Combustion 2000
Phase II

Volume I of II

DE-AC22-95PC95144

Final Technical Report

June 20, 1995 – March 31, 2001

Prepared for

National Energy Technology Laboratory
Pittsburgh, Pennsylvania

United Technologies Research Center
411 Silver Lane, East Hartford, Connecticut 06108

Acknowledgement

This program was carried out under DOE contract DE-AC22-95PC95144, the Engineering Development of Coal-Fired High Performance Power Systems (HIPPS). The contract was supervised by the National Energy Technology Laboratory (NETL) as represented by Arun Bose, Larry Ruth and Andy Karish.

The work of the program and its success was the result of a concerted team effort consisting of:

Alstom (formerly ABB/Combustion Engineering) - A. Levasseur and S. Goodstine

Nexant (a Bechtel Company) - J. Ruby and M. Nawaz

PSI - C. Senior

KWS - F. Robson, S. Lehman and W. Blecher

FluorDaniel - W. Fugard and A. Rao

University of Utah and Reaction Engineering International - A. Sarofim, P. Smith, D. Pershing, E. Eddings and M. Cremer

UND/EERC - J. Hurley, G. Weber, M. Jones, M. Collings, D. Hajicek, A. Henderson and P. Klevan

UTRC - D. Seery, B. Knight, R. Lessard, J. Sangiovanni, A. Dennis, C. Bird, W. Sutton, N. Bornstein, F. Cogswell, C. Randino and S. Gale.

All of the above should be considered as co-authors of this report.

Several additional contributors were involved in the Phase I study that immediately preceded this work. In particular, a special recognition should be made for the contributions of the late Mike Heap, whose insights were so important in the early stages of this program. His energy and enthusiasm will be missed.

Executive Summary

This report is a presentation of work carried out on Phase II of the HIPPS program under DOE contract DE-AC22-95PC95144 from June 1995 to March 2001. The objective of this report is to emphasize the results and achievements of the program and not to archive every detail of the past six years of effort. These details are already available in the twenty-two quarterly reports previously submitted to DOE and in the final report from Phase I. The report is divided into three major foci, indicative of the three operational groupings of the program as it evolved, was restructured, or overtaken by events. In each of these areas, the results exceeded DOE goals and expectations.

HIPPS Systems and Cycles (including thermodynamic cycles, power cycle alternatives, baseline plant costs and new opportunities)

HITAF Components and Designs (including design of heat exchangers, materials, ash management and combustor design)

Testing Program for Radiative and Convective Air Heaters (including the design and construction of the test furnace and the results of the tests)

There are several topics that were part of the original program but whose importance was diminished when the contract was significantly modified. The elimination of the subsystem testing and the Phase III demonstration lessened the relevance of subtasks related to these efforts. For example, the cross flow mixing study, the CFD modeling of the convective air heater and the power island analysis are important to a commercial plant design but not to the R&D product contained in this report. These topics are of course, discussed in the quarterly reports under this contract.

The DOE goal for the High Performance Power Plant System (HIPPS) is high thermodynamic efficiency and significantly reduced emissions. Specifically, the goal is a 300 MWe plant with > 47% (HHV) overall efficiency and ≤ 0.1 NSPS emissions. This plant must fire at least 65% coal with the balance being made up by a premium fuel such as natural gas.

To achieve these objectives requires a change from complete reliance of coal-fired systems on steam turbines (Rankine cycles) and moving forward to a combined cycle utilizing gas turbines (Brayton cycles) which offer the possibility of significantly greater efficiency. This is because gas turbine cycles operate at temperatures well beyond current steam cycles, allowing the working fluid (air) temperature to more closely approach that of the major energy source, the combustion of coal. In fact, a good figure of merit for a HIPPS design is just how much of the enthalpy from coal combustion is used by the gas turbine.

The efficiency of a power cycle varies directly with the temperature of the working fluid and for contemporary gas turbines the optimal turbine inlet temperature is in the range of 2300-2500 °F (1260-1371 °C). These temperatures are beyond the working range of currently available alloys and are also in the range of the ash fusion temperature of most coals. These two sets of physical properties combine to produce the major engineering challenges for a HIPPS design.

The UTRC team developed a design hierarchy to impose more rigor in our approach. Once the size of the plant had been determined by the choice of gas turbine and the matching steam turbine, the design process of the High Temperature Advanced Furnace (HITAF) moved ineluctably to a down-fired, slagging configuration. This design was based on two air heaters: one a high temperature slagging Radiative Air Heater (RAH) and a lower temperature, dry ash Convective Air Heater (CAH). The specific details of the air heaters are arrived at by an iterative sequence in the following order:

- Starting from the overall Cycle requirements which set the limits for the combustion and heat transfer analysis
- The available enthalpy determined the range of materials, ceramics or alloys, which could tolerate the temperatures
- Structural Analysis of the designs proved to be the major limitation
- Finally the commercialization issues of fabrication and reliability, availability and maintenance.

The program that has sought to develop and implement these HIPPS designs is outlined below.

Power Cycle Analyses

During Phase I of the HIPPS program, a nominal 300 MW HIPPS Commercial Plant Design (CPD) was developed. This plant used essentially off-the-shelf technology in all of its components with the exception of the High Temperature Advanced Furnace (HITAF). The CPD met all of the Phase I DOE goals for performance (47% HHV), emissions (one-fourth of NSPS) and cost (COE no more than 90% of a comparable PC plant).

In Phase II, the CPD was updated to meet more stringent emission standards, now one-tenth NSPS, and some changes to the configuration were made for reasons of operability; e.g., the gas turbine exhaust was no longer split into two streams. Rather, all the exhaust was sent to a HRSG and an air preheater was used to preheat combustion air. This change resulted in elimination of a historically troublesome diverter valve in the exhaust and also allowed a slight gain in performance to 47.4%. The HIPPS approach defined by the CPD, which has a fuel diversity capability, lends itself to the use of advanced technology. Thus, during Phase II, a number of power cycle alternatives were investigated.

Higher performance gas turbines such as intercooled aeroderivative (ICAD) types were identified as having performance advantages over frame engines operating at the same turbine conditions. The ICAD engine was used with both the existing steam system and advanced steam systems having technology demonstrated in another DOE-sponsored program on advanced steam systems. An advanced HIPPS/ICAD with a 6200 psi/1300 °F (42,750 kPa/705 °C) steam topping turbine had an estimated performance of 53% (HHV) using a 55/45 coal /gas fuel split.

The ICAD also lends itself to use in an advanced gas turbine cycle called the Humid Air turbine (HAT) cycle. In this cycle, low-grade heat from the gas turbine is used to saturate the compressor discharge air, which is subsequently recuperated against the turbine exhaust. Both the efficiency and the power output are significantly increased. A variety of HIPPS/HAT

configurations were investigated. When the coal/gas ratio was decreased to approximately 62/38, and the HITAF radiator outlet temperature increased to 2000 °F (1093 °C), HIPPS/HAT efficiencies of over 54% (HHV) were projected.

These advanced technology approaches were used in an investigation of repowering older steam stations. Aging PC plants with efficiencies of 32-35% could be repowered with HIPPS/ICAD resulting in increased output and increased efficiencies usually in the 45-50% range, depending on the steam conditions of the repowered plant. The HIPPS/HAT could also be used, but this approach is not as attractive in the repowering applications because use of the existing steam turbine and boiler, while having capital cost advantages, reduce overall efficiency. Economic analyses indicate that the cost of repowering appears to be competitive with the more normal approach of using natural gas fueled gas turbines.

A major goal of Combustion 2000 was the identification of an "all coal" plant. Again, a variety of HIPPS configurations were considered. When HITAF radiator outlet temperatures were limited to the 1700 °F (927 °C) level, all coal HIPPS had efficiencies in the 41-43% (HHV) range. When advanced materials are used for the radiator and temperatures are allowed to reach 2000 °F (1093 °C), efficiencies of 44-45% are projected. When HIPPS/HAT configurations are identified, efficiencies over 48% are estimated. These estimates are made for systems with no natural gas used to further heat the radiator outlet. If even a small amount of gas is used, say 5%, the performance would increase to over 50%.

The investigation into the all coal HIPPS lead to the modular HIPPS Today concept. HIPPS Today would use only the convective heater in the HITAF, thereby reducing the technical risk and the cost of the system. System performance would be limited to that of gas turbines with operating inlet temperatures of < 1600 °F (871 °C) for current heater materials to 1800 °F (982 °C) for advanced material convection heat exchangers. There are a number of small (< 25 MW) gas turbines that have these conditions including several aeroderivative types. By using the aeroderivative engines, a modular approach can be defined. In this approach, the turbine and the remainder of the components are designed for factory assembly and shipment as modules. Assembly-line plants of nominally 100 MW size would be designed in "cookie cutter" fashion thereby reducing production costs and subsequent erection costs. These plants would have performances of 40-44% (HHV) on all coal or, potentially, coal/biomass mixtures. Costs would be reduced by about 10% over the more traditional approach. Because of the relative simplicity and reduced maintenance, these plants could be candidates for use in developing economies where they would use indigenous fuels. Because of their higher efficiency compared to plants typical in these areas, overall fuel use could be reduced, as would the emissions of CO_2.

HIPPS can be a technology for use in the DOE's Vision 21 program. The major goal of this program is the generation of power at least 60% (HHV) using coal or 75% (LHV) using gas. Emissions are to be essentially zero, including Greenhouse gases. One of the methods of potentially reaching these goals is by using a hybrid cycle. The hybrid combines a thermodynamic cycle, e.g., a Brayton cycle, with an electrochemical cycle such as a high temperature fuel cell. In the HIPPS/Hybrid, the compressor discharge air is heated in the HITAF to 1800 °F (982 °C) and then goes to a Solid Oxide Fuel Cell (SOFC) where it is reacted with H_2 from a steam/natural gas reformer. The effluent from the SOFC is at approximately 1850 °F (1010 °C) and contains some unreacted H_2 and CH_4. When burned, temperatures to perhaps 2100 °F (1149 °C) are possible. When additional gas is added, the temperature can be raised to

the level typical of modern gas turbines. These systems consumed significant fractions of natural gas. At a 40/60 coal/gas ratio, the efficiency is over 61% (HHV of coal plus gas mixture). As the coal/gas ratio increases, the efficiency decreases; 55% at 50/50 and 51% at 60/40. This is because the SOFC participation decreases since SOFC fraction is a direct function of the natural gas flow.

The HIPPS approach, from the CPD to Vision 21, offers the highest power plant efficiencies of any coal-based design. Coal gasification, even when used with the "H" class frame machines, identified in the DOE Advanced Turbine System program, reaches efficiencies in the mid-40%'s.

HITAF Components and Design

Modeling

One of the first steps after generating a basic HITAF configuration was to determine if the design could be translated into a practical commercial plant. In addition to the cycle analysis, previously mentioned, there is always the need to model the detailed combustion process and the related questions of slag flow, NO_x formation and carbon burnout. Although the program was restructured to eliminate the larger scale testing and the Phase III demonstration, the modeling study continued for the insights it provides on the HIPPS process and with the hope that a future HIPPS program could take advantage of the work. This effort is discussed in Section 6.

The improved models developed as part of this contract have been incorporated, together with developments in parallel programs, into the codes used by Reaction Engineering International to simulate boilers for the electrical utility industry. These codes have been successful in simulating actual performance in practical power plant combustors. In particular, they have been able to simulate alternative low NO_x control technologies, including low-NO_x burners, the use of closely coupled and separated over-fire air ports, and the optimum positions for introducing reagents for SNCR. This success has led the industry to accept simulations as an important element in retrofitting boilers.

An example of the success of these tools is a program for a consortium of electrical generation utilities, organized by the Electric Power Research Institute (EPRI), which predicted effects of operating a cyclone-fired boiler under low-NO_x firing conditions. Under baseline conditions, the cyclone barrels are operated fuel lean, whereas under staged conditions, the cyclone barrels are operated fuel-rich and the make-up combustion air is added through over-fire air ports. The REI model was applied to guide the placement of the over-fire air ports and the impact of different degrees of staging. Excellent agreement was obtained between predictions and measurements of NO_x, made after implementation of the optimized designs for several units. The use of such tools has resulted in 80 percent of all cyclone fired furnaces being retrofitted with overfire air ports. The success in the simulation of cyclone barrels is particularly relevant to the future designs of a HITAF, since it has been shown that the cyclones provide a means to rapidly obtain the high fluxes required for the radiant air heaters. Traditionally cyclones have been viewed as being high emitters of NO_x. The REI simulations and the implementation of the staged combustion in the field show that this is not necessarily the case. Indeed, the high residence time at high temperatures that would be involved in a HITAF, in combination with staging, could result in very low NO_x levels, even prior to downstream reagent injection.

Air Heater Designs and Test Modules

The rationale for the selection of heat exchanger concepts and the design of test modules is presented in Section 7. The approach to transferring heat from coal combustion products to high pressure air for driving the gas turbine is determined primarily by the types of mineral deposits and the associated temperature regimes of the hot combustion gas. Depending on the temperature of coal combustion products, there are two general types of deposits, molten or liquid slag at high temperatures and dry ash at low temperatures, with varying amounts of the two types of deposits present at intermediate temperatures. For most coals, the distinction between the two types of mineral deposits can be controlled by regulating the temperature of the combustion gas stream within two fairly broad temperature regimes. Specifically, liquid slag is predominant at high temperatures above about 2200 to 2600 °F (1204 to 1427 °C) and dry ash prevails at lower temperatures below about 1800 °F (982 °C). Therefore, heat exchanger concepts and materials of construction will be chosen so as to be compatible with the types of mineral deposits present in the combustion gas stream, the corrosive nature and mechanisms of the prevailing type of deposit, the temperature regime, and the optimum modes of heat transfer available. In general, the RAH is best suited for the high temperature molten slag regime while the CAH is appropriate for the lower temperature regime with dry ash.

After a series of unsuccessful designs, the alloy-based "tubes-in-a-box" with ceramic tile protection emerged as the prime candidate.

In order to validate the air heater designs, the program called for extensive small scale testing of prototype components. To this end RAH and CAH test modules were designed and fabricated for tests at conditions that simulate actual conditions in a utility combustor. The RAH panel is a scaled version of the commercial design but using only three tubes in the heat exchanger. The CAH test module is a straightforward scaled version of the tube and shell heat exchanger in the commercial design.

The design, heat transfer analysis and structural analysis are presented in Section 7.

Air Heater Materials

Materials are the key enabling technology for successful operation and commercialization of the HIPPS system. The use of high temperature heat exchangers in a coal combustion environment, coupled with the cost constraints, make proper materials selection a considerable challenge. Nonetheless, utilization of state-of-the-art materials and joining methods, as well as advanced oxidation and corrosion resistant coatings, can yield reasonable compromises.

The choice of materials for the RAH panel was inescapable. Once the alloy/refractory "tubes-in-a-box" design was selected, the choice became inevitable. For alloys, only the oxide dispersion strengthened (ODS) materials have the required high temperature strength for the design. The Inco MA754 was chosen for its availability and our expectation that we could develop a welding technique for it. The material for the refractory tiles which protect the alloy tubes was determined to be a fusion cast alumina based on the Phase I testing. The RAH must tolerate running coal slag on it's surface, while providing protection and reasonable heat transfer to the working fluid (air) contained in the alloy tubes. After consultation with several vendors, the Monofrax M was the first choice for testing, based on availability, corrosion resistance and thermal properties.

Beyond the testing of the RAH panel with MA754 tubes and Monofrax M tiles for protection, there was a continuing search for lower cost alternatives. An obvious target was to find a cheaper material than the nickel based MA754. An alternative ODS material is the MA956 ferritic alloy which we have tested for coal ash corrosion and found it very promising. In addition we have developed a TLP welding technique for joining this material, which offers the potential of significant cost reduction.

The fusion cast alumina Monofrax M has performed very well, however, improved corrosion resistance and reduced machining are obvious improvements needed for a practical design. At our request, the Kyocera Industrial Ceramics Corp. has fabricated a high chrome alumina that can be cast in "near net shape". This material has shown excellent corrosion resistance in early testing, but its thermal shock properties are poor, probably because of the narrow size distribution of the initial particles. A wider distribution of the particle sizes of the original material should greatly improve its thermal shock resistance. The potential for a tile material that resists corrosion and does not require machining could provide a major cost reduction in a commercial HIPPS plant.

The discussion of the materials evaluation is contained in Section 8.

Ash Management

The ash management aspects of our HIPPS design are complicated by the desire to be compatible with a wide range of US coals typical of current power plant usage. To be generally useful in the US market it was felt that the design should accommodate the full range of bituminous coals not just the Illinois #6 design coal. Our final design is in fact applicable to any solid fuel.

The wide range of coals also means a wide variation in the ash produced in the HITAF. For the high temperature regime the ash will be molten and free flowing. For the design coal, the slag layer will be only about 1mm thick on the furnace walls and the RAH tiles. In the HITAF, about half of the ash will be collected by the slag tap as runoff from the walls and the slag screen. Any ash particles that get past the slag screen will either deposit on the CAH tubes or be collected in the baghouse. All of this collected flyash will then be recycled into the fuel inlet so that all of the ash removed from the HITAF will have passed through the slag tap. This vitrified ash is a commercially viable product and therefore the ash disposal problem is resolved.

Initial sootblowing studies of the dry ash deposits on the CAH tubes indicate that these deposits can be readily removed and collected. A full discussion of the ash management part of the program is given in Section 9.

Duct Heater

The design of the HIPPS cycle has assumed that materials limitations would require a boost heater to raise the RAH exhaust temperature to an appropriate inlet temperature. The state-of the-art gas turbines in the baseline cycle have turbine inlet temperatures around 2500 °F (1371 °C), well above the working temperature of available RAH containment materials. In the DOE requirements for the program 65% of the fuel input must be coal and 35% can be a premium fuel such as natural gas. The baseline UTRC HIPPS design, natural gas is used to boost the air temperature from 1700 °F to 2500 °F. The technical challenge is to mix the fuel (natural gas) with the high temperature air rapidly enough to avoid forming NO_x.

The hot air stream must be mixed with the fuel gas to form a very lean (stoichiometry < 0.2) mixture in a time that is shorter than the NO_x formation time. In our designs, the centrifugal mixing approach was chosen to achieve this goal. Based on some experiments and detailed chemical kinetic calculations the UTRC duct heater design can mix rapidly enough to avoid significant chemical reaction at near stoichiometric conditions. The experimental studies on the duct heater mixing were ultimately truncated because of the program restructuring.

The discussion of the Duct Heater effort is presented in Section 10

Component Testing Program

Pilot Scale Furnace

The testing of the individual air heater components were carried out with scale model test modules in a specially constructed furnace at UND/EERC. The pilot-scale slagging furnace system (SFS) consists of eight main components: 1) slagging furnace, 2) slag screen/slag tap, 3) dilution-quench zone, 4) process air preheaters, 5) convective air heater (CAH) section, 6) radiant air heater (RAH) panel, 7) tube-and-shell heat exchangers, and 8) pulse-jet baghouse.

The design and fabrication of the pilot-scale slagging furnace and the performance of the CAH test module, and RAH panel are presented in Section 11.

The pilot-scale slagging furnace design is intended to be as fuel-flexible as possible, with maximum furnace exit temperatures of 2700 to 2900 °F (1482 to 1593 °C) to maintain the desired heat transfer to the RAH panel and slag flow. The furnace has a nominal firing rate of 2.5 MMBtu/h (2.65 x 10^6 kJ/hr) and a range of 2.0 to 3.0 MMBtu/h (2.12 x 10^6 to 3.18 x 10^6 kJ/hr) using a single burner. The furnace design was based on Illinois No. 6 bituminous coal (11,100 Btu/lb, 26,018 kJ/kg) and a nominal furnace residence time of 3.5 sec. Flue gas flow rates range from roughly 425 to 645 scfm (12.0 to 18.3 m^3/min), with a nominal value of 535 scfm (15.1 m^3/min), based on 20% excess air. Firing a subbituminous coal or lignite increases the flue gas volume, decreasing residence time to roughly 2.6 sec. However, the high volatility of low-rank fuels results in high combustion efficiency (> 99%).

RAH and CAH testing results

The RAH and CAH have been tested in the SFS for more than 2000 hrs while firing natural gas and for more than 1500 hrs firing coal and lignite. The heat transfer from both test modules was very close to the design estimates for the CAH and RAH. The implication of this is that our cycle anlaysis is realistic and that thermal efficiencies equal to or greater than 50% are achievable with our HIPPS design.

The test modules held up structurally with no apparent deterioration except slag corrosion of the protective tiles. The thermal expansion was accommodated by the design and the horizontal and vertical seams did not bind up with hardened slag. The corrosion rate of the tiles (especially the high chrome tiles) was acceptable for most coals. The damage to the tiles came mostly from thermal cycling which induced cracks. The ceramic manufacturers believe this is a correctable flaw, and that with a blending of different particle size distributions in the initial material there would be a significant improvement in thermal shock resistance.

HIPPS Achievements

- Accomplished or exceeded all C2000 contractural performance goals; i.e. eff. > 47% HHV, 1/10 NSPS, when ready for deployment, the UTRC HIPPS concept would achieve efficiencies exceeding 47% HHV, 1/10 NSPS, at a competitive COE
- Assembled an outstanding team in all the specialty technologies
- Designed and tested a high temperature air heater, which is an enabling technology goal of the Vision 21 Program
- Demonstrated RAH and CAH that match heat transfer requirements for 55% eff. (HHV) cycles within materials and COE envelope
- Tested air heaters for ~1500 hrs for three coals and exit temperatures 1700 - 2000 °F (1093 °C)
- Identified repowering designs compatible with market desire to increase efficiency from 30% to 44% at competitive COE
- Identified options for Vision 21(e.g., very high temperature heat exchanger designs, coal-based hybrid SOFC cycles, cofiring of biomass and opportunity fuels etc.)
- The UTRC HIPPS concept design is compatible with CO_2 mitigation strategies and fuel cell combinations

Table of Contents - Vol I

Table of Contents - Vol I (Continued)

List of Exhibits-Vol I

List of Tables-Vol I

Section 1 - HIPPS Program

Abstract

This section presents work carried out under Task 1.3 of contract DE-AC22-95PC95144 "Engineering Development of Coal-Fired High Performance Systems Phase II and III." The goals of the program were to develop a coal-fired high-performance power generation system (HIPPS) that is capable of:

thermal efficiency (HHV) ≥ 47%

NOx, SOx, and particulates ≤ 10% NSPS
(New Source Performance Standard)

coal providing ≥ 65% of heat input

all solid wastes benign

cost of electricity ≤ 90% of present plants

During Phase I of the HIPPS program, a nominal 300 MW HIPPS Commercial Plant Design (CPD) was developed. This plant used essentially off-the-shelf technology in all of its components with the exception of the High Temperature Advanced Furnace (HITAF). The CPD met all of the Phase I DOE goals for performance (47% HHV), emissions (one-fourth of NSPS) and cost (COE no more than 90% of a comparable PC plant).

In Phase II, the CPD was updated to meet more stringent emission standards, now one-tenth NSPS, and some changes to the configuration were made for reasons of operability; e.g., the gas turbine exhaust was no longer split into two streams. Rather, all the exhaust was sent to a HRSG and an air preheater was used to preheat combustion air. This change resulted in elimination of a historically troublesome diverter valve in the exhaust and also allowed a slight gain in performance to 47.4%. The HIPPS approach defined by the CPD, which has a fuel diversity capability, lends itself to the use of advanced technology. Thus, during Phase II, a number of power cycle alternatives were investigated.

Higher performance gas turbines such as intercooled aeroderivative (ICAD) types were identified as having performance advantages over frame engines operating at the same turbine conditions. The ICAD engine was used with both the existing steam system and advanced steam systems having technology demonstrated in another DOE-sponsored program on advanced steam systems. An advanced HIPPS/ICAD with a 6200 psi/1300 °F (42,750 kPa/705 °C) steam topping turbine had an estimated performance of 53 % (HHV) using a 55/45 coal /gas fuel split.

The ICAD also lends itself to use in an advanced gas turbine cycle called the Humid Air turbine (HAT) cycle. In this cycle, low-grade heat from the gas turbine is used to saturate the compressor discharge air, which is subsequently recuperated against the turbine exhaust. Both the efficiency and the power output are significantly increased. A variety of HIPPS/HAT configurations were investigated. When the coal/gas ratio was decreased to approximately 62/38, and the HITAF radiator outlet temperature increased to 2000 °F (1093 °C), HIPPS/HAT efficiencies of over 54% (HHV) were projected.

Introduction

There is a growing need for additional electric power generating capacity. For the present and short term needs, gas turbine combined cycle plants will provide the major source of this capacity. However, several projections indicate that the rising cost of natural gas will present opportunities for additional coal-based capacity. It is clear that, whether this additional capacity is in a Greenfield plant or a repowered plant, the final configuration will have to operate at a higher thermal efficiency and with greatly reduced pollutant emissions.

The Department of Energy (DOE) has recognized that this need to improve the overall efficiency of coal-burning plants while decreasing their environmental burden can only be achieved using Brayton Cycles (gas turbines) rather than Rankine Cycles (steam turbines). To reach their goals, the National Energy Technology Laboratory (NETL) has initiated a research program for the High Performance Power Generating System (HIPPS) which utilizes gas turbines but excludes all coal combustion products from the working fluid. This exclusion avoids the expense of hot gas cleanup and/or the corrosion of turbine blades by coal ash.

Because the gas turbine working fluid (air) is heated indirectly, the highest air temperature that can be reached by coal combustion is limited by heat exchanger materials and will fall short of the ideal turbine inlet temperature for highest efficiency. To achieve the desired turbine inlet temperature (approximately 2500 °F or 1371 °C) the program allows for up to 35% use of a premium fuel (e.g., natural gas or no. 2 heating oil) in a topping cycle. The design is still required to have a growth path to all coal as improvements in materials allow for a high temperature, corrosion-resistant heat exchanger. For the near term (< 5 years) it is unlikely that there will be a structural ceramic available that can withstand molten coal ash at temperature >2700 °F (1482 °C) for long times (10,000 hours). Therefore today's designs must be based on materials available now and accept temporary limitations on the maximum air temperature.

The program as originally devised by DOE had three phases:

Phase I - Concept Definition and Preliminary R&D, begun in 1992;

Phase II - Engineering Development and Testing, which started in 1995; and,

Phase III - Prototype High Performance Power Plant, which was canceled.

For Phase II the HIPPS designs are required to meet or exceed the goals listed in Table 1-1.

Table 1-1
DOE Goals for HIPPS Program

	Phase I	Phase II	NSPS
Pollutant Emissions			
NO_X (lbs NO_2/MBtu fuel)	0.15	0.06	0.6
SO_X (lbs SO_2/MBtu fuel)	0.15	0.06	0.6
Particulates (lbs/MBtu fuel)	0.0075	0.003	0.03
Thermal efficiency (HHV) > 47%			
All solid wastes benign			
Coal must be > 65% total fuel (and path to 95% coal)			
COE < 90% present cost for NSPS plant			

There are several topics that were part of the original program but whose importance was diminished when the contract was significantly modified. The elimination of the subsystem testing and the Phase III demonstration lessened the relevance of subtasks related to these efforts. For example, the cross flow mixing study, the CFD modeling of the convective air heater and the power island analysis are important to a commercial plant design but not to the R&D product contained in this report. These topics are of course, discussed in the quarterly reports under this contract.

The following sections deal with the overall HIPPS system starting with the updated version of the HIPPS Commercial Plant Design described in the Phase 1 Final Report (Seery, et al, 1995). The technology of the commercial plant was based on off-the-shelf components with the exception of the radiant air heater (RAH) and convective air heater (CAH) portions of the High Temperature Advanced Furnace (HITAF). Advanced versions of HIPPS were investigated using more aggressive gas turbine and steam turbine conditions to achieve efficiencies of 50% or more. The basic HIPPS configuration was also changed to accommodate more advanced cycles. Again, the efficiencies were increased to values approaching 58% (HHV) using turbine technology that would appear in the early 21st century.

To broaden the potential market penetration of the HIPPS beyond new Greenfield plants, investigations were made of repowering older steam stations using the HIPPS technology. It was found that older plants having efficiencies of 30-35% could be repowered and achieve efficiencies of 42-47%, while retaining much of the original plant equipment.

The HIPPS Commercial Plant design concept uses approximately 35% natural gas to boost the air temperature from the RAH to levels typical of modern gas turbines. The ultimate goal of the DOE HIPPS program is to use only coal. Several all-coal design concepts were investigated and, when based on advanced RAH designs and materials, efficiencies over 50% could be identified.

The all-coal approach was also used in the HIPPS Today configuration. In HIPPS Today, the high technical risk RAH was eliminated and only the CAH was used. This limited temperatures

of the heated air to values between 1550 and 1800 °F (816 and 982 °C), but configurations having efficiencies of 43-44% were identified. This value is some 25% greater than pulverized coal (pc) steam stations using similar technology.

An additional application of the HIPPS technology has recently emerged. The DOE has initiated an ambitious program aimed at ultra high efficiency, near zero emission power plants for use in the early 21st century. Called Vision 21, the program has as a goal, coal-based power system efficiencies of 60% (HHV) and gas-based power systems efficiencies of 75% (LHV). The HIPPS concept was used as a basis of hybrid power systems having solid oxide fuel cells (SOFC), gas turbines, and steam turbines. Efficiencies approaching 60% (HHV) were identified in systems having 50% coal energy input.

HIPPS Commercial Plant Design

Introduction

The basic plant layout and configuration remains much as described in the Phase 1 Report (Seery, et al., 1995). Only two changes of note were made. The first was the elimination of the gas turbine exhaust as a source of combustion air for the HITAF. This was done mainly to improve plant reliability by negating the need for a costly and historically unreliable diverter valve in the GT exhaust. The combustion air is now supplied in the more conventional manner by fans and an air preheater. The second was the addition of a selective catalytic reactor (SCR) for NO_x control. The SCR was added for further NO_x control and reduction of ammonia slip from the SCNR.

The initial design was developed based on a thermodynamic optimization study of a combined cycle 300 MW plant using a conventional frame type gas turbine and a commercially available steam turbine. At least 65% of the fuel is coal and the working fluid is heated using both radiative and convective air heaters. As a result of continuous analysis and cycle improvement, the designs for the commercial operating plant evolved to include a modern intercooled aeroderivative gas turbine, a convective air heater constructed of ferritic alloy and a radiative air heater. It was determined that the radiative air heater (RAH) can be constructed from Ni-based alloy as long as it is protected by a ceramic refractory coating.

The three major elements of the system are the High Temperature Air Furnace (HITAF), the gas turbine, and the steam turbine. The HITAF supplies 55% of the temperature rise required by the gas turbines, bringing the compressor discharge air to 1700 °F (927 °C). The air then goes to a duct burner where natural gas combustion boosts the temperature to that required by the turbine. The turbine exhaust stream, along with that from the HITAF, furnishes waste heat to a heat recovery steam generator (HRSG) and steam turbine. The overall efficiency of this system exceeds 47%, significantly better than typical pc plants.

A simplified schematic of the HIPPS is shown in Exhibit 1-1. There, it can be seen that the compressor discharge air is sent to a convective air heater in the HITAF exit stream. From there, it goes to a radiant heater located in the highest temperature portion of the HITAF and then to the duct heater where the temperature is raised to the required combustor exit level. In this schematic, unlike the final HIPPS configuration, the exhaust from the gas turbine is split; one portion is sent to a “clean” HRSG while the remainder is used as preheated combustion air for

the coal (Illinois No. 6) in the HITAF. The exhaust from the HITAF is sent to a "dirty" HRSG, baghouse, and FGD. To maintain the temperature required for a selective non-catalytic converter in the HITAF, as well as assure that the temperature for the convective section does not exceed 1800 °F (982 °C), a portion of the HITAF exhaust is recirculated. The steam bottoming system is atypical of currently installed combined cycles, with higher operating conditions of 2400 psi/1000 °F /1000 °F (16547 kPa/538 °C /538 °C) made possible by the HITAF exhaust temperature level.

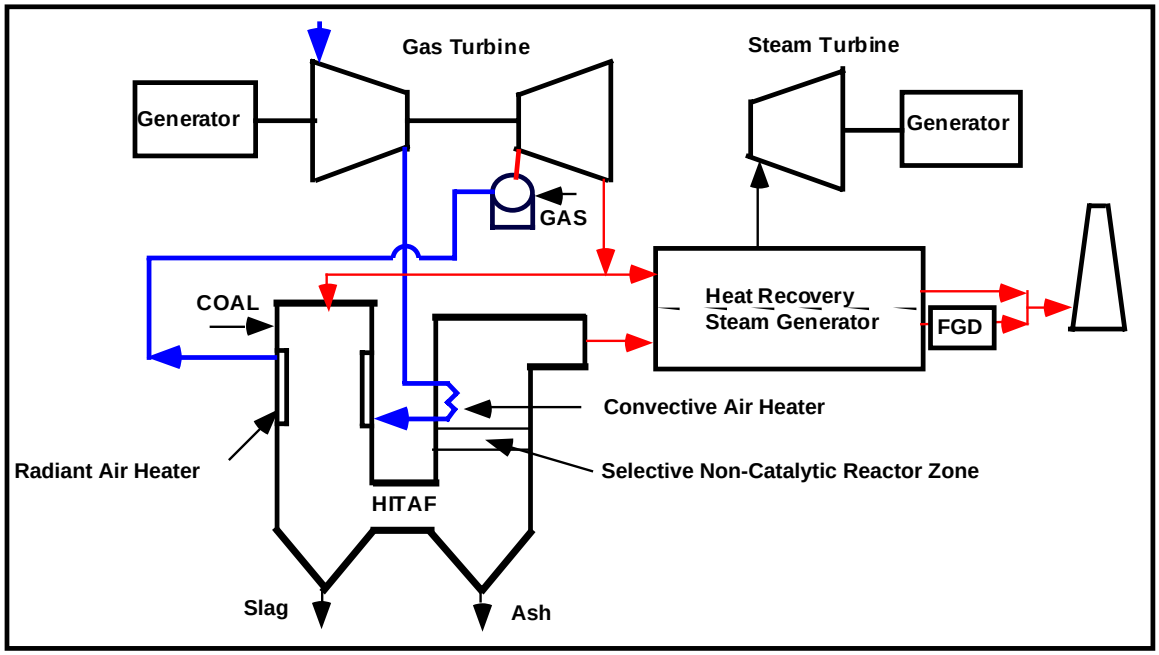

Exhibit 1-1
Simplified HIPPS

The plant design scope is a non site-specific, Greenfield power generation plant and includes all facilities required for power production. Consistent with the June, 1993 EPRI TAG , the HIPPS plant boundaries for design and cost estimates include all the major operating systems, such as:

- the HITAF unit,
- heat recovery steam generators,
- gas turbine,
- environmental control equipment,
- auxiliary equipment, and
- all support facilities needed to operate the plant (shops, offices, cafeteria, fuel handling and storage equipment, water intake structures, and waste treatment facilities).

The plant includes the high voltage buss of the generator step-up transformer, but not the switchyard and transmission lines. The switchyard and lines are generally influenced by transmission system specific conditions and hence are not included with the cost or design.

Balance of Plant

The nominal generating capacity of the HIPPS plant is 300 MWe. The plant is planned for a baseloaded duty cycle with limited cycling capability.

The conceptual engineering concentrated on the balance of plant and other items supporting the HITAF and the GT. Process data for HITAF and the GT were developed as part of the in initial HIPPS Commercial Plant Design efforts. In many areas, technical and economic criteria prepared for the study use the EPRI TAG™, Volume 1: Rev. 7; June 1993 as a basis.

Accompanying the following discussion are several appendices containing individual topical studies. The appendices are:

- Appendix A: Major Equipment List, HIPPS Commercial Plant Conceptual Design
- Appendix B: An Emissions Control Technology Screening, which documents the selection of control systems for the HIPPS plant.
- Appendix C: An examination of Makeup Water Treatment Systems which apply to the HIPPS plant.
- Appendix D: The Coal Pulverization System for HIPPS was examined and documented to define the impact of coal quality (moisture and Btu content) on plant performance and to evaluate the need for coal drying prior to combustion.
- Appendix E: A Market Study for application of the HIPPS technology in the U.S. was completed to examine the timing and options for commercial use.
- Appendix F: CO_2 Separation Technologies were evaluated for use with the HIPPS conceptual plant and as part of a potential CO_2 sequestration requirement.
- Appendix G: An assessment of Enriched Oxygen Combustion Gas Turbine Cycles
- Appendix H: An examination of Plant Operations and HITAF Control Systems

Site Location and Conditions

Except as noted in later parts of the report, the design calculations, plant location and site conditions are taken from the EPRI TAG™, and are as follows:

Site related

- Plant site — Central USA[1]
- Site elevation (above mean sea level) — 600 feet
- Seismic zone — 0 (UCB)[2]
- Water transportation — Lake Michigan
- Water makeup source[3] — Lake Michigan
- Electric power source for startup — Grid
- Fuel Storage Capacity — 40 Days (live and long term)[4]
- Unit train coal delivery with rotary dump cars

1. EPRI identified region: E/W Central US (Kenosha, WI)
2. Uniform Building Code.
3. Representative analysis is shown in Table 1-2.

Reduced from the EPRI TAG™ capacity is 60 days at 100%

Meteorological

- Average annual conditions
  - dry bulb temperature 60 °F (16 °C)
  - wet bulb temperature 52 °F (11 °C)
  - atmospheric pressure 14.4 psi (99.3 kPa)
  - rainfall 31 inch/yr (78.8 cm/yr)
- Other meteorological data
  - max. dry bulb temperature 95 °F (35 °C)
  - max. wet bulb temperature 75 °F (24 °C)
  - minimum temperature for performance 20 °F (-7 °C)
  - minimum temperature for freeze protection -20 °F (-29 °C)

Table 1-2
Representative Water Analysis

	mg/l	mg/l as $CaCO_3$
Silica (SiO_2)	6.8	--
Calcium (Ca)	76.0	89.0
Magnesium (Mg)	16.0	68.0
Sodium (Na)	20.0	44.0
Potassium (K)	2.9	3.7
Bicarbonate (HCO_3)	246.0	202.0
Sulfate (SO_4)	56.0	58.0
Chloride (Cl)	26.0	37.0
Nitrate (NO_3)	6.9	5.6
Total dissolved solids	457.0	
Total hardness	255.0	
pH	8.0	
Temperature range	40 - 80 °F	

Plant Performance Criteria

The following are the major criteria specified for the design and cost assessments.

- Service conditions: The plant was to be designed for baseload operation. However, in recent years an important market aspect has surfaced in the power generation business. Load profiles are increasingly indicating a need for flexible plant operations, and for new plant designs that account for daily output requirement swings. Thus, a minimum turndown of 50% and operational flexibility are very desirable features.
- Plant design life: The plant is designed for a nominal life of 30 years.
- Target efficiency: The net efficiency of the reference commercial plant was designed to be 47 percent or higher maximum heat rate 7,260 Btu/kWh, (7,660 kJ/kWh) HHV, at ISO conditions.

- Environmental criteria: Environmental limits are shown in Table 1-3 for the conceptual design and for comparison to the new source performance standards.
- Design basis fuel: The plant burns Illinois No. 6 bituminous coal as the primary fuel. Coal is burned to supply 65 percent or more of the total heat input to the HIPPS system. Properties of the design coal are listed in Table 1-4.

Table 1-3
Summary of Environmental Performance Requirements

	New Source Performance	Phase II
Sulfur Oxides (lb/MMBtu)	0.40*	0.06
Nitrogen Oxides (lb/MMBtu)	0.50	0.06
Particulate (lb/MMBtu)	0.03	0.003
Solid Wastes	Benign	Benign

** Based on 90% reduction of the total sulfur in the fuel with the design coal (5.98 pounds of SO_2 per MMBtu; or 2.57 kg of SO_2 per million kJ) and a 65/35 ratio of coal and natural gas.*
Liquid discharges are treated to meet NSPS requirements.

Solid wastes (ash and FGD sludges) are to be stabilized and shipped for off site disposal.

Table 1-4
Design Coal Properties

(Illinois No. 6 Bituminous Coal from 1993 EPRI TAG™)

Proximate analysis		**Average**
Higher heating value (Btu/lb)		10,982
Sulfur %wt		3.28
SO_2/MMBtu		5.98
Grindability index (Hardgrove)		51
		% wt
Moisture		12.25
Ash		10.97
Fixed carbon		41.48
Volatile matter		35.30
	TOTAL	100.00
Ultimate analysis (%wt)		
Moisture		12.25
Carbon		61.00
Hydrogen		4.25
Nitrogen		1.25
Chlorine		0.07
Sulfur		3.28
Ash		10.97
Oxygen		6.93
	TOTAL	100.00
Ash analysis (%wt)		
SiO_2		50.66
Al_2O_3		19.00
TiO_2		0.83
Fe_2O_3		20.30
CaO		2.42
MgO		0.89
Na_2O		0.67
K_2O		2.54
$P2O_3$		0.17
SO_3		1.90
Undetermined		0.58
	TOTAL	99.96

Ash fusion temperature (°F)	Reducing	Oxidizing
Initial deformation	1,950	2,250
Softening (H=Q)	2,030	2,300
Fluid	2,150	2,450

(Ash fusion data from 1989 TAG)

Natural gas serves as auxiliary and warm-up fuel. Natural gas could provide up to 35 percent of the energy requirements at the HIPPS system design point. Composition and properties of natural gas are listed in Table 1-5.

Table 1-5
Natural Gas Composition

Ultimate analysis (%wt)		
C		73.25
H		24.26
N		1.87
O		0.62
	TOTAL	100.00
Composition (mole %)		
CH_4		96.67
C_2H_6		1.80
C_3H_8		0.11
CO_2		0.32
H_2S		0.0004
N_2		balance
	TOTAL	100.00
Average molecular weight		16.55
Higher heating value		
(dry gas at 60 °F (15.6 °C), 30 inches Hg)		
Btu/scf		1,013
Btu/lb		23,189

Code of Accounts

Table 1-6 presents the code of accounts, or identification system employed with the HIPPS plant. The account numbers are used to increase consistency and understanding of the plant's technical and cost estimating scopes.

Table 1-6
HIPPS Commercial Plant Code of Accounts

POWER GENERATION

1.0 Steam Generation/HITAF
- 1.1 High Temperature Furnace
- 1.2 HITAF Heat Recovery Steam Generator #2

2.0 Gas Turbine System
- 2.1 Gas Turbine Generator
- 2.2 Gas Turbine Heat Recovery Steam Generator # 1

3.0 Steam Turbine System
- 3.1 Steam Turbine Generator
- 3.2 Circulating Water
- 3.3 Condensate
- 3.4 Feedwater
- 3.5 Condensate Transfer and Storage

BALANCE OF PLANT

4.0 Flue Gas Emissions Control
- 4.1 Ammonia Scrubbing for Particulate and SO_2 Removal
- 4.2 NO_X Reduction

5.0 Solids Material Handling
- 5.1 Coal Feed
- 5.2 Coal Handling
- 5.3 Bottom Ash/Slag Handing
- 5.4 Flyash Handling

6.0 Process Water Systems
- 6.1 Demineralized Water
- 6.2 Condensate Polisher
- 6.3 Raw Water
- 6.4 Softener
- 6.5 Chemical Additives

7.0 Miscellaneous Process Support
- 7.1 HVAC
- 7.2 Diesel Fuel Storage
- 7.3 Fire Protection
- 7.4 Wastewater

8.0 Other Process Systems
- 8.1 Process Piping
- 8.2 Instruments and Controls
- 8.3 Electrical Equipment
- 8.4 Electrical Materials
- 8.5 Service and Instrument Air

9.0 Civil and Structural

Process Design and Performance

The goal of the HIPPS plant is to produce power using a gas turbine in such a way that most of the heat energy normally supplied by natural gas is replaced by heat from coal combustion. In the commercial plant design this is done by heating the gas turbine air to 1,700 °F (927 °C) in a coal-fired furnace (the HITAF), and then sending the heated air to a natural gas-fired combustor/heater to increase the temperature of the air from 1,700 to 2,495 °F (927 to 1,368 °C). The proportion of natural gas is limited to 35% of the total energy input by the design criteria.

Exhibit 1-2 is a simplified block diagram for the HIPPS operation. The major components are shown, and dashed lines used to illustrate the boundaries for code of account groupings. The exhibit shows two HITAF units, each with a HRSG. There is a single GT and its associated HRSG. While each of the HITAF HRSG is expected to have individual NO_x control systems installed, there will be a single SO_2 reduction operation for flue gases from both HITAFs. Steam from the HITAFs and HRSG units is used in a single steam generator-turbine, which has systems for feedwater, condensate and other operations.

The process operation and interaction among the various components is more completely shown in the process flowsheet, Exhibit 1-3. The code of account items and major systems are described in later sections of the report.

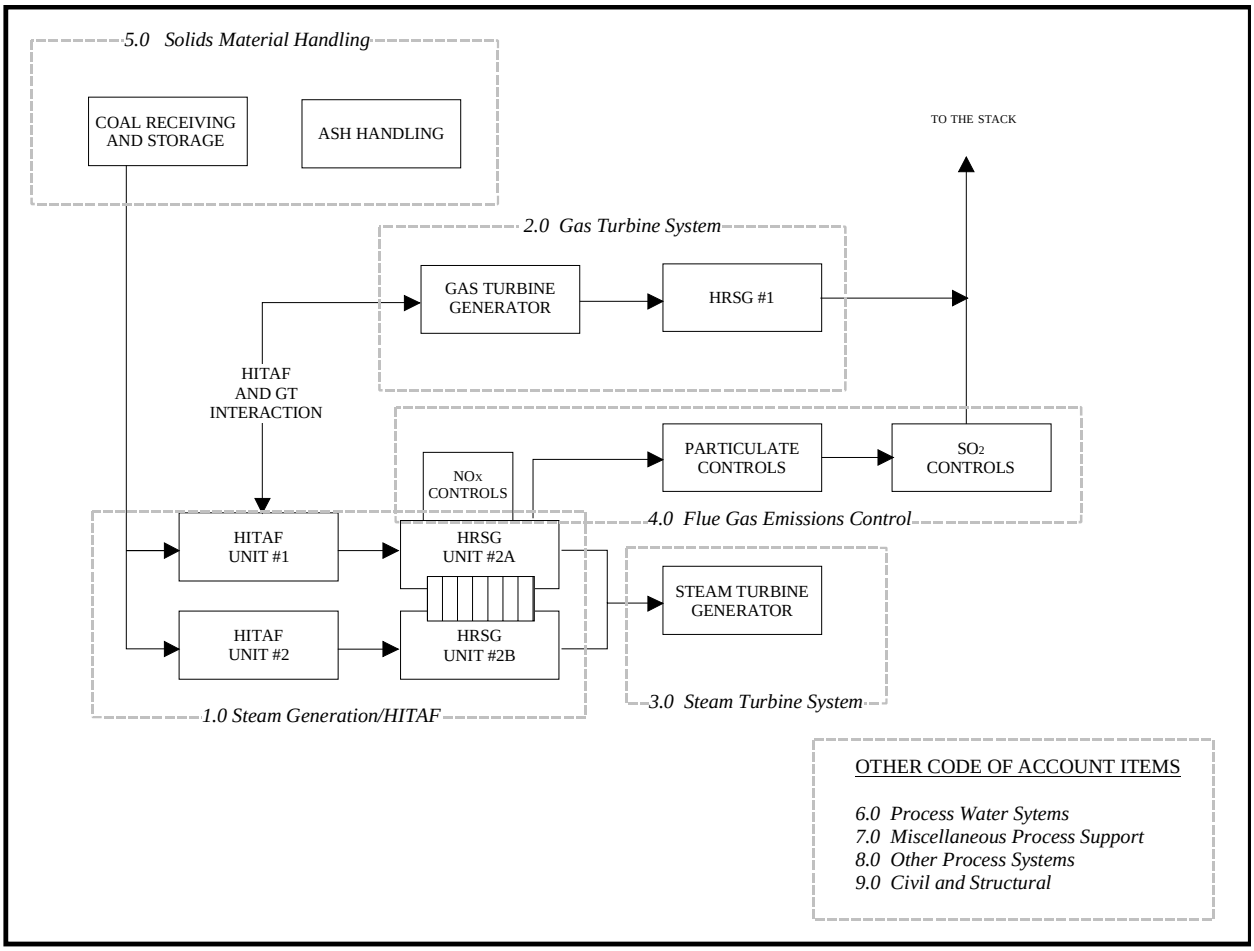

Exhibit 1-2
HIPPS Plant Block Diagram

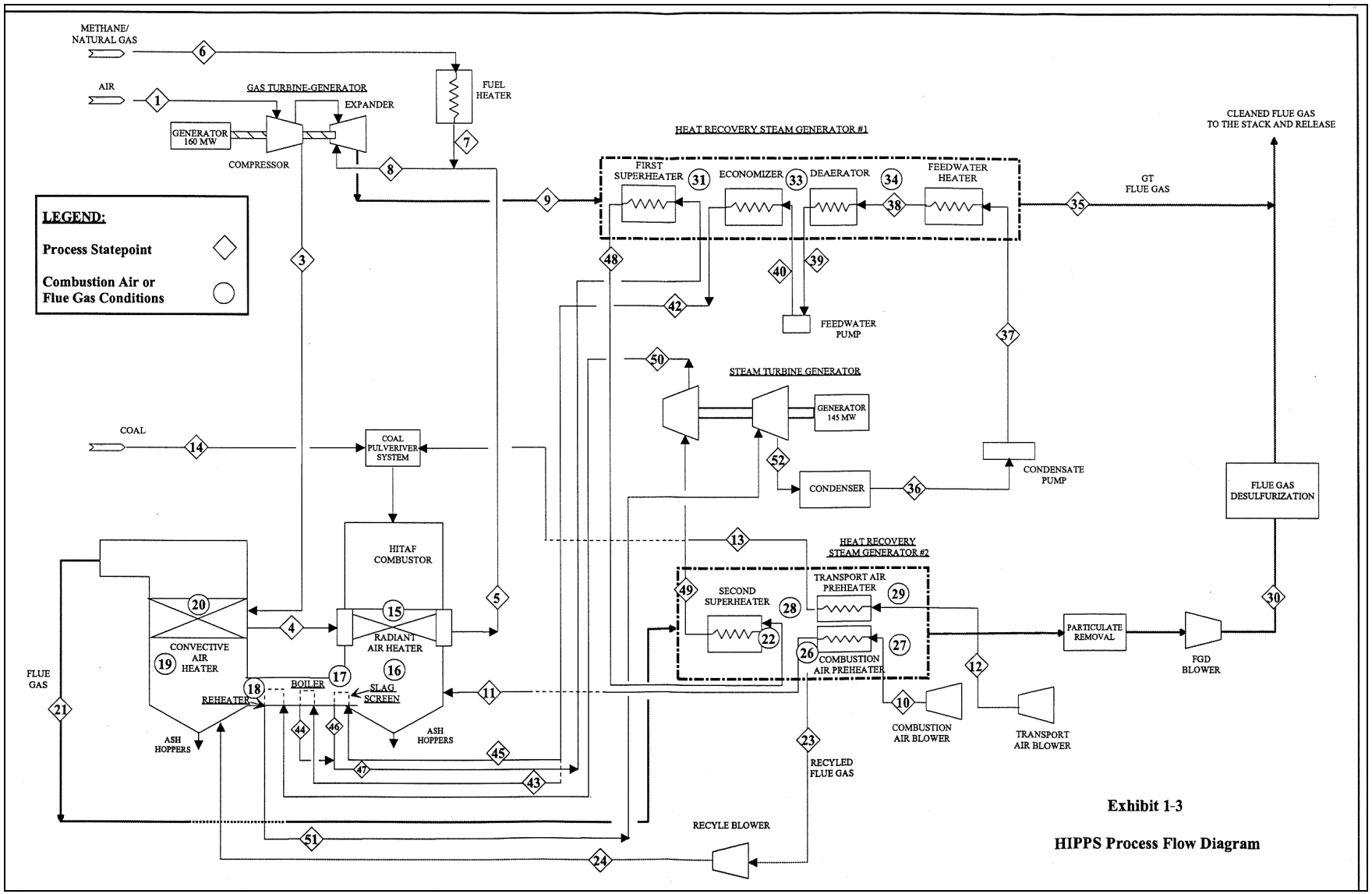

Exhibit 1-3

HIPPS Process Flow Diagram

Process Flow Diagram and Process Description

The process flow diagram of the 300 MWe power plant is shown in Exhibit 1-3, and provides significantly more detail than the block diagram. However, it should be noted that "process" operations are shown, and where there is more than one physical unit, for example the two HITAFs, only a single operation is shown.

As earlier noted, the heated air exits the natural gas combustor at 2,495 °F (1,368 °C). The hot, compressed air then enters the gas turbine expander where it expands to produce electric power. The flue gas leaves the GT expander at 1,003 °F (539 °C). Heat from the flue gas is recovered in the gas turbine HRSG as the gas is cooled to 180 °F (82 °C) before being sent to the stack. The heat recovered from the gas turbine flue gas is used to preheat the HITAF feedwater to 682 °F (361 °C). The feedwater is sent to evaporators (HITAF water walls and slag screens) where saturated steam at 2,400 psia (16,547 kPa) is generated. This steam is sent to a superheater, which is located in the gas turbine HRSG. Thus the waste heat of the gas turbine flue gas is used to heat feedwater and to (partly) superheat the steam.

The above describes gas turbine operation; the following describes the HITAF operation.

Coal, which contains 12.25% moisture, is fed to two operating pulverizers using transport air preheated to 575 °F (302 °C). The heat in the transport air vaporizes most of the moisture from the coal, and the vaporized moisture travels with the transport air. The transport air sweeps the coal from the pulverizers and carries the pulverized coal to the HITAF burners. Combustion air is added at the burners and the coal is fired.

The heat transfer surfaces for the following HIPPS components are located inside the HITAF.

- Radiant air heater
- Slag screen walls
- Steam reheater
- Convection air heater

The radiant air heater is located nearest the burners where the furnace temperature is the highest. The convective air heater is the farthest from the burners and sees the lowest temperature in the furnace. As the combustion products flow past the components, energy is transferred from the gases to the heat transfer surfaces. To develop the required temperature profile in the HITAF furnace, part of the combustion gas is recycled from the downstream HITAF HRSG, and is injected into the HITAF between the steam reheater and convective air heater.

The surface areas and locations of the slag screens and water walls are designed so that the slag produced from the coal flows on, and does not scale the radiant air heater and convective air heater. After the radiant heater and before the convective air heater, the flowing slag combines with other bottom slag. The flue gas exits the HITAF at 1,105 °F (596 °C). The heat in HITAF flue gas is recovered in the HITAF HRSG and used for heating the coal combustion air, coal transport air, and heating the partly superheated steam to 1,000 °F (538 °C). The HITAF HRSG also contains a selective catalytic reactor which destroys any NO_x present in the flue gas. The

SCR is located upstream of the air preheaters. The HITAF flue gas leaves the HRSG at 300 °F (149 °C) and then goes to a flue gas desulfurization (FGD) unit.

The flyash in the flue gas is removed by a particulate removal device prior to the FGD process, which removes the sulfur compounds present in the flue gas. In the conceptual commercial design, an ammonia based FGD and electrostatic precipitator are used. The cleaned flue gas is sent to a stack and released.

The superheated steam from the second superheater is sent to the high pressure section of the steam turbine at 2,400 psia/1,000 °F (16,550 kPa/538 °C). The steam leaves the HP section at 540 psia (3723 kPa); it then is sent to the reheater, which is located in the HITAF, and the steam is reheated to 1,000 °F (538 °C). The reheated steam is sent to the intermediate pressure section of the steam turbine at 540 psia (3,722 kPa). The steam passes through IP and low pressure sections of the steam turbine and is then exhausted to the steam condenser. The condensate and necessary make-up water is sent to the gas turbine HRSG and the steam cycle is repeated continuously.

Statepoint Table

The heat and mass balance, which was developed by UTRC, for the HIPPS 300 MWe power plant is shown in Table 1-7. The corresponding statepoint locations are shown in Exhibit 1-3. Coal, natural gas and compositions of other items were presented earlier: Compositions of the gas turbine flue gas and HITAF flue gas are respectively shown in Tables 1-8 and 1-9.

Power Plant Performance

A summary of the commercial HIPPS plant performance is listed below. A more complete list of performance is provided in Table 1-10.

Gas turbine power output, MWe	160.2
Steam turbine power output, MWe	143.1
Total power output, MWe	303.3
Net power output, MWe	292.2
Gross power efficiency based on HHV, %	49.2
Net power efficiency based on HHV, %	47.4

Table 1-7
Heat and Materials Balance Statepoint Table

State Point Number	State Point Description	Flow lb/h	Temp. °F	Pressure Psia	Enthalpy Btu/lb
					GAS TURBINE
1	Gas Turbine Compressor Inlet Air	3,304,620	59	14.7	124.6
2	Not Used				
3	Air to Convection Air Heater	2,615,436	732	230.9	290.8
4	Air to Radiant Air Heater	2,615,436	1,300	230.9	441.4
5	Air to Gas Turbine Combustor	2,615,436	1,700	230.9	552.6
6	Fuel Gas to Fuel Gas Heater	31,767	70	250.0	256.6
7	Fuel Gas to Gas Turbine Combustor	31,767	611	250.0	595.1
8	Combustion Products to Gas Turbine Expander	2,647,224	2,495	225.1	804.5
9	Gas Turbine Expander Exhaust	3,336,408	1,003	15.6	367.8
	HITAF COMBUSTION SYSTEM				
10	HITAF Combustion Air to Air Preheater	1,054,944	59	14.7	124.0
11	HITAF Combustion Air from Air Preheater	1,054,944	731	14.7	288.5
12	Transport Air to Transport Air Preheater	186,858	138	22.0	143.0
13	Transport Air from Transport Air Preheater	186,858	575	22.0	249.5
14	Coal to Pulverizer	124,574			
15	HITAF Combustion Products	1,352,124	3,014	14.7	1,009.4
16	HITAF Combustion Products to Slag Screen	1,352,124	3,014	14.7	1,009.4
17	HITAF Combustion Products to Water Walls	1,352,124	2,914	14.7	975.6
18	HITAF Combustion Products to Reheater	1,352,124	2,503	14.7	835.8
19	HITAF Combustion Products before Quench	1,352,124	2,143	14.7	722.6
20	HITAF Combustion Products to Convective Air Heater	1,861,380	1,800	14.7	618.1
	HITAF HRSG: GAS SIDE				
21	HITAF Flue Gas to Superheater	1,861,380	1,105	14.7	406.3
22	HITAF Flue Gas from Superheater	1,861,380	832	14.7	328.1
26	HITAF Flue Gas to Combustion Air Preheater	1,213,056	832	14.7	328.1
27	HITAF Flue Gas fm Combustion Air Prehter	1,213,056	300	14.7	185.0
28	HITAF Flue Gas to Transport Air Preheater	139,057	832	14.7	328.1
29	HITAF Flue Gas ex Transport Air Preheater	139,057	300	14.7	185.0
30	HITAF Flue Gas to FGD	1,352,113	300	14.7	185.0
23	Flue Gas to Recirculation Fan	509,256	832	14.7	332.0
24	Recycled Flue Gas to Quench	509,256	862	16.2	340.6

Table 1-7 (Continued)
Heat and Materials Balance Statepoint Table

State Point Number	State Point Description	Flow lb/h	Temp. °F	Pressure Psia	Enthalpy Btu/lb
	GAS TURBINE HRSG: GAS SIDE				
31	Gas Turbine Flue Gas to Economizer	3,336,372	820	14.8	318.8
33	Gas Turbine Flue Gas to Deaerator	3,336,372	301	14.8	186.1
34	Gas Turbine Flue Gas to Feedwater Heater	3,336,372	236	14.8	169.8
35	Gas Turbine Flue Gas to Stack	3,336,372	180	14.8	156.1
	GAS TURBINE HRSG: STEAM SIDE				
36	Condensate from Steam Condenser	784,404	91	0.74	59.7
37	Condensate to Feedwater Heater	784,404	91	17.0	59.8
38	Condensate to Deaerator	784,404	150	17.0	118.3
39	Feedwater from Deaerator	784,404	219	17.0	187.7
40	Feedwater to Economizer	784,404	224	3,160	199.6
42	Feedwater from Economizer	784,260	682	2,749	763.8
	HITAF HRSG: STEAM SIDE				
43	Feedwater to Water Wall Evaporator	633,276	682	2,749	763.8
44	Steam from Water Wall Evaporator	626,940	682	2,749	1,063.1
45	Feedwater to Slag Screen Evaporator	150,984	682	2,749	763.8
46	Steam from Slag Screen Evaporator	149,476	682	2,749	1,063.1
47	Steam to First Superheater	776,484	677	2,667	1,063.1
48	Steam to Second Superheater	776,484	782	2,667	1,273.6
49	Superheated Steam to Steam Turbine	776,484	1,000	2,400	1,461.1
50	Steam from Steam Turbine to Reheater	776,484	643	540	1,322.2
51	Reheated Steam from Reheater	776,484	1,000	540	1,519.3
52	Steam Turbine Exhaust to Steam Condenser	776,484	91	0.74	1,003.1

Table 1-8
Composition Of Gas Turbine Flue Gas

Components	mol %
O_2	17.17
N_2	75.77
Ar	0.92
CO_2	1.64
H_2O	4.49
Total	99.99

Table 1-9
Composition Of HITAF Flue Gas

Components	mol %
O_2	3.14
N_2	72.94
Ar	0.88
CO_2	13.95
H_2O	8.80
SO_2	0.28
Total	99.99

Table 1-10
Power Plant Performance

Heat Input:	
Coal input, lb/h	124,574
High heating value (HHV) of coal, Btu/lb	10,982
Total HHV of coal, million Btu/h	1,368
Natural gas input, lb/h	31,767
High heating value (HHV) of natural gas, Btu/lb	23,189
Total HHV of natural gas, million Btu/h	737
Total HHV of coal and natural gas, million Btu/h	2,105
Power Output	
Gas turbine power output, MW_e	160.2
Steam turbine power output, MW_e	143.1
Total plant power output, MW_e	303.3
In-plant power consumption, MW_e	11.1
Net plant power output, MW_e	292.2
Gross efficiency, %	49.2
Net efficiency, %	47.4

Major HIPPS Plant Components

In this section, major components and equipment of the conceptual commercial HIPPS plant are described. The sequence follows the code of accounts list.

Code of Accounts Item 1.0 Steam Generation/High Temperature Advanced Furnace

1.1 High Temperature Advanced Furnace

The Radiant Air Heater and Convection Air Heater are discussed in Section 7. Steam generation in the slag screen, the water walls, and the reheater are discussed elsewhere in this Section.

1.2 HITAF Heat Recovery Steam Generator

This HRSG heats the partially superheated steam from 770 to 1,000 °F (410 to 538 °C), and also heats the coal combustion air and coal transportation air. (Steam is initially superheated in the gas turbine HRSG.) The HRSG has the following major components:

- Combustion air preheater
- Transport air preheater
- Second superheater

Because HITAF burns pulverized coal, the flue gas contains particulate, SO_x, and NO_x. The temperature is 1,105 °F (546 °C). Because of the SO_x, the flue gas will cause corrosion problems if cooled below 300 °F (149 °C). This somewhat limits the heat recovery capability of the unit.

The fluid flow path in the HITAF HRSG is as follows: A combustion air blower pushes the coal combustion air through the combustion air preheater, and a transport air blower pushes the transport air through the transport air preheater. In the combustion air preheater, the coal combustion air is heated to 731 °F (388 °C) and in the transport air preheater, the coal transport air is heated to 575 °F (302 °C). The two air preheaters are positioned in the HRSG such that flow of the flue gas exiting the second superheater is divided among the two air preheaters in proportion to their heat loads. The preheated coal combustion air is sent to the HITAF burners and the preheated transport air is sent to the coal pulverizers.

Steam at 782 °F (417 °C) arrives from gas turbine HRSG, where the first superheater is located. The steam is further superheated in the HITAF HRSG's superheater (termed the "second" HRSG). The flue gas entering the HITAF HRSG heats the superheated steam to 1,000 °F (538 °C). The superheated steam at 1,000 °F (538 °C), is sent to the HP section of the steam turbine.

Combustion Air Preheater

The function of the combustion air preheater is to raise the temperature of the combustion air to 731 °F (388 °C). The combustion air preheater cools the flue gas to 300 °F (149 °C) and heats the combustion air to 731 °F (388 °C). Its heat duty is 184 million Btu/h (194 million kJ/h) and its total heat transfer surface area is 240,000 square feet (22,300 square meters). The heat transfer surface material of the combustion air preheater is carbon steel.

Transport Air Preheater

The function of the transport air preheater is to raise the temperature of the transport air to 575 °F (302 °C). The transport air preheater is a finned tube heat exchanger which cools the flue gas to 300 °F (149 °C) and heats the transport air to 575 °F (302 °C). Its heat duty is 11.4 million Btu/h (12 million kJ/h) and its total heat transfer surface area is 57,600 square feet (5,350 square meters). The heat transfer surface material of the transport air preheater is carbon steel SA-106B.

HITAF (Second) Superheater

The function of the second superheater is to raise the temperature of the partially superheated steam coming from first superheater to 1,000 °F (538 °C). The second superheater is a finned tube heat exchanger which cools the flue gas from 1,105 to 832 °F (596 to 444 °C) and heats the

steam from 782 to 1,000 °F (417 to 538 °C). Its heat duty is 160 million Btu/h (169 million kJ/h) and its total heat transfer surface area is 301,000 square feet (27,960 square meters). The heat transfer surface material is alloy steel SA-335-P11 for the colder section and stainless steel 304 for the hot section.

Attemperators are installed downstream of the second superheater to control the superheated steam temperature at 1000 °F (538 °C). These attemperators control the steam temperature by injecting water taken from the economizer into the superheated steam line.

2.0 Gas Turbine System

2.1 Gas Turbine Generator

The gas turbine description remains as described in the Phase I Report (Seery, et. al., 1995).

2.2 Gas Turbine HRSG

The function of this HRSG is to transfer heat from the gas turbine exhaust gas to the feedwater. The HRSG has the following components:

- Feedwater heater
- Deaerator
- Economizer
- First superheater

Because the gas turbine uses clean natural gas to boost the air temperature, the flue gas is free from particulate and SO_x. The flue gas temperature is 1,000 °F (538 °C). Because this flue gas is clean, it can be cooled to a temperature of 180 °F (82 °C) without corrosion on the heat exchange surface or in the flue gas stack, which discharges the flue gas to the atmosphere. The GT flue gas is used to heat steam to 782 °F (417 °C). As noted above, a second superheater is required to achieve the 1,000 °F (538 °C) steam temperature designed for the steam turbine.

The fluid flow path in the gas turbine HRSG is as follows: A condensate pump pumps the condensate from the steam condenser hotwell to the deaerator via the condensate polisher and feedwater heater. In the deaerator, pressure is 17.0 psia (117.2 kPa), and the temperature of the heated and deaerated water is 219 °F (104 °C). A boiler feedwater pump draws the deaerated water from deaerator and pumps it into the economizer. Temperature of water exiting the economizer is 682 °F (361 °C). The heated water from the economizer goes to the steam drum and from there is sent to the slag screen and water walls of the HITAF, where the water is vaporized to saturated steam at 682 °F (361 °C). The saturated steam goes to the first superheater in the gas turbine HRSG, where it is heated to 782 °F (417 °C).

Feedwater Heater

The function of the feedwater heater is to raise the temperature of the condensate coming from the steam condenser (via a condensate polisher) to 150 °F (66 °C). The feedwater heater is a finned tube heat exchanger which cools the flue gas from 236 to 180 °F (113 to 82 °C) and heats the feedwater to 150 °F (66 °C). Its heat duty is 47 million Btu/h (50 million kJ/h) and its total heat transfer surface area is 183,500 square feet (17,050 square meters). The heat transfer surface material of the feedwater heater is carbon steel SA-106B.

Deaerator

The function of the deaerator is to raise the temperature of the feedwater coming from the feedwater heater to 224 °F (107 °C) and to reduce the oxygen content to .001 cubic inch/gal (0.005 cc/liter) of deaerated water. The deaerator is a finned tube heat exchanger which cools the flue gas from 301 to 236 °F (149 to 113 °C) and heats the feedwater to 219 °F (104 °C). Its heat duty is 55 million Btu/h (58 million kJ/h) and its total heat transfer surface area is 214,700 square feet (19,950 square meters). The heat transfer surface material of the deaerator is carbon steel SA-106B.

Economizer

The function of the economizer is to raise the temperature of the feedwater exiting the deaerator to 682 °F (361 °C). The economizer is a finned tube heat exchanger which cools the flue gas from 820 to 301 °F (438 to 149 °C) and heats the feedwater to 682 °F (361 °C). Its heat duty is 450 million Btu/h (475 million kJ/h) and its total heat transfer surface area is 1,791,700 square feet (166,450 square meters). The heat transfer surface material of the economizer is carbon steel SA-106B.

The heated feedwater from the economizer is sent to the steam drum, from there it is sent to the slag screen and water walls of the HITAF where it is evaporated to saturated steam at 682 °F (361 °C).

First Superheater

The saturated steam from the slag screen and water walls of the HITAF goes to the steam drum and is sent to the first superheater, which is part of the gas turbine HRSG.

The function of the first superheater is to raise the temperature of the saturated steam to 782 °F (417 °C). The first superheater is a finned tube heat exchanger which cools the flue gas from 1,003 to 820 °F (539 to 438 °C) and heats the saturated steam from 682 to 782 °F (361 to 417 °C). Its heat duty is 154 million Btu/h (163 million kJ/h) and its total heat transfer surface area is 257,600 square feet (23,930 square meters). The heat transfer surface material of the first superheater is carbon steel SA-106B for the colder section and alloy steel SA-335-P11 for the hot section.

Attemperators are installed downstream of the first superheater to control the partly superheated steam temperature at 770 °F (410 °C). These attemperators control the steam temperature by injecting water taken from the economizer into the partly superheated steam line.

3.0 Steam Turbine System

The steam turbine-generator consists of a steam turbine and a generator. The function of the steam turbine is to expand steam from 2,400 psia (16,550 kPa) to 0.75 psia (5.17 kPa) and rotate the generator which produces electric power. The system also includes components for condensate and feed water operations.

3.1 Turbine Generator

Steam Turbine

The steam turbine consists of three sections: a high pressure (HP) section, an intermediate pressure (IP) section and low pressure (LP) section, connected in tandem.

Steam at 2,400 psia/1,000 °F (16,550 kPa/538 °C) enters the HP section of the steam turbine and exits at 540 psia (3,723 kPa). The 540 psia (3,723 kPa) steam is sent to the reheater section of the HITAF where its temperature is increased to 1,000 °F (538 °C). Attemperators are installed downstream of the reheater to control the reheated steam temperature at 1000 °F (538 °C). These attemperators control the steam temperature by injecting the water taken from the economizer into the reheated steam line. The reheated steam at 540 psia/1,000 °F (3,722 kPa/538 °C) enters the IP steam and then goes to the LP section.

The exhausted steam leaves the LP section at 0.74 psia (5.1 kPa) and enters the condenser. Generally, in pulverized coal based power plants, steam is extracted from various stages of the steam turbine and used for heating the boiler feedwater. In the HIPPS plant, the feedwater is heated with flue gas. Therefore no steam is extracted from any of the turbine stages. This feature benefits the turbine operation: The turbine operates more smoothly because of consistent steam loading of all the stages, which results in a slightly higher efficiency and a longer equipment life.

Turbine Generator

Generally the steam turbine generator is supplied by the manufacturer who manufactures the steam turbine. The turbine generator is rotated by the steam turbine at 3,600 revolutions per minute to produce about 150 MWe at 22,000 volts, 60 Hz, 3 phase power.

The steam turbine generator unit includes a protective valve system, a control system and an emergency trip system. The equipment package also has an electro-hydraulic system, a lube oil system, a gland sealing system, a turbine drain system, and a turning gear. Supervisory instruments for monitoring position, eccentricity, vibration and differential expansion of the turbine rotor, and turbine instruments for pressure and temperature measurements are included.

3.2 Circulating Water Subsystem

The circulating water system supplies cooling water to the steam turbine condenser and various heat exchangers including the generator exciter, hydrogen, stator and steam turbines lube oil coolers. The circulating water exiting the heat exchangers becomes warm. The warm circulating water is cooled in the cooling tower. A flow diagram of the system is shown in Exhibit 1-4.

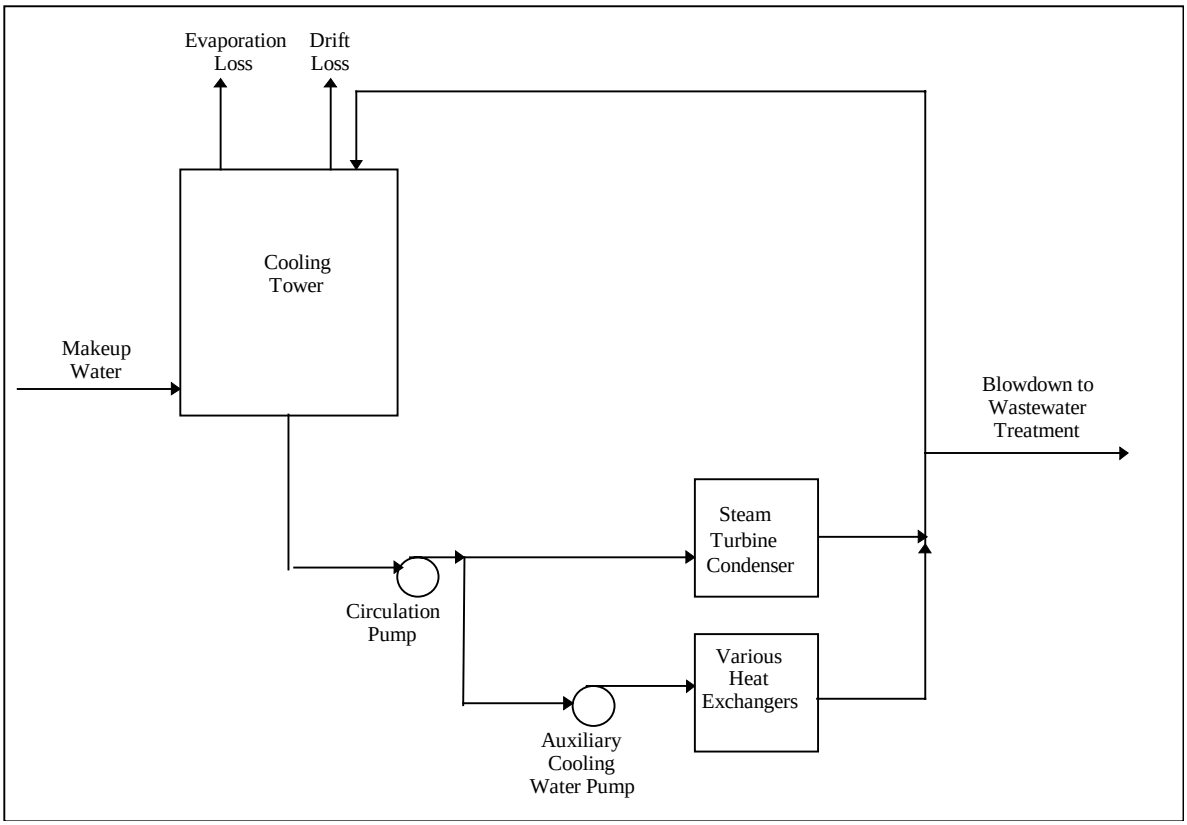

Exhibit 1-4
Circulating Water Process

Cooling Tower

The cooling tower consists of six cells with auxiliary equipment that includes fans with motors and gear drives, water distribution system, piping and instrumentation, NFPA-214 fire protection system, and all structural components necessary for complete tower installation. The basic structural material is wood. Polyvinyl chloride (PVC) is used for fill and drift eliminators.

Warm circulating water is discharged from manifolds to a warm water distribution basin which is located directly over the fill area. The water from the warm water basin is distributed evenly over the fill by means of polypropylene nozzles. The air drawn upward by the induced fans contacts the falling water. The falling water gives up its heat to the contacting air by evaporation and by sensible heat transfer, and is collected in the cold water basin located at the base of the tower. From the cold water basin, the cold circulating water is returned to the heat exchangers by the circulating water pump.

About ninety percent of the circulation water is sent to the main steam condenser. The remaining ten percent of the water is sent to the following exchangers:

- Bearing cooling water heat exchanger
- Exciter air cooler
- Generator stator cooling water coolers
- Generator hydrogen coolers, and

- Turbine lube oil coolers.

Cooling tower design data is listed below.

Circ. water required flow rate, gpm (m^3/h)	82,000	(18,624)
Circ. water design flow rate, gpm (m^3/h)	85,000	(19,306)
Circ. water inlet temperature, °F (°C)	83	(28)
Circ. water exit temperature, °F (°C)	63	(17)
Required heat load, million Btu/h (million kJ/h)	820	(865)
Design heat load, million Btu/h (million kJ/h)	850	(897)
Number of cells	6	
Number of fans	6	
Fan motors, HP each	150	
Pumping head from the tower base, ft (m)	22	(6.7)
Air flow, ft^3/minute/fan (m^3/minute/fan)	1,275,900	(36,129)
Fill volume, ft^3 (m^3)	66,700	(1,889)
Wetted surface area, ft^2 (m^2)	3,112,700	(228,179)
Water flow rate, gpm/ft^2 (gpm/ m^2)	5.1	(0.5)
Liquid/Gas ratio	1.415	
Evaporation loss, gpm (m^3/h)	1,515	(344)
Drift loss, gpm (m^3/h)	5	(1.14)
Blowdown, gpm (m^3/h)	340	(77)
Total makeup water requirement, gpm	1,860	(422)
Overall tower dimensions:		
Length, ft (m)	330	(100.6)
Width, ft (m)	60	(18.2)
Height, ft (m)	51	(15.5)
Shipping weight, lb (kg)	891,000	(404,151)
Operating weight, lb (kg)	1,485,000	(673,585)
Concrete basin dimensions:		
Length, ft (m)	336	(102.4)
Width, ft (m)	66	(20.1)
Depth, ft (m)	4	(1.2)

Circulation Pump

Circulation pumps draw water from the cooling tower concrete basin and push it through the heat exchangers before it is discharged at the top of cooling tower. There are three, 50% capacity, circulation water pumps, two operating and one standby. The two operating pumps circulate 100% of the circulating water. About 90% of this water is sent to the steam condenser and the remaining 10% is sent to the auxiliary cooling water pump, which pushes the water through the other heat exchangers. The circulation water from the steam condenser and the

circulation water from the other heat exchangers is combined and pumped to the top of the cooling tower.

The design data for the circulation pumps are as follows:

Number of operating pumps	2
Number of standby pumps	1
Type	vertical, axial flow
Liquid pumped	circulating water
Liquid temperature, °F (°C)	63 (17.2)
Flow rating, gpm/pump ((m3/h)/pump)	45,000 (10,221)
Suction pressure, psig (kPa)	0 (0)
Discharge pressure, psig (kPa)	35 (241)
Case material	carbon steel
Shaft material	stainless steel
Impeller material	bronze
Motor, HP	1,300

Auxiliary Cooling Water Pump

The auxiliary cooling water pump takes water from the circulation water pump, boosts its pressure, pushes it through the heat exchangers (other than the steam condenser) and returns it to the discharge line of the circulating water pump. There are three, 50% capacity, auxiliary cooling water pumps, two operating and one standby.

The design data for the auxiliary cooling water pumps are as follows:

Number of operating pumps	2
Number of standby pumps	1
Type	centrifugal
Liquid pumped	circulating water
Liquid temperature, °F (°C)	63 (17.2)
Flow rating, gpm/ pump ((m3/h)/pump)	4,500 (1,022)
Suction pressure, psig (kPa)	35 (241)
Discharge pressure, psig (kPa)	60 (414)
Case material	stainless steel
Barrel material	steel
Shaft material	stainless steel
Impeller material	bronze
Motor, HP	100

3.3 Condensate Subsystem

The condensate system transfers condensate from the condenser hotwell through the condensate polisher and feedwater heater to the deaerator. The system also maintains proper

levels of condensate in the hotwell. It is also used as a source of water for the steam packing exhaust desuperheater and for the turbine exhaust hood spray.

The condensate is pumped to the deaerator by condensate pumps. Three pumps are provided, each 50% capacity. Normally two pumps will be operating. The condensate pumps are sized in excess of full load with a 4% margin in flow to allow for system surge, and a 4% margin in flow to allow for pump wear. Pump head is based on normal flow plus 8% surge margin only.

The condensate system piping, valves and heat exchanger tubes have a design pressure determined by the condensate pump shutoff pressure plus 5% overpressure margin. The design temperature is based on the saturation temperature, corresponding design pressure of the heat exchanger shell plus a margin. The condensate system piping sizes are selected to achieve velocities that will economically minimize noise levels and friction losses.

The condensate system consists of:

- Steam condenser
- Three 50% capacity condensate pumps
- The condensate polisher
- Steam jet air ejector condensers
- Feedwater heater
- Associated piping, valves, controls and instrumentation.

Steam Condenser

The steam condenser condenses the turbine exhaust steam, and maintains a low level of oxygen concentration in the condensate. The condenser is a single shell, single pressure and single pass deaerating type, located under the LP section of the steam turbine. The hotwell storage is equivalent to one minute of total storage at the design flow of the condensate. The exhaust from the steam turbine is directed downward into the hotwell, such that any condensation in the lines is drained by gravity to the condenser. The shellside of the steam condenser is designed for a pressure of 15 psig (205 kPa) to vacuum. The design temperature is in excess of the saturated temperature corresponding to the design pressure. At normal water level, the condenser hotwell has a storage capacity equivalent to the flowrate required by the condensate pumps for 10 minutes with the system operating at full load. The steam condenser data are listed below:

Type: Single pressure, single shell, single pass

• Effective surface, ft^2 (m^2)	53,550	(4.970)
• Circulating water		
• Inlet temperature, °F (°C)	63	(17.2)
• Return	80	
• Flow, gpm (m^3/h)	94,900	(21,554)
• Water pressure, psia (kPa)	45	(310)
• Tubes		
• Overall length, ft (m)	34.25	(10.44)
• Water velocity, ft/s (m/s)	10.0	(3.05)

- Steam flow rate, lb/h (kg/h) 800,000 (362,874)
- Condenser duty, million Btu/h (million kJ/h) 800 (844)

Steam Condenser Air Removal

The condenser air removal system establishes the initial vacuum on the shell (steam) side of the condenser by removing air, and maintains vacuum during operation by continuously removing air and non-condensable gases. The function of the waterbox priming system is to create a vacuum in top portion of the condenser waterboxes to facilitate complete filling of the waterboxes to prevent formation of air pockets.

The condenser air removal system consists of one main ejector unit and one startup (hogging) ejector. Condenser vacuum is initiated by use of steam to the hogging ejector. Once a pressure of about 7.5 psia (51.7 kPa) has been established in the condenser, the main air ejector is brought into action. It takes about two hours to reduce condenser pressure from 15 to 7.5 psia (103 to 51.7 kPa) and additional two to three hours to reduce pressure from 7.5 to 0.74 psia (51.7 to 5.1 kPa). The main air ejector consists of two first stage jets, one inter-condenser, two second stage jets and one after-condenser. The amount of steam required to maintain the vacuum is about 1,300 lb/h (590 kg/h) saturated and dry steam at 100 psia (690 kPa).

The waterbox priming system consists of two 100% capacity liquid ring type vacuum pumps with seal water coolers and a vacuum tank. Each pump is designed to remove 20 cfm (0.57 m^3/m) of air at 60 °F (15.6 °C) with suction pressure of 2 psia (13.8 kPa).

The condensate pumps are constant speed electric motor driven, vertical, canned suction, centrifugal type, each rated at 50% capacity. The pumps are capable of running individually or in parallel. A recirculation system is provided for each pump to protect the pump from overheating and instability at low pump flows. The pumps have mechanical seals that are supplied with seal water to cool the seals and to prevent air leakage. The seal water is supplied from the condensate transfer system any time a condensate pump is idle.

The condensate polisher, located immediately downstream of the condensate pumps, minimizes scale formation and fouling of equipment in the condensate system, the feedwater system and the boiler systems by removing impurities from condensate.

Each condensate pump receives suction from individual connections on the condenser hotwell and discharges to a common header. During normal plant operation, two condensate pumps will operate, and third will be standby. Condensate flow to the deaerator is regulated by a level control valve downstream of the feedwater heater.

Demineralized makeup water is supplied from the condensate transfer pump discharge header to the condenser hotwell. If during normal operation, condensate level in the hotwell rises too high, excess condensate will be transferred to the condensate storage tank through a condensate reject valve.

The quality of condensate is controlled by injection of neutralizing amine and oxygen scavenger chemical, from a chemical feed system, into the condensate header upstream of the steam jet air ejector.

During normal operation, condensate passes through the condensate polisher before entering the feedwater heater.

Seal water supply at 5-10 psig (35-70 kPa) and up to 1 gpm (0.2 m^3/h) is continuously required for each standby pump to provide sealing in the stuffing box to prevent air from entering the system on suction side which is under vacuum. A pressure regulator valve on the seal water supply header is provided to reduce the condensate transfer pump discharge pressure to the required seal injection pressure. A relief valve with set pressure of 25 psig (274 kPa) is provided on the seal water header to protect the pump stuffing boxes from over-pressure in case of regulator failure.

During startup, the condenser hotwell is initially filled from the condensate storage and transfer system via the condensate transfer pumps. Seal water for the idle pump(s) is supplied from the condensate transfer pump discharge header.

3.4 Feedwater Subsystem

The feedwater system pumps feedwater from the deaerator storage tank through the economizer, the steam drum and to the HITAF boiler (i.e., to water walls and slag screens of the HITAF). The system controls feedwater flow and pressure in response to turbine load, and maintains proper water level in the steam drum.

The feedwater system is designed to supply an uninterrupted flow of feedwater to the HITAF boiler such that the HITAF boiler may continuously supply steam to the steam turbine. The feedwater flowrate is 784,260 lb/h (355,740 kg/h).

Auxiliary outlets from the fourth intermediate pressure stage are provided on the boiler feed pumps (BFPs) to supply spray water for the boiler reheat steam temperature control systems.

The deaerator is designed to heat the feedwater to 219 °F (104 °C), and provide deoxygenated feedwater with a maximum oxygen content of 0.001 in^3/gal (0.005 cc/liter) at all loads. The deaerator storage tank is sized to store enough volume to supply feedwater to the BFPs' suction header for 5 minutes with the pumps operating at their design flow-rate with no flow entering the tank. The deaerator and the storage tank are designed for full vacuum and 30 psig (308 kPa) positive pressure. The deaerator and the storage tanks are made of carbon steel.

The feedwater system, which supplies heated deaerated water through the economizer to the HITAF boiler consists of the following:

- Deaerator
- Deaerator storage tank
- Three 50% capacity boiler feedwater pumps
- Associated piping, valves, controls and instrumentation.

Deaerating Feedwater Heater and Storage Tank

The deaerating feedwater heater, described under the gas turbine HRSG, is provided with suitable overpressure protection and vented to atmosphere. From the bottom of the deaerator, the hot water flows into the deaerator storage tank. The storage tank is a horizontal tank with capacity for a minimum of 5 minutes storage between normal level and pump suction nozzle.

Boiler Feedwater Pumps

Three 50% capacity, motor driven boiler feedwater pumps are installed in parallel. They are horizontal, constant speed, radially split, double barrel, 11 stage centrifugal pumps. Each pump is designed to deliver 850 gpm (193 m^3/h) flowrate at 2700 psig (18,712 kPa) discharge pressure. They take suction from the bottom of the deaerator storage tank. The BFPs pump water through the economizer and into the steam drum. They are sized to have a discharge pressure high enough to overcome pressure drop in the economizer, boiler drum operating pressure, and static head. Each pump is provided with two seal coolers and a forced type lube oil system.

During normal operation, condensate is pumped from the condensate system into the deaerator, via the feedwater heater. By using signals from the level transmitters on the deaerator storage tank and from the feedwater control system, the required level of water is maintained in the deaerator storage tank.

3.5 Condensate Transfer and Storage Subsystem

The condensate transfer and storage system receives, stores, and supplies demineralized water to the HITAF boiler, the auxiliary boiler, the condenser and other miscellaneous plant users. Product water from the demineralizer system is collected and stored in the condensate storage tank. Condensate transfer pumps distribute water to the various plant users.

The condensate transfer pumps are designed for 500 gpm (114 m^3/h) flowrate. The condensate storage tank is designed to provide 12 hours of storage capacity for continuous demands. The design product water from the makeup demineralizer system to the condensate storage tank is as follows:

Total dissolved solids	0.1 ppm
Conductivity	<0.5 micromho per cm
pH @ 77°F (°C)	5 to 8
Silica (as SiO_2)	0.02 ppm

The condensate transfer and storage system consists of the following:

- Condensate storage tank
- Two 100% capacity condensate transfer pumps
- Associated piping, valves, and instrumentation

The condensate storage tank collects product water from the demineralizer system. During normal operation, one of the condensate transfer pumps takes suction from the condensate storage tank and directs the water mostly to the main condenser. The other intermittent consumers served by the pump are: Auxiliary boiler, stator cooling system, backwash header and precoat mixing tank in the condensate polisher system.

4.0 Emissions Control System

Emissions control are for particulate, SO_x and NO_x. Particulate and SO_x are removed by an ammonia scrubbing process and NO_x is removed by selective catalytic reduction (SCR) process.

4.1 Ammonia Scrubbing for Particulate and SO_x Removal

General Electric and others have developed flue gas desulfuization processes based on ammonia scrubbing. A block diagram for an ammonia-based scrubbing system is shown in Exhibit 1-5.

One of the features of the ammonia based flue gas scrubbing systems is that ammonium sulfate, a valuable chemical used in fertilizer manufacturing and other industries, can be produced as a by-product. The quality of the by-product ammonium sulfate can be controlled to meet agricultural and fertilizer specifications regarding nitrogen content and impurities. The sulfate can be used in solid crystalline form, compacted or granulated, or in liquid form as ammonium sulfate solution or slurry, depending on the market requirements. The process is considered commercial, and is in operation at several locations outside the U. S.

The cost estimate prepared for the HIPPS plant excludes the by-product production costs and estimates for revenue from sales. While the system promises cost benefits to the plant concept, the application of ammonia-based scrubbing is not unique to HIPPS, and similar costs/benefits could be achieved with ammonia scrubbing at pulverized coal plants. Thus, the by-product does not significantly impact comparisons between HIPPS and PC power plants.

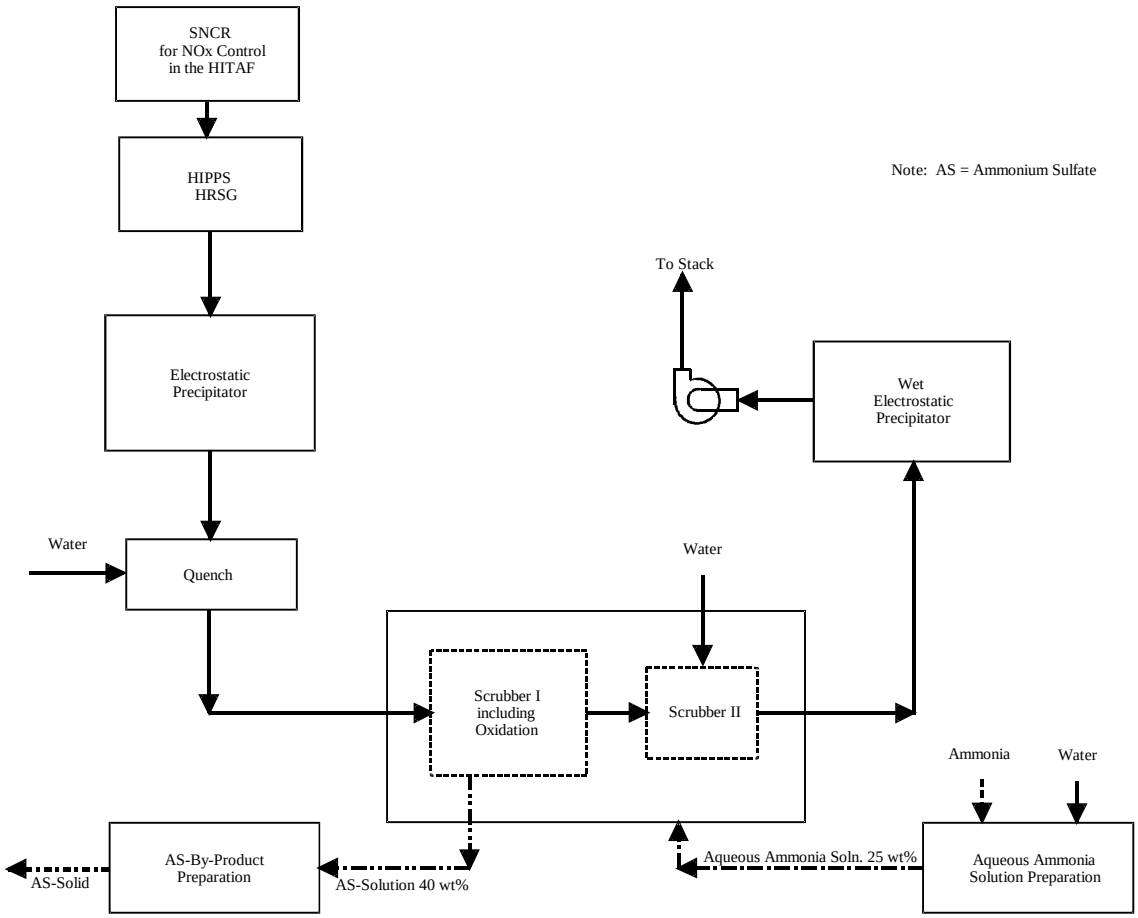

Exhibit 1-5
Block Diagram for Ammonia Scrubbing System

The FGD in the HIPPS plant design uses an unsaturated aqueous ammonium sulfate solution to absorb SO_2 from the flue gas. The absorbed SO_2 reacts with ammonia, which is introduced into the absorber with the oxidation air. Upon reacting, SO_2 and ammonia produce ammonium sulfite which is oxidized to ammonium sulfate by the oxidizing air. The ammonium sulfate product is recovered from solution by evaporation and centrifuging the crystals.

More detail is shown in Exhibit 1-6. The flue gas from the HITAF HRSG passes through an electrostatic precipitator. The precipitator removes fine particulate from the flue gas prior to its entering the FGD plant. The flue gas from the precipitator enters a prescrubber just above liquid level. The hot flue gas is contacted with a recirculating spray of ammonium sulfate slurry. In this vessel, the flue gas becomes saturated by evaporation of water from the recirculating spray of ammonium sulfate slurry. The pH of this slurry is low (~ 1.0). The saturated flue gas leaves the prescrubber through a mist eliminator designed to remove any slurry which was entrained in the flue gas.

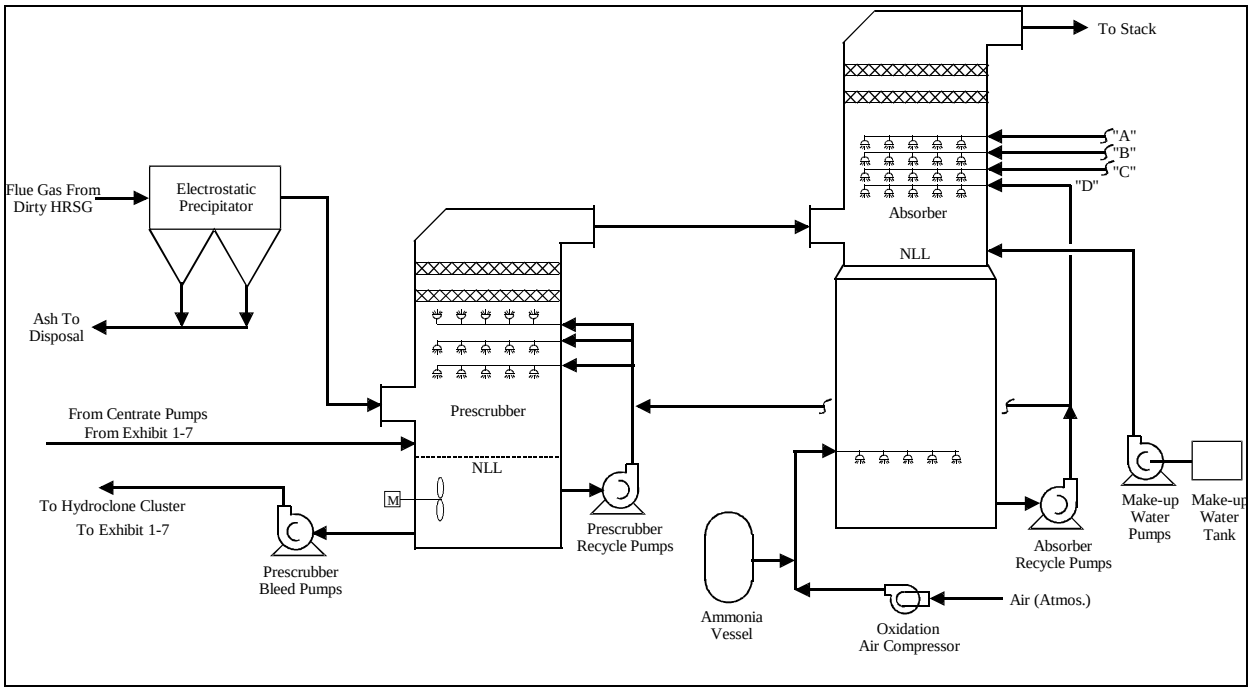

Exhibit 1-6
Ammonia-Based Process Absorber Area Process

After leaving the prescrubber, the flue gas enters a counter-current absorber, where it is contacted by a recirculating unsaturated ammonium sulfate liquor. Ammonia is added with the oxidation air to maintain the recycle liquor at a pH of 5.2 to 5.8, thus ensuring the required SO_2 removal. The cleaned flue gas passes through two stages of high efficiency mist eliminators to remove any entrained droplets.

The primary purpose of the prescrubber is to separate the process of SO_2 absorption and oxidation, which take place in the absorber, from the process of ammonium sulfate crystallization. The oxidation rate of ammonium sulfite deteriorates as the concentration of dissolved salts increases, and approximately 45 wt% dissolved ammonium sulfate is required

before solids will crystallize. By a separate oxidation step, the oxidation rate can remain high in an unsaturated solution in the absorber.

Thermal energy from the HITAF flue gas evaporates water from the prescrubber slurry, and the flue gas becomes saturated with the evaporated water. The evaporation of water causes crystallization of ammonium sulfate products and liquid level reduction in the prescrubber vessel.

The unsaturated ammonium sulfate solution in the absorber is used to wash the prescrubber mist eliminator and maintain prescrubber vessel liquid level. As a result, unsaturated ammonium sulfate solution is introduced into the prescrubber where the excess water is evaporated and crystallization of product occurs.

The process steps of SO_2 absorption and oxidation take place in the dilute liquor phase in the absorber. In the absorber, the flue gas SO_2 reacts with ammonia, which is introduced in gaseous form with the oxidation air. The ammonia is highly reactive and sensitive to pH. The ammonia is stored in a pressurized or refrigerated vessel and pumped as a liquid to a vaporizer. The vaporizer typically uses steam to vaporize the ammonia prior to mixing with the oxidation air.

Oxidation air is introduced into the absorber to oxidize the ammonium sulfite to ammonium sulfate. Ammonium sulfate solution (10 - 25 wt% dissolved solids) is bled from the absorber to the prescrubber to maintain level in the prescrubber tank. The fresh make up water required by the process is added to the absorber reaction tank to maintain tank level.

Exhibit 1-7 shows the process for dewatering the liquid-solids slurry.

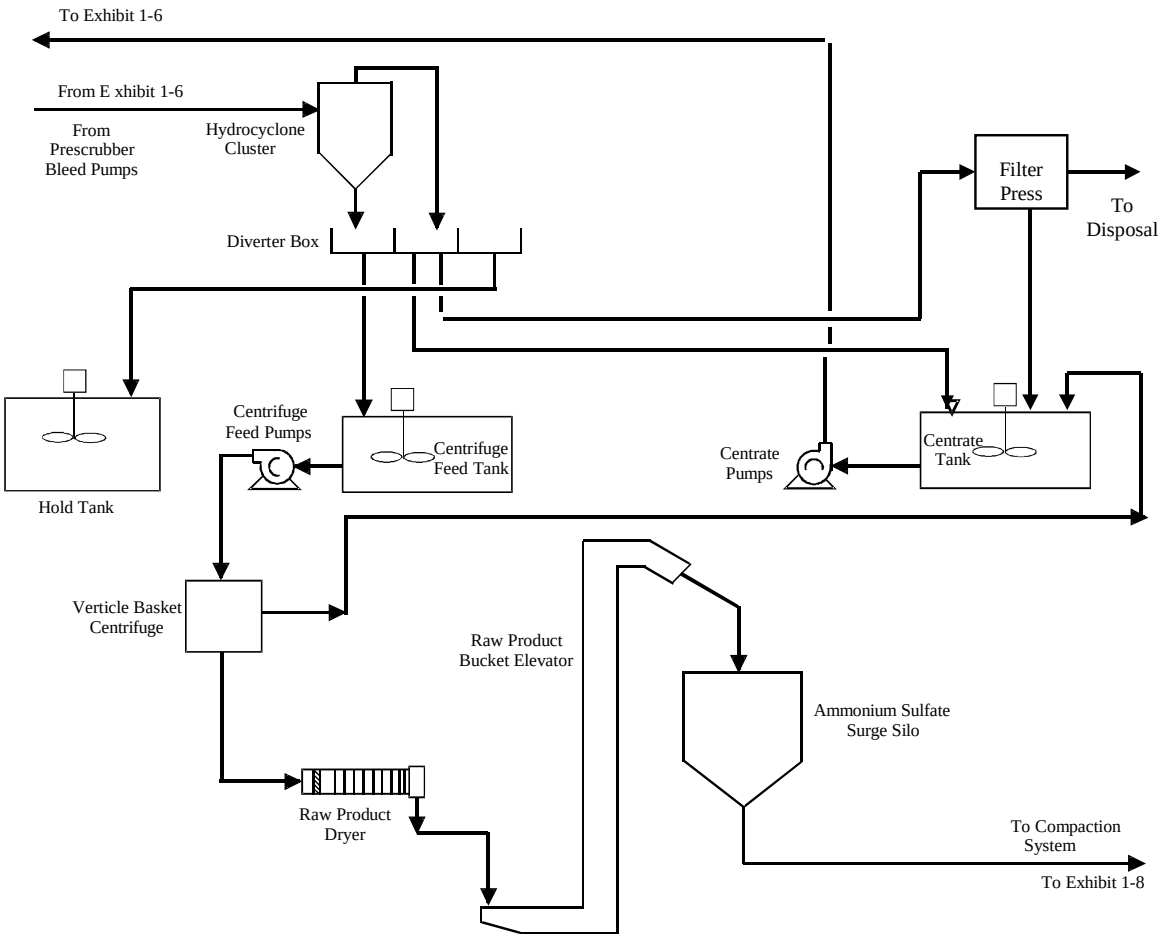

Exhibit 1-7
Ammonia-Based Process Dewatering Area Process

Slurry is bled from the prescrubber to a dewatering hydroclone, which increases solids concentration in the slurry from 10 to 35 wt% solids. The purpose of the hydroclone is twofold: First, the hydroclone dewaters the slurry from the prescrubber to optimize the centrifuge feed slurry density. Secondly, the hydroclone separates the fine particulate (primarily flyash in the flue gas) from the product, thus maintaining product purity. The underflow of the hydroclone is directed via a diverter box to the centrifuge feed tank. The overflow of the hydroclone is diverted to the centrate tank. In the event that the prescrubber solids density is lower than 10 wt%, the hydroclone underflow is combined with the hydroclone overflow and returned to the prescrubber via the centrate tank.

The slurry from the centrifuge feed tank is pumped to a series of basket centrifuges where the slurry is dewatered to 97 - 98% solids. The centrifuges then discharge the material immediately into the rotary drum dryer where heated air is passed over the crystals to dry the material to less than one per cent moisture. The dry material is conveyed to a small surge silo where the material is stored prior to final processing in the compaction system.

To maintain product purity, a portion of the hydroclone overflow can be diverted to a centrate filter press which captures the fine particulate matter, washes it, dewaters it and discharges the filter cake (50 wt% solids) into a bin for disposal.

To maximize the product value, the ammonium sulfate material in the surge silo must be converted from sugar like crystals to the larger granular crystals. To accomplish this, the raw unprocessed ammonium sulfate in the surge silo is fed to the compaction system, which is illustrated in Exhibit 1-8**.** In this system, the fresh feed of ammonium sulfate material is combined with the fine particles from the compaction process and fed to a pug mill mixer to insure that the recycle and fresh feed material are fully mixed prior to entering the compactor. The recycle and fresh feed ratio is controlled to produce the ammonium sulfate product of the desired particle hardness.

The material from the pug mill mixer is fed to a compactor feed screw system that forces the material between the two rolls that compact the solids into a hard flake. The hard flake from the compactor is discharged into a flake breaker which breaks the large flake into smaller pieces. The small pieces are then sized in a series of sizing mills.

The sized material is then fed to a sizing screen which separates the on-size material from the fines. The fines are recycled to the beginning of the compaction process. The on-size product passes through a dryer and then a cooler, which ensure the moisture of the final product to meet the industry standards of less than one per cent. Prior to final storage, the on-size material is passed through a final screening process to insure the final product size of 1 to 3 millimeters. The final on-size product is sent to a large storage dome. From the storage dome, the material is loaded on to either trains or trucks for transportation to market.

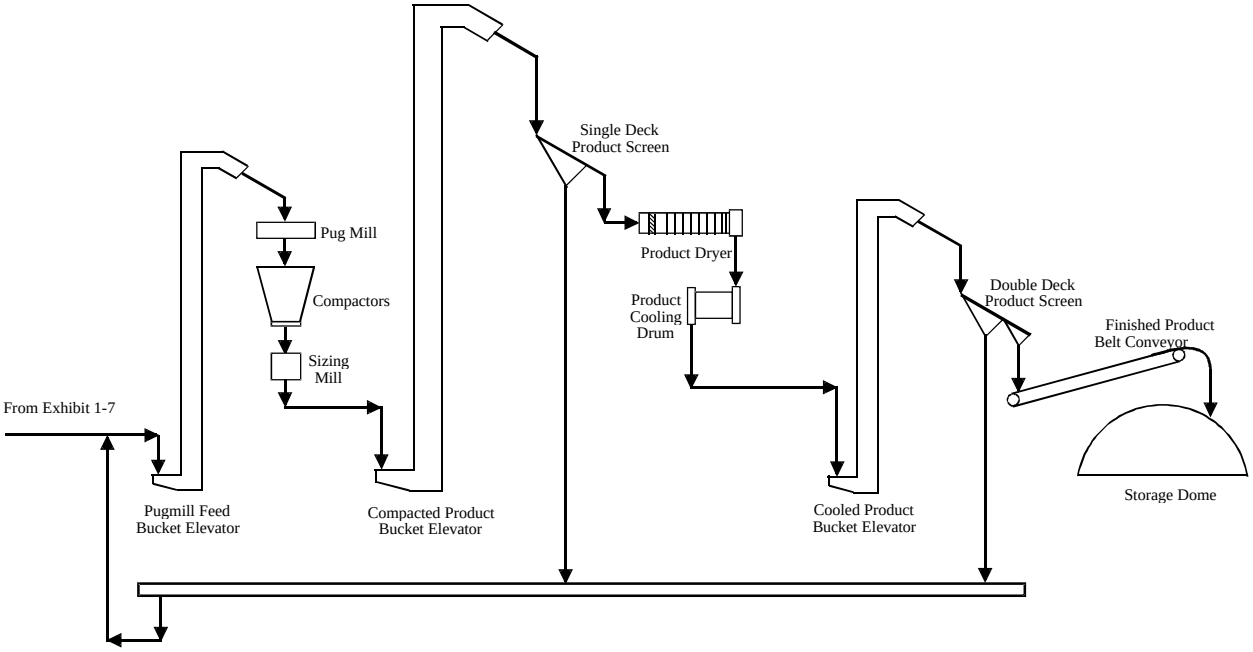

Exhibit 1-8
Ammonia-Based Process Compaction Area Process

Process Chemistry

The SO_2 from the flue gas is absorbed in the spray tower by water and sulfurous acid, H_2SO_3, is formed:

$$SO_2 + H_2O \text{ -----> } H_2SO_3$$

The sulfurous acid, H_2SO_3, then reacts with ammonia to form ammonium sulfite, $(NH_4)_2SO_3$:

$$H_2SO_3 + 2\ NH_3 \text{ -----> } (NH_4)_2SO_3$$

The ammonium sulfite, $(NH_4)_2SO_3$, further reacts with H_2SO_3 to form ammonium bisulfite, $(NH_4)HSO_3$:

$$H_2SO_3 + (NH_4)_2SO_3 \text{ -----> } 2\ (NH_4)HSO_3$$

The ammonium sulfite, $(NH_4)_2SO_3$, also is oxidized in the absorber to form ammonium bisulfate, $(NH_4)_2SO_4$:

$$(NH_4)_2SO_3 + 1/2\ O_2 \text{ -----> } 2\ (NH_4)_2SO_4$$

Similarly, ammonium bisulfite, $(NH_4)HSO_3$, also is oxidized in the absorber to form ammonium bisulfate, $(NH_4)HSO_4$:

$$(NH_4)HSO_3 + 1/2\ O_2 \text{ -----> } (NH_4)HSO_4$$

The ammonium bisulfate, $(NH_4)HSO_4$, can be further neutralized by ammonia to form ammonium sulfate, $(NH_4)_2SO_4$:

$$(NH_4)HSO_4 + NH_3 \text{ -----> } (NH_4)_2SO_4$$

All of these reactions take place in the absorber vessel in a solution phase. The ammonium sulfate is crystallized when the excess water is evaporated in the prescrubber.

4.2 NO_x Reduction Subsystem

The NO_x reduction system is selective catalytic reduction (SCR), which uses a mixture of ammonia vapor and hot air sufficient to maintain the HIPPS NO_x emission rate at 0.06 lb/MM Btu (25.8 ng/J) of total input energy. Aqueous ammonia (28% ammonia by weight) is supplied from ammonia storage and supply system.

Sufficient ammonia injection is required to lower the NO_x emission from 0.3 lb/MM Btu (129 ng/J) from the burners to below 0.06 lb/MM Btu (25.8 ng/J) in the range of 30 to 100% of maximum continuous rating (MCR) of the HITAF. The SCR process is illustrated in Exhibit 1-9.

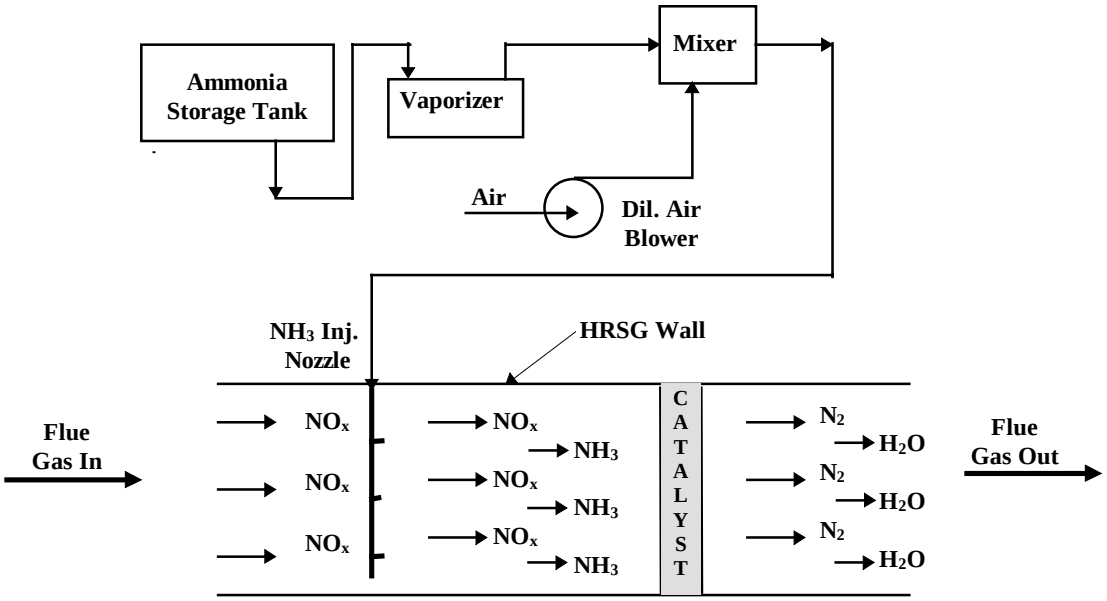

Exhibit 1-9
Typical SCR Process

An initially supplied first layer of SCR catalyst is sufficient for a three year operation period. A second and third layer will be provided in the future to compensate for the spent catalyst. A catalyst management plan permits the SCR to satisfy the NO_x performance requirements for a period of 10 years. The plan is to have the top catalyst layer full and the middle and lower level empty for the first three years. At the end of the year three, a half layer is added to the top of the middle layer, while retaining the same full top layer and the empty lower layer. At the end of 6.5 years, another half layer is added to the middle layer making it a full layer, while retaining the same full top layer and the empty bottom layer. This arrangement remains to achieve the ten year performance.

The ambient air design temperature is 60 °F (15.6 °C). The operating temperature of flue gas leaving the air preheater is 300 °F (149 °C). The SCR is designed to reduce the NO_x level to 0.06 lb/MM Btu (25.8 ng/J) heat input with less than 5 ppmvd ammonia slip at 7% O_2 on a three hour average. SO_2 to SO_3 conversion through the SCR catalyst will be less than 1%.

Ammonia Storage and Transfer System

The ammonia storage and supply system stores and supplies liquid aqueous ammonia to the SCR unit for the pulverized coal-fired HITAF. The ammonia system is designed to provide aqueous ammonia (28% by weight of ammonia) to the SCR system.

The ammonia tank and pump skid are installed outdoors. The ammonia tank is designed per ASME Section VIII requirements. The 25 psig (274 kPa) design pressure is based on maximum vapor pressure corresponding to tank liquid temperature of approximately 140 °F (60 °C) to account for heat gain from the solar heat gain in the tank. The ammonia unloading, storage tank, and supply pump areas are designed to contain any ammonia spills.

The ammonia supply pumps are gear type pumps with magnetic drive/coupling to eliminate the need for shaft seals and thus minimize leakage of ammonia.

The ammonia tank material is carbon steel with 1/8" (0.32 cm) corrosion allowance. Piping is A312 stainless steel. The ammonia pumps are made of corrosion resistant composite material "PPS" (reinforced polyphenylylene sulfide)

The ammonia storage and transfer system consists of the following:

- Truck unloading rack to one aqueous storage tank
- Two skid mounted 100% capacity aqueous ammonia supply pumps
- Associated piping, valves and instrumentation

The truck rack is provided with a liquid fill line to unload aqueous ammonia from the delivery truck to the storage tank. The rack also has a vapor balance line that allows equalization of pressure between the vapor space of the storage tank and the vapor space of the delivery truck to facilitate unloading of aqueous ammonia. The liquid fill line enters the storage tank from the top.

The storage tank has a useable storage capacity of 15,000 gallons (56.8 m^3) and has a vapor space to contain any vapor released from the aqueous ammonia. The vapor pressure inside the tank varies with ambient temperature accordingly, the storage tank is provided with a vapor pressure relief/vacuum breaker vale. The tank is provided with access ladders and platforms, and is shop painted white on the exterior surface.

The two 100% capacity ammonia supply pumps are skid mounted complete with drive motors, motor starters, instruments and controls. Instruments and controls are provided to operate the ammonia system automatically, allowing local supervision and control by a plant operator and remote monitoring.

The ammonia system operates on a continuous basis to supply aqueous ammonia to the SCR system during operation of the HITAF. The storage tank is approximately 15 days' storage capacity to support the HITAF operating at full load. The tank can be replenished with aqueous ammonia by ammonia delivery trucks having a capacity of 8,500 gallons (32.2 m^3) each in an 8-hour shift.

5.0 Solids Material Handling

5.1 Coal Feed Subsystem

The coal feed system supplies the burners with pulverized coal and primary air. The hot primary air comes from the air preheater located in the HITAF HRSG. A natural gas igniter system is used to ignite the coal during HITAF startup, or to stabilize the flame during normal operation. Each pulverizer is furnished with structural attachments, a pulley and a motorized wire rope hoist suitable for safely removing and maintaining pulverizer rollers.

The coal feeders are operated and monitored from the burner management system (BMS) and locally from the control panel.

There are three 50% capacity pulverizers. Two pulverizers operate to fire two furnaces. The third pulverizer is a common standby spare. A description of the nominally selected pulverizer (Riley MPS) is given below.

The Riley MPS pulverizer is a vertical mill with a rotating classifier and hydraulic roller loading. Raw coal, which is pulverized between the rollers and ring, is fed through a central coal inlet at the top of the pulverizer and falls by gravity to the rotating grinding table. Centrifugal action forces the coal outward to the grinding ring where it is pulverized between the ring and three grinding rollers.

A nozzle ring on the outer perimeter of the grinding ring feeds primary air to the pulverizer. Primary air enters the mill through an aerodynamically-ported nozzle. The swirl induces larger particles to return to the grinding track. During this first stage of classification, fine particles are carried upward in the housing in the stream of air and coarse particles fall back to the table for grinding. In the second stage of classification, the air velocity decreases and larger particles drop out. In the final stage of classification, those particles which are sufficiently pulverized for transport to the burners are separated from the rest and sent to the burners. The others are returned to the grinding zone. The technical data for this mill are as follows:

- Mill type: ring-roller mill with internal classifier
- Mill model: 170 MPS
- Mill motor: 400 HP
- Air pressure drop: 8 - 10 in (20.3 – 25.4 cm) w.c.
- Mill weight: 191,000 lb (86,639 kg)
- Mill foot print: 16 ft by 18 ft (4.9 m by 5.5 m)

5.2 Coal Handling Subsystem

The function of the coal handling system is to receive, store, process and supply coal to meet fuel requirements for the HITAF unit operating at maximum continuous rating.

The coal handling system is designed to support a HITAF firing rate of 62.3 tph (56.5 tonne/h). The coal specifications are listed below. Some items have been altered from the EPRI TAG™ list of criteria to reflect changes in the power generation industry.

- Bituminous coal size distribution
- As received 2” x 0” (5.08 x 0 cm) nominal; passing 1/4” (.64 cm, 50% max.
- After crushing 1-1/4” x 0”, 3/4” nominal
- Bulk densities, lb/ft^3 (kg/m^3)
- For volumetric calculations for:
- hoppers, bins and silos 50 (801)
- conveyor speed sizing 50 (801)
- For conveyor drive calculations 60 (961)
- For structural calculations 65 (1041)
- Flowability angles, degrees
- Angle of repose 38
- Surcharge angle 20
- Drawdown angle 45

Coal unloading capabilities are based on receiving three unit trains of coal every two weeks with each car having a rated capacity of 100 tons (91 tonnes) and an average capacity of 98 tons (89 tonnes). The system is designed to unload each train (85 cars maximum) in approximately eight hours.

The coal storage building is sized to enclose an approximate 16,000-ton (14,500 tonnes) pile of coal. The pile capacity represents an approximate 10-day plant operation requirement. Reclaimed coal can be transferred to two coal silos to provide a supply capacity of 16 hours when both silos are in use.

The system design includes equipment to divert/store/reclaim coal using an emergency stackout pile. The pile is located outdoors and sized to accommodate up to 15 carloads of incoming coal. The same equipment is also capable of establishing an inactive coal pile, representing a 30-day coal requirement.

Coal is delivered to the coal handling system by train in bottom dump rail cars. The rail cars are pulled into the unloading building by a locomotive and individually spotted over the unloading hoppers where the cars are unloaded. Coal is removed from the hoppers by two 27 inch (69 cm) wide unloading belt feeders and is discharged to a 24 inch (61 cm) unloading conveyor. The unloading conveyor transfers coal to a transfer tower where the coal can be discharged either to the active coal storage building via a 24 inch (61 cm) wide stacking conveyor and its associated traveling belt tripper, or to an emergency stackout pile via a 48 inch (122 cm) wide emergency stackout conveyor and its associated telescopic chute.

Coal is reclaimed from the emergency stackout pile using mobile equipment discharging into an emergency reclaim hopper and 48 inch (122 cm) wide emergency reclaim belt feeder. The emergency reclaim belt feeder discharges the coal into the coal storage building forming an active storage pile. Coal is reclaimed from the active storage pile using a portal scraper/reclaimer which discharges to a 18 inch (46 cm) wide reclaiming conveyor. The reclaiming conveyor conveys the coal to a transfer point where the coal is discharged to either or both of two 12 inch (30 cm) wide crusher feed conveyors.

In the event that the portal scraper/reclaimer is out of service, coal is reclaimed from the active storage pile using mobile equipment and discharged into an emergency reclaiming hopper and 18 inch (46 cm) wide emergency reclaiming conveyor. The emergency reclaiming conveyor discharges the reclaimed coal on to only one of the two 12 inch (30 cm) wide crusher feed conveyors. The two crusher feed conveyors convey the coal to the crusher building and discharge into the crusher surge bin. Coal is discharged from the surge bin on to the two 24 inch (61 cm) wide crusher belt feeders with each feeding a separate coal crusher. The crushers are fitted with diverter gates which allow the coal to be diverted past either crusher. The crushed (or bypassed) coal is then discharged to either of the two 12 inch (30 cm) wide plant feed conveyors which convey the coal to the boiler building. The plant feed conveyors discharge the coal to a 24 inch (61 cm) wide silo feed conveyor and its associated traveling belt tripper. The traveling belt tripper sequentially discharges the coal into four coal storage silos.

5.3 Bottom Ash/Slag Handling System

The bottom ash/slag handling system collects the bottom ash/slag discharged from the HITAF bottom and conveys it to the bottom ash/slag bunker for storage and disposal.

A submerged mechanical flight conveyor and a transfer belt conveyor in series are used to convey bottom ash/slag to the bottom ash/slag bunker at a design removal rate of 3 tons/h (2.7 tonnes/h) with a catch-up removal rate of 6 tons/h (5.4 tonnes/h). The system is designed to operate continuously and to have adequate storage to allow for normal maintenance without interrupting HITAF operation. The bottom ash/slag conveyor seal trough maintains a water seal against HITAF differential pressure.

The conveyors are capable of starting from rest with 8 hours of ash/slag accumulation. Conveying equipment is designed for services at the following conditions:

Ash/slag bulk densities:

- For volumetric calculations 55 lb/ft^3 (881 kg/m^3)
- For mechanical drive calculations 75 lb/ft^3 (1201 kg/m^3)
- For structural calculations 120 lb/ft^3 (1922 kg/m^3) (drag chain conveyor)
- 90 lb/ft^3 (1442 kg/m^3) (transfer conveyor)

Design for the bottom ash/slag handling system is based on continuous operation and employs a mechanical ash/slag removal system for bottom ash/slag evacuation. Bottom ash/slag is discharged by gravity from the HITAF into the submerged drag chain conveyor. The submerged drag chain conveyor is designed for removal and transport of bottom ash/slag to the bottom ash/slag transfer conveyor. The drag chain conveyor consists of a water filled trough through which steel flight bars connected by chains are pulled. The ash/slag is quenched by the water, thereby breaking up large ash/slag agglomerations. The ash/slag is pulled along by the flights and up an inclined section prior to discharge to the transfer conveyor. The incline allows the ash/slag to dewater, thus reducing the amount of makeup water required.

The dewatered ash/slag from the inclined section of the drag chain conveyor discharges on to a 24 inch (61 cm) wide belt transfer conveyor with a hood cover. The transfer conveyor has a 6 tons/h (5.4 tonne/h) maximum capacity and will unload the dewatered ash/slag into an enclosed bottom ash/slag bunker sized to accommodate an 8-day ash/slag capacity. A front end loader will enter through the bunker's roll-up door to reclaim and load the stored ash/slag into rail cars (the rail cars are part of the incoming coal and outgoing ash/slag trains).

The bottom ash/slag hopper is furnished with wheels and rails running perpendicular to the conveyor travel. This allows the hopper to be moved from under the HITAF for maintenance. The drag chain conveyor is designed to allow routine repairs without removing the assembly from the HITAF (i.e., with the HITAF remaining on line). Items that can be maintained in this manner include:

- Chain tensioning and aligning
- Motor repairs
- Sprocket repairs
- Take-up mechanism repairs
- Accessible chain flight repairs

The drag chain conveyor can remain shut down while HITAF continues to operate, until the ash/slag buildup approaches the hopper capacity. The drag chain conveyor is designed to start from rest when fully loaded with ash/slag (8 hours).

Makeup water is used to provide a sufficient water level in the seal trough for maintaining a water seal against the HITAF operating pressure and to also limit the water temperature in the horizontal section of the submerged drag chain conveyor to a maximum of 140 °F (60 °C).

5.4 Flyash Handling Subsystem

The fly ash handling system removes flyash that has been collected in various hoppers and conveys the flyash via a pneumatic conveying system to a storage silo for storage and disposal. The system encompasses the removal of ash from baghouse hoppers, air heater hopper and superheater hopper. Each hopper is furnished with level sensors providing a signal to the ash handling controls.

The design conveying capacities for the flyash removal system is based on total ash removal through the use of two simultaneously operating 25 tons/h (22.7 tonne/h) vacuum systems. Conveying equipment is designed for services at the following flyash design densities:

- For volumetric calculations 40 lb/ft^3 (641 kg/m^3)
- For mechanical drive calculations 60 lb/ft^3 (961 kg/m^3)
- For structural calculations 90 lb/ft^3 (1442 kg/m^3)

Flyash removal from the above mentioned hoppers is by direct introduction into the pneumatic vacuum system through ash intake assemblies. The system generates an air pickup velocity of not less than 3,800 fpm (19.3 m/s) for flyash at any point in the conveying pipeline. The flyash from the baghouse hoppers is directed to the ash silo. The ash passes through receiving/separating equipment before being discharged into the silo. The designed net capacity of the flyash storage silo is a nominal 2000 tons (1,814 tonnes) and is based on providing a 7-day ash storage at full load operation. The rate of unloading ash from the storage silo is a minimum 125 tons/h (113 tonne/h).

The flyash handling system is designed to convey ash from ash hoppers to a storage silo. A vacuum system transports the ash from the hoppers to the collectors by having outside air drawn into the pipeline through the air intake valve at the beginning of each branch line. The ash intake valve under the hopper to be evacuated opens up and ash is introduced into the pipeline and carried by the air flowing with a minimum pickup velocity of 3,800 fpm (19.3 m/s). The ash and air mixture coming from all ash intake valves reaches the collector in a very short time and enters the separator section where, due to sudden volume expansion, the ash velocity drops abruptly and approximately 85 to 90% of the ash falls down into the collector. The ash particles suspended in the carrying air are retained by the filter bags as the clean air continues its way toward the vacuum blowers located on the unloader floor.

The flyash silo receives and temporarily stores fly ash. As fly ash falls into the silo from the collector, displaced air exits through a bag vent filter. Heated air is introduced into the bottom of the silo through aeration slide assemblies that are arranged in a radial array around unloading ports in the silo floor. The ash is unloaded into pressure differential rail cars (or, as an option,

into enclosed trucks) using dry dust unloaders with a capacity of 125 tons/h (113 tonne/h). A vent fan is connected to the chute to return any fugitive dust to the silo.

6.0 Process Water Systems

6.1 Demineralized Water Subsystem

The demineralized water system produces high purity makeup water for the condensate transfer and storage system to meet HITAF boiler and other miscellaneous needs. During normal operation, the demineralizer feedwater system is required to meet the following concurrent demands for demineralized water:

- Boiler blowdown 20 gpm (4.54 m^3/h)
- Miscellaneous condensate demands 60 gpm (13.63 m^3/h)
- Total 80 gpm (18.7 m^3/h)

However, the system is designed to supply 190 gpm (43.1 m^3/h) to meet the startup and emergency demands. The demineralizer feed tank is designed to provide a surge capacity for demineralizer's normal operation of 100 minutes.

A flow diagram of the system is shown in Exhibit 1-10. There are two trains: One train is operating while the second train is being regenerated. Only one train is shown on the figure. Water from the demineralizer feed tank is pumped to a multimedia filter to remove particles as small as 10 microns. The filter contains a multi-layer bed with a coarse top layer of anthracite, an intermediate layer of quartz filter sand and a fine bottom layer of garnet. The bed structure causes particulate to be trapped in all the three beds.

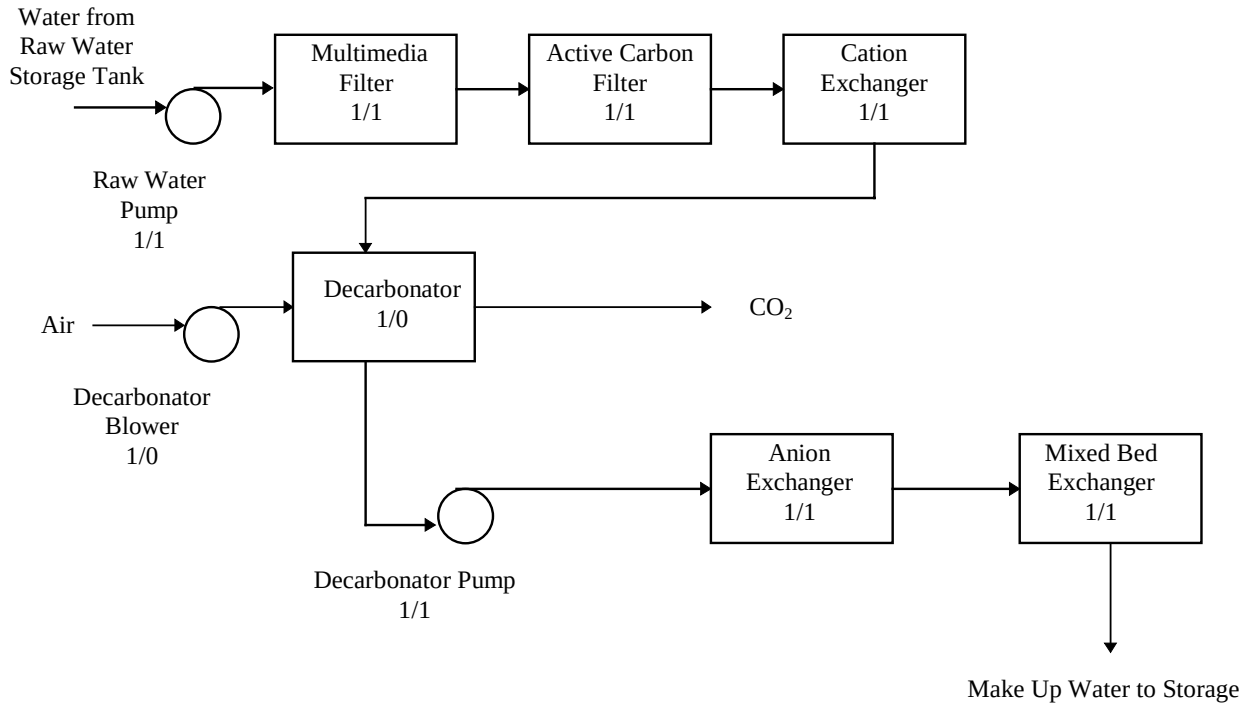

Exhibit 1-10
Demineralized Water System

The filtrate from the multimedia filter is directed to an activated carbon filter. This filter contains a bed of activated carbon to absorb chlorine and organic matter from the water. Chlorine is removed to prevent it from oxidizing the ion exchange resin, or certain types of reverse osmosis membranes, which would reduce their performance. Organic matter is removed to avoid fouling ion exchange resins or reverse osmosis membranes.

The filtrate from the activated carbon filter is sent to a strong acid cation exchanger. The cations, such as calcium, magnesium and sodium, are removed in this exchanger by the following ion exchange reaction:

$$H_2Z + CaSO_4 \text{ -----> } CaZ + H_2SO_4$$

where the cation resin is denoted by Z. The decationized water from the cation exchanger is sent to a forced draft decarbonator.

In the decarbonator, CO_2 is removed from the water by contacting air supplied by the decarbonator blower. The forced draft decarbonator unit reduces carbon dioxide by more than 90%. CO_2 is removed from the water to prevent it acting as an anion, and thereby increasing the ionic load of the anion exchanger. An increased ionic load would require a larger anion exchanger, increased regenerating reagent (sodium hydroxide) consumption and would produce more waste water.

The decarbonated water is pumped to an anion exchanger where anions such as bicarbonates, sulfates, chlorides and soluble silica are removed by the following ion exchange reaction:

$$H_2SO_4 + 2R.OH \text{ -----> } R.SO_4 + H_2O$$

where R is the anion removing resin.

After treatment in the two ion exchangers, the mostly deionized water is sent to a mixed bed ion exchanger. The mixed bed ion exchanger contains strong acid cation and strong base anion resins thoroughly mixed together in a single unit. Because of the mixture, the mixed bed process is comparable to having many pairs of cation and anion exchangers arranged in series. In the mixed bed ion exchanger, the water contacts pairs of cation and anion resin beads as it passes through the bed. When the water contacts the resin bead pairs, it is repeatedly deionized, and each contact reduces the level of ionic contamination. Thus, the mixed bed ion exchanger polishes the water after a primary deionization by separate cation and anion exchangers. The polished water is sent to a demineralized water storage tank.

When the operating train's exchangers' deionization performance is exhausted, they are replaced by the second train's fresh ion exchangers. The exhausted ion exchangers are regenerated with 3% to 6% solutions made from the following regenerating agents:

- Cation exchanger 93% H_2SO_4
- Anion exchanger 100% NaOH
- Mixed bed exchanger 93% H_2SO_4 and 100% NaOH

Regeneration wastes from the mixed bed vessels are directed to the water treatment building's chemical waste sump. The demineralized water system consists of the following items:

- Demineralizer feed tank
- Three 100% capacity multimedia filter feed pumps
- Two 100% capacity multimedia filter vessels
- Two 100% capacity active carbon filter vessels
- Two 100% capacity cation exchange vessels
- One 100% capacity decarbonator blower
- One 100% capacity decarbonator
- Two 100% capacity decarbonator pumps
- Two 100% capacity anion exchange vessels
- Two 100% capacity mixed bed vessels
- Bulk acid storage tank
- Two 100% capacity acid feed pumps
- Bulk caustic storage tank with heater
- Two 100% capacity caustic feed pumps
- Two 100% capacity regeneration water pumps
- Caustic dilution water heater tank with heater
- Associated piping, valves and instrumentation

The bulk acid and caustic tanks, acid and caustic feed pumps, and regeneration water pumps are part of the regeneration system. During normal operation, one of the demineralizer feed pumps takes suction from the demineralizer feed tank and directs water through the in-service demineralizer train to the condensate storage tank. Flow to the demineralizer train is controlled by the level in the condensate storage tank.

6.2 Condensate Polisher Subsystem

The condensate polisher system removes impurities from the condensate water prior to it entering the feedwater heater. Removal of the impurities minimizes scale formation and fouling of equipment in the condensate, feedwater and boiler systems. Condensate from the condenser is pumped by the condensate pumps through the polisher vessel before entering the feedwater heater train. The condensate polisher uses a precoat media (ion exchange resin and/or fibrous material) to simultaneously filter suspended solids impurities and remove dissolved solid impurities from the condensate. An advance precoat system is furnished as an integral part of the polisher system and is used to remove exhausted resin from the polisher vessel and to apply fresh resin to the vessels.

The condensate polisher system is designed to remove suspended and dissolved impurities from the condensate flow. The condensate polisher vessels are each designed to purify the design condensate flow of 1,700 gpm (386 m^3/h). The maximum pressure drop through the system is 40 psi (276 kPa).

The media used in the condensate polisher has an extremely fine particle size (30-80 micron). The media is applied to cylindrical elements within the polisher vessel which act as septa. The small pore size of the resulting precoat acts as a filter to remove suspended solids. Many types of media are available with varying ratios of inert fibrous material to ion-exchange resin. The ratio of cation to anion exchange capacity for the resin can also be adjusted. The media is selected based on the operating conditions. Normally a cation resin in the ammonia form and an anion resin in the hydroxide form are used, with a cation to anion ratio between 2:1 and 1:1. The thickness of the precoat on the septa can also be varied depending upon the suspended solids loading. To keep the precoat on the septa, each vessel is equipped with a hold pump to provide a minimum flowrate of water through the vessel.

The advance precoat system is designed to remove exhausted resin from and apply fresh resin to the septa. The amount of resin used in the vessels is sufficient to allow system operation for 14 days under normal conditions before the resin is exhausted. The condensate polisher system consists of the following items.

- Two 100 percent capacity condensate polisher vessels
- Two 100 percent capacity hold pumps (one pump for each polisher vessel)
- Precoat injection pump
- Recycle pump
- Advance precoat tank with mixer
- Auxiliary tank, an air surge tank
- Four sample coolers
- Associated piping valves and instrumentation.

The precoat injection pump, recycle pump, advance precoat tank, auxiliary tank and air surge tank are all part of the advance precoat system. Analytical instrumentation monitors system performance and alerts the operator when the in-service vessel must be taken out of service.

At 100 percent capacity operation, condensate from the condenser is pumped by two of the condensate pumps through the in-service polisher vessel to feedwater heater. Suspended and dissolved solids impurities in the condensate are removed by the media in the polisher vessel.

Each condensate polisher vessel contains 200 cylindrical elements upon which the media (precoat) is built up and maintained. To keep the precoat on the septa, each vessel is equipped with a hold pump which starts automatically when the condensate flowrate through the vessel falls below a preset minimum. The hold pump takes suction from the vessel discharge piping and discharges flow to the vessel inlet piping, creating recirculation of flow through the vessel.

When the ion exchange capacity of the media in the vessel is exhausted, or the pressure drop across the vessel exceeds the design point due to suspended solids buildup, the vessel is taken out of service and the exhausted resin removed by backwash.

Water for the backwash and precoating steps is obtained from the condensate transfer pumps. Backwash waste from the condensate polisher vessel along with wastes from the advance precoat

tank and auxiliary tank are directed to the condensate polisher backwash sump and forwarded to the wastewater system.

6.3 Raw Water Subsystem

The raw water supply system furnishes makeup water to the plant by pumping river water from the river intake to the cooling water pond or directly to the water softener. A flow diagram of the system is shown in Exhibit 1-11.

The raw water consumers are as follows.

- Evaporative loss in the cooling tower
- Water consumed in the flue gas cleaning system
- Evaporative loss in the cooling water storage pond, wastewater storage pond and coal pile runoff basin

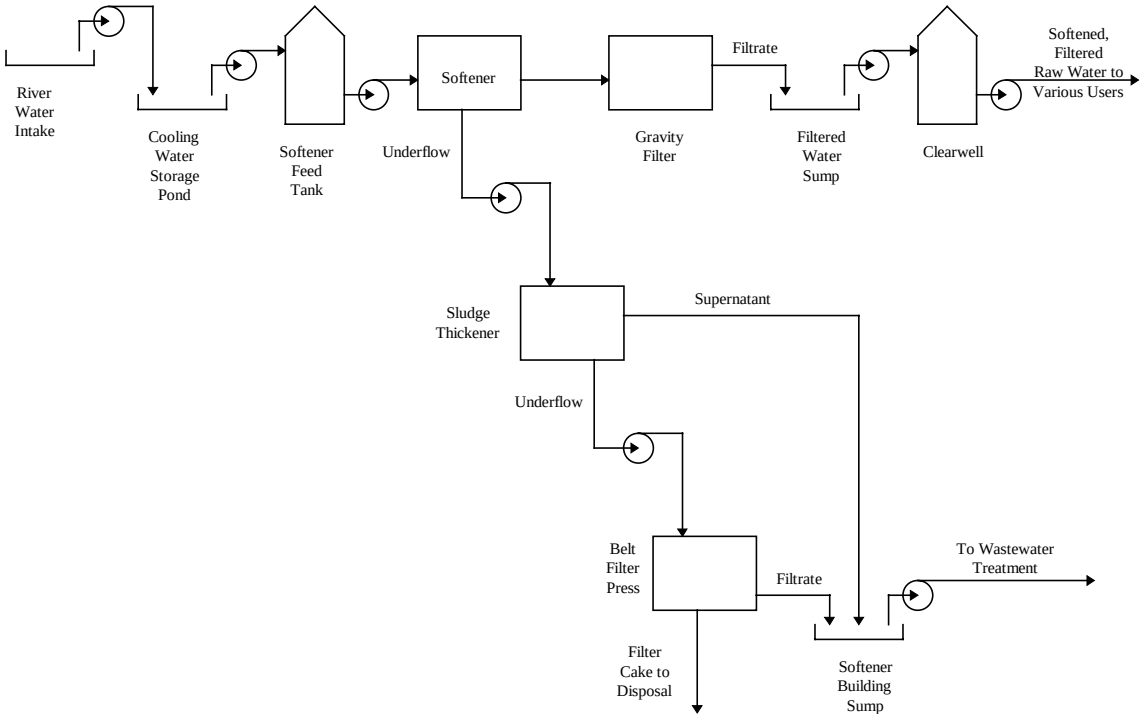

Exhibit 1-11
Raw Water and Water Softener System

Along with the plant makeup water, suspended and dissolved solids are brought and must be managed to prevent scaling or plugging of piping and equipment. The sinks for suspended and dissolved solids include:

- Filter cake from the softener system
- Dissolved solids in the cooling tower drift
- Residual solids which collect in basins and sumps

Raw water from the river is treated in the softener and gravity filter for use as cooling tower makeup and filtered water.

The cooling water pond pumps are designed to meet the following concurrent demands:

- Evaporative losses in cooling tower 1,500 gpm (341 m^3/h)
- FGD process 200 gpm (45 m^3/h)
- Miscellaneous 300 gpm (68 m^3/h)
- Total 2,000 gpm (454 m^3/h)

The average demand from either the river pumps or the cooling water storage pond pumps is about 2,000 gpm (454 m^3/h). The softener feed pumps are sized to meet the design flowrate of the softener system or 2,000 gpm (454 m^3/h). The softener feed tank is designed to provide one hour of surge capacity at the design softener feed pump flow. The clearwell transfer pumps are designed to meet the same demands as for the cooling water pond pumps.

The cooling tower blowdown rate used to size the clearwell transfer pumps is equivalent to the cooling tower operating at about 4 cycles of concentration (COC) to allow for the periods of high blowdown to correct circulating water chemistry problems. The clearwell is designed to provide one hour of surge capacity at the design filtered water feed pump flow.

Sodium hypochlorite is injected to control biofouling in the softener feed tank and softener system. The makeup water sodium hypochlorite metering pumps are designed to inject up to 10 ppm dose of sodium hypochlorite. The makeup water sodium hypochlorite storage tank is designed to provide two weeks of storage (the approximate shelf life of sodium hypochlorite) at a 5 ppm dose. Sodium hypochlorite is typically purchased as a 12-15 trade percent solution, which degrades rather quickly in high temperatures. Sodium hypochlorite is injected via an injection quill into the makeup water piping before it enters the softener feed tank.

The raw water supply system consists of the following items.

- Two 100% capacity river intake screens
- Two 100% capacity river pumps
- Two 100% capacity cooling water storage pond pumps
- Softener feed tank
- Two 100% capacity softener feed pumps
- Clearwell
- Two 100% capacity clearwell transfer pumps
- Two 50% capacity river air receivers
- Makeup water sodium hypochlorite storage tank
- Two 100% capacity makeup water sodium hypochlorite metering pumps
- Associated piping, valves and instruments.

The river pumps take suction from the river intake and discharge into the pipeline to the plant. An air burst system is provided to backwash the screens at the river water intake. The makeup water from the river is directed either to the cooling water storage pond (or if needed directly to the softener). The cooling water storage pond pumps take suction from the intake structure in the pond and discharge into the softener feed tank.

The softener feed pumps take suction from the softener feed tank and supply water to the softener. Product water from the softener system is pumped by the gravity filter transfer/backwash pump to the clearwell, which stores the softened water. The clearwell transfer pumps transfer softened water from the clearwell to the cooling tower.

The river intake, pumps and pipeline are not included in the cost estimate's scope. Water and the other services; natural gas, liquid fuels and grid power are assumed to available at the plant fenceline.

6.4 Softener Subsystem

The softener system reduces the concentration of iron, calcium, magnesium, silica, alkalinity and suspended solids in water for use as cooling tower makeup and filtered water. Water from the softener feed tank is pumped to the softener. Product water from the softener is treated in the gravity filter and transferred to the clearwell. Sludge removed by the softener is thickened and dewatered for disposal. A flow diagram of the system was shown with the raw water system in Exhibit 1-11.

The softener system is designed to meet the following concurrent demand of the circulating water system and filtered water system.

- Cooling tower evaporative losses 1,500 gpm (341 m^3/h)
- Cooling tower blowdown 300 gpm (68 m^3/h)
- Flue gas cleanup 200 gpm (45 m^3/h)
- Total 2,000 gpm (454 m^3/h)

The softener is a solids contact clarifier with a maximum overflow rate of 1.25 gpm/ft^2 (3.05 $m^3/h/m^2$) at the effluent launders. Water fed to the softener is mixed with hydrated lime, soda ash, and a polymer (which aids in coagulating the precipitated solids). In addition to these primary chemical feed systems, a coagulant feed system is provided to feed ferric sulfate to enhance coagulation.

The lime feed system is designed to feed up to 400 lb/h (181 kg/h) of 93% powdered hydrated lime at a minimum density of 35 lb/ft^3 (561 kg/m^3). Similarly the soda ash feed system is designed to feed up to 675 lb/h (306 kg/h) of 98% soda ash at a minimum density of 65 lb/ft^3 (1042 kg/m^3). Both chemicals are fed as 20% solutions. The lime and soda ash storage silos are designed to provide 5 days of storage at the design usage rate.

The sludge thickener is designed for a loading of 50 lb solids/ft^2/day (244 kg/m^2/day) and to achieve a thickened sludge concentration in the range of 7-15% solids. The belt filter press is designed to dewater 25,000 lb/day (11,340 kg/day) of dry solids in the thickened sludge to 40% dry solids over a period of 16 hours. The gravity filter is designed so that the flowrate through each filter cell is no higher than 4.5 gpm/ft^2 (11 m^3/m^2-h) at the design flowrate of 2,000 gpm

total (4893 m^3/m^2-h). The backwash system is capable of providing a flowrate of up to 20 gpm/ft^2 (48.9 $m^3/h/m^2$) to remove accumulated solids.

The softener system consists of the following items

- Softener
- Two 100% capacity softener sludge pumps
- Eight 12.5% capacity gravity filter cells
- Two 100% capacity filter air scour blowers
- Three 100% capacity gravity filter transfer/backwash pumps
- One sludge thickener
- Two 100% capacity belt press feed pumps
- One belt filter press
- Associated chemical feed systems, piping, valves and instrumentation.

The lime feed system consists of these items:

- Lime volumetric feeder
- Lime dilution tank
- Lime slurry pumps located within an enclosed skirt at the base of the lime storage silo which is equipped with a dust collector, lime vibrator unloader. The enclosure is equipped with a heater and a vent fan.

The soda ash feed system consists of the following.

- Soda ash volumetric feeder
- Soda ash dilution tank
- Soda ash slurry pumps located within an enclosed skirt at the base of the soda ash storage silo which is equipped with a dust collector, soda ash vibrator unloader, soda ash delumper. The enclosure is equipped with a heater and a vent fan.

The coagulant feed system consists of a coagulant feed tank and coagulant feed pumps. The polymer feed for the softener is self-contained system that dilutes and conditions polymer, then pumps it to the softener. The sulfuric acid feed system consists of an acid storage tank and sulfuric acid transfer pumps.

Spray water booster pumps are provided to supply high pressure spray water to the belt filter press. The polymer feed for the belt press is a self-contained system that dilutes and conditions polymer, then injects it into the feed line to the belt filter press.

During normal operation, water from the softener feed tank is pumped by the softener feed pumps to the softener. The water is vigorously mixed with the feed chemicals (lime, soda ash, polymer and/or coagulant) to precipitate the hardness ions and alkalinity. From the mixing well, the water flows to a quiescent zone where the suspended particles settle to the bottom. Softened water flows out of the softener through an effluent weir to the gravity filter, while the settled

solids are scraped to a sludge pit in the center of the softener. At the gravity filter, the softened water is distributed to the individual cells (normally all eight cells in service) and flows down through the filter media to the filtered water sump, from where the water is pumped to the clearwell. When the pressure drop through a cell rises above a setpoint (determined by high water level above the media), the cell is taken out of service and backwashed. Backwash water is obtained from the discharge header of the gravity filter backwash/transfer pumps. Each filter cell is expected to be backwashed about once a day when the clarifier is operating effectively. Underflow from the softener is pumped to the sludge thickener. A long residence time in the sludge thickener allows the solids to further thicken. Supernatant from the sludge thickener overflows to the softener building sump. Thickened sludge is periodically pumped to the belt filter for dewatering.

6.5 Condensate, Feedwater, and Circulating Water Chemical Addition Subsystem

The chemical addition system is used with the operation of several other systems:

- Circulating water system
- Service water system
- Condensate system
- Feedwater system
- Auxiliary boiler system

The boiler chemical additives control corrosion and prevent formation of deposits and scale in the boiler feedwater and condensate systems. The purpose of the circulating water chemical additives is to prevent scale formation and inhibit biological growth in the circulating service water systems. These functions are accomplished by feeding chemicals to the systems at the proper location in the appropriate amounts.

Boiler Chemical Addition

The boiler chemical additives control pH and dissolved oxygen in the boiler feedwater system. The additives work with the condensate polisher system to control silica and metals concentration in feedwater system piping. The additives also remove any alkalinity which may be present and prevent deposition of hardness scale species (calcium, magnesium and iron) on boiler tubes.

A coordinated pH/phosphate program is utilized to accomplish the feedwater and boiler water control. The boiler chemical additive consists of a blend of phosphate and polymer dispersant, volatile oxygen scavenger and a blend of neutralizing amines. The phosphate additive system is designed to feed 0.5 ppm concentrated phosphate solution to the steam drum. A dilution tank is provided to allow a greater range of feed rates ad reduce the chance of clogging the feed line with the concentrated solution. The dilution tank is sized to provide up to 24 hours of a 2% solution to the boiler. The phosphate storage tank is sized to provide six months storage capacity for the boiler usage.

The oxygen scavenger feed system is designed to feed 0.1 ppm of an ascorbic acid solution to either the suction piping of the feedwater booster pump or the condensate pump discharge piping.

The oxygen scavenger solution is fed (without diluting) to the injection point. The oxygen scavenger storage tank is sized to provide two months storage capacity for the boiler usage.

The neutralizing amine feed system is designed to feed 1.0 ppm of blended amines to the condensate pump discharge piping. The neutralizing amine solution is fed (without diluting) to the injection point. The neutralizing amine storage tank is sized to provide two months storage capacity for the boiler usage.

Boiler Chemical Additive

Boiler chemical treatment includes a number of operations.

- Neutralizing amine additive system
- Oxygen scavenger additive system
- Phosphate additive system

The neutralizing amine feed system includes the following.

- Neutralizing amine storage tank
- Two 100% capacity HITAF boiler neutralizing amine metering pumps
- One auxiliary boiler neutralizing amine metering pump
- Associated piping, valves and instrumentation

During normal operation, one of the neutralizing amine metering pumps draws the neutralizing amine from the neutralizing amine storage tank and injects into the discharge piping of the condensate pump.

The oxygen scavenger feed system includes the following.

- Oxygen scavenger storage tank
- Two 100% capacity HITAF boiler oxygen scavenger metering pumps
- One auxiliary boiler oxygen scavenger metering pump
- Associated piping, valves and instrumentation

During normal operation, one of the oxygen scavenger metering pumps draws the oxygen scavenger from the oxygen scavenger storage tank and injects into the discharge piping of the condensate pump.

The phosphate feed system includes the following.

- Phosphate storage tank
- Two 100% capacity HITAF boiler phosphate metering pumps
- One phosphate dilution tank
- Two 100% capacity HITAF boiler phosphate injection pumps
- Two auxiliary boiler phosphate injection pump
- Associated piping, valves and instrumentation

During normal operation, one of the phosphate metering pumps draws the phosphate solution from the phosphate dilution tank and injects into the discharge piping of the condensate pump

Circulating Water Chemical Addition

The circulating water chemical additives with the softener system to maintain a quality of water that prevents scaling and corrosion within the circulating water system and service water system.

The circulating water chemical additives consist of sulfuric acid and sodium hypochlorite. Sulfuric acid is added in the cooling tower basin to achieve the desired pH-alkalinity combination in the circulating water system. The sulfuric acid feed system is designed to feed up to 2 gph. The design capacity of the storage tank is 30 day supply.

Sodium hypochlorite is added in the circulating water pumphouse forebay to control biofouling in the circulating and service water systems. Although blowdown from he cooling tower is not discharged to the environment, design of the circulating water sodium hypochlorite feed system is based on a 5 ppm dose of 10 trade % sodium hypochlorite for two hours per day. Since sodium hypochlorite has a shelf life of about two weeks, the storage tank size is 5,000 gallons (18.9 m^3). As the strength of the solution decreases, more solution may be required to achieve the same effect.

Circulation Water Chemical Additives

Circulating water chemical treatment includes the following.

- Circulating water sulfuric acid feed system
- Circulating water sodium hypochlorite feed system

The circulating water sulfuric acid feed system includes:

- Sulfuric acid storage tank
- Two 100% capacity circulating water sulfuric acid metering pumps
- Associated piping, valves and instrumentation

The sulfuric acid storage tank is equipped with a desiccant breather on the tank vent.

During normal operation, one of the sulfuric acid metering pump is in operation and one is in standby mode. The operating sulfuric acid metering pump draws sulfuric acid from the sulfuric acid storage tank sends to a dilution trough in the cooling tower from where it mixes with the circulating water.

The circulating water sodium hypochlorite feed system consists of the following.

- Sodium hypochlorite storage tank
- Two 100% capacity circulating water sodium hypochlorite metering pumps
- Associated piping, valves and instrumentation

During normal operation, one of the sodium hypochlorite metering pump is in operation and one is in standby mode. The operating sodium hypochlorite metering pump draws sodium

hypochlorite from the sodium hypochlorite storage tank and sends it to a dilution trough in the cooling tower from where it is mixed with the circulating water.

7.0 Miscellaneous Process Support

7.1 HVAC Subsystem

The heating, ventilating, and air conditioning (HVAC) system provides air movement, temperature, and humidity control as applicable for various facility areas for the proper functioning of operating equipment year-round, and for personal comfort. For the plant areas containing electronic equipment requiring a temperature-controlled environment, air conditioning during summer and heating during winter are provided, as required.

The HVAC system is designed for an outside design dry bulb temperature of 92 °F (33.3 °C) and 41 °F (5 °C) during summer and winter respectively. Design summer wet bulb temperature is 77 °F (25 °C). Design winter wind velocity is 15 mph (24 km/h).

Various facility areas will be heated in winter and cooled in summer (by outside air ventilation or air conditioning as required) to maintain the required inside ambient design conditions. All air conditioning units are designed to maintain 50 ± 10 % relative humidity in summer. The ventilation equipment for the softener building and water treatment building is designed to provide 10 air changes per hour. The design criteria for sizing ventilating equipment for all other ventilated areas is to prevent inside air temperature from going higher than 104 °F at design ambient conditions and maximum equipment heat load.

The major components of the heating, ventilating, and air conditioning systems include:

- Packaged air conditioning units
- Roof mounted exhaust fans
- Wall mounted supply/exhaust fans
- Electric heaters

The HVAC system services the following areas:

- Control building
- Admin. Building/warehouse office area/I&C shop area
- Water treatment building
- Softener building
- Switchgear rooms/MCC room in coal silo area
- Battery room
- Tripper gallery area and elevator machinery room

7.2 Diesel Fuel Storage Subsystem

The diesel storage and supply system stores and supplies diesel fuel for use by mobile (yard) equipment. The system also serves as a backup for supplying diesel fuel to the locomotive used to position rail cars for coal unloading.

Diesel fuel is unloaded into a 1000 gallon (3.8 m^3) capacity diesel fuel storage tank from commercial trucks using the pump in the truck. One 100% capacity diesel pump shall be used to supply fuel from the storage tank to the mobile equipment or locomotive as required. The diesel fuel pump is a UL listed, self-contained single hose pump with positive displacement meter. The pump is capable of delivering approximately 20 gpm (4.5 m^3/h).

The diesel fuel storage tank is equipped with a flame arrestor. The fuel oil storage tank area is designed to contain any fuel spills in compliance with the State Law.

7.3 Fire Protection Subsystem

The fire protection systems protect structures and personnel from the effects of fire. The system includes both automatic and manual features to provide alarm, detection and suppression capabilities consistent with building code requirements, NFPA guidance, and typical industrial engineering practices.

In general, design requirements for the fire protection system are based on NFPA recommendations. The following design requirements represent the most significant NFPA recommendations which have been incorporated into the system design.

Fire water shall be supplied to the fire protection system by two 100% capacity fire pumps. One pump shall be motor driven and serve as the main fire pump. The other pump shall be diesel engine driven and serve as a backup to the motor driven pump. Each pump shall develop the following three operating conditions:

- 2000 gpm at 120 psi (454 m^3/h at 827 kPa)
- 750 gpm at 155 psi (35 m^3/h at 1069 kPa)
- 0 gpm at 170 psi (0 m^3/h at 1172 kPa)

A jockey pump shall be provided to maintain system pressure in the supply piping during normal operation.

The fire protection system shall utilize a reliable and dedicated fire water supply.

The fire pumps shall be sized to serve the largest single automatic suppression system demand, concurrent with a nominal demand of 500 gpm (114 m^3/h) for outside fire hose streams.

The following means of suppression and detection shall be provided in accordance with the local building code and NFPA requirements: Automatic fire suppression systems shall be provided for the following.

- HITAF burner fronts
- Turbine building
- Administration building/visitor's center
- Dirty lube oil area
- Water treatment building (lab., office, storage room)
- Auxiliary boiler burner fronts
- Transformers (main, auxiliary, startup and station service)
- Cooling tower
- Coal unloading conveyor
- Coal storage stackout conveyor
- Emergency stackout conveyor

- Reclaim and emergency reclaim conveyors
- Crusher feed conveyors
- Plant feed conveyors
- Coal silo feed conveyor
- Coal dust collection baghouse

The fire protection system consists of a fire water source, a pumping system, a distribution network of piping and fire suppression systems and equipment. Additionally, the system incorporates all necessary controls including fire detection and alarm. The fire protection system provides fire detection warning to plant personnel and provides fire suppression of the appropriate capacity and capability to minimize the adverse effect of fires and prevent them from spreading.

The facility is serviced by an underground yard main loop which encircles the main plant site. Fire hydrants are provided at intervals along the main loop. Distribution headers off the main loops provide water to the hose stations, manual and automatic sprinkler systems, and the propane tank water cannon system.

Selected areas of the main plant have fire detection systems installed that provide alarm signals at the control room fire alarm panel. The fire alarm signals also initiate any associated pre-action sprinkler system. Fire alarm pull boxes and horns are located throughout the plant and alarm at the control room fire alarm panel.

The cooling water storage pond of the raw water supply system serves as the source of fire fighting water. A jockey pump maintains firemain pressure during periods of system standby operation. During periods of fire water demand, system flow and pressure is provided by an electric motor driven fire pump and a backup diesel engine driven fire pump.

The fire protection system is divided into zones. Each zone concentrates on a particular area of the facility and is designed for that area's particular needs for protection and detection. In areas best served by manual use of hose stations, only a detection system is used.

7.4 Wastewater Subsystem

The wastewater treatment system performs the following operations.

- Collects process wastewater including floor and equipment drains
- Collects potentially contaminated storm water runoff from the plant yard and solids handling area
- Treats potentially oily process water
- Neutralizes acidic or basic process wastewater
- Transfers all collected wastewater during outages and abnormal operating conditions

The wastewater treatment system is designed to collect, treat, store and transfer process wastewater and potentially contaminated stormwater runoff during startup, normal operation, and plant outages for reuse as plant makeup water.

The wastewater treatment system includes the following items.

- Thirteen pairs of sump pumps (nominally two 100% capacity duplex sump pumps)
- Three single sump pumps for small sumps
- One oil/water separator
- Two pumps each in the coal pile runoff and storm water management basin #1
- Two 50% capacity air preheater wash sump pumps
- One large transfer pump in the wastewater storage pond
- One neutralization tank
- Two 100% capacity neutralization recirc/transfer pumps
- One wastewater equalization tank
- Two 100% capacity waste equalization tank transfer pumps
- Associated piping, valves and instrumentation.

The water treatment building and steam turbine/HITAF area and chemical waste sump pumps direct potentially acidic or caustic waste to the neutralization tank for pH adjustment. The steam turbine area equipment and floor drain sumps, flyash silo sump, bottom ash storage building sump, HITAF area sump and auxiliary area equipment and floor drain sump direct potentially oil contaminated wastewater to the oil/water separator.

Collected wastewater from other sumps is combined with the oil/water separator effluent and with neutralized wastewater from the neutralization tank and then directed to the wastewater equalization tank. Collected wastewater from the equalization along with water from various ponds and the softener building sump is transferred to the softener feed tank for treatment and reuse as plant makeup water. Alternatively, it is transferred to the cooling water storage tank.

Oil/Water Separation

The oil/water separator utilizes a coalescing media pack to remove free and mechanically emulsified oil and grease from the wastewater flow. Flow through the unit is by gravity to the condensate polisher backwash sump. An adjustable skimmer directs the separated oil to an oil storage compartment. A manually controlled oil pump transfers the oil to drums for off-site disposal in accordance with the state and local regulations. Suspended solids in the wastewater may accumulate in the bottom of the oil/water separator. A manually controlled sludge pump transfers accumulated solids to a container. The accumulated solids may be dewatered in the softener system or otherwise disposed of in accordance with state and local regulations.

The condensate polisher backwash sump collects backwash and other precoat waste streams from the condensate polisher along with effluent from the oil/water separator. Two 100% capacity condensate polisher backwash sump pumps transfer the wastewater to the wastewater equalization tank.

Neutralization

The wastewater neutralization tank is equipped with a mixer to mix its contents. Two 100% capacity neutralization recirc/transfer pumps initially recirculate the tank contents through the acid and caustic injection tees and back to the neutralization tank. Upon completion of neutralization, the discharge valve opens and flow is directed to the wastewater equalization tank. A detailed operating description of the regeneration system and neutralization system

control is provided in the Operation and Maintenance Manual for the Makeup Demineralizer System.

Wastewater Equalization

The wastewater equalization tank collects wastewater from the following sources.

- Condensate polisher backwash sump (including oil/water separator effluent)
- Neutralization tank
- Overflow from the filtered water storage tank

Two 100% capacity waste equalization tank transfer pumps transfer the collected wastewater to the softener feed tank. When wastewater in the equalization tank is not suitable for the softener feed tank, it is transferred to the cooling water storage pond.

Wastewater Recycling to the Softener Feed Tank

The softener building sump collects wastewater from the following sources for recycle to the softener system.

- Backwash from the gravity filters
- Supernatant from the sludge thickener
- Filtrate from the belt filter press
- Floor drains in the softener building
- Area drainage

Two 100% capacity softener building sump pumps transfer collected wastewater either to the softener feed tank or to the cooling water storage pond. Suspended solids from the various waste streams may accumulate in the sump. The solids level in the sump is monitored and the accumulated material is periodically removed. The solids may be dewatered in the sludge thickener or disposed off in accordance with state and local regulations.

Wastewater Storage Pond

This pond performs the following functions.

- Stores plant makeup water from the water source for use later when this source is not available
- Stores cooling tower blowdown(short term) if an evaporator is taken off-line
- Stores plant wastewater during startup outages

During startup, the wastewater storage pond collects and stores wastewater. During normal operation, the wastewater storage transfer pump is used to transfer the wastewater to the softener feed tank for treatment and reuse in the plant.

8.0 Other Process Systems

For design and cost estimating, the following items are grouped in Item 8.

- 8.1 Process piping
- 8.2 Instruments and controls
- 8.3 Electrical equipment
- 8.4 Electrical materials
- 8.5 Service air and instrument air

Only the last item is described in this section. The other items are equipment and materials that are used plant-wide.

8.5 Service Air and Instrument Air Subsystem

The service and instrument air systems satisfies the various plant needs for compressed air by providing a continuous, sufficient supply of clean, oil-free compressed air to plant equipment, controls, and utility services with minimum vibration and noise.

The compressed air systems are designed to provide oil-free compressed air while maintaining a minimum of 100 psig (791 kPa) pressure in the distribution headers and operating continuously during all modes of operation. Individual compressor ratings are based on ambient temperatures of 105 °F (40.6 °C) maximum and 40 °F (4.4 °C) minimum, and shall be capable of providing 500 scfm (14 m^3/m) at a discharge pressure to the dryers at 125 psig (963 kPa). The compressors will take air from inside the steam turbine building, which is exposed to ambient conditions.

The compressed air is dried to a dew point of -40 °F (-40 °C) using heatless desiccant dryers. The dryers shall have a flow capacity of 1580 scfm (44 m^3/m) based on inlet conditions of 125 psig (963 kPa) and 100% humidity at 100 °F (38 °C).

The compressors are powered from the plant 4160 V distribution system. In order to maintain continuous operation during all modes of operation, two compressors are fed from one 4160 V bus and the third compressor is fed from a separate 4160 V bus.

The primary components of the service air and instrument systems are:

- Three compressors
- Two desiccant air dryers (with pre-filters and after-filters)
- Instrument air receiver tank
- Service air receiver tank

Three Kobelco Northwest compressors, or their equivalent, each with a rated capacity of 500 scfm (14 m^3/m) at 125 psig (963 kPa) supply air to the dryers. The compressors are skid mounted, two-stage, oil free, rotary screw machines with an intercooler, aftercooler and

lubrication system. The lubrication system utilizes a separate motor driven oil pump and is for the bearings and gears only. Oil is not used in the compression chamber therefore the unit produces oil-free air.

The compressors discharge to two individually skid mounted, dual tower, desiccant-type dryers designed for heatless regeneration, which provide instrument quality air at dew point of -40 °F (-40 °C). Dual pre-filters and after-filters are also mounted on the dryer skid to remove entrained water and oil droplets and to prevent any carryover of granular desiccant into the air stream. The dryer's discharge a common header which feeds the air receivers provided for each system. The air receivers provide surge protection and accumulation of air. Each receiver is equipped with relief valves to protect the tank from overpressurization.

The balance of both the instrument and service air systems consists of piping headers that encircle the power block. Branches supply specific areas within the power block and other buildings located on the site.

Service Air System

The service air system receives clean dried air from the common air dryers and supplies air to the steam turbine building service air loop which also is connected to boiler building loop. These loops feed branch headers that supply air to various areas of the plant. Low points in the loops and branch lines are designed to drain any condensate collected in the piping by means of float type drain traps. The loop arrangement allows sections of the header to be isolated without affecting service air supply to other sections of the header.

In addition to supplying service air to various quick disconnect stations throughout the steam turbine building, the steam turbine building loop supplies the following users:

- Condensate polisher
- Warehouse/maintenance building
- Water treatment building
- Circulating water pump house (includes circulating water sodium hypochlorite feed pumps)
- Softener building (includes belt filter press, and ash silo filter)

In addition to supplying service air to various quick disconnect stations throughout the HITAF building, the HITAF building loop supplies the following users.

- Quick disconnects for emergency mill drives
- Auxiliary boiler area
- Flyash silo area (includes bag filters)
- Spray dryer absorber area
- Baghouse and ID fan areas

Instrument Air System

The instrument air system receives clean dried air from the common air dryers and supplies air to the steam turbine building instrument air loop which also is connected to HITAF building

loop. These loops feed branch headers that supply air to various areas of the plant. Low points in the loops and branch lines are designed to drain any condensate collected in the piping by means of float type drain traps. The loop arrangement allows sections of the header to be isolated without affecting instrument air supply to other sections of the header.

In addition to supplying instrument air to various quick disconnect stations throughout the steam turbine building, the steam turbine building loop supplies the following users.

- Steam turbine area
- Warehouse/maintenance building
- Water treatment building
- Circulating water pump house
- Softener building
- Primary air fans
- Cooling tower fire protection system

In addition to supplying instrument air to various quick disconnect stations throughout the HITAF building, the HITAF building loop supplies the following users.

- HITAF building
- Coal silo bay area
- SCR system
- Forced draft fan areas
- Auxiliary boiler
- Flyash silo area (includes unloader floor and collectors)
- Baghouse and induced draft fan areas
- Stack/continuous emissions monitoring (CEMS) area

9.0 Civil and Structural

Item 9 covers site preparation including piling, roads and finish grading; concrete including forms, embeds, rebar and other requirements; steel for structures and miscellaneous uses and architectural requirements. There are no process descriptions for Item 9.

HIPPS Estimated Costs and Economics

HIPPS Cost Estimate

The estimate for the commercial HIPPS plant was prepared using informal budget quotes from equipment suppliers and Nexant/Bechtel's experience from recent coal-fired and gas turbine combined cycle power plant work. Costs reflect price and wage level of 1999.

Slightly more than 80% of the equipment (excluding the HITAF) was priced from budget quotes. From another perspective, nearly 50% of the total direct cost is comprised of data from

the same set of equipment quotes. Equipment and material costs estimated from past work are based on a recent 330 MW pulverized coal-fired power plant. The historical costs were adjusted for scope and capacity to match the HIPPS requirements.

The equipment cost estimate for the HITAF is to be provided by UTRC, and they may revise the estimate to recalculate the plant cost. The HITAF is estimated as a range so economic evaluations can be performed. As is shown by varying the HITAF cost, the HIPPS plant total constructed cost is 10% less than an equivalent pulverized coal plant if the HITAF cost is $25 million; PC plant and HIPPS costs are equal if the HITAF is $50 million; and the HIPPS plant is 10% more than a PC plant if the HITAF cost is $75 million.

The HIPPS plant costs are for the Nth plant of its kind, and thus, there are no special, one-time costs associated with engineering, constructing and operating the 1st of a kind facility. While the PC technology is available today, and while the future changes to HIPPS or PC plant costs can not be predicted, it is expected that the gas turbine portion of the HIPPS plant is more likely to have lower future costs than the coal-fired portions of either HIPPS or PC technology.

Other costs shown in the estimate are defined below.

Indirect Costs

These are costs associated with construction that can not be assigned to a particular facility, but are known from experience to be needed. Examples of indirect cost items are buildings and structures for construction, mobile equipment, tools, laydown areas, security, health and safety requirements. A cost of $82 per kW was used for both the HIPPS plant and the PC comparison plant. The cost is from recent experience.

Engineering Services

The cost of home office and field engineering and fees are accounted for in this category. The cost is calculated at 8% for both the HIPPS and the PC plants.

Project Contingency

Depending on the level of engineering and technology maturity, a percentage contingency will be added to account for costs which are expected to be defined when more detailed engineering is accomplished. A contingency factor of 15% is used with both plants. This is in variance with the EPRI TAG methodology of project and process uncertainty, but is thought to provide a more consistent comparison, and better reflect the current nature of the power generation market: A HIPPS plant will have to be demonstrated to the degree that its uncertainty will be equal to a PC plant with the same generation and emissions performance standards before the industry will consider it ready for the market.

Allowance for Funds During Construction

The cost of interest on funds spent during the construction period, when there are no revenues, is estimated from experience as 8% of the TPC.

Owner Costs

These costs include the following items.

- Preproduction or startup costs
- Inventory capital

- Initial catalyst and chemicals cost
- Land

The costs are presented in Table 1-11. A value of $30 million or $100 per kW has been assigned to the HITAF unit to complete the estimate.

Table 1-11
HIPPS Commercial Plant Total Construction Cost Estimate

Code of Account Items	300 MW HIPPS PLANT		300 MW PC PLANT	
	Cost in Thousands	$ per kW	Cost in Thousands	$ per kW
POWER GENERATION				
1.0 Steam Generation/HITAF				
1.1 High Temperature Furnace	30,000	100.00	-	0.00
1.2 HITAF HRSG #2	10,000	33.30	-	0.00
1.3 Heaters and Boilers	2,200	7.30	50,800	169.30
2.0 Gas Turbine System				
2.1 Gas Turbine Generator	35,200	117.30	-	0.00
2.2 Gas Turbine HRSG # 1	8,000	26.70	-	0.00
2.3 Natural Gas Supply System	500	1.70	-	0.00
3.0 Steam Turbine System				
3.1 Steam Turbine Generator	15,000	50.00	28,000	93.30
3.2 Condenser	1,000	3.30	2,100	7.00
3.3 Pumps	2,800	9.30	4,800	16.00
4.0 Flue Gas Emissions Control				
4.1 SO_2, NO_X and Particulate Controls	23,000	76.70	51,400	171.30
BALANCE OF PLANT				
5.0 Coal and Ash Handling	6,000	20.00	11,200	37.30
6.0 Water Treatment	4,100	13.70	7,100	23.70
7.0 HVAC, Tanks, Insulation, Stack	7,000	23.30	5,200	17.30
8.0 Other Process Systems				
8.1 Process Piping	7,800	26.00	11,700	39.00
8.2 Instruments and Controls	4,100	13.70	3,700	12.30
8.3 Electrical Equipment	4,400	14.70	4,400	14.70
8.4 Electrical Materials	2,500	8.30	2,500	8.30
9.0 Civil and Structural				
9.1 Concrete	5,000	16.70	4,800	16.00
9.2 Steel and Site Preparation	28,300	94.30	26,900	89.70
TOTAL DIRECT COST	196,900	656.30	214,600	715.30
Indirect Costs	24,600	82.00	24,600	82.00
TOTAL FIELD COST	221,500	738.30	239,200	797.30
Home Office Engineering	17,300	57.70	19,100	63.70
TOTAL CONSTRUCTION COST	238,800	796.00	258,300	861.00

Additional Capital Cost Items

Items shown in Table 1-12 are added to the Construction Cost Estimate to complete the capital cost.

Table 1-12
Total Capital Cost Calculations

	HIPPS Plant		PC Plant	
Item	$1,000s	$/kW	$1,000s	$/kW
Total Construction Cost -TCC (from Table 1-11)	238,800	796	258,300	861.00
Project Contingency @ 15% of TCC	35,820	119	38,745	129
Total Plant Cost -TPC	274,620	915	297,045	990
Allowance For Funds During Construction @ 8% of TPC	21,970	73	23,764	79
Total Plant Investment -TPI	296,590	989	320,809	1,069
Owner Costs @ 5% of TPI	14,829	49	16,040	53
Total Capital Cost	311,419	1,038	336,849	1,123

With the data on Tables 1-11 and 1-12, the delta between the HIPPS and the PC plant is a little more than 8% or $85 per kW lower cost for the HIPPS plant, keeping in mind the $30 million arbitrary valued used for the HITAF component.

Economic Analysis and Comparisons

Exhibit 1-12 shows the Energy Information Administration's (EIA) Annual Energy Outlook 1998; with projections to 2020, dated December 1997, reference case prices for pipeline natural gas (PNG) and steam coal delivered for power generation. As shown on the figure, coal prices are nearly constant, declining slightly in the 1996 to 2020 timeframe. The EIA estimates are calculated in 1996 dollars. The forecast cost for coal and gas are used to select a range of energy prices to compare the HIPPS plant with more conventional pulverized coal-fired plant and a gas turbine combined cycle plant, burning natural gas. The EIA reference case forecast prices for 2005 are $1.14 and $2.63 per million Btus for coal and natural gas, respectively.

The method chosen for comparing the plants is a present worth calculation. The year 2005 is set as the starting point for calculations: The HIPPS plant, or one of the other types of plants, is to be finished construction and begin operation at 2005. Capital costs, operating and maintenance costs and fuel costs are discounted to their present worth. The cost of money and term of analysis are varied as parameters. Factors for O&M and fuel escalation were taken from the EIA report.

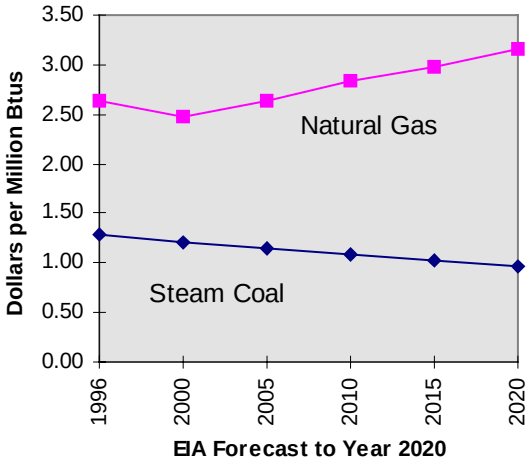

Exhibit 1-12
Delivered Fuel Prices --EIA Annual Energy Outlook Report 1998

Summary of Plant Data for Comparison

The plants used for comparison are the HIPPS commercial plant, which has been fully described in previous sections; a modern pulverized coal-fired plant with New Source Performance Standard emissions controls, and a modern gas turbine combined cycle plant with SCR for NO_x control. The performance data for the PC plant and the GTCC plant are from in-house spreadsheet models. The major performance items are listed in Table 1-13.

Table 1-13
Plant Comparison Data Summary

		300 Mw HIPPS Plant	300 Mw PC Plant	300 Mw GTCC Plant
Gas Turbine Generation	MWe	160.2		
Steam Turbine Generation	MWe	143.1		
Total Generation	MWe	303.3	316	305
Net Power Generation	MWe	292.2	292	300
Total Fuel Requirement	Btu/year	16.6E+12	24.6E+12	16.9E+12
Coal Requirement	Btu/year	10.8E+12	24.6E+12	
Gas Requirement	Btu/year	5.81E+12		16.9E+12
Gross Plant Heat Rate HHV	Btu/kWh	6,942	9,120	7,043
Gross Plant Efficiency HHV	Btu/kWh	49.2%	37.4%	48.5%
Net Plant Heat Rate HHV	Btu/kWh	7,200	9,870	7,160
Net Plant Efficiency HHV	Btu/kWh	47.4%	34.6%	47.7%
Capacity Factor		90%	90%	90%
Coal Price	$/MMBtu	1.14	1.14	Not Used
Natural Gas Price	$/MMBtu	2.63	Not Used	2.63

Operating and Maintenance Costs

Operating and maintenance cost data is shown on Exhibit 1-24. The O&M costs are taken from the EPRI TAG™. Fuels costs are calculated from the fuel used and the unit prices given in Table 1-13, from the EIA reference case in 2005. The Total Capital Cost is repeated for convenience. The capital cost for the GTCC plant is taken as $800 per kW. Data from Gas Turbine World 1999-2000 Handbook and Nexant/Bechtel experience are the basis for the cost, which includes the indirect costs shown on Table 1-14 that are added to the construction cost.

Table 1-14
Operating and Maintenance Cost Data

		300 Mw HIPPS Plant	300 Mw PC Plant	300 Mw GTCC Plant
Fixed Cost	$/kW-Yr	38.7	47.2	26.5
Incremental Cost	Mills/kWh			
• Variable Cost		1.3	2.0	0.4
• Consumables		1.3	2.0	0.4
• Byproducts		0.0	0.0	0.0
Total Incremental Cost		2.6	4.0	0.8
Annual O&M	$1,000s	17,845	23,621	9,842
Fuel Cost	$1,000s			
• Coal		12,295	28,032	
• Natural Gas		15,282		44,539
Total Fuel Cost		27,577	28,032	44,539
Total Capital Cost	$1,000s	311,419	336,849	240,000

Present Worth Comparison

Table 1-15 shows the results from present worth calculations with several parameters analyzed. Two costs of money, 8 and 15 percent and two investment durations, 10 and 20 years were used in calculations for year 2005 natural gas prices of $2.50, $3.00 and $3.50 per million Btus. The 2005 price for steam coal is $1.14 per million Btu from the EIA forecast, and is not used as a variable parameter.

On the table all the present worth values are negative; they represent costs incurred over the investment period. Differences between the technologies are shown in the “Delta” columns. For all sets of parameters, the HIPPS plant has a higher present worth (costs less) than the PC plant. Examining the deltas between the HIPPS plant and the GTCC plant shows that the HIPPS plant is most competitive when interest rates are low, and/or the investment horizon is long. This is logical as these conditions lessen the impact of the HIPPS plant’s higher capital cost. Also, it is

clear that higher natural gas prices have a strong impact on the GTCC case. The HIPPS and the GTCC are competitive at $3.00 gas, and the HIPPS is clearly the more economical plant when gas is $3.50. Finally, it should be remembered that the economics are based on a HITAF cost of $30 million. However, doubling the cost of the HITAF does not change the economic trends among the three plants.

Table 1-15
Present Worth Calculation Results for Selected Parameters
(HITAF Equipment Cost of $30 million)

	300 Mw HIPPS Plant	300 Mw PC Plant	DELTA HIPPS - PC	300 Mw GTCC Plant	DELTA HIPPS - GTCC
At $2.50 Natural Gas Price					
Present Worth; 8%, 10 years	($598,143)	($674,676)	$76,534	($573,293)	($24,850)
Present Worth; 8%, 20 years	($721,320)	($826,595)	$105,275	($713,258)	($8,061)
Present Worth; 15%, 10 years	($527,254)	($590,370)	$63,116	($491,163)	($36,092)
Present Worth; 15%, 20 years	($576,838)	($651,108)	$74,270	($547,752)	($29,086)
At $3.00 Natural Gas Price					
Present Worth; 8%, 10 years	($617,036)	($674,676)	$57,640	($628,359)	$11,322
Present Worth; 8%, 20 years	($748,417)	($826,595)	$78,177	($792,235)	$43,818
Present Worth; 15%, 10 years	($541,454)	($590,370)	$48,916	($532,549)	($8,905)
Present Worth; 15%, 20 years	($594,342)	($651,108)	$56,766	($598,766)	$4,424
At $3.50 Natural Gas Price					
Present Worth; 8%, 10 years	($635,930)	($674,676)	$38,746	($683,425)	$47,495
Present Worth; 8%, 20 years	($775,515)	($826,595)	$51,080	($871,211)	$95,696
Present Worth; 15%, 10 years	($555,654)	($590,370)	$34,716	($573,935)	$18,281
Present Worth; 15%, 20 years	($611,845)	($651,108)	$39,263	($649,780)	$37,935

The impact of doubling the cost of the HIPPS HITAF is illustrated in Exhibit 1-13. On the graph: Bar 1 is delta present worth between HIPPS and the PC plant where the HITAF cost is $30 million; bar 2 compares HIPPS and PC when the HITAF cost is $60 million. For both comparisons, HIPPS has a positive delta, showing it costs less than the PC plant.

Graph bars 3 and 4 are the delta present worths between HIPPS, first with a $30 million HITAF, and then with a $60 million unit cost, and the GTCC plant. The deltas are negative, showing that the HIPPS plant costs more with either HITAF.

The first set of 4 bars is for a cost of money of 8% and a 10 year investment period; the second set of 4 bars is the same delta present worth comparison with 8% cost of money and a 20 year duration. The first 8 bars are calculated for a year 2005 gas price of $2.50 per million Btus. The bar graphs are recalculated for gas prices of $3 and $3.50 in the next two sets of 8 bars.

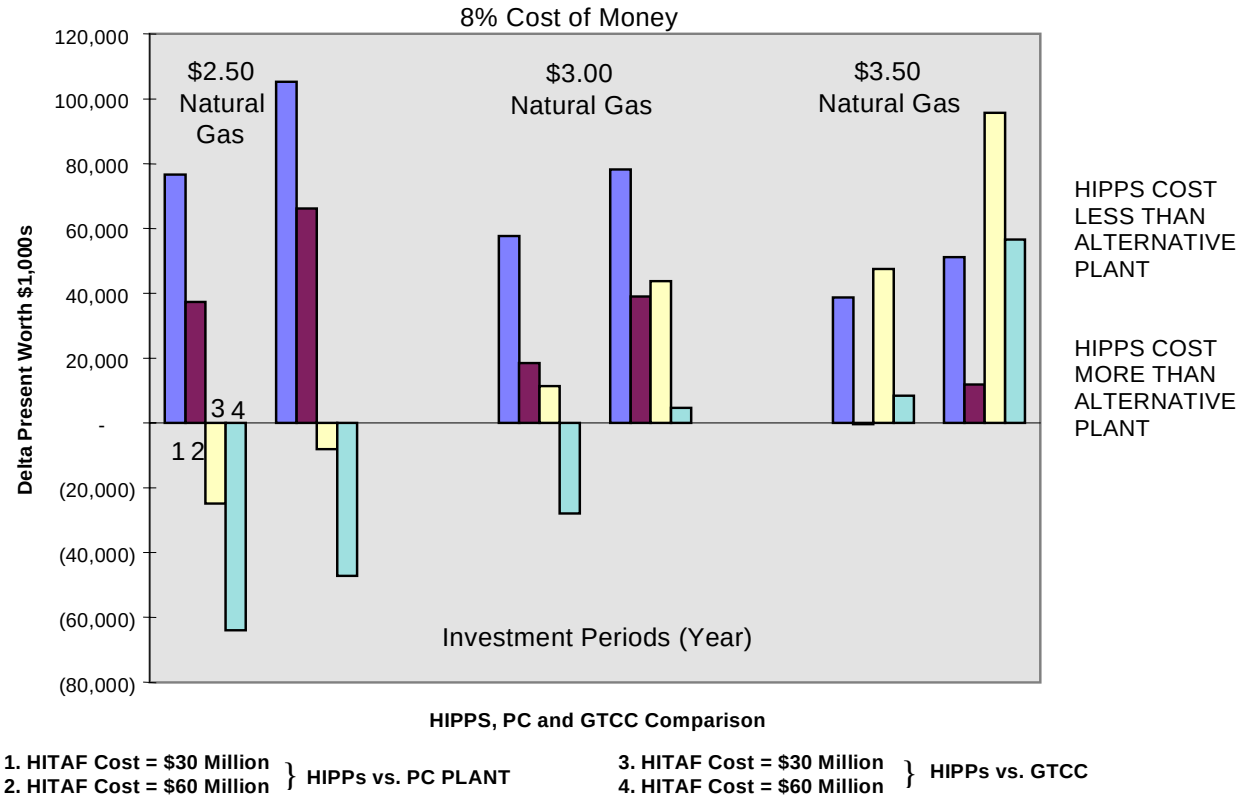

Exhibit 1-13
Comparison of HIPPS, PC and GTCC with Two HITAF Costs

The graph shows that doubling the HITAF cost estimate only slightly impacts the delta present worths used to compare the technologies. At $3.00 per million Btu for gas, the HIPPS is competitive unless a $60 million HITAF is combined with a short 10 year investment duration. It is also noted that the delta between the HIPPS and the PC plant decreases as the gas price increases; this is due to the 35% natural gas and 65% coal fuel split for HIPPS. At a $3.50 gas price, 8% cost of money and 10 years, the PC and HIPPS are roughly equal if the higher $60 million HITAF is used in the estimate.

Advanced HIPPS Configurations

Introduction

The Commercial Plant design was based on the philosophy of low risk in every element except the HITAF. Thus, the gas turbine conditions and the steam cycle conditions were chosen from commercially available equipment. While the operating conditions of the steam system were advanced as far as use as the bottoming portion of a combined cycle (2400 psi/1000 °F /1000 °F; 16,547 kPa/538 °C/538 °C), they did not approach the super critical conditions of many large plants (>3500 psi /1050 °F /1050 °F; 24, 131 kPa/566 °C/566 °C). Newer technology approaches were considered for advanced HIPPS.

Advanced frame and aero-derivative gas turbines were investigated for use in HIPPS that could appear in the latter part of the first decade of the 21st century. These engine configurations are based on the DOE Advanced Turbine Systems program and the EPRI/Utility Consortium-

sponsored Collaborative Advanced Gas Turbine (CAGT). The CAGT uses technology from the latest 80-100,000 lb thrust aero engines for the large wide-body civil aircraft, but incorporate industrial features that could allow turbine temperatures approaching 3000 °F (1649 °C) and pressure ratios over 50/1.

These HIPPS, using either frame or aero-derivative technology, have performances well above present PC plants and approach currently installed combined cycles (47-50% HHV). A number of technology development programs such as AST, CAGT program, and several Department of Defense programs will provide new materials and gas turbine cooling technologies for frame and aero-derivative gas turbines. By taking advantage of these advances in technology, both the air heater and gas turbine portions of the HIPPS could be improved, resulting in significant performance gains. In addition, development of advanced steam cycle components is underway (Valenti, 1996) and use of this technology will also boost HIPPS performance.

The use of the ICAD engine also allows the consideration of different power cycles such as the Humid Air Turbine (HAT) cycle. The HAT cycle offers the potential of higher efficiencies and lower capital costs than the more conventional combined cycle system.

Advanced GT and Steam

In the last five years, several efforts have been initiated to advance technology for industrial gas turbine application. Most notable are the ATS Program of the DOE and the CAGT Program sponsored by an international consortium of energy companies and the Electric Power Research Institute with input from DOE and the Gas Research Institute. The goal of both programs was essentially the same - power systems capable of producing electricity at overall efficiencies of 60% (LHV) - but the approach has been different. The ATS program in its later phases has selected the heavy frame gas turbine in combined cycle configuration for the large-scale base load type power producer while the CAGT has focused on the ICAD gas turbine in several configurations for mid range applications. UTRC has been involved in various phases of both programs (Robson, 1993; TPM, 1993). In these studies, the FT4000 has been analyzed in numerous configurations including simple cycle, various intercooled cycles, and complex cycles involving multiple fluids with regeneration and reheat. The technologies in materials and cooling ranged from that currently used to very advanced engines using the technology derived from military aircraft engines. The following configurations use some of these FT4000 configurations in the HIPPS application.

The Commercial Plant using off the shelf gas turbine technology has an efficiency of 47.3% (HHV). Introduction of advanced technology gas turbines such as the ICAD results in an efficiency gain (Exhibit 1-14) to 48.5% (HHV), the rest of the system remaining the same.

The use of advanced steam conditions also can result in significant efficiency gains. The steam system for the baseline HIPPS, while atypical of current combined cycle use, was selected because it is commercially available, thereby reducing operational risk for the initial HIPPS. New steam plants, especially in Europe, often have supercritical operating conditions, some as high as 4500 psi (31,000 kPa) and 1150 °F (620 °C). In this country, effort by Innovative Steam Technologies, funded in part by DOE, have led to a demonstration of a High Performance Steam System (HPSS) consisting of a turbine and once-through boiler (Valenti, 1996). This unit, with

capabilities of operation at over 6000 psi (41,369kPa) and 1300 °F (704 °C) or 3600 psi (124,821kPa) and 1500 °F, (816 °C) has been demonstrated in a 4 MW size at 1500 psi/1500 °F (10,342 kPa/816 °C). The HPSS is aimed for use as a topping turbine with standard steam equipment in new or repowering applications. This technology has been used to top the steam system in the HIPPS for both the frame-type and ICAD HIPPS.

In Exhibit 1-15, the HPSS operating at 5500 psi/1294 °F (37,921kPa/701 °C) exhausts directly into the 2400 psi/1000 °F turbine (16,547kPa/538 °C) of the baseline system. Matching of flow conditions results in that turbine now operating at slightly over 950 °F (510 °C) in the HP section; the reheat is increased to 1050 °F (560 °C). A net gain in output of approximately 18 MW is achieved and the HIPPS efficiency is increased to 51.4%.

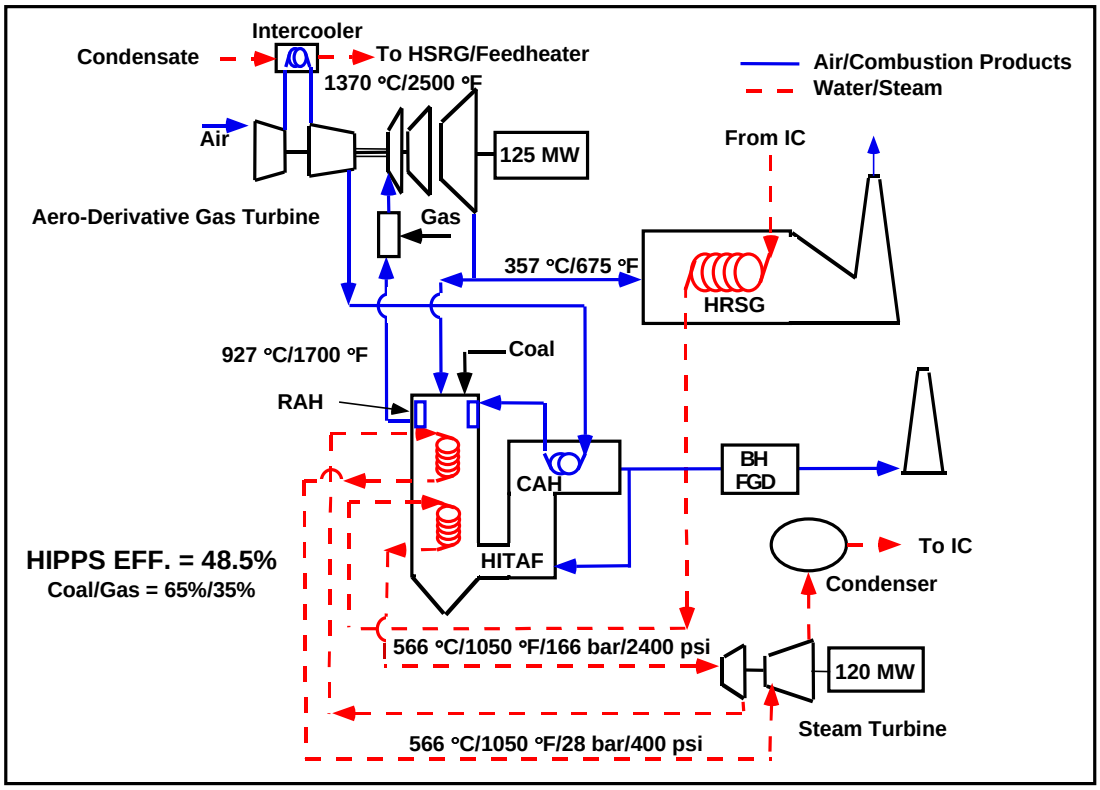

Exhibit 1-14
HIPPS with ICAD Engine

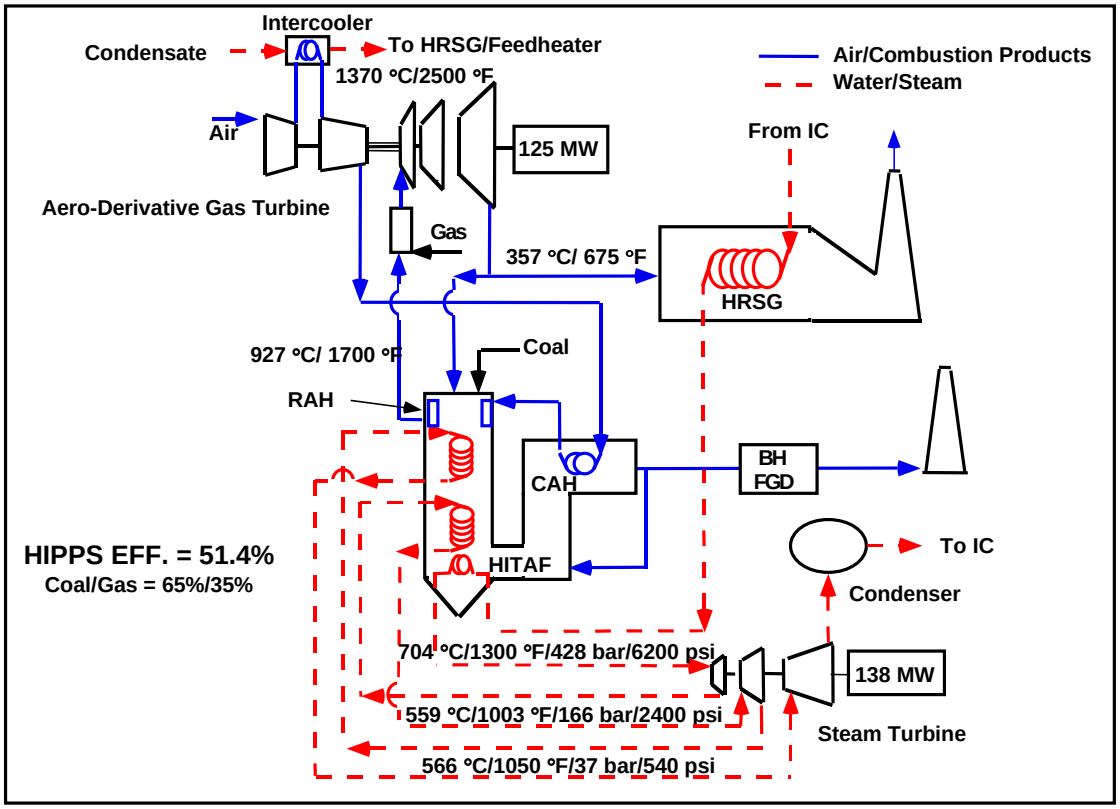

Exhibit 1-15
ICAD HIPPS with Advanced Steam

A HIPPS using an advanced ICAD engine configuration described in both the ATS and CAGT efforts is shown in Exhibit 1-16. This ICAD version has single crystal material technology with thermal barrier coatings and cooling techniques adapted from aircraft turbines to operate at combustor exit temperatures of 2900 °F (1593 °C) and pressure ratio approaching 50. This technology level could be introduced into industrial gas turbines in the 2005 time frame. The HITAF also operates with advanced conditions: the radiator has an outlet temperature of 2000 °F (1093 °C) and steam is raised for the HPSS at 6200 psi (42,747kPa) and 1300 °F (704 °C). A gas-fired reheater is used to bring the temperature into the power turbine to 2200 °F (1204 °C). The overall efficiency of this configuration is 53%, the highest among a number of combined-cycle configurations evaluated.

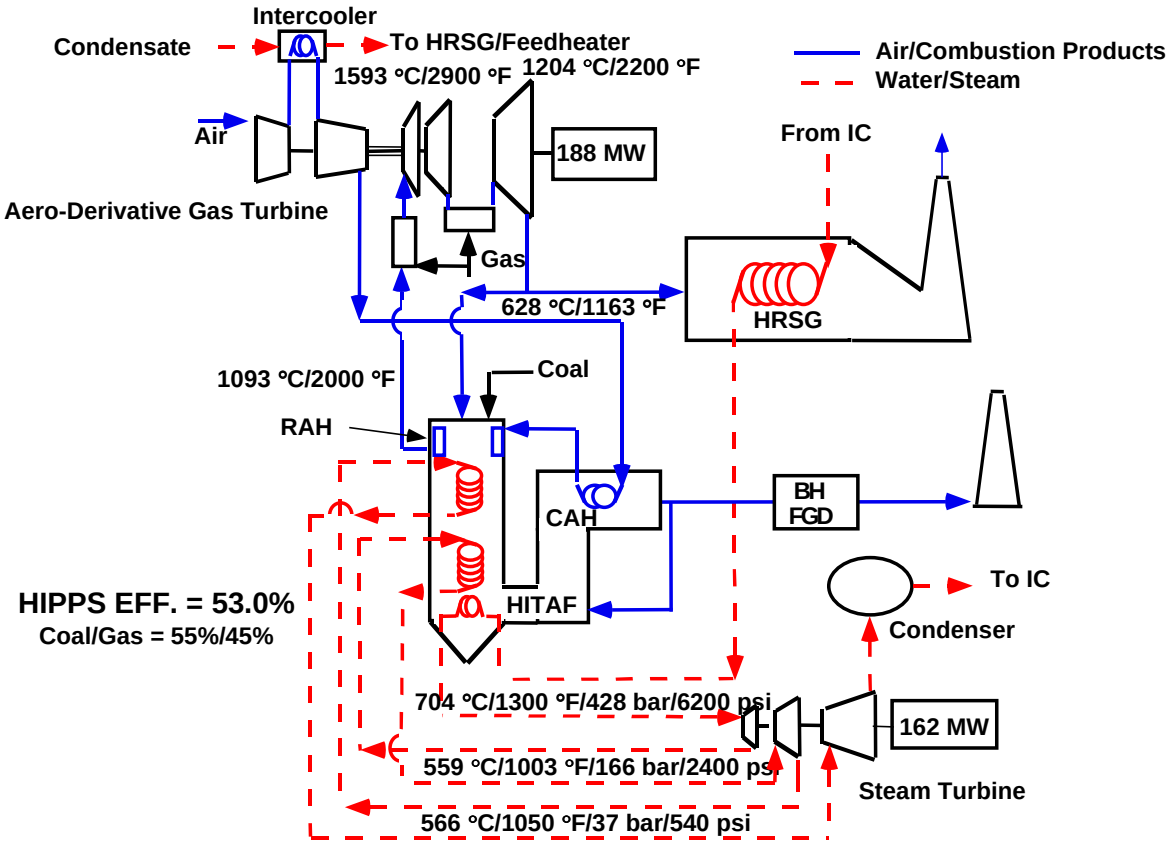

Exhibit 1-16
Advanced ICAD and Advanced Steam HIPPS

HAT

The Humid Air Turbine (HAT) cycle involves the recovery of low grade heat from the gas turbine for use in a humidifier that saturates the compressor discharge air with water prior to a regenerator (Exhibit 1-17). The HAT cycle offers the opportunity to get high efficiencies and low capital cost.

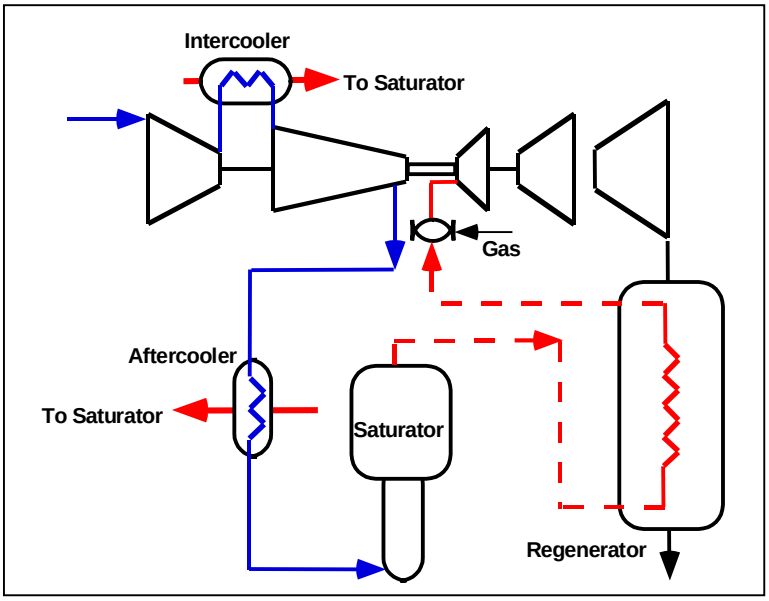

Exhibit 1-17
Simplified HAT Cycle

The initial HIPPS/HAT configuration is based on a state of the art ICAD, i.e., one that has a turbine inlet of 2500 °F (1371 °C). Basically, an ICAD configuration uses low grade heat to humidify the compressor discharge stream, adding significant mass to the stream (approximately 20% of inlet flow). This stream is then regenerated by the gas turbine exhaust. Depending on ICAD technology level, efficiencies over 55% (HHV) can be projected. One of the advantages of the HAT cycle is that these high efficiencies can be attained without the need for steam bottoming equipment. Also, it should be noted that water recovery techniques are available that would return over 85% of the water to the system, with little impact on efficiency and small additional cost. In these cases, water consumption is well below typical combined cycle levels.

The HIPPS/HAT configuration shown in Exhibit 1-18 uses current technology in the ICAD. Because of the water vapor in the working fluid, additional gas must be burned to attain the required combustor temperatures. To meet the DOE goal of 65% coal utilization, more coal heat must be put into the cycle. Since steam bottoming is not desirable, a higher radiator exit temperature is needed. In addition, coal heat is added to the humidified stream in the HITAF and some stack heat is used for the saturator. The efficiency of this configuration is 49.3%; only slightly higher than the ICAD combined cycle. This is mainly due to higher than desired stack temperature from the HITAF.

As part of the CAGT program, a HAT cycle was identified having a reheater in front of the power turbine (see Exhibit 1-19). The HAT turbine had some advanced materials and cooling techniques allowing it to operate at a higher combustor exit temperature (2780 °F, 1527 °C). As before, the radiator outlet temperature was 2000 °F (1093 °C); also, additional coal heat was used in the HAT as the HITAF supplied a portion of the reheat. Some steam raised in the HITAF was also introduced just before the reheater. An efficiency of over 54% could be realized with coal furnishing 62% of the cycle heat.

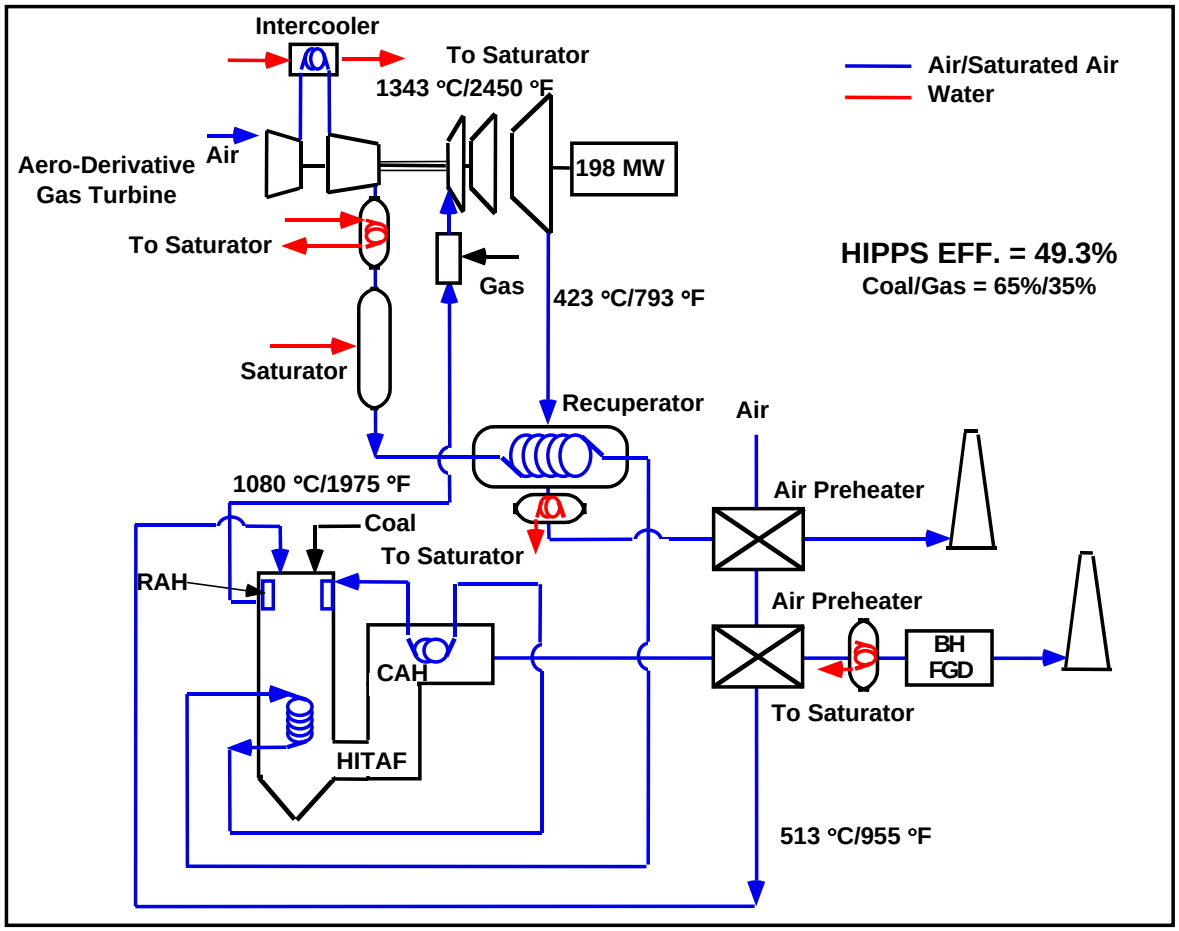

Exhibit 1-18
State-of-the-Art ICAD in HIPPS/HAT

The advanced turbine technology described for a combined cycle application was used for a HIPPS/HAT cycle (Exhibit 1-20). In this configuration, the temperature in front of the power turbine is too high (<2000 °F, 1093 °C) to allow any coal heat to be used. Also, the turbine exhaust is hot enough to regenerate the stream to a temperature typical of convection heater inlet. Thus, cycle efficiency of 54.3% was attained at a coal/gas ratio of 53%/47%.

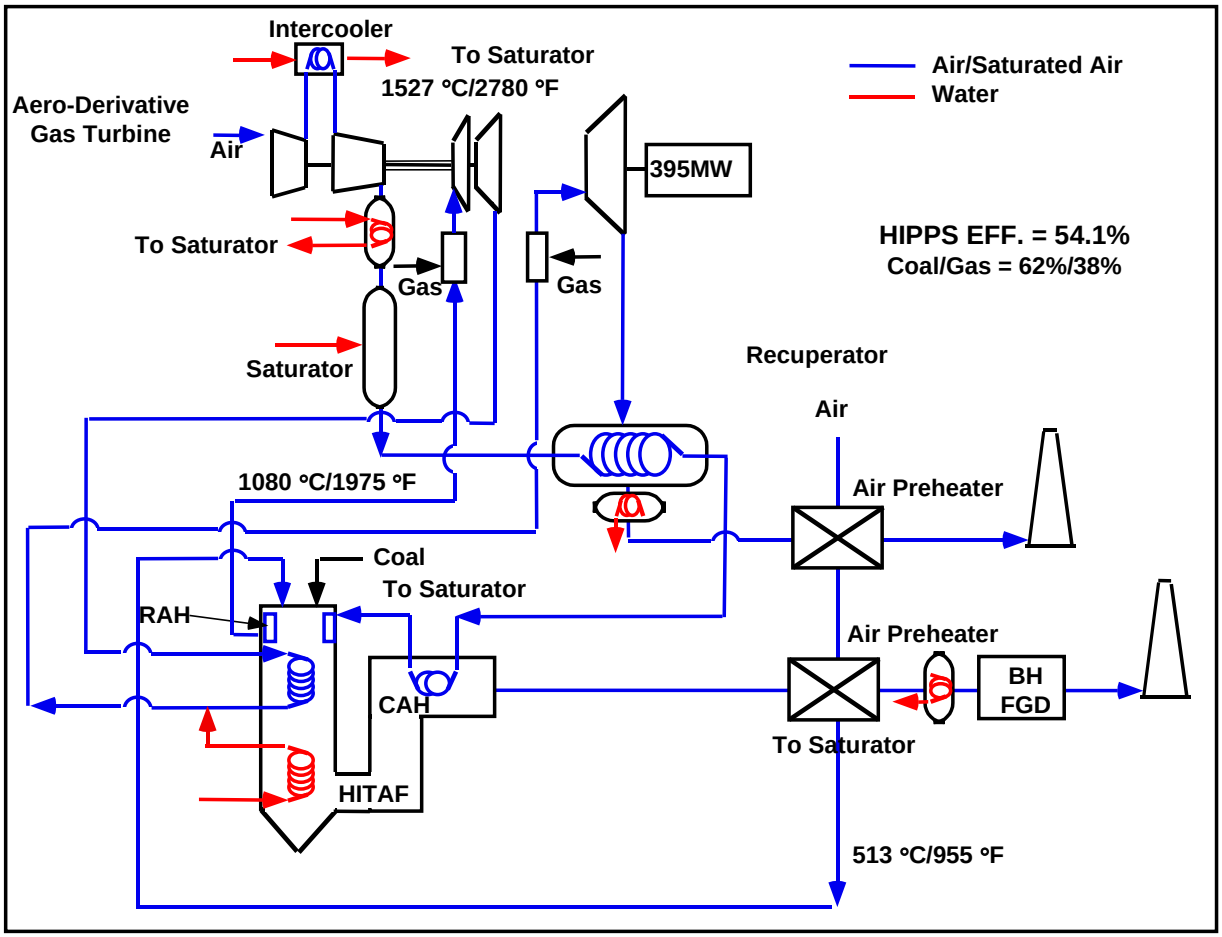

Exhibit 1-19
Advanced ICAD in a HIPPS/HAT

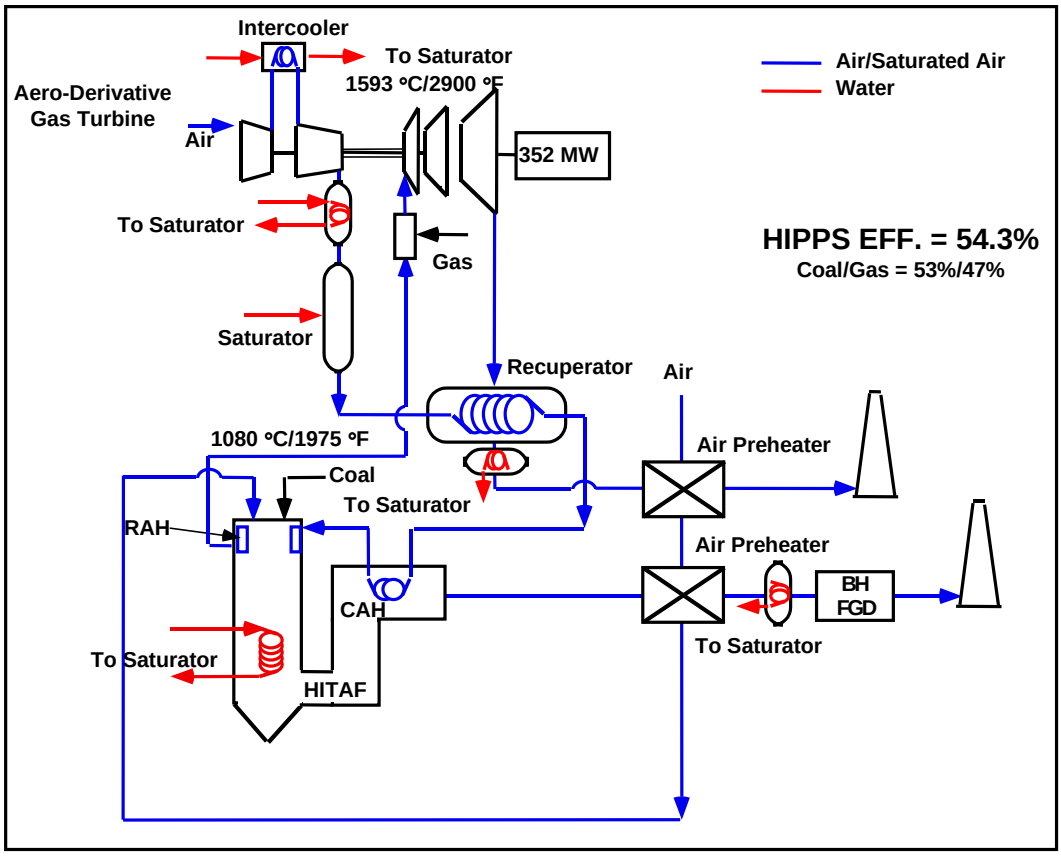

Exhibit 1-20
Advanced ICAD in HIPPS/HAT

The advanced HIPPS described in the foregoing do not exhaust the variety of configurations that could be identified. For example, both the combined cycle HIPPS and the HIPPS/HAT could include other bottoming technologies, such as Kalina or bi-phase turbines. These could add one or two points to cycle efficiencies at increased complexity (cost). In Phase 1, the allowable incremental equipment cost ($/kW) to gain one point in efficiency was determined as a function of starting point (base efficiency) and fuel cost. It was easy to justify the additional costs to move from 35% to near 50%, especially when these efficiency gains could be realized at less cost than current coal-fired plants. The allowable incremental cost, however, decreases as efficiency increases. As long as fuel costs remain within the range projected through 2015, the inducement to increase efficiency through cycle complexity becomes less and less.

Of more interest than ultimate efficiency is how the HIPPS compares to other coal-fired alternatives. Such a comparison is shown in Exhibit 1-21 (Maude, 1993). Here, we see that the various HIPPS technologies have projected efficiencies that are better than most of the other alternatives and are comparable to the goals of the gas-fired systems of ATS and CAGT.

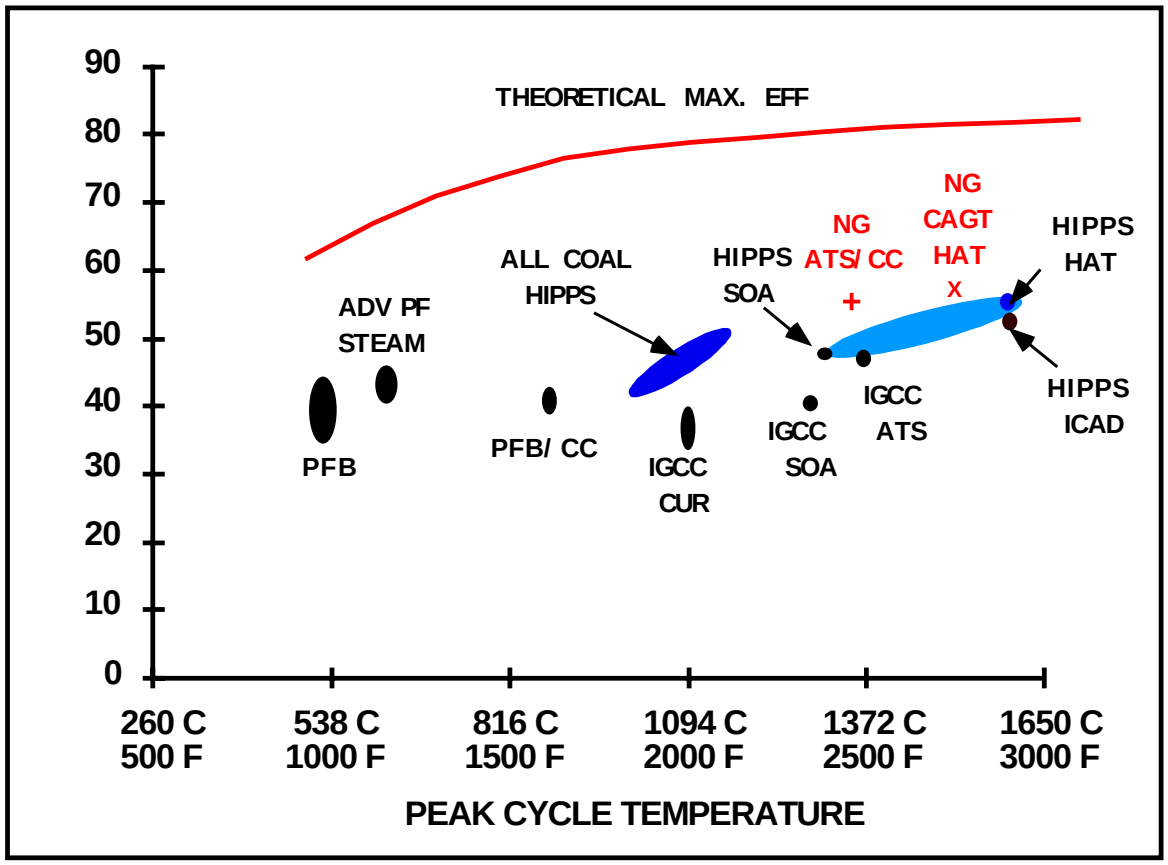

Exhibit 1-21
Comparison of Coal-Based Cycle Performance

Summary

The advanced HIPPS described in the previous sections offer performance advantages over most of the alternative coal-based power plants. The development of this advanced technology is very dependent on the form that the electric power industry assumes over the next decade. Many of the projected operating scenarios would have few, if any, new base-load plants built until the current reserve margin is reduced from near 20% to around 5%. New capacity would be added for peaking (1000 - 2500 hr/yr.) and mid-range (2500 - 4000 hr/yr.). In this market driven scenario, generators would be competing to meet customer demands for blocks of MW/hr at varying times of day. Ideally, these plants would be low cost, have high efficiency and quick startup capabilities to minimize consumption of costly (usually natural gas) fuel.

The advanced HIPPS configurations could meet the criteria arising from this new power industry scenario. The gas turbine could be brought on-line using gas, supplying part (or all in the HAT version) of the power demand in a matter of minutes. As the HITAF comes on-line, coal provides a major portion of the energy further reducing energy production costs. Applications of these technologies to repowering of older coal plants, which would have a variety of benefits, appears to offer a major opportunity to realize HIPPS, both in the near term using state-of-the-art technology as well as future, very high performance systems.

References

Seery, D.J., et al., Coal-Fired High Performance Power Generating System, Final Report, United Technologies Research Center, August 31, 1995

Robson, F.L., Advanced Turbine Systems Study - System Scoping And Feasibility Study, Doe Contract De-Ac21-92mc29247, United Technologies Research Center, March 1993

Maude, C., Advanced Power Generation – A Comparative Study of Design Options for Coal, IEA Coal Research, 1993

TPM, Collaborative Advanced Gas Turbine Phase 1 Final Report, Dec. 1993

Valenti, M., Pouring on the Steam, Mechanical Engineer, Feb. 1996

Appendix A - Major Equipment List
HIPPS Commercial Plant Conceptual Design

Code of Accounts	Description	Quantity	Motor HP	Total Operating HP	Total Installed HP
1.0	**Steam Generation/HITAF**				
1.1	High Temperature Advanced Furnace				
	Process data from UTRC				
	Operating	2			
	Spare	0			
	Flows are per HITAF element				
	Radiant Air Heater (RAH):				
	Air flow rate: 1,307,718 lb/h (593,171 kg/h)				
	Air inlet temperature: 1,300 °F (704 °C)				
	Air outlet temperature: 1,700 °F (927 °C)				
	Duty: 145.3 MMBtu/h (153.3 million kJ/h)				
	Material: TBD				
	Slag Screen Evaporator				
	Feedwater flow rate: 73,166 lb/h (33,166 kg/h)				
	Feedwater inlet temperature: 682 °F (361 °C)				
	Steam outlet temperature: 682 °F (361 °C)				
	Duty: 21.7 MMBtu/h (22.9 million kJ/h)				
	Material: TBD				
	Water Walls Evaporator				
	Feedwater flow rate: 325,386 lb/h (147,593 kg/h)				
	Feedwater inlet temperature: 682 °F (361 °C)				
	Steam outlet temperature: 682 °F (361 °C)				
	Duty: 96.4 MMBtu/h (101.7 million kJ/h)				
	Material: TBD				
	Reheater:				
	Steam flow rate: 394,596 lb/h (178,986 kg/h)				
	Steam inlet temperature: 643 °F (339 °C)				
	Steam outlet temperature: 1,000 °F (538 °C)				
	Duty: 77.8 MMBtu/h (82.1 million kJ/h)				
	Material: TBD				

Code of Accounts	Description	Quantity	Motor HP	Total Operating HP	Total Installed HP
	Convective Air Heater (CAH):				
	Air flow rate: 1,307,718 lb/h (593,171 (kg/h)				
	Air inlet temperature: 732 °F (389 °C)				
	Air outlet temperature: 1,300 °F (704 °C)				
	Duty: 197.0 MMBtu/h (207.8 million kJ/h)				
	Material: TBD				
1.2	HITAF Heat Recovery Steam Generator No. 2				
	"Dirty HRSG"				
	Operating	2			
	Spare	0			
	Superheater:				
	Steam inlet temperature: 770 °F (410 °C)				
	Steam outlet temperature: 1,000 °F (538 °C)				
	Duty: 160 MMBtu/h (168.8 million kJ/h)				
	Surface area: 301,000 ft^2 (27,964 m^2)				
	Tube surface: finned				
	Material: Alloy Steel SA-335-P11 and Stainless 304				
	Combustion Air Preheater				
	Air inlet temperature: 59 °F (15 °C)				
	Air outlet temperature: 776 °F (413 °C)				
	Duty: 184 MMBtu/h (191.1 million kJ/h)				
	Surface area: 320,000 ft^2 (29,729 m^2)				
	Plate Heat Exchanger				
	Material: Carbon Steel				
	Transport Air Preheater				
	Air inlet temperature: 59 °F (15 °C)				
	Air outlet temperature: 555 °F (291 °C)				
	Duty: 11.4 MMBtu/h (12.0 million kJ/h)				
	Surface area: 57,600 ft^2 (5,351 m^2)				
	Tube Surface: finned				
	Material: Carbon Steel SA-106B				

2.0 Gas Turbine System

2.1 Gas Turbine Generator

Heavy frame type machine; process data from UTRC

Operating	1
Spare	0

Nominal capacity: 150 MWe

2.2 Gas Turbine Heat Recovery Steam Generator No. 1

"Clean HRSG"

Operating	1
Spare	0

Superheater:

Steam inlet temperature: 682 °F (361 °C)
Steam outlet temperature: 770 °F (410 °C)
Duty: 154 MMBtu/h (162.5 million kJ/h)
Surface area: 257,600 ft^2 (23,932 m^2)
Tube surface: finned
Material: Carbon Steel SA-106B and Alloy Steel SA-335-P11

Economizer:

Water inlet temperature: 224 °F (107 °C)
Water outlet temperature: 682 °F (361°C)
Duty: 450 MMBtu/h (474.8 million kJ/h)
Surface area: 1,791,700 ft^2 (166,454 m^2)
Tube surface: finned
Material: Carbon Steel SA-106B

Deaerator:

Water inlet temperature: 150 °F (66 °C)
Water outlet temperature: 224 °F (107 °C)
Duty: 55 MMBtu/h (58 million kJ/h)
Surface area: 214,700 ft^2 (19,946 m^2)
Tube surface: finned
Material: Carbon Steel SA-106B

Feedwater Heater

Water inlet temperature: 91.4 °F (33 °C)
Water outlet temperature: 150 °F (66 °C)
Duty: 47 MMBtu/h (49.6 million kJ/h)
Surface area: 183,500 ft^2 (17,048 m^2)
Tube surface: finned
Material: Carbon Steel SA-106B

3.0 Steam Turbine System

3.1 Steam Turbine Generator

Operating	1			
Spare	0			

Nominal generator output: 150 MWe
Type: Reheat/condensing
HP turbine inlet steam 1,000 °F, 2400 psia (538 °C, 16547 kPa)
IP turbine inlet steam 1,000 °F, 580 psia (538 °C, 3999 kPa)
LP turbine inlet steam
Design Flow: 800,000 lb/h (362,874 kg/h)
Actual Flow: 720,342 lb/h (326,742 kg/h)
Generator: 3600 RPM; 150 MWe
22,000 Volt; 60 Hertz; 3 phase

3.2 Circulating Water Subsystem

Cooling Tower:

Operating	1			
Spare	0			

6-cells including all auxiliary equipment
Design flow rate, 85,000 gpm (19,306 m^3/h)
Inlet water temperature, 83 °F (28 °C)
Outlet water temperature, 63 °F (17 °C)
Duty, 850 million Btu/h (896.8 million kJ/h)

Tower fans	6	150	900	900

Material: Wood with PVC fill and drift eliminators

Circulation Pump

Operating	2	1,300	2,600	3,900
Spare	1			

Type: Vertical, axial flow
Liquid pumped: Circulating water
Liquid temperature, 63 °F (17 °C)
Flow rating, 45,000 gpm/pump (10,221(m^3/h)/pump)
Suction pressure, 0 psig (0 kPa)
Discharge pressure, 35 psig (241 kPa)
Case material: Carbon steel
Shaft material: Stainless steel
Impeller material: Bronze

Auxiliary Cooling Water Pump

Operating	2	100	200	300
Spare	1			

Type; centrifugal
Liquid pumped: Circulating water
Liquid temperature, 63 °F (17 °C)
Flow rating, 4,500 gpm/pump (1,022 (m^3/h)/pump)

Suction pressure, 35 psig (241 kPa)
Discharge pressure, 60 psig (413.7 kPa)
Case material: Stainless steel
Shaft material: Stainless steel
Impeller material: Bronze

3.3 Condensate Subsystem

Steam Condenser

Operating	1			
Spare	0			

Type: Single pressure, single shell, single pass
Effective surface, 53,550 ft^2 (4975 m^2)
Circulating water:
Inlet temperature, 63 °F (17 °C)
Return 80 °F (27 °C)
Flow, 94,900 gpm (21,554 m^3/h)
Water pressure, 45 psia (310 kPa)
Tubes
Overall length, 34.25 ft (10.45 m)
Water velocity, 10 ft/s (3.05 m/s)
Steam flow rate, 800,000 lb/h (362,874 kg/h)
Condenser duty, 800 million Btu/h (844 million kJ/h)

The condensate subsystem also includes:
· Three 50% capacity condensate pumps
· The condensate polisher
· Steam jet air ejector condensers
· Feedwater heater
· Associated piping, valves, controls and instrumentation.

3.4 Feed Water Subsystem

Boiler Feedwater Pump

Operating	2	2,000	4,000	6,000
Spare	1			

Type: Barrel
Capacity: 850 gpm (193 m^3/h)
Inlet pressure: 20 psia (138 kPa)
Discharge pressure: 2,700 psia (18,616 kPa)
Motor: 2,000 HP

Boiler Feedwater Intermediate Storage Tank

Operating	1
Spare	0

Capacity: 50,000 gallons (189.2 m^3)
Size: 20 ft ID x 24 ft Ht (6.10 m ID x 7.32 m Ht)
30 minute storage
Material: CS

Blowdown Storage Tank

Operating	1			
Spare	0			

Flow: 20 gpm (4.5 m^3/h)
8 hours storage
Capacity: 10,000 gallons (37.8 m^3)
Size: 10 ft ID x 17 ft Ht (3.05 m ID x 5.18 m Ht)
Material: CS

Blowdown Transfer Pump

Operating	1	1.5	1.5	1.5
Spare	0			

Capacity: 20 gpm (4.5 m^3/h)
Inlet pressure: 20 psia (138 kPa)
Discharge pressure: 60 psia (414 kPa)
Motor: 1.5 HP

3.5 Condensate Transfer and Storage Subsystem

Condensate Storage Tank

Operating		1		
Spare		0		

Capacity: 30,000 gallons (113.6 m^3)
Size: 16 ft ID x 20 ft Ht (4.88 m ID x 6.10 m Ht)
1.5 fills storage
Material: CS

Makeup Feedwater Storage Tank

Operating	1			
Spare	0			

Capacity: 10,000 gallons (37.8 m^3)
Size: 10 ft ID x 16 ft Ht (3.05 m ID x 4.88 m Ht)
4 hours storage
Material: CS

Condensate Pump

Operating	2	35	70	105
Spare	1			

Type: Vertical, canned
Capacity: 850 gpm (193 m^3/h)
Temp: 92 °F (33.3 °C)
Inlet pressure: 0.74 psia (5.1 kPa)
Discharge pressure: 50 psia (345 kPa)
Impeller material: A-296 Gr CA 15
Case material: Series B-145 Alloy 836
Motor: 35 HP

4.0 Flue Gas Emissions Control

4.1 Ammonia Based SO2 and Particulate Removal Subsystem

5.0 Solids Material Handling

5.1 Coal Feed Subsystem

Coal Feed Bin

Operating	2			
Spare	0			

Capacity: 35 tons (31.75 tonnes)
Cone slope: 55°
12 ft ID x 30 ft Ht (3.66 m ID x 9.14 m Ht)
Cylindrical Ht: 20
Construction: steel plate-3/8 in (0.95 cm) thick
Liners: 1/4 in (0.64 cm) AR

Weigh Belt Feeder

Operating	2	5	10	10
Spare	0			

Capacity: 40 tph (36.29 tonnes/h)
Length: 10 ft (3.05 m)
Motor: 5 HP

Combustion Air Blower

Operating	1	120	120	120
Spare	0			

Flow rate: 44,200 acfm (1,226.1 m^3/minute)
Discharge pressure: 14.8 psia (102.04 kPa)
Inlet pressure: 14.4 psia (99.28 kPa)
BHP: 96
Motor: 120

Day Bins

Operating	4
Spare	0

Size: 25 ft ID x 45 ft Ht (7.62 m ID x 13.72 m Ht)
Cone slope: 55°
Construction: Steel plate-3/8 in (0.95 cm) thick
Liners: 1/4 in (0.64 cm) AR

Pulverizer

Operating	2	400	800	1200
Spare	1			

Capacity: 32 tph (20.03 tonnes/h) (with integral classifier)
Motor: 400 HP

Primary Air Blower

Operating	1	1,900	1,900	1900
Spare	0			

Flow rate: 43,300 acfm (1,226.1 m^3/minute)
Disch pressure: 22 psia (151.68 kPa)
Inlet pressure: 14.4 psia (99.28 kPa)
BHP: 1,568
Motor: 1,900

5.2 Coal Handling Subsystem

Dump Hopper

Operating	1
Spare	0

Live capacity: 300 tons (272.2 tonnes)
Plan: 16 ft x 90 ft (4.88 m x 27.43 m)
Vertical side: 14 ft (4.27 m)
Outlets: 6
Construction: concrete and steel plate
Steel sloping sides: 3/8 in (0.95 cm) thick, 55°
Liners for sloping sides: 1/4 in (0.64 cm) thick AR
Structural steel supports for rail track included
Bar grids over dump hoppers: 8 in (20.32 cm) opening
6 in x 1/2 in (15.24 cm x 1.27 cm) flats- welded

Coal Silo

Operating	2
Spare	0

Capacity: 12,500 tons (11,340 tonnes) /each
Diameter: 65 ft (19.81 m)
Height: 165 ft (50.3 m)
Outlets: 2
Cone slope: 55°
Construction: 3/8 in (0.95 cm) thick steel plate
Liners: 1/4 in (0.64 cm) AR

Dump Hopper Feeders

Operating	6	15	90	90
Spare	0			

Type: vibrating
Delivers to: dump hopper conveyor
Material: coal, 4 in x 0 (10.16 cm x 0 cm)
Capacity: adjustable from 0 to 500 tph (0 to 454 tonnes/h)
Enclosure: dust tight
Liners: repacable, abrasion resistant steel

Dump Hopper Conveyor

Operating	1	25	25	25
Spare	0			
Type: belt conveyor				
Capacity: 2,000 tph (1814 tonnes/h)				
Width: 60 in (18.29 cm)				
Length: 90 ft (27.43 m)				
Speed: 650 fpm (198 m/minute)				
Lift: zero				
Emergency Pile Feed Conveyor				
Operating	1	200	200	200
Spare	0			
Type: belt conveyor				
Capacity: 2,000 tph (1814 tonnes/h)				
Width: 60 in (18.29 cm)				
Length: 300 ft (91.44 m)				
Lift: 20 ft (6.10 m)				
Speed: 650 fpm (198 m/minute)				
Belt Scale				
Operating	1			
Spare	0			
Capacity: 2,000 tph (1814 tonnes/h)				
Belt width: 60 in (18.29 cm)				
Tramp Iron Magnet				
Operating	1	5	5	5
Spare	0			
Type: self cleaning				
Belt width: 60 in (18.29 cm)				
Coal flow rate: 2,000 tph (1814 tonnes/h)				
Coal size: 4 in (10.16 cm)				
Silo Feed Conveyor				
Operating	2	500	1,000	1000
Spare	0			
Type: belt conveyor				
Capacity: 2,000 tph (1814 tonnes/h)				
Width: 60 in (18.29 cm)				
Length: 500 ft (152.4 m)				
Lift: 95 ft (28.96 m)				
Speed: 650 fpm (198 m/minute)				

Sampling System				
Operating	1	45	45	90
Spare	1			
Coal size: 4 in x 0 (0.16 cm x 0)				
Flow rate: 2,000 tph (1814 tonnes/h)				
Includes primary sampler, sample crusher, and secondary sampler				
Motorized Gate				
Operating	3	10	30	30
Spare	0			
Type: two way				
Coal flow: 2,000 tph (1814 tonnes/h)				
Vibrating Bin Bottoms				
Operating	2	10	20	40
Spare	2			
Type: Kinergy or equal				
Reclaim Feeders				
Operating	4	5	20	40
Spare	4			
Type: belt feeder				
Capacity: 100 tph (90.8 tonnes/h)				
Width: 42 in (106.7 cm)				
Length: 25 ft (7.62 m)				
Lift: zero				
Speed: 100 fpm (30.58 m/minute)				
Emergency Feeders				
Operating	0		0	0
Spare	2			
Type: belt feeder				
Capacity: 100 tph (90.8 tonnes/h)				
Width: 42 in (106.7 cm)				
Length: 15 ft (4.58 m)				
Lift: zero				
Speed: 100 fpm (30.58 m/minute)				

Reclaim Conveyor				
Operating	1	15	15	15
Spare	0			
Type: belt conveyor				
Capacity: 100 tph (90.8 tonnes/h)				
Width: 24 in (60.96 cm)				
Length: 300 ft (91.44 m)				
Lift: 50 ft (15.24 m)				
Speed: 250 fpm (76.2 m/minute)				
Emergency Reclaim Conveyor				
Operating	1	15	15	30
Spare	1			
Type: belt conveyor				
Capacity: 100 tph (90.8 tonnes/h)				
Width: 24 inch (60.96 cm)				
Length: 300 ft (91.44 m)				
Lift: 40 ft (12.19 m)				
Speed: 250 fpm (76.2 m/minute)				
Plant Feed Conveyor				
Operating	2	10	20	20
Spare	0			
Type: belt conveyor				
Capacity: 100 tph (90.8 tonnes/h)				
Width: 24 in (60.96 cm)				
Length: 275 ft (83.82 m)				
Lift: 40 ft (12.19 m)				
Speed: 250 fpm (76.2 m/minute)				
Dump Area Dust Suppression System				
Operating	1	40	40	40
Spare	0			
Includes: a 5 gpm (1.14 m^3/h) proportioning pump, mixing tank, a 200 gpm (45.42 m^3/h) distribution pump, spray nozzles				
Johnson Marsh, Chemjet or equal				

5.3 Bottom Ash and Slag Handling Subsystem

Part of the HITAF equipment package: 3 tph (2.72 tonnes/h) design rate as described in the commercial plant conceptual report.

5.4 Fly Ash Handling Subsystem

Part of the HITAF equipment package: 50 tph (43.36 tonnes/h) design rate as described in the commercial plant conceptual report.

6.0 Process Water System

6.1 Demineralized Water Subsystem

Supplier package consisting of the following:

· Demineralizer feed tank
· Three 100% capacity multimedia filter feed pumps
· Two 100% capacity mutimedia filter vessels
· Two 100% capacity active carbon filter vessels
· Two 100% capacity cation exchange vessels
· One 100% capacity decarbonator blower
· One 100% capacity decarbonator
· Two 100% capacity decarbonator pumps
· Two 100% capacity anion exchange vessels
· Two 100% capacity mixed bed vessels
· Bulk acid storage tank
· Two 100% capacity acid feed pumps
· Bulk caustic storage tank with heater
· Two 100% capacity caustic feed pumps
· Two 100% capacity regeneration water pumps
· Caustic dilution water heater tank with heater
· Associated piping, valves and instrumentation

6.2 Condensate Polisher Subsystem

Supplier package consisting of the following:

· Two 100 percent capacity condensate polisher vessels
· Two 100 percent capacity hold pumps (one pump for each polisher vessel)
· Precoat injection pump
· Recycle pump
· Advance precoat tank with mixer
· Auxiliary tank, an air surge tank
· Four sample coolers
· Associated piping valves and instrumentation.

6.3 Raw Water Subsystem

Supplier package consisting of the following:

· Two 100% capacity river intake screens
· Two 100% capacity river pumps
· Two 100% capacity cooling water storage pond pumps
· Softener feed tank
· Two 100% capacity softener feed pumps
· Clearwell
· Two 100% capacity clearwell transfer pumps
· Two 50% capacity river air receivers
· Makeup water sodium hypochlorite storage tank
· Two 100% capacity makeup water sodium hypochlorite metering pumps
· Associated piping, valves and instruments.

6.4 Softener Subsystem

Supplier package consisting of the following:

· Softener
· Two 100% capacity softener sludge pumps
· Eight 12.5% capacity gravity filter cells
· Two 100% capacity filter air scour blowers
· Three 100% capacity gravity filter transfer/backwash pumps
· One sludge thickener
· Two 100% capacity belt press feed pumps
· One belt filter press
· Associated chemical feed systems, piping, valves and instrumentation.
· lime feed system
· soda ash feed system

6.5 Chemical Addition Subsystem

Supplier package consisting of the following:

· Neutralizing amine additive system
· Oxygen scavenger additive system
· Phosphate additive system
· Circulating water sulfuric acid feed system
· Circulating water sodium hypochlorite feed system

7.0 Miscellaneous Process Support

7.1 HVAC Package Including:

- · Packaged air conditioning units
- · Roof mounted exhaust fans
- · Wall mounted supply/exhaust fans
- · Electric heaters

7.2 Diesel Fuel Storage Package

7.3 Fire Protection Package

7.4 Wastewater Package Including:

- · Thirteen pairs of sump pumps (nominally two 100% capacity duplex sump pumps)
- · Three single sump pumps for small sumps
- · One oil/water separator
- · Two pumps each in the coal pile runoff and storm water management basin #1
- · Two 50% capacity air preheater wash sump pumps
- · One large transfer pump in the wastewater storage pond
- · One neutralization tank
- · Two 100% capacity neutralization recirc/transfer pumps
- · One wastewater equalization tank
- · Two 100% capacity waste equalization tank transfer pumps
- · Associated piping, valves and instrumentation.

Appendix B - Emissions Control Technology Screening

Summary and Introduction

The Emissions Control Technology Screening report presents results from collecting, assimilating and comparing the data provided by a number of air emissions control system suppliers. From a screening evaluation of these data, and the evaluation of other cost and performance factors, the primary flue gas cleaning candidates for the HIPPS commercial plant conceptual design are lime absorbent flue gas desulfurization (FGD) combined with selective catalytic reduction (SCR) for NO_x control, and ammonia based FGD processes with selective noncatalytic reduction (SNCR) for NO_x. These processes have the lowest annualized costs and power consumption among the screened technologies. The ammonia based process costs are most competitive when the by-product ammonium sulfate is successfully marketed. This makes the ammonia process likely to be more sensitive to site specific conditions than the lime and SCR system. However, successful marketing of the by-product also eliminates a large stream of waste materials, which would otherwise require treatment and disposal.

The economic results of the screening study are shown in Exhibit B-1. The estimated annual costs are compared for the following.

- Series 1 = Lime based process for SO_2 and SCR for NO_x.
- Series 2 = Ammonia process for SO_2 and SNCR for NO_x.
- Series 3 = Wet limestone forced oxidation for SO_2 and SCR for NO_x.

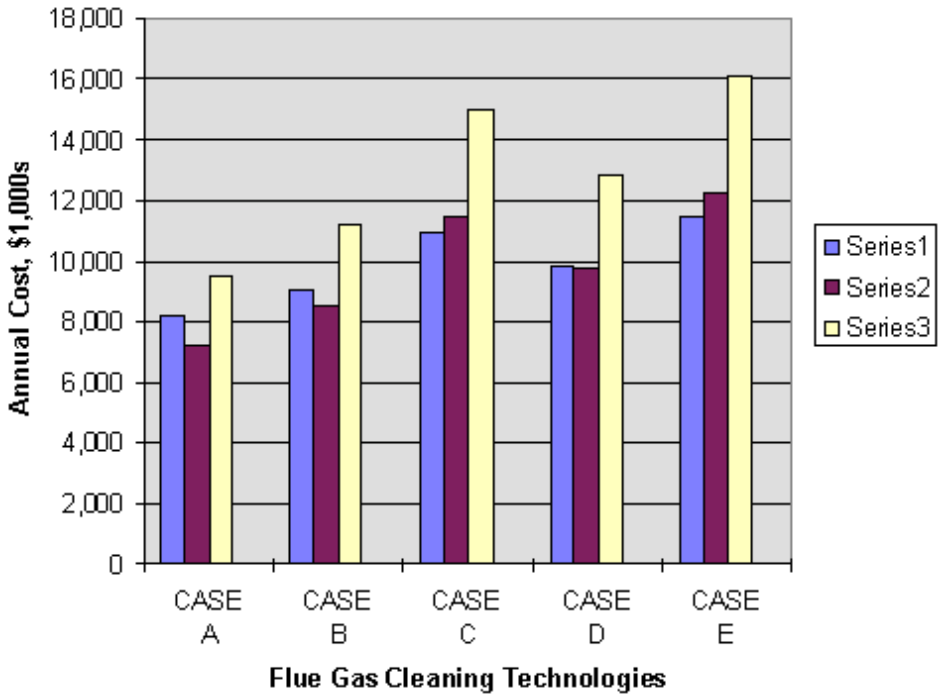

Exhibit B-1
Summary of Annual Costs for FGD Technologies

In Exhibit B-1, series 1 is a lime process FGD and SCR, 2 is an ammonia FGD process and SNCR, and 3 is wet limestone forced oxidation FGD and SCR. Cases A, B, C, D, and E use variations in the cost of money and investment time frame as part of the annual cost calculations. Cost estimate details and annual cost calculations are reported further in the section on Flue Gas Cleaning Cost and Economic Data. Before making the comparison reported above, a dozen potential suppliers were contacted with results reported in later sections.

Air Emissions Control Technology Screening

The data reported here will be used by the HIPPS team to screen and select the air emissions control technologies for the conceptual commercial HIPPS plant. The emissions control systems are examined for the three major power plant pollutants. The emission limits are those in Table B-1, which are based on 65% coal and 35% natural gas energy input to the system.

Table B-1
Summary of Environmental Performance Requirements

	New Source Performance	Phase I	Phase II
Sulfur Oxides (lb/MMBtu)	0.40*	0.10	0.06
Nitrogen Oxides (lb/MMBtu)	0.50	0.125	0.06
Particulate (lb/MMBtu)	0.03	0.008	0.003
Solid Wastes	Benign	Benign	Benign

- *Based on 90% reduction of the total sulfur in the fuel with the design coal (5.98 pounds of SO_2 per MMBtu) and a 65/35 ratio of coal and natural gas.*
- *Liquid discharges are treated to meet NSPS requirements. Solid wastes, such as coal ash and flue gas treatment sludges are to be stabilized and sent to offsite disposal.*

Sulfur Dioxide

The flue gas desulfurization (FGD) process will be designed for 105% of the calculated gas flow. For an all coal-fired plant and the design coal, SO_2 capture would need to be 99% if the emissions requirement is 0.06 lb/MMBtu (25.80 ng/J). However for the near term HIPPS design, as much as 35% of the total plant fuel can be natural gas burned to raise the GT inlet air temperature to GT inlet conditions. For the 65/35 coal and gas scenario, a SO_2 capture of 98.5% is sufficient to meet the Phase II standard.

Nitrogen Oxide

In the commercial plant configuration, NO_x is formed by the coal combustion process, and negligible in the GT operation. Thus, post combustion controls will be needed only for the coal flue gas stream. To obtain the required NO_x control, commercial and developing NO_x capture processes are examined. NO_x reduction of 60% is needed for the 65/35 coal and gas scenario to reach the 0.06 lb/MMBtu (25.80 ng/J) emission limit.

Particulate

With the control limit of 0.003 lb per MMBtu, (1.3 ng/J) or an order of magnitude increase of the current regulations, the particulate control system will require capture efficiencies of 99.9 to 99.99%. The strict limit is also consistent with the project objective to minimize the release of potentially hazardous trace elements or heavy metals.

Flue Gas Composition and Flow

For the 300 MW scale commercial plant, the composition and flow rate of the flue gas produced by burning Illinois No. 6 coal is shown in Table B-2. Illinois No. 6 was selected in Phase I as representative of a widely available high sulfur coal. Table B-2 also shows the permissible flow rates of the pollutants in the coal flue gas after cleaning.

Table B-2
Flue Gas Data Sheet

(Illinois No. 6 Coal)

	Normal	Design
Dirty Flue Gas		
Gas inlet temperature, °F	300	300
Gas inlet pressure, psia	14.8	14.8
O_2, lbmol/h	1,450.9	1,523.4
N_2, lbmol/h	38,674.2	40,607.9
Ar, lbmol/h	470.1	493.6
CO_2, lbmol/h	7,048.2	7,400.6
H_2O_{gas}, lbmol/h	5,611.5	5,892.1
SO_2, lbmol/h[1]	127.7	134.1
NO_2, lbmol/h[3]	6.7	7.1
Total, lbmol/h	53,389.3	56,058.7
Total, lb/h	1,568,353	1,646,771
Mol. Wt., lb/lbmol	29.376	29.376
Volumetric flow rate, scfh	20,261,233	21,274,295
Volumetric flow rate, acfh	29,412,487	30,883,111
Particulate, lb/h[5, 7]	7,132	7,489
Particulate, gr/scf	2.35	2.35
Particulate, gr/acf	1.82	1.82
Cleaned Flue Gas		
SO_2 in exit gas, lbmol/h[2]	1.98	1.98
NO_x in exit gas, lbmol/h[4]	2.75	2.75
Particulate in exit gas, lb/h[6]	6.33	6.33

Notes:

1. SO_2 in dirty flue gas is equivalent to 3.9 lb/million Btu
2. SO_2 in cleaned flue gas is equivalent to 0.06 lb/million Btu
3. NO_x in dirty flue gas is equivalent to 0.15 lb/million Btu
4. NO_x in cleaned flue gas is equivalent to 0.06 lb/million Btu
5. Particulate in dirty flue gas is equivalent to 3.4 lb/million Btu
6. Particulate in cleaned flue gas is equivalent to 0.003 lb/million Btu
7. Size distribution of particulate in dirty flue gas is as follows:

Microns	Mesh	Cumulative, %
<10		40
<20		70
<44	325	80
<74	200	97
<149	100	100

Flue Gas Cleaning Process Developers

The following potential providers of processes/equipment were contacted with varying results.

1. General Electric Environmental Systems, Lebanon, PA
2. ABB Environmental Systems, Knoxville, TN
3. AirPol Inc., Parsippany, NJ
4. Environmental Elements Corporation, Baltimore, MD
5. Krupp Koppers, Essen, Germany
6. NOXSO Corporation, Bethel Park, PA
7. General Electric Environmental Systems, Lebanon, PA for their Ammonia Process
8. Babcock & Wilcox, Barberton, OH
9. Belco Technologies Corporation, Parsippany, NJ
10. Dravo Lime Company, Pittsburgh, PA
11. Haldor Topsoe, Inc. Houston, TX
12. Pure Air, Allentown, PA
13. Chiyoda Corporation, Tokyo, Japan

Of the above companies, the first six recommended flue gas cleaning systems and supplied technical and cost information. SCR suppliers were also contacted and the results are reported in the section on GE's Ammonia Desulfurization Process. The recommended processes are described in the following sections.

Flue Gas Cleaning Processes

Process descriptions, performance and cost data provided by the first six organizations listed above are reported below. After each process description, a table is presented documenting the data provided by process developers, and some areas where information has been augmented by Bechtel from other sources. All costs are for 1997 price and wage levels.

GE's Limestone Flue Gas Desulfurization Process

The flue gas desulfurization system proposed by General Electric Environmental Systems utilizes wet limestone slurry with insitu forced oxidation to produce disposable gypsum. Exhibits B-2 and B-3 show the gas flow paths and the liquid flows in the absorber area. Exhibit B-4 shows the dewatering of gypsum and Exhibit B-5 illustrates the sorbent preparation system. Table B-3 provides data about the flue gas cleaning process.

Process Description

Sorbent preparation and handling: Pebble limestone is fed to a closed circuit wet grinding system. The system includes a ball mill and cyclone classifiers. The limestone is ground to 90% passing 325 mesh. The slurry from the ball mill is discharged at 30% solids into the limestone slurry storage tank.

A continuously circulating slurry loop feeds the absorber intermittently. Limestone slurry is added to the absorber to replenish limestone consumed by sulfur dioxide. The slurry addition rate is controlled by a feed forward controller based on the amount of sulfur dioxide in the flue

gas. The control is overridden by a feed backward controller based on pH of the absorber recycle slurry.

GE's flue gas desulfurization process: The flue gas from the HIPPS dirty HRSG flows through an ESP to the FGD inlet duct, continues to the absorber, and finally to a stub stack mounted on top of the absorber.

The dirty flue gas is treated first in the ESP to remove most of the flyash particles. The flue gas leaving the ESP enters the absorber where it is contacted by countercurrent sprays of limestone slurry. The flue gas enters the absorber at 300 °F (149 °C) and discharges in a saturated condition at 132 °F (56 °C). The gas travels upward through two levels of slurry spray where SO_2 is absorbed by the limestone slurry. The gas next passes through two chevron-type mist eliminators at the top of the absorber where water droplets entrained in the gas are removed. The cleaned gas exits the system via the absorber stub stack.

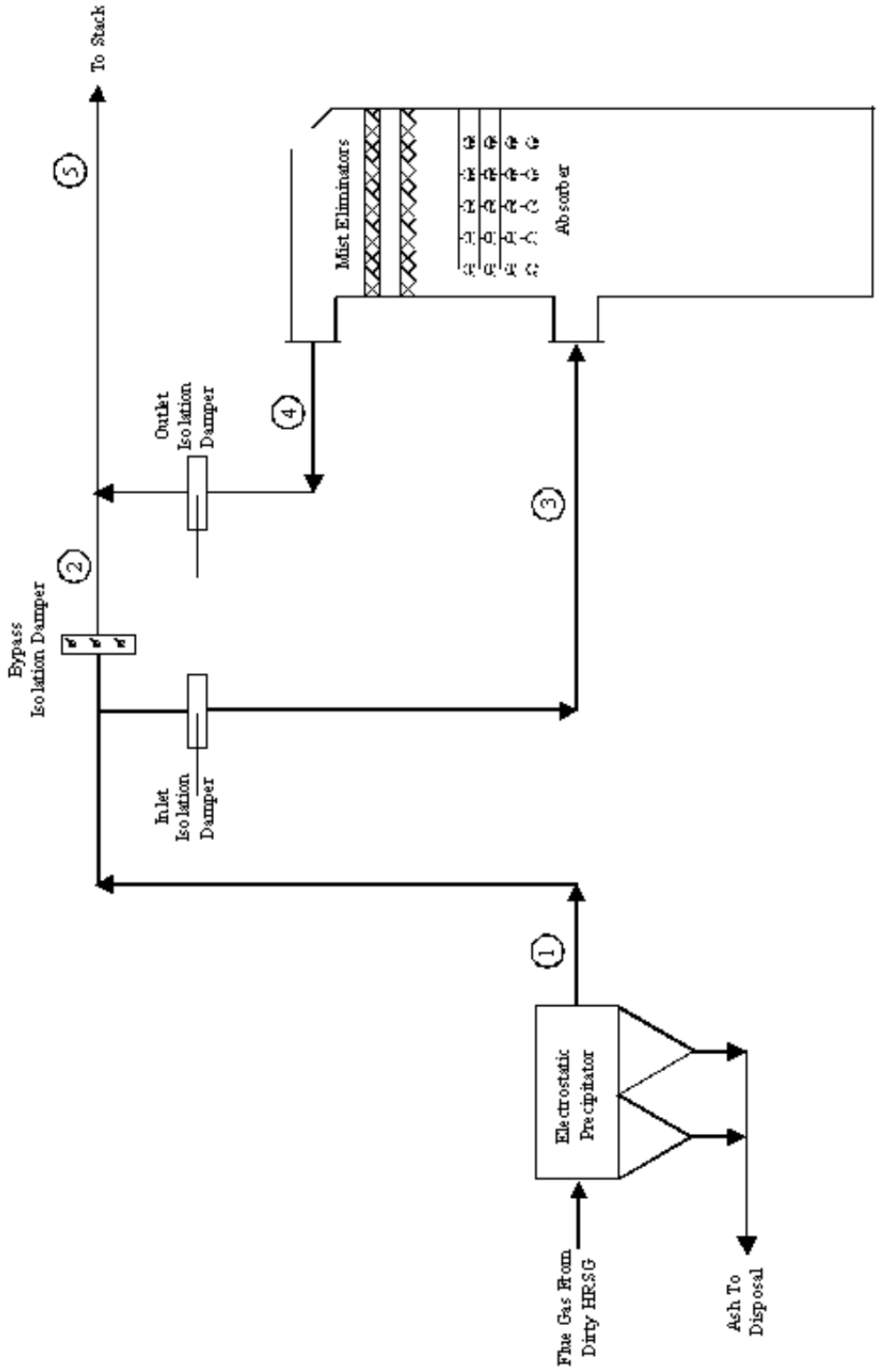

Exhibit B-2
GE's Limestone Process - ESP and Absorber Gas Flow Path

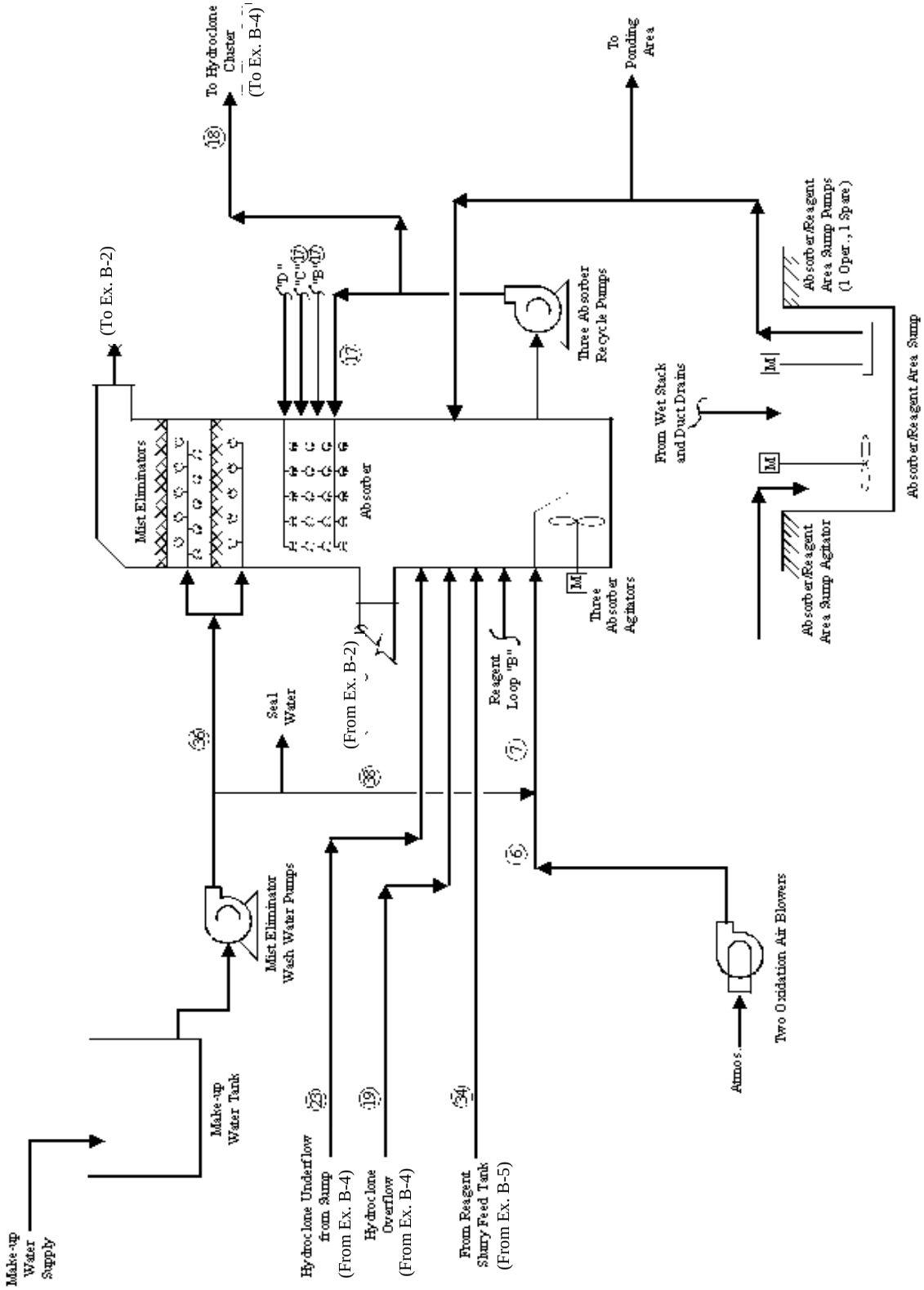

Exhibit B-3
GE's Limestone Process - Liquid Flow Path in Absorber Area

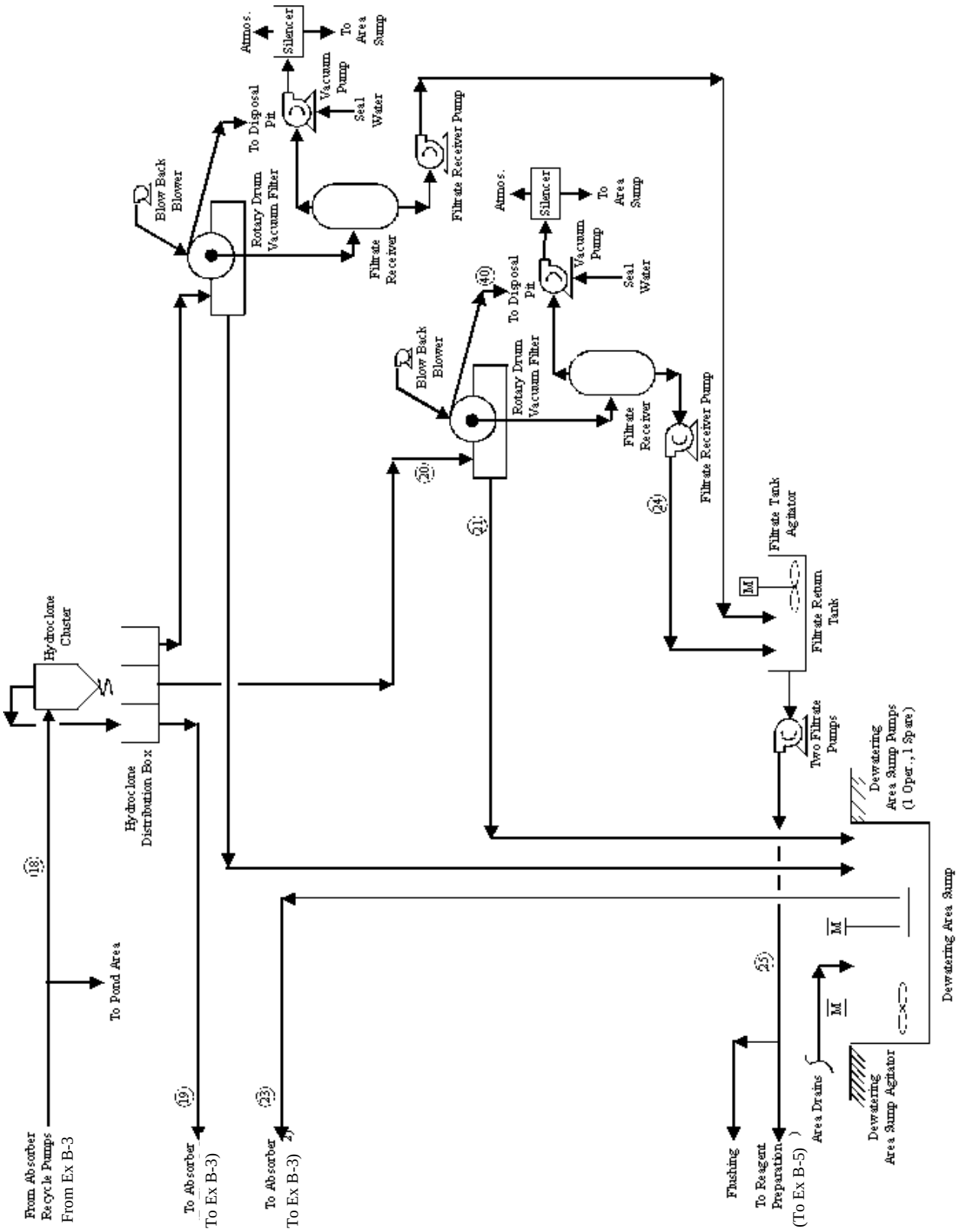

Exhibit B-4
GE's Limestone Process - Dewatering Area

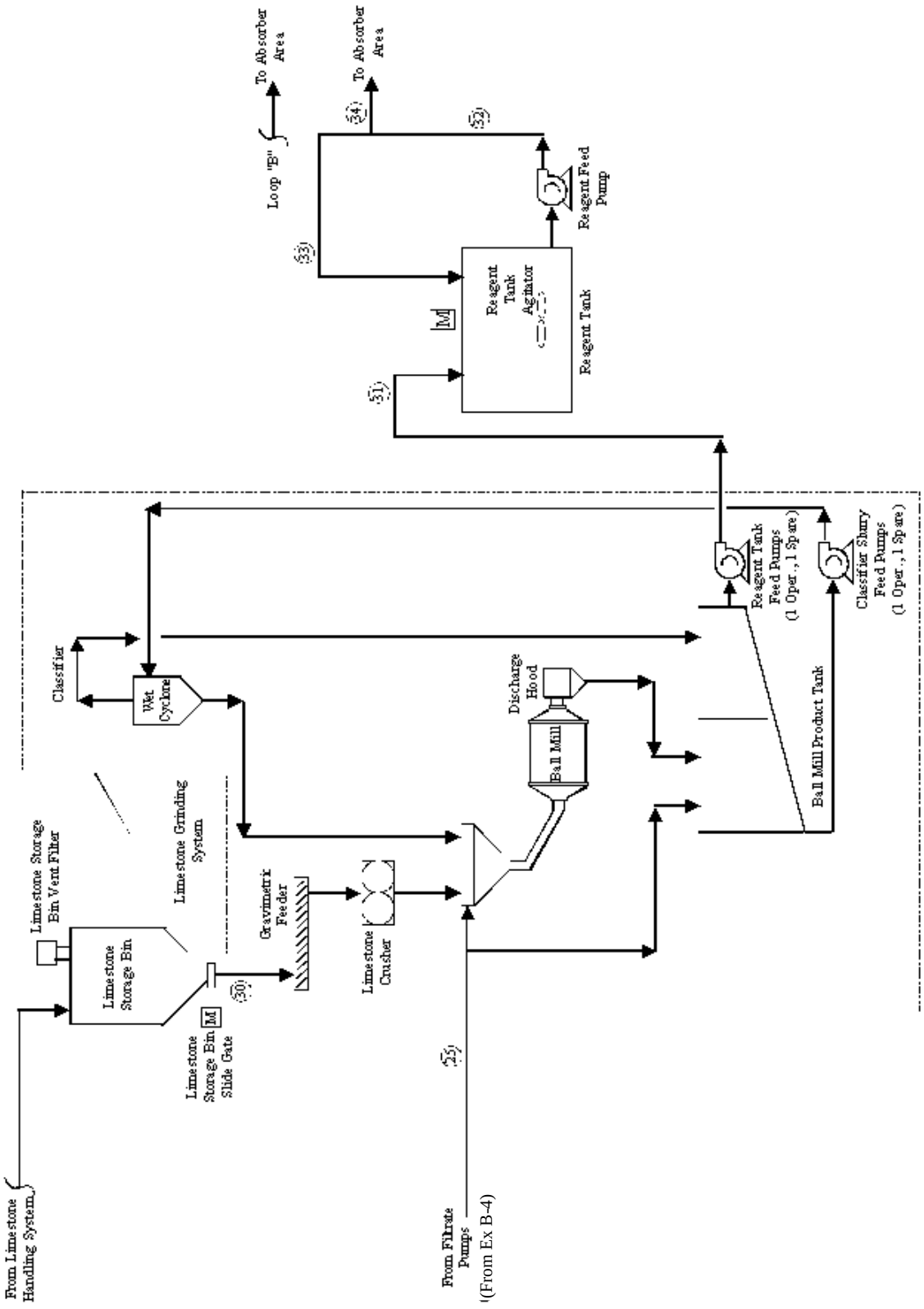

Exhibit B-5
GE's Limestone Process - Reagent Preparation Area

The absorber design and internal arrangement are crucial to successful SO_2 capture. Flue gas enters the absorber near the bottom of the spraytower and flows upward to react with a descending spray of finely divided droplets of recycle slurry. The slurry contains the alkali needed to react with SO_2. The slurry spray also saturates and cools the gas from an inlet temperature of 300 to 132 °F (149 to 56 °C). Intimate contact of the flue gas with the alkaline limestone slurry is achieved in two successive spray zones. Each spray bank has a series of spray nozzles designed to achieve proper atomization of the recycle slurry. Recycle slurry to the absorber is provided by two operating and one spare recycle pumps. The absorber recycle tank is designed for sufficient residence time and adequate agitation to ensure optimum utilization of limestone as well as crystallization and precipitation of gypsum.

Oxidation of calcium sulfite to calcium sulfate or gypsum is also accomplished in the recycle tank. Oxidation air compressors supply air to the oxidation air lances submerged in the recycle tank. A stream of slurry from the recycle pump removes the gypsum produced and controls the percent solids in the absorber at 15%. The gypsum slurry is sent to a disposal pond by the absorber recycle pump.

A two-stage mist eliminator is provided at the top of the absorber. The first stage mist eliminator removes the bulk of the entrained liquid droplets from the gas stream. The second stage removes fine droplets carried over from the first stage. The mist eliminators are washed intermittently to maintain clean surfaces and low gas-side pressure losses. Spray banks and wash nozzles wash both the bottom and the top of the first stage mist eliminator and the bottom of the second stage mist eliminator. The frequency of the washing cycle is adjustable and its control is based on the system water demand.

Process chemistry: The main function of the absorber is to remove sulfur dioxide from the flue gas using a slurry, pH 5.2 to 6.0, containing limestone (calcium carbonate). The absorber reaction tank is designed to promote calcium carbonate dissolution, forced oxidation, and solid precipitation. The overall reactions that take place in the absorber are:

$$SO_2 + CaCO_3 \longrightarrow CaSO_3 + CO_2$$
$$SO_3 + CaCO_3 \longrightarrow CaSO_4 + CO_2$$

Many intermediate steps also take place. Calcium ions are formed in the aqueous solution.

$$CaCO_3(s) \longrightarrow CaCO_3(aq)$$
$$CaCO_3(aq) + H_2O \longrightarrow Ca^{++} + HCO_3^{'} + OH^{'}$$

The SO_3" anions form at the flue gas/liquid interface in the absorber.

$$SO_2(g) \longrightarrow SO_2(aq)$$
$$SO_2(aq) + H_2O \longrightarrow HSO_3' + H^+$$
$$HSO_3' \longrightarrow H^+ + SO_3"$$

Gypsum, the primary precipitate, is formed in the insitu forced oxidation environment.

$$SO_3" + 1/2\ O_2 \longrightarrow SO_4"$$
$$Ca^{++} + SO_4" + 2\ H_2O \longrightarrow CaSO_4.2H_2O(s)$$

The sulfite ion also combines with the calcium ion to form calcium sulfite hemihydrate.

$$Ca^{++} + SO_3" + 1/2\ H_2O \longrightarrow CaSO_3.1/2H_2O(s)$$

In addition to sulfur dioxide, the absorber can also remove hydrogen chloride and hydrogen fluoride from the flue gas. This may be important for certain coals. Calcium carbonate is required to neutralize these acid gases in the following manner.

$$2\ HCl + CaCO_3 \longrightarrow CaCl_2 + H_2O + CO_2$$

$$2\ HF + CaCO_3 \longrightarrow CaF_2 + H_2O + CO_2$$

Experience

GE has extensive experience with limestone-based FGD plants. Their first commercial limestone based plant was commissioned in 1982. GE has installed 13 limestone-based FGD plants with a total capacity of 9,500 MW in the USA and 40 plants with a total capacity of 20,000 MW in other countries, for a total of 53 plants with a total capacity of about 30,000 MW. In addition to the limestone-based FGD plants, GE has also installed venturi scrubbers, lime scrubbers and water scrubbers, the water scrubbers having been installed in the early 70's. When these plants are also included, the GE's scrubber experience comes to some 50,000 MW.

Table B-3
GE's Limestone Flue Gas Cleaning Process Data

- Process Scope:
  - SO_x removal
  - Particulate removal
- Equipment Scope:
  - Limestone grinding
  - Limestone slurry preparation
  - Scrubber
  - ESP
- Pressure Drop: = 8.5 in. w. c.
- Raw Material Consumption:
  - Limestone = 7.6 ton/h
- By-product/Waste Production:
  - Waste = 14.5 ton/h
- Utilities Consumption:
  - Power = 3,800 + 708 = 4,508 kW
  - Water = 147 gpm
- Cost, millions:

Equipment cost	= $ 15.0
Grinding System	= $ 1.9
Installation	= $ 10.0
ESP Allowance[1]	= $ 1.5
Total	= $ 28.4

- Manpower: = 1.5 operators per shift
- Footprint:

FGD = 50 ft wide x 60 ft long
ESP = 50 ft wide x 70 ft long x 50 ft high

Note:
1. The GE recommended system limits particulate emissions to 15.0 lb/h. To increase particulate capture and limit the emissions to 6.33 lb/h, $1.5 million is added for additional ESP fields.

ABB's Limestone Flue Gas Desulfurization Process: LS-2

ABB recommended its LS-2 limestone slurry process, which is an enhanced forced oxidation process using a high velocity absorber and other process improvements to reduce the life cycle cost. The LS-2 process is installed on a 130 MW scale unit at Ohio Edison's Niles Station.

Process Description

Sorbent preparation and handling: Ground limestone is delivered and fed to a small tank (2 hours capacity) where it is mixed with water to create a 30% solids (by weight) slurry. (ABB's system scope begins with a ground limestone. In later cost comparisons, a grinding facility is added to make ABB and GE more consistent and comparable.) Limestone slurry is transported from the tank to the absorber with a recirculating feed loop. Slurry velocities are constantly maintained in the loop while at the same time providing the required feed to the absorber.

Slurry is added to the absorber in response to two control signals. The primary control is the SO_2 concentration in the flue gas entering the FGD system. The other control is the pH in the reaction tank which trims the feed valve. The pH trimmed system responds rapidly and is highly stable.

ABB's flue gas desulfurization process: ABB recommended the LS-2 process with the following design basis:

- The FGD system uses ground limestone (95% less than 325 mesh) delivered to the site by truck. The purchase of ground limestone avoids an investment in grinding facilities, and is economically attractive for small plants. The 300 MWe HIPPS plant decision to install facilities or purchase grinding services is not definitive. For comparisons, HIPPS has chosen to add grinding to the system costs provided by ABB.
- With SO_2 removal efficiency specified at 98.5%, organic acid (dibasic or adipic acid) enhancement is recommended. When added in small quantities, the acid reduces power requirements and pressure drop in the absorber.
- The flue gas cleaning plant is designed without reheat. This is the most common approach in the U. S. and it avoids the substantial capital and operating cost of reheat equipment with no environmental or performance penalty.
- Product will be gypsum containing at least 95% $CaSO_4.2H_2O$.
- Sparing philosophy: All critical pieces of rotating equipment (pumps, blowers, etc.) have an installed standby spare.

The process flow diagram for the LS-2 process is shown in Exhibits B-6 and B-7. Process data are provided in Table B-4. Flue gas from the HRSG is ducted to an ESP. The gas from the ESP outlet is directed to the inlet ductwork of a single absorber train and subsequently to the stack. Provision has been made for the flue gas to bypass the absorber. The absorber is 23 feet (7 m) in diameter by 42 feet (12.8 m) high. The reaction tank is 27 feet (8.2 m) in diameter by 39 feet (11.9 m) high.

The flue gas from the ESP enters the spray tower near the bottom through an inlet zone made of nickel alloy that resists the corrosion that can take place at the wet/dry interface. In the absorber, the hot flue gas is immediately quenched as it travels upward countercurrent to a

continuous spray of the recycle slurry produced by multiple spray banks. The recycle slurry (a 15% concentration slurry of calcium sulfate, calcium sulfite, unreacted alkali, inert materials, flyash and various dissolved materials) absorbs the sulfur dioxide from the flue gas. The absorbed sulfur dioxide reacts with the dissolved alkali (calcium carbonate) to form dissolved calcium sulfite.

The design liquid-to-gas ratio (L/G) is provided by three operating recycle spray levels fed by three dedicated recycle spray pumps; a fourth pump and spray level is provided as an installed standby spare. Each spray level consists of a bank of nitride-bonded silicon carbide spray nozzles. The spray nozzles are designed to provide proper sized droplets for SO_2 absorption, typically a $d_{50} < 2{,}000$ μm. The spray nozzles are arranged so that spraying is in both con-current and countercurrent directions, to maximize turbulence and gas/liquid contact.

The recycle slurry falls from the spray zone into the reaction tank which forms the base of the absorber. This tank is sized to provide sufficient residence time for all of the FGD chemical reactions to take place. Fresh reagent slurry is added to the reaction tank where it reaches equilibrium with the bulk of the recycle slurry prior to being returned to the spray banks via the recycle pumps.

Forced oxidation of the recycle slurry in a limestone wet FGD system produces a more manageable reaction product. To produce the fully oxidized product, rotary lobe blowers supply compressed air to a sparging system in the reaction tank. The oxygen in the air converts the dissolved calcium sulfite ($CaSO_3$) to calcium sulfate ($CaSO_4$), which then crystallizes as gypsum ($CaSO_4.2H_2O$).

ABB's oxidation air injection system utilizes open sparging lances located adjacent to each of the side-entering reaction tank agitators. The agitators provide a uniform distribution of air within the tank. The lance system is superior to sparge grids or assemblies submerged in the reaction tank in that there are no small holes that can plug or massive pipes or support structures that can corrode or break.

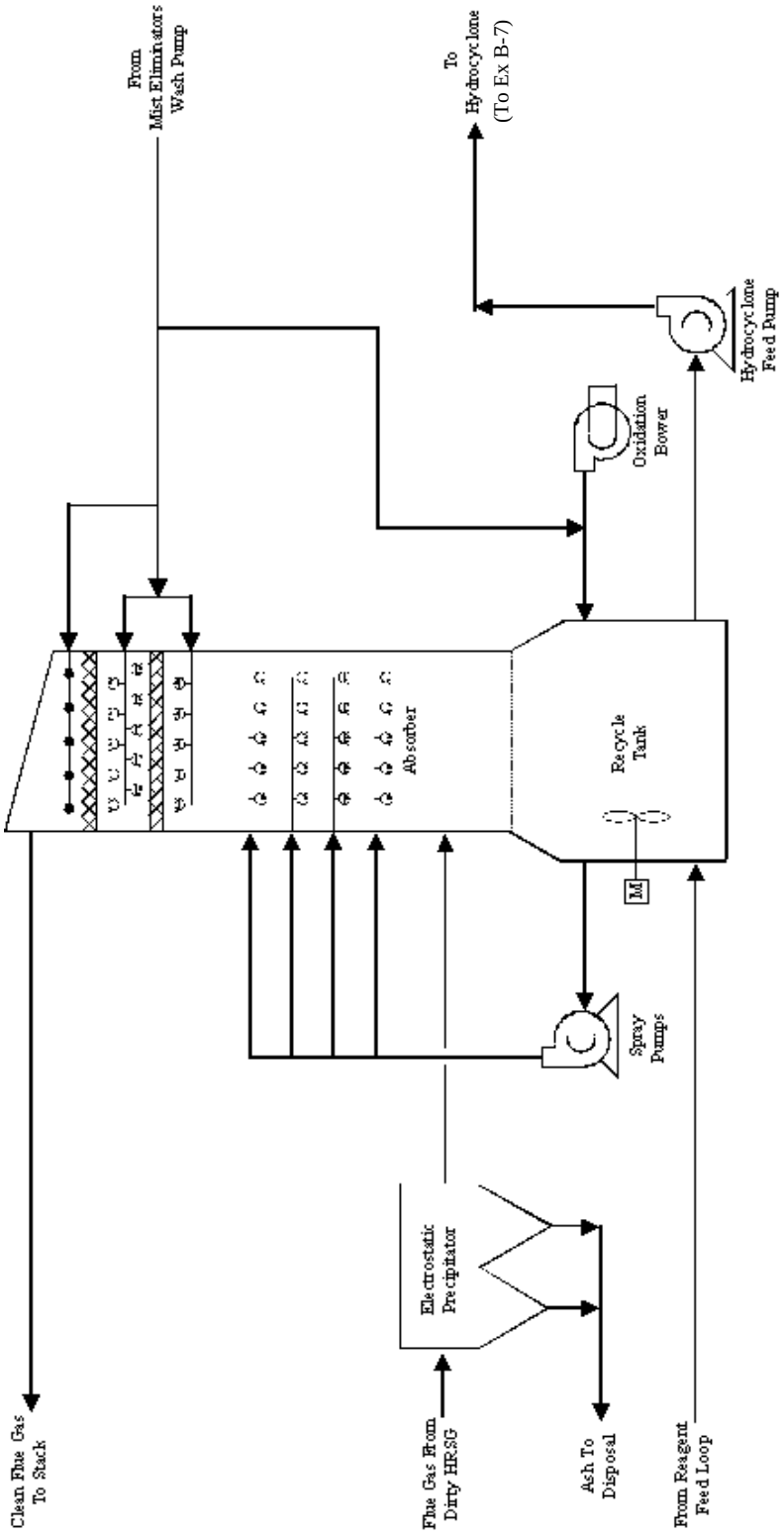

Exhibit B-6
ABB's LS-2 Process

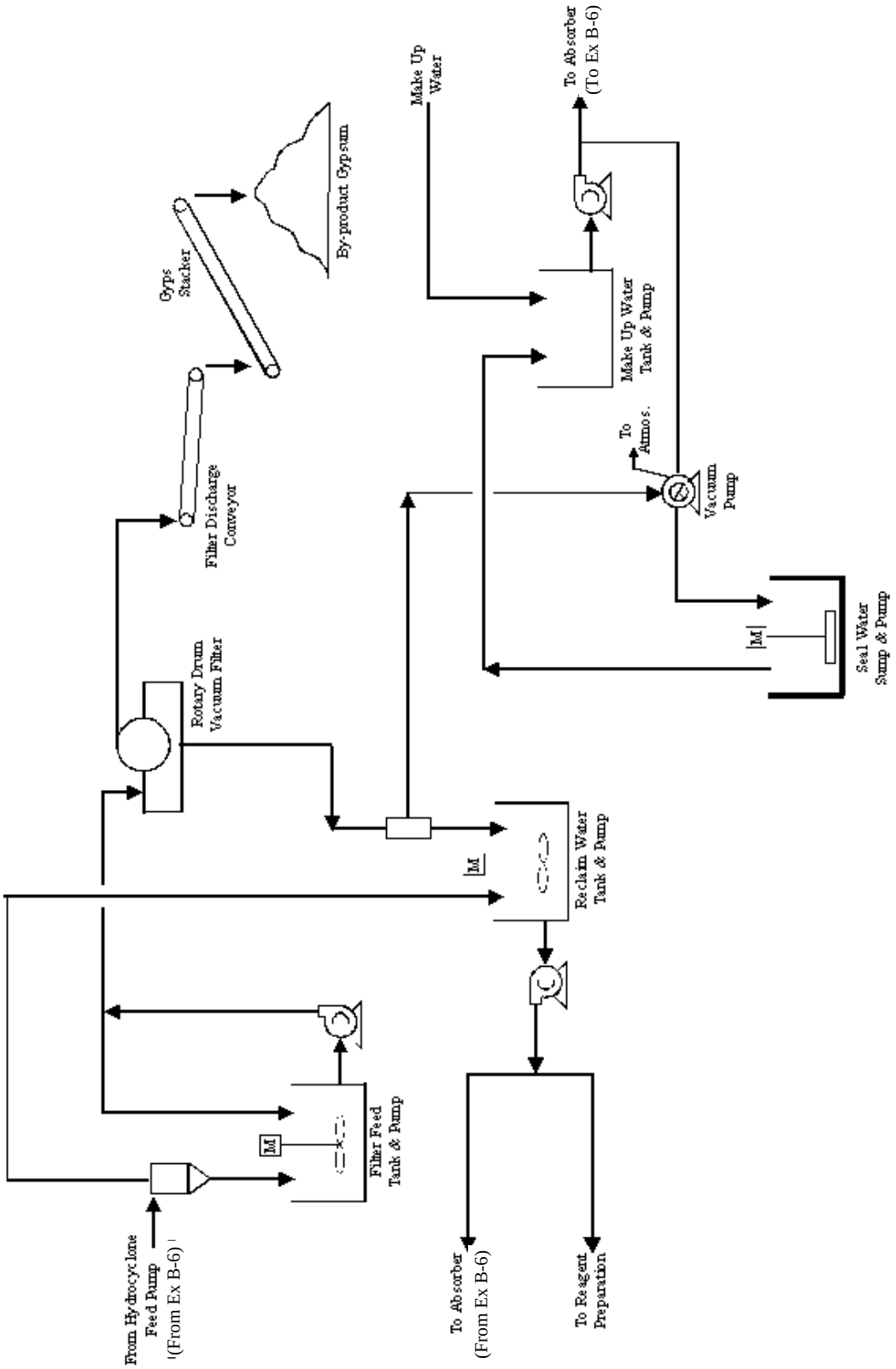

Exhibit B-7
ABB's LS-2 Process - Dewatering of Gypsum

Upon leaving the absorption zone, the gas flows upward through a two-stage mist elimination system. The first stage provides primary separation of large entrained slurry drops and functions as a gas distributor for the second stage. The second stage is a horizontal flow, multipass chevron mist eliminator designed to achieve outlet loadings less than 50 mg/Nm^3. The first stage mist eliminator is an open single pass design with wide spacing between the blades; this stage is washed from below with a high pressure stream of make up water. The second stage which consists of multipass chevron blades, is washed from the front and back with a high pressure stream of fresh water.

Process chemistry: The chemistry of the ABB process is basically the same as for General Electric's limestone desulfurization system. However, ABB's perception is that the reaction tank provides the residence time to complete the following reactions:

limestone dissolution:

$$CaCO_3 + H^+ \text{ -----> } Ca^{++} + HCO_3'$$

sulfite oxidation:

$$SO_3^{"} + 1/2\ O_2 \text{ -----> } SO_4^{"}$$

gypsum precipitation:

$$Ca^{++} + SO_4^{"} + 2\ H_2O \text{ -----> } CaSO_4.\ 2H_2O$$

Experience

ABB's gas/liquid contacter is a vertical, countercurrent, spray tower absorber which is widely used for ABB's wet limestone FGD systems. The wet limestone process has been installed by ABB for more than 28,000 MW. The absorbers range in size from 18 feet (5.5 m) to 65 feet (19.8 m) in diameter, and are constructed with various types of alloys, stainless steels, and mild steel with corrosion/erosion resistant linings. The LS-2 process described above has been installed for demonstration at Ohio Edison's Niles Station, and began operation in 1995. The LS-2 system treats flue gas from Units 1 and 2, with a capacity of 130 MW. The systems design includes production of wallboard grade gypsum.

The ESP is based on ABB's rigid-frame design which is installed on over 100,000 MW of capacity worldwide.

Table B-4
ABB's LS-2 Process Data

- Process Scope:
  - SO_x removal
  - Particulate removal

- Equipment Scope:
  - Limestone slurry preparation
  - Scrubber
  - ESP

- Pressure Drop:

Scrubber + ductwork	= 9.0 in. w.c.
ESP	= 1.5 in. w.c.
Total	= 10.5 in. w.c.

- Raw Material Consumption:

Limestone	= 7.2 ton/h
Adipic acid	= 8.5 lb/h

- By-product/Waste Production:

Waste	= 13.2 ton/h

- Utilities Consumption:
  - Power = 1,373 + 866 = 2,239 kW
  - Water = 174 gpm

- Cost, millions:

Scrubber	= $ 21.0
ESP [1]	= $ 6.0
Grinding Addition [2]	= $ 1.9
Installation	= $ 9.5
Total	= $ 38.4

- Manpower = 1 to 2 operators per shift

- Footprint:
  ESP = 50 ft wide x 70 ft long x 50 ft high
  Scrubber = 27 ft tank dia, 23 ft upper dia, 85 ft high + 15 ft high exit bend
  Slurry preparation and product handling = 40 ft wide x 70 ft long x two story high

Note:
1. The ABB recommended system limits particulate emissions to 63.3 lb/h. To increase the capture and limit emissions to 6.33 lb/h, an allowance of $1.5 million dollars is included for additional ESP fields.
2. Grinding facilities are added to the ABB data for later comparisons.

AirPol's Gas Suspension Absorber (GSA) Flue Gas Desulfurization Process

The AirPol process for removing particulate and SO_2 uses a gas suspension absorber (GSA) with lime as the adsorbent. For HIPPS, the required SO_2 removal of 98.52% cannot be met by the GSA without exorbitant lime consumption. Therefore, AirPol recommended adding a wet absorber downstream of the GSA. The wet absorber will act as a SO_2 polisher. A bleed from the wet scrubber will be used in the GSA as make up water and the system will have no liquid discharges.

Process Description

The process layout is as follows: GSA, baghouse, ID Fan, wet absorber with a top mounted stack. The process flow sheet is shown in Exhibit B-8. Process data are provided in Table B-5.

Sorbent preparation and handling: The GSA system is designed for the use of pebble (quick) lime or hydrated lime. The lime is delivered to the plant by truck and is pneumatically loaded into the silo. A pulse-jet type bin filter is located on top of the silo for cleaning the air displaced during loading.

The lime preparation system will be equipped with two slakers (one operating, one spare) and one slurry tank with agitator all enclosed in the skirt of the silo. The lime is metered as needed to either one of the slakers. The slaker mixes the lime with the water to produce a smooth hydrated milk-of-lime slurry, which can be adjusted to appropriate consistency. The mixing of the lime and water results in an exothermic reaction. The heat from the reaction preheats the water entering the slaker. The heated water speeds up the slaking process. The water temperature is controlled automatically.

The lime slurry is then transferred to an oscillating positive removal grit screen. With the help of a warm water spray, the grit is rejected and removed for disposal via a screw conveyor to a grit bin. The screened hydrated lime slurry flows down to a slurry tank, where an agitator keeps the slurry suspended and prevents "hot spots". A slurry transfer pump, with installed standby unit, conveys the slurry in a closed loop line back to slurry tank. The loop line is connected to a small feed tank located immediately adjacent to the GSA reactor. The feed tank is equipped with a level controller and a valve, connected to the slurry loop line, maintaining proper level in the tank.

The lime slurry feed pump, with connected standby, conveys the slurry from the feed tank to the spray nozzle in the GSA reactor.

The AirPol GSA flue gas cleaning process: The AirPol process is a semi-dry system. The flue gas enters the bottom of the GSA reactor and flows upward through a restriction (venturi) in the vessel. An injection lance with a single nozzle is located in the center of the venturi spraying concurrently with the gas flow. The injection lance assembly is connected to lime slurry, cooling water and compressed air feed lines. The slurry and water mixture is atomized by the compressed air in the dual-fluid nozzle.

Recycled solids from the feeder box (see Exhibit B-8) are introduced into the reactor just above the venturi where the solids become coated with the lime slurry. When the flue gas comes in contact with the lime coated solids, the lime chemically reacts with SO_2, HCl, and other acids in the flue gas to capture and neutralize these acid gases. The water in the slurry starts to

evaporate and simultaneously cool the gas. The reactor provides the necessary reaction and drying retention time before the solids enter the GSA cyclone. The suspended solids are carried upward in the GSA reactor by the turbulent gas.

The reactor is 20 feet (6.1 m) inside diameter by 100 feet (30.5 m) high.

The flue gas flows through the GSA cyclone where the solids are separated from the gas stream. Approximately 99% of the solids are fed back to the reactor via the feeder box. The remaining solids continue with the gas to the particulate filter (baghouse). The solids collected in the baghouse are still reactive and continue to neutralize acid in the flue gas, thus minimizing the need for fresh lime. The by-product is a dry powder with very low moisture content (less than 1%) consisting of calcium sulfite/sulfate, calcium chloride and fly ash.

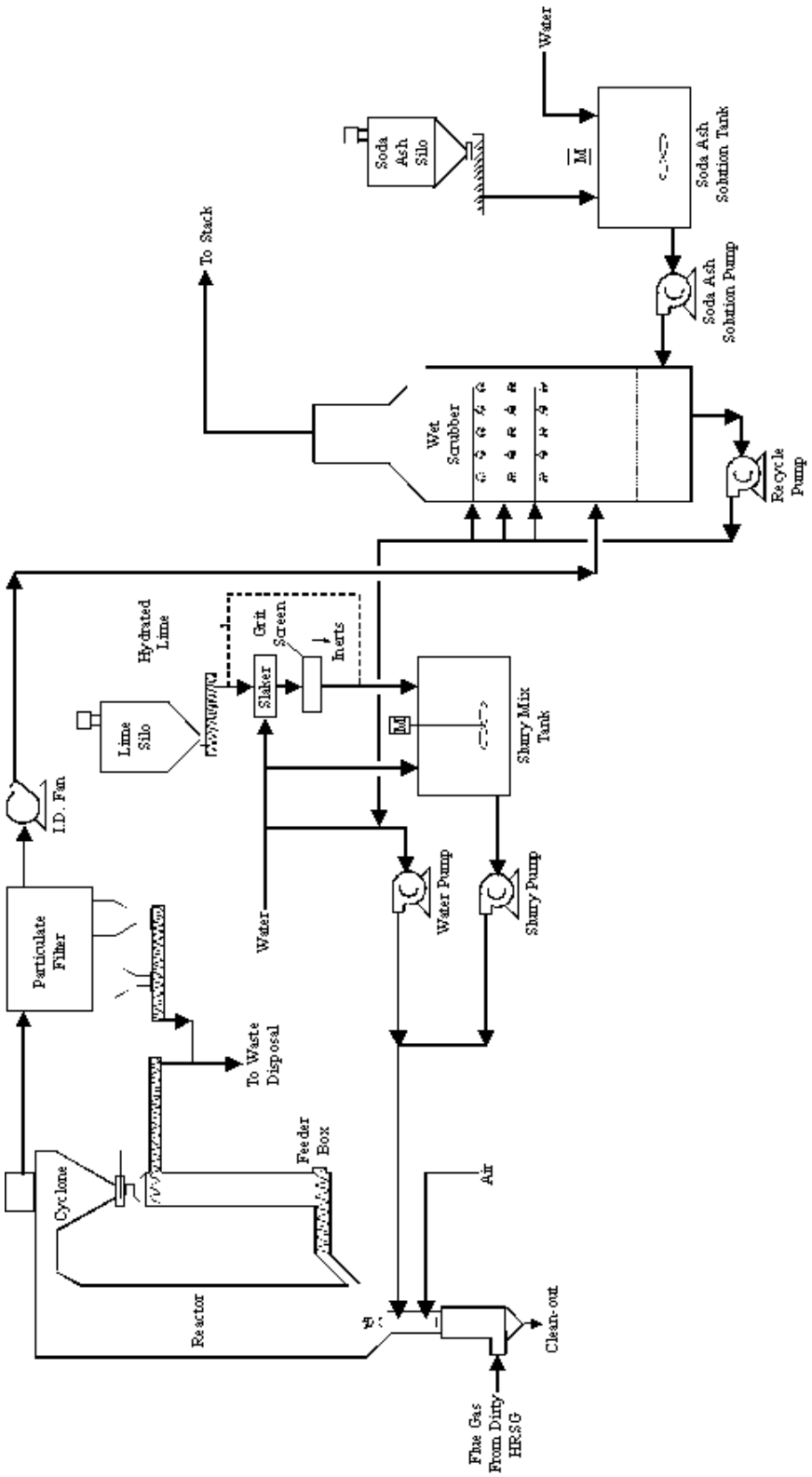

Exhibit B-8
AirPol's Lime System & Soda Ash Wet Scrubber

The flue gas is drawn from the cyclone through the particulate filter by an induced draft fan, which overcomes the pressure drop of the flue gas through the system. The fan discharges the partially cleaned flue gas to the wet scrubber.

Wet scrubber: The wet scrubber is located downstream of the ID fan and is a vertical spray tower with three spray zones, exposing the flue gas to a recycle liquid containing soda ash (sodium carbonate). At the bottom of the scrubber is a reservoir from which recycle pumps supply liquid to each spray zone. The wet scrubber is a final SO_2 removal step.

The soda ash slurry is prepared in a soda ash preparation system. This system consists of a soda ash silo for pneumatic truck unloading, metering device, and slurry tank with agitator. The slurry is pumped to the wet scrubber from a closed loop pipe line, with a control valve administering the correct slurry flow to the scrubber.

Absorption of SO_2 takes place in and between the scrubber's spray zones. The SO_2 is converted to soluble sodium salts (sulfite, bisulfite, and sulfate). The concentration of these salts is maintained at 10% by controlling the bleed from the system. This is accomplished via an electrical conductivity type density controller located in the recycle loop. The bleed is pumped over to the GSA as make up water. There is thus no liquid discharge from the system. It is important to maintain the alkalinity of the scrubbing liquid at a pH of about 8.0. This is accomplished by adding a 12% soda ash slurry to the recycle via a control valve at the scrubber. The control valve receives signal from a pH controller, also located in the recycle loop.

Above the spray zones is a mist eliminator, that will remove virtually all liquid droplets from the flue gas before the gas enters the exhaust stack. The mist eliminator is provided with a wash spray header, which will efficiently remove any possible build up of reaction salts. This spray is intermittent and is controlled by a timer.

The scrubber is of 29 feet (8.8 m) inside diameter by 60 feet (18.3 m) high.

A stack is mounted directly on top of the scrubber. The gas velocity in stack has been selected at approximately 34 feet per second (10.4 m/s). The gas leaving the scrubber is saturated and water will condense on the inside stack wall, and run back into the scrubber. The stack is of 16 feet (4.9 m) inside diameter by 100 feet (30.5 m) high.

Process chemistry: When lime (CaO) is mixed with water in the slaker, it reacts with water to form slaked lime, $Ca(OH)_2$. The slaked lime and water are added to the slurry mixing tank to make a lime slurry of the required concentration. When the lime slurry is injected into the GSA reactor, the $Ca(OH)_2$ reacts with sulfur dioxide to form calcium sulfite ($CaSO_3$). Calcium sulfite is oxidized to calcium sulfate by the oxygen in the slurry injecting air, as shown in the following reactions:

$$CaO + H_2O \text{ -----> } Ca(OH)_2$$

$$Ca(OH)_2 + SO_2 \text{ -----> } CaSO_3 + H_2O$$

$$CaSO_3 + 1/2\ O_2 \text{ -----> } CaSO_4$$

The first reaction takes place in the lime slaker and the last two reactions take place in the GSA reactor and continue in the filter cake of the baghouse.

In the wet scrubber, a solution of soda ash reacts with the remaining SO_2 in the flue gas leaving the GSA and forms sodium sulfite by the following reaction:

$$Na_2CO_3 + SO_2 \text{ -----> } Na_2SO_3 + CO_2$$

The sodium sulfite solution is injected into the GSA reactor where it is oxidized by the air in the GSA reactor to sodium sulfate by the following reaction:

$$Na_2SO_3 + 1/2\ O_2 \text{ -----> } Na_2SO_4$$

Experience

AirPol's parent company FLS miljo Inc. has over 1400 wet scrubber installations in successful operation in North America, of which more than 400 are for flue gas desulfurization, the great majority of them sodium based. FLS miljo has installed 26 GSA units since 1988, mostly in Europe. Many of the European GSA units process flue gases from incinerators and boilers. Some installations are for steel and cement production. There are two GSA installations in the U. S. One is a 10 MW demonstration unit at TVA's Shawnee plant, and the other is a 50 MW commercial unit in Hamilton, Ohio.

Table B-5
AirPol's GSA Process Data

- Process Scope:
  - SO_x removal
  - Particulate removal
- Equipment Scope:
  - Lime slurry preparation
  - Soda ash slurry preparation
  - Gas suspension absorber (GSA)
  - Soda ash scrubber
  - Baghouse
- Pressure Drop:

GSA	= 7.2 in. w.c.
Baghouse	= 6.0 in. w.c.
Soda ash scrubber	= 2.5 in. w.c.
Ductwork	= 2.3 in. w.c.
Total	= 18.0 in. w.c.

- Raw Material Consumption:

Lime	= 9,930 lb/h
Soda ash	= 1,920 lb/h

- By-product/Waste Production:

Waste	= 15.5 ton/h

- Utilities Consumption:

Power	= 1,792 kW
Water	= 166 gpm

- Cost, millions:

Total equipment	= $ 6.8
Installation [1]	= $ 6.8
Total	= $ 13.6

- Manpower = 1 to 2 operators per shift

Footprint: 80 ft wide x 150 ft long x 160 ft high

Note:
1. Added to Airpol's input as 100% of equipment cost.

EEC's Flue Gas Desulfurization Process: CDS

The Environmental Elements Corporation's Circulating Dry Scrubber (EEC's CDS) process uses dry hydrated lime to contact the flue gas and remove SO_2. The scrubber is followed by an electrostatic precipitator. Most of the solids collected in the ESP are recycled to the scrubber, giving the solids more contact time with the flue gas.

Process Description

The process flow diagram is shown in Exhibit B-9. Process data are provided in Table B-6.

Sorbent preparation and handling: Pebble lime is delivered to a lime storage silo at the power plant. The lime characteristics are: 90% (minimum) CaO; 3/4 inch (1.9 cm) maximum size; and 55 lb/ft^3 (269 kg/m^3) density. The silo has a 7 day capacity. One hydrator is located beneath the outlet of the silo. After the metered pebble lime has been hydrated to approximately 0.5% moisture, the product is pneumatically conveyed to a hydrate lime storage silo which has a capacity of 12 hours. The hydrated lime is transferred onto the ash recirculation airslide conveyors. The hydrated lime mixes with the ash as it enters the venturi section of the circulating dry scrubber. The flow rate of the hydrated lime to the scrubber is controlled by the flow rate of the SO_x of the flue gas entering the scrubber.

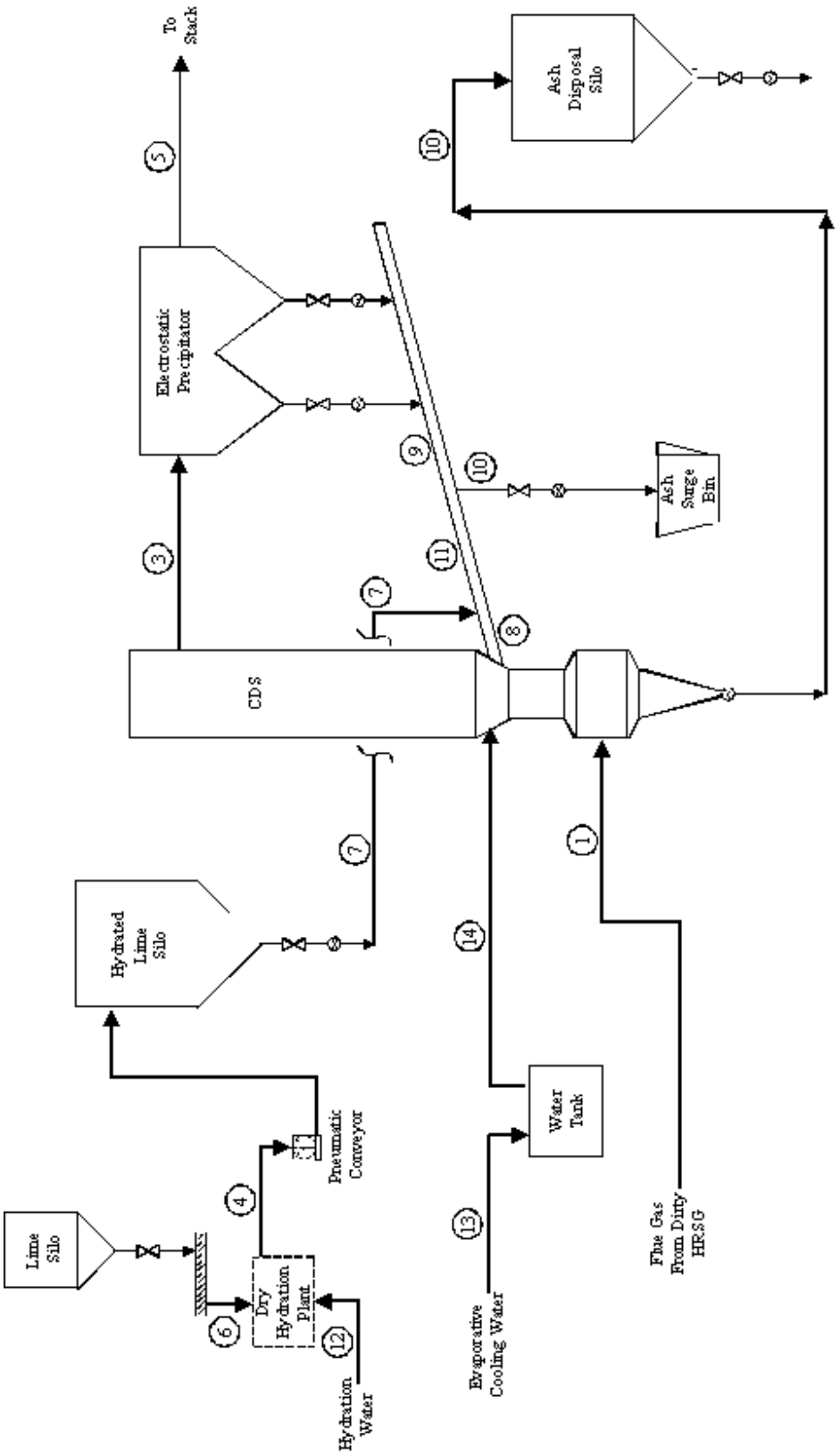

Exhibit B-9
EEC's Circulating Dry Scrubber Process Flow Diagram

EEC's flue gas cleaning process: The gas passes through the scrubber vessel, 24 feet (7.3 m) inside diameter by 62 feet (18.9 m) high, followed by an ESP and then to the stack. The hot gases which enter the scrubber are cooled by water spray nozzles. These nozzles reduce the temperature inside the scrubber vessel to the optimum temperature required for the SO_2 and $Ca(OH)_2$ reaction. The water injection system is independent of the introduction of reagent and recirculating ash in the scrubber. The gas temperature at the scrubber exit controls the amount of water injected through nozzles into the bottom of the scrubber.

Ash (for this process ash = flyash plus unreacted lime plus calcium salts produced by the chemical reactions) which is produced as a result of the scrubbing process is collected in a downstream electrostatic precipitator. The ash falls from the ESP hoppers onto a series of airslides which are designed to recirculate the ash back into the scrubber. A portion of the ash is diverted from the airslides or precipitator hoppers and sent to a product surge bin. The product surge bins hold 12 hours of ash. The flow rate of the ash discharged from the ESP is controlled by the solids loading of the scrubber. This is measured by the pressure drop across the absorber height which is kept at a constant value. The solids loading divided by the solids feed rate (product plus flyash) gives the solids retention time of the scrubber. The retention time can be varied over a wide range, limited by the pressure drop of the gas and efficiency of the ESP.

Process chemistry: The reactions in the EEC's circulating dry scrubber (CDS) are similar to those of AirPol's gas suspension absorber (GSA): When lime (CaO) is hydrated with water in the hydration plant, it reacts with water to form $Ca(OH)_2$. The hydrated lime, $Ca(OH)_2$, is injected into the CDS reactor along with the recirculating solids from the electrostatic precipitator, the $Ca(OH)_2$ reacts with sulfur dioxide to form calcium sulfite ($CaSO_3$) and calcium sulfate ($CaSO_4$) mixture, as shown in the following reactions:

$$CaO + H_2O \text{ -----> } Ca(OH)_2$$

$$Ca(OH)_2 + SO_2 \text{ -----> } CaSO_3 + H_2O$$

$$CaSO_3 + 1/2\ O_2 \text{ -----> } CaSO_4$$

The first reaction takes place in the hydration plant and the last two reactions take place in the CDS reactor.

Experience

The CDS process was developed by Lurgi in Germany. The process has been used commercially since 1984 in the European countries where Lurgi has installed eight CDS plants with capacities ranging from 50 to 140 MW. Most of these plants are for utilities. In the USA, the first commercial plant (80 MW) was installed by EEC at the Black Hills Power and Light Company site in 1995. Two plants (165 MW each) in Austria are scheduled for start up during 1998.

Table B-6
EEC's Circulating Dry Scrubber (CDS) Process Data

- Process Scope:
  - SO_x removal
  - Particulate removal
- Equipment Scope:
  - Lime hydration
  - Lime slurry preparation
  - Circulating dry scrubber
  - ESP
- Pressure Drop: = 6.0 in. w. c.
- Raw Material Consumption:
  - Lime = 6.3 ton/h
- By-product/Waste Production:
  - Waste = 12.9 ton/h
- Utilities Consumption:
  - Power = 1,250 + 600 = 1,850 kW
  - Water = 126 gpm
- Cost:

Equipment cost	= $ 5.25
Allowance[1]	= $ 0.50
Installation	= $ 5.75
Total	= $ 11.50

- Manpower:
  - Manpower = 0.5 operators per shift
- Footprint:
  - FGD = 50 ft wide x 60 ft long
  - ESP = 55 ft wide x 68 ft long x 57 ft high

Note:
1. The EEC's recommended system limits particulate emissions to 12.3 lb/h. To limit emissions to 6.33 lb/h, $ 0.5 million is added (EEC's estimated cost) for two more ESP fields.

Krupp Uhde's Flue Gas Desulfurization Process: AMASOX®

The Krupp Uhde process uses an aqueous ammonia solution to absorb SO_2 from the flue gas. The process produces ammonium sulfite and ammonium sulfate, both of which are water soluble. Ammonium sulfite is oxidized to ammonium sulfate by air. The ammonium sulfate solution is evaporated and crystallized. The crystals are then dried to produce fertilizer grade ammonium sulfate. Krupp Uhde also provided data for a system with both SO_2 and NO_x control. This system combines the AMASOX® desulfurization process with a SNCR located in the HITAF.

Process Description

The process diagram is shown in Exhibit B-10; process data are provided in Table B-7.

Sorbent preparation and handling: The liquid ammonia is received in pressurized tank cars and transferred to the aqueous ammonia mixing tank. The tank cars are filled with nitrogen gas as the liquid ammonia is removed. After the liquid ammonia transfer is complete, the connecting piping is also purged with nitrogen.

The aqueous ammonia solution for gas scrubbing has an NH_3 concentration of approximately 10 to 32 wt %, the preferred concentration is about 25 wt %. The liquid ammonia and water are mixed using a ratio controller in a mixer/cooler at a pressure about 15 psi (103 kPa) above the vapor pressure of ammonia. This prevents the formation of gas bubbles during mixing. The

aqueous ammonia solution is stored in a rubber-lined carbon steel tank. Storage capacity of the tank is one week.

Krupp Uhde's flue gas cleaning process: A SNCR process is used in the HITAF for NO_x control. The SNCR process is described later in the section on the ammonia desulfurization process. After exiting the HITAF, a blower, designed to overcome system pressure drop, moves the flue gas through the AMASOX® scrubbing system.

The flue gas from the HIPPS dirty HRSG is saturated in a quencher by injecting process water or scrubbing solution from scrubber II (see Exhibit B-10). The saturated flue gas enters scrubber I where most of the acidic components are removed by a solution of ammonia salts. The solution is injected through nozzles located at the top of the scrubber. Apart from these nozzles, scrubber I has no other internals.

Process Chemistry: The reactions which take place in this process are as follows:

$$HCl_{(g)} + H_2O \longrightarrow H^+ + Cl^- + H_2O \quad (1)$$

$$SO_2 + (NH_4)_2SO_3 + H_2O \longrightarrow 2\,NH_4HSO_3 \quad (2)$$

$$NH_4HSO_3 + NH_4OH \longrightarrow (NH_4)_2SO_3 + H_2O \quad (3)$$

The scrubbing solution is oxidized by reacting with atmospheric oxygen in accordance with reaction 4 below. The resulting ammonium hydrogen sulfite is converted to ammonium sulfate by the addition of aqueous ammonia solution and atmospheric oxygen per reaction 5 below.

$$2\,(NH_4)_2SO_3 + O_2 \longrightarrow 2\,(NH_4)_2SO_4 \quad (4)$$

$$2\,NH_4HSO_3 + O_2 + 2\,NH_4OH \longrightarrow 2\,(NH_4)_2SO_4 + 2\,H_2O \quad (5)$$

The resulting ammonium salts are highly soluble in water and therefore remain in the scrubbing solution. The scrubbing solution is circulated by a pump to maintain the liquid/gas ratio in the scrubber. The required liquid/gas ratio is calculated by a processor and is controlled using measurements of the volumetric flow and SO_2 concentration of the flue gas. The pH value of the solution is maintained at about 4.8 - 5.5 by the addition of aqueous ammonia to the circulating solution. Depending on the process requirements, the concentration of dissolved ammonium salts is maintained at 30 to 40 wt % by a density controller which regulates draining the scrubbing solution of scrubber I to another vessel. The level in the sump of scrubber I is kept constant with the scrubbing solution from scrubber II.

The scrubbed flue gas leaves scrubber I via a knock out drum which removes 99.9% of all droplets larger than 10 µm. The liquid collected in the knock out drum is returned to scrubber I. The flue gas leaving the knock out drum enters scrubber II where the scrubbing solution is sprayed from the top. The main function of this scrubber is to minimize ammonia slip from the AMASOX® process. If needed, aqueous ammonia solution can be added to the scrubbing solution to remove residual traces of SO_2. The pH value of the scrubbing solution for this scrubber is kept less than 4.5. The level in this scrubber is maintained by the addition of water. The scrubbed flue gas leaves scrubber II via a knock out drum which removes 99.9% of all droplets larger than 10 µm. The liquid collected in the knock out drum is returned to scrubber II.

Both the scrubbers are made of carbon steel lined with 0.16 in (4 mm) thick soft rubber. All the scrubbing solution piping is made of fiberglass reinforced plastic.

Aerosols removal: In the flue gas scrubbing process, salt aerosols may be formed in scrubber I by the reaction of gaseous ammonia with gaseous sulfur oxides and halogens. These aerosols consist of water droplets with dissolved ammonium salts whose diameter is less than 10 µm. These aerosols cannot be removed by conventional knock out drums. If their concentration in the cleaned flue gas is high, they might produce a visible plume. To prevent that, the aerosol droplets are captured in a wet electrostatic precipitator specially developed for this purpose.

The wet electrostatic precipitator is designed as a plate filter. The clean gas from the scrubber flows horizontally through the precipitator and the aerosols are collected at the plates. These plates also have to be cleaned and this is done periodically using water or scrubbing solution from scrubber II. The cleaning fluid is then returned to the scrubber.

Ammonium sulfate production: The solution from the flue gas scrubber is initially stored in an ammonium sulfate solution tank. The solution in the tank can be supplied directly to the customer without further treatment. Alternatively, the solution can be crystallized. The proposed unit consists of crystallizers designed on the basis of Swenson's (crystallizer manufacturer) experience for the production of ammonium sulfate crystals. The crystals are separated from the solution by a centrifuge. The wet salt crystals from the centrifuge are dried in a crystal dryer to the required moisture content of less than 3%.

Experience

Krupp Uhde has installed three flue gas cleaning plants using the ammonia scrubbing process described above. One of the plants is a demonstration unit in Italy. The other plants are commercial units operating in Germany. Their total operating experience is some 70,000 hours. The quality of the by-product ammonium sulfate meets agricultural specifications as well as fertilizer specifications stipulated by the European Union, regarding nitrogen content and impurities. The sulfate can be used in solid crystalline form, compacted or granulated, or in liquid form as ammonium sulfate solution or slurry, depending on the market requirements.

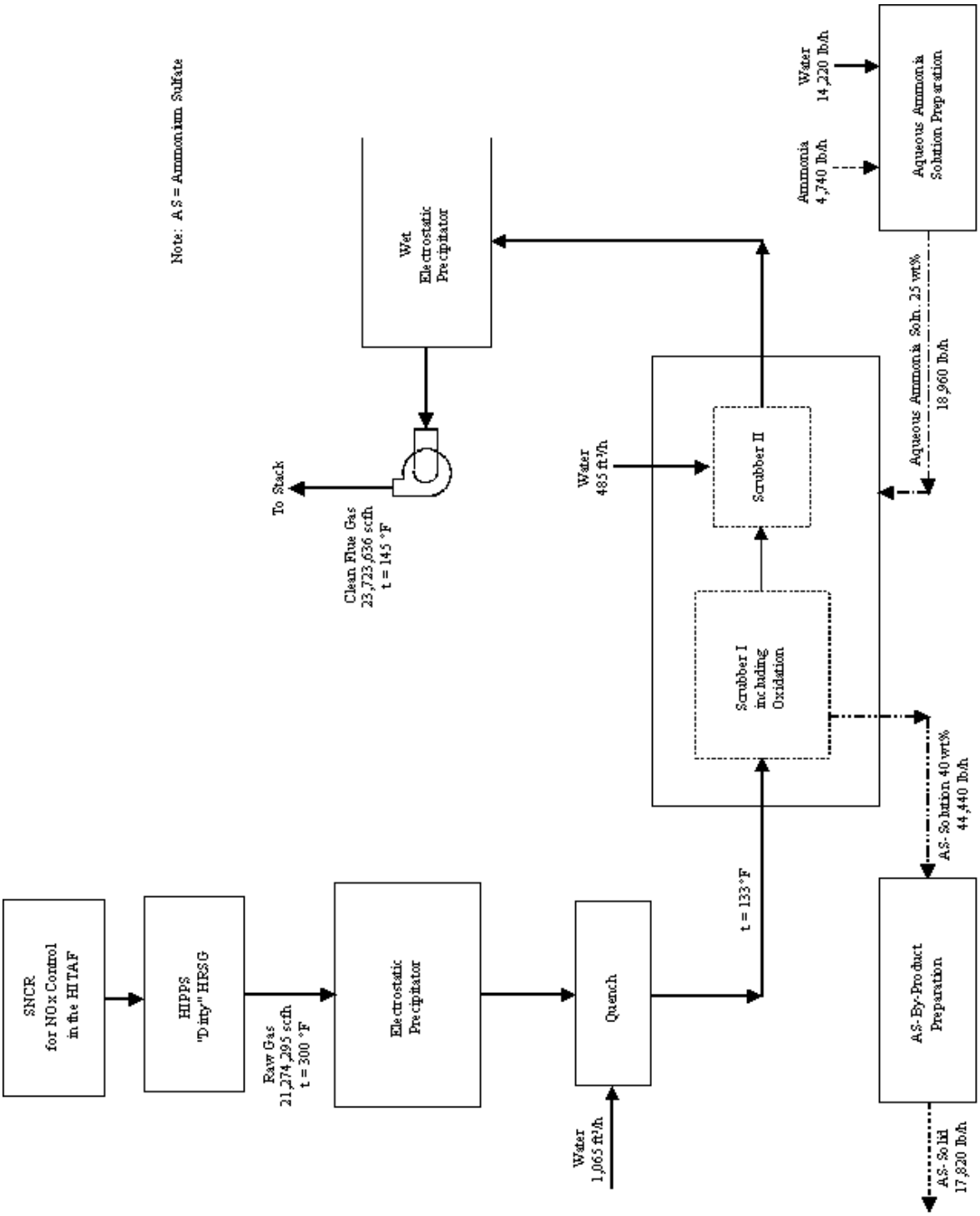

Exhibit B-10
Krupp Uhde's Ammonia Process - Block Flow Diagram

Table B-7
Krupp Uhde's AMASOX® Process Data

- Process Scope:
  - NO_x removal with SNCR
  - SO_x removal
  - Particulate removal
- Equipment Scope:
  - Dry ESP + wet ESP
  - Ammonia scrubbers (two)
  - Aqua ammonia solution preparation
  - Ammonium sulfate product
  - SNCR
- Pressure Drop:
  - Scrubber + ductwork = 7.7 in. w.c.
  - 2 ESPs = 1.7 in. w.c.
  - Total = 9.4 in. w.c.
- Raw Material Consumption:
  - Ammonia for deSO_x = 4,520 lb/h
  - Ammonia for SNCR = 320 lb/h
- By-product/Waste Production:
  - Ammonium sulfate = 8.1 ton/h
- Utilities Consumption:
  - Power = 1900 kW
  - Water = 194 gpm
  - Steam = 19,800 lb/h
  - Cooling water = 1,238 gpm
  - Compressed air = 800 lb/h
- Cost, millions:
  - Dry ESP = $ 1.9
  - Ammonia preparation, scrubber and ESP = $ 15.8
  - Ammonium sulfate production = $ 5.9
  - SNCR = $ 1.2
  - Installation = $ 5.6
  - Total = $ 30.4
- Manpower: = 2 operators per shift
- Footprint, overall: = 18,200 ft^2

NOXSO Corporation's Flue Gas Cleaning Process: NOXSO

The NOXSO process is a dry, flue gas treatment process that uses a regenerable sorbent to simultaneously remove SO_2 and NO_x from the flue gas. The SO_2 is converted to elemental sulfur and the NO_x is reduced to nitrogen and oxygen.

Process Description

The process flow diagram is shown in Exhibit B-11; process data are provided in Table B-8.

Sorbent preparation and handling: The NOXSO process sorbent is used for thousands of adsorption/regeneration cycles. The life of the sorbent is dictated by mechanical and thermal stresses experienced within the process. The fate of attrited sorbent is discussed below. For the HIPPS system, the total attrition rate is 165 lb/h (74 kg/h) out of a total system inventory of 560 tons (508 tonnes) of sorbent. Thus, the system inventory is replaced on average every 9 months. The sorbent make up is added in batches on a daily basis. A sorbent storage tank with two weeks sorbent make up capacity is provided.

NOXSO flue gas cleaning process: The NOXSO module has two adsorbers, each 43 feet (13 m) in diameter. (For simplicity, the process flow diagram in Exhibit B-11 shows a single

adsorber.) Flue gas is routed through the mechanical separators (cyclone type) to the two flue gas booster fans and into the two NOXSO adsorbers. The adsorber vessels are three-stage fluidized bed reactors that contact the flue gas with a proprietary NOXSO sorbent. SO_2 and NO_x are simultaneously adsorbed on the sorbent and the clean flue gas passes through a pulse jet baghouse before being routed to the plant stack.

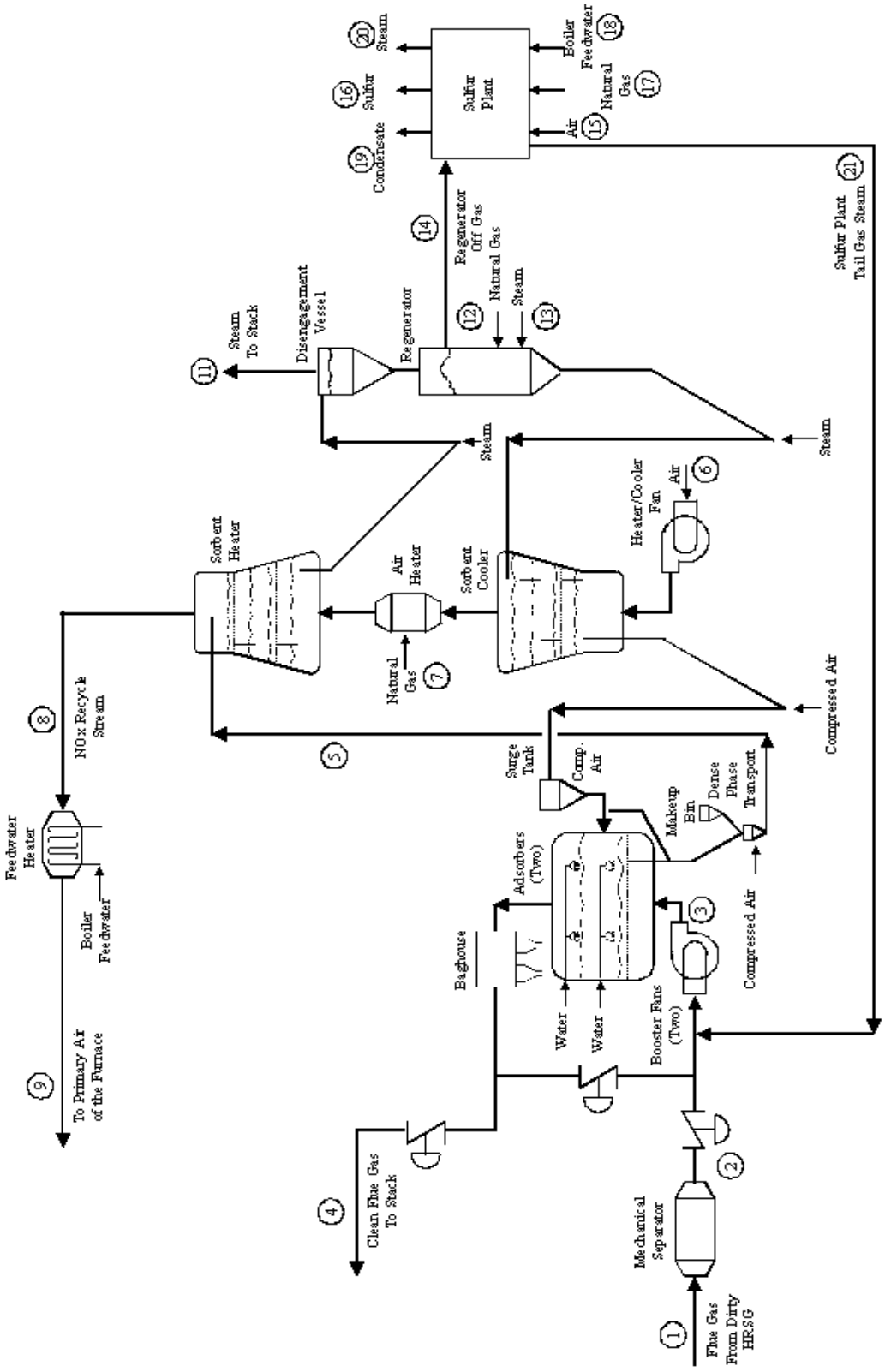

Exhibit B-11
NOXSO Process Flow Diagram

The cyclone separator removes most of the solids prior to the NOXSO adsorbers. The purpose of the baghouse is to prevent attrited sorbent and residual flyash from exiting the stack by first removing it from the flue gas and directing it to the plant's ash disposal system, which also handles the ash collected by the cyclone separator. The mass of sorbent exiting the system is only about 1% (by weight) of the combined bottom ash/flyash generated by typical boilers. Because all of the chemical components found in NOXSO sorbent are also found in coal ash, the mixture of ash and sorbent is chemically indistinguishable from ash itself. Both NOXSO sorbent and sorbent/ash mixtures have been subjected to TCLP tests and have been characterized as non-toxic based on the results of these tests.

The two NOXSO adsorption trains, consisting of a cyclone separator, forced draft fan, adsorber vessel, baghouse and connecting ductwork, each have isolation dampers that will allow either train to be operated independent from the other. In addition, each train has a bypass line, located downstream of the cyclone separator, that will allow the NOXSO system to operate in hot standby mode when the gas is not available. The bypass duct allows ambient air to be circulated through the adsorber in a closed loop. A bleed-off stream is used to control temperature in this mode of operation with ambient air providing the required make up.

This bypass duct also allows the system to be brought up to temperature during a cold start-up prior to the introduction of flue gas. Ambient air is again circulated through the adsorbers and mechanical energy from the FD fans provides heat to the system. This preheating of the system prevents acid condensation which could happen if flue gas is introduced into cold ductwork. The adsorber and associated ductwork are constructed from carbon steel. Flue gas temperature is maintained above the acid dew point until it reaches the first absorber bed. Once in the bed SO_3, SO_2, and NO_x are adsorbed, reducing the dew point to below the bed operating temperature. In this manner, the need for special materials of construction is avoided.

The temperature of the adsorber beds is controlled by spraying water directly into each bed. The water spray volume is small compared to the flue gas (<2.5%) and water evaporates instantaneously in the flue gas stream occupying the fluid beds. An array of nozzles is used to achieve complete coverage of the bed's cross-section. Temperature is a key parameter relating to NO_x removal efficiency with lower temperature promoting higher removals. Because of the low NO_x loading in this application, virtually no cooling is required. At an adsorber bed temperature of 325 °F (163 °C), the overall NO_x removal efficiency is 92%.

Sorbent treatment/regeneration: The remainder of the NOXSO system is used to regenerate the sorbent and provide ultimate disposition of the adsorbed NO_x and SO_2. Spent sorbent from the adsorbers is pneumatically conveyed in dense phase transport systems to the top bed of the sorbent heater. The sorbent heater is a four stage fluidized bed reactor that raises the sorbent temperature to 1150 °F (621 °C) for regeneration purposes. The vessel consists of a tapered design such that the variable cross-sectional area at each stage accounts for the change in gas volume due to temperature and pressure variations within the vessel, thereby maintaining a constant velocity of 3 ft/s (0.9 m/s) at each stage. The average diameter of the sorbent heater is 36 feet (11 m).

During the heating process, adsorbed NO_x is driven from the sorbent and exits the vessel in the sorbent heater off-gas. The sorbent heater off-gas is at a temperature of 434 °F (223 °C). Heat can be recovered from this stream by heating a slipstream of boiler feed water from the

condensate system. After heating the slipstream of BFW, the temperature of the sorbent heater off-gas is 140 °F (60 °C).

The sorbent heater off-gas stream is then returned to the power plant as a part of the combustion air. NO_x destruction is then achieved by one of two mechanisms. The first mechanism takes advantage of the NO_x formation reaction equilibrium. By injecting NO_x into the combustion chamber, a situation is created where the NO_x concentration is higher than the equilibrium value. NO_x formation is thereby suppressed in the combustor and some NO_x is destroyed through the reaction shown below.

$$2\ NO \longrightarrow N_2 + O_2$$

In addition, free radicals are present in the fuel rich portion of the flame which can also reduce NO_x to nitrogen and water.

Once the sorbent has reached a temperature of 1150 °F (621 °C) in the sorbent heater, it is transported by steam to the regenerator vessel via the disengagement vessel. The transport steam is piped to the stack and the sorbent gravity flows through a standpipe into the regenerator vessel. Separating the steam from the sorbent at this point prevents it from mixing with the regenerator off-gas, reducing the volume of gas sent to the sulfur recovery unit (SRU). In addition, because the sulfur formation reaction is an equilibrium controlled reaction with H_2O as a product, reducing the H_2O concentration of the feed gas increases the conversion achieved in the SRU.

Sorbent in the regenerator is contacted first with natural gas and then with steam in a countercurrent moving bed. Natural gas reacts the with adsorbed sulfur compounds on the sorbent to form primarily SO_2, H_2S, CO_2, and H_2O as reaction products. Approximately 90-95% of the sulfur is removed from the sorbent through reaction with steam. The product of the steam reaction is H_2S.

The disengagement vessel and regenerator vessel both have carbon steel shells with internal refractory lining. The disengagement vessel has an inside diameter of 19 feet (5.8 m) while the regenerator vessel has an inside diameter of 26 feet (7.9 m). The two vessels are in a stacked configuration.

The regenerator off-gas is piped to a sulfur recovery unit where SO_2 and H_2S are converted to elemental sulfur. Heat recovery in the SRU is done by generating steam. The steam generated is of sufficient quantity to provide all of the process steam required in the NOXSO process. Sulfur is the end product from the NOXSO process. Approximately 50 tons (45.4 tonnes) per day will be produced.

The final sorbent treatment/regeneration step of the NOXSO process is cooling the sorbent. After regeneration, sorbent is transported from the regenerator to the sorbent cooler. The sorbent cooler is a four stage fluidized bed reactor that utilizes an ambient air stream to reduce the sorbent temperature to 320 °F (160 °C). The cooler, like the sorbent heater, has a tapered wall design to maintain a constant gas velocity at each stage. The average diameter of the sorbent cooler vessel is 33 feet (10 m). Ambient air is provided by two 50% capacity blowers. A third 50% capacity blower is provided as a spare for the two operating units.

The air exits the sorbent cooler at 950 °F (510 °C). The air stream then passes through a natural gas-fired in-duct air heater that raises the temperature to 1,325 °F (718 °C). This air

stream is then used to raise the sorbent temperature to 1,150 °F (621 °C). The sorbent cooler, air heater and sorbent heater are also in a stacked arrangement.

Sorbent exiting the sorbent cooler vessel is transported to one of two surge tanks by compressed air. The surge tanks are a source and sink for sorbent so that a constant inventory can be maintained in all the process vessels during periods of variable sorbent circulation rates.

Finally, sorbent is transported from the surge tanks back to the adsorber vessels completing one full cycle. Again, compressed air is used for transport.

Process Chemistry: The solid sorbent is a proprietary sodium aluminate ($NaAlO_2$) material which is prepared from sodium carbonate (Na_2CO_3) and gamma-alumina (γ-Al_2O_3). In the adsorber, the sorbent removes SO_2 according to the following reactions:

$$2\ NaAlO_2\ (s) + H_2O\ (g)\ \text{-----}>\ 2\ NaOH\ (s) + Al_2O_3\ (s)$$

$$NaOH\ (s) + SO_2\ (g)\ \text{-----}>\ NaHSO_3\ (s)$$

$$NaHSO_3\ (s) + 1/2\ O_2\ (g)\ \text{-----}>\ NaHSO_4\ (s)$$

$$NaHSO_4\ (s) + NaOH\ (s)\ \text{-----}>\ Na_2SO_4\ (s)\ + H_2O$$

The adsorbed SO_2 reacting with $NaAlO_2$ produces temporary NO_x sorption sites where NO_x is adsorbed.

In the sorbent heater, where the bed temperature is maintained at 1,300 °F (704 °C), the adsorbed NO_x is driven out. The liberated NO_x is sent to the furnace along with the primary air. In the regenerator, methane from the natural gas reacts with alumina (Al_2O_3) and sodium sulfate (Na_2SO_4) as follows:

$$Na_2SO_4\ (s) + Al_2O_3\ (s) + 1/4\ CH_4\ (g) \longrightarrow\ 2\ NaAlO_2\ (s) + 1/2\ H_2O\ (g) + SO_2\ (g) + 1/4\ CO_2\ (g)$$

$$Na_2SO_4\ (s) + Al_2O_3\ (s) + CH_4\ (g)\ \text{-----}>\ 2\ NaAlO_2\ (s) + H_2O\ (g) + H_2S\ (g) + CO_2\ (g)$$

$$Na_2SO_4\ (s) + CH_4\ (g)\ \text{-----}>\ Na_2S\ (s) + 2\ H_2O\ (g) + CO_2\ (g)$$

The gaseous products (H_2O, H_2S and CO_2) in the above reactions leave the regenerator with the reactor effluent and go to the sulfur recovery unit while the solid product (Na_2S) remains on the sorbent. The sodium sulfide on the sorbent is reduced to H_2S by the steam injected in the regenerator:

$$Na_2S\ (s) + Al_2O_3\ (s) + H_2O\ (g)\ \text{-----}>\ 2\ NaAlO_2\ (s) + H_2S\ (g)$$

The H_2S produced in the above reaction also goes to the sulfur recovery unit.

Experience

Process development began in 1979 with laboratory-scale tests and progressed to pre-pilot-scale tests (3/4-MW) and a life-cycle test. Each of these programs has provided data for the process design. Tests of the NO_x recycle concept, which is inherent to the NOXSO process, have been conducted on small boilers at the Pittsburgh Energy Technology Center (PETC) and at the Babcock & Wilcox Research Center in Alliance, Ohio.

A 5 MW Proof-of-Concept (POC) pilot plant test at Ohio Edison's Toronto Power Plant in Toronto, Ohio, was completed in 1993. Based on more than 7,000 hours of operation with flue gas, it was claimed that the process can economically remove more than 95% of the acid rain precursor gases from the flue gas.

The NOXSO Clean Coal Project was to be the final step in commercialization of the process. The project was selected during Round III of the Department of Energy's Clean Coal Technology Program with the NOXSO Corporation as the prime contractor, project manager and process supplier. The project host was the Alcoa Generating Corporation at their Warrick Power Plant near Evansville, Indiana. The plan was for the NOXSO plant to treat the flue gas from a 150 MW unit.

The project has been indefinitely postponed because NOXSO has not been able to arrange for the 50% cost share required from private industry.

Table B-8
NOXSO Corporation's NOXSO Process Data

- Process Scope:
  - NO_x removal
  - SO_x removal
  - Particulate removal
- Equipment Scope:
  - NO_x + SO_x adsorbers and one baghouse
  - Sorbent heater and sorbent cooler
  - Sorbent regenerator
  - Sulfur plant
- Pressure Drop:
  - NO_x + SO_x adsorbers = overcome by the booster fan
  - Baghouse = overcome by the booster fan
  - Sorbent cooler = overcome by the heater/cooler fan
  - Sorbent heater = overcome by the heater/cooler fan
  - Regenerator = overcome by steam
  - Total = overcome by vendor supplied equipment
- Raw Material Consumption:
  - Sorbent = 165 lb/h
- By-product/Waste Production:
  - By-product (sulfur) = 2.1 ton/h
  - Steam (615 psia, 489 °F) = 1,500 lb/h
- Utilities Consumption:

Power	= 4,000 kW
Water	= 75 gpm
Cooling water	= 50 gpm
Natural gas	= 1,850 scfm

- Cost, millions:

Total equipment	= $ 20.0
Installation[1]	= $ 26.3
Total	= $ 46.3

- Manpower = one operator per shift
- Footprint, overall: =
  - 150 ft wide x 200 ft long x 160 ft high

Note:
1. Installation cost is based on vendor's assumption that concrete, ductwork, piping, the control building, electrical and instrumentation, and insulation are not equipment.

GE's Ammonia Desulfurization Process

GE's FGD process based on ammonia scrubbing uses an unsaturated aqueous ammonium sulfate solution to absorb SO_2 from the flue gas. The absorbed SO_2 reacts with ammonia which is introduced into the absorber with the oxidation air. On reacting, SO_2 and ammonia produce ammonium sulfite which is oxidized to ammonium sulfate by the oxidizing air. The ammonium sulfate product is recovered by concentrating the solution by evaporation and then centrifuging the precipitated crystals. While GE did not provide data for a combined SO_2 and NO_x system, a SNCR could be added in the HITAF, as discussed for the Krupp process.

Process Description

The process flows are illustrated by Exhibits B-12 to B-14; process data are provided in Table B-9.

The flue gas leaving the dirty HRSG goes to an electrostatic precipitator. The precipitator removes fine particulate from the flue gas stream prior to the flue gas desulfurization plant (Exhibit B-12). The flue gas from the precipitator enters the prescrubber just above liquid level. The hot flue gas is contacted with a recirculating spray of ammonium sulfate slurry and becomes saturated by evaporation of water. The pH of the slurry is low (~ 1.0). The saturated flue gas leaves the prescrubber through a mist eliminator designed to remove slurry materials entrained in the flue gas.

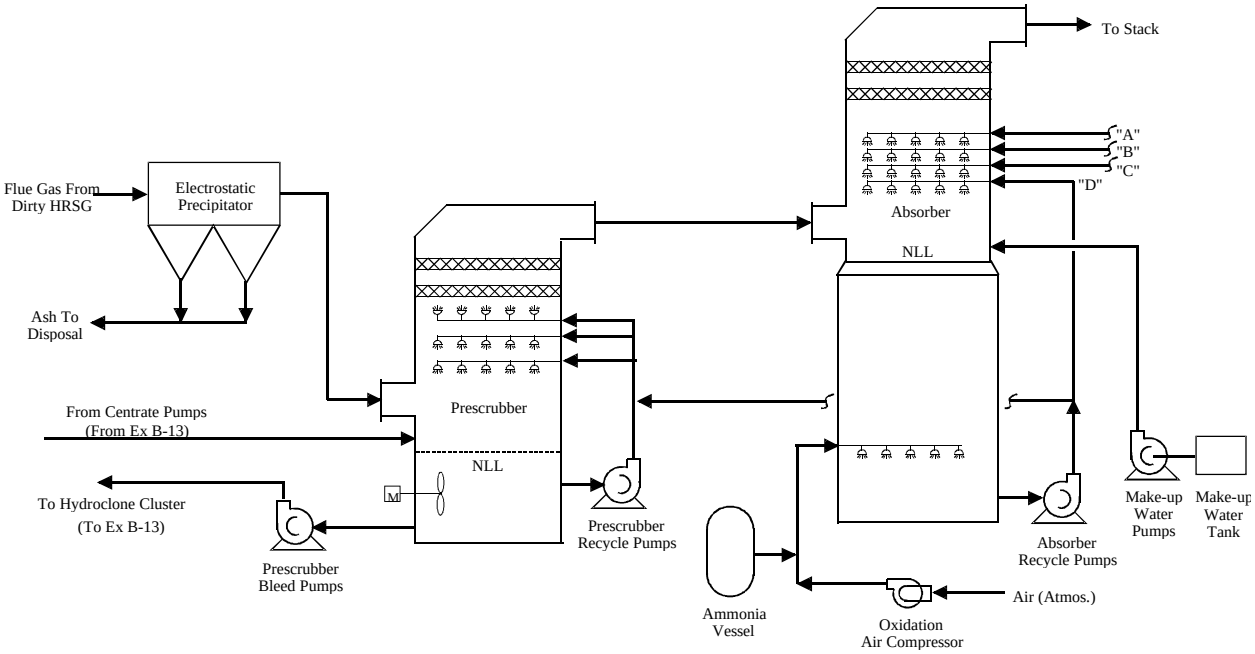

Exhibit B-12
GE's Ammonia Based Process Absorber Area

After leaving the prescrubber, the flue gas enters a countercurrent absorber where it is contacted by a recirculating unsaturated ammonium sulfate liquor. Ammonia is added with the

oxidation air to maintain the recycle liquor at the pH of 5.2 to 5.8, thus ensuring the required SO_2 removal. The cleaned flue gas then passes through two stages of high efficiency mist eliminators to remove entrained droplets.

The primary purpose of the prescrubber is to separate the process functions of SO_2 absorption and oxidation, which take place in the absorber, from the function of ammonium sulfate crystallization. The oxidation rate of ammonium sulfite deteriorates as the concentration of dissolved salts increases. Approximately 45 wt % dissolved ammonium sulfate is required before solids will crystallize. By separating the oxidation step, the oxidation rate remains high in an unsaturated solution in the absorber.

The thermal energy of the flue gas evaporates water from the prescrubber slurry and saturates the flue gas with the evaporated water. The evaporation of water causes crystallization of ammonium sulfate product.

The unsaturated ammonium sulfate solution in the absorber is used to wash the prescrubber mist eliminator and maintain the prescrubber vessel liquid level. As a result, unsaturated ammonium sulfate solution is introduced into the prescrubber where the excess water is evaporated and crystallization of product occurs.

The process steps of SO_2 absorption and oxidation take place in the dilute liquor phase in the absorber. In the absorber, the flue gas SO_2 reacts with ammonia which is introduced in gaseous form with the oxidation air. The ammonia is highly reactive and sensitive to pH. The ammonia is stored in a pressurized or refrigerated vessel and pumped as a liquid to a vaporizer. The vaporizer typically uses steam to vaporize the ammonia prior to introducing it into the oxidation air.

Oxidation air is introduced into the absorber to oxidize the ammonium sulfite to ammonium sulfate. Ammonium sulfate solution (10 - 25 wt % dissolved solids) is bled from the absorber to the prescrubber to maintain level in the prescrubber tank. The fresh make up water required by the process is added to the absorber reaction tank to maintain tank level.

Slurry is bled from the prescrubber to a dewatering hydroclone which increases solids in the slurry from 10 to 35 wt % solids (Exhibit B-13). The purpose of the hydroclone is two fold. First, the hydroclone is designed to dewater the slurry from the prescrubber to optimize the centrifuge feed slurry density. The second purpose of the hydroclone is to separate the fine particulate (primarily flyash in the flue gas) from the product, thus maintaining product purity. The underflow of the hydroclone is directed via a diverter box to the centrifuge feed tank. The overflow of the hydroclone is diverted to the centrate tank. In the event that the prescrubber solids density is lower than 10 wt %, the hydroclone underflow is combined with the hydroclone overflow and returned to the prescrubber via the centrate tank.

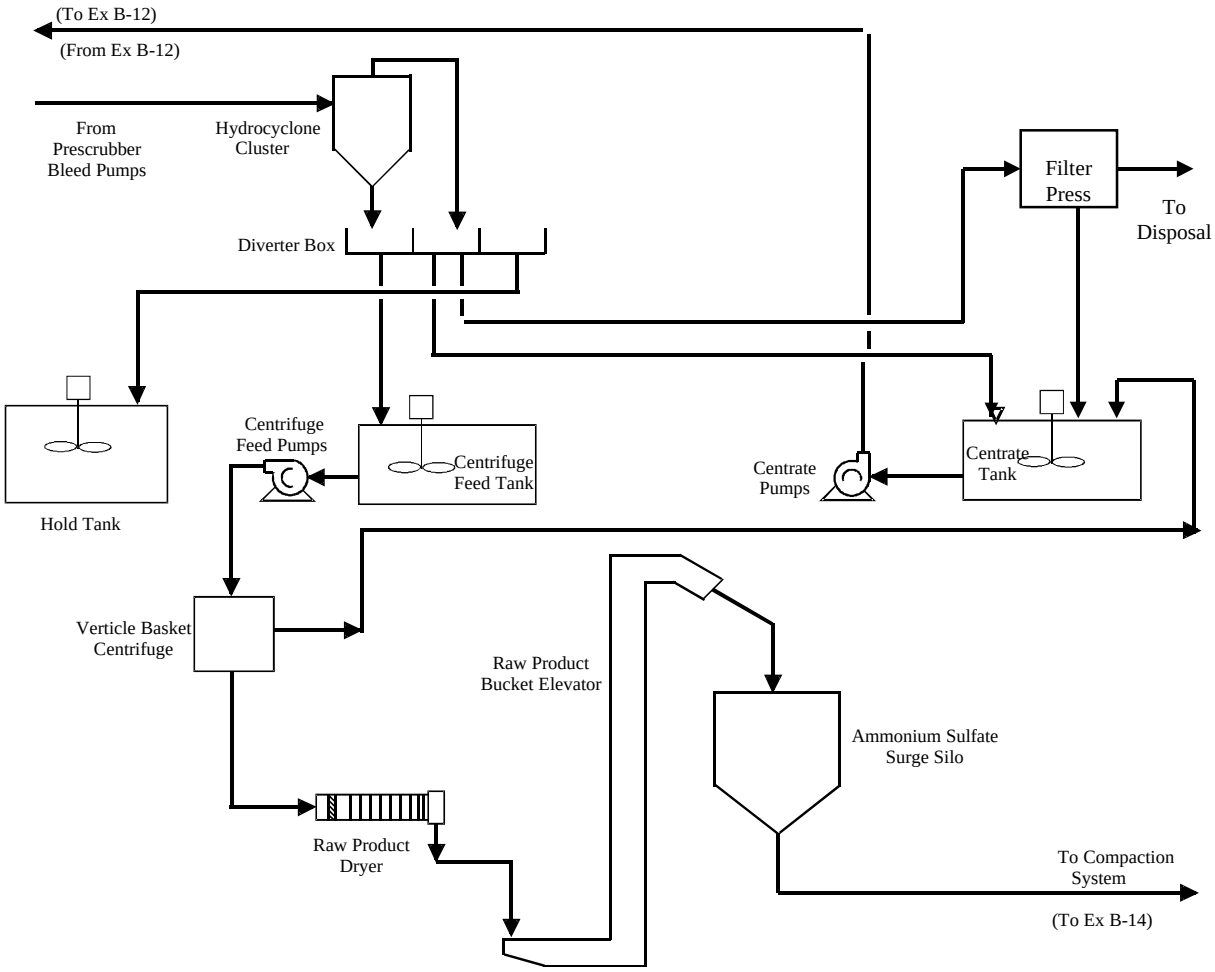

Exhibit B-13
GE's Ammonia Based Process Dewatering Area

The slurry from the centrifuge feed tank is pumped to a series of basket centrifuges where the slurry is dewatered to 97 - 98% solids. The centrifuges then discharge the material immediately into the rotary drum dryer where heated air is passed over the crystals to dry the material to less than one per cent moisture. The dry material is conveyed to a small surge silo where the material is stored prior to final processing in the compaction system.

To maintain product purity, a portion of the hydroclone overflow can be diverted to a centrate filter press which captures the fine particulate matter, washes it, dewaters it and discharges the filter cake (50 wt % solids) into a bin for disposal.

To maximize the product value, the ammonium sulfate material in the surge silo must be converted from sugar like crystals to the larger granular crystals. To accomplish this, the raw unprocessed ammonium sulfate in the surge silo is fed to the compaction system (Exhibit B-14). In this system, the fresh feed of ammonium sulfate material is combined with the fine particles from the compaction process and fed to a pug mill mixer to insure that the recycle and fresh feed

material are fully mixed prior to entering the compactor. The recycle and fresh feed ratio is controlled to produce the ammonium sulfate product of the desired particle hardness.

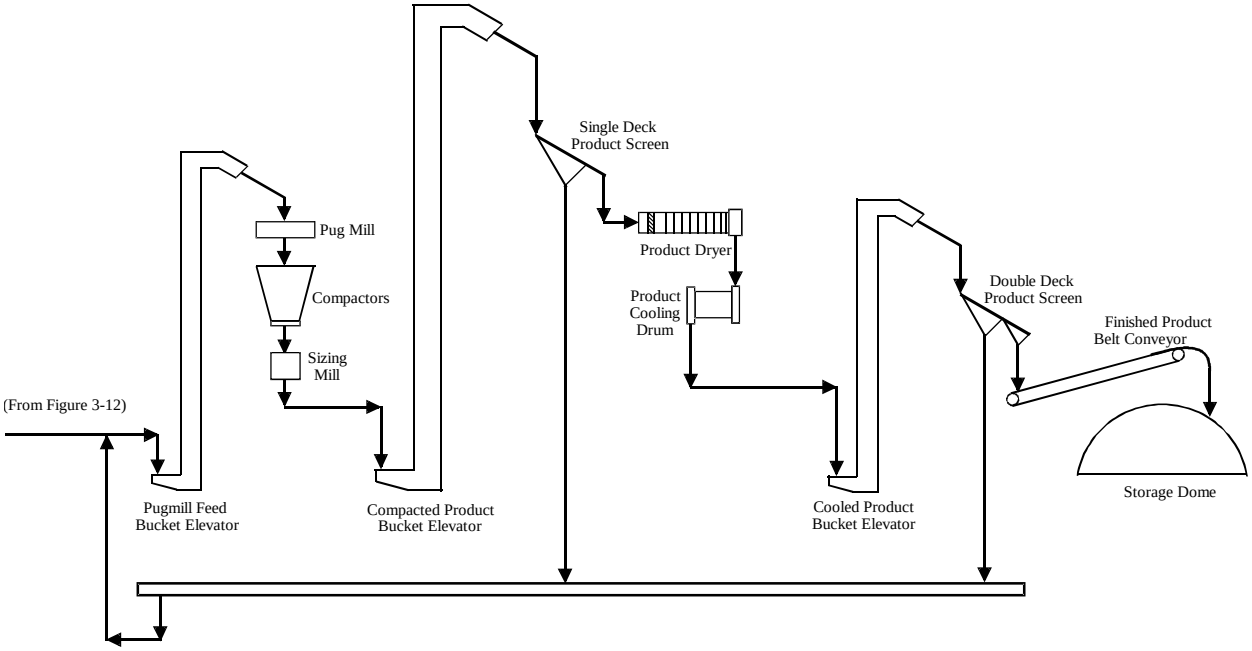

Exhibit B-14
GE's Ammonia Based Process Compaction Area

The material from the pug mill mixer is fed to a compactor feed screw system that forces the material between the two rolls that compact the solids into a hard flake. The hard flake from the compactor is discharged into a flake breaker which breaks the large flake into smaller pieces. The small pieces are then sized in a series of sizing mills.

The sized material is then fed to a sizing screen which separates the sized material from the fines. The fines are recycled to the beginning of the compaction process. The sized product passes through a dryer and then a cooler which ensure the moisture of the final product meets the industry standards of less than one per cent. Prior to final storage, the sized material is passed through a final screening process to insure the final product size of 1 to 3 millimeter. The final sized product is sent to a large storage dome. From the storage dome, the material is loaded on to either trains or trucks for transportation to market.

Process Chemistry: The SO_2 from the flue gas is absorbed in the spray tower by water contained in the ammonium sulfate spray drops, forming sulfurous acid, H_2SO_3:

$$SO_2 + H_2O \text{ -----> } H_2SO_3$$

The sulfurous acid, H_2SO_3, then reacts with ammonia to form ammonium sulfite, $(NH_4)_2SO_3$:

$$H_2SO_3 + 2\ NH_3 \text{ -----> } (NH_4)_2SO_3$$

The ammonium sulfite, $(NH_4)_2SO_3$, further reacts with H_2SO_3 to form ammonium bisulfite, $(NH_4)HSO_3$:

$$H_2SO_3 + (NH_4)_2SO_3 \text{ -----> } 2\ (NH_4)HSO_3$$

The ammonium sulfite, $(NH_4)_2SO_3$, is oxidized in the absorber to form ammonium sulfate, $(NH_4)_2SO_4$:

$$(NH_4)_2SO_3 + 1/2\ O_2 \text{ -----> } 2\ (NH_4)_2SO_4$$

Similarly, ammonium bisulfite, $(NH_4)HSO_3$, is oxidized in the absorber to form ammonium bisulfate, $(NH_4)HSO_4$:

$$(NH_4)HSO_3 + 1/2\ O_2 \text{ -----> } (NH_4)HSO_4$$

The ammonium bisulfate, $(NH_4)HSO_4$, can be further neutralized by ammonia to form ammonium sulfate, $(NH_4)_2SO_4$:

$$(NH_4)HSO_4 + NH_3 \text{ -----> } (NH_4)_2SO_4$$

All of these reactions take place in the absorber vessel in a solution phase. The ammonium sulfate is crystallized when the excess water is evaporated in the prescrubber.

Table B-9
GE's Ammonia Process Data

- Process Scope:
  - SO_x removal
  - Particulate removal
- Equipment Scope:
  - Flue gas prescrubbing
  - Ammonia scrubbing
  - Ammonium sulfate recovery
  - Ammonium sulfate crystal sizing
  - ESP
- Pressure Drop: = 8.0 in. w. c.
- Raw Material Consumption:
  - Ammonia = 2.25 ton/h
- By-product/Waste Production:
  - Product = 8.75 ton/h
- Utilities Consumption:
  - Power = 2,350 + 710 = 3,060 kW
  - Water = 200 gpm
  - Steam = 3,500 lb/h
  - Natural gas = 53 lb/h
- Cost, millions:

Equipment cost	= $ 17.0
Installation	= $ 14.4
Allowance[1]	= $ 1.5
Total	= $ 32.9

- Manpower:
  - Manpower = 1.5 operators per shift
- Footprint:
  - Ammonia scrubbing[2] = 50 ft wide x 60 ft long
  - ESP = 50 ft wide x 70 ft long x 50 ft high

Notes:
1. The GE recommended system limits particulate emissions to 12.0 lb/h. To limit emissions to 6.33 lb/h, an allowance of $1.5 million is added for additional ESP fields.

2. The vendor did not supply the footprint. GE's Limestone process footprint is used as a default.

Experience

In March 1994, GE Environmental Systems (GEESI), Morrison Knudsen Corporation (MK) and Dakota Gasification Company (DGC) entered into a contract to build the first commercial size ammonia scrubbing system at DGC's Great Plains Synfuels plant located near Beulah, North Dakota. It was started in June 1996. This is GE's first ammonia-based FGD commercial plant. It has a 300 MW capacity and burns heavy resid. GE has guaranteed a 93.0% sulfur removal and a 99.0% purity of ammonium sulfate product.

NO_x Flue Gas Cleaning

Unless the flue gas cleaning technology combines SO_2 and NO_x removal, a separate process is needed to remove NO_x. Discussions with process providers, and review of the literature indicates that at the present time, the use of SNCR with coal-fired boiler flue gases has many uncertainties. However, with the HITAF, it should be possible to "design in" a SNCR system if it is desired when the furnace is more defined, later in Phase II. Thus, for the present screening study, SCR technology for NO_x control is used with the wet limestone FGD and with the lime based FGD. The ammonia based SO_2 systems (Krupp, GE) are combined with SNCR technology (in the HITAF) for NO_x removal.

In addition to the SNCR and SCR processes, a combination, called hybrid SNCR/SCR, is discussed in the literature. In the hybrid process, part of the NO_x is reduced by the SNCR injection of ammonia in the furnace and the remaining NO_x is removed by the SCR in the HRSG. Except for possible special cases, the hybrid system lacks industrial performance and economic incentives for use in the HIPPS conceptual design.

SNCR Summary

The SNCR process directly injects ammonia or urea into a part of the HIPPS furnace where the flue gas temperature ranges from 1,700 to 1,800 °F (927 to 982 °C): At a temperature lower than 1,600 °F (871 °C), reagent slips through unreacted, and above 2,000 °F (1093 °C), NO_x conversion and reagent utilization decreases.

The SNCR process reactions are:

Ammonia reactions:

$$4\ NO + 4\ NH_3 + O_2 \ \text{-----}> \ 4\ N_2 + 6\ H_2O$$
$$2\ NO_2 + 4\ NH_3 + O_2 \ \text{-----}> \ 3\ N_2 + 6\ H_2O$$

Urea reactions:

$$4\ NO + 2\ CO(NH_2)_2 + O_2 \ \text{-----}> \ 4\ N_2 + 2\ CO_2 + 4\ H_2O$$
$$2\ NO_2 + 2\ CO(NH_2)_2 + O_2 \ \text{-----}> \ 3\ N_2 + 2\ CO_2 + 4\ H_2O$$

The main advantage of SNCR is that no catalyst is needed, giving an initial low cost. However, operating and maintenance costs can be high. For a reasonable reagent consumption,

SNCR requires the reaction zone in the furnace be large enough to provide a residence time of at least one second for the reactants. Also, the flue gas flow regime in the reaction zone must be turbulent enough to thoroughly mix NO_x with the reagent. Such requirements make it difficult to efficiently use SNCR for existing furnaces. New furnaces can be especially designed for SNCR, but such design changes to suit SNCR have not been implemented by industry. Also, if the furnace must operate over a range of firing rates, the furnace/SNCR design must maintain process conditions over the range in the zone established for the SNCR reactions.

SNCR costs for the ammonia based FGD process were provided by Krupp Uhde.

SCR Process Description

In the SCR process, a catalyst is located in the HIPPS dirty HRSG at a location where the flue gas temperature is about 700 to 800 °F (371 to 427 °C). Unlike a SNCR zone in a furnace, the flue gas temperature remains constant in the catalyst because there are no heat sinks inside the catalyst bed. The volume of catalyst material is such that there is sufficient residence time. SCR has a relatively high initial cost and high operating cost because of the catalyst, but in spite of this, SCR is being used for high removal (up to 90%), reliable, efficient NO_x reduction. The process flow diagram for a typical SCR is shown in Exhibit B-15.

Most of the SCR catalysts used to remove NO_x from coal based flue gas contains catalytically active vanadium pentoxide (V_2O_5), and titanium dioxide (TiO_2) which acts as a support for the active constituent. The actual catalyst composition varies among manufacturers, and can consist of many active metals and support materials. Some catalyst manufacturers include tungsten oxide (WO_3), which inhibits oxidation of sulfur dioxide to sulfur trioxide and imparts thermal and mechanical stability to the catalyst. The catalyst manufacturers can adjust proportions of vanadium pentoxide, titanium dioxide and tungsten dioxide in the catalyst to suit a given SCR application.

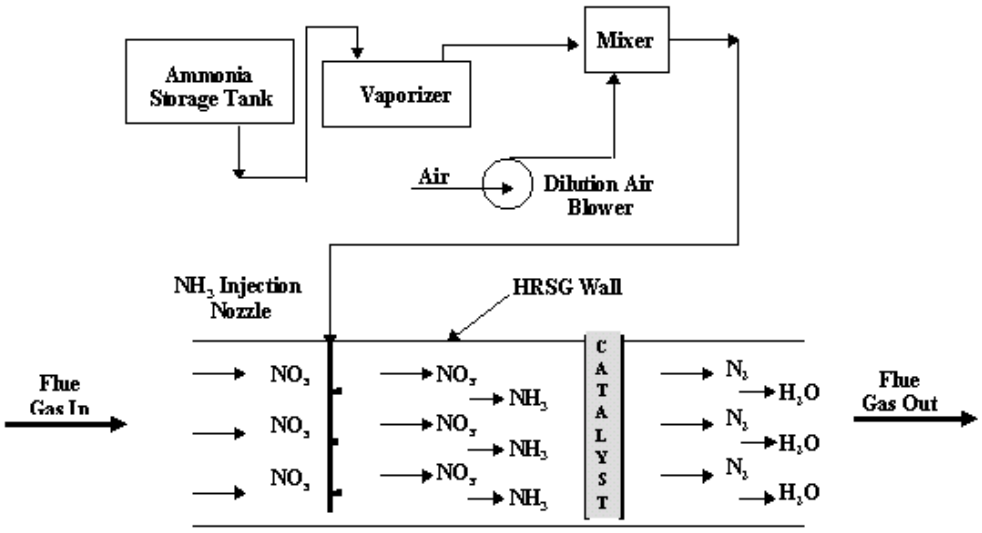

Exhibit B-15
Process Flow Diagram of the SCR Process for NO_x Removal

Process Chemistry: In the presence of a catalyst, NO_x is removed by its reaction with ammonia:

$$4\ NO + 4\ NH_3 + O_2 \ \text{-----}> \ 4\ N_2 + 6\ H_2O$$
$$2\ NO_2 + 4\ NH_3 + O_2 \ \text{-----}> \ 3\ N_2 + 6\ H_2O$$

To collect process data, several equipment providers were informally contacted and asked for cost and process information. They were provided with the flue gas data from Table B-2 and other project information. As noted earlier, permissible NO_x concentration is 0.06 lb NO_x/million Btu (25.8 ng/J) of fuel input. Reviewing the data provided in Table B-2 for the raw and cleaned flue gas, the allowed NO_x in the cleaned gas is 2.75 lbmol/h. This was the performance objective for the SCR suppliers.

SCR Process Providers

The following organizations were contacted and asked to provide data.

1. Mitsubishi Heavy Industries, Newport Beach, CA/Cormetech Inc., Durham, NC
2. Steag AG, Washington, DC/Black & Veatch, Kansas City
3. Wahlco Environmental Systems Inc., Leawood,
4. ABB Combustion Engineering Systems, Windsor, CT
5. Aqua Chem Inc. Cleaver-Brooks Div., Milwaukee, WI
6. Johnson Matthey Inc., Wayne, NJ
7. Lechler Inc., St. Charles, IL
8. Peerless Manufacturing Company, Dallas, TX

Of the eight companies, the first three supplied technical information and budget-level costs. The three SCR systems are described below. Data for the three processes are reported in Addendum A on Equipment and Cost Data for SCR Processes.

Mitsubishi/Cormetech: Cormetech supplies the catalyst. Mitsubishi Heavy Industries assembles the NO_x reduction system and supplies it to the customer.

In the Mitsubishi/Cormetech NO_x reduction system, the SCR catalyst housing is located within the HRSG where the optimum flue gas temperature can be obtained, independent of the furnace operating load. The housing is arranged so the flue gas flows downward. The catalyst modules are installed in two initial layers. Space for one spare layer is provided for future catalyst addition. A "dummy" layer is provided at the inlet of the SCR catalyst to streamline the flue gas flow and reduce erosion of the elements. Final arrangement and location of the housing will be determined by studying the arrangement of other equipment and ducting. The present arrangement assumes a single housing located within the HRSG.

The flue gas will enter the SCR inlet transition duct and then flow into the SCR housing from the top of the housing. The SCR catalyst elements are fitted into steel frame modules at the shop and shipped to the job site by truck. The catalyst modules are installed in the housing through catalyst loading doors located on the side of the housing. Soot blowers are installed for each catalyst layer. Steam conditions for the soot blowers are the same or similar to that for the boiler soot blowers.

The ammonia injection grid (AIG) can be located at the inlet of the SCR housing or upstream of the SCR housing within the HRSG tube banks. (The AIG location will be finalized after review of the total HRSG and SCR arrangement, and flue gas flow guide vanes will be installed at the SCR inlet and/or at the AIG if necessary to reduce flow distribution balance.) The flue gas from the outlet of the SCR housing is returned to the downstream portion of the HRSG.

Anhydrous ammonia is used for the SCR system. Ammonia is supplied from the ammonia tank and diluted with air at the ammonia dilution skid. An ammonia dilution fan is used to mix and dilute the anhydrous ammonia with ambient air and then transport the diluted ammonia into the flue gas duct. Ammonia distribution headers are located at the AIG. Ammonia distribution within the duct is adjusted by manual flow control valves at the header outlet.

The control logics and wiring diagrams for the SCR system are provided as part of the scope of supply. The logic is incorporated into the furnace DCS system. The SCR system is operated automatically and does not require any designated operators for normal operation.

Planned maintenance includes adding the third catalyst layer after three years of operation and replacing the first layer 8.5 years after initial operation. The catalyst replacement interval is estimated to be three to four years thereafter. On this schedule, approximately four additional or replacement layers will be required over 20 years.

MHI has extensive experience designing and installing NO_x reduction systems. In the USA, they have installed 80 NO_x reduction systems for gas turbines. In Japan they have installed NO_x reduction systems for gas and oil-fired utility boilers (18,000 MW), for gas and oil-fired industrial boilers producing 1,500 ton/hour steam (1,362 tonne/h), for gas turbines (4,500 MW), and for industrial gas turbines and diesel engines (375 MW). For coal-fired units, MHI has installed NO_x reduction units for utility boilers (7,600 MW) and for industrial boilers (1,560 ton/hour steam (1,416 tonne/h)).

Steag AG/Black & Veatch: Steag is an independent power producing company in Germany, with an office in Washington, DC. Steag works with Black and Veatch (B&V) who buys the catalyst from a catalyst manufacturer and then designs and supplies complete NO_x reduction systems.

For the Steag/B&V NO_x reduction system, anhydrous ammonia is delivered to the plant by a truck and stored in an ammonia storage tank. Ammonia from the ammonia storage tank is vaporized by an electrically heated ammonia vaporizer. The vaporized ammonia is mixed in a muffler-like mixer with the dilution air. The dilution air is supplied by a dilution air fan, which compresses atmospheric air to about 2 to 3 psig (115 to 122 kPa). The dilution air is added to make a 5 percent concentration of ammonia in the mixture.

The air and ammonia mixture is sent to the AIG, which is located ahead of the SCR catalyst. In the Steag/B&V NO_x reduction system, the AIG is a grid of pipes with small holes through which the air/ammonia mixture is introduced into the flue gas stream. The grid stands vertically and distributes the air/ammonia mixture over the cross section of the HRSG. The SCR catalyst is located in the HRSG where the flue gas temperature is about 700 °F (371 °C). The catalyst is contained in two vertical sections called layers, each layer about four feet deep. The two layers are separated by a distance of about five feet. This distance is to accommodate the soot blowers.

There are 10 soot blowers which are operated for about an hour each day to remove the fly ash deposited on the catalyst layers.

When the catalyst is freshly charged, the ammonia slip is zero. With the passage of time, the catalyst becomes slightly deactivated and traces of ammonia start appearing in the deNO_xed flue gas. As the deactivation progresses, the ammonia slip increases until it is equal to the design allowance of 2 ppm. The time for the slip to reach its design allowance is estimated to be about three years. At that time the deactivated catalyst is replaced by fresh catalyst.

B&V has installed SCR and SNCR at a number of fossil fueled plants. They have provided SCR design services for 13 plants (2,300 MW) and SNCR design services for 9 plants (670 MW). Their experience includes design, procurement, installation and startup of the largest SCR system in the United States on the 460 MW Orlando Utilities Commission Stanton Energy Center Unit 2, which is coal-fired. Since 1992, B&V has teamed with Steag for design and installation of SCR systems. Steag owns and operates 13 coal-fired units (5,400 MW). All of these units are equipped with SCR based NO_x reduction systems. Since 1984, Steag has designed SCR systems for a total of 12,000 MW of power production capacity.

Wahlco Environmental Systems Inc.: Wahlco buys catalyst from a catalyst manufacturer and designs and installs the NO_x reduction system.

For the Wahlco NO_x reduction system, the ammonia injection system consists of an ammonia vaporization skid and an injection grid. The AIG is located in the dirty HRSG. The reactor section is approximately 30 by 60 feet. Aqueous ammonia at about 27 percent by weight concentration is vaporized in a hot air stream from a dilution air fan and electric heaters which heat ambient air. The air/NH_3 mixture is routed to the AIG through a series of valves used to distribute and mix the NH_3 flow with the flue gas NO_x flow so that a uniform NH_3/NO_x distribution is achieved at the catalyst. Inside the HRSG are two separate banks of catalyst elements separated by approximately 5 feet of space. The catalyst plates are oriented vertically to minimize flyash deposition. Metal frames secure the catalyst in place.

The catalyst is a plate type. It consists of a metal substrate covered by catalyst. The active catalytic materials are titanium dioxide and molybdenum/vanadium oxide.

The success of the SCR system is dependent upon the operation of a complex soot blowing system. Air operated soot blowers are located ahead of the first and second catalyst banks to periodically clean the catalyst plates of ash build up.

Wahlco has installed SCR systems at two gas-fired utility plants (110 MW and 390 MW) and at two coal-fired utility plants (100 MW and 560 MW). In addition, Wahlco has extensive experience injecting reagents to condition the flue gas going to an electrostatic precipitator. They have supplied 367 flue gas conditioning systems using SO_3 injection and 58 systems with NH_3 injection. The combined total capacity of the conditioned plants is some 110,000 MW.

SCR Process Screening Results

NO_x reduction with SCR is a proven technology and there are a number of SCR catalyst and system manufacturers. The catalysts are very similar and the suppliers can tailor the catalyst to suit a given SCR application.

For the three companies that responded to requests for data, two companies use anhydrous ammonia and one uses a 27% ammonia solution in water. This supplier can also supply a system based on anhydrous ammonia. The amount of commercial experience varies among companies, but from an industry perspective SCR use and experience is extensive.

The cost data from the SCR providers varied over a range of $5 to $10 million. Reasons for the variance were not fully investigated for the screening. For the HIPPS conceptual commercial plant design, a SCR similar to the MHI/Cormetech process will be used. The installed cost for the system is estimated to be $7.5 million. Operating and maintenance, including ammonia and catalyst replacement is estimated to be $250,000 per year.

Other Flue Gas Desulfurization Processes

Brief process descriptions for those companies which were unable to provide data are presented in this section.

Babcock & Wilcox. B&W is currently testing a 10 MW prototype of LIDS™ as part of their Low Emission Boiler System (LEBS). However, this process is not applicable to HIPPS because the sorbent is fed directly to the furnace. Feeding the sorbent directly to the furnace would require redesign of the HITAF furnace.

B & W recommended wet scrubbers using limestone slurry containing adipic acid as an additive. B&W has extensive experience with wet limestone plants, and they would be interested to propose a system when the plant is to be built. For the study, B&W declined providing further information.

Belco Technologies Corporation. They have installed acid gas cleaning systems having deSO_x efficiencies up to 92% on Municipal Solid Waste (MSW) incinerators. The Belco process uses a Spray Dryer Absorber (SDA). For HIPPS, the deSO_x requirement is 98.5%. To achieve that level, Belco needs a baghouse downstream of the SDA. They declined to provide data for a system with a baghouse.

Dravo Lime Company. In the 1995/1996 period, Dravo Lime Company, in cooperation with Ohio Coal Development Office and Cinergy Corporation, conducted evaluations of high gas velocity scrubbing with a magnesium-enhanced lime FGD process at a 4.5 MW pilot plant. These studies showed a significant decrease in the quantity of liquor required to scrub the same volume of gas as the gas velocity in the scrubber increases. During this operation they achieved 98% SO_2 removal at gas velocities of 10 to 25 ft/s (3 to 7.6 m/s) in both vertical and horizontal scrubbers. Dravo has not responded to requests for data.

Haldor Topsoe. Haldor Topsoe developed a flue gas cleaning process called SNOX. This process removes 95% of both the sulfur and the nitrogen oxides in the flue gas. Particulates are also removed from the flue gas. The sulfur is recovered as concentrated commercial grade sulfuric acid using Haldor Topsoe's WSA-2 process, while the NO_x is removed by reduction with ammonia into free nitrogen and water vapor using selective catalytic reduction (SCR). The SNOX process has been used commercially since 1987. Haldor Topsoe did not provide data.

Pure Air™. Pure Air is a partnership between Air Products & Chemicals and Mitsubishi Heavy Industries America Inc., and sells Mitsubishi's flue gas desulfurization process. In June 1992, their advanced flue gas desulfurization (AFGD) system at Northern Indiana Service

Company's Bailly Generating Station began to process flue gas. The process uses dry pulverized limestone as a sorbent, and a high flue gas velocity of 20 ft/s (6.1 m/s), resulting in reduced absorber height. The gypsum produced is of wallboard grade. Due to other commitments, Pure Air did not provide data.

Chiyoda Corporation. Chiyoda manufactures FGD equipment, but did not provide data. In the Chiyota process, limestone slurry is reacted with the flue gas sulfur dioxide to form calcium sulfate. The reaction is performed in Chiyota's jet bubbling reactor (JBR). In the JBR, the flue gas and the oxidation air are bubbled through a limestone slurry, which is circulating in the reactor. The JBR process also removes particulates from the flue gas, eliminating the need for other particulate controls.

Flue Gas Cleaning Cost and Economic Data

Cost data were provided by the process developers. Some of the costs are highlighted in the data tables for each process, and data from the developers is consolidated in the section on Data for Flue Gas Desulfurization Processes. Other costs needed to complete a system, or make the estimates more comparable, have been provided by Bechtel. At the present level of conceptual design and informal communications with potential flue gas cleaning process developers, the screening comparison for this topical report is limited to the generic systems noted in Table B-10. The costs are based on the developers' inputs with adjustments for completeness and consistency. However, the costs are not tied to a single process developer. Typically there are more than one possible supplier of a SO_2 or NO_x technology, and more design and procurement work is required to select from among the available specific choices.

Table B-10 below summarizes the equipment and installation costs as the Investment_Cost. The Annual Operating and Maintenance Cost in Table B-10 is the sum of previously reported variable costs; operating labor at $200,000 per year for each process; and maintenance costs at 2% of the FGD Investment Cost.

In Table B-10, annualized costs are calculated on the right-hand portion of the table for five cases. The economic and financial variables for the cases are cost of funds and investment duration. The values for the variables used in each case are listed below the case.

Table B-10
Flue Gas Cleaning Cost and Economics

Item	Emissions Technology	Annual Operating and Maintenance Cost -$1,000s	Investment Cost - $1,000s	ANNUALIZED COST 1,000's				
				CASE A	CASE B	CASE C	CASE D	CASE E
1	Lime based desulfurization system with SCR NO_x control	5,850	20,000	8,199	9,045	10,908	9,835	11,451
2	Ammonia based SO_x and SNCR NO_x control with ammonium sulfate byproduct*	3,600	31,000	7,241	8,553	11,440	9,777	12,282
3	Wet limestone desulfurization with SCR NO_x control	4,750	40,500	9,507	11,220	14,993	12,820	16,093
	Economic and Financial Variables							
	Cost of Funds			10%	15%	25%	15%	25%
	Investment Term Years			20	20	20	10	10

Economic and Financial Variables

Cost and Economics Discussion

The screening study uses data provided by the technology providers, with limited modifications to make the technical scopes and costs as consistent as possible for comparison. The major adjustments to the providers' data are:

- The ABB scope and costs were increased to add a limestone grinding system. ABB had specified the use of delivered, ground limestone. This was done for an equal comparison with GE's limestone system.
- Additions were made to providers to increase particulate removal rates to match the HIPPS requirements.
- Installation costs were added to equipment costs, if the installation cost was not provided in the data.
- Operating labor and maintenance costs were added to all the technologies.
- For technology screening, the costs of specific processes were combined and rounded to obtain the values in Table B-10.

Thus, the "investment cost" estimated in Table B-10 is equal to EPRI's TAG "bare erected cost" item. Engineering, contingency and owner's costs will be added when the complete HIPPS plant cost estimate is prepared. Depending on future HITAF design decisions, further data may be obtained from one or more process suppliers.

Based on the economics, the ammonia based system has the lowest annual costs except for cases where the cost of money is very high. This is expected from the nature of the calculations as processes with high investment costs are sensitive to the cost of funds and investment

duration. Perhaps more important in a practical sense, it is noted that the ammonia based system's economics are strongly dependent on the sale of by-product ammonium sulfate, making the use of this technology especially site and market specific. The combined SO_x and NO_x technology represented by NOXSO Corporation has been screened out of the study because of the current lack of progress toward commercialization.

Table B-11 summarizes the energy requirements and wastes or by-products from the technologies. Efficiency is a major concern in the HIPPS project, and Table B-11 was prepared to see if there was a conflict between process cost and process energy consumption, which will reduce overall plant efficiency. There is no apparent conflict, as the two low cost processes are also low energy consumers.

Table B-11
Flue Gas Cleaning Energy Requirements and Waste/By-product Production

Emissions Technology	Energy Requirements	Production tons/hour
Lime based desulfurization system with SCR NO_x control	1,800 kW	12 (Waste)
Ammonia based SOX and NOX flue gas cleaning with ammonium sulfate by-product	2,000 kW	8 (Ammonium sulfate by-product)
Wet limestone desulfurization with SCR NO_x control	4,300 kW	14 (Waste)

Conclusions and Recommendations

For the conceptual design screening objective, NOXSO and wet limestone processes are eliminated by their higher cost and energy consumption. Also, the NOXSO Corporation's financial status is questionable, with recent news articles indicating problems funding further technology development.

Ammonia based process technologies such as Krupp's and General Electric's have competitive costs and energy requirements, and will be retained for future evaluations. However, inclusion of an ammonia based process in the conceptual design would require a separate review of the potential for the ammonium sulfate by-product in the U. S. market. In addition to the real by-product issue, ammonia based processes must overcome perceptions about handling "toxic" and "dangerous" materials, which from an engineering viewpoint and experience in other industries should not be a primary concern, but when combined with the larger project objective to commercialize an advanced power generation concept, could become a problem.

The leading companies and their technologies: EEC and AirPol (lime processes) and Krupp and GE (ammonia processes) are all experienced pollution control organizations with sound financial and technical bases.

Addendum A - Calculations and Background Information

Appendix B

Operating Cost Unit Prices

The following unit prices were used with estimated quantities of materials required by the flue gas cleaning processes.

Adipic acid[1], $/lb	0.70
Anhydrous ammonia, wholesale tanks[1], $/ton	225.00
Ammonium sulfate, granular[1], $/ton	45.00
Lime[1], $/ton	57.00
Limestone[2], $/ton	15.00
Natural gas[2], $/million Btu	2.90
Soda ash, bulk[1], $/ton	105.00
Sulfur, crude recovered[1], $/ton	47.00
Steam[4], $/ton	5.30
Water, cooling[5], $/1000 gal	0.40
Water, raw[2], $/1000 gal	0.80
Waste solids[2], $/ton	10.00
Electricity[4], $/kWh	0.05
NOXSO sorbent[3], $/ton	2,000

References:

1. Chemical Market Reporter, February 10, 1997.
2. TAG™ - Technical Assessment Guide, EPRI, 1993.
3. Communication with NOXSO corporation.
4. TAG™ - Technical Assessment Guide, EPRI, 1986
5. In-house data.

Data for Flue Gas Desulfurization Processes

Details for the flue gas cleaning processes provided by the suppliers are contained in this section. Costs are provided by the suppliers, or are calculated from quantities of materials and the unit rates from the section on Operating Cost Unit Process.

ABB Environmental Systems, Knoxville, TN	Quantity	$1,000
Limestone, ton/h	7.2	946
Adipic acid, lb/h	8.5	52
Electricity, kWh	2,239	981
Raw water, gpm	174	73
Cooling water, gpm	0	0
Waste solids, ton/h	13.2	1,156
Annual operating cost		**3,208**
Equipment cost		**27,000**

GE Environmental Services, Lebanon, PA	Quantity	$1,000
Limestone, ton/h	7.6	999
Electricity, kWh	4,508	1,975
Raw water, gpm	147	62
Cooling water, gpm	0	0
Waste solids, ton/h	14.5	1,270
Annual operating cost		**4,305**
Equipment cost		**14,600**

AirPol, Parsippany, NJ	Quantity	$1,000
Lime, ton/h	4.97	2,479
Soda ash, ton/h	0.96	883
Electricity, kWh	1,792	785
Raw water, gpm	166	70
Cooling water, gpm	0	0
Waste solids, ton/h	11.8	1,034
Annual operating cost		**5,251**
Equipment cost		**6,800**

Environ. Elements Corp, Baltimore, MD	Quantity	$1,000
Lime, ton/h	6.27	3,131
Electricity, kWh	1,850	810
Raw water, gpm	126	53
Cooling water, gpm	0	0
Waste solids, ton/h	12.9	1,129
Annual operating cost		**5,123**
Equipment cost		**5,750**

Krupp Uhde, Dortmund, Germany	Quantity	$1,000
Version I - with SO_2 removal only		
Anhydrous ammonia, ton/h	2.26	4,454
Electricity, kWh	1,900	832
Raw water, gpm	194	82
Cooling water, gpm	1238	260
Ammonium sulfate, ton/h	8.1	-3,193
Annual operating cost		**2,435**
Equipment cost		**21,300**

Krupp Uhde, Dortmund, Germany	Quantity	$1,000
Version II - addition for NO_x removal		
Anhydrous ammonia, ton/h	0.16	315
Electricity, kWh	0	0
Raw water, gpm	5	2
Cooling water, gpm	0	0
Ammonium sulfate, ton/h	0	0
Annual operating cost		**2,753**
Equipment cost		**22,500**

NOXSO Corporation, Bethel Park, PA	Quantity	$1,000
Sorbent	0.08	1,445
Electricity, kWh	4,000	1,752
Raw water, gpm	75	32
Cooling water, gpm	50	11
Natural gas, scfm	1,850	2,820
Sulfur, ton/h	2.1	-865
Steam, lb/h	1,500	-35
Annual operating cost		**5,160**
Equipment cost		**20,000**

GE Environmental Services, Lebanon, PA	Quantity	$1,000
(ammonia based desulfurization process)		
Anhydrous ammonia, ton/h	2.25	4,445
Electricity, kWh	3,060	1,340
Raw water, gpm	200	84
Natural gas, scfm	21	30
Steam, lb/h	3,500	81
Ammonium sulfate, ton/h	8.74	-3,450
Annual operating cost		**$3,530.0 0**
Equipment cost		**17,000**

Equipment and Cost Data for SCR Processes

Data from the suppliers for the SCR processes are contained in this section.

MHI/Cormetech's NO_x Reduction System

Catalyst layer orientation	Horizontal
Flue gas flow direction	Vertically downward
Reagent	Anhydrous ammonia
Reagent slip	5 ppmv
Reagent consumption	75 lb/h
Pressure drop	2.6 in. w.c.
Catalyst type	Titanium based extruded honeycomb
Catalyst life	3 years
Catalyst volume	3,500 ft^3
Equipment cost	2.9 million $
Installation cost	2.0 million $
Total cost	4.9 million $
Catalyst replacement cost	135,000 $/year
Steam for soot blowers	1,000 lb/day/blower
No. of soot blowers	5

Steag/B&V's NO_x Reduction System

Catalyst layer orientation	Vertical
Flue gas flow direction	Horizontal
Reagent	Anhydrous ammonia
Reagent slip	2 ppmv
Reagent consumption	75 lb/h
Pressure drop	3 to 4 in. w.c.
Catalyst type	Titanium based plate or extruded honeycomb
Catalyst life	3 years
Catalyst volume	6,400 ft^3
Equipment cost	4.0 million $
Installation cost	3.6 million $
Total cost	7.6 million $
Catalyst replacement cost	330,000 $/year
Steam for soot blowers	14,000 lb/day
No. of soot blowers	10

Wahlco's NO_x Reduction System

Catalyst layer orientation	Vertical
Flue gas flow direction	Horizontal
Reagent	27% ammonia solution
Reagent slip	10 ppmv
Reagent consumption	75 lb/h (NH_3)
Pressure drop	5.0 in. w.c.
Catalyst life	2 years
Catalyst type	Titanium/molybdenum/vanadium
Catalyst volume	5,300 ft^3
Equipment cost	5.5 million $
Installation cost	4.5 million $
Total cost	10.0 million $
Catalyst replacement cost	not provided
Air for soot blowers	2,500 scfm at 150 psi and 130 °F
No. of soot blowers	not provided

Appendix C - HITAF Makeup Water Treatment System

Introduction and Summary

The HIPPS plant steam properties are 2,400 psia (16,547 kPa) and 1,000 °F (537.8 °C). For the heat recovery steam generation (HRSG) equipment to perform adequately, steam production requires high purity make up boiler water. Table C-1 gives an analysis of the Lake Michigan raw water, as provided by the Electric Power Research Institute's Technical Assessment Guide . The purity of the water required for the HIPPS plant is summarized in Table C-2.

Table C-1
Raw Water Analysis

Compound	Analysis, ppmw
Silica (SiO_2)	1.80
Iron (Fe)	0.09
Manganese (Mn)	0
Calcium (Ca)	39
Magnesium (Mg)	10
Sodium (Na)	3.30
Potassium (K)	0.70
Carbonate (CO_3)	0
Bicarbonate (HCO_3)	132
Sulfate (SO_4)	23
Chloride (Cl)	7.20
Fluoride (F)	0.10
Nitrate (NO_3)	0
Hardness as $CaCO_3$	
Equivalents:	
Total	168
Noncarbonate	30
Total suspended solids	10
Total dissolved solids	215
Color	1 unit
pH	7.9
Turbidity	0
Specific conductance @ 25°C	275 µ Ohm

ppmw = parts per million by weight

Table C-2
Boiler Feed Water Quality Required

Item	Limit
Total dissolved solids	50 ppbw max.
Suspended solids	minimum, preferably 0.0
Hardness	0 ppbw
Organic	0 ppbw
Free Caustic	0 ppbw
Dissolved oxygen	7 ppbw max.
Carbon dioxide	minimum, preferably 0.0
Total silica (as SiO_2)	20 ppbw max.
Total iron (as Fe)	10 ppbw max.
Total copper (as Cu)	2 ppbw max.
pH value* **	normally 9.0 to 9.5 @ 77 °F

* Adjusted to obtain 10 ppbw iron maximum.
** Obtained by addition of an alkaline volatile material such as ammonia.

Glegg Water Conditioning, Inc. was contacted, and graciously provided recommendations for an appropriate water conditioning system. Glegg was given the data shown in Table C-1 and Table C-2, and asked to provide technical and cost data for a system producing 100 gallons per minute of treated water. Glegg provided three alternatives for water treatment systems:

- Demineralization water treatment system,
- Reverse osmosis/mixed bed ion exchange water treatment system, and
- Reverse osmosis/E-Cell water treatment system.

The equipment costs for the systems ranged from about $450,000 to a little more than $550,000:

Water Treatment System	Equipment Cost
1. Demineralization	$551,000
2. Reverse osmosis/mixed bed ion exchange	$519,000
3. Reverse osmosis/E-Cell	$455,000

The estimated operating and maintenance costs for the systems vary from $35,000 to $85,000 per year. The reverse osmosis/E-Cell system is selected for the HIPPS commercial plant. Installed costs are estimated to be $650,000 and annual costs are $60,000. As there are only small economic differences among the systems, the RO/E-Cell system has the advantage of minimal waste effluents.

Gregg also provided data for a condensate polishing system. The installed cost is estimated to be $300,000 and annual O&M is $25,000.

The three water treatment systems are described below. The condensate polishing system is summarized in the last section.

Demineralization Water Treatment System

A flow diagram of the system is shown in Exhibit C-1. There are two trains: One train is operating while the second train's ion exchange materials are being regenerated. Only one train is shown on the exhibit. The number of operating and spare (being regenerated) pieces of equipment are indicated as 1/1, 1/0 and so on.

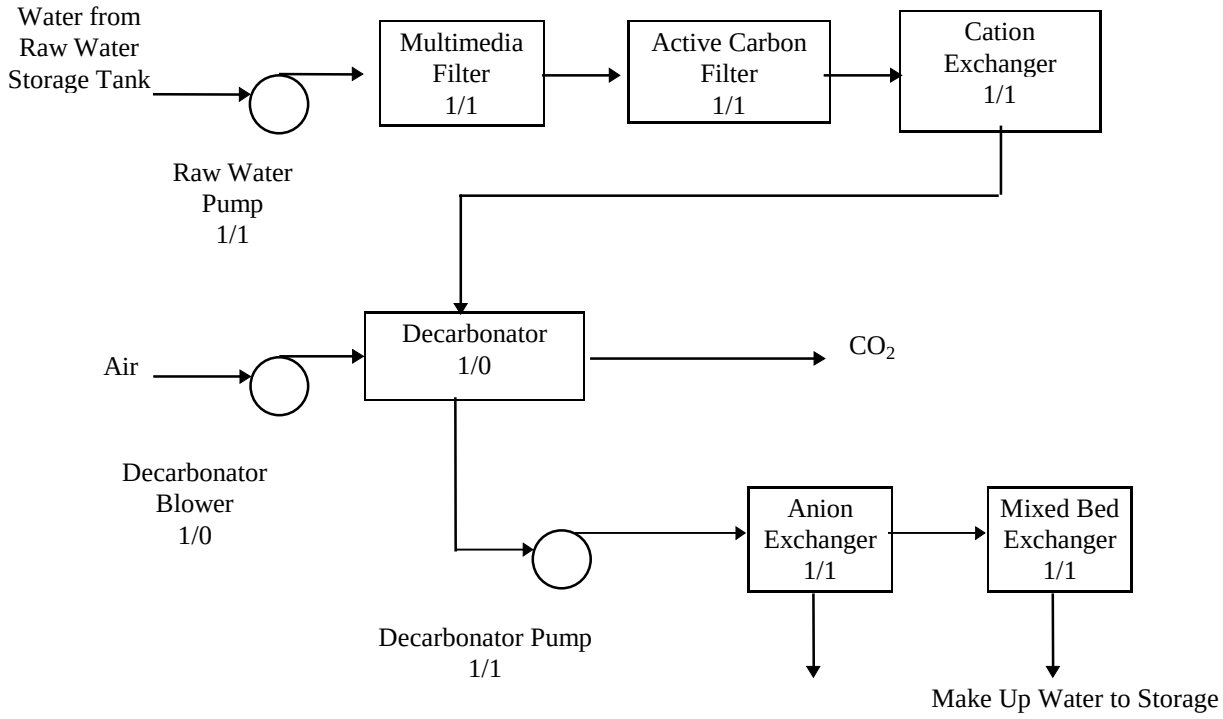

Exhibit C-1
Demineralization Water Treatment System

Process Description

Water from the raw water storage tank is pumped to a multimedia filter to remove particles as small as 10 microns. The filter contains a multi-layer bed with a coarse top layer of anthracite, an intermediate layer of quartz filter sand and a fine bottom layer of garnet. The bed structure causes particulate to be trapped in all the three beds.

The filtrate from the multimedia filter is directed to an activated carbon filter. This filter contains a bed of activated carbon to absorb chlorine and organic matter from the raw water. Chlorine is removed to prevent it from oxidizing the ion exchange resin, or of oxidizing certain types of reverse osmosis membranes, which would reduce their performance. Organic matter is removed to avoid fouling ion exchange resins or reverse osmosis membranes.

The filtrate from the activated carbon filter is sent to a strong acid cation exchanger. The cations, such as calcium, magnesium and sodium, are removed in this exchanger by the following ion exchange reaction:

$$H_2Z + CaSO_4 \text{ -----> } CaZ + H_2SO_4$$

where the cation resin is denoted by Z. The decationized water from the cation exchanger is sent to a forced draft decarbonator.

In the decarbonator, CO_2 is removed from the water by contacting air supplied by the decarbonator blower. The forced draft decarbonator unit reduces carbon dioxide by more than 90%. CO_2 is removed from the water to prevent it acting as an anion, and thereby increasing the ionic load of the anion exchanger. An increased ionic load would require a larger anion exchanger, increased regenerating reagent (sodium hydroxide) consumption and would produce more waste water.

The decarbonated water is pumped to an anion exchanger where anions such as bicarbonates, sulfates, chlorides and soluble silicas are removed by the following ion exchange reaction:

$$H_2SO_4 + 2R.OH \text{ -----> } R.SO_4 + H_2O$$

where R is the anion removing resin.

After treatment in the two ion exchangers, the mostly deionized water is sent to a mixed bed ion exchanger. The mixed bed ion exchanger contains strong acid cation and strong base anion resins thoroughly mixed together in a single unit. Because of the mixture, the mixed bed process is comparable to having many pairs of cation and anion exchangers arranged in series. In the mixed bed ion exchanger, the water contacts pairs of cation and anion resin beads as it passes through the bed. When the water contacts the resin bead pairs, it is repeatedly deionized, and each contact reduces the level of ionic contamination. Thus, the mixed bed ion exchanger polishes the water after a primary deionization by separate cation and anion exchangers. The polished water is sent to a demineralized water storage tank.

When the operating train's exchangers' deionization performance is exhausted, they are replaced by the second train's fresh ion exchangers. The exhausted ion exchangers are regenerated with 3% to 6% solutions made from the following regenerating agents:

Cation exchanger	93% H_2SO_4
Anion exchanger	100% NaOH
Mixed bed exchanger	93% H_2SO_4 and 100% NaOH

Waste liquids from regeneration are sent to a neutralization tank. The water treatment system includes the following items for regeneration.

- One rotary lobe blower,
- One acid regeneration system with two 100% metering pumps, and
- One caustic regeneration system and two 100% metering pumps.
- One waste neutralizing system with pH control.

Process Costs

Cost of the demineralization water treatment system is $551,000. The cost includes instrumentation, an electrical equipment skid and a PLC based control system. Taxes and freight to the job site are excluded.

Reverse Osmosis/Mixed Bed Ion Exchange Water Treatment System

A flow diagram of the system is shown in Exhibit C-2. The system consists of one train.

Process Description

The raw water from the water supply tank is pumped through a multimedia filter and then through an activated carbon bed filter. The filters are the same as described for the demineralization system.

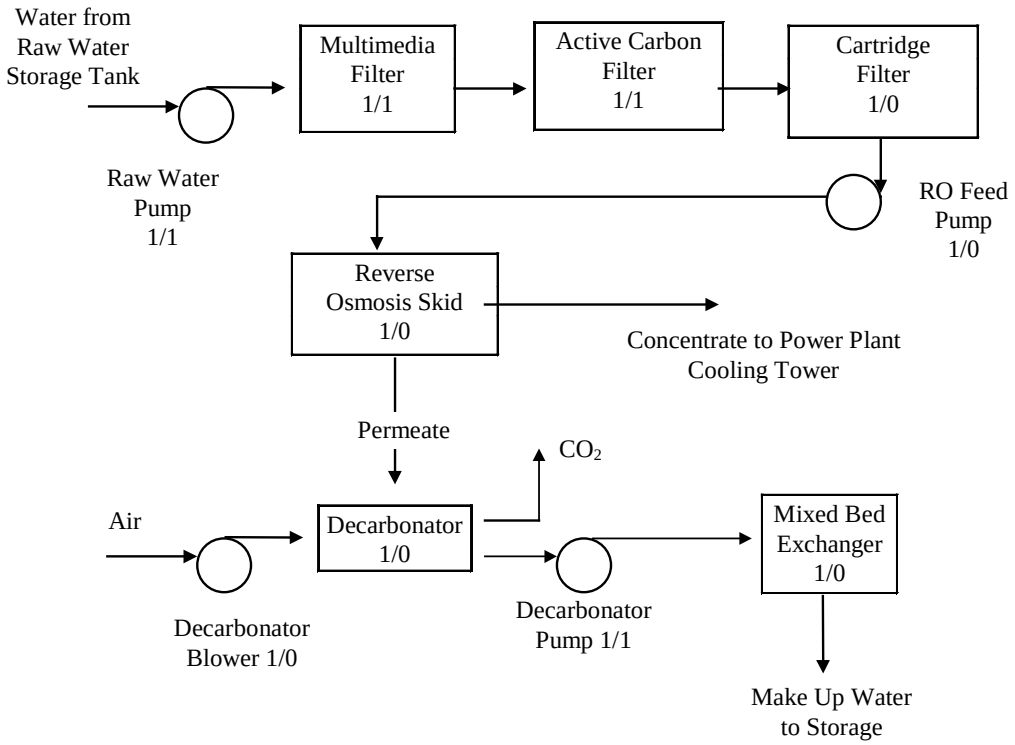

Exhibit C-2
Reverse Osmosis/Mixed Bed Ion Exchange Water Treatment System

Filtrate from the activated carbon filter is passed through a cartridge filter to remove particulates larger than 5 microns. The filtrate from the cartridge filter is pumped by a reverse osmosis feed pump to the reverse osmosis skid. The reverse osmosis (RO) process purifies water using the natural tendency of a fluid to pass through a semi-permeable membrane when the fluids on opposite sides of the membrane have different concentrations. By pressurizing the feed stream, the natural osmotic effect is reversed, and the process continuously removes contaminants from the fluid. The RO skid replaces the cation exchanger and anion exchanger

described in the demineralization water treatment system section. The RO process is especially attractive if the dissolved solids level of the raw water is high. The advantage of RO (for high dissolved solids) is its low chemical consumption compared with ion exchange demineralization systems. The low chemical consumption equates to lower operating costs and less waste water generation.

The concentrate from the RO skid is sent to the power plant's cooling tower make up water stream, and the permeate is polished further by passing it through a forced draft decarbonator and then through a mixed bed ion exchanger. Operation of the decarbonator and the mixed bed exchanger are the same as described in the previous section. The deionized water from the mixed bed ion exchanger is sent to the demineralized water storage tank.

This water treatment system includes the equipment for the regeneration of the mixed bed ion exchanger. Regeneration of the exchanger is performed weekly. For regeneration, which only takes about an hour, the exchanger is bypassed by the rest of the system.

Process Costs

Cost of the water treatment system is $519,000. The cost includes instrumentation, the electrical equipment and a PLC based control system. However, it does not include taxes and freight.

Reverse Osmosis/E-Cell Racks Water Treatment System

A flow diagram of the system is shown in Exhibit C-3.

Process Description

The treatment system has one train, and is identical to that described in the previous section, up to, and including the RO skid. Concentrate from the RO skid goes to the cooling tower make up, and the RO permeate is polished by passing it through a pair of E-Cell racks with a total capacity of 100 gpm water. (The E-Cell racks replace the mixed bed ion exchanger described earlier.) The water treatment system does not require a regeneration step. The E-Cells operate on the electrodeionization (EDI) principle. In EDI, the ion exchange media is continuously regenerated electrochemically with ion exchange membranes. EDI has no chemical consumption and the pure water recovery is higher compared with the systems using mixed bed ion exchangers.

The EDI permeate is sent to the demineralized water storage tank.

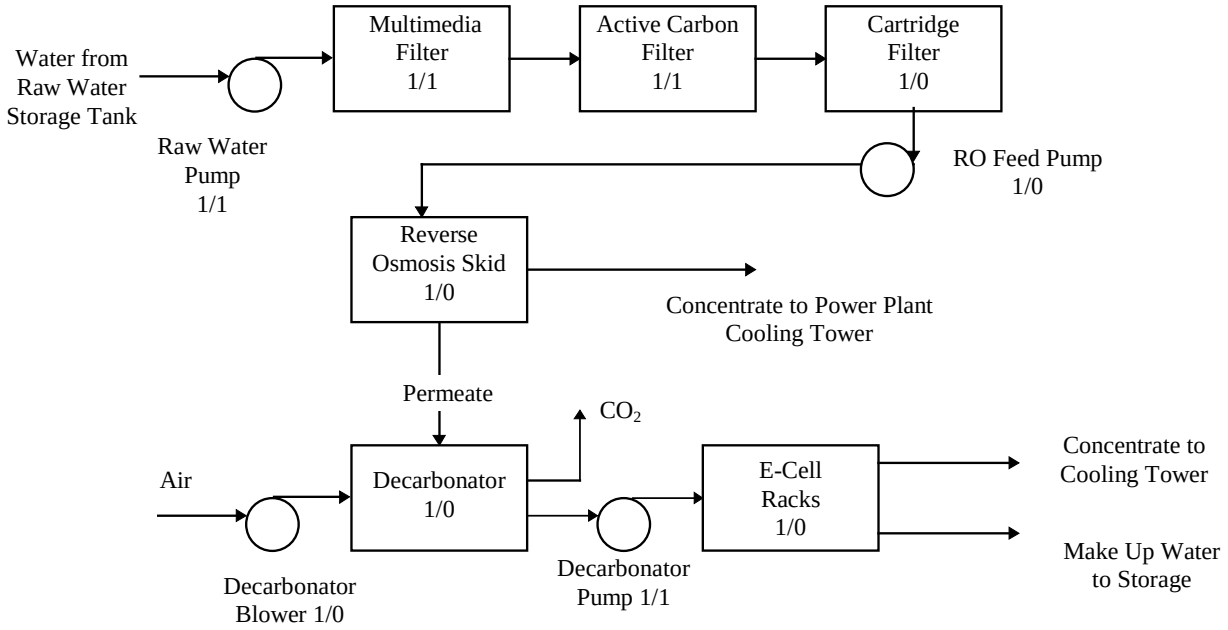

Exhibit C-3
Reverse Osmosis/E-Cell Based Water Treatment System

Process Costs

Cost of the E-Cell water treatment system is $445,000. The cost includes instrumentation, electrical equipment and a PLC based control system. It does not include taxes and freight.

Condensate Polishing System

Budget quotes were also requested for a condensate polishing system with a 1,600 gpm (363.4 m^3/h) capacity. Glegg recommended two, 100 percent capacity trains. Each train has a strong acid exchanger with 300 cubic feet of sodium zeolite. Exchanger beds are regenerated once a day with 3,000 lbs of 26% concentration brine. The brine regeneration system includes two metering pumps. The equipment cost, excluding taxes and freight, is $264,000. The installed cost is estimated to be $300,000 and the annual O&M is $25,000.

Appendix D - Coal Pulverization System

Introduction and Summary

As part of the HIPPS commercial plant conceptual design, balance of plant equipment is to be specified and costs estimated. As part of the BOP design, coal pulverization and drying data was collected from several equipment manufacturers. Coal received at the plant has a one inch topsize. It must be reduced to 70 percent passing 200 mesh (74 micron) to meet high temperature advanced furnace (HITAF) burner requirements.

Coal pulverizers use hot air to dry the coal; to classify coal particle size; to sweep the mill of properly sized coal, and transport the ground coal to the furnace. The coal's surface moisture must be reduced to eliminate material handling problems in the mill and during coal transport. Hot air is introduced into the pulverizer mill to remove moisture and allow the ground coal to flow freely. (For the energy balance, the moisture is not "removed or reduced"; moisture is only freed from the coal and entrained with the hot air. The coal, air and moisture all eventually go to the combustion process.) The temperature of the hot air depends on the amount of moisture to be removed and the amount of air needed to transport the coal. In conventional pulverized coal boilers, a bleed of hot air from the air preheater is tempered with ambient air to reach the required air temperature. An air preheater is not used in the HIPPS plant, so other methods are needed to heat the pulverizer air.

A system with roller mill coal pulverizers and plate-type air preheaters will be used with the HIPPS conceptual plant design. The total installed cost for three pulverizers and two air preheaters required by the design is $8.33 million.

HIPPS Coal Pulverization Process

If the HITAF primary (combustion) air is used for pulverizer and coal transport air, the temperature required for the design coal (Illinois No. 6; total moisture of 12.25%) is 555 °F (290.6 °C). In the HIPPS plant, flue gas exiting the coal-fired HITAF enters a "dirty" heat recovery steam generator (HRSG) at 1200 °F (648.9 °C). The gas is cooled to 300 °F (148.9 °C) and sent to the flue gas cleaning system. A bleed of flue gas from a location, with a flue gas temperature of about 700 °F (371.1 °C), in the dirty HRSG will be used in a heat exchanger (air preheater) to raise the primary air temperature to 555 °F (290.6 °C). Primary air enters the air preheater at 60 °F (15.6 °C). The flue gas enters the air preheater at 700 °F (371.1 °C). It is cooled to 300 °F (148.9 °C) and combined with the flue gas leaving the dirty HRSG for the flue gas cleaning system.

Exhibit D-1 shows a simple diagram of the HIPPS coal pulverization scheme.

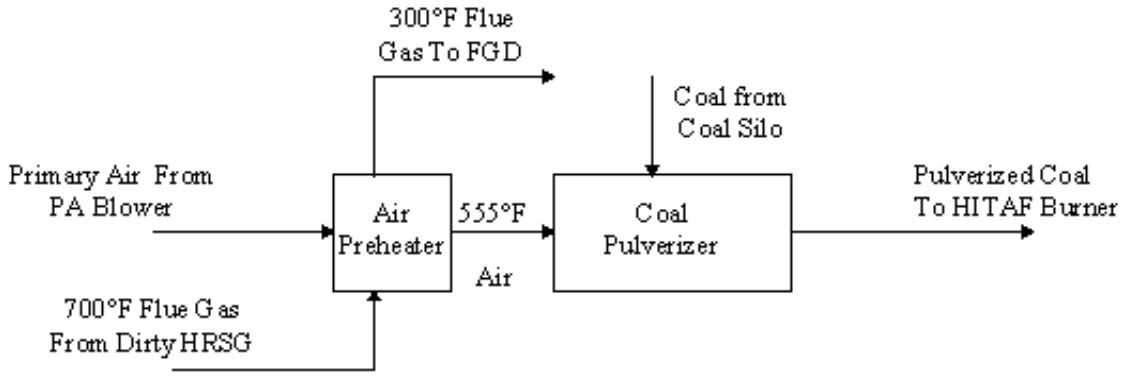

Exhibit D-1
HIPPS Coal Pulverization Scheme

Equipment Specification

The HIPPS plant design uses two furnaces. For increased reliability, design includes three pulverizers, two operating and one common standby spare. The coal pulverization system specification is summarized in Table D-1 and the feed coal data for Illinois No. 6 coal is given in Table D-2. Pulverizer equipment suppliers were asked to recommend equipment to meet the specifications of Tables D-1 and D-2, and provide performance and cost data.

The HIPPS design includes two air preheaters, one for each furnace. The primary air heater specification is summarized in Table D-3. Air preheater equipment suppliers were asked for data and recommendations based on the specifications.

Table D-1
Coal Pulverization System Data

Number of operating furnaces	2	Primary air flow rate to one operating pulverizer system	26.15 lb/s
Number of pulverizing systems	3	Primary air pressure	22 psia
Operating pulverizer systems	2	Primary air temperature	60 °F
Spare pulverizer systems (common to both ops units)	1	Primary air heat source	flue gas
Source of pulverizer feed coal	feeder		
Pulverized coal destination	classifier exit	Flue gas inlet temperature	700 °F
Coal feed rate to one operating pulverizer system	17.325 lb/s	Flue gas exit temperature	300 °F
		Flue gas acid dew point	300 °F
Size of coal feed to pulverizer	3/4 to 1 inch	Flue gas pressure	15.2 psia
Pulverized coal size	70% through 200 mesh	Flue gas heat capacity	0.2606 Btu/lb °F

Table D-2
Feed Coal Data

Coal type	Illinois No. 6	
Coal size, inch	3/4 to 1	
Proximate Analysis		
Higher heating value (Btu/lb)	10,982	
Sulfur % wt	3.28	
SO_2/million Btu	5.98	
Grindability index (Hardgrove)	51	
(% wt)		
Moisture	12.25	
Ash	10.97	
Fixed carbon	41.48	
Volatile matter	35.30	
TOTAL	100.00	
Ultimate Analysis (% wt)		
Moisture	12.25	
Carbon	61.00	
Hydrogen	4.25	
Nitrogen	1.25	
Chlorine	0.07	
Sulfur	3.28	
Ash	10.97	
Oxygen	6.93	
TOTAL	100.00	
Ash Analysis (% wt)		
SiO_2	50.66	
Al_2O_3	19.00	
TiO_2	0.83	
Fe_2O_3	20.30	
CaO	2.42	
MgO	0.89	
Na_2O	0.67	
K_2O	2.54	
P_2O_3	0.17	
SO_3	1.90	
Undetermined	0.58	
TOTAL	100.00	
Ash fusion temperature, °F	**Reducing**	**Oxidizing**
Initial deformation	1,950	2,250
Softening (H=W)	2,030	2,300
Fluid	2,150	2,450

Table D-3
Primary Air Preheater Data

Number of operating air preheaters = Two
Number of spare air preheaters = None

Data For One Primary Air Preheater:

Primary air preheater heat load	= 11.4 million Btu/h
Primary air flow rate	= 94,140 lb/h
Primary air inlet temperature	= 60 °F
Primary air outlet temperature	= 553 °F
Primary air inlet pressure	= 22.0 psia
Primary air heat capacity	= 0.2453 Btu/lb °F
Primary air viscosity	= 0.028 centipoise
Flue gas flow rate	= 109,224 lb/h
Flue gas inlet temperature	= 700 °F
Flue gas outlet temperature	= 300 °F
Flue gas inlet pressure	= 15.2 psia
Flue gas heat capacity	= 0.2606 Btu/lb °F
Flue gas viscosity	= 0.026 centipoise

(Air Preheater Data continued)
Flue Gas Composition:

Components	Volume %
O_2	2.72
N_2	72.44
Ar	0.88
CO_2	13.20
H_2O	10.51
SO_2	0.24
NO_2	0.01
Total	100.00
Flyash, gr/scf	2.35

Data Requests

Several equipment suppliers were contacted and data for the HIPPS plant design were requested.

Pulverizers

The following vendors were contacted to collect information about the coal pulverizers.

- ABB Raymond, Lisle, IL
- DB Riley Inc., Worcester, MA
- Svedala Ind. Inc., Grinding Division, York, PA
- Williams Patent Crushers and Pulverizer Co., St Louis, MO

Air Preheater

The following vendors were contacted to collect information about the air preheaters.

- ABB Air Preheater Inc., Wellsville, NY
- American Schack Company, Wexford, PA
- DB Riley Inc., Worcester, MA
- Hudson Products, Houston, TX
- Kvaerner Pulping Inc., Williamsport, PA

Data Collection

The following pulverizer equipment suppliers responded to the request for technical information and budgetary prices.

DB Riley Inc.

The Riley MPS™ pulverizer is a vertical mill with a rotating classifier and hydraulic roller loading. Raw coal is fed through a central coal inlet at the top of the pulverizer and falls by gravity to the rotating grinding table. Centrifugal action forces the coal outward to the grinding ring where it is pulverized between the ring and three grinding rollers.

A nozzle ring on the outer perimeter of the grinding ring feeds primary air to the pulverizer. Primary air enters the mill through an aerodynamically-ported nozzle. The swirl induces larger particles to return to the grinding track. During this first stage of classification, fine particles are carried upward in the housing by the stream of air, and coarse particles fall back to the table for grinding. In a second stage of classification, the air velocity decreases and larger particles drop out. In a final classification, those particles which are sufficiently pulverized for transport to the burners are separated and sent to the burners. The technical data for this mill are as follows.

Mill type:	Ring-roller mill with internal classifier
Mill model:	170 MPS
Mill motor:	400 HP
Air pressure drop:	8 - 10 in (20.32 – 25.40 cm) w.c.
Mill weight:	191,000 lb (86,636 kg)
Mill foot print:	16 ft by 18 ft (4.88 m x 5.49 m)
Price of 3 mills:	$3,817,000

Svedala Ind. Inc.

Svedala recommended dry ball mills for coal grinding. A ball mill uses a horizontal cylinder whose diameter is roughly equal to its length, lined with heavy liner plates. In a ball mill, grinding results from the impact the cascading balls and coal and the attrition between balls, coal and liners. Ball mill grinding is a low speed, low wear type of pulverization. An air-swept grinding system simultaneously dries, grinds and classifies the coal in a closed circuit with a non-mechanical air separator. The technical data for this mill are as follows:

Mill type:	Ball mill
Mill model:	11 ft diameter by 15 ft grinding length (3.35 m x 4.57 m)
Mill motor:	800 HP
Air pressure drop:	10.6 in (29.92 cm) w.c.
Mill foot print:	25 ft wide by 45 ft long by 50 ft high (7.62 m x 13.72 m x 15.24 m)
Price of 3 mills:	$6,500,000

Williams Patent Crushers and Pulverizer Co.

The Williams pulverizer is based on a roller mill. A feeder introduces coal into a grinding chamber in the base of the roller mill. Plows located ahead of each roller direct the material upward, between the grinding rolls and the heavy alloy steel bull ring where the coal is ground to size. The grinding rolls are free to swing out centrifugally. The centrifugal movement forces the rolls to bear upon and grind the coal. Once ground to size, the coal is swept out of the mill by the primary air. The air entrained ground coal passes through an adjustable spinner separator. In the separator, product size coal is conveyed away from the roller mill, while oversize coal is returned for additional grinding.

The technical data for this mill are as follows.

Mill type:	Roller mill with internal classifier (spinner separator)
Mill model:	DF-85
Mill motor:	400 HP
Air pressure drop:	8 to 10 in (20.32 – 25.40 cm) w.c.
Mill weight:	105,000 lb (47,627 kg)
Mill foot print:	16 ft wide by 20 ft long (4.88 m x 6.10 m)
Price of 3 mills:	$2,340,000

Air Preheaters

The following air preheater equipment suppliers responded to the request for the technical information and budgetary prices.

ABB Air Preheater

ABB makes APEX® plate air preheaters. APEX® uses welded plates as compared to other plate heat exchangers where the plates are sealed with rubber gaskets. The welded plates minimize leakage, which is a significant problem in conventional pulverized coal-fired boilers. The plate heat transfer coefficients are about three times larger than for corresponding tubular heat exchangers. ABB makes the plate air preheaters in modules. The modular construction facilitates replacement of a corroded or damaged plate in the preheater. The data on the heat exchanger is as follows.

Type:	Plate
Model:	APEX-LP-CC-XC-4
Air side pressure drop:	2.2 in (5.6 cm) w.c.
Flue gas pressure drop:	1.8 in (4.6 cm) w.c.
Heat transfer surface:	4,876 ft^2 (453 m^2)
Air side material of construction:	LACR steel*
Flue gas side material of construction:	LACR steel*
Overall dimensions:	4 ft wide by 13.5 ft long by 19 ft high (1.22 m x 4.11 m x 5.79 m)
Weight of one air preheater:	106,000 lb (48,081 kg)
Price of two air preheaters:	$364,000

* LACR = low alloy corrosion resistant

American Schack Company

The company makes tubular heat exchangers which are installed vertically. The recommended air preheater is made from a welded tube bundle enclosed in a casing with a plenum. The data on the heat exchanger is as follows.

Type:	Tubular
Model:	- not provided
Air side (casing) pressure drop:	5.0 in (12.7 cm) w.c.
Flue gas (tube side) pressure drop:	4.0 in (10.16 cm) w.c.
Heat transfer surface:	11,637 ft^2 (1,081 m^2)
Air side (casing) material of construction:	A-36 carbon steel
Flue gas side (tube) material of constr'n:	carbon steel
Overall dimensions:	8 ft diameter by 55 ft high (2.44 m x 16.76 m)
Weight of one air preheater:	100,000 lb (45,359 kg)
Price of two air preheaters:	$800,000

DB Riley Inc

Riley recommended a tubular heat exchanger with two legs, each leg containing one pass. The air in the shell side and the flue gas passes through tubes. Tubes in the first pass are carbon steel; those in the second pass are made of stainless steel. The stainless steel is a precaution to avoid corrosion if the dew point temperature limit is exceeded. The data on the heat exchanger is as follows.

Type:	Tubular
Model:	- not provided
Air side (casing) pressure drop:	4 in (10.16 cm) w.c.
Flue gas (tube side) pressure drop:	4 in (10.16 cm) w.c.
Heat transfer surface:	- not provided
Air side (casing) material of construction:	carbon steel
Flue gas side (tube) material of constr'n:	carbon steel
Overall dimensions:	1st pass: 6 ft wide by 7 ft long by 20 ft high (1.83 m x 2.13 m x 6.10 m) 2nd pass: 6 ft wide by 7 ft long by 16 ft high (1.83 m x 2.13 m x 4.88 m). The two passes are 5.5 ft (1.52 m) apart
Weight of one air preheater:	- not provided
Price of two air preheaters:	$332,000

Hudson Products

Hudson makes air preheaters based on the heat pipe principle. In a heat pipe, a volatile liquid like water is sealed in a tube. Part of the external surface of the sealed tube is exposed to a hot flue gas and the remaining external surface of the sealed tube is exposed to the cooler air. The water in the tube section exposed to the hot flue gas is vaporized and travels towards the section which is exposed to the cold air. The water vapor transfers its heat to the cold air through the tube wall, and then condenses to liquid water. The liquid water returns towards the section of the tube exposed to the hot flue gas, and the heat transfer process is repeated. A wick is inside the sealed tube to assist the movement of liquid water. The commercial heat exchanger is a bundle of sealed tubes. A tube sheet divides the tube bundle into two sections and keeps the flue gas separate from the air.

The data on the heat exchanger is as follows.

Type:	Heat pipe with finned tubes
Model:	1-HO-1-320-16 x 20-2-22-SAE x 11 x 3/4 -SCW x 3 x 3/4-6-0
Air side pressure drop:	1.0 in (2.54 cm) w.c.
Flue gas pressure drop:	1.1 in (2.79 cm) w.c.
Heat transfer surface:	- not provided
Air side material of construction:	SA 178 Gr. C
Flue gas side material of constr'n:	SA 178 Gr. C
Overall dimensions:	26 ft long by 12 ft wide by 10 ft high (7.92 m x 3.66 m x 3.05 m)
Weight of one air preheater:	62,725 lb (28,452 kg)
Price of two air preheaters:	$410,000

Kvaerner Pulping Inc.

They make tubular heat exchangers installed vertically. Their recommended air preheater is made from a welded tube bundle enclosed in a rectangular casing with a plenum.

The data on the heat exchanger is as follows:

Type:	Tubular
Model:	- not provided
Air side (casing) pressure drop:	2.1 in (2.54 cm) w.c.
Flue gas (tube side) pressure drop:	3.0 in (2.79 cm) w.c.
Heat transfer surface:	18,471 ft^2 (1,716 m^2)
Air side (casing) material of construction:	carbon steel
Flue gas side (tube) material of construction:	carbon steel
Overall dimensions:	11.5 ft deep by 40 ft high by 12 ft wide (3.5 m x 12.19 m x 3.66 m)
Weight of one air preheater:	920,000 lb (417,305 kg)
Price of two air preheaters:	$470,000

Data Evaluation

Pulverizers

Technical data for the pulverizer equipment is summarized on Table D-4. The data clearly shows that the ball mill is more costly and requires the most auxiliary power. The Williams roller mill requires an air to coal ratio of more than 2.0, whereas the air to coal ratio in the current furnace design is 1.5. A roller mill of the type recommended by Riley will be used in the conceptual design and cost estimate. Installation costs equal to equipment cost ($3.8 million) are estimated for a total pulverizer system cost of $7.6 million.

Table D-4
Comparison of Pulverizers

Vendor	Type	Motor, HP	Air ΔP, Inch wc	Equipment Price of Three Mills
DB Riley	Ring roller	400	8 - 10	$3,817,000
Svedela	Ball	800	10.6	$6,500,000
Williams	Roller	400	8 - 10	$2,340,000

Air Preheaters

The technical data for the air preheaters is summarized on Table D-5. The heat exchanger manufacturers performed detailed calculations to determine the size of their exchangers except for the Riley exchanger, which is based on less detailed calculations. Table D-5 lists a cost range of about $330,000 to $800,000, and a pressure drop of from about 2 to 5 inches (5.08 – 12.70 cm) of water. Considering price and pressure drop, an air preheater such as recommended by ABB will be used in the HIPPS design. With installation, the cost for the preheater system is estimated as $730,000.

Table D-5
Comparison of Air Preheaters

Vendor	Type	Air-side ΔP, Inch wc	Gas-side ΔP, Inch wc	Equipment Price of Two Preheaters
ABB	Plate	2.2	1.8	$364,000
Am. Schack	Tubular	5.0	4.0	$800,000
DB Riley	Tubular	4.0	4.0	$332,000
Hudson	Heat pipe	1.0	1.1	$410,000
Kvaerner	Tubular	2.1	3.0	$470,000

Appendix E - Market Study for HIPPS Technology

HIPPS Market Study Summary

The HIPPS market study examines the current state of electric power generation in the United States, and forecasts for future changes to the industry. The Energy Information Administration (EIA) of the U. S. Department of Energy was the source of most raw data. The EIA data is collected from utilities, and usually does not reflect power generation by independent producers or others outside the regulated utility field. Seventeen States were selected as a focus of the study, and that selection was reduced to seven States where the effort can be concentrated to market the HIPPS technology. HIPPS is shown in the study as being competitive with other power generation technologies, including gas turbine combined cycle power plants.

Estimates and Forecasts for the HIPPS Market

The following significant issues were used in the study, or result from estimates made in the study.

Market size:

- 403,000 megawatts of capacity will be required by 2020 in the U. S. to replace older units and provide for growth. Of that total new capacity, 49,000 megawatts is forecast as coal-fired. Consequently, for the HIPPS market to have the best opportunity to grow, HIPPS will have to compete with, and capture some of the forecast natural gas-fired capacity.
- The market for HIPPS could range from 8,000 megawatts (20% of the planned coal-fired additions) to 80,000 megawatts (about 20% of the total capacity addition).
- The megawatt range above equates to a cost range of from about $6 to $60 billion (in 1997 dollars) over the period from now to 2020.

Market timing:

- Because of the planned retirements of existing units, more than half of the added capacity will occur in the 2010 to 2020 period. This allows time for HIPPS to demonstrate its performance and economic advantages.

Repowering Market:

- There are several thousand megawatts of opportunity for HIPPS in the near term (now to 2006) as utilities plan to change the capacity of existing units. (Data about repowering beyond 2006 was not available and markets were not estimated.)
- There are unknown opportunities in the non-utility power generating industry if HIPPS can show successful experience and competitive costs compared with other technologies, including gas turbine combined cycle.

Location:

- While not examined in detail, there may be major opportunities for HIPPS in the European and Asian markets where fuel prices and environmental limits drive power generation plants to the most efficient systems.
- In the U. S., the States of Ohio, Indiana, Pennsylvania, Illinois, Missouri, Tennessee and Wisconsin were selected as having the best conditions for HIPPS to enter the power generation market.

Competitive Standing:

- From estimates made for the conceptual plant design, HIPPS is clearly more economical than integrated gasification combined cycle and pulverized coal-fired technology on both a capital cost and cost of electricity basis.
- While having a higher capital cost, HIPPS is also competitive with gas turbine combined cycle plants based on the present value cost of electricity calculated in a range of power generation scenarios.
- The cost of electricity for HIPPS is competitive with the average prices paid for electricity in the 17 States examined by the study.

Vital Statistics

A large amount of data was examined during the study with a lesser, but still significant amount reported. The items below further distill the data to illustrate areas of special importance to the forecasts of a HIPPS market.

- The installed coal-fired capacity of the U. S. is 302,000 megawatts, or about 43 percent of the Nation's total capacity in 1997. About 30 percent of the coal-fired capacity began operation in, or prior to 1960.
- In general, the utility industry is a low growth area of our mature economy. Some of the low growth of electric power demand can be allocated to efficiency and other advances in generation and consumption technologies.

The study selected 17 States in the U. S. to focus the work of estimating the market for HIPPS technology power plants. Data about the 17 States was examined to show:

- Some 44,500 megawatts of coal-fired capacity started operation in 1960 or earlier.
- As indicated by fuel (coal and natural gas) use, growth in the 17 States has a wide variation. The variability may indicate areas of opportunity in an overall slow growth industry.
- Fuel prices in the 17 States follow a National trend for coal price to decline while natural gas price increases.
- Average electricity prices charged to the ultimate consumers in the 17 States ranged from 4 to 8 cents per kilowatt hour (kWh).
- The EIA forecasts that (nationally) plants with an operating and maintenance cost greater than 4 cents per kWh will be retired in the next decade.

- There are some 5,000 megawatts of coal-fired capacity planned for addition during 1997 to 2006 in the U. S. Four thousand megawatts is planned in the 17 States. For natural gas-fired plants (gas turbines and gas turbine combined cycle) the Exhibits are much higher; 32,000 megawatts for the U. S. and 22,000 megawatts for the 17 States.
- In addition to the planned additions in the 17 States, some 6,200 megawatts are planned for changes to their installed coal-fired capacity.

Introduction and Background

A market study using published data was performed as part of the work to produce a commercially viable design for the HIPPS technology. The study assesses how present U. S. industry conditions and utilities' plans for new generation and changed or repowered generation may impact opportunities for HIPPS to enter the power production market.

The study used data from several Energy Information Administration (EIA) databases where electric power and fuel data is collected from utility inputs. The EIA data has been reorganized and consolidated to evaluate the HIPPS market. The following major sets of data are explored in the study.

- Selection of States by installed coal-fired generation capacity and coal use: To narrow the scope of the study, 17 States were selected for more extensive study based on their use of coal for power generation.
- Aging of steam generation units: As a gauge of possible repowering and greenfield HIPPS applications, the age of existing power plants in the 17 States was documented.
- Power generation growth: States with higher growth rates may be more likely to require adding generation capacity and using HIPPS. Power generation growth rates are calculated from EIA data.
- Fuel prices: The difference in prices between utility natural gas and coal fuels is a crucial parameter for HIPPS to compete with other new power generation and repowering technologies. The price rate change was determined for the States as another factor in the potential market for HIPPS.
- Cost of Electricity/ utility revenue: The COE for HIPPS has been estimated in earlier tasks. The HIPPS COE is considered in perspective with existing plants. As the cost of electricity is not available by State, prices are used to assess the market opportunities for HIPPS versus existing price structures.
- Planned generation capacity additions: The EIA data includes utilities' estimates for adding capacity. This information is used to help estimate the size and location of HIPPS markets.
- Planned utility changes: EIA also provides the utility information on repowering, retirement, reactivation and increases/decreases planned for existing units. This data is reported and used to estimate the HIPPS market.

Overview of U. S. Utility Power Generation

United States electric utility power generation capacity totaled 712,033 megawatts as of January 1, 1997. Some 12,800 megawatts of this total are classified as inactive. Net generation for 1997 was 3,123 billion kilowatt hours (kWh); an increase of 1% from 1996. Categorized by energy source, the totals are in Table E-1.

Table E-1
Overview of Utility Capacity and Generation

Energy Source	Megawatts Capacity	Percent of Total Capacity	Percent of Total Generation
Coal-Fired	302,523	42	57
Gas-Fired	142,566	20	9
Nuclear	100,756	14	20
Renewables	75,448	11	11
Petroleum	69,480	10	2
Pumped Storage Hydro	21,110	3	1

The capacity data included almost 4,800 megawatts of new (added in 1997) capacity, with this added generation split as 34 % coal; 36 % gas; 23 % nuclear and 7 % from other energy sources.

Renewables (water, geothermal, solar, biomass and wind) total about 1 % of the capacity and less than 1 % of the generation when conventional hydroelectric is separated from the renewables category.

The data reviewed in this report is largely from EIA utility data. However, non-utility power generation is significant and growing. Non-utility capacity is about 73,000 megawatts (approximately 10% of utility power generation capacity) and net generation (sales) was 383 billion kWh (approximately 12% of utility net generation). Unless noted, the data used in this study is from the EIA utility industry database published on EIA's web pages.

Coal-Fired Power Generation

An underlying assumption of the market study is that HIPPS will be most likely to enter and build a market in areas of the country where coal is already in wide use. EIA data is presented in Table E-2 for 17 States where coal is important to present and likely future power generation.

In Table E-2, the first 15 States are ordered by the amount coal-fired generation. The last two States, Utah and New Mexico are listed to represent Western U. S. bituminous coals in States where coal-fired power production is significant.

Table E-2
State Coal Consumption and Power Generation

EIA Data for 1997			
		Coal-Fired Generation 10^9 kWh	Coal Use 10^6 Tons
1	Texas	135.7	96.5
2	Ohio	124.9	52.9
3	Indiana	108.9	54.8
4	Pennsylvania	105.5	42.6
5	Kentucky	87.9	38.3
6	West Virginia	87.7	34.5
7	Illinois	76.1	41.0
8	Alabama	71.6	30.8
9	North Carolina	70.2	27.2
10	Georgia	66.2	30.6
11	Florida	66.0	27.4
12	Michigan	65.6	31.9
13	Missouri	59.9	35.2
14	Tennessee	58.9	24.5
15	Wisconsin	40.8	23.6
16	Utah	32.1	14.3
17	New Mexico	27.1	15.8

Aging Power Generation Units

Another potential criteria for influencing the HIPPS greenfield and repowering markets is the age of existing coal units that might be replaced by HIPPS (Table E-3). Clearly, not all units will be replaced as they age, nor can all the units that are replaced use the HIPPS technology. Additionally, the "retirement age" varies widely among coal-fired units.

Table E-3
Aging of Utility Coal-Fired Units for 17 States

	1997 EIA Data	Number of Units	Average Age years	Average Capacity MW	Oldest Unit	Total MW of Units 1960 and Earlier	Newest Unit
1	Texas	36	17	576	1971	0	1992
2	Ohio	99	35	240	1933	5,994	1991
3	Indiana	78	34	265	1925	3,804	1995
4	Pennsylvania	50	37	374	1948	4,019	1980
5	Kentucky	58	32	278	1950	2,427	1990
6	West Virginia	33	36	453	1943	2,859	1980
7	Illinois	41	34	257	1948	2,376	1982
8	Alabama	39	37	323	1908	3,768	1991
9	North Carolina	45	40	278	1940	3,085	1983
10	Georgia	38	35	381	1941	1,505	1989
11	Florida	31	25	380	1953	621	1996*
12	Michigan	48	35	257	1943	3,066	1985
13	Missouri	43	33	261	1948	1,091	1986
14	Tennessee	33	41	293	1951	6,105	1973
15	Wisconsin	48	40	141	1935	1,645	1985
16	Utah	9	23	451	1954	189	1987
17	New Mexico	10	26	428	1963	0	1984
	Total/Average	739	31	313	---	44,514	---

** One of the two units starting operation in 1996 is a integrated gasification combined cycle plant (Tampa Electric's Polk Plant)*

The data shown in Table E-3 are augmented in Addendum A wherein coal-fired capacity by state and first year operation are displayed. The graphs illustrate the number and size (name plate capacity) of units and their ages. In general, many of the oldest units are relatively small and the biggest units have been more recently built. It is clear from the data in the last column that utility construction of new coal-fired units has not been extensive in the last 10 years.

However, there are some signs of improved market conditions for coal-fired units if they are clean and economical. Tractebel Energy of Houston, Texas recently announced (Power, 1998) the start of construction of a 440 MW facility using two circulating fluid bed boilers. The facility is near Chester, Mississippi. Southern Indiana Gas & Electric Company of Evansville, Indiana is reported as purchasing a 100 MW CFB for a new plant near Mount Vernon, Indiana. These units were not shown in the EIA utility data, and their construction holds promise for a larger coal-fired power generation market than can be inferred only from EIA data.

Electric Power Generation Growth

Growing markets, where the demand for power generating capacity is increasing, are likely to be attractive for HIPPS to gain a market position. A caveat for the growth criteria is that historical growth may not reflect future plans, and indeed, the past growth may satisfy demand for the future, and thus be a reason to exclude HIPPS or other generating capacity additions.

Table E-4 illustrates generation growth by presenting the average annual increase/decrease for coal and natural gas used by utilities for power generation. The fuel data was used rather than generation data to examine how coal and natural gas are changing in relation to each other for power generation.

Table E-4
Average Annual Change of Utility Fuel Consumption

	EIA Data for Years 1993 Through 1997	Coal	Natural Gas
1	Texas	0.9%	-0.3%
2	Ohio	0.5%	2.9%
3	Indiana	2.2%	-5.5%
4	Pennsylvania	1.5%	-1.6%
5	Kentucky	1.6%	15.5% *
6	West Virginia	3.9%	-30.0% *
7	Illinois	4.5%	12.8%
8	Alabama	2.1%	10.0%
9	North Carolina	3.1%	6.7%
10	Georgia	3.5%	11.8%
11	Florida	1.7%	8.3%
12	Michigan	2.0%	8.6%
13	Missouri	7.5%	6.7%
14	Tennessee	0.5%	-5.0% *
15	Wisconsin	3.8%	16.2%
16	Utah	0.4%	-9.3%
17	New Mexico	1.1%	3.2%

In Table E-4, the average annual changes are simple calculations of the average for a 5 year period, 1993 – 1997. Other calculations were examined to avoid misleading results that could be caused by highly variable yearly numbers. The simple average i.e.

(Consumption Year 5 – Consumption Year 1) / Consumption Year 5/5

provided results consistent with the data and the other calculating options.

Utilities in the three States marked with * consumed less than 3,000 million cubic feet of natural gas in 1997, and the percentage changes may not reflect a "real" trend, as small absolute changes can lead to large percentage changes.

Fuel Price Changes

A HIPPS market is expected to be strongly influenced by the relative prices for coal and natural gas. Coal is the main fuel for HIPPS; natural gas is the fuel for HIPPS' main competitor in today's market – gas turbine combined cycle power plants. Table E-5 shows the average annual changes for coal and gas in the 17 States for the years 1993 through 1997.

Table E-5
Average Annual Change of Utility Fuel Prices

	EIA Data for Years 1993 Through 1997	Coal	Natural Gas
1	Texas	-2.4%	1.6%
2	Ohio	-1.7%	4.2%
3	Indiana	-2.0%	2.8% *
4	Pennsylvania	-1.5%	2.5%
5	Kentucky	-2.6%	2.2% *
6	West Virginia	-3.1%	-6.0% *
7	Illinois	-3.2%	0.5%
8	Alabama	-3.9%	1.5%
9	North Carolina	-4.0%	-2.5%
10	Georgia	-3.2%	-4.3%
11	Florida	-0.8%	1.2%
12	Michigan	-2.9%	-3.3%
13	Missouri	-9.0%	3.3%
14	Tennessee	-3.2%	14.4% *
15	Wisconsin	-2.5%	3.2%
16	Utah	-1.7%	-2.1%
17	New Mexico	-0.3%	3.1%

As for the previous data exhibit, a simple 5 year average change appears to fairly represent the data and show how fuel prices have increased or decreased in the States during that time.

States marked with * consumed relatively little natural gas, and the average change may be affected by variations in the small amounts.

Electricity Prices

The costs of electricity have been estimated for HIPPS and other generation technologies. The price of electricity is shown in Table E-6 for the 17 States. The table data reflects utility revenues from all sectors of consumers, and includes generation from all energy sources –fossil, nuclear, renewables. Costs comparable to the HIPPS cost of electricity are not part of the EIA database.

Table E-6
Average State Electricity Price

	EIA Data for 1997	Cents per kWh	Comparison Ratio*
1	Texas	6.17	1.01
2	Ohio	6.25	1.03
3	Indiana	5.29	0.87
4	Pennsylvania	7.99	1.31
5	Kentucky	4.03	0.66
6	West Virginia	5.02	0.82
7	Illinois	7.71	1.27
8	Alabama	5.33	0.88
9	North Carolina	6.48	1.06
10	Georgia	6.37	1.05
11	Florida	7.19	1.18
12	Michigan	7.04	1.16
13	Missouri	6.09	1.00
14	Tennessee	5.31	0.87
15	Wisconsin	5.22	0.86
16	Utah	5.17	0.85
17	New Mexico	6.80	1.12

** The ratio of each State's electricity price to the average price of 17 States.*

For HIPPS to compete in a State, its COE should be substantially less than the prices above, as they include transmission and distribution, overhead and profit and other items included with the price of electricity to the ultimate consumer. The commercial 300 MW conceptual HIPPS design's COE ranges from 3 to 5 cents per kWh, based on present value calculations over a range of fuel costs and financial criteria.

Utility Planned Capacity Additions.

Table E-7 shows EIA data for the U. S. for additions of capacity over the years 1997 through 2006, and is presented to illustrate the overall planning by utilities for the near term future. As is clear, the largest planned additions are to be natural gas-fired units, some 32,000 out of the

42,000 megawatts total. Thus, in addition to the planned coal-fired additions, and changes to units discussed later, there is a large HIPPS market opportunity if some of the utilities planning to build gas-fired units can be convinced that HIPPS is a better business and economic choice.

Table E-7
Planned Additions by Utilities

EIA Data for Utilities --1997 through 2006	Existing Number of Units	Nameplate Capacity MW	Number of Units to be Added	Nameplate Capacity MW
U.S. Total.....	10,422	756,484	370	42,079
Coal.....	. 1,214	326,457	11	4,924
Petroleum.....	. 3,282	77,683	40	2,146
Gas.....	. 2,205	145,639	231	32,000
Water (Pumped Storage Hydroelectric).....	. 140	18,387	1	204
Water (Conventional Hydroelectric).....	. 3,340	72,566	64	767
Nuclear.....	. 110	108,976	--	--
Waste Heat.....	. 55	4,548	13	1,941
Other Renewable2/.....	. 76	2,228	10	97

Table E-8 reports the data for coal and natural gas additions to utility plants in the 17 States being examined. Consistent with the National data, the natural gas plant additions far outweigh the coal additions. Further, the six additions planned for Texas are likely to use lignite or other low rank coals, and because of the typical low ash fusion temperatures of these coals, they are less than optimum fuels for HIPPS installations. Again, it appears that for the HIPPS market to have a significant impact on power generation, some of the utilities planning to increase gas-fired capacity need to be convinced that coal-fired HIPPS is more attractive.

Table E-8
Planned Coal and Gas Additions by Utilities

EIA Data for Utilities --1997 through 2006		Coal		Natural Gas	
		Number of Units to be Added	Nameplate Capacity MW	Number of Units to be Added	Nameplate Capacity MW
1	Texas	6	4,151	21	2,413
2	Ohio	--	--	5	383
3	Indiana	--	--	23	3,406
4	Pennsylvania	--	--	5	602
5	Kentucky	--	--	8	1,007
6	West Virginia	--	--	--	--
7	Illinois	--	--	16	2,704
8	Alabama	--	--	5	554
9	North Carolina	--	--	12	3,041
10	Georgia	--	--	10	2,074
11	Florida	1	157	15	2,934
12	Michigan	--	--	--	--
13	Missouri	--	--	12	1,734
14	Tennessee	--	--	--	--
15	Wisconsin	1	60	13	1,190
16	Utah	--	--	--	--
17	New Mexico	1	233	1	103
	Totals	9	4,601	146	22,145

Utility Planned Changes

EIA also reports the changes that are planned by utilities for ten year periods. The information on coal-fired units and the 17 States is summarized below in Table E-9. The changes indicated in the table include retirements, decreases and increases in capacity and reactivation of units. No repowering of coal-fired units is planned by utilities in these 17 States.

Table E-9
Planned Changes by Utilities

	EIA Data for Utilities -- 1997 through 2006	Number of Units to be Changed	Nameplate Capacity MW
1	Texas	1	600
2	Ohio	2	888
3	Indiana	8	809
4	Pennsylvania	6	610
5	Kentucky	4	1,436
6	West Virginia	2	1,140
7	Illinois	--	--
8	Alabama	1	125
9	North Carolina	--	--
10	Georgia	--	--
11	Florida	--	--
12	Michigan	4	583
13	Missouri	--	--
14	Tennessee	--	--
15	Wisconsin	1	30
16	Utah	--	--
17	New Mexico	--	--
		29	6,221

The only coal-fired units listed in the EIA data for repowering are in the State of Delaware: Two 80 MW units at the Indian River (Sussex) Station of Delmarva Power and Light Company. The Delmarva repowering is planned for 2001 (unit 2) and 2003 (unit 1).

Table E-10 shows some of the details for planned changes to the coal-fired units.

Table E-10
Details for the Planned Changes by Utilities

EIA Data for Utilities --1997 through 2006

State, Utility, Station(s)	Unit Number	Name Plate Capacity MW	Type of Planned Change	Year for Planned Change
Texas	1	600		
Central Power & Light Co.				
Coleto Creek (Goliad)	1	600	D	1997
Ohio	2	888		
Columbus Southern Power Co.				
Conesville (Coshocton)	5	444	A	1997
Conesville (Coshocton)	6	444	A	1997
Indiana	8	809		
PSI Energy Inc.				
Edwardsport (Knox)	7	40.3	RT	2004
Edwardsport (Knox)	8	69	RT	2004
Noblesville (Hamilton)	1	50	RT	2006
Noblesville (Hamilton)	2	50	RT	2006
R Gallagher (Floyd)	1	150	D	2003
R Gallagher (Floyd)	2	150	D	2003
R Gallagher (Floyd)	3	150	D	2003
R Gallagher (Floyd)	4	150	D	2003
Pennsylvania	6	610		
Duquesne Light Co.				
F R Phillips (Allegheny)	1	69	RA	1999
F R Phillips (Allegheny)	2	81.3	RA	1999
F R Phillips (Allegheny)	3	81.3	RA	1999
F R Phillips (Allegheny)	4	179.7	RA	1999
Pennsylvania Electric Co.				
Seward (Indiana)	5	156.2	RT	2001
Warren (Warren)	1	42.3	RT	2000
Kentucky	4	1,436		
East Kentucky Power Coop Inc.				
Dale (Clark)	3	66	A	1997
H L Spurlock (Mason)	1	305.2	A	1997
H L Spurlock (Mason)	2	508.3	D	2000
Kentucky Utilities Co.				
Ghent (Carroll)	2	556.4	D	2000
West Virginia	2	1,140		
Virginia Electric & Power Co.				
Mt Storm (Grant)	1	570.2	D	2005
Mt Storm (Grant)	2	570.2	D	2004

Table E-10 (Continued)
Details for the Planned Changes by Utilities

State, Utility, Station(s)	Unit Number	Name Plate Capacity MW	Type of Planned Change	Year for Planned Change
Alabama	1	125		
Alabama Power Co.				
Gorgas (Walker)	6	125	RT	2006
Michigan	4	583		
Consumers Power Co.				
B C Cobb (Muskegon)	4	156.3	A	1999
B C Cobb (Muskegon)	5	156.3	D	1997
Detroit Edison Co.				
Conners Creek (Wayne)	15	135	RA	2000
Conners Creek (Wayne)	16	135	RA	2000
Wisconsin	1	30		
Wisconsin Public Service Corp.				
Pulliam (Brown, subbituminous)	4	30	RT	1999

RT = Retire
RA = Reactivate
A = Add capacity
D = Decrease capacity

HIPPS Market Assessment

While the EIA data used in the preceding sections is valuable and interesting, it does not by itself say anything about a market for HIPPS technology, because potential HIPPS users are unaware of the HIPPS costs and performance. The costs and performance of HIPPS, while still uncertain and under development, are another part of the market study, and values estimated in Phase I and revised in Phase II will be used in following sections forecast a market for HIPPS.

The market assessment portion of the study seeks answers to the following major issues.

- What are the markets for HIPPS plants?
- How large might the HIPPS market become?
- What is the timeframe for a HIPPS market?
- Where are the best HIPPS opportunities?
- What are the competitors to HIPPS in the power generation market? And, how does HIPPS compare to the competition?

Future Markets

The HIPPS technology is well suited to both new plant and repowering applications. For repowering cases, HIPPS would be most attractive where added capacity (generation capacity greater than from the existing steam turbine generator) is desired.

The HIPPS plants will operate mostly in base-load for several reasons. There will be a desire to operate the high temperature furnace with few start-and-stop cycles. Since HIPPS will be one of the most efficient and low cost plants in a generation system, the economic dispatch will indicate a high usage. However, with the combination of a gas turbine and conventional steam system, HIPPS will be more flexible than a typical base-load plant such as a pulverized coal plant for example, the gas turbine and part of the steam turbine generator system could run solely on natural gas.

The technology and the current power generation market indicate that HIPPS units will be moderate in size, say 100 to 300 megawatts. However, HIPPS is well suited for use as a modular component of a phased construction scheme, and could be used for much larger plants. If properly planned and executed, major economies of scale are possible in a large phased construction plant. For example, a single flue gas desulfurization system could be used for several HIPPS modules, or the gas turbines could be operated while the coal portion of the plant is being installed.

For the foreseeable future, HIPPS plants will be fueled with a combination of coal and natural gas. The all-coal HIPPS requires special materials development and engineering solutions to a number of problems before the all coal case is feasible. Thus, the plant location should be sufficiently large for coal storage facilities and possibly ash disposal, and systems for supplying coal and gas should be reasonably near the plant site.

HIPPS is designed to operate as a good friend to the local community and the environment. The design criteria is 1/10 of the current emission limits for new coal plants. Systems to perform that level of control are included with the price and efficiency estimates for HIPPS. The high efficiency reduces greenhouse gas emissions compared to other coal-based systems. Environmental cleanliness is one of the strong points for marketing HIPPS.

The HIPPS technology can be used in the U. S. and most other parts of the world. There are no special, high-tech equipments that need special operation and maintenance or training. HIPPS looks and operates very much like a conventional power plant. As long as the estimates for performance and economics hold true as the technology develops, a wide range of owners will want to use HIPPS. Utilities, independent producers, merchant plants and others will consider HIPPS for cases where coal is available and other conditions are favorable to adding electric power generation.

Future Market Size

One estimate of the potential market's limits can be done by examining EIA's estimates (Annual Energy Outlook, 1997) for 1996 to 2020 where some 403,000 megawatts or about 1,300 new plants (assuming an average capacity of 300 MW) will be needed in response to growth and replacement of retired plants. EIA also assumes that plants with operating and maintenance cost above 4 cents per kWh will be retired in the next decade. The retirements include 73,000

megawatts of fossil generation. This estimate for new plants is in addition to repowering and life extensions or other actions that power generators may take to reduce the need for new plants.

Almost 50% of the additions will be required in the 2010 to 2020 time because of planned nuclear plant retirements. The EIA forecast is that 85% of the new power will be from gas turbines and gas turbine combined cycle plants. Only 49,000 megawatts of new coal-fired capacity is forecast, and 58 percent of that generation will come online in the 2010 to 2020 time.

Thus for the new plants, the bottom of the HIPPS market is some portion of the 49,000 megawatts of coal-fired additions. Using 20 percent as an estimate of the portion of the total market available for HIPPS, that would mean that some 10,000 megawatts of capacity could be built, mostly in the 2010 to 2020 time period. If for example, 8,000 megawatts is built in that 10 year period, it would mean about 2 to 3 HIPPS plants would have to be installed each year (assuming an average capacity of 300 MW). Even at such a conservative estimate, HIPPS would seem to be a good business venture, and the timing is about right for industry to demonstrate and accept the technical and economic attributes of the technology. Given earlier HIPPS plant estimates of slightly less than $800 per kW, total installed cost, the 8,000 megawatts would equal costs for a buyer, or revenues to a seller of $6.4 billion (1998 dollars).

The HIPPS market could expend significantly if the technology is able to replace some of the new capacity planned for gas turbine combined cycle plants, which is about 354,000 megawatts. Even winning 5% or 10% of this capacity would more than double or triple the installation of new HIPPS plants, and based on cost of electricity estimates, HIPPS should be very competitive with gas turbine combined cycle for a number of scenarios.

In the nearer term, from the present to 2006, the potential market for replacements of existing coal plants is smaller. Tables E-8 and E-9 illustrate this, showing only 9,200 megawatts of additions and 12,440 megawatts of change over the 10 year period. However, if HIPPS is technically ready and economically proven for this timeframe, there are also about 44,000 megawatts of gas-fired capacity additions that would be open to competition by a clean, economical HIPPS system.

Other technologies may also win portions of the demand for new capacity: Distributed power generation, using a number different generators – fuel cells, microturbines, diesel and gas engines, may have a significant role in future power generation. For one example, Allied Signal has commitments for 3,000 microturbine generator units in 1999 and 10,000 units in 2000 (T&D Electric World, 1998). Each unit produces only 75 kW of power and their widespread use requires solutions of a number of issues, but they are part of the overall competition that makes any forecast of markets difficult and out-of-date relatively quickly if not periodically updated.

The repowering market, and the role of HIPPS in that market are more difficult to define. EIA data (EIA Inventor of Power Plants in the US, 1997) shows only about 2,000 megawatts of capacity planned for repowering or life extension for the 1996 to 2006 period, and very few coal units are included in the estimate. There may be more repowering and upgrading work planned by non-utility generators, but no data was found to define this. EIA did report that non-utility generators planned to add 4,000 megawatts of capacity in the years 1997 to 1999. For comparison, non-utility generating capacity in 1996 was about 73,000 megawatts.

Another target for repowering could be a portion of the 73,000 megawatts of fossil-steam (coal, oil and gas) capacity scheduled for retirement over the 1996 to 2020 period. However, each plant would require site specific analysis to evaluate that possibility.

In summary, for the repowering market, because of the variability of site and unit specific conditions it is difficult to estimate a future market. However, while it appears that the repowering market will be relatively small, it could be an important one for HIPPS to gain a foothold in the generation business. Even if just one of the plants planned for repowering or life extension in the next ten years were to use the HIPPS technology, that would benefit the future market. Over the longer term, to 2020, more repowering opportunities for HIPPS are likely. However, it is noted that adding repowered capacity is likely to replace or substitute for new plant capacity described in earlier paragraphs.

One conclusion that can be fairly drawn is that the combined new plant and repowering market for HIPPS, which as reasoned above is to be conservatively on the order of $6 to 7 billion in the 2010 to 2020 period, should be large enough to attract business interest. Other market factors are examined next, but purely from the size of a potential market, HIPPS is worth pursuing.

Future Market Timing

As reported above, the EIA forecasts a major need for additional capacity in the 2010 to 2020 period, largely because of planned nuclear plant retirements. HIPPS technology should be available to meet part of the requirement.

As with all developing technologies, schedules depend on many internal and external factors, but the sequence and milestones below reasonably estimate HIPPS progress.

- Engineer, install and test a near commercial scale HIPPS system by the end of year 2003.
- Install the first commercial unit using tax incentives or other subsidies by 2006.
- Install first unsubsidized system by 2008.
- Beyond this, the rest of the success for HIPPS will depend on its performance and changing conditions in the industry: gas turbine and other technological advances; fuel prices; electric power supply and demand; and numerous others.

If HIPPS can develop and become commercial by approximately 2008, the technology would be sufficiently tested in commercial conditions to be deployed on as large as scale as made feasible by the demand for electric power and competing generation systems.

While the present discussion is limited to U.S. markets, the foreign market may have large impacts of the size and time table for commercializing HIPPS. As the technology advances, its applications outside of the U.S. should be more closely examined.

Future Market Locations

For the United States, there are significant data from which one may estimate and forecast markets for HIPPS technology. However, it needs to be continuously remembered that such forecasts are only the best guesses of the forecaster, and they are more useful in comparing technologies or marketing opportunities than for the absolute values: A market study is only one

part of the decision making process that may lead to a market plan followed by eventual manufacturing and sales of the products.

Forecasting location(s) for a market is a section of the market study that would benefit the most from person-to-person communications to discuss plans for future power plants. However, the study's scope is limited to examining available data. A summary of the data is shown on Table E-11, the methodology is explained below.

To forecast the locations for future HIPPS plants, the table was used as follows to estimate which States might offer the best opportunity for HIPPS plants. First, any State that had a planned coal unit addition received a "boxed" value in that column. Next, the three largest values for each column are highlighted with boxes. (The second column, Utility Consumption, is not used in the selection.) For example in the two growth rate columns, the coal and natural gas rates are combined to select three States with the largest values. For price growth, a negative coal price rate increase was considered favorable when combined with a positive gas price rate increase, so for Ohio, -2.4 and 1.6 total to one of the high values as 4.0. Missouri and Tennessee have even wider spreads and received boxes.

Finally, those States with two boxed values (Ohio, for example, has a high price growth rate and a high count of MW built before 1960.) are themselves boxed in the first column: Ohio, Indiana, Pennsylvania, Illinois are major coal producers and users; less obvious without the data, Missouri, Tennessee and Wisconsin also have two boxed values and may be high potential places to market the HIPPS technology.

Table E-11
Summary of Data from EIA Sources

		Utility Consumption 1997 Data		Utility Annual Growth Rates 1993-1997		Utility Annual Price Growth 1993-1997		Units to be Added	Capacity MW	Units to be Added	Capacity MW	Units to be Changed	Capacity MW	Total MW of Units 1960 or before.
								EIA Data for 1997 Through 2006						
		Generation 10^9 kWh	Coal Use 10^6 Tons	Coal	Natural Gas	Coal	Natural Gas	Coal		Natural Gas		Coal		Coal
1	Texas	135.7	96.5	0.9%	-0.3%	-2.4%	1.6%	6	4,151	21	2,413	1	600	0
2	Ohio	124.9	52.9	0.5%	2.9%	-1.7%	4.2%	--	--	5	383	2	888	5,994
3	Indiana	108.9	54.8	2.2%	-5.5%	-2.0%	2.8%	--	--	23	3,406	8	809	3,804
4	Pennsylvania	105.5	42.6	1.5%	-1.6%	-1.5%	2.5%	--	--	5	602	6	610	4,019
5	Kentucky	87.9	38.3	1.6%	15.5%	-2.6%	2.2%	--	--	8	1,007	4	1,436	2,427
6	West Virginia	87.7	34.5	3.9%	-30.0%	-3.1%	-6.0%	--	--	--	--	2	1,140	2,859
7	Illinois	76.1	41.0	4.5%	12.8%	-3.2%	0.5%	--	--	16	2,704	--	--	2,376
8	Alabama	71.6	30.8	2.1%	10.0%	-3.9%	1.5%	--	--	5	554	1	125	3,768
9	North Carolina	70.2	27.2	3.1%	6.7%	-4.0%	-2.5%	--	--	12	3,041	--	--	3,085
10	Georgia	66.2	30.6	3.5%	11.8%	-3.2%	-4.3%	--	--	10	2,074	--	--	1,505
11	Florida	66.0	27.4	1.7%	8.3%	-0.8%	1.2%	1	157	15	2,934	--	--	621
12	Michigan	65.6	31.9	2.0%	8.6%	-2.9%	-3.3%	--	--	--	--	4	583	3,066
13	Missouri	59.9	35.2	7.5%	6.7%	-9.0%	3.3%	--	--	12	1,734	--	--	1,091
14	Tennessee	58.9	24.5	0.5%	-5.0%	-3.2%	14.4%	--	--	--	--	--	--	6,105
15	Wisconsin	40.8	23.6	3.8%	16.2%	-2.5%	3.2%	1	60	13	1,190	1	30	1,645
16	Utah	32.1	14.3	0.4%	-9.3%	-1.7%	-2.1%	--	--	--	--	--	--	189
17	New Mexico	27.1	15.8	1.1%	3.2%	-0.3%	3.1%	1	233	1	103	--	--	0

While this market study does not include assessment of foreign opportunities, the first markets for HIPPS may be outside the U. S. In parts of Asia, especially, natural gas and liquefied natural gas are expensive and domestic distribution systems are limited, but coal mining and coal transportation are more developed mature industries. Also, most of the developing countries with coal, gas and oil resources would prefer to sell the gas and oil for dollars, which can be used for imports and investment funding. The demand for energy and environmental improvements is high in Asia and Europe, both of which could benefit from coal-fired HIPPS.

Competitors in the Market

The main competition for HIPPS are plants using gas turbine combined cycle power plant technology, and the future GTCC systems which will be cleaner, more efficient and may cost the same or less than today's GTCC plants. In some special markets, for example where the owner has determined that coal will be used as the primary fuel, HIPPS will be competing against pulverized coal-fired plants, integrated gasification combined cycle and possibly, systems using atmospheric and pressurized fluid bed combustion technologies.

Table E-12 presents a summary of the estimated investment costs. The HIPPS plant is clearly less expensive than the pulverized coal-fire plant. Published and in-house data was used to estimate the gas turbine combined cycle plant, and $800 per kW was used for a Total Capital Cost, consistent in definition with the other technologies. The three plants are also consistent in capacity and environmental requirements. While the GTCC plant has the lowest capital cost, its fuel is more expensive.

Earlier work did not include an estimate for coal gasification combined cycle, but even the more optimistic estimates for IGCC are some $200 per kW more that the HIPPS and PC plants. The IGCC efficiency is lower than for HIPPS, and to show reasonable economics, the IGCC plant needs to be significantly larger capacity, thus increasing the magnitude of the investment required.

Table E-12
Cost Estimates from Commercial Plant
Conceptual Design and Estimating Task

Cost Estimates from Task 1.3.2 for 300 MW Commercial HIPPS Plant Conceptual Design	HIPPS Plant		Pulverized Coal Plant		Gas Turbine Combined Cycle Plant	
	Thousands of 1997 Dollars	$ per kWh	Thousands of 1997 Dollars	$ per kWh	Thousands of 1997 Dollars	$ per kWh
TOTAL CONSTRUCTION COST	238,800	796	258,300	861		
Project Contingency 15 % of TCC	35,820	119	38,745	129		
Total Plant Cost	274,620	915	297,045	990		
Allowance For Funds During Construction 8%	21,970	73	23,764	79		
Total Plant Investment	296,590	989	320,809	1,069		
Owner Costs 5% 0f TPI	14,829	49	16,040	53		
Total Capital Cost	311,419	1,038	336,849	1,123	240,000	800

To account for the differences in fuels and performance, cost of electricity (COE) was calculated for several scenarios as part of the conceptual design and costing task. Exhibit E-1 presents the results comparing HIPPS, PC and GTCC. The graphs show the results of calculating COE present values for three prices of natural gas, and four sets of cost of money and investment time period criteria (Indicated by A, B, C and D on the graphs.).

Exhibit E-1
Present Value Costs of Electricity for Different Scenarios

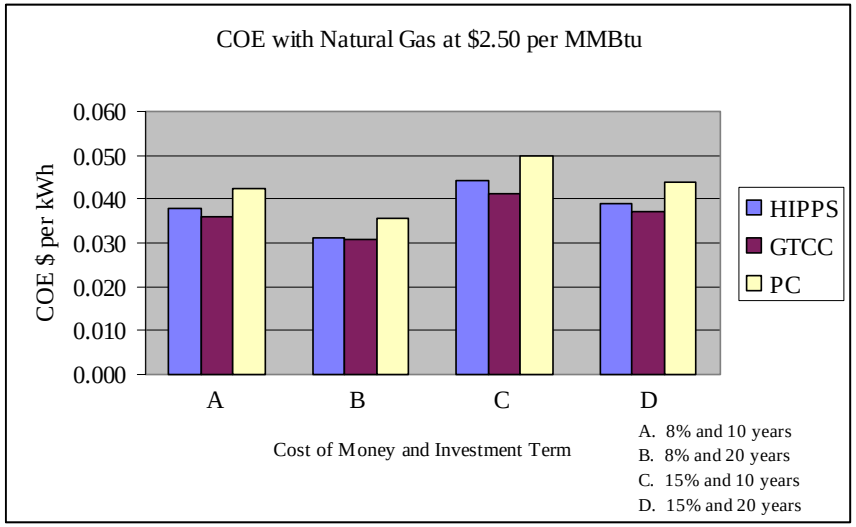

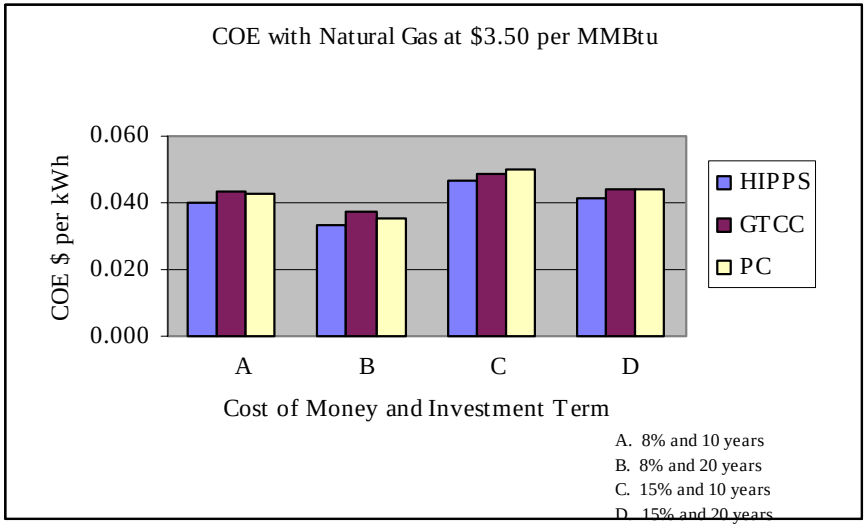

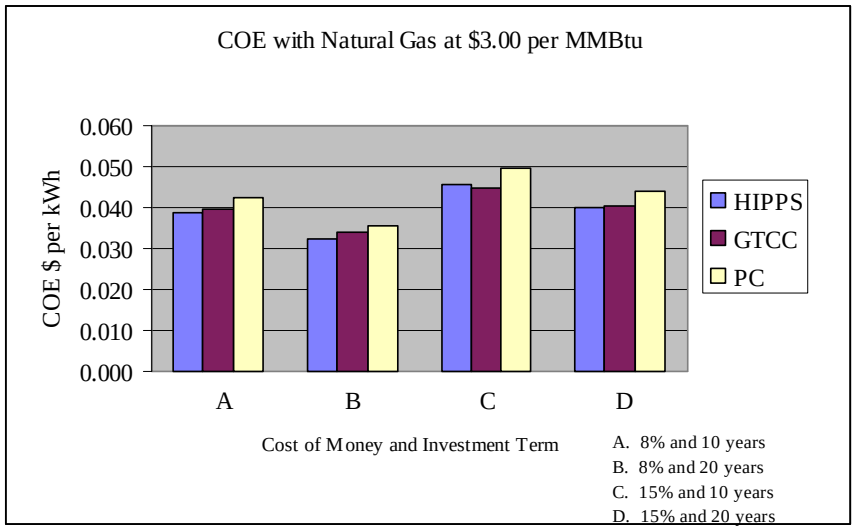

From Exhibit E-1, the relatively small difference between costs of electricity for HIPPS and GTCC power is clear. While the pulverized coal-fired COE is almost always the highest, the COE for HIPPS and GTCC plants sometimes give the advantage to one, and in other scenarios to the other technology. High natural gas prices favor HIPPS (and even PC plants at the highest price per million Btus); low costs of money and longer investment horizons also favor HIPPS as they reduce the impact of its higher capital costs. Conversely, the higher costs of money and shorter investment periods favor the less capital intense GTCC.

Referring back to Table E-6, where the reported average electricity prices were give for the 17 States as between $.04 and .08 per kWh, it is not surprising that for the study parameters, the HIPPS and GTCC plants are competitive with existing power generators. Even with reasonable additions to the HIPPS and GTCC COEs for transmission and distribution and profits, the estimated COEs will be less than a number of existing plants' prices for electricity.

Coal was priced at $1.14 per million Btus for the HIPPS conceptual design and estimates. For reference, the average price of natural gas delivered to U. S. utilities in 1997 was $2.76 per million Btus (Electric Power Annual, 1997).

While the calculations show that HIPPS and GTCC technologies are close competitors, it must be fairly noted that HIPPS is still a developing system, while GTCC plants are in many commercial operations. Both HIPPS and GTCC technologies will continue to advance; increasing efficiencies; reducing emissions and lowering costs of electricity. The selection of HIPPS, once it is commercially available, or GTCC will likely be decided on site, fuel, and plant owner's requirement specifics.

References

Annual Energy Outlook 1998, with Projections to 2020; December, 1997. All values are from the EIA reference case.

EIA Inventory of Power Plants in the United States – As of January 1, 1997.

Electric Power Annual 1997 Volume 1 by the EIA

Power, November/December 1998, page 4.

T&D Electric World, December 1998 Volume 212; A publication of the McGraw-Hill Companies.

Addendum A - Graphs Showing Coal-Fired Units by State and Their First Year of Operation

(Appendix E)

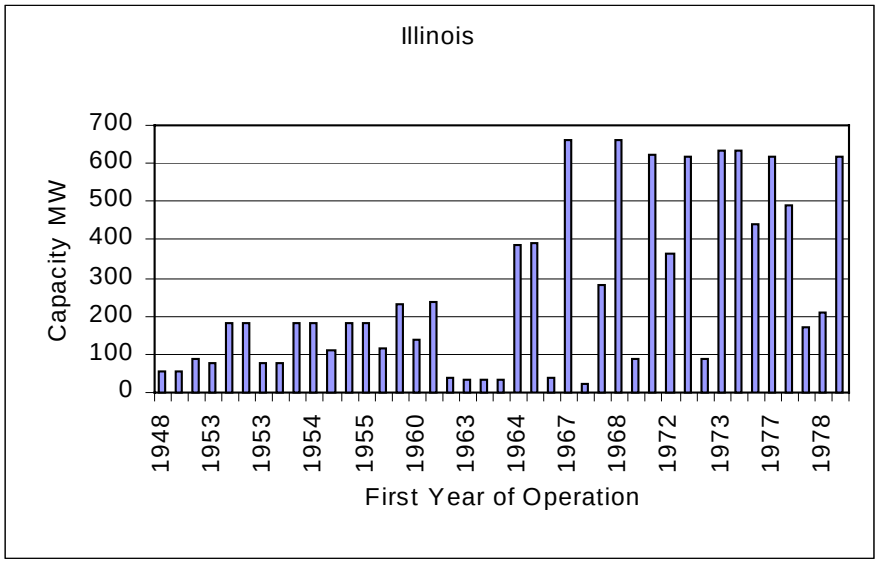
Illinois
Capacity MW
0
100
200
300
400
500
600
700
1948
1953
1953
1954
1955
1960
1963
1964
1967
1968
1972
1973
1977
1978
First Year of Operation

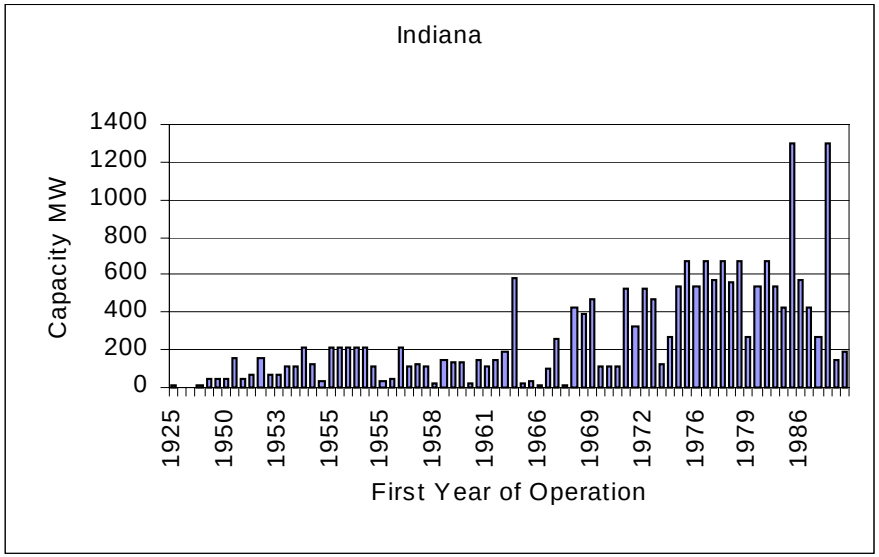
Indiana
Capacity MW
0
200
400
600
800
1000
1200
1400
1925
1950
1953
1955
1955
1958
1961
1966
1969
1972
1976
1979
1986
First Year of Operation

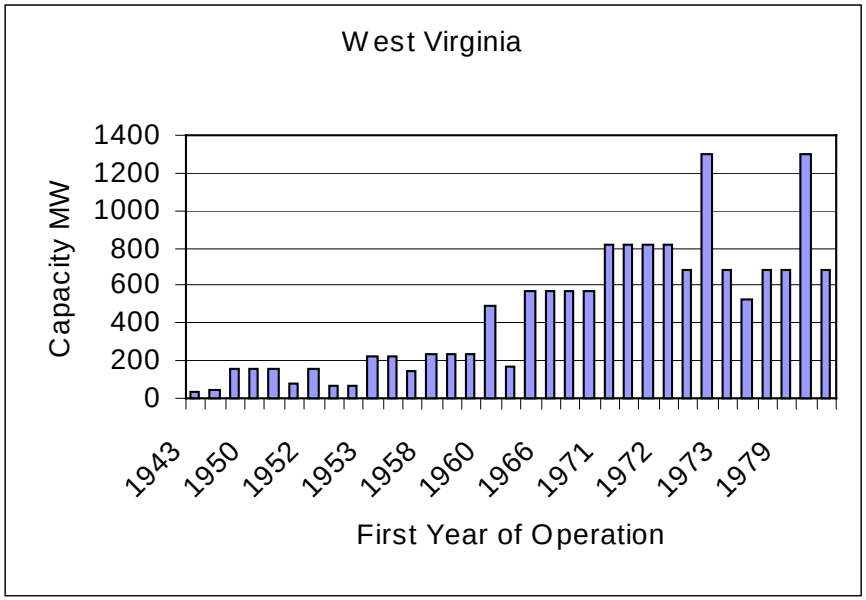
West Virginia
Capacity MW
0
200
400
600
800
1000
1200
1400
1943
1950
1952
1953
1958
1960
1966
1971
1972
1973
1979
First Year of Operation

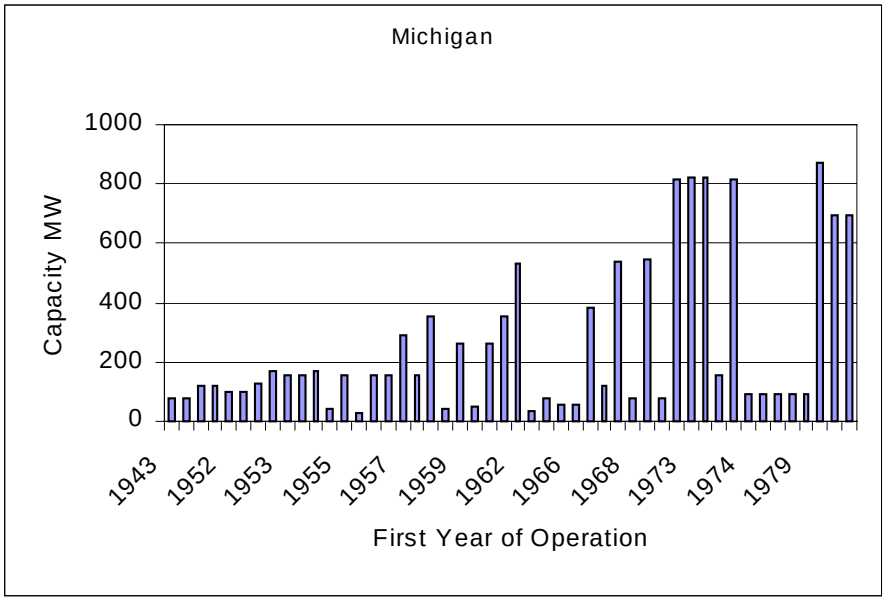
Michigan
Capacity MW
0
200
400
600
800
1000
1943
1952
1953
1955
1957
1959
1962
1966
1968
1973
1974
1979
First Year of Operation

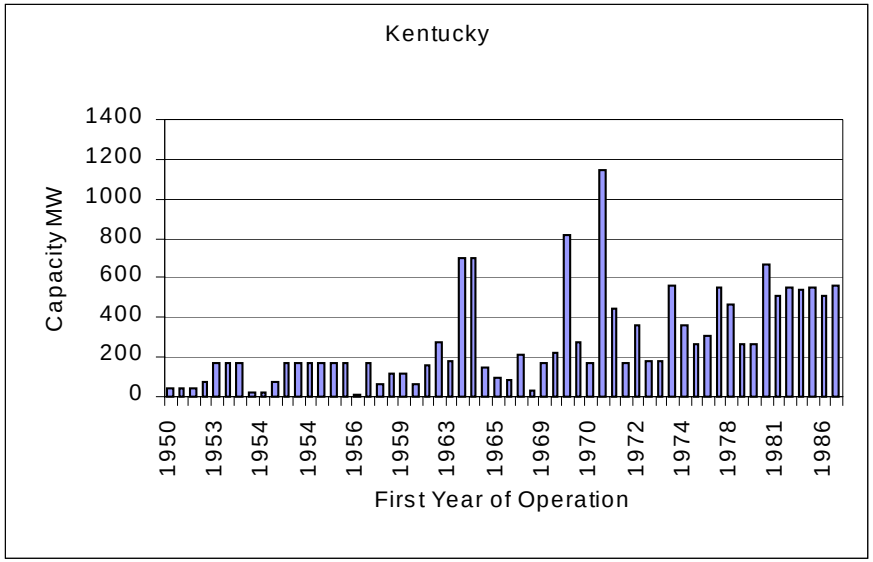
Kentucky
Capacity MW
1400
1200
1000
800
600
400
200
0
1950 1953 1954 1954 1956 1959 1963 1965 1969 1970 1972 1974 1978 1981 1986
First Year of Operation

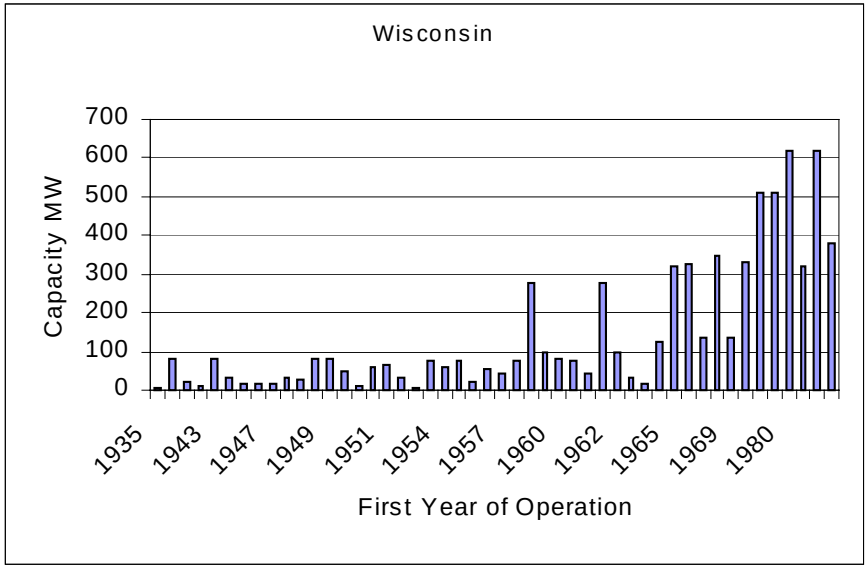
Wisconsin
Capacity MW
700
600
500
400
300
200
100
0
1935 1943 1947 1949 1951 1954 1957 1960 1962 1965 1969 1980
First Year of Operation

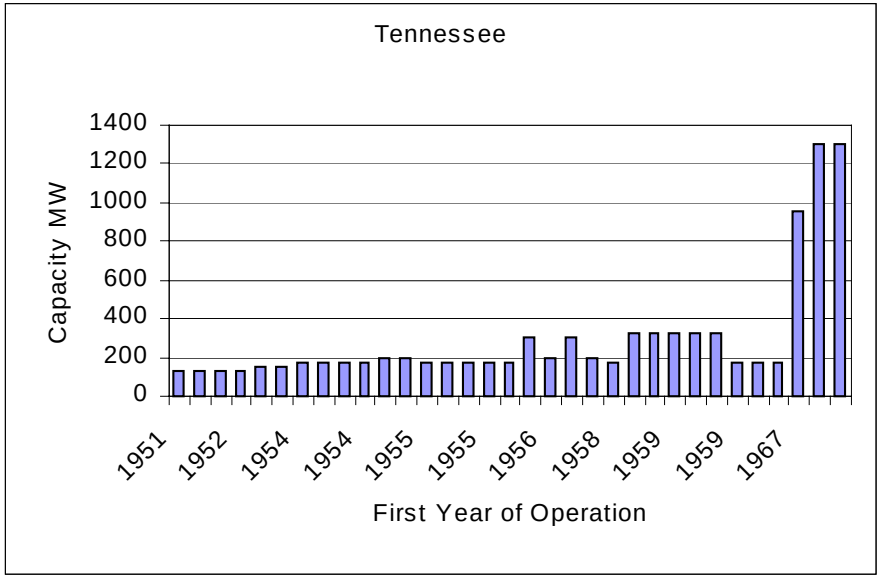
Tennessee
Capacity MW
1400
1200
1000
800
600
400
200
0
1951 1952 1954 1954 1955 1955 1956 1958 1959 1959 1967
First Year of Operation

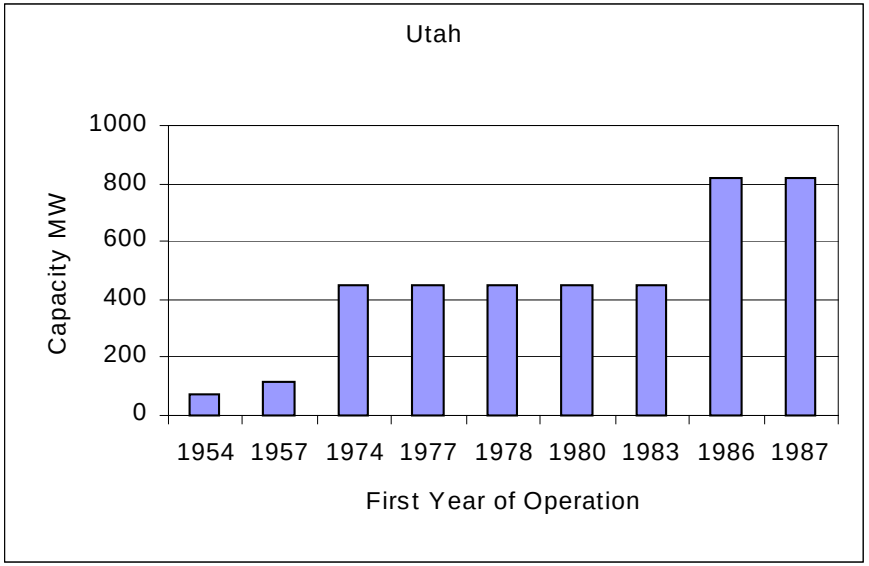
Utah
Capacity MW
1000
800
600
400
200
0
1954 1957 1974 1977 1978 1980 1983 1986 1987
First Year of Operation

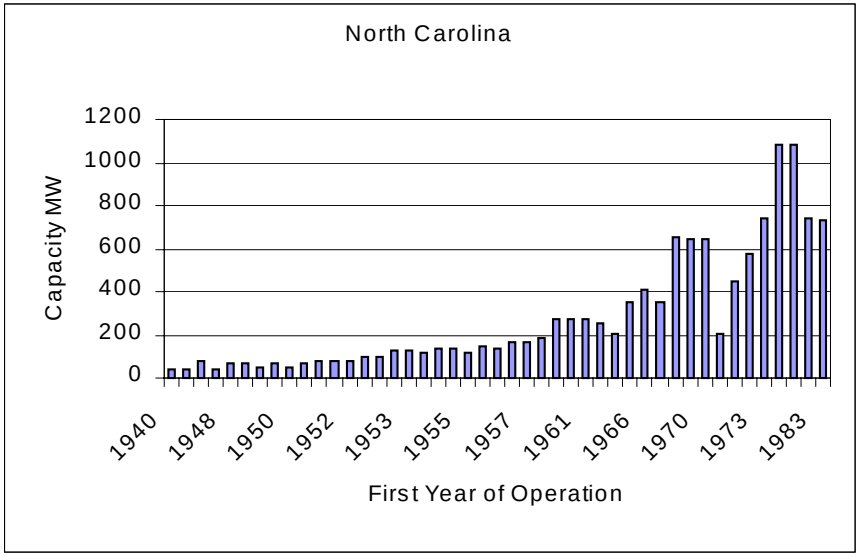
North Carolina
Capacity MW
1200
1000
800
600
400
200
0
1940
1948
1950
1952
1953
1955
1957
1961
1966
1970
1973
1983
First Year of Operation

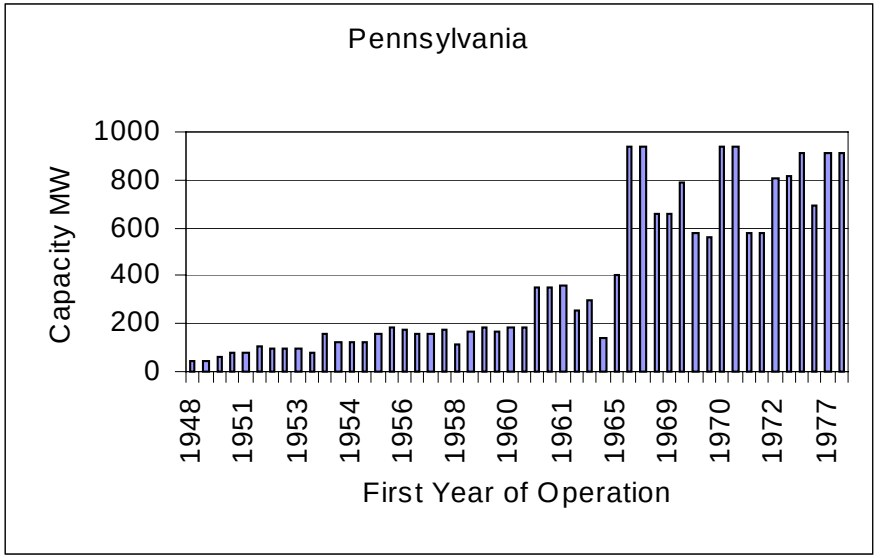
Pennsylvania
Capacity MW
1000
800
600
400
200
0
1948
1951
1953
1954
1956
1958
1960
1961
1965
1969
1970
1972
1977
First Year of Operation

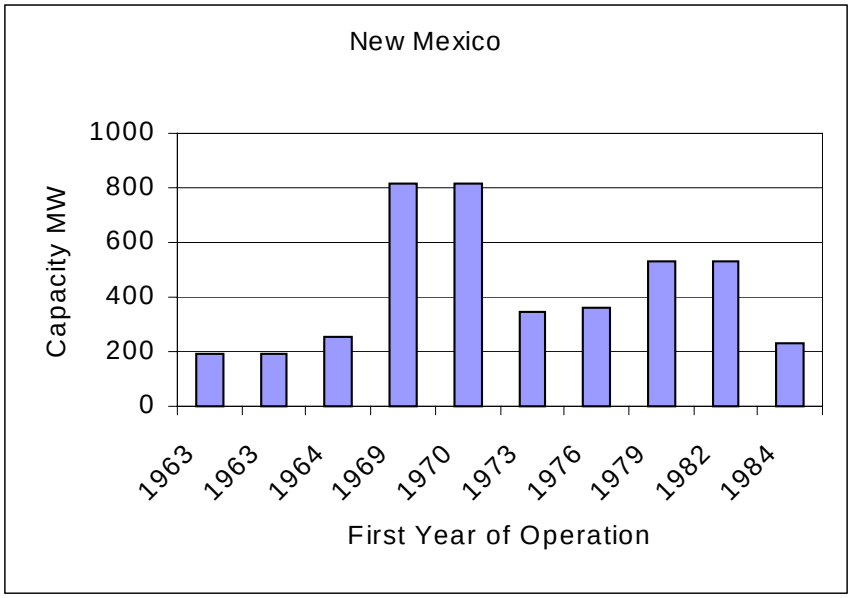
New Mexico
Capacity MW
1000
800
600
400
200
0
1963
1963
1964
1969
1970
1973
1976
1979
1982
1984
First Year of Operation

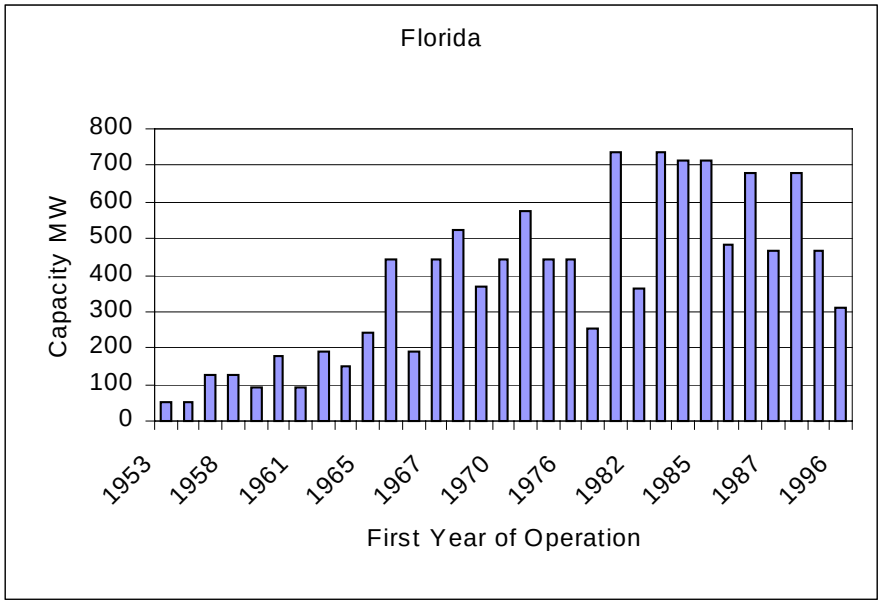
Florida
Capacity MW
800
700
600
500
400
300
200
100
0
1953
1958
1961
1965
1967
1970
1976
1982
1985
1987
1996
First Year of Operation

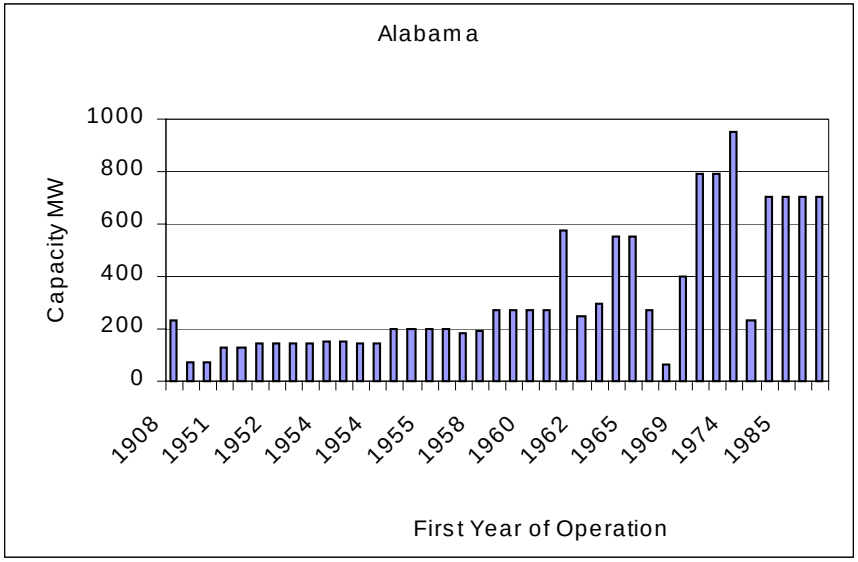
Alabama
Capacity MW
1000
800
600
400
200
0
1908
1951
1952
1954
1954
1955
1958
1960
1962
1965
1969
1974
1985
First Year of Operation

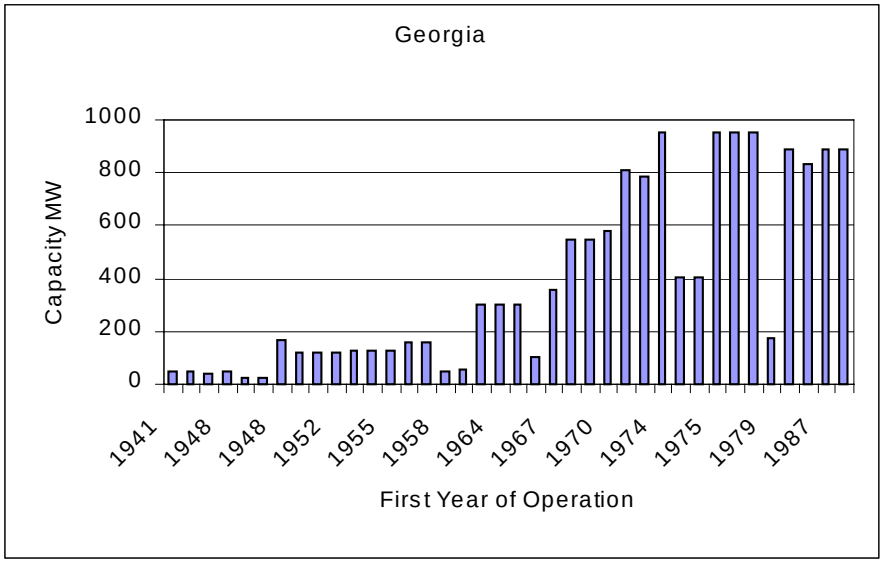
Georgia
Capacity MW
1000
800
600
400
200
0
1941
1948
1948
1952
1955
1958
1964
1967
1970
1974
1975
1979
1987
First Year of Operation

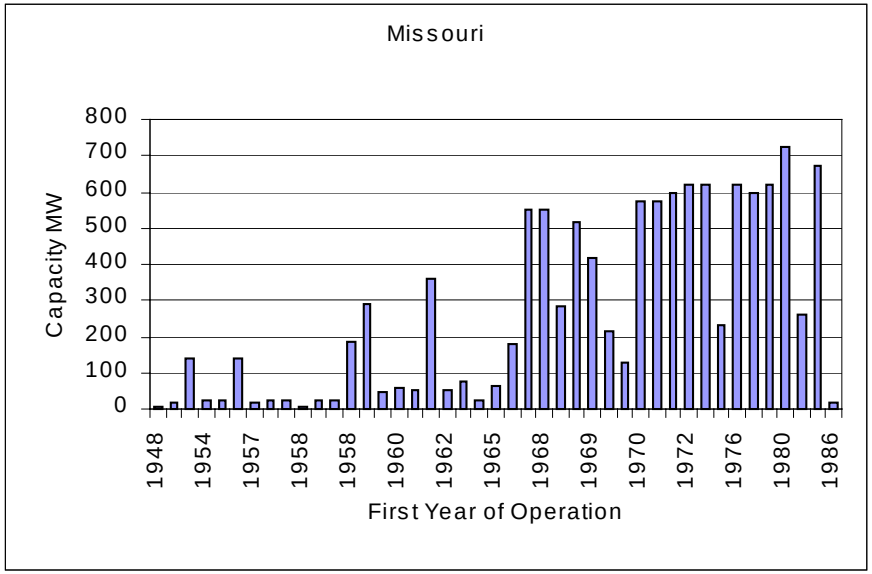
Missouri
Capacity MW
800
700
600
500
400
300
200
100
0
1948
1954
1957
1958
1958
1960
1962
1965
1968
1969
1970
1972
1976
1980
1986
First Year of Operation

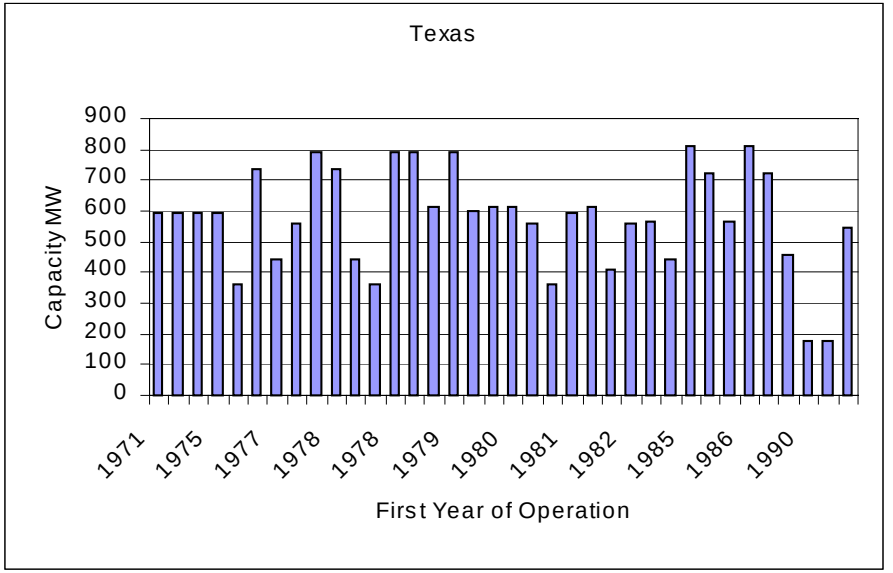
Texas
Capacity MW
900
800
700
600
500
400
300
200
100
0
1971
1975
1977
1978
1978
1979
1980
1981
1982
1985
1986
1990
First Year of Operation

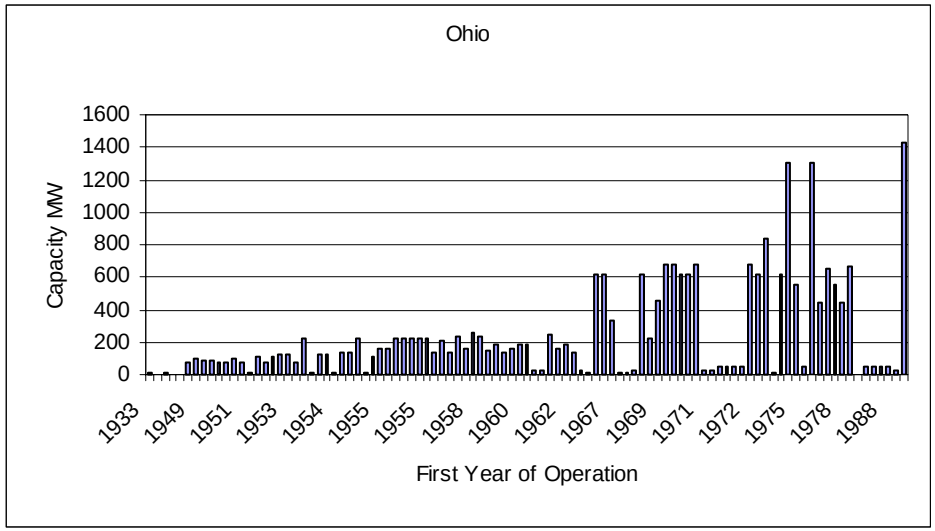
Ohio
Capacity MW
1600
1400
1200
1000
800
600
400
200
0
1933
1949
1951
1953
1954
1955
1955
1958
1960
1962
1967
1969
1971
1972
1975
1978
1988
First Year of Operation

Appendix F – Commercial Plant Design, CO_2 Separation and Capture Issues

The High Performance Power Systems (HIPPS) electric power generation technology integrates a combustion gas turbine and heat recovery steam generator (HRSG) combined cycle arrangement with an advanced coal-fired furnace. A unique feature of the HIPPS plant is the partial heating of gas turbine (GT) compressor outlet air using energy released by firing coal in the high temperature advanced furnace (HITAF). The compressed air is additionally heated prior to entering the GT expander section by burning natural gas. Thermal energy in the GT exhaust and in the HITAF flue gas is used in a steam cycle to maximize electric power production. The HIPPS plant arrangement is thus a combination of existing technologies (gas turbine, heat recovery units, conventional steam cycle) and new technologies (the HITAF including its air heaters, and especially the heater located in the radiant section of the furnace).

The HIPPS plant operation is briefly described below. The discussion applies to the commercial plant conceptual design prepared for Phase I, updated and used in Phase II as the basis for a variety of power cycles and economic comparisons. The design is relatively conservative: it uses commercially available equipment, except for the HITAF; the steam cycle conditions are moderate, and the plant efficiency only meets the minimum DOE requirement of slightly more than 47% on a higher heating value basis. Conceptual designs with more advanced equipment and cycle conditions have potential efficiencies approaching 60% (HHV).

Gas Turbine Operation

A block diagram of the 300 MWe power plant is shown in Exhibit F-1. Air is heated in the natural gas combustor to 2,495 °F (1,368 °C). The hot, compressed air then enters the gas turbine expander where it expands to produce electric power. The flue gas leaves the GT expander at 1,003 °F (539 °C). Heat from the flue gas is recovered in the gas turbine heat recovery steam generator (HRSG) as the gas is cooled to 180 °F (82 °C) before being sent to the stack. The heat recovered from the gas turbine flue gas is used to preheat the HITAF feedwater to 682 °F (361 °C). The feedwater is sent to evaporators (HITAF water walls and slag screens) where saturated steam at 2,500 psia (17,232 kPa) is generated. This steam is sent to a superheater, which is located in the gas turbine HRSG. The waste heat of the gas turbine flue gas is used to heat feedwater and to (partly) superheat the steam.

The following describes the HITAF operation.

HITAF Operation

Coal, which contains 12.25% moisture, is fed to two operating pulverizers using transport air preheated to 575 °F (302 °C). The heat in the transport air vaporizes most of the moisture from the coal, and the vaporized moisture travels with the transport air. The transport air sweeps the coal from the pulverizers and carries the pulverized coal to the HITAF burners. Combustion air is added at the burners and the coal is fired.

The heat transfer surfaces for the following HIPPS components are located inside the HITAF.

- Radiant air heater
- Slag screen walls

- Steam reheater
- Convection air heater

The radiant air heater is located nearest the burners where the furnace temperature is the highest. The convective air heater is the farthest from the burners and sees the lowest temperature in the furnace. As the combustion products flow past the components, energy is transferred from the gases to the heat transfer surfaces. To develop the required temperature profile in the HITAF furnace, part of the combustion gas is recycled from the downstream HITAF HRSG, and is injected into the HITAF between the steam reheater and convective air heater.

The surface areas and locations of the slag screens and water walls are designed so that the slag produced from the coal flows on, and does not scale the radiant air heater and convective air heater. After the radiant heater and before the convective air heater, the flowing slag combines with other bottom slag. The flue gas exits the HITAF at 1,105 °F (596 °C). The heat in HITAF flue gas is recovered in the HITAF HRSG and used for heating the coal combustion air, coal transport air, and heating the partly superheated steam to 1,000 °F (538 °C). The HITAF HRSG also contains a selective catalytic reactor which destroys any NO_x present in the flue gas. The SCR is located upstream of the air preheaters. The HITAF flue gas leaves the HRSG at 300 °F (149 °C) and then goes to a flue gas desulfurization (FGD) unit.

The flyash in the flue gas is removed by a particulate removal device prior to the FGD process, which removes the sulfur compounds present in the flue gas. In the conceptual commercial design, an ammonia-based FGD and an electrostatic precipitator are used. The cleaned flue gas is sent to a stack and released.

The superheated steam from the second superheater is sent to the high pressure section of the steam turbine at 2,400 psia/1,000 °F (16,550 kPa/538 °C). The steam leaves the HP section at 580 psia (4,000 kPa). The 580 psia (4,000 kPa) steam is sent to the reheater, which is located in the HITAF, and the steam is reheated to 1,000 °F (538 °C). The reheated steam is sent to the intermediate pressure section of the steam turbine at 540 psia (3,722 kPa). The steam passes through IP and low pressure sections of the steam turbine and is then exhausted to the steam condenser. The condensate and necessary make-up water is sent to the gas turbine HRSG, and the steam cycle is repeated continuously.

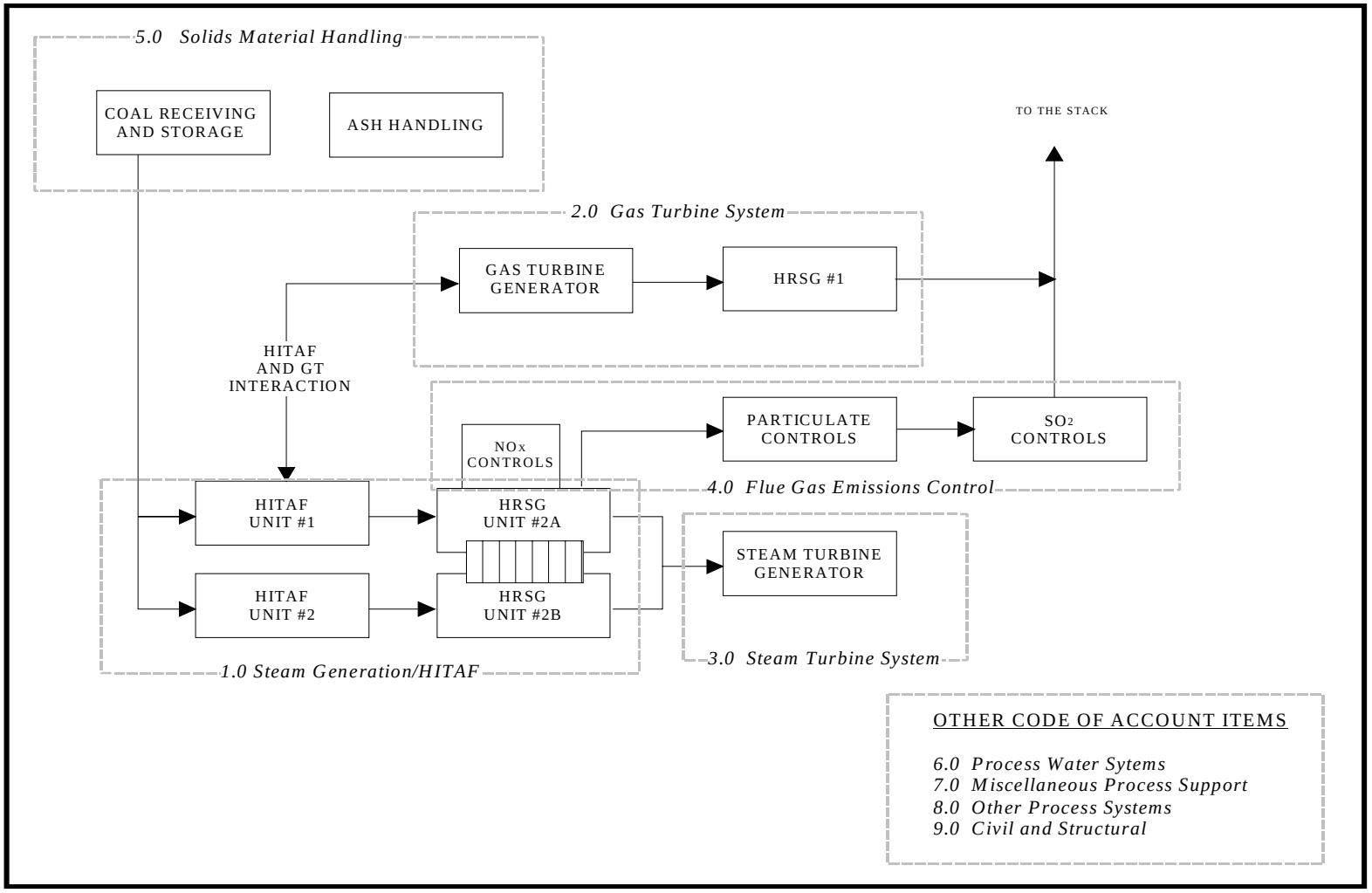

Exhibit F-1
HIPPS Commercial Plant Block Diagram

CO_2 Separation from Flue Gas at the 300 MW HIPPS Plant

U. S. Department of Energy Vision 21 and Climate Change Issues

The U. S. DOE is preparing strategic plans for "Vision 21", a concept to define DOE's role in the Federal Government's energy programs. As part of the DOE concept, climate change or greenhouse gases issues will require investigation and the creation of engineering and cost data to support decision making.

The ongoing HIPPS program has clear advantages in the area of greenhouse gas (carbon dioxide) reduction compared to other coal-fired power generation designs because of its high efficiency (Robson, 1997). In the work presented here, it also appears that the HIPPS concept has significant cost benefits. Using conventional CO_2 separation technology, MEA absorption, and the conservative HIPPS commercial plant cycle, the cost per ton of CO_2 avoided is estimated to be about $10. The cost of electricity increases 9 mills or about 20 percent, from 42 (base case HIPPS) to 51(HIPPS with MEA absorption) mills per kWh. Both calculations are based on 10% cost of money and 20 year investment period. Bearing in mind that only the CO_2 from the coal combustion is treated by the MEA absorption, the cost per ton of carbon avoided and cost of electricity are substantial, but appear promising, with room for process optimization to significantly reduce costs.

To explore the potential for HIPPS technology to impact the reduction of CO_2 from power generation stations, a topical study was performed to assess several CO_2 separation methods, and evaluate how they might be used in the HIPPS power plant. The technical and economic findings from the study are reported in the following pages along with conclusions drawn by the HIPPS team. The study uses conceptual design and cost data; published information; engineering experience and judgement; and informal contacts with technology developers. Cost estimates are order-of magnitude approximations for plants with mature technologies i.e. not first-of-a-kind plant costs. Considering the level of engineering and cost estimating, and the variability of parameters used to compute the cost of electricity, and the cost per ton of CO_2 avoided, the results should be used in the full context of the topical report.

Introduction

The main greenhouse gas contained in the flue gas created by fossil fuel power plants is CO_2. (Tables F-1 and F-2 show the HIPPS flue gas components.) To reduce the emission of CO_2, it has to be separated from the flue gas, and then transported to a location where it can be either used for manufacturing products or sequestered in long term (several hundred years) storage. The amounts of CO_2 from power plants is so large that even with very optimistic projections for use, large quantities of unconsumed CO_2 are likely to require sequestration. Assessments of sequestration are not part of the present study, but are being examined in other work by DOE and others. Nonetheless, because the sequestration method may impact the separation step, the major schemes for sequestration are listed below. The state of the CO_2 – gas or liquid, and the pressure will have to be considered for their impact on the steps to be taken after separation, and before transportation, sequestration, or use.

The major sequestration concepts are:

- Injection into depleted oil and gas reserves. Gaseous CO_2 can be compressed and injected into the field. Use of CO_2 for enhanced recovery (flooding) is not really applicable, because the injected CO_2 is recovered with the hydrocarbons and must be continuously separated and recycled to avoid atmospheric emissions.
- Injection into deep, unminable coalbeds. Gaseous CO_2 can be compressed and injected into the coalbeds. Other work at DOE and elsewhere is investigating displacement and recovery of coalbed methane from the sequestration process.
- Magnesium carbonate fixation. Magnesium present in ultramafic rocks can be reacted with CO_2 to produce magnesium carbonate which can be disposed of as an inert solid.
- Deep ocean disposal. CO_2 can be converted to hydrates and injected deep into the ocean, or it may be injected as a liquid. Much work remains to prove the potential for this concept, technically and environmentally.
- Deep aquifer injection. CO_2 can be injected into deep groundwater aquifers if the geological conditions are such that the gas does not leak back to the atmosphere, nor cause damage to useful ground water.

For the first three options, the captured CO_2 will be sequestered in gaseous form, and for the last two options, it is in liquid form. As this study is limited to separation and capture of CO_2 from the flue gas, and because the end use of the CO_2 is very site specific, the temperature, pressure and physical state of the captured CO_2 is left as it is after the separation/capture process.

Objective

The study objective is the technical and economic evaluation of commercially available processes, and processes that may become available in the near term for the separation of CO_2 from HIPPS flue gases.

Conclusions

The main conclusions drawn from the study are summarized below.

- Absorption processes with MEA have the lowest cost and greatest technical feasibility for the HIPPS design.
- The oxygen combustion concept holds promise for improved CO_2 capture, and should be examined in future work.

Costs for the MEA absorption and oxygen combustion process are summarized below.

Annualized Cost of Reference HIPPS Plant	$97,262,000
Cost of Electricity for Reference HIPPS Plant	42 mills/kWh
Annualized Cost with MEA Added to the HIPPS Plant	$107,113,000
Cost of Electricity with MEA Added to the HIPPS Plant	51 mills/kWh
Cost per Ton of CO_2 avoided with MEA Absorption	$9.20
Annualized Cost with Oxygen Combustion at the HIPPS Plant	$107,205,000

Cost of Electricity with Oxygen Combustion at the HIPPS Plant	52 mills/kWh
Cost per Ton of CO_2 avoided with Oxygen Combustion	$6.30

CO_2 Production at the HIPPS Plant

The HIPPS commercial power plant produces electricity by burning coal and natural gas, and using the thermal energy in a combined cycle type of operation. The flue gas from coal combustion in the HITAF furnace is cleaned to limit particulate, NO_x and SO_x. The composition, temperature, pressure and flow rate of the cleaned coal-based flue gas is shown in Table F-1. The flue gas exhausted by the gas turbine is passed through a HRSG. Composition, temperature, pressure and flow rate of the natural gas-based flue gas at the HRSG exit is shown in Table F-2. The data in the tables are from a United Technologies Research Center report (Seery, 1998). For detailed information about the HIPPS commercial plant and about the processes used for the removal of particulate, NO_x and SO_x from the flue gas, the reader is referred to this report.

Tables F-1 and F-2 show the coal-based flue gas containing 6,352 lb-mol/h (2,881 kg-mol/h) CO_2 and the natural gas-based flue gas containing 1,913 lb-mol/h (868 kg-mol/h). That is, 77% of the CO_2 is contained in the coal-based flue gas and 23% in the natural gas-based flue gas. Also, the concentration of CO_2 in the coal-based flue gas is 12.9% (wet) whereas in natural gas-based flue gas, it is only 1.6% (wet).

Table F-1
Cleaned Coal-Based Flue Gas

Components	lb-mol/h	lb/h	lb-mol%
O_2	1,431	45,791	2.91
N_2	33,208	930,369	67.51
A	402	16,040	0.82
CO_2	6,352	279,537	12.91
H_2O	7,801	140,547	15.86
Totals	49,194	1,412,284	100.00
Temperature	132 °F		
Pressure, Psia	14.8		
ACFM	351,377		

Table F-2
Natural Gas-Based Flue Gas

Components	lb-mol/h	lb/h	lb-mol%
O_2	20,016.0	640,513	17.17
N_2	88,322.5	2,474,444	75.77
A	1,073.5	42,881	0.92
CO_2	1,912.8	84,182	1.64
H_2O	5,237.1	94,352	4.49
Total	116,562.0	3,336,372	100.00
Temperature,	180 °F		
Pressure, Psia	14.8		
ACFM	900,072		

Except for energy consumption, impacts on the operation outside of the CO_2 capture are not examined in the present study. However, there are clearly scenarios where CO_2 capture could strongly affect the overall plant: For example, if oxygen-enriched combustion is part of the CO_2 reduction concept, the gas for sequestration likely does not need NO_x and SO_x removed. The capital and operating costs for NO_x and SO_x removal could be avoided if that is the case.

Separation Technology Status

The study focused on five separation technologies, and a combustion modification concept for producing a pure or highly concentrated stream of CO_2 directly from the combustion process. The areas of interest and a brief evaluation of their potential role for CO_2 separation as part of a greenhouse gas reduction program are itemized below. The technologies are examined in more detail as the report proceeds (also see Addendum A).

Gas Absorption is the most mature separation technology, and appears to be the only one of the separation concepts that could be economically viable in the near term. The other separation technologies and the combustion modification concept require extensive improvement/innovation and testing to reduce costs and increase performance.

Cryogenic Cooling is used for air separation to produce oxygen, nitrogen and other gases, and it is used to separate volatiles from mixed gas streams. Discussions with process developers indicated that cryogenic systems would not be feasible for greenhouse gas reduction. This was confirmed by conceptual work in the study.

Membrane Separation was discussed with technology developers and the consensus was that current technologies were not suited to greenhouse gas reduction. Equipment costs and operating costs make the concept too expensive. Developers are well aware of the potential market for an economical CO_2 separation membrane, but from the available information much more research and development is needed to obtain such units.

Membrane Separation with Gas Absorption (MGA) developers are pursuing the combined technologies as a new approach to reducing CO_2 in the context of greenhouse gas reduction. Researchers in several countries are studying and testing the technology, and several papers have been presented. However, present estimates of cost and performance indicate that it is still too expensive for power plant scenarios for CO_2 separation. The TNO Institute of Environmental Sciences in the Netherlands believes they have a near-commercial process with major cost savings, and their work should be followed by interested industry organizations.

Pressure Swing Adsorption (PSA) is another commercial separation technology, but the application for greenhouse gas separation is not attractive.

Oxygen Combustion with CO_2 Recycle is a promising concept for producing a CO_2 rich stream for disposal or use. While an air separation plant is required for the supply of oxygen, there are several potential advantages that could be gained in the power generation plant that would partly compensate for the costs of the system to produce the CO_2 gas stream. This concept should be looked at in more detail by the HIPPS team if DOE interest is sufficient to allocate the necessary resources. The concept could be applied to both the coal-fired furnace and the gas turbine. A number of issues about the combustion process itself are uncertain and require R&D efforts for data to support the engineering evaluations.

CO_2 Removal Limits

An early technology screening indicated that the concentration of CO_2 in the natural gas-based flue gas was too low for practical CO_2 removal, and that gas stream was excluded from the evaluation: Only the coal-based flue gas was used as the source of CO_2 for treatment.

In practice, a 100 % CO_2 removal from any stream is not feasible. Depending on the separation technology, the recovery of CO_2 can range from 90 (or less) to 99%. For the coal-based flue gas, 90% removal was chosen as the design point. The HIPPS commercial plant is based on 65% coal combustion and 35% natural gas combustion. Therefore, a 90% CO_2 removal from the coal-based flue gas is equivalent to about 70% overall CO_2 removal at the power plant. If the HIPPS commercial power plant is designed for 100% coal combustion, 90% of all the CO_2 produced could be captured.

Also in practical terms, producing a 100% pure substance is not reasonable. Depending on the technology, the practical purity of the recovered CO_2 can range from as low as 50% for membrane and PSA processes, to as high as 99.9% for gas absorption and cryogenic cooling processes. The design point for the captured CO_2 stream is 90% purity on a dry basis.

CO_2 Separation and Removal Technologies

There are two primary concepts for removing CO_2 from flue gas. One concept separates CO_2 from the other components present in a mixed gas stream. An alternative method modifies the combustion process so that the flue gas produced is largely CO_2, so that a separation step is not required.

Overview of CO_2 Separation Technologies

Five separation technologies were examined for CO_2 removal from the coal-based flue gas produced at the HIPPS commercial plant.

Gas Absorption

Gas absorption processes are commonly used in commercial plants to remove CO_2 from mixed gas streams. Gas absorption can treat streams with high or low pressures, and with high or low CO_2 concentrations. Gas absorption works by contacting the mixed gas stream containing CO_2 with a liquid solvent in which CO_2 is soluble. Two types of solvents are often used for CO_2 removal: Physical solvents and chemically reactive solvents. Physical solvents dissolve CO_2 but do not react with it. Chemically reactive solvents first dissolve CO_2 and then react with it. Physical solvents are more suitable for mixed gas streams which are under high pressure. The elevated pressure increases CO_2 solubility, which in turn reduces the solvent circulation rate. The performance of chemically reactive solvents is not affected by the pressure.

If the mixed gas stream containing CO_2 is at elevated pressure, the physical solvent can be recovered by simply flashing to a liquid at a lower pressure. Chemically reactive solvents require heat to separate the dissolved gas. Commercial experience indicates that the physical solvent process is more economical if the CO_2 partial pressure is above 200 psia (1,379 kPa). At low inlet CO_2 partial pressure, and where a very low outlet concentration of CO_2 is required, chemically reactive solvent processes are more likely to be selected.

Cryogenic Cooling

CO_2 can be separated from a mixed gas stream by liquefaction when the CO_2 concentration is sufficient. CO_2 can be liquefied at any temperature between its triple point –70 °F (-57 °C) and its critical point 88 °F (31 °C) by compressing it to the corresponding liquefaction pressure, and removing the heat of compression and condensation. There are two common commercial liquefaction processes. In the first process, the CO_2 is liquefied near the critical temperature and cooling water is used for cooling. This process requires compression of the CO_2 gas to about 1,100 psia (7,582kPa). A second liquefaction process operates with temperatures from 10 to 70 °F (-12 to 21 °C), and with liquefaction pressure of about 250 to 350 psia (1,723 to 2,413 kPa). This process requires dehydration of the feed stream with activated alumina or silica gel dryer and distillation of the condensate in a stripping column.

Another cryogenic method for CO_2 removal is to cool the mixed gas stream to such a low temperature that CO_2 condenses out of the gas phase. This method is used to remove vapors of organic compounds from vent gases and for other operations.

Membrane Separation

Membrane separation of mixed gases often competes with cryogenic air separation units and pressure swing adsorption units when medium quantities of low purity product gas is required. For large quantities and high purity products, the number of stages and the recycle flow rates increase to such an extent that membrane separation does not compete with cryogenic air separation units.

A pressure drop ranging from 50 to 400 psia (345 to 2,757 kPa) across the membranes is required for the separation of mixed gases. Membrane separation technology is thus more suited for treating mixed gas streams feed from a high pressure source.

Membrane Separation with Gas Absorption (MGA)

The partial pressure difference of the gas drives the separation of mixed gas streams with membranes: The greater the partial pressure difference across the membrane is, the greater is the flux of the gas passing through it. One method of increasing the partial pressure difference is to dissolve the CO_2 passing through the membrane in a liquid solvent, so that the partial pressure of CO_2 is virtually zero on the permeate side. The solvent can be a physical solvent or a chemically reactive solvent. This method of gas separation is called membrane separation with gas absorption (or MGA, for short). This process is suitable for gaseous streams at low pressure.

Pressure Swing Adsorption (PSA)

Like the membrane separation, this process also competes with cryogenic air separation units which produce oxygen and nitrogen. For high purity products, the number of stages and the recycle flow rates increase to such an extent that the PSA process does not successfully compete with the cryogenic air separation unit.

Combustion Modification Technologies

Substitution of oxygen for all or part of the combustion air has been proposed in some concepts as a method to produce a CO_2 rich flue gas that requires no separation, and the combustion gas can be sent directly to use or sequestration.

Oxygen Combustion

Conventional air combustion process produces flue gas which contains predominantly nitrogen and excess oxygen in addition to CO_2 and water. The separation technologies have to separate CO_2 from these other components. If the air is replaced by oxygen, the nitrogen content of the flue gas is zero and the flue gas is predominantly CO_2 with a small amount of excess oxygen and combustion water.

While schemes for oxygen combustion, usually with the recycle of flue gas for combustion control, have been conceptually examined, there are no field units. Commercial plant feasibility may be difficult to justify under most conditions because of the auxiliary power consumption of the air separation unit needed to produce the oxygen.

Evaluation of CO_2 Separation Technologies

The following parts of the report provide detailed discussions of the technologies.

Gas Absorption Technology

There are several commercial gas absorption processes currently used for removing CO_2 from mixed gas streams. Some of the more commonly used processes are listed in Table F-3.

The first four processes in the table use solvents which physically absorb the CO_2 present in a mixed gas stream. Because these processes do not involve chemical reactions, little if any heat is

required to recover the solvent. In most cases, lowering the pressure of the rich solvent stream is sufficient to release the dissolved CO_2. The recovered solvent is recirculated to absorb more CO_2. These processes are used for mixed gas streams which are under high pressure and contain a high concentration of CO_2. The solvent circulation rates for these processes are generally high.

For the other processes in the table, a chemically reactive solvent is used which acts in two steps. In the first step the solvent absorbs CO_2, and in a second step it chemically reacts with the absorbed CO_2. The compound produced by the chemical reaction is decomposed with heat to liberate the solvent and CO_2. The liberated solvent is reused for further CO_2 absorption. Because the CO_2 chemically combines with the solvent, these processes require substantial quantities of heat for the solvent recovery. Theoretically, all of the chemical absorption processes can be used at atmospheric pressure, but in practice they are used for mixed gas streams which are under substantial pressure. Two examples of use are the removal of CO_2 from natural gas and from synthesis gas.

Alkanolamines (a group of amines) which are used for CO_2 removal are monoethanolamine (MEA), diethanolamine (DEA), diglycolamine (DGA), diisopropanolamine (DIPA), and triethanolamine (TEA). Of these amines, MEA is the most alkaline; that is, it has the highest dissociation constant and the highest pH in water solution. The others are progressively less alkaline in the order listed. Other properties which bear on the use of these amines follow in the same order as their akalinities. The chemical reaction with CO_2 is fastest with MEA and decreases with the others. The overall mass transfer coefficients for various packings (K_Ga's) for MEA are 2 to 2 1/2 times greater than those for DEA. For these reasons, MEA based processes are the most popular. The MEA absorber/stripper unit was selected for the assessment as a representative of the gas absorption processes.

Table F-3
Gas Absorption Processes for CO_2 Removal

No.	Process	Owner	Use	Remarks
1	Sulfinol	Shell Oil Company	Natural gas, refinery gases and synthesis gases.	Shell reported that there were 180 commercial units in operation or under construction in 1996.
2	Selexol	UOP	Natural gas, refinery gases and synthesis gases	UOP reported that 53 commercial units had been installed by 1992.
3	Rectisol	Lurgi GmbH and Linde AG	Heavy oil partial oxidation process of Shell and Texaco, also Lurgi gasification	Lurgi and Linde reported that there were more than 100 commercial units in operation or under construction in 1996.
4	Purisol	Lurgi GmbH	Natural gas, hydrogen and synthesis gases	Lurgi reported that there were seven commercial units in operation or under construction in 1996.
5	Catacarb	Eickmeyer & Associates, Kansas	Any gaseous stream	
6	Benfield	UOP	Synthesis gas, hydrogen, natural gas, town gas and others	UOP reported that there were 600 commercial plants which had been installed by 1992.
7	Alkanolamines (a group of amines)	Not owned by any entity	Any gaseous stream	Alkanolamines are a group of amines produced by chemical companies like Dow, Du Pont, Union Carbide etc. These chemical companies supply the chemically reactive solvents but not the process equipment.

MEA-Based Absorber/Stripper

Process Description.

A process flowsheet for the MEA absorber/stripper is shown in Exhibit F-2. Coal-based flue gas from the FGD unit at 132 °F (56 °C) is drawn by the booster fan, which increases the flue gas pressure by 5 psia to 19.7 psia (35 to 136 kPa). The boosted gas is cooled to 143 °F (62 °C) in the after-cooler and then fed to the absorber where it is contacted with the lean MEA solution flowing downward. The lean MEA solution contains 30 weight percent MEA. More than 90% of the CO_2 present is absorbed by the MEA solution. The CO_2-cleaned flue gas is discharged to atmosphere. The rich MEA solution from the bottom of absorber is pumped to the stripper via the MEA/MEA exchanger. The stripper reboiler produces water vapor, which strips the rich

MEA solution coming down the stripper. The free CO_2 and water vapor go to the condenser. Condensed water is separated from CO_2 in the gas/liquid separator. Water condensate from the separator is pumped back to the stripper top as a reflux and CO_2 is ready for further processing downstream.

The lean MEA solution from the stripper bottom exchanges its heat with the cooler rich MEA solution in the MEA/MEA exchanger. The lean MEA solution is further cooled in the lean MEA cooler and fed to the absorber.

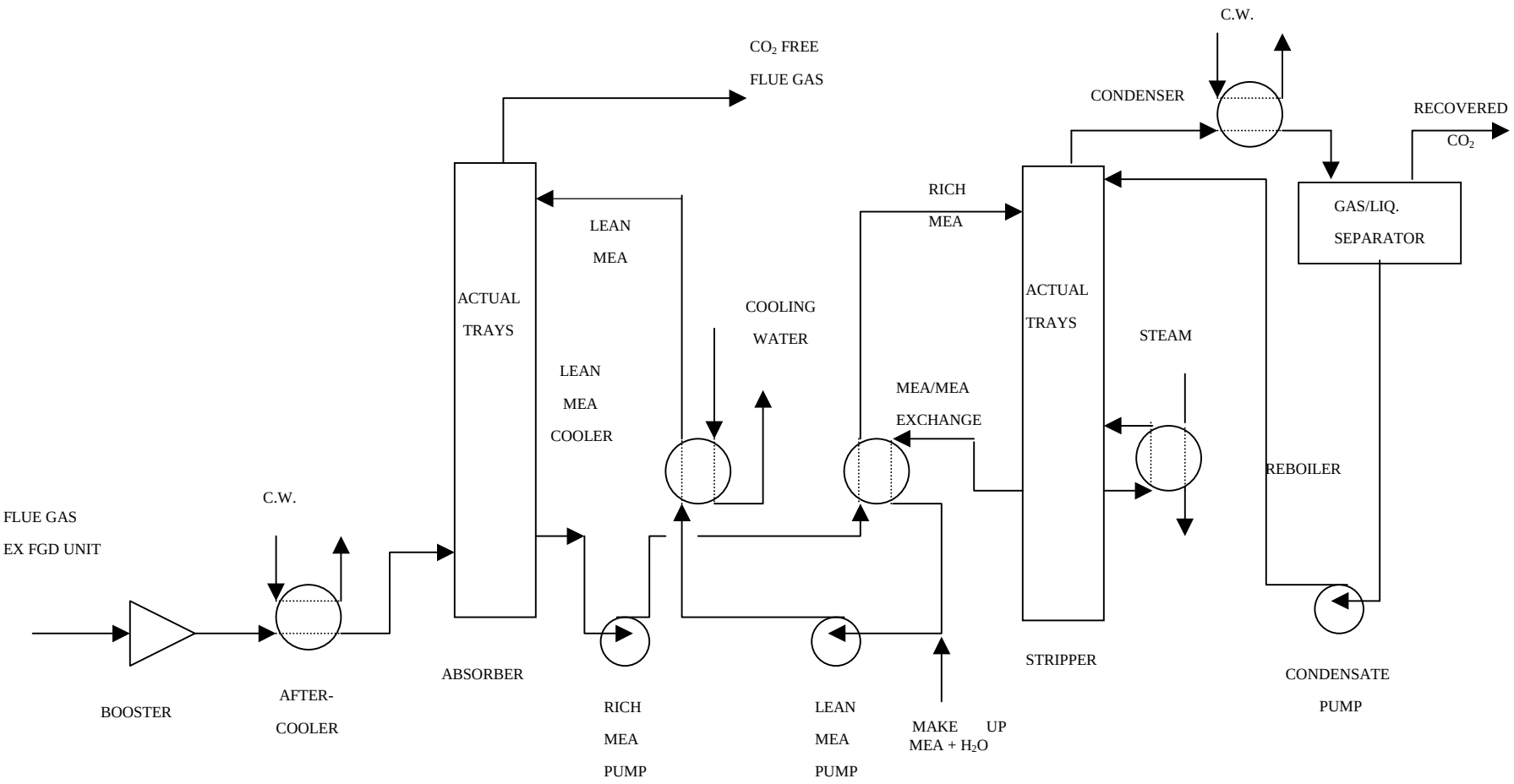

Exhibit F-2
Process Flow Diagram of CO_2 Removal by MEA Absorber/Stripper
(One of Six Trains)

Major Stream Flows

Major stream flow rates for the MEA-based absorption/stripping unit are shown in Table F-4. The total flow rate of the coal-based flue gas from the HIPPS 300 MW plant is too large to be handled in one MEA train: Six trains are needed for sufficient capacity. The flow rates in the table are for one of the six trains. The data was developed from the heat and material balances calculated by Aspen Plus™ program simulating the MEA-based absorption/stripping unit.

Major Equipment

The major equipment list is presented in Addendum B and lists the equipment in one train. Installed spare equipment is not used because of the number of lines. One exception is that all the pumps have 100% installed spares.

For sizing the heat exchangers, heat transfer coefficients were calculated using detailed calculation methods given in Kern's *Process Heat Transfer* book. The number of theoretical and actual trays required for the absorber and stripper are based on data from Kohl's *Gas Purification* book (5^{th} ed.). The diameters of the absorber and stripper were estimated with Aspen Plus. Their heights were determined using Bechtel standards. The remainder of the equipment items (pumps and tanks etc.) is also sized from Bechtel standards.

Table F-4
CO_2 Removal by MEA Absorber/Stripper
Major Stream Flow Rates

	1	2	3	4	5	6	7	8	9	10
	Flue Gas ex FGD Unit	**Boosted Flue Gas**	**Cooled Flue Gas**	**CO_2 Free Flue Gas**	**Absorber Bottoms**	**Rich MEA to Stripper**	**Stripper Bottoms**	**Lean MEA to Absorber**	**Stripper Overhead Vapor to Condenser**	**Recovered CO_2**
	Gas	Gas	Gas	Gas	Liquid	Liquid	Liquid	Liquid	Gas	Gas
H_2O	23,424	23,424	23,424	33,676	397,327	397,327	396,517	407,578	42,310	811
MEA	0	0	0	75	174,807	174,807	174,807	174,882	1	0
CO_2	46,590	46,590	46,590	4,508	59,244	59,244	17,148	17,148	42,141	42,082
O_2	7,632	7,632	7,632	7,632	0	0	0	0	0	0
N_2	155,060	155,060	155,060	155,060	0	0	0	0	0	0
A	2,673	2,673	2,673	2,673	0	0	0	0	0	0
Total flow, lb/h	235,379	235,379	235,379	203,624	631,378	631,378	588,472	599,608	84,452	42,893
Total flow, lbmol/h	8,199	8,199	8,199	7,814	26,262	26,262	25,261	25,876	3,306	1,001
Temperature, °F	131	175	143	154	149	200	246	95	212	95
Pressure, psia	14.7	19.7	18.95	14.95	18.95	24.7	24.7	15.7	20.7	19.0

Table F-4 (Continued)
CO_2 Removal by MEA Absorber/Stripper
Major Stream Flow Rates

	11	12	(Note 2) 13	(Note 2) 14	(Note 2) 15	16	17	18
	Condensate ex Gas/Liq Separator	**Steam to Reboiler**	**Cooling Water to After-Cooler**	**Cooling Water to Lean MEA Cooler**	**Cooling Water to Stripper Condenser**	**Make up MEA and Water**	**Lean MEA ex Exchanger**	**Lean MEA to Cooler**
	Liquid	Gas	Liquid	Liquid	Liquid	Liquid	Liquid	Liquid
H_2O	41,499	188,271	95,000	2,340,000	5,795,000	11,063	396,517	407,578
MEA	0	0	0	0	0	76	174,807	174,882
CO_2	60	0	0	0	0	0	17,148	17,148
O_2	0	0	0	0	0	0	0	0
N_2	0	0	0	0	0	0	0	0
A	0	0	0	0	0	0	0	0
Total flow, lb/h	41,559	188,271	95,000	2,340,000	5,795,000	11,139	588,472	599,608
Total flow, lbmol/h	2,305	10,451	5,273	129,890	321,671	615	25,261	25,876
Temperature, °F	95	281	63	63	63	60	186.5	184
Pressure, psia	19.0	50.0	75.0	75.0	75.0	14.7	24.7	24.7

NOTES.

1. Processing of all the coal-based flue gas produced at the HIPPS commercial plant requires six trains. The flow rates in Table F-4 are for one of the six trains.
2. Cooling water enters the heat exchanger at 63 °F and exits at 83 °F.

Major Equipment Cost

The estimates for major equipment costs are summarized in Table F-5. The cost of the vessels, such as the absorber, stripper and tanks are estimated based on their weight and materials of construction. Heat exchangers were priced from the cost data received with recent vendor quotations of heat exchangers. Cost of pumps and their motors were determined from *The Richardson Rapid Systems*.

Table F-5 shows the equipment cost for one train to be about $5 million. Thus, the equipment cost for the 6 trains needed for the HIPPS plant is about $31 million.

Table F-5
Major Equipment Costs
CO_2 Removal by MEA Absorber/Stripper
(1 of 6 Trains)

Equipment	Quantity	Cost 1999 Dollars
Absorber	1	210,000
Stripper	1	17,000
MEA Make up Tank	1	29,000
After Cooler	1	127,000
MEA Cooler	1	344,000
MEA/MEA Exchanger	1	481,000
Condenser	1	1,921,000
Reboiler	1	1,324,000
Booster	1	601,000
Rich-MEA Pump	2	34,000
Lean-MEA Pump	2	31,000
Condensate Pump	2	6,000
Total major equipment cost		5,125,000

Annual Consumption of Utilities

Estimates for the annual consumption of utilities and their costs are summarized in Table F-6. The cost for utilities consumption is $5 million per year for one train, or $30 million for the 6 train design. Generic unit costs are applied to the annual quantities of utilities to calculate cost. Later discussions in the report used the utilities' costs to calculate operating and maintenance costs, as inputs to the estimates of cost of electricity and cost per ton of CO_2 avoided.

Table F-6
Annual Utilities Cost
CO_2 Removal by MEA Absorber/Stripper
(1 of 6 Trains)

	Units	Quantity/train	Cost, $
Annual MEA consumption	lb/year	61,000	40,000
Annual process water consumption	1,000 gal/year	10,500	2,000
Annual power consumption	kWh/year	9,118,000	456,000
Annual steam consumption	1,000 lb/year	1,484,300	4,156,000
Annual cooling water consumption	1,000 gal/year	7,817,500	391,000
Total for one train			5,045,000
1999 Dollars			

Other Solvents-Based Absorber/Stripper Processes

Several manufactures of amine solvents for the removal of CO_2 from mixed gas streams were contacted. The solvents are used in an absorber/stripper process similar to the MEA-based absorber/stripper. The results of the discussions are described below:

Dow Solvent Based Absorber/Stripper Process

Dow manufactures amines and other solvents which are used for the removal of CO_2 from mixed gas streams. They also offer the GAS/SPEC CS-2000 process, which can be used to remove CO_2. However, when Dow was asked for a quotation for the removal of CO_2 from the HIPPS flue gas, they declined, saying that the presence of oxygen in the flue gas made it unsuitable for the GAS/SPEC CS-2000 process.

Union Carbide Solvent Based Absorber/Stripper Unit

Union Carbide manufactures amines and other solvents which are used for the removal of CO_2 from mixed gas streams. To assist with the study, Union Carbide very graciously performed a simulation for the coal-based flue gas produced at the HIPPS commercial plant using their proprietary solvent UCARSOL® AP-814.

The process flowsheet of Union Carbide's unit is shown in Exhibit F-3. Coal-based flue gas from the FGD unit at 132 °F (56 °C) is drawn by the compressor, which increases the flue gas pressure from 14.8 to 60.7 psia (102 to 418 kPa). The compressed gas is cooled to 132 °F (56 °C) in the after-cooler and then fed to the absorber where it is contacted with the lean UCARSOL® solution flowing downward. The lean UCARSOL® solution in Stream 8 contains 50 wt% UCARSOL®. More than 90% of the CO_2 present is absorbed by the UCARSOL® solution. The CO_2 cleaned flue gas is discharged to atmosphere. Rich UCARSOL® solution from the bottom of absorber is pumped to the stripper via the Lean/Rich exchanger. The stripper

reboiler produces water vapor which strips the rich UCARSOL® solution coming down the stripper. The free CO_2 and water vapor go to the condenser. The condensed water is separated from CO_2 in the gas/liquid separator. The water condensate from the separator is pumped back to the stripper top as a reflux and CO_2 is ready for further processing downstream.

The lean UCARSOL® solution from the stripper bottom stream exchanges heat with the cooler rich UCARSOL® solution in the Lean/Rich exchanger. The lean UCARSOL® solution is further cooled in the Lean Solvent Cooler and fed to the absorber.

It should be noticed that in the UCARSOL® based process the flue gas is pressurized to 60.7 psia (418 kPa) whereas in the MEA process it is pressurized to 19.7 psia (136 kPa). Therefore this process uses more power than the MEA process. Furthermore, in the UCARSOL® based process, the CO_2 free flue gas is at a pressure of 55 psia (379 kPa) whereas in the MEA based process, the same stream is at a pressure of 15 psia (103 kPa).

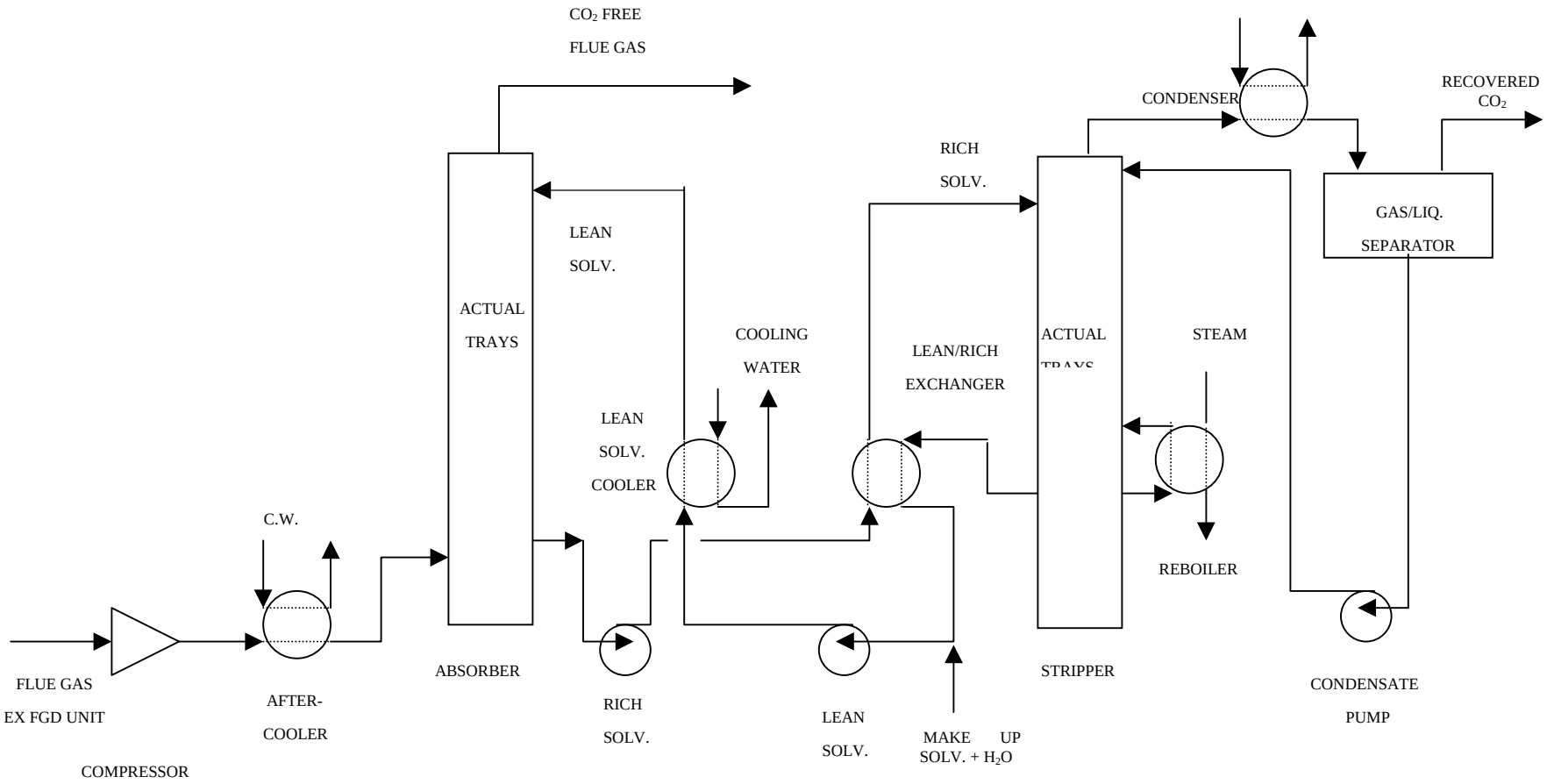

Exhibit F-3
CO_2 Removal by U.C. Solvent Absorber/Stripper
(One of Five Trains)

Major Equipment The major equipment list for the Union Carbide process is contained in Addendum C, and lists equipment for one train. Only pumps are spared with 100% installed spares used.

For sizing the heat exchangers, heat transfer surfaces were calculated using the same heat transfer coefficients as were used in the MEA process. The number of the actual trays required for absorber and stripper were provided by Union Carbide during their simulation work. The diameters of the absorber and stripper were also estimated by Union Carbide. The heights of the absorber and stripper were determined using Bechtel standards. The remainder of the equipment items was also sized using Bechtel methods.

Major Equipment Cost The estimated cost for major equipment cost is shown in Table F-7. The cost of the vessels such as the absorber, stripper and tanks was estimated by their weight and materials of construction. Heat exchangers were priced from the heat exchanger cost data from recent vendor quotations. The cost of pumps and their motors were determined from *The Richardson Rapid Systems*.

Table F-7 displays the equipment cost of one of the five trains (about $6 million). For the five trains, the equipment cost is $30 million.

Table F-7
Major Equipment Cost
CO_2 Removal by UCARSOL Absorber/Stripper
(1 of 5 Trains)

Equipment	Quantity	Cost 1999 Dollars
Absorber	1	307,700
Stripper	1	16,700
Solvent Make up Tank	1	65,100
After Cooler	1	941,800
Lean Solvent Cooler	1	290,400
Lean/Rich Exchanger	1	670,100
Condenser	1	319,700
Reboiler	1	581,900
Compressor	1	2,646,000
Rich-Solvent Pump	2	39,600
Lean-Solvent Pump	2	38,600
Condensate Pump	2	6,400
Total major equipment cost 1999 Dollars		5,924,000

Annual Consumption of Utilities The annual consumption of utilities and their estimated cost is shown in Table F-8. With the cost for one train at $5.25 million, the cost for 5 trains is about $26.25 million.

Table F-8
Annual Utilities Cost
CO2 Removal by UCARSOL Absorber/Stripper
(1 of 5 Trains)

	Units	Quantity/train	Cost 1999 Dollars
Annual solvent consumption	lb/year	73,000	164,000
Annual process water consumption	1,000 gal/year	3,032	500
Annual power consumption	kWh/year	58,098,000	2,905,000
Annual steam consumption	1,000 lb/year	679,822	1,904,000
Annual cooling water consumption	1,000 gal/year	5,523,549	276,000
Total for one train			5,249,500
1999 Dollars			

Cryogenic Cooling

Three industrial organizations were approached to propose a cryogenic process for the removal of CO_2 from the HIPPS coal-based flue gas. Only BOC Gases responded.

BOC Gases supplies equipment and offers a process called cryocleaning. The process is used to remove volatile organic compounds (VOCs) by cooling the VOC laden gas with liquid nitrogen, which, during the process, is vaporized to the gaseous state. The process is typically used where quantities of VOCs are small and the vaporized nitrogen can be used elsewhere in the plant.

To apply the cryocleaning process for flue gas CO_2 removal, the flue gas with CO_2 will be cooled in a heat exchanger by vaporizing the liquid nitrogen. By a preliminary estimate, BOC Gases found that

- the amount of nitrogen required is very large, and
- the number of cryocleaning units required is very large, and
- the vaporized nitrogen gas could not be used at the power plant.

Based on the above, BOC concluded that the cryocleaning process will not be economically feasible for HIPPS CO_2 removal, and they declined to provide a budgetary quotation for the study.

To examine the cryogenic concept, basic principles of heat transfer were used to prepare a conceptual design of a cryogenic cooling system to cool the flue gas to so that 90% of the CO_2 present will be condensed. The study did not optimize the designed cryogenic cooling system.

Process Principles

Major components of the cleaned dry flue gas are CO_2, N_2, O_2 and A. The physical data (Isalski, 1989) of the components are given in Table F-9. The exhibit shows that the boiling point of CO_2 is the highest of all the components of the flue gas. That means, that as flue gas is cooled, the first component to condense will be CO_2. Furthermore, since the boiling point of CO_2 is about 200 °F (93 °C) higher than the other components, very little of the other components will condense with CO_2 and the condensate will be virtually pure CO_2. The CO_2 condensate should not require further purification.

Table F-9
Physical Data of Flue Gas Components

Component	Boiling Point °F	Critical Temp. (T_c), °F	Critical Pressure (P_c), psia
CO_2	-109.3	87.8	1,070
N_2	-320.4	-232.6	493
O_2	-297.4	-182.2	732
A	-302.8	-188.3	705

The vapor/liquid equilibrium calculation shows that to condense 90% CO_2 under atmospheric pressure, the flue gas needs to be cooled to –180 °F (-118 °C). The cooling of flue gas down to -180 °F (-118 °C) to condense 90% CO_2 is shown in the process flow diagram (Exhibit F-4).

Process Description

The flue gas from the FGD unit of the power plant is drawn by a centrifugal booster that increases the flue gas pressure from 14.7 to 16.7 psia (101 to 115 kPa). The boost in the flue gas pressure is required to overcome the pressure drop in the downstream equipment. The compressed gas is cooled in an aftercooler to 70°F (21°C) wherein part of the water vapor is condensed. The condensate is removed from the flue gas in the condensate separator. The gas leaving the condensate separator is saturated with water vapor at 70°F (21°C). This water vapor is removed in the flue gas dryer system which consists of a glycol dryer and a packed bed dryer. The saturated flue gas enters the glycol dryer and leaves it with a moisture content of 150 ppmv. The gas exiting the glycol dryer enters the packed bed dryer which contains a UOP adsorbent called molsiv. (This is the same as the commercially known molecular sieve 4A.) The molsiv packing reduces the water content of the flue gas to less than a 0.1 ppmv. The flue gas water removal is required to avoid the plugging of the downstream heat exchangers operating at low temperatures.

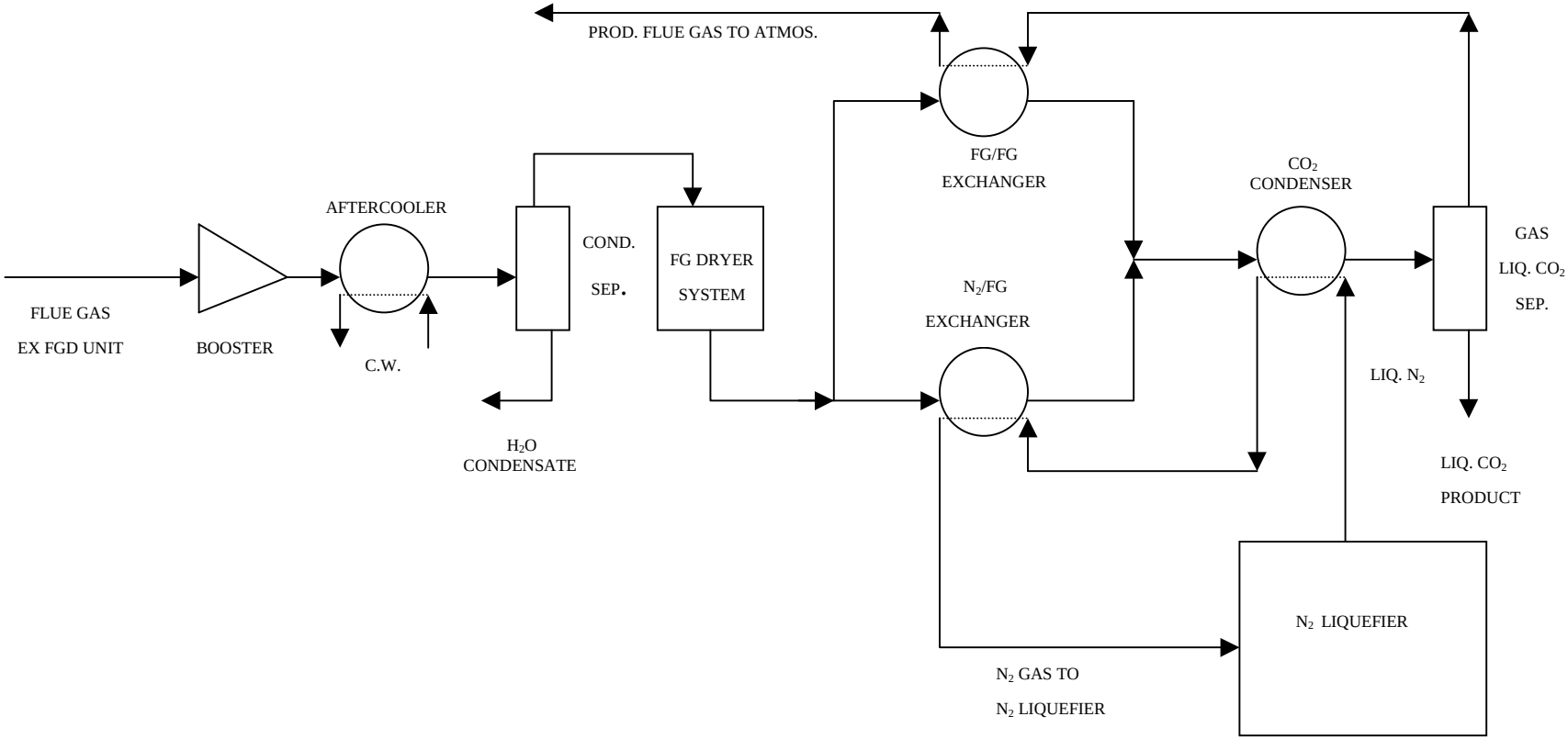

Exhibit F-4
CO_2 Removal by Cryogenic Cooling
(One of Six Trains)

The dry flue gas leaving the flue gas dryer is split into two streams. One stream goes to the FG/FG exchanger and the other goes to the N_2/FG exchanger. Both these exchangers pre-cool the flue gas from 70 to –175 °F (21 to –115 °C). The pre-cooled flue gas streams exiting the FG/FG exchanger and the N_2/FG exchanger are combined into a single stream and passed through the CO_2 condenser. In the CO_2 condenser, the latent heat of CO_2 condensation is supplied by the latent heat of N_2 boiling. The condensed CO_2 and the uncondensed flue gas exit the CO_2 condenser at –180 °F (-118 °C) and enter the gas/liquid CO_2 separator where the CO_2 condensate is removed from the bottom as the liquid CO_2 product and the cold flue gas exits from the top. The cold flue gas is directed to the FG/FG exchanger where it pre-cools the incoming dry flue gas. Nitrogen leaves the CO_2 condenser as vaporized gas and enters the N_2/FG exchanger to pre-cool the incoming dry flue gas.

The liquid nitrogen entering the CO_2 condenser comes from a nitrogen liquefier unit. After passing through the CO_2 condenser and the N_2/FG exchanger, it is returned to the N_2 liquefier unit as a gas at 0 F (18 °C).

The most common way to produce liquid nitrogen is to split air into gaseous oxygen and gaseous nitrogen in an air separation unit. The gaseous nitrogen produced in the air separation unit is then liquefied in a N_2 liquefier. For the present study, it was assumed that air separation unit is not needed. Only the N_2 liquefier unit is required. Thus, at the time of the unit start up, liquid N_2 will be imported to fill the N_2 liquefier unit.

It was noted that both the product flue gas exiting the FG/FG exchanger, and N_2 gas exiting the N_2/FG exchanger are at 0 °F (18 °C). A calculation showed that if the product flue gas exits the FG/FG exchanger at 50 °F (10 °C), then N_2 gas exiting the N_2/FG exchanger will be at –77 °F (-61 °C). Thus it will reduce the heat load on the liquefier by about 2.1 million Btu/h (2.2 million kJ/h) per train. However, what impact will this have on the power consumption and equipment size of the N_2 liquefier is not known. The impact of the redistribution of heat duties of the FG/FG exchanger and N_2/FG exchanger will be to increase the total heat transfer area from 31,400 to 64,300 ft^2 (2,917 to 5,974 m^2) per train. It is very likely that the cost of the increase in the surface area of the two heat exchangers will be offset by the savings caused by the reduction of the heat load of the N_2 liquefier, but to prove this requires a more detailed study.

For the cryogenic cooling process, liquid nitrogen was selected as a refrigerant for the following reasons:

- It is commercially used in the BOC Gases cryocleaning process.
- It is commercially available.
- It is a non-greenhouse gas. Most of the other refrigerants are harmful to the ozone layer.

Major Stream Flows

Major stream flow rates for the cryogenic cooling process is shown in Table F-10. The total flow rate of the HIPPS coal-based flue gas is too large to be handled in one train. It requires six trains. The flow rates in this table represent one of the six trains. This table was developed from calculated heat and material balances.

Table F-10
Major Stream Flow Rates
CO_2 Removal by Cryogenic Cooling

Stream	1	2	3	4	5	6	7	8	9
	Flue Gas ex FGD Unit	Boosted Flue Gas	Cooled Flue Gas	Water Condensate	Dried Flue Gas	Dry FG to FG/FG Exchanger	Dry FG to N_2/FG Exchanger	Pre-cooled FG to CO_2 Condenser	Liquid N_2 to CO_2 Condenser
	Gas	Gas	Gas/Liquid	Liquid	Gas	Gas	Gas	Gas	Gas
H_2O	23,424	23,424	2,764	20,660					
CO_2	46,590	46,590	46,590		46,590	28,254	18,336	46,590	
O_2	7,632	7,632	7,632		7,632	4,628	3,004	7,632	
N_2	155,060	155,060	155,060		155,060	94,034	61,026	155,060	107,529
A	2,673	2,673	2,673		2,673	1,621	1,052	2,673	
Total flow, lb/h	235,379	235,379	214,719	20,660	211,955	128,537	83,418	211,955	107,529
Total flow, lbmol/h	8,199	8,199	7,052	1,147	6,899	4,184	2,715	6,899	3,839
Temperature, °F	131	154	70	70	70	70	70	-175	-315
Pressure, psia	14.7	16.7	16.3	16.3	16.2	16.2	16.2	15.7	19.7

Table F-10
(continued)

Stream	9	10	11	12	13	14
	Liquid N_2 to CO_2 Condenser	Liquid CO_2 Product	Cold FG to FG/FG Exchanger	Product FG to Atmosphere	Cold N_2 Gas from CO_2 Condenser	N_2 Gas to N_2 Liquefier
	Gas	Liquid	Gas	Gas	Gas	Gas
H_2O						
CO_2		41,941	4,649	4,649		
O_2			7,632	7,632		
N_2	107,529		155,060	155,060	107,529	107,529
A			2,673	2,673		
Total flow, lb/h	107,529	41,941	170,014	170,014	107,529	107,529
Total flow, lbmol/h	3,839	953	5,946	5,946	3,839	3,839
Temperature, °F	-315	-180	-180	0	-185	0
Pressure, psia	19.7	15.2	15.2	14.7	16.7	15.7

NOTES

1. Processing of all the coal-based flue gas produced at the HIPPS commercial plant requires six trains. The flow rates in Exhibit F-4 are for one of the six trains.

Major Equipment

The major equipment list is contained in Addendum D. The addendum lists equipment for one of the six trains. The only equipment that is spared is the flue gas dryer, which requires regeneration after every eight hours. The flue gas dryers were sized by UOP. The remainder of the equipment items was sized using Bechtel standards.

Major Equipment Cost

Major equipment estimated cost is shown in Table F-11. Cost of the vessels such as dryers and separators was estimated by their weight and materials of construction. Heat exchangers were priced from cost data in recent vendor quotations of heat exchangers. Cost of the liquid nitrogen unit was obtained from published literature (Blakey, 1990).

Table F-11 estimates equipment cost of one of the six trains, or about 13 million dollars. Therefore for the six trains, the equipment cost is 78 million dollars.

Table F-11
Major Equipment Cost
CO_2 Removal by Cryogenic Cooling
(1 of 6 Trains)

Equipment	Quantity	Cost 1999 Dollars
Feed Flue Gas Dryer System	1	467,000
Product FG-Liquid CO_2 Separator-A	1	21,000
Product FG-Liquid CO2 Separator-B	1	30,000
After Cooler	1	1,103,000
CO_2 Condenser	1	630,000
FG/FG Exchanger	1	2,015,000
N_2/FG Exchanger	1	1,159,000
Booster	1	312,000
Nitrogen liquefier unit	1	7,184,000
Total major equipment cost		12,921,000
1999 Dollars		

Annual Consumption of Utilities

Annual consumption of utilities and their cost are estimated in Table F-12. This exhibit shows the cost of utilities consumption is $7.5 million per year. For the six trains, it is $45 million per year. It is noted that most of utilities cost is for the electricity consumed by the nitrogen liquefier.

Table F-12
Annual Utilities Costs
CO_2 Removal by Cryogenic Cooling
(1 of 6 Trains)

	Units	Quantity/train	Cost 1999 Dollars
Annual power consumption	1,000 kWh/year	149,926	7,496,000
Annual cooling water consumption	1,000 gal/year	1,176,044	59,000
Total utilities cost			7,555,000

Membrane Technology

Several membrane technology developers were contacted with requests for technical and commercial information about their technologies. The results of these contacts are summarized below:

UOP Gas Separation Membranes

UOP operates three commercial units for removing CO_2 from natural gas. A fourth unit is being shipped to a site in Pakistan. UOP membranes are called Separex Membranes. UOP declined to provide a budgetary quote because their membrane requires that the feed flue gas be compressed to 400 psia (2,757 kPa), and based on their experience, the compression requirement would make their process uneconomical. For example, natural gas feed to the separation membrane could be 1000 psia (6,893 kPa) or even higher because of geological pressure, and the pressure greatly enhances the membrane separation economics.

Medal Gas Separation Membranes (Medal = MEmbrane Systems Du Pont Air Liquide)

According to Medal, they have made numerous estimates for this type of application, but none have been implemented. Therefore they declined to develop a budgetary quotation for this study.

SEHAN Membrane Technology, Seoul, Korea

Offers PCFD membrane modules for the separation of CO_2 from mixed gas streams. SEHAN did not respond to several requests for information. Upon further investigation it was noted that SEHAN deals with gas separation in small quantities (liters) which are primarily for hospital application and perhaps that was the reason they never responded.

Permea Gas Separation Membranes

Air Products and Chemicals' Permea Division supplies membranes based separators called PRISM® separators. These separators operate on the principle of selective gas permeation. Every gas entering the PRISM® separator has a characteristic permeation rate that is a function of its ability to dissolve in, diffuse through and dissolve out of the hollow fiber membrane. The permeation rate is the product of the solubility and diffusivity rates of the gas in the membrane.

PRISM® separators utilize these relative permeation rates to selectively separate a "fast" gas, such as hydrogen from the "slow" gas components, such as nitrogen, in a gaseous stream. Relative rates of permeation for some common gases are shown below:

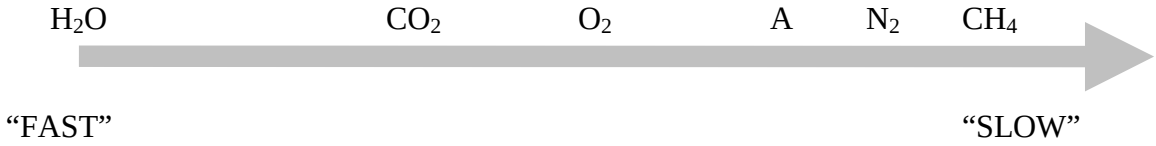

The driving force for gas separation is the difference between the partial pressure of each stream component on either side of the hollow fiber membrane.

The PRISM® separator module (Exhibit F-5) consists of a compact bundle of hollow fibers which are sealed at one end and open at the other. The open ended fibers are held in a tube sheet. The bundle is contained within a coded pressure vessel. The pressurized feed gas enters at the side inlet of the PRISM® separator and flows up through the PRISM® separator on the outside of the fibers (shell side). The fast gases selectively permeate through the membrane into the inside of the hollow fibers (bore side) which is at lower pressure. The permeate stream is collected in a manifold at the lower end of the PRISM® separator. The retentate gas exits through the upper end of the PRISM® separator at essentially the same pressure as the feed gas.

Each PRISM® separator employs hundreds of thousands of these small diameter hollow fibers to provide the maximum separation surface in a compact module. To obtain the desired performance, an appropriate number of PRISM® separator, arranged in series, parallel or cascade, are assembled into a skid mounted system.

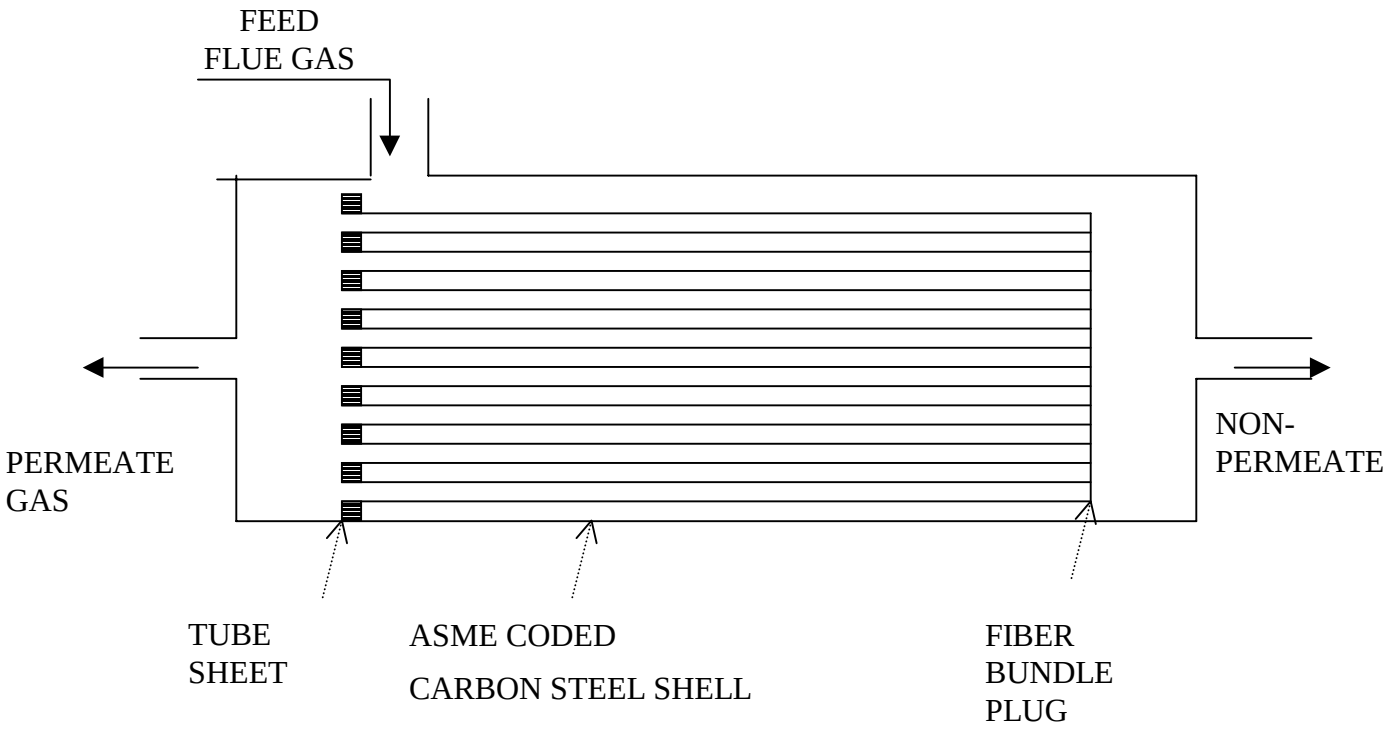

Exhibit F-5
PRISM Module

Water, at any level up to saturation, in the gas stream does not impair operations nor require pre-treatment. The system can accept particulates in suspension without pre-filtration. The presence of any liquid droplets requires mist elimination. Heavier liquid loading requires the use of a liquid knock out vessel prior to the membrane.

For the system proposed by Permea, the flue gas is compressed to 165 psia (1,137 kPa) and then fed to one end of PRISM® separator module. Almost 100% of water vapor and 90% of the CO_2 in the compressed feed flue gas passes through as a permeate gas. The remaining components of the flue gas exit the separator as the retentate stream. Pressure of the permeate (CO_2 and water vapor) is about 16 psia (110 kPa) and that of the retentate about 145 psia (999 kPa). The recovered CO_2 contains about 10% impurities on dry basis. Exhibit F-6 shows the process operations for the Permea system.

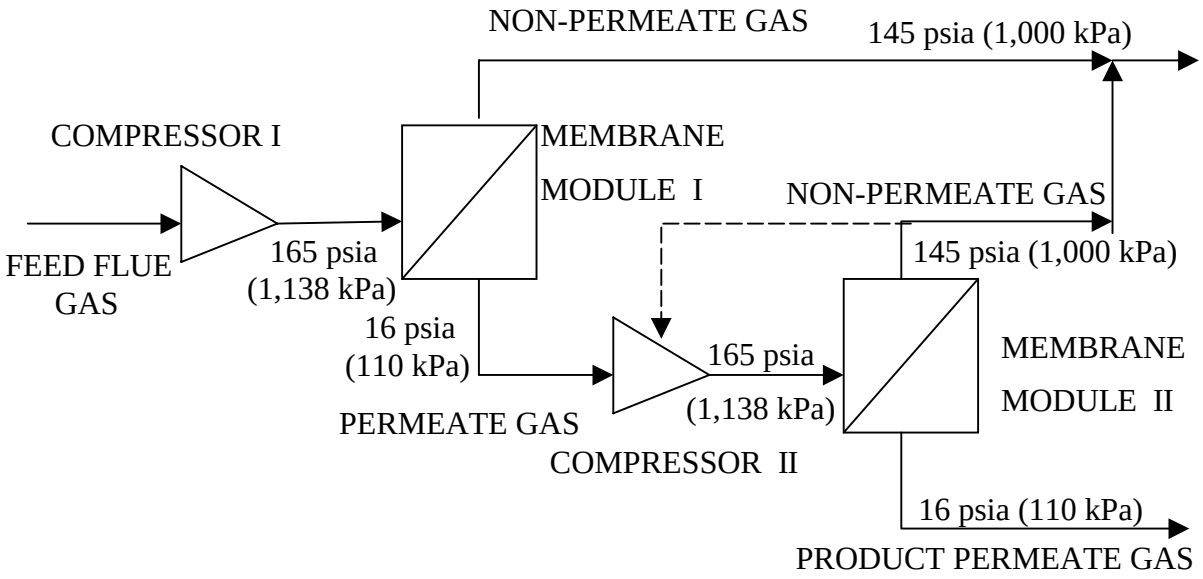

Exhibit F-6
Permea Membrane CO_2 Process

The membrane modules can be arranged in several schemes. One of the schemes is shown in Exhibit F-6. In this figure, flue gas from the FGD unit of the power plant is drawn by compressor I. This compressor increases the flue gas pressure from 14.7 to 165 psia (101 to 999 kPa). The pressurized flue gas is fed to the membrane module I. The non-permeate gas leaves membrane module I at 145 psia (199 kPa) and the permeate gas leaves at 16 psia (110 kPa). The CO_2 concentration in the non-permeate gas is lower than that in the feed flue gas and the CO_2 concentration in the permeate gas is higher than that in the feed flue gas. The permeate gas is compressed by compressor II to 165 psia (999 kPa) and fed to membrane module II.

The non-permeate gas leaving the second membrane module is at 145 psia (999 kPa) and has a higher CO_2 concentration in the non-permeate gas from the first membrane module. This non-permeate gas can either be returned to the first compressor for recycling (as indicated by the dotted line) or it can be combined with the non-permeate gas from the first membrane module and released to atmosphere as shown. The permeate gas exiting the second membrane module is at 16 psia (110 kPa) and has a CO_2 concentration much higher than that of the permeate gas of the first membrane module. If the CO_2 concentration of the permeate is still lower than what is required, it is subjected to another compression and fed to another membrane module. However, if the CO_2 concentration in the permeate stream from the second membrane module is acceptable, then it is regarded as the product stream, as shown. The product stream is now ready for further processing like liquefaction or transportation.

Permea did not supply information about the stream flows or the major equipment. Permea did provide the capital cost of one of the six trains in million of dollars as follows:

PRISM® separator modules	$48
Compressors	$115
Total	$163 million

Therefore the capital cost of the six trains in million dollars is:

PRISM® separator modules	$290
Compressors	$690
Total	$980 million

The utilities cost for one train is $34 million, and for six trains the cost is about $200 million.

Membrane Gas Absorption Technology

Several membrane gas absorption technology developers were contacted with requests for technical and commercial information about their technology. The results of the contacts are summarized below:

Kvaerner Water Systems (a division of Kvaerner) is developing a system for the separation of CO_2 from flue gas produced by a gas turbine operating on an offshore platform (Falk-Andersen, 1996). In the process, Kvaerner proposes to combine amine (MEA) absorption, amine desorption and gas separation membrane. They are using a Gore-Tex membrane made by W.L. Gore to make the CO_2 separation into amine more efficient, and more compact than the conventional method of passing the gas through a solution in a packed column. The membranes can be packed tightly; the unit works over a wider range of gas and liquid rates; and there is no foaming, channeling or other disturbances found in large columns. An amine solution is passed through very fine tubes of membrane, over which the gas is passed. CO_2 in the gas is preferentially absorbed by the amine solution through the membranes.

Kvaerner's preliminary conclusions about the process are as follows:

- An amine (MEA) absorption process is the best process
- Membrane gas/liquid contactors are the best alternatives to conventional absorption columns
- Membrane gas/liquid contactors are the best alternatives to conventional desorber columns (*i.e.*, strippers)

A demonstration trial with high pressure gas started earlier in 1998 at the Sage terminal for North Sea gas in Scotland. A trial on the flue gas separation at Statoil's gas terminal at Karstee, Norway, should have started in the Summer of 1998, and a further trial with flue gas is likely to start at a British Petroleum's site in 1999 (Miller, 1998).

Technical and cost information was requested several times from Kvaerner, but they did not respond to contacts.

At their membrane laboratories, the Research Institute of Innovative Technology for the Earth (RITE) are developing a RITE process for recovering CO_2 from flue gas by gas separation membranes. Their objective is to develop a process to produce 99.9% pure CO_2 to be used in methanol production.

The process flow sheet for the RITE process is shown in Exhibit F-7. Coal-based flue gas from the power plant is drawn by the booster fan, which increases the flue gas pressure by a few psi to overcome the pressure drop in the low pressure membrane module. The permeate gas leaving the low pressure membrane module is enriched in CO_2 content. The non-permeate gas is deprived of CO_2 and is discharged to the atmosphere.

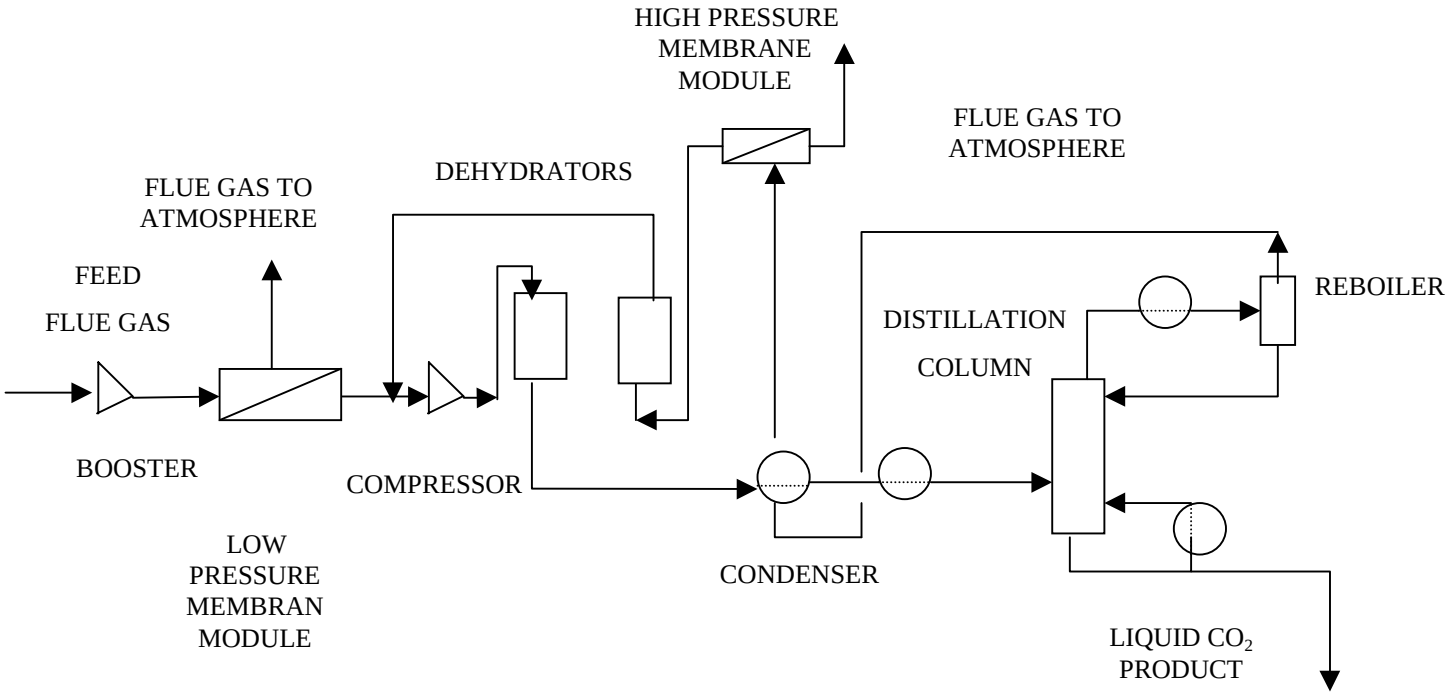

Exhibit F-7
RITE Process for CO_2 Separation

The CO_2 enriched part of the flue gas is compressed to a high pressure and is passed through a suitable dehydrator because of the cryogenic distillation downstream. There are two sets of dehydrator beds. While one bed is adsorbing the water vapor from the flue gas, the other bed is being regenerated with the permeate gas coming from the high pressure membrane module. The dehydrated gas leaving the dehydrator bed is cooled to liquefy, and is then fed to the cryogenic distillation column. Bottoms from the distillation column are 99.9% pure CO_2 and the overhead noncondensables are fed to the high pressure membrane module. In the high pressure membrane module, the permeate gas is recycled via the spent dehydrator. The non-permeate gas from the high pressure membrane module is discharged into the atmosphere as flue gas.

As the process flow diagram indicates, only a fraction of the original flue gas is compressed to a high pressure. Though it is not known how much additional membrane is required to minimize the power consumption for compression, the idea seems to be right.

RITE was asked for process and cost information to process 49,194 lb-mol/h (22,314 kg-mol/h) of flue gas, or one sixth of total HIPPS coal-based flue gas. Composition of the feed flue gas (supplied by Bechtel to RITE) and composition of the permeate gas coming out of the low pressure membrane (calculated by RITE) are shown in Table F-13. The exhibit shows that the

flow rate of the permeate gas is 14,500 lbmol/h (6,577 kg-mol/h) which is about 29% of the feed flue gas.

RITE did not supply information about the major equipment. RITE estimated the major equipment cost for processing the above flue gas flow rate as about $125 million. That means, for processing the total, six train flue gas flow rate, the major equipment cost will be about $750 million.

Table F-13
Composition of Feed Flue Gas and Permeate Gas
Exiting the Low Pressure Membrane of the RITE Process
(1 of 6 Trains)

	Feed Flue Gas	Permeate Gas
O_2, lbmol%	2.9	5.3
N_2, lbmol%	68.3	39.9
CO_2, lbmol%	12.9	39.8
H_2O, lbmol%	15.9	14.9
Total, lbmol%	100.0	100.0
Flow rate, lbmol/h	49,194	14,500

RITE estimated the operating cost as about $40 million per year for processing the above flue gas flow rate. That means, for processing the total flue gas flow rate, the operating cost will be about $240 million per year.

TNO Institute of Environmental Sciences, Appledoorn, the Netherlands, is developing a process for recovering CO_2 from flue gas. The new process is based on the combination of two known processes, membrane separation and gas absorption. In the TNO process, CO_2 is brought in contact with a suitable absorption liquid via a membrane. TNO has developed and tested several absorption liquids called CORAL (**CO**$_2$ **R**emoval **A**bsorption **L**iquid.) With this combination, the process developers are expecting to achieve a 3-fold to 10-fold equipment size reduction compared to the size of amine absorption/stripping process. The reduced size of the equipment should also lead to reduced equipment cost. The expected operational benefits include the avoidance of channeling, foaming, flooding and entrainment. The membrane gas absorption units are being supplied by an equipment manufacturing company Cirmac, Appledoorn, the Netherlands.

In the process, the flue gas travels on the one side of the low pressure membrane and liquid travels at the other side of the membrane. As the CO_2 in the flue gas permeates through the membrane from the gas side to the other side where CO_2 is dissolved by the liquid flowing over that side. The permeation of CO_2 gas from one side of the membrane to the other side depends upon the difference of CO_2 partial pressure across the membrane. As the diffused CO_2 is dissolved away by the liquid, the partial pressure of CO_2 on the liquid side of the membrane is reduced in accordance with the CO_2 solubility in and the CO_2 reactivity with the flowing liquid.

This dissolution and reaction of CO_2 with the liquid increases the rate of CO_2 permeation from gas side to the liquid side and reduces the amount of membrane surface required.

According to Cirmac, the membrane modules are cubical in shape in which membrane surfaces are arranged like the plates and frames in a plate-and-frame filter press or like the plates in a plate heat exchanger. Each module is provided with four ports. Two ports are for the entry and exit of the flue gas and the two ports for the entry and exit of the absorbing liquid. Cirmac is currently offering module size about 1.25 ft x 1.25 ft x 1.25 ft (40 cm x 40 cm x 40 cm). The module size suitable for processing the flue gas flow rates of this study will be about 2.5 ft x 2.5 ft x 2.5 ft (80 cm x 80 cm x 80 cm). Cirmac will be offering the larger module size in a couple of years.

The process flow diagram for the membrane gas absorption process developed by TNO is shown in Exhibit F-8. The flue gas from the FGD unit of the HIPPS commercial plant is drawn by a blower which increases its pressure slightly above atmospheric pressure so that the gas can pass through the membrane absorber module. In the membrane module the gas flows over one side and the lean CORAL flows over the other side. The CO_2 free gas leaves the module and is discharged to the atmosphere. The rich CORAL is directed to the stripper via the lean/rich exchanger. The liberated CO_2 leaves the stripper via condenser as the product stream ready for further processing steps. The liberated CORAL is drawn from the stripper bottoms and sent to the membrane absorber via lean/rich exchanger and lean CORAL cooler. The process is thus continued indefinitely.

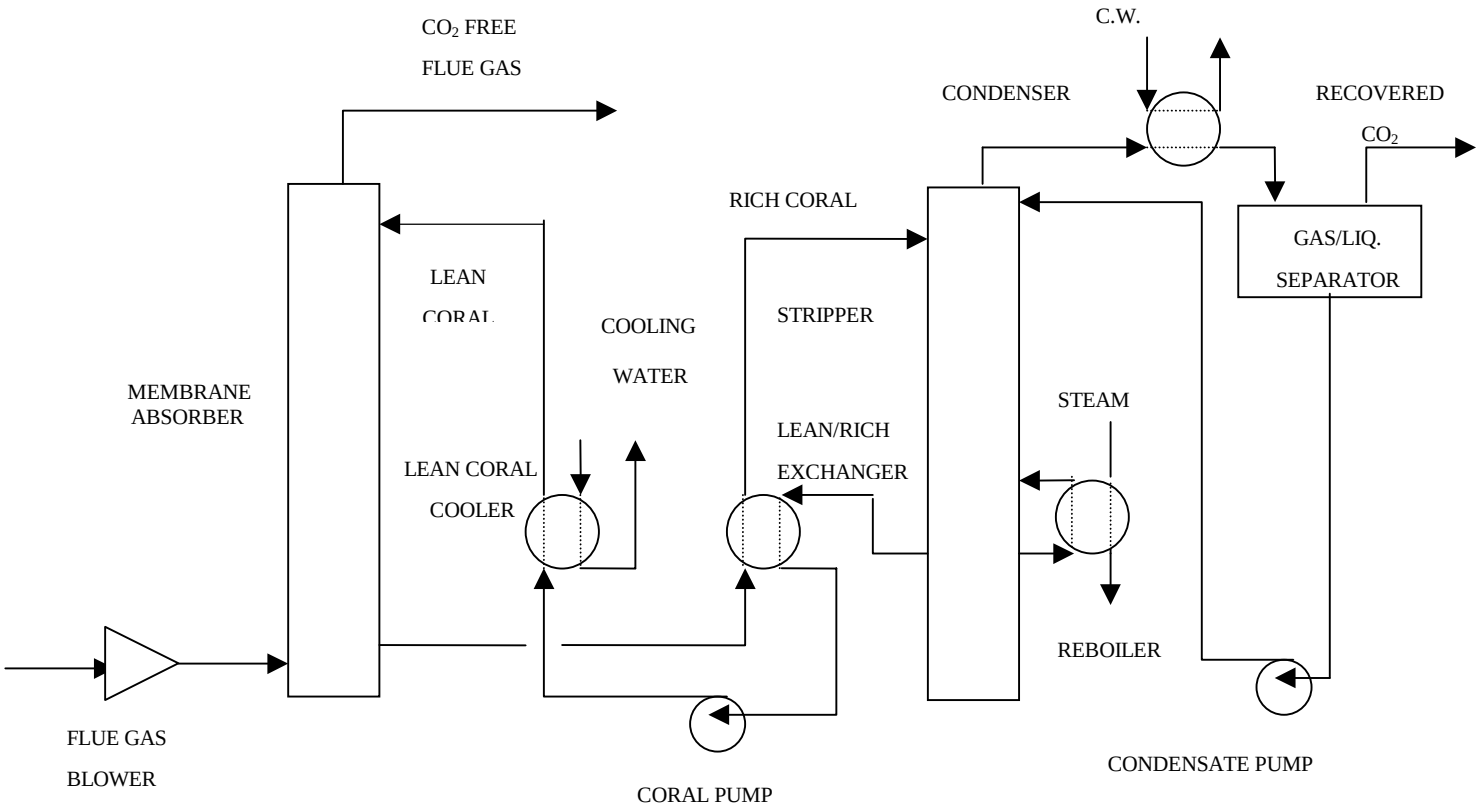

Exhibit F-8
Membrane Gas Absorption Process
(TNO/Cirmac)

Neither TNO nor Cirmac supplied any information about the major equipment for this study. Though in a letter of April 19, 1999 to Mr. Nawaz of Bechtel, Dr. Feron of the TNO Institute stated, "If you require more detailed information we would advise a research feasibility study dedicated to your flue gas problem."

In an article (Feron, 1998), TNO Institute has published information on the conceptually designed commercial plant. The capacity to produce CO_2 of this conceptual plant is such that to process all the coal-based flue gas produced at the commercial HIPPS plant would require 11 of these units. By using the figures given in the article, investment cost for processing the total coal-based flue gas comes at about $80 million.

However, it is pointed out here that the reported TNO conceptual unit processed a flue gas which has the CO_2 concentration of 3.5%. The HIPPS plant flue gas has a CO_2 concentration of about 13%. The CO_2 concentration difference of the two flue gases could reduce the TNO equipment cost for CO_2 removal. Furthermore, the TNO conceptual unit removed only 50% of the CO_2 present in the flue gas. The HIPPS study requires a 90% CO_2 removal. The higher percentage removal of CO_2 could significantly increase the equipment cost of the TNO unit. Thus the two differences between TNO conceptual unit, and the HIPPS commercial plant are likely to largely cancel each other.

From the information given in the TNO article, the operating and maintenance cost of the units required for the coal-based flue gas produced at the HIPPS plant is estimated as $35 million per year.

PSA Technology

PSA, or pressure swing adsorption, technology is a commercial process for air drying, hydrogen purification, n-paraffin removal, and small- to medium-scale air fractionation. Depending on the feed gas and the species to be adsorbed two vessels are filled with an adsorbent such as silica gel, molecular sieves or molecular sieve carbon. One vessel serves as an adsorbing bed, with the feed entering at pressure; up to 150 psia (1,034 kPa). When the bed is saturated, the feed is switched to the second vessel. Pressure in the first (spent) vessel is lowered to release the adsorbed species. The adsorbent in the vessel is regenerated and the vessel is pressurized to make it ready for another cycle. The process is repeated in the second vessel.

CarboTech, Industrieservice GmbH, Essen, Germany, is a supplier of pressure swing adsorption (PSA) units: Their representative, Gas Land in Fairfield, California was contacted for technical information and a budget quotation for the removal of CO_2 from the flue gas. CarboTech opined that the natural gas-based flue gas is too dilute for CO_2 removal, and although the CO_2 concentration was better in the coal-based flue gas, its flow rate and a 90% recovery is a very difficult job. Recovery would require a very large number of PSA units which will create operational problems and the cost will be very high. Therefore, CarboTech declined to prepare a budget quotation for this study.

Oxygen Combustion

Except for gasification installations, existing commercial power plants use air for combusting coal, with the major coal combustible components being carbon and hydrogen. The oxygen in air combines with the carbon and and hydrogen to produce carbon dioxide and water wapor. The nitrogen in the air is 79 mole percent of the total, and acts as a diluent and keeps the adiabatic flame temperature low. Nitrogen in the combustion air becomes the major component of the flue gas, making the flowrate very large, and removal of CO_2 difficult. If the coal is burned with oxygen instead of air, the major components of the flue gas will be CO_2 and water vapor only. The CO_2 from this mixture can be removed by compressing and cooling, followed by glycol dehydration. The adibatic flame temperature can be moderated by recirculating a part of the recoverd CO_2.

For a rigorous evaluation of the oxygen, or enriched air combustion technology and the removal of CO_2, one needs to account for the effect of oxygen combustion on the following items at the HIPPS commercial power plant.

- thermodynamic cycle.
- size of the furnace.
- sizes of the heat exchangers

The scope of the present study only allows for a more simplified approach as described below.

The adiabatic flame temperature was estimated for the HIPPS coal based on 20% excess air. This calculation showed that for no loss of heat and for no dissociation of the combustion products, the adiabatic flame temperature was about 3,000 °F (1,649 °C). Another calculation was made for the same coal being burned with 98% pure oxygen from an air separation unit. To the oxygen case products of combustion, clean CO_2 was added until the adiabatic flame temperature of 3,000 °F (1,649 °C) was reached. By keeping the same flame temperature (3,000 °F (1,649 °C) in both the combustion calculations, the total enthalpy of the combustion products of both the calculations are the same, and it is very likely that the size of the heat transfer equipment will be the same also.

In the oxygen based combustion calculation, 98% oxygen was used because of power consumption considerations (John McKetta's Encyclopedia of Chemical Processing and Design, 1990). Power consumption rises sharply for an oxygen purity exceeding 98%. For the production of oxygen with a purity lower than 98%, the power consumption curve becomes flat. Therefore 98% oxygen was used in the calculation to minimize the amount of nitrogen (impurity in oxygen) in the flue gas and at the same minimize the power consumption by the oxygen producing unit. More detailed trade-off work is required to validate the oxygen specification if the issue is further studied.

Results of the air and oxygen combustion calculations are shown in Table F-14.

Table F-14
Comparison of Air Combustion and Oxygen Combustion
Basis: 100 lb HIPPS Coal

	Air Combustion	Oxygen Combustion
Adiabatic flame temperature, °F	3,000	3,000
Mass of gas combustion products, lb	1,290	1,223
Moles of gas combustion products, lbmol	43.8	29.8
CO_2 concentration in dry flue gas, mol%	12.4	94.3
High-emissivity components, mol%	18.2	95.2

A comparison of the two combustion calculations shows that the mass of CO_2 required to achieve the 3,000 °F (1,649 °C) flame temperature is less than that of the nitrogen in the air. This is because the mass heat capacity of CO_2 is higher than that of nitrogen. Moreover, because the molecular weight of CO_2 is higher than that of N_2, the molar flow rate of CO_2 required to maintain the same adiabatic flame temperature is lower than that of nitrogen. Thus, the molar and volumetric flow rate of gaseous combustion products inside the furnace will be much lower than that for air combustion. Therefore, for the same amount of heat transfer, the pressure drop for oxygen combusion will be less than for air combustion.

Table F-14 also shows that the CO_2 concentration in flue gas increases from 12.4 mol% with air combustion to 94.3 mol% with oxygen combustion. The remaining components of the oxygen-based flue gas are the excess oxygen, nitrogen impurities in the combustion oxygen, and the nitrogen in coal. If the excess oxygen is reduced say from 20 to 10%, the CO_2 concentration in the oxygen-based flue gas will be higher. It should be noticed that even with 20% excess oxygen, the CO_2 concentration in the oxygen based flue gas is so high that it can be regarded as the product CO_2 ready for further treatment or sequestering.

In the chapter on Furnace Calculations, Kern's *Process Heat Transfer* book reads as follows:

"The diatomic gases such as O_2, N_2, and H_2 have very poor emissivities, so low that they may be considered zero in furnace-design work. On the other hand, H_2O, CO_2, and SO_2 have good emissivities (though much poorer than most solid materials), and CO has a fair emissivity. The sources of radiation may be referred to specifically as the radiating constituents in the combustion products. Ordinarily H_2O and CO_2 are the only radiating constituents which need be considered, since the small amount of sulfur in most fuels is negligible and furnaces are generally operated with sufficient excess air to eliminate CO."

Table F-14 shows that comparing air combustion to oxygen combustion, the high emissivity components of flue gas increase from 18% (air combustion) to 95% (oxygen combustion). The increased emissivity will mean an increased heat transfer coefficient and less heat transfer equipment. This agrees with the findings (Kiga, 1996) of T. Kiga who conducted experiments on the combustion of coal with oxygen and recycled flue gas (i.e., CO_2). Their experiments used a horizontal, cylindrical type furnace with a water wall lined with refractory. The furnace inside diameter was 4.25 ft (1.3 m) and length 25 ft (7.5 m). The exhaust gas entered a stack through a flue gas cooler, a tubular air preheater, a multi-cyclone dust collector and a bag filter. Part of flue gas was removed downstream of the bag filter and recycled as the primary gas for transporting pulverized coal and secondary gas for combustion. Oxygen was supplied by evaporating liquid oxygen. Part of oxygen was mixed with the secondary gas for combustion and another part was directly injected into the burning area of the furnace. Combustion tests were performed at the firing rate of 220 lb/h (100 kg/h) using three kinds of bituminous coal.

Their combustion results showed that air-blown combustion produced a large amount of NO_x in the flame while oxygen/recycled flue gas combustion produced a remarkably small amount of NO_x. This is mainly due to the decomposition of recycled NO_x in the flame. When the air combustion was carried out with staging, the NO_x produced was only 25% of the NO_x produced in air combustion without staging. However, the reduction of NO_x in the oxygen/recycled flue gas staged combustion was only 50%. It is thought that the NO_x recycled in the oxygen/recycle flue gas staging was not decomposed because there is a lack of reducing components like hydrocarbons.

On the basis of the experimental results they simulated the performance of a 48 ft (14.5 m) deep by 108 ft (32.9 m) wide by 221ft (67.5 m) high furnace and concluded that oxygen combustion might reduce the furnace size.

Equipment Cost of the Oxygen Supply Unit

Without considering the cost and performance benefits of factors discussed above, the equipment cost of the oxygen production unit, which is the major piece of equipment required for

switching from the air-based combustion to the oxygen-based combustion, was estimated. The oxygen production unit is a cryogenic air separation system producing 98% pure oxygen gas. The 300 MW_e HIPPS plant uses 124,574 lb/h (57507 kg) coal. To burn this much coal with 20% excess oxygen, 3,500 tons/day (3,175 tonnes/day) 98% pure oxygen is required. It was assumed that there will be two trains of air separation units, each producing 1,750 ton/day (1,588 tonne/day) 98% pure oxygen. Equipment cost of the two air separation units is estimated to be $27.5 million.

Utilities Cost of the Oxygen Supply Unit

Again without trying to account for the cost and performance issues, an estimate of 745,000 kWh per day was made for the electricity required to operate the two oxygen units. For 300 operating days per year and $.05 per kWh, the estimated cost is about $11.2 million per year.

Comparison of Various CO_2 Removal Processes

To review, seven processes are examined in this topical report. Comparisons are made and explained in the following pages. Capital costs and other issues are shown in Table F-15. The first six processes in the table remove CO_2 from the flue gas; the seventh process produces flue gas which is nearly pure CO_2. The first six processes are grouped for discussion first. The oxygen combustion process will be discussed last.

Table F-15
Comparison of CO_2 Removal Processes

	Process	Removal Rate %	CO_2 Gas Stream Purity %	Capital Cost $ millions	State of the CO_2 Product
1	MEA Absorption	90	100	63	Gas
2	UCARSOL Absorption	90	100	61	Gas
3	TNO Membrane Gas Absorption	90	100	81	Gas
4	Permea Membrane	90	90	1,980	Gas
5	Cryogenic Cooling	90	100	158	Liquid
6	RITE Membrane	90	100	1,520	Liquid
7	Oxygen Combustion with CO_2 Recycle	100	94	57	Gas

The capital costs based on earlier equipment cost data are very much order-of-magnitude estimates with high potentials for changes when manufacturing economies of scale, detailed engineering, trade studies and other work is applied to the estimates.

The table shows the gas absorption processes (MEA-based and Ucarsol-based), which have been in commercial operation for several years, require the lowest capital cost; about $60 million. The TNO process based on membrane gas absorption and is near commercialization, is a close second in capital cost. The cryogenic separation capital cost is much higher, about $160 million. The cryogenic process examined in the study is not optimized, and there is room for cost reductions which might make the cryogenic process promising from a capital cost aspect.

The two membrane processes (Permea and RITE) require high capital costs. It is noted that although the RITE process produces liquid CO_2, the developers estimate a lower capital cost than for the Permea process which produces gaseous CO_2. This may be due to the low pressure membrane operation of the RITE process.

CO_2 Separation Costs – Cost per ton of CO_2 Avoided and Cost of Electricity

Capital costs are only one of the criteria needed to evaluate CO_2 separation systems. The cost of CO_2 avoided by the installation of a separation system has become a quasi-industry standard to compare technologies, and the resulting increase in the cost of electric power is a major issue for judging commercial feasibility of the separation operation. The International Energy Agency (IEA) published several reports on its web page () and compared costs per tonne for CO_2 avoided. While there was not enough detail in the IEA material to be sure that an equivalent comparison can be made with HIPPS, the writer feels that there was sufficient information that considering the accuracy of IEA's estimates and those of the study, a valid approximate comparison can be made.

Table F-16 shows the data summarized from the IEA web material. The IEA figures reflect fuel costs of $2.50 per GJ for coal, and $3.50 per GJ for natural gas. The calculations used a discounted cash flow basis of 10% cost of money. The table data does not include costs for CO_2 liquefaction, transport nor disposal.

Table F-16
IEA Comparison of CO2 Separation Technologies

IEA Plant Type and Data	PF + FGD	GTCC	IGCC	O2 with CO_2 Recycle
Size (MWe)	500	465	503	500
SO_2 % Reduction	90	not required	99	
Reference Power Cost (without CO_2 separation, mills per kWh	49	35	53	78
Reference Plant Efficiency, lower heating value basis	40	52	42	33
CO_2 Separation Technologies:				
Monoethanolamine (MEA) Absorption Data				
MEA CO_2 Captured	90%	85%	90%	99%
Cost CO_2 Avoided $/tonne [1]	35	55	87	16
Power Cost with MEA Mills per kWh	74	53	112	94
Pressure Swing Adsorption (PSA) Data				
PSA CO_2 Capture	95%	95%	95%	95%
Cost CO_2 Avoided $/tonne [1]	84	544	205	21
Power Cost with PSAMills per kWh	114	140	201	98
Membrane Data				
Membrane CO_2 Capture	80%	80%	80%	80%
Cost CO_2 Avoided $/tonne [1]	47	335	125	9
Power Cost with Membrane Mills per kWh	83	125	129	90
Cryogenic Data				
Cryogenic CO_2 Capture	na	na	85%	85%
Cost CO_2 Avoided $/tonne [1]	na	na	23	26
Power Cost with Cryogenics Mills per kWh	na	na	78	109

1. Cost per tonne of CO2 avoided is the difference between plants with and without CO_2 removal, including the performance penalty of reduced efficiency caused by power consumed in the CO_2 separation and capture operation.

MEA for Separation

Calculations for the HIPPS case with MEA for separation were made following the IEA methodology as closely as the information permitted (Table F-17 and Table F-18). The calculations are explained in relative detail for future reference, or review and revision should another method be applied.

Table F-17
Basis for HIPPS Cost of CO_2 Avoided

ITEM	VALUE
Capacity MWe (net)	292.2
HIPPS Capital Cost 1,000s	$311,500
HIPPS O&M Including Fuels 1,000s	$65,145
HIPPS Power Production kWh/year	2.30E+09
HIPPS COE @ 10%, 20 years	$0.042
MEA Energy Requirement MWe	24
MEA Capital Cost 1,000s	$62,800
MEA O&M 1,000s	$3,000
HIPPS Power Production kWh/year	2.11E+09
HIPPS COE @ 10%, 20 years	$0.051
CO_2 avoided tons per year	1,073,200
CO_2 avoided tonnes per year	975,600

The HIPPS plant capacity and power production without CO_2 separation, and the capital and O&M costs are from the HIPPS commercial plant conceptual design. Power production is the product of capacity times 365 days, 24 hours and a 0.9 factor for estimated on-line baseload operations. The HIPPS cost of electricity, COE, is the present value of the capital cost and O&M including fuel. The cost number is divided by the present value of kWs produced to obtain 42 mills, or 4.2 cents per kWh.

The MEA energy requirement, capital and O&M costs are from data collected in the present study. The COE for the HIPPS plant with MEA separation is calculated the same as for the reference plant with the costs for MEA added, and the power production reduced by the energy requirements of the MEA separation process. The accounting for energy consumed by the absorption process is an issue for the cost calculations: The MEA process needs steam (heat) to release the CO_2 and recycle the absorbent. To calculate the reduction of the power plant capacity caused by increased auxiliary power requirements, the steam was equated to electric power. A

detailed process investigation of the HIPPS plant with MEA absorption might result in different impacts on the plant's energy production.

Finally, the annual cost is calculated in Table F-18 below as the product of the power produced and the unit COE for the reference HIPPS plant and for one with MEA CO_2 separation added. The unit cost for CO_2 avoided is calculated by dividing the difference in costs by the amount of CO_2 removed. This amount is some 1.1 million tons per year (975 thousand tonnes per year), which is 90% of the coal-fired furnace flue gas CO_2 removed by the MEA process (including additions to the base case for CO_2 generated by the power consumed in the MEA system). The gas turbine exhaust is too dilute to be treated, and is released to the atmosphere.

Table F-18
Costs for CO2 Avoided

ITEM	COST
Annualized Cost of Reference Plant	$97,262,000
Annualized Cost with MEA Added	$107,113,000
Cost per ton of CO_2 avoided	$9.90
Cost per tonne of CO_2 avoided	$10.90

The estimated unit cost of about $11 per tonne compares favorably with the IEA estimates. However, any comparison should note that for HIPPS only the coal-based portion of the fossil fuel used is treated, and thus, only about 70% of the total potential CO_2 removal is accomplished. If the HIPPS plant design is used with higher efficiency cycles, the costs of CO_2 separation are expected to be reduced, but cost estimates have not been performed for advanced HIPPS and the degree of the reduction is not presently known.

Oxygen Combustion Process

The oxygen combustion concept, differs from the other CO_2 capture processes by instead of removing CO_2 from a flue gas, the concept produces a flue gas which is mostly CO_2. Therefore, it is not the cost of the CO_2 separation, but it is the cost of switching from air combustion to oxygen combustion. The delta capital cost (largely the installation of an air separation plant) of this process is estimated at $57 million and the CO_2 recovery cost as about $6 to $7 per ton of CO_2 avoided. The estimate does not include any possible benefits from oxygen combustion to reduce the furnace size and the heat exchangers sizes at the HIPPS commercial power plant. The relatively low cost numbers, and the potential for cost reduction by more detailed engineering make oxygen combustion (or enriched air combustion) a strong candidate for future CO_2 removal trade studies. Also, use of oxygen for combustion could allow removal of the CO_2 generated by both natural gas and coal at the HIPPS plant. For consistency with the MEA HIPPS removal case, only enough oxygen production is costed to support the coal portion of the HIPPS plant fuel consumption.

Tables F-19 and F-20 show data for the oxygen combustion concept similar to the MEA process case.

Table F-19
Basis for HIPPS Cost of CO2 Avoided
Oxygen Combustion Concept

ITEM	VALUE
Capacity MWe (net)	292.2
HIPPS Capital Cost 1,000s	$311,500
HIPPS O&M Including Fuels 1,000s	$65,145
HIPPS Power Production kWh/year	2.30E+09
HIPPS COE @ 10%, 20 years	$0.042
Oxygen Combustion Energy Requirement MWe	31
Oxygen Combustion Capital Cost 1,000s	$56,700
Oxygen Combustion O&M 1,000s	$4,000
HIPPS Power Production kWh/year	2.06E+09
HIPPS COE @ 10%, 20 years	$0.052
CO_2 avoided tons per year	1,586,100
CO_2 avoided tonnes per year	1,441,900

Table F-20
Costs for CO2 Avoided
Oxygen Combustion Concept

ITEM	COST
Annualized Cost of Reference Plant	$97,262,000
Annualized Cost with Oxygen Combustion Added	$107,205,000
Cost per ton of CO_2 avoided	$6.30
Cost per tonne of CO_2 avoided	$6.90

Conclusions

The primary conclusions from the study are listed below.

There are several technologies that can remove CO_2 from the HIPPS flue gas. From the currently available commercial processes, and those processes with near term potential for technical feasibility, MEA absorption and oxygen combustion have the least impacts on cost of electricity, and lowest costs per ton of CO_2 captured.

Compared to conventional pulverized coal-fired power systems and IGCC, the HIPPS plant design has relative advantages for CO_2 reduction because of its higher efficiency, and opportunity to capture the CO_2 concentrated in the coal-derived flue gas.

There are areas in the HIPPS design with CO_2 capture (MEA absorption and oxygen combustion) where optimization engineering could potentially lower costs.

To fully evaluate the impact of CO_2 capture on HIPPS and other technologies, a more site specific comparison with liquefaction of the CO_2 gas, transportation and sequestration all included.

A detailed methodology for computing CO_2 capture costs would be useful to the US DOE and industry so that comparable figures can be calculated for different cases.

While the increases for the cost of electric power are substantial when CO_2 capture is added to the HIPPS plant, the higher cost does not appear prohibitive if environmental benefits can be proven by the CO_2 removal. In addition to the approximately 20% increase of the cost of electricity from CO_2 capture, there will be significant and very site specific costs for liquefaction, transport and sequestration, which could easily double the COE increase.

References

Blakey, P. G. and Mostello, R.A., "*Nitrogen, Oxygen, and Argon Production from Air*" in John McKetta et al, *Encyclopedia of Chemical Processing and Design,* Volume 31, p. 205, Dekker, New York, 1990.

Falk-Pedersen, O. and Dannstrom, H., "Separation of Carbon dioxide from Offshore Gas Turbine Exhaust", *Proceedings of the Third International conference on Carbon Dioxide removal*, Cambridge, MA, USA, 9-11 September 1996, Pergamon.

Feron, Paul H.M. and Jansen, Albert E., *Techno-Economic Assessment of Membrane Gas Absorption for the Production of Carbon Dioxide from Flue Gas*, Fourth International Conference on Greenhouse Gas Control Technologies, Interlaken, Switzerland, August 30-September 2, 1998.

Isalski, W. H., *Separation of Gases*, Clarendon Press, Oxford, 1989.

John McKetta's Encyclopedia of Chemical Processing and Design, p.214 Volume 31, Dekker, 1990 contains a graph showing oxygen purity versus power required for the production of oxygen.

Kiga, T., et al (Characteristics of pulverized-coal combustion in the system of oxygen/recycled flue gas combustion, *Proceedings of the Third International Conference on Carbon Dioxide Removal*, Cambridge, MA, 9-11 September 1996).

Miller, Andrew article, "The gas that no one wanted", Re*view* April – June, 1998, p. 11.

Robson, F.L., Ruby, J., and Seery, D.J., *Greenhouse Gas Reduction Through the Use of High Performance Power Systems (HIPPS)*, ASME IJPGC, Denver, Co., Nov. 1997.

Seery, D. J., et al *Final Engineering Development of Coal-Fired High Performance Power Systems, Phase II and III*, Quarterly Progress Report, January 1 – March 31, 1998.

.

Addendum A - CO_2 Removal Literature

(Appendix F)

The following lists published sources and Internet web sites that were found/reviewed during the study. Extracts from some of the literature are presented to document issues especially relevant to the HIPPS CO_2 removal work.

- IEA Greenhouse Gas R&D Program Summary Reports posted at the web site: http://www.ieagreen.org.uk/sr1p.htm.
- Proceedings of the Third International Conference on Carbon Dioxide Removal, Cambridge, MA 9-11 September 1996**.**
- Proceedings of the Advanced Coal-Based Power and Environmental Systems '98 Conference, Morgantown, July 21-23, 1998.
- Proceedings of The Fourth International Conference on Greenhouse Gas Control Technologies, Interlaken, Switzerland, August 30 – September, 1998, were not available at the time of this writing.

The following are extracts from articles in the above literature.

IEA Greenhouse Gas R&D Program, "Greenhouse Gas Emissions from Power Stations," the first in a series of public summaries of work, September 1998. From the internet www site: http://www.ieagreen.org.uk/sr1p.htm

This report has the following sections.

- Greenhouse Gases & Oxides of Nitrogen
- Greenhouse Gas Emissions from Pulverized Coal Power Plant
- Criteria for the Case Studies
- Greenhouse Gas Emissions from Natural Gas Fired Combined Cycle Power Plant
- Greenhouse Gas Emissions from Integrated Gasification Combined Cycle Power Plant
- Greenhouse Gas Emissions from Carbon Dioxide Recycle Power Plant
- Greenhouse Gas Emissions Comparison of the Power Plants

Greenhouse Gases & Oxides of Nitrogen

Global warming potential (GWP) is a concept which aims to measure the possible warming effect of a gas relative to CO_2. It takes into account the energy absorption capacity of the gas and its lifetime in the atmosphere. GWP should thus always be quoted for a specific time period. It is useful for comparing the relative strengths of greenhouse gases on a molar basis. [p. 1]

Coal derived CO_2, is believed to contribute about 20% of the enhanced greenhouse effect. It has been estimated that global fossil fuel emission in 1989 and 1990 were 6.0 ($\pm$ 0.5) gigatonnes of carbon (GtC) in 1987. To put these figures in perspective, the atmosphere contains about 750 GtC and deforestation annually releases about 2 GtC to the atmosphere. [p. 1]

The GWP of CH_4 is 11 relative to CO_2 over 100 years.

Nitrous oxide has a GWP 270 times that of CO_2 over 100 years. The emissions of N_2O from stationary sources due to combustion of fossil fuels, is very small. Soils are the main source of N_2O emissions. [p. 1]

Criteria for Case Studies

The specifications that were given to the contractors performing the power generation case studies are only outlined here. It was important that each scheme used the same assumptions, so that meaningful comparisons of the results could be made. Contractors were asked to use state of the art technology and state of the art emissions control. Current European environmental legislation is assumed.

The base case was a 500 MW (electricity sent out from the) power plant, with a 35 years working life. Costs are given in US dollars, nominally set at the first quarter of 1992. The power plant is assumed to be seawater cooled and located on the coast in Western Europe. The ambient conditions are 59 °F, 14.692 psi (15 °C, 1.013 bar) relative humidity 60% and the cooling water is available at 59 °F (15°C). The design fuel is an Australian bituminous coal of 0.86% as-received sulfur content from the Drayton mine. Plant emissions are controlled to comply with current EEC Directives as a minimum. Also, 90% removal of SO_2 is specified.

The analysis of the coal used is as given in the following table.

Comments on the table are:

1. Total of the Ultimate Analysis, Dry Ash-Free Basis, should be 100.0 but the table shows 87.0.
2. Asterisks mark the heating value entries in the table. According to the top entry, low heating value (LHV) of the coal is 11,114 Btu/lb (25.85 MJ/kg). This value falls within the range of the heating values of coal. However, the heating value entries near the bottom of the table are 3,035 and 2,515 Btu/lb (7.06 and 5.85 MJ/kg, respectively). It is likely that these values are typed incorrectly in the original article. The correct values are probably 11,634 and 11,114 Btu/lb (27.06 and 25.85 MJ/kg, respectively).

Drayton Mine Coal Analysis

Moisture (in as received coal), %weight	9.5
Ash (in as received coal), %weight	1.2
Heating value (LHV), MJ/kg	25.85
Ultimate Analysis, Dry Ash-Free Basis	
C, % weight	82.5
H, % weight	0.60
O, % weight	0.97
S, % weight	1.10
N, % weight	1.80
Cl, % weight	0.03
Total	87.00
Higher heating value (as received basis), MJ/kg	7.06
Lower heating value (as received basis), MJ/kg	5.85
Hardgrove index	45
Chlorine (as received basis), % weight	0.03

Greenhouse Gas Emissions from Pulverized Coal Power Plant

This was the base line study of four power generation plants selected to ensure a wide range of CO_2 conditions in the exhaust/flue gas. The plant is a seawater cooled, conventional pulverized coal-fired steam plant with limestone/gypsum flue gas desulfurization. The net power is 500 MW.

The boiler module provides steam for a condensing steam turbogenerator. Flue gas from the boiler module, (after particulate separation in electrostatic precipitators) is cooled, scrubbed in a flue gas desulfurization unit, reheated and then sent to the stack. The plant includes all the necessary auxiliary power, water and waste treatment systems. The boiler is a conventional drum type, utilizing natural circulation. NO_x control is by combustion measures only. The following table summarizes key results discussed in the study overview.

Summary of Key Results for a Fuel Cost of 2$/GJ

Plant	SO_2 % Removal	Size MW_e	Efficiency %	Cost, $/kW	CO_2 Emissions kg/MWh	Power Cost mills/kWh
Subcritical	90	500	40	1060	830	49
Subcritical	95	500	40	1080	830	50
Subcritical	90	250	40	1300	830	59
Supercritical	90	500	40	1060	770	47

Most of this carbon dioxide shown in the above table comes from coal, although about 0.5% is released by the limestone.

The capital cost of the reference plant has been estimated from the plant mass and energy flows and a breakdown is given in the following table.

Capital Cost of the Reference Plant

	$ (million 1991)
Coal receiving and storage	24
Coal handling	3
Boiler plant	124
Electrostatic precipitators	24
Steam turbine generator	107
Cooling system	11
Water treatment and waste water plant	7
Electrical distribution	20
Controls and instrumentation	11
FGD plant	56
Miscellaneous (buildings, fire protection, fuel oil system, support systems, mobile equipment, building services)	72
Total	458
Contingency	46
Total plant cost	504
Land clearance etc.	25
Total excluding interest during construction and commissioning	529
Specific investment cost, $/kW	1,060

Breakdown of the generating costs for 90% sulfur removal in mills/kWh is as follows:

Electricity Generating Cost for 10% DCF

Item	mills/kWh
Capital	21
Fixed operating	9
Variable operating	1
Fuel ($2.5/net GJ)	22
Total	53

[p. 3]

Greenhouse Gas Emissions from Natural Gas Fired Combined Cycle Power Plant

The study considered North Sea natural gas being burnt in a modern combined cycle power station, equipped with two gas turbines, two heat recovery steam generators and one steam turbine. Steam is generated at two pressure levels. The composition of the fuel gas is shown below.

Fuel Gas Composition of a Typical North Sea Brent Natural Gas

Component	Symbol	Volume %
Nitrogen	N_2	0.9
Carbon dioxide	CO_2	0.7
Methane	CH_4	82.0
Ethane	C_2H_6	9.4
Propane	C_3H_8	4.7
Butane	C_4H_{10}	1.6
Pentane +	C_5H_{12} +	0.7

The design plant performance is given in the following table. This table shows that net efficiency of the GTCC power plant is 52% (LHV basis).

Plant Energy Balance

Item	MW
Gas turbines	294
Steam turbine	177
Plant total, gross	470
Boiler feed pump	-2
Cooling water pump	-1
Auxiliaries	-2
Plant total, net	465
Fuel LHV input	894
Net efficiency, %	52

The CO_2 emissions are about 400 kg/MWh. The high excess air levels necessary for gas fired turbines result in a low concentration of CO_2 in the exhaust gas and a high mass flow rate per unit of power generated (2 kg s/MW compared to a value of 1 kg/s/MW for the equivalent coal fired unit).

[p. 1, 2 The above units are documented as they are in the report. But they seem incorrect. To find the correct units: The above table shows a fuel LHV input of 894 MW. Assuming a coal HHV of 11,000 Btu/lb containing 70% carbon, the CO_2 emission is 322,840 kg/h. This corresponds to 360 kg/h/MW input. Then the article figure of 400 kg MWh is perhaps 400 kg/h/MW. Therefore, units for the other figure are kg/s/MW.]

The cost of a turnkey combined cycle power plant varies from case to case, but the specific cost is in the range 400-600 $/kW. The IEA study used 600 $/kW. Typical cost distribution for a turnkey combined cycle power plant consisting of 2 gas turbines, 2 HRSGs and one steam turbine is as follows:

Typical Cost Distribution for a Turnkey Combined Cycle Power plant (2 GTs + 2 HRSGs + 1 ST)

Item	%
Gas turbine auxiliary equipment	26
HRSG + piping + auxiliary equipment	17
Steam turbine + generator + piping + condenser	21
Electric and supervisory equipment + transformer	12
Civil engineering	6
Erection + supervision	18
Total	100

With a real rate of return equal to 10%, cost of electrical power before adding the fuel cost is 15 mills/kWh, as shown in the following table.

Cost of Electrical Power Before Adding the Fuel Cost (@ Real Rate of Return of 10%)

Cost Item	Mills/kWh
Total capital investment	10
Taxation and insurance	1
Maintenance	1
Labor cost – administration	1
Power cost without fuel cost	15

The power cost is in the range of 25-45 mills/kWh if a typical fuel cost (natural gas) of 10-18 cents/Sm^3 is used.

Greenhouse Gas Emissions from Integrated Gasification Combined Cycle Power Plant

This plant consist of a Texaco based IGCC power plant with integration of the air separation unit. The 500 MW IGCC power plant involves two Texaco gasification trains, processing about 4000 t/d of coal, and is integrated with a power block incorporating two Siemens V94.2 gas turbines, one heat recovery steam generation section, one set of steam turbines and an elevated pressure air separation unit.

The overall mass balance is summarized in the following table.

Mass Balance of the Texaco Based IGCC Power Plant

Input	Kg/s	Output	Kg/s
Coal	47	Stack gas	1028
Water (in coal slurry)	18	Waste water	26
Air	990	To sulfur recovery	4
Water (venturi scrubber)	10	ASU condensate	1
		Ash	5
Total input	1065	Total output	1065

A coal slurry is fed to the gasifiers with oxygen and raw fuel gas is produced. Ash is removed from the raw coal gas. Fresh water is mixed with condensate in the gas cleaning section and fed to the venturi scrubber, resulting in waste water.

In the Selexol unit, a mixture of H_2S/CO_2 is removed and treated in the sulfur recovery unit. After the gas cleaning section, clean fuel gas flows through the expanders to the gas turbine section. In the air compressor of the gas turbine section, cold air is compressed from which some is sent to the air separation unit and the bulk sent to the combustion chamber of the gas turbine. The nitrogen product from the air separation unit is admixed for NO_x control and to increase the power output. The total amount of flue gas is 1030 kg/s. [p. 1]

The waste heat recovered from the gasifier is combined with the HRSG steam and sent to steam turbines. The net output of the steam turbines is 272 MW.

An overview of the power balance is given in the following table which shows that the net plant efficiency is about 42%. [p. 1]

Power Balance of the Texaco Based IGCC Power Plant

Input		Output	
Coal, MW	1206	Expander, MW	10
		Gas turbine, MW	289
		Steam turbine, MW	272
		Gross output, MW	571
		Plant consumption, MW	68
		Net output, MW	503
		Net efficiency, %	42

As the ASU is responsible for 60% of the ancillary power consumption, the overall power plant efficiency will be sensitive to for further improvements in the air separation plant efficiency.

New gas turbine combine cycle can operate on clean fuel at 50 to 52% (LHV). Today gasification processes operate with gasification efficiencies from 75 to 92% (based on LHV). [p. 2]

The CO_2 emission is 790 g/kWh. The main CO_2 emission source (97%) in an IGCC power plant is the stack, emitting the cooled exhaust gas of the gas turbines. The remaining 3% is emitted by the acid gas removal plant. [p. 3]

The gasification processes integrated in IGCC power plant systems are operating at elevated pressures, favoring the recovery of CO_2 by means of physical absorbents like Selexol or Purisol and by membranes. The recovered CO_2 can be delivered at higher pressure resulting in lower energy demand for the compression of CO_2 for disposal.

To recover CO_2 from coal gas, the IGCC power plant has to be extended with shift reactors and a CO_2 recovery or removal unit. However, the requirements for the shift reduce the overall efficiency of the system.

When 90% of the CO in the coal gas is shifted (in two steps and with 50% excess steam), the CO_2 concentration will rise to approximately 34 mol% in the wet coal gas (40% in the dry coal gas). The total investment costs of this shift section will be about $30 million and the annual catalysts costs about $1 million. [p. 3]

The power production costs for a 500 MW IGCC power plant is summarized in the following table.

Investments of a Texaco Based, 500 MWe, State of the Art IGCC Power Plant

Gasification	$Million
Coal treatment	19
Gasifier/sulfur cooler	108
Syngas purifying/sulfur recovery	68
Waste water treatment	10
Oxygen production	88
Combined cycle:	
Gas turbines	86
HRSG/steam turbines	127
Storage/transport	32
Support systems	37
Common supplies	65
Bare costs (BC)	640
Engineering, procurement, etc. (5% BC)	32
Capital investment (CI)	672
Fees (2% of CI)	13
Land purchase, site preparation (5% of CI)	34
Contingencies (10% of CI)	67
Total plant cost (TPC)	786
Allowance for funds during construction	177
Total capital requirement (TCR)	963
Total capital requirement ($/kW net)	1910

Power production costs for a real rate of return at 10% is 59 mills/kWh as shown in the following table. [p. 3, 4]

Power Production Cost for a 500 MWe, Texaco Based IGCC Power Plant

(@ a 10% Rate of Return)

Fuel costs, million $/year	87.4
O and M costs, million $/year	41.6
Capital costs, million $/year	90.3
Total costs, million $/year	219.3
Net production, GWh/year	3747
Power costs, mills/kWh	59

Greenhouse Gas Emissions from Carbon Dioxide Recycle Power Plant

This study characterizes power generation in a coal combustion plant fed by oxygen and using recycled carbon dioxide as the means of temperature control. The base case is atmospheric PF combustion in oxygen. It is based on speculative long term technology rather than existing or medium term technology.

From storage, the coal is pulverized and transferred in a mixture of recycled flue gases and oxygen to low NO_x burners. Some of the unburned coal and ash is removed from the base of the furnace, and the rest of the ash is carried forward with the hot gases and removed in the electrostatic precipitators (ESP). Before reaching the ESP these hot gases are cooled, then partially recycled back to the furnace, with any excess being exhausted to the atmosphere. The volume of the flue gases recycled back to the furnace is adjusted to maintain the boiler conditions. Oxygen from a cryogenic plant air separation unit is added to maintain normal excess oxygen levels. The steam from the superheater tubes goes to the steam turbine. [p. 1]

The base case plant operating a recycled CO_2 system has a design efficiency of 33%(LHV) compared to the base case (PF + FGD) efficiency for the study of 40%. A study based on a supercritical plant with SCR, reports that the adoption of CO_2 recycle reduces an initial plant efficiency of 39% to 31% (HHV). It has been calculated that fitting CO_2 recycle to an existing 500 MW unit would reduce the plant efficiency from 38% to 27% (LHV). In both cases the CO_2 is produced as a pure liquid suitable for pipeline disposal.

Results of the mass and energy balance calculations are summarized in the following table and are given together with the corresponding results for the standard air fired PF coal fired combustor.

Mass and Energy Balance Summary

Item	Air Fired	O_2/CO_2 Fired
Pressure in combustor, bar abs.	1	1
Heat input (MW, LHV)	1260	1524
Electricity generated, MW	522	654
Ancillary Consumption:		
O_2 Separation, MW	0	126
Coal/ash system, MW	3	3
Fans/compressors, MW	3	3
Condensate pumps, MW	12	15
Cooling water, MW	22	154
Overall results:		
Net electricity, MW	500	500
Overall efficiency, %	40	33
CO_2 emission, kg/kWh	1	1
NO_x, g/kWh	1	1
SO_x, g/kWh		

The efficiency of the oxygen fired system is improved due to the recycling of hot flue gases back to the combustion chamber. In the air fired system these hot gases are used to preheat the combustion air. The flue gas analysis is summarized in the following table.

Flue Gas Analysis

Item	Air	O_2/CO_2
Pressure, bar abs.	1	1
Temperature, °C	132	166
Density, kg/m^3	1	1
Flow rate, kg/s	552	178
Dew point, °C		
Flue Gas Composition , Mol%:		
Argon		
CO_2	14	63
H_2O	8	32
N_2	74	0.6
O_2	3	4.5
SO_x	0.07	0.3

The table shows that the CO_2 content of the flue gas has increased from 14 to 63 mol%, with the majority of the remaining flue gas being water vapor at 32 mol%. The total flow of flue gas has decreased from 550 to 180 kg/s, and the high moisture content of the flue gas has increased the flue gas dew point from 50 to 80°C. Subsequent downstream processing of the flue gas, especially if it involves cooling and compression, will mean that most of the SO_x together with some of the CO_2 will be dissolved in the condensed water phase. Special consideration of the materials of construction of this downstream processing will be required.

Although referred to for convenience as stack gas, following downstream recovery of CO_2 and condensation of the water, the gases that will actually be vented to the stack are minimal.

Although there are high levels of nitrogen and sulfur oxides in the flue gas, they are not comparable to the results of previous studies because there are no clean-up facilities. It has been suggested that the high levels of NO_x in the recycled gas lead to a reduction in the net quantity of NO_x produced.

A beneficial feature of this concept is the small volume of gas that needs to be treated to recover/condition the CO_2. The mass flow rate of purged gas requiring further processing is less than 0.4 kg/s/MW compared to three times this number for the PF case studied earlier and twice this again for the gas fired case. [p. 3]

The capital cost and operating cost factors used are considered to be study estimates. A summary of these capital costs are given in the following table.

Summary of Cost

Item	Million $
Solids handling	72
Boiler house	255
Steam and condensate system	55
Steam turbines and generators	213
Cryogenic air separation unit	290
Cooling water system	22
Total system cost	907

The break even electricity generation cost is 83 mills/kWh for a plant size of 500 MW. The specific capital cost of the CO_2 recycle power plant is 2040 $/kW which is significantly greater than the figures quoted for the other power generation technologies.

Including CO_2 liquefaction, IGCC based technology is quoted as having overall efficiencies in the 30-33% (LHV) region. If O_2/CO_2 recycle in conjunction with supercritical steam plant can reach efficiencies such as this, it could well be attractive for new plants as well as retrofit situations. [p. 4]

Greenhouse Gas Emissions Comparison of the Power Plants

Results from the four power generation options studied are compared with each other and with alternative power generation schemes.

Generating Efficiency

The efficiency of PF + FGD systems is generally quoted as being limited to about 45%. Efficiencies of up to 50% could be achieved depending upon the extent to which better steels enable steam temperatures and pressures to be increased and steam turbines to be improved. The study evaluated the PF + FGD system at 40%, the NGCC at 52%, IGCC at 42% and CO_2 recycle at 33%.

CO_2 Emissions

In the absence of any recovery, the amount of CO_2 released for a given fuel is inversely proportional to the process efficiency. The following table illustrates the CO_2 emissions for each of the base cases examined and shows the range obtained with each option. As can be seen, the natural gas fired option produces significantly less CO_2 per unit of power generated, than the coal fired options. The coal fired options show a considerable range of CO_2 emissions as a result of significant variations in the efficiency of power generation. The results illustrate the often suggested ‘fuel substitution’ argument; that use of a fuel with a low carbon to hydrogen ratio, significantly reduces the emissions of CO_2.

Flue Gas Data

	PF + FGD	GTCC	IGCC	CO_2 Recycle
CO_2 in flue gas, kg/s	115	52	108	139
CO_2 in flue gas, kg/s MW	0.23	0.11	0.21	0.28

CO_2 in the Flue Gas

The composition of the flue gas leaving the power generation section of the plant, could have a significant effect on the ease and hence the cost of recovering CO_2. The higher the partial pressure, the easier it will be to recover CO_2. Other constituents of the gas stream act as diluent and/or interfere with the recovery method which increases the cost. The total quantity of the gas stream to be treated directly effects the size of the downstream processing plant required. As can be seen from the following table, the two process technologies which rely on gas turbine combustion, result in considerably more gas requiring treatment than the steam cycle based processes. This is because of the high excess air levels in gas turbines necessary to control their inlet temperature. (NOTE: This study recycled CO_2 in the PC boiler only. CO_2 was not recycled in gas turbine. Can a gas turbine also use recycled CO_2? The CO_2 recycle to gas turbine will reduce the mass feed to the gas considerably. It might change turbine to a very different machine.)

Flue Gas Data

Items	PF + FGD	GTCC	IGCC	CO_2 Recycle
Flue gas flow rate, kg/s	607	1007	1028	178
Flue gas flow rate, kg/s MW	1.2	2.2	2.0	0.4
CO_2 in flue gas, volume % wet	13	3	7	63
CO_2 in flue gas, volume % dry	14	4	7	91

Although the standard 500 MW GTCC produces about half the CO_2 of the PF and IGCC alternatives, it is only at a very low concentration in a relatively large gas stream.

This means that the gas will be costly to handle and the CO_2 difficult to recover. The potential advantage of recirculating CO_2 can be seen clearly; at 91% (vol. dry) CO_2 content, the CO_2 does not require further recovery as such and the processing equipment is determined by the level of impurities that can be tolerated in an impure CO_2 gas for disposal.

Related Articles

The following articles appeared in *Proceedings of the Third International Conference on Carbon Dioxide Removal*, Cambridge, MA 9-11 Sep. 1996.

- **Miesen, Axel and Xiaoshan Shuai, "Research and Development Issues in CO_2 Capture,"** p. S37**.** (The authors are from The University of British Columbia, Canada.)

The article reviews the principal CO_2 capture technologies and then makes recommendations for future R&D to make those technologies more suitable for CO_2 capture from single point sources. Following are the notes from the article:

Introduction: The role of CO_2 in global warming is one of the most important contemporary environmental issues and it is therefore necessary to have available technology which minimizes the discharge of CO_2 into the atmosphere. Amongst the anthropogenic sources of CO_2, electric power stations utilizing fossil fuels, petroleum refineries, natural gas plants and certain chemical plants are the largest single-point sources of CO2 and therefore deserve particular attention. In the aforementioned cases, the CO_2 is discharged into the atmosphere in the form of mixtures with other constituents (principally N_2, H_2O, O_2, CO, SO_x, NO_x and/or particulate) near atmospheric pressure and at elevated temperatures (typically above 100°C).

Absorption Processes. Chemical and/or physical absorption processes are widely used in the petroleum, natural gas and chemical industries for the separation (capture) of CO_2. Chemical absorption is based on reactions between CO_2 and one or more basic absorbents such as aqueous solutions of mono-, di-, or tri-ethanol amines, diisopropanol amine, sodium hydroxide, sodium carbonate and potassium carbonate. Typical physical solvents are methanol, N-methyl-2-pyrrolidone, polyethylene glycol dimethylether, propylene carbonate and sulfolane.

A favorable characteristic of absorption is that, with the choice of proper absorbents, the absorption can be reversed by sending the CO_2-rich absorbent to a desorber (or stripper) where the pressure is reduced and/or the temperature is raised. The regenerated absorbent is then returned to the absorption tower thereby creating a fully continuous process.

There are presently only two major industrial installations in which CO_2 is captured by means of chemical solvents; they are the ABB Lummus Crest (1995) design based on aqueous monoethanolamine (MEA) solutions at Torna (California) and Shady Point (Oklahoma). The plants are claimed to be working well but given their limited number and the purity of the flue gases, absorption is not yet well proven technology for the capture of CO_2 from the flue gases.

Adsorption Processes. Adsorption processes are based on intermolecular forces between gases (including CO_2) and the surfaces of certain solid materials (such as molecular sieves and activated carbon). The adsorbents are normally arranged as packed beds of spherical particles. In pressure swing adsorption (PSA), the gas mixture flows through the beds at elevated pressures and low temperatures until the adsorption of the desired constituent approaches equilibrium conditions at the bed exit. The beds are then regenerated by stopping the flow of the feed mixture, reducing the pressure and elutriating the adsorbed constituents with a gas having a low adsorptivity. Once regenerated, the beds are ready for another adsorption cycle. By contrast, in temperature swing adsorption (TSA), the adsorbents are regenerated by raising their temperature utilizing a hot inert gas or external heating. Riemer and Webster found that PSA was superior to TSA in all cases due to the high energy requirements and low speed of regeneration in TSA.

Adsorption is not yet a highly attractive approach for CO_2 removal in the large scale industrial treatment of flue gases because the capacity and CO_2 selectivity of available adsorbents is low.

Gas Separation Membranes. Gas separation membranes are solids and operate on the principle that their porous structure permits the preferential permeation of mixture constituents. The main design and operational parameters are their selectivity and permeability. Membrane separation of CO_2 from light hydrocarbons has met with success in the petroleum, natural gas and chemical industries because of the inherent simplicity resulting from steady state operation, absence of moving parts and modular construction. The CO_2 bearing gas mixture is introduced at elevated pressure into the membrane separator consisting typically of a large number of hollow cylindrical membranes arranged in parallel. The CO_2 passes preferentially through the membranes and is recovered at reduced pressure on the shell side of the separator.

Gas separation membranes have thus far not been widely explored for CO_2 capture from flue gases due to the comparatively high mixture flows and the need for flue gas pressurization. Feron et al. Found in their exploratory study that a two-stage system was needed to achieve good separation and that the costs were double those of conventional amine separation processes. The principal cost component was compression energy.

Gas Absorption Membranes. Gas absorption membranes consist of microporous solid membranes in contact with a liquid absorbent. The gas component to be separated diffuses through the solid membrane and is then absorbed into and removed by the liquid absorbent. This arrangement results in independent control of gas and liquid flows and minimization of entertainment, flooding, channeling and foaming. The equipment also tends to be more compact than conventional membrane separators. Feron, et al. and Nishikawa, et al. considered gas absorption membranes for CO_2 capture from flue gases and found them to be promising but still requiring considerably more research.

Cryogenic Processes. Cryogenic separation of gas mixtures involves compressing and cooling the gas mixtures in several stages to induce phase changes in CO_2 and, in the case of flue gases, invariably other mixture components. Depending on the operating conditions (the CO_2 critical temperature and triple point are 31.1 and 56.6 °C, respectively), the CO_2 may arise as a solid or liquid together with other components from which it may be distilled. Water vapor in the CO_2 feed mixture leads to the potential formation of solid CO_2 clathrates and ice which, together with solid CO_2 particles, can result in major plugging problems.

The basic advantage of cryogenic processes is that, provided the CO_2 feed is properly conditioned, high recovery of CO_2 and other feed constituents is possible. However, cryogenic processes are inherently energy intensive.

CO_2/O_2 Combustion. The use of oxygen significantly improves the combustion of fossil fuels, because it leads to higher combustion rates, higher combustion temperatures and therefore thermal efficiencies, lower thermal NO_x formation and smaller combustion equipment since atmospheric nitrogen is absent or reduced. [I doubt about the higher thermal efficiencies and lower thermal NO_x formation. Are these claims factual? Or just an opinion?] To moderate the combustion temperatures, part of the product gases which are rich in CO_2 can be recycled. Depending on the composition of the fuel and the ultimate disposition of the CO_2, the product gases may need to undergo further treatment including particulate, SO_x and NO_x removal (Nakayama et al. 1992). In the case of pulverized coal combustion, drying of the recycle gas was also found to be a major consideration.

An important inherent disadvantage of the CO_2/O_2 combustion is the need for oxygen which is still relatively expensive to produce from air. It has been estimated (USDOE, 1993) that 20% of the net electric power output of a conventional fossil fuel power plant would be needed for the production of oxygen.

- **Pruschek, R., "CO_2 Abatement Investigations Under the Framework Program of the RTD Policy of the EU, in Particular Under the Joule II Program (1993 to 1995),"** p. S43. (The author is from the University of Essen, Germany.)

This article describes the Joule II program "Minimum emission power production from fossil fuel sources". The results will be published when they become available.

- **Leci, Colin L, "Development Requirements for Absorption Processes for Effective CO_2 Capture from Power Plants,"** p. S45. (The author is from ICEL Developments Ltd., UK.)

This article describes a sensitivity analysis to identify the key parameters for the major development requirements of current commercial absorption technology for CO_2 capture from flue gases based on the MEA solvent. This analysis utilized the identical economic models derived for the earlier reported studies for the overall plant export capacity of 500 MW. It focused on the impact of reducing the MEA solvent circulation rate by increasing the solvent concentration.

The article concluded that the most significant area for future R&D for solvent absorption process for effective CO_2 capture from conventional pulverized fuel power stations is that of the development of a solvent which can be used at flue gas low operating pressures at high solution concentration. The significant being twofold in that not only are the utility requirements for such a stand alone plant considerably reduced, but more significant, is that the parasitic demands made on the power plant in terms of both power and steam by the former is drastically reduced.

- **Chakma, Amit, "CO_2 Capture Processes, Opportunities for Improved Energy Efficiencies,"** p. S51. (The author is from University of Regina, Canada.)

In this article suggestions are made to reduce the energy requirements for the conventional MEA based technologies for the capture of CO_2. The suggestions include the use of a pre-contactor, injection of external steam and use of mixed solvents. The author estimated that the combined effect of these options can reduce the regeneration energy requirement by 30% compared to the conventional MEA process.

- **Tomio Mimura, Hidenobu Simayoshi, Taiichiro, Masaki Iijima and Sigieki Mituoka, "Development of Energy Saving Technology for Flue Gas Carbon Dioxide recovery in Power Plant by Chemical Absorption Method and Steam System,"** p. S57. (The authors are from MHI and Kansai Electric Power Co., Japan)

The main theme of the chemical absorption method is reduction of its high regeneration energy requirement. The regeneration energy required for CO_2 recovery by MEA is about 900 kcal/kg-CO_2, which is equivalent to about 20% of the boiler combustion energy of the thermal power plant.

With the aim of developing energy efficient absorbent which is essential for the power plant CO_2 recovery, laboratory screening tests were made which focused on the sterically hindered

amine (SHA). After testing 80 alkanolamine specimens in laboratory, they selected the promising sterically hindered amine and subjected them to bench-scale tests. Subsequently performance tests have been carried by many utility companies in Japan from April 1995 in a pilot plant showed excellent characteristics of KS-1. Compared with MEA, KS-1 requires approximately 20% less energy to recover CO_2.

After the development of KS-1, KS-2 was developed and had its performance confirmed. KS-2 has a higher degree of steric hindrance than that of KS-1, therefore it should require less regeneration energy than that required for KS-1. The pilot plant tests for KS-2 showed that the regeneration energy of KS-2 is about 700 kcal/kg-CO_2 recovered which is about 20% less than MEA solution. This figure is almost same as that of KS-1 absorbent. However, the regeneration temperature of the KS-2 absorbent is lower therefore steam required for regeneration is extracted at a lower pressure. This gives a loss of power plant output about 5 to 6 percentage points only.

- **Arashi, N., Naoki Oda, Mutsuo Yamada, "Evaluation of Test results of 1000 m^3N/h Pilot Plant for CO_2 Absorption Using an Amine-Based Solution**," p. S63. (The authors are from Hitachi Ltd. and Babcock Hitachi, Japan.)

CO_2 recovery plants in which alcanole amine is used as an absorption solution are already being used at some thermal power stations (Clair et al., 1983, Kaplan, 1982). A problem has been, however, the deterioration of absorbent by SO_2 in the flue gas (Barchas et al., 1992). Subsequently, Tokyo Electric Power Company and Hitachi Ltd. developed an amine based absorption solution which is not affected by SO_2 (Yamada et al., 1996).

The 620 scfm (1000 m^3N/h) pilot plant tests in which this new absorption solution was used were carried out at the Yokosuka Thermal Power Station of Tokyo Electric Power Company. The objectives of these pilot plant tests were to prove the applicability of the new absorption solution to SO_2 containing flue and to obtain the engineering data needed for design work. The test data showed that the solution is sufficiently SO_2 durable and saves energy.

In these pilot plant tests the flue gas was taken from a 265 MW power plant which used coal oil mixture (COM) as the fuel. The gas is previously cooled to 40 °C to decrease its moisture content before being introduced into the absorber. The absorber contains a ring shaped stainless steel packing (1 inch in diameter). In the absorber, CO_2 in the flue gas is absorbed by the solution at temperatures between 40 and 50 °C. CO_2 loaded solution is then extracted from the bottom of the absorber and transferred to the regenerator through a heat exchanger in which the solution temperature is raised to 100 and 110 °C. In the regenerator, the solution contacts with steam which comes from the reboiler and CO_2 is stripped from the solution.

Based on the data from the pilot plant, the authors prepared a conceptual deign of the CO_2 recovery plant for a 1000 MW coal fired power plant. The design required eight pairs of absorbers and regenerators. Each absorber was equipped with a booster blower, and each regenerator with a pump. Two pairs of absorbers and regenerators had one heat exchanger. The footprint of the plant was found to be 170 m by 110 m.

[The article includes a flowsheet of the pilot plant and a layout for the 1,000 MW CO_2 recovery plant. These figures are not copied in these notes.]

- **Buzek, J., J. Podkanski, K. Warmuzinski, "The Enhancement of the Rate of Absorption of CO_2 in Amine Solutions due to the Marangoni Effect,"** p. S69. (The authors are from Academy of Sciences, Poland.)

The experimental and theoretical results described in this paper concern the liquid surface instabilities (cellular convection) during gas absorption in liquids accompanied by a chemical reaction. Surface instability, if it does occur, can increase mass transfer rates during gas chemisorption in liquids by a factor of two and more (for liquid-liquid systems, a factor as high as 75 is reported).

The investigation of these authors were focused on the practically important mechanism inducing the surface instability during gas chemisorption in liquids – the so called Marangoni instability (MI): the concentration disturbances on the interface affect the local values of surface tension, which may, in turn produce instability.

The authors studied CO_2–amines (MEA, DEA) system theoretically and experimentally. They found that the occurrence of MI during the absorption of CO_2 in MEA and DEA solutions. MI can enhance significantly mass transfer rate (by 100% in certain parts of the absorption column), but it can easily be dampened by a surface active agent. Therefore the authors recommended that amine solutions used for absorption should not be contaminated by even traces of surfactants.

- **Aroonwilas, Adisorn and Paitoon Tontiwachwuthikul, "Mass Transfer Studies of High Performance Structured Packing for CO_2 Separation Processes,"** p. S75. (The authors are from University of Regina, Canada.)

Of the hindered amines, 2-amino-2-methyl-propanol (AMP) is the most promising solvent because it has some excellent characteristics compared with the primary amine MEA. On the basis of stoichiometry, AMP can react with CO_2 at a theoretical ratio of one mole CO_2 per mole of amine. This becomes a superior characteristic of the hindered amine to the conventional MEA whose each mole can react with only one-half mole of CO_2. Besides its outstanding absorption capacity, AMP also induces less corrosion which is considered the major operational problem in the conventional CO_2 absorption plants.

The replacement of the conventional alkanolamine MEA with the hindered amine AMP is very attractive, however, one limitation for use of AMP is that its absorption rate is lower than that of MEA. To make the replacement feasible, the rate of CO_2 absorption into the AMP solution must be improved. Therefore the primary objective of this article was to investigate the role of a high-efficiency structured packing in improving of CO_2 absorption process. The authors evaluated the performance of the structured packing by absorption CO_2 into sodium hydroxide solutions and into AMP solutions. They found that in the CO_2-NaOH system, the structured packing (EX type) provides an overall mass transfer coefficient which is higher than the coefficient for random packing by a factor of 10 to 33. In the CO_2-AMP system, the structured packing shows at least 6 fold superior performance to random packing (1/2" Berl Saddles).

- **Falk-Pedersen, O., and H. Dannstrom, "Separation of Carbon Dioxide from Offshore Gas Turbine Exhaust,"** p. S81. (The authors are from Kavaerner Water Systems, Norway.)

In 1989 the Norwegian Government initiated the objective that the total CO_2 emission in Norway will be established at the 1989 level in the year 2000. This led to the introduction of the CO_2-tax in 1991. The total CO_2-tax paid by the Norwegian oil companies is assumed to be US$ 369 – 382 million in 1996, which is equal to a53 US$/tonne generated CO_2.

In 1992, Kvaerner Engineering initiated a joint effort program for CO_2 separation between major North Sea operators and the Norwegian authorities. The study is at present in phase four and will be finished in November 1996.

The main target of the study is to optimize the process with respect to size, weight and cost. (Size and weight are important because the 21 MW power plant based on LM2500 PE gas turbine is to be located on an offshore platform.) The development work focused on the absorption unit, the desorption unit and the total process.

The optimization study found that combined cycle with 40% recycling of exhaust is the best power generation system of the options investigated in connection with the removal of CO_2 on offshore installations. Both General electric and Rolls Royce have in general agreed that the recycle ratio (40%) will not significantly influence gas turbine performance, though detailed testing is necessary to verify this.

The optimization study investigated use of several membranes gas/liquid contactor for use as absorber. The membranes examined were polypropylene, polyether sulphone, silicon rubber and GORE-TEX ePTFE. Of these materials, GORE-TEX ePTFE was selected because of their high mass transfer coefficient, chemical stability and not getting wet by the absorption liquid. Also their modules have good mechanical stability and low production cost. This resulted in 72% reduction in size and 66% reduction in weight compared with a conventional absorption column.

In order to further minimize space and weight, membrane gas/liquid contactor based desorber was selected which was also made of GORE-TEX ePTFE.

It was concluded that that the economic feasibility of the project seems promising.

- **Chan, Christine and Patrick Lau, "Implementations of Advisory System for the Solvent Selection of Carbon Dioxide Removal Processes,"** p. S87. (The authors are from University of Regina, Canada.)

This article describes the solvent selection advisory system (SSAS) which is a decision support system for aiding users in the preliminary selection of optimal solvents for carbon dioxide removal processes given different user specification and plant conditions. This article is not relevant to our needs of the present study.

- **Feron, P.H.M. and A.E. Jansen, "The Production of Carbon Dioxide from Flue Gas by Membrane Gas Absorption,"** p. S93. (The authors are from TNO-Institute of Environmental Sciences, The Netherlands.)

This article is about the use of absorption liquids which are used with membranes. The authors are of the view that a stable membrane gas absorption system cannot be achieved with the combination of commercially available polyolefin membranes and the usual absorption liquid, monoethanolamine (MEA). TNO Institute has come up with a range of liquids which show stable operation with commercially available polyolefin membranes. These liquids named CORAL (CO_2 Removal Absorption Liquid) are suitable for carbon dioxide recovery from flue

gas but also from other gas streams such as biogas and natural gas. From this range of liquids a number of liquids have been selected and assessed for CO_2–removal. This selection has been based on the measurement of the mass transfer coefficient as this determines the size of the equipment and hence the investment costs. The authors claim that CORAL has the following advantage over the MEA solution: CORAL is oxygen resistant to air while MEA solution is degraded when exposed to air. CORAL is less corrosive than MEA, therefore CORAL handling equipment can be made of carbon steel.

- **Burchell, Timothy D. and Roddie R. Judkins, "A Novel Carbon Fiber Based Material and Separation Technology,"** p. S99. (The authors are from Oak Ridge National Laboratory, USA.)

This article describes the preparation of a new carbon based material that can be used for absorbing CO_2 from CH_4. The article also gives data on the material but does not say what or how much advantage this new adsorbing material has over the existing materials used for the same purpose.

- **Sarkar, S.C. and A. Bose, "Role of Activated Carbon in Carbon Dioxide Removal,"** p. S105. (The authors are from Jadavpur University, India.)

This article describes development of activated carbon from coconut shell for the purpose of adsorbing CO_2 from air/CH_4/CO_2 mixture and then desorbing it by PSA. The preliminary data reported in the article shows that purity of CO_2 in the adsorbed gases was about 57%. The data on the desorbed gas composition is not reported n the article.

- **Tokuda, Y., E. Fujisawa, N. Okabayashi, N. Matsumiya, K. Takagi, H. Mano, K. Haraya and M. Sato, "Development of Hollow Fiber Membranes for CO_2 Separation,"** p. S111. (The authors are from National Institute of Materials and Chemical Research, Japan.)

The authors are developing hollow membranes for the separation of CO_2 from the CO_2/N_2 mixture. They have developed polymers using different kinds of Cardo polyimides. They have also developed methods for making hollow fiber membranes from these polyimides based polymers. These membranes have high selectivity for CO_2. Their computer simulation results show that 80 to 90% CO_2 purity is achieved in a two stage module. They have assembled a pilot plant where they will verify the computer simulation results and obtain design data for a CO_2 separation plant.

- **Andries, J., J.G.M. Becht and P.D.J. Hoppesteyn, "Pressurized Fluidized Bed Combustion and Gasification of Coal Using Flue Gas Recirculation and Oxygen Injection,"** p. S117. (The authors are from Delft University of Technology, The Netherlands.)

This article describes experimental work on coal combustion and coal gasification carried out in a test rig. The test rig consists of a 0.4 m diameter fluidized bed reactor operating at a pressure of up to 10 bar, a high temperature ceramic filter, a high temperature ammonia removal system, a pressurized toping combustor, a scrubber, a booster compressor and an atmospheric combustor.

The oxygen supplied to the bed is mixed with air (when enriched air is used as fluidizing gas) or recirculated flue gas (when a CO_2/O_2 mixture is used as fluidization gas). Recirculation of the

flue gas implies recirculation of water vapor formed during the combustion of the coal and/or the fuel gas. The water concentration can become as high as 30 volume % at 8 bar. Because of the high dew point of the resulting flue gas this could result in severe corrosion in the system. Furthermore the water concentration in the flue gas strongly influences the composition of the fuel gas produced by the gasifier. To control the water vapor concentration, the flue gas is passed through scrubber. By injecting water and cooling the resulting gas below the dew point, the water vapor concentration can be controlled and be kept below a few percent. The scrubber will also remove SO_2 and remaining dust particles from the gas stream thus protecting the booster compressor from the erosion and corrosion.

During the commissioning of the test rig a number of combustion experiments were performed. All the combustion experiments were done at a bed temperature of 850 °C, a fluidization velocity of 0.8 m/s, with air (21% oxygen), oxygen-enriched air (24% oxygen) or oxygen enriched recirculated flue gas (24 and 27% oxygen) as fluidizing gas and Kiveton Park coal mixed with Middleton limestone (97% $CaCO_3$). Preliminary conclusions based on the results from these combustion experiments are:

- There seems to be no influence of the amount of recirculated NO on the emission of NO.
- The input of fuel-N and the oxygen level in the outlet determine together the emission of NO.
- The oxygen level at the inlet of the reactor seems to have no influence on the NO emission.
- The processes which determine the net emission of NO are not influenced by the replacement of nitrogen by carbon dioxide

During the future experiments (second half of 1996) the authors plan to investigate the carbon conversion in the fluidized bed and combustion characteristics of the low calorific value fuel gas in the pressurized topping combustor.

- **Okawa, M., N. Kimura, T. Kiga, S. Takano, K. Arai and M. Kato, "Trial Design for a CO_2 Recovery Power Plant by Burning Pulverized Coal in O_2/CO_2,"** p. S123. (The authors are from utility companies and Center for Coal Utilization, Japan.)

This article describes designing of a conceptual power plant in which part of CO_2 in the flue gas is recycled to the boiler and the remaining is recovered for disposal into ground.

The O_2/CO_2 pulverized coal fired power plant consists of four main processes: oxygen generation, O_2/CO_2 combustion, flue gas treatment, and CO_2 recovery/disposal. The most efficient and technically feasible processes are shown in Figure 1 (not reproduced in these notes). The authors adopted wet recycling method although it requires gas coolers and dehumidifiers. For the oxygen supply, cryogenic air separation method was selected. Optimization showed that 97.5% pure oxygen should be produced in the cryogenic plant. Because the CO_2 would be disposed of underground by gas compression, the system does not need SO_x removal unit. For this scheme, the authors found that the footprint of the power plant is equal to that of the conventional pulverized coal fired power plant.

In the oxygen combustion method, the amount of flue gas decreases because of absence of nitrogen. It therefore reduces thermal heat loss in the flue gas and reduces power consumption thus improving boiler efficiency. However, it requires a great deal of power for oxygen

generation and CO_2 compression, so the net efficiency falls from the 39.6% of the conventional power plant to 29.1%.

- **T. Kiga, S. Takano, N. Kimura, K. Omata, M. Okawa, T. Mori and M. Kato, "Characteristics of Pulverized-Coal Combustion in the System of Oxygen/Recycled Flue Gas Combustion,"** p. S129. (The authors are from utility companies and Centers for Coal Utilization, Japan.)

This article describes the experimental work that was carried to study oxygen/recycle flue gas combustion for the removal of CO_2 from pulverized-coal firing power plants, combustion characteristics of pulverized coal and the heat absorption of boiler furnace.

Figure 4 in the article shows the flow diagram of the industrial-scale combustion test facilities. (Figure 4 was not reproduced in these notes.) The furnace is a horizontal cylindrical type with water wall lined with refractory. Its inside diameter is 1.3 m and length is 7.5 m. The exhaust gas enters a stack through an flue gas cooler, a tubular air preheater, a multi-cyclone dust collector and a bag filter. A part of flue gas is taken out downstream of the bag filter and recycled as the primary gas for transporting pulverized coal and secondary gas for combustion. Oxygen is supplied by evaporating liquid oxygen. Part of oxygen is mixed with the secondary gas for combustion and another part is directly injected into the burning area of the furnace. Combustion tests were performed at the firing rate of 100 kg/h using three kinds of bituminous coal.

The combustion results showed that air-blown combustion produced a large amount of NO_x in the flame while oxygen/recycled flue gas combustion produced a remarkably small amount of NO_x. This is mainly due to the decomposition of recycled NO_x in the flame. When the air combustion was carried out with staging, the NO_x produced was only 25% of the NO_x produced in air combustion without staging. However, the reduction of NO_x in the oxygen/recycled flue gas staged combustion was only 50%. It is thought that the NO_x recycled in the oxygen/recycle flue gas staging was not decomposed because there is a lack of reducing components like hydrocarbons.

Another effect of oxygen/recycle flue gas combustion is that the heat absorption in furnace increases as wind box O_2 concentration increases. When the oxygen concentration in the wind box is 30%, heat absorption is almost same as that in air-blown combustion. The result indicates that there is a possibility of reducing furnace size if O_2 concentration can be increased.

- **Jody, B. J., E. J. Daniels and A. M. Wolsky, "Integrating O_2 Production with Power Systems to Capture CO_2,"** p. S135. (The authors are from Argonne National Laboratory, USA.)

This article is doing a loud thinking on the subject of integrating O_2 production with power system. The article mentions several theoretical cycles which could be used for the above integration. Thermochemical cycles for O_2 production from water and air can be integrated with high temperature power cycles to facilitate the production of commercial grade CO_2. Such integrated systems can achieve internal separation of the air or water while minimizing the overall energy consumption of the integrated system. This process might (under the right operating conditions) be more efficient than the use of conventional O_2 separation technology to produce O_2 for use in conventional fossil-fuel fired power generation systems. The article ends

with the remark that the lack of technical data at this time does not permit the evaluation of the economic competitiveness of such systems.

- **Iantovski, E. and Ph. Matheieu, "Highly Efficient Zero Emission CO_2-Based Power Plant,"** p. S141 (The authors are from University of Liege, Belgium.)

This article proposes a CO_2–based power plant promising zero emissions and removal of 80 to 90% CO_2. The removed CO_2 is then is then injected into a deep aquifer or into empty gas fields. The authors estimate around 2% of the processed crude oil is rejected as waste in oil refineries, the resulting low grade fuels would be produced at an annual rate of 100 Mtons. In addition large amounts of municipal solid wastes, which are currently disposed of in landfills, could be available for incineration. Large sources of such bad fuels, which are to some extent noxious even before combustion and are polluting land and water, can now be used for power production.

The proposed power plant consists of a recuperative CO_2 gas turbine associated with a topping CO_2–like Rankine cycle. The CO_2 gas turbine is made of a quasi-isothermal compressor, a O_2/CO_2 combustion chamber and an expander which is not on the same shaft as the compressor. The heat content of the exhaust gas, mainly a mixture of CO_2 and H_2O is transferred partly to the toping cycle and partly to the compressed CO_2 in a recuperator.

Another option is to use an oxygen blown gasifier of coal, biomass or low grade fuels in order to produce a syngas fuel. Here, instead of using water or steam in the gasification process, which generate large losses due to a very large heat of evaporation impossible to recuperate, CO_2 is used as a gasification agent.

The authors calculate the power plant efficiency at 54%. They suggest modification of the gas turbine expander which results in an expander of a smaller dimensions and the rotational speed is reduced by 12%. The authors think that such a gas turbine could be developed by a gas turbine manufacture within two to three years.

- **Meratla, Z., "Combining Cryogenic Flue Gas Emission Remediation with a CO_2/O_2 Combustion Cycle,"** p. S147 (The author is from CDS Research Ltd., Canada.)

The author of this paper describes a patented process for the removal of CO_2. Like all patent holders, the author does not give any technical or economic information and keeps indulging into day dreams. His process flowsheet shows oxygen combustion in the boiler with recycle flue gas for controlling the temperature. He gets oxygen from the non-existing Canadian hydroelectric power plants which will electrolyze water into hydrogen and oxygen. Hydrogen will be sold as a source of energy and oxygen will be sold to author's patented power plants for burning fossil fuel. The question is, if one has cheap electricity why bother to use fossil fuel to produce electricity. Why not sell electricity. Secondly, with oxygen combustion the power plant produces nearly pure CO_2, therefore it does not need any separation. Then what is this talk about cryogenic separation. [I think the CDS Research LTD is a one man company. And that one man is the author himself.]

- **Pruschek, R., G. Oeljeklaus, G. Haupt, G. Zimmermann, D. Jansen and Ribberink, "The Role of IGCC in CO_2 Abatement,"** p. S153 (The authors are from University of Essen, Germany; Siemens AG, Germany; and Netherlands Research foundation, The Netherlands.)

Annual worldwide CO_2 emissions from energy use of fossil fuels are in the order of magnitude of 22 Gt (1988), corresponding to a carbon inventory of some 6 Gt C. About 20% of them come from electric power generation in coal-fired power plants representing 1.2 Gt C in the fuel. In contrast, carbon used worldwide for raw materials of the chemical industry such as ethylene, propylene, methanol amounts to only 0.09 Gt C. These figures show that only a small fraction of the CO_2 emitted by power plants would be necessary as a feedstock for the production of chemicals, which would not justify demonstration of CO_2 reuse technology on technical scale.

The only potential worth analyzing more closely is substitution of mineral oil based fuels in the transportation sector by methanol, as the major part of the carbon requirement of 1.2 Gt C could be met from power plant emissions. For this purpose, CO_2 and H_2 are converted into the liquid energy carrier methanol which can be stored more easily and which is therefore more suitable to application in today's transportation sector infrastructure. Bound carbon would then be ultimately released into atmosphere by subsequent combustion. Required H_2 must of course be produced using a carbon-free or low-carbon energy source (e.g. by hydropower driven water electrolysis) in order to reduce CO_2 emissions of the overall system.

Stoichiometric conversion of hydrogen and carbon dioxide to methanol following the chemical reaction equation

$$3\ H_2 + CO_2 \rightarrow CH_3OH + H_2O + 49.9\ kJ/mol$$

requires $2.1 m^3$ H_2/kg CH_3OH. Assuming e.g., the whole fuel demand of Germany's traffic sector to be covered by methanol, about 220 billion m^3 H_2 annually is required, which is eleven times the present annual H_2 production in Germany.

The pre-basic designed afterwards is based on a 300 MW-class IGCC power plant with a Siemens Model 94.3A gas turbine-generator with 1190 °C (2175 °F) ISO inlet temperature. Gas generation and treatment include:

- Pittsburgh No. 8 coal is gasified in a pressurized entrained flow (PRENFLO) oxygen-blown gasifier.
- The sensible heat of coal-derived gas is used for steam generation by raw gas cooling.
- Dust is primarily removed by cyclone and candle filter arrangements.
- Alkali compounds and residual fine dust are separated in a Venturi (water) wash.
- CO and H_2O are converted into CO_2 and H_2 in a water gas shift reactor system.
- Sulfur compounds (H_2S, COS) and CO_2 are simultaneously removed by Rectisol wash.

By this means, around 88% CO_2 (related to C input by coal) are removed and extracted in gas phase with acceptable amount of energy and investment costs. The following table compares salient data of IGCC with CO_2 removal a standard IGCC as a reference case. The incorporation of CO_2 separation results in a 6 percentage points lower efficiency.

Salient Data of IGCC with CO_2 Removal Compared to the Reference Case

Items	Reference Case	With CO_2 Removal
CO_2 emission from stack, kg/s	72.9	8.4
CO_2 emission from stack, kg/kWh	0.69	0.09
Coal heat input, MJ/s	811.2	876.1
Gross power output from gas turbine, MW	238.8	234.1
Gross power output from steam turbine, MW	177.7	170.2
Total gross power output, MW	416.5	404.3
Auxiliary power requirement, MW	37.8	49.1
Power requirement for gas treatment, % Aux. power	3	24
Net power output, MW	378.6	355.2
Net efficiency, %	46.7	40.5

The CO_2 based methanol plant is integrated into the IGCC. The two plants are liked through CO_2 fraction removed and imported/exported steam. Hydrogen as reactant is imported as 100% pure H_2 at 66 bar pressure.

Salient data of the coproduction system are:

- Coal input, tonnes/day 2300
- Hydrogen input, tonnes/day 780
- CO_2 (intermediate product), tonnes/day 5500
- Methanol product (>99.85 wt %) 3800
- Gas turbine gross power output, MW 234
- Steam turbine gross power output, MW 120
- Total gross power output, MW 354
- Total net power output, MW 310

Total investment costs for coproduction of power and methanol/gasoline costs of IGCC with CO_2 removal and of methanol synthesis/MTG plant. Specific costs of coproduced methanol/gasoline strongly depend on hydrogen price. CO_2 from IGCC could be considered as for free in case extra costs caused by CO_2 removal are allocated to generating costs. In the present case, a simplified cost calculation model has been used which is solely based on investment costs for the additional equipment of the methanol system and hydrogen production costs depending on the different sources. Taking into account that the CO_2 stream has been provided by adding a CO_2 removal plant to a standard IGCC, the specific methanol production

costs estimated as described above are penalized by thereby higher generating costs according to the ratio of electricity and coproduced methanol/gasoline.

In Figure 3 (not reproduced in these notes), methanol/gasoline production costs are plotted against hydrogen price (1 ECU = 1.25 US$). General target should be that methanol costs are below market price and gasoline costs are below market price including tax. Both comparative figures are indicated in the diagram showing that even with today's cheapest hydrogen produced from natural gas by steam reforming (not CO_2-free), methanol is not competitive. Synthetic gasoline is only below market price if based on this hydrogen source and not charged with tax.

In Figure 4 (not reproduced in these notes), primary energy requirements and accompanying CO_2 emissions for different cases of interest are collected. It turns out that only power generation via IGCC and parallel use of cars fuelled with hydrogen from a CO_2-free source show a slightly lower CO_2 output than IGCC with coproduction of electric power and methanol as substitute for oil based gasoline.

The article concludes by stating that CO_2 removal from IGCC makes drastic CO_2 reduction possible as required by the IPCC in the next century if it can be disposed of. A conceivable CO_2 disposal strategy apart from deep sea dumping and underground storage is reutilization of extracted CO_2, which is of course a more expensive way, and CO_2 emission abatement of the overall system is less pronounced.

- **Bracht, M. P.T. Alderliesten, R. Kloster, R. Pruschek, G. Haupt, E. Xue, J.R.H. Ross, M.K. Koukou and N. Papayannakos, "Water Gas Shift Membrane Reactor for CO_2 Control in IGCC Systems: Techno-Economic Feasibility Study,"** p. S159. (The authors are from University of Essen, Germany; Siemens A.G., Germany; University of Limerick, Ireland; and University of Athens, Greece.)

Conventional process schemes for CO_2 removal for oxygen blown entrained bed gasifiers comprise low temperature gas cleaning, a separate water gas shift conversion to convert the CO with steam in the fuel gas mixture into CO_2 and H_2, followed by CO_2 removal for example by scrubbing with solvents. The extent of the shift conversion determines the final CO concentration in the fuel gas and thus the maximum level of CO_2-control. The thermodynamic equilibrium conversion of CO decreases as temperature increases. In order to achieve high CO conversion, a two-step catalytic process is usually employed.

One of the methods to circumvent conversion limitations is to enforce an equilibrium displacement to the product side. From an energy efficiency viewpoint, this should be achieved by continuous removal of one of the product components directly at the place where it is formed.

One approach to reach this is the use of a catalytic membrane reactor, in which the water gas shift reaction is combined with H_2 separation from the reaction mixture in one reactor, using ceramic membranes selectively permeable to hydrogen.

The authors propose the layout of the membrane reactor as shown in Figure 3 (which has not been reproduced in these notes.) In this layout, a shift reactor, cooler and membrane reactor are shown. In the first shift reactor bulk of the shift conversion is carried out which causes a large temperature rise. The effluent from the first reactor is cooled in the cooler and then fed to the membrane reactor. In the membrane reactor hydrogen is removed and the shift reaction is pulled

over the thermodynamic equilibrium. The temperature rise in the membrane reactor will be moderate. The pressure drop across the membrane is 15 bar.

The IGCC plant incorporating the membrane reactor is as follows:

- Gasification process is PRENFLO, entrained-flow, oxygen blown gasification with dry coal dust.
- Synthesis gas cleaning system is conventional wet gas cleaning (low temperature) or advanced dry gas cleaning (elevated temperature).
- CO_2 delivery is either at 15 °C, 1 bar (i.e., gaseous) or 15 °C, 150 bar (i.e., liquid).

To enhance the hydrogen recovery of the membrane reactor, a sweep gas is fed at the low pressure side of the membranes in countercurrent flow mode. The sweep gas consists of the nitrogen fraction from the air separation unit, saturated with water to increase the available mass flow and for NO_x suppression in the gas turbine combustor. The unconverted and unseparated gas stream from the membrane reactor still contains CO and H_2 which is burned with the oxygen from the air separation unit in a catalytic burner. The exhaust gas from the gas turbine and catalytic combustor is sent to the HRSG.

The following table summarizes performance of the IGCC containing membrane reactor.

Results of IGCC Calculation

IGCC Configuration	Net Power Efficiency %	Overall CO_2 Recovery %
No CO_2 removal	46.7	-
Conventional CO_2 removal	40.5	88
Shift & membrane reactors with conventional gas cleaning	42.8	80
Shift & membrane reactors with dry gas cleaning	43.4	80

This table shows that the incorporation of shift and membrane reactors in the IGCC system is attractive for CO_2 removal as compared to conventional options. Although the rate of CO_2 removal is a little lower than the conventional case, the efficiency of the novel system is significantly higher.

Results of the economic evaluation are summarized in the following table.

Results of Economic Analysis

Item	Base Case	Conventional CO_2 Removal	Membrane Reactor CO_2 Removal with Conventional Gas Cleaning
CO_2 recovery (Note 1)	-	88	80
CO_2 state	-	Gaseous	Gaseous
Net power, MW	379	355	433
Net efficiency, % LHV	46.7	40.5	42.8
Investment, ECU/kW (Note 2)	1560	1869	1594
Cost of electricity, ECU/kWh	0.0787	0.0867	0.0835

Notes:

1. Based on coal input.
2. European Currency Unit, 1ECU = 1.27 US$, 30 July 1996,

The additional equipment which was included in the above economic analysis of the IGCC is as follows. Saturation system, CO shift reactor, membrane reactor, catalytic burners, and two HRSGs. The analysis shows that investment cost and cost of electricity is not much higher than the base case.

- **Gaudernack, Bjorn and Steinar Lynum, "Natural Gas Utilization without CO_2 Emissions,"** p. S165. (The authors are from Institute for Energy Technology, Norway; and Kvaerner Engineering, Norway.)

This paper describes two methods of natural gas utilization without CO_2 emissions. The first is o produce hydrogen by steam reforming of natural gas. The second method is to produce hydrogen and carbon by cracking natural gas.

Advances in Steam Reforming of Natural Gas. Steam reforming is the dominant method for hydrogen production, and the technology is well proven. Nonetheless, developments and improvements are taking place. Conventional steam reformers are large and operate at high temperatures with poor heat transfer and emission of CO_2 and NO_x. They are being replaced by more compact reformers of the heat exchanger type. It has also been proven advantageous to carry out the reforming in two stages, adding oxygen for autothermal reforming in one of the stages. These features are being incorporated in ICI Katalco's Leading Concept Hydrogen (LCH) process, using the specially designed Gas-Heated Reformer (GHR) in the first stage. These reformers will reduce the investment and operating costs (Abbishaw et al., 1996).

The possibilities of incorporating selective sorbents or membranes into steam reformers or shift reactors are being investigated. Selective removal of one of the products (H_2 or CO_2) will shift the equilibrium and create more favorable thermodynamic conditions, permitting lower operating temperatures. An example is the Sorption Enhanced Reaction Process (SERP) being developed by Air Products and Chemicals, where a special CO_2-selective sorbent has been developed. This is expected to result in lower operating temperatures, reduced downstream

purification, less expensive construction materials (Anand et al., 1996). An alternative is to remove hydrogen selectively through H2-permeable membranes. Thin supported membranes of a Pd-Ag alloy have been investigated with promising results (Laegsgaard Jorgensen et al. 1995)

The paper also mentions two studies which calculated the cost of the CO_2 avoidance at a GTCC plant as 80 US$/tonne CO_2 (Holloway, 1996) and the cost of capture of CO_2 in a hydrogen plant as 20 US$/tonne CO_2 (Audus et al., 1996).

One suggestion for the use of hydrogen is to mix it with natural gas (call it hythane) and send it from Norway to other parts of Europe by means of hythane pipeline. According to the paper many European countries are interested in the use of hythane.

[The latter part of the paper describes advances in natural gas cracking to produce carbon black, proposed uses of carbon black etc.]

- **Gottlicher, G. and R. Pruschek, "Comparison of CO_2 Removal Systems for Fossil-Fuelled Power Plant Processes,"** p. S173. (The authors are from University of Essen, Germany.)

This article summarizes the data published in some 300 articles on the subject of CO_2 removal systems for fossil fueled power plants. The article divided the CO_2 removal processes into five groups, as follows.

Process Group I comprises processes with CO shift or steam reforming before CO_2 removal. The resulting hydrogen rich fuel gas can then be combusted with air after H_2/CO_2 separation. Also the option of H_2/CO separation without CO shift is possible.

Process Group II covers processes where fuel is combusted in an atmosphere of oxygen mixed with recycled CO_2 or steam.

Process Group III includes all kinds of fossil-fuel-fired power generation systems in which CO_2 is removed from the flue gas after combustion at the exhaust end of the plant.

Process Group IV includes the so-called Hydrocarb processes whereby carbon is separated from the fuel prior to combustion.

Process Group V deals with CO_2 separation in fuel cells suitable for the use of fossil-fuel-derived gases.

Efficiency Reduction due to CO_2 Removal.

CO_2 separation processes applied to a fossil-fuel-fired power plant give rise to additional energy consumption and to the direct reduction of power output. Assuming a pipeline pressure of 110 bar, the energy requirement for liquefaction by intercooled 5-stage compression starting from 1 bar amounts to about 0.12 kWh/kg CCO_2. Thus, in the case of 90% CO_2 removal, the CO_2 liquefaction reduces the efficiency of coal-fuelled power plants by 3.2 to 5.1 percentage points. The efficiency of natural gas fired power plants is reduced by 2.2 to 2.8 percentage points. These values of efficiency reduction depend on the carbon content and heating value of the fuel and the CO_2 removal extent. The following figures on efficiency reduction are based on the assumption that the CO_2 removed is at 1 bar (gaseous).

Process Group I. The efficiency reduction due to CO_2 removal is predominantly caused by:

- Exergy destruction is due to steam reforming or gasification and CO shift. Overall efficiency reduction of 2.5 to 5 percentage points.
- Energy demand of the gas separation process (i.e., regeneration, compression). Efficiency reduction of about 1 percentage point.
- Volume displacement of the separated carbon dioxide. Efficiency reduction of about 1 percentage point.

The efficiency reductions for Process Group I are

- In the range of 4 to 7.4 percentage points for an IGCC with CO shift (CO_2 removal: 80 to 90%).
- And around 14.5 percentage points for a natural gas fired combined cycle with steam reforming, CO shift and absorption by MDEA (CO_2 removal below 60%).

Process Group II. The efficiency reductions due to O_2/CO_2 firing (as cited in the literature and as calculated by the authors) are in the range of 4.8 to 8.5 points for IGCC power plants and about 6 percentage points for natural gas fired plants.

Process Group III. In this process scheme the bulk of the proposals apply flue gas scrubbing with amine-based chemical sorbent. Such removal processes consume up to two thirds of steam as extraction steam (2 – 5 bar) for solvent regeneration. Efficiency figures cited in the literature are in the range of 8 to 11 percentage points when 80 to 90% of the CO_2 is removed from coal-powered plants, or 5.5 to 11 percentage points when removed from GTCCs.

Process Group IV. Processes like "Hydrocarb" (Steinberg et al. 1991) aim at the separation of carbon from the fuel. This option, however, is reasonable approach only for a fuel mix consisting of biomass and natural gas or oil, where the CO_2 released is generated from the biomass and the sequestered fossil carbon is disposed. According to Steinberg, the conversion efficiency (energy of produced methanol divided by energy input of natural gas and biomass input, LHV) amounts to 60.9%. To compare this process with the other CO_2 removal options as discussed before, one has to multiply this conversion efficiency with a cycle or plant efficiency (reciprocating engines, steam and gas turbine cycles).

Process Group V. Phosphoric acid fuel cells (PAFC), molten carbonate fuel cells (MCFC) or solid oxide fuel cells (SOFC) can be operated with fossil fuel derived gases. The efficiency of power plants with PAFC is below the efficiencies of other combined cycles. MCFC or SOFC combined cycles are expected to achieve higher efficiencies. In all three cases the extra energy demand in the range of 0.05 to 0.11 kWh/kg CO_2 is required for the necessary separation of residual fuel and CO_2 removal rate is probably limited to around 80% with specific CO_2 emissions of 0.15 to 0.17 kg of CO_2 per kWh.

Efficiencies of power plants incorporating CO_2 removal based on today's available technology (efficiencies without CO_2 removal: IGCC = 50%, GTCC = 58%) and respective CO_2 emissions are depicted in Fig. 1 (not reproduced in these notes) and listed in more detail in the following two tables.

Estimate of Efficiencies, CO_2 Emissions and Costs

Based on Present Status of Technology
Process Group I: CO_2 Removal from Fuel Gas Before Combustion

Processes with CO_2 Removal (Liquid CO_2, 110 bar)				Reference Processes			Cost of CO_2 Avoid. DM/t
	DM/ kW	$KgCO_2$/ kWh	Efficiency %	DM/ kW	$KgCO_2$/ kWh	Efficiency %	
IGCC-CO-Shift, Wet Quench	3300	0.108	31.4	2350	0.83	38.9	48
IGCC-CO-Physical Absorption	3595	.102	40.2	2700	0.64	50.0	58
IGCC-CO-Shift, Sea Water*	3330	0.095	41.8	2700	0.64	50.0	43
IGCC-CO-Shift, Chemical Absorption	3720	0.055	39.2	2700	0.64	50.0	61
IGCC-CO-Shift, Membrane, HG Clean up	3400	0.110	41.1	2700	0.64	50.0	48
IGCC-CO-Shift, Membrane Reactor	3360	0.175	42.6	2700	0.64	50.0	49
IGCC-CO-Shift, Cryogenic Distillation*	3600	0.121	39.7	2700	0.64	50.0	61
IGCC-CO-Shift, Adsorption*	4800	0.136	29.8	2700	0.64	50.0	151
Air Blown IGCC-CO-Shift, Chemical Absorption	3440	0.179	34.4	2300	0.69	46.7	82
IGCC, H_2/CO Membrane*	3500	0.060	41.8	2700	0.64	50.0	47
Natural Gas Fired Processes							
Steam Power Plant, Reformer*	2660	0.053	33.3	2000	0.46	45.0	115
GTCC, Reformer	1600	0.156	42.0	940	0.36	57.5	207

Estimate of Efficiencies, CO_2 Emissions and Costs

Based on Present Status of Technology
Process Group II: O_2 /CO_2 Firing

Processes with CO_2 Removal (Liquid CO_2, 110 bar)				Reference Processes			Cost of CO_2 Avoid. DM/t
	DM/ kW	$KgCO_2$/ kWh	Efficiency %	DM/ kW	$KgCO_2$/ kWh	Efficiency %	
Steam Power Plants	3660	0.007	33.6	2400	0.72	45.0	64
Direct Coal-Fired Combined Cycle*	3090	0.007	40.6	2000	0.61	52.5	63
MHD Combined Cycle	3110	0.007	38.2	2000	0.64	50.7	63
IGCC+ PFBC (Partial Gasification)	3690	0.007	34.8	2300	0.69	46.7	71
IGCC-O_2/H_2O–Blown Gasification	3900	0.007	39.9	2700	0.64	50.0	63
IG-STIG-O_2/H_2O–Blown Gasification*	4210	0.007	28.2	2700	0.84	38.4	66
IGCC-CO_2/H_2O–Blown Gasification	3890	0.007	40.1	2700	0.64	50.0	63
Natural Gas Fired Processes							
Steam Power Plants*	2580	0.007	37.1	2000	0.46	45.0	74
GTCC	1590	0.007	48.6	940	0.36	57.5	84
Evaporative Cycle*	1540	0.007	45.8	900	0.37	56.0	89
Internal Combustion Rankine Cycle	3620	0.007	34.1	940	0.36	57.5	337

The following articles were copied from the following web site.
http://www.ieagreen.org.uk/sr1p.htm

- **Riemer, Pierce, "Greenhouse Gas Mitigation Technologies. An Overview of the CO_2 Capture, Storage and Future Activities of the IEA Greenhouse Gas R&D Program,"** paper presented in 1995. September 1998. (The author is from IEA, France.)

- **Freund, Paul, "Abatement and Mitigation of Carbon Dioxide Emissions from Power Generation," paper presented at the Power-gen conference, Milan, June 1998.** September 1998. (The author is from IEA, France.)
- **IEA Greenhouse Gas R&D Program, "Carbon Dioxide Capture from Power Stations," the second in a series of public summaries of work,"** September 1998.

This report consists of the following sections:

- Introduction
- Design and Chemistry
- Criteria for Case Studies
- Absorption Technologies
- Adsorption Technologies
- Cryogenic Technologies
- Membrane Systems
- Comparing the Capture Options
- Conclusions

Introduction:

This is the second in a series of public summaries of work carried out by the IEA Greenhouse Gas R&D Program. Selected power generation, CO_2 capture, and CO_2 disposal options are evaluated, relating them to whether they are a presently available technology, likely to be available in the near future or long term prospects requiring considerable development.

The four schemes were selected to represent a wide range of CO_2 concentrations as shown in the following table. The starting point for this report is where the CO_2 has actually been produced.

Flue Gas Rates and CO_2 in Flue Gas

Items	PF + FGD	GTCC	IGCC	CO_2 Recycle
Flue gas flow rate, kg/s	607	1007	1028	178
Flue gas flow rate, kg/s MW	1.2	2.2	2.0	0.4
CO_2 in flue gas, vol.% wet	13	3	7	63
CO_2 in flue gas, vol.% dry	14	4	7	91

The studies concentrate on the overall impact of capture processes (for specifically removing or isolating CO_2) on power generation. The combined power generation and scrubbing plant should have a net output of 500 MW. The original studies on power generation plants were based on this output and hence will need to be scaled up in size to allow for the power consumed in the gas scrubbing process. The need to meet emission standards is considered, in particular,

the most appropriate technology for CO_2 capture from coal fired plant takes account of the need to remove SO_2. [p. 1]

Design and Chemistry:

Processing techniques for the capture of CO_2 are significantly influenced by the concentration or partial pressure of the gas to be captured. For example at low concentrations such as that applying to the exhaust from a natural gas fired turbine, a large amount of inert gas has to be treated which has a significant cost penalty on the size of any downstream scrubbing, heat recovery equipment, etc. However, the quantity of adsorbent or absorbent required is a function of the quantity of CO_2 to be removed. Chemical solvents are likely to be preferred for cases with low concentrations or amounts of CO_2 in the combusted gases and do not gain significant advantage by operating at elevated pressure. Whereas, physical solvents are favored by high pressures and low concentrations of inert gases such as nitrogen.

The solvent regeneration (or gas recovery) step is relatively simple for physical absorption as it is carried out by pressure let down and, for example, as in Selexol process can be arranged in more than one stage to optimize energy requirements. For chemical absorption, significant quantities of heat are needed to dissociate the chemical complex formed by reaction with the CO_2.

Membranes use partial pressure as the driving force for separation and consequently will be most effective at high concentrations and pressure of CO_2. They are not very selective at separating individual components of a gas stream and if low residual CO_2 and/or high CO_2 purity is required, a number of separation stages are required. There is a strong possibility that a combination of processes such as membranes and monoethylamine (MEA) absorption, or cryogenics will be attractive as they would combine the bulk CO_2 removal characteristics of membranes with the ability to CO_2 down to low levels.

The presence of other acid gases and their concentration relative to the amount of CO_2 is likely to be a key factor in determining the optimum CO_2 recovery process. Chemical solvents tend to react with both SO_x and NO_x to form heat stable salts which are not easily recoverable. This can result in unacceptable solvent losses unless SO_x and NO_x are removed upstream. SO_2 is generally much more soluble than CO_2 in physical solvents. For example SO_2 is about 100 times more soluble than CO_2 in Selexol and is not easily recovered other than by thermal means. Hence very low levels of SO_2 are necessary (in the 5-10 ppmv region) prior to CO_2 recovery. NO_x compounds are not particularly soluble in physical solvents such as Selexol and in general are less of a handicap to CO_2 recovery than SO_x.

Criteria for Case Studies:

The base case was 500 MW electricity sent out from the power plant, with a 35 years working life. Costs are given in US dollars, nominally set at the third quarter of 1992; accuracy is believed to be ± 30%. Ambient conditions, natural gas analysis and coal analysis, fuel cost etc. are the same as described in the first report.

Absorption Technologies:

The CO_2 can be physically absorbed in a solvent according to Henry's law and then regenerated using either or both heat or pressure reduction. Typical solvents are Selexol (dimethylether of polyethylene glycol) and Rectisol (cold methanol) which are applied at high pressure. At lower pressures, the chemical absorption processes are more economical. The Selexol physical solvent process is frequently specified for coal gasification applications.

Hybrid solvents combine the best characteristics of both the chemical and physical solvents and are usually composed of a number of complementary solvents. Hybrid solvents have outperformed existing solvents. Currently the tendency has been to develop tailor-made solvents using complementary solvents where the proportions are varied to suit the application. Typical solvents are A-MDEA, Purisol, Sulfinol, and UCARSOL.

All the processes operate in essentially the same manner by scrubbing the flue gas in absorption towers to collect the CO_2 and then regenerating the solvent and releasing the CO_2.

Figures arrived for the cost incurred per tonne of CO_2 release to atmosphere avoided range from 16-87$/tonne as shown in the following table. They do not include the cost of CO_2 liquefaction and disposal. [p. 2]

Carbon Dioxide Releases and Cost of Avoidance
(Efficiencies as %LHV)

Items	PF + FGD	GTCC	IGCC	CO_2/ O_2	IGGC Selexol
Reference efficiency, %	40	52	42	33	42
Efficiency after CO_2 capture, %	29	42	28	30	36
CO_2 captured, %	90	85	90	99	82
CO_2 in product CO_2, %	99.2	99.4	99.8	99.9	96
Cost CO_2 avoided, $/tonne	35	55	87	16	23
Power cost, ref. mills/kWh	49	35	53	78	53
Power cost, mills/kWh	74	53	112	94	63
Investment cost of ref. case, $/kW	1058	702	1561	2044	1561
Invest. cost of CO_2 removal case, $/kW	1842	1367	3254	3102	2400

The key criteria in evaluating options are the amount of CO_2 vented to atmosphere per unit of power sent out and the cost of the power. As can be seen from the above table the CO_2 recycle system reduces CO_2 emissions but at a cost which is twice as expensive as the cost of generating power in the base case PF + FGD plant. It is not feasible to get down to such low levels of CO_2 release using absorption systems on the PF + FGD and GTCC plants but good CO_2 emissions can be obtained at a cost of 74 and 53 mills/kWh, respectively.

The dramatic increase in the power cost for the IGCC case shows that using absorption on the gas turbine exhaust is not an effective way to capture CO_2. Hence alternative schemes are based on treating the gasifiers product gas to concentrate the carbon before combustion and take advantage of the operating pressure.

An additional exercise looked at an IGCC system where the fuel gas was shifted in a high and low temperature shift reactor and then cleaned in a Selexol unit. The H_2S and CO_2 leave the unit in separate streams. The cleaned fuel gas (mainly H_2) is burned in the gas turbine. The heat of the flue gases is transmitted to the steam system, for power generation in the steam turbines. The separated CO_2 is dried and compressed ready for storage. [p. 2]

For the CO_2 removal from an IGCC power plant some additional investments are needed. The shift reactors, the CO_2 separation section of the Selexol unit and the CO_2 compression and drying section have to be added. Also, the steam system has to be modified slightly. The costs of the IGCC are 113 million US$ higher than for the reference base case. The overall efficiency from the IGCC with CO_2 removal by means of scrubbing is 36%. The efficiency drop due to CO_2 removal is 6%. [p.3]

Adsorption Technologies:

Typical gas-solid adsorption systems which may be applicable for removal of CO_2 from power plant flue gas employ adsorbent beds of alumina, zeolite or activated carbon. Other solid materials used commercially in gas separation processes are alumina gel and silica gel. However, processes using these gels are a hybrid of adsorption and absorption.

There are several adsorption methods used commercially in the process industries that may be applicable for removing CO_2 from power plant flue gases. These employ adsorbent beds of alumina and zeolite molecular sieves (natural or manufactured aluminosilicate).

Four methods are used commercially for regeneration. Pressure swing regeneration or adsorption (PSA) involves lowering the pressure in the vessel containing the saturated bed until trapped gases are pulled off the bed. Technologies requiring a vacuum to regenerate are called VPSA units. The regeneration cycles are relatively short and are typically measured in seconds. Thermal (or temperature) swing adsorption (TSA) employs high temperature regeneration gas to drive off trapped gases. The regeneration cycles are quite long (measured in hours), and result in larger quantities of adsorbent being required than with PSA systems. The third method employs a stream of fluid that does not contain any of the trapped gas in an effort to “wash” the bed. The final method involves using a gas stream that contains a material that can “bump” the trapped gas from its place in the bed and is essentially a chromatographic procedure.

Most commercial units use either a PSA type regeneration, or a combined thermal swing/wash method that regenerates at reduced pressure, known as thermal swing. The chromatographic method of bumping captured gas is usually employed for small services. The commercial alumina and commercial gel processes employ thermal swing regeneration exclusively.

The mass of gas adsorbed per unit weight of solid is a key factor in the assessment of potential sorbents. As molecular sieves have a capacity for CO_2 adsorption about five times that of alumina, it was decided to concentrate on the use of molecular sieve based systems. Energy is released during adsorption which means that isothermal adsorption is not practical. This leads to

lower effective mean adsorption capacities than predicted for constant temperature operation and a requirement to optimize the adsorption/desorption cycle. Similar to the absorption process, the adsorption can be primarily chemical or physical with physical adsorption being the less energy intensive to reverse. The driving force for regeneration is obtained either by raising the temperature (TSA) or reducing the pressure (PSA).

The calculated power cost shows that the use of state of the art adsorption technology for CO_2 capture is not at all attractive. All the options considered except the CO_2 recycle case, more than double the cost of power. Even the CO_2 recycle case is not attractive, as in practice, a system based on condensation of the water followed by removal of trace gases would be used.

The PSA system is more attractive than the TSA system because of the nature of the regeneration cycles (see the following table). TSA requires two to three times more energy than PSA and the regeneration gas used in TSA dilutes the product. The physical size of the TSA plants are about ten times the PSA equivalent due to the difference in quantity of adsorbent required.

Comparison of PSA and TSA Technology Against the Base Case Technologies (Efficiencies as % LHV)

Items	PF + FGD	GTCC	IGCC	CO_2/O_2
Reference efficiency, %	40	52	42	33
Efficiency after CO_2 capture using PSA, %	28	33	26	29
Efficiency after CO_2 capture using TSA, %	29	39	29	-
CO_2 captured, %	95	95	95	95
CO_2 in product CO_2, %	75	50	60	97
Cost CO_2 avoided using PSA, $/tonne	84	544	205	21
Cost CO_2 avoided using TSA, $/tonne	264	401	361	-
Power cost of reference case, mills/kWh	49	35	53	78
Power cost using PSA, mills/kWh	114	140	201	98
Power cost using TSA, mills/kWh	179	241	215	-
Investment cost for reference case, $/kW	1058	702	1561	2044
Invest. cost for CO_2 removal using PSA, $/kW	1369	1200	2150	2189
Invest. cost for CO_2 removal using TSA, $/kW	2363	1548	3031	-

It is apparent that state of the art adsorption technology has little attraction for the schemes examined here. However, there is the possibility that work on metal oxide gels may be of interest whether as a membrane, adsorbent, or in a combined role.

Cryogenic Technologies:

Cryogenic methods for only IGCC and the combustion in O_2/CO_2. Cryogenic systems use a low temperature physical approach, in which the CO_2 is separated directly or by using a solvent. Methane is difficult to separate from CO_2 but some processes have been developed specially for the methane-CO_2 system. Water also presents problems in cryogenic systems, so the feed gas must be dried before being cooled.

Carbon dioxide can be physically separated from other gases by condensing the CO_2 at cryogenic temperature. The minimum CO_2 mole fraction in the gas phase is achieved by

lowering the temperature and raising the total pressure as much as practical, but in most situations it is not practical reduce the temperature below the freezing point of CO_2 (-56.6°C). Alternatively it can be achieved by compression to a supercritical fluid followed by distillation (with lower associated energy temperature), with power recovery on the gas phase. [p. 1.]

The base IGCC plant has a design efficiency of 42% (LHV) and total CO_2 emissions of 790 kg/MWh. When cryogenics are applied to remove the CO_2 the efficiency is reduced to 36% and the cost of electricity increases, as shown in the following table. The Selexol unit used to collect the H_2S also removes about 15% of the CO_2 in the gas stream and vents this to the atmosphere. Hence not all of the CO_2 reaches the cryogenic plant. {Surely, it can be redirected to the cryogenic plant.] A dual system (Ryan Holmes process) was utilized. It involves contacting the dry de-sulfurized synthesis gas/CO_2 mixture with a C_4 hydrocarbon which absorbs 97% of the CO_2. The liquid hydrocarbon and CO_2 then pass to a second column and the pressure is raised to 140 bar where the hydrocarbon is stripped out and CO_2 is in liquid form ready for disposal.

Comparison of IGCC and Combustion in Oxygen Base Case Studies Using Cryogenics to Remove the Flue Gas CO_2

(Efficiencies as % LHV)

Items	IGCC	CO_2/O_2
Reference efficiency, %	42	33
Efficiency after CO_2 capture, %	36	27
CO_2 captured, %	85	85
CO_2 in product CO_2, %	97	99
Cost CO_2 avoided, $/tonne	23	26
Power cost, reference mills/kWh	53	78
Power cost, mills/kWh	78	109
Specific investment cost, reference case, $/kW	1561	2044
Specific investment cost, CO_2 removal case, $/kW	2763	3597

The efficiency of the power plant in which oxygen is used for combustion was 33% (LHV basis), which is about 7% less than the conventional PF plant. The CO_2 leaving the recycle process is at a concentration of 91% by volume (dry basis). When cryogenics are applied to remove CO_2 the efficiency is reduced to 27% and the cost of electricity rises. [p. 1.]

Membrane Systems:

Two membrane operations which appear to have potential are gas separation and gas adsorption.

Gas Separation Membranes. Gas separation membranes rely on a difference in physical or chemical interaction between components present in a gas mixture with the membrane material,

causing one component to permeate faster through the membrane than another (component). The gas component dissolves into the membrane material and diffuses through it to the other side.

The membrane divides the feed gas stream in two – the permeate stream and the retentate stream. The quality of the separation is determined by the selectivity and by two process parameters: the ratio of the permeate flow to the feed flow; and the ratio of permeate pressure to the feed pressure. Usually the selectivity of the membrane is insufficient to achieve the desired purity and recovery and multistage plants with or without recycle of the permeate are necessary. This leads to increased recompression costs and increased capital costs. There are a number of different types of gas separation membranes currently available. Some have only been examined on the laboratory scale. In the descending order of commercialization, they are polymer membranes, palladium membranes, facilitated transport membranes and molecular sieves. [p. 1]

The gas separation membranes used were polyphenyleneoxide and polydimethylsiloxane. The former has good CO_2/N_2 separation characteristics (with very low CO_2 content in the gas stream (which gas stream?) and costs about 150 US$/m^2. The latter at 300 US$/m2 is a good CO_2/O_2 separator. These two were selected for their properties and the requirement that commercially available technology should be applied where possible. [p.2]

Gas Absorption Membranes. Gas absorption membranes are used as contacting devices between a gas flow and a liquid flow. The separation is caused by the presence of an absorption liquid on one side of the membrane which selectively removes certain components from a gas stream on the other side of the membrane. In contrast with gas separation membranes, it is not essential that the membrane has any selectivity at all. It is merely intended to provide a contacting area without mixing gas and absorption liquid flow. The selectivity of the process is derived from the absorbing liquid.

Comparison of Four Base Case Studies Using Membrane and Membrane/MEA Combinations to Remove the Flue Gas CO_2.

(Efficiencies as % LHV)

Items	PF + FGD	GTCC	IGCC	CO_2/O_2
Reference efficiency, %	40	52	42	33
Efficiency after CO_2 capture with membrane, %	31	31	26	31
Efficiency after CO_2 capture with membrane/MEA, %	30	47	32	30
CO_2 captured, %	80	80	80	80
CO_2 in product CO_2, %	55	16	30	97
Cost CO_2 avoided with membrane, $/tonne	47	335	125	9
Cost CO_2 avoided with membrane/MEA, $/tonne	45	31	42	16
Power cost of reference case, mills/kWh	49	35	53	78
Power cost with membrane, mills/kWh	83	125	129	90
Power cost with membrane/MEA, mills/kWh	81	45	84	94
Investment cost for reference case, $/kW	1058	702	1561	2044
Invest. cost for CO_2 removal with membrane, $/kW	2103	3116	4855	2213
Invest. cost for CO_2 removal with membrane/MEA, $/kW	1644	-	2736	-

Removal of flue gas components like SO_2 or CO_2 is achieved through the use of porous, hydrophobic membranes in combination with suitable absorption liquids, such as sulphite, carbonate or amine solutions.

The CO_2 is removed from each process with the aid of gas absorption membranes (in combination with MEA). For the gas absorption membrane case porous polypropylene was selected.

The results of both types of membranes are summarized in the above table. The above table shows that the energy requirements for both the IGCC and GTCC systems are high when gas separation membranes are used due to the high compression requirements of the gas flow. The PF + FGD is better although the best is the CO_2 recycle case where the CO_2 is already concentrated in the exhaust flow.

The CO_2 removal using gas absorption membranes in conjunction with MEA were all significantly better than the membrane on its own. There is still a significant decrease in power output although this reduction depends on the amount of CO_2 in the flue gas. The combination of MEA and membranes seems the best removal option for all of the technologies (except for the CO_2 recycle where gas separation membranes are superior) in terms of power cost, CO_2 removed and the cost of CO_2 avoided. This is particularly promising as new improved gas absorption membranes are expected on the market shortly.

Comparing the Capture Options:

The following table illustrates some results for the CO_2 capture alternatives as applied to just PF + FGD option**.**

Typical Capture Data for PF + FGD System Incorporating CO_2 Capture

Item	Efficiency %	Power Cost Mills/kWh	Cost CO_2 Avoided $/tonne	CO_2 Emission Rate g CO_2/kWh
PF + FGD Base Case	40	49.0	-	829
+ Membrane	31	77.6	45.0	194
+ Membrane & MEA	30	74.7	42.3	222
+ Absorption (MEA)	29	74.0	35.0	116
+ Cryogenics	-	-	-	-
+ Adsorption PSA	28	114.0	84.0	57
+ Adsorption TSA	29	179.0	264.0	335

The following articles appeared in *Proceedings of the Advanced Coal-Based Power and Environmental Systems '98 Conference*, Morgantown, July 21-23, 1998.

- **Lackner, Klaus S. et al, *"Mineral Carbonates as Carbon Dioxide Sinks."*** (The authors are from Los Alamos National Laboratory, Los Alamos, NM 87544.)

In contrast to a generally held belief, carbon dioxide is not the lowest energy state of carbon. Instead the formation of carbonates from carbon dioxide and many common magnesium or calcium bearing silicate minerals is exothermic and thermodynamically favored. Consequently, CO_2, is not the unavoidable end product of combustion. On geological time scales mineral carbonation happens spontaneously and represents an important part of the overall carbon cycle. We plan to accelerate this natural process in an industrial setting to the point that it can absorb anthropogenic CO_2 emission.

We are developing an industrial process that binds CO_2 in an exothermic reaction. The result is a thermodynamically stable and environmentally benign carbonate formed from readily available mineral rocks like serpentinite or peridotite. These magnesium silicates ores are rich in magnesium; they are chemically reactive and are readily accessible in quantities that far exceed

even the most optimistic estimate of coal reserves. One promising implementation is based on an HCl extraction in which magnesium is obtained as $MgCl_2$. HCl is quantitatively recovered while $MgCl_2$ is transformed into $Mg(OH)_2$. The hydroxide is carbonated in a gas-solid reaction that provides the energy consumed in recovering the HCl. The overall process is exothermic and our goal is process design that does not require external supply of energy. We are also considering direct carbonation of serpentinite rock. If successful, the latter process would be a net energy producer.

- **Doctor, Richard D. et al, *"Hydrogen Production and Carbon Dioxide Recovery from KRW Oxygen-Blown Gasification."*** (The authors are from Argonne National Laboratory, Argonne, IL 60439.)

An oxygen-blown (Kellogg-Rust-Westinghouse) KRW coal-gasification plant producing hydrogen, electricity, and supercritical CO_2, was studied in a full-energy cycle analysis extending from the coal mine to the final destination of the gaseous product streams. A location in the mid-western United States 160 km from Old Ben #26 mine was chosen. Three parallel gasifier trains, each capable of providing 42% of the plant's 413.5 MW nominal capacity consume 3,700 metric tonnes/stream day of Illinois #6 coal from this mine. The plant produces a net of 151 MW of power for sale. At an 85% capacity factor, the plant also produces 3.7 million standard cubic m/day of 99.999% purity hydrogen. This is sent 100 km by pipeline at 34 bars, and 2.7 million standard cubic m/day of supercritical CO_2 at 143 bars, which is sequestered in enhanced oil recovery 500 km away.

- **Adams**, **E. Eric et al *"Ocean Sequestration of Carbon Dioxide."*** (The authors are from MIT Energy Laboratory, Cambridge, MA 02139.)

The ocean contains 40,000 GtC (Billion tonnes of carbon) compared with annual worldwide anthropogenic emissions of about 6 GtC. Discharging CO_2 directly to the ocean would accelerate the ongoing, but slow, natural processes by which over 90% of present-day emissions are currently entering the ocean indirectly and would reduce both peak atmospheric CO_2 concentrations and their rate of increase.

The issues:

- Impact on the marine organism
- Sequestration efficiency. That is, what is the residence time of the injected CO_2?

- **Gupta**, **Neeraj, et al, *"Feasibility of Long Term Carbon Dioxide Storage in Deep Saline Formation."*** (The authors are from Battelle Memorial Institute, Columbus, OH 43201.)

Deep aquifer sequestration of carbon dioxide, generated from power plant and other industrial emissions, is being evaluated as one of the potential options for the reduction of atmospheric greenhouse gas emissions. The major advantages of using deep aquifers are that the disposal facilities can be located close to the sources. It is a long –term/permanent sequestration option, because a large fraction of the injected CO2 may be fixed into the aquifer by dissolution or mineralization. The major limitations include the potentially high cost, the risk of upward migration, and the public perception of risk. Most of the cost is due to the need to separate CO2 from other flue gases, rather than the actual cost of disposal.

Aquifer disposal involves finding geologically suitable formations for sequestering large amounts of CO2 for a long period, without a significant environmental risk at a reasonable cost. Usually such aquifers are deep, regionally extensive, filled with saline waters, and separated from freshwater and other formations of economic interest by low permeability cap-rock. For CO_2 disposal applications, a minimum depth of 800 meters (1150 psia) is required to maintain the pressure and temperature for retaining CO_2 in a dense supercritical phase. Other siting criteria include detailed evaluation of geologic, hydro-geologic, geo-chemical, and seismic issues.

It is worth noticing that hazardous and non-hazardous liquid waste and acid gas disposal in deep sedimentary formations is well established practice. As an example, in Ohio more than 35 million metric tonnes of waste (88% of which are hazardous) has been injected in wells at class I facilities. Much greater amounts have been injected in other types of injection wells such as the oil and gas drilling related wells. There are also numerous facilities for storage of natural gases in depleted oil and gas reservoirs. The only current facilities for aquifer disposal of CO_2 is the offshore injection well at Sliepner Vest in the North Sea in Norway, operated by Statoil. The data and experience obtained from the existing deep-waste disposal facilities and from the Sliepner Vest site form a strong foundation for further research and development on CO2 responsible for this behavior. This would also not be desirable for the same reasons mentioned. [There seems to be something missing here.

It seems, somehow, there are no cracks or other structural defects which could cause the gas leakage.]

- **Byrer, C. W., et al, "Carbon Dioxide Sequestration Potential in Coal-bed Deposits."** (The authors are from USDOE, FETC, Morgantown, WV 26507)

The concept of using coal deposits for CO_2 sequestration while enhancing or initiating methane production from the coal-beds may be a viable near-term economic system for industry consideration. … Estimated coal resources in the US total 6 trillion tons to depth of 6,000 feet with 90% of this amount considered unmineable because it is not economically feasible with current technology. The unmineable coals represent a widely dispersed potential sink for CO_2, and at the same time, a significant potential source of additional natural gas.

During the last decade, coal-bed methane has been commercially produced in many of the coal-bearing countries, most notably, the U.S. and Australia. More than one trillion cubic feet (Tcf) per year of coal-bed methane is now produced in the U.S., meeting about 5% of the total natural gas demand. Coal-bed methane resources in the U.S. total over 400Tcf of which more than 15 Tcf are classified as proved reserves.

During this period, industry proprietary research has shown that the recovery of coal bed methane can be enhanced by the injection of CO_2 via vertical wells into coal deposits. Coal has a 2:1 sorption selectivity for CO_2 over CH_4. Sequestering CO_2 emissions into unmineable coal-beds potentially can be a viable geological disposal option while significantly enhancing the production of coal-bed methane as an energy source.

Worldwide coal resources with a high affinity for CO_2 may be an attractive natural sink for sequestering emissions of CO_2 as disposal options are evaluated.

Addendum B - Equipment List, CO_2 Removal by MEA Absorber/Stripper
Appendix F

(1 of 6 Trains)

Vessels/Tanks

Absorber	
Number required	1
Fluids handled	MEA, flue gas
Orientation, vertical/horizontal	Vertical
Operating temperature, ° F (°C)	155 (68.33)
Operating pressure, psia (kPa)	19.7 (135.8)
Inside diameter, ft (m)	13.75 (4.19)
Total height, ft (m)	58 (17.68)
Number of actual trays	18
Material of lower 1/3 of shell	SS
Material of upper 2/3 of shell	CS
Material of trays	CS
Stripper	
Number required	1
Fluids handled	MEA, CO_2
Orientation, vertical/horizontal	Vertical
Operating temperature, °F (°C)	246 (118.89)
Operating pressure, psia (kPa)	24.7 (170.3)
Inside diameter, ft (m)	14 (4.27)
Total height, ft (m)	58 (17.68)
Number of actual trays	18
Material of shell	SS
Material of trays	SS
Gas-Liquid Separator	
Number required	1
Fluid handled	CO_2, water
Orientation, vertical/horizontal	Vertical
Operating temperature, °F (°C)	95 (35)
Operating pressure, psia (kPa)	19.0 (131)
CO_2 flow rate, lb/h (kg/hr)	42,893 (19,456)
Water flow rate, lb/h (kg/hr)	41,559 (18,851)
Inside diameter, ft (m)	4.0 (1.22)
Height, ft (m)	11.0 (3.35)
Material	CS

MEA Make up Tank

Number required	1
Fluid handled	100% MEA
Orientation, vertical/horizontal	Vertical
Operating temperature, °F (°C)	60 (15.56)
Operating pressure, psia (kPa)	14.7 (101.4)
Holdup time, days	30
Tank inside diameter, ft (m)	8 (2.44)
Tank height, ft (m)	23 (7.01)
Material	CS

Heat Exchangers

After Cooler

Number required	1
Number of shells per heat exchanger	1
Heat duty, million Btu/h (mkJ)	1.9 (2.005)
Tubeside fluid	Water
Shellside fluid	Flue gas
Tubeside inlet temperature, °F (°C)	63 (17.22)
Tubeside exit temperature, °F (°C)	83 (28.33)
Tubeside flow rate, lb/h (kg/hr)	95,000 (43.091)
Tubeside operating pressure, psia (kPa)	***75 (517)***
Shellside inlet temperature, °F (°C)	175 (79.44)
Shellside exit temperature, °F (°C)	143 (61.67)
Shellside flow rate, lb/h (kg/hr)	235,379 (106,766)
Shellside operating pressure, psia (kPa)	19.7 (135.8)
Shell inside diameter, in (cm)	41 (104.14)
Tube length, ft (m)	14 (4.27)
Heat transfer area, ft^2 (m^2) / shell	1,246 (115.8)
Total heat transfer area, ft^2 (m^2) / heat exchanger	1,246 (115.8)
Shell material	SS
Tube material	SS

MEA Cooler

Number required	1
Number of shells per heat exchanger	1
Heat duty, million Btu/h (mkJ)	46.8 (49.377)
Tubeside fluid	Lean MEA
Shellside fluid	Water
Tubeside inlet temperature, °F (°C)	184 (84.44)
Tubeside exit temperature, °F (°C)	95 (90.56)
Tubeside flow rate, lb/h (kg/hr)	597,806 (271,160)
Tubeside operating pressure, psia (kPa)	24.7 (170.3)
Shellside inlet temperature, °F (°C)	63 (17.22)
Shellside exit temperature, °F (°C)	83 (28.33)
Shellside flow rate, lb/h (kg/hr)	2,340,000 (1,061,406)
Shellside operating pressure, psia (kPa)	75 (517)
Shell inside diameter, in (cm)	52 (132.1)
Tube length, ft (m)	12 (3.66)
Heat transfer area, ft^2 (m^2) / shell	4,080 (379)
Total heat transfer area, ft^2 (m^2) / heat exchanger	4,080 (379)
Shell material	CS
Tube material	CS

MEA/MEA Exchanger

Number required	1
Number of shells per heat exchanger	1
Heat duty, million Btu/h (mkJ)	31.9 (33.656)
Tubeside fluid	Lean MEA
Shellside fluid	Rich MEA
Tubeside inlet temperature, °F (°C)	246 (118.89)
Tubeside exit temperature, °F (°C)	187 (86.11)
Tubeside flow rate, lb/h (kg/hr)	588,472 (266,926)
Tubeside operating pressure, psia (kPa)	24.7 (170.3)
Shellside inlet temperature, °F (°C)	149 (65)
Shellside exit temperature, °F (°C)	200 (93.33)
Shellside flow rate, lb/h (kg/hr)	631,378 (286,388)
Shellside operating pressure, psia (kPa)	24.7 (170.3)
Shell inside diameter, in (cm)	55 (139.7)
Tube length, ft (m)	16 (4.88)
Heat transfer area, ft^2 (m^2) / shell	6,081 (564.9)
Total heat transfer area, ft^2 (m^2) / heat exchanger	6,081 (564.9)
Shell material	SS
Tube material	SS

Condenser

Number required	1
Number of shells per heat exchanger	2
Heat duty, million Btu/h (mkJ)	115.9 (122.281)
Tubeside fluid	Cooling water
Shellside fluid	Gas
Tubeside inlet temperature, °F (°C)	63 (17.22)
Tubeside exit temperature, °F (°C)	83 (28.33)
Tubeside flow rate, lb/h (kg/hr)	5,795,000 (2,628,568)
Tubeside operating pressure, psia (kPa)	75 (517)
Shellside inlet temperature, °F (°C)	212 (100)
Shellside exit temperature, °F (°C)	95 (35)
Shellside flow rate, lb/h (kg/hr)	84,452 (38,307)
Shellside operating pressure, psia (kPa)	20.7 (142.7)
Shell inside diameter, in (cm)	67 (170.2)
Tube length, ft (m)	24 (7.32)
Heat transfer area, ft^2 (m^2) / shell	13,882 (1,289.7)
Total heat transfer area, ft^2 (m^2) / heat exchanger	27,763 (2,579.3)
Shell material	SS
Tube material	SS

Reboiler

Number required	1
Number of shells per heat exchanger	1
Heat duty, million Btu/h (mkJ)	174 (183.580)
Tubeside fluid	Steam
Shellside fluid	Strip. Bottoms
Tubeside inlet temperature, °F (°C)	245 (118.33)
Tubeside exit temperature, °F (°C)	245 (118.33)
Tubeside flow rate, lb/h (kg/hr)	235,340 (106,748)
Tubeside operating pressure, psia (kPa)	50 (344.7)
Shellside inlet temperature, °F (°C)	281 (138.33)
Shellside exit temperature, °F (°C)	281 (138.33)
Shellside flow rate, lb/h (kg/hr)	188,270 (85,398)
Shellside operating pressure, psia (kPa)	24.7 (170.3)
Shell inside diameter, in (cm)	86 (218.4)
Tube length, ft	24 (7.32)
Heat transfer area, ft^2 (m^2) / shell	20,358 (1,891)
Total heat transfer area, ft^2 (m^2) / heat exchanger	20,358 (1,891)
Shell material	SS
Tube material	SS

Pumps/Blowers

Booster

Number required	1
Number of operating boosters	1
Number of spare boosters	0
Booster type	Centrifugal
Fluid handled	Flue gas
Flue gas flow rate, scfm (m^3N/h)	51,790 (83,532)
Flue gas design flow rate, scfm (m^3N/h)	56,970 (91,887)
Flue gas inlet temperature, °F (°C)	131 (55)
Flue gas inlet pressure, psia (kPa)	14.7 (101.4)
Flue gas discharge pressure, psia (kPa)	20 (137.9)
Fractional efficiency, E	0.90
BHP	1,413
Motor horsepower, HP	1,700
Impeller material	SS
Casing material	SS

Rich-MEA Pump

Number required	2
Number of operating pumps	1
Number of spare pumps	1
Pump type	Centrifugal
Fluid handled	Rich MEA
Fluid flow rate, lb/h (kg/hr)	631,378 (286,388)
Specific gravity of fluid	0.94
Volumetric flow rate, gpm (m^3/h)	1,341 (304.6)
Design flow rate, gpm (m^3/h)	1,470 (333.9)
Fluid inlet temperature, °F (°C)	149 (65)
Fluid inlet pressure, psia (kPa)	19 (131)
Total pressure difference, psia (kPa)	70 (482.6)
Fractional efficiency, E	0.80
BHP	75
Motor horsepower, HP	100
Impeller material	SS
Casing material	SS

Lean-MEA Pump

Number required	2
Number of operating pumps	1
Number of spare pumps	1
Pump type	Centrifugal
Fluid handled	Lean MEA
Fluid flow rate, lb/h (kg/hr)	597,806 (271,160)
Specific gravity of fluid	1.02
Volumetric flow rate, gpm (m^3/h)	1,168 (265.3)
Design flow rate, gpm (m^3/h)	1,280 (291)
Fluid inlet temperature, °F (°C)	184 (84.44)
Fluid inlet pressure, psia (kPa)	24.7 (170.3)
Total pressure difference, psia (kPa)	61 (420.6)
Fractional efficiency, E	0.80
BHP	57
Motor horsepower, HP	75
Impeller material	SS
Casing material	SS

Condensate Pump

Number required	2
Number of operating pumps	1
Number of spare pumps	1
Pump type	Centrifugal
Fluid handled	Condensate
Fluid flow rate, lb/h (kg/hr)	41,559 (18,851)
Specific gravity of fluid	0.99
Volumetric flow rate, gpm (m^3/h)	84 (19.1)
Design flow rate, gpm (m^3/h)	90 (20.4)
Fluid inlet temperature, °F (°C)	95 (35)
Fluid inlet pressure, psia (kPa)	19.0 (131)
Total pressure difference, psia (kPa)	68 (468.8)
Fractional efficiency, E	0.8
BHP	5.4
Motor horsepower, HP	7.5
Impeller material	SS
Casing material	SS

MEA Make up Pump

Number required	2
Number of operating pumps	1
Number of spare pumps	1
Pump type	Centrifugal
Fluid handled	100% MEA
Fluid flow rate, lb/h (kg/hr)	76 (34.47)
Specific gravity of fluid	1.02
Volumetric flow rate, gpm (m^3/h)	0.15 (0.034)
Design flow rate, gpm (m^3/h)	0.16 (0.036)
Fluid inlet temperature, °F (°C)	60 (15.56)
Fluid inlet pressure, psia (kPa)	14.7 (101.4)
Fluid discharge pressure, psia (kPa)	30.0 (206.8)
Fractional efficiency, E	0.50
BHP	0.01
Motor horsepower, HP	0.50
Impeller material	CS
Casing material	CS

Addendum C - Equipment List, CO_2 Removal by UCARSOL Absorber/Stripper (Appendix F)

(1 of 5 Trains)

Vessels/Tanks

Absorber

Number required	1
Fluids handled	Solvent, flue gas
Orientation, vertical/horizontal	Vertical
Operating temperature, °F (°C)	145 (62.78)
Operating pressure, psia (kPa)	59.7 (411.6)
Inside diameter, ft (m)	14.5 (4.42)
Total height, ft (m)	63 (19.20)
Number of actual trays	20
Material of lower 1/3 of shell	SS
Material of upper 2/3 of shell	CS
Material of trays	CS

Stripper

Number required	1
Fluids handled	Solvent, CO_2
Orientation, vertical/horizontal	Vertical
Operating temperature, °F (°C)	230 (110)
Operating pressure, psia (kPa)	25.7 (177.2)
Inside diameter, ft (m)	14.5 (4.42)
Total height, ft (m)	63 (19.20)
Number of actual trays	20
Material of shell	SS
Material of trays	SS

Gas-Liquid Separator

Number required	1
Fluid handled	CO_2, water
Orientation, vertical/horizontal	Vertical
Operating temperature, °F (°C)	95 (35)
Operating pressure, psia (kPa)	19 (131)
CO_2 flow rate, lb/h (kg/hr)	53,360 (24,204)
Water flow rate, lb/h (kg/hr)	17,523 (7,948)
Inside diameter, ft (m)	5 (1.52)
Height, ft (m)	8 (2.44)
Material	CS

Solvent Make up Tank

Number required	1
Fluid handled	100% Solvent
Orientation, vertical/horizontal	Vertical
Operating temperature, °F (°C)	60 (15.56)
Operating pressure, psia (kPa)	14.7 (101.4)
Holdup time, days	30
Tank inside diameter, ft (m)	14 (4.27)
Tank height, ft (m)	50 (15.24)
Material	CS

Heat Exchangers

After Cooler

Number required	1
Heat duty, million Btu/h (mkJ)	41.8 (44.101)
Tubeside fluid	Water
Shellside fluid	Flue gas
Tubeside inlet temperature, °F (°C)	63 (17.22)
Tubeside exit temperature, °F (°C)	83 (28.33)
Tubeside flow rate, lb/h (kg/hr)	2,092,000 (948,915)
Tubeside operating pressure, psia (kPa)	75 (517.1)
Shellside inlet temperature, °F (°C)	428 (220)
Shellside exit temperature, °F (°C)	132 (55.56)
Shellside flow rate, lb/h (kg/hr)	282,457 (128,120)
Shellside operating pressure, psia (kPa)	60.7 (418.5)
Total heat transfer area, ft^2 (m^2)	13,552 (1,259)
Shell material	SS
Tube material	SS

Lean Solvent Cooler

Number required	1
Heat duty, million Btu/h (mkJ)	54.9 (57.293)
Tubeside fluid	Lean solvent
Shellside fluid	Water
Tubeside inlet temperature, °F (°C)	196.6 (91.44)
Tubeside exit temperature, °F (°C)	120 (48.89)
Tubeside flow rate, lb/h (kg/hr)	804,224
Tubeside operating pressure, psia (kPa)	117 (806.7)
Shellside inlet temperature, °F (°C)	63 (17.22)
Shellside exit temperature, °F (°C)	83 (28.33)
Shellside flow rate, lb/h (kg/hr)	2,745,000 (1,245,111)
Shellside operating pressure, psia (kPa)	75 (517.1)
Total heat transfer area, ft^2 (m^2)	3,328 (309.2)
Shell material	CS
Tube material	CS

Lean/Rich Exchanger

Number required	1
Heat duty, million Btu/h (mkJ)	43.3 (45.684)
Tubeside fluid	Lean solvent
Shellside fluid	Rich solvent
Tubeside inlet temperature, °F (°C)	254.2 (123.44)
Tubeside exit temperature, °F (°C)	196.6 (91.44)
Tubeside flow rate, lb/h (kg/hr)	804,224 (364,790)
Tubeside operating pressure, psia (kPa)	117 (806.7)
Shellside inlet temperature, °F (°C)	160 (71.11)
Shellside exit temperature, °F (°C)	219.2 (104)
Shellside flow rate, lb/h (kg/hr)	854,389 (387,544)
Shellside operating pressure, psia (kPa)	88 (606.7)
Total heat transfer area, ft^2 (m^2)	9,028 (838.7)
Shell material	SS
Tube material	SS

Condenser

Number required	1
Heat duty, million Btu/h (mkJ)	19.6 (20.679)
Tubeside fluid	Cooling water
Shellside fluid	Gas
Tubeside inlet temperature, °F (°C)	63 (17.22)
Tubeside exit temperature, °F (°C)	83 (28.33)
Tubeside flow rate, lb/h (kg/hr)	978,000 (443,613)
Tubeside operating pressure, psia (kPa)	75 (517.1)
Shellside inlet temperature, °F (°C)	202.7 (94.83)
Shellside exit temperature, °F (°C)	120 (48.89)
Shellside flow rate, lb/h (kg/hr)	70,883 (32,152)
Shellside operating pressure, psia (kPa)	25.7 (177.2)
Total heat transfer area, ft^2 (m^2)	3,733 (346.8)
Shell material	SS
Tube material	SS

Reboiler

Number required	1
Heat duty, million Btu/h (mkJ)	78.64 (82.970)
Tubeside fluid	Steam
Shellside fluid	Stripper bottoms
Tubeside inlet temperature, °F (°C)	298 (147.78)
Tubeside exit temperature, °F (°C)	298 (147.78)
Tubeside flow rate, lb/h (kg/hr)	86,228 (39,112)
Tubeside operating pressure, psia (kPa)	64.7 (446.1)
Shellside inlet temperature, °F (°C)	254 (123.33)
Shellside exit temperature, °F (°C)	255 (123.33)
Shellside flow rate, lb/h (kg/hr)	804,224 (364,790)
Shellside operating pressure, psia (kPa)	27.7 (191)
Total heat transfer area, ft^2 (m^2)	7,628 (708.7)
Shell material	SS
Tube material	SS

Pumps/Compressors

Compressor

Number required	1
Number of operating boosters	1
Number of spare boosters	0
Booster type	Centrifugal
Fluid handled	Flue gas
Flue gas flow rate, scfm (m^3N/h)	62,148 (100,238)
Flue gas design flow rate, scfm (m^3N/h)	68,360 (110,258)
Flue gas inlet temperature, °F (°C)	131 (55)
Flue gas inlet pressure, psia (kPa)	14.7 (101.4)
Flue gas discharge pressure, psia (kPa)	60.7 (418.5)
Fractional efficiency, E	0.9
BHP	9,705
Motor horsepower, HP	11,000
Impeller material	SS
Casing material	SS

Rich-Solvent Pump

Number required	2
Number of operating pumps	1
Number of spare pumps	1
Pump type	Centrifugal
Fluid handled	Rich solvent
Fluid flow rate, lb/h (kg/hr)	801,537 (363,571)
Specific gravity of fluid	1.03
Volumetric flow rate, gpm (m^3/h)	1,560 (354.315)
Design flow rate, gpm (m^3/h)	1,720 (390.655)
Fluid inlet temperature, °F (°C)	161 (627.22)
Fluid inlet pressure, psia (kPa)	59.7 (411.6)
Total pressure difference, psia (kPa)	88 (606.7)
Fractional efficiency, E	0.8
BHP	92
Motor horsepower, HP	125
Impeller material	SS
Casing material	SS

Lean-Solvent Pump

Number required	2
Number of operating pumps	1
Number of spare pumps	1
Pump type	Centrifugal
Fluid handled	Lean solvent
Fluid flow rate, lb/h (kg/hr)	694,980 (315,238)
Specific gravity of fluid	0.891
Volumetric flow rate, gpm (m^3/h)	1,560 (354.315)
Design flow rate, gpm (m^3/h)	1,720 (390.655)
Fluid inlet temperature, °F (°C)	197 (91.67)
Fluid inlet pressure, psia (kPa)	28 (193.1)
Total pressure difference, psia (kPa)	62 (427.5)
Fractional efficiency, E	0.8
BHP	78
Motor horsepower, HP	100
Impeller material	SS
Casing material	SS

Condensate Pump

Number required	2
Number of operating pumps	1
Number of spare pumps	1
Pump type	Centrifugal
Fluid handled	Condensate
Fluid flow rate, lb/h (kg/hr)	17,348 (7,869)
Specific gravity of fluid	0.993
Volumetric flow rate, gpm (m^3/h)	35 (7.949)
Design flow rate, gpm (m^3/h)	40 (9.085)
Fluid inlet temperature, °F (°C)	95 (35)
Fluid inlet pressure, psia (kPa)	25 (172.4)
Total pressure difference, psia (kPa)	95 (655)
Fractional efficiency, E	0.8
BHP	2.8
Motor horsepower, HP	5
Impeller material	SS
Casing material	SS
Casing material	CS

Solvent Make up Pump

Number required	2
Number of operating pumps	1
Number of spare pumps	1
Pump type	Centrifugal
Fluid handled	100% solvent
Fluid flow rate, lb/h (kg/hr)	558 (253)
Specific gravity of fluid	1
Volumetric flow rate, gpm (m^3/h)	1 (0.227)
Design flow rate, gpm (m^3/h)	1 (0.227)
Fluid inlet temperature, °F (°C)	60 (15.56)
Fluid inlet pressure, psia (kPa)	14.7 (101.4)
Fluid discharge pressure, psia (kPa)	44.7 (308.2)
Fractional efficiency, E	0.5
BHP	0.04
Motor horsepower, HP	0.50
Impeller material	CS
Casing material	CS

Addendum D - Equipment List, CO_2 Removal by Cryogenic Cooling

(Appendix F)

(1 of 6 Trains)

Vessels/Tanks

Feed Flue Gas Dryer System

Number required	12
Fluid handled	Flue gas/adsorb.
Orientation, vertical/horizontal	Vertical
Operating temperature, °F (°C)	70 (21.11)
Operating pressure, psia (kPa)	15.2 (104.8)
Flue gas in-flow rate, lb/h (kg/hr)	214,720 (97,395)
Flue gas out-flow rate, lb/h (kg/hr)	211,978 (96,152)
Water adsorption rate, lb/h (kg/hr)	2,742 (1,244)
Inside diameter, ft (m)	10 (3.05)
Height, ft (m)	6 (1.83)
Material	SS

Product FG-Liquid CO_2 Separator-A

Number required	1
Fluid handled	FG/liquid CO_2
Orientation, vertical/horizontal	Vertical
Operating temperature, °F (°C)	-180 (-117.78)
Operating pressure, psia (kPa)	15.2 (104.8)
Liquid CO_2 flow rate, lb/h (kg/hr)	41,941 (19,024)
Product flue gas flow rate, lb/h (kg/hr)	170,016 (77,118)
Inside diameter, ft (m)	8 (1.44)
Height, ft (m)	8 (2.44)
Material	CS

Product FG-Liquid CO_2 Separator-B

Number required	1
Fluid handled	Empty
Orientation, vertical/horizontal	Vertical
Operating temperature, °F (°C)	-180 (-117.78)
Operating pressure, psia (kPa)	15.2 (104.8)
Liquid CO_2 flow rate, lb/h (kg/hr)	Empty
Product flue gas flow rate, lb/h (kg/hr)	Empty
Inside diameter, ft (m)	12 (3.66)
Height, ft (m)	12 (3.66)
Material	CS

Heat Exchangers

After Cooler

Number required	1
Number of shells per heat exchanger	--
Heat duty, million Btu/h (mkJ)	24.9 (26.271)
Tubeside fluid	Cooling water
Shellside fluid	Flue gas
Tubeside inlet temperature, °F (°C)	63 (17.22)
Tubeside exit temperature, °F (°C)	83 (28.33)
Tubeside flow rate, lb/h (kg/hr)	1,243,070 (563,847)
Tubeside operating pressure, psia (kPa)	61 (420.6)
Shellside inlet temperature, °F (°C)	154 (67.78)
Shellside exit temperature, °F (°C)	70 (21.11)
Shellside flow rate, lb/h (kg/hr)	235,381 (106,767)
Shellside operating pressure, psia (kPa)	16.7 (115.1)
Shell inside diameter, in (cm)	--
Tube length, ft (m)	--
Heat transfer area, ft^2 (m^2) / shell	--
Total heat transfer area, ft^2 (m^2)	16,364 (1,520.3)
Shell material	SS
Tube material	SS

CO_2 Condenser

Number required	1
Number of shells per heat exchanger	--
Heat duty, million Btu/h (mkJ)	12.70 (13.999)
Tubeside fluid	Liquid nitrogen
Shellside fluid	Feed flue gas
Tubeside inlet temperature, °F (°C)	-315 (-192.78)
Tubeside exit temperature, °F (°C)	-185 (-120.56)
Tubeside flow rate, lb/h (kg/hr)	107,529 (48.774)
Tubeside operating pressure, psia (kPa)	16 (110.3)
Shellside inlet temperature, °F (°C)	-175 (-115)
Shellside exit temperature, °F (°C)	-180 (-117.78)
Shellside flow rate, lb/h (kg/hr)	211,957 (96,142)
Shellside operating pressure, psia (kPa)	22 (151.7)
Shell inside diameter, in (cm)	--
Tube length, ft (m)	--
Heat transfer area, ft^2 (m^2) / shell	--
Total heat transfer area, ft^2 (m^2)	5,170 (480.3)
Shell material	SS
Tube material	Aluminum

FG/FG Exchanger

Number required	1
Number of shells per heat exchanger	--
Heat duty, million Btu/h (mkJ)	7.7 (8.124)
Tubeside fluid	Product flue gas
Shellside fluid	Feed flue gas
Tubeside inlet temperature, °F (°C)	-180 (-117.78)
Tubeside exit temperature, °F (°C)	0
Tubeside flow rate, lb/h (kg/hr)	170,016 (77,118)
Tubeside operating pressure, psia (kPa)	15.2 (104.8)
Shellside inlet temperature, °F (°C)	70 (21.11)
Shellside exit temperature, °F (°C)	-175 (-115)
Shellside flow rate, lb/h (kg/hr)	128,537 (58,303)
Shellside operating pressure, psia (kPa)	16.2 (111.7)
Shell inside diameter, in (cm)	--
Tube length, ft (m)	--
Heat transfer area, ft^2 (m^2) / shell	--
Total heat transfer area, ft^2 (m^2)	20,700 (1,923.1)
Shell material	SS
Tube material	Aluminum

N_2/FG Exchanger

Number required	1
Number of shells per heat exchanger	--
Heat duty, million Btu/h (mkJ)	5.0 (5.275)
Tubeside fluid	N_2 gas
Shellside fluid	Feed flue gas
Tubeside inlet temperature, °F (°C)	-185 (-120.56)
Tubeside exit temperature, °F (°C)	0
Tubeside flow rate, lb/h (kg/hr)	107,529 (48,774)
Tubeside operating pressure, psia (kPa)	15.7 (108.2)
Shellside inlet temperature, °F (°C)	70 (21.11)
Shellside exit temperature, °F (°C)	-175 (-115)
Shellside flow rate, lb/h (kg/hr)	83,420 (37,839)
Shellside operating pressure, psia (kPa)	16.2 (111.7)
Shell inside diameter, in (cm)	--
Tube length, ft (m)	--
Heat transfer area, ft^2 (m^2) / shell	--
Total heat transfer area, ft^2 (m^2)	10,700 (994.1)
Shell material	SS
Tube material	Aluminum

Pumps/Blowers

Blower

Number required	1
Number of operating blowers	1
Number of spare blowers	0
Blower type	Centrifugal
Fluid handled	Flue gas
Flue gas flow rate, scfm (m^3N/h)	51,790 (83,532)
Flue gas design flow rate, scfm (m^3N/h)	56,970 (91,887)
Flue gas inlet temperature, °F (°C)	131 (55)
Flue gas inlet pressure, psia (kPa)	14.7 (101.4)
Flue gas discharge pressure, psia (kPa)	16.7 (115.1)
Fractional efficiency, E	0.9
BHP	601
Motor horsepower, HP	750
Impeller material	SS
Casing material	SS

Appendix G - HIPPS Commercial Plant Design
Enriched Oxygen Combustion Gas Turbine Cycle Assessment

Background

A limited study was undertaken to determine the impact of using an oxygen enriched-air turbine cycle. The chief purpose is to produce a product gas with a sufficiently high concentration of carbon dioxide to facilitate capture for reuse or sequestration.

Turbines Examined

The bulk of the work performed on the oxygen-enriched analysis examined the impact on performance to gas turbine combined cycle (GTCC) systems. Two turbines were examined to determine what, if any, effect compression ratio and combustion temperature might have. The turbines examined were GE's LM6000 aeroderivative machine and their conventional PG6561 Frame 6 turbine. These two turbines, that are approximately the same size (nominally 60 MWe), provided information on compression ratios ranging from 12, for the Frame 6, to over 29 for the LM6000. The corresponding combustor outlet temperatures ranged from 1938 °F to 2378 °F (1060 °C to 1300 °C). These ranges provide information that should be applicable to the majority of turbines currently available. If DOE requested future work, the performance and economic impacts of these cycles on HIPPS would be examined.

Configurations

Five models were developed for each of the two turbines and the system performance was determined using ASPEN PLUS. The configurations were:

- Case 1 – Air with no flue gas recycle
- Case 2 – Air with flue gas recycle
- Case 3 – 40% oxygen with flue gas recycle
- Case 4 – 75% oxygen with flue gas recycle
- Case 5 – 98% oxygen with flue gas recycle

To provide consistency, certain parameters were held constant for all of the configurations being examined for a specific turbine. To determine these values, a run was made using GATE's internal parameters for each turbine on a conventional GTCC cycle running on air. The flows, temperatures and pressures were recorded and the following items were then held constant for the remaining runs:

- Volume flow (moles) to the expanders
- Temperature from the combustors
- Temperature of flue gas from the HRSG (110 °F (45 °C))
- The oxygen content in the exhaust gas leaving the combustor was maintained at 4%vol.
- Efficiencies of the compressor and expander
- Percentage of gas from the compressor used for cooling air in the expander

For simplicity, pure methane was used to fuel the turbines. Also, oxygen is produced at 98% purity in a conventional cryogenic air separation system with nitrogen and argon making up the remaining 2 percent.

Description of Configurations

The configurations used for the systems incorporating a recycle of flue gas (Cases 2-5) are shown in Exhibits G-1 and G-2.

Exhibit G-1
LM6000 Cycle

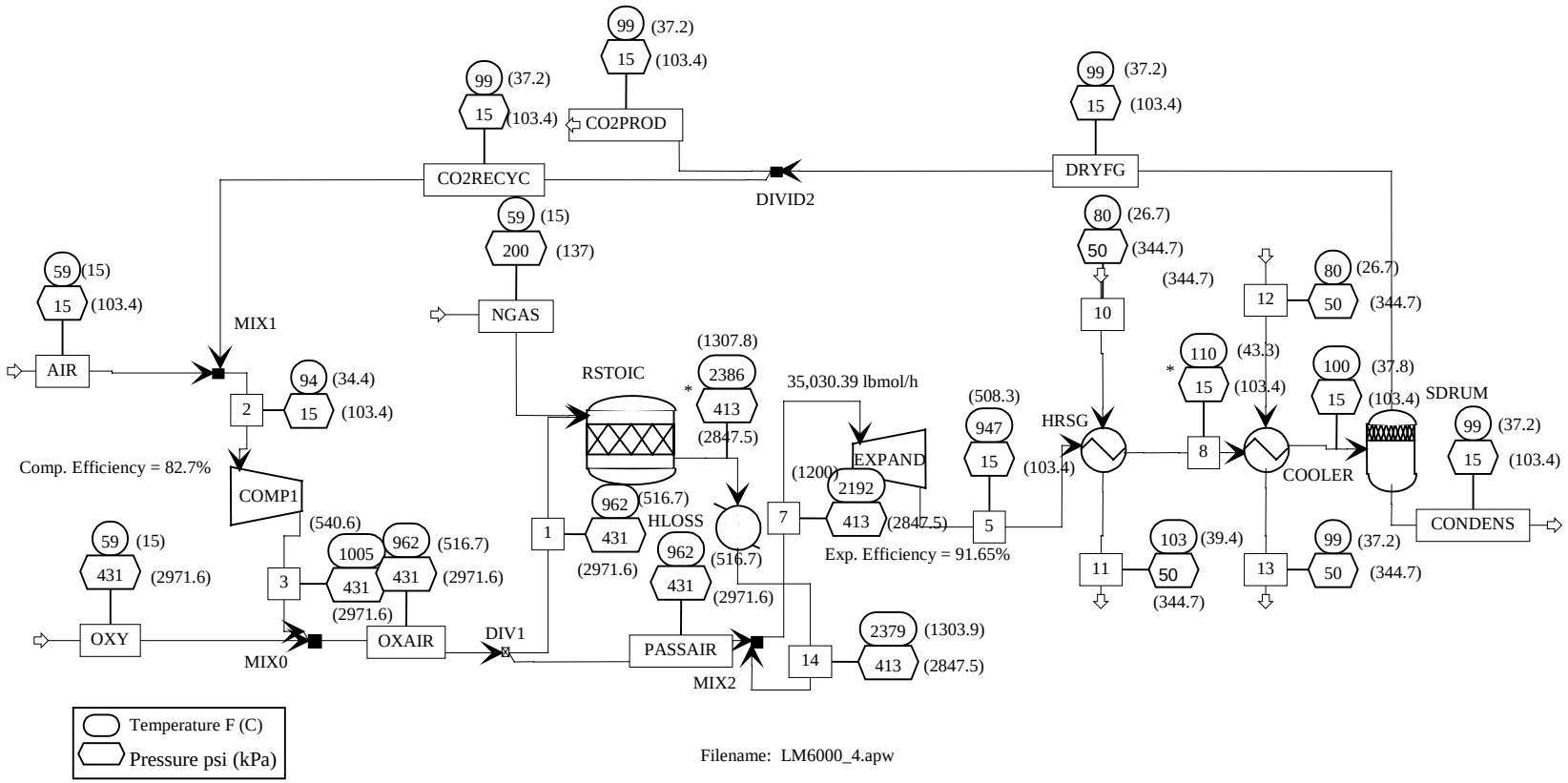

Filename: LM6000_4.apw

Exhibit G-2
Frame 6 (GE PG6561) Cycle

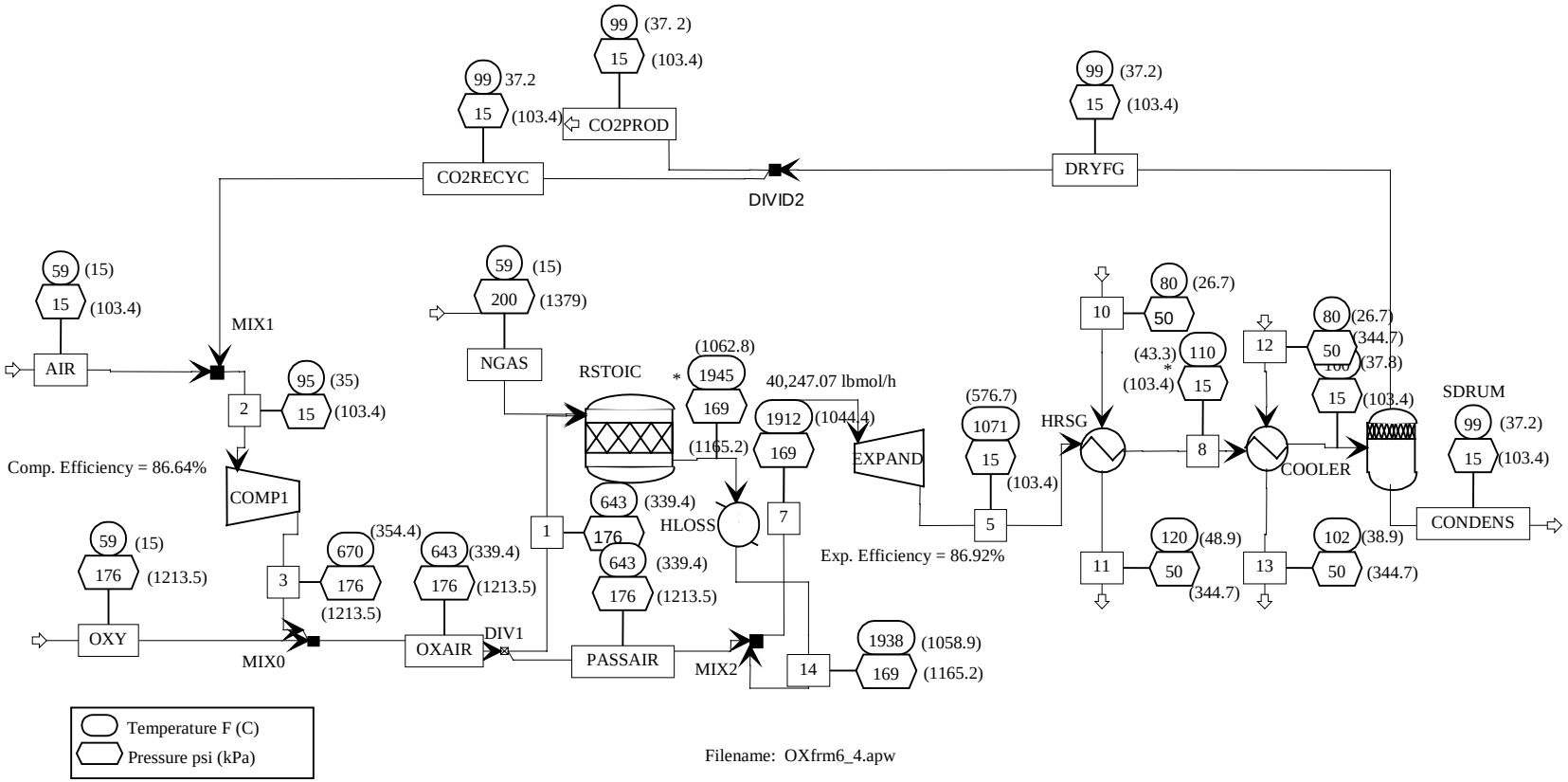

Filename: OXfrm6_4.apw

Included in the diagrams are the values held constant for each of the turbines.

The ability to capture carbon dioxide using current technologies is largely dependent on its concentration in the product gas. The only way to increase the concentration of CO_2 is to reduce the concentration of other components, chiefly nitrogen. However, gas turbines are designed for 200-300 percent excess air to provide the desired volume required to drive the turbine. The excess air also tempers the temperature from the combustor along with control of the fuel. Reducing the amount of nitrogen available through the use of enriched air means the nitrogen must be replaced by another gas to maintain the proper flow through the turbine. This is accomplished by recycling flue gas from the back end.

As seen in both exhibits, only air and recycle flue gas are introduced to the system compressor. Oxygen is introduced to the system downstream of the compressor in sufficient quantity to bring the oxygen concentration going to the combustor to the level desired for the case being examined. It was assumed that oxygen was available from liquid storage and could be pumped to the desired pressure without need for compression.

Methane is introduced to the combustor in sufficient quantity to maintain the outlet temperature set for each of the two turbines. For the sake of simplicity, the cooling air from the compressor is mixed with the combustor product gases upstream of the expander. The gas exiting the expander is passed directly to a HRSG for recovery of the sensible heat in the exhaust gases. To simplify the system it was assumed that sufficient pressure was available in the gas leaving the HRSG to allow a portion of the gas to be recycled directly to the compressor suction without the need of a ID fan. While such a system could be designed, it is likely that if such a system were to be built, that an ID fan would be incorporated on the recycle stream. However, it was felt that the absence of an ID fan would not taint the general understanding of the impact of enhanced oxygen on the performance of a GTCC system.

General Results

A summary of the results is included in Tables G-1 and G-2. It should be noted that the efficiencies are based on gross power as they only have allowances for losses in the generators and other systems directly connected to the turbines and do not take into account auxiliary power demands, the largest of these being the those associated with the air separation unit. The results incorporating these additional loads will be discussed later but a number of interesting results can be obtained from an examination of Tables G-1 and G-2.

Table G-1
Enriched Oxygen GTCC – LM6000

Basis for Cycle Calculations			Results from Cycle Calculations					
Computer program	Aspen Plus 10		Aspen Plus Filenames	OXLM6000_1	OXLM6000_2	LM6000_4	OXLM6000_5	OXLM6000_6
				Non Recycle		Recycle Cases		
Combustor exit temperature, F	2,378		Turbine:	21% O_2	21% O_2	40% O_2	75% O_2	98% O_2
Fuel gas	Pure CH_4		Air to compressor suction, lb/h	980,953	388,900	147,250	36,974	0
LHV fuel gas, Btu/lb	21,510		Recycle gas to compressor suction, lb/h	0	594,317	836,887	1,051,820	1,208,440
Compression ratio	29.31		Oxygen to compressor discharge, lb/h	0	0	54,294	96,854	124,646
Temperature of flue gas at HRSG exit, F	110		Fuel gas flowrate, lb/h	16,573	16,820	19,190	24,462	29,465
Recycle gas temperature, F	99.4		Expander inlet flowrate, lb/h	997,526	1,000,037	1,057,621	1,210,110	1,362,551
Expander inlet flowrate, lbmol/h	35,030.39		Combustor outlet temperature, F	2,378	2,378	2,379	2,379	2,379
Heat rate of recoverd heat, Btu/kWh	9,700		Expander inlet temperature, F	2,198	2,202	2,192	2,175	2,164
GT generator losses, MW	0.877		Expander outlet temperature, F	856	888	947	1,071	1,172
GT aux & BOP losses, MW	0.140		Expander temperature drop, F	1,342	1,314	1,245	1,104	992
ST generator losses, %	1.000		Compressor power, MW	-70.007	-72.290	-67.816	-61.415	-56.658
ST aux & BOP losses, %	9.357		Expander power, MW	113.897	115.402	117.731	122.563	126.368
			GT power, MW	43.890	43.112	49.916	61.147	69.710
Oxgen Composition, vol%:			Steam power, MW	19.825	22.402	26.742	36.072	45.392
Oxygen	98.0		Total gross power, MW	63.715	65.514	76.658	97.220	115.102
Nitrogen	1.0		GT power loss, MW	1.017	1.017	1.017	1.017	1.017
Argon	1.0		Steam power loss, MW	2.053	2.320	2.770	3.736	4.701
Total	100.0		Total net power, MW	61.662	63.194	73.888	93.484	110.400
			CO_2 Product:					
			CO_2 product flowrate, lb/h	993,785	380,337	183,185	105,628	88,785
			CO_2 conc in CO_2 product, vol%	3.0	8.0	20.2	51.4	83.6
			Efficiency:					
			LHV input, MMBtu/h	356.49	361.80	412.78	526.18	633.79
			Power output, MW	**61.66**	**63.19**	**73.89**	**93.48**	**110.40**
			Heat rate, Btu/kWh	5,781	5,725	5,587	5,629	5,741
			Efficiency, %LHV	**59.02**	**59.60**	**61.08**	**60.62**	**59.43**

Table G-2
Enriched Oxygen GTCC – FRAME 6, GE PG6561

Basis for Cycle Calculations			Results from Cycle Calculations					
Computer program	Aspen Plus 10		Aspen Plus Filenames	OXfrm6_1	OXfrm6_2	OXfrm6_4	OXfrm6_5	OXfrm6_6
				Non Recycle	Recycle Cases			
Combustor exit temperature, F	1,938		Turbine:	21% O_2	21% O_2	40% O_2	75% O_2	98% O_2
Fuel gas	Pure CH_4		Air to compressor suction, lb/h	1,126,390	417,500	162,672	39,899	0
LHV fuel gas, Btu/lb	21,510		Recycle gas to compressor suction, lb/h	0	713,389	973,412	1,226,800	1,415,070
Compression ratio	11.99		Oxygen to compressor discharge, lb/h	0	0	59,981	104,516	132,543
Temperature of flue gas at HRSG exit, F	110		Fuel gas flowrate, lb/h	19,400	19,668	21,802	26,800	31,675
Recycle gas temperature, F	99.4		Expander inlet flowrate, lb/h	1,145,790	1,150,557	1,217,867	1,398,015	1,579,288
Expander inlet flowrate, lbmol/h	40,247.07		Combustor outlet temperature, F	1,937	1,938	1,938	1,938	1,938
Heat rate of recoverd heat, Btu/kWh	9,700		Expander inlet temperature, F	1,911	1,912	1,912	1,910	1,910
GT generator losses, MW	1.201		Expander outlet temperature, F	999	1,024	1,071	1,169	1,248
GT aux & BOP losses, MW	0.163		Expander temperature drop, F	912	888	841	741	662
ST generator losses, %	1.000		Compressor power, MW	-49.044	-50.930	-48.248	-44.669	-41.969
ST aux & BOP losses, %	9.357		Expander power, MW	88.621	89.527	91.118	94.344	96.857
			GT power, MW	39.577	38.597	42.870	49.675	54.888
Oxgen Composition, vol%:			Steam power, MW	27.320	30.577	35.247	45.495	55.680
Oxygen	98.0		Total gross power, MW	66.896	69.175	78.118	95.170	110.568
Nitrogen	1.0		GT power loss, MW	1.364	1.364	1.364	1.364	1.364
Argon	1.0		Steam power loss, MW	2.829	3.167	3.651	4.712	5.767
Total	100.0		Total net power, MW	64.067	66.008	74.467	90.458	104.801
			CO_2 Product:					
			CO_2 product flowrate, lb/h	1,140,700	406,179	201,556	113,415	93,904
			CO_2 conc in CO_2 product, vol%	3.1	8.8	20.9	52.6	85.4
			Efficiency:					
			LHV input, MMBtu/h	417.29	423.06	468.96	576.47	681.33
			Power output, MW	**64.07**	**66.01**	**74.47**	**90.46**	**104.80**
			Heat rate, Btu/kWh	6,513	6,409	6,298	6,373	6,501
			Efficiency, %LHV	**52.38**	**53.24**	**54.18**	**53.54**	**52.48**

The first thing to be noted is that allowing for the expected increase in performance for the LM6000 over the Frame 6 turbine, the general trends observed for both machines are identical. Although admittedly connected to a simple system, this would indicate that the impact of using enhanced oxygen is consistent no matter what turbine or turbine conditions are used. This is rather a broad statement based on only limited data but the two turbines do cover a relatively representative span of compression ratios and combustor temperatures and as such while there may be exceptions that this evaluation did not address, it appears a reasonable conclusion. This said, we can concentrate on the observations for one of the turbines realizing the trends will also be observed in the other. For the purpose of the following observations, data for the LM6000 will be used for illustration.

There are probably a number of ways of approaching the amount of recycle gas to be recycled for any particular case but only two were considered here. One method would be to provide sufficient recycle to maintain the oxygen concentration in the combustor effluent at approximately the same level as the base case, or about 13%v or 15%wt. The problem with this method is that oxygen from an air separation facility is expensive and underutilizing it is uneconomical and therefore unacceptable. The alternate approach is to determine a lower limit on the oxygen level leaving the combustor that could be maintained and use it for those cases using recycle flue gas. For the purpose of this study we chose a level of 4%v oxygen from the combustor. This is a level common to furnaces burning everything from gas to coal, and was reasonable for the current evaluation.

Accepting this value as a design basis, an interesting set of data is generated when comparing Case 1 with Case 2. Both systems are based on standard air with no enriched oxygen, however, since Case 2 includes sufficient recycle to reduce the oxygen content leaving the combustor down to 4%v, the concentration of CO_2 in the product gas nearly triples, going from 3%v to 8%v. Also noticed is the fact that the fresh air to the compressor drops by 60 percent with the residual made up from recycled product gas. It is also worth noting that the apparent efficiency of the system with recycle gas is marginally more than the conventional system. It is believed that this is due to the simplicity of the system modeled but it is an intriguing result that might be useful in some circumstances.

Going from Case 1 to Case 2, the amount of recycle goes from zero to about 600,000 lb/hr for the LM6000 system. As can be seen in Exhibit G-3, going from Case 2 using air to Case 5 using 98% oxygen only doubles this amount. However, the corresponding concentration of CO_2 in the recycle and product gas increases from 8%v to almost 84%v or 89%wt. The weight percent of CO_2 is shown in Exhibit G-4 for the various cases.

Exhibit G-3
Flue Gas Recycle

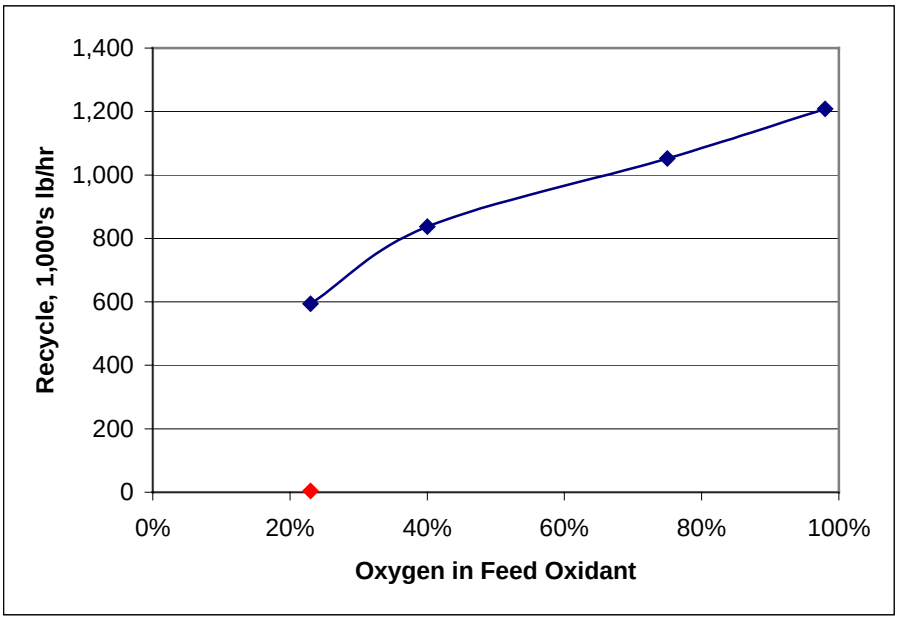

Exhibit G-4
CO2 in the Flue Gas

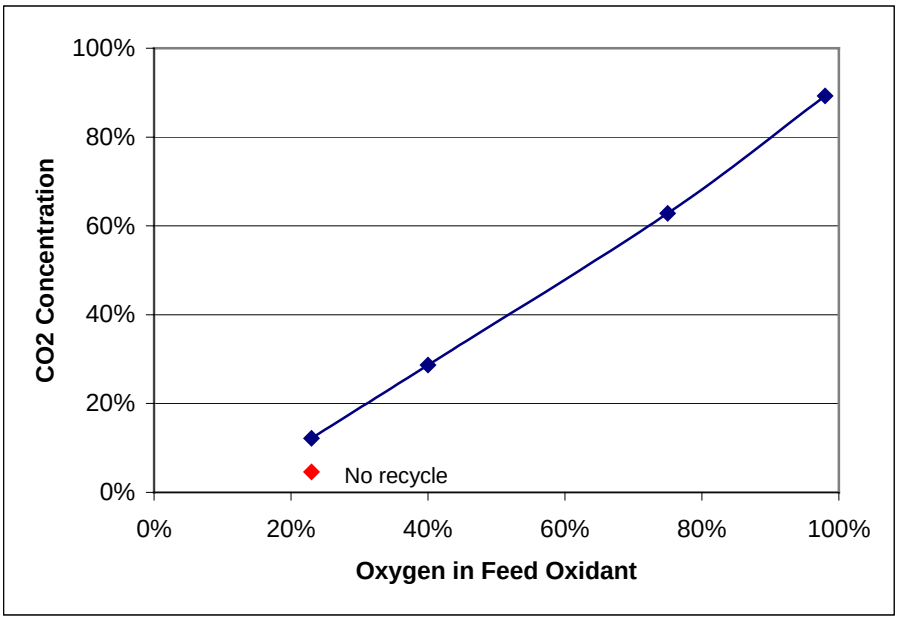

One of the simplifying assumptions made for the current analysis was that we would maintain the volume or moles of gas entering the expander. With the increase in CO_2 content of the gas being recycled, while the volume remains unchanged, the mass increased by about 35% between Cases 2 and 5, as shown in Exhibit G-5. While certainly both the compressor and expander are volumetric machines there are undoubtedly limits based on power considerations or at least changes in efficiency that should accompany this level of change. Should refinements in the current results be required these changes would have to be taken into account and would most likely have to be obtained from the turbine vendor.

Exhibit G-5
Mass to Expander

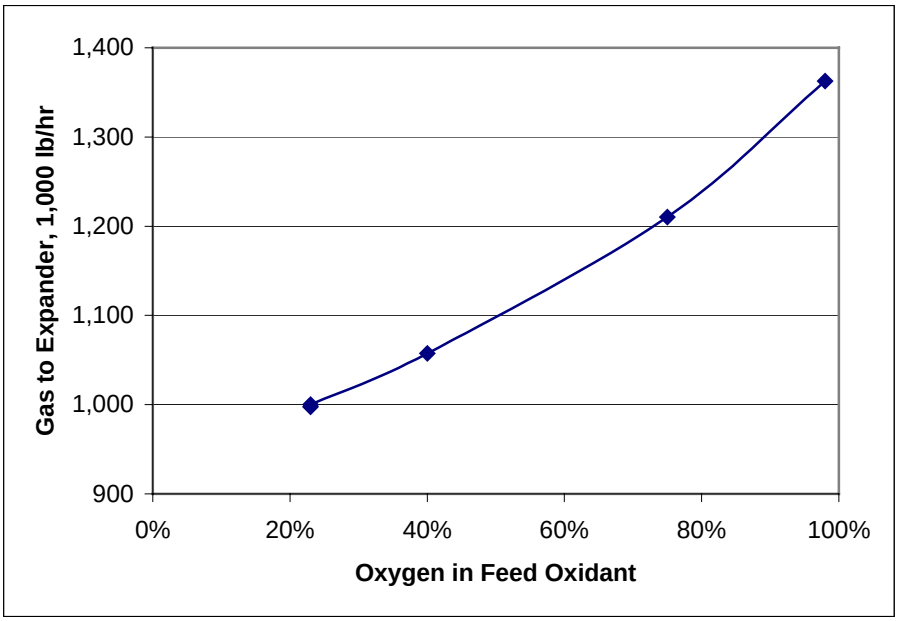

The mass of gas passing through the compressor increased as the level of carbon dioxide increased in the recycle for the higher oxygen cases. However, the mass of bypass gas also increased, and so the corresponding temperature of the blended gas entering the expander tended to drop slightly.

Performance

The bulk of the performance calculations made by ASPEN PLUS ignored auxiliary power demands. Although slightly more pronounced for the LM6000, the results shown in Exhibit G-6 indicate the general trend seen for both turbines. For both turbines, a maximum system efficiency based on gross power production is found around the 40% oxygen level.

The apparent reason for this is a combination of two effects occurring simultaneously. As the oxygen is increased the power required by the compressor is reduced. This reduction is largely due to the fact that although more mass is passing through the compressor, it processes less volume. Since the volume to the expander is maintained the same, the increased mass due the change in molecular weight causes a slight increase in the expander power. The combination of less compressor requirement and greater expander power provides a net increase in power

from the gas turbine. Parallel with this increase is a corresponding increase in the size of the HRSG and steam turbine. However, as the oxygen content gets higher the change in molecular weight becomes more severe resulting in more energy being required by the combustor to achieve the design temperature. This means more methane feed. Essentially the level of increase in fuel demands begins to overshadow the gains in power production somewhere around the 40% oxygen case.

Exhibit G-6
Relative Gross Efficiencies

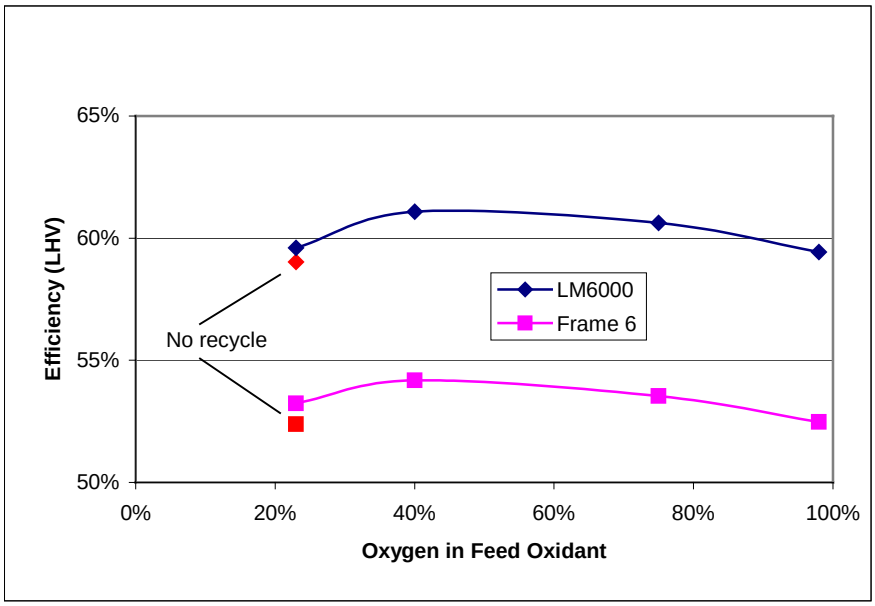

However, as noted, this does not take into account auxiliary power requirement, specifically those associated with the air separation plant. A brief examination of previous studies involving air separation plants indicated that we have consistently used values of 0.185 kW/lb/hr of O_2 produce for standalone systems and 0.152 kW/lb/hr of O_2 produced for integrated systems. It is unclear whether such a system could be integrated into such a power plant, but a value of 0.152kW/lb/hr was assumed to determine the net overall efficiency for the various cases. The results are shown in Exhibit G-7 for both turbines. As can be seen, the efficiency drops of rapidly once oxygen is introduced into the system. The degree of decrease being a direct function of the amount of oxygen required.

These results do not include any additional auxiliary power demands required by an ID fan or by a CO_2 compressor that will likely be required for capture and/or sequestration. If added in this would only reduce the overall plant efficiency even further.

Exhibit G-7
Net Plant Efficiencies

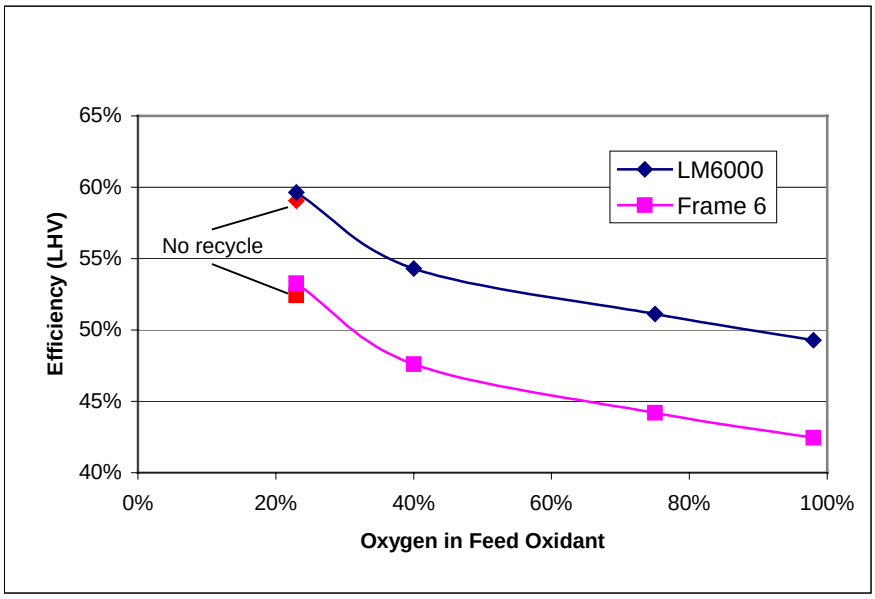

Comments

Although the evaluation was very basic and included a number of simplifying assumptions, the results indicate that unless a source of oxygen is available, which requires considerably less power, the use of enhanced oxygen to facilitate CO_2 capture does not appear attractive. Ceramic membranes may offer this flexibility but since the gross efficiency is relatively flat, albeit there is a slight increase up to 40% oxygen, almost any extra power demands will mean the overall efficiency will be less than the base system. This would mean that either a significant byproduct credit for CO_2 would have to be realized to offset this loss in efficiency or the government would have to regulate the necessity through CO_2 penalties or offsetting credits.

Appendix H - HIPPS Operation and Control

HIPPS Commercial Plant Operations Review

This review examines the conceptual commercial HIPPS plant from the standpoint of plant operations: If the plant is to be commercially feasible, it must be designed to be safe, reliable and operable in a manner similar to other utility power generating stations. With this goal in mind, the operations review is limited to those plant features and components related to the new technologies and combinations of existing technologies in new arrangements, as follows:

- Combustion gas turbine.
- High temperature advanced furnace and the air heaters.
- Heat recovery steam generators.

The responses of these components to various HIPPS operating conditions, and, in turn, the restrictions on operations caused by equipment limitations are examined in the context of the overall HIPPS conceptual design. In particular, the HITAF's convective air heater (CAH) and radiant air heater (RAH) will be sensitive to operating transients, and attention to plant design and safety features is required. Other systems, such as the steam turbine, are considered only in relation to the three components noted above.

Major Operating Issues

The main design feature of concern in the HIPPS plant operations is the HITAF, and its function to preheat gas turbine combustion air.

The HITAF is a slagging furnace and is designed to provide 65 % of the total plant heat input. The remaining gas turbine heat input is provided by combustion of natural gas in a combustor, as part of, or near the gas turbine. The target efficiency of the HIPPS plant is 47 % at ISO conditions, and to achieve this efficiency the temperature of gas turbine combustion air leaving the HITAF needs to be about 1700 °F (927 °C). To reach the desired temperature, the HITAF includes a convective air heater and a radiant air heater. These increase the air temperature to the required 1700 °F (927 °C) inlet conditions to the gas turbine combustion air duct burner.

A major concern with HIPPS plant operability is related to the ability of CAH and RAH materials to withstand temperature transients. The RAH in particular will operate at very high temperatures due to the low film coefficient on the air side of the RAH (compared to waterwalls in a conventional boiler).

Another area of concern is the steam cycle. The HIPPS design concept combines a high thermal mass system, the HITAF and HRSG #2, with a low thermal mass system, the gas turbine and HRSG #1. The stability of these systems during transients is very important to the success of the design concept.

Air Heater Materials

The RAH and CAH are critical components of the HIPPS plant and are expected to be the design items with the most impact on plant operation considerations.

The RAH will be constructed of alloy metals with a ceramic coating, or refractory tile covering, to protect the tubing from overheating. Rapid temperature fluctuations are likely to cause problems with ceramic coatings or tiles, especially at the interface with the alloy tubes.

High temperature in either the coating or tubes during temperature excursions or surges, whether rapidly or slowly occurring, may cause overstress due to thermal growth or lowering of allowable stress values.

Due to the low heat transfer characteristics of air (as compared to boiling water), RAH materials will operate at higher temperatures than waterwall boiler tubes in a typical steam plant boiler, which may leave a low margin of difference between operating temperatures and maximum allowable temperature limits. In addition, because there is no inventory of heat exchange fluid in the HITAF system (i.e., gas turbine combustion air), as is provided by water in the boiler steam drum and waterwalls of a conventional boiler, the RAH will be very sensitive to changes in gas turbine combustion air flow.

Similar issues could also exist for CAH tubing (although ceramic coatings are not required for the CAH). Plant design and operating procedures will address the limits on RAH and CAH temperatures and rate of temperature changes.

Steam Cycle Issues

The HIPPS plant is configured to use heat from gas turbine exhaust and from the HITAF flue gas to obtain throttle conditions of 2400 psia/1000 °F /1000 °F (16,550 kPa/538 °C /538 °C) in a reheat steam cycle. To achieve these steam cycle operating conditions HRSG #1 (gas turbine exhaust) interacts with HRSG #2 (HITAF flue gas) at the reheaters. These interactions are required because of the low gas turbine exhaust temperature, which is insufficient to achieve the required 1000 °F (538 °C) steam conditions

One consideration for all steam generation systems is the prevention of overheating in superheater and reheater tubes. The temperature of gas turbine exhaust will not be high enough during transients to damage tubes in properly designed exhaust ducting, superheaters and reheaters. However, flue gas at the outlet of the HITAF could damage reheater and superheater tubes. Protection of HITAF reheater and superheater tubes can be covered by typical fired boiler startup and operating procedures not unique to the HIPPS plant.

The gas turbine and HRSG #1 and HITAF and HRSG #2 have different thermal operating characteristics. The gas turbine and HRSG #1 arrangement is a low thermal mass system and is capable of rapid startups and load changes. The HITAF and HRSG #2 arrangement is a high thermal mass system and will not be as responsive to changes in heat input or changes originating in the steam piping system. To accommodate these differences, plant design and operating procedures will be required to assure capability to independently remove heat from both HRSGs #1 and #2 during periods of transition or mismatched operation.

Plant Startup

Plant startup is a process of alternately ramping up the gas turbine and HITAF to an initial holding condition. Subsequent loading of the units would be in parallel, with appropriate holding points during the ramp ups for temperature equalization, soak periods, and so forth as required by the equipment manufacturers. An important startup consideration is to limit thermal

stress in the RAH and CAH during their heat up. Due to the difference in startup rates between the gas turbine and HITAF, steam flows between these components will be mismatched, and a system for removing heat from the HITAF and HRSGs (via the steam system) will be required.

With the HRSGs and HITAF filled with water and ready, the HITAF would be placed in service using natural gas fired startup burners. The HITAF would be fired at a rate to slowly raise the temperature of the RAH and CAH. Following the initial gas firing of the HITAF, the gas turbine would be started. The HITAF firing rate would be held constant while the gas turbine ramps to the first holding level for warm up of HRSG #1.

As HRSG #1's pressure increases, a majority of steam is generated in the low pressure portion of the system. The LP steam turbine, however, cannot accept steam until the HP steam turbine stop valves are opened, which does not occur until HP steam from the HITAF has adequate superheat; generally 90 to 110 °F (32 to 43 °C). Any steam generated in HRSG #1 prior to steam turbine operation is bypassed to the main condenser in a steam bypass system.

At the end of the first HRSG #1 holding level, the gas turbine and HITAF will ramp up at a rate consistent with maintaining RAH, CAH, and HP drum stress levels within allowable limits (IP and LP drums are generally thin walled and not subject to overstress during startup). During low load gas turbine operation, combustion air flow is reduced by modulation of the gas turbine inlet guide vanes, hence air flow through the CAH and RAH would be below design values. At this time, however, HITAF heat input is low and sufficient gas turbine combustion air will be flowing through the CAH and RAH to prevent overheating. The steam turbine is not yet in operation, so HITAF and HRSG #2 steam would be bypassed to the main condenser.

The gas turbine and HITAF will increase load in parallel until HITAF HP steam is admitted to the steam turbine. The steam turbine requires a ramped warm up period, and during initial steam turbine operation excess steam generated in the HITAF and HRSGs will be bypassed to the main condenser. Loading would continue up to full load, with the ramp rate limited by either steam turbine heat up rates or HITAF heat up rates.

The startup sequence will be semi-automated so that plant operators do not have to manually balance the operation of the numerous plant components. Instrumentation in critical areas will monitor ramp rates. Predetermined hold points, based on design input and data collected during initial commissioning, will be maintained automatically. Typical plant instrumentation used in modern power plants is sufficient for automatic startup sequencing with additional temperature elements in critical areas of the RAH and CAH.

An item which may cause problems during startup (and normal operation) is unbalanced combustion air flow in various portions of the CAH and RAH. The potential problem would be worse during startup where air flow through the CAH and RAH is reduced by gas turbine operation at low load. As a minimum, instrumentation is required to verify adequate air flow and heat removal in all areas of the CAH and RAH, otherwise local overheating may lead to material failures. The location of the thermocouples will be determined by analysis and model testing of the CAH and RAH. Modeling and tests may also show that during startup, the gas turbine may be raised more rapidly so that full load rate combustion air is flowing to the HITAF air heaters. If this is the case, the steam bypass system would dump generated steam prior to steam turbine operation.

The steam bypass system consists of piping, isolation valves, control valves, desuperheaters, and discharge connections in the main condenser. Steam bypass system sizing will depend on the final plant process design, the startup sequence, the need to minimize the impacts of transients during operation at load, and the desired operating flexibility for integration of the HIPPS plant with the local utility grid. The steam bypass system will be sized to accommodate the maximum bypass flow requirements as determined by reviewing each operating mode requiring bypass operation. Due to the very high energy in bypass steam, the impact of the steam bypass system operation on the main condenser design criteria and sizing must be considered.

Normal Plant Operation

During normal plant operation at design conditions, the gas turbine, HITAF, HRSGs, and steam turbine are operating at full load.

HITAF heat input will normally be controlled by the HP superheater outlet pressure. The gas turbine will be base loaded and controlled by gas turbine inlet temperature limits. HRSGs #1 and #2 will be in sliding pressure operation. Pressures in the HRSGs will not be controlled, and will follow conditions established by the gas turbine and HITAF control systems.

Reduced Load Operation

The conceptual commercial plant design includes a requirement for the plant to be able to cycle down to 50 percent capacity.

Initial turndown of the plant power output would be most easily accomplished by reducing load on the gas turbine. Gas turbine combustion air would remain at full load flow until modulation of the compressor inlet guide vanes (IGV) occurs. At this point, HITAF load would be reduced to match lower air flow through the CAH and RAH caused by gas turbine IGV modulation.

Further load reduction would be accomplished by downward load ramping of the HITAF and gas turbine. The maximum combustion air temperature exiting the RAH will be maintained to preserve overall plant efficiency. The operation will be automatically controlled at a rate to prevent thermal shocking of critical components. An operator would select the target load and ramp rate (within prescribed ramp rate limits). Instrumentation may be used during the load change to verify stress levels are within allowable limits (similar to instrumentation to regulate plant startup).

Rapid Load Changes

The HIPPS plant will allow for rapid load changes. However, the magnitude of incremental changes will likely be limited to avoid thermal stresses in equipment and materials.

For the CAH and RAH, rate and degree of load changes will be partly dependent on changes to the gas turbine compressor air flow. Load changes, which do not modulate the gas turbine IGVs, will not substantially change the flow or temperature of gas turbine combustion air and ramp rates within this range can be achieved rapidly.

Rapid load reductions will be accomplished by ramping the HITAF and gas turbine simultaneously. To enhance stability of steam conditions in the HP steam system during rapid load reduction, modulation of the steam turbine control valves will be integrated into the control

system to minimize HITAF HP steam system pressure swings. Excess steam generation during rapid load reductions will be bypassed to the main condenser. Steam temperature drops due to control valve throttling may limit the range of such load reductions.

Rapid load increases are subject to the same restraints covering startup, and the responsiveness of the plant will depend on the plant output at the start of the load change. In general, the higher the plant output, the faster the expected ramp rate.

The ability of the HITAF and steam systems to accomplish rapid load changes and determining ramp rate limits will require additional study. Dynamic modeling will help clarify the interactions between plant components and determine ramp rate limits and interactive control schemes that assure stability.

Normal Plant Shutdown

The same issues discussed for normal plant startup also apply to plant shutdown. The shutdown procedure is essentially the reverse of the normal startup procedure.

Emergency Conditions

Emergency conditions are defined as abnormal operating conditions, which could cause personnel injury and/or equipment damage. While plant equipment is designed with sufficient margin to withstand many excursions beyond normal limits, instrumentation is required to monitor critical plant parameters, and to initiate control actions to protect the equipment from damage or failure during extreme excursions. For vessels and piping, safety valves are provided as a final pressure relief protective feature. This review considers HIPPS plant crucial components unique to the plant. Other equipment and processes, which are typically of power plants and usually controlled by design codes and standards, are not included in the discussion of emergency conditions.

The HIPPS plant control alarm system will be designed to notify plant operators when operating conditions exceed normal limits. Alarm set points are chosen just beyond the normal operating band to prevent nuisance alarms, but also below the maximum limits to allow the operators the time to assess the condition and to take corrective action. Trip set points are the maximum limits to initiate automatic, emergency actions to prevent further failures. The most drastic emergency action is tripping (turning off) a piece of equipment as fast as possible, without regard to normal shutdown procedures. For the HIPPS plant, tripping the following items would be major events.

- Gas turbine
- HITAF
- Steam turbine

In addition to abnormal operating conditions in the units, their tripping can be required because of conditions in other equipment such as the:

- Draft fans (ID, FD)
- Gas turbine auxiliary equipment: Lube oil, control oil, fuel systems, etc.

- Steam turbine auxiliary equipment (similar to gas turbine equipment)
- Balance of plant equipment, such as feed water and cooling water pumps, vacuum equipment, etc.
- Instrument failures related to the above items

require an emergency plant shutdown. The following paragraphs consider the consequences of major equipment trips and design features to prevent or limit damage.

Gas Turbine Trip

Gas turbine protection includes a control system provided by the turbine supplier, and for most events, damage to the turbine is unlikely. The main concern following a gas turbine trip is the loss of combustion air flow from the turbine to the CAH and RAH. Following a gas turbine trip, the HITAF will also need to be tripped, or the firing-rate rapidly reduced to decrease heat input to the CAH and RAH. In any scenario, residual heat in the HITAF can cause overheating of the air heater materials, unless an emergency source of air is provided to cool the CAH and RAH.

The extent of cooling and source of cooling air will be the subject of further studies to determine maximum temperature limits and allowable cool down rates in the CAH and RAH under various conditions.

Several options for providing emergency cooling to the CAH and RAH are available. For example, warm air from the HITAF primary or forced draft fan discharge duct could be one source of cooling air. The fans are not available if there is a blackout, and a separate, limited capacity fan, driven by a reliable power source is anticipated. A source of heat to warm the air supply may be required to prevent shocking the CAH or RAH with air that is too cool compared to the air heater material temperatures.

For a scenario where the HITAF is operated at reduced load following a gas turbine trip, future work needs to determine the effect of losing heat input to the HRSG #1 reheater and economizers. There are concerns that loss of heat input to the HRSG #1 reheater may cause water induction, which precludes continued steam turbine operation. Similarly, loss of heat input to the HP steam system economizers may cause unacceptable low feed water temperatures for the HP drum.

HITAF Trip

A HITAF trip, for example caused by failure of the ID fan, will cause a pressure decay of the HP steam system. Operation of the steam turbine is possible for a short time with the significant residual heat present in the HITAF. Unless the problem is rapidly solved and the HITAF placed back on-line, the steam turbine will be tripped and further cool down accomplished using the steam bypass lines to the main condenser.

Following a HITAF trip, the gas turbine can remain on line with HRSG #1 steam dumping to the main condenser until the HITAF returns to operation.

Loss of External Electrical System -Load Rejection

The HIPPS plant design will include the capability to shut down, without equipment damage, following a loss of the external electrical system, termed a site blackout.

All normal AC power will be lost during the blackout, and a backup power supply is needed for the following critical items, as a minimum:

- The instrument and control system
- The lube oil systems for bearings of the gas turbine generator, steam turbine generator, and large mechanical equipment (such as fans, boiler feed pumps where forced lubrication is provided in the design)
- The feed water supply to the HITAF for residual heat removal
- The emergency cooling air supply to the CAH and RAH.

Emergency power can be provided by a number options, or combination of options, including:

Batteries

Batteries can provide several hours of power to a minimal number of plant components. At other power plants the control system and DC driven emergency lube oil pumps use batteries for emergency power. The battery power provides lubrication to turbine generator and other equipment bearings until the equipment stops rotating. Battery power is also used to operate the control system. The batteries are recharged with AC inverters, and eventually require re-establishment of normal AC power from the external electrical system for recharging.

Standby diesel generator

A standby diesel generator will supplement the battery system and provide the additional power necessary for other loads, such as emergency feed water to the HITAF and emergency cooling air to the CAH and RAH. Diesel generators are very reliable, and well suited to the type of occasional service required by emergency conditions.

Steam turbine drives (emergency feed water pump and cooling air supply fan)

Steam turbine drives may be provided for emergency feed water and cooling air service. Steam for the drives could be generated from the residual heat in the HITAF. The auxiliary equipment for the steam turbines use DC motors with backup power provided by batteries (for operation under site blackout conditions, similar to steam and gas turbine lube oil systems). The decision to use steam turbine drives rather than AC drives in combination with a standby diesel generator will be studied as a site specific design issue.

HITAF Sensors and Controls

Control System Design

HIPPS presents a very dynamically complex system with many unknown factors and non-linearities. The novel HITAF furnace will be combined with conventional power plant subsystems (steam turbine, HRSG, gas turbine, emission control equipment, etc.). Even when it is clearly know and understand the behavior of individual parts and components, it is difficult to predict and understand how changes in design or operation affect the whole system, particularly the transient behavior of the system. Usually these problems are resolved experimentally via expensive, time-consuming and sometimes dangerous field testing.

Dynamic simulation was proposed to aid in the identification of needed sensors and control elements and by elucidating the transient behavior during start-up, shutdown, and load changes. The dynamic simulation model can identify sensor and control needs appropriate for the transient behavior of the system in terms of time scales for measurement, required accuracy, and number and location of sensors. Once identified, the system can be reconfigured or specific tests can be done *in the design stage*, thus avoiding dangerous and/or expensive problems with the demonstration unit.

The HIPPS system must produce electricity from coal, providing a minimum of 65% of the thermal input, at a busbar efficiency of 47% or better. The plant must be able to maintain an availability comparable to conventional power plants and must be capable of 50% turndown. As far as the HITAF is concerned, these requirements mean that the furnace must produce hot air at a minimum temperature of 1700 ^{o}F (927 ^{o}C) while meeting the availability targets. To meet the turndown requirements, the HITAF may need to be capable of achieving 50% load. Furthermore, the HITAF will have certain targets for NO_x emissions and unburned carbon in the ash that must be met.

The HITAF must meet targets for performance and emissions. The ease and cost of meeting these targets will be influenced by the combustor control system. The HITAF is a new furnace design, one that has never been built. While the task of designing such a system may seem daunting, the fact that HITAF is being designed "from scratch" provides an unprecedented opportunity to instrument the furnace and to create a control system which takes maximum advantage of advances in sensors and diagnostics. Design of the control system begins with a clear statement of the control philosophy.

The overall combustion control system will include several control subsystems that are interdependent: any changes or disturbances in one of them affect operation of other systems and the overall HITAF performance. To achieve the target NO_x emissions while maintaining high efficiency and availability, operation of all subsystems must be coordinated. In Phase II, a system integration approach was taken to design the combustion / NO_x control system.

The following technical issues were identified:

- Optimum set-point settings for individual subsystems versus load
- Burner turndown vs. burner out of service (BOOS) strategy for load swings
- Distribution of various air flows (primary, secondary, staging, dilution) versus load
- Flue gas recirculation versus load
- Slagging limitations for individual subsystems.

A number of innovative measuring concepts, presently under development, were considered for the HITAF application, including the following:

- Coal and air flow measurements for individual burners
- Fuel-air ratio for individual burners based on temporal flame frequency spectra analysis
- OH imaging for individual burner flames
- Gas temperature, O_2, NO_x, CO, unburned carbon measurements at furnace exit

- Gas temperature, NO, NH_3, N_2O measurements at SNCR exit.

It is anticipated that the HITAF control system will consist of several major subsystems: base combustion control, burner balancing and adjustment system, NO_x control, and turbine air temperature control.

The **base combustion control** system for each combustor will be organized similar to a conventional boiler control system: several control loops (fuel, airflow and draft) will operate in parallel following the HITAF load demand generated by the unit load controller. The fuel (or firing rate) controller will maintain desirable load distribution between coal and natural gas. The pulverizer controller for each mill will meet the coal flow demand by maintaining the feeder weight. The primary air flow controller will modulate the primary fan to maintain the required burner stoichiometry and the pulverizer temperature controller will modulate the hot air flow to maintain the pulverizer outlet temperature. The gas turbine exhaust could be used as the source of hot air to pulverizers. The total combustion airflow controller with an O_2 trim will modulate the staging airflow to maintain the optimum excess air. The ID Fan controller will maintain the air-flue gas balance by maintaining the constant (slightly negative) pressure at the combustor exit downstream of the slag screen.

The **burner balancing and adjustment system** will scan operation of individual burners and will equalize the values of fuel to air ratio and flame radiational characteristics for all burners by incremental positioning of available burner adjustments (such as secondary air dampers and swirl vanes) of individual burners. It is envisioned that this system would autonomous and relatively slow, operating only when the base system is in operation and the unit is in the steady-state mode. The operator will be able to intervene by changing the criteria of burner balancing and adjustment.

The **NO_x control system** will be the most sophisticated, it will combine a central logic with several analog control loops. The system will incrementally and sequentially modulate controllable factors affecting NO_x formation in search of the best compromise between the lowest values of NO_x and unburned carbon at the combustor exit. These controllable factors may include airflow staging and distribution, reburn fuel flow, flue gas recirculation to the radiant zone. It is envisioned that this system would be implemented as an expert system operating when the combustor is in the steady-state mode. Depending on the research and design data and combustor operating conditions (FEGT and ash deposit values), the system would select the controllable parameters and would determine the sequence, directions and rates of changes for their adjustments.

Further NO_x reduction to the target level will be achieved in the post-combustion systems (SNCR and SCR). Each of them will be equipped with their own controls. The optimum thermal conditions for their operation (temperature windows) will be maintained by modulating the quenching air and FGR flow to the dilution zone.

The **turbine air temperature control system** will be designed to ensure sufficient heat transfer to the turbine air in the radiant and convective air heaters which is critical for achieving high process efficiency in the HITAF. A key component in this control system is control of the radiant heat flux distribution in order to avoid overheating of the radiant panels. The axial and circumferential variations in radiant heat flux must be kept within a certain tolerance. A system of perimeter monitoring will have to be developed to ensure protection of the radiant panels. It is

anticipated that specialized radiant heat flux sensors would have to be developed / selected and tested. An autonomous radiant heat transfer balancing system is being contemplated: when an imbalance in radiant heat transfer (or an overheated portion in the radiant air heater) is detected, this system will tilt or reposition the individual burner flames to restore the balance of heat distribution in the combustor.

Turbine air from the gas turbine exhaust passes through convective and radiant air heaters and the duct burner. The temperature of air exiting the duct burner and entering the gas turbine is one of the main cycle parameters. This temperature will be affected by many factors, such as the flame temperature and emissivity in the radiant zone, thickness of ash deposits in both air heaters, combustor outlet temperature and the quench air / FGR flows, operation of sootblowers. The most direct and dynamically effective method of maintaining this temperature is by the fuel supply to the duct burner. Other methods may include burner flame adjustments, fuel biasing between burners and reburners, airflow distribution and convective air heater bypass. The optimum temperature control method (or combination of several methods) would have to be determined and the corresponding control system will have to be designed.

Ash deposits must be continuously monitored and controlled to maintain sufficient radiant heat transfer and optimum turbine air temperature. The ash management control system must assure effective ash deposit removal from the convective air heater and from the radiant air heater. Sensors will have to be developed/selected, tested, and evaluated to measure physical properties of deposits, including deposit thickness or deposit emissivity. The optimum cleaning strategies will have to be developed and analyzed. Cleaning procedures for the convective air heater will be tested on small-scale combustors.

Critical Issues for Control System Design

HIPPS is more complex than a conventional pulverized coal power plant or even a gas turbine-combined cycle due to the coupling of a "slow" (i.e., high thermal inertia) combustor with "fast" gas and steam turbines. The way in which the HITAF is controlled must be determined in the very beginning of the design process because the control philosophy determines what equipment will be needed in the commercial plant and what the performance criteria will be for subsystems. Both affect the capital and operating costs for the commercial plant. The combustor control philosophy is shaped by the need to accommodate following factors:

- Rapid load changes (startup, shutdown, equipment failure)
- Load following
- Heat flux distribution in radiant zone
- Integration of NO_x control subsystems

Procedures and equipment for starting up or shutting down (in either planned or unplanned mode) must be identified. The most critical needs fall in the area of emergency shutdown resulting from a failure in some component or subsystem. A failure of the gas turbine will result in rapid loss of vitiated combustion air to the furnace and of cooling air in the air heater. The airflow must be maintained at some level using a back up compressor or fan until the combustor can be cooled down. The combustor will have a maximum rate of temperature change,

determined by the behavior of the refractory, the air heater, joints and seals, etc. On the other hand, in the event of a HITAF failure, provision must be made to continue running the gas turbine by increasing the output of the duct burner. As mentioned above, the dynamic simulator provides guidance in designing start-up and shutdown procedures, in predicting the ability of the system to change load, and in identifying system response to component or subsystem failure.

Load changes down to 50% must be accommodated in the HIPPS. There are several options for dropping load as far as operation of the HITAF is concerned. First, the turbine inlet temperature can be changed while keeping the airflow relatively constant. The natural gas supply to the duct burner is reduced, but the coal and airflow to the HITAF remains relatively constant. Although the overall efficiency decreases, the least expensive fuel, coal, is being used. Second, the turbine airflow can be reduced while keeping turbine exhaust temperature constant. As a consequence, the coal and airflow to the HITAF are changed as is the natural gas flow to the duct burner. The minimum load may be determined by flame stability and/or by slag freezing on the radiant air heater.

In a multiple burner furnace, the radiant heat flux will not be constant over the entire high temperature heat transfer surface which may cause hot or cold spots. The former could result in loss of refractory and structural failure and the latter may cause build up of frozen slag with the related problems for heat transfer and structural integrity. The new materials under development for the radiant air heater subsystem will have limitations on temperature. In turn, these considerations will affect the control required for individual burners in the firing system and may affect the choice of sensors for the high temperature furnace environment.

To meet the NO_x emissions level of 0.06 lb/MMBtu (0.026 kg/10^6 kJ) a multi-step approach must be taken, both to minimize the cost and to lower the technical risk. The total NO_x reduction strategy must include a low-NO_x firing system in combination with one or more of the following subsystems: air staging, reburning, SNCR and SCR. Performance and cost analysis determine which subsystems are included. Each of these technologies has its own control requirements and limitations, each of them must be maintained at optimum conditions. For example, optimum stoichiometry on a burner-per-burner basis must be maintained for the firing system to achieve the lowest level of NO_x without increase in unburned carbon. Vertical temperature profile should be monitored for the air staging and reburning systems, optimum temperature windows must be maintained for the SNCR or SCR system.

Sensor/Instrumentation Needs

Monitoring the following parameters will be critical to the operation and control of HITAF and to managing the interaction between the heat recovery steam generators and HITAF:

- Convective air heater exit temperature
- Radiant air heater exit temperature
- Coal air distribution to the HITAF burners
- HITAF burner operation
- HITAF exit gas composition (CO, O_2, NO_x, NH_3)

- HITAF exit gas temperature
- Slag screen conditions
- Temperature of steam flows between HRSG 1 and 2.

Temperature

The ability to monitor and control the HITAF and combined cycle system relies on accurate temperature measurement of the working fluid (air) in the range 1000 to 2000 ^{o}F (538 to 1093 ^{o}C). Typical measurement requirements are as follows.

1. Measuring the temperature in the convective and radiant air heaters provides an indication of the distribution between convective and radiative heat transfer and will be necessary to control the firing rate.
2. Measuring the temperature in individual radiant air heater panels will provide a valuable cross check to other measurements of fuel and air distribution as well as providing warning of tube failure.
3. Measuring steam temperatures in lines transporting steam to heat recovery steam generators 1 and 2 will be necessary for dynamic control of the system.
4. Measuring the air exit temperature from the radiant air heater will be necessary for controlling the firing rate in the duct heater.

Thermocouples have had a poor record of long term stability and survivability at high temperature. Typical lifetimes at high temperature have ranged from 3 to 6 months and accuracy was maintained for shorter periods. The degradation in measurement accuracy of unstabilized thermocouples can be as much as 10 °F (6 °C) in 10 days. For example, during the 1980's, Riley Stoker embarked on an aggressive project to characterize furnace heat transfer. This required installation of hundreds of chordal thermocouples in the water wall tubes of two utility boilers. After only a month or two, about half the thermocouples had failed. High failure rates and unreliable readings after relatively short periods of time have always plagued steam temperature readings. Recent advances in thermocouple technology have yielded new thermocouples with higher stability.

Stabilized thermocouples will be needed for operation of HITAF. These can achieve a drift in the calibration of less than 1.8 °F (1 °C) after 3200 hours at 980 °F (527 °C) and 5.4 °F (3 °C) after 240 hours at 2240 °F (1227 °C). Thermo Electric Corporation manufactures stabilized type K and type E thermocouples.

As discussed in more detail below, an accurate measurement of the flue gas temperature entering the SNCR zone is critical for maximizing NO_x reduction and minimizing ammonia slip.

Deposit Monitoring

Two methods have been identified to date for monitoring deposits in the radiant air heater or slag screen. Diamond Power Product's Flameview^{TM} takes an infrared image of an object's surface and computes a temperature distribution. The resulting image is color-coded to give a temperature map of the surface. The absolute accuracy of the temperatures reported by

Flameview™ is not known, but this instrument does provide information on the uniformity of slag coverage.

Pyro Instrument Company's Pyro Laser™ is an infrared pyrometer used primarily in the metals processing industry for monitoring product quality. The device operates by shining a laser (0.865 micron) at the object's surface. The reflected laser light is used to determine the emissivity of the surface. The wavelength of the laser is chosen to avoid absorption of the laser energy by gaseous combustion products. (It is not yet known whether the presence of ash particles in the gas will affect the measurement.) Knowing the emissivity of the surface allows accurate measurement of the surface temperature. Pyro Laser™ might be used to characterize not only the temperature, but the thickness and nature of the slag using surface temperature, working fluid temperature, and emissivity of the slag.

Burner Operation

Burner operation is best monitored using the signal from the flame scanner. Fuel and airflow can (and should) be monitored, but they do not always represent actual flame conditions. Over years of research, PSI had demonstrated that the information contained in the flame scanner signal is directly related to the turbulent mixing in the burner ignition zone. Mixing is a sensitive indicator of air-fuel ratio, burner instability, and NO formation in the flame. The flame radiation information, when properly processed, provides a fingerprint of burner aerodynamics.

Air Flow

Measuring airflow to individual burners will be necessary to achieve minimum NO_x emissions; the technology is commercially available. Air Monitor makes low pressure drop airflow measurement devices for both clean and dirty gas environments. Currently, Air Monitor's probes are used by all major burner manufacturers to measure primary and secondary air in low-NO_x coal burners.

Coal Flow Measurement

EPRI sponsored a Coal Flow Measurement program in which three measurement methods are being developed: microwave, acoustic, and nuclear magnetic resonance (NMR).

The microwave method differs from current practice by using an active receiver across the duct. The Doppler shift and signal attenuation are both measured and used to calculate the mass flow of solids.

The acoustic method relies on analysis of the amplitude of acoustic power in both the time and frequency domains. Chaos theory is used to interpret the time domain and analysis of the power spectrum is used to interpret the frequency domain. Both analyses are used to infer the solid flow rate.

To date the NMR method has only been evaluated analytically. The microwave and acoustic methods have been tested on bench scale apparatus. In the near future the microwave and acoustic methods will be tested in a closed-loop pneumatic transport system at Lehigh University.

Currently there is a solids flow meter (Granuflo) available from Ramsey Technology which uses the Doppler shift of reflected microwave energy to deduce the solids flow rate and the signal

intensity to measure solids concentration. At constant air velocity, this device can provide a reliable coal flow signal.

Furnace Exit Gas Composition

Stack measurements are not adequate for process control. In any coal-fired power system that utilizes an induced-draft fan to pull flue gas to the stack (the vast majority of existing boilers, and the specification for HITAF), outside air will be drawn into the flue gas through leaks in the duct work or expansion joints thus diluting the flue gas. Since in-leakage is determined by local diluting pressure which is highly variable, ppm values measured in the stack can also vary unpredictably with such factors as ID/FD fan balance, ash deposits on convective tubes, excess air levels, or mills in services. In the worst case, leakage amounts may be coupled to the combustion control scheme.

Therefore, either HITAF NO_x control systems or conventional boiler combustion or post-combustion control systems are best served by gas concentrations measured at the furnace outlet. Since probe maintenance is a potential problem at furnace exit gas temperatures, the preferred measurement location for process control is the economizer outlet duct in conventional boilers. In the HITAF, such measurements should be made upstream of the HRSG.

An open path instrument that gives an across-the-duct measurement will prove superior to a point measurement (e.g., an extractive sample) in meeting these needs. Several commercial instruments that measure one or more gas species using an open path system are discussed below.

There are no reliable, accurate techniques that can measure two or more of these gases simultaneously. The instrument closest to commercial acceptance as a multi-species analyzer is the OPSIS instrument. OPSIS uses a technique called Differential Optical Absorption Spectroscopy (DOAS) to measure concentrations of several species along the same optical path. Light from a broadband source is collimated and directed across the duct to an optical fiber at the receiver. Absorption spectra are then deconvoluted using an on-board computer based on reference spectra for all gas components. Since broadband absorption has little spectral structure and can be difficult to differentiate from scattering by ash particles, the DOAS technique only uses the narrow band structure. The measurement signal is created by dividing the raw signal by a reference signal and then looking at the difference between the sample signal and a 5th order polynomial fitted to the signal.

The problem with OPSIS and other techniques that utilize the UV spectrum is the overlap of absorption lines from a large number of flue gas species. In essence, the computer must guess one specie (usually SO_2) in order to back out other gas concentrations. If the guess is too far off, the solution algorithm will not converge or reach a unique solution for other gases. Trace species like ammonia are likely to suffer the largest error.

The most important gas component of the flue gas that cannot presently be measured non-intrusively is O_2. The lack of a non-intrusive O_2 monitor means that O_2 cannot be measured upstream of the staging air where temperatures will be in excess of 2780 ^oF (1527 ^oC). The addition of staging air before a gas analysis can be made will eliminate a direct measurement of burner operation. Therefore the performance of burners and fuel and air distribution cannot be monitored directly based on composition. Because furnace exit gas composition cannot be used

to monitor burner operation, it will be necessary to use measurements of fuel and airflow along with flame signature information to control the burners.

New Instrumentation for NOx Control in HITAF

Introduction

Application of urea or ammonia injection is being designed as part of an integrated NO_x control system for the High Temperature Advanced Furnace (HITAF) being developed by the United Technologies Combustion 2000 team. Ammonia or urea is injected into the boiler through existing ports at temperatures where NO_x will react with the chemical reagent to form N_2. Since ammonia slip results from injecting excessive reagent and/or low injection temperatures, the NH_3 measurement allows on-line tuning of the NO_x reduction process. A well-tuned non-catalytic NO_x reduction process is capable of 30 to 50% NO_x reduction before excess ammonia appears in the flue gases. Reagent utilization (the percentage of reagent that actually reacts with NO_x) depends on the time/temperature distribution available in each boiler, but usually ranges from 15 to 40% in retrofit applications.

By designing the NO_x reduction region for rapid reagent mixing, constant temperature, and feedback/feedforward control, much greater NO_x reductions and higher reagent utilization are possible. Under ideal laboratory conditions at the University of Utah, 90% NO_x reduction and 70% reagent utilization have been measured. The HITAF could be designed to approach ideal NO_x reduction conditions, but advanced sensors and controls will be required to hold these conditions throughout the operating range of the HITAF.

The design of a preliminary NO_x control system must address sensor needs and constraints associated with the following:

- Gas species to be monitored and controlled
- Location of optical paths
- Issues relative to instrument location
- Issues relative to process control.

HITAF NOx Control System Overview

Coal is combusted in the HITAF for the primary purpose of heating compressed air. The heated air is then expanded through a gas turbine to generate electricity. Additional heat is extracted from the flue gas in a steam bottoming cycle, resulting in a combined cycle efficiency of 47 to 52% (HHV). Although the HITAF concept is simple, the actual design places constraints on the NO_x control system.

High compressed air temperatures require high combustion temperatures to drive the radiative heat transfer. High combustion temperatures are best achieved using high heat release burners tuned to near-stoichiometric air-fuel ratios. This type of combustion generates high NO_x emissions, typically above 1.0 lb/MMBtu (0.43 kg/10^6 kJ)or at least ten times higher than systems fired by natural gas. The goal of the HITAF system is to achieve NO_x emissions below 0.06 lb/MMBtu (0.026 kg/10^6 kJ).

To achieve this NO_x goal, the HITAF will apply the following technologies in series:

- Low-NO_x burners with separate air-fuel ratio control
- Coal reburning
- Adiabatic selective non-catalytic reduction
- Hybrid selective catalytic reduction.

Each technology is discussed below.

Low-NO_x Burners

The 300 MW conceptual plant design consists of two HITAFs, each fired by five low-NO_x burners. These burners will be fed by separate air and fuel ducts so that air-fuel ratios can be controlled on a per-burner basis. The burners are arranged on the top of the furnace with one central burner that is surrounded by four equally spaced outer burners.

In the preliminary design, all ten burners are fired at a stoichiometric air/fuel ratio of about 1.0 in order to maximize flame temperature. Alternatively, firing the central burner at a stoichiometric ratio of about 0.90 and the outer burners at 1.025 may be a better compromise between furnace temperature and lower initial NO_x. In either case, close control of individual burner air-fuel ratios will be required to minimize NO_x and maximize heat transfer to the radiant air heater.

Initial burner testing and modeling performed by Reaction Engineering predicts a baseline NO_x of about 0.4 lb/MMBtu ($0.17 kg/10^6$ kJ) for the HITAF. This prediction was based on a single burner per HITAF (i.e., without radial staging effects), so it should be considered slightly conservative.

The key to low-NO_x burner performance is flame attachment. Unless burner ignition is established at the coal nozzle, the fuel and secondary combustion air can premix causing NO_x emissions to increase. Flame standoff will also shift the heat release downstream, thus degrading the performance of the radiant air heater.

An array of 15 intelligent flame scanners has been specified for monitoring and controlling the burners as shown in Exhibit H-1. Each burner will have a conventional flame scanner located on the burner front to tie in with the flame safety system. The primary function of the burner-mounted scanners is to assure the presence of individual flames. If a flame goes out, a controller will shut off fuel flow to the affected burner in order to prevent a possible explosion. In addition, ten advanced scanners will be aimed from the furnace sidewalls at a point at the base of each flame (two aimed at each burner). The main purpose of the sidewall scanners is to assure tight flame attachment by sending a signal calling for burner adjustment if the flame wanders too far downstream. In addition, advanced software in each burner scanner will process oscillations in the flame signal to monitor changes in burner air/fuel ratio, mixing rate, or flame shape. These parameters can then be optimized for both burner and radiant air heater performance.

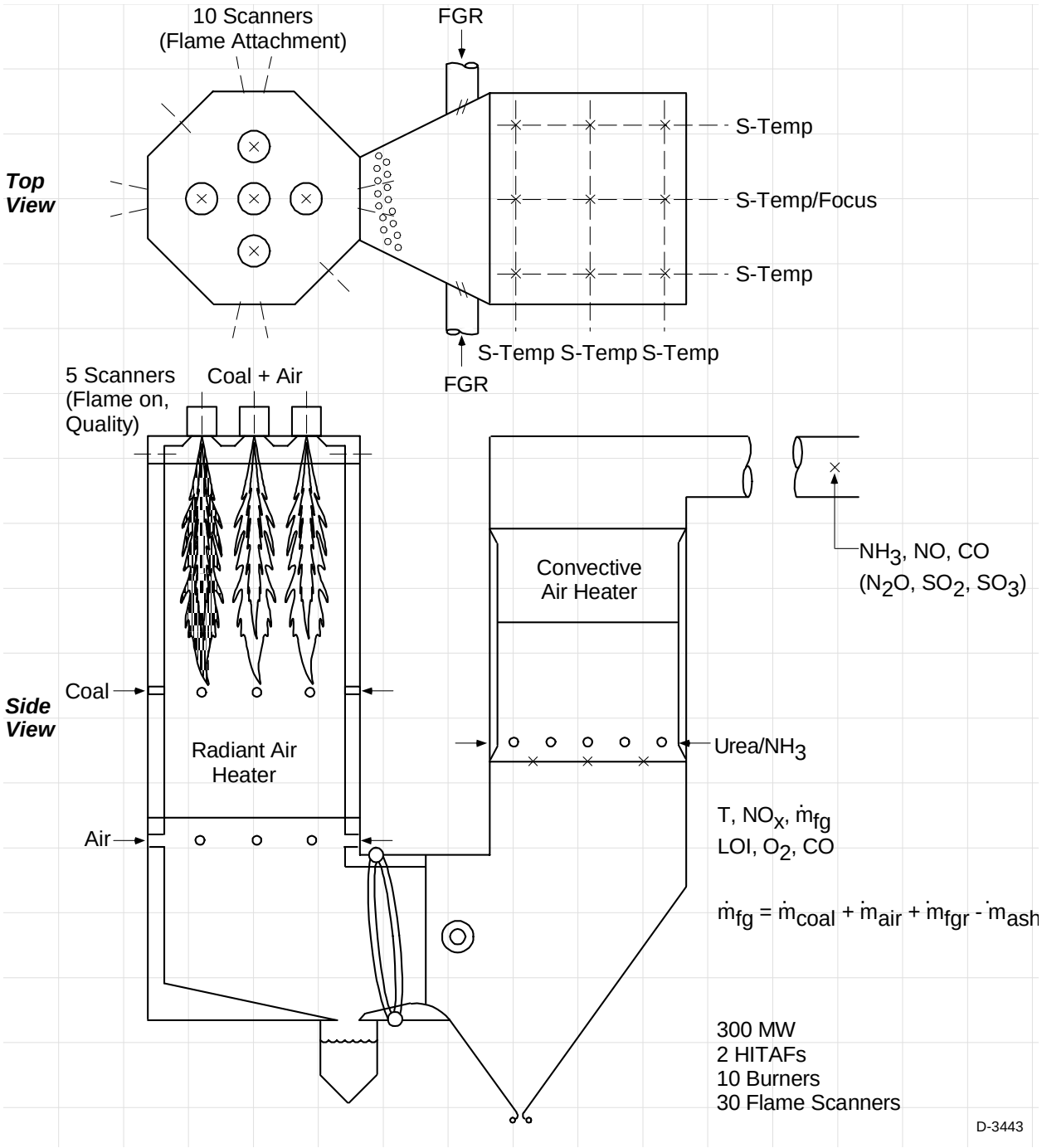

Exhibit H-1
Measurement Needs for NOx control system in HITAF.

Reburning

NO_x is further reduced to about 0.2 lb/MMBtu (0.086 kg/10^6 kJ) by injecting additional pulverized coal into the HITAF through eight wall openings in each HITAF just downstream of the flame zone. Coal volatile matter reacts with NO_x in the post-flame gases to convert 50 to 70% of the NO_x to N_2 or to reduced nitrogen species such as HCN or NH_3. This process is called

reburning. The ideal air-fuel stoichiometric ratio for reburning is about 0.70 to 0.85 (higher furnace temperatures favor higher stoichiometric ratios) but the HITAF will be designed to maintain reburn zone stoichiometric ratios above 0.90 to maximize heat transfer to the radiant air heater. Staging air to complete combustion is injected from staging air ports located in the eight furnace sidewalls at the bottom of the radiant furnace. Some NO_x will reform when the staging air reacts with reduced nitrogen species. Uniform dispersion of staging air within the furnace cross section will be required to minimize CO and unburned carbon leaving the combustion zone.

SNCR

The radiant furnace is designed for wet ash removal. Flue gas recirculated at a temperature of about 260 °F (127 °C) is injected downstream of the radiant furnace to quench any molten ash droplets that escape the screen tubes at the furnace outlet. The amount of flue gas recirculation will be controlled based on temperature measurements from an array of SpectraTemp[7] instruments located just upstream of the SNCR section. Thus, the amount of dispersion of FGR can be controlled to achieve the optimum temperature profile for NOx reduction the SNCR region.

The SNCR region is refractory-lined to maintain constant gas temperature for a minimum residence time of 0.5 seconds. In addition to temperature profiles, the SNCR control system will require the following continuous data:

- Inlet NO_x concentration
- Inlet flue gas flow rate (total, not just FGR)
- Outlet NO_x concentration
- Outlet NH_3 concentration.

Urea-based systems need to minimize inlet CO since this gas inhibits the NO_x reaction chemistry, effectively changing the temperature window for maximum NO_x reduction.

From the inlet NO_x and flue gas flow measurements, the controller can calculate the moles of NO_x per second passing through the reactor. The reagent flow rate can then be adjusted to maintain a constant mole ratio of reagent nitrogen to NO_x. Given constant temperature and rapid dispersion of reagent into the flue gas stream, a 50% NO_x reduction should be possible at reagent stoichiometric ratios below 1.0 (greater than 50% reagent utilization).

Reagent that does not react with NO_x will either pass through unreacted as ammonia or burn to N_2 (and a little more NO_x). A fraction of the inlet NO_x (2 to 8%) is partially reacted to nitrous oxide (N_2O) in urea-based retrofit SNCR systems. The amount of N_2O in the exit gases is related to the rate of temperature quench (i.e., it is highest when urea is injected into convective pass cavities where superheater/reheater tubes rapidly reduce gas temperatures). In the HITAF application, only about 1 to 5 ppm of N_2O is expected because the NO_x reduction reactions take place at constant temperature.

It will be critical in the HITAF application to monitor and minimize NH_3 slip downstream of the SNCR section. Not only is NH_3 indicative of wasted reagent, it can also cause long-term operating difficulties in downstream equipment. Ammonia combines with SO_3 to form ammonium sulfate and bisulfate, a white submicron-sized fume that will deposit or condense on

heat transfer surfaces at temperatures below about 450 °F (232 °C). Deposits on economizer or feedwater heater surfaces in the heat recovery steam generator (HRSG) may lead to plugging, derating (due to increased gas-side pressure drop), and eventual shutdown for water washing. Ammonia salt contamination of fly ash has been a problem in a few retrofit SNCR applications because the ammonia odor made it difficult for the utility to sell its fly ash.

Hybrid SCR

Ammonia measurement at the SNCR outlet will also be critical if selective catalytic reduction (SCR) is required to achieve NO_x emission limits below 0.06 lb/MMBtu (0.026 kg/10^6 kJ). SCR can only achieve very low NO_x emissions if ammonia and NO_x are intimately mixed upstream of the catalyst section. In retrofit applications, this requirement has been met by installing an ammonia injection grid in front of multiple catalyst layers. Both the grids and the catalyst represent a significant capital cost that may be avoidable.

In the HITAF, a small catalyst section has been designed as part of the HRSG, located between the reheater and economizer sections where the flue gas temperature is expected to be about 700 °F (371 °C). In-situ monitoring of both ammonia and NO_x in a grid upstream of the catalyst can be used to send a signal to the SNCR control system. Reagent flow to various SNCR injectors could be biased according to these feedback signals to produce ammonia and NO_x flow profiles more conducive to lower overall NO_x reduction. Thus, target NO_x values could be achieved without increasing total reagent flow, without installing a separate ammonia handling and injection system, and using the minimum amount of catalyst surface.

In-Furnace Monitoring of NO_x Control

Ammonia slip occurs when reagent flow is too high or when gas temperature is too low. The ammonia measurement is used to decrease urea flow rate until the ammonia concentration is below a critical value (say 5 ppm at 3% sample O_2). If NO_x emissions then increase above the regulated value, the injection location is moved to a higher temperature zone and urea flow is increased until the NO_x limit is met. The result is compliance at a reagent utilization of about 30% (as compared to 10 to 20% reagent utilization without SpectraScan®).

Better reagent utilization would be possible if a more representative flue gas sample could be obtained. Any extractive sampling system can only obtain a tiny fraction of the total gas stream. Nalco FuelTech addresses the sampling problem by locating the sampling probe where ammonia emissions are likely to be highest. Therefore, the NO_x control system is less likely to emit excess ammonia but more likely to over-control and waste reagent.

A better, more economical control system could be implemented if ammonia concentrations could be measured in-situ using multiple optical paths. First, a line-of-sight NH_3 measurement is more representative of the total flow gas than an extracted sample would be. Since measurement paths could be associated with specific injectors, multiple measurement paths would allow the control system to decrease urea flow for a path showing high ammonia, and increase urea flow for a path showing low ammonia. Therefore, an in-situ NH_3 instrument could greatly enhance the cost-effectiveness of retrofit SNCR systems.

The open path technology must be adapted from relatively clean and cool ambient weather conditions to the high temperature, high velocity, and dusty environment typical of flue gas ducts

from a coal-fired boiler. Special ports coupling the instrument transceiver and retro-reflector to the duct wall must be designed to compensate for vibrations or other alignment problems.

Criteria for selecting the gas species to be measured by the prototype multi-species instrument are listed below:

1. The measurement will benefit process control (HITAF, SNCR, and SCR) for Combustion 2000.
2. Gases to be measured are present in many boiler or SNCR systems, and measurement is desirable for process control.
3. There are no adequate substitute technologies for measuring these gas species simultaneously.
4. The gases need to be measured upstream of the stack.
5. The gases can be measured concurrently along a single optical path.

Each criterion will be discussed below. Then candidate gas pairs will be nominated and evaluated against the selection criteria. The gas pairs will then be rank ordered.

HITAF NO_x System Control

Achieving NO_x emissions below 0.06 lb/MMBtu (0.026 kg/10^6 kJ) will require integrating at least three and maybe four NO_x control technologies. In the combustion zone, air and fuel must be distributed among the burners and reburners to simultaneously minimize NO_x, CO, and unburned carbon leaving the slagging section. Operation will be further constrained by the need to achieve the desired compressed air temperature within the radiant air heater as well as free-flowing slag through the slag tap.

The SNCR NO_x reduction performance will be dependent on the ability of operators to control temperature and reagent distribution in the reaction zone. The presence of carbon monoxide (CO) in the flue gas can also be detrimental to urea-based SNCR, especially when NO_x emissions below 0.1 lb/MMBtu (0.043 kg/10^6 kJ) are desired. In order to optimize the SNCR system operation, inlet NO_x, CO, and temperature distributions must be measured and *controlled*. Temperature distribution can be controlled by varying the amount of momentum (axial vs. radial) of recycled flue gas injected. Response to changes in CO or NO_x distribution, however, must include burner adjustments, staging airflow damper modulation, and/or reagent injection flow control. These controllable parameters will also be trimmed to minimize NH_3, NO_x, and CO concentrations downstream of the SNCR section.

In the event that SCR is required to reach NO_x emission limits, the amount and distribution of NO_x and NH_3 going into the reactor section (within the HRSG) must be measured and controlled. This will require controlling FGR flow to minimize SNCR reagent combustion instead of minimizing outlet NO_x. Reagent loss is minimized at lower SNCR zone temperatures around 1610 °F (877 °C). FGR flow will be constrained by convective air heater performance, thus requiring a tie-in to the air temperature control subsystem. Also reagent flow to the SNCR section will be controlled to maintain the SCR outlet NO_x concentration below the emission limit, while minimizing NH_3 emissions.

Gases that must be monitored and included in the control system boil down to: NO_x, CO, O_2, and NH_3. Table H-1 summarizes the HITAF gas measurement requirements and the location of each measurement.

Table H-1
Gases Whose Measurement Will Help Control HITAF

Combustion Control	NO_x, CO, O_2 at combustion zone outlet (same as SNCR zone inlet)
SNCR Control	CO, NO_x at inlet NH_3, NO_x, CO at outlet
Hybrid SCR Control	NH_3, NO_x at inlet (same as SNCR outlet) NH_3, NO_x at outlet

Conventional Boiler/SNCR Systems

Note that all the gases listed in Table H-1, except NH_3, are supervised by the continuous emission monitors required for existing coal-fired boilers. Ammonia monitoring is not required for emission compliance in the United States, but ammonia instruments are being applied to prevent NH_3 slip from both SNCR and SCR retrofit installations. Therefore, NO_x, CO, CO_2, and NH_3 meet the criterion of being present in conventional boiler systems.

All these gases are also useful inputs to conventional combustion or emission process control systems. Many utility boilers have O_2 sensors mounted in the economizer outlet ducts. The O_2 measurements are used to trim total airflow in order to minimize boiler heat rate. Many boilers also employ CO monitors at the same location to assure that excess air is not lowered to the point where unburned combustibles are emitted with the flue gas or fly ash.

NO_x measurements have not been used directly for combustion control, but software packages have been developed to characterize and optimize boiler and burner operation. Predictive emission monitoring systems (PEMS) have been used to relate boiler operation to NO_x emissions measured during a comprehensive test program. Once "calibrated", these PEMs give boiler operators the opportunity to minimize NO_x by tighter control over operating parameters that have the largest impact on NO_x emissions.

New software products such as ULTRAMAX and GNOCIS go one step further. These products can be used in either a control or advisory mode to simultaneously constrain NO_x emissions while operating at the lowest possible net plant heat rate. ULTRAMAX creates statistical models relating controllable parameters to both NO_x and heat rate. GNOCIS employs adaptive neural network and fuzzy logic technology to create an adaptive model of boiler operation and NO_x production. Both these software systems require fast and accurate measurement of NO_x, O_2, and CO.

Ammonia measurement is also required for process control. Nalco FuelTech is incorporating an ammonia slip measurement into their newest SNCR installations. Ammonia slip measurements in SCR installations are also being used by operators to tune the ammonia injection grid for the desired NH_3/NO ratio. A robust continuous ammonia slip monitor could be

incorporated into SCR control systems. Another use for ammonia slip data is to monitor catalyst activity to indicate the time interval for catalyst cleaning or replacement.

Recommendations

Table H-2 shows the gas pairs that could be measured and used in a HITAF control system. The preferred measurement location and how the measurement could be used for control are information distilled from previous sections of the report for inclusion in this table.

Table H-2
Candidate Gas Pairs

Gas Pair	**Measurement Location**	**Purpose**
CO-O_2, CO-CO_2	Combustion zone outlet	Burner/staging air control (CO relates to air/fuel bias)
NH_3-CO	SNCR outlet (downstream of convective air heater)	Reagent flow trim FGR port control (urea systems only)
NH_3-N_2O	HRSG plenum	Reagent flow trim FGR port control
NH_3-SO_3	SCR outlet	Sootblow convective air heater Reagent flow trim FGR port control
NO-CO	SNCR inlet	Simultaneous combustion - SNCR control (feedback-feedforward)
NO-NH_3	SNCR outlet	Ideal SNCR optimization and control

These six gas pairs were then rank-ordered according to the evaluation criteria in Table H-3. NO-CO was judged most important for HITAF because the measurements were useful for controlling both combustion and post-combustion NO_x reduction. The other gas pairs were ranked according to their usefulness for controlling combustion, SNCR, or hybrid SCR separately.

Most conventional boiler systems do not utilize post-combustion NO_x control (although many will choose SNCR in response to seasonal NO_x regulations expected to be imposed in ozone non-attainment areas of the U.S.). Therefore, gas pairs that are important for combustion optimization received the highest ranking for usefulness in conventional systems.

Table H-3
Ranking the Gas Pairs

Gas Pair	HITAF Usefulness	Ranking			
		Usefulness in Conventional Systems	Upstream Measurement Required	No Completing Technology	Overall
NO-CO	1	1	1	5	1
NO-NH_3	2	3	2	1	1
CO-O_2	4	2	3	6	4
NH_3-CO	3	4	4	2	3
NH_3-N_2O	5	5	5	3	5
NH_3-SO_3	6	6	6	4	6

Section 2 - Repowering of Existing Plants with HIPPS Technology

Abstract

The work reported in this section was performed under program tasks 6.2, 6.3 and 6.4. Advanced gas turbines such as intercooled aeroderivative (ICAD) or the Humid Air Turbine (HAT) cycle were used in an investigation of repowering older steam stations. Aging PC plants with efficiencies of 32-35% could be repowered with HIPPS/ICAD resulting in increased output and increased efficiencies usually in the 45-50% range, depending on the steam conditions of the repowered plant. The HIPPS/HAT could also be used, but this approach is not as attractive in the repowering applications because use of the existing steam turbine and boiler, while having capital cost advantages, reduce overall efficiency. Economic analyses indicate that the cost of repowering appears to be competitive with the more normal approach of using natural gas fueled gas turbines.

Introduction

This section describes an analysis of technical and market/economic issues for the repowering of existing power plants. A more detailed market assessment is contained in Appendix E - Market Study for HIPPS Technology. The first sections of this report presents results from a review of repowering information from public literature and data from the UTRC Combustion 2000 team members. Additional sections contain flowsheets and an energy and materials balance for major process flow streams of a HIPPS power generation cycle evaluated by the UTRC team. A list of major equipment and cost data for the repowering case is also provided. The generic site performance and cost data indicate that repowering with HIPPS has positive economic and environmental impacts on power generation. However, more detailed site-specific work would be required to assess individual cases where HIPPS might be applied.

Power Plant Repowering Background

There are some 30 to 40 GW of oil and gas fired power generation capacity, and more than 50 GW of coal-fired capacity that is 30 or more years old. The total of 30-year old capacity represents over 8% of the current U.S. generating capability. While not all these mature units are suited to repowering, even a reasonable portion of the total would be a significant market for repowering concepts. Table 2-1 shows the average age of fossil power plants smaller than 300 MW in North America.

Table 2-1
Fossil Power Plant Average Age Data

Size, MW	1 to 99	100 to 199	200 to 300
Number of Units	380	430	175
Average Age, years	40	35	30

In addition to a future replacement of aging power producers, utilities are assessing repowering as one way to comply with the Clean Air Act and other environmental requirements.

Clearly, repowering with new technology can markedly increase generation capacity and reduce environmental emissions. However, the technology options need careful study. For example, it is now assumed that for any significant repowering effort, the new plant will need to meet Federal New Source Performance Standards (NSPS). Exhibits 2-1 and 2-2 were published by General Electric Company in Power Engineering, February 1993, but the relationships remain valid today. Exhibit 2-1 shows estimates of how heat rate increases (and efficiency declines) as the steam generator ages. Exhibit 2-2 displays forced outages as a function of age.

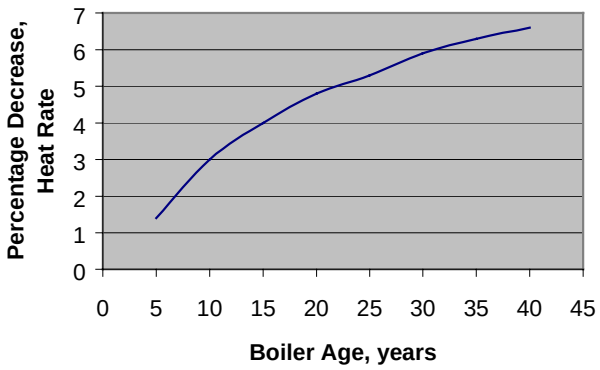

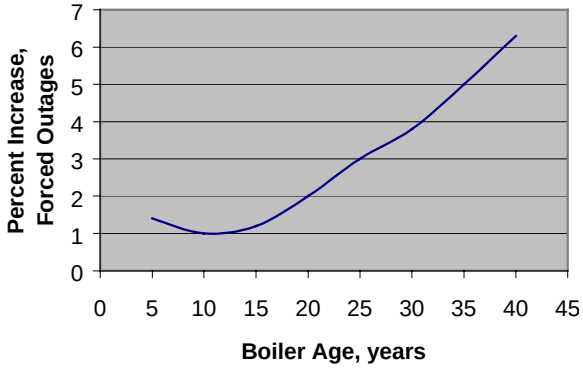

Exhibit 2-1
Heat Rate Decrease vs. Boiler Age

Exhibit 2-2
Forced Outage Increase vs. Boiler Age

Other important incentives for considering repowering options are listed below.

- The cost of Greenfield power plants is relatively high compared to repowering. In many cases, repowering will be the least cost option for utilities in today's market.
- The difficulty to permit and site new plants typically causes large schedule delays and cost increases. If a utility can repower an existing facility, permitting can often be facilitated.
- With the pressure imposed by a competitive market, and threats of CO_2 limits and other regulated restrictions, utilities are more prone to improve unit and system efficiencies.
- Repowering an existing unit can give the utility a competitive advantage over independent power producers and merchant plants.

Current Repowering Practices

Much of the present (1999/2000) repowering activity now going on in the U.S. and the world uses natural gas fired turbines with combined cycle (GTCC). Such plants have rapid load-change and startup abilities. They are reliable; have low air emissions and offer net plant efficiencies of 45% (HHV).

Repowering with GTCC equipment can increase existing plant efficiency by 20 to 30 percent and in some cases double or triple the output i.e. the capacity of the gas turbine is usually twice that of the steam generator. Of course, it may not be possible to exactly match the repowering gas turbine with existing steam generators/turbines, and some cases the existing steam plant will be derated. Alternatively, existing equipment may be upgraded with to take more complete

advantage of repowering. The upgrades, and more routine refurbishing of existing turbines and generators, also increase the cost for repowering.

Three common types of repowering concepts are discussed next based on data published in a Bechtel paper by H. Wen and R. Gopalarathinam (1992).

Windbox Repowering

In windbox type repowering, the hot exhaust from a new gas turbine is sent to an existing boiler. The thermal energy from the exhaust replaces fired boiler combustion gases, and is used to generate steam. Exhibit 2-3 shows an example of a windbox type of repowering. Boiler and windbox modifications are used with the concept, and usually include the addition of a gas cooler, or small heat recovery steam generator (HRSG), to keep the turbine exhaust temperature within the windbox design limits.

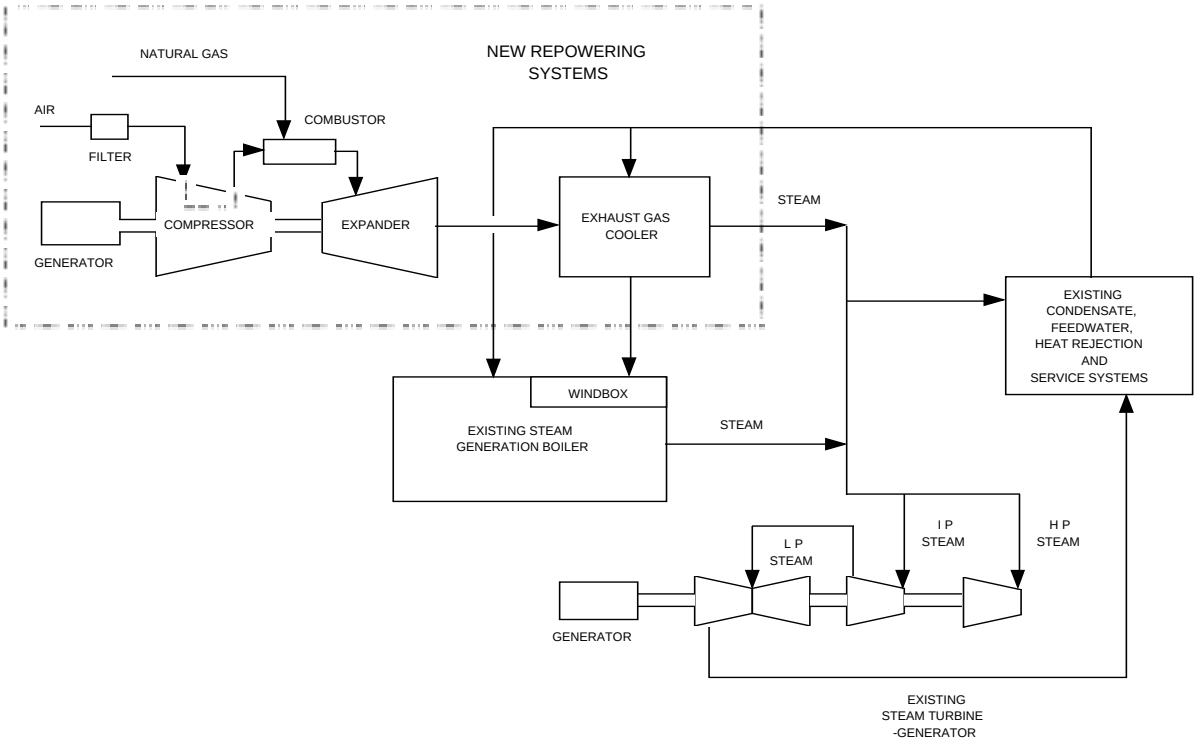

Exhibit 2-3
Windbox Repowering Concept

Usually 60 to 70% of the turbine exhaust heat is recovered in the form of steam. The steam is sent to the existing steam turbine-generator and associated equipment to produce power. The resulting increase in plant capacity from addition of the gas turbine to the steam cycle is limited by the need to closely match the gas turbine with the combustion air requirements of the boiler. If coal is being replaced by natural gas as the fuel for windbox repowering, emissions are greatly reduced. The exception may be CO_2 emissions, which could remain high because of the increased capacity and energy consumption by the addition of the gas turbine. The amounts of CO_2 will vary depending on the plant efficiency.

The following generic plant costs are estimated by examination of a number of published and in-house data points.

- Gas Turbine Installation 40 MW
- Total New Capacity 130 MW
- Net Capacity Increase 40 %
- Investment $30 Million
- Incremental Cost $750 to $900 per kW

Windbox repowering is not as attractive for many utility applications as are other options because the incremental cost per kW is higher than for new construction; the increased capacity is limited; and fewer environmental benefits are possible.

Feedwater Heating/Repowering

For many existing plants, steam (thermal energy) is extracted from the steam turbine system to preheat the boiler feedwater. When the exhaust from a gas turbine is used to do the feedwater heating, there is no need to divert energy, and all of the generated steam is sent to the steam turbine to make electric power. Exhibit 2-4 shows one of the concepts for feedwater heating with gas turbine exhaust.

In a Bechtel study of a 518 MW power plant, a net gain of 55 MW and a 4 percent heat rate improvement were found in the steam turbine. However, the incremental cost per kW was higher than for new construction, and all else equal, there were few environmental advantages.

The following data for a feedwater-heating example of repowering was compiled from consolidating a number of published and in-house sources. The values are nearly the same as for the windbox repowering case.

- Gas Turbine Installation 40 MW
- Total New Capacity 130 MW
- Net Capacity Increase 40 %
- Investment $40 Million
- Incremental Cost 700 to $900 per kW

Because maintenance records show in older plants that boiler outages are the leading cause of lost availability, repowering by keeping the existing boiler is not actively pursued by many utilities.

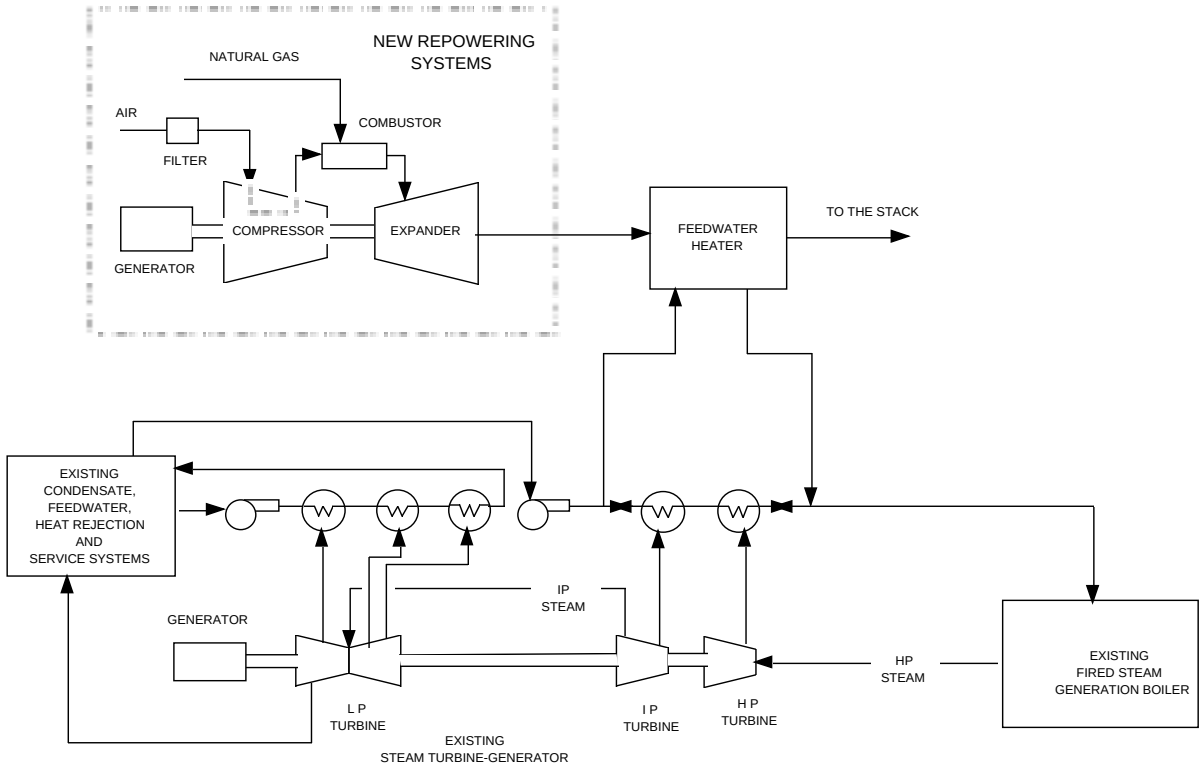

Exhibit 2-4
Feedwater Repowering Concept

Full Repowering

For full repowering, the existing steam generator is replaced by a new heat recovery steam generator (HRSG). The repowered plant has most of the benefits of a new construction GTCC plant, including a long service life, added generating capacity and lower environmental emissions. Exhibit 2-5 illustrates one of the various possible full-repowering concepts.

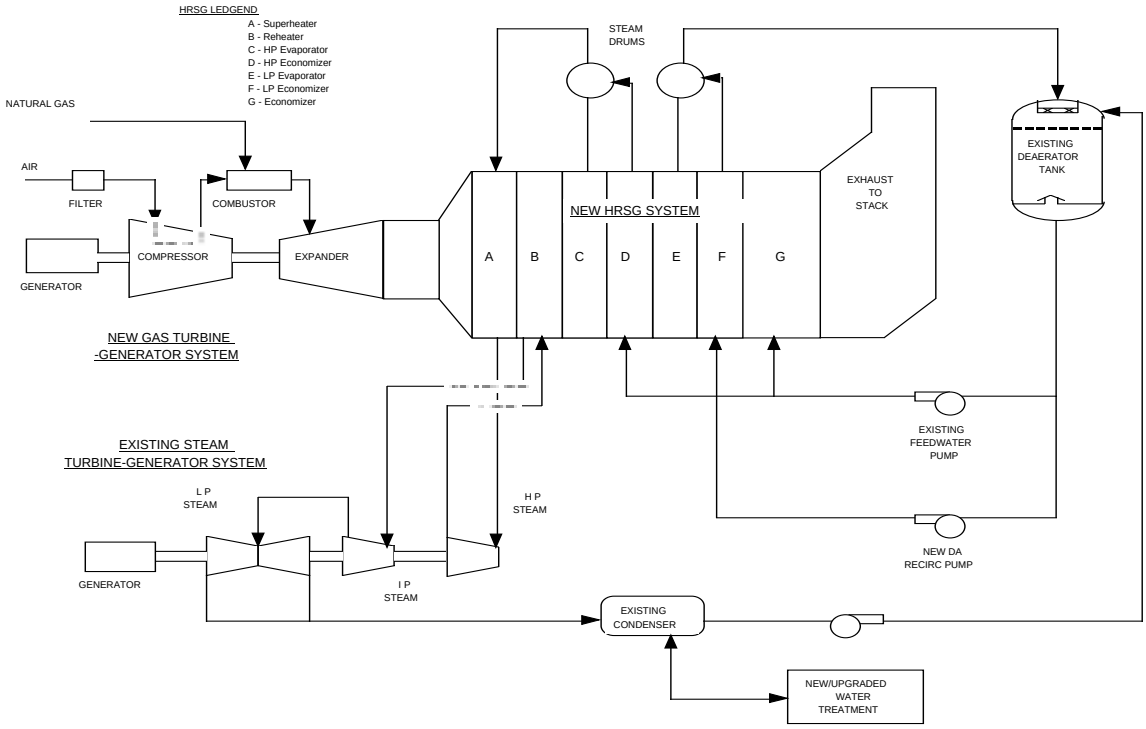

Exhibit 2-5
Full Repowering Concept

Compared to a new GTCC plant, the repowering project cost is usually attractive because the existing site and infrastructure can be used.

Data from several sources were consolidated and are approximated below for an example of full repowering.

- Gas Turbine Installation 160 MW
- Total New Capacity 240 MW
- Net Capacity Increase 150 to +200 % for others
- Investment $90 Million
- Incremental Cost $600 to $700 per kW

Thus, when utilities are examining repowering, full repowering (with variations) is usually the most attractive option. Performance data for one such repowered plant, summarized from a Bechtel American Power Conference paper, are shown in Table 2-2.

Table 2.2
Full Repowering Performance Summary

Existing Plant Conditions			
Existing Plant Capacity MW	100	200	300
Steam Conditions (psig/°F/°F)	1,450/1,000/1,000	2,400/1,000/1,000	2,400/1,000/1,000
Heat Rate, Btu/kWh	11,130	10,200	9,700
Repowered Plant Conditions			
Gas Turbine, MW	160	2 x 170	3 x 170
Number of HRSG's	1	2	3
Steam Conditions (psig/°F/°F)	1,450/1,000/1,000	1,515/980/980	1,515/980/980
Steam Turbine, MW	80	160	242
Net Plant, MW	230	490	740
Plant Heat Rate, Btu/kWh	7,320	7,500	7,460

Two other repowering cost data points reported in the news are:

- San Diego Gas and Electric's South Bay Station with 171 MW existing capacity will be repowered to add 503 MW for a cost of $410 million, or some $815 per kW of added capacity.
- Public Service Electric and Gas Company's Bergen Station with 225 MW of existing capacity will add 425 MW and cost some $400 million, or some $940 per kW of added capacity.

HITAF Repowering

The above review of current utility repowering alternatives concludes that the repowering of aging steam stations with modern gas turbines may now present the better opportunity to provide the additional power that is required for the future. The ability to use existing facilities and infrastructure and, in many cases, use locations near load centers that already have needed environmental permitting makes repowering attractive. Although the process is much simpler at sites with permits to generate power, environmental permits are still required for repowering. As part of the HIPPS program, preliminary investigations were made indicating that the HIPPS/HITAF approach can be successfully applied to repowering. First, preliminary studies identified the operating characteristics and performance of a HITAF/aeroderivative gas turbine combination for repowering. A specific steam power plant was then used as the basis for a repowering study to estimate potential performance using an actual steam power system.

Preliminary Analysis

As described in the section on Advanced HIPPS Configurations, HIPPS based on an advanced aeroderivative gas turbine have a performance advantage over one based on a heavy frame machine. Thus, for the repowering analysis, a single FT4000 I/C (intercooled) was used as the gas turbine. The investigation identified the ranges of steam plant sizes, steam conditions, and repowered plant configurations that could be accommodated with a single engine. Other sizes would then be scaled accordingly. Steam turbine outputs from 90 to 200 MW with steam conditions ranging from 1250 psi/950 °F (8618 kPa/510 °C) non-reheat to 2400 psi/1050 °F/1050 °F (16547 kPa/566 °C/566 °C) reheat were identified (Exhibit 2-6). Station efficiencies

in the 42-47% range (HHV) are possible (Exhibit 2-7). While the cost of electricity is application specific, it should be significantly less than the original station at emission levels one-tenth of current New Source Performance Standards.

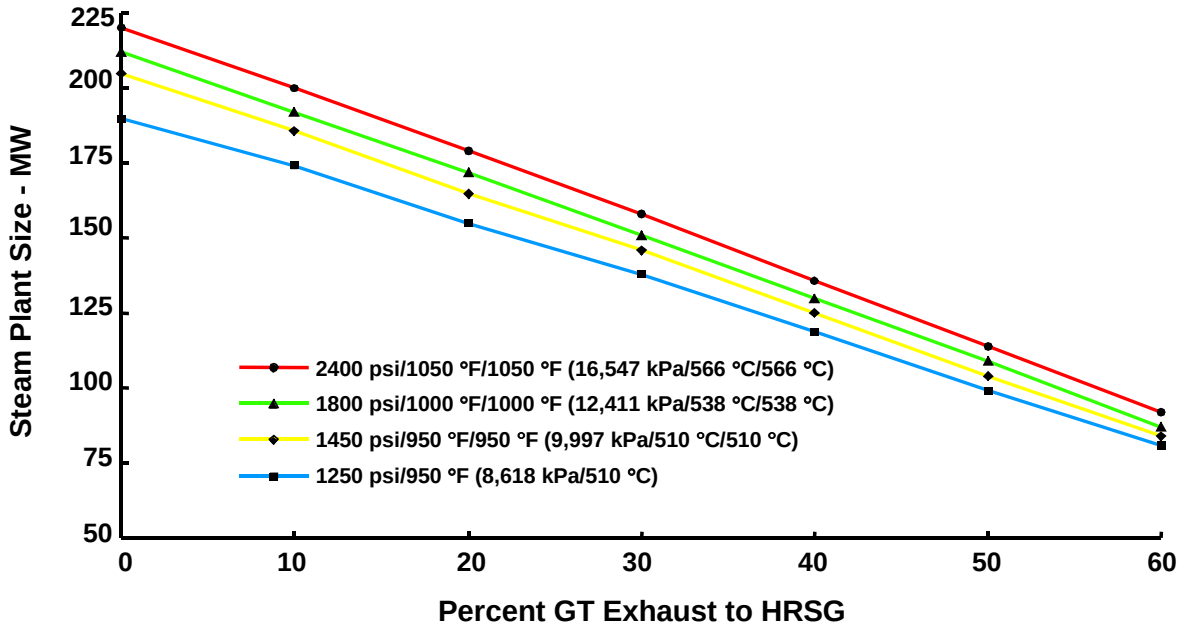

Exhibit 2-6
Potential Size Range for Repowering with One FT4000 I/C

The preliminary analysis of repowering with aeroderivative engines has shown as much as 10 or 12 points (around 30-35%) can be added to the efficiencies of older steam stations. In several cases, the repowering configurations do not use the radiator heat exchangers simplifying the HITAF, which should result in systems having lower overall cost of electricity than current repowering alternatives. These advantages are realizable with coal providing 60-70% of the cycle input heat requirement.

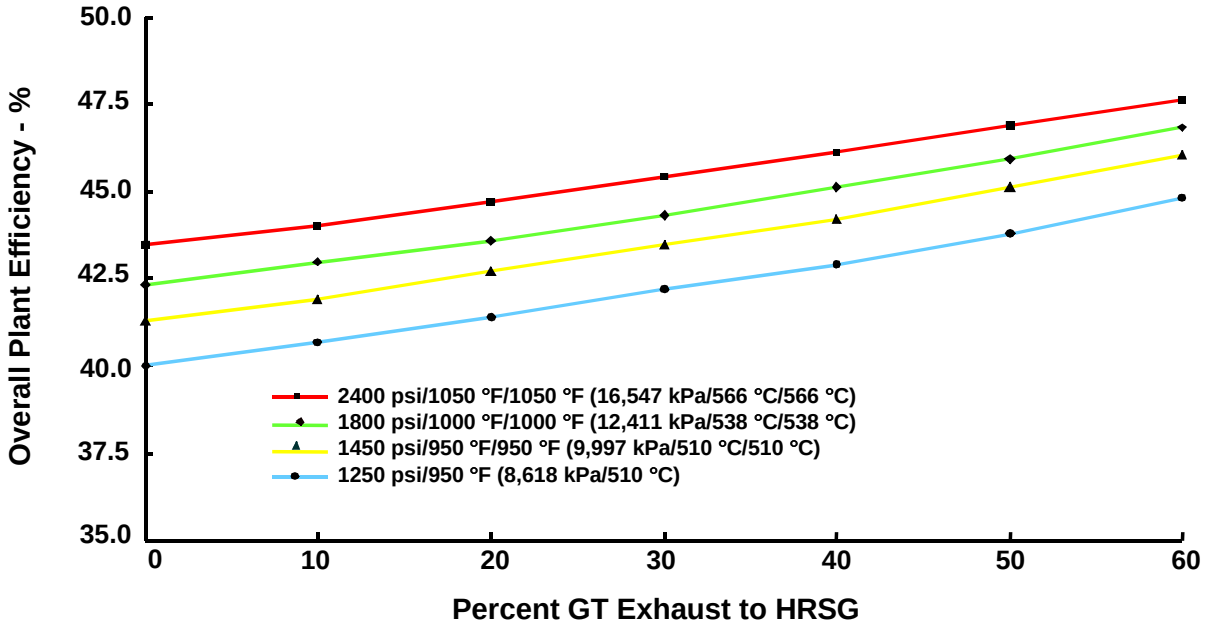

Exhibit 2-7
Potential Efficiency Range for Repowering with One FT4000 I/C

In actual operation, compromises between operational considerations and performance will have to be made. These compromises will be predicated on type of repowering application, e.g., baseload, mid-range, etc. and also on the experience of the specific utility or other user. The real-life configuration and operation, and thus, the economics, will be very site (application) specific.

For the HITAF technology, this indicates that the conceptual design for repowering with HITAF should also strive to use the existing steam turbine with feedwater, heat rejection, condensate and other selected auxiliaries, and the important site and infrastructure features at an existing power generation plant. Combustion 2000 HITAF Repowering

HIPPS Repowering with FT 4000 Advanced Gas Turbine

Process and Cycle Repowering Design

Exhibit 2-8 illustrates the process selected to evaluate HITAF repowering. The overall power generation concept is similar to that conceived for the grassroots 300 MW plant. The repowering process includes a high temperature furnace with radiant and convective air heating exchanges, heat recovery steam generation and an advanced aeroderivative gas turbine - the FT 4000.

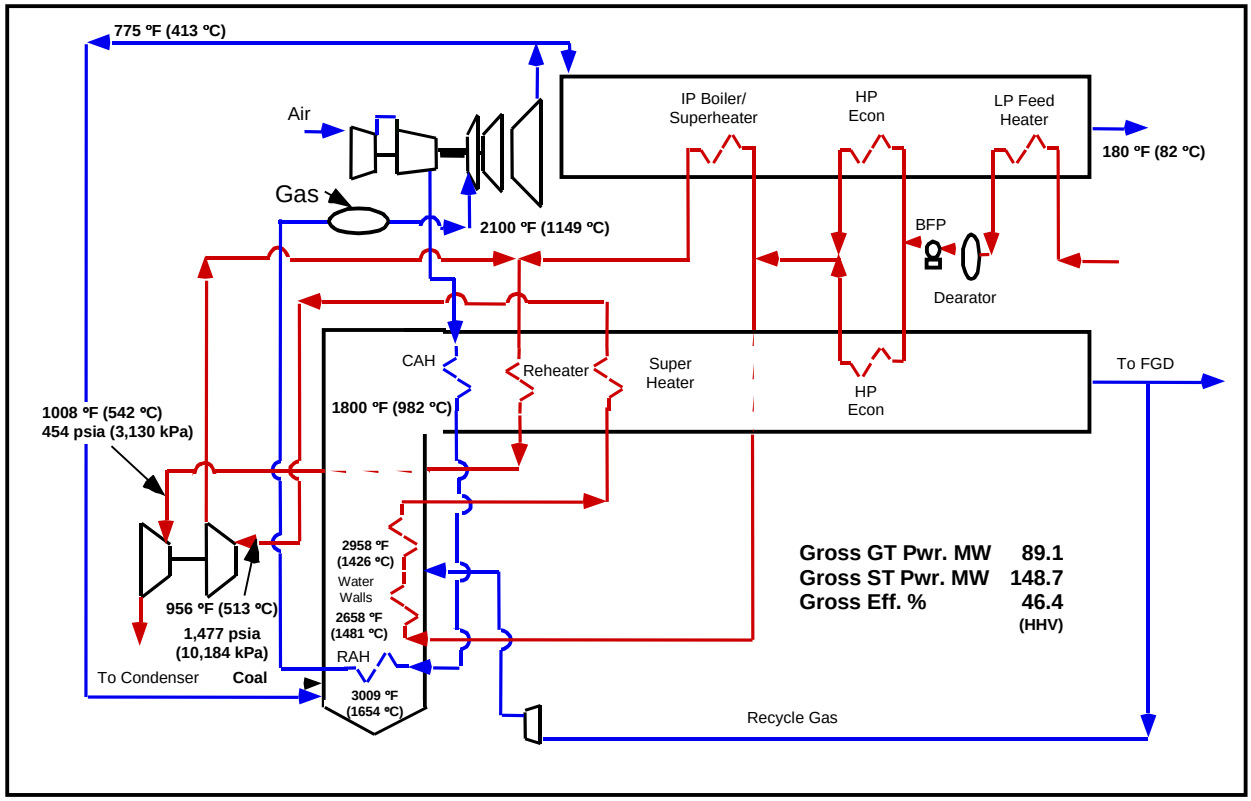

Exhibit 2-8
Schematic of HIPPS Repowering of Existing Steam Station

Major parts of the existing plant are kept and used in the repowering design. The existing steam turbine and electric generator are one such system. Other parts of the existing plant kept for the repowering operation include:

- The coal receiving, storage and handling system.
- Cooling water and heat rejection.
- Water supply and treatment.
- Effluent treatment.
- Much of the plant support systems, and
- The site and most of the buildings and structures.

Emission controls for particulate, SO_2, and NO_X have been added to the repowered plant.

Performance

A summary of repowering performance is given in Table 2-3.

Table 2-3
Repowered Plant Performance Summary

(Estimates are at 100% of Design Capacity)

Resources	
As Received Coal	
Tons per day	49.33
HHV, millions of Btu/h	1,083
Pipeline Natural Gas	
scfm	9,620
HHV, millions of Btu/h	583
Limestone, tons per hour	5.6
Raw water requirement, gpm	2,327
Wastes/Effluents	
Bottom Ash, tons per hour	1.1
Fly Ash, tons per hour	4.3
Treated Wastewater, gpm	1,252
Power Generation, MW	
Gross Power	237.8
Steam Turbine	148.7
Gas Turbine	89.1
In-plant Power Consumed	11.5
Net Power to the Grid	226.3
Plant Efficiency (HHV)	
Net Heat Rate, Btu/kWh	7,362
Thermal Efficiency, %	46.4

Table 2-4 provides some of the details of the estimates used to calculate the in-plant power consumption.

Environmental Factors

The estimated emissions and discharges from the repowered plant are presented in Table 2-5. The annual emission numbers are bases on a plant operating capacity of 65%.

Table 2-4
In-Plant Power Consumption

ITEM	kW Auxiliary Power
Induced draft fan	1,020
Recirculated flue gas fan	880
Transport air fan	830
Condensate pump*	60
Boiler feedwater pump*	1,900
Makeup water pump	1120
Cooling tower circulation pump*	500
Waterwall circulation pump	310
Cooling tower fans*	890
Miscellaneous pumps*	200
Coal Preparation equipment	800
Flue gas desulfurization equipment	2,500
Water treatment equipment*	375
Coal dryer fan	100
Plant lighting*	1,000
Rounded Total	11,500

* Some or all of this equipment is part of the existing plant.

Table 2-5
Repowered Plant Environmental Summary

Sulfur Oxides -SO_2	Values
Tons per year	285
lb per million Btu	0.06
Particulates	
Tons per year	14
lb per million Btu	0.003
Liquid Effluents, gpm	
Cooling water blowdown	1,179
Neutralization waste	1.0
Other process effluents	73
Total	1,253
Solid Wastes, tons per year	
Bottom ash	7,200
Fly ash	24,675
FGD sludge	43,940
Total	75,815

Repowering Conceptual Cost Data

Costs for the base case 300 MW HITAF plant and the repowering case are presented in Table 2-6. The repowering case costs are briefly explained below.

- Solids Feeding and Removal - These costs are calculated from the base case using coal flow as a criteria for the estimate.
- Steam Generation Island/HITAF - Budget quotes from equipment manufacturers are used to estimate the HRSG systems, the stacks and the ID fan (the cost also includes other fans). The high temperature furnace is estimated by adjusting the base case estimate.
- High Temperature Heat Exchanges - Cost information of the HITAF is unchanged.
- High Temperature Piping and Ducting - The cost is calculated from the base case data.
- Process Systems - The burner is priced from the base case data.
- Gas Turbine-Generator - The FT 4000 cost is based on information from the CAGT.
- Emissions Control Systems - The three systems (SO_2, NO_X and particulate) were priced based on budget quotes from manufacturers. As evidenced on the table, costs for the baghouse and SCNR/SCR are considerably less than were estimated for the base case. The base case costs were taken from EPRI data.
- Solids Material Handling - The repowering design utilizes existing coal facilities. The other material handling systems are calculated from the base case.
- Water Systems - Existing systems at the plant are used with some additions in the repowering design.
- Support Systems and Civil/Structural - Parts of the existing plant's systems will be used, and costs for repowering are included as an allowance. Also, an allowance of $10 million is included for demolition of other existing facilities.

It is also noted that several of the other existing systems are likely to require additions, modifications or upgrades. However, they can not be quantified at this time. When a site(s) has been selected for possible repowering, more complete and detailed design and cost estimating can be accomplished.

Table 2-6
Conceptual Costs of Repowered Plant

1999 Conceptual Costs	300 MW HIPPS PLANT		REPOWERING COSTS	
Code of Account Items	Cost $1,000s		Cost $1,000s	
1.0 Steam Generation/HITAF	42,200		34,200	
2.0 Gas Turbine System	43,700		36,700	
3.0 Steam Turbine System	18,800		0	
4.0 Flue Gas Emissions Control	23,000		18,600	
5.0 Coal and Ash Handling	6,000		1,500	
6.0 Water Treatment	4,100		900	
7.0 HVAC, Tanks, Insulation, Stack	7,000		1,800	
8.0 Other Process Systems	18,800		8,800	
9.0 Civil and Structural	33,300		24,100	
TOTAL DIRECT COST	196,900		126,600	
Indirect Costs	24,600		19,800	
TOTAL FIELD COST	221,500		146,400	
Home Office Engineering	17,300		11,700	
		$/kW		$/kW
TOTAL CONSTRUCTION COST	238,800	796	158,100	527
Project Contingency 15 % of TCC	35,800		23,700	
TOTAL PLANT COST	274,600		181,800	
Allowance For Funds During Construction 8%	22,000		14,500	
TOTAL PLANT INVESTMENT	296,600		196,300	
Owner Costs 5% 0f TPI	14,800		9,800	
TOTAL CAPITAL COST	311,400	1,038	206,100	687

In addition to the repowering case above, a HIIPS repowering of an older Atmospheric Fluid Bed Combustor power plant was investigated. The plant to be repowered is shown in Exhibit 2-9.

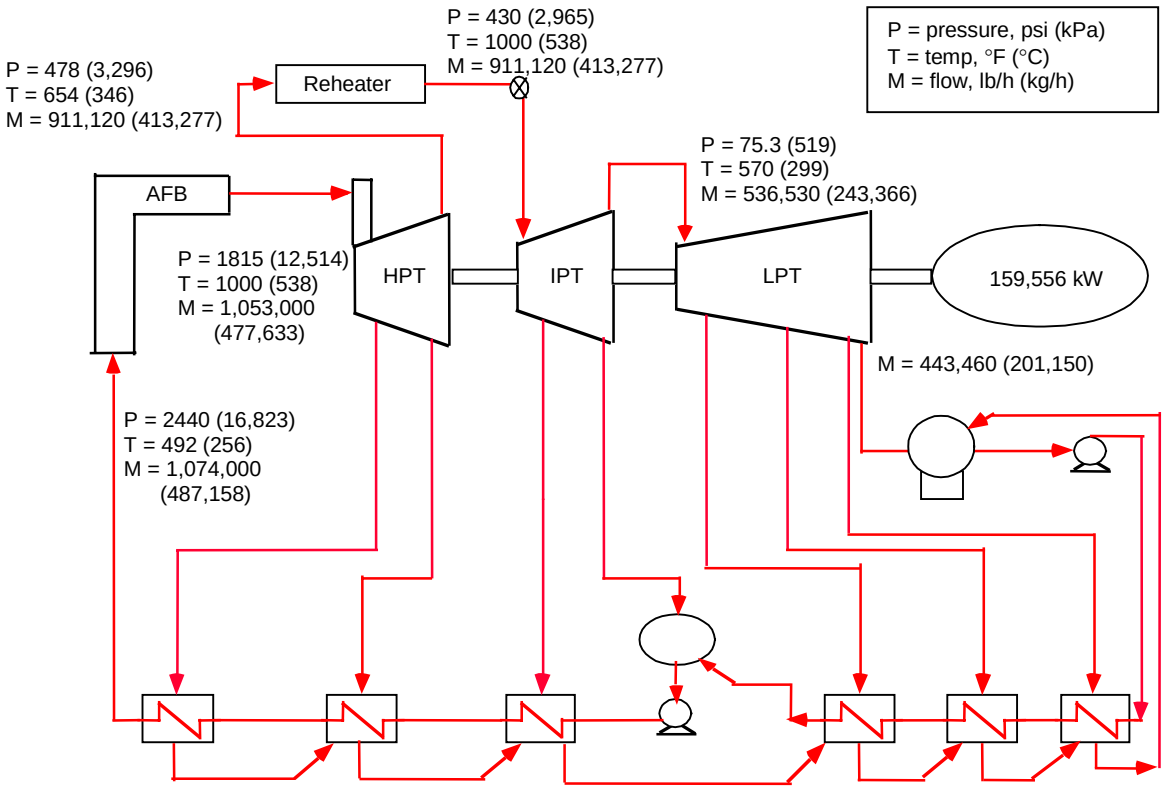

Exhibit 2-9
AFB Plant for HIPPS Repowering

The heat rate of the AFB plant was 10,600 Btu/kWh (11,184 kJ/kWh), 32% (HHV) with a nominal output of 150 MW. The steam plant requires the flow of two FT4000 I/C engines so that the HIPPS repowered plant had an output of 421 MW and an estimated efficiency of 45.4% (HHV). The repowered plant had a coal/gas ratio of 77%/23%. In this repowered plant, it was assumed that the back end of the steam turbine had been modified to take the increased flow due to the replacement of the extraction heaters by the HRSG.

Summary

The use of HIPSS to repower older steam stations is an attractive option and probably will be the manner in which HIPPS will have the widest application. The ability to use existing sites and equipment goes a long way in keeping down the cost of power. The potential to add incremental power at less than $700/kW is very attractive. Also, the fuel flexibility allows coal to provide a large portion of the plant energy, a very significant cost factor as natural gas prices rapidly increase. The cost of electricity from a HIPPS repowering plant has the potential to be among the lowest among fossil fuel plants.

Reference

Wen, H. and R. Gopalarathinam, *Repowering Options For Steam Power Plants.* Proceedings of the American Power Conference, 1992

Section 3 - All Coal Designs

Abstract

The work reported in this section was performed under program task 1.3. A major goal of Combustion 2000 was the identification of an "all coal" plant. Again, a variety of HIPPS configurations were considered. When HITAF radiator outlet temperatures were limited to the 1700 °F (927 °C) level, all coal HIPPS had efficiencies in the 41-43% (HHV) range. When advanced materials were used for the radiator and temperatures were allowed to reach 2000 °F (1093 °C), efficiencies of 44-45% were projected. When HIPPS/HAT configurations were identified, efficiencies over 48% were estimated. These estimates were made for systems with no natural gas used to further heat the radiator outlet. Were even a small amount of gas used, say 5%, the performance would increase to over 50%.

Introduction

The HIPPS Commercial Plant design concept described in the section titled HIPPS Commercial Plant Design, uses approximately 35% natural gas to boost the air temperature from the RAH to levels typical of modern gas turbines. The ultimate goal of the DOE HIPPS program is to use only coal. Several all-coal design concepts were investigated and, when based on advanced RAH designs and materials, efficiencies over 50% could be identified.

All-Coal HIPPS

The desire to use coal alone as the fuel for the HIPPS places additional requirements on the HITAF portion of the system. The designs of the HIPPS to date have limited the temperature of the air from the HITAF to a range of 1700 °F to 1975 °F (925 °C to 1065 °C). Tests of a radiator segment in a coal-fired furnace at the Energy and Environmental Research Center at the University of North Dakota have demonstrated the soundness of the UTRC design. Air has been successfully heated to temperatures of over 1700 °F (927 °C). While not all the questions of refractory durability and structural design have been answered, these tests have demonstrated the technologies needed in a coal-fired, high temperature air heater.

Other tests using ODS materials for high temperature heaters have been carried out. At the Research Center for British Gas, a radiator capable of 2100 °F (1149 °C) gas outlet temperatures was used to supply heated air to a closed-cycle gas turbine (Mabbutt, 1995). In addition to the MA754 used in the current design, materials experts at UTRC have identified several advanced alloys currently capable of commercialization (e.g., PM 2000 and MA 6000) which would be suitable for radiator tubes with gas outlet temperatures of 2100 °F (1149 °C). Thus, a series of analyses were made of HIPPS configurations with HITAF's having radiators with 2100 °F (1149 °C) outlet temperatures.

Conventional HIPPS

The "conventional" HIPPS is one based on the combined cycle configuration; i.e., one that uses the GT exhaust to supply heat to a steam cycle. Note that the gas turbine used in these configurations is based on a multi-shaft aeroderivative design such as that which could be derived from the 100,000 lb. thrust class aircraft engines such as the General Electric 90, the Pratt & Whitney 4000, and the Rolls Royce Trent As previously mentioned, industrialized

versions of these engines using intercoolers would offer high efficiency and high power density. The ICAD could also offer better performance at "off-design" conditions than the single shaft frame machines. Operation at 2100 °F (1149 °C), rather than the engine design point of 2300 to 2500 °F (1260 °C to 1371 °C) represents a part load, or off design operating point). This engine type also lends itself to greater flexibility in cycle configuration. On the other hand, at a given inlet temperature, the lower pressure ratios of frame machines allow more heat in the gas turbine exhaust and could result in better steam conditions for a combined cycle. The following analyses are indicative of all coal HIPPS performance, but do not necessarily represent the optimum match of gas turbine with steam cycle.

In Exhibit. 3-1, for example, the HITAF is designed to burn only the amount of coal needed to heat the gas turbine compressor discharge to the desired temperature; i.e., no additional heat is added for the purpose of raising steam. Thus, the steam conditions are not representative of modern systems. An efficiency approaching 39% is attained. While this is not particularly attractive compared to newer coal-fired alternatives, this configuration could be the basis of repowering applications that could result in appreciable increases in existing site efficiency.

By adding a reheater to this configuration, a system with an efficiency of nearly 42% can be identified, Exhibit 3-2. Once again, the heat for steam raising from the HITAF is only that available after heating the GT air. The additional heat in the GT exhaust allows for a better performing steam system. Again, this configuration could be of interest for repowering.

A third configuration was investigated (Exhibit 3-3). The gas turbine with reheat was used in conjunction with an ultra-critical steam cycle (1300 °F/6200 psi (704 °C/42747 kPa)); (Valenti, 1996) using technology being developed, in part, under DOE sponsorship. The performance of this configuration is projected to be 48%, a value well above other pc-fired steam stations.

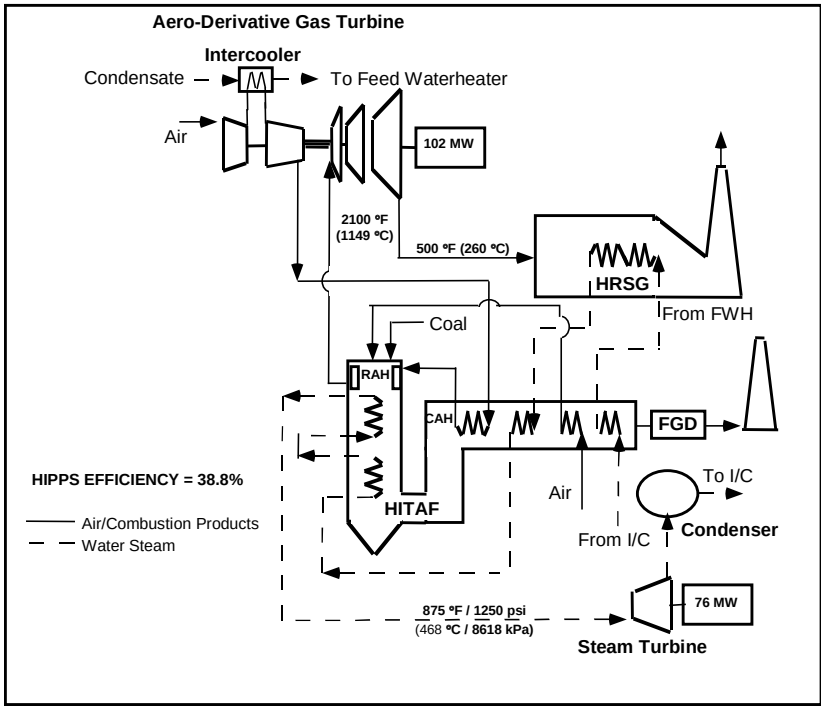

Exhibit 3-1
All Coal HIPPS

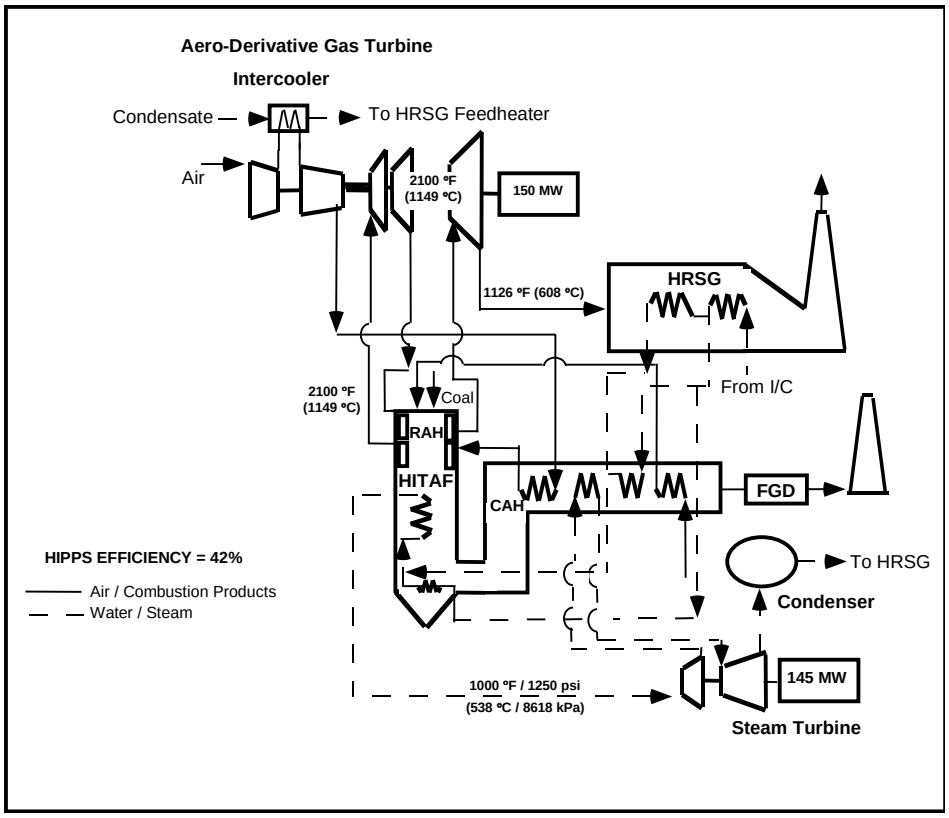

Exhibit 3-2
All Coal HIPPS with Reheat Gas Turbine

Advanced HIPPS

The use of the aeroderivative engine such as the FT4000 IC also allows consideration of advanced cycle HIPPS for the all coal case. Once again, the Humid Air Turbine cycle offers high performance with out the need for additional steam system equipment.

The first configuration considered is shown in Exhibit 3-4. Here the system efficiency is over 45% and the output approaches 350 MW. For much the same reason as in the combined cycle, the efficiency is affected by the low exhaust temperature. In this case, the amount of regeneration is reduced. On the plus side, the power is up significantly. This is because of the added water that can be used in the all coal case. The applications that require the humid air to be part of the combustion process are limited to their moisture content by flame stability requirements. Generally, with natural gas at least 4% excess oxygen is required for flame stability. The actual amount is a function of air preheat, type of burner etc., but there is a limitation for moisture. In the all coal case, the mixture is externally heated and the moisture amount is limited only by the low-grade heat available to the saturator.

Similar to the combined cycle, the use of a reheater results in significant performance increase, Exhibit 3-5. This increase in efficiency is due mainly to the increased regeneration because of the higher GT exhaust temperature. The efficiency of 51% is very attractive as is the output of 387 MW.

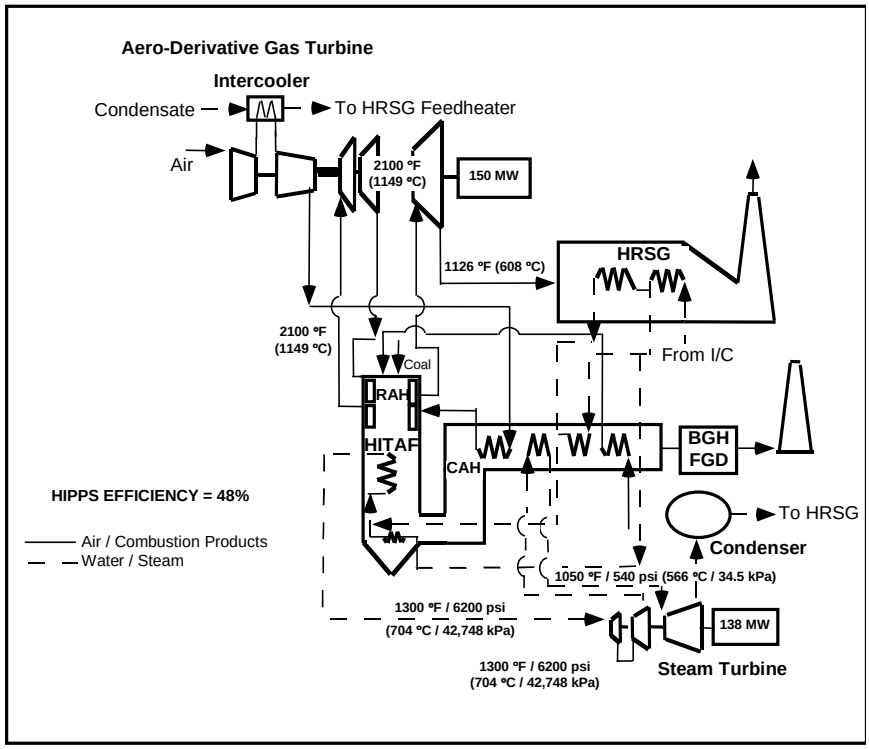

Exhibit 3-3
All Coal HIPPS with Reheat GT and Advanced Steam System

The configurations discussed so far have one common denominator, a radiator with an outlet temperature of 2100 °F (1149 °C). Depending on the cycle, the pressure in this radiator can vary from 600 to 700 psi (4137 kPa to 4826 kPa). These pressures result in stresses that are at the edge of the performance envelope for the MA 6000-type alloy. While it is anticipated that the material properties will be improved over time, it is worthwhile to investigate cycles that have operating regime more compatible with known performance limitations. One such cycle is the Cascaded Humidified Advanced Turbine (CHAT) cycle (Nakhamkin, 1996).

The HIPPS/CHAT uses the low pressure spool of the FT4000. The air is from the LP compressor is sent to the intercooler, then, rather than going to the high pressure section of the FT4000 (high spool), it goes to a "balanced shaft" turbo-compressor (TC) set. "Balanced shaft" means that there is no net work from the TC. The TC consists of a multi stage intermediate pressure (IP) centrifugal compressor, a high pressure (HP) barrel compressor and a turboexpander. The air is intercooled between the IP stages. From the HP compressor, which operates at a pressure somewhat higher than the FT4000 IC design pressure, the air is sent to an aftercooler and then to the saturator. The saturated air is recuperated and then heated in the HITAF to 1750 °F (954 °C), and then expanded to drive the TC set. The turboexpander exhaust is reheated at a reduced pressure to 2100 °F (1149 °C) and further expanded in the FT4000 LP turbine. Performance is essentially the same as the HIPPS/HAT with the reheater.

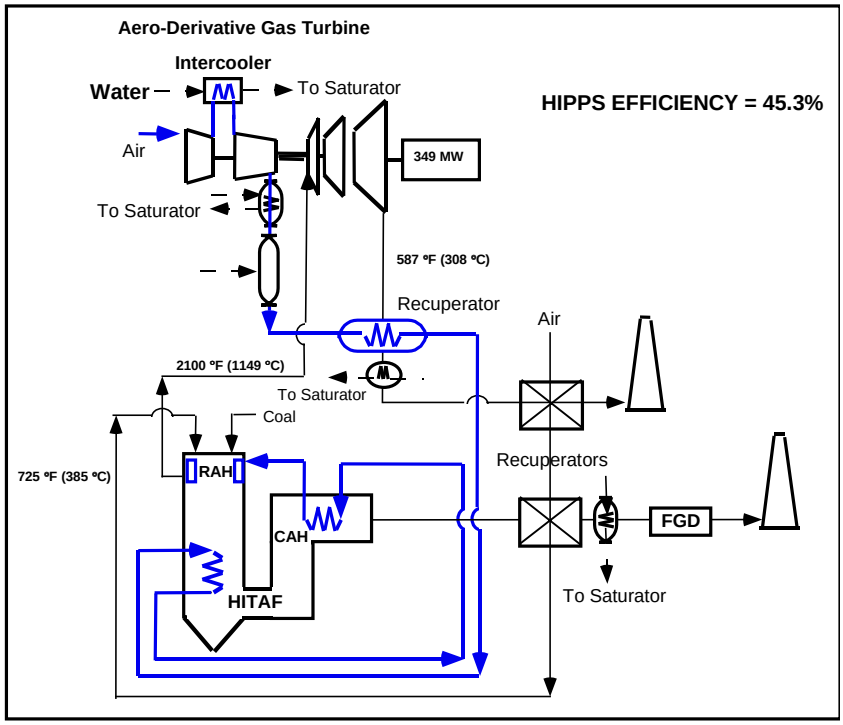

Exhibit 3-4
HIPPS with Humid Air Turbine

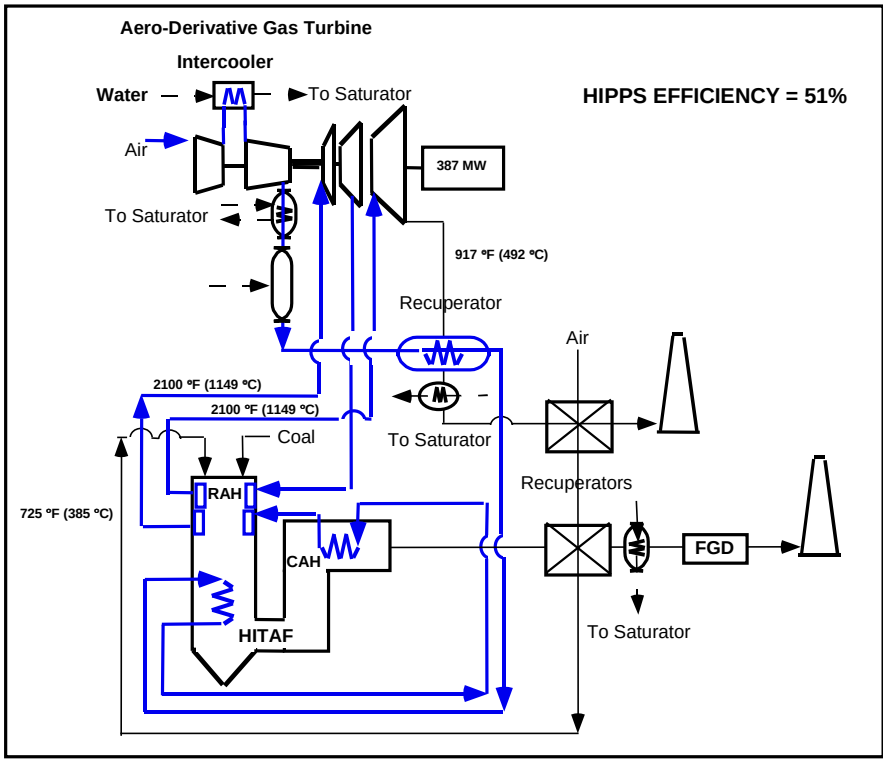

Exhibit 3-5
HIPPS with Reheat Humid Air Turbine

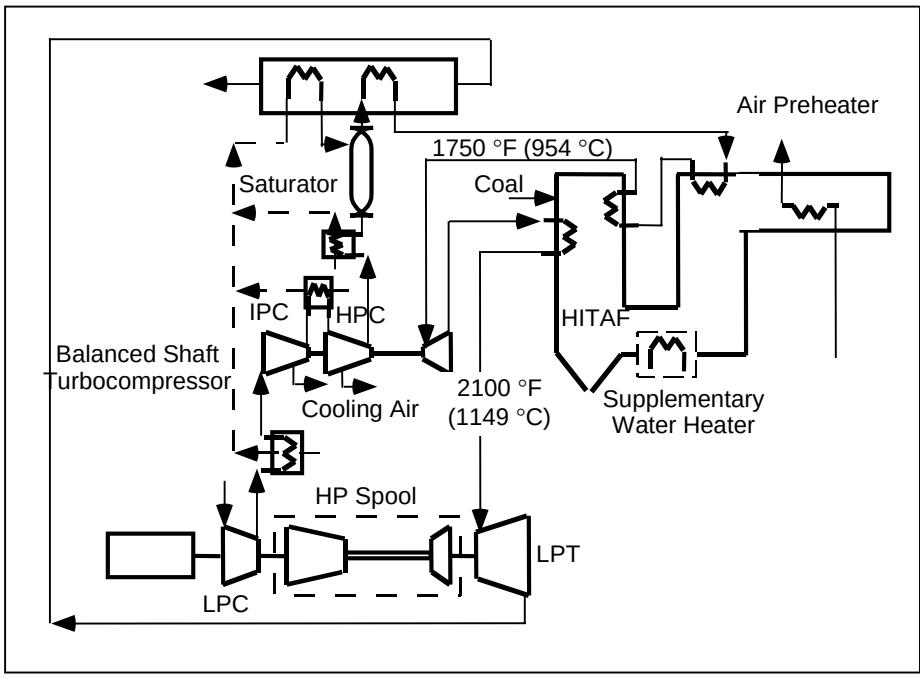

Exhibit 3-6
Schematic of HIPPS/CHAT

Concluding Remarks

A path to an all-coal HIPPS has been identified. Systems with efficiencies of over 50% can be postulated even with the limitations set by materials constraints. Implementation of the earlier generations of HIPPS will give impetus to development of high temperature alloys for heater tubes and temperatures beyond 2100 °F (1149 °C) could be possible in the 2010 - 2015 time frame.

The all coal HIPPS, like its predecessors, would be an obvious candidate for repowering older, low-to-intermediate performance steam stations. If desired, the gas turbine could be equipped with conventional burners to allow rapid start up on premium fuel, producing revenue during the shift to coal fuel. While the high efficiency would dictate base load operation, the flexibility would also allow mid-range and load-following operation.

Another aspect of fuel flexibility is the HITAF can be designed to burn low-grade fuels and renewable resources such as biomass, either as the sole fuel or in a mixture with coal. This ability could make the approach very attractive for many of the emerging economies.

The emissions from the all-coal HIPPS are significantly less than those from other pc-fired plants. This is the result of the increased efficiency of the HIPPS plant. Another benefit would be the reduction in CO_2 compared to typical coal-fired plants. The all-coal HIPPS has the potential of reducing these emissions by 20% or more.

The research currently being carried out on the High Performance Power Systems has identified and demonstrated many of the technologies required to achieve high efficiency power generation using coal, the number one energy resource in the world. These systems would not only produce electrical power at lower costs than today's plants, they would also contribute significantly less to greenhouse gases and other harmful pollutants.

References

Mabbutt, Q. J., Cost 501 Work Package IV Final Report - O.D.S Closed Cycle Heat Exchanger Programme, Bgplc Research & Technology, July, 1995

Nakhamkin, M. and Swensen, E., The Cascaded Humidified Advanced Turbine (CHAT), Journal of Engineering for Gas Turbines and Power, July, 1996

Valenti, M., Pouring on the Steam, Mechanical Engineer, Feb. 1996

Section 4 - Modular HIPPS, the HIPPS Today Approach

Abstract

The work reported in this section was performed under program task 6.4. The investigation into the all coal HIPPS lead to the modular HIPPS Today concept. HIPPS Today would use only the convective heater in the HITAF, thereby reducing the technical risk and the cost of the system. System performance would be limited to that of gas turbines with operating inlet temperatures of <1600 °F (871 °C) for current heater materials to 1800 °F (982 °C) for advanced material convection heat exchangers. There are a number of small (<25 MW) gas turbines that have these conditions including several aeroderivative types. By using the aeroderivative engines, a modular approach can be defined. In this approach, the turbine and the remainder of the components are designed for factory assembly and shipment as modules. Assembly-line plants of nominally 100 MW size would be designed in "cookie cutter" fashion thereby reducing production costs and subsequent erection costs. These plants would have performances of 40-44% (HHV) on all coal or, potentially, coal/biomass mixtures. Costs would be reduced by about10% over the more traditional approach. Because of the relative simplicity and reduced maintenance, these plants could be candidates for use in developing economies where they would use indigenous fuels. Because of their higher efficiency compared to plants typical in these areas, overall fuel use could be reduced, as would the emissions of CO_2.

Introduction

As has been described in previous sections, the RAH and CAH have been demonstrated at small-scale at the Energy and Environmental Research Center at the University of North Dakota with a wide variety of coals and lignite. Air temperatures as high as 2012 °F (1100 °C) have been reached in the radiator and nearly 1400 °F (760 °C) in the convective heater. The metallurgy and joining technologies demonstrated should allow the CAH to reach nearly 1652 °F (900 °C) using metallic heat exchangers made from commercially available materials. With only a small stretch in materials, temperatures of 1832 °F (1000 °C) or more could be attained. Use of the CAH alone would allow the HITAF to more closely resemble typical boiler configuration, resulting in lower costs and less technical risk.

This lower technology, lower risk approach gives rise to the HIPPS Today approach, configurations that use only coal, or coal and biomass. These configurations have gas turbines operating at relatively low inlet temperatures of 1517 °F to 1832 °F (825 °C to 1000 °C) and use, in many cases, only a convective air heater. Based on smaller aero-derivative gas turbines such as the Alstom GT 35 or the Pratt & Whitney FT8, HIPPS of 75-125 MW with efficiencies of 42% to 45% have been identified. This type of configuration lends itself to being “modularized”, i.e., factory assembly of components allowing for rapid construction on site. In this way, a series of nominal 100 MW plants using indigenous fuels could be rapidly built in developing countries. Because of the high efficiencies, especially when compared to existing plants in these areas, air and water emissions, including CO_2, are greatly reduced. These HIPPS Today characteristics would be important to countries such as China and India.

Coal makes up the bulk of China’s energy supply, and China is both the largest consumer and largest producer of coal in the world producing roughly one third of the world total. One of China's main priorities as it enters the 21st century is developing environmental technologies to

solve the major environmental challenges it is currently facing and will face in the future. These efforts are focused on technologies that will treat wastewater, prevent air pollution and improve environmental monitoring systems. Although the Chinese government is aiming at a policy of larger (600 MW and bigger) central plants and a nation wide interconnected grid, there could be a need to replace small diesel or coal-fired plants which were opened by provincial or municipal governments and have been recently shut down. These plants are relatively inefficient and polluting.

As in China, coal is the dominant commercial fuel in India, satisfying more than half of India's energy demand. Power generation accounts for about 70% of India's coal consumption. Increased coal consumption over the past four decades has led to a nine-fold increase in energy-related carbon emissions. Environmental effects due to the relatively high use of coal in the energy mix are exacerbated by the low energy efficiency of coal-based electricity generating plants. Inefficient plants are one of the contributing factors to a steadily increasing energy consumption per unit of output (i.e., energy intensity). With the high costs associated with replacing existing coal-based plants, it is realistic to assume that these plants will continue running for the next couple of decades. The advent of HIPPS today and its modular capability could be an attractive alternative to operating these older polluting plants.

Modular HIPPS

In the commercial plant and in subsequent advanced HIPPS concepts, the RAH design uses a "tube in a box" approach in which metallic tubes are protected from the coal slag by refractory plates (e.g., Monofrax M). The tube material in this design is an oxygen dispersion strengthened (ODS) alloy, INCO MA754. The use of metallic heat exchangers, rather than ceramic, was based on the capability of joining the tubes with complex headering using new technology developed in the program.

The refractory and tubes have operated for several thousand hours in a nominal 2.5 x 10^6 Btu/hr (2.6 x 10^6 kJ/hr) HITAF pilot plant at the University of North Dakota Energy and Environmental Research Center (UNDEERC). The HITAF has operated routinely producing 1832 °F (1000 °C) air with a variety of coals, including lignite, with no significant problems that would require redesign. In these tests at UNDEERC, the UTRC design has also furnished air at over 2012 °F (1100 °C) (Chem. Eng., 1999). The numerous startups and shutdowns typical of testing have not resulted in thermally induced damage to the metallic tubes.

There is an opportunity to take a less technically challenging approach using only the convective heat exchangers in the HIPPS. This lower risk, albeit lower performance HIPPS approach requires only a modest stretch of current heat exchanger technology to achieve efficiencies that are on a par with the most modern ultra-critical steam plants. In these plants, the outlet temperatures of the CAH can be several hundred degrees lower than configurations with the radiator. This means that the gas turbines would operate at relatively low inlet temperatures of 1517 °F to 1832 °F (825 °C to 1000 °C). There are a large number of older frame-type and aeroderivative turbines that operate in or near this range and could form the basis of smaller (~100 – 150 MW) power plants. Because of the smaller size and weight of the gas turbine, much of this type of configuration could be modularized, i.e., components would be factory assembled and transported to the site, thereby reducing on-site construction time and costs.

Convective Heat Exchanger

The major technology in the modular HIPPS is the convective heat exchanger, which not only must heat air to as much as 1832 °F (1000 °C), but also must operate in dust (coal ash) laden air. To minimize the ash carryover, the HITAF will still operate in the slagging regime and have a slag screen upstream of the CAH. In the HITAF, the highest temperature portion of the CAH would be downstream of the steam superheater and the slag screen, which would remove much of the carry over. Nonetheless, it is probable that soot blowing would be necessary and the design of the convector is based on an 8-hr soot-blowing cycle.

Considerable analyses were carried out to establish the limits of ash deposition on the CAH (Seery, 1995). Since deposition reduces the heat transfer, only a certain thickness can be tolerated. A maximum deposit thickness of 0.4 in (1 cm) was identified as the limit before soot blowing. A deposition rate of 0.02 in/hr (0.06 cm/hr) was predicted by the modeling for the leading tubes, indicating that the 1-cm limit would not be exceeded in the 8-hour soot blowing cycle. Since the ash densification and fluidity are both coal type and temperature dependent, the flue gas temperature to the CAH is limited by the desire to keep the deposition to the 0.4-in (1-cm) level. A flue gas temperature of approximately 1800 °F (980 °C) was identified as the desired maximum flue gas temperature for the Illinois No. 6 coal. More frequent soot blowing can be used to allow higher flue gas temperatures.

The proposed design is shown in Exhibit 4-1. The CAH is a modified shell and tube heat exchanger with the compressor discharge air flowing inside the tubes and the HITAF exhaust flowing perpendicular to the tubes on the outside. The tubes are joined in a finned tube arrangement, which results in a number of benefits:

1. the increased surface area provides a heat conductance that helps balance the nearly four to one difference in heat transfer coefficients between the inside and outside of the tube, reducing the CAH size by about one-third;
2. the finned tube is more rigid, reducing vibrational stresses and also reducing susceptibility to circumferential thermal stress; and
3. the smoother surface of the finned tube sheet is aligned with the hot gas streamlines and there are no spaces for recirculation, thus, ash deposits are significantly reduced.

The design effectiveness of the CAH is a very conservative 53%. This allows a two-pass, cross-counter current flow, with two air passes and one hot gas pass. While additional passes would reduce the CAH size, the added pressure drop in the compressor discharge could unduly penalize performance. A detailed cost benefit analysis would be required to finalize the CAH design.

The materials for the hot initial section of the CAH would be similar to those mentioned for the RAH, probably an ODS type. Other materials, depending on desired temperature out, would be Inconel 617, 800, 802, etc., which have better resistance to the harsh environment than the less expensive stainless steels. Stainless steel would be required for the somewhat cooler middle portion of the CAH, and less expensive carbon steels would suffice for the much cooler (~ 750 °F, 400 °C) back end.

For the selected coal, the exhaust from the slag screen section of the HITAF must be quenched to 1800 °F (980 °C). This is accomplished by recirculating a portion of the total HITAF exhaust stream extracted just prior to the FGD. This also balances the hot side (HITAF

exhaust) and the cold side (compressor discharge) flows, contributing to the reasonable effectiveness for the CAH of 53%. The mixing of the recirculation stream also provides a zone at 1800 °F (980 °C) where a Selective Non-Catalytic Reactor (SNCR) can be used to further reduce NO_x from the HITAF.

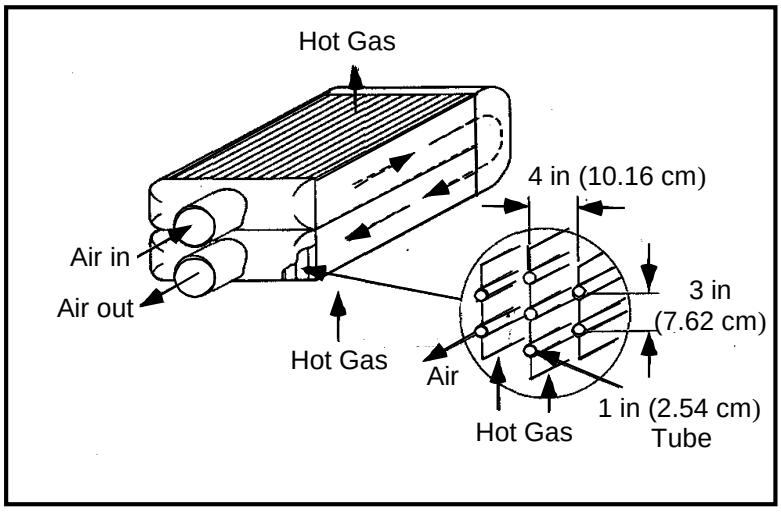

Exhibit 4-1
Conceptual Design of the Convective Air Heater

HIPPS Today

The HIPPS today concept is based on the use of an HITAF with only the convective heat exchanger. While in the commercial plant design the outlet temperature was limited to around 1301 °F (705 °C), the materials could easily allow over 1472 °F (800 °C). Although this temperature is not equal to that used in today's state of the art gas turbines, there are a number of turbines available that operate near that range. Of particular interest are the aero-derivative type turbines that are relatively compact and easily transportable. Two examples of this type to be considered are the Alstom-ABB GT35, a 17 MW engine with a turbine temperature of approximately 1562 °F (850 °C) and the FT8, a nominal 25 MW engine with a design turbine temperature over 2102 °F (1150 °C) (Exhibit 4-2). In addition, a small relatively compact frame machine, the nominal 25 MW Alstom-ABB GT10 was considered. It also has a design operating temperature over 2102 °F (1150 °C).

A simplified schematic of the concept is shown in Exhibit 4-3. As in prior HIPPS concepts, the compressor discharge is heated in the HITAF. In this configuration, however, only the CAH is used. Several variations were analyzed and the one giving the best performance had the GT exhaust split, some of the flow was used as preheated combustion air for the HITAF and the remainder was used in a HRSG for the feed water heater and the economizer. Because of the relative small GT size, two engines were used in conjunction with a nominal 70 MW reheat steam system. The resulting system has a net output of slightly over 100 MW at an efficiency of 43.2% (HHV). Use of a non-reheat steam system would reduce performance by approximately 1.5 percentage points.

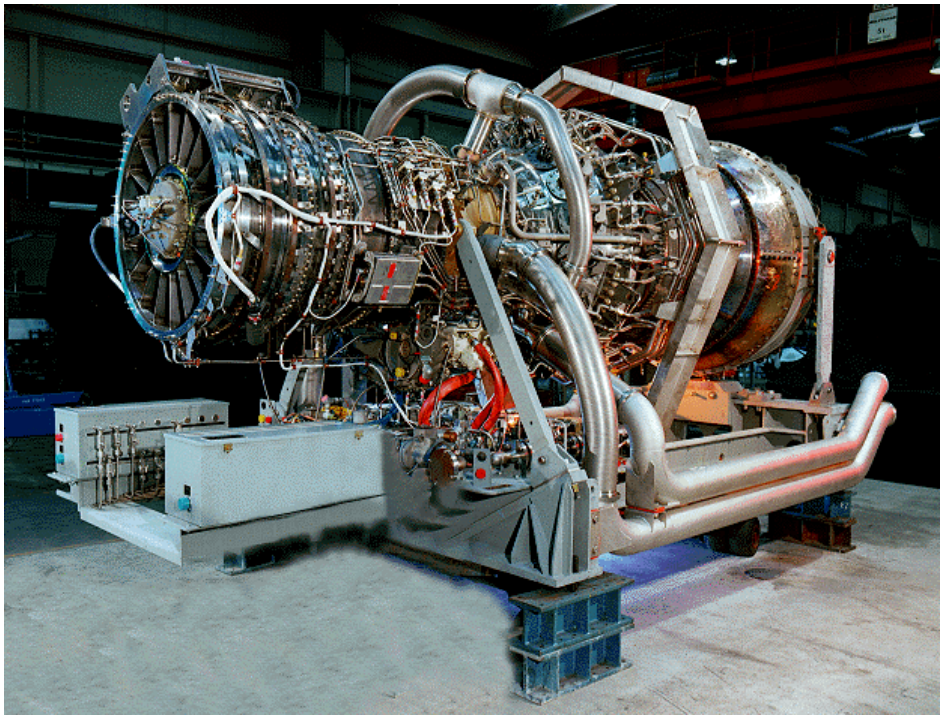

Exhibit 4-2
The Pratt & Whitney FT8, a 25 MW Aeroderivative Engine

The system configuration chosen for the FT8 is similar to that shown in Exhibit 4-3. This system was aimed at a higher output of around 150 MW. While the FT8 has a higher output than the GT35 at design point, at the reduced operating temperature from the CAH, a value here of 1796 °F (980 °C), the output drops to about 15 MW. The 1796 °F (980 °C) CAH outlet temperature would require the use of the ODS materials identified for use in the radiator. Four FT8 engines and a nominal 90 MW reheat steam system result in an output of 143.9 MW at an efficiency of 44% (HHV). The CAH effectiveness is increased to nearly 80%, requiring another cold gas pass and a slight reduction in performance because of the higher pressure drop.

The GT10 turbine is a compact, low-weight heavy-duty industrial gas turbine, nominally rated in the 25 MW class, with 34,2% open-cycle efficiency. The GT10 is designed as a compact, twin-shaft unit suitable for electrical and mechanical drive applications. In the HIPPS Today configuration, the turbine temperature was reduced to 1697 °F (925 °C), resulting in a reduction in output to approximately 15 MW. Again, the system schematic would be similar to Exhibit 4-3. Two GT10's and a nominal 65 MW reheat steam turbine result in an overall system output of 89 MW at an efficiency of 43.1% (HHV). The CAH effectiveness would be around 68% and a third pass would be required. Materials would include smaller amounts of the ODS tubing.

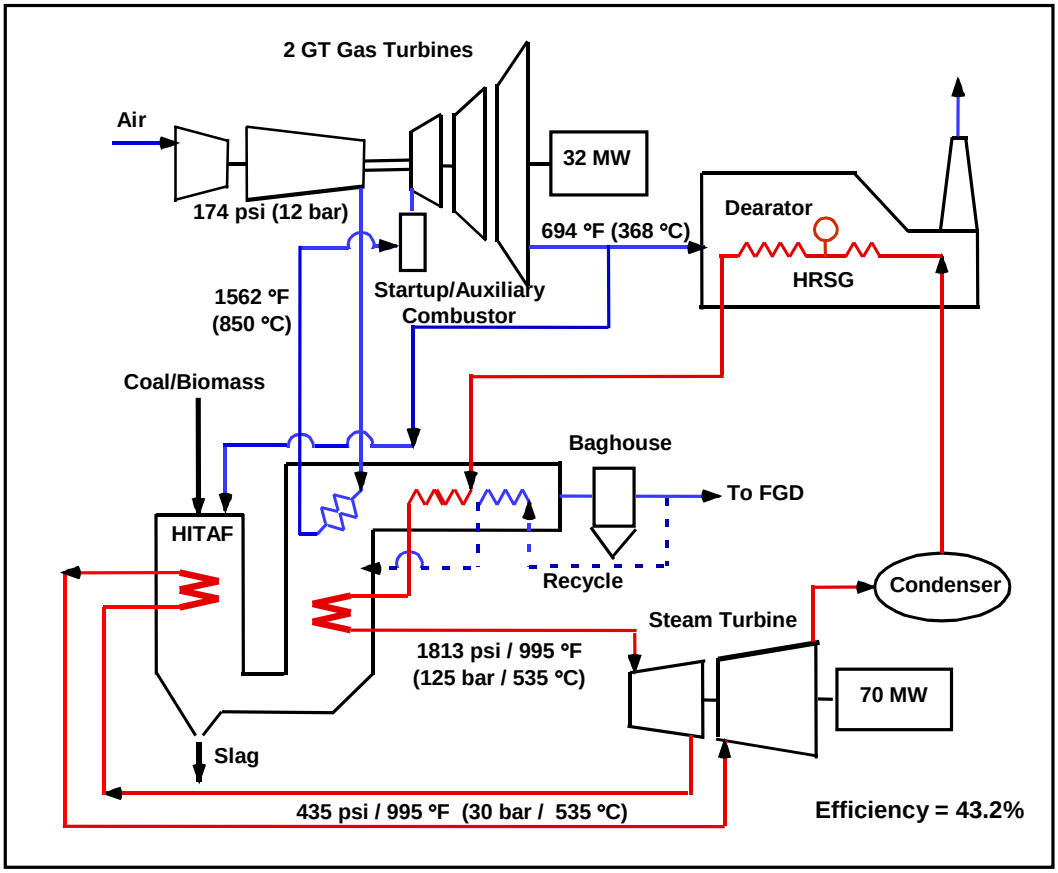

Exhibit 4-3
Schematic of the Modular HIPPS Today

The three examples described would be typical of HIPPS systems using only current state of the art technology in convective air heaters. The projected performances of over 43% (HHV) are higher than nearly any steam station in operation or planned. Only those steam stations operation at ultra-critical pressures and temperatures of over 1148 °F (620 °C) approach this value.

Modular HIPPS

The HIPPS Today approach can also be used with much larger gas turbines and could, in fact, be used to repower older, lower temperature gas-fired installations with coal, thus, reducing the coat of power. But the major reason for investigating the smaller, more compact gas turbines was the concept of developing HIPPS modules.

Modularization can reduce costs in two ways, affecting both production and engineering elements. Historically, each plant has been individually tailored to meet the demands of the client. But like clothes, the tailor-made approach is more expensive than the off-the-rack. The automobile industry has moved to platform engineering where many models use essentially the same basic design and share many modules, significantly reducing engineering and production costs. Thus, the HIPPS Today approach can benefit from platform engineering using common modules, many of which can be factory assembled, further saving design and construction costs. This approach has been credited with savings of 10% or more (World Bank, 2000).

For example, by concentrating on powerplants of 75-100MW, manageable sized pieces of equipment could be factory assembled and shipped to the site for final construction. This approach would seem to be especially appropriate for us in developing economies where indigenous solid fuel including biomass could be used. While auxiliary liquid or gaseous fuel would be needed for startup or boost power (the GT could be taken to design conditions for additional MW's), there would not be the requirement for dedicated use of fuels that represent export potential.

The economies in the Asian Pacific region provide examples of this. Both China and India are major users of coal in the region with more than 70% of their electrical power generated from coal. Indonesia will increase its coal use as it substitutes coal for oil in power generation, thereby freeing up the oil for export. The emphasis in China in power generation will be on the addition of larger supercritical steam technology, but there is a potential market for smaller systems, especially ones that would replace older, very low efficiency (<20%) plants. Because of the rapid increase projected for the generation of power in China, there is need to insure that emissions including greenhouse gases are reduced (IEA, 1998). The HIPPS Today approach would meet the overall DOE goal of one-tenth NSPS for coal-fired steam stations and would reduce CO_2 emissions by 15-20% over typical coal-fired alternatives.

Economic Considerations

The cost of small coal-fired power plants are of the order of $1800-$2200/kW (Rao, 2000), depending on steam conditions, stack gas treatment, coal pretreatment, etc. The estimated cost of the 300 MW HIPPS plant was on the order of $1050/kW (Seery, 1998). This included the radiator with the attendant refractory materials and additional construction cost for supports, etc. The HIPPS Today with only the convective heater should cost some 8-10% less, or about $975/kW. Using the scaling guidelines from DOE (DOE, 1999), the cost for a nominal 100 MW HIPPS Today would be approximately $1900/kW. If the modular approach was used and the 10% cost savings were realized, the plant would be $1710/kW. However, small GT's are more expensive per kW than the large frame type GT, so that a reasonable cost for the plant would be on the order of $1925 /kW.

Small steam plant efficiencies are typically 32-34% for reheat units. The cost of coal is dependent on numerous factors, but is generally in the range of $1.00 - $1.25 MMBtu ($0.95 to $1.18/$10^6$ kJ). For our comparison, a value of $1.14 MMBtu ($1.08/10^6 kJ) was selected. This is the coal cost projected by the EIA for 2005 (EIA, 2000). Again, because of scale effects, the operation and maintenance costs for the small plant are higher than for the large plants. The ratio of costs between the PC plant and the HIPPS is assumed to be the same, even though the HIPPS Today plant has no radiator with its higher maintenance refractory. Because of the uncertainties in the costing, a relative cost of electricity has been estimated (Exhibit 4-4). Here, the COE for the PC plant is defined as unity and the HIPPS Today plant is some fraction of the value. Also shown in Exhibit 4-4 are the relative COE's for a combined cycle plant. This plant was assumed to have an output of 100 MW at an efficiency of 52% (LHV). In Exhibit 4-4, it can be seen that the HIPPS Today has a COE approximately 18% less than the PC plant. The combined cycle plant has a lower COE than the HIPPS Today does at gas costs of approximately $2.75/MMBtu ($2.62/10^6 kJ) and below (gas/coal cost ratio of approximately 2.5). At a gas/coal cost ratio greater than 2.5, which is currently the case and is projected to continue in the future, the HIPPS Today would offer lower COE's than the combined cycles.

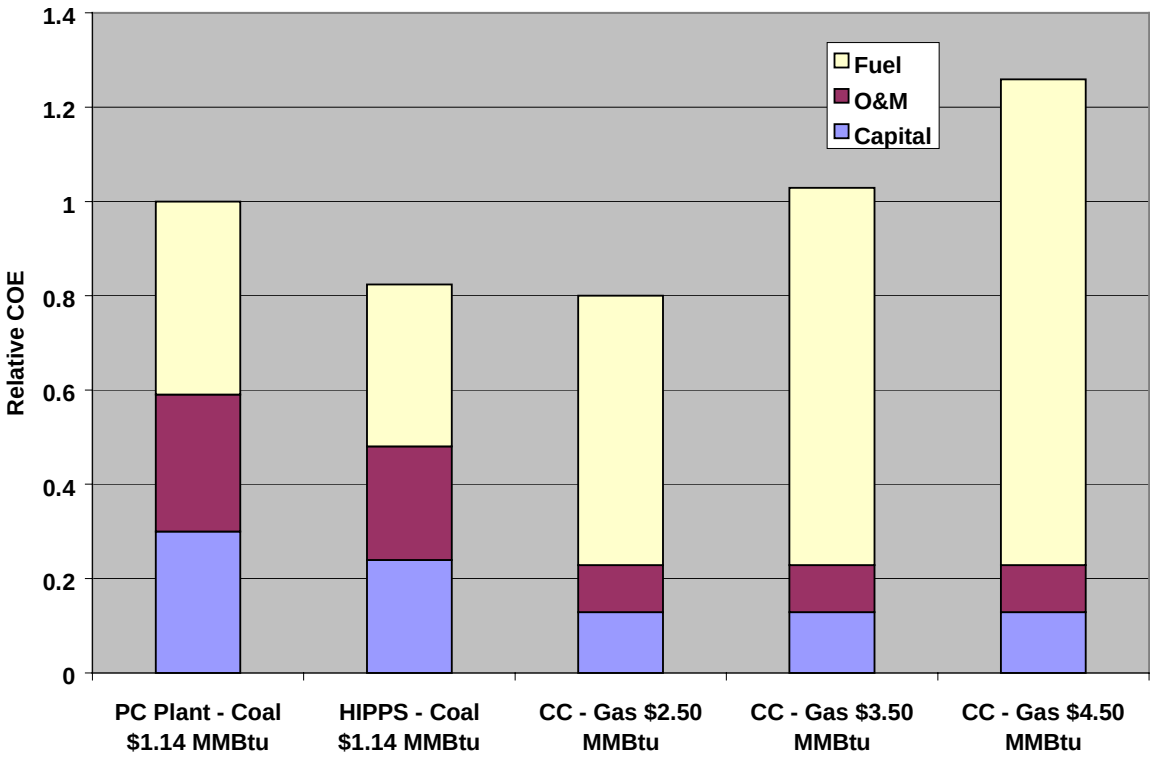

Exhibit 4-4
Relative Cost of Electricity

Emissions

Estimates of the emissions (g/kWh) for the three plants are shown in Table 4-1. It is assumed that the PC Plant meets the NSPS and that the HIPPS Today Plant meets the DOE goals of one-tenth current NSPS. The emissions for the combined cycle plant are based on typical levels for aeroderivative gas turbines burning natural gas.

The reduction of greenhouse gases, particularly CO_2, is of intense interest. Several alternatives have been investigated for mitigation in HIPPS (Klara, 1994), but the costs associated with CO_2 removal are not well defined. For example, cost ranging from $31.8/ton ($35/tonne) to over $227/ton ($250/tonne) have been identified (IEA, 1998). The carbon tax of 350 NOK/tonne ($50/ton or $55 /tonne) of CO_2 set by the government of Norway on emissions from combustion falls within this range. The COE shown in Fig. 4.5 has been recalculated with a CO_2 removal cost at the $50/ton ($55/tonne) value. The lower CO_2 emissions of the combined cycle, due to both a higher efficiency and a fuel with lower carbon content, result in lower COE's. A breakeven COE, i.e., one at which the HIPPS Today and the combined cycle have equal costs, is shown in Exhibit 4-6. For the range of gas/coal costs projected by IEA, roughly 3-5, the CO_2 removal cost must be below the $50/ton ($55/tonne) value for the HIPPS to have a lower COE.

Table 4-1
Emissions from Power Plants
g/kWh

	SO_x	NO_x	Particulates	CO_2
PC Plant	2.7	2.7	1.4	1025
HIPPS Today	0.22	0.22	0.14	850
CC	0	0.06	0.01	420

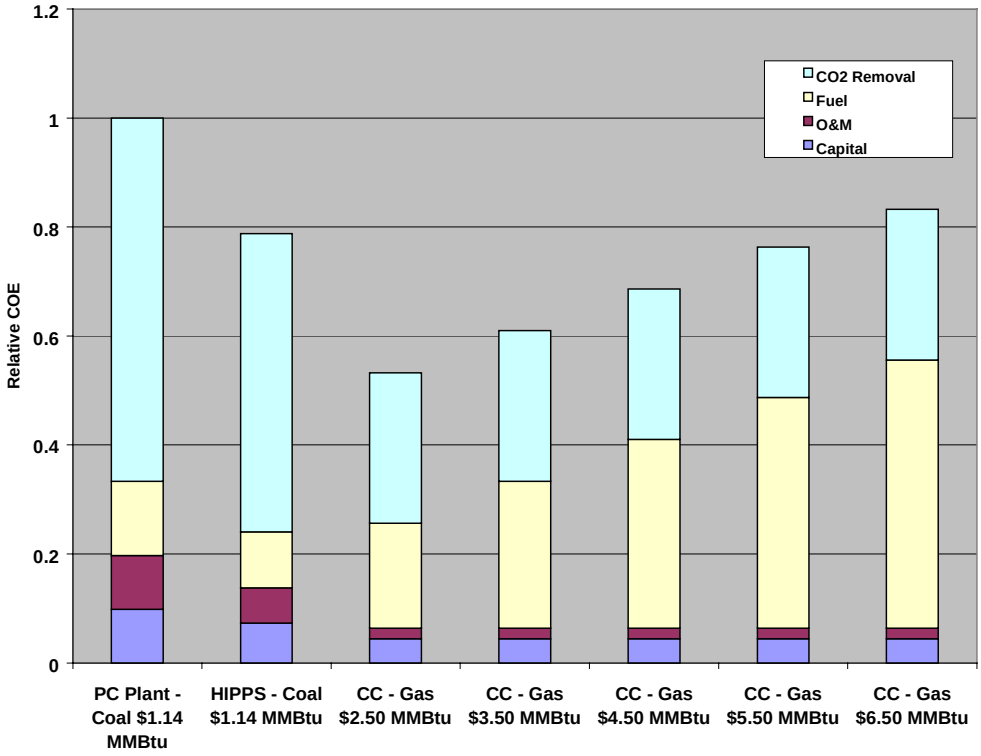

Exhibit 4-5
Relative COE with CO_2 Removal

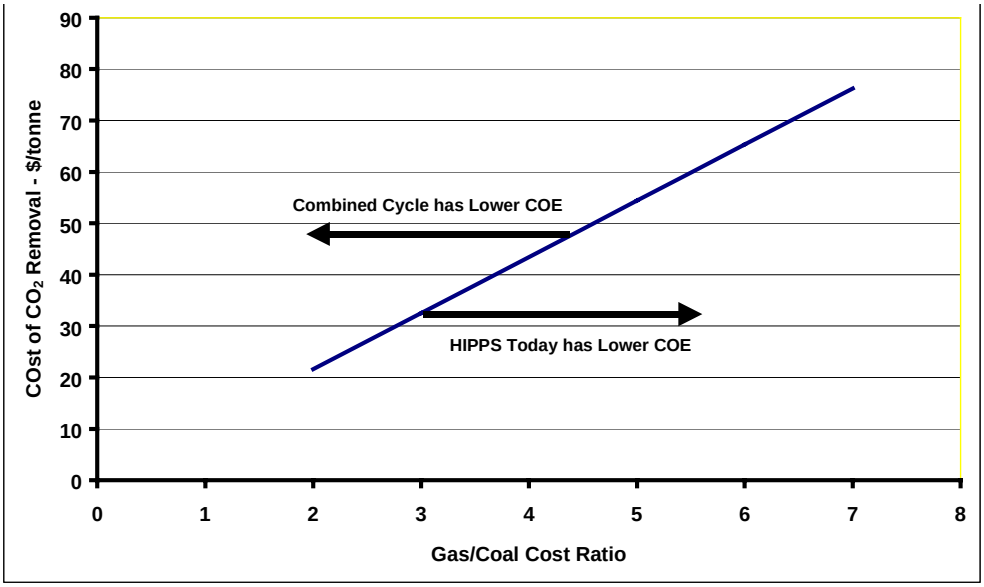

Exhibit 4-6
Breakeven CO_2 Removal Costs

The COE, however, would not be the only consideration in many developing economies. In those locations having both fuels available, the choice of power plant, i.e., coal-fired or gas fired, would have to also consider the incremental cost of CO_2 removal and its equivalent worth as "CO_2 credits". If the CO_2 credits are worth more than the fuel, then a gas-fired plant would be chosen. However, if the CO_2 credits were not as valuable as the export value of the gas, then the coal-fired plant would be built. The coal-fired plant has the potential advantage of using biomass as a fraction of the fuel, thereby further reducing the COE.

Conclusion

The HIPPS Today concept offers the opportunity of early application of the coal-fired combined cycle with its increased efficiency and reduced emissions vis-a-vis traditional pc steam plants. By using a modular approach, the cost of the HIPPS Today can be further reduced, adding to its attractiveness.

References

Anon., Hot Air Boosts Efficiency in Power Generation, Chemical Engineering, February, 1999

DoE, Energy Information Agency, Annual Energy Outlook 2000 With Projections to 2020, Dec. 2000

DoE, Market-Based Advanced Coal Power Systems, 1999

IEA, Carbon Dioxide Capture from Power Stations, 1998

Klara, Scott and Van Bibber, Lawrence, Carbon Dioxide Capture from High Performance Power Systems, Global Climate Change Conference, 1994

Rao, A., Private Communication to F.L. Robson, Sept. 2000

Seery, D.J., et al., Coal-Fired High Performance Power Generating System, Final Report, United Technologies Research Center, August 31, 1995

Seery, D.J., et al, Coal-Fired High Performance Power Generating Systems, Quarterly Report No. 13, Contract DE-AC92-92PC91155, Dec. 1998.

World Bank, Reducing the Cost and Construction time of Thermal Power Plants, June, 2000

Section 5 - Integration of High Performance Power Systems (HIPPS) into Vision 21

Abstract

The work reported in this section was performed under program task 6.4. HIPPS can be a technology for use in the DOE's Vision 21 program. The major goal of this program is the generation of power at least 60 % (HHV) using coal or 75 % (LHV) using gas. Emissions are to be essentially zero, including Greenhouse gases. One of the methods of potentially reaching these goals is by using a hybrid cycle. The hybrid combines a thermodynamic cycle, e.g., a Brayton cycle, with an electrochemical cycle such as a high temperature fuel cell. In the HIPPS/Hybrid, the compressor discharge air is heated in the HITAF to 1800 °F (982 °C) and then goes to a Solid Oxide Fuel Cell (SOFC) where it is reacted with H_2 from a steam/natural gas reformer. The effluent from the SOFC is at approximately 1850 °F (1010 °C) and contains some unreacted H_2 and CH_4. When burned, temperatures to perhaps 2100 °F (1149 °C) are possible. When additional gas is added, the temperature can be raised to the level typical of modern gas turbines. These systems consumed significant fractions of natural gas. At a 40/60 coal/gas ratio, the efficiency is over 61% (HHV of coal plus gas mixture). As the coal/gas ratio increases, the efficiency decreases; 55 % at 50/50 and 51 % at 60/40. This is because the SOFC participation decreases since SOFC fraction is a direct function of the natural gas flow.

The HIPPS approach, from the CPD to Vision 21, offers the highest power plant efficiencies of any coal-based design. Coal gasification, even when used with the "H" class frame machines, identified in the DOE Advanced Turbine System program, reaches efficiencies in the mid-40 %'s.

Introduction

The DOE's Office of Fossil Energy has identified a new approach to producing energy that emphasizes the reduction of emissions of all types, including Greenhouse gases such as CO_2, as an integral part of the energy production. This approach, Vision 21 (V21), will build on the advances of the ongoing programs such as Combustion 2000 and the Advanced Turbine Systems to develop new types of facilities that integrate power production with pollution control and provide, where economic, byproducts and thermal energy (DOE, 1999). The V21 plant could use a single fuel or a combination of fuels such as coal, gas, or biomass to produce higher value products as electric power, chemical feedstocks, hydrogen, as well as secondary products such as steam or hot air for industrial use. There will be no single V21 design; rather the goals will be to integrate the emerging technologies into power plants that minimize or eliminate the pollution associated with the use of fossil fuels and maximize the efficiency of producing high value products. The goal is to use as much of the fuel energy as possible.

The following sections describe an initial attempt at defining a near term V21 application based on the integration of several ongoing or suggested DOE programs to repower older steam plants.

HIPPS in V21

While there are a wide variety of possible applications of the V21 approach, one that is recognized as a candidate for the nearer term (2010) is the repowering of existing coal-fired steam stations. Repowering can vary in scope from complete site leveling and replacement of everything to refurbishment of existing boilers and steam equipment and the addition of a topping gas turbine. In the V21 concept to be described, the coal handling and steam turbine sections would be saved/upgraded. The boiler would be replaced by a new HITAF. The constraints placed on the system design by the desire to use the existing turbine and coal systems could reduce the efficiency benefits of HIPPS application versus a new greenfields plant. Nonetheless, repowering represents a realistic entry for HIPPS and V21. A progression of V21 repowering scenarios is briefly described to show the potential for integrating a portfolio of technologies.

A nominal 125 MW steam station located in upstate New York has been chosen for repowering. It operates at 1475 psi/1000 °F/1000 °F (10169 kPa/538 °C/538 °C) with a heat rate of 10157 Btu/kWh (10.716 MJ/kWh). In the repowered configuration, the HRSG supplies feedwater heating. Because steam is normally extracted for this, the back end of the steam turbine cannot handle the added flow, unless upgraded. The first repowering configuration (Exhibit 5-1) uses a nominal 125 MW gas turbine based on an aeroderivative design first described in the Collaborative Advanced Gas Turbine (CAGT) program (Davidson, 1966). The technology for engines such as this could be realized in a planned DOE initiative on the Next Generation Turbine System, a logical follow on to the ATS program and an enabling V21 technology.

The HITAF in this version has a radiator section with an outlet temperature of 1700 °F (930 °C). Other repowering schemes have been considered that do not include a radiator and use only the convective heat exchanger in the HITAF. In the configurations under consideration, the exhaust from the gas turbine is not used for preheated combustion air in the HITAF. The GT can be "decoupled" from the coal side and, when desired, the GT can be run alone as a peaker, adding a great deal of operational flexibility to the concept. This configuration has an output of 130 MW from the GT and 80 MW from the steam turbine. (Analysis indicated that better overall efficiency could be obtained with the reduced steam flow). The plant has a net output of 204 MW at a net efficiency of 44.8% (HHV), a value approximately 32% better than the original station. Coal furnishes 76% of its heat input. The repowered plant would be retrofitted with pollution control devices such as those being demonstrated in the LEBS program to meet the goal of 1/10th NSPS. This near term application demonstrates the transition of technologies to meet the V21 goals of higher efficiency and lower emissions.

The next repowering configuration integrates a new technology, the solid oxide fuel cell (SOFC) into the HIPPS and LEBS combination. The use of the SOFC as a topping cycle for a gas turbine is widely described in the literature (George, 1999; Hirschenhofer, 1998). In most of those applications, however, natural gas is the only fuel considered. In the HIPPS repowering schemes considered the combustion of coal furnishes a significant amount of the energy to the fuel cell and furnishes at least 50% of the total system energy input.

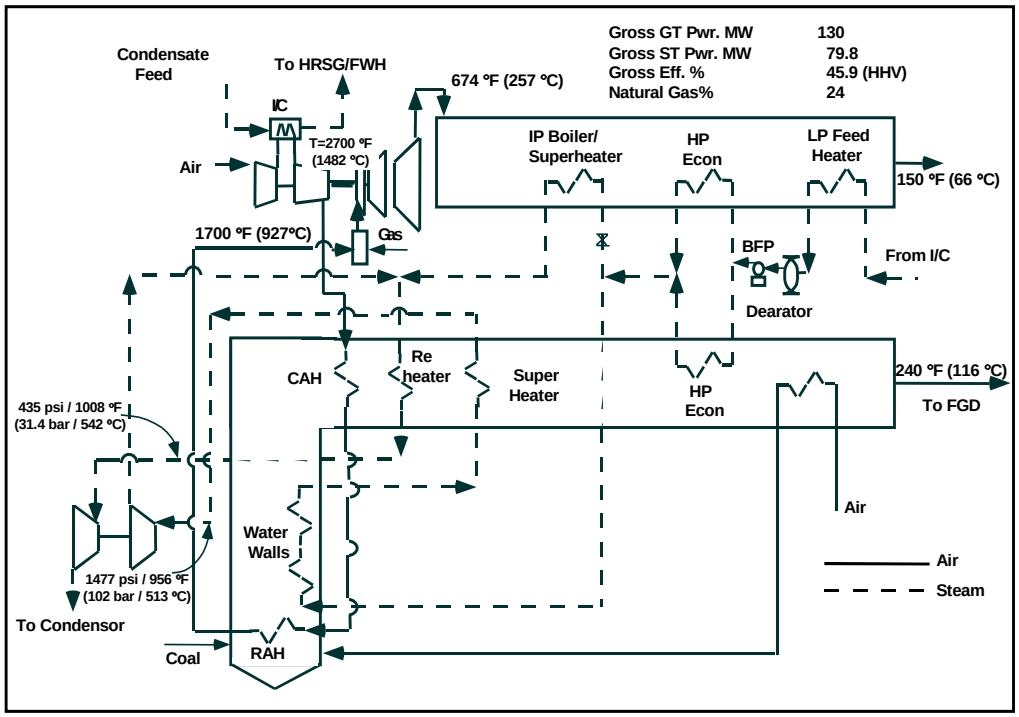

Exhibit 5-1
Schematic of HIPPS Repowering with NGT Technology

With the SOFC in the system (Exhibit 5-2), the compressor discharge air is heated in the HITAF to around 1800 °F (980 °C) and sent to the cathode of the SOFC. Natural gas is desulfurized, preheated and mixed with steam, then enters a pre-reformer before going to the anode side of the SOFC. The SOFC exhaust contains small amounts of CH_4 and H_2 as well as water vapor and CO_2. Additional methane is added and the mixture is combusted in the duct burners to reach desired turbine temperature. Because of the added moisture, NO_x production in the gas turbine combustor is quite low (Bhargava, 1999). The moisture also results in an increase in turbine output and in the turbine exhaust temperature. In the system with coal furnishing 65% of the overall energy input (DOE goal for the HIPPS commercial plant), the repowered station has an output of 266 MW (33.5 MW SOFC/137 MW GT/102 MW ST) at an efficiency of 47.9% (HHV). This is a 41% increase over the base steam system and a 3-percentage point increase over the HIPPS repowering. Over 70% of the energy into the fuel cell is from coal.

In the present analysis, the original steam turbine throttle flow was not exceeded, but when needed, the back end was allowed to be enlarged to handle increased flow. Also, the coal-handling infrastructure was kept within the capability of the original system. When the DOE HIPPS goal of 65% coal input was relaxed, a significantly different system resulted. Natural gas flow was increased up to a value of 50% of total energy input, resulting in a larger fraction of the power generated by the fuel cell and gas turbine. When the coal flow and gas flow energies were the same, the resulting system output was increased to 431 MW (171 MW SOFC/154 MW GT/ 113 MW ST) with an efficiency of 55.6% (HHV). Thus, the repowered plant has an output nearly four times the original plant at an efficiency that is 65% better. While these systems demonstrate the performance and environmental potential of integrated V21 power plants, it

would be instructive to compare the system economics to see if the DOE goal of reduced costs is met.

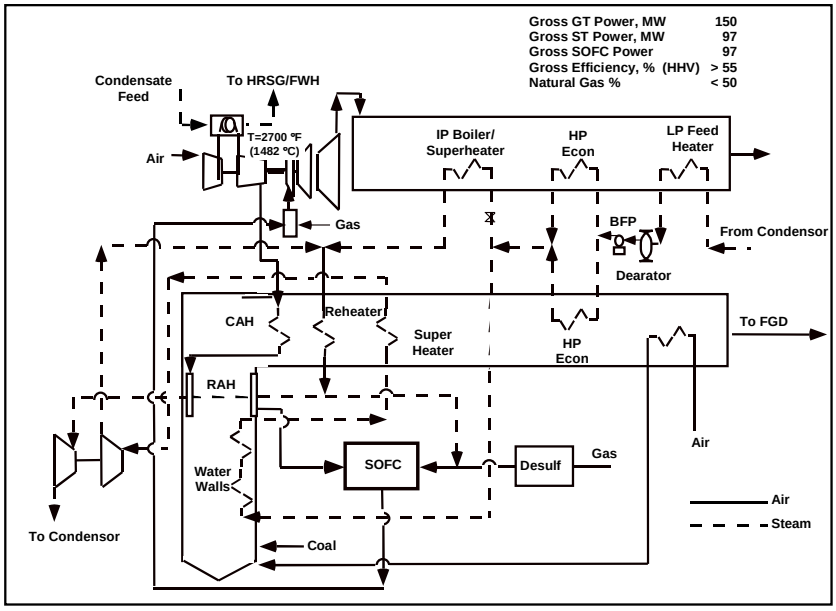

Exhibit 5-2
Schematic of HIPPS/SOFC Repowering with NGT Technology

Economic Comparison

Because of the lack of actual cost information on the advanced power systems, a simplistic approach was taken for the economic analysis. The original steam plant was assumed to have an overnight cost of $1200/kW, fuel cost of $1.00/million Btu, and non-fuel O&M costs of 4 mills/kWh. The cost of power was calculated for a load factor of 65% and normalized to a value of one. The cost of electricity (COE) for the V21 repowered systems was then compared on this normalized basis.

The cost of repowering with HIPPS has been estimated to be between $600 and $800/kW of incremental power, depending on what upgrading was required by the existing infrastructure (Seery, 1998). The $800/kW value was used for the HIPPS repowering, as the switchyard required upgrading. For the SOFC/HIPPS, $810/kW was used, as the steam turbine also required upgrading. The non-fuel O&M costs were assumed to be 7 mills/kWh including an allowance for refractory replacement in the HITAF. Cost estimates for the SOFC range from hundreds of dollars per kW to over $3000/kW. Based on updating a SOFC repowering study (Moss, 1992) a value of $1000/kW was assumed. The non-fuel O&M costs for the SOFC were assumed to be 9 mills/kWh. This includes an allowance for materials to replace the fuel cell modules after 40,000 hr.

Coal gasification is an alternative approach to repowering as demonstrated by the Destec Wabash plant (Keeler, 1997). This plant is presently owned by Global Energy, Inc. and the process is called E-GAS™ Technology. The lower efficiency of this plant, 42%, the very high

O&M costs, and the uncertainty as to the real costs of the gasification bloc mitigated against an economic comparison at this time.

Aside from more accurate values for equipment costs, the major variable in the COE calculation is the cost of fuel. Currently, natural gas is plentiful and its cost is roughly twice that of coal. Predictions are that gas supplies will remain plentiful, but infrastructure costs and competition for end use could increase the costs. The Energy Information Agency projects the cost of gas for utility use could increase by 40% over the next twenty years (Exhibit 5-3; EIA, 2000). Coal costs are predicted to remain nearly constant and could actually drop as fuel competition increases.

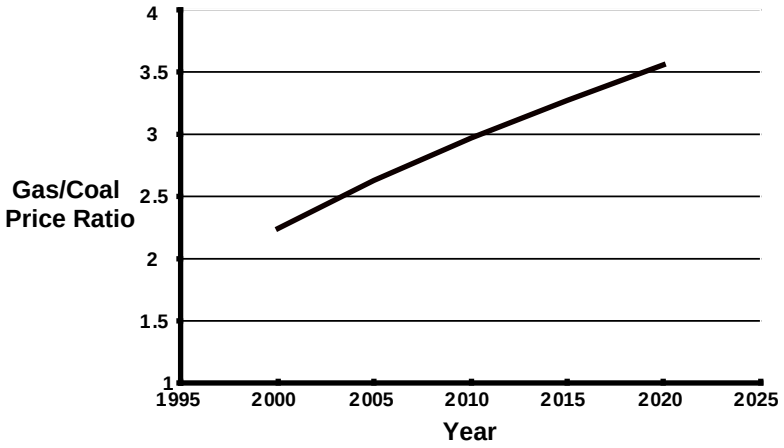

Exhibit 5-3
Projected Fuel Cost Ratio

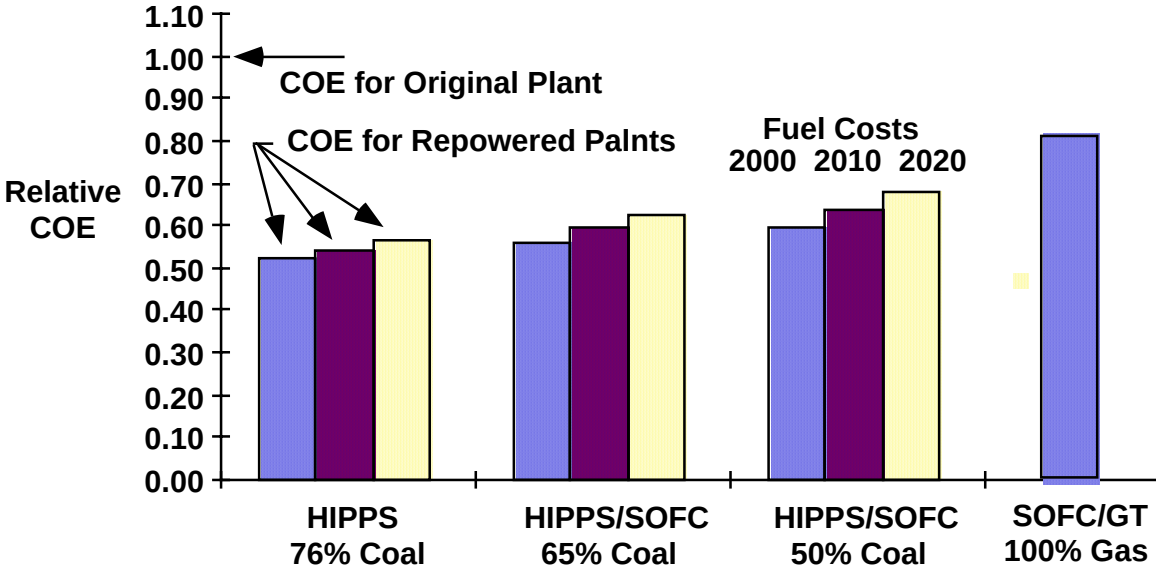

Exhibit 5-4
Relative Cost of Electricity

The analysis shown in Exhibit 5-4 uses gas-to-coal cost ratios projected for the year 2000 (2.5), for 2010 (3.0), and 2020 (3.5) to compare COE for the repowering cases. The use of gas in combination with the coal makes a good deal of economic sense in repowering. The GT or GT/SOFC portion of the plant can be operated independently, creating a revenue stream during planned, or forced, outages of the coal portion. This duel fuel approach offers a good deal of operating flexibility. The COE for the HIPPS repowering is lower than those for the HIPPS/SOFC repowering for all fuel cost ratios. The higher capital costs of the HIPPS/SOFC and the higher cost of gas relative to coal are not offset by the efficiency gains. An all gas repowering scenario (SOFC/GT, but no HIPPS) had a lower capital cost and an efficiency of 61.4% (HHV). Its COE was still higher than those schemes using coal, even at the lowest gas/coal cost ratio. It is worth noting the effect on COE when CO_2 removal is considered. At this time the costs for CO_2 reduction are not well defined.

One method of assessing the impact of emissions of CO_2 on COE can be seen by imposing a "carbon tax"; e.g., a tax of 350 NOK/tonne ($50/ton or $55/tonne) of CO_2 has been set by the government of Norway on emissions from combustion. The effect of assessing such a tax on the repowering scenarios is shown in Exhibit 5-5. The emissions of CO_2 are based on the data from (Dehle, 1996). For example, a coal-fired plant having an efficiency of 34% (the plant to be repowered) would have CO_2 emissions of about 2.2 lb/kWh (1 kg/kWh). At a tax of $50/ton ($55/tonne), the additional cost would be approximately $0.055/kWh, a value that would more than double the cost of electricity. Since the object is to compare the various HIPPS configurations, once again the cost of electricity has been normalized against the original plant cost, this time with three values for CO_2 removal, $50, $25, $12.50/ton ($55, $27.50 and $13.75/tonne) CO_2. As before, the added efficiency of the configurations with the SOFC do not overcome their higher capital and fuel costs, although the percentage differences in the relative costs have been reduced because of the lower costs of CO_2 removal from the more efficient configurations.

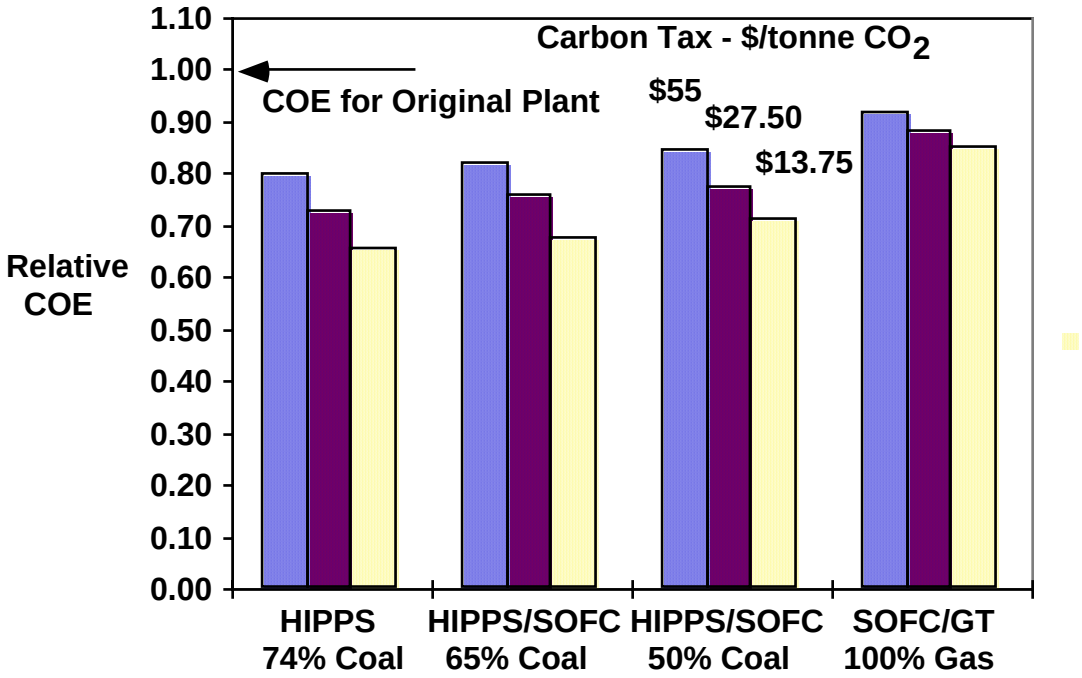

Exhibit 5-5
Relative COE with CO_2 Removal

Perspective on V21 Repowering Technologies

The portfolio of technologies represented by Vision 21 can be successfully used to repower the generation of older steam stations that will reach the end of their economic life in the early decades of the 21st century. Both the HIPPS and SOFC/HIPPS approaches result in higher efficiency and lower emission power plants. It is obvious from the simplistic approach used in the foregoing analysis that the economics of these new generations of power plants will have to be carefully defined. It should be noted, however, that it would take relatively large changes in cost estimates to change the overall results. Also, as plants become more efficient, the allowable cost to obtain a gain in efficiency becomes smaller (the savings in fuel cost per point in efficiency change becomes smaller as efficiency increases). Unless "clean" fuel costs are very high, at least a factor of two beyond those used, the new, higher efficiency technologies can not have capital costs that are significantly different from today's plants if they are to compete successfully in the increasingly competitive deregulated market for electricity. This is true even with high cost CO_2 removal.

Advanced V21 Configurations

While the repowering application offers the earliest opportunity for applying V21 technologies, there are other configurations more suitable for Greenfield use. In the previous configurations, the SOFC was pressurized by the GT compressor. That technology has been demonstrated on a small scale, <200 kW GT, and at low pressure ratios, mostly under 10 and more often around 3. The use of an atmospheric pressure SOFC in the HIPPS is shown in Exhibit 5-6.

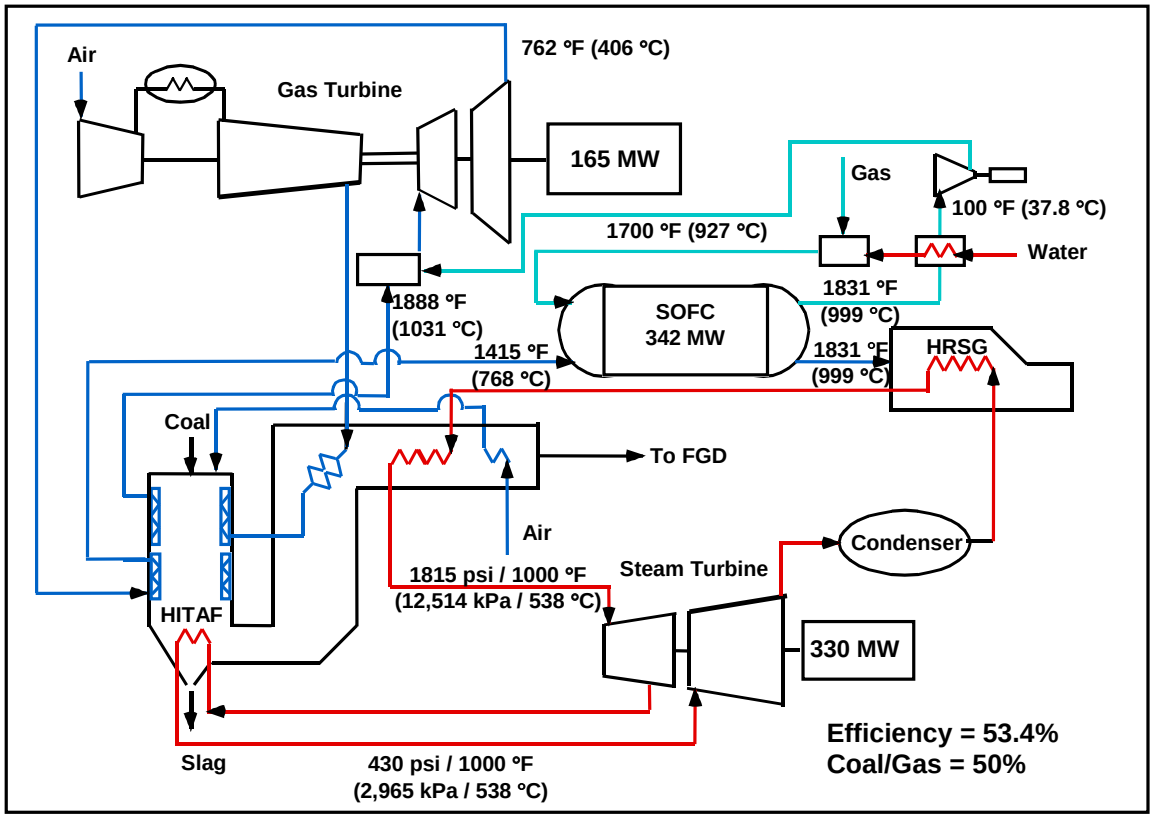

Exhibit 5-6
HIPPS/Hybrid with Atmospheric Pressure SOFC

In this power plant, the compressor discharge is heated in the HITAF as in normal HIPPS operation. The temperature is boosted to the desired level by gas. The GT exhaust is sent back to the HITAF where it is reheated to over 1400 °F (760 °C) using coal and then sent to the SOFC as preheated oxidant. The exhaust from the SOFC is used in an HRSG to heat feed water. This steam is mixed with that raised in the HITAF and expanded in a steam turbine. With an atmospheric SOFC and modest steam conditions, an efficiency of over 53% can be achieved with 50% of the input energy derived from coal.

The efficiency is dependent on the amount of gas used. This because the SOFC can only use gas and, as the most efficient energy converter, the more gas, the higher the efficiency. This is seen in Table 5.1. In the first three configurations, the GT temperature is kept at the design level of over 2700 °F (1482 °C). Because the exhaust of the SOFC contains insufficient fuel to raise that temperature, additional fuel is used in the GT combustor. Because the goal for HIPPS is to maximize coal use, as the coal/gas ratio increases, less gas is sent to the SOFC (it becomes smaller) and more to the GT. This reduces overall efficiency. The last configuration in Table 5-1 shows that when the GT temperature is set by the available fuel in the SOFC exhaust, i.e., to around 2200 °F (1204 °C), the efficiency increases.

Table 5-1
HIPPS/SOFC Performance

	HITAF	HITAF	HITAF	HITAF
Engine Type	NGT Tech	NGT Tech	NGT Tech	NGT Tech
Type of fuel	Coal & Gas	Coal & Gas	Coal & Gas	Coal & Gas
%Gas	61.0	50.0	40.0	37.9
Inlet Air Flow/engine, lbs/sec	610.3	610.3	610.3	610.3
OPR, PR(HPC*LPC)	60.3	60.3	60.3	60.3
GT Turbine Inlet Temp, F	2716	2716	2716	2200
System Performance				
Total net power, MW (@gen)	647.8	431.4	309.9	322.9
Gross Gas Turbine power, M	176.4	154.1	141.7	97.5
Gross Steam Turbine power, MW	128.3	113.1	104.9	99.4
Gross Fuel Cell power, MW	351.2	171.4	70	132.1
Cycle Efficiency, gross (HHV c&g)	61.2	55.6	50.3	52.4
Gas Turbine Performance				
GT HPT temp, F	2716	2716	2716	2200
GT LPT temp, F	1964	1895	1852	1422
GT exhaust temp, F	775	726	696	505
GT Stack temp, F	180	180	180	180
Fuel flow/engine, lbs/sec	26.00	15.65	10.00	0
HITAFF Combustor				
Coal flow rate, lbs/sec	31.4	29.6	28.4	29.3
Radiant sect., GT Outlet temp, F	1634	1754	1803	1774
Convective HX outlet temp, F	1300	1300	1300	1300
HITAF HRSG stack temp, F	596	551	517	429
Steam System				
HP Throttle flow, lbs/sec	198.1	174.7	162.2	153.8
HP pressure/temp, psia/F	1477/956	1477/956	1477/956	1477/956
LP Steam flow, lbs/sec	198.1	174.7	162.2	153.8
LP pressure/temp, psia/F	454/1008	454/1008	454/1008	455/1008

A more complex HIPPS/Hybrid configuration is shown in Exhibit 5-7. The ICAD NGT has been changed to include a reheat section in the GT. The compressor discharge air is heated in the HITAF to approximately 1800 °F (982 °C) and sent to the SOFC. The exhaust is burned and partially expanded in the GT. The lower pressure exhaust is reheated in the HITAF and sent to a lower pressure SOFC where much of the remaining oxygen is used. The unburned fuel is combusted with the remaining oxygen and expansion completed in the GT power turbine. Only very preliminary estimates have been made for this configuration, but it has the potential for over 60% efficiency (HHV of the fuel mixture) with more than 50% of the energy coming from coal combustion.

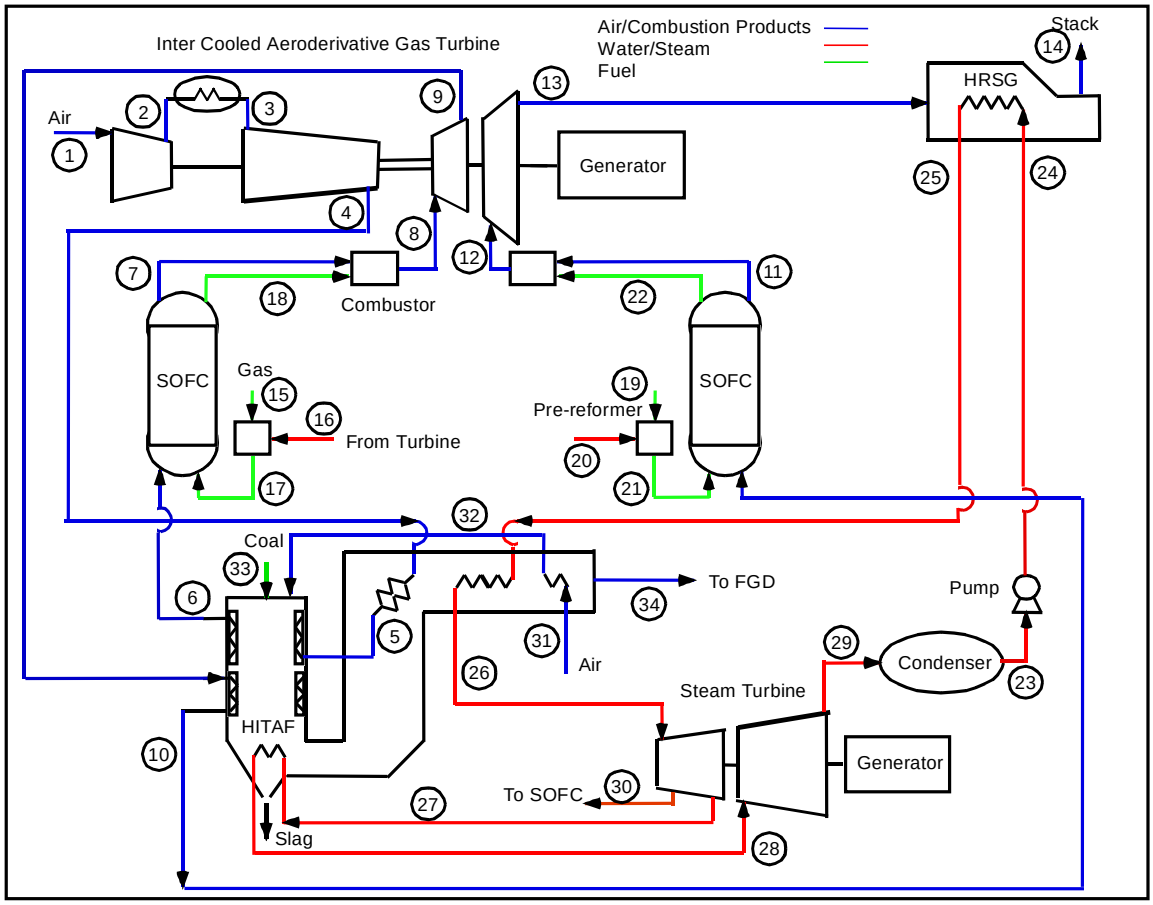

Exhibit 5-7
HIPPS/Hybrid with HP and IP SOFC's

Ultra HIPPS

The last V21 configuration considered is based on a V21 enabling technology goal of a heat exchanger capable of 3000 °F (1649 °C) metal (ceramic) temperatures. The configuration is similar to the commercial plant design, but the HITAF has a radiator capable of reaching significantly higher temperatures.

In these applications coal is the only fuel supply. The gas turbine used is similar to the latest intercooled NGT engines. The HITAF configuration was modified to include convective and radiant HITAF sections, which were assumed capable of gas outlet temperatures of 2000 °F (1093 °C) and 2800 °F (1538 °C) respectively. The combination of these "Ultra" heaters was assumed to be capable of heating the gas turbine compressor discharge air to 2800 °F (1538 °C) for entry to the high pressure turbine without any downstream gas combustion.

The baseline gas turbine and HAT cycles using the FT4000 gas turbine are shown in Table 5-2, Cases 1, and 2. In these cases, the convective and radiant heat exchanger outlet temperatures are 1300 °F (704 °C) and 2100 °F (1149 °C) respectively. This study examined the performance benefits which would be realized if these two critical components were capable of higher outlet conditions. The radiant section was assumed to produce air outlet conditions of 2800 °F (1538 °C) and satisfy the gas turbine firing condition without the need for any natural gas combustion.

In each case considered, the power system was designed to minimize the HITAF participation and provide just enough heat from the coal to supply the necessary heat for the gas turbine and use the remaining heat for steam generation. For completeness, several cycles were configured in which the steam portion was eliminated and a gas turbine air-to-air regenerator was used. In all of the HITAF cases, the gas turbine exhaust is de-coupled from the coal combustor. Combustion air for the HITAF is supplied by an air pre-heater.

In the first HITAF application (Case 3), the gas turbine exhaust is the only source of steam generation and is allowed to provide heat down to a stack temperature of 180 °F (82 °C). The all-coal configuration has a gross cycle efficiency of 49.4% (HHV). This combination of the HAT cycle and the combined cycle was the most efficient all-coal configuration identified in the study. However, when the steam cycle was replaced with an air/air regenerator using the gas turbine exhaust gas, Case 4, a cycle efficiency of 51.5% (HHV) was estimated. Other advanced regenerative simple cycle and intercooled versions are also shown in Cases 5 & 6. These configurations also produce high efficiency HITAF power plants in which no steam is required. The regenerative single shaft, simple cycle configuration results in a gross cycle efficiency of 48.1% (HHV) while the two-spool intercooled version results in a gross cycle efficiency of 50.9% (HHV). These three Ultra-HIPPS cycles, which do not require steam generation equipment but do include an air/air gas turbine regenerator all result in cycle efficiencies which are higher than any previously examined all-coal configurations. In all of the foregoing cases, the effectiveness of all heaters was assumed to be 90%.

These cycles should be examined further to understand better the cycle and cost effects and may represent good candidates for DOE Vision 21 (V21) applications.

Table 5-2
Ultra-HIPPS

	1	2	3	4	5	6
Engine Type	FT4000	FT4000	FT4000	FT4000	NGT - S/S	NGT-FT60KIC
Fuel	Gas	Gas	All Coal	All Coal	All Coal	All Coal
%Gas	100.0	100.0	0.0	0.0	0.0	0.0
Inlet Air Flow- 1 engine, lbs/sec	610.3	610.3	610.3	610.3	610.3	610.3
Compressor Overall Pressure Ratio	60.3	60.3	60.3	60.3	19.2	53.8
GT Turbine Inlet Temp, °F	2715	2715	2800	2800	2800	2800
Cycle Configuration	Simple	HAT	HAT	HAT	HAT	HAT
System Performance						
Total net power, MW (@ generator)	144.6	271.3	260.6	245.7	222.3	255.8
Gross Gas Turbine power, MW	147.5	274.0	234.6	249.5	225.8	259.8
Gross Steam Turbine power, MW	NA	NA	31.0	0.0	0	0
Cycle Efficiency, gross (LHV gas)	47.5	57.9				
Cycle Efficiency, gross (HHV coal & gas)			49.4	51.5	48.1	50.9
Gas Turbine Parameters						
GT HPT temp, °F	2715	2715	2800	2800	2800	2800
GT Power Turbine temp, °F	1865	2071	2018	2035	NA	2015
GT exhaust temp, °F	710	808	752	760	1134	844
GT Stack temp, °F	710	250	180	180	180	180
Turbine Cooling (% Inlet)	26.2	26.2	27.8	28.4	25.4	23.9
Fuel (nat. gas) flow- 1 engine, lbs/sec	14.30	21.50	0.00	0.00	0.00	0.00
Saturator: Steam Flow, lb/sec	0	137.3	119.6	136.8	160.9	148.7
Percent Saturation, (Rel to inlet flow), %	0	22.50%	19.60%	22.40%	26.40%	24.40%
HITAFF Combustor						
Coal flow rate, lbs/sec	0	NA	40.4	36.3	35.3	38.3
Radiant sect., GT Outlet temp, °F	NA	NA	2800	2800	2800	2800
Convective HX outlet temp, °F	NA	NA	2000	2000	2000	2000
Convective HX Effectiveness, %	NA	NA	90.0	90.0	90.0	90.0
HITAF HRSG stack temp, °F	NA	NA	238	236	236	236
Stm from HITAF combustor, lbs/sec	NA	NA	0.0	0.0	0.0	0.0
Stm from HITAF HRSG. lbs/sec	NA	NA	0.0	0.0	0.0	0.0
Stm from GT HRSG, lbs/sec	NA	NA	53.0	0.0	0.0	0.0
% Steam split, HITAF comb/HRSG	NA	NA	0.0	0.0	0.0	0.0
Steam System						
HP Throttle flow, lbs/sec	0	0	53.0	NA	NA	NA
HP pressure/temp, psia/°F	NA	NA	1250/950	NA	NA	NA
LP Steam flow, lbs/sec	0	0	53.0	NA	NA	NA
LP pressure/temp, psai/°F	NA	NA	540/950	NA	NA	NA

References

Bhargava, A., Colket, M., Sowa, W., Maloney, D. and Castleton, K., An Experimental and Modeling Study of Humid Air Premixed Flames, ASME IGTI 1999, Indianapolis, IN. June, 1999

Davidson, Barry and George Hay, Advanced Aeroderivatives and the CAGT Programme**,** Innovative Repowering Strategies with Advanced Gas Turbines, Washington, D.C., June 4-5, 1996

Dehle, M., Future Development by CO_2 Emissions in the European Electricity Economy, VDI-Report 1321, Advanced Energy Conversion and Utilization, Vol. 3, 1996

DoE, Energy Information Agency, Energy Projections for 2000, Jan. 2000

George, R.A., Hybrid Power Systems, International Colloquium and Exhibit on Environmentally Preferred Advanced Energy Generation, March 23, 1999

Hirschenhofer, J.H., Stauffer, D.B., Engleman, R.R., and Klett, M.G., Fuel Cell Handbook – Fourth Edition, DOE/FETC – 99/1076, November, 1998

Keeler, C.G., Wabash River in Its Fourth Year of Operation, Proceedings of the 1999 Gasification Technology Council, October, 1999

Moss, W.E, Solid Oxide Fuel Cell Repowering of Highgrove Generating Station, Pacific Coast Electrical Association E&O Conference, March 18-20, 1992

Seery, D.J., et al, Coal-Fired High Performance Power Generating Systems, Quarterly Report No. 13, Contract DE-AC92-92PC91155, Dec. 1998

Combustion 2000
Phase II

Volume II of II

DE-AC22-95PC95144

Final Technical Report

June 20, 1995 – March 31, 2001

Prepared for

National Energy Technology Laboratory
Pittsburgh, Pennsylvania

United Technologies Research Center
411 Silver Lane, East Hartford, Connecticut 06108

Combustion 2000
Phase II

Volume II of II

DE-AC22-95PC95144

Final Technical Report

June 20, 1995 – March 31, 2001

Prepared for

National Energy Technology Laboratory
Pittsburgh, Pennsylvania

United Technologies Research Center
411 Silver Lane, East Hartford, Connecticut 06108

Table of Contents-Vol II

Table of Contents-Vol II (Continued)

List of Exhibits-Vol II

List of Tables-Vol II

Section 6 - HITAF Modeling

Abstract

The work reported in this section was performed under program task 2.1.2. One of the first steps after generating a basic HITAF configuration was to determine if the design could be translated into a practical commercial plant. In addition to the cycle analysis, previously mentioned, there is always the need to model the detailed combustion process and the related questions of slag flow, NOx formation and carbon burnout. Although the program was restructured to eliminate the larger scale testing and the Phase III demonstration, the modeling study continued for the insights it provides on the HIPPS process and with the hope that a future HIPPS program could take advantage of the work.

The improved models developed as part of this contract have been incorporated, together with developments in parallel programs, into the codes used by Reaction Engineering International to simulate boilers for the electrical utility industry. These codes have been successful in simulating actual performance in practical power plant combustors. In particular, they have been able to simulate alternative low NOx control technologies, including low-NOx burners, the use of closely coupled and separated over-fire air ports, and the optimum positions for introducing reagents for SNCR. This success has led the industry to accept simulations as an important element in retrofitting boilers.

An example of the success of these tools is a program for a consortium of electrical generation utilities, organized by the Electric Power Research Institute (EPRI), which predicted effects of operating a cyclone-fired boiler under low-NO_X firing conditions. Under baseline conditions, the cyclone barrels are operated fuel lean, whereas under staged conditions, the cyclone barrels are operated fuel-rich and the make-up combustion air is added through over-fire air ports. The REI model was applied to guide the placement of the over-fire air ports and the impact of different degrees of staging. Excellent agreement was obtained between predictions and measurements of NO_X, made after implementation of the optimized designs for several units. The use of such tools has resulted in 80 percent of all cyclone fired furnaces being retrofitted with overfire air ports. The success in the simulation of cyclone barrels is particularly relevant to the future designs of a HITAF, since it has been shown that the cyclones provide a means to rapidly obtain the high fluxes required for the radiant air heaters. Traditionally cyclones have been viewed as being high emitters of NO_X. The REI simulations and the implementation of the staged combustion in the field show that this is not necessarily the case. Indeed, the high residence time at high temperatures that would be involved in a HITAF, in combination with staging, could result in very low NO_X levels, even prior to downstream reagent injection.

Nomenclature

a_1, a_2	β-PDF distribution parameters
A	rate specific preexponential factor
A_c	surface area of carbon-rich core
A_D	thermal annealing model preexponential factor
A_p	particle surface area
b	temperature exponent

B	overall burnout
C	gas-phase concentration
C_D	drag coefficient
C_f	numerical constant
C_{g1}, C_{g2}	turbulent combustion model constants
D	dimension of the PDF
D_{Yi}	diffusivity
d_p	particle diameter
d_c	shrinking carbon rich core diameter
D_e	effective diffusivity in the bulk phase
D_{eff}	effective diffusivity in the ash film layer
E	activation energy
E_D	thermal annealing model activation energy
f	transport scalar
f	mixture fraction
$\bar{f}$	mean value of transport scalar, the first moment of PDF
f_E	normalized frequency distribution function
f_p	mixture fraction of primary stream
F	upper mean of f
g	gravitational acceleration
g	second moment about the mean, variance
G	upper variance
h	enthalpy
H	upper mean of η
k	turbulent kinetic energy generation rate
k	reaction rate coefficient
k_m	mass transfer coefficient
k'_m	corrected mass transfer coefficient
K	equilibrium constant
m_p	mass flow rate of primary stream
m_s	mass flow rate of secondary stream
m, m_0, m_{c0}	
M_i	molecular mass of species i
n	
N	total number of physical streams
N	total number of sites available for char oxidation
N_t	total molar flux
N_p	number of particular active sites
N_p	total number of differentiable primary streams
N_s	total number of differentiable secondary streams
p	pressure
P(f)	probability density function, PDF
$\dot{q}$	particle number flow rate
$\tilde{q}$	fluctuating Favre-averaged turbulent scalar energy
q_i	particle burnout rate, or reactivity

Q_{r_j}	radiation to the surface of the particle
Q_j	convection and conduction from the particle to the gas phase
r_c	carbon rich core radius
r_j	rate of depletion of the particular component
r_j	total mass flow rate out of the particle
r_p	particle radius
r_p^{ϕ}	rate of change of particle property ϕ
R	universal gas constant
R_{ij}^{p}	particle velocity correlation function
Re	Reynolds number
S	sum of squares of the mean mixture fractions
S_p^k	the k^{th} appropriate mass and momentum source terms
$S_{p,ijk}^{\varphi}$	particle source term
t	time
T	temperature
u	velocity component in i-direction
U	fluid velocity
v	velocity component
V	particle velocity
V	volume
w_A	rate of reaction
W_i	overall rate of reaction
$\overline{W_i}$	time mean rate of reaction
$W(x_i,t)$	weight function
x	spatial coordinate
X	mass fraction in solid phase
X	mole fraction
Y	volatile yield
Y	instantaneous mass fraction
Y_i^f	fully achievable mass fraction
Z_ϕ	

Greek symbols

α	mode of burning parameter
α	intermittency
α_I	intermittency of streams other than coal off-gas
α_j	coal property
β_p	scalar value in pure primary stream
β_s	scalar value in pure secondary stream
δ	ash film thickness
ε	turbulent energy dissipation rate

ε_I	error in calculated species concentration
ϕ	any general fluid property
Φ	combined parameter
η	mixture fraction
$\widetilde{\eta}_{vol}$	progress variable, mass fraction of coal off-gas originating from the devolatilization process
φ_e	stoichiometric coefficient
λ	thermal annealing parameter
μ	viscosity
μ_e	turbulent eddy viscosity
μ_f	fluid viscosity
π	spatial linearization constant
θ	correction coefficient, or blowing parameter
θ_{af}	ash film porosity
ρ	density
ρ_f	fluid density
ρ_p	particle density
σ_f, σ_{gf}	turbulent Schmidt number
σ_{ij}	variance, or second moment of the particle position PDF
τ	dummy variable for time
ω	mass fraction
ζ	fractional conversion

Other symbols

-	mean value
’	fluctuating part
~	Favre-averaged value
$\langle\ \rangle$	ensemble average properties
[ ]	species concentration
∞	bulk value

Subscripts and superscripts

0	initial
a	adiabatic
a	ash
ap	apparent
c	pure coal off-gas
c	carbon
g	bulk (gas) phase
h	heterogeneous; char
i, j, k	respective component
o	oxidant
p	primary stream

p	particle
r	residual
s	secondary stream
vol	volatile

Acronyms

CARM	Computer Assisted Reduction Method
CFD	Computational Fluid Dynamics
CBK	Carbon Burnout Kinetics model
HIPPS	High-Performance Power System
HITAF	high temperature advanced furnace
IFRF	International Flame Research Foundation
ILDM	Intrinsic Low-Dimensional Manifolds
LOI	Loss on Ignition
NSR	Nitrogen Stoichiometric Ratio ([N]/[NO])
PDF	Probability Density Function
SNCR	Selective Non-Catalytic Reduction

Introduction

The UTRC-led Combustion 2000 team was assembled to develop an advanced high-performance power generation system (HIPPS) with a high efficiency and minimal pollutant emissions to enable the U.S. to use its abundant coal resources to satisfy current and future demand for electric power. The original concept was to use of a combined cycle using either a frame-type gas turbine or an inter-cooled aeroderivative gas turbines with clean air as the working fluid that is heated by a coal-fired high temperature advanced furnace (HITAF). In addition to a greenfields design of a HIPPS cycle, options for HIPPS repowering cycles in which a gas turbine is used to supply additional power as well heated air for use in a steam bottoming cycle, either alone or in combination with a high temperature fuel cell, were examined.

The numerical modeling efforts were originally set up to provide simulation of the HITAF furnace. The high temperatures in the radiant section provide major challenges to the achievement of the low NOx required for the next generation low-emitting power plants. Simulation tools were developed to provide guidance for the design of the coal-fired radiant heater, the slag screen, the dilution zone, the convective heater, and the SNCR zone. The development of the model was conducted under Tasks 2.1.2.1 and Tasks 2.1.2.4 of the Contract.

The original contract work plan would have used the tools developed to simulate the firing system for the HITAF, to come up with an optimized design for the radiant heater; to Model the Pilot Scale System to guide the pilot scale design and test plan and to provide data for the model validation; to the Commercial Plant HITAF; and to Model the Prototype HITAF.

In light of the contract modification to eliminate the task involving the simulation of the pilot plant and HITAF designs, the models on NO formation and carbon burnout have been tested against data from Imperial College and the International Flame Research Foundation and the improved formulation of the probability density functional (PDF) methods tested against the

University of Utah pilot scale data. The adequacy of the SNCR models has been tested with laboratory, pilot scale, and field data.

Finally, the applicability of the models for the original objectives of designing the HITAF and HIPPS repowering cycles is discussed by showing the success of the application of the improved model in parallel programs involving pulverized-coal fired systems.

Pulverized-Coal Modeling Basics

Accurately modeling the complex physical phenomena during pulverized-coal combustion requires models that couple turbulent fluid flow, chemical reaction, heat transfer and mass transfer. The governing equations are discretized and solved on a computational mesh. Since the computational expense of solving the turbulent reacting systems directly for all time and length scales is too great, various models have been developed. This section briefly describes the salient issues for mathematical modeling pulverized-coal combustion.

Gas Phase Fluid Dynamics

The description of the conservation of mass and momentum for a continuum fluid is given by the Navier-Stokes Equations. For the process of pulverized- coal combustion, which involves the liberation of coal off-gas into the gas phase, the equations of motion are given by

$$\frac{\partial}{\partial t}(\rho v_i)+\frac{\partial}{\partial x_j}(\rho v_i v_j)-\frac{\partial}{\partial x_j}\left[\mu\left(\frac{\partial v_i}{\partial x_j}+\frac{\partial v_j}{\partial x_i}\right)\right]\frac{\partial p}{\partial x_i}=\rho g_i+S_p^{V_i},\quad i=1,2,3 \qquad (1)$$

and

$$\frac{\partial \rho}{\partial t}+\frac{\partial}{\partial x_j}(\rho v_j)=S_p^m \qquad (2)$$

where S_p^k represents the k^{th} appropriate mass and momentum source terms. These source terms are required for the proper coupling of the gas phase fluid mechanics to the heterogeneous process of coal combustion.

In turbulent flows, the equations of motion are time averaged due to the inability to resolve the fine time and length scales that characterize the physical cascade of energy (Gatski et al., 1996; Bird et al, 1960). The variables are separated into a time mean and fluctuating part,

$$\phi=\bar{\phi}+\phi' \qquad (3)$$

This relation is substituted into the equations of motion to obtain a time averaged set of equations.

The separation of variables into a mean and fluctuating part give rise to cross terms known as Reynolds stresses (Bird et al., 1960). These newly created terms are an artifact of the Reynolds averaging procedure and must be adequately modeled. For example, consider the following convection term of the equations of motion: $\rho v_i v_j$. Substituting the properties of Eq. (3) and time averaging this quantity yields,

$$\overline{\rho v_i v_j} = \overline{\rho}\,\overline{v_i}\,\overline{v_j} + \overline{\rho v_i' v_j'} \tag{4}$$

where $\overline{\rho v_i' v_j'}$ is the Reynolds stress term. The proper modeling of the cross terms is known as the classic closure problem of turbulent fluid mechanics since there exists no account for these terms within the equations of motion. In variable-density flows, cross terms involving a fluctuating density appear. In such cases, use of Reynolds averaged Navier Stokes equations (RANS) typically involves neglecting these cross terms (Bird et al., 1960).

The technique of Favre averaged variables (Bilger, 1976; Favre, 1969) eliminates this complication by weighing the fluctuating quantities by the instantaneous density before the time averaging step,

$$\tilde{\phi} = \frac{\overline{\rho\phi}}{\overline{\rho}} \tag{5}$$

Therefore, upon Favre-averaging, for example, in the convection term in Eq. (1) the following cross terms arise:

$$\overline{\rho v_i v_j} = \overline{\rho}\,\tilde{v}_i \tilde{v}_j + \overline{\rho}\left(\widetilde{v''_j v''_i} \right) \tag{6}$$

where the tilde, ~, represents Favre-averaging. Upon Favre-averaging the equations of motion, triple correlations involving a variable density are eliminated and the resulting partial differential equations are identical to the RANS equations under the assumption of a non-fluctuating density field. In this coal combustor simulator, turbulent momentum closure is obtained using Bousinesq gradient diffusion with a nonlinear *k*-ε model (Harlow and Nakayama, 1968; Speziale, 1987) and the code is able to handle both Favre and Reynolds averaged properties. Details of the solution technique and turbulent model formulations may be found in Kumar (1999), Smith (1990) and Smoot and Smith (1985).

Progress Variable Turbulent Transport

In turbulent diffusion flame applications, the fuel and air are initially separated from each other. Traditionally, the fuel stream is designated as the primary stream while the secondary stream contains the oxidizing source. Assuming that the reaction process is micromixing limited, the chemical state of the particular node in the reactor domain can be calculated based on equilibrium considerations alone given the degree of "mixidness" (Smoot and Smith, 1985). Under the assumptions of equal mass diffusivities, individual transport equations for the species present in each stream can be replaced by a single transport scalar, *f*. This conserved mixture fraction progress variable is defined as

$$f = \frac{m_p}{m_p + m_s} \tag{7}$$

where m_p is the mass flow rate of primary stream and m_s is the mass flow rate of secondary stream. Therefore, the conserved mixture fraction progress variable *f* is the mass fraction of fluid

elements originating from the primary stream. From a locally calculated value of *f*, any conserved scalar can be calculated by

******* $$\hat{\beta} = f\hat{\beta}_p + (1-f)\hat{\beta}_s \tag{8}$$

where β_p and β_s represent the particular scalar value in pure primary and secondary stream, respectively.

Assuming Crocco similarity (Smoot and Smith, 1985), i.e., equal boundary conditions and like turbulent species diffusivities, the turbulent transport of the primary mixture fraction can be calculated from (Smoot and Smith, 1985)

$$\frac{\partial}{\partial x_j}\left(\overline{\rho}\tilde{v}_j\tilde{f} - \frac{\mu_e}{\sigma_f}\frac{\partial\tilde{f}}{\partial x_j}\right) = 0 \tag{9}$$

where σ_f is the turbulent Schmidt number and μ_e is the turbulent eddy viscosity. The turbulent Schmidt number is frequently taken to be 0.9 (Smoot and Smith; 1985).

Although any conserved scalar can be calculated given a unique local value of f using Eq. (8), in a turbulent environment the mixture fraction is fluctuating randomly about its mean value. Therefore, to properly account for the random fluctuations the statistics of the fluctuations must be resolved. Therefore, a subgrid mixing model must be implemented such that turbulent fluctuations and subgrid spatial in-homogeneities are properly resolved.

The mixing model used in this application is a presumed probability density function to describe the statistics of the turbulent micromixing. The PDF, therefore, is defined as

P(f)df = fraction of time interval in which f(t) is within the range (f, f+df). (10)

The integration of the PDF is, by definition, equal to unity,

$$\int_0^1 P(f)\,df = 1 \tag{11}$$

Moreover, the first moment of the PDF is defined as the mean value, $\bar{f}$

$$\int_0^1 fP(f)\,df = \bar{f} \tag{12}$$

and the second moment about the mean, or variance g_f, is defined as

$$\int_0^1 (f-\bar{f})^2 P(f)\,df = g_f \tag{13}$$

The specific shape of the individual PDF is defined by a mean and variance. The variance is calculated by a formulation from the *k*-ε turbulence model (Launder and Spalding, 1972; Bilger, 1975; Smoot and Smith, 1985) and is given by

$$\frac{\partial}{\partial x_j}\left(\overline{\rho}\widetilde{v}_j\widetilde{g}_f - \frac{\mu_e}{\sigma_{g_f}}\frac{\partial \widetilde{g}_f}{\partial x_j}\right) = C_{g_1}\mu_e\left(\frac{\partial}{\partial x_j}\widetilde{f}\right)^2 - \frac{C_{g_2}\overline{\rho}\varepsilon g_f}{k^2} \tag{14}$$

where σ_{gf} is the turbulent Schmidt number; C_{g1} and C_{g2} are the turbulent combustion model constants.[1]

Solving Eq. (9) and Eq. (14) together with the fluid mechanics model allows calculation of the mean flow field state space variables such as temperature, species concentration, equivalence ratio, etc., given a prescribed PDF shape. Therefore, mean variables, which are uniquely a function of the mixture fraction, can be obtained by convolution over the univariate PDF,

$$\widetilde{\beta} = \int_0^1 \beta(f)\widetilde{P}(f)df \tag{15}$$

For coal combustion applications, an analogous mixture fraction is defined that represents the mass fraction of fluid elements originating from the coal off-gas:

$$\eta = \frac{m_c}{m_c + m_p + m_s} \tag{16}$$

where m_c is the total mass of coal off-gas liberated from the combusting coal particle. The appropriate transport equation for the mean value of the coal off-gas and its variance are given by Eq. (17) and Eq. (18).

$$\frac{\partial}{\partial x_j}\left(\overline{\rho}\widetilde{v}_j\widetilde{\eta} - \frac{\mu_e}{\sigma_\eta}\frac{\partial \widetilde{\eta}}{\partial x_j}\right) = S_p^m \tag{17}$$

$$\frac{\partial}{\partial x_j}\left(\overline{\rho}\widetilde{v}_j\widetilde{g}_\eta - \frac{\mu_e}{\sigma_g}\frac{\partial \widetilde{g}}{\partial x_j}\right) = C_{g_1}\mu_e\left(\frac{\partial}{\partial x_j}\widetilde{\eta}\right)^2 - \frac{C_{g_2}\overline{\rho}\varepsilon\widetilde{g}_f}{k^2} \tag{18}$$

In coal combustion applications that involve both a primary and secondary stream, the mixture fraction *f* is not a conserved scalar and Eq. (9) is not the appropriate transport equation. A new transport equation is solved for the mixture fraction of primary stream, f_p, which is defined as

$$f_p = \frac{m_p}{m_p + m_s + m_c} \tag{19}$$

Assuming that f_p and η are statistically independent, the mean mixture fraction, *f* can be obtained by

[1]The turbulent Schmidt number is frequently taken to be 0.9 while the two constants are taken to be 2.8 and 1.92 (Smoot and Smith, 1985).

$$\tilde{f} = \frac{\tilde{f}_p}{1-\tilde{\eta}} \tag{20}$$

As before, any local property that is uniquely a function of *f* and η can be calculated by the following equation:

$$\beta = \beta_c \eta + (1-\eta)[f\beta_p + (1-f)\beta_s] \tag{21}$$

where the subscript *c* represents pure coal off-gas.

The time mean gas properties can be obtained, analogous as before in Eq. (15), by convolution over the joint PDF,

$$\tilde{\beta} = \int_0^1 \int_0^1 \beta(f,\eta)\tilde{P}(f,\eta)\,df\,d\eta \tag{22}$$

Methods and applications for the construction and application of a joint PDF are discussed later in this report. Assuming statistical independence (Smith, 1990; Smoot and Smith, 1985; Smith et al., 1980), Eq. (22) is written as

$$\tilde{\beta} = \int_0^1 \int_0^1 \beta(f,\eta)\tilde{P}(f)\tilde{P}(\eta)\,df\,d\eta \tag{23}$$

This formulation assumes that the joint PDF may be approximated by the product of the individual uncorrelated PDF in *f* and η.

Equilibrium Chemistry

For type B flames, which are characterized as micromixing limited, the chemical kinetic process can be removed in favor of local equilibrium chemistry that is obtained via a minimization of Gibbs free energy (Smoot and Smith, 1985). In other words, the micromixing limited assumption implies that the turbulent time scale is much larger than the reaction rate time scale. Therefore, as soon as molecules coalesce, they subsequently react. Although this is not true for trace nonequilibrium species such as the oxides of nitrogen and sulphur, it is a reasonable approximation for major species in turbulent coal-combustion applications (Smoot and Smith, 1985).

For a Gibbs free energy minimization technique, only the energy state, elemental composition and pressure are required to specify the thermodynamic properties of the system. Given an adiabatic system, the energy state is uniquely a function of the two local mixture fractions calculated,

$$h_a = h_c \eta + (1-\eta)[fh_p + (1-f)h_s] \tag{24}$$

For nonadiabatic operations, however, an energy transport equation must be solved and proper Favre-averaged properties are obtained through the convolution over the joint-compositional and enthalpy PDF,

$$\widetilde{\beta} = \int_{0}^{1}\int_{0}^{1}\int_{0}^{1} \beta(f,\eta,h)\,\widetilde{P}(f,\eta,h)\,df\,d\eta\,dh \qquad (25)$$

In practice, however, the enthalpy appearing in the joint PDF, Eq. (25), is replaced by the mean residual enthalpy that is defined as

$$h_r = h - h_a \qquad (26)$$

Moreover, the fluctuations of the residual enthalpy are assumed to be negligible and the joint PDF is written as

$$P(f,\eta,h) = P\left(f,\eta,\widetilde{h}_r\right) \qquad (27)$$

Details of the solution of the energy equation and further exposition on the modeling process of nonadiabatic processes may be found at Smoot and Smith (1985) and Smith (1990).

In the following section, the choice of PDF and assumptions associated with constructing the joint PDF are presented.

Prescribed PDF Shape and Joint PDF Construction

In the previous sections, the subgrid mixing model was presented. In coal combustion simulations that include a primary and secondary stream, mean value state space variables are obtained via the convolution of the state space function over the joint PDF, Eq. (22). The prescribed shape of the PDF and the construction of the joint PDF are presented below.

Clipped Gaussian PDF

In turbulent systems, there can exist spatial regions over time that display a finite probability of pure streams. This intermittency is directly caused by eddies of unmixed gasses passing through a given control volume. Therefore, the probability of having an eddy of pure stream *i* passing through position x is defined as the intermittency of stream *i* at position x. The chosen PDF shape must include a formulation to account for this physical phenomena.

The clipped Gaussian PDF formulation has been used extensively throughout the combustion field for many years (Smoot and Smith, 1985; Smith et al., 1980; Kent and Bilger, 1971). Recall, however, that the range of a continuous Gaussian distribution is between -∞ and ∞ (Abramowitz and Stegun, 1970). The clipped Gaussian formulation assumes that the intermittency of stream *i* can be represented by the portions of the integrals that are beyond the physical limits of *f* and η (Smoot and Smith, 1985; Smith et al., 1980). Therefore, the continuous PDF can be expressed as

$$P(f) = \alpha_p + \alpha_s + P(f)\Big|_{0+}^{1-} \qquad (28)$$

where α_p and α_s are the intermittency of the primary and secondary streams, respectively, and are defined as

$$\alpha_p = \int_{1+}^{\infty} P(f)\,df \qquad (29)$$

and

$$\alpha_s = \int_{-\infty}^{0-} P(f)\,df \tag{30}$$

Likewise, the intermittency of coal off-gas, α_c and intermittency of streams other than coal off-gas , α_I, are defined as

$$\alpha_c = \int_{1^+}^{\infty} P(\eta)\,d\eta \tag{31}$$

and

$$\alpha_I = \int_{-\infty}^{0^-} P(\eta)\,d\eta \tag{32}$$

The process of clipping the continuous Gaussian distribution artificially shifts the first moment of the PDF and the second moment about the mean. The mean and variance obtained by the appropriate turbulent PDE must, therefore, be corrected.

Table 6-1 represents the required parameters for the mathematical description of constructing the clipped Gaussian PDF for both *f* and η. In practice, a table is constructed such that a properly shifted mean and variance is interpolated during the simulation, given the calculated mean and variance through the turbulent progress variable mixture fraction PDE.

β-PDF

Since the physical range of the mixture fraction is the same as the continuous portion of the β-PDF, the process of clipping the PDF, as described in the previous section, is moot. Intermittency is a natural feature of the β-PDF and occurs when any distribution parameter is less than unity (Chen et al., 1994). The one-dimensional Favre-averaged β-PDF is given by:

$$\tilde{P}(\eta) = \frac{\Gamma(a_1 + a_2)}{\Gamma(a_1)\ (a_2)} \eta^{a_1 - 1}(1-\eta)^{a_2 - 1} \tag{33}$$

where the distribution parameters a_1 and a_2 are defined as

$$a_1 = \tilde{\eta}\left(\frac{\tilde{\eta}(1-\tilde{\eta})}{\tilde{g}_\eta} - 1 \right) \tag{34}$$

and

$$a_2 = (1 - \tilde{\eta})\left(\frac{\tilde{\eta}(1-\tilde{\eta})}{\tilde{g}_\eta} - 1 \right) \tag{35}$$

Table 6-1
Parameters for the Clipped Gaussian Probability Density Function

$$P(\phi) = \frac{1}{\sqrt{2\pi G_\phi}} \exp\left\{\frac{-Z_\phi^2}{2}\right\}$$

$$\alpha = \frac{1}{\sqrt{2\pi}} \int_L^U \exp\left\{\frac{-Z_\phi^2}{2}\right\} dZ_\phi$$

Intermittency	ϕ	U	L	Z
α_p	f	$+\infty$	$(1-F)/\sqrt{G_f}$	$(f-F)/\sqrt{G_f}$
α_s	f	$-F/\sqrt{G_f}$	$-\infty$	$(f-F)/\sqrt{G_f}$
α_c	η	$+\infty$	$(1-H)/\sqrt{G_\eta}$	$(\eta-H)/\sqrt{G_\eta}$
α_I	η	$-H/\sqrt{G_\eta}$	$-\infty$	$(\eta-H)/\sqrt{G_\eta}$

With F and G_f obtained from

$$\tilde{f} = \alpha_p + \frac{1}{\sqrt{2\pi G_f}} \int_{0^+}^{1^-} f \exp\left\{\frac{-(f-F)^2}{2G_f}\right\} df$$

$$\tilde{g}_f = \alpha_c - \tilde{f}^2 + \frac{1}{\sqrt{2\pi G_f}} \int_{0^+}^{1^-} f^2 \exp\left\{\frac{-(f-F)^2}{2G_f}\right\} df$$

With H and $G\eta$ obtained from

$$\tilde{\eta} = \alpha_c + \frac{1}{\sqrt{2\pi G_\eta}} \int_{0^+}^{1^-} \eta \exp\left\{\frac{-(\eta-H)^2}{2G_\eta}\right\} d\eta$$

$$\tilde{g}_\eta = \alpha_c - \tilde{\eta}^2 + \frac{1}{\sqrt{2\pi G_\eta}} \int_{0^+}^{1^-} \eta^2 \exp\left\{\frac{-(\eta-H)^2}{2G_\eta}\right\} d\eta$$

The β function is extensively used (Rawat, 1997; Coelho and Carvalho, 1995; Baurle et al., 1994; Chen et al., 1994) and is the shape employed in such commercial codes as FLUENT.

Joint PDF Convolution

As described in Eq. (22), the time mean gas properties can be obtained by convolution over the joint PDF. In the original formulation of Smith et al. (1980) it was assumed that the joint PDF of *f* and η are not correlated and can, therefore, be written as

$$\mathrm{P}(\mathrm{f},\eta) = \mathrm{P}(\mathrm{f})\mathrm{P}(\eta) \tag{36}$$

Upon substitution of Eq. (36) into Eq. (22) and using the definition of the clipped Gaussian PDF as given in Eq. (28), the mean gas properties can be obtained by

$$\begin{aligned}\widetilde{\beta}(\mathrm{f},\eta) = \alpha_c\beta_c + \alpha_I\Bigg[\alpha_p\beta_p + \alpha_s\beta_s + \int_{0+}^{1-}\beta(\mathrm{f},\eta)\widetilde{\mathrm{P}}(\mathrm{f})\,\mathrm{df}\Bigg] + \alpha_p\int_{0+}^{1-}\beta(1,\eta)\widetilde{\mathrm{P}}(\eta)\,\mathrm{d}\eta \\ + \alpha_s\int_{0+}^{1-}\beta(0,\eta)\widetilde{\mathrm{P}}(\eta)\,\mathrm{d}\eta + \int_{0+0+}^{1-1-}\beta(\mathrm{f},\eta)\widetilde{\mathrm{P}}(\mathrm{f})\widetilde{\mathrm{P}}(\eta)\,\mathrm{df}\,\mathrm{d}\eta\end{aligned} \tag{37}$$

In 1991, Girimaji developed a general process of constructing a joint β-PDF that has been used by various researchers (Rawat, 1997; Baurle et al., 1994). This concept and formulation is described in detail later in this report.

Particle Cloud Tracking Technique

During the process of heterogeneous pulverized-coal combustion, combustible material is released from the particle to the gas phase. Accurate simulation of the turbulent particle dispersion is necessary to adequately describe the placing of combustible coal off-gas mass source terms on the Eulerian mesh. Coupling between the heterogeneous phase and the gas phase is accomplished by including particle source/sink terms as described in Eq. (1) and Eq. (2).

The approach used in this simulation code is to solve a Lagrangian equation of motion for an ensemble of particles that describes the mean trajectory and variance for a cloud of particles. As the ensemble of particles pass through the Eulerian mesh, the coal off-gas mass source terms are accumulated at the respective mesh node. This mathematical description is equivalent to the particle source in cell technique as outlined by Crowe et al. (1977).

Mehrotra (1998) implemented a stochastic particle dispersion model within the combustion simulator using Monte Carlo simulations to account for particle dispersion effects such as inertia, crossing trajectories and the continuity effect. For computational efficiency, however, a Lagrangian cloud dispersion model has been developed (Baxter, 1989) and implemented within a three-dimensional code by Jain (1997).

A particle cloud is characterized by a mean position and a variance. Particles within a cloud at a given mean residence time are assumed to share uniform physical characteristics such as diameter, temperature and velocity. The mean or expected value of the particle cloud position can be computed from the ensemble averaged particle velocity as defined by an equation of motion,

$$\langle x_i(t)\rangle = \int_0^t \langle V_i(\tau)\rangle d\tau + \langle x_i(0)\rangle \tag{38}$$

where the angled brackets, $\langle\ \rangle$, represent ensemble average properties.

The ensemble particle velocity is simply obtained via Newton's second law of motion. For coal combustion applications, the appropriate forces are only aerodynamic drag and gravity. Additional forces such as virtual mass, thrust, Magnus, Basset, Saffman, etc. contribute less than 1% and are therefore neglected (Jain, 1997). Thus, the governing equation for the mean location of the cloud is

$$\frac{d}{dt}\langle V_i\rangle = \frac{3C_D\rho_f}{4\rho_p d_p}\left(\langle U_i\rangle - \langle V_i\rangle\right) + \left(1 - \frac{\rho_f}{\rho_p}\right) g_i \tag{39}$$

where U_i, V_i , ρ_f , ρ_p and d_p are the fluid and particle velocities, the fluid and particle densities and the particle diameter, respectively. The drag coefficient is defined as (Wallis, 1969)

$$C_D = \frac{24}{Re}\left(1 + 0.15\, Re_p^{0.687}\right) \tag{40}$$

where Re_p, the particle Reynolds number, is given by

$$Re_p = \frac{d_p |V - U| \rho_f}{\mu_f} \tag{41}$$

Each Lagrangian cloud trajectory is computed through the computational flow field by solving the set of ordinary differential equations governing the particle motion, Eq. (38) and Eq. (39) along with the relationships described in Eq. (40) and Eq. (41).

Particle Dispersion

The variance, or second moment of the particle position PDF that defines the dispersion or spread of particles can be related to the particle velocity correlation function, R_{ij}^p, of the cloud of particles and is given by

$$\sigma_{ij} = 2\int_0^t (t - \tau) R_{ij}^p(\tau)\, d\tau \tag{42}$$

The particle velocity correlation function is defined as the rate at which the instantaneous velocity loses correlation with time. Wang (1990) has developed a method to determine the particle velocity correlation function by relating it to the fluid particle correlation function. For more detailed information regarding the Lagrangian cloud dispersion model, the reader is referred to Jain (1997).

Particle Continuity Equations

As described in the previous section, the coupling of heterogeneous coal combustion to the gas phase fluid motion is accomplished by accumulating mass source terms on the Eulerian mesh (Crowe et al., 1977). Therefore, along with the solution of the particle equation of motion, a number of continuity equations are solved for each coal component. A continuity equation is solved for each component of the coal that includes: liquid, coal, char, ash and volatiles. The continuity equations for each coal component are of the following form:

$$\frac{d\alpha_j}{dt} = r_j \tag{43}$$

where *j* represents the respective component. The right hand side of Eq. (43) simply represents the rate of depletion of the particular component. The rate of mass depletion of a coal particle during pulverized-coal combustions is defined by two major reactions, devolatilization and char oxidation.

Devolatilization represents the process by which raw coal is converted to residual char by the release of heavy tars and volatiles by one or more reactions. The physical process of devolatilization has been studied and reaction rates and volatile yields, Y_j , have been determined for a wide range of coals (Solomon et al., 1992; Kobayashi, et al., 1977; Ubhayakar et al., 1977).

It is imperative that at least a two-step mechanism is used to insure particle history effects through two competing devolatilization reaction pathways. Therefore, a unique overall volatile yield can be calculated given a particle time/temperature history. In contrast, the use of one devolatilization reaction pathway insures a constant split between char and volatiles.

The second main pathway for the release of coal off-gas to the gas phase is through the process of char oxidation. Char reacts heterogeneously, after diffusion of an oxidant to the particle surface, by one or more reactions. The process of char oxidation is, in general, assumed to be modeled by two rate limiting steps: 1) diffusion of oxidant to the surface of the char followed by 2) heterogeneous reaction. Details of the char oxidation rate laws are given later in this report.

As noted earlier, an ODE describing the mass of liquid evolved from the coal particle is solved and is given by the classic expression,

$$\text{liquid} \rightarrow \text{vapor}. \tag{44}$$

Moreover, it is assumed that the rate of particle mass depletion due to ash loss is zero, i.e. the mass of ash is constant throughout the Lagrangian cloud trajectory.

Eulerian Particle Source Terms

As described earlier, the particle equation of motion and continuity equations for each coal component are calculated in a Lagrangian reference frame. The particle source terms are accumulated at the Eulerian mesh and used in the gas phase continuity and motion equations, Eq. (1) and Eq. (2). The particle source term, $S^{\varphi}_{p,ijk}$, is obtained by summing the differences in the property ϕ of all particles that traverse the particular Eulerian cell at location x_i. This sum is weighted by the particle position PDF, $P(x_i, t)$. The weight function accounts for the number of

particles at a given computational volume within the overall cloud PDF. The particle source term for property, ϕ is spatially varying and is defined by

$$S_{p,ijk} = \int_{-\infty V}^{+\infty} \dot{q}\, r_p^{\phi}\, W(x_i, t)\, dV\, dt \qquad (45)$$

where $\dot{q}$ is the particle number flow rate, r_p^{ϕ} is the rate of change of particle property ϕ, e.g. overall mass, char mass, etc. and $W(x_i, t)$ is the weight function. The time integration bounds are formally written for all time, $-\infty$ to $+\infty$.

Particle Energy Equation

A particle energy conservation equation in Lagrangian form is solved to obtain the particle temperature used in the devolatilization and char oxidation reaction rates. The particle energy equation accounts for radiation to the surface of the particle, Q_{r_j}; the convection and conduction from the particle to the gas phase, Q_j; and the enthalpy loss to the gas phase by transfer of mass due to particle reaction, $r_j h_{g_j}$,

$$\frac{d}{dt}(\alpha_j h_j) = Q_{r_j} - Q_j - r_j h_{g_j} \qquad (46)$$

Nitrogen Oxide Submodel for Pulverized-Coal Flames

Although the instantaneous chemistry assumption outlined previously is appropriate for most major species in pulverized-coal flames, this technique is not applicable to trace nonequilibrium species such as nitrogen oxide (Smoot and Smith, 1985). A typical homogeneous reaction rate time scale for the formation and destruction of nitric oxide is on the order of 1 ms while turbulent time scales in pulverized-coal furnaces are within the 10 ms range (Smoot and Smith, 1985). The concept of a local instantaneous equilibrium state, therefore, is not appropriate for nitrogen oxide pollutant formation simulations. Successful nitrogen oxide simulations require the coupling of a physical micromixing model to a detailed chemical kinetic mechanism.

Detailed chemical kinetic sets exist for the formation and destruction of nitric oxide in various types of flames (Mitchell, 1998; Miller and Bowman, 1989; Saliman and Hanson, 1980; Heap et al., 1977). The use of a detailed chemical kinetic reaction mechanism requires solving individual transport equations for each of the intermediate and major species involved within the entire reaction mechanism. To calculate the mass fraction of any species, an appropriate conservation equation can easily be derived. Such a transport equation for species *i* is given by Eq. (47):

$$\frac{\partial}{\partial t}(\omega_i \rho) + \nabla \cdot (\omega_i \rho v) = W_i \qquad (47)$$

Equation (47) is equally valid for a turbulent reacting system; however, in turbulent systems, proper consideration for fluctuating variables must be included. This is accomplished by decomposing each of the fluctuating variables into their respective mean and fluctuating

components. The resulting equation is then time averaged to obtain an equation for the time mean mass fraction of species *i*.

Upon time averaging Eq. (47) , care must be taken in obtaining the proper overall time mean rate of reaction for species *i*. To illustrate this principle, take for example the following elementary reaction between species A and B, to yield species C:

$$A + B \rightarrow C \tag{48}$$

The instantaneous rate of reaction assuming an Arrhenius rate law is given by Eq. (49).

$$w_A = k_0 \rho^2 \omega_A \omega_B \exp\left(\frac{-E}{RT}\right) \tag{49}$$

Although this rate expression is fully valid for determining the instantaneous rate of reaction for species A in both laminar and turbulent flows, obtaining the time mean rate of reaction again requires a Reynolds decomposition for each fluctuating variable. The time averaged rate of reaction is not simply the product of individually averaged variables as shown in Eq. (50) .

$$\overline{w}_A = \overline{k_0 \rho^2 \omega_A \omega_B \exp\left(\frac{-E}{RT}\right)} \neq \overline{k}_0 \overline{\rho}^2 \overline{\omega}_A \overline{\omega}_B \exp\left(\frac{-E}{R\overline{T}}\right) \tag{50}$$

Instead, after proper Reynolds decomposition and time averaging, we obtain:

$$\overline{w}_A = \overline{k}_0 \overline{\rho}^2 \overline{\omega}_A \overline{\omega}_B \exp\left(\frac{-E}{R\overline{T}}\right)\left[1 + \frac{\overline{\rho'^2}}{\overline{\rho}^2} + \frac{\overline{\omega'_A \omega'_B}}{\overline{\omega}_A \overline{\omega}_B} + \frac{2\overline{\rho' \omega'_A}}{\overline{\rho}\,\overline{\omega}_A} + \frac{2\overline{\rho' \omega'_B}}{\overline{\rho}\,\overline{\omega}_B} + \cdots\right] \tag{51}$$

Not shown are the terms arising from a fluctuating temperature and the triple correlations that appear in the fluctuating variables: ω_A , ω_B , and ρ. For a *n*-dimensional reaction set, *n* time-averaged rate equations must appear. For the extremely large reaction set of nitrogen oxide formation and destruction[2], a more computationally feasible technique must be explored.

One such technique was developed by Bilger (1977) and was implemented within a nitrogen oxide pulverized-coal simulation package by Smith *et al*. (1982) whereby the mean reaction rates are obtained via the convolution of the instantaneous rate equation over the joint PDF. The time mean reaction rate for any reaction *i* is

$$\overline{w}_i = \overline{\rho} \int_{f_1} \int_{f_2} \cdots \int_{f_{N-1}} \frac{w_i\left(f_1, f_2, \ldots, f_{N-1}, \tilde{h}_r\right)}{\rho\left(f_1, f_2, \ldots, f_{N-1}, \tilde{h}_r\right)} \tilde{P}\left(f_1, f_2, \ldots, f_{N-1}, \tilde{h}_r\right) df_1 df_2 \ldots df_{N-1} \tag{52}$$

where w_i is the instantaneous rate, ρ is the instantaneous density, $\tilde{P}$ is the Favre-averaged joint-probability distribution function and N is the total number of distinguishable mixture fraction progress variables. This technique assumes that the reaction rates are strictly a function of local stoichiometry and that a suitable shape of the PDF is available. Smith et al. (1985, 1982, 1980)

[2] Detailed chemical reaction mechanisms can approach well over 200 reactions.

further assumed that the joint-PDF appearing in Eq. (52) can be written as the product of all individual probability distribution functions,

$$\widetilde{P}(f_1, f_2, \ldots, f_{N-1}) = \prod_{i=1}^{N-1} \widetilde{P}(f_i) \qquad (53)$$

where N is the total number of physical streams and f_i is a particular mixture fraction of stream i.

Since rates of reactions are given as a function of species concentration and not overall mixture fractions, another relationship is required to evaluate w_i in Eq. (52). The specific technique used is outlined in detail below.

The nitrogen oxide submodel is cast within a postprocessor simulation package (Smith et al., 1982). The composition of nitrogen oxide in pulverized-coal furnaces is frequently within the parts per million range and does not appreciably affect major flow field variables such as velocity and state space variables, e.g., gas phase temperature and major species concentration (Smoot and Smith, 1985). The nitric oxide model simulation, therefore, can be "decoupled" from the main flow field simulation and is run after the main combustion code has sufficiently converged (Smith, 1990; Smoot and Smith, 1985; Smith et al., 1982).

NO Formation Mechanism for Pulverized-Coal Applications

Although the prescribed PDF approach in calculating time mean reaction rates is extendable to a *n*-dimensional reaction set, this technique is computationally intensive. The use of a detailed chemical reaction mechanism has been successfully demonstrated in hydrocarbon turbulent diffusion flames (Rawat, 1997) using the technique of Intrinsic Low Dimensional Manifolds, ILDM (Maas and Pope, 1994). The ILDM implemented by Rawat (1997) has not been applied to coal combustion simulations. In hydrocarbon flames, the chemical composition of the entering fuel is clearly known. In contrast, during coal combustion the knowledge of the exact chemical species liberated during coal devolatilization and char oxidation is unclear. Several coal devolatilization studies propose species evolution rates; however, these models have not been coupled to a detailed chemical reaction mechanism (Niksa, 1994; Niksa, 1991; Solomon et al., 1991).

Although the use of a detailed chemical reaction mechanism is unavailable in coal combustion simulations, global reaction rates have been developed for three primary reaction pathways (Fennimore, 1976; DeSoete, 1975; Zeldovich, 1947). The three primary reaction pathways of nitric oxide formation and destruction are: thermal, prompt, and fuel NO. Therefore, the entire homogeneous reaction mechanism for nitrogen oxide production in pulverized coal flames can be distilled to a few, key global rates. This dramatically reduces the number of species transport equations that need to be solved and also reduces the number of individual time-mean reaction rates that need to be computed via convolution over the joint PDF. The salient elements of the global nitrogen oxide mechanism applicable to pulverized-coal combustion will now be described.

Thermal NO

Thermal NO is the pathway whereby molecular nitrogen, originating from the primary and secondary air source, is oxidized by the incoming oxygen at relatively high temperatures (Miller

and Bowman, 1989). Thermal NO is modeled by the widely used and accepted Zeldovich two-step mechanism (Sawyer, 1981; Zeldovich et al., 1947).

$$N_2 + O = NO + N \tag{54}$$

$$N + O_2 = NO + O \tag{55}$$

Newell and Shaded (1971) found that these two principle reaction pathways accurately accounted for thermal NO production in both fuel rich and fuel lean combustion flame conditions. Furthermore, Lavoie et al. (1970) proposed that in addition to the Zeldovich pathways, the following reaction:

$$N + OH = NO + H \tag{56}$$

could be included for further accuracy of thermal NO production for fuel-rich combustion flame conditions. These combined reactions are known as the extended Zeldovich mechanism. Reaction rate constants have been determined for each of the above reactions by the groups of Hanson and Salmon (1984), in addition to Baulch et al. (1973).

The extended Zeldovich mechanism typically shows good agreement with experimental data when measured oxygen radical concentrations are available (Bowman, 1973). However, when detailed measurements of oxygen radicals are not available (as is the case with most practical simulation efforts) the concentration of oxygen radicals must be calculated.

The combustion code used in this simulation study provides equilibrium compositions of oxygen and hydroxide radicals (Jain, 1998, Mehrotra, 1998; Smoot and Smith, 1985; Smith et al., 1980). In fact, nonequilibrium effects exist over a wide range of combustion temperatures and thermal NO is frequently under predicted when only equilibrium chemistry is used (Miller and Bowman, 1989; Drake et al., 1987; Bowman, 1973). Therefore, the ability to accurately calculate thermal NO is limited by the ability to predict non-equilibrium compositions of oxygen and hydroxide radicals (Miller and Bowman, 1989; Drake et al., 1987; Bowman, 1973).

Under the assumptions of steady state for the nitrogen atom in reactions Eq. (54) through Eq. (56), the rate of nitric oxide is given by:

$$\frac{d}{dt}[NO] = \frac{2k_1[O][N_2]}{k_{-1}[NO]}\left\{1 - \frac{k_{-1}[NO]}{k_2[O_2] + k_3[OH]}\left(\frac{k_{-2}[NO]}{k_1[N_2]} + \frac{k_{-3}[NO][H]}{k_3[O][N_2]}\right)\right\} \tag{57}$$

Assuming that the reaction:

$$O + OH = O_2 + H \tag{58}$$

is fast compared to Eq. (54-56), the overall nitric oxide rate can be expressed as (Bowman, 1975):

$$\frac{d}{dt}[NO] = 2[O]\left\{\frac{k_1[N_2] - \frac{k_{-1}k_{-2}[NO]^2}{k_2[O_2]}}{1 + \frac{k_{-1}[NO]}{k_2[O_2] + k_3[OH]}}\right\} \tag{59}$$

Limited success has been reported based on the assumption that when nitric oxide is far from equilibrium, only the forward process of the rate limiting step, Eq. (54), is important (Quan, et al., 1973).

$$\frac{d}{dt}[NO] = 2k_1[N_2][O] \tag{60}$$

Again, the difficulty in modeling thermal nitric oxide is not in the inability to understand the chemical mechanism, rather in calculating the appropriate species concentrations of O and OH appearing in Eq. (59) (Dupont, 1993).

In fuel-lean secondary combustion zones, the concentration of oxygen radicals can be assumed to be in equilibrium with O_2 (Boardman and Smoot, 1988; Caretto et al., 1968),

$$O_2 + M = O + O + M \tag{61}$$

where M is an inert chain propagating radical. Hence, the concentration of O atoms is

$$[O] = \{K_{61}[O_2]\}^{1/2} \tag{62}$$

where K_{61} is the equilibrium constant defined as the ratio of the forward to reverse reaction rate constants, k_{61}/k_{-61}.

In regions of hydrocarbon consumption, Eq. (62) significantly under predicts the concentration of oxygen. Following the work of Iverach et al. (1973), the following reactions are assumed to be close to equilibrium:

$$H + O_2 = OH + O \tag{63}$$

$$CO + OH = CO_2 + H \tag{64}$$

yielding:

$$[O] = \frac{K_{63}K_{64}[O_2][CO]}{[CO_2]} \tag{65}$$

The concentration of the hydroxide radical can also be obtained using a partial equilibrium assumption (Sarofim and Pohl, 1973; Schott, 1960). In this approach, the radical concentrations of O and OH can be related to the concentration of the stable species.

$$H + O_2 = OH + O \tag{66}$$

$$O + H_2 = OH + H \tag{67}$$

$$H_2 + OH = H_2O + H \quad (68)$$

$$CO + OH = CO_2 + H \quad (69)$$

Again, assuming Eq. (66) through Eq. (68) are significantly faster than Eq. 69, the system is in partial equilibrium and the OH radical concentration can be given by,

$$[OH] = \left\{ \frac{K_{66} K_{67} K_{69}}{K_{68}} \frac{[O_2][CO][H_2O]}{[CO_2]} \right\}^{1/2} \quad (70)$$

As indicated earlier, the concentration of oxygen and hydroxide radicals can be obtained from equilibrium considerations alone. As this assumption has been shown to frequently under predict thermal NO, the options described in Eq. (62), Eq. (65) and Eq. (70) are preferred.

Since most pulverized-coal applications operate under fuel rich environments and within the lower temperature range of 1600 - 1800 K, the extended Zeldovich thermal NO pathway does not appear to be a significant source of nitric oxide (Wendt, 1980; Hayhurst and Vice, 1980). In a study conducted by Milne and Beachy (1977), argon was substituted for nitrogen within a premixed coal burner. Nitric oxide measurements with and without the presence of molecular nitrogen did not appreciably change indicating the overall contribution of thermal NO in pulverized coal-combustion systems can be small.

Modern pulverized-coal nitric oxide modeling efforts as recent as 1999 often neglect thermal NO (Visona and Stanmore, 1999 and 1996; Antifora et al., 1997). A past study does indicate; however, that for a stoichiometric ratio of 1.2, approximately 15% of the total nitric oxide can be attributed to the thermal NO pathway (Pershing et al., 1975). This study also showed that at a stoichiometric ratio of 1.0, nearly no thermal nitric oxide was produced. In an effort to retain all possible production pathways of nitrogen oxide, regardless of how small the potential contribution, the current simulation does include the extended Zeldovich thermal NO mechanism.

Prompt NO

During the course of devolatilization, tiny fragments of hydrocarbons from the parent coal can react with molecular nitrogen to form nitric oxide (Fenimore, 1976). Fenimore, and numerous others have shown the predominance of prompt nitric oxide is formed due to reactions between molecular nitrogen and hydrocarbon radicals (Hayhurst and Vince, 1980; Fenimore, 1976; Hayhurst and Mclean, 1974; Iverich et al., 1973). Hydrocarbon radicals and nitrogen react to form cyano-compounds that can be converted to nitric oxide via the DeSeote fuel nitric oxide pathway, to be discussed below (DeSoete, 1975).

Prompt NO is usually prevalent in fuel rich hydrocarbon flames since the mechanism requires hydrocarbon fragments to initiate the reaction pathway. Moreover, in most practical pulverized coal flames, prompt NO accounts for approximately 5% of the total nitric oxide formed (Hayhurst and Vince, 1980). Due to the potentially small overall prompt NO contribution, past and present nitric oxide models have ignored its contribution (Visona and Stanmore, 1996 and 1999; Smoot and Smith, 1985).

New low NO_x furnace designs may necessitate utilization of a prompt NO mechanism. One such nitrogen oxide abatement strategy technique is known as staging whereby fuel-rich zones are created by introducing only a fraction of the combustion air through the main burners (Wendt, 1980). The residual air, as required for complete combustion, is introduced downstream. This constructed fuel-rich environment allows partial oxidation of fuel and presumably favors the conversion of fuel-bound nitrogenous species to the formation of N_2 rather than to NO. The next stage is that of a fuel-lean environment where the lower temperatures potentially inhibit thermal NO formation. Wendt (1980) showed that the use of staging dramatically reduced the amount of nitrogen oxide emission and the principle has been applied with some success to utility boilers as early as 1976 (LaChapelle, 1976). Staged combustion techniques can, therefore, favor the formation of prompt NO.

Fenimore (1976) originally suggested a prompt NO reaction pathway whereby hydrocarbon radicals and molecular nitrogen form the nitric oxide precursor cyano-compound, hydrogen cyanide.

$$CH_i + N_2 = HCN + N \quad (71)$$

Blauwens et al. (1977) also postulated that another path existed for the production of HCN from hydrocarbon radicals:

$$CH_2 + N_2 = HCN + NH \quad (72)$$

Miller and Bowman (1989) suggested that due to the 1,3 hydrogen shift from nitrogen to carbon, an intrinsic energy barrier exists and Eq. (72) is commonly ignored.

Fuel NO

Fuel NO is the process by which devolatilized nitrogen is oxidized to nitrogen oxide and generally accounts for approximately 60-80% of the total nitrogen oxide formed in pulverized-coal flames (Smoot and Smith, 1985). Nitrogen that is released from the coal during the devolatilization process is usually assumed to be quickly converted to HCN (Fenimore, 1976; DeSoete, 1975). Hydrogen cyanide can decay to ammonia species that react through competing pathways to either NO or N_2 (Fenimore, 1979; Levy, 1980; Rees et al., 1981). Various elementary reactions have been proposed to describe the salient features of the decay of HCN (Caretto, 1976; Levy, 1980); however, it is generally accepted that the rate expression proposed by DeSoete (1975) adequately describes the decay of HCN to nitric oxide.

$$\text{Coal (fuel N)} \rightarrow HCN \quad (73)$$

$$HCN + O_2 \rightarrow NO + \ldots \quad (74)$$

$$HCN + NO \rightarrow N_2 + \ldots \quad (75)$$

DeSoete, in 1975, further provided that the order of the reaction involving HCN and O_2, Eq. (74), is dependent on the local oxygen mole fraction. The reaction order of oxygen in Eq. (74) is 0.0 for mole fractions of oxygen greater than 18,000 ppm and 1.0 for oxygen mole fractions less than 2500 ppm. For values in between this range, a cubic spline interpolation of the DeSoete data

set is used to determine the order of Eq. (74)[3]. Although DeSoete's study was produced in 1975, to this day his mechanism represents the predominant choice of fuel nitric oxide simulation studies (Visona and Stanmore, 1999 and 1996; Antifora et al., 1997; Abbas et al., 1996; Eddings et al., 1994; Smoot and Smith, 1985; Smith et al., 1982)

Char-Nitrogen NO Formation

Char nitrogen can account for approximately 25% of the overall fuel nitric oxide produced in practical coal flames (Pershing and Wendt, 1979). The production of nitrogen oxide from char-nitrogen can not be neglected. The exact mechanism of char-nitrogen conversion to the oxides of nitrogen, however, is unresolved. The ongoing debate rests on whether the process of nitric oxide production attributed to char-nitrogen conversion occurs heterogeneously at the surface of the char particle or if HCN is released from the char matrix and subsequently enters the homogeneous NO pathway.

Many researchers believe the process of nitrogen oxide production occurs analogously to that of char oxidation (DeSoete et al., 1997; Johnson, 1994; Goel et al., 1994). They propose that nitrogen in the char is oxidized to NO where it can enter the gas phase and be reduced to N_2 and/or N_2O (DeSoete et al., 1997; Johnson, 1994; Goel et al., 1994).

Goel and Sarofim (1997) propose the formation of a surface complex between oxygen and char-nitrogen that can be split to NO or can be hydrolyzed in the presence of water vapor to form HCN. Amand (1994) simply suggest that HCN is produced by a heterogeneous reaction of the char matrix with oxygen. Visona and Stanmore (1999) recently reported two equally successful modeling procedures in dealing with the homogeneous vs. heterogeneous char-nitrogen conversion to the oxides of nitrogen debate. In their first approach, all of the char-nitrogen is assumed to be oxidized to nitric oxide and subject to the surface reduction reaction of Chan et al. (1983). The second approach tested was the specification of all char-nitrogen to evolve as HCN which is subject to the gas-phase reaction process. Both approaches fit equally well with the experimental data. Winter et al. (1996) propose that both paths, indeed, occur. For a more detailed exposition on this topic, the reader is referred to Spinti (1997).

Char-Nitrogen NO Destruction

Nitric oxide can be reduced at the surface of char (Levy et al., 1981; Chan et al., 1983). Recent theoretical work has indicated that nitric oxide reduction can potentially occur at the surface of soot (Ostberg et al., 1998). Wang et al. (1994) suggest that both surface area and the intrinsic reactivity of the char are important in determining the reduction of NO on carbon during combustion. Simulation studies conducted by Visona and Stanmore (1999, 1996) that incorporate heterogeneous reduction of NO within the surface of a pore have shown success. In this study, an effectiveness factor (as developed for porous solids) is incorporated within the char/NO reduction mechanism of Chan et al. (1983).

There is a community of investigators who propose that nitric oxide destruction can occur by a heterogeneous char-nitrogen process to yield N_2O in the presence of O_2 (Goel and Sarofim, 1995; Goel et al., 1994). The former generation NO model (Smith et al., 1982), which was based on the axisymetric combustion simulator JASPER, used the heterogeneous reduction rate of nitric oxide that has been reported in the literature by Levy et al. (1981),

[3] In the 1975 DeSoete publication, the functionality of the order of reaction Eq. (74) is provided as a function of oxygen concentration.

$$\text{Char} + \text{NO} \rightarrow \text{N}_2 + \ldots \quad (76)$$

Past NO simulation studies indicate that the heterogeneous NO reduction pathway is not significant (Smith, 1997). In this simulation study, the overall contribution of heterogeneous NO reduction at the surface of char has been neglected.

Reburn

Reburning is the nitrogen oxide abatement strategy that involves the introduction of a fuel in the downstream combustion zone. This downstream addition provides a fuel rich zone where nitric oxide can react with the hydrocarbon radicals to form HCN. Typical fuels include wood, heavy fuel oil, coal and natural gas (U.S. Dept. of Energy, 1995; Syverud et al., 1994; Smart et al., 1994). The hydrogen cyanide produced can enter the fuel NO mechanism where it can be reduced to N_2 through Eq. (75) (a further NO sink) or be oxidized to nitric oxide via Eq. (74).

Successful NO reduction through reburning requires lower temperatures and longer nitric oxide residence times in the reducing environment (Miller et al., 1998). Problems with this technique include refractory deterioration due to the fuel rich reducing environment and the increased manufacturing cost associated with preliminary building and retrofitting. Nevertheless, reburning is a viable nitrogen oxide abatement strategy capable of a nitric oxide reduction up to 90% (Smart et al., 1994).

Rate parameters for the reburning reaction,

$$\text{CH}_i + \text{NO} \rightarrow \text{HCN} + \ldots \quad (77)$$

were determined by Chen et al. (1995). In the group's study, Chen et al. proposed that CH radical concentrations are proportional to the inlet hydrocarbon concentrations. For fuel-rich zones, i.e., an equivalence ratio greater than 1.0, the NO reburn model described in Eq. (77) is used.

Thermal De-NO_x

The last global reaction pathway of nitric oxide formation and destruction involves the use of ammonia that is injected into the downstream combustion zone to reduce nitric oxide to N_2. This technique is known as thermal De-NO_x and is described in detail by Lyon (1987). In this simulation study, the thermal De-NO_x mechanism is not warranted.

Computational Modeling of Nitrogen Oxide

As described in the beginning of this section, a turbulent transport equation for each major species is calculated. Equation (78) describes such a transport equation in Favre- averaged, steady state form for species *i*.

$$\nabla \cdot \left(\overline{\rho}\widetilde{v}\text{Y}_i\right) - \nabla \cdot \left(\overline{\rho}\text{D}_{\text{Y}_i}\nabla\text{Y}_i\right) = \overline{\text{W}_i} \quad (78)$$

The time mean rate of reaction, $\overline{\text{W}_i}$, is simply the difference between the rates of production and consumption of species *i*,

$$\overline{W}_i = \overline{w}_i^{\text{production}} - \overline{w}_i^{\text{consumption}} \qquad (79)$$

The exact number of chemical species transport equations depends on the physics of the chemical process that is to be simulated. For cases involving neither reburning nor thermal De-NOx, the minimum number of species transport equations is two. The two transport equations calculated for a typical case study are for NO and HCN.

HCN Mass Source Terms

Although the individual global mechanisms for nitrogen oxide formation and destruction applicable to pulverized-coal combustion have been developed, how nitrogen appears in the homogeneous gas phase remains an issue and will now be presented.

The original model implemented by Smith et al. (1982) assumes that the rate of HCN production is proportional to the total rate of mass release from the coal particle, $\overline{S}_p^m$. Therefore, the mass source of HCN is based on the combined mechanisms of devolatilization and char oxidation. The mass source term of HCN is described mathematically by:

$$\overline{w}_{HCN} = \left(\frac{M_{HCN}}{M_N}\right)\left\{\omega_N \overline{S}_p^m\right\} \qquad (80)$$

This model implicitly assumes that HCN is released into the gas phase during the char oxidation process.

The model developed by Philip J. Smith and described in Eddings et al. (1994) incorporates the ability to distinguish between char nitrogen and volatile nitrogen by the incorporation of a new progress variable, $\tilde{\eta}_{vol}$. This progress variable is defined as the mass fraction of coal off-gas originating from the devolatilization process. Furthermore, the conversion of devolatilized-nitrogen to HCN is dependent on a user-supplied parameter, ζ. In this formulation, the source of HCN via the char oxidation pathway is removed. The mass source term of HCN is, therefore, given by,

$$\overline{w}_{HCN} = \varsigma\left(\frac{M_{HCN}}{M_N}\right)\left\{\omega_N^{vol} \overline{S}_p^{\tilde{\eta}_{vol}}\right\} \qquad (81)$$

Compositional effects for volatile nitrogen are included by determining a volatile nitrogen mass fraction, ω_N^{vol}, based on an overall coal conversion to char.

NO Mass Source Terms

The fractional conversion of char-nitrogen to nitric oxide is obtained through the user specified parameter, ζ_h provided the ability to distinguish between char-nitrogen is available, i.e., $\tilde{\eta}_{vol}$ is calculated. The ability to distinguish between the products of devolatilization and char oxidation allows the mass source term of nitrogen dioxide from char-nitrogen to be easily calculated. The rate of NO production through the homogeneous pathway of char-nitrogen is:

$$\overline{w}_{HCN} = \varsigma_h \left(\frac{1}{M_N} \right) \omega_N^{char} \left(\overline{S}_p^m - \overline{S}_p^{vol} \right) \qquad (82)$$

The mass fraction of nitrogen in the char, ω_N^{char}, is user specified and can be obtained from experimental data (Mitchel et al., 1992).

The first generation nitric oxide model developed by Smith et al. (1982) does not use a specified conversion of char-nitrogen to NO, ζ_h. The heterogeneous conversion of char-nitrogen is solely modeled as char-nitrogen evolving as HCN as was previously described.

Global NO Model

Exhibit 6-1 describes the global mechanism of nitric oxide production in a pulverized-coal system. This mechanism includes contributions of thermal, prompt, and fuel NO; reburning, thermal De-NOx and the fuel NO pathway of Mitchel and Tarbell (1982). Instantaneous reaction rates and the accompanying parameters are given in Tables 6-2 and 6-3. This global model represents the final distilled reaction mechanism that the NO simulation code is currently capable of utilizing.

Table 6-2
NO Rate Parameters

Description	Equation
Thermal NO (production of NO)	$w_1 = \left(\frac{1}{M_{mix}}\right) 2\rho X_O \left\{ \frac{k_1 X_{N_2} - \frac{k_{-1} k_{-2} X_{N_2} X_{NO}^2}{k_2 X_{O_2}}}{1 + \frac{k_{-1} X_{NO}}{k_2 X_{N_2} X_{O_2} + k_3 X_{N_2} X_{OH}}} \right\}$
Prompt NO (formation of HCN)[a]	$w_2 = \left(\frac{1}{M_{mix}}\right) \rho (1.35 \times 10^6) X_{N_2} X_{CH_i} \exp\left(\frac{-30}{RT}\right)$
Fuel NO (destruction of HCN/formation of NO)[b]	$w_3 = \left(\frac{1}{M_{mix}}\right) \rho (1.0 \times 10^{11}) X_{HCN} X_{O_2}^b \exp\left(\frac{-67}{RT}\right)$
(destruction of HCN/destruction of NO)	$w_4 = \left(\frac{1}{M_{mix}}\right) \rho (3.0 \times 10^{12}) X_{HCN} X_{NO} \exp\left(\frac{-60}{RT}\right)$
NO-Char reduction (destruction of NO)	$w_5 = \alpha_p n_p A_E (4.18 \times 10^7) \tilde{\rho}_{NO} \exp\left(\frac{-34.7}{RT}\right)$
Reburn NO (destruction of NO)	$w_6 = \left(\frac{1}{M_{mix}}\right) \rho (2.7 \times 10^3) X_{NO} X_{CH_i} \exp\left(\frac{-18}{RT}\right)$
Mitchell and Tarbell Fuel NO (destruction of HCN)	$w_7 = \left(\frac{1}{M_{mix}}\right) \rho (1.94 \times 10^{15}) X_{HCN} X_{O_2} \exp\left(\frac{-18}{RT}\right)$
(destruction of NH_3/formation of NO)	$w_8 = \left(\frac{1}{M_{mix}}\right) \rho \frac{(3.48 \times 10^{20}) X_{NH_3} X_{O_2} \exp\left(\frac{-100}{RT}\right)}{1 + (6.9 \times 10^{-6}) X_{O_2} \exp\left(\frac{-42}{RT}\right)}$
(destruction of NH_3/destruction of NO)	$w_9 = \left(\frac{1}{M_{mix}}\right) \rho (6.22 \times 10^{14}) X_{NO} X_{NH_3} \exp\left(\frac{-55}{RT}\right)$

[a] R is given as [=] kcalgmol^{-1}K^{-1}
[b] For [O_2] greater than 18,000 ppm, b is 0.0; for [O_2] less than 2,500 ppm, b is 1.0.

Table 6-3
Thermal NO Rate Parameters

	k_1	k_{-1}	k_2	k_{-2}	k_3
Preexponential factor, $m^3kgmol^{-1}s^{-1}K^{-1}$	$1.36x10^{11}$	$1.6x10^{10}$	$6.4x10^{6}$	$1.5x10^{6}$	$3.28x10^{10}$
Activation energy, kcal-$gmol^{-1}$	75.4	1.025	6.25	38.7	0.0

Mixing Model Coupling

The transport equation of Eq. (78) requires an overall time mean reaction rate. Recall, the overall time mean rate of reaction for species *i* is obtained by the net difference between the averaged rates of production and consumption of species *i*, Eq. (79). For example, $\overline{W}_{HCN}$, in the absence of the Mitchell and Tarbell fuel NO mechanism, is given by:

$$\overline{W}_{HCN} = \overline{w}_{HCN} + (\overline{w}_2 + \overline{w}_6 - \overline{w}_3 - \overline{w}_4)M_{HCN} \tag{83}$$

where the individual mean reaction rates are obtained via convolution over the joint PDF, Eq. (52). The overall mean reaction rate for NO is

$$\overline{W}_{NO} = \overline{w}_{NO} + (\overline{w}_1 + \overline{w}_3 - \overline{w}_4 - \overline{w}_5 - \overline{w}_6)M_{NO} \tag{84}$$

Recall that this technique assumes that the reaction rates are strictly a function of local stoichiometry and that a suitable shape of the PDF is available (Bilger, 1979 and 1980; Smoot and Smith, 1985).

Since rates of reactions are given as a function of species mole fractions and not overall mixture fractions, we must convert the instantaneous mixture fraction used in Eq. (52) to an instantaneous mole fraction. Using the current instantaneous mixture fraction(s) within the integration loop, we calculated the instantaneous temperature and mole fractions of N_2, O_2 and CH_i appearing in Table 6-2 using full equilibrium. The mole fraction of O and OH are calculated based on the desired model.

Instantaneous mole fractions for HCN and NO are calculated by assuming that the local instantaneous mass fraction of species *i* is a linear function of its fully achievable mass fraction, Y_i^f:

$$Y_i = \pi_i Y_i^f \tag{85}$$

where π_i is a spatial linearization constant and Y_i is the required instantaneous mass fraction. The mass fractions are first converted to mole fractions and are used in the appropriate instantaneous reaction rate as given in Table 6-2 (Smith et al., 1982).

For example, Y^f_{HCN} represents the instantaneous maximum mass fraction HCN can achieve at a given spatial location. This variable is only a function of stoichiometry and can be obtained from the instantaneous mixture fraction progress variable during the integration process of Eq. (52). The instantaneous fully achievable mass fraction of HCN depends on the assumption of how HCN enters the homogeneous pathway and which coal off-gas mixture fractions are in use during the integration process. Assuming that HCN enters the gas phase through the contribution of both devolatilization and char oxidation, then Y^f_{HCN} is given by:

$$Y^f_{HCN} = \varsigma M_{HCN}(\omega_N \eta) \tag{86}$$

The coal off-gas mixture fraction, η, appearing in Eq. (86), represents the instantaneous value within the integration algorithm. The fully achieved NO mole fraction, Y^f_{NO}, is calculated by assuming that all HCN is converted to NO:

$$Y^f_{NO} = Y^f_{HCN}\left(\frac{M_{NO}}{M_{HCN}}\right) \tag{87}$$

In the study reported by Eddings et al. (1994), Y^f_{HCN} is calculated based on a mean volatile mixture fraction, $\tilde{\eta}^{vol}$, that is consistent with the stated assumption that fluctuations in the volatile off-gas are neglected. The maximum instantaneous fully achievable mass fraction for HCN when the $\tilde{\eta}^{vol}$ option is in use is given by Eq. (88):

$$Y^f_{HCN} = \varsigma M_{HCN}\left(\omega^{vol}_N \tilde{\eta}^{vol}\right) \tag{88}$$

Implications of this assumption are presented later, however, at the very least it is clear that using the $\tilde{\eta}^{vol}$ option does not calculate an instantaneous fully achieved HCN or NO composition. In essence, the only fluctuation effect when this option is active appears in the fluctuating temperature and the fluctuation effect of the species O_2, OH, N_2 and CH_i.

The variable, π_i. in Eq. (85) is a local linearization constant and assumed to be independent of turbulent fluctuations (Smoot and Smith, 1985; Smith et al., 1982). Therefore, the spatial variable linearization constant is obtained from the time-mean mass fraction field:

$$\tilde{\pi}_i = \frac{Y_i}{\tilde{Y}^f_i} = \pi_i \tag{89}$$

The mean fully achieved mass fractions of HCN, assuming the ability to distinguish between char-nitrogen and devolatilized nitrogen, is given by:

$$\tilde{Y}^f_{HCN} = \varsigma M_{HCN}\left(\omega^{vol_1}_N \tilde{\eta}^{vol}\right) \tag{90}$$

or, assuming that the $\tilde{\eta}^{vol}$ formulation is not in effect

$$\tilde{Y}^f_{HCN} = M_{HCN}(\omega_N \tilde{\eta}) \tag{91}$$

In each case, the mean value of the fully achieved NO mass fraction is given by Eq. (92):

$$\widetilde{Y}_{NO}^{f} = \widetilde{Y}_{HCN}^{f}\left(\frac{M_{NO}}{M_{HCN}}\right) \tag{92}$$

The mean mixture fraction, $\widetilde{Y}_i$, is calculated from the transport Equation (78) with the appropriate overall mean rate of reaction, for example Eq. (83).

NO Solution Algorithm

The algorithm for calculating the trace nonequilibrium mole fraction of HCN and NO at a given point in the computational grid is as follows:

1. Obtain the mean value of the fully achieved mass fractions, $\widetilde{Y}_{HCN}^{f}$ and $\widetilde{Y}_{NO}^{f}$ based on the mean values of the implemented coal off-gas mixture fraction progress variables, Eq. (90) or (91) and Eq. (92).
2. Use the current value of $\widetilde{Y}_{NO}$ and $\widetilde{Y}_{HCN}$ based on the transport PDE, Eq. (78), to calculate each respective linearization constant, π_i.
3. Within integration loop, calculate instantaneous fully achieved mass fractions for Y_{HCN}^{f} and Y_{NO}^{f}.
4. Use the respective calculated linearization constant from step 2 and calculate the instantaneous mass fractions of HCN and NO, Eq. (85).
5. Calculate equilibrium state space variables to be used in rate expressions listed in Table 6-2 based on the current value of the mixture fraction progress variable within the integration loop; use major species compositions to determine the appropriate non-equilibrium mole fractions of OH and O, if applicable, and convert all mass fractions to mole fractions.
6. Calculate instantaneous rates, w_1, w_2, w_3, etc.
7. Assign appropriate PDF weight to instantaneous rate and return to step 4 until the full integration loop is terminated.
8. With the mean values of the individual rates of reactions in hand, construct $\overline{W}_{HCN}$ and $\overline{W}_{NO}$.
9. Solve $\widetilde{\eta}^{vol}$ transport equation, if applicable.
10. Solve respective transport equation for $\widetilde{Y}_{NO}$ and $\widetilde{Y}_{HCN}$. If convergence is reached, terminate. Otherwise return to step 1.

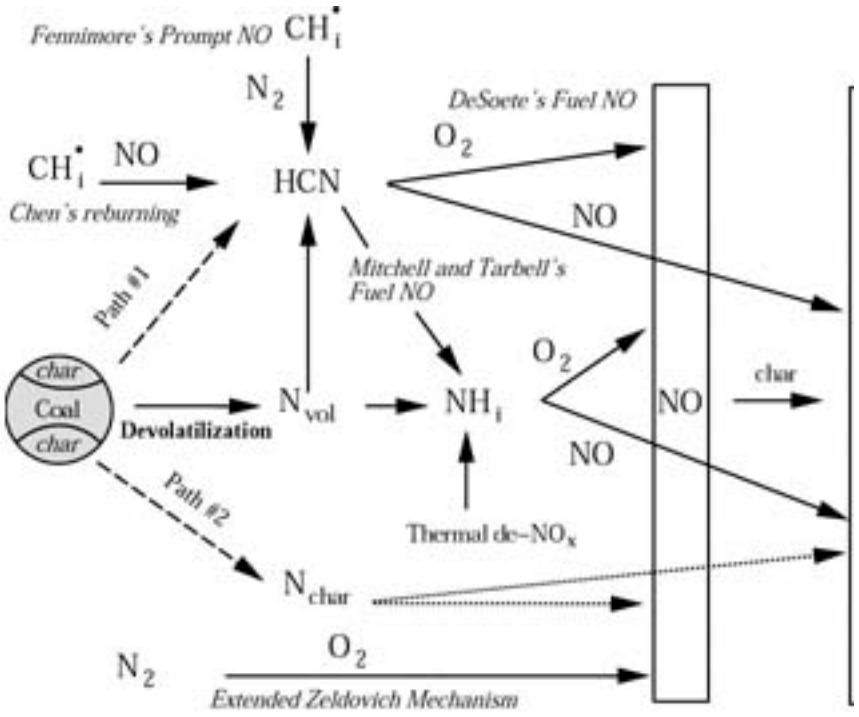

Exhibit 6-1
Global nitric oxide mechanism applicable to pulverized-coal combustion

Carbon Burnout Formulation

The original char oxidation model that requires updating will now be presented. In this original model, the coal particle is modeled as a porous particle that burns out with variable density and near-constant particle diameter. The ordinary differential equation describing the rate of mass change for a single particle with the near-constant particle diameter behavior is

$$\frac{dm_p}{dt} = \frac{d}{dt}\left(\rho_{ap} V_p\right) = V_p \frac{d\rho_{ap}}{dt} = -r_p \qquad (93)$$

where m_p is the mass of the particle V_p, is the volume of the particle, ρ_{ap} is the apparent density and r_p is the overall particle reaction rate. This ordinary differential equation is integrated within the Lagrangian particle dispersion model and is ensemble averaged over the entire domain of the cloud.

The right hand side of Eq. (93) represents the rate of decrease of particle mass and is strictly a function of the rate of devolatilization and of the heterogeneous char oxidation. The burnout process has been modeled as a two-step, diffusion limited rate process on a spherical particle. The two rate steps include the external mass transfer of oxidant to the surface of the particle and the subsequent surface chemical kinetic rate.

The rate of mass transfer to the surface of the particle must include the effect of high mass transfer on the mass transfer coefficient. Thus we seek to obtain a mass transfer coefficient, k_m,

by expressing it as the product of the intrinsic mass transfer coefficient, k_m^o and the correction coefficient, θ, or blowing parameter,

$$k_m = \theta k_m^o \tag{94}$$

The intrinsic mass transfer coefficient corresponds to conditions of vanishingly small mass transfer rates where distortions to the concentration profile are minimal and are frequently given by correlations of mass transfer data (Taylor and Krishna, 1993). Equation (94) defines the intrinsic mass transfer coefficient, which is a function of the Sherwood number, Sh , the effective diffusivity to the surface of the particle, D_e and the outer diameter of the reacting particle, d_p,

$$k_m^o = \lim_{mt \to 0} \frac{Sh\, D_e}{d_p} \tag{95}$$

The correction coefficient factor to account for the finite fluxes on the intrinsic mass transfer coefficient can be derived by solving the one-dimensional, mass transfer of oxidant to the surface of a reacting particle problem,

$$\frac{\partial C_o}{\partial t} + \nabla \cdot (N_o) = R_o \tag{96}$$

Assuming steady-state application of Fick's law of diffusion and that appropriate boundary conditions are available (the concentration of oxidant at the surface of the char particle is $C_{o,ps}$ and the bulk oxidant concentration is $C_{o,\infty}$), we solve Eq. (96) in spherical coordinates to yield:

$$N_o(r) = \frac{N_t}{C_g \Phi}\left[(\Phi + 1)C_{o,ps} - C_{o,\infty}\right] \tag{97}$$

where N_t is the total molar flux and Φ is defined as

$$\Phi = \exp(\psi) - 1 \tag{98}$$

and

$$\psi = \frac{N_t r^2}{r_p D_e C_g} \tag{99}$$

The correction coefficient is obtained by solving Eq. (97) at the surface of the char particle and fitting the rate of mass transfer of oxidant to the surface of the particle to the following form:

$$r_o = k_m^o \theta A_p M_o \left(C_{o,\infty} - C_{o,ps}\right) - \frac{r_j C_{o,ps} M_o}{\rho_g} \tag{100}$$

yielding

$$\theta = \frac{\phi}{e^{\phi} - 1} \tag{101}$$

where ϕ is defined by Eq. (102) and is a strict function of the total mass flow rate out of the particle, r_j (either by devolatilization reactions or char oxidation), ρ_g is the density of the bulk phase, A_p is the surface area of the coal particle and M_o is the molecular weight of oxidant.

$$\phi = \frac{r_j}{2\pi d_p \rho_g D_e} \tag{102}$$

With the rate of mass transfer to the surface of the particle defined, the next step is to outline the rate of heterogeneous chemical char oxidation. Equation (103) represents the rate law for the chemical kinetic oxidation of carbon as integrated within the cloud model,

$$r_h = A \exp\left(\frac{-E}{RT_p}\right) C_{o,ps} \tag{103}$$

where A and E are the rate specific preexponential factor and activation energy, respectively. Chemical kinetic oxidation rate parameters are given for oxygen, carbon dioxide and water by Baxter et al. (1987), Lewis et al. (1949) and Field et al. (1967).

The final rate of mass transfer of oxidant to the surface of the coal particle, evaluated at the surface of the particle (kg/s) is given by

$$r_o = k_m A_p M_o \left(C_{o,\infty} - C_{o,ps}\right) - \frac{r_j M_o C_{o,ps}}{\rho_g} \tag{104}$$

The last term on the right of Eq. (104) represents the total convective flux of mass out of the particle including both heterogeneous char oxidation and devolatilization effects that act to retard the flux of oxygen to the outer surface of the particle. At this point, no multicomponent interactions have been implemented within the model solely due to the uncertain knowledge of the exact liberated chemical species of devolatilization.

Equations (103) and (104) are combined, along with the mass balance relationship of the surface flux of oxygen and the chemical char oxidation reaction, Eq. (105), to eliminate the surface concentration of oxygen.

$$r_h = \frac{\varphi_e r_o M_h}{M_o} \tag{105}$$

The overall rate of heterogeneous chemical char oxidation is

$$r_h = \frac{\varphi_e A_p^2 M_h \rho_g k_m k_j C_{o,\infty}}{\rho_g A_p \left(k_j - k_m\right) + r_j} \tag{106}$$

The user determined value of the stoichiometric coefficient, φ_e to be used within all temperature regimes of the reactor is chosen to be: $1.0 \le \varphi_e \le 2.0$. Values of φ_e close to unity indicate mostly CO_2 is liberated from the coal particle during char oxidation while values near 2 indicate a predominance of CO. For the high temperature regimes of pulverized coal combustion, values near 2.0 are appropriate (Smoot and Smith, 1985).

Advanced Carbon Burnout Model Rate Equation

The carbon burnout model of Hurt et al. (1996; 1998) uses an empirical burning rate equation that can include an intrinsic distribution of reactivity and thermal annealing of a particular reactivity by the augmentation of the preexponential factor. The single particle burnout rate for a particular preexponential factor, or reactivity, is

$$q_i = A_i \exp\left(\frac{-E}{RT_p}\right)\left(C_{o,ps} R T_p\right)^{0.5} \tag{107}$$

Kinetic rate parameters are given for oxygen as the sole oxidizer. Primary differences between the two rate expressions, Eq. (103) and Eq. (107) include the functionality of oxidizer concentration at the surface of the combusting particle and the capability of a distribution of preexponential values that have been obtained from detailed analysis of the Sandia coal char combustion database (Hurt et al., 1998; Mitchell et al., 1992).

Incorporation of the CBK model with its coal specific char oxidation parameters allows the use of Eq. (107) in conjunction with the ash film resistance and thermal annealing model. When the ash film submodel is not active, the model mimics the original two-step diffusion resistance model (diffusion to the outer coal particle surface followed by the surface char oxidation reaction).

The surface functionality of oxygen used in the rate expression defined by Eq. (107) does not allow direct elimination of the surface oxygen concentration and; therefore, a numerical procedure such as Newton's method must be used to converge the oxygen surface concentration.

When the ash film resistance model is in use, another mode of mass transfer resistance is included, specifically, the transfer of oxygen to the carbon rich core through an ash film. Therefore, Eq. (94) and Eq. (95) need to be re-formulated to include this new diffusional resistance layer. The process in obtaining the intrinsic mass transfer coefficient and correction factor is analogous to the procedure outlined in the previous section. A one-dimensional transport equation is solved, assuming steady state, in spherical coordinates. The resulting equation for the molar flux of oxidant is solved at the surface of the carbon rich core and the equation is again forced into the form resembling Eq. (104).

The intrinsic mass transfer coefficient through the ash film is given by

$$k_m^o = \frac{Sh\, r_p\, D_{eff}}{d_c\left(r_p - r_c\right)} \tag{108}$$

where d_c is the shrinking carbon rich core diameter, D_{eff} is the effective diffusivity through the ash film; r_p and r_c are the particle and carbon rich core radius, respectively. Within the context of the ash film resistance model, ϕ' is now defined as:

$$\phi' = \frac{r_c\left(r_p - r_c\right) r_j}{r_p D_{eff} \rho_g A_c} \tag{109}$$

where A_c represents the surface area of the carbon rich core shrinking diameter. The correction coefficient for the mass transfer coefficient, within the context of the ash film resistance submodel, is of the same form as Eq. (101) ,

$$\theta' = \frac{\phi'}{e^{\phi'} - 1} \tag{110}$$

The corrected mass transfer coefficient, $k_m^{0\,\prime}$, is of the same form as Eq. (94),

$$k'_m = \theta' k'^{o}_m \tag{111}$$

Again, equations (103), (104), and (107) are used to iteratively solve for the carbon rich core surface concentration of oxygen and therefore the chemical rate of char oxidation.

CBK Burnout Model

The germane elements of the CBK model implemented within the cfd simulator including reactivity distribution, thermal annealing and ash film resistance model will now be described.

Reactivity Distribution

Hurt et al. (1996, 1998) propose that within a particle size distribution of a coal, there can exist a distribution of char oxidation preexponential factors due to the distribution of macerals for a given coal type at a given geographic location. A statistical model of particle reactivity distribution has been developed through experiments at the Combustion Research Facility at Sandia National Laboratory for ten different coal types over the last several years (Hurt et al., 1996; Mitchell et al., 1992). Results showed that within a general class of coal type, statistical effects were important and the distribution in reactivity was correlated to a gamma distribution (Hurt et al., 1996).

The correlations detailed by Hurt et al. provide information for ten US coals and also include rank-dependent correlations for the mean value of char reactivity for coal types outside the studied database (Hurt et al., 1998). The mean value of the preexponential factor distribution is correlated to the weight fraction of carbon, ω_c, on a dry, ash-free basis,

$$\ln\left(A_{mean}\right) = 10.96 - 0.0713\omega_c \tag{112}$$

Thermal Annealing

The time scale of heterogeneous char oxidation reactions in commercial boilers is on the order of several seconds. Variations in reactivity over this time scale will result in variation in residual carbon in ash. The acute phenomenon of thermal annealing of carbon and char is well known and has been the subject of many studies in years past (McCarthy, 1981; Radovic, 1983; Hecker et al., 1992). A decrease in char oxidation reactivity subsequent to high temperature treatment in both commercial and pilot scale boilers has been observed (Hurt and Gibbons, 1995; Jones et al., 1995). Chemical kinetic studies that have attempted to quantify this decrease in reactivity have accredited this loss primarily to loss of surface area per unit volume and destruction of active carbon sites (Suuberg et al., 1989). Thermal deactivation of the burning

char particle occurring as the mean particle trajectories cross high temperature regions has been postulated (Hurt and Davis, 1995).

Beeley et al. (1996) recently demonstrated that char reactivity is quite sensitive to the preparation technique employed prior to combustion. The effect of thermal deactivation mechanisms was isolated from oxidative mechanism by using and inert environment. It was found that deactivation of char reactivity was on the order of 30–50 times after only two seconds of treatment between the temperature range of 963 °F–1407 °F [(1546 °C–2346 °C) (1273 K–2073 K)]. Comparison of the reactivities between the high temperature combusted char and boiler fly ash indicated that a thermal deactivation mechanism was significant.

The approach taken in modeling the thermal annealing process is largely based on the work of Suuberg (1991). In his original model the number of particular active sites, N_p, with a unique value of energy of activation, E_D, undergoing char oxidation are consumed by a first order deactivation process,

$$\frac{dN_p}{dt} = -N_p A_D \exp\left(\frac{-E_D}{RT_p}\right) \tag{113}$$

Although all sites share a single valued annealing preexponential factor, A_D, it is postulated that there exists a continuous distribution in energy of activation for the deactivation thermal annealing process.

At any time t, the ratio of active sites remaining, N, to the initial number of active sites present in the unburned char, N_0, represents the current fraction of remaining active sites available for heterogeneous char oxidation. This ratio is determined by integration over the normalized frequency distribution function for active sites (Hurt et al., 1998).

$$\frac{N}{N_0} = \int_0 f_E(t, E_D)\,dE_D \tag{114}$$

Of course, at time equal to zero, integration of Eq. (114) yields a ratio of unity. Since different sites anneal at different rates, the log-normal Gaussian distribution of active sites loses its characteristic shape over time. Equation (113) is recast to

$$\frac{\partial}{\partial t} f_E(t, E_D) = -f_E A_D \exp\left(\frac{-E_D}{RT_p}\right) \tag{115}$$

and integration of Eq. (114) results in a ratio of active sites that approaches zero as exposure time within the hot environment proceeds (Hurt et al., 1998). The reactivity at any time and location along the reactor, A_i, depends on this ratio of remaining sites to initial sites.

$$A_i = A_{i0}\left(\frac{N}{N_0}\right)^{\lambda} \tag{116}$$

For the relative high temperatures of char combustion and for rates determined by surface reaction and pore diffusion (the so-called zone II region) and for thermal annealing effects

controlled by a decrease of intrinsic surface reactivity, classical Thiele analysis suggests a value of 0.5 for λ (Hurt et al., 1998).

Ash Film Resistance

Chemical kinetic studies in a one-dimensional entrained-flow reactor indicates that thermal annealing and reactivity distribution effects alone are incapable of capturing the complete magnitude of char oxidation deactivation during the late stages of combustion (Hurt et al., 1998). Vleeskens et al. (1986) suggest that there exists a net inhibitory effect of ash on char oxidation. Mineral effects described as ash decarburization decrease the number of carbon islands from a coherent ash framework thereby reducing the ratio of carbon surface area to particle volume (Hurt and Davis, 1994).

The ash film resistance model of Hurt et al. (1998) attempts to quantify this observed experimental evidence. Within the ash film submodel, the char particle is modeled as a shrinking carbon rich core surrounded by a developing porous ash film. The model introduces three parameters: the critical ash porosity, the minimum ash film thickness that corresponds to the characteristic grain size and the mode of burning parameter (Hurt et al. 1998). Coal specific values of the critical ash porosity vary from 0.16 to 0.26 and the minimal ash film thickness has been determined for a wide range of coals to be 1μm.

Coal specific values for the mode of burning parameter have been determined for ten US coals and fall within a somewhat narrow range (between 0.0 to 0.4) (Mitchell et al., 1992). This narrow range is consistent with the older studies of Hamor et al. (1973) and Smith (1971) who also predicted near zero behavior. Values of the mode of burning parameter close to unity result in near constant diameter behavior while shrinking core behavior is seen for values of near zero. The displayed range of the model of burning paramter indicates that during the combustion process, both the char density and particle diameter are changed significantly. For unknown coals outside the Sandia data base, a value of 0.20 is recommended (Hurt et al., 1998).

Conceptually, the model works as follows: Initially, when carbon burnout is low there exists a highly porous sparse ash film that does not appreciably retard the mass transfer of oxygen across the ash film boundary. As the extent of carbon burnout increases, this sparse ash film envelopes the coal particle until a uniform coal specific critical ash porosity is reached. At this point the ash film begins to grow past the critical thickness. The resulting ash film porosity directly affects the rate at which the oxidizer can diffuse to the surface of the combusting particle.

The ash film thickness, δ, is explicitly calculated based on the knowledge of the particle diameter and core diameter (Hurt et al., 1998),

$$\delta = \frac{\left(d_p - d_c\right)}{2} \tag{117}$$

Assuming that the ash film at any time t is equal to the critical ash film porosity, the shrinking core diameter is calculated by local mass balance considerations,

$$d_c = d_p\left(\frac{X_a\rho - \rho_{at}(1-\theta_{af})}{X_{a0}\rho_0 - \rho_{at}(1-\theta_{af})}\right)^{1/3} \tag{118}$$

where ρ is the current overall particle density, ρ_o is the initial overall density, θ_{af} is the ash film porosity, and ρ_{at} is the apparent density of the nonporous ash (taken to be 2.6 g/cm^3).

The current particle diameter is obtained by geometric considerations alone,

$$\frac{d_p}{d_{p0}} = \left(\frac{m\rho_0}{m_0\rho}\right)^{1/3} \tag{119}$$

The current density of carbon, ρ_o, within the particle is related to the extent of carbon conversion and is given by an empirical equation with the coal specific mode of burning parameter, α, that can vary between zero and one (Mitchell et al., 1992).

$$\frac{\rho_c}{\rho_{c0}} = \left(\frac{m_c}{m_{c0}}\right)^{\alpha} \tag{120}$$

With the current carbon density calculated from Eq. (120), the overall current density of the reacting coal particle can be calculated,

$$\frac{1}{\rho} = \frac{1-X_a}{\rho_c} + \frac{X_a}{\rho_a} \tag{121}$$

where X_a is the mass fraction of ash and ρ_a is the ash density assuming the existence of a critical ash porosity.

If the calculated ash thickness is less than the minimum ash film thickness, then Eq. (117) is solved for the core diameter assuming that the ash film thickness is equal to the characteristic grain size of 1 μm. Using the newly calculated core diameter, rearrangement of Eq. (118) yields the actual ash film porosity (Hurt et al., 1998),

$$\theta_{af} = 1 - \left[\frac{X_a\rho - X_{a0}\rho_0\left(1-\frac{2\delta_m}{d_p}\right)^3}{\rho_{at} - \rho_{at}\left(1-\frac{2\delta_m}{d_p}\right)^3}\right] \tag{122}$$

The effective diffusivity of oxidant through the ash film is a function of the ash film porosity and is calculated by (Hampartsoumian, 1989):

$$D_{eff} = D_e\theta_{af}^{2.5} \tag{123}$$

Char Oxidation Simulation Results

In this section, simulation results for three variations in the carbon burnout model are presented. An experimental data set from the International Flame Research Foundation (IFRF) long pulverized-coal flame experimental study and the large-scale pulverized-coal axial fired cylindrical combustor of the Imperial College of Science and Technology's are used in conjunction with the combustion simulator, under various burnout model assumptions, to evaluate potential mechanisms controlling the residual carbon in ash. The three simulation cases are labeled as follows: external, anneal CBK, and ash CBK. The former simulation model represents the two step external char oxidation model that was discussed in the previous section, Eq. (103), with rate parameters based on Baxter et al. (1987). Both the anneal CBK and ash CBK are the models based on the kinetic burnout rate law of Eq. (107). The CBK models each use three reactivity bins and utilize a detailed stoichiometric coefficient. Both CBK cases include the effects of thermal annealing (Hurt et al., 1998).

All simulation cases were run on an SGI Octane workstation. The finite difference equation for the gas-phase velocities, u, v, w; pressure and pressure correction, p and p^c; production and dissipation of kinetic energy, k and ε; mixture fractions and respective variances, f, η, g_f, g_η and the enthalpy, h, were solved until the maximum of all the finite difference equation residuals was less than 3.5 (Smith, 1990). Most residuals, however, were on the order of 3.0. Case ash CBK differs only with case anneal CBK in that the effect of the additional ash film resistance is included within the calculation of the oxygen surface concentration.

Imperial College Simulation Study

The Imperial College of Science and Technology large-scale pulverized-coal axial fired cylindrical combustor consists of ten, 0.3 m water cooled segments of an internal diameter of 0.6 m (Hassan et al., 1985). To assist in the stabilization of the coal flame, the upper most five segments are refractory lined. The burner gun, 22.2 mm ID, sits concentrically within a 56 mm diameter 24^o quarl section to further stabilize the flame and contains a moveable block swirl generator (Godoy et al., 1989). The experimental case is flame B1, where Gedling coal was fired (Godoy et al., 1991). The experimental conditions included a swirl number of 1.03 and a primary coal mass flow rate of 12 kg coal/ hr. Mass flow rates of secondary and primary air are 102.0 kg air/hour and 27.6 kg air/hour; the excess air ratio is 1.10.

All of the reported cfd simulation cases include a particle size distribution (9 bins) ranging from 13 to 200 μm. There are five initial Lagrangian cloud starting locations for each particle size and for each reactivity. The modeling parameters used for this study are summarized in Table 6-4. The CBK mean char oxidation parameter, which is obtained by Eq. (112), is 257 g/s-cm^2-$atm^{0.5}$. The char oxidation rate constant that is used for the external model is $0.7545\exp\left(\frac{-6.37\times10^7}{RT}\right)$. Grid independent result, which is the point at which simulation results are independent of the chosen grid size, was found to be at a grid size of 50x37x37.

Table 6-4
Imperial College Simulation Parameters

Moisture (%)	Ash (%)	Fixed carbon (%)	Volatile matter (%)	Calorific Value Btu/lb
6.3	4.2	53.7	35.8	12,468
Mass(%) d.a.f.				
Carbon	Hydrogen	Nitrogen	Oxygen	Sulphur
75.78	5.27	1.35	15.98	1.62
CBK parameters				
Bin	Reactivity, G/s-cm^2-atm$^{0.5}$	Distribution	θ_{af}^{c}	α
1	103.14	0.04	0.21	0.20
2	216.72	0.29		
3	283.62	0.67		
Particle size distribution				
Bin	Diameter (μm)	Weight		
1	13	0.087		
2	18	0.1005		
3	29	0.335		
4	45	0.155		
5	61	0.107		
6	95	0.0700		
7	120	0.0531		
8	160	0.0600		
9	199	0.0324		

LOI Trajectory Simulation Results: anneal CBK vs. external

Exhibit 6-2 through Exhibit 6-5 are individual plots of loss on ignition trajectories for a cloud of particles originating at the center of the burner throat. The exhibits contain particles with an initial diameter of 13, 45, 95 and 160 m, respectively. Each exhibit contains the external kinetic burnout model, (●); and the anneal CBK model. The exhibits each show all three reactivity bins for the anneal CBK model, which are provided in Table 6-4, and are labeled as follows: R1, (■); R2, (▲) and R3, (+).

Since common particle sizes display comparable heat-up rates in each of the simulations (the burnout model did not dramatically affect the temperature history) the simulations that used lower reactivities within each particle class consistently display a lengthened axial distance before complete or near complete burnout.

Notice that in the 13 μm particle size class all CBK reactivity trajectories burn out at a lower rate when compared to the external case. The trend of lengthening time to complete burnout, when comparing the CBK reactivity bins and external case, for small particles is explained by the observed trend depicted in Exhibit 6-6. In this figure, the functional dependence of thermal

annealing and particle diameter is shown. During practical combustion conditions, smaller particles anneal more rapidly since the smaller particles reach higher temperatures earlier in their combustion time/temperature history. This increased residence time at higher temperatures causes a more pronounced thermal annealing effect that, in turn, decreases the overall rate of carbon burnout. Larger particles, which have longer heat up times, anneal at lower rates.

The two compared simulation cases, anneal CBK and external, neither display nor explain any transition at the late stages of carbon burnout as is evident by the consistent trend of rather smooth LOI trajectory curves through to complete burnout. There is no display of a decrease in char oxidation kinetics at or near complete burnout as is expected in practical coal furnaces (Hurt et al., 1998). Results also indicate that the weighted average of the three reactivity trajectories computed in the anneal CBK case would yield a single trajectory very similar to the single external model trajectory. As evident by the overall computed LOI (38.37% for anneal CBK and 38.29% for external) there exists a self-consistency between each of the kinetic data sets. Lastly, the shown behavior of the LOI trajectories is consistent with the observations of Hurt et al. (1996 and 1998). In their studies, there was an inability to describe the late stages of combustion when only the thermal annealing model was active.

LOI Trajectory Simulation Results: ash CBK vs. external

Exhibit 6-7 through Exhibit 6-10 are LOI trajectories for the same four particle clouds as presented in the previous section. For the ash CBK model, there is a general trend of a smooth decrease in carbon content in the particles throughout the axial length of the reactor followed by a dramatic flattening of this curve at the late stages of carbon burnout. This behavior is unique to the ash CBK case that couples thermal annealing, reactivity distribution and an ash film resistance mechanism.

The ash film resistance model used in the simulation case ash CBK incorporates three overall competing mechanisms: 1) the effect of a decreasing carbon rich core surface area and its subsequent effect on the ash film and bulk mass transfer coefficient, 2) mass transfer of oxygen to the core surface inhibited by a developing ash film porosity and 3) the chemical kinetic rate of carbon burnout per unit surface area. These coupled effects cause the lengthening of the LOI trajectories.

As each particle size and reactivity class approaches complete burnout, the ash film resistance model accounts for islands of ash nodules that coalesce and the resulting ash layer reaches complete coverage of the external surface area of the particle. As the ash layer grows, its porosity decreases and approaches a minimum value at full coverage. The critical porosity of the ash corresponding to the inherent porosity of the individual ash nodules was taken to be 0.21 as suggested by Hurt et al. (1998). At the realization of complete coverage, the ash film begins to grow at this constant critical porosity. The increase of the ash film distance dramatically decreases the ash film effective diffusivity.

Exhibit 6-11 illustrates the approach to the critical ash porosity for a 13, 45 and 95 μm initial particle diameter for reactivity bin #1. The 45 μm particle, (■); obtains its critical ash porosity at approximately 1.7 m. Recall that upon realization of the critical ash porosity, the ash film layer surrounding the carbon rich core begins to grow in excess of the minimal ash film distance of 1 μm. This increase in the ash film distance corresponds to a dramatic flattening of the LOI curve

as originally described in Exhibit 6-10, (■); again at an axial distance of 1.7 m. This trend was demonstrated by neither simulation case external nor simulation case anneal CBK.

Although the dramatic deflection in the LOI trajectories is attributed to the growth of a critical porosity ash film layer, the diffusional resistance effect of a decreasing ash porosity is also significant. The reader is again referred to Exhibit 6-11, now for the 13 μm, (●); size class. This size class is unique in that it reaches its critical ash porosity very near complete burnout. Although, a flattening of the LOI trajectory can be seen (see Exhibit 6-9, (○); at approximately 1.1 m), this particle size class spends the majority of time with only a developing ash film.

The effects of the developing ash film can be identified by contrasting the LOI trajectories between the 13 μm size class for each of the ash and anneal CBK models. Comparing the LOI trajectories between case ash CBK and anneal CBK for reactivity 1, (■); the axial distance corresponding to complete burnout is shifted from approximately 0.8 m to 1.1 m (see Exhibit 6-2 and Exhibit 6-7). This shift, therefore, represents the diffusional effect of the ash film resistance model. Although a developing ash film does affect the larger particle size class, the effects seem to be less dominating. For example, consider the LOI trajectories for the R1 reactivity bin, (■); for a 160 μm particle in Exhibit 6-5 and Exhibit 6-10. The respective LOI trajectories are nearly identical and each display an exit LOI of approximately 88%.

Exhibit 6-11 affirms that the developing ash film porosity for the 95 μm particle reaches only approximately 0.6. This porosity appears to have only a slight resistance effect. Reactivity 2, (▲); and 3, (+); however, each display a more pronounced diffusional effect of a developing ash film, see Exhibit 6-9. This is true since a higher reactivity results in a larger degree of carbon burnout and, therefore, larger ash film coverage.

Overall Exit LOI Imperial College Simulation Results

Godoy et al. (1991) reported overall burnout values as given by the following equation:

$$B = \frac{1 - \frac{\omega_a}{\omega_{a0}}}{1 - \omega_{a0}} \tag{124}$$

where B is the overall burnout, ω_a is the ash mass fraction in the collected char and ω_{ao} is the initial mass fraction of ash in the raw coal. Loss on Ignition is computed by solving for the mass fraction of ash in the char sample and is simply defined as the residual weight of carbon in the ash,

$$LOI = 100(1.0 - \omega_a) \tag{125}$$

Exhibit 6-12 compares the overall exiting loss on ignition values for both the simulated predictions and the available experimental data. The converted loss on ignition for the experimental case B1 is 45%. This value compares quite well to the ash CBK simulation case, 44.41%. The simulated external and anneal CBK case predicted LOI values very similar to each other: 38.29 and 38.37%, respectively. Each of the anneal CBK and external models were unable to predict the higher level of residual carbon in ash as experimentally observed (Godoy et al., 1991).

IFRF Simulation Study

Detailed IFRF combustion experiments have been performed on IFRF furnace #1 (Michel and Payne, 1980). It is a refractory tunnel of approximate dimensions: 6.23 x 6.23 x 20.51 ft (1.9 x 1.9 x 6.25 m) (Michel and Payne, 1980).

The IFRF furnace is tangentially fired and the primary and secondary ducts are concentric. A high volatile bituminous coal from the Saar-region in Germany was used in the IFRF study. The coal composition lies in the range typical US coals (32 and 7.6%, dry; volatiles and ash content). The flame chosen for this simulation study is flame A1. This flame is characterized by a high secondary air velocity (greater than 82 ft/s [25 m/s]). The experimental conditions included a coal mass flow rate of 458.03 lb/h (207.76 kg/h).

Mass flow rates of secondary and primary air are 4,550 and 562 lb (2,064 and 255 kg) air/h, respectively. The inlet secondary and primary temperatures are 301 °F and 914 °F [(423 °C and 490 °C) (423 and 763 K)], respectively. All of the reported cfd simulation cases include a particle size distribution (5 bins) ranging from 25 to 250 μm. There are five Lagrangian cloud starting locations for each particle size and for each reactivity. The modeling parameters used for this study are summarized in Table 6-5. Grid independent results were found to be at a grid size of 40 x 36 x 36 (the simulation case geometry was 6.23 x 6.23 x 20.83 ft (1.9 x 1.9 x 6.25 m).

Table 6-5
IFRF Simulation Parameters

Moisture (%)	Ash (%)	Fixed carbon (%)	Volatile matter (%)	Calorific Value Btu/lb
Trace	7.6	60.4	32.0	13,330
Mass(%) d.a.f.				
Carbon	Hydrogen	Nitrogen	Oxygen	Sulphur
80.79	5.086	1.21	11.99	0.92
CBK parameters				
Bin	Reactivity, G/s-cm^2-atm$^{0.5}$	Distribution	θ_{af}^{c}	α
1	72.13	0.04	0.20	0.20
2	153.61	0.29		
3	198.37	0.67		
Particle size distribution				
Bin	Diameter (μm)	Weight		
1	25.0	0.5		
2	62.5	0.2		
3	100	0.17		
4	162.5	0.09		
5	250	0.04		

Loss on Ignition Trajectory Simulation Results

Exhibits 6-13 and 6-14 are individual plots of loss on ignition vs. axial location for a cloud of particles starting at a location centered within the burner throat. The exhibits shown are for particles with an initial diameter of 25 and 100 μm. Each Exhibit compares the external, ash CBK and anneal CBK char oxidation submodels. LOI trajectories for both the anneal and ash CBK model represent the second reactivity bin, as previously defined in Table 6-5.

As in the Imperial College simulation study, neither the external model nor the anneal CBK display any transition at the late stages of carbon burnout as is evident by the consistent trend of rather smooth LOI vs. axial distance curve through to complete burnout. The ash CBK model, however, again displays lengthened LOI trajectories.

At the realization of a complete coverage, the ash film begins to grow at the constant critical porosity of 0.20. Exhibit 6-15 describes the approach to the critical ash film porosity for the conditions of Exhibit 6-13. Notice at approximately 12.47 ft (3.8 m), the ash film reaches its critical ash film porosity and marks the point where the critical ash film begins to grow past the model parameter of 1.0 μm. Again, this point is exactly where the LOI plot of Exhibit 6-13 turns over.

The trends outlined in the IFRF simulation case are exactly those of the Imperial College simulation cases. The use of the ash CBK model is the only char oxidation formulation that predicts a transition during the late stages of char combustion. The trend of a smooth LOI trajectory that is followed by a flattening is unique to ash CBK.

Axial Burnout Profile Results

Exhibit 6-16 is a plot of the available IFRF axial burnout data with the three simulated case studies: ash CBK, anneal CBK and external. The simulated case including ash film resistance, thermal annealing and three reactivity bins represents the model that best matches both the early and late stages of carbon burnout. These case study simulation results indicate that use of a char oxidation model that includes a diffusional resistance of oxidant to the surface via a developing ash film is key in accurately predicting the early and late stages of char oxidation. Each of the anneal CBK and external simulations severely over predicts the early stages of carbon burnout.

Exit Loss on Ignition Results

Although detailed axial profile simulation data are useful in quantifying different mechanisms of the char oxidation process, overall exit LOI represents the parameter that is most used in assessing design efficiency. Exhibit 6-17 is a bar graph comparing outlet LOI values for each of the three simulated cases with the IFRF experimental data set (Michel and Payne, 1980). The results confirm that the ash CBK model (50%) performs most accurately when compared to the experimental data (49%). Both the external case (27%) and the anneal CBK case (20%) again over predict the extent of carbon burnout.

Char Oxidation Conclusion

It has been shown that incorporation of specific elements of the advanced carbon burnout model of Hurt et al. (1996, 1998) within a cfd simulator does increase the accuracy of predicted overall loss on ignition and axial burnout profiles. Moreover, the models implemented neatly

incorporate observable physical phenomena paramount to the accurate prediction of LOI during both the early and the late stages of carbon burnout.

The ash CBK model represents the sole char oxidation model that predicts a somewhat dramatic turnover in the LOI simulation trajectories. This turnover is attributed to the increased diffusional resistance of the growing ash film and the attainment of a critical ash film porosity. It is evident that use of the ash CBK model reduces the char oxidation rate during the late stages of carbon burnout. This near-extinction behavior is not apparent in the two other simulation cases.

Although it was anticipated that the ash CBK model would be required for the accurate predictions of late stages of carbon burnout, results indicate that accurate prediction of axial burnout at the near burner region also require use of the ash CBK model as shown in Exhibit 6-16. The use of the ash CBK model has proven most capable of predicting exit furnace LOI while the anneal CBK and external model dramatically under predict exit LOI.

The three bin reactivity distribution, preexponential reactivities, critical ash film thickness, mode of burning parameter and porosity used in this study have been taken directly from the Hurt et al. (1998) formulation and guidelines. This study did not afford manipulation of the aforementioned parameter values. However, simulation cases were run to superficially determine the sensitivity of exit LOI and burnout profiles to different values of the mode of burning parameter and the critical ash film porosity. Varying these model parameters did not appreciably change the overall trend of lengthened LOI trajectories. Rather, only the exact point at which the LOI trajectory turnover occurred and the overall exit LOI were affected.

The relative importance of the reactivity distribution model was also explored by reducing the number of reactivity bins used for the ash CBK cfd IFRF simulation case from three bins to one bin. When only the mean value of the preexponential factor was tracked (a value of 180.34 $g/s\text{-}cm^2\text{-}atm^{0.5}$) the predicted exit LOI in the ash CBK three bin simulation case increased approximately from 49.8% to 58.7% LOI. This indicates that inclusion of a reactivity distribution, as suggested in the Hurt et al. (1996; 1998) statistical kinetics model, does affect predicted exit LOI. For all simulations, the computational expense in tracking more Lagrangian clouds must be balanced with the anticipated augmented prediction capability. In this simulation study, including a three bin reactivity distribution is computationaly manageable. The three bin reactivity model seems to adequately capture the effect of a distributed preexponential reactivity.

For simulations of low NO_x aerodynamic burner designs, predicting the subsequent reactivity of the coal particle after it has left the hot recirculation zone is key. Capturing the time/temperature thermal annealing effects coupled with an increasing resistance to oxidant diffusion is imperative. Predicted NO concentrations in coal-fired furnace applications are sensitive to the type of char oxidation submodel used (Domino and Smith, 1997). The ability to accurately predict nitrogen oxide in complex coal-fired furnaces requires an accurate carbon burnout prediction (Smoot and Smith, 1985). The ash CBK simulation case provides all of the intuitive mechanistic attributes to capture the controlling history of the overall coal particle reactivity and subsequent oxidation.

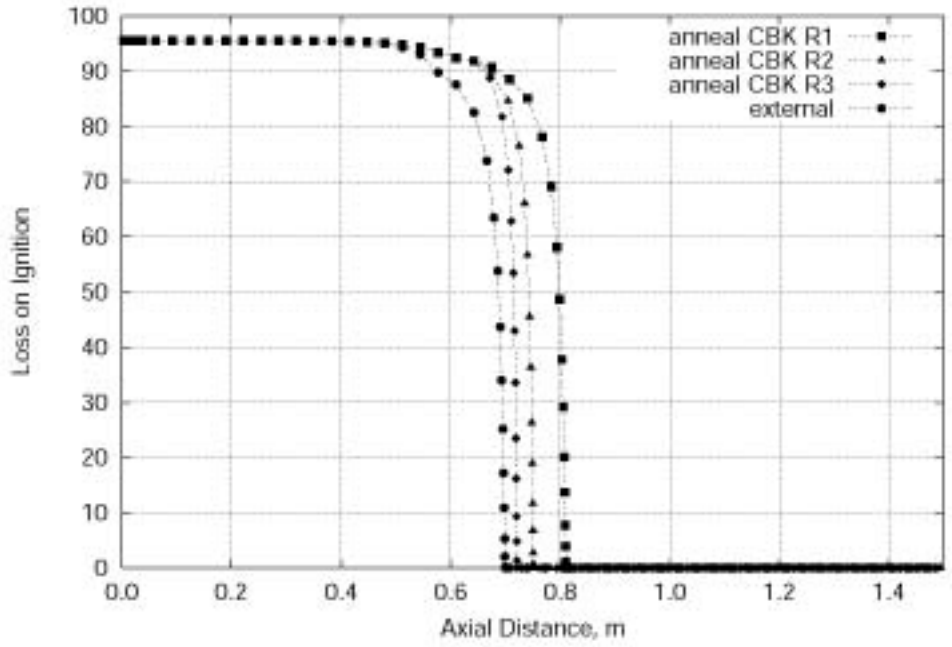

Exhibit 6-2
Loss on ignition plot for a 13 µm particle size class; trajectories shown are for simulation case external and anneal CBK

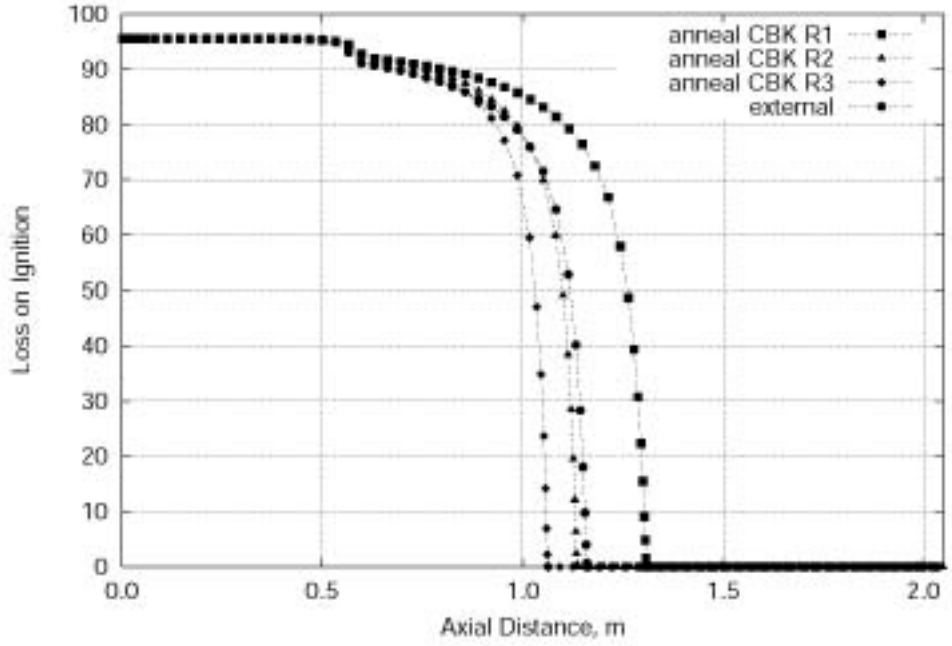

Exhibit 6-3
Loss on ignition trajectory plot for a 45 µm particle size class; trajectories shown are for simulation case external and anneal CBK

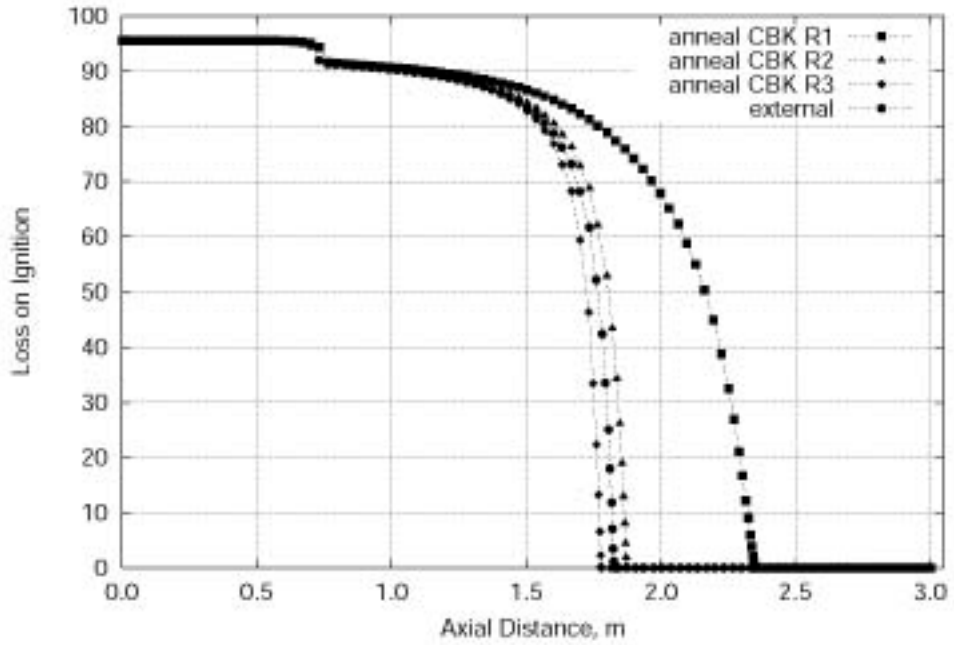

Exhibit 6-4
Loss on ignition trajectory plot for a 95 µm particle size class; trajectories shown are for simulation case external and anneal CBK

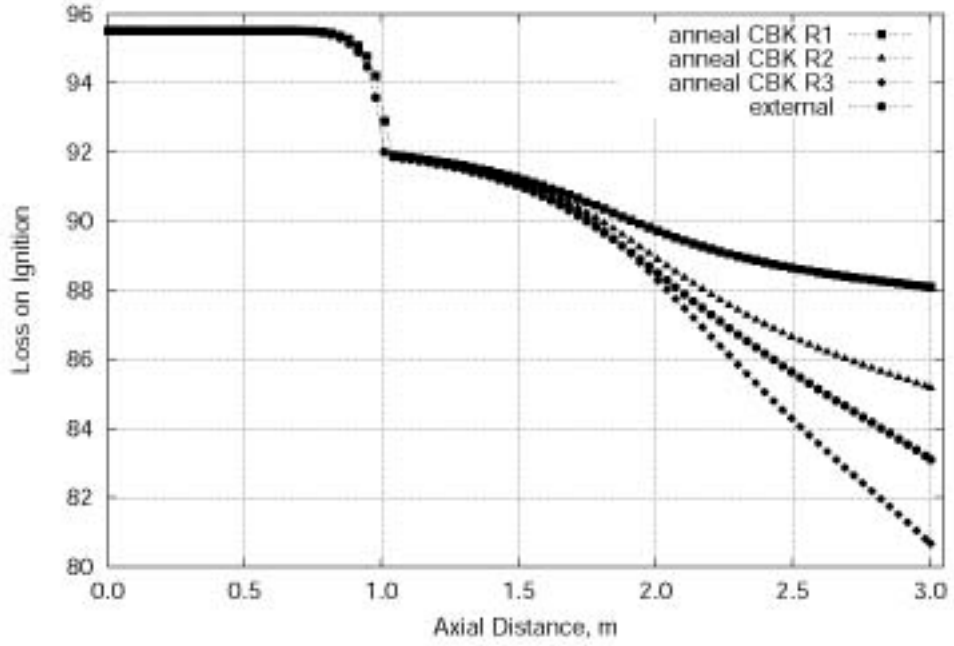

Exhibit 6-5
Loss on ignition trajectory plot for a 160 µm particle size class; trajectories shown are for simulation case external and anneal CBK

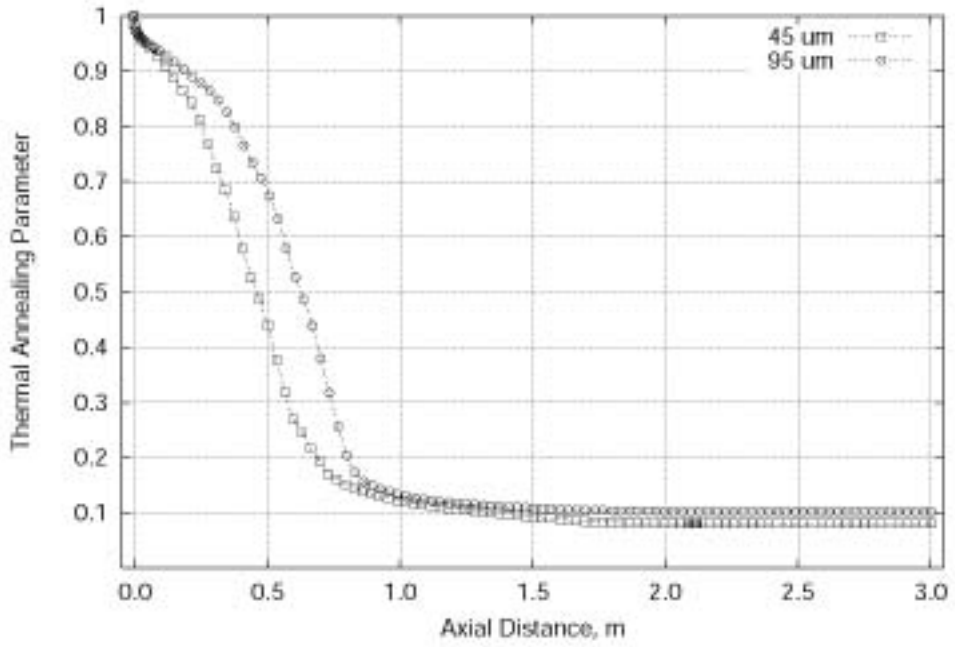

Exhibit 6-6
Thermal annealing functional dependence on particle diameter

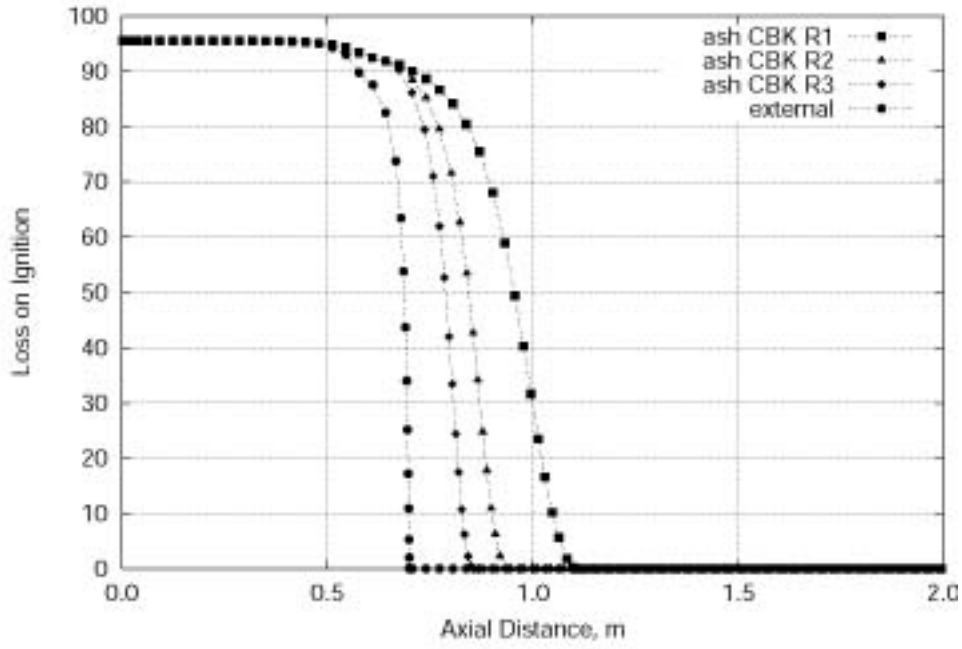

Exhibit 6-7
Loss on ignition trajectory plot for a 13 µm particle size class; trajectories shown are for simulation case external and ash CBK

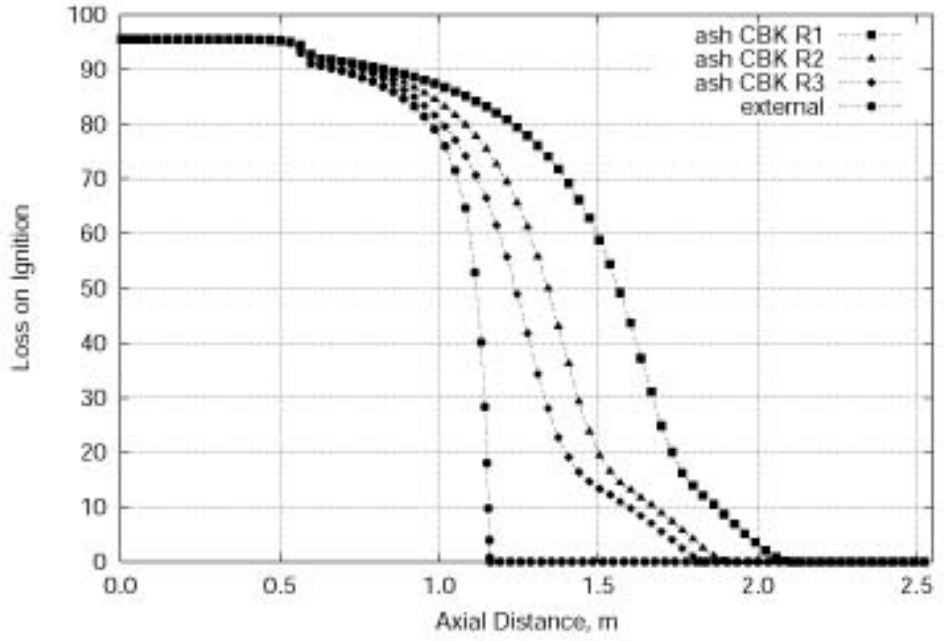

Exhibit 6-8
Loss on ignition trajectory plot for a 45 µm particle size class; trajectories shown are for simulation case external and ash CBK

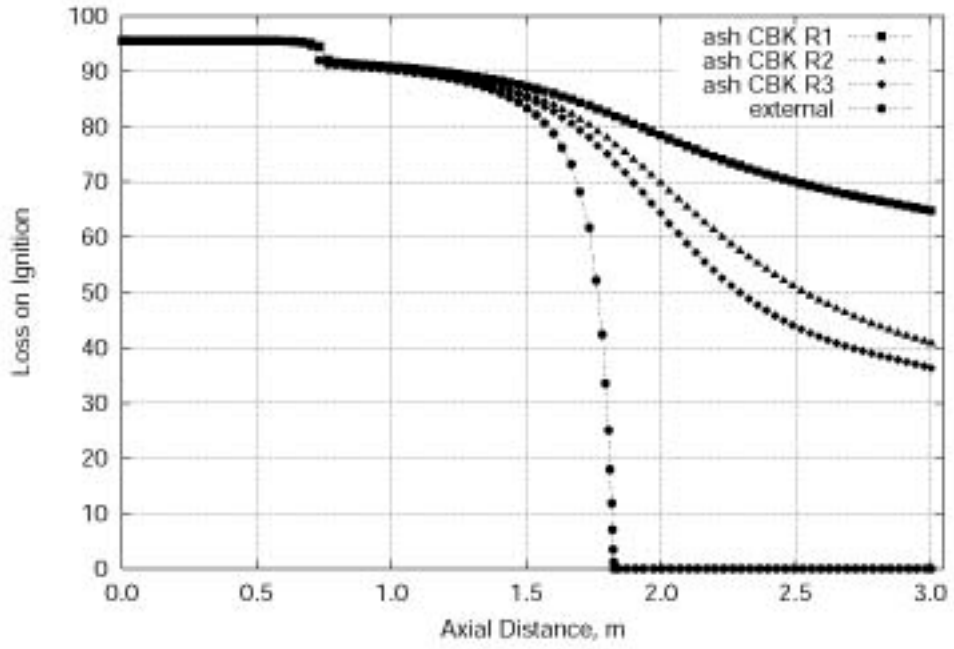

Exhibit 6-9
Loss on ignition trajectory plot for a 95 µm particle size class; trajectories shown are for simulation case external and ash CBK

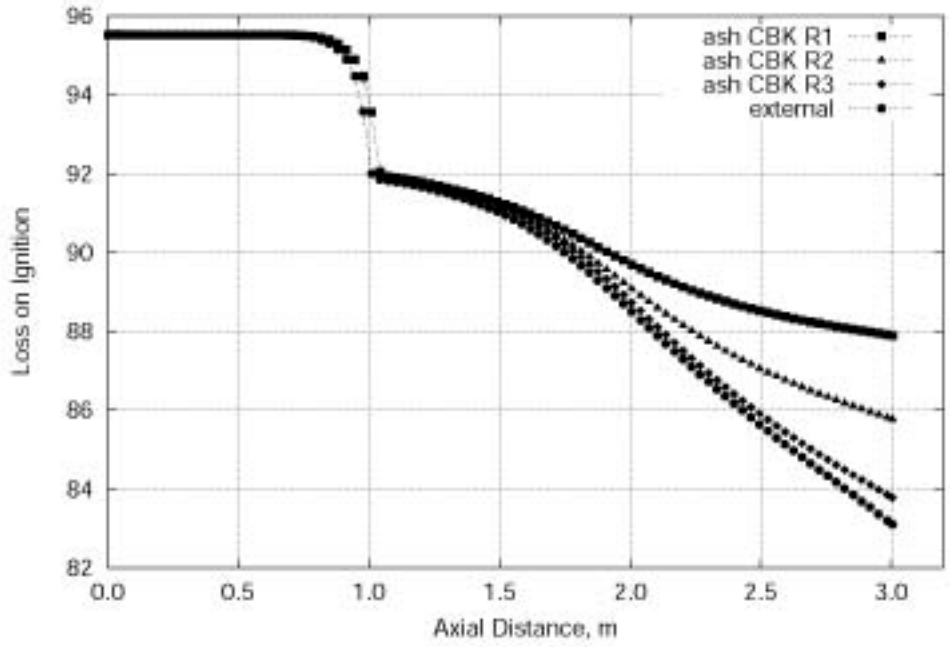

Exhibit 6-10
Loss on ignition trajectory plot for a 160 µm particle size class; trajectories shown are for simulation case external and ash CBK

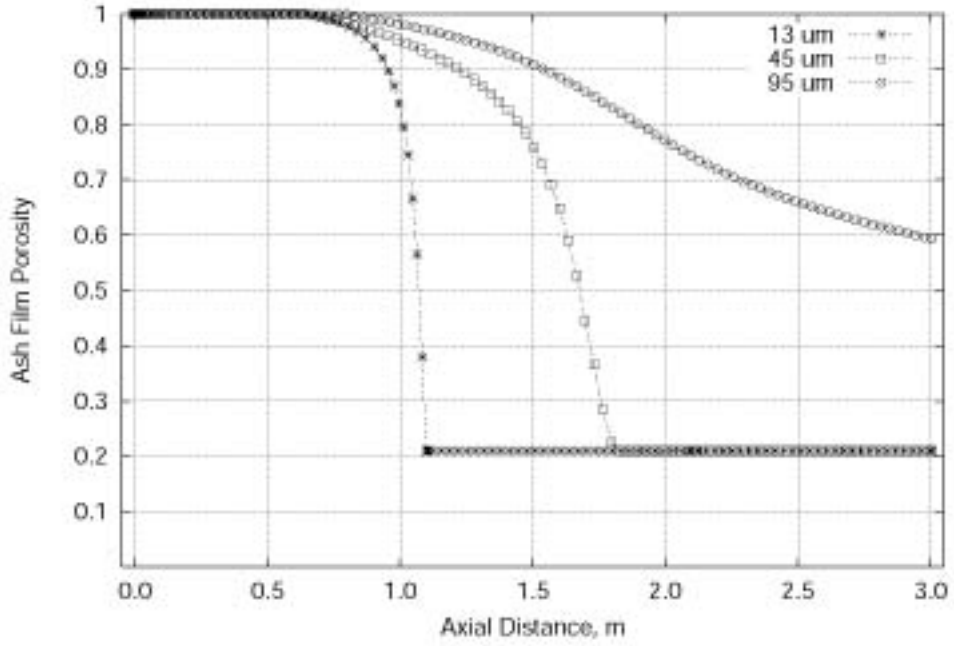

Exhibit 6-11
Critical ash film comparison

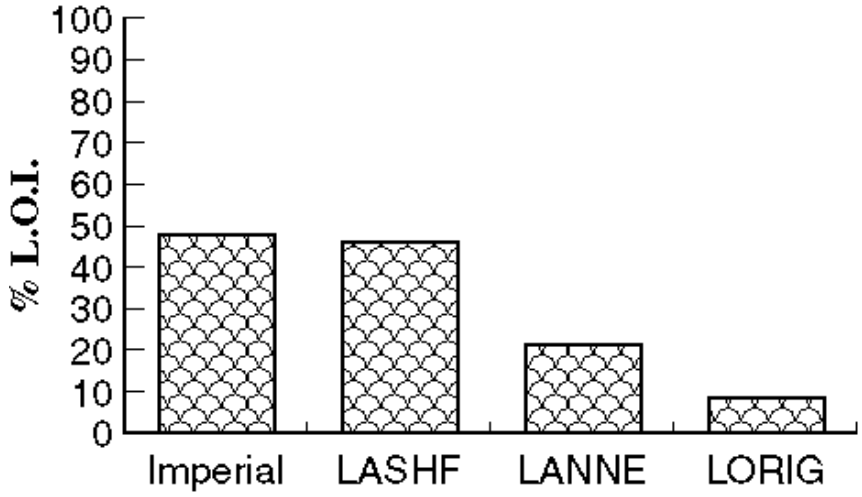

Exhibit 6-12
Overall LOI comparisons

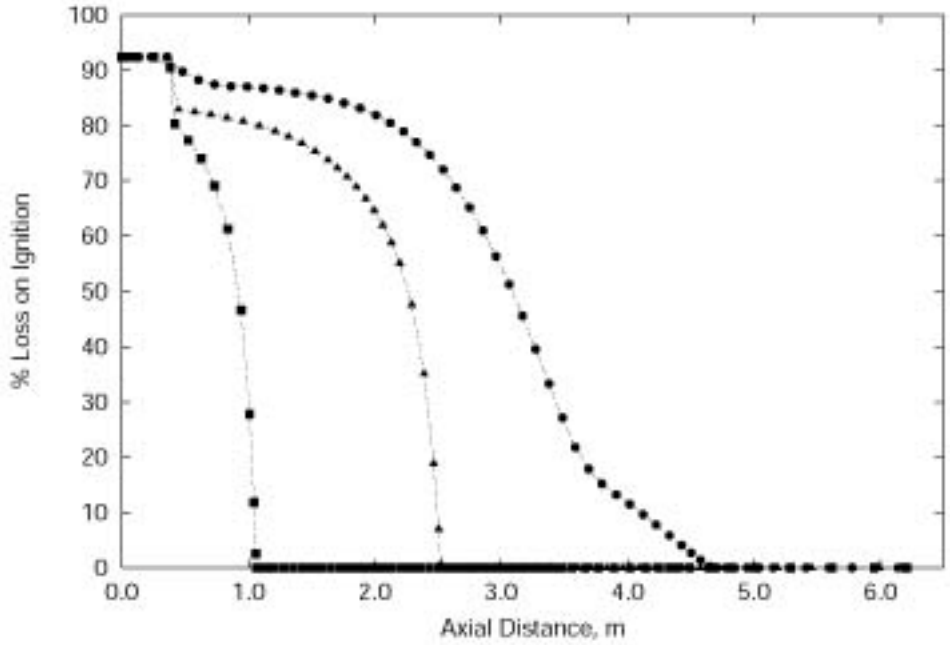

Exhibit 6-13
Loss on ignition trajectory plot for a 25 µm particle size class; trajectories shown are for simulation case external, anneal CBK, and as CBK

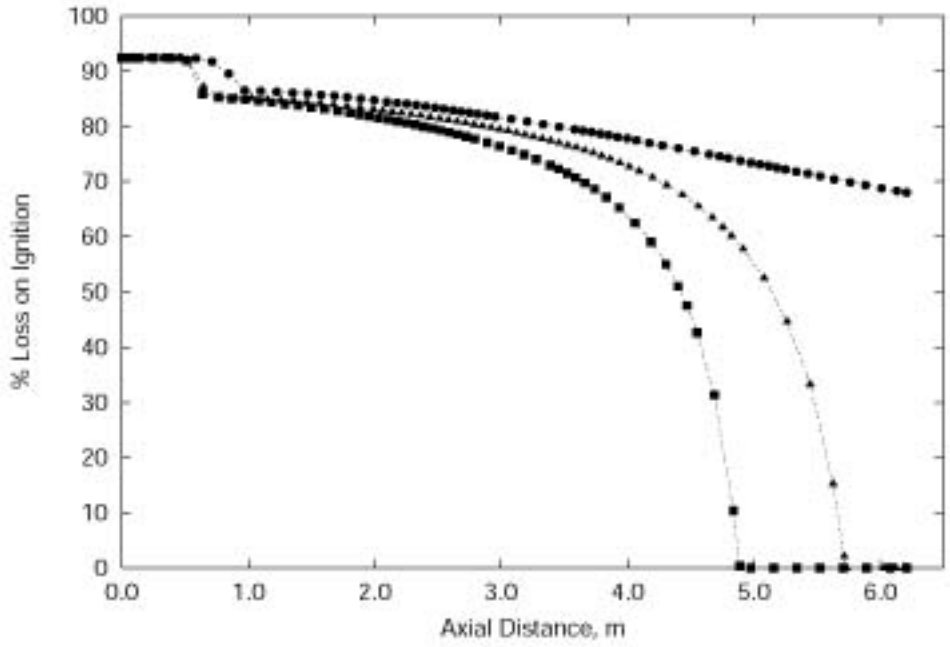

Exhibit 6-14
Loss on ignition trajectory plot for a 100 µm particle size class; trajectories shown are for simulation case external, anneal CBK, and CBK

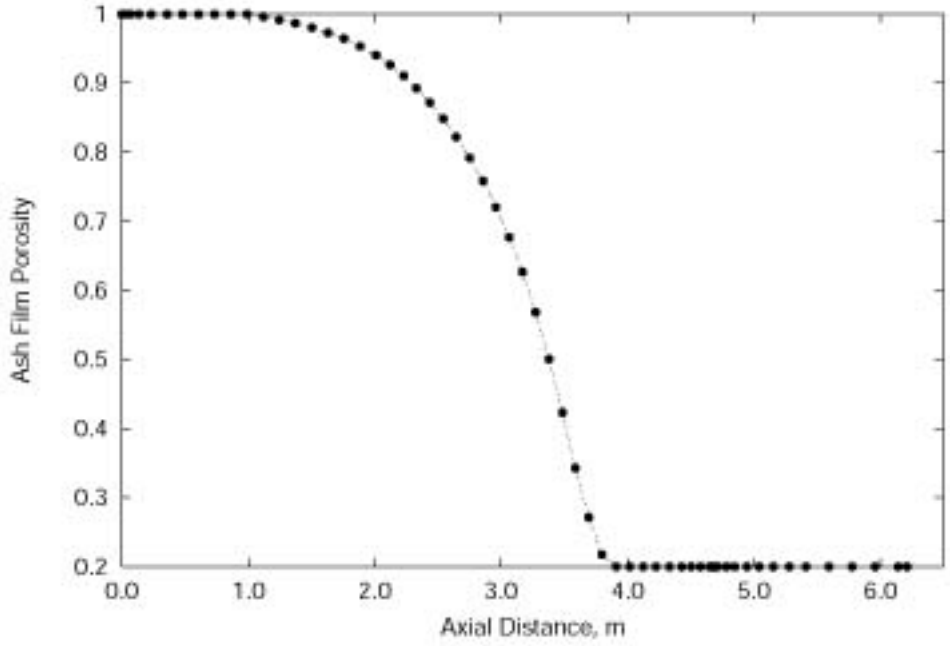

Exhibit 6-15
Ash film porosity for conditions of Exhibit 6-13

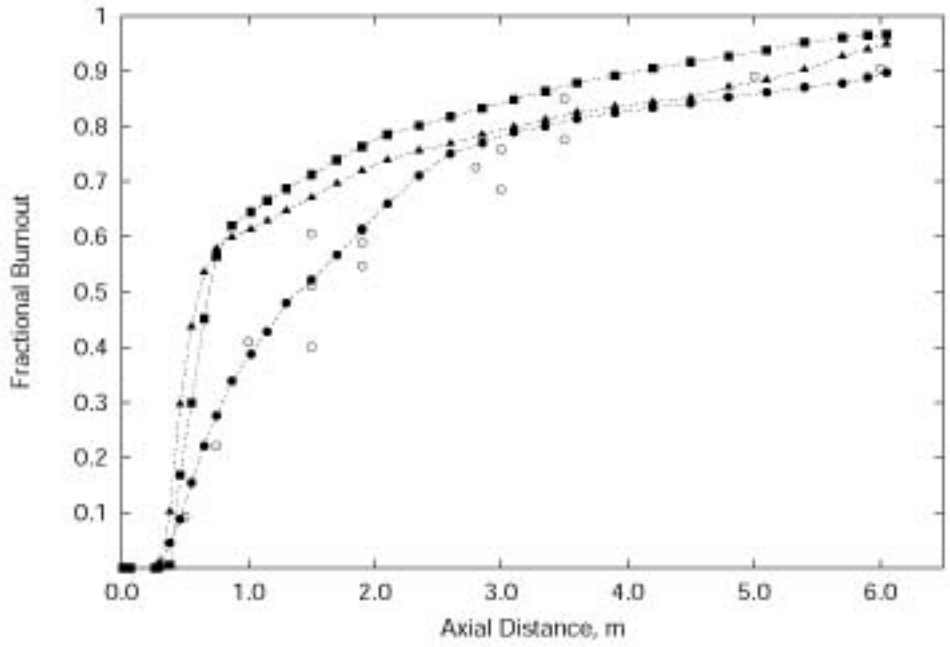

Exhibit 6-16
Centerline axial burnout profiles comparing the IFRF data set, ○, with the simulation cases: ash CBK, ●,anneal CBK, ■, and external, ▲

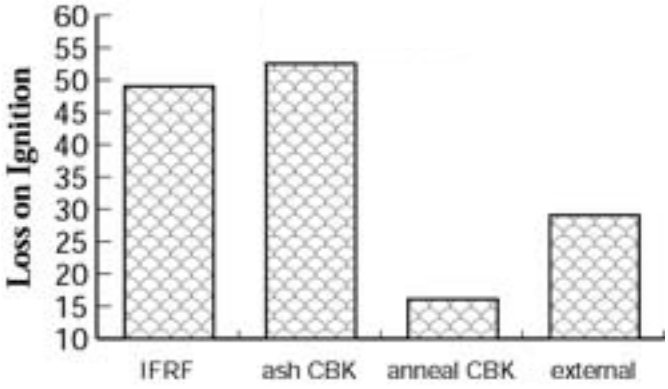

Exhibit 6-17
IFRF flame A1 overall simulated and experimentally reported LOI

Multiple Coal Off-Gas Mixture Fraction Formulation

Multiple Coal Off-Gas Mixture Fraction

Exhibit 6-18 is a schematic of a multiple coal off-gas mixture fraction formulation. The exhibit illustrates four total individual pathways for the liberation of coal off-gas assuming two competing devolatilization pathways.

Studies providing the residual composition of char exists and do not distinguish between the char formed through the mathematical construct of different devolatilization pathways (Mitchell et al., 1992; Spinti, 1997). Therefore, the multiple-η formulation requires the specification of one char composition and the calculation of the resulting two devolatilization pathways. The three coal off-gas mixture fractions computed are as follows: the mixture fraction of mass originating from devolatilization stream 1, 2 and char oxidation stream, η_1, η_2 and η_3, respectively.

Devolatilization pathways, as described previously, include the specification of a volatile yield and reaction rate coefficients (Kobayashi, et al., 1977; Ubhayakar et al., 1977). Assuming that the volatile yield for pathway *j* and the specification of the residual char are provided, then the composition of volatile stream *j* is

$$\omega_{V_j}^i = \frac{\omega_c^i - (1 - Y_i)\omega_h^i}{Y_j} \tag{126}$$

where *i* represents a particular element, i.e., carbon, oxygen, etc., ω_c^i is the mass fraction of element *i* in the raw coal, Y_j is the volatile yield for pathway *j* and ω_h^i is the residual char mass fraction for element *i*.

As described earlier, a turbulent transport equation for a coal off-gas stream is derived:

$$\frac{\partial}{\partial x_j}\left(\overline{\rho}\widetilde{v}_j\widetilde{\eta}_k - \frac{\mu_e}{\sigma_{\eta_k}}\frac{\partial\widetilde{\eta}_k}{\partial x_j}\right) = S_p^{\eta_k} \tag{127}$$

where $\widetilde{\eta}_k$ is the k^{th} Favre-averaged coal off-gas mixture fraction given by Eq. (128) and $S_p^{\eta_k}$ is the mass source term of the k^{th} coal off-gas stream originating from the respective pathway (char oxidation or either devolatilization stream 1 or 2).

$$\widetilde{\eta}_k = \frac{m_c^k}{\sum_i m_i} \tag{128}$$

The determination of mean state space variables is, therefore, given by the convolution of the compositional joint PDF as similarly in Section 2. Due to the increased number of turbulent coal off-gas mixture fractions, the dimension of the PDF is

$$d = (N_p + N_s + 3) - 1 \tag{129}$$

where N_p and N_s are the total number of differentiable primary and secondary streams, respectively. The number three appearing in the above equation is simply the contributions of the

three coal off-gas mixture fractions introduced in this section. Therefore, a simulation case involving a premixed coal burner has a total dimension of 3.

Independent Clipped Gaussian Coupling

As was discussed previously, a prescribed clipped Gaussian PDF mixing model has been developed (Smith, 1990). Moreover, the joint compositional PDF has been assumed to be uncorrelated and able to be written as the product of the independent probability density functions,

$$\widetilde{P}(f_1, f_2, ..., f_{N-1}) = \prod_{i=1}^{N-1} \widetilde{P}(f_i) \tag{130}$$

Therefore, the required multiple-η integration for a premixed coal burner simulation is

$$\widetilde{\beta} = \int_0^1 \int_0^{1-\eta_1} \int_0^{1-\eta_1-\eta_2} \beta(\eta_1, \eta_2, \eta_3)\, \widetilde{P}(\eta_1, \eta_2, \eta_3)\, d\eta_1\, d\eta_2\, d\eta_3 \tag{131}$$

Joint β-PDF Formulation

One approach to a joint β-PDF is to assume independence of the state variables. For this case

$$\widetilde{P}(\eta) \sim \widetilde{P}(\eta_1, \eta_2, ...) \sim \widetilde{P}(\eta_1)\widetilde{P}(\eta_2)... \tag{132}$$

Since the work involved in constructing a multiproduct independent clipped Gaussian PDF integration is too great (Brewster et al., 1988) methods to construct a joint PDF are warranted.

The formulation described by Girimaji (1992) provides a technique whereby the univariate β-PDF is extended to an arbitrary dimensional joint β-PDF. The joint PDF, which can be used to model the mixing of N scalars, is given by:

$$P(f_1, f_2, \ldots, f_{N-1}) = \frac{\Gamma(a_1 + a_2 + \cdots + a_N)}{\Gamma(a_1)\Gamma(a_2)\ldots\Gamma(a_N)} f_1^{a_1-1} f_2^{a_2-1} \ldots f_N^{a_N-1} \tag{133}$$

where f_i is the mass fraction of species originating from stream *i* and a_i are the joint β-PDF distribution parameters given by Eq. (134).

$$a_i = \widetilde{f}_i\left(\frac{1-S}{Q} - 1\right) \tag{134}$$

The variable S is the sum of squares of the mean mixture fractions,

$$S = \sum_{i=1}^{N} \widetilde{f}_i^{\,2} \tag{135}$$

and the fluctuating Favre-averaged turbulent scalar energy, $\widetilde{q}$, is defined as the sum over all mean variances

$$\widetilde{q} = \sum_{i=1}^{N} \widetilde{g}_i \qquad (136)$$

As presented, the construction of the joint β-PDF only requires the solution of N-1 transport equations and the Favre-average fluctuating turbulent scalar energy, $\widetilde{q}$. The variable $\widetilde{q}$ can either be calculated by solving the individual N variance equations as provided previously or the suggested transport equation given by Girimaji (1991) that calculates $\widetilde{q}$ directly,

$$\frac{\partial}{\partial t}\widetilde{q} + \widetilde{u}_j \frac{\partial}{\partial x_j}\widetilde{q} = \sum_{i=1}^{N} \frac{\partial}{\partial x_j}\left(-\widetilde{f_i'' f_i''}\right) - 2\sum_{i=1}^{N} u_i' f_i' \frac{\partial \widetilde{f}_i}{\partial x_i} - 2\varepsilon_f \qquad (137)$$

The first term on the right hand side represents the transport of scalar energy due to velocity fluctuations and can be modeled by a gradient-diffusion model. The next term on the right hand side is the production of turbulent scalar energy. The last term on the right hand side is the dissipation of turbulent scalar energy and is modeled by

$$\varepsilon_f = C_f \frac{\varepsilon}{k}\widetilde{q} \qquad (138)$$

where ε is the turbulent energy dissipation, k is the turbulent energy production and C_f is a numerical constant. The reader will note the similarly between Eq. (137) and Eq. (14). In fact, the modeling assumptions in determining the right hand side terms are analogous to those used in Eq. (14) (Launder and Spalding, 1972; Bilger, 1975; Smoot and Smith, 1985).

Joint β-PDF Integration

As shown in Exhibit 6-19, there exists a sensitivity to the total amount of Gaussian Quadrature points in the evaluation of the state space convolution. The number of Gaussian quadrature points required to accurately perform the integration represented in Eq. (131) depends on the PDF dimension. Exhibit 6-19 is a plot that displays excellent accuracy for the three-dimensional fixed 10-point Gaussian quadrature integration algorithm (Abramowitz and Stegun; 1970). Shown in this exhibit is the mean value of $\widetilde{\eta}_1$ calculated by two different methods. Method 1 calculates $\widetilde{\eta}_1$ from a transport equation while method 2 uses the definition of a mean variable within the context of a PDF integration,

$$\widetilde{\eta}_1 = \int_0^1 \int_0^{1-\eta_1} \int_0^{1-\eta_1-\eta_2} \eta_1 \widetilde{P}(\eta_1, \eta_2, \eta_3)\, d\eta_1\, d\eta_2\, d\eta_3 \qquad (139)$$

Unfortunately, when the dimension of the integration is increased, the accuracy dramatically decreases at fixed Gaussian quadrature points.

β-PDF Robustness

As described in Eq. (133), the β-PDF requires a gamma function evaluation for individual distribution parameters, $\Gamma(a_i)$ and sums of distribution parameters, $\Gamma(a_i + a_2 + \ldots + a_N)$. Unfortunately, at mean values with low variances, the calculated distribution parameters give rise to numerical overflow when the gamma function evaluation is attempted. Machine overflow

occurs at approximately Γ(170). Typical distribution parameters can range from less than unity to greater than 1000.

Various techniques can be used in extending the point at which machine overflow occurs. One such method is to replace the entire gamma function evaluation by an integration. Using a fundamental definition of a PDF,

$$1 = \int_0^1 \int_0^{1-\eta_1} \cdots \int_0^{1-\eta_1-\eta_2-\cdots-\eta_{N-1}} \tilde{P}(\eta_1, \eta_2, \ldots, \eta_{N-1})\, d\eta_1\, d\eta_2 \ldots d\eta_{N-1} \qquad (140)$$

and the definition of the joint β-PDF yields the following equation:

$$\int_0^1 \int_0^{1-\eta_1} \cdots \int_0^{1-\eta_1-\eta_2-\cdots-\eta_{N-1}} \tilde{P}(\eta_1, \eta_2, \ldots, \eta_{N-1})\, d\eta_1\, d\eta_2 \ldots d\eta_{N-1} = \frac{\Gamma(a_1)\Gamma(a_2)\ldots\Gamma(a_N)}{\Gamma(a_1 + a_2 + \cdots + a_N)} \qquad (141)$$

This definition is substituted into Eq. (133), thus eliminating the need for a gamma function evaluations.

Another technique that has been proposed by Chen et al. (1994) is renormalization of the distribution parameters. In this technique, the overflow problem is circumvented by normalizing the maximum β-PDF distribution parameter to a value that will not result in machine overflow. In this procedure, each distribution parameter is normalized such that the ratio of any two distribution parameters is conserved, however, results in suitably low parameters to prevent machine overflow.

Take for example, a one-dimensional β-PDF that has distribution parameters a_1 and a_2 equal to 300 and 1000, respectively. The process of renormalization defines a maximum distribution parameter value, for example 600, and renormalizes the maximum distribution parameter to that value. Therefore, the distribution values used in the PDF function evaluation are a_1 and a_2 equal to 180 and 600, respectively. Notice the ratio of distribution parameters has been preserved and that this process artificially augments the physical mixing effect. Nevertheless, this technique has been reported in the literature to perform well when the integration of Eq. (143) fails due to a high distribution factor and low mixture fraction (Chen et al., 1994).

Summary of the Multiple-η Formulation

In this section, the concept of a multiple-coal off-gas mixture fraction, which is required to incorporate the mixing and reaction effect of a variable coal off-gas stream, is developed. Moreover, the feasibility of constructing the joint PDF and incorporating it within a mixing model is clearly demonstrated.

Simulation results indicate that it is improper to neglect turbulent fluctuations in the char off-gas stream. This assumption was justified by Flores (1992) by assuming the following: 1) that the char reactions are very slow in comparison to the fluctuating state space variables; 2) the "oxidizer and carbon from the char must already be mixed at the char surface for reaction to occur, and fluctuations are not needed"; and 3) "experience in comprehensive coal combustion calculations has shown that the turbulent fluctuations are generally only significant (greater than 5% of the mean) in the near-burner regions where devolatilization occurs (Flores and Fletcher, 1995). The first assumption more appropriately addresses the reason why fluctuations are not included in the heterogeneous char oxidation process, while the third explanation is purely anecdotally based.

The calculation of the distribution factors needed for the proper description of the joint β-PDF can be obtained either from one single modeled equation (Girimaji, 1991) or by the calculation of N individual variance partial differential equations. The computation of a single PDE to determine the joint β-PDF distribution factors is highly preferred.

Simulation results indicate that the accuracy of the joint PDF integration is compromised at higher dimensions. There also exists a state space sensitivity to the prescribed PDF as simulation results comparing the clipped Gaussian and β-PDF resulted in significantly different state space profiles.

The following sections present the coupling between the joint PDF mixing model and to the postprocessor NO model. Lastly, coal off-gas stream compositional effects are explored via a detailed simulation study.

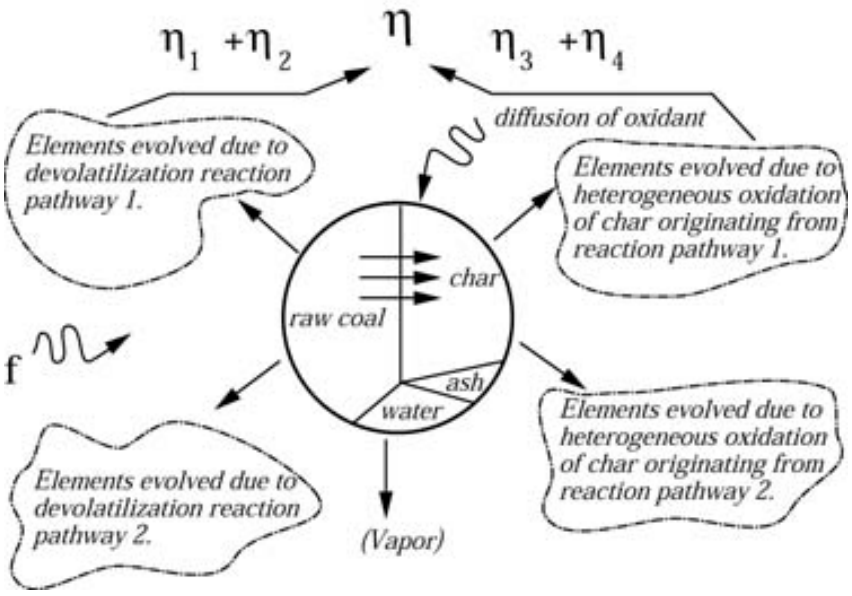

Exhibit 6-18
General Schematic of coal combustion illustrating the concept of the multiple coal off-gas mixture fraction

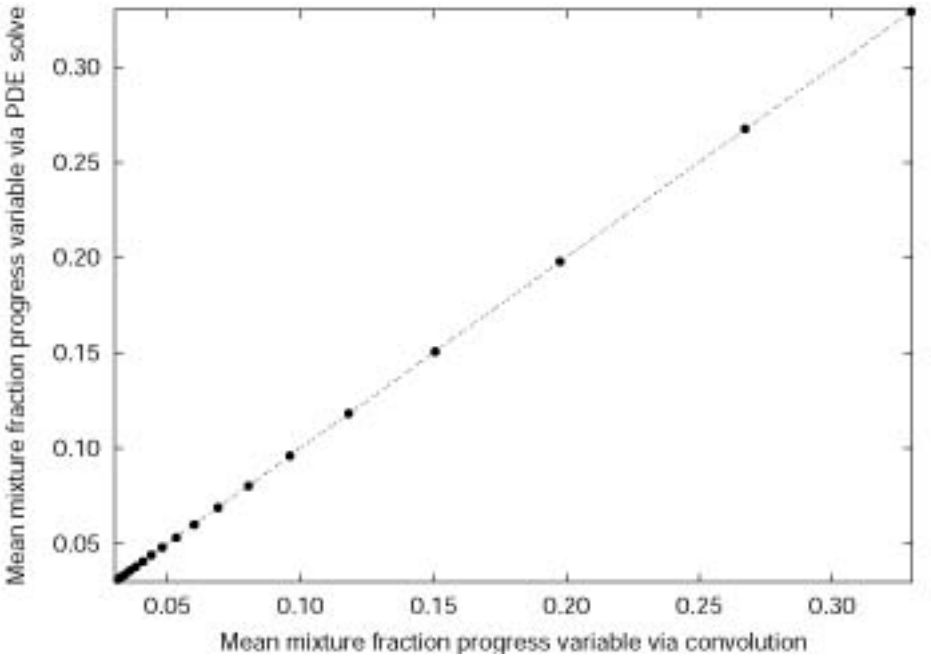

Exhibit 6-19
Error in 3-dimensional convolution over mean mixture fraction variable; 10 Gaussian quadrature points

Multiple-η NO Submodel For Pulverized-Coal Flames

The nitrogen oxide model within the multiple-η formation contains all of the global NO rate laws as described previously. As before, individual turbulent transport equations for each species in Favre averaged form are calculated:

$$\nabla \cdot \left(\overline{\rho}\widetilde{\mathbf{v}}\widetilde{Y}_i\right) - \nabla \cdot \left(\overline{\rho} D_{Y_i} \nabla \widetilde{Y}_i\right) = \overline{W}_i \tag{142}$$

To review, the time mean rate of reaction, $\overline{w}_i$, is simply the difference between the rates of production and consumption of species *i*,

$$\overline{W}_i = \underset{i}{\overline{w}_i^{\text{production}}} - \underset{i}{\overline{w}_i^{\text{consumption}}} \tag{143}$$

The individual mean production and consumption reaction, w_i are obtained by convolution over the joint compositional β-PDF. Assuming that the system is a pre-mixed coal burner, there exist four total streams.[4] The integration is performed using Gaussian quadrature as previously explained. The appropriate integration of an individual instantaneous rate is given by:

$$\overline{w}_i = \overline{\rho} \int_0^1 \int_0^{1-\eta_1} \int_0^{1-\eta_1-\eta_2} \frac{w_i\left(\eta_1, \eta_2, \eta_3, \widetilde{h}_r\right)}{\rho\left(\eta_1, \eta_2, \eta_3, \widetilde{h}_r\right)} \widetilde{P}(\eta_1, \eta_2, \eta_3)\, d\eta_1\, d\eta_2\, d\eta_3 \tag{144}$$

As previously noted by Coelho and Carvalho (1995) and Jones (1979), mean NO reaction rates are extremely sensitive to the effect of temperature and, therefore, these rates may be quite sensitive to the assumed PDF shape. Coalho and Carvalho (1995) presented limited comparison plots of a clipped Gaussian and β-PDF and found NO compositional differences of up to 50 ppm (approximately 10%).

HCN Mass Source Terms

The newest approach is similar to that of Eddings et al. (1994); however, the definition of two coal off-gas mixture fractions originating from two competing devolatilization reactions affords use of the exact mass fraction of devolatilized nitrogen. Therefore, there exists full coupling of the known compositional effects between the coal combustion simulation and the NO model. The specification of an overall yield of devolatilized nitrogen to HCN (the parameter ζ) is retained. Equation (147) represents the new rate of HCN production, assuming a two-step devolatilization mechanism.

$$\overline{w}_{HCN} = \varsigma\left(\frac{M_{HCN}}{M_N}\right)\left(\omega_N^{vol_1}\overline{S}_p^{\tilde{\eta}_1} + \omega_N^{vol_2}\overline{S}_p^{\tilde{\eta}_2}\right) \tag{145}$$

[4] In the multiple-η formulation, the total number of inlet streams is defined by: 3+S, where S is the number is differentiable air inlet streams and 3 streams and 3 represents the contribution of 2 volatile streams and 1 char off-gas stream. Recall, the dimension of the integration over the joint-PDF is defined by the number of independent mixture fraction progress variables. For the case of a permitted coal burner, the PDF has a dimension of 3.

NO Mass Source Terms

In the nitric oxide multiple-η model, the fractional conversion of char-nitrogen to nitric oxide is obtained through the user specified parameter, ζ_h. Recent modeling studies indicate that NO formation through the oxidation of char-nitrogen is a viable modeling assumption (Visona and Stanmore; 1996 and 1999). The rate of NO production through the homogeneous pathway of char-nitrogen is:

$$\overline{w}_{NO} = \zeta_h \left(\frac{1}{M_N} \right) \omega_N^{char} \left(\overline{S}_p^{char} \right) \tag{146}$$

The mass fraction of nitrogen in the char, ω_N^{char}, is the user specified nitrogen mass fraction and is provided by Mitchell et al. (1992) for a suite of 10 coal types.

Mixing Model Coupling

Instantaneous mole fractions for HCN and NO are calculated by assuming that the local instantaneous mass fraction of species *i* is a linear function of its fully achievable mass fraction, as previously described. To review, Y_i is given by Eq. (147).

$$Y_i = \pi_i Y_i^f \tag{147}$$

where Y_i^f is the fully achievable mass fraction of species *i* and π_i is a linearization parameter.

The instantaneous fully achievable mass fraction of HCN again depends on the assumption of how HCN enters the homogeneous pathway. Assuming that HCN enters the gas phase through a specified conversion of devolatilized nitrogen and that the multiple-η formulation is in use, then Y_{HCN}^f is given by:

$$Y_{HCN}^f = \zeta M_{HCN} \left(\omega_N^{vol_1} \eta_1 + \omega_N^{vol_2} \eta_2 \right) \tag{148}$$

The coal off-gas mixture fractions appearing in Eq. (148), η_1 and η_2 represent instantaneous values of each volatile off-gas mixture fraction within the integration algorithm loop.

The fully achieved NO mole fraction, Y_{NO}^f, is again calculated by assuming that all HCN is converted to NO,

$$Y_{NO}^f = Y_{HCN}^f \left(\frac{M_{NO}}{M_{HCN}} \right) \tag{149}$$

Unlike the $\tilde{\eta}_{vol}$ formulation, the fully achieved instantaneous mass fraction of HCN and NO are correctly calculated from the instantaneous volatile mixture fractions as defined within the integration loop.

The mean fully achieved mass fractions of HCN and NO are

$$\widetilde{Y}_{HCN}^f = \zeta M_{HCN} \left(\omega_N^{vol_1} \tilde{\eta}_1 + \omega_N^{vol_2} \tilde{\eta}_2 \right) \tag{150}$$

and

$$\widetilde{Y}_{NO}^{f} = \widetilde{Y}_{HCN}^{f}\left(\frac{M_{NO}}{M_{HCN}}\right) \tag{151}$$

The algorithm for calculating the trace nonequilibrium mole fraction of HCN and NO at a given point in the computational grid for the multiple-η nitrogen oxide model is very similar to the algorithm outlined previously. The only differences are the way in which the fully achievable mean and instantaneous values are computed. Since all progress variables are available at run time, there is no need to solve a PDE for the transport of any coal off-gas mixture fraction progress variable. The appropriate algorithm is as follows:

1. Obtain the mean value of the fully achieved mass fractions, $\widetilde{Y}_{HCN}^{f}$ and $\widetilde{Y}_{NO}^{f}$ based on the mean values of $\widetilde{\eta}_1$ and $\widetilde{\eta}_2$; Eq. (150) and (151).
2. Use the current value of $\widetilde{Y}_{NO}$ and $\widetilde{Y}_{HCN}$ based on the species transport PDE, Eq. (144), to calculate each respective linearization constant, $\widetilde{\pi}_i$.
3. Within integration loop, calculate instantaneous fully achieved mass fractions for Y_{HCN}^{f} and Y_{NO}^{f}, Eq. (148) and (149), based on the appropriate instantaneous value of η_1 and η_2.
4. Use the respective calculated linearization constant from step 2 along with instantaneous fully achieved mass fractions and calculate the instantaneous mass fractions of HCN and NO, Eq. (147).
5. Calculate equilibrium state space variables to be used in rate expressions listed in Table 6-2, based on the current values of the mixture fraction progress variables within integration loop; use major species compositions to determine the appropriate nonequilibrium mole fractions of OH and O, if applicable and convert all mole fractions to mass fractions.
6. Calculate instantaneous rates, w_1, w_2, w_3, etc.
7. Assign appropriate PDF weight to instantaneous rate and return to step 4 until the full integration loop is terminated.
8. With the mean values of the individual rates of reactions in hand, construct $\overline{W}_{NO}$ and $\overline{W}_{HCN}$.
9. Solve each respective transport equation for $\widetilde{Y}_{NO}$ and $\widetilde{Y}_{HCN}$. If convergence is reached, terminate. Otherwise return to step 1.

β-PDF Simulation Case Study

Simulation cases of the University of Utah bench scale test facility coal fired furnace are presented to evaluate the sensitivity of state space variables and nitric oxide compositions to a varying mixture fraction coal off-gas composition. Sensitivity of state space variables to the

chosen PDF (clipped Gaussian or joint β) is explored through global simulation studies. Fundamental differences in the clipped Gaussian and β-PDF are addressed by individual PDF shape studies given a common mean and variance.

The University of Utah multifuel combustion research furnace is down-fired with a nominal firing rate of 29 kW. The combustion chamber is 0.52 ft (0.16 m) in diameter and has a U configuration. The overall length of the furnace is 23.95 ft (7.3 m). Ports along the length of the furnace are available for extracting samples and injecting air or fuel. Detailed plans of the University of Utah bench scale furnace may be found at Spinti (1997) and Veranth (1998). In this experimental case, Pittsburgh #8 coal was fired at a coal mass flow rate of 7.78 lb/hr (3.53 kg/hr) through a premixed coal burner. The incoming primary air flow rate was 1165 SCFM (32.99 m^3/m) and the inlet temperature was taken to be 449 °F (232 °C, 505 K).

Each of the reported simulation cases includes a six particle-sizes bin with five Lagrangian cloud starting locations for each particle size and reactivity. The char oxidation submodel is the CBK (Hurt et al., 1998; 1996) with thermal annealing, ash film resistance and reactivity distribution. Details of the coal compositions and CBK parameters may be found in Table 6-6.

The course mesh size is 20x17x17 and all cases were run on an SGI Octane workstation. The finite difference equations for u, v, w, k, e, p, p^c and all appropriate mean mixture fraction and variance progress variables were solved until the maximum of all the finite difference equation residuals were less than 3.5 (Smith, 1990).

Table 6-6
Pittsburgh #8 Coal Parameters

Moisture (%)	Ash (%)	Fixed carbon (%)	Volatile matter (%)	Calorific Value Btu/lb
1.72	8.06	53.57	36.65	13,296
Mass(%) d.a.f.				
Carbon	Hydrogen	Nitrogen	Oxygen	Sulphur
81.93	5.35	1.74	10.0	0.98
CBK parameters				
Bin	Reactivity, G/s-cm^2-atm$^{0.5}$	Distribution	θ_{af}^{c}	α
1	69.2	0.04	0.16	0.19
2	147.3	0.29		
3	190.3	0.67		
Particle size distribution				
Bin	Diameter (μm)	Weight		
1	3.8	0.0011		
2	18.6	0.1006		
3	37.6	0.2800		
4	71.4	0.3668		
5	135.5	0.2011		
6	280.8	0.0504		

Uniform Coal Off-Gas Mixture Fraction Case Study

State space variable sensitivity to the shape of the assumed PDF is explored through comparisons of a single clipped Gaussian PDF and a multi-dimensional β-PDF with all coal off-gas stream compositions set to that of the parent coal. Therefore, specification of the residual char to be that of the parent coal for the multiple- formulation, as described earlier, allows direct shape comparison with the single clipped Gaussian PDF mixing model. To review, the multiple-η coal off-gas mixture fraction formulation calculates three turbulent coal off-gas mixture fractions originating from the two devolatilization and single char oxidation streams. The uniform-η formulation uses one mixture fraction to describe the uniform transport of all coal off-gas.

Exhibit 6-20 is a comprehensive plot of all uniform composition simulation cases run. The simulation cases presented are as follows: no mixing model, single clipped Gaussian PDF, joint β-PDF with renormalization, joint β-PDF without renormalization, joint β-PDF with three assumed independent clipped Gaussian at distribution parameter overflow, robust joint β-PDF method (to be explained in this section) and, lastly, three independent clipped Gaussian probability distribution functions that neglect intermittency effects.

The axial temperature plots shown in Exhibit 6-20 are fully converged cases that include multiple particle iterations. The use of particle iterations is unlike the previous plots presented earlier where no particle chemistry was included. Small changes in state space variables, therefore, are expected to drastically effect devolatilization and char oxidation rates.

The simulation case using the robust β-PDF involves recasting the joint PDF to natural logarithm form, thus eliminating the overflow problem with large distribution factors. Function evaluations of the joint β-PDF, as required for any chosen integration algorithm, are obtained by first taking the natural logarithm of the joint β-PDF,

$$\ln\left(P\left(\eta_1,\eta_2,\ldots,\eta_{N-1}\right)\right)=\ln\left(\frac{\Gamma\left(a_1+a_2+\cdots+a_N\right)}{\Gamma\left(a_1\right)\Gamma\left(a_2\right)\cdots\Gamma\left(a_N\right)}\eta_1^{a_1-1}\eta_2^{a_2-1}\cdots\eta_N^{a_N-1}\right) \qquad (152)$$

The precise function evaluation of the β-PDF is simply obtained by taking the exponential of Eq. (152). This novel formulation perfectly extends the use of the β-PDF to an arbitrarily high distribution factor.

The process of renormalization, as proposed and developed by Chen et al. (1994), represents only a partial fix to the overflow problem. Recall, that Chen et al. (1994) proposed that the overflow problem can be overcome by normalization of the maximum β-PDF distribution parameter to a value that will not result in machine overflow. In this procedure, each distribution parameter is normalized such that the ratio of any distribution parameter is conserved, however, is suitably low to prevent machine overflow.

Comparison of the individual temperature plots, as shown in Exhibit 6-20, indicates that utilizing the robust β-PDF formulation is quite similar to the case of renormalization. Using mean values, however, does appear to yield slightly different outlet temperature. Therefore, at machine overflow, there does exist a slight mixing effect that is captured by the renormalization technique, yet missed by the utilization of mean values.

Exhibit 6-20 also includes a case using three independent clipped Gaussian independent probability distribution functions without the effects of intermittency. The exact disparity between this case and others is unknown and was not pursued due to the non-intuitive numerical algorithm needed to calculate 4(2(N-1)-1) total terms (Brewster et al., 1988)[5].

Variable Composition

The calculation of multiple coal off-gas mixture fraction progress variable via a PDE solve affords the specification of a residual char composition. The ability to distinguish individual coal off-gas mixture fractions allows capturing the known compositional disparity throughout the devolatilization and char oxidation combustion regime (Mitchell, 1992). The specification of the char composition for Pittsburgh # 8 coal was given in Spinti (1997) and the values used in this simulation study are given in Table 6-7. Exhibit 6-21 and Exhibit 6-22 are axial plots of centerline temperature comparing the effect of a varying coal off-gas composition. The simulations shown are for the cases of with and without the use of renormalization. Each plot also shows the experimental data provided within the dissertation of Spinti (1997).

[5] N again represents the total number of physical streams. In the case of three coal off-gas mixture fractions and one inlet stream, the total number of terms for the triple independent clipped Gaussian formulation is 15.

Table 6-7
Individual Stream Compositions

Component (%)	η	η_1	η_2	η_3
C	81.93	62.23	78.64	95.06
H	5.35	11.70	6.41	1.12
O	10.00	22.57	12.09	1.62
N	1.74	2.01	1.79	1.56
S	0.98	1.49	1.07	0.64

Although the state space variable temperature is rather insensitive to both the choice of mixing model used at distribution overflow and the use of a multiple coal off-gas composition, other state space variables such as oxygen are not. Exhibit 6-23 and Exhibit 6-24 are simulation plots comparing axial oxygen profiles for cases with and without renormalization.

Joint β-PDF NO Case Study

Nitric oxide sensitivity to the use of a variable coal off-gas composition and the choice of mixing model will now be presented. Exhibit 6-25 is a plot that demonstrates the nitric oxide sensitivity of a variable coal off-gas composition and the mixing model effect of renormalization. The exhibit indicates a substantial sensitivity of predicted nitric oxide compositions to the choice of mixing and compositional model used. The use of a varying coal off-gas composition, for example, can lead to differences in predicted NO levels of up to 300 ppm. Moreover, the use of renormalization can change outlet NO levels by more than 350 ppm.

Although simulation centerline profiles are useful for comparison with experimental data, integrated profiles can add insight to global behavior. The overall trend displayed by each of the multiple-η NO axial profiles, where the centerline nitric oxide composition rises to a maximum and subsequently drops to a lower outlet nitric oxide composition, is due to local mixing effects.

PDF Shape Sensitivity

Obviously, as shown in the Exhibits of the previous section, in absence of numerical error associated with convolution of the state space variables over the PDF, there exists a sensitivity of state space variables to the prescribed PDF shape. The sensitivity of state space variables to the assumed shape of the PDF has not been well documented. For example, Coelho and Carvalho (1995) simply state that it is widely accepted that the precise form of the PDF chosen has a negligible effect on the mean temperature, density and major species concentration fields. No sources within Coelho and Carvalho (1995) are provided to document this conclusion.

There exists no detailed shape sensitivity study between the β-PDF and clipped Gaussian PDF. Coelho and Carvalho (1995) do conclude, however, that due to the high temperature sensitivity of NO formation rates, mean formation rates may be quite sensitive to the shape of the chosen PDF. Similar logic can hold true for the devolatilization and char oxidation rate process since there does exist an acute sensitivity of the devolatilization process on mean temperatures. Moreover, the mean concentration of oxidant can dramatically affect the rate of carbon burnout.

This is especially true for the CBK model as the burnout rate is a function of square root of oxygen concentration at the surface of the char.

In the following sections, state space variables sensitivity to the assumed shape of the PDF are explored in absence of the aforementioned arguments of reaction rate and coal combustion process sensitivity. Three specific examples will be presented to describe different physical processes common within a typical simulation that can explain the global shape sensitivity already demonstrated. The three cases are: 1) substantial intermittency effects, 2) slight intermittency effects and, 3) non-intermittent effects.

To review, the one dimension Favre averaged β-PDF is given by:

$$\widetilde{P}(\eta) = \frac{\Gamma(a_1 + a_2)}{\Gamma(a_1)\Gamma(a_2)} \eta^{a_1 - 1} (1 - \eta)^{a_2 - 1} \tag{153}$$

where

$$a_1 = \widetilde{\eta}\left(\frac{\widetilde{\eta}(1 - \widetilde{\eta})}{\widetilde{g}_\eta} - 1 \right) \tag{154}$$

and

$$a_2 = (1 - \widetilde{\eta})\left(\frac{\widetilde{\eta}(1 - \widetilde{\eta})}{\widetilde{g}_\eta} - 1 \right) \tag{155}$$

The use of the clipped Gaussian PDF does not afford the natural feature of intermittency and must, therefore, be constructed. See previous section, entitled "Clipped Gaussian PDF". The Gaussian PDF is described by a mean and variance and is given by:

$$P(\eta) = \frac{1}{\sqrt{2\pi \widetilde{g}_\eta}} \exp\left[\frac{-(\eta - \widetilde{\eta})^2}{2\widetilde{g}_\eta} \right] \tag{156}$$

Case 1: Intermittency

In turbulent systems, there can exist spatial regions over time that display a finite probability of pure streams. This intermittency is directly caused by eddies of unmixed gasses passing through a given control volume. Intermittency is a natural feature of the β-PDF and occurs when any distribution parameter is less than unity (Chen et al., 1994).

Table 6-8 provide results comparing a clipped Gaussian PDF and a β-PDF for the specific case of $\widetilde{\eta}$ = 0.1 and $\widetilde{g}_\eta$ = 0.01. The corresponding distribution parameters for the β-PDF, intermittency term for the clipped Gaussian-PDF and state space variables are given in Table 6-8. Integration of each respective PDF using 80-point Gaussian Quadrature (Abramowitz and Stegun; 1970) yields the appropriate unity value. Nevertheless, convolution of state space variable over the respective PDF indicates a significant difference in temperature, density and oxygen concentration as shown in Table 6-8.

Table 6-8
State Space Variable Sensitivity to the Chosen PDF

		Assumed shape	$\widetilde{T}$, (K)	$\overline{\rho}$, (kg-m^{-3})	$[\widetilde{O}_2]$ kgmol-m^{-3})	$\int P(\eta)$	α_I
Mean Variance	0.01 0.01	clipped Gaussian	1633	0.31	0.12	1.0	0.34
a_1 a_2	0.8 7.2	β-PDF	1661	0.24	0.14	1.0	Na
Mean Variance	0.1 0.001	clipped Gaussian	2042	0.18	0.041	1.0	0.005
a_1 a_2	8.9 80.1	β-PDF	2111	0.17	0.025	1.0	na
Mean Variance	0.4 0.01	clipped Gaussian	971	0.35	0.0	1.0	0.00
a_1 a_2	95.6 143.5	β-PDF	971	0.34	0.0	1.0	na

Case 2: Slight Intermittency

The maximum function value of the β-PDF, assuming each of the distribution parameters is greater than unity, can be obtained by differentiation of Eq. (156) with respect to the mixture fraction, η,

$$\frac{\mathrm{d}}{\mathrm{d}\eta}\widetilde{\mathrm{P}}(\eta)=\frac{\mathrm{d}}{\mathrm{d}\eta}\left(\frac{\Gamma(\mathrm{a}_1+\mathrm{a}_2)}{\Gamma(\mathrm{a}_1)\Gamma(\mathrm{a}_2)}\eta^{\mathrm{a}_2-1}(1-\eta)^{\mathrm{a}_2-1}\right)=0.0 \qquad (157)$$

Applying the chain rule for differentiation of Eq. (157) and solving for η yields the mixture fraction corresponding to the maximum function value of the β-PDF,

$$\eta_{\mathrm{m}}=\frac{\mathrm{a}_1-1}{\mathrm{a}_1+\mathrm{a}_2-2} \qquad (158)$$

Using the appropriate distribution parameters in Eq. (158) for the case of $\widetilde{\eta}=0.1$ and $\widetilde{g}_{\eta}=0.001$ yields a function maximum occurring at a mixture fraction of 0.0908. This is a natural property of the β-PDF and, in fact, the maximum function value of the β-PDF occurs at or near the mean only as the ratio of distribution parameters approaches unity.

Similarly, the mixture fraction corresponding to the maximum function value can be obtained for the clipped Gaussian PDF. It is immediately obvious through inspection of Eq. (156) that the maximum function value occurs at the mean.

Although the calculated temperatures are within 95% of each other, the calculated oxygen mole fractions are different by an order of approximately 2. In both Case 1 and 2, the use of the β-PDF calculated higher temperatures that could drastically affect the rate of coal devolatilization.

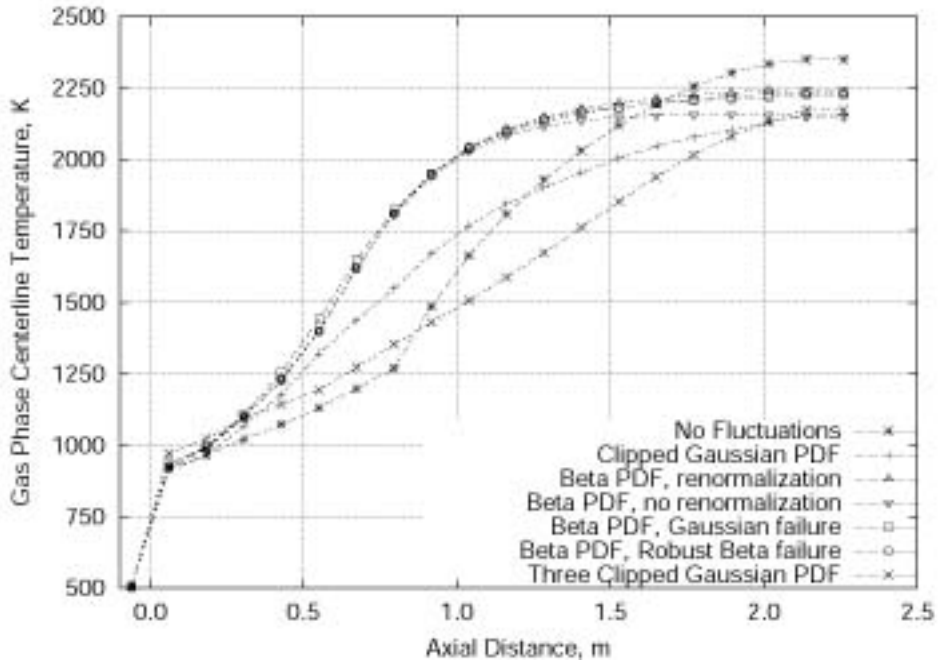

Exhibit 6-20
Summary of the University of Utah bench scale furnace simulation cases

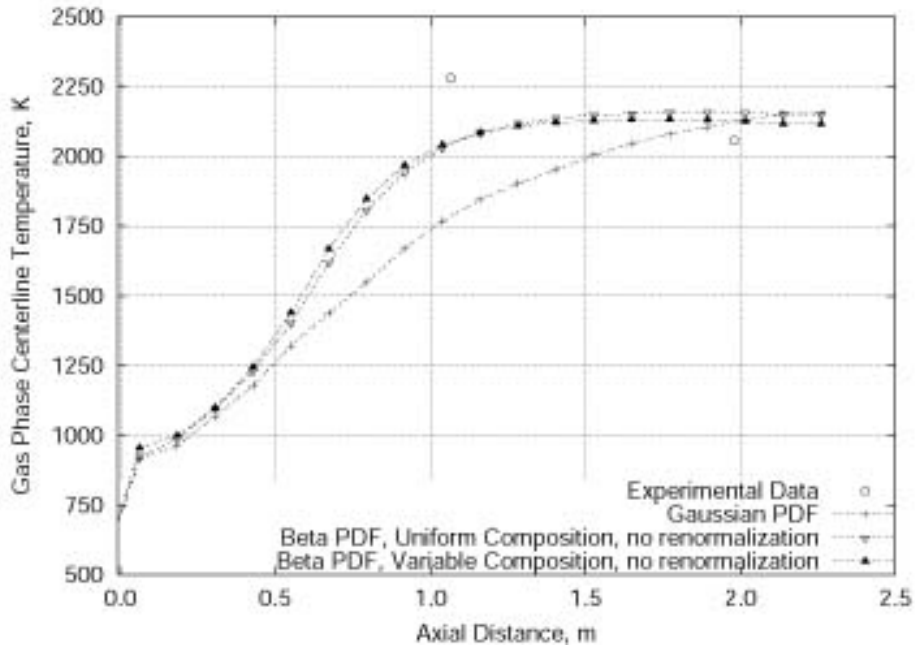

Exhibit 6-21
Simulation axial temperature profiles comparing clipped Gaussian and β-PDF without renormalization

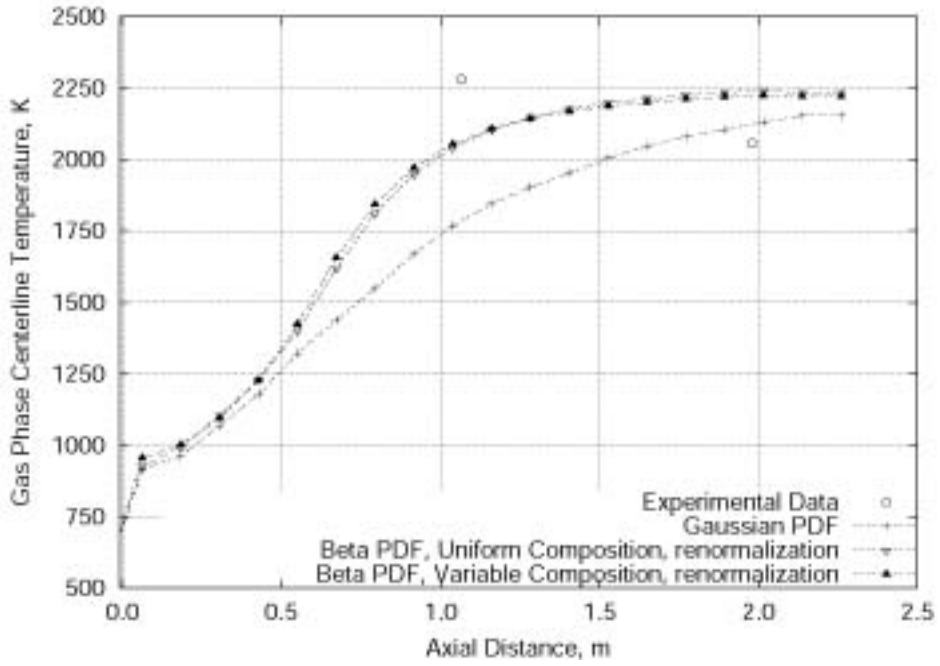

Exhibit 6-22
Simulation axial temperature profiles comparing clipped Gaussian and β-PDF with renormalization

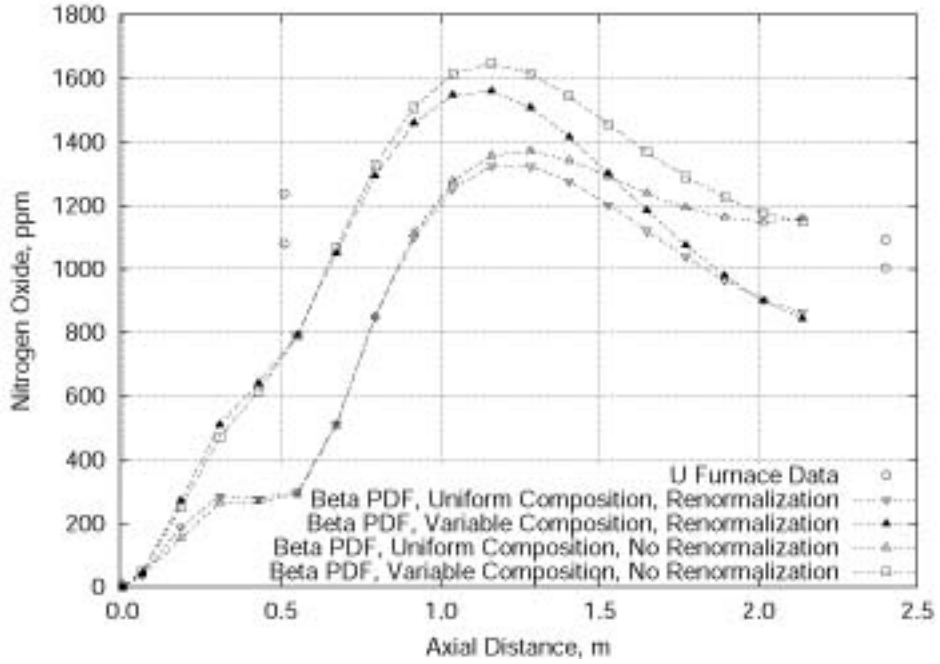

Exhibit 6-23
NO Beta-PDF case to illustrate the sensitivity to coal off-gas composition and mixing model application

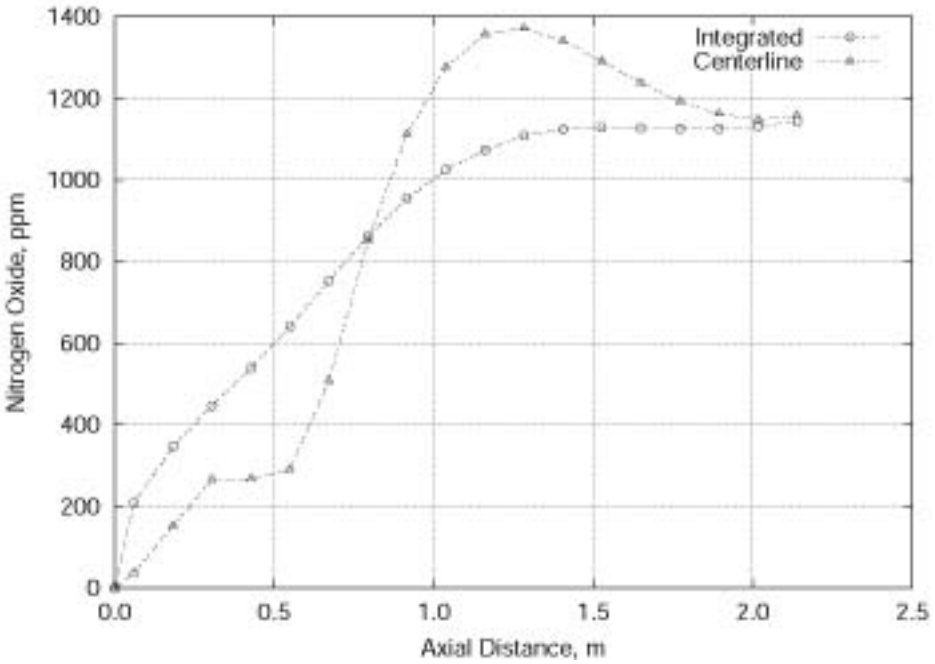

Exhibit 6-24
Centerline and integrated nitric oxide compositions for uniform coal off-gas streams and no renormalization

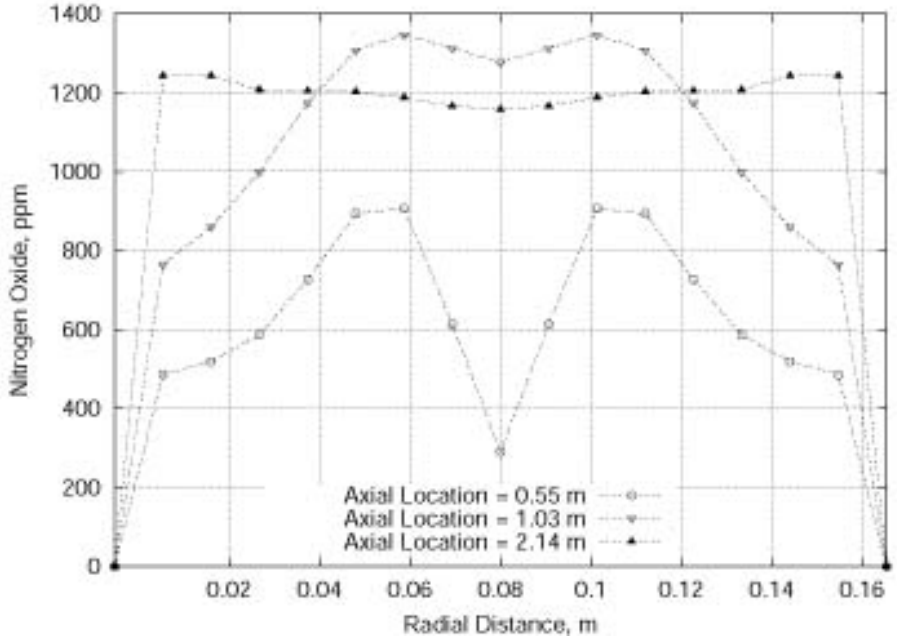

Exhibit 6-25
Radial nitric oxide profiles for uniform coal off-gas composition without renormalization

SNCR Simulation And Validation

Conditions for the selective noncatalytic reduction (SNCR) of NO to N_2 by ammonia in the presence of excess oxygen were first identified by Lyon nearly twenty-five years ago [Lyon, 1975]. Since that time, researchers have investigated the effectiveness of other reagents, such as urea [Muzio, et al., 1976] and cyanuric acid [Perry and Siebers, 1986] and effects of process parameters such as temperature, residence time, normalized stoichiometric ratio (i.e. chemical N/NOx molar ratio, NSR), equivalence ratio, initial NOx level, and various additives [Zamansky et al., 1999]. There has been significant industrial interest in SNCR as a low-cost, effective, and retrofittable NOx control strategy. SNCR has demonstrated NOx reduction capabilities from 25% to 75% over a range of industrial applications including: 1) utility boilers, 2) refinery process units and industrial boilers, 3) municipal waste combustors, 4) wood-fired/co-gen plants, and the 5) chemical industry [ICAC, 1994]. SNCR is a critical component with staged air addition in order to achieve the design goals of 0.06 lbs/MMBtu for the HIPPS cycle. The variation in observed NOx reduction capability depends on site-specific considerations and the amount of unreacted ammonia (ammonia slip) that is considered tolerable.

Although simple in concept, the design of actual SNCR installations can become quite complicated. Non-uniformities in velocity and temperature at the reagent injection location can pose operational difficulties because of the inherent sensitivity of the process to these parameters. The physical location of the optimal temperature window depends on operating factors such as unit load, fuel type, burner firing strategy, etc. Generally, these factors require the utilization of multiple injection elevations in full-scale systems, especially for those boilers or furnaces operated with a cycling load profile. There are also other balance-of-plant issues including: 1) ammonia contamination of fly-ash in coal-fired boilers, 2) air heater pluggage in regions of high ammonia slip, 3) formation of ammonium chloride plumes, and 4) the emission or production of undesirable byproducts, such as NH_3 or N_2O [Muzio and Quartucy, 1997; Teixera et al., 1991]. These are concerns that must be considered in the design and operation of an SNCR system.

In practical combustion systems, NOx reduction efficiencies are primarily dependent on three factors: 1) mixing, 2) temperature, and 3) residence time. Efficiencies increase when all three act in concert so that the reagent is fully mixed with the flue gas at optimum temperatures over a sufficient residence time. In practical combustion systems, severe design constraints are placed on the reagent injection system that must disperse the reagent throughout the entire combustion product stream while the gases are within the appropriate temperature window. Thus, the design of an SNCR injection system requires an analysis capability that takes into account the nonlinear coupling between these processes. Accurate representation of mixing, temperature, and residence time requires coupling between turbulent fluid mechanics, radiative and convective heat transfer, spray droplet dynamics, and gas phase chemistry.

CFD-Based SNCR Models

Overview

In the Twenty-sixth International Combustion Symposium Brouwer et al. [1996] outlined the development and implementation of a seven step global mechanism for SNCR chemistry into a steady state, three-dimensional, turbulent reacting, computational fluid dynamics (CFD) code (GLACIER) [Smith et al., 1995]. GLACIER fully couples reacting gases, solids, and liquids with

turbulent mixing and radiative heat transfer. Coupling turbulence and heat transfer with finite-rate reaction chemistry requires the number of chemical kinetic steps to be relatively small. GLACIER uses a set of reduced kinetic steps for slow reactions and minimizes Gibbs free energy for all other species. Mean species concentrations, density, and temperature are calculated using an assumed probability density function (PDF) approach. One important difference between this model and other CFD-based SNCR models is that the SNCR chemistry is incorporated and coupled into the CFD calculation.

Brouwer et al. used the 7 step global chemistry within GLACIER and compared predictions with new pilot scale data. Effects of reagent composition, injection temperature, thermal quench rate, mixing rates, and CO concentration were examined and the comparisons showed overall good agreement with measured data.

Application of SNCR Model to Large-scale Systems

Following the implementation of the 7 step global chemistry into GLACIER, a number of investigations of SNCR performance in coal fired utility boilers have been conducted using GLACIER. These investigations have been used to assess expected performance of SNCR in particular boiler geometries and to aid in the design of actual SNCR injection systems. Many boiler types and sizes have been investigated including tangentially-fired, wall-fired, cyclone-fired and turbo-fired boilers ranging in size from 150 to 600 MW. In several of the studies, CFD simulations were combined with in-boiler measurements of temperature, CO, O2, and NOx, as well as cold flow measurements in subscale models to quantify effects of injection location on reagent mixing [Cremer et al., 1995; Cremer et al., 1999, and Cremer et al., 1999].

The overall results of these investigations indicated that NOx reductions from 20-45% with less than an average of 5 ppm ammonia slip were possible. Conditions that limited the effectiveness of SNCR in these boilers included:

- Existence of convective surfaces that limited reagent mixing,
- Large cross-sectional areas over which reagent needed to be mixed,
- Infeasibility of injector placement in “optimal” locations due to existing hardware, and
- High furnace exit gas temperatures followed by fast temperature quench in the convective section.

The advantage of the use of GLACIER over other commonly used models [Comparato et al., 1998] for prediction of SNCR performance is the level of coupling that exists within the model. In particular, mechanisms controlling reagent mixing (i.e. turbulence, droplet dynamics) are coupled to the finite rate calculations of SNCR chemistry. The importance of coupling the calculations of reagent mixing with the finite rate chemistry has been observed and it has been shown that poor mixing can result in lower NO reduction compared to ideal mixing [Østberg, 1996].

The importance of this degree of coupling can be seen in Exhibit 6-26, which shows calculations of NOx reduction versus nitrogen stoichiometric ratio (NSR) for a 600 MW tangentially fired coal utility boiler [Cremer et al., 1999]. The GLACIER results (with the incorporated 7 step global SNCR chemistry) show the range of predicted overall NOx reductions in this boiler. These predictions are compared to corresponding Chemkin [Kee et al., 1989]

calculations along computed streamlines originating in locations of urea release predicted in the GLACIER calculations. The time/temperature history along these representative streamlines was used within Chemkin calculations, assuming a specified initial NSR for urea. Both the 7 step global SNCR chemistry and the detailed chemistry on which it was based were used in these streamline calculations. Exhibit 6-26 shows that for all of the streamlines chosen in the region of the urea release, the predicted NOx reduction along the streamline was higher than that predicted in the GLACIER simulations at the same NSR. This difference highlights the role of mixing limitations on SNCR performance and the necessity of utilizing an analysis tool that couples mixing with chemistry.

An additional observation that can be made from Exhibit 6-26 is the difference in predictions of NOx reduction along the streamlines due to the chemical kinetics. Streamline calculations were performed using both detailed and global chemistry at NSR=1. In the figure, the data are offset slightly along the abscissa from NSR=1 to distinguish the symbols even though the calculations were indeed for NSR=1. The difference in these results is a direct indication of inadequacies in the global chemistry in its representation of the detailed chemistry over the nonisothermal history of the streamlines.

Exhibit 6-26 motivates the remaining discussions in this paper that describe the methods used to improve the reduced SNCR chemistry as well as the actual implementation procedures and results obtained with the new reduced chemistry.

Improved Global Chemistry for SNCR

In Brouwer's previous work, he developed a reduced seven step mechanism describing SNCR chemistry for typical reagents (NH_3 (ammonia), NH_2CONH_2 (urea), and $(HNCO)_3$ (cyanuric acid)). The simplified mechanism and its rates were derived from the mechanism of Miller and Bowman [1989] with recent literature modifications [Dean et al., 1991; Miller and Melius, 1986] through sensitivity analysis and curve fitting using SENKIN [Kee et al., 1989]. The global mechanism as presented by Brouwer is reproduced in Table 6-9 below.

Table 6-9
Rate parameters for the global SNCR model [Brouwer et al., 1996]

Reaction	A	b	E_a
1. $NH_3+NO \rightarrow N_2+H_2O+H$	4.24E+08	5.3	83,600
2. $NH_3+O_2 \rightarrow NO+H_2O+H$	3.500E+05	7.65	125,300
3. $HNCO+M \rightarrow H+NCO+M$	2.400E+14	0.85	68,000
4. $NCO+NO \rightarrow N_2O+CO$	1.000E+13	0.00	-390
5. $NCO+OH \rightarrow NO+CO+H$	1.000E+13	0.00	0
6. $N_2O+OH \rightarrow N_2+O_2+H$	2.000E+12	0.00	10,000
7. $N_2O+M \rightarrow N_2+O+M$	6.900E+23	-2.50	64,760

Units are A = cm-mol-s-K; E_a = cal/mol

For several relatively small boilers on which the model was used, the predictions of NOx reduction and NH3 slip appeared to be quite good. However, in several studies, the model was

applied to large (>300 MWe) coal-fired utility boilers. For two particular boilers, temperature measurements taken near the furnace exit (near the nose) under normal operation at 100% load, were relatively high (near or exceeding the upper limit of the SNCR temperature window) in agreement with the model predictions. In conventional SNCR injection, ammonia or urea are injected in the vicinity of the furnace exit so that the reagent is given suitable residence time to mix and react with the flue gases. Examination of several injection scenarios in which ammonia was injected in the vicinity of the furnace exit indicated little to no net NOx reduction and net NOx formation in some cases. Upon comparison of these cases with calculations using SENKIN with detailed chemistry at the temperatures seen in the tested injection locations indicated that the CFD model was over-predicting NH3 oxidation at these temperatures.

This in fact was confirmed upon comparison between the detailed and global mechanisms within SENKIN. Exhibit 6-27 shows that the results of isothermal SENKIN plug flow reactor (PFR) simulations over a range of temperatures comparing predictions obtained using the detailed mechanism and the global mechanism (Table 6-9) for a typical flue gas composition given in Table 6-10. For temperatures greater than 1900 °F (1038 °C), the global mechanism, which for this case involves only the first two reaction steps shown in Table 6-9, significantly over-predicts the rate of NH_3 oxidation. As a result, NOx reduction and NH_3 slip are both under-predicted by the global mechanism.

A similar comparison between the reduced and detailed chemistry, for a different inlet composition was considered by Brouwer et al. [1996]. This composition, given in Table 6-11, has no initial OH, O, or CO, and for this case, the SENKIN results are quite different. Results for this comparison are shown in Exhibit 6-27. This comparison is similar to Exhibit 6-4 in Brouwer, et al. [1996].

Table 6-10
Typical flue gas composition

Chemical Species	Mole %
N_2	77.06
CO_2	13.57
H_2O	7.09
O_2	2.25
OH	4.5E-05
O	1.0E-06
NO	3.19E-02
NH_3	3.19E-02
CO	1.54E-04

Table 6-11
Gas composition taken from Brouwer, et al. [1996]

Chemical Species	Mole %
He	98.70
O_2	1.23
NO	2.25E-02
NH_3	4.50E-02

For this composition, it can be seen in Exhibit 6-28 that agreement for NOx reduction as well as NH_3 slip is very good. For temperatures higher than 2100 °F (1149 °C), the global mechanism begins to over-predict NH_3 oxidation, but overall agreement with the detailed chemistry is much better. This difference in prediction due to composition is suggestive of a deficiency in the global mechanism in not being able to properly account for effects of intermediate radical concentrations (such as OH) on NOx reduction and NH_3 slip.

For a typical flue gas composition as shown in Table 6-10, it is clear that the global SNCR mechanism yields poor predictions, particularly for temperatures above 1900 °F (1038 °C). To improve upon these predictions, while retaining the same global steps (steps 1 and 2 for NH3) that are shown in Table 6-9, a series of SENKIN calculations were carried out to obtain improved curve fits to the data obtained from the detailed calculations. The objective was to determine values for A, b, and Ea, for reaction steps 1 and 2, that yielded the best agreement with the detailed mechanism.

The procedure used to obtain the improved kinetic values is now outlined. By the definition of k_i as the rate constant for the i^{th} reaction, the following equations for k_1 and k_2 were obtained:

$$k_1 = -\frac{1}{2}\frac{d([NH_3]+[NO])}{dt}\frac{1}{[NH_3][NO]} \tag{159}$$

$$k_2 = \frac{1}{2}\frac{d([NO]-[NH_3])}{dt}\frac{1}{[NH_3][O_2]} \tag{160}$$

Using SENKIN, values of k_1 and k_2 were tabulated as functions of temperature by computation of the RHS of Eqs. (162) and (163) over a range of temperatures. Using these data in combination with a modified Arrhenius expression for k given by

$$k = AT^b e^{-Ea/RT} \tag{161}$$

provided a means of estimating the best A and E_a by computing the least squares line through a plot of $\ln(k/T^b)$ vs. 1/T. The slope of this line is $-E_a/R$, while the y-intercept is ln(A). The effect of varying the temperature exponent, b, could be determined by repeating this approach for various values of b.

Exhibit 6-29 shows the result of this approach. Revised Arrhenius parameters were obtained from the curve fits shown in Exhibit 6-29. The temperature exponent, b, was held fixed for both k_1 and k_2, retaining the values shown in Table 6-9. Exhibit 6-30 shows the effect of the revised rate constants on predictions of NOx reduction and NH_3 slip as compared to the detailed mechanism. Improved agreement with the results of the detailed mechanism is obvious both in terms of NOx reduction and NH_3 slip. It is apparent in Exhibit 6-29 that for both rate constants, assumption of a linear relationship between $\ln(k/T^b)$ and 1/T is not very good over the temperature range shown. The data can be better represented by breaking the curve fits into two temperature ranges, with the cut-off being at 1900 °F (1038 °C). The benefit achieved in doing this can be seen in Exhibit 6-29 in which agreement with the detailed chemistry is improved over the entire temperature range. The revised Arrhenius parameter values are given in Table 6-12.

Effects of Initial NO Level

For an initial NOx concentration, in the flue gas, of 300 ppm, the prediction of NOx reduction and NH_3 slip using the modified global mechanism (Table 6-12) was quite good in comparison with the detailed chemical mechanism. However, in application to situations in which the initial NOx level was significantly less than 300 ppm, required examination of the fidelity of the modified global mechanism. In a specific application, the model was applied to a large (600 MWe) coal-fired utility

Table 6-12
Rate Parameters for the Modified Global SNCR Model

Reaction	A	b	E_a
1a. $NH_3 + NO \rightarrow N_2 + H_2O + H$ ($T < 1900^oF$)	1.12	5.3	37,450
1b. $NH_3 + NO \rightarrow N_2 + H_2O + H$ ($T > 1900^oF$)	1.68E-05	5.3	8,552
2a. $NH_3 + O_2 \rightarrow NO + H_2O + H$ ($T < 1900^oF$)	1.90E-01	7.65	95,253
2b. $NH_3 + O_2 \rightarrow NO + H_2O + H$ ($T > 1900^oF$)	5.97E-11	7.65	37,120
3. $HNCO + M \rightarrow H + NCO + M$	2.40E+14	0.85	68,000
4. $NCO + NO \rightarrow N_2O + CO$	1.00E+13	0.00	-390
5. $NCO + OH \rightarrow NO + CO + H$	1.00E+13	0.00	0
6. $N_2O + OH \rightarrow N_2 + O_2 + H$	2.00E+12	0.00	10,000
7. $N_2O + M \rightarrow N_2 + O + M$	6.90E+23	-2.50	64,760

Units are A=cm-mol-s-K; E_a = cal/mol

boiler with an initial NOx concentration of approximately 100 ppm. Comparisons of calculations using SENKIN with the detailed mechanism, and calculations using BANFF with the modified global mechanism shown in Table 6-12 indicated that the global mechanism was under-predicting the NOx reduction over the range of temperatures existing in the boiler.

Exhibits 6-31 and 6-32 show the comparison of results of isothermal SENKIN plug flow reactor (PFR) simulations and isothermal BANFF plug flow reactor (PFR) simulations for a residence time of 150 ms. The comparisons cover a range of temperatures and assume a typical flue gas composition as given in Table 6-13. These Exhibits show that the global mechanism

significantly under-predicts the NOx reduction at temperatures greater than 1750 °F (954 °C) and 1900 °F (1038 °C) using NH_3, and urea, respectively although the NH_3 slip predicted using global mechanism is in reasonable agreement with the values predicted using detailed mechanism.

To improve upon these predictions, a series of SENKIN calculations, using the detailed mechanism, was carried out to obtain improved values, through curve fitting, for the values of A, b, and E_a, for each reaction step shown in Table 6-12. The same detailed procedure described previously was used to obtain the improved rates. The revised global mechanism is given in Table 6-14. The same global steps were

Table 6-13
Typical Flue Gas Composition from Coal-Fired Boiler

NH_3 as a reagent		Urea as a reagent	
Chemical Species	Mole %	Chemical Species	Mole %
N_2	70.48	N_2	70.48
O_2	2.89	O_2	2.89
CO_2	14.19	CO_2	14.19
H_2O	12.43	H_2O	12.43
OH	1.0E-03	OH	1.0E-03
O	1.0E-04	O	1.0E-04
NO	1.2E-02	NO	1.2E-02
NH_3	1.44E-02	NH_3	7.2E-03
HNCO	0.0	HNCO	7.2E-03

retained except for step 5 in which O_2 was used as the oxidizer instead of OH. The benefit achieved in using the revised global mechanism is shown in Exhibits 6-33 - 6-38. The results in the Exhibits are for a residence time of 150 ms and utilize the flue gas composition shown in Table 6-13 except the mole fraction of NH_3 (and HNCO) may change for different normalized stoichiometric ratios (NSR). Overall, the agreement between the detailed mechanism and the revised global mechanism, for NOx reduction and NH_3 slip, is improved for a range of NSRs, temperatures, and for both NH_3 and urea as reagents.

Table 6-14
Rate Parameters for the Revised Global SNCR Model

Reaction	A	b	E_a
1a. $NH_3 + NO \rightarrow N_2 + H_2O + H$ ($T < 1900^oF$)	1.12	5.3	38246
1b. $NH_3 + NO \rightarrow N_2 + H_2O + H$ ($T > 1900^oF$)	2.99	5.3	40746
2a. $NH_3 + O_2 \rightarrow NO + H_2O + H$ ($T < 1900^oF$)	1.90E-01	7.65	95,253
2b. $NH_3 + O_2 \rightarrow NO + H_2O + H$ ($T > 1900^oF$)	1.45E-07	7.65	59340
3. $HNCO + M \rightarrow H + NCO + M$	6.02E+10	0.85	47,899
4. $NCO + NO \rightarrow N_2O + CO$	1.00E+13	0.00	-390
5. $NCO + O_2 \rightarrow NO + CO_2$	2.08E+04	2.0	6,158
6. $N_2O + OH \rightarrow N_2 + O_2 + H$	2.00E+12	0.00	10,000
7. $N_2O + M \rightarrow N_2 + O + M$	6.90E+23	-2.50	64,760

Units are A=cm-mol-s-K; E_a = cal/mol

Development of a Reduced Mechanism for SNCR

The detailed NOx mechanism that we have been using to evaluate the kinetics governing reactions between ammonia or urea and coal flue gases containing NOx, is the mechanism of Miller & Bowman [1989] with literature modification [Dean et al., 1991; Miller and Melius, 1986]. This detailed mechanism contains over 60 chemical species and 250 reversible elementary reactions [http://wwww.reaction-eng.com/downloads/htm, see REI Detailed Mechanism for SNCR Chemistry (REI97)]. Implementation of this chemical mechanism into a CFD code, which would require the solution of transport equations for the same number of species that exist in the mechanism, is prohibitive from the standpoint of both CPU time and memory. Thus, a reduced description of the detailed chemistry is necessary.

The approach that we have taken is based on the assumption that certain species contained within the detailed mechanism are in steady state (i.e. rate of production equals rate of destruction) [Smooke, 1991]. This is a more rigorous and universal approach than curve-fitting approaches that are often used to generate simple global mechanisms. Historically, reduced mechanism methods have been difficult to generate due to the amount of human time necessary in deriving them. To overcome this difficulty, we have been using an approach that automates the reduction process. The Computer Assisted Reduction Method (CARM) [Chen, 1988] automates this process and produces FORTRAN source code for the calculation of the chemical source terms defined by the reduced mechanism. The inputs for the subroutine are pressure, temperature, and the mass fractions of the major species. The output is the instantaneous reaction rate for the major species.

To faithfully represent behavior in the furnace corresponding to fuel rich or fuel lean NH_3 (or urea) injection, the reduced mechanism must be robust enough to capture the kinetics of NO reduction/formation in both fuel rich and fuel lean regions with and without the presence of NH_3. Using CARM, we have constructed and evaluated several reduced mechanisms over a wide range of conditions. CARM uses a set of input test problems (perfectly stirred reactor, PSR solutions) to rank species by the errors, ε_I, introduced by assuming they are in steady state. This error is evaluated by the expression

$$\varepsilon_i = X_i \frac{\left|\omega_i^p - \omega_i^c\right|}{\max\left(\left|\omega_i^p\right|, \left|\omega_i^c\right|\right)} \qquad (162)$$

where ω_i^p and ω_i^c are respectively the rates of production and consumption for species *i*, and X_i is the mole fraction. To create reduced mechanisms for modeling SNCR chemistry, fixed temperature PSR solutions covering the range of temperatures (1100-1700 K) and flue gas stoichiometric ratios (1-1.5, lean conditions) were obtained, where the stoichiometric ratio is defined as the inverse of the fuel equivalence ratio. A number of reduced mechanisms were developed and tested, utilizing an imposed error criterion of ε_i = 1.e-7. Although the test problems utilized by CARM are based on PSR solutions, the resulting reduced mechanisms were tested under both PSR and plug flow reactor (PFR) conditions. A six step reduced mechanism retaining 10 major species (48 species in steady-state) was found to give excellent agreement with the detailed chemistry. The six steps of this reduced mechanism are:

$2OH = 0.5O_2 + H_2O$ (R1)

$CO_2 = CO + 0.5O_2$ (R2)

$NO = 0.5O_2 + 0.5N_2$ (R3)

$CO + OH + 0.5N_2 = 0.5O_2 + HNCO$ (R4)

$N_2O = 0.5N_2 + NO$ (R5)

$2OH + 0.5N_2 + HNCO = CO + 0.5O_2 + NO + NH_3$ (R6)

The steady-state species, although not shown in the six-step mechanism, play a direct role in the computation of the chemical reaction rates of the 10 major species, which are computed by CARM.

Exhibits 6-39 and 6-40 compare results in an isothermal PFR configuration representing urea injection into a typical lean flue gas composition. Results using detailed, reduced, and 7 step global chemistry are compared. For these calculations, it was assumed that urea decomposes into equal parts NH_3 and HNCO. Exhibit 6-39 shows that the 10-species reduced mechanism gives excellent agreement with the detailed chemistry over the SNCR temperature window, while the global model fails for temperatures above 1080 °F [(1027 °C) (1300 K)]. Exhibit 6-40 makes a similar comparison between detailed, reduced and global chemistry with variation in the initial CO concentration in the flue gas. Again, the global model works well over the narrow range of conditions for which it was developed, but is unable to predict the increase in NO at higher CO concentrations that is accurately predicted by both the reduced and detailed mechanisms. Similar improvement over the global model was found when varying initial O_2 and NO concentrations, as well as the NSR. Other species of interest such as NH_3, HNCO, and N_2O (not shown) show similar agreement between the reduced and detailed chemistry and similar improvement over the global model. The reduced mechanism has also been found to yield excellent results under fuel rich conditions.

Implementation Into a CFD Model

The four primary issues that were addressed regarding implementation of the reduced mechanism were:

1. Calculation of chemical reaction rates for major species
2. Accounting for turbulence/chemistry interaction in calculation of mean reaction rates
3. Solution of additional transport equations for the major species
4. Addressing numerical "stiffness" problems associated with solution of new transport equations

The CPU time required by the reduced mechanism can become expensive when it is integrated into a CFD code and used for predictions in a full-scale application. In a "post-process" implementation, in which the temperature and velocity fields are assume fixed, the calculation of the chemical reaction rates can take up to 80% of the total CPU time of the simulation. Of this time, about 90% is spent on converging the steady-state species concentrations and about 10% is spent on calculating the elementary forward and backward reaction constants. The time needed to converge the steady-state species concentrations depends on the number of steady-state species, the initial guess, the convergence criteria, and the iteration method. The use of good initial guesses for the steady-state species concentrations, for example, can make a significant reduction in the overall CPU time required.

Since the rates of reaction associated with the SNCR chemistry are the same order of magnitude as the rates of turbulent mixing, the effects of turbulence can have a significant effect on the mean rates of chemical reaction. Based on the approach developed by Smoot and Smith [1985], *GLACIER* uses an assumed probability density function (PDF) approach to account for the effects of turbulence. The mean reaction rates ($\overline{\omega}_i$) for turbulent reacting gases are approximated by convoluting the instantaneous rates over the mixture fraction PDFs, as shown in Eq. (163),

$$\overline{\omega}_i = \overline{\rho} \int_f \int_\eta \frac{\omega(f,\eta,h)}{\rho(f,\eta,h)} \widetilde{P}(f)\,\widetilde{P}(\eta)\,d\eta\,df \qquad (163)$$

where f and η represent two mixture fraction variables used within *GLACIER* and ~ denotes Favre averaging. This PDF approach is extremely CPU intensive and can require up to approximately a factor of 20-25 times increase in CPU time over the assumption of laminar chemistry (not accounting for turbulence effects on the mean reaction rates).

The addition of transport equations for the new species is a relatively straightforward procedure. However, the stiffness associated with the chemical reaction rates can cause some difficulty in converging the new transport equations. In the current approach, only six species transport equations (CO, OH, NO, N_2O, HNCO, and NH_3) are solved with chemical source terms while the other four species in the reduced mechanism (CO_2, O_2, H_2O, and N_2) are calculated through the principle of conservation of atoms. The use of conservation of atoms reduces the number of transport equations that must be solved and improves the overall convergence of the remaining transport equations.

Application to Simple Plug Flow Geometry

To compare the reduced SNCR mechanism implemented into *GLACIER* with the detailed chemistry on which it was based, plug flow calculations over a range of conditions were performed. The detailed chemistry calculations were performed in Chemkin, while the *GLACIER* calculations were performed in a pipe flow geometry under the same conditions. Exhibit 6-41 shows the comparisons over a range of temperatures and NSRs utilizing NH_3 as the SNCR reagent. Exhibit 6-42 shows the corresponding calculations of NH_3 slip for the same conditions as in Exhibit 6-41. The agreement between the *GLACIER* calculations and the detailed chemistry calculations is quite remarkable and it is important to note that in Exhibit 6-42, the results are nearly indistinguishable. Exhibit 6-43 shows a similar comparison using urea reagent for three different initial NO levels. Again, agreement is extremely good. Note that the effect of reduction in the initial NO, seen in Exhibit 6-43, is to decrease the maximum NO removal and to reduce the optimal temperature where NO removal is a maximum, in agreement with reported data [Quartucy et al., 1990]. Exhibit 6-44 shows similar comparisons over a range of CO levels. The reduced chemistry performs very well in capturing the effect of increased CO in both lowering and narrowing the SNCR temperature window. Comparisons with NH_3, HNCO, and N_2O concentrations show similar agreement. Comparisons also show excellent under fuel rich conditions as shown in Exhibit 6-45.

Conclusions

Practical constraints such as imperfect reagent dispersion, nonuniform and nonisothermal temperature profiles, and local flue gas composition can have a significant effect on SNCR performance in industrial furnaces and boilers. The heat transfer, extent of mixing, and finite rate chemistry control the effectiveness of SNCR. Since these controlling mechanisms are tightly coupled, it is important that predictions of SNCR performance take it into account. Decoupling the mixing from the chemistry can significantly impact the predictions. However, over-simplification of the finite rate chemistry can also lead to erroneous predictions.

To develop an improved description of reduced SNCR chemistry, an automated strategy that utilizes conventional reduced mechanism techniques to reduce detailed chemical mechanisms (CARM) was utilized in this study. Using CARM, a 10-specie reduced mechanism describing SNCR chemistry within both the fuel rich and fuel lean regions of a furnace was developed and implemented into a CFD-based turbulent reacting flow code (*GLACIER*). Comparisons with detailed chemistry calculations show that the reduced mechanism is able to represent the detailed chemistry over a much wider range of conditions than was previously obtained with a 7 step global mechanism. Effects of gas temperature, CO concentration, initial NO concentration and local stoichiometry on NO and NH_3 concentrations are represented very well in a simple plug flow geometry. The greatly enhanced capability of the enhanced SNCR model combined with those described for the NO codes in the earlier sections has improved the predictive capabilities of the model to the point it can be used with fair confidence in guiding the design and optimization of HIPPS cycles with a combination of staged air addition and SNCR downstream reductions. These tools have been applied on parallel programs with remarkable success as will be described in the following section.

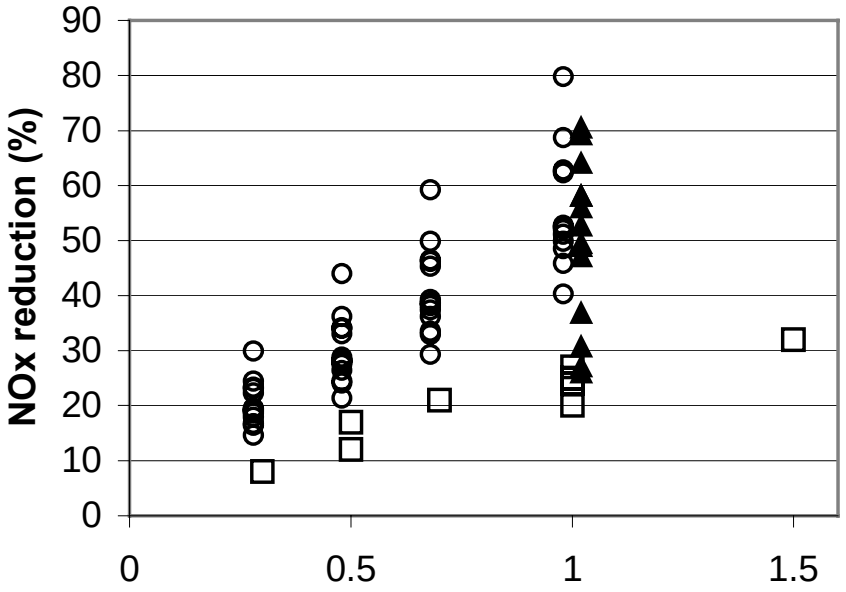

Exhibit 6-26
Comparison of NOx predictions using *GLACIER* (□), 7 step global chemistry along streamlines (○), and detailed NOx chemistry along streamlines (▲) as a function of nitrogen stoichiometric ratio (NSR). Initial properties for the streamline calculations were based on the local conditions computed by the CFD model. The global and detailed calculations at NSR = 1 are offset only to distinguish the data

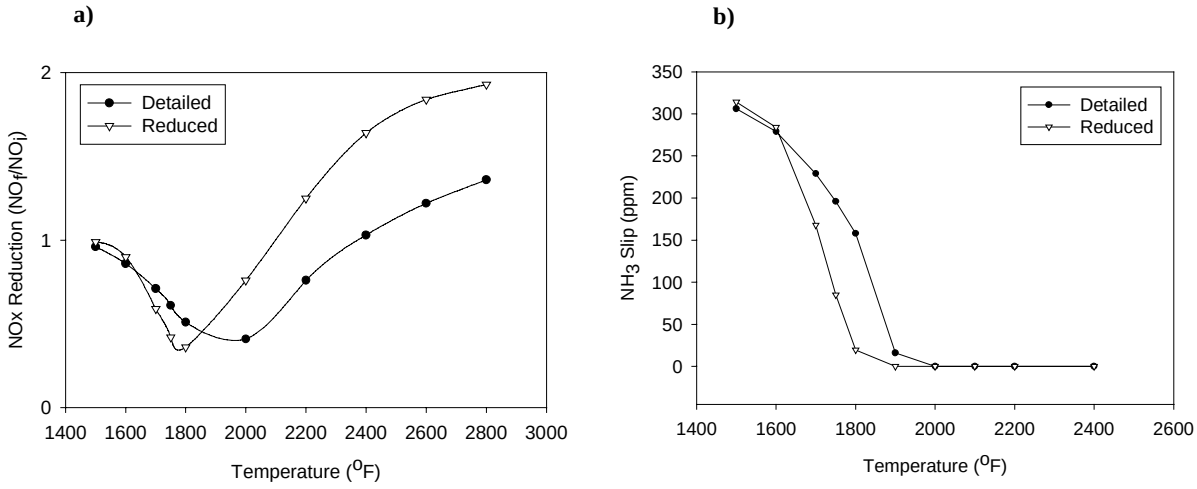

Exhibit 6-27
Comparison between reduced and detailed chemistry for isothermal, homogeneous conditions for NSR = 1 and a typical flue gas composition as given in Table 6-10 (residence time = 50 ms). a) NOx reduction; b) NH_3 slip.

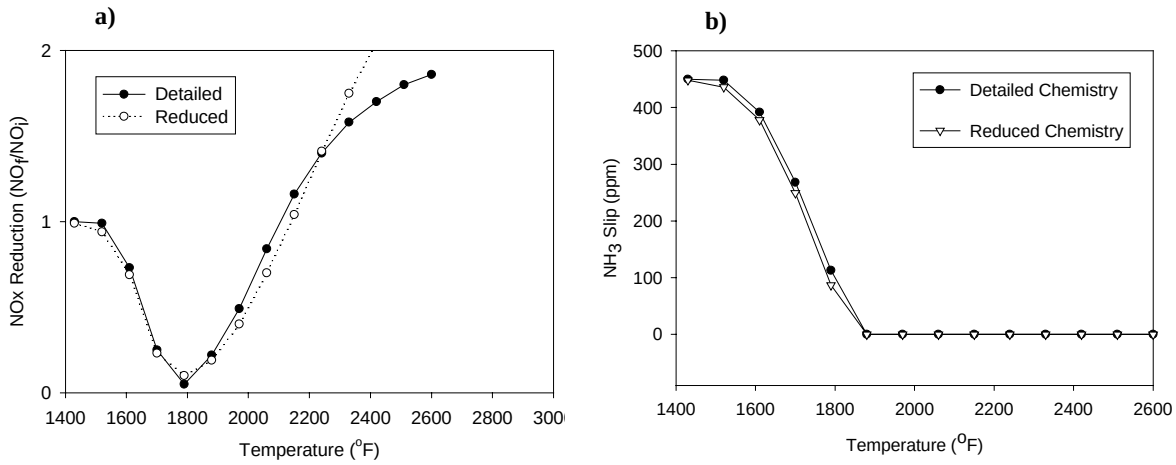

Exhibit 6-28
Comparison between reduced and detailed chemistry for isothermal, homogeneous conditions for NSR = 1 and a gas composition as given in Table 6-11. a) NOx reduction; b) NH_3 slip.

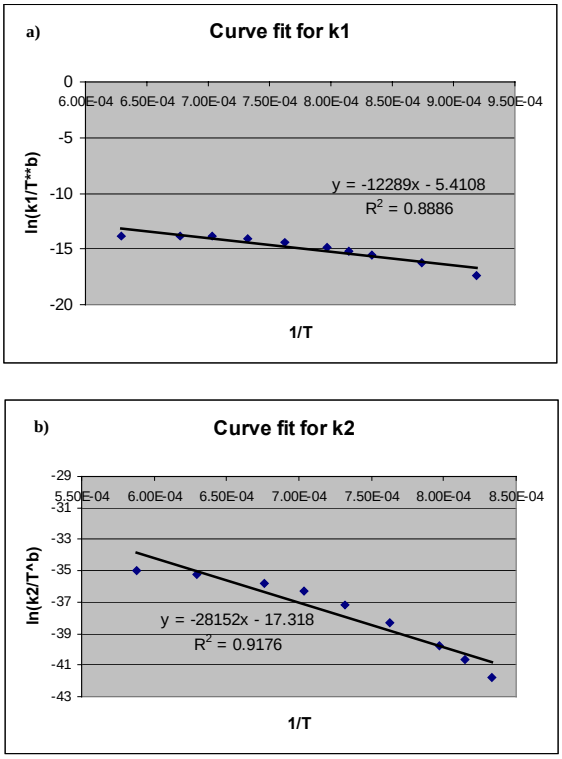

Exhibit 6-29
Revised curve fits for the rate constants for steps 1 and 2 of Table 6-9. a) Curve fit for k_1; b) Curve fit for k_2.

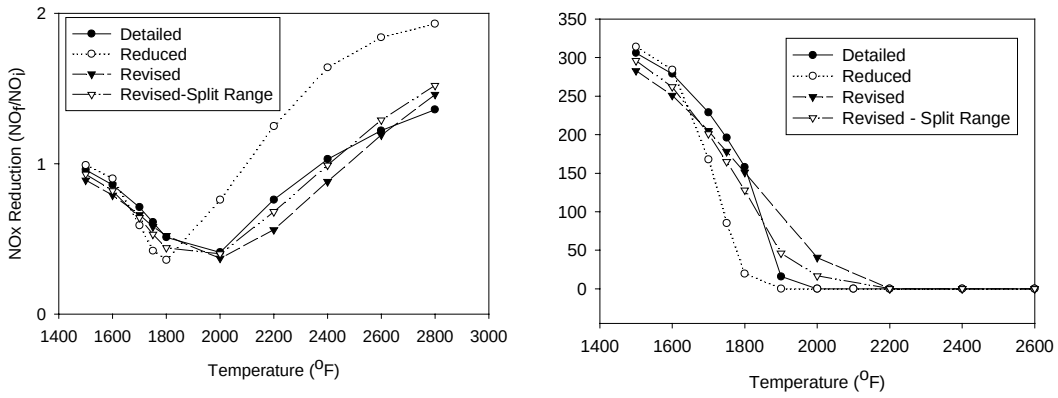

Exhibit 6-30
Comparison between detailed and 3 reduced mechanisms for isothermal, homogeneous conditions for NSR = 1 and a gas composition as given in Table 6-10. The points labeled reduced correspond to the original reduced mechanism shown in Table 6-9. The points labeled revised correspond to the reduced mechanism with improved Arrhenius parameter values for steps 1 and 2, as shown in Table 6-12. Revised – split range corresponds to Arrhenius parameters defined over two temperature ranges, with the cut-off at 1900 °F (1038 °C). a) NOx reduction; b) NH_3 slip.

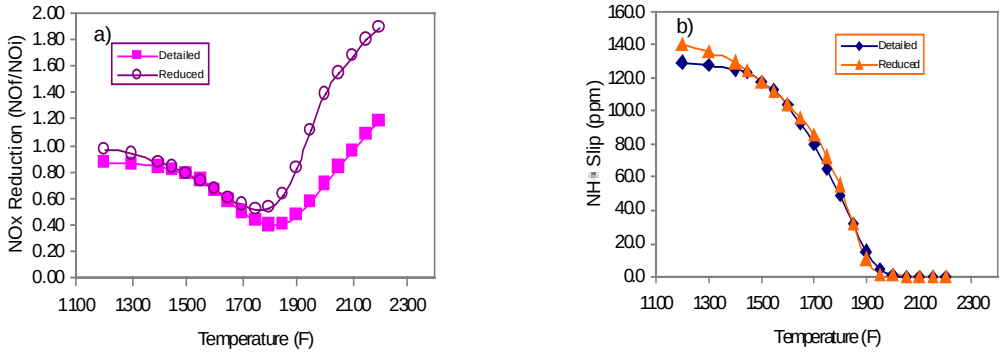

Exhibit 6-31
Comparison between global mechanism (Table 6-12) and detailed mechanisms for NH_3 at NSR = 1.2. a) NOx Reduction; b) NH_3 Slip.

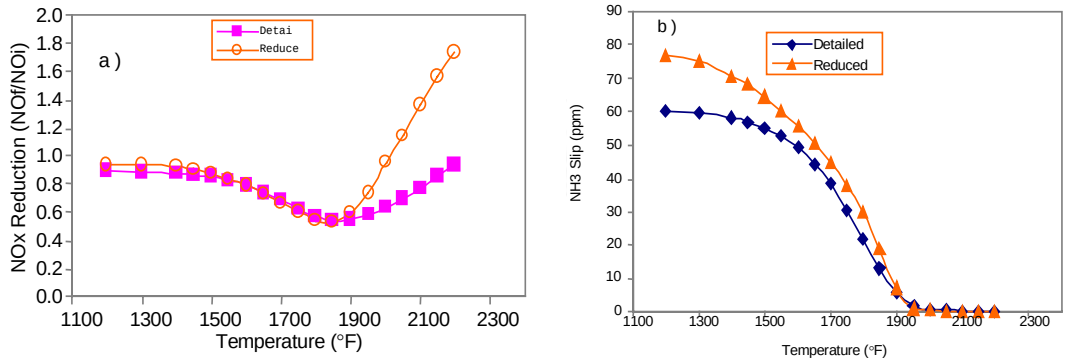

Exhibit 6-32
Comparison between global and detailed mechanisms for urea at NSR = 1.2. a) NOx Reduction; b) NH_3 Slip.

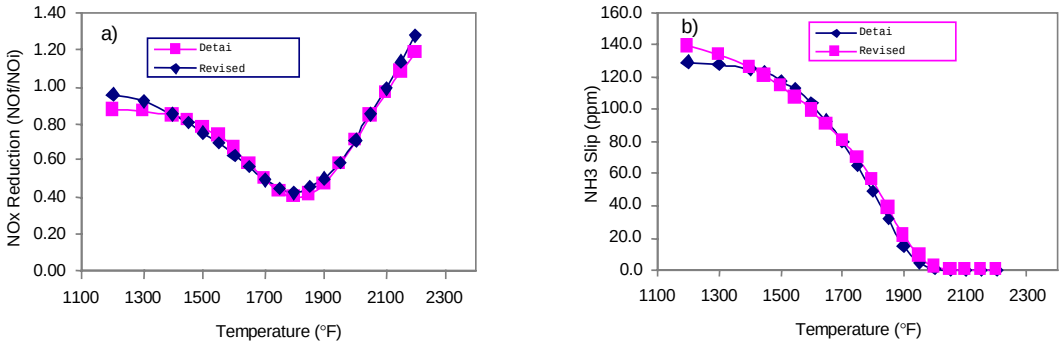

Exhibit 6-33
Comparison between the revised-global and detailed mechanisms for NH_3 at NSR = 1.2. a) NOx Reduction; b) NH_3 Slip.

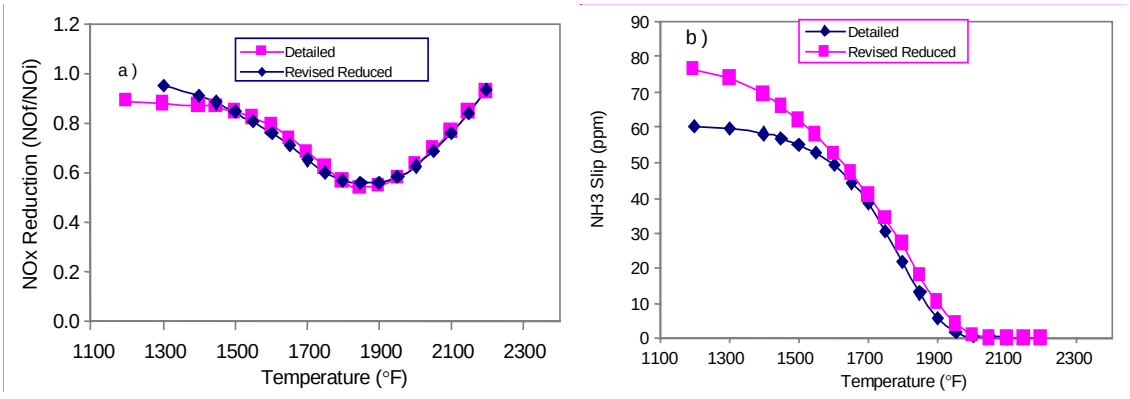

Exhibit 6-34
Comparison between revised-global and detailed mechanisms for urea at NSR = 1.2. a) NOx Reduction; b) NH_3 Slip.

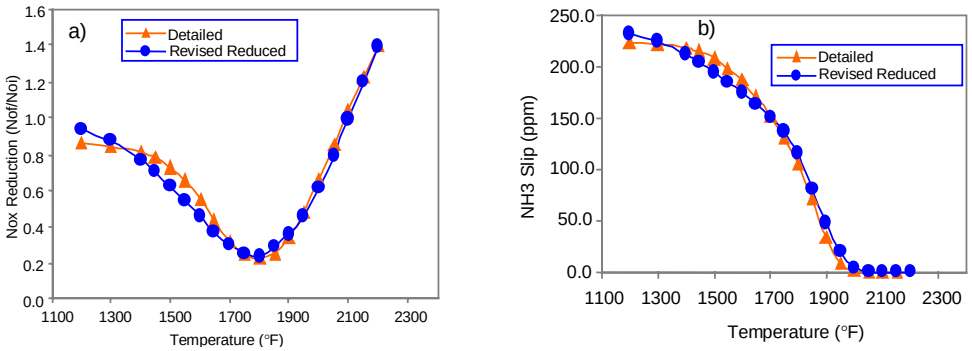

Exhibit 6-35
Comparison between revised-global and detailed mechanisms for ammonia at NSR = 2.0. a) NOx Reduction; b) NH_3 Slip.

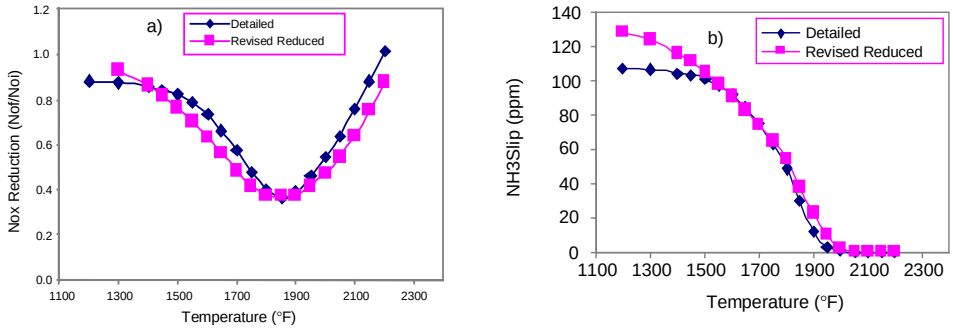

Exhibit 6-36
Comparison between revised-reduced and detailed mechanisms for urea at NSR = 2.0. a) NOx Reduction; b) NH_3 Slip.

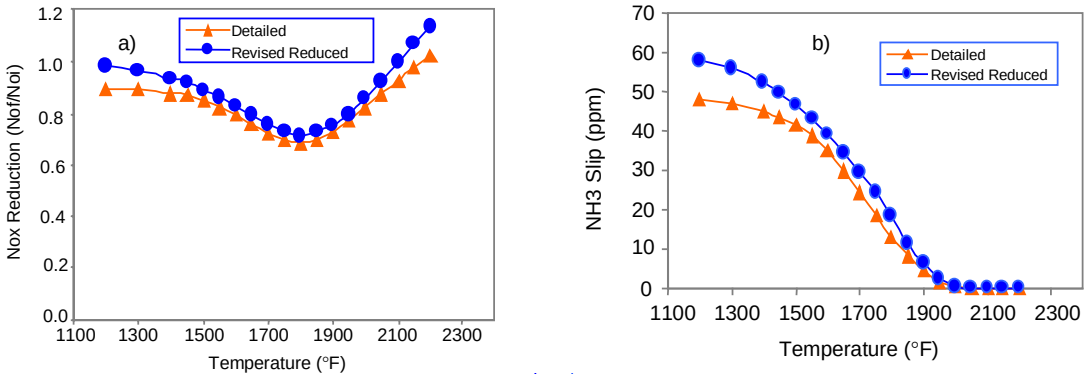

Exhibit 6-37
Comparison between revised-global and detailed mechanisms for NH3 at NSR = 0.5. a) NOx Reduction; b) NH3 Slip.

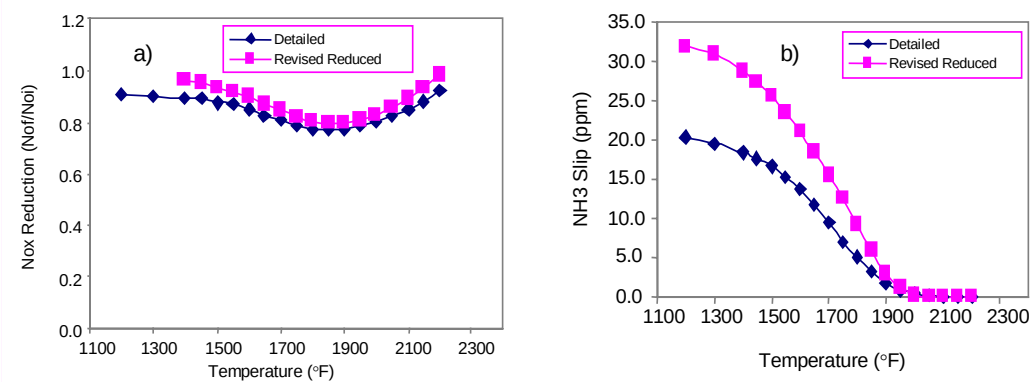

Exhibit 6-38
Comparison between revised-global and detailed mechanisms for urea at NSR = 0.5. a) NOx Reduction; b) NH_3 Slip.

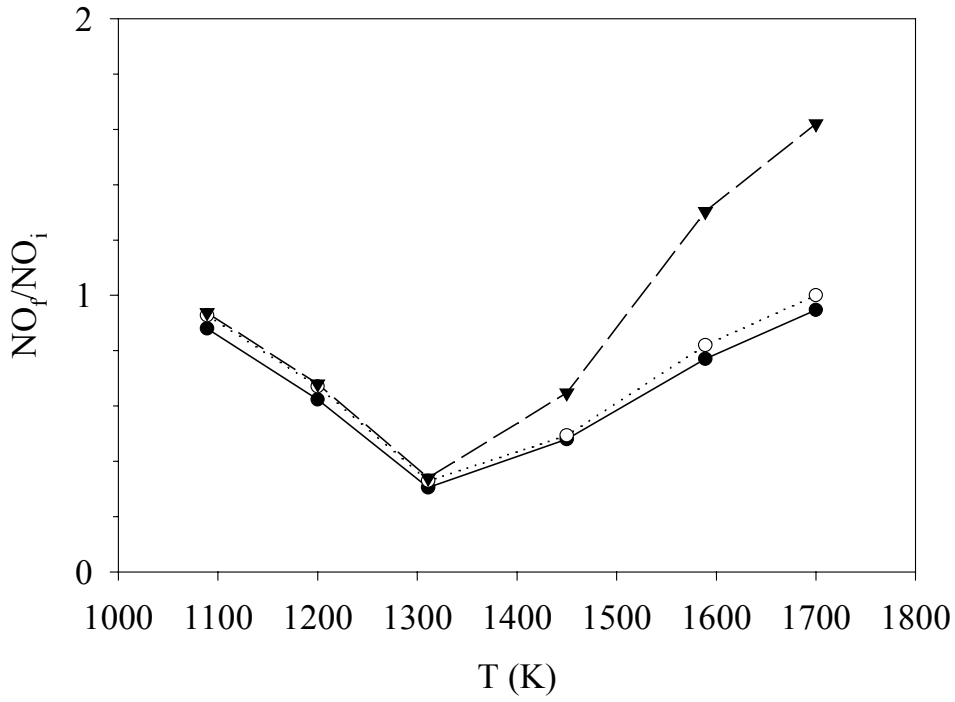

Exhibit 6-39
Comparison of isothermal plug flow calculations in Chemkin using seven-step global (▼), 10 specie reduced (○), and detailed (●) chemistry versus gas temperature for a residence time of 0.1 sec. The initial flue gas composition was that of equilibrated coal products with 3% O_2, 300 ppm NO, 150 ppm NH_3 and, 150 ppm HNCO-

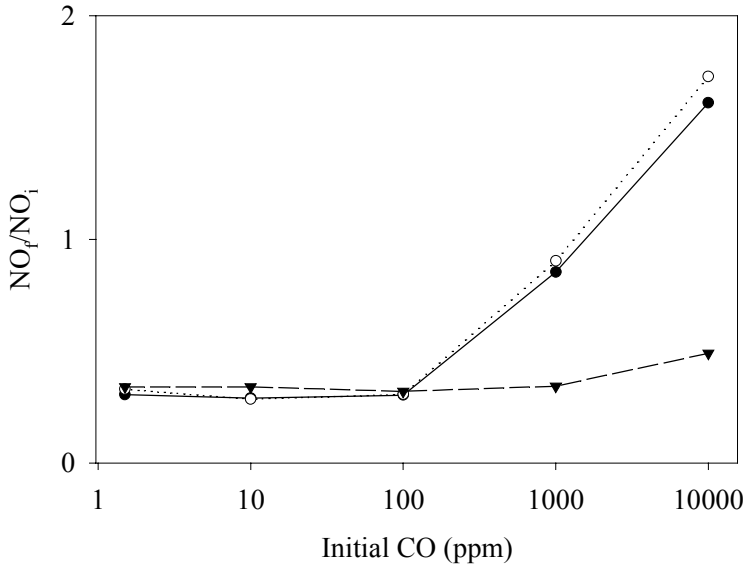

Exhibit 6-40
Comparison of isothermal plug flow calculations in Chemkin using seven-step global (▼), 10 specie reduced (O), and detailed (●) chemistry versus initial CO concentration for a residence time of 0.1 s. Initial flue gas composition corresponded to that of equilibrated coal products with 3% O_2, but varying levels of CO from 2-10,000 ppm, 300 ppm NO, 150 ppm NH_3, and 150 ppm HNCO at T = 1311 K

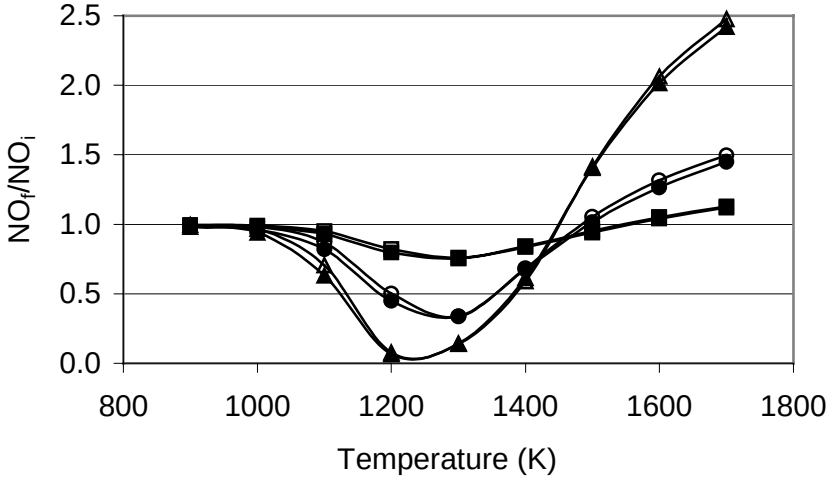

Exhibit 6-41
Comparison of NOx predictions for isothermal plug flow with initial coal flue gas composition CO_2:14.19%, H_2O:12.43%, N_2:70.46%, O_2:2.89%, NO_i:200 ppm, NH_3/NO_i = 0.3, 1.0, or 3.0 at residence time 0.2 s. (■ ~ Detailed with NSR = 0.3, □ ~ Reduced with NSR = 0.3, ● ~ Detailed with NSR = 1.0, ○ ~ Reduced with NSR = 1.0, ▲~ Detailed with NSR = 3.0, Δ~ Reduced with NSR = 3.0)

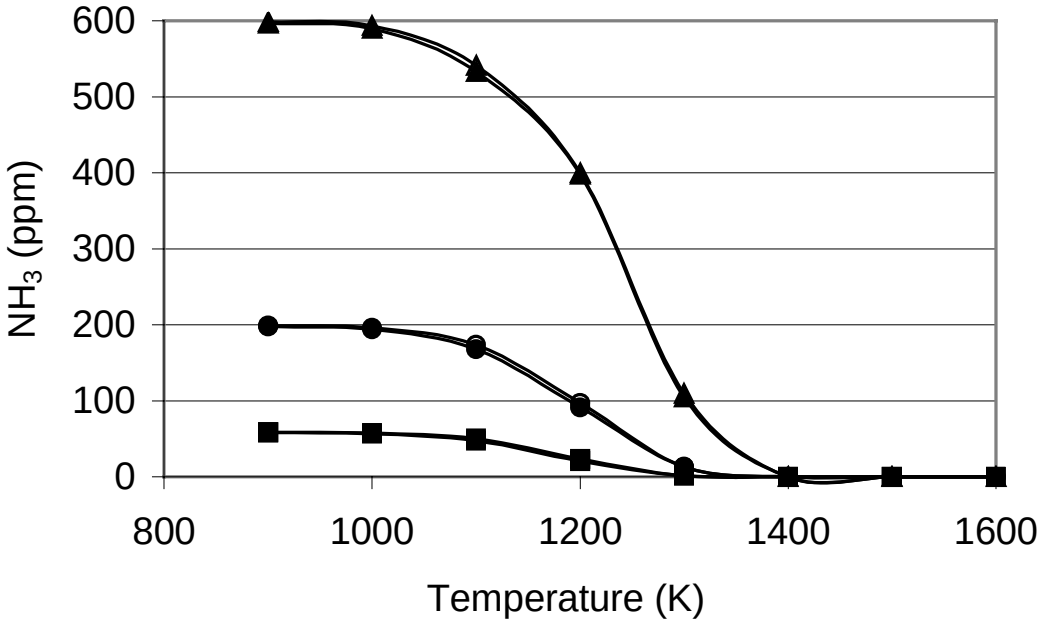

Exhibit 6-42
Comparison of NH_3 slip predictions for the same conditions as in Exhibit 6-65

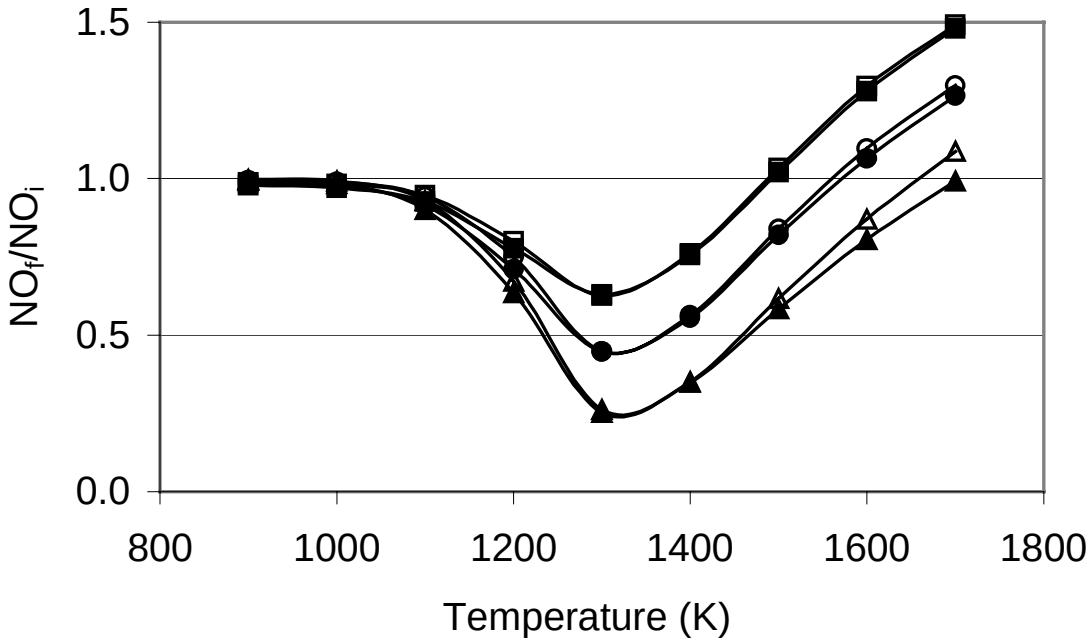

Exhibit 6-43
Comparison of NOx predictions for isothermal plug flow with initial composition CO_2:14.19%, H_2O:12.43%, N_2:70.46%, O_2:2.89%, NO_i:100ppm, 200ppm, or 500 ppm, Urea/NO_i:0.5 at residence time 0.2 s (■ ~ Detailed with NO_i = 100 ppm, □ ~ Reduced with NO_i = 100 ppm, ● ~ Detailed with NO_i = 200 ppm, ○ ~ Reduced with NO_i = 200 ppm, ▲~ Detailed with NO_i = 500 ppm, Δ~ Reduced with NO_i = 500 ppm)

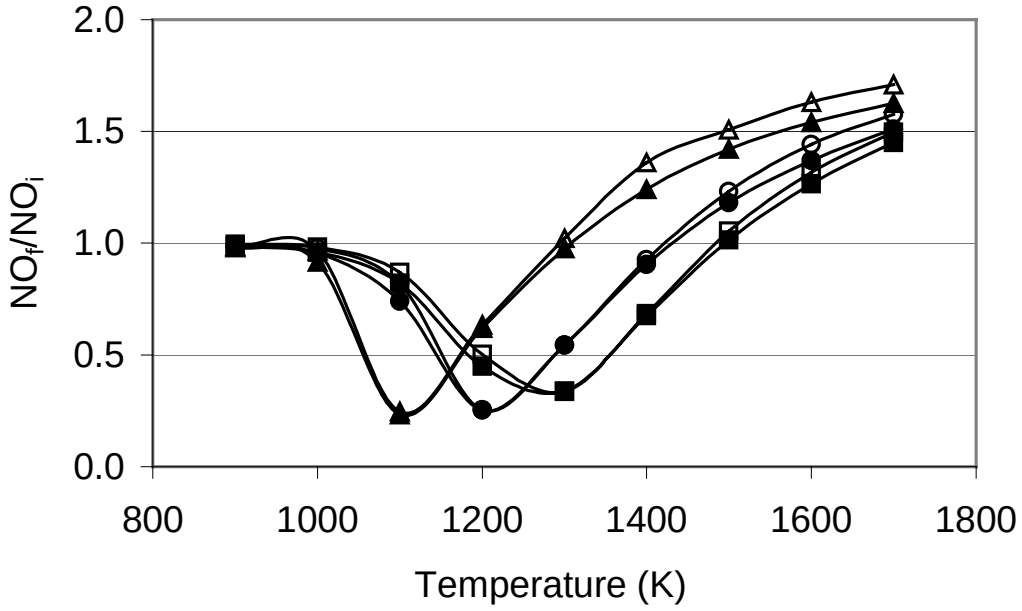

Exhibit 6-44
Comparison of NOx predictions for isothermal plug flow with initial composition CO_2:14.19%, H_2O:12.43%, N_2:70.46%, O_2:2.89%, NO:200 ppm, $NH3/NO_i$:1.0, CO:0 ppm, 100 ppm, 500 ppm at residence time 0.2 s (■ ~ Detailed with CO = 0 ppm, □ ~ Reduced with CO = 0 ppm, ● ~ Detailed with CO = 100 ppm, ○ ~ Reduced with CO = 100 ppm, ▲~ Detailed with CO = 500 ppm, Δ~ Reduced with CO = 500 ppm)

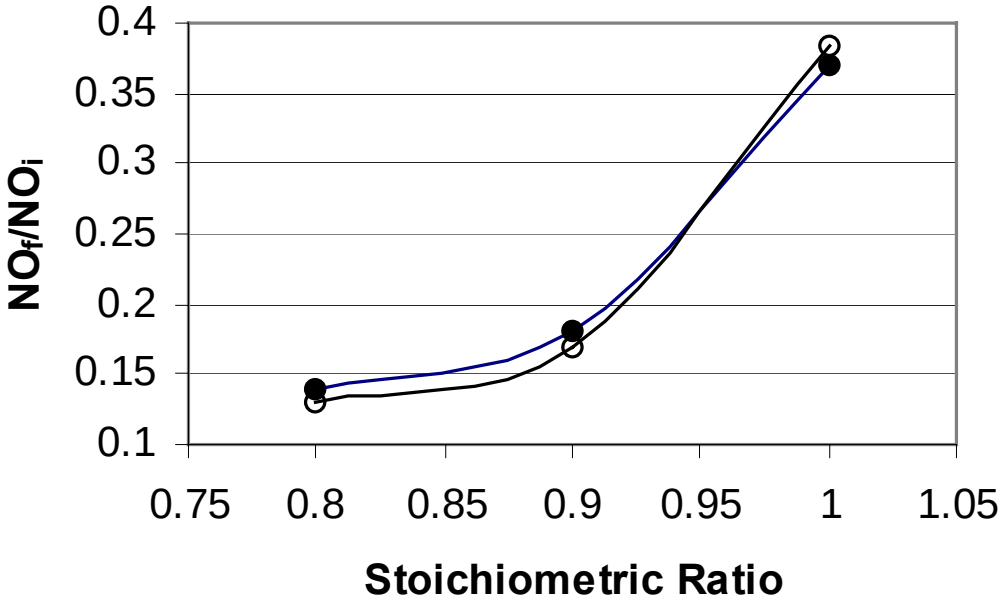

Exhibit 6-45
Comparison of NOx predictions for isothermal plug flow under fuel rich (coal) conditions, T = 1800 K, with urea/NO_i:1.0, NOi = 600 ppm, at a residence time 0.5 s (● ~ Detailed, ○ ~ Reduced)

Concluding Comments

The improved model was developed to assist the development of the HITAF, HIPPS repowering facilities, and to assist in the design of test plans and interpretation of data from the pilot Boiler Simulation Furnace (BSF) that were to be carried out at ABB's (now Alstom's) test facilities at Windsor, CT. These tests would have provided confidence in the predictive capabilities of the model and its potential for having industry accept the risk inevitably involved with the introduction of any new technology.

The models developed as part of this contract have been incorporated, together with developments in parallel programs, into the codes used by Reaction Engineering International to simulate boilers for the electrical utility industry. The success of these codes to simulate performance, in particular to simulate alternative low NOx control technologies, including low-NOx burners, the use of closely coupled and separated over-fire airports, and the optimum positions for introducing reagents for SNCR has led the industry to accept simulations as an important element in retrofitting boilers. Some of these successful simulations will be described below because they are pertinent to the future demonstrations of HIPPS.

One example of the success of the application of theses tools on a program for a consortium of electrical generation utilities organized by the Electric Power Research Institute (EPRI) is shown in Exhibit 6-46, which illustrates the predicted effects of operating a cyclone-fired boiler under low-NOx firing conditions. Under baseline conditions, the cyclone barrels are operated fuel lean, whereas under staged conditions, the cyclone barrels are operated fuel-rich and the make-up combustion air is added through over-fire air ports. The REI model was applied to guide the placement of the overfire air ports and the impact of different degrees of staging. Exhibit 6-46 shows the excellent agreement between predictions and measurements of NOx that were made **after** implementation of the optimized designs for several units. The use of such tools have resulted in 80 percent of all cyclone fired furnaces being retrofitted with overfire air ports. The success in the simulation of cyclone barrels is particularly relevant to the future designs of a HITAF, since it has been shown that the cyclones provide a means to rapidly obtain the high fluxes required for the radiant air heaters. Traditionally cyclones have been viewed as being high emitters of NOx. The REI simulations and the implementation of the staged combustion in the field show that this is not necessarily the case. Indeed, the high residence at high temperatures that would be involved in a HITAF, in combination with staging, could result in very low NOx levels, even prior to downstream reagent injection.

A measure of how the tools developed here can be applied to the retrofit applications of HIPPS is given below. Existing furnaces will need to operate with the combustion air replaced by vitiated air from the gas turbine. The questions that need to be addressed are the impact of this change on NOx emissions, flame attachment, temperature profiles, and flame profiles.

Simulation of the Hammond furnace operation has been performed using the CFD program Glacier. Utilizing the fact that the furnace has vertical symmetry plane, only one half of the furnace was used to run the simulation. The computational mesh had 507,000 cells.

Two modes of furnace operation are analyzed: combustion with normal air, and combustion with vitiated air. Composition, temperature and flow rate of inlet streams for the two cases are presented in Table 6-15.

Table 6-15
Inlet stream properties

Property	Case	
	Normal air	Vitiated air
Inlet flow rate, [kg/s]		
Primary air	54.3	
Secondary air	207	250
Coal	22.4	
Air temperature, [K]		
Primary	350	
Secondary	620	811
Secondary air composition, [%]		
O_2	21.0	17.6
N_2	78.9	77.7
H_2O	0.1	3.2
CO_2	0	1.5

In a simulation of a HIPPS plant the oxidant stream would be the exhaust from the gas turbine. In order to show the capability to simulate a hot gas stream with lower oxygen content we have arbitrarily created a vitiated air by combustion of methane in the secondary air stream, resulting in oxygen concentration in the secondary air stream reduced to 17.6 % and temperature is increased to 998 °F (537 °C, 810 K). In order to maintain the overall stoichiometric ratio at 1.1, the flow rate of the secondary air has to be increased from normal-air value of 463 lb/s (210 kg/s) to 551 lb/s (250 kg/s) for vitiated air. Table 6-16 presents main flow and thermal parameters for the two analyzed operation modes.

Table 6-16
Flow and thermal parameters

Property	Case	
	Normal air	Vitiated air
Global Re	570000	657000
Particle loading	0.0858	0.0737
T_{ad}, [K]	2325	2242
T_{max}, [K]	2248	2223
$T_{out,\ integrated}$, [K]	1640	1657
Thermal output, [MW]	717	797

Even though the secondary air temperature is higher for the vitiated air case, the lower oxygen contents causes -316 °F (-193 °C, 80 K) lower adiabatic flame temperature as compared to the normal air case. The two competing effects are balanced and the temperature profiles for two cases are similar, as seen in -6.47.

The peak flame temperature, which is achieved close to the burners, is only slightly higher (-424 °F [-253 °C, 20 K]) for the normal air case, despite much higher adiabatic flame temperature (-316 °F [-193 °C, 80 K]). Here the higher temperature of the vitiated air effectively compensates for 17% lower oxygen contents. The same factors lead to equally well near-burner behavior for the two cases. As seen in Exhibit 6-48, in both cases the flames are attached.

Exhaust stream properties are presented in Table 6-17.

Table 6-17
Furnace exhaust stream properties

Property	Case	
	Normal air	Vitiated air
Exhaust gas composition		
dry O_2, [%]	4.3	4.2
dry CO, [ppm]	1518	48
dry NO_x, [ppm]	319	234
NO @ 3% O_2, [ppm]	344	250
Carbon burnout, [%]	97.93	97.81
Carbon in ash, [%]	16.53	17.32

Nitrogen oxides formation has been simulated in the post-processing phase, using established flow and temperature field. While temperature field looks very similar for the two cases (Exhibits 6-47), NOx emissions differ significantly. Combustion using vitiated air produces 26% less NOx. Exhibit 6-49 shows the nitrogen oxide distribution through the furnace at a representative cross-section.

Having in mind the similar temperature profile and only 1% lower N_2 concentration, one may expect nearly equal NOx emissions. However, NOx formation is happening on the time scale of the order of magnitude longer than for the hydrocarbon combustion process. Higher flow rate of the secondary stream in the vitiated air case necessary to maintain the stoichiometry at 1.1, corresponds to the 70% higher gas velocity, which means to the same extent shorter residence time. Thus, NOx formation process has less much time to take place in the vitiated air case, and the resulting NOx concentration is significantly lower. NOx formation rate for the same furnace cross-section is presented in Exhibit 6-50.

The highest NOx formation rate in both cases occurs in the mixing layer between coal and secondary air stream, where both temperature and NOx-related radicals concentration are high. Away from the burners, NOx generation for the two cases differs significantly. The difference in the shape of NOx generation zone above the burners is caused by slightly different flow field, which is due to different gas velocities. The large difference in size of that zone in two cases is consistent with the difference in oxygen concentration presented for the same cross-section of the furnace in Exhibit 6-51. While the NOx generation rate in the zone above the burners is significantly lower than around the flames, volume of that zone is large enough to be a significant NOx source.

NOx destruction rate for the two cases are compared in Exhibit 6-52. According to these results, NOx destruction occurs only in the fuel-rich portion of the flame. Both the size of the NOx destruction zone and the rate of destruction are similar for two cases, thus not contributing significantly to the calculated difference in the NOx concentration at the exhaust.

In summary, a comparison of the results of these two simulations indicates that the use of vitiated air in combustion can result in reduced NOx emissions without a significant increase in unburned carbon. An evaluation of the use of a vitiated oxidant, however, must also consider the impact of increased flow rates on heat transfer to the downstream equipment in the boiler. Capacity of existing ID fans and air pollution control devices may prohibit a simple retrofit and require a much greater capital investment to accommodate the required flow rates.

Similar conclusions have been reached in earlier experimental studies (Floris, 1980). The NOx reduction observed by Floris was attributed to reduced oxygen concentrations, with consequently lower flame temperatures and lower thermal NOx formation rates. While the burner in that study promoted intensive early mixing of primary and secondary streams, their overall trends of lower NOx emissions and only slightly higher amount of carbon in ash observed during vitiated air combustion, are supportive of our findings.

A measure of the acceptance by industry of the simulation tool is the simulation by REI for the utility industry of a total of 66 boilers, involving 9.5 GW cyclone fired, 6.5 GW wall-fired, and 6.0 GW corner-fired. The value to the energy industry of simulations will be much greater during the development of the next generation of high efficiency, low emission, energy plants such as HIPPS.

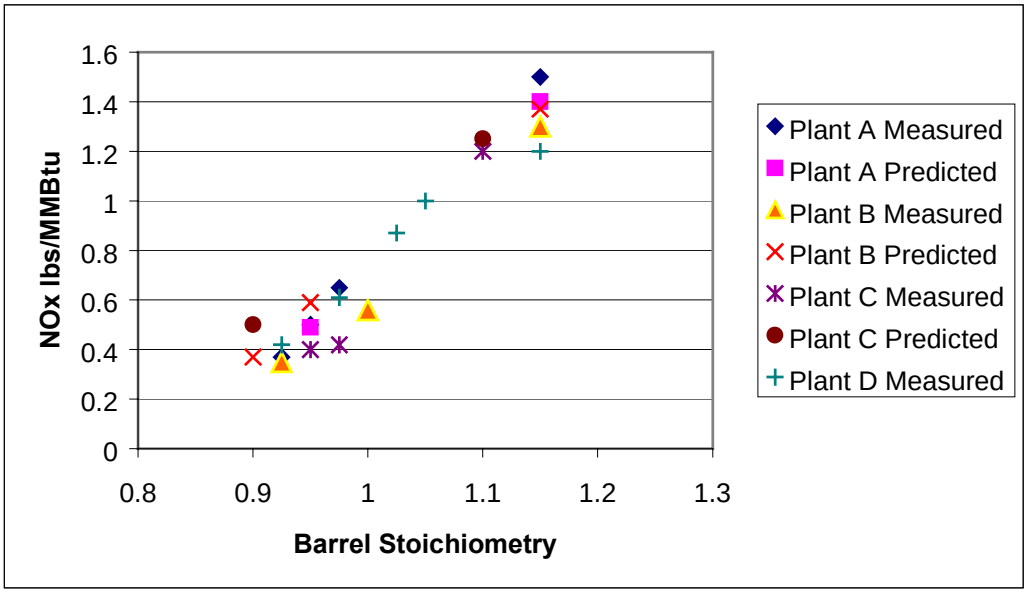

Exhibit 6-46
Comparison between predicted and measured NOx emissions for several cyclone fired furnaces under staged and unstaged conditions. The measured emissions have been found to agree very well with predictions

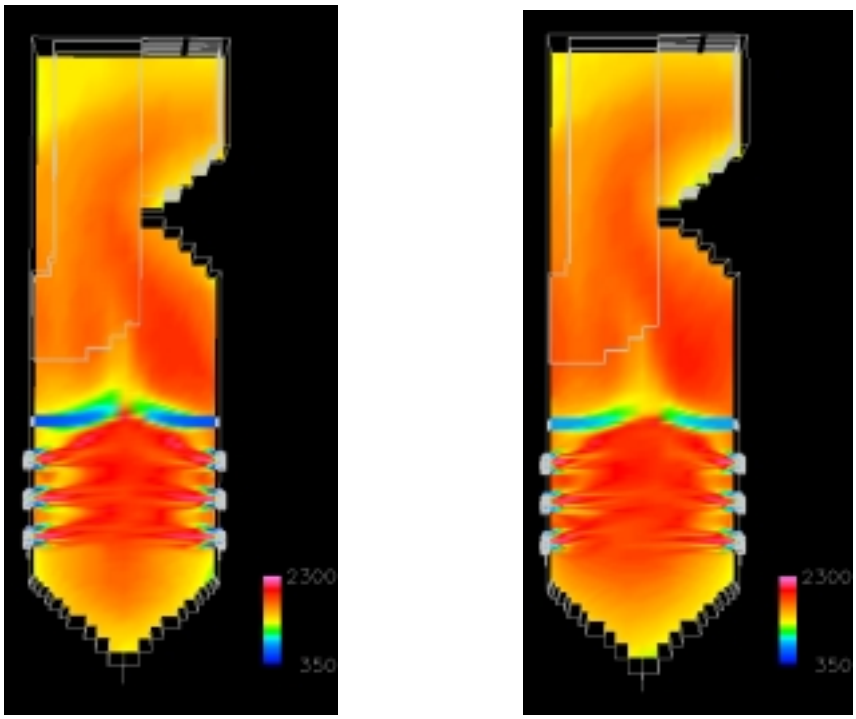

Exhibit 6-47
Temperature profile for the vertical cross-section through the set of opposing burners closer to the symmetry plane. Scale is in K. (left – normal air case; right – vitiated air case)

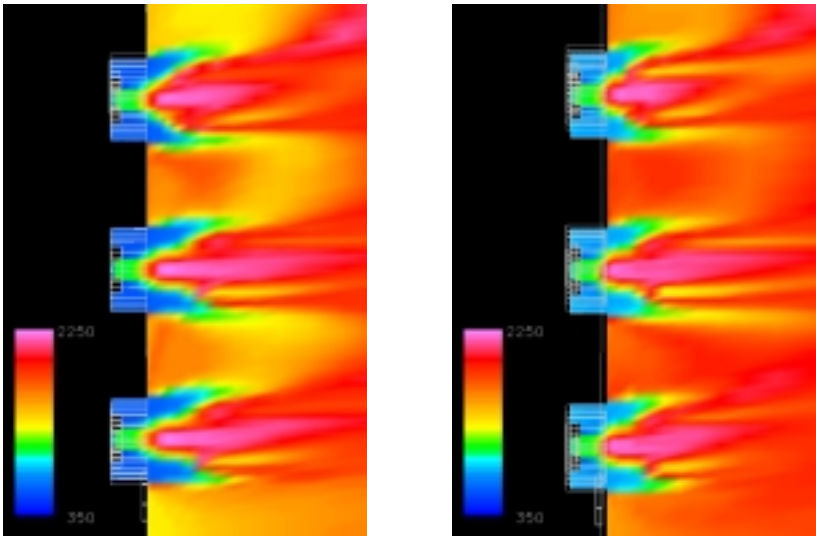

Exhibit 6-48
Near-burner temperature profiles. Front-wall near symmetry line set of burners. Scale is in K. (left – normal air case; right – vitiated air case)

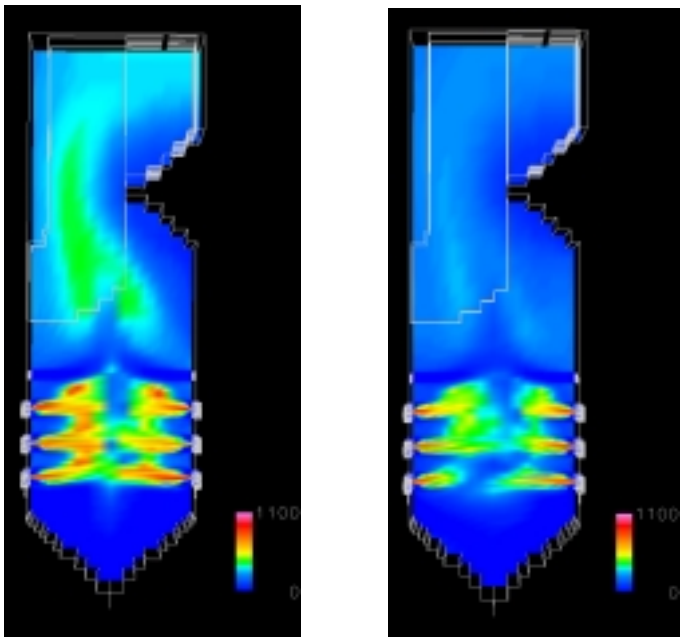

Exhibit 6-49
NOx concentration profile for the vertical cross-section through the set of opposing burners closer to the symmetry plane. Scale is in ppm. (left – normal air case; right – vitiated air case)

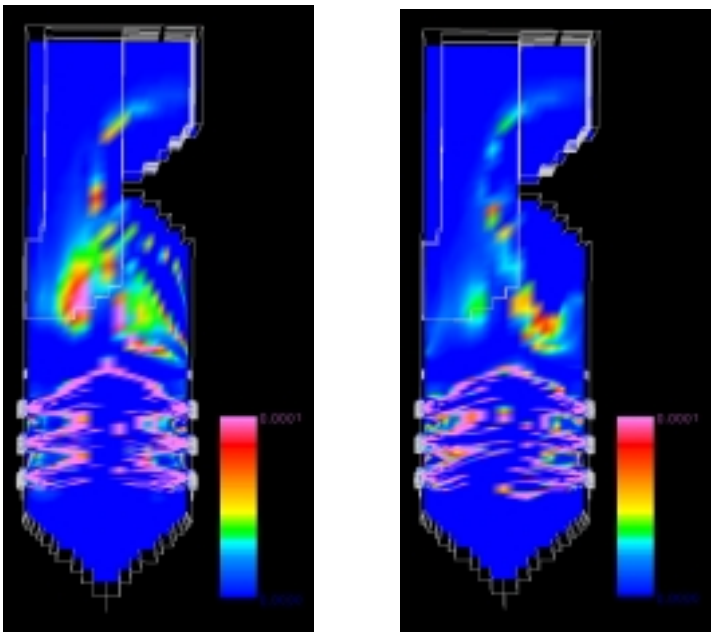

Exhibit 6-50
NOx generation rate for the vertical cross-section through the set of opposing burners closer to the symmetry plane. Scale is in kg/m^3·s. (left – normal air case; right – vitiated air case)

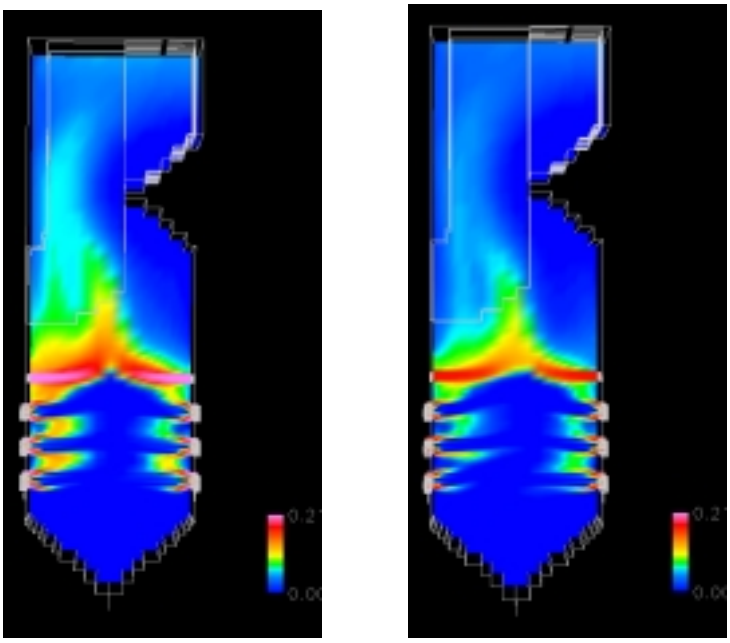

Exhibit 6-51
O_2 concentration profile for the vertical cross-section through the set of opposing burners closer to the symmetry plane. Scale is in %. (left – normal air case; right – vitiated air case)

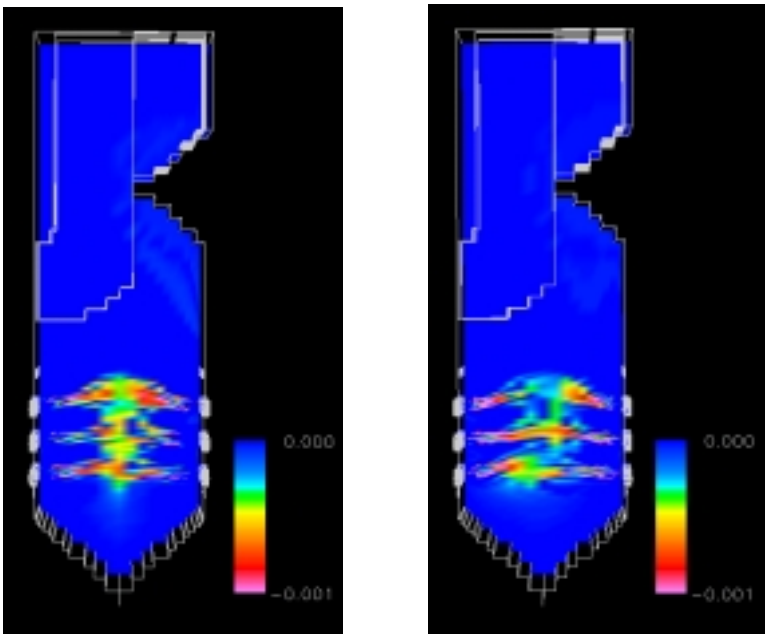

Exhibit 6-52
NOx destruction rate for the vertical cross-section through the set of opposing burners closer to the symmetry plane. Scale is in kg/m^3·s as NOx generation – more negative numbers represent faster NOx destruction. (left – normal air case; right – vitiated air case)

References

Abbas, T. N.; Costen, P. G.; Kandamby, N.; Lockwood, F. C.; Yosuf, S.; Benos, G.; Perera, A. "NO_x Abatement Through Fuel-Staging in Pulverized Coal-Fired Furnaces"; presented at the ASME International Joint Power Generation Conference and Exposition, Houston, TX, 1996.

Abramowitz, M.; Stegun, I. A. *Handbook of Mathematical Functions*; Dover Publications: New York, 1970.

Antifora, A.; Sala, M.; Perera, A.; Vigevano, L. "NO_x Emissions in Combustion Systems of Coal Fired Furnaces with a Reburning Environment: Predictions and Measurements"; presented at the Fourth International Conference on Technologies and Combustion for a Clean Environment, San Francisco, CA, 1977.

Baulch, D. L.; Drysdale, D. D.; Horne, D. G.; Loydt, A. C., *Evaluated Kinetic Data for High Temperature Reaction*s; CRC Press: Cinncinati, 1973.

Baurle, R. A.; Alexopoulus, G. A.; Hassan, H. A. *J. of Prop. Power* **1994**, 10, 777.

Baxter, L. L. Ph. D. Dissertation, Brigham Young University, 1987.

Bilger, R. W. *Prog. Energy Combust. Sci.* **1976**, 1, 87.

Bilger, R. W. *Prog. Aster. Aero.* **1977**, 53, 49.

Bilger, R. W. *Combust. Sci. Technol.* **1979**, 19, 89.

Bilger, R. W. In *Topics in Applied Physics: Turbulent Reacting Flow*; Libby, P. A.; Williams, F. A., Eds; Springer-Verlag: New York, 1980; Vol. 44, p 65.

Bird, R.B.; Stewart, W. E.; Lightfoot, E. N. *Transport Phenomena*; John Wiley and Sons: New York, 1960.

Blauwens, J.; Smets, B.; Peters, J. *Sixteenth Symposium (International) on Combustion*; The Combustion Institute: Pittsburgh, 1977; p 1055.

Bowman, C. T. *Fourteenth Symposium (International) on Combustion*, The Combustion Institute: Pittsburgh, 1973; p 729.

Bowman, C. T. *Prog. Energy Combust. Sci.* **1975**, 1, 33.

Brewster, B. S.; Baxter, L. L.; Smoot, L. D. *Energy Fuels* **1988**, 2, 362.

Brouwer, J., Heap, M.P., Pershing, D.W., and Smith, P.J., *Proc. Combust. Inst.* 26:2117-2124 1996).

Caretto, L. S.; Sawyer, R. F.; Starkman, E. S. University of California at Berkely Technical Report No. TS-68-1; University of California at Berkely: Berkely, CA, 1968.

Caretto, L. S. "Modeling Gas-Phase Kinetics of Fuel-Nitrogen"; presented at the Western States Section/The Combustion Institute, Salt Lake City, UT, 1989.

Chan, C. C.; Lee, Y. Y. Presented at the Proceedings of the IASTED International Conference, Santa Barbara, CA, 1985.

Chan, L. K.; Sarofim, A. F.; Beer, J. M., *Combust. Flame* **1983,** 52, 37.

Chen, C-S.; Chang, K-C.; Chen, J-Y. *Combust. Flame* **1994** 10, 375.

Chen, J.-Y., *Combust. Sci. and Tech.* 57:89-94 (1988).

Chen, J.-Y., Workshop on Numerical Aspects of Reduction in Chemical Kinetics, CERMICS-ENPC, Cite Descartes, Champus sur Marne, France,1997.

Chen, S. L.; Heap, M. P.; Pershing, D. W.; Martin, G. B. *Nineteenth Symposium (International) on Combustion*; The Combustion Institute: Pittsburgh, 1981; p 1263.

Chen, W.; Smoot, L. D.; Hill, S. C.; Fletcher, T. H. *Energy Fuels* **1996**, 10, 1046.

Coelho, P. J.; Carvalho, M. G. *Combust. Sci. Technol.* **1995**, 108, 363.

Comparato, J.R., Boyle, J.M., and Michels, W.F., *1998 U.S. DOE Conference on SCR and SNCR for NOx Control*, Pittsburgh, PA, 1998.

Cremer, M.A., Eddings, E., Martz, T., Muzio, L.J., Quartucy, Q., Hardman, R., Cox, J., and Stallings J., *1998 U.S. DOE Conference on SCR and SNCR for NOx Control*, Pittsburgh, PA, 1998.

Cremer, M.A., Wang, D.H., Phillips, R.A., Smith, R.C., Boll, D.E., Martz, T., and Muzio, L.J., and Stallings J., *1999 U.S. DOE Conference on SCR and SNCR for NOx Control*, Pittsburgh, PA, 1999.

Cremer, M.A., Heap, M.P., Ciarlante, V., Zoccola, M., *1999 U*

Crowe, C. T.; Sharma, M. P.; Stock, D. E. *J. Fluids Eng.* **1977**, 99, 325.

Dean, A.J., Hanson, R.K., and Bowman, C.T., *J. Phys. Chem*. 95:3180-3189 (1991).

Drake, M. C.; Correa, S. M.; Pitz, R. W.; Shyy, W.; Fennimore, C. P. *Combust. Flame* **1987**, 69, 347.

DeSoete, G. G. *Fifteenth Symposium (International) on Combustion*; The Combustion Institute: Pittsburgh, 1975; p 1093.

DeSoete, G. G.; Croiset, E.; Richard, J.-r. Presented at the Seventh International Workshop on Nitrous Oxide Emissions, Koln, Germany, April 1997.

Domino, S. P.; Smith, P. J. "Improved NO Simulations in Pulverized-Coal Combustion"; presented at the Western States Section/The Combustion Institute, Diamond Bar, CA, 1997.

Domino, S. P.; Smith, P. J. "Char Oxidation Model Validation in Detailed Coal Simulations"; presented at the ASME International Mechanical Engineering Congress and Exposition, Nashville, TN, 1999.

Eddings, E. B.; Smith, P. J.; Heap, M. P.; Pershing, D. W.; Sarofim, A. F. "An Improved Model for Predicting NO_x Formation in Practical Coal Flames"; presented at the ASME Conference, Snowbird, UT, 1994.

Favre, A. In *Problems of Hydrodynamics and Continuum Mechanics;* Society for Industrial and Applied Mathematics, Philadelphia, 1969.

Fenimore, C. P. *Combust, Flame* **1976** 26, 249.

Fenimore, C. P. *Seventeenth Symposium (International) on Combustion*; The Combustion Institute: Pittsburgh, 1979; p 661.

Field, M. A.; Gill, D. W.; Morgan, B. B.; Hawksley, P. G. W. *Brit. Coal Util. Res. Assoc. Monogr. Bull.* **1967**, 31, 285.

Flores, D. V.; Fletcher, T. H. "A Two Mixture Fraction Approach for Modeling Turbulent Combustion of Coal Volatiles and Char Oxidation Products"; presented at the Spring Meeting of the Central States/Western States/Mexican National Section of the Combustion Institute and the American Flame Research Committee, San Antonio, TX, 1995.

Floris F., "The effect of vitiated air on the combustion of pulverized coal for applications to coal fired combined cycle steam generators", Eighteenth Symposium (International) on Combustion; The Combustion Institute: Pittsburgh, 1980; p 1313.

Fletcher, T. H.; Solum, M. S.; Grant, D. M.; Crichfield, S.; Pugmire, R. J. *Twenty-third Symposium (International) on Combustion*, The Combustion Institute: Pittsburgh, 1990; p 1231.

Gatski, T.B.; Grosch, C. E.; Rose, M. E. *J. Comp. Phys.* **1989**, 82, 298.

Genetti, D.; Fletcher, T. H.; Pugmire, R. J. *Energy & Fuels* **1999***,* 13, 60.

Girimaji, S. S. *Combust. Sci. Technol.* **1991**, 78, 177.

Goel, S. K.; Sarofim, A. F. *A Single Particle Model for Studying Char Nitrogen Chemistry at Pulverized Fuel Combustion Conditions*; Department of Energy Report No. DOE/PC/94223-1; United States Department of Energy: Pittsburgh, PA, 1995.

Goel, S. K.; Morihara, A.; Tullin, C. J.; Sarofim, A. F. *Twenty-fifth Symposium (International) on Combustion*; The Combustion Institute: Pittsburgh, 1994; p 1051.

Goel, S. K.; Sarofim, A. F. "Comparison of Four Mechanisms for Nitrogen Chemistry During Char Combustion.", personal communication, 1997.

Godoy, S. G.; Hassan, M.A.; Ismail, M.A.; Lockwook, F. C. *Combust. Sci. Technol.* **1991**, 80, 137.

Godoy, S. G.; Ismail, M.; Lockwood, F. C. *Combust. Sci. Technol.* **1989**, 67, 59.

Hampartsoumian, E.; Pourkashanian, M.; Williams, A. *J. Inst. Energy* **1989**, March, 48.

Hanson, R. K.; Salimian, S. In *Combustion Chem*istry, W. C. Gardiner, Jr. Ed.; Springer: New York, 1984.

Hassen, M.A.; Hirji, K. A.; Lockwood, F. C.; Moneib, H. A. *Experiments in Fluids* **1985** 3, 153.

Harlow, F.H.; Nakayama, P.I. *Transport of Turbulence Energy Decay Rate*, Los Alamos national Laboratory Technical Report No. LA-3854; Los Alamos National Laboratory: Los Alamos, New Mexico.

Hayhurst, A. N.; Mclean, H. G. *Nature* **1974**, 251,303.

Hayhurst, A. N.; Vince, I. M. *Prog. Energy Combust. Sci.* **1980**, 6, 35.

Heap, M. P.; Tyson, T. J.; Cichanowicz, J. E.; Gershman, R.; Kau, C. J. *Sixteenth Symposium (International) on Combustion*; The Combustion Institute: Pittsburgh, 1977; p 535.

http://www.reaction-eng.com/downloads.htm.

Hurt, R. H.; Sun, J. K.; Lunden, M.; *Combust. Flame* **1998**, 113, 181.

Hurt, R. H.; Lunden, M.; Brehob, E. G.; Maloney, D. J. *Twenty-sixth Symposium (International) on Combustion*; The Combustion Institute: Pittsburgh, 1996; p 3169.

Hurt, R, H.; Gibbons, J. R. *Fuel* **1995**, 74, 471.

Hurt, R. H.; Davis, K. A.; Yang, N. Y. C.; Headly, T. R.; Mitchell, G. D. *Fuel* **1995**, 74, 1297.

Hurt, R. H.; Davis, K. A. *Twenty-fifth Symposium (International) on Combustion*; The Combustion Institute: Pittsburgh, 1994; p 561.

Institute of Clean Air Companies (ICAC), SNCR Committee, "Selective Non-Catalytic Reduction (SNCR) for Controlling NOx Emissions," 1994.

Iverach, D.; Kirov, N. K.; Haynes, B. S. *Combust. Sci. Technol.* **1973**, 8, 139.

Jain, S. Ph. D. Dissertation, University of Utah, 1997.

Johnson, J. E., *Fuel* **1994** 73, 1398.

Kee, R.J.; Miller, J.A.; Jefferson, T.H. *Chemkin User's Manual,* Sandia National Laboratories Report No. SAND80-8003; Sandia National Laboratories: Livermore, CA, 1980.

Kee, R.J., Rumpley, F.M., and Miller, J.A., "Chemkin-II: A Fortran Chemical Kinetics Package for the Analysis of Gas Phase Chemical Kinetics," Sandia National Laboratories Report No. SAND89-9009B, 1989.

Kent, J. H.; Bilger, R. W. Department of Mechanical Engineering Report No F-37; University of Sydney: Sydney, Australia, 1971.

Kennedy, I. M.; Kent, J. H. "Laser Scattering Measurements in Turbulent Diffusion Flames"; presented at the AIAA Eighteenth Aerospace Sciences Meeting, Pasadena, CA, 1980.

Kinkaid, D.; Cheney, W. *Numerical Analysis, Mathematics of Scientific Computing*; Brooks/Cole: Pacific Grove, California, 1991.

Kobayashi, H.; Howard, J. B.; Sarofim, A. F. *Eighteenth Symposium (International) on Combustion*; The Combustion Institute: Pittsburgh, 1977; p 411.

Kumar, S. Ph. D. Dissertation, University of Utah, 1999.

LaChapelle, D. G. Presented at the EPRI Nitric Oxide Control Technology Seminar, San Francisco, CA, 1976.

Launder, B.E.; D.B. Spalding, *Mathematical Models of Turbulence*; Academic Press: London, 1972.

Lavoie, G. A.; Heywood, J. B.; Keck, J. C. *Combust. Sci. Technol.* **1970**, 23, 313.

Levy, J. M. "Modeling of Fuel-Nitrogen Chemistry in Combustion: The Influence of Hydrocarbons"; presented at the Fifth EPA Fundamental Combustion Research Workshop, Newport Beach, CA, 1980.

Lewis, W. K.; Gillilang, E. R.; McBride, G. T. *Ind. Eng. Chem.* **1949**, 41, 1213.

Lyon, R.K., U.S. Patent No. 3,900,544 (1975).

Mair, H.; Spliehoff, H.; Kicherer, A.; Fingerle, A.; Hein, K. R. G. *Fuel* **1994,** 73, 1447.

Makansi, L. *Power* **1994**, August, 37.

Mass, U.; Pope, S. B. *Twenty-fifth Symposium (International) on Combustion*; The Combustion Institute: Pittsburgh, 1994; p. 1349.

Mehrotra, V. Ph. D. Dissertation, University of Utah, 1998.

Miller, J. A.; Bowman, C. T. *Prog. Energy Combust. Sci.* **1989,** 15, 287.

Miller, J. and Melius, C., *Proc. Combust. Inst.* 21:919-927 (1986).

Miller, C. A.; Touati, A. D.; Eand Wendt, J. O. L. *Twenty-seventh Symposium (International) on Combustion*; The Combustion Institute: Pittsburgh, 1980; p 1265.

Milne, T. A.; Beachy, J. E. *Combust. Sci. Technol.* **1977,** 16, 139.

Mitchell, S. C. *Nitrogen Oxide in Pulverized Coal Combustion, in Perspectives*, IEQ Coal Research, 1998.

Mitchell, J. W.; Tarbell, J. M. *AIChE J.* **1982,** 28, 302.

Mitchell, R. E.; Hurt, R. H.; Baxter, L. L.; Hardesty, D. R. *Compilation of Sandia Coal Char Combustion Data and Kinetic Analysis*, Sandia National Laboratory Report No. SAND92-8208; Sandia National Laboratories: Livermore, CA, 1992.

Muzio, L.J., Arand, J.K., and Teixeira, D.P., *Proc. Combust. Inst.* 16:199-208 (1976).

Muzio, L.J. and Quartucy, G.C., *Prog. Energy Combust. Sci*. 23:233-266 (1997).

Newhall, H. K.; Shahad, S. H. *Thirteenth Symposium (International) on Combustion*; The Combustion Institute: Pittsburgh, 1971; p 381.

Niksa, S. *Energy Fuels* **1991**, 5, 647.

Niksa, S. *Twenty-fifth Symposium (International) on Combustion*; The Combustion Institute: Pittsburgh, 1994; p 537.

Orendt, A. M.; Solum, M. S.; Sethi, N. K.; Pugmire, R. J.; Grant, D. M. *Advances in Coal Spectroscopy*; Plemum Press: New York, 1991.

Østberg, M. Ph.D thesis, Department of Chemical Engineering, Technical University of Denmark, 1996

Østberg, M.; Glarborg, P.; Tensen, A.; Johnson, J. E.; Pederson, L. S.; Dam-Johansen, K. *Twenty-seventh Symposium (International) on Combustion*; The Combustion Institute: Pittsburgh, 1998; p 3027.

Patankar, S.V. *Numerical Heat Transfer and Fluid Flow*; McGraw-Hill: New York, 1980.

Perry, R.A. and Siebers, D.L., *Nature* 324:657-666 (1986).

Pershing, D. W.; Martin, G. B.; Berkau, E. E. *AIChE Symposium Series* **1977**, 16, 139.

Pershing, D. W.; Wendt, J. O. L. *Sixteenth Symposium (International) on Combustion*; The Combustion Institute: Pittsburgh, 1977; p 389.

Peters, N. and Rogg, B, (Eds.) *Reduced Kinetic Mechanisms for Applications in Combustion Systems*, Springer, 1993.

Piessens, C.; Uberhuber; Kahaner, D. *QUADPACK: A Subroutine Package for Automatic Integration*; Springer: Berlin, 1980.

Quan, V.; Marble, F.; Kliegel, J. R. *Fourteenth Symposium (International) on Combustion*; The Combustion Institute: Pittsburgh, 1973; p 851.

Quartucy, G.C., Montgomery, T.A., and Muzio, L.J., *Joint Spring Meeting of the Canadian and Western States Sections*/The Combustion Institute, Banff, Alberta, 1990.

Rawat, R. Ph.D. Dissertation, University of Utah, 1997.

Rees, D. P.; Smoot, L. D.; Hedman, P. O. *Eighteenth Symposium (International) on Combustion*; The Combustion Institute: Pittsburgh, 1981; p 1305.

Sarofim, A. F.; Pohl, J. H. *Fourteenth Symposium (International) on Combustion*; The Combustion Institute: Pittsburgh, 1973; p 739.

Sawyer, R. F. *Eighteenth Syposium (International) on Combustion*; The Combustion Institute: Pittsburgh, 1981; p 1.

Schott, G. L. *J. Chem. Phys*. **1960**, 32, 710.

Sethi, D. M.; Pugmire, R. J.; Facelli, J. C.; Grant, D. M. *Anal Chem* **1988**, 60, 1574.

Sikorski, K.; Schuster, G.; Sun, Y. *Geophysics* **1997**, 62, 918.

Smart, J. P.; Morgan, D. J. *Fuel* **1994**, 73,1437.

Smith, J.D.; Smith, P. J.; Hill, S. C. *AIChE J.* **1993**, 39, 1668.

Smith, P. J.; Fletcher, T. H.; Smoot, L. D. *Eighteenth Symposium (International) on Combustion*; The Combustion Institute: Pittsburgh, 1981; p 1285.

Smith, P. J., Hill, S. C.; Smoot, L. D. *Nineteenth Symposium (International) on Combustion*; The Combustion Institute: Pittsburgh, 1982; p 1263.

Smith, P. J. *User Manual for Three-Dimensional Combustion Code, BANFF*, Department of Chemical and Fuels Engineering Report, University of Utah: Salt Lake City, UT, 1990.

Smith, P.J., Adams, B.R., and Eddings, E.G., *User Guide for GLACIER 2.5*, Reaction Engineering International, 1995.

Smith, P. J. Personal Communication (1997).

Smooke, M.D. (Ed*.), Reduced Kinetic Mechanisms and Asymptotic Approximations for Methane-Air Flames*, Springer, 1991.

Smoot, L. D.; Smith, P. J. *Coal Combustion and Gasification*; Plenum Press: New York, 1985.

Solomon, P. R.; Serio, M. A.; Suuberg, E. M. *Prog. Energy Combust. Sci.* **1992**, 18, 133.

Speziale, C. G. *J. F. M.*, 1987, 178, 459.

Spinti, J. Ph. D. Dissertation, University of Utah, 1997.

Storm, R. F. *Power* **1993**, 53, 1.

Suuberg, E. M. In *Fundamental Issues in Control of Carbon Gasification Reactivity*; Lahaye, J.; Ehrburger, P. Eds.; Klauwer Academic: The Netherlands, 1991; p 269.

Suuberg, E. S.; Wojtowicz, M.; Calo, J.M. *Carbon* **1989**, 27, 431.

Syverud, T.; Thomassen, A.; Gantestad, T. *World Cement* **1994**, 25, 39.

Taylor, R. and Krishna, R., *Multicomponent Mass Transfer*; John Wiley and Sons: New York, 1993.

Teixeira, D.P., Muzio, L.J., and Montgomery, T.A., AFRC/JFRC International Conference on Environmental Control of Combustion Processes, Honolulu, HI, 1991.

Ubhayakar, S. K.; Stickler, D. B.; Von Rosenberg, C. W.; Gannon, R. E. *Sixteenth Symposium (International) on Combustion*; The Combustion Institute: Pittsburgh, 1976; p 427.

Veranth, J. Ph. D. Dissertation, University of Utah, 1998.

Visona, S. P.; Stanmore, B. R. *Combust. Flame* **1996**, 105, 92.

Visona, S. P.; Stanmore, B. R. *Chem. Eng. Sci.* **1998**, 53, 2013.

Visona, S. P.; Stanmore, B. R. *Combust. Flame* **1999**, 118, 61.

Wallis, G. B. *One-Dimensional Two-Phase Flow*; McGraw-Hill: New York, 1969.

Wang, W.; Brown, S. D.; Hindmarsh, C. J.; Thomas, K. M. *Fuel*, 1994, 73, 1381.

Wang, L. P. Ph. D. Dissertation, Washington State University, 1990.

Wendt, J. O. L. *Prog. Energy Combust. Sci.* **1980**, 6, 201.

Wendt, J. O. L.; Pershing, D. W. *Combust. Sci. Technol.* **1977**, 16, 111.

Winter, F.; Wartha, C.; Loffler, G.; Hofbauer, H. *Twenty-sixth Symposium (International) on Combustion*; The Combustion Institute: Pittsburgh, 1996; p 3325.

Yue, G. X.; Pereira, F. J.; Sarofim, A. F.; Beer, J. M. *Combust. Sci. Technol.* **1990**, 100, 231.

Zamansky, V.M., Lissianski, V.V., Maly, P.M., Ho, L., Rusli, D., and Gardiner, W.C., Jr., *Combust. Flame* 117:821-831 (1999).

Zeldovich, Ya. B.; Bladt, G. I.; Librovich, V. B.; Makhviladze, G. M. *The Mathematical Theory of Combustion and Explosions*; Consultants Bureau: New York, 1985; p 30.

Zeldovich, Ya. B.; Sadovnikov, P. Ya.; Frank-Kamenetskii, D. A. *Oxidation of Nitrogen in Combustion, translated by M. Schelef;* Academy of Sciences of the USSR: Moscow, 1947.

Section 7 - Air Heater Design and Test Models

Abstract

The work reported in this section was performed under program tasks 2.2.1, 2.2.3 and 2.2.6. The rationale for the selection of heat exchanger concepts and the design of test modules is presented. The approach to transferring heat from coal combustion products to high-pressure air for driving the gas turbine is determined primarily by the types of mineral deposits and the associated temperature regimes of the hot combustion gas. Depending on the temperature of coal combustion products, there are two general types of deposits, molten or liquid slag at high temperatures and dry ash at low temperatures, with varying amounts of the two types of deposits present at intermediate temperatures. For most coals, regulating the temperature of the combustion gas stream within two fairly broad temperature regimes can control the distinction between the two types of mineral deposits. Specifically, liquid slag is predominant at high temperatures above about 2200 to 2600 °F (1204 to 1427 °C) and dry ash prevails at lower temperatures below about 1800 °F (982 °C). Therefore, heat exchanger concepts and materials of construction will be chosen so as to be compatible with the types of mineral deposits present in the combustion gas stream, the corrosive nature and mechanisms of the prevailing type of deposit, the temperature regime, and the optimum modes of heat transfer available. In general, the RAH is best suited for the high temperature molten slag regime while the CAH is appropriate for the lower temperature regime with dry ash.

After a series of unsuccessful designs, the alloy-based "tubes-in-a-box" with ceramic tile protection emerged as the prime candidate.

In order to validate the air heater designs, the program called for extensive small scale testing of prototype components. To this end RAH and CAH test modules were designed and fabricated for tests at conditions that simulate actual conditions in a utility combustor. The RAH panel is a scaled version of the commercial design but using only three tubes in the heat exchanger. The CAH test module is a straightforward-scaled version of the tube and shell heat exchanger in the commercial design. The design, heat transfer analysis and structural analysis are presented in this section.

Introduction

Since the high temperature products of coal combustion will provide the heat source for the proposed HITAF concept, the air heaters must be capable of operation under unusually severe conditions. While conventional coal-fired steam power plants experience similar operating conditions, the air temperature required from the HITAF is of the order of 1700 °F (927 °C) or more compared to only about 1000 °F (538 °C) for steam, and air is a poor heat transport fluid compared to steam. The process of transferring heat from coal combustion products at about 3000 °F (1649 °C) to high pressure air will require special structural design of the air heaters in order to avoid excessive mechanical and thermal stresses. Moreover, the mineral content of most coals at typical combustion temperatures produces ash particles in the effluent stream, resulting in potential for heat transfer degradation, as well as corrosion and erosion of air heater surfaces. Although erosion of air heater surfaces by impinging ash particles is not expected to be a

problem because gas and particle velocities are relatively low, special provisions will be made to minimize heat transfer degradation and to prevent corrosion.

In order to produce the high air temperature required for acceptable gas turbine efficiency, the coal combustion temperature will have to be in a regime which produces molten slag. This slag can potentially foul and corrode heat transfer surfaces. Since the entire air heater cannot be maintained hot enough to produce continuous slag flow from all heat transfer surfaces, the transition from wet slag to dry ash will be controlled by separation into two different types of air heaters which will be designed to deal exclusively with slag or ash. The radiant air heater (RAH) will operate at the higher temperature levels required, while the convective air heater (CAH) will function at the lower temperature regime. A slag screen will be located between the two air heaters to establish the wet-dry interface (wet slag to dry ash) and to remove most of the ash from the hot gas stream before it can enter the convective air heater. To prevent excessive sintering of ash deposits on CAH surfaces and to provide a suitable temperature zone for selective non-catalytic reduction of NO_X, the combustion gas temperature will be reduced to about 1800 °F (982 °C) by introducing flue gas recirculation immediately upstream of the convective air heater. This arrangement of the air heaters and the slag screen is shown schematically in Exhibit 7-1 along with expected operating temperature levels. The rationale for this arrangement of the air heaters, their respective operating conditions, and unique design features are discussed below in relationship to operating temperature levels and slag and ash environments.

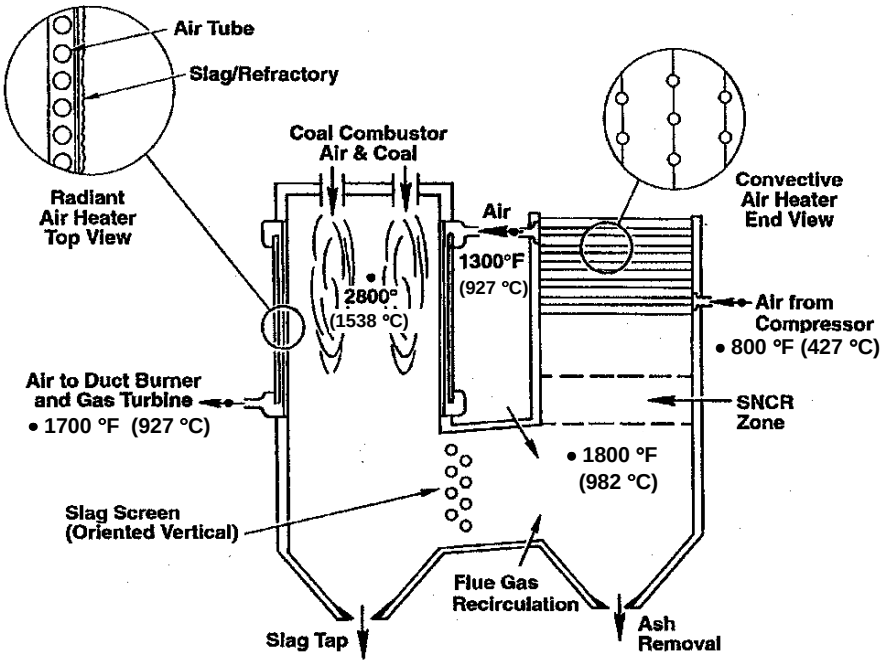

Exhibit 7-1
Arrangement of HITAF Components

The selection of heat exchanger concepts for transferring the heat from coal combustion products to high pressure air is based primarily on the types of mineral deposits and the associated temperature regimes of the hot combustion gas. Depending on the temperature of

coal combustion products, there are two general types of deposits, molten or liquid slag at high temperatures and dry ash at low temperatures, with varying amounts of the two types of deposits present at intermediate temperatures. For most coals, the distinction between the two types of mineral deposits can be controlled by regulating the temperature of the combustion gas stream within two fairly broad temperature regimes. Specifically, liquid slag is predominant at high temperatures above about 2200 to 2600 °F (1204 to 1427 °C) and dry ash prevails at lower temperatures below about 1800 °F (982 °C). Therefore, heat exchanger concepts and materials of construction will be chosen so as to be compatible with the types of mineral deposits present in the combustion gas stream, the corrosive nature and mechanisms of the prevailing type of deposit, the temperature regime, and the optimum modes of heat transfer available. In general, radiation heat transfer is best suited for the high temperature regime while convective heat transfer is appropriate for the lower temperature regime.

The radiant heat transfer mechanism offers several ideal features for transferring heat from coal combustion gases at the highest temperature regime to the gas turbine air. First, since radiant heat transfer is most efficient at high temperatures, the percentage of high quality heat from coal combustion, which can be transferred to the Brayton cycle, is unrestricted by thermal conductance. Second, since radiant heat transfer is a non-contact process which acts at a distance, slag deposition on heater surfaces can be minimized by proper design and location of the heater and the coal combustor. Third, since some amount of slag deposition on heater surfaces is unavoidable, ceramic refractory coatings can provide long-term protection of heater surfaces from slag-induced corrosion. Ceramic refractory coatings are currently used to protect radiant-heated steam boilers from slag-induced corrosion. Although the thermal resistance of the refractory reduces the heat flux somewhat, the refractory serves the more important dual functions of preventing corrosion of the underlying structural air passages and maintaining a sufficiently high heater surface temperature to ensure slag removal by gravity-induced flow. The latter function is important because slag cannot be allowed to solidify in thick layers on heater surfaces since this will impede heat transfer adversely and solidified slag is difficult to remove. In practice the refractory will gradually dissolve into the flowing slag and the refractory will have to be replaced periodically. By proper selection of the refractory, however, experience with steam boilers and glass melting furnaces has shown that the cost and frequency of replacement of the refractory can be acceptable.

The coal combustion product gas in the lower temperature regime is characterized by a gas temperature below about 1800 °F (982 °C), dry ash deposits, and potential for alkali-induced corrosion. Since the temperature of the gas in this second regime is too low for efficient radiant heat transfer, this air heater will have to be based on convective heat transfer. Since heat flux levels for convective heat transfer are typically low, compared to radiant heat transfer, deposition of ash on convective air heater surfaces will have to be controlled. Fortunately, techniques and equipment are readily available for cleaning of coal ash deposits from heater surfaces. By limiting the combustion gas temperature to a maximum of about 1800 °F (982 °C), ash deposits will not densify excessively beyond 75% of full density in about eight hours and the ash deposits will be removable from heater surfaces by conventional soot-blowing methods at reasonable time intervals.

Conceptual designs for the radiant and convective air heaters are shown in Exhibits 7-2 and 7-3, respectively. The radiant air heater will consist of many long hollow structural panels, which will line the inside walls of the coal combustion furnace. The gas turbine air will be

distributed to the many small passages within these panels by an arrangement of headers, manifolds, and ducts, which will be staged to avoid excessive thermal stresses. Ceramic refractory tiles will form the firesides of the hollow panels to prevent slag-induced corrosion. Although the radiant air heater is adaptable for either parallel or counter flow of the hot and cold gas streams, parallel flow will enhance draining of liquid slag from the radiant heater surface by producing the highest surface temperature at the lowest point of the heater. A massive structural shelf at the bottom of the furnace, probably consisting of furnace brick masonry will provide structural support for the entire radiant air heater. The high temperature coal combustion products at 2800 °F (1538 °C) or higher will heat the panels by radiant transfer and, as the gas turbine air flows through the panels, the air will be heated by forced convection from about 1300 °F (704 °C) to 1700 °F (927 °C) or higher, depending on heater material and availability of supplemental heating by direct combustion of natural gas or oil. If the air temperature out of the radiant heater is limited to 1900 °F (1038 °C), state-of the-art metal alloys can be used to withstand an expected maximum heater temperature up to 2200 °F (1204 °C). As shown in Exhibit 7-3, the heat transfer surface configuration for the convective air heater is a modification of the shell and tube heat exchanger where the air flows through the tubes and the hot combustion gas flows over and perpendicular to banks of tubes. This simple modification of the shell and tube heat exchanger, which is called the finned-tube-sheet configuration, consists of a sheet or fin extension between adjacent tubes in rows along the direction of the hot gas flow. There are a number of advantages to using the finned-tube-sheet configuration for the convective air heater. First, because the heat convection coefficient for the hot gas side is only about one-fourth of the coefficient for the air side, the enhanced surface provides an overall heat conductance which is closer to the ideal balance for minimizing the convective air heater size. This enhanced surface area has been estimated to reduce the convective air heater size by about one-third as compared to a plain tube configuration. Second, the integrated structure is stronger and more rigid than plain tubes and less susceptible to circumferential thermal stresses. Joining adjacent tubes together by fin sheets (i.e. connecting the hottest and coldest circumferential positions together) will reduce circumferential temperature gradients in tube walls. Third, because the smooth external surface contour of the finned-tube-sheet is aligned with the hot gas streamlines and there are no spaces between tubes for gas recirculation, ash deposition on air heater surfaces will be dramatically reduced. Finally, by limiting the hot gas temperature to 1800 °F (982 °C), the finned-tube-sheet configuration can be manufactured in modular units from metal alloys using conventional fabrication processes. In summary, use of the finned-tube-sheet configuration for the convective air heater will increase the hot gas side surface area, provide additional structural integrity, reduce circumferential thermal stresses in the tubes and reduce ash deposition, resulting in a smaller, stronger, more reliable, and lower cost heater.

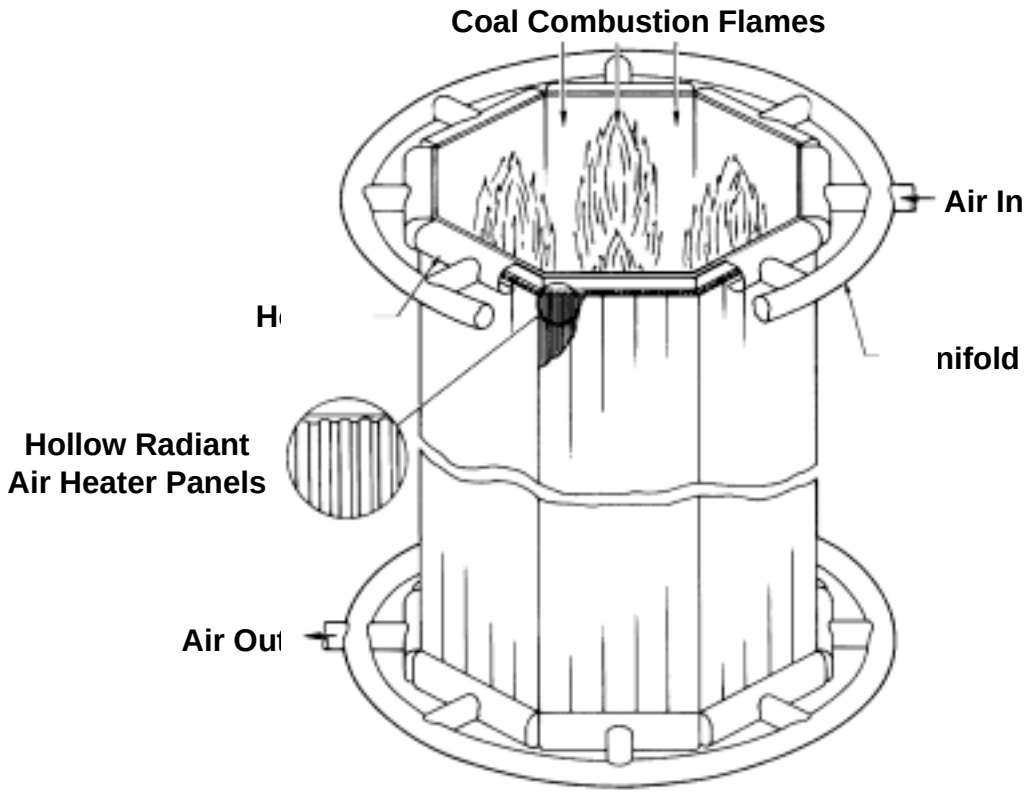

Exhibit 7-2
Radiant Air Heater Conceptual Design

For the rather modest effectiveness requirement of 53 % for the convective air heater, a two-pass, cross-counter flow arrangement, with two air passes and one hot gas pass as shown in Exhibit 7-3, will produce the desired heating and temperature rise of the gas turbine air with a reasonable size heater. While additional passes of the gas turbine air could slightly reduce the size of the convective air heater, this would increase the air side pressure drop and require additional return headers. As shown in Exhibit 7-3, large domed headers will collect and distribute the gas turbine air to the convective air heater passes. Since the maximum air side temperature is not expected to exceed 1500 °F (816 °C), the structural shell of these headers will be constructed of metal alloy, similar to the alloy to be used for the convective air heater tubes.

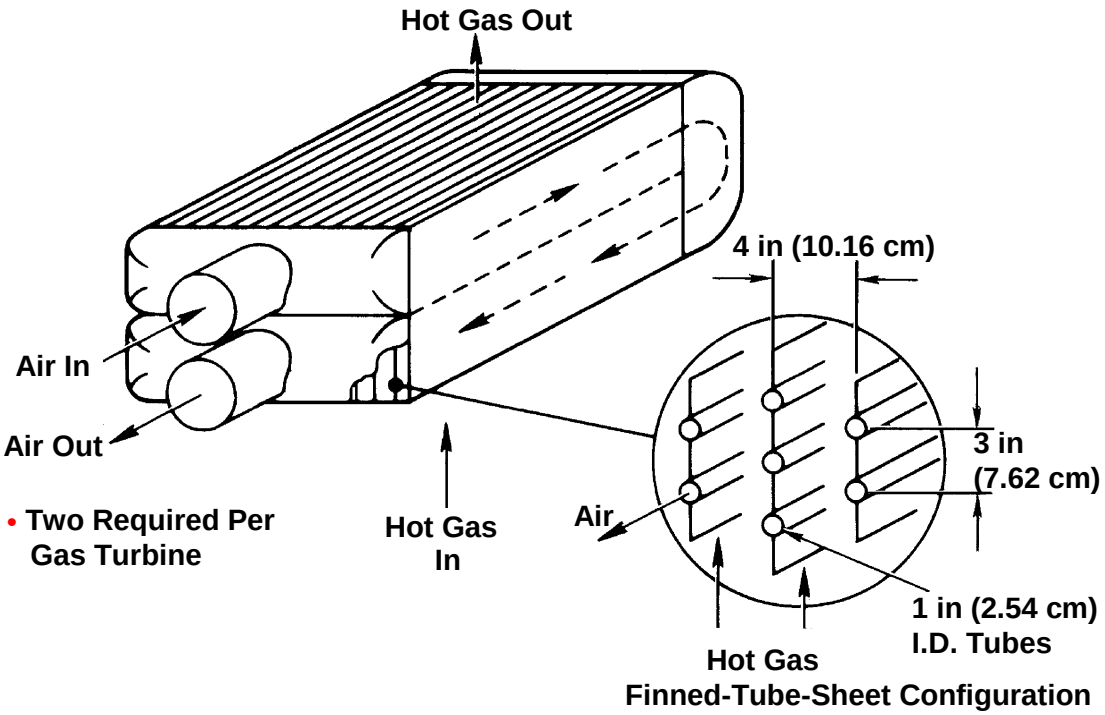

Exhibit 7-3
Convective Air Heater Conceptual Design

RAH Scale Model Test Panel

A scaled-down version of the RAH was designed and fabricated for testing as part of the overall component testing phase of the program. A CAD drawing of the RAH test panel is shown in Exhibit 7-4 and an open view of the heat transfer tubes is pictured in Exhibit 7-5. A schematic showing the cross section is presented in Exhibit 7-6. The schematic shows the tubes, enclosure and supporting side rails and clarifies why this arrangement is referred to as the "tubes in a box". This design was selected as most promising and has the following advantages:

- Since the tubes and refractory are not mechanically coupled, they need not be constrained with respect to each other. This results in lower thermal stresses, and easier assembly with less clamping required.
- The alloy tubes receive heat from all sides by radiation, reducing the thermal gradient and partially compensating for the heat transfer loss due to the tube spacing.

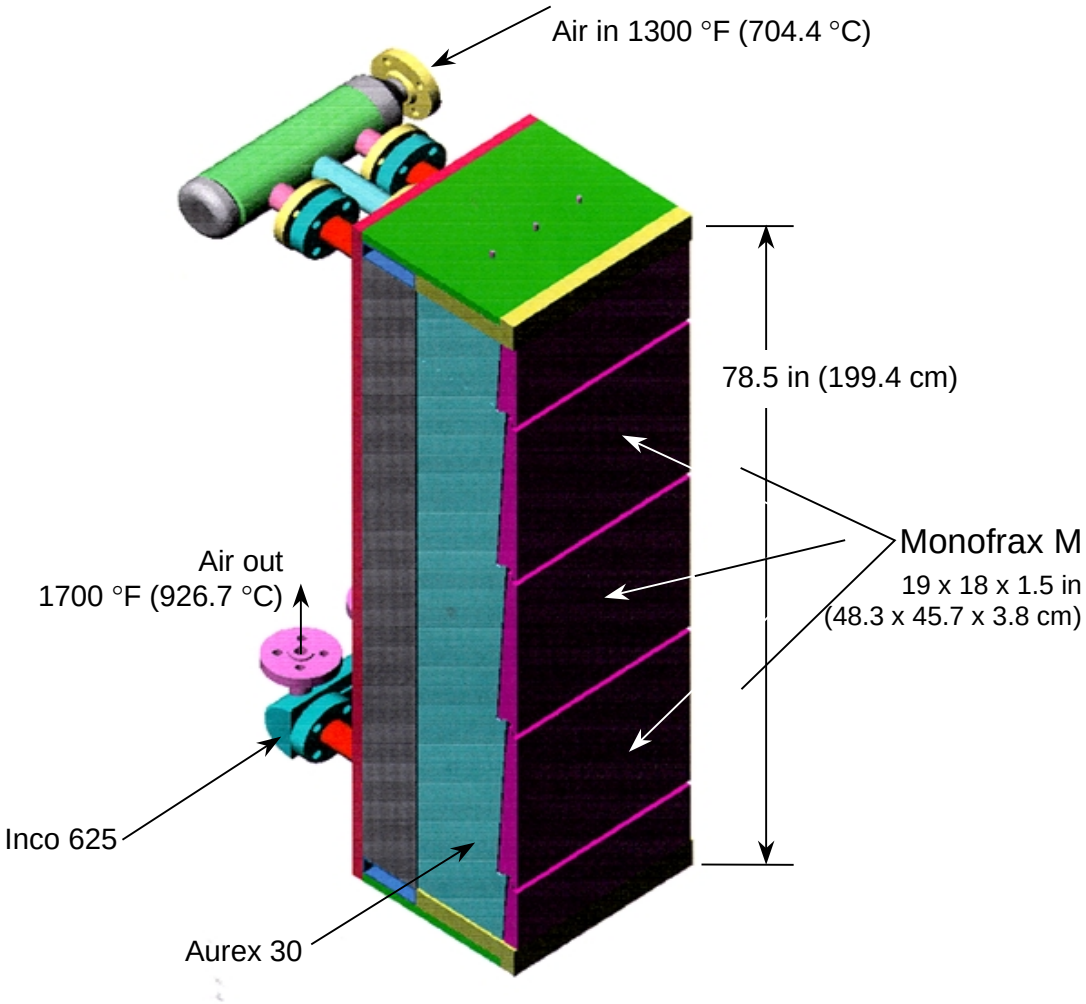

Exhibit 7-4
Design Drawing of Radiant Air Heater Test Module

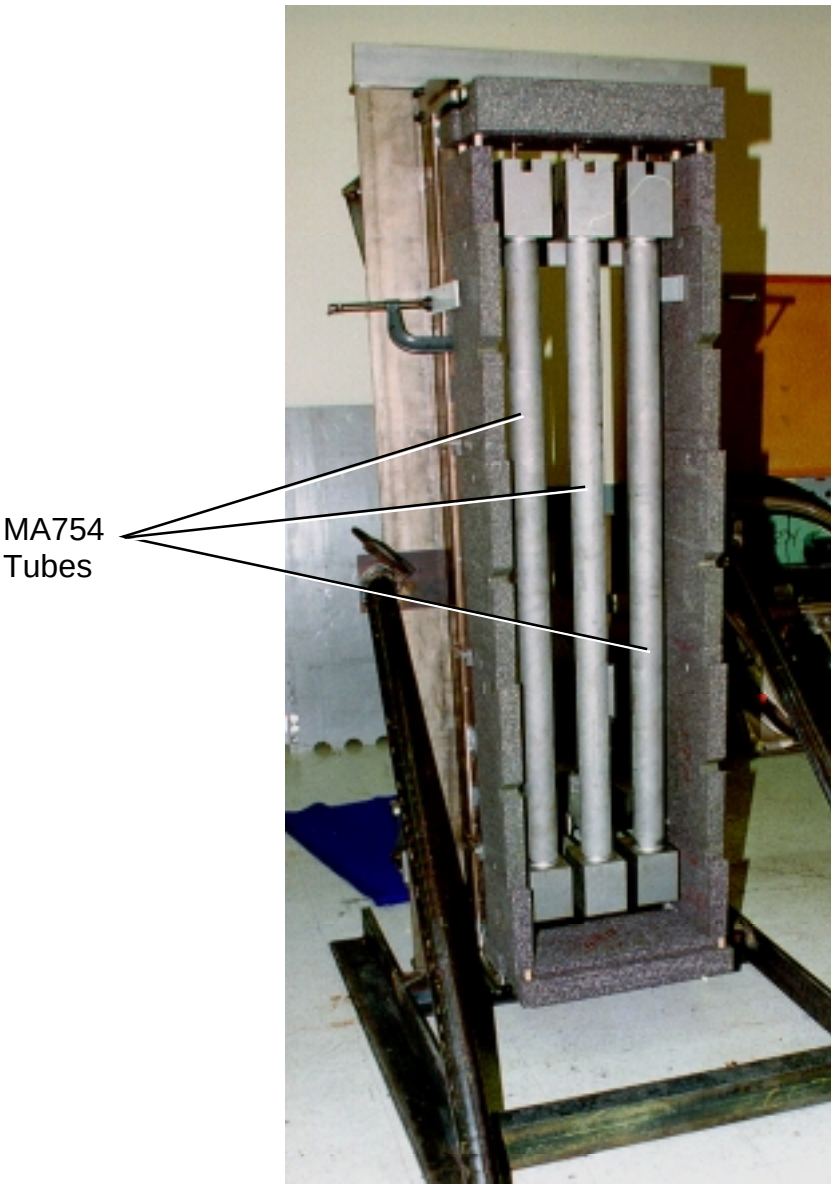

Exhibit 7-5
Open View of RAH Test Panel

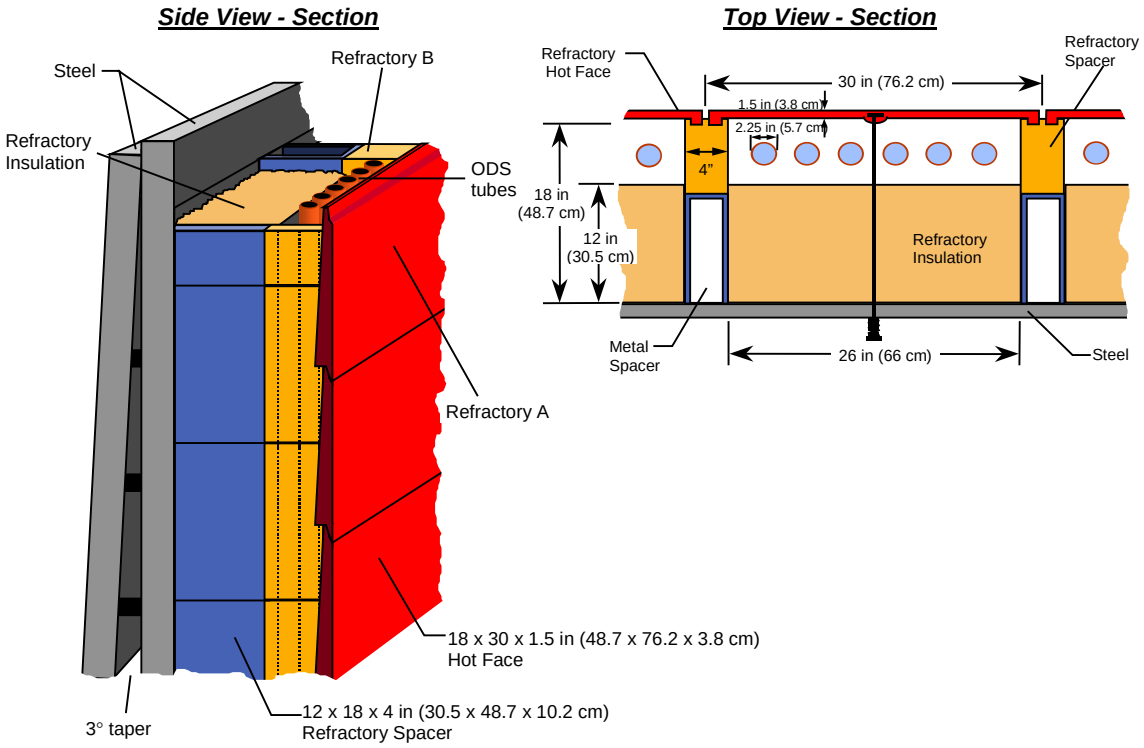

Exhibit 7-6
Schematic of Hot Sections of Radiant Air Heater

Radiation Modeling

A radiation program has been created to determine and optimize the heat transfer from the outer refractory wall to the air in the tubes. The total heat transfer per unit RAH surface area is represented as a function of: (a) temperature of the hot surface facing the top of the tubes, (b) geometric parameters, (c) the air-side convection coefficients, and (d) the air temperature.

From this an effective convective coefficient is expressed as a function of the hot refractory surface temperature and the air temperature for a given geometry and material properties, and air-side convection coefficient.

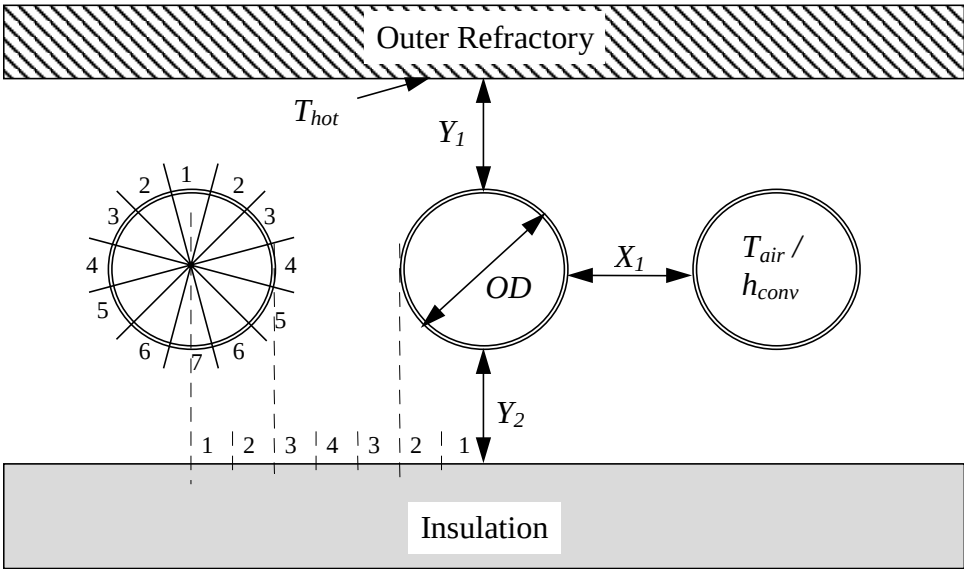

Exhibit 7-7
Schematic of Radiation Transfer Sub-Problems

The following parameters define the geometry of the radiation problem:

Y_1: space between tubes and hot refractory

Y_2: space between tubes and refractory insulation (re-radiating surface)

X_1: space between tubes

OD: the diameter of the tubes

The boundary conditions are specified as:

T_{hot}: *temperature of the hot surface facing the top of the tubes,*

T_{air}: temperature of the air inside the tubes,

h_{conv}: convection coefficient from the inside of the tube to the air, the net radiative heat flux to the insulation (re-radiating wall) is zero, and the net radiative heat flux to the tube wall elements is equal to that which convects to the air.

the tube wall thickness and conductivity is entered as an added resistance to heat transfer.

The tube is broken into a total of 12 elements of equal circumference. The top element is #1, and the bottom element is #7. A symmetry plane exists vertically through each tube, and therefore only 7 independent elements need to be defined. Each tube element may have its own temperature and emittance.

The re-radiating plane is also broken into elements. There are 4 equally sized elements under each tube, and 3 equally sized elements in the space between the tubes. Again due to symmetry, only 4 independent elements need to be defined. Each refractory element may have its own temperature and emittance. The hot surface is treated as a single element.

For each element, radiation shape factors are determined as functions of the geometry parameters, defined from the element's center. Since there are many interactions, an iterative method of solution was developed where the following sub problems are solved separately:

- The re-radiating plane temperature distribution is found assuming that the tube temperature distribution is known and fixed.
- A single tube temperature distribution is found assuming that the other tubes and the re-radiating plane is known and fixed.

Within each sub-problem, the temperature of each element is relaxed until the prescribed boundary heat flux is obtained. Iteration is required at each sub-problem level, and between the two sub-problems. The temperature distribution of the neighboring tubes is taken as the previous iteration solution.

The results of the analysis are:

- Increasing the tube spacing (X_1) increases the temperature of the re-radiating surface, which increases the transfer to the "cold" side of the tubes. As the tube spacing increases, the amount of heat transfer per tube increases, but the number of tubes per RAH area decreases. Overall, it was found that the heat transfer per unit RAH decreases with increasing space between the tubes, but the tube temperature profile became more uniform.
- With increasing RAH size, and decreasing normal heat flux, the refractory can provide more insulation, and therefore can be thicker.
- Increasing the tube to wall spacings (Y_1, Y_2) increases the uniformity of the refractory temperature profile. It was found that a spacing of approximately 1 tube diameter is sufficient.
- The emittance of both the hot surface and the tubes determines (together with the geometry) the effective gap resistance. The emittance of the re-radiating surface (assuming negligible heat loss) does not. The lowest gap resistance is for black surfaces (emissivity = 1).
- The emittance of the tube can be varied to even out its temperature distribution by providing a low emissivity coating on the top surface, and a high emissivity coating on the lower surface. The total heat transfer per unit tube can be maximized by then raising the hot refractory surface temperature. Although this leads to smallest RAH size and minimizes the tubes stresses and deflections, the increased gap resistance requires a thinner refractory.

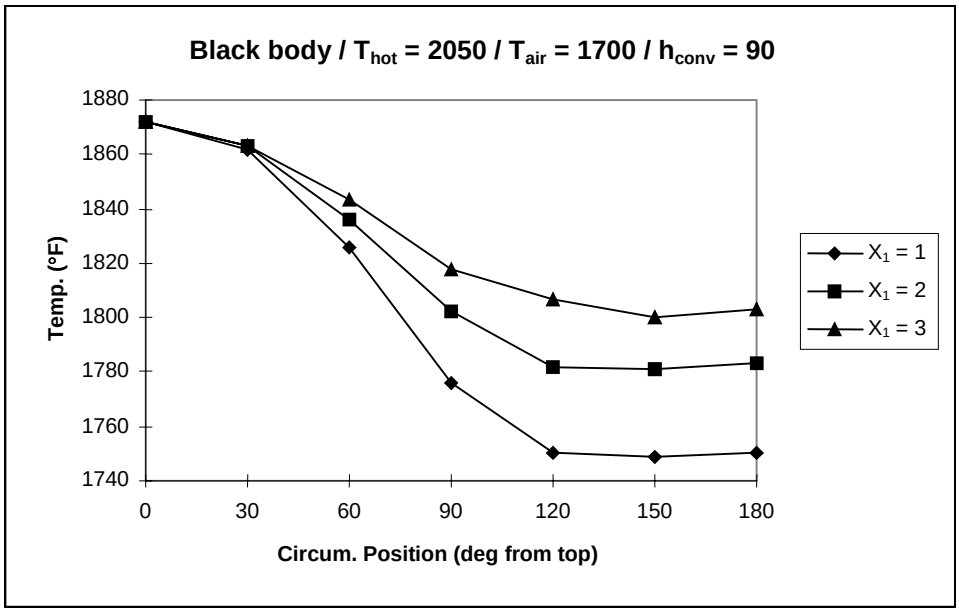

Exhibit 7-8
Temperature Distribution Around Single Alloy Tube

Exhibit 7-8 shows the temperature profiles of the tube (black body) for various tube spacings.

In the RAH design, various material constraints must be considered. Since the "tubes-in-a-box" design relieves the stress problem in the alloy tubes, the tube properties no-longer constrain the problem. The current design is being constrained by the minimum allowable refractory thickness. Because of this it is not expedient to vary the emissivity of the tubes since it leads to higher overall gap resistance.

The radiation program has been run with

- the emittance of the tubes uniform = 0.85
- the emittance of the hot refractory surface = 0.85, and
- the emittance of the re-radiating surface = 0.40.

for

- T_{air} = 1300, 1500, 1700 °F (704, 816, 927 °C)
- $T_{wall} = T_{air} + (300 \rightarrow 600)$, and
- h_{conv} = 70, 100, 130 Btu/h-ft^2-F (400, 571, 743 W/m^2-K)

It was found that the effective heat transfer conductance between the hot refractory and the air (through the tubes) could be well represented as a function of

- geometry,
- air side convection coefficient, and
- a single temperature function => $T_{avg} = 0.65\ T_{hot} + 0.35\ T_{air}$.

Exhibit 7-9 shows this relation.

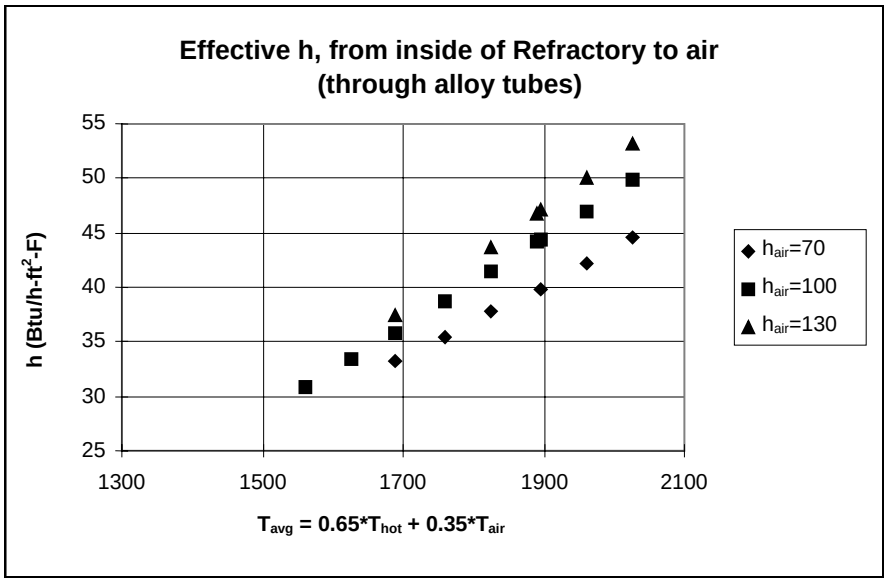

Exhibit 7-9
Heat Transfer Conductance

Since the radiation program results could be easily parameterized, two codes were combined by: (a) converting the radiation code to a subroutine, and (b) inserting a call to this subroutine before each iteration, after the geometries have been set by the Optimizer, and the convection coefficient calculated.

A preliminary sizing of the RAH was performed. The following geometry assumptions were used:

- Thickness of Monofrax M (k = 7 W/m-K) was used for the refractory wall.
- Each refractory brick was 30 in (76.2 cm) wide by 18 in (45.7 cm) tall.
- Support rails (each 4 in (10.2 cm) wide) occurred every 30 in (76.2 cm) to support the bricks.
- The width of each box was therefore 26 in (66 cm).
- No credit was taken for extra heat transfer that might occur to the tubes at the end of each box (since the support rails will be hotter than the neighboring brick).
- Tube wall thickness = 1/8 in (0.318 cm).

The results of this sizing for the commercial plant design were:

- Overall size of (1/2) RAH = 60 ft (18.3 m) tall, by 36 ft (11 m) diameter. This is ~30% larger than the flat plate design studied earlier (but this design has not been fully optimized).
- The tube size is ~2 in (~5.08 cm) ID, OD = 2.25.
- With 6 tubes in a box, tube spacing = 26 / 6 = 4.33 in (11 cm), this allows for ~2 in (~5.08 cm) between tubes (which is sufficient).

For the RAH scale model this would require a heat transfer rate of 98,000 Btu/hr (103,396 kJ/hr) to be consistent with the overall plant efficiency of >47%HHV.

Insulation Thickness, and Supports

In Exhibit 7-6, the schematic of the RAH cross-section, the radiation box as shown, must be insulated from the steel support structure, and the steel support structure must be insulated from the outside world. The refractory support rails are dense, and have a relatively high thermal conductivity. Therefore, they must be thermally isolated from the steel support (by hollow metal-alloy spacers). The total heat transfer, and required insulation values were calculated by assuming:

- radiation box = 2000 °F (1093 °C)
- steel support structure = 700 °F (371 °C)
- outside surface = 175 °F (79.4 °C) (OK to touch), and
- outside air = 75 °F (23.9 °C).

The outside convection coefficient was calculated to be 1.2 Btu/h-ft^2-F (6.9 W/m^2-K).

The heat flux per unit area is then 120 Btu/h-ft^2 (less than 1% of the total heat transfer through the hot refractory).

The required resistance value for the refractory insulation

= (2000 - 700) / 120 = 10.8 (hr-ft^2-F/Btu).

Low density refractory can have conductivity values of between 0.1 and 0.2 W/m-K. Assuming 0.15 W/m-K (or 0.086 Btu/h-F-ft), the required thickness is 10.8 * 0.086 = 0.93 ft (0.28 m) or 11 in (27.94 cm).

RAH Panel Air Temperatures

The air temperatures in the tubes were calculated using the same code that was developed for the commercial plant design with a few modifications. The reduced scale design uses concentric tubes with the middle tube plugged. The flow area, perimeter, and equivalent diameter for pressure drop and convection calculations become:

$$A_c = \frac{\pi}{4}\left(D_1^2 - D_2^2\right) \qquad P = \pi\left(D_1 + D_2\right)$$

$$D_e \equiv \frac{4\,A_c}{P} = \frac{D_1^2 - D_2^2}{D_1 + D_2} = D_1 - D_2$$ which is 2 times the gap.

Spiral spacers will be necessary to mix the flow from the tubes hot side (facing the hot brick) to its cold side (facing the re-radiating insulation). This mixing occurs naturally in an open tube, but in the concentric tube design it is possible for the air to be at different temperatures circumferentially around the tubes. With spiral spacers at angle θ (θ = 0 is no spiral, θ = 90 is blocked) the flow area and length are modified as:

$$A_c = \frac{\pi}{4}\left(D_1^2 - D_2^2\right) * \cos(\theta)$$

Length = L0 / cos(θ)

The mixing length is the axial distance per ½ turn: $L_{mix} = \frac{\pi D}{2 \tan(\theta)}$.

For 2 in (5.1 cm) tubes:

θ	L_{mix}
30°	5.44 in (13.8 cm)
45°	3.14 in (7.8 cm)

RAH Code Inputs

Table 7-1
RAH Code Input

Outer Tube OD	2.5 in	6.4 cm
Outer Tube ID	2.0 in	5.1 cm
Inner Tube OD	1.625 in	4.1 cm
Spiral Angle	45 degrees	
Length of Active Heat Exchanger	54 in	137 cm
Flow rate air (was varied in order to obtain the desired output temperature)	890 #/hr (195 scfm)	0.112 kg/s
Refractory Thickness	1.5 in	3.8 cm
Refractory Conductivity	3.2 (Btu/h-ft-F)	5.5 W/m-K
Air-side convection, based on spiraled thin annular gap (derivation not shown here).	70 (Btu/h-ft^2-F)	400 W/m^2-K
Radiation box transfer coefficient is determined from another code (not shown here) and is a function of temperature.		

RAH Code Output:

Exhibit 7-10 is a graph of the output temperature profiles from the Modified RAH code. The metal temperature is not shown but lies in the range between the refractory temperature and the air temperature. It is hotter on the side which faces the refractory. The Profiles shown here mimic those expected in commercial design, except that they occur over 5 ft (1.52 m) rather than 60 ft (18.3 m).

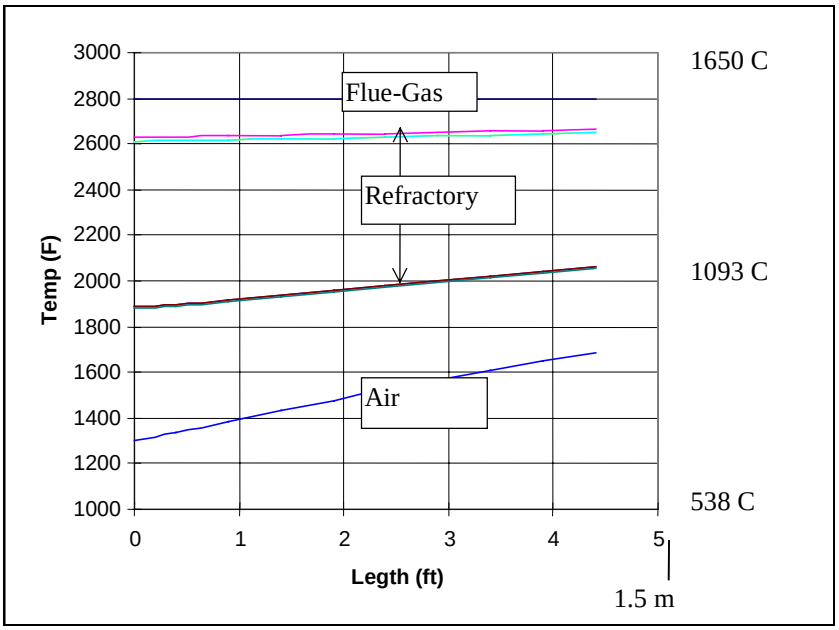

Exhibit 7-10
RAH Panel Temperature Profiles (flow = 890 #/hr (0.112 kg/s))

The Wedge-Shaped Brick:

To align the bricks with the support rails, and to minimize the number of support rails, it is necessary to stack the bricks so that they are aligned directly on top of the brick below, with no horizontal overlap. This situation was cause for concern, since a failed brick would result in a collapse of an entire vertical section. Various schemes for staggering were investigated, but were ultimately rejected. The primary concern was that due to the large amount of thermal bending expected for each brick, it would not be possible to maintain a seal at each vertical brick interface (at each side) where there was no support rail.

The solution to the problem of preventing catastrophic failure of the tile assembly was supporting each brick individually by shelves on the support rail. This idea was pursued with the following criteria:

- The effective thermal conductance of the design must be maintained.
- The horizontal brick interfaces (top and bottom) must create a slag seal.

The design that ultimately emerged was the Wedge. In this design the entire brick is wedge shaped (nominal 1 to 2 in (2.54 to 5.08 cm) thickness variation). The thick part of the wedge is down, and rests on the support shelf. This design creates thermal variations over the height of each brick, the implications of which are considered in the testing program.

Finite-Element analysis has been used to study the heat transfer and thermal stresses of the bricks in both two and three dimensions. The heat transfer from each end of the box, through the support rails is an important design parameter for the commercial plant.

Ceramic Material Analysis

A three dimensional model of a wedge shaped brick made from a modified Monofrax M material was constructed. A thermal analysis was performed to determine the temperature

profile through the brick. These results were read into a second model that calculated the resulting stress and deflections. A summary of the geometry and thermal boundary conditions follows.

Geometry

Ceramic shape	Wedge Rectangular	18 in by 30 in by 1.0 to 2.0 in thick (45.7 cm by 76.2 cm by 3.8 cm)

No vertical slip joints, horizontal slip joints

Thermal Boundary Conditions

<u>Hot side</u>	
Sink temp	2800 °F (1520 °C)
Convective heat transfer coefficient	21.2E-5 Btu/sec/in^2/°F (625 W/m^2/°C)
<u>Cold side (directly exposed to tubes)</u>	
Sink temp	1700 °F (900 °C)
Convective heat transfer coefficient	9.6E-5 Btu/sec/in^2/°F (284 W/m^2/°C)
<u>Cold side (covered by support brick)</u>	
Sink temp	1700 °F (900 °C)
Convective heat transfer coefficient	4.8E-5 Btu/sec/in^2/°F (142 W/m^2/°C)

Analysis

Due to symmetry, only ½ of the brick was modeled. The face of the brick lies in the y-z plane. The thickness of the brick lies in the x direction. The brick was constrained by the symmetry plane in the y direction. One node was fixed in the z direction and 2 nodes were fixed in the y direction. A minimum number of constrains was used to avoid inducing additional stress. The model assumes the material has infinite strength and that the deformation is elastic. The results of this analysis are presented in Table 7-2

Table 7-2
Model Results

Modified Monofrax M	
Deflection	**inch (cm)**
y deflection each edge (width)	0.17 (0.43)
z deflection (height)	0.16 (0.41)
x max. deflection at center	0.13 (0.33) 0.000 at four corners
Stress	**psi (kPa)**
Max Tensile Sigma X	2,800 (16,500)
Max Compressive Sigma X	-1,000 (-6,900)
Max Tensile Sigma Y	8,600 (59,300)
Max Compressive Sigma Y	-1,900 (-13,100)
Max Tensile Sigma Z	2,800 (19,300)
Max Compressive Sigma Z	-800 (-5,500)
Max Von Mises	8,519 (58,800)
Temperature	**°F (°C)**
Hot Face	2,650 (1,454) 2,773 (1,523) over lap
Cold Face	2,000 (1,204) 1,830 (999) under lap
Delta Temp Center	650 (360)

The model indicates that Modified Monofrax M results in low levels of stress. The under lap area of the brick does have high tensile loads. These loads result from thermal stress. The under lap area is cooler than the rest of the brick and the thermal expansion is less than the hotter sections of the brick. Cracking at flaws maybe a problem in this area. The modified Monofrax M is expected to have tensile strengths of greater than 3500 psi (24,132 kPa) at 2750 °F (1510 °C) and 5,000 psi (34,474 kPa) at 2400 °F (1316 °C). The high stress underlap area is less than 1900 °F (1038 °C). Testing is needed to determine if cracking is a problem in the underlap area.

Design Layout of the RAH

A design layout for the RAH is shown in Exhibit 7-11 and 7-12, showing all the major components and orientations as required for the initial tests. The material for the flanges, elbows

and the three vertical radiation tubes is an Inconel alloy type MA 754. This material was selected because of its high strength and good oxidation resistance at elevated temperatures.

The air manifold that feeds the inlet and exit lines of the radiant tubes outside the RAH door assembly is made of an Inconel 625 alloy material

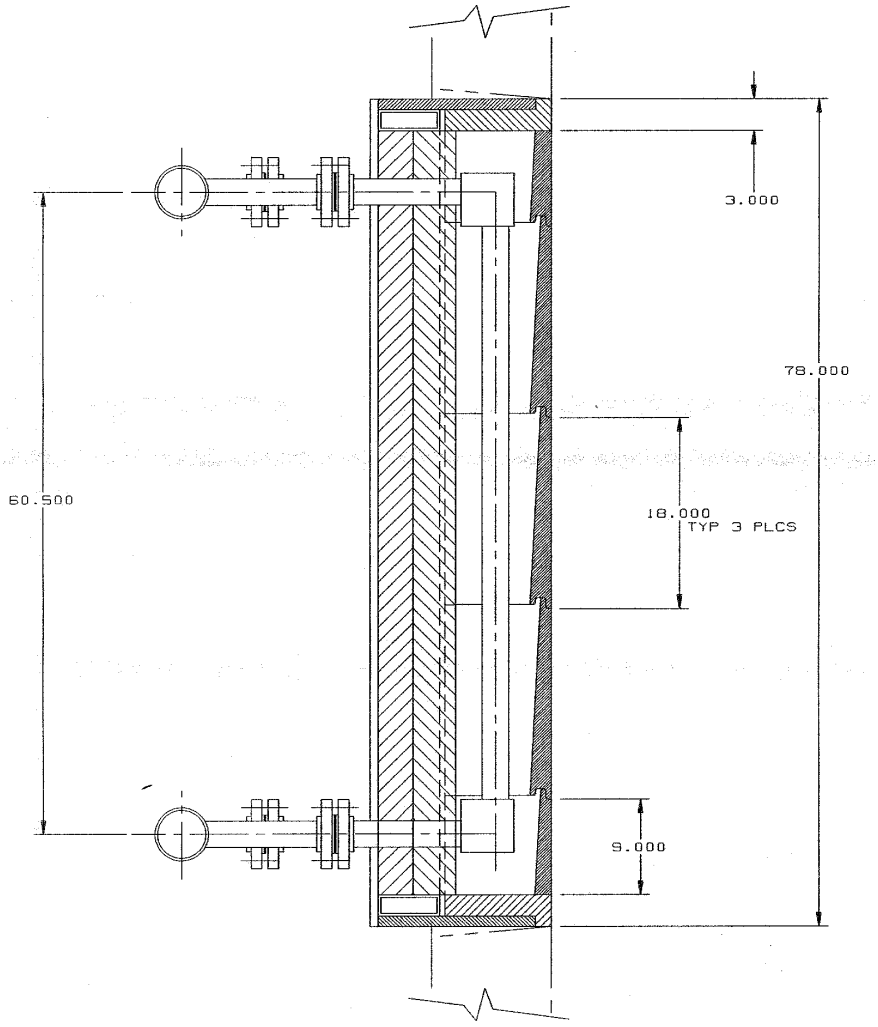

Exhibit 7-11
Design of RAH Test Unit - Side View

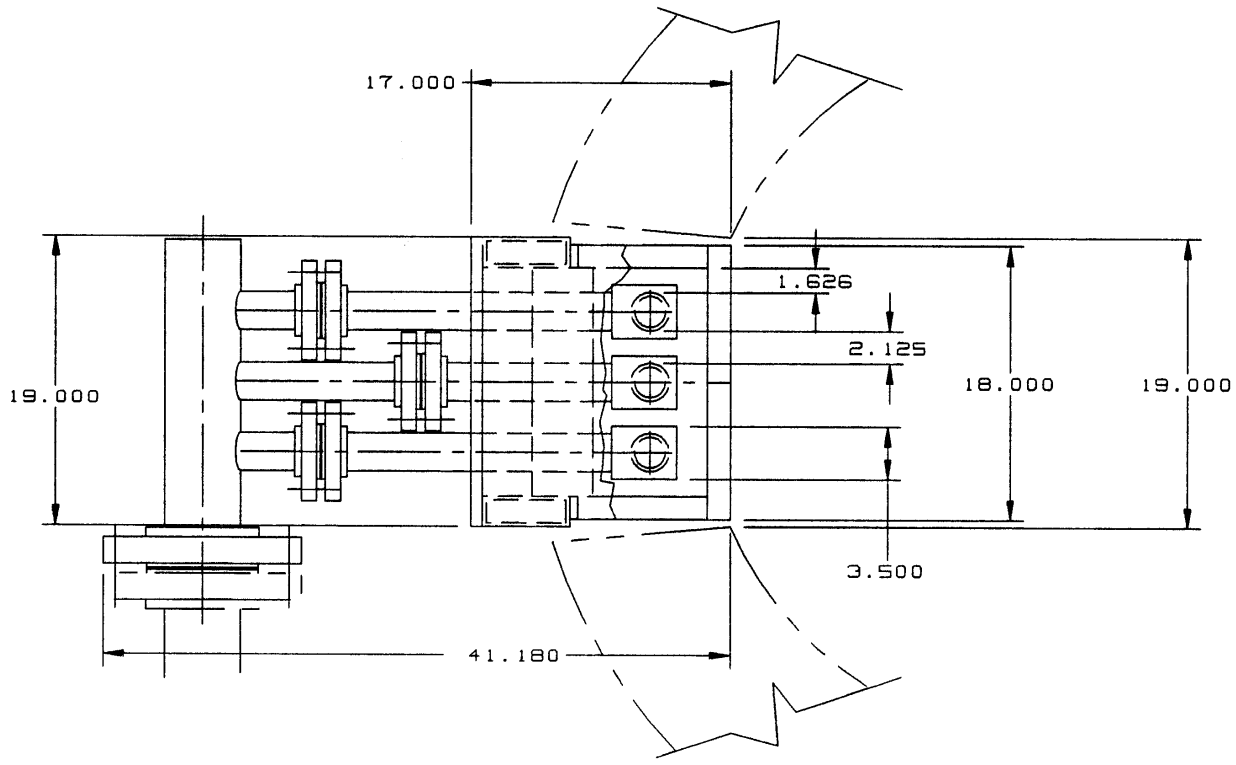

Exhibit 7-12
Design of RAH Test Unit - Top View

CAH Test Model

The design for the CAH test model is a relatively straightforward shell and tube heat exchanger. The design drawing showing a cross section of the scaled test model is presented in Exhibit 7-13 Because the pressure vessel was required to conform to the Boiler Code, the fabrication was subcontracted to Taylor Forge, Kansas City, Mo. This vendor has welders available who are certified tom weld Inco 625 alloy.

The concentric tube arrangement added an additional complication to the heat transfer analysis. At the operating temperature {T(tube surface) = 1600 °F (871 °C) and T(air exit) = 1300 °F (704 °C)} the inner tube became both a radiation sink and a convective source.

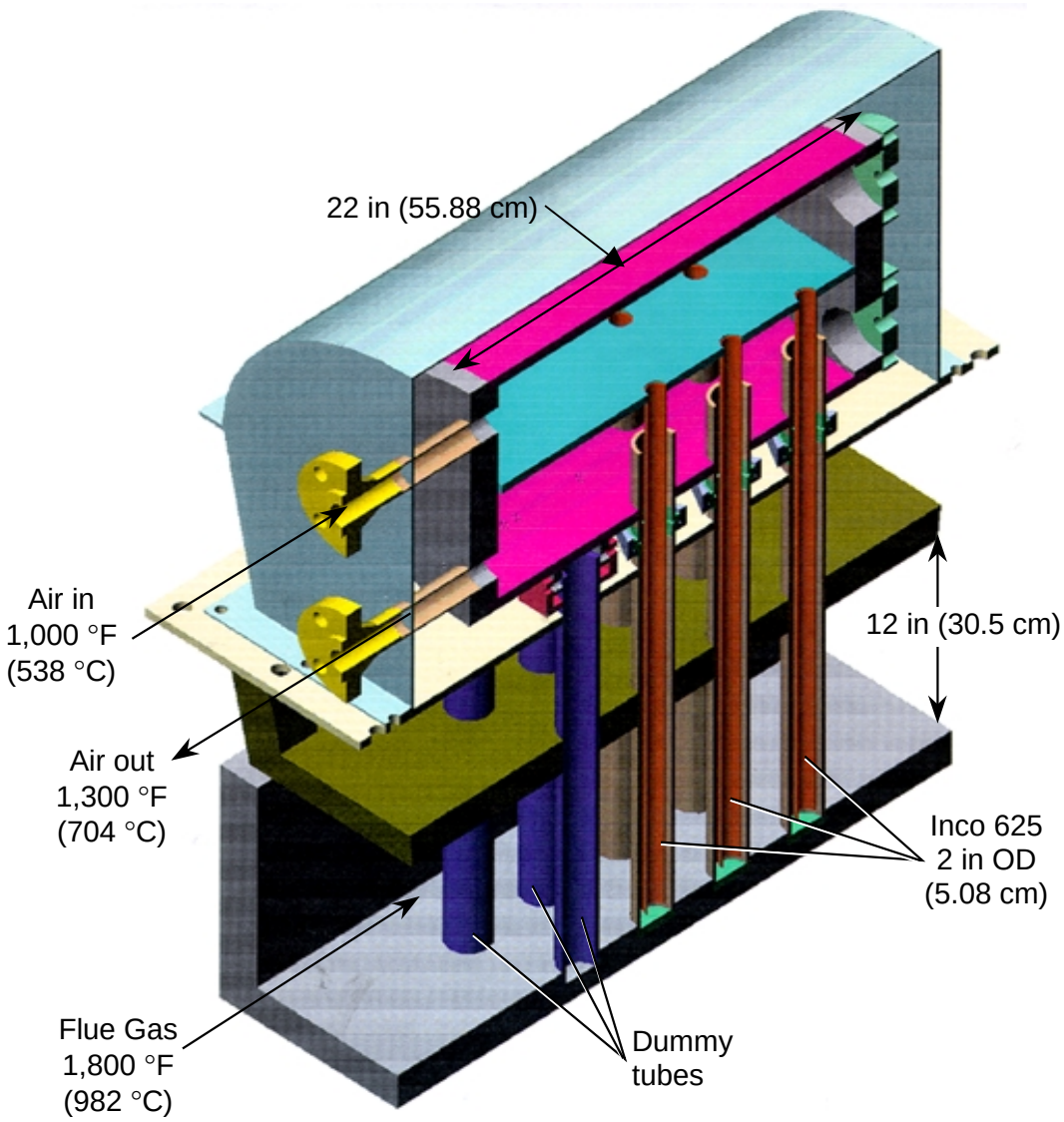

Exhibit 7-13
Schematic of Convective Air Heater Test Module

CAH Test Model

The primary goals of the CAH model testing are to:

1. determine the outside (flue-gas to tubes) convective coefficient,
2. determine the rate of coal deposition on the tubes, and
3. test the metal alloy tube which is exposed to the slag for resistance to corrosion at key temperatures. (The hottest tube wall temperature in the commercial design is expected to be ~1600 °F (871 °C). Materials will also be tested at lower temperatures where corrosive alkalies form.

It is believed that the internal convective heat transfer is easily calculated and need not be explicitly checked in the pilot scale tests.

The commercial plant CAH design requires (according to the Phase II proposal) that the compressed air be heated from 730 to 1300 °F (388 to 704 °C), while the flue gas is cooled from 1800 down to 1200 °F (980 to 650 °C). Depending upon the convection coefficient achieved on the flue-gas side, the tube temperature will likely vary from ~1000 to ~1600 °F (540 to 870 °C). In this reduced scale it will not be possible to test the full range of tube temperatures during a single run. Each test condition will simulate a single section of the full CAH.

Each exposed section of tube will be 13 in (33 cm) long. The CAH will have 7 active tubes, and 5 dummy tubes. The reason for fewer active tubes is to increase the air-flow per tube and therefore have less axial temperature gradient over each tube length. The dummy tubes help set up the proper turbulent flow regime over the tubes which will be monitored for heat transfer.

The CAH compressed air is supplied at 1000 °F (538 °C). A tube design was found (see below) which will heat air from 1000 to just under 1200 °F (538 to 648 °C) in a single pass (using bayonet style tube-within-a-tube) with the maximum tube wall temperature at ~1600 °F (871 °C). Multiple path arrangements were not attempted in this small scale due to the headering complexities which would arise. The cooler tube temperatures can easily be achieved by lowering the inlet air temperature to the CAH.

CAH Model Heat Transfer Testing

The CAH model was designed using two codes. The Kays code, which automates standard calculations found in the literature, was used to find the convective coefficient between the flue-gas and the outside of the tubes. A second program was then written to determine the temperature profiles as a function of axial position along the tubes. This program simply solves for the net heat flux to each wall element by following the air flow (down the inside tube, and then back up the annulus between the two tubes) and then relaxes the tube wall temperatures with time until a steady-state solution is found. Tables 7-3 and 7-4 display the input to the code and the output from the temperature profile code, respectively. Tables 7-5 and 7-6 display the input and the output to the Kays' code.

Table 7-3
Inputs to the Temperature Profile Code

Outside Tube OD	2 in	5.08 cm
Outside Tube Wall Thickness	3/16 in	0.48 cm
Active Heat Exchange length	13 in	33 cm
Length for Pres. Drop. Calc.	20 in	51 cm
Spiral Angle	45 deg	
Total air flow	100 scfm	0.057 kg/s
Temp Air Entering	1000 °F	538 °C
Temp Flue Gas	1800 °F	982 °C
h convection outside (from Kays' code, see below)	23 Btu/h-ft^2-°F	130 W/m^2-K
k tube is high.		

Table 7-4
Outputs from Code Temperature Profile

#	Number of Active Tubes	OD of inner tube (in)	Temp Air out (°F)	Temp Tube bottom (°F)	Temp Tube Top (°F)
1	5	1.25	1185	1405	1490
2	7	1.25	1218	1459	1545
3	7	1.125	1192	1505	1571
4	**7**	**1.0**	**1173**	**1538**	**1591**
5	5	1.0	1149	1488	1543
metric:					
4	7	2.54 cm	634 °C	837 °C	866 °C

Case #4 was chosen for the CAH design.

Table 7-5
The Inputs for Kays' Code

type of cross flow	Single Pass
Cross-sectional area	13 X 14 (in)
Length	16 (in) (4 deep)
Flue Gas flow rate	4720 (#/hr)
Flue Gas Properties • density • viscosity • specific heat • Pr • Pressure	 0.018 (#/ft^3) 0.28 (#/ft-hr) 0.29 (Btu/#-°F) 0.74 15 (psia)
Tube designation used	T31 and T24 (nominally 1 in tubes with 2 in spacings)
Scaling factor	X 2

Table 7-6
Outputs from Kays' Code for Outside of Tubes

	T31	T24
Reynold's Number	27,000	27,000
Convection Coefficient	22.3	23.3

(Actual desired tube arrangement lies between case T24 and T31.)

Tube stress analysis

The analysis done above implied that there is no circumferential variation in tube temperature or flux. In fact, the convective coefficient provided by Kays' code is an integrated average. Although sufficient for determining the net heat flux, in order better represent the tube wall temperature distribution for determining thermal stress, the outside convective coefficient was re-generated as a function of circumference around the tube. A function was derived which matched the profile found in *Kreith,* Principle of Heat Transfer, and which was scaled to give the same integrated average value as calculated by Kays' code.

The finite element code MARC was used to solve for the thermal stresses of the outside tube as indicated in the Structural Analysis section. The following were provided as boundary conditions:

Outside convective coefficient = function of circumferential position around the tube

Inside convective coefficient = constant

Outside Temperature = 1800 °F (982 °C).

Inside temperature = function of axial position.

Structural Analysis

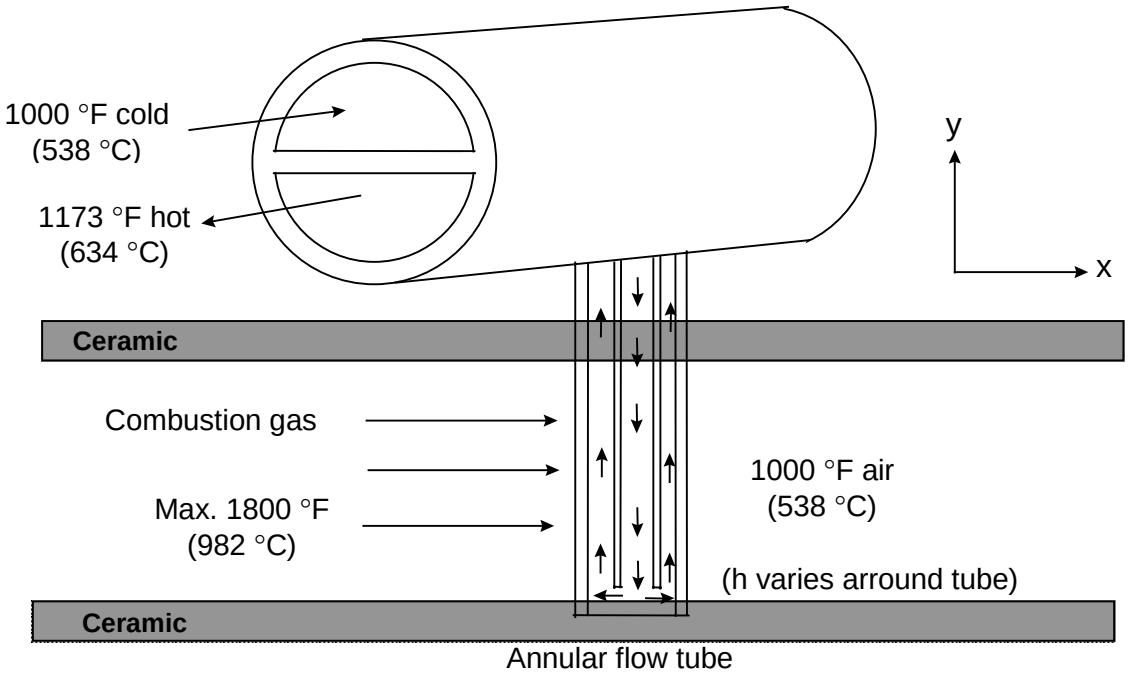

Exhibit 7-14
Convective Air Heater

Exhibit 7-14 is a sketch of the convective air heater design. The sketch shows the header and one of several annular flow tubes supplied by the header. The header is a partitioned cylinder. The top compartment distributes the cool inlet air flow and the lower compartment collect the heated outlet flow. The tubes are a tube in a tube design where the cool air travels down the center and is returned to the top through the outer annular flow area. A spiral vain in the annulus will force the air to circle the tube as it travels upward. This was done to encourage even heating of the air flow. The header is supported by a saddle that is not shown in the figure. The tubes are inserted directly in to the combustion gas stream.

Header Analysis

A 2D model of the cross section of the header was constructed. This model was used to find the bending stress in the cylindrical header caused by thermal gradients.

Geometry

Partitioned cylinder	OD (y direction)	15 in (38.1 cm)
	OD (x direction)	14 in (35.6 cm)
	Length	22 in (55.9 cm)

Material

Haynes 214

Thermal Boundary Conditions

Hot side

Air flow temp 1173 °F (634 °C)

Cold side

Air flow temp 1000 °F (538 °C)

OD of header is perfectly insulated

Analysis

Due to symmetry, only ½ of the header was modeled. The cross section of the header lies in the x-y plane. The axial length of the header lies in the z direction. The header was constrained in the x direction by a symmetry plane. One node was fixed in the y direction. A minimum number of constrains was used to avoid inducing additional stress. Both thermal and stress analyses were performed. Generalized plane strain elements were used. The cylinder was allowed to expand in the z direction. The cross section must remain planer but it is allowed to rotate about the x and y axis. The model assumes the material has infinite strength and that the deformation is elastic. The results are presented below.

Table 7-7
Header Model Results

Haynes 214	
Deflection	**inch (cm)**
y deflection each edge (height)	0.060 (0.152)
x deflection each edge (width)	0.061 (0.155)
z max. (total increase in length)	0.188 (0.478)
Stress	**psi (kPa)**
Max Tensile Sigma X	3,614 (24,915)
Max Compressive Sigma X	-1,430 (-9,858)
Max Tensile Sigma Y	3,189 (21,985)
Max Compressive Sigma Y	-461 (-3,178)
Max Tensile Sigma Z	3,953 (27,252)
Max Compressive Sigma Z	-3,219 (-22,192)
Max Von Mises	4,833 (33,319)
Max Tresca	5,839 (40,254)
Temperature	**°F (°C)**
Maximum	1,165 (629)
Minimum	1,008 (598)
Safety Factor	12.75

Tube Analysis

A 2D model of the cross section of a tube was constructed. This model was used to find the bending stress in the tube due the thermal gradients caused the circumferential variation in convective heat transfer coefficient (h). Away from the ceramic duct walls there is no axial variation in h.

Geometry

Cylindrical tube	Outside Diameter	2.0 in (5.08 cm)
	Wall thickness	1875 in (0.476 cm)
	Length	19 in (0.48.26 cm)

Material

Haynes 214

Thermal Boundary Conditions

Hot (outside) side	
Air flow temp	1800 °F (982 °C)
Cold (inside) side	
Air flow temp	1000 °F (538 °C)

Analysis

Due to symmetry, only ½ of the tube was modeled. The cross section of the tube lies in the x-y plane. The axis of the tube lies in the z direction. The tube is constrained by the symmetry plane in the y direction. One node was fixed in the x direction. A minimum number of constrains was used to avoid inducing additional stress. Both thermal and stress analyses were performed. Generalized plane strain elements were used. The cylinder was allowed to expand in the z direction. The cross section must remain planer and it is not allowed to rotate about the x and y axis. This boundary condition was imposed because the tube end fits into a pocket in the ceramic. The tube may expand deeper into the pocket but bending will be prevented. The model assumes the material has infinite strength and that the deformation is elastic. The results are presented below.

Table 7-8
Tube Model Results

Haynes 214	
Deflection	**inch (cm)**
y deflection each edge (height)	0.0070 (0.018)
x deflection each edge (width)	0.0068 (0.017)
z max. (total increase in length)	0.132 (0.335)
Stress	**psi (kPa)**
Max Tensile Sigma X	3,499 (24,122)
Max Compressive Sigma X	-1,881 (-12,968)
Max Tensile Sigma Y	3,237 (22,316)
Max Compressive Sigma Y	-1,503 (-10,362)
Max Tensile Sigma Z	4,901 (33,787)
Max Compressive Sigma Z	-6,801 (-46,886)
Max Von Mises	6,419 (44,253)
Max Tresca	6,469 (44,597)
Temperature	**°F (°C)**
Maximum	1,554 (846)
Minimum	1,513 (823)
Safety Factor	8.3

Simple horizontal slip joints

0.25 in (0.635 cm) ceramic pins

Thermal Boundary Conditions

Hot side

Sink temp	2800 °F (1520 °C)
Convective heat transfer coefficient	21.2E-5 Btu/sec/in^2/°F
	110 Btu/h/ft^2/°F (625 W/m^2/C)

Cut out and over lap surfaces

Sink temp	2000 °F (900 °C)
Convective heat transfer coefficient	2.12E-5 Btu/sec/in^2/°F
	5.0 Btu/h/ft^2/°F (28.4 W/m^2/C)

Cold side (covered by support brick)	
Sink temp	1700 °F (900 °C)
Convective heat transfer coefficient	4.8E-5 Btu/sec/in^2/°F
	25 Btu/h/ft^2/°F (142 W/m^2/C)

Design Layout of the CAH

The design layout of the CAH is presented in Exhibit 7-15. The design is 90% an all stainless steel assembly, minus the radiation tubes. Because of the combination of temperatures and pressures that are expected, stainless steel has its limitations and therefore other more materials have been investigated.

Alternative materials such as the Inconel Alloy's 617, 800, 802, 601, 601GC, 333 and Haynes 214 were considered. These materials are preferred over the stainless steels, because they have better resistance to the harsh environments and have better mechanical properties at the high temperatures.

The operating conditions show a design of 7 active radiation tubes and 5 dummy tubes. The outside tube dimension is 2.0 in (5.08 cm) OD x 0.188 in (0.478 cm) wall. The inner tube dimension is 1.0 in (2.54 cm) x 0.065 in (0.165 cm) wall. The temperature of the air flowing into the inner radiation tube from the inlet plenum is 1000 °F (538 °C) and the temperature of the air in terms of the exit plenum from the radiation tubes is 1173 °F (634 °C).

A threaded joint interface which incorporates a high temperature metal o-ring has been designed. This will permit two dissimilar materials to be connected.

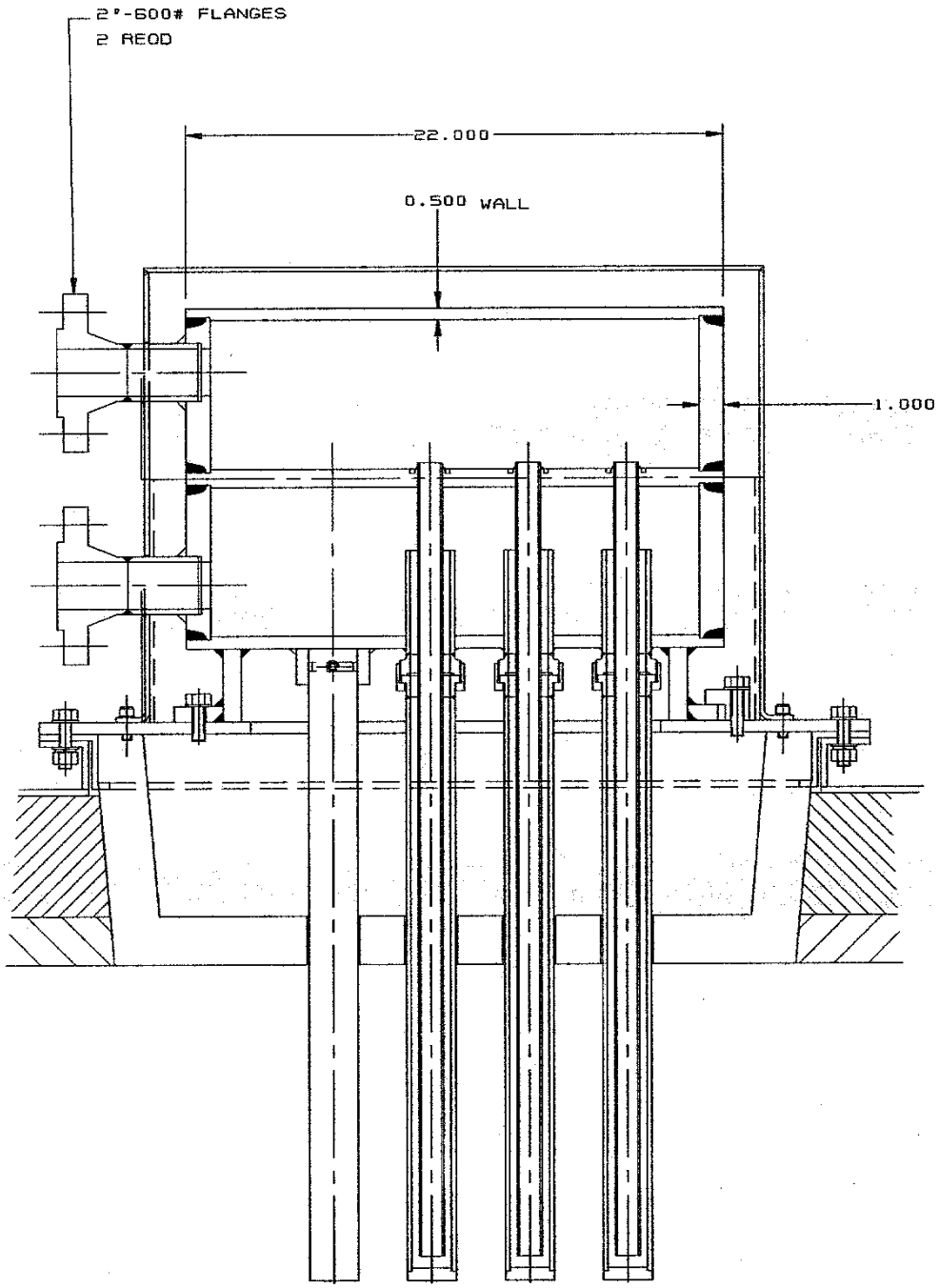

Exhibit 7-15
Design of CAH Test Unit - Side View

Section 8 - Air Heater Materials

Abstract

The work reported in this section was performed under program task 2.2.5. The choice of materials for the RAH panel was inescapable. Once the alloy/refractory "tubes-in-a-box" design was selected, the choice became inevitable. For alloys, only the oxide dispersion strengthened (ODS) materials have the required high temperature strength for the design. The Inco MA754 was chosen for its availability and our expectation that we could develop a welding technique for it. The material for the refractory tiles that protect the alloy tubes was determined to be a fusion cast alumina based on the Phase I testing. The RAH must tolerate running coal slag on it's surface, while providing protection and reasonable heat transfer to the working fluid (air) contained in the alloy tubes. After consultation with several vendors, the Monofrax M was the first choice for testing, based on availability, corrosion resistance and thermal properties.

Beyond the testing of the RAH panel with MA754 tubes and Monofrax M tiles for protection, there was a continuing search for lower cost alternatives. An obvious target was to find a cheaper material than the nickel based MA754. An alternative ODS material is the MA956 ferritic alloy which we have tested for coal ash corrosion and found it very promising. In addition we have developed a TLP welding technique for joining this material, which offers the potential of significant cost reduction.

The fusion cast alumina Monofrax M has performed very well, however, improved corrosion resistance and reduced machining are obvious improvements needed for a practical design. At our request the Kyosera Industrial Ceramics Corp. has fabricated a high chrome alumina that can be cast in "near net shape". This material has shown excellent corrosion resistance in early testing, but its thermal shock properties are poor, probably because of the narrow size distribution of the initial particles. A wider distribution of the particle sizes of the original material should greatly improve its thermal shock resistance. The potential for a tile material that resists corrosion and does not require machining could provide a major cost reduction in a commercial HIPPS plant.

Introduction

Materials are the key enabling technology for successful operation and commercialization of the HIPPS system. The use of high temperature heat exchangers in a coal combustion environment, coupled with the cost constraints, make proper materials selection a considerable challenge. Nonetheless, utilization of state of the art materials and joining methods, as well as advanced oxidation and corrosion resistant coatings, can yield reasonable compromises.

The RAH must tolerate running coal slag on it's inner surface, while providing protection and reasonable heat transfer to the working fluid (air) contained near the outer walls of the coal combustor. Phase I efforts have indicated several potential approaches for this component: 1) use of metal tubing with protective coating(s) and refractory ceramic lining(s), 2) use of structural ceramics such as silicon carbide or silicon carbide /alumina particulate composites, with a protective refractory ceramic lining, and 3) use of fusion cast ceramics such as those used for glass furnace tank linings.

The use of a metallic based RAH, particularly under moderated temperatures and environments afforded by the 65% coal combustion case offers several advantages: 1) ease of fabrication, (i.e. conventional processes can be used to shape and weld components); 2) existence of a significant supplier base; and 3) high strength under moderate (65% coal) system conditions. These alloys offer superior performance compared to the steels, currently utilized in similar applications such as water wall slagging coal combustors. However, for the radiant air heater section, a system of refractory ceramic linings (with or without supplemental thin coatings on the base alloy) will be required to protect the alloy for a slagging coal ash environment.

The use of structural ceramics and/or fusion cast refractories for the RAH tubes has some disadvantages. Joining and sealing technologies are not well developed for these materials. For structural ceramics, while a supplier base exists for producing relatively large tubes, production costs remain high. Moreover, fusion cast ceramics are not normally produced as hollow shapes. Nonetheless, the allowable use temperatures of these ceramic materials make them the primary alternatives for use in the "all coal" combustion case when the working fluid is heated to 2300 °F (1260 °C) or higher.

The metal based approach to the RAH clearly offers a high probability of success for fabricating and operating a prototype HIPPS system. All of the various material elements (metals, coatings, and ceramics) that make up this approach to the RAH wall will require careful testing to determine survivability in coal combustion environments. In addition to selecting and testing of metals, coatings, and refractory ceramic liners, consideration must be given to both on-line and off-line repair of the materials during use. Techniques for bonding, joining and attaching both the dissimilar materials of construction and individual wall subsections will require development and validation.

Metals for the Radiant Air Heater

Several types of alloys have been considered for use in construction of the metal alloy based RAH. Initially, the high strength, oxidation resistant cast nickel based superalloys, such as B-1900, were the choice. While the high temperature strength of these materials is adequate for some applications they fell short of the requirements of the HIPPS design.

A new class of high temperature alloys came into existence during the 1960’s with the invention of oxide dispersion strengthened alloys (ODS) using insoluble metal oxides. Two methods were developed to produce alloys, a chemical process invented by Dupont and a mechanical alloying process invented by Inco. The processes produce a product that exhibits a high grain aspect ratio, textured microstructure, and a stable oxide dispersion to produce combinations of properties previously unattainable in a single alloy. The alloys seem well suited to application as a high temperature heat exchanger.

The alloy chosen for our initial testing is Inco MA 754, essentially Ni-20Cr-0.3 Al-0.5Ti containing a dispersion of Y2O3 particles for high temperature strength. Although the normal composition of MA754 suggests that it should be readily weldable, this is not so. An inherent problem with ODS alloys is related to the distribution of the oxide strengthening phase, in this case Y2O3. Conventional fusion welding results in agglomeration of the dispersed oxide as well as loss of directionality of the alloy grains. These changes cause a loss of the outstanding high temperature creep strength at the location of a fusion weld.

There are several techniques whereby ODS alloys can be joined and retain a large fraction of their high temperature properties. The approaches that were examined for joining the MA 754 components of the RAH were:

- Threading the members
- Transient liquid metal bonding, or transient liquid metal processing (TLP)
- The use of threads and sealers
- Metallurgically sealed threads and

To check the feasibility of these approaches, threads were machined in a number of trial components, with male threads on 1 in. diameter rods and corresponding female threads machined into the blocks that represent the elbows. Although this alloy has a strong tendency to gall, Class 1 threads resisted galling. The use of high temperature gaskets was investigated, but rejected since the coefficient of thermal expansion of the commercially available materials was less than that of MA754, such that there was a gap present at elevated temperatures. Experiments were run to simultaneously evaluate the metallurgical sealing of threaded members as well as conventional sleeve brazing . The initial brazing operations were performed in vacuum at 1925 °F (1052 °C). The configuration was held at temperature for approximately 45 minutes, then heated to 2250 °F (1232 °C) and held at temperature for an additional 255 minutes prior to furnace cooling. In order to facilitate the TLP process, a jig was constructed that allowed the tubes, elbows and end plates to be assembled and held in position with a minimum of movement.

Based on the results of these tests, the joining technique chosen was TLP. This technique was originally developed for the joining of gas turbine blade components, and significant practical experience exists in its application. For TLP joining, the principal component of the braze alloy diffuses into the matrix, this strongly influences the liquation process temperature. The decrease in this element raises the melting point of the union. In most cases, the incipient melting point is equal to that of the matrix alloy so that, in effect, the braze becomes a weld. In this case the composition of the braze was Ni-9.5Cr-3.0Al-4.9Ti-7(Mo+W) +4.5Si +0.7B, and its melting point was 1900 °F (1038 °C).Tube assemblies were joined using a specially designed jig, and a large vacuum furnace.

While the MA754 alloy performed well in all the RAH testing program, there has been a continuing search for lower cost alloys with comparable high temperature properties. The Fe-base alloys ODM 751 and PM 2000 provide a good compromise between strength and formability with an excellent oxidation resistance provided by the formation of a compact, continuous and adherent alumina scale. Alumina former alloys are preferred for applications above 1830 °F (1000 °C) since they are not subjected to scale volatilization under oxidizing conditions. Scale adherence due to the presence of yttria has also been has also been reported for these types of materials (Kazimierzak, 1992).

Bennett et al. (1991) studied the isothermal oxidation kinetics of the ODS alloys MA 956 (18% Cr, 4.4% Al), ODM 751 (16% Cr, 4.6% Al) and PM 2000 (19% Cr, 4.7% Al) in the temperature range 2190 to 2550 °F (1200 to 1400 °C). The tests were carried out in both flowing air and carbon dioxide for a period of 100 to 200 hours. After a short transition oxidation period, the kinetics of all alloys followed parabolic behavior with the formation of single-phase α-

Al_2O_3 (Corundum) scales. No systematic relation was established between alloy composition and oxidation kinetics.

The mechanical properties of these alloys is intimately related to the addition of an oxide dispersion, in this particular case yttria (Y_2O_3), which is thermodynamically more stable than strengthening particles such as "gamma-prime" and carbides in conventional alloys. The addition of yttria during mechanical alloying provides good high temperature strength since agglomeration or dissolution of these particles does not occurred. The addition of yttrium in conventional alloys has been shown to increase scale adherence by the formation of "pegs" or protrusions formed around the rare-earth-metal containing particles extending from the oxide scale into the metal, pinning the scale to the underlying metal. Quadakkers et al. (1989) evaluated the oxidation mechanism of Alloy MA956 in synthetic air at 1830 and 2010 °F (1000 and 1100 °C) tagging the gaseous environment with radioactive ^{18}O to study the scale growth mechanism. Yttrium-containing phases were incorporated into the scale improving scale adherence and reducing scale growth rate. The presence of yttrium suppressed cation transport through the scale favoring the selective oxidation of Al leading to the formation of a single-phase oxide scale instead of mixed Al-Fe spinels resulting in low oxidation kinetics (Lowell, 1990). A decrease in cation transport also minimized the formation of voids at the metal/scale interface improving scale adherence with a less convoluted scale. The effective role of yttria in scale growth and adherence was sensitive to the appropriate amount and distribution of the oxide dispersion. High amounts of yttria have been associated with thicker oxide scales due to enhanced inward growth (Quadakkers, 1989).

The experiments with the oxygen radioactive tracer suggested that the role of yttria additions on the scale formation mechanism was related to the incorporation of yttrium into the scale preferentially at grain boundaries. The entrapped or absorbed dispersoid reduces diffusion of cations through the scale with oxide growth taking place at the scale-metal interface by exclusive inward oxygen transport with minimal growth stresses from alumina nucleation within the existing scale (Quadakkers, 1989). The presence of yttrium at the scale grain boundaries retards grain boundary migration resulting in fine grain scales where growth stress are more effectively relieved by diffusional plastic flow improving scale adherence (Malik, 1990).

Quadakkers (1990) and Versaci et al. (1993) have shown that the Kp values vary with exposure time. They measured sub-parabolic time dependence for the oxidation of MA 956 for an exposure of 1000 hours. The parabolic rate constant decreased with time due to an increase in alumina oxide grain size that in turn was related to the presence of yttrium at the scale grain boundaries. Continued research (Weinbruch, 1999; Garcia-Alonso, 2000) has further elucidated the oxidation mechanisms for ODS alloys.

As described above, ODS alloys exhibit good resistance to oxidation and corrosion in relatively clean environments but there is little evidence on behavior in the environments typical of coal combustion where sulfur levels may be high and impurities such as alkalis, and chlorides may be present. The study described here involved exposure of candidate ODS alloy samples MA 754, ODM751 and PM2000 to controlled environments for times up to 5000 h at temperatures of 1740 to 1920 °F (950 to 1050 °C) with weight change measurements at periodic intervals. Metallographic examination was carried out on selected test pieces to determine the extent of penetration of corrosive attack. Similar exposures were carried out with the test pieces exposed to coal ash and in this case metallographic analysis was the principal analysis technique.

Experimental Procedure

Three alloys were selected for study in this program, two iron-based and one nickel-based. Nominal composition of the alloys is presented in Table 8-1.

Table 8-1
Nominal Alloy Composition

Alloy Designation	PM2000	ODM 751	MA 754
Source	Plansee	Durametal	Inco
Nominal Composition – Wt %			
Chromium	20	17	20
Aluminum	5	5	0.3
Titanium	0.5	0.5	0.5
Yttrium	0.5	0.5	0.5
Iron	Balance	Balance	1
Nickel	----------	----------	Balance

The materials were obtained in tubular form, with specimens fabricated as arc sections of the tube approximately 3 cm long. The specimens were placed into an alumina tray for insertion into the test furnace. The test furnaces were standard tube furnaces, 50 mm ID x 1 m long. One furnace was operated at 1740 °F (950 °C) and the at 1920 °F (1050 °C). Temperature profiling of the heated zone showed a variation of less than ±40 °F (±5 °C) over the active length. The gaseous environment was controlled to that expected from combustion of an Illinois Number 6 coal. The target gas composition is presented in Table 8-2. The gas was synthesized from compressed gas cylinders with part of the gas humidified to achieve the final composition.

Table 8-2
Gas Composition

Constituent	Concentration – Wt %
N_2	73.5
CO_2	13.8
H_2O	9.1
O_2	3.3
SO_2	0.31

Selected samples were immersed in coal ash powder. The composition of the ash is given in Table 8-3.

Table 8-3
Ash Composition

Constituent	Concentration – Wt %
SiO_2	44.9
Al_2O_3	19.9
Fe_2O_3	24.0
CaO	3.3
MgO	0.7
Na_2O	0.5
K_2O	1.7
TiO_2	0.9
P_2O_5	0.7
SO_3	2.9
Total	99.8

Sample exposure was performed for approximately 5000 hours. Periodically, the samples were cooled to ambient temperature, removed and weighed, and then returned to the furnace for continued exposure. Finally, selected samples were destructively examined by optical microscopy and SEM.

Results

Average weight gain data for the test specimens are presented in Exhibits 8-1 - 8-3.

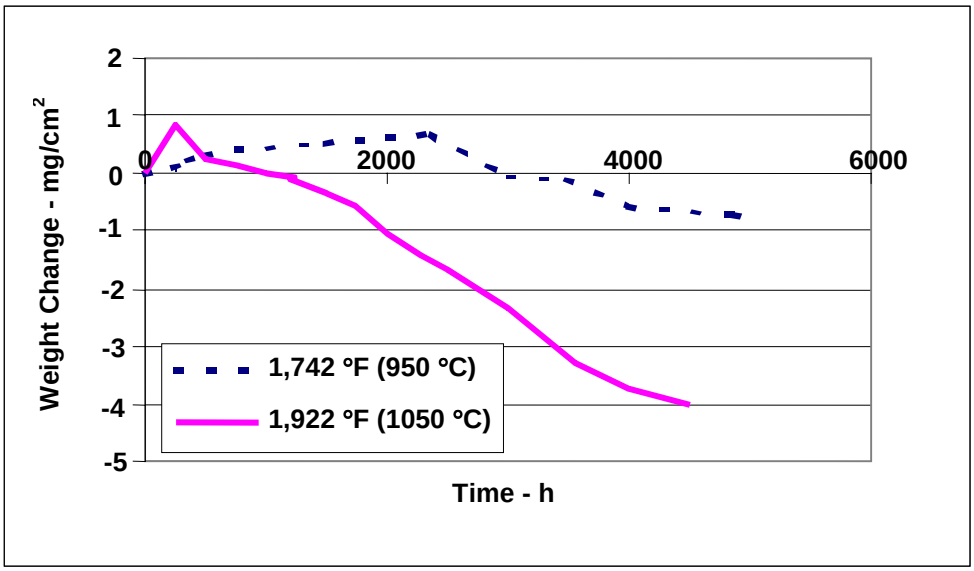

Exhibit-8.1
Weight gain data for MA 754

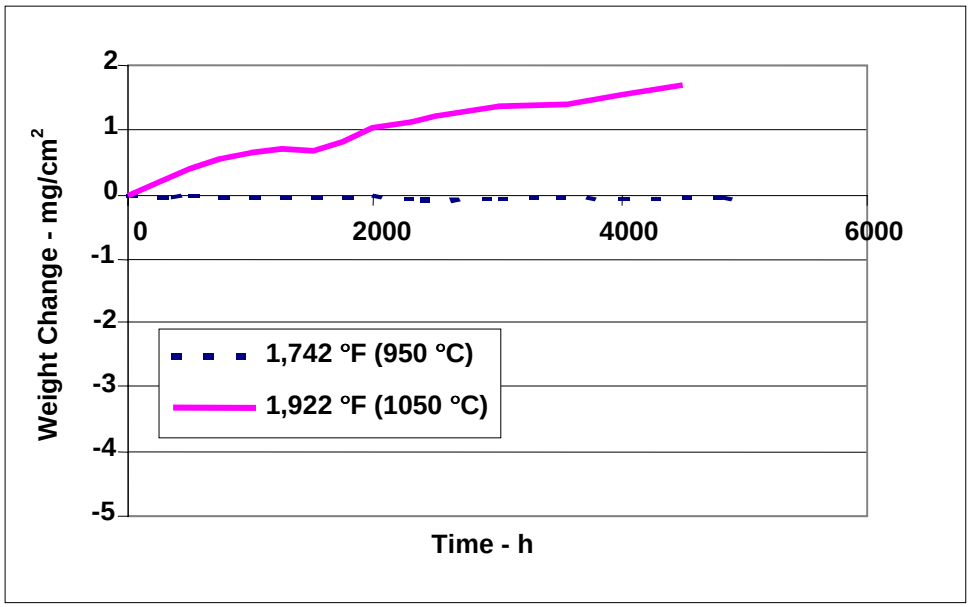

Exhibit 8-2
Weight gain data for PM2000

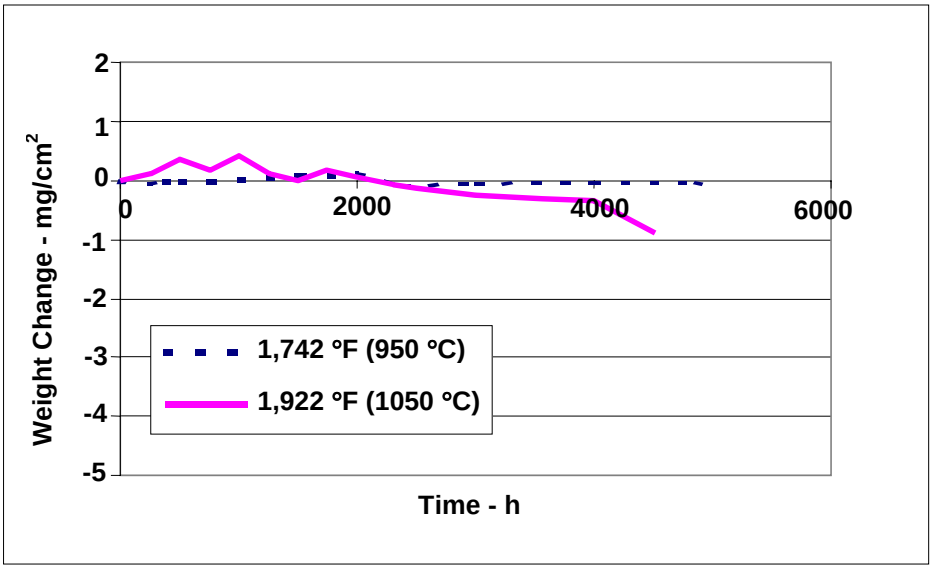

Exhibit 8-3
Weight gain data for ODM 751

The weight change data is generally consistent with that observed for oxidation in air, i.e. very low oxidation rates particularly at 1740 °F (950 °C). The combustion gas environment does not appear to have adversely impacted the oxidation rate. Alloys MA 754 and ODM 751 ultimately experience weight loss with time during exposure at 1920 °F (1050 °C). This is due to exfoliation of the oxide scale and, in the case of MA 754, the likely additional loss of volatile chromium oxyhydroxide species. PM 2000 did not show evidence of scale exfoliation with continued gain in weight at 1920 °F (1050 °C).

Metallographic examination was performed on selected samples after completion of 5,000 hours exposure at 1740 °F (950 °C) and 4,500 hours exposure at 1920 °F (1050 °C), respectively. Results are documented in the Appendix (following the section "Metals for the RAH") in Exhibits 8-4 - 8-13. The micrographs shown in these Exhibits generally illustrate the formation of an oxide scale at the sample surface. The layers are more uniform for the 1740 °F (950 °C) exposure and show evidence of spallation in the 1920 °F (1050 °C) samples. The sample of ODM 751 exposed to coal ash exhibited small areas of internal oxidation, Exhibits 8-11 and 8-12 at scattered locations of the surface.

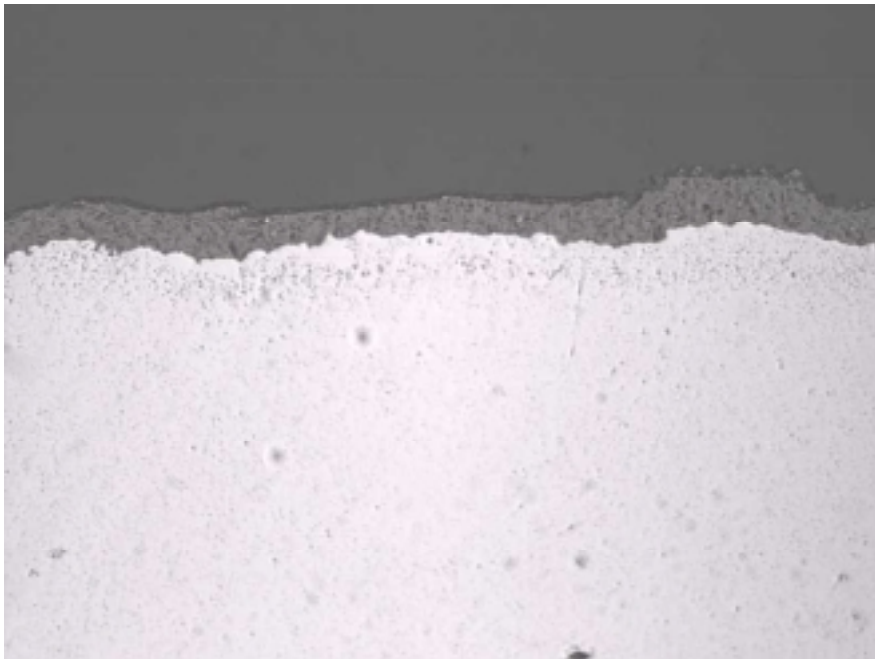

Exhibit 8-4
MA 754, 1740 °F (950 °C), 500x

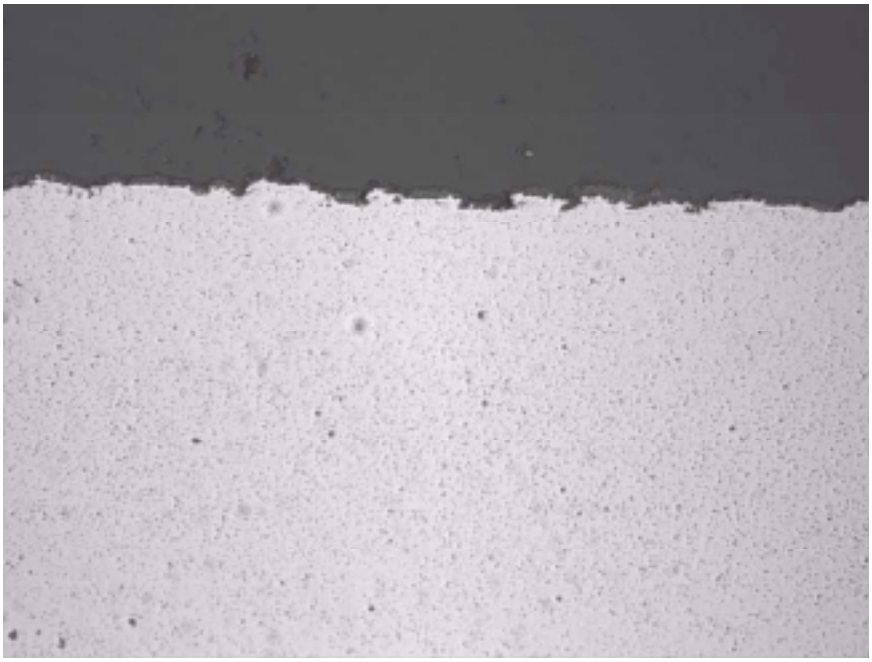

Exhibit 8-5
ODM 751, 1740 °F (950 °C), 500x

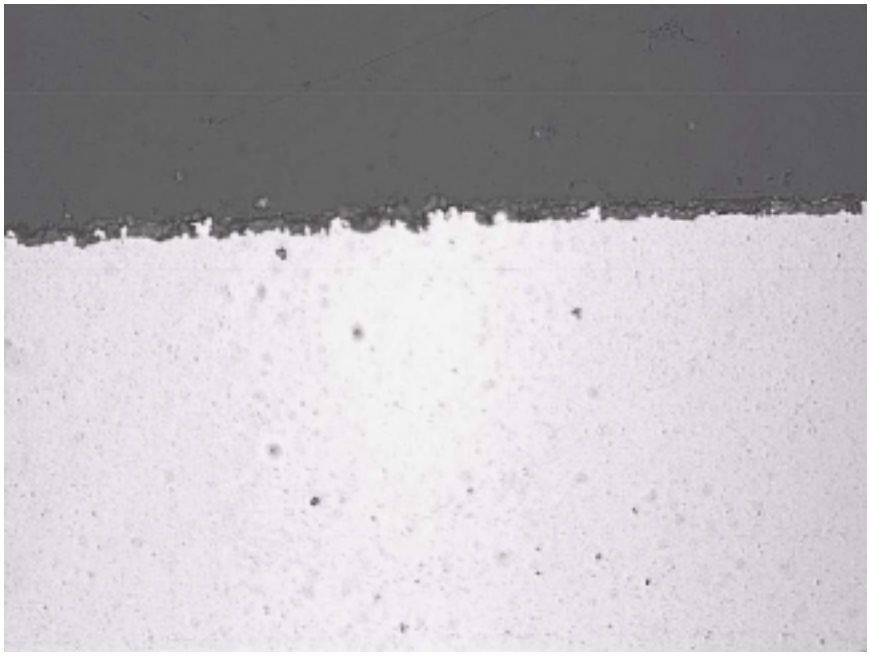

Exhibit 8-6
PM 2000, 1740 °F (950 °C), 500x

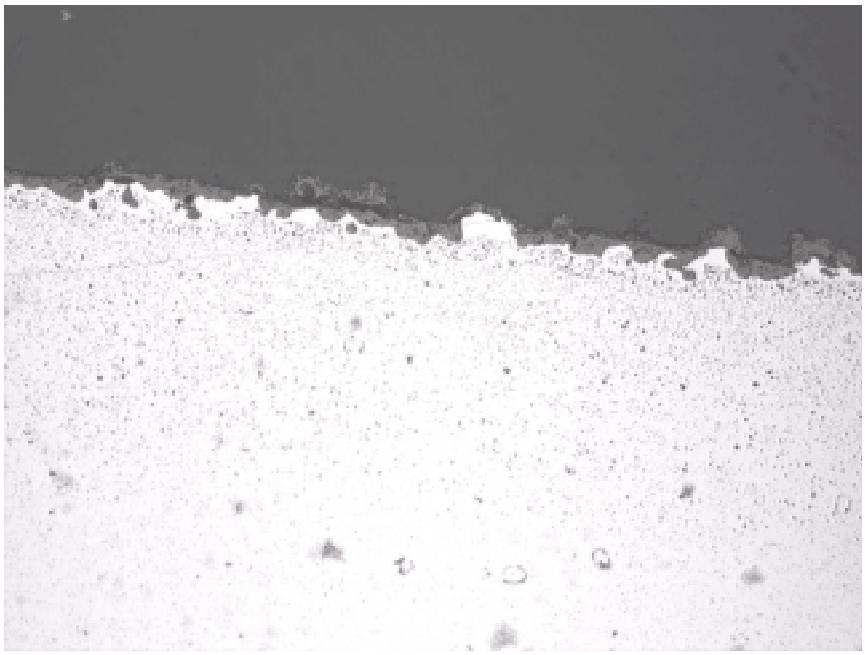

Exhibit 8-7
MA 754, 1920 °F (1050 °C), 500x

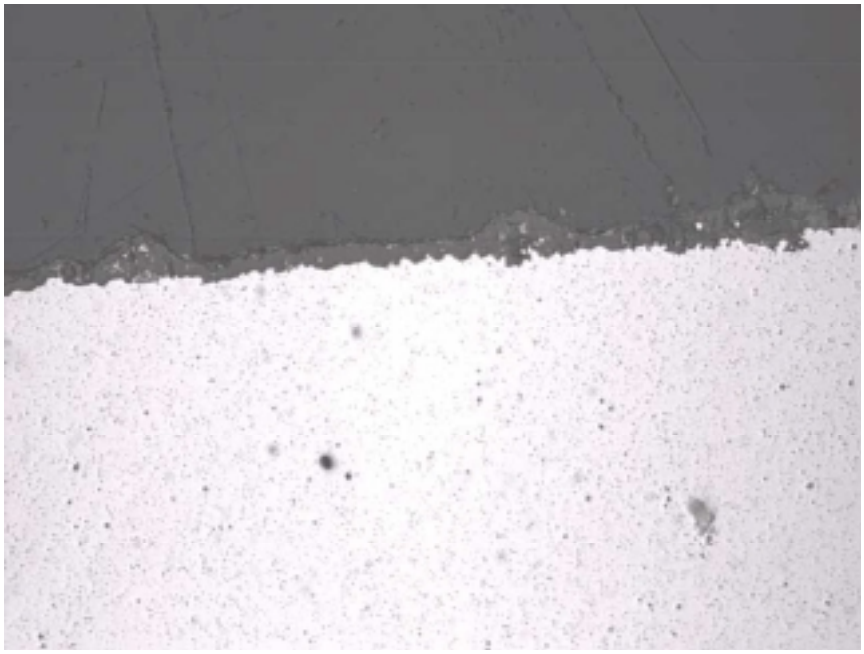

Exhibit 8-8
ODM 751, 1920 °F (1050 °C), 500x

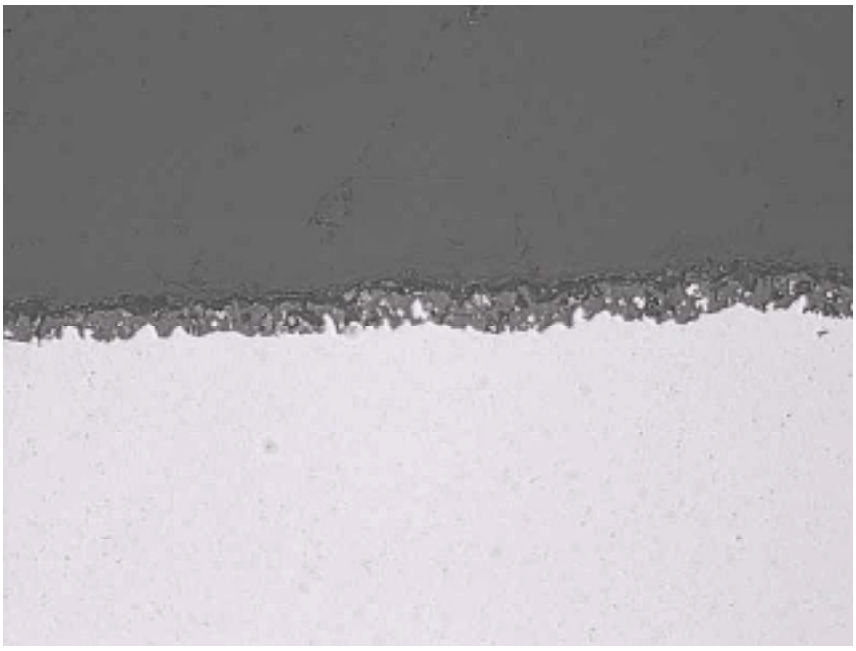

Exhibit 8-9
PM 2000, 1920 °F (1050 °C), 500x

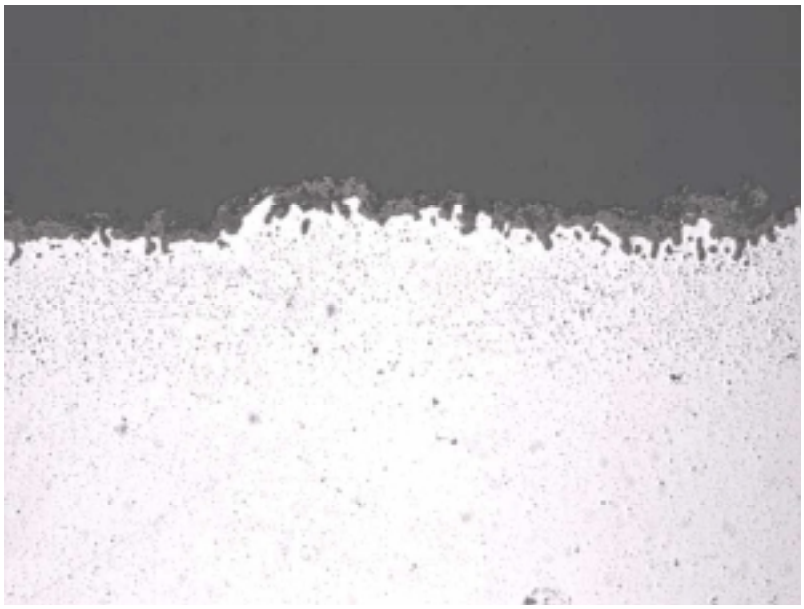

Exhibit 8-10
MA 754, 1920 °F (1050 °C) with ash, 500x

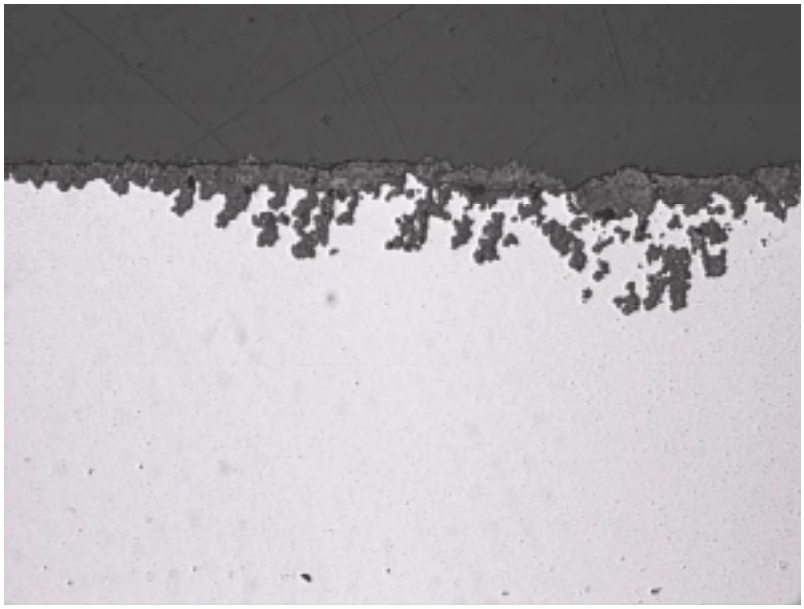

Exhibit 8-11
ODM 751, 1920 °F (1050 °C) with ash, 100x

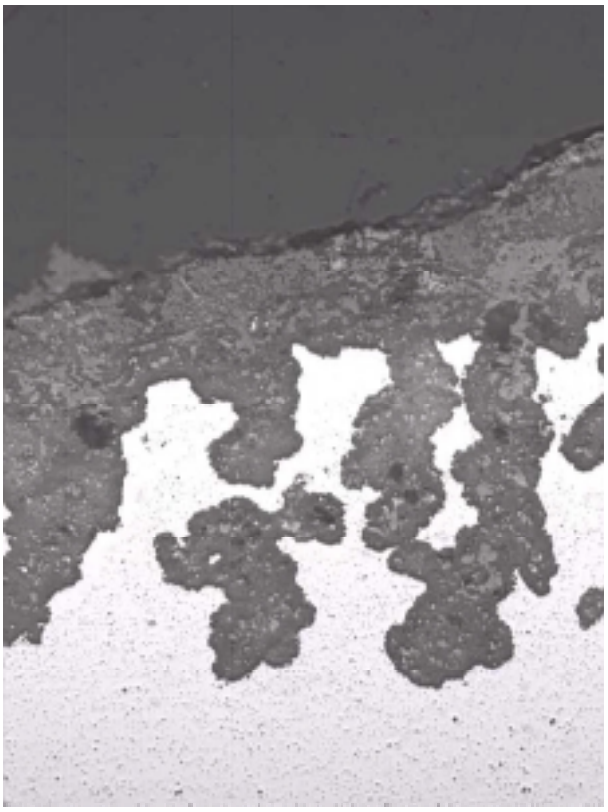

Exhibit 8-12
ODM 751, 1920 °F (1050 °C) with ash, 500x

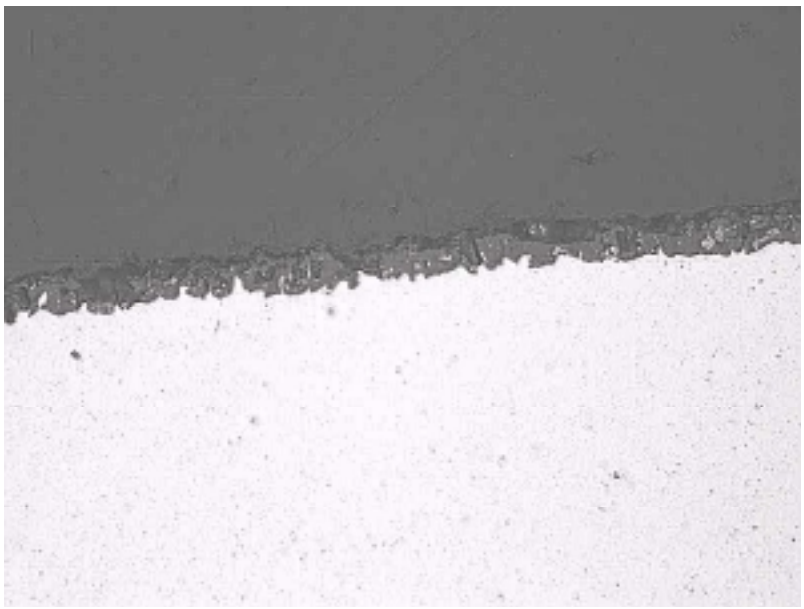

Exhibit 8-13
PM 2000, 1920 °F (1050 °C) with ash, 500x

Samples of the three alloys under study were examined by SEM, with the results shown in Exhibits 8-14 - 8-16. These figures document that the oxide layers are predominately composed of alumina for alloys PM 2000 and ODM 751 and chromia for alloy MA 754, as expected.

In summary, these results do not reveal any significant adverse interaction of the ODS alloys with the products of coal combustion.

Joining

The joining of ODS alloys is a problem that limits their application. The very concept that makes the alloys desirable for high temperature use, perversely, makes joining so difficult.

Fusion welding methods such as electron beam, laser, tungsten inert gas, plasma arc and resistance welding have proved to be extremely difficult and in many cases impossible to do. Fusion welding procedures result in a solidification grain structure more or less perpendicular to the welding direction. The oxide dispersion, essential for the high temperature properties, agglomerates in the fusion zone to such an extent that mechanical properties are no longer acceptable for highly stressed components. Even partial melting can produce semi-continuous oxide networks that can contribute to premature weld failures. In addition, melting may release entrapped gases from the mechanically alloyed base metal, producing fine porosity in either the weld pool or along the edge of the fusion zone. Moreover, fusion welding often results in grain boundaries that lie transverse to the direction of maximum applied loads, seriously degrading the high temperature performance of the joint.

Liquation destroys the texture of the alloy and the cast structure lacks the distribution of dispersoid, which provides high temperature strength. Brazing, transient liquid phase bonding (also known as diffusion brazing) and diffusion bonding are considered to be the most suitable processes for joining ODS materials. Brazing is the term used to describe liquid phase joining techniques that do not require any additional heat treatments. It is a useful process to produce joints of limited high temperature capabilities. In diffusion brazing (TLP Processing), the interlayer (braze alloy) melts and isothermally resolidifies at the bonding temperature. Diffusion welding is a solid-state process in which an inter-layer may be present, but liquation does not occur. The process is usually carried out at temperatures in the range of 0.5 to 0.8Tm.

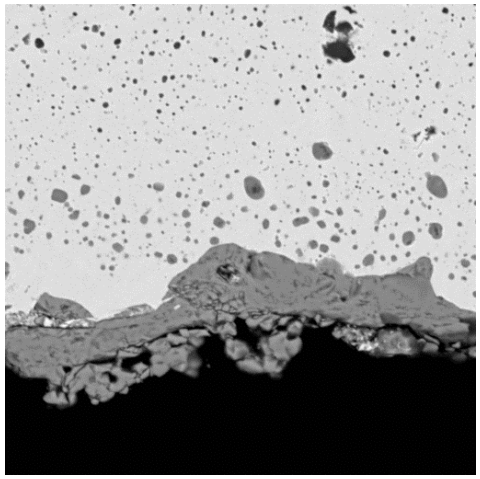

Backscatter Image 2000X

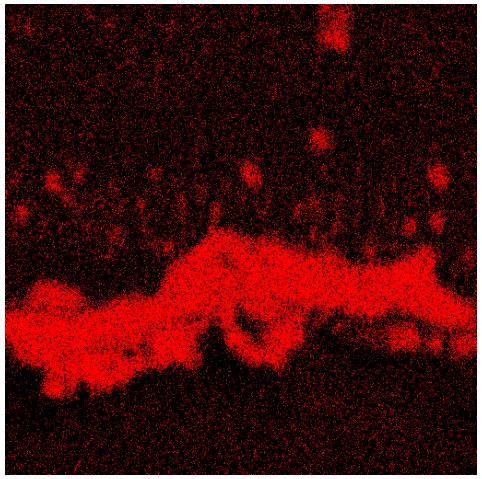

O_kα 2000X

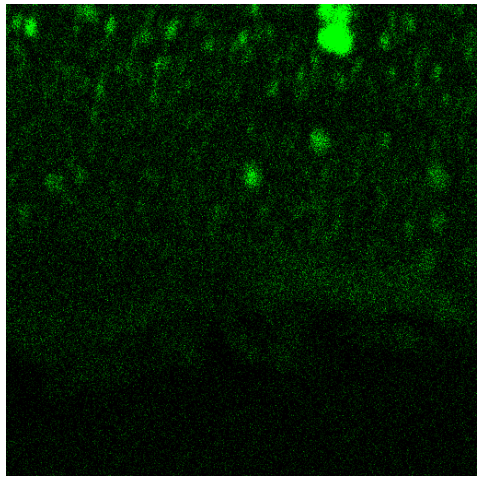

Al_kα 2000X

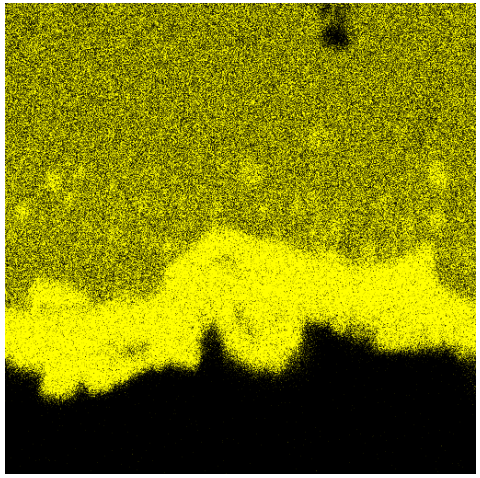

Cr_kα 2000X

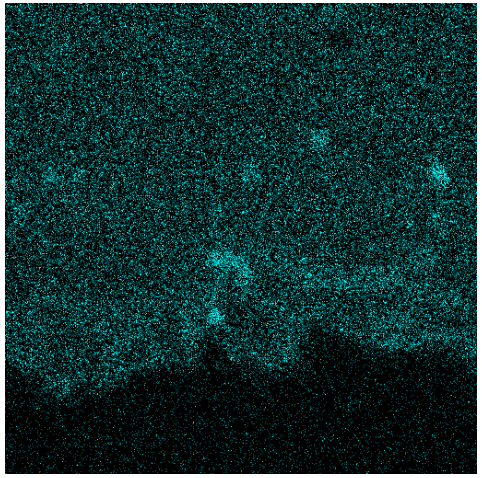

Ti_kα α 2000X

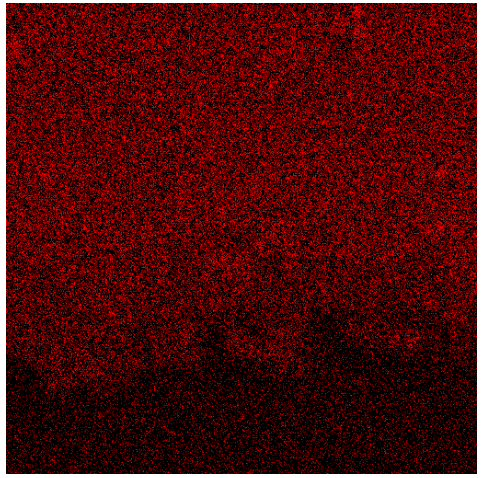

Y_lα 2000X

Exhibit 8-14
Elemental X-Ray Mapping, MA 754, 1920 °F (1050 °C)

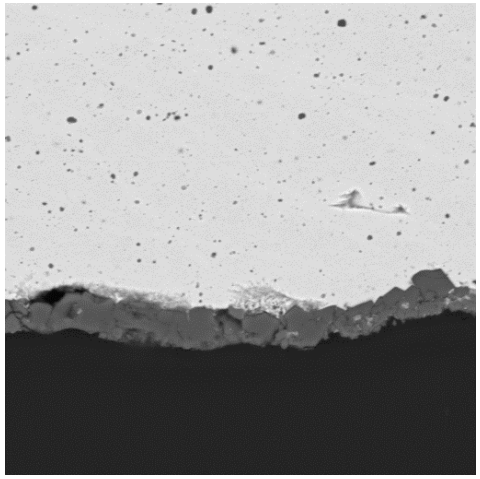

Backscatter Image 2000X

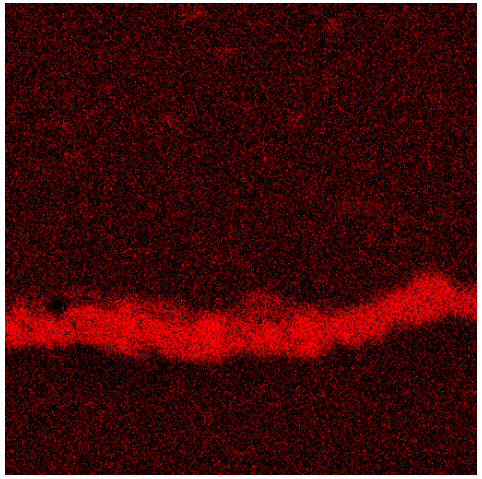

O_kα 2000X

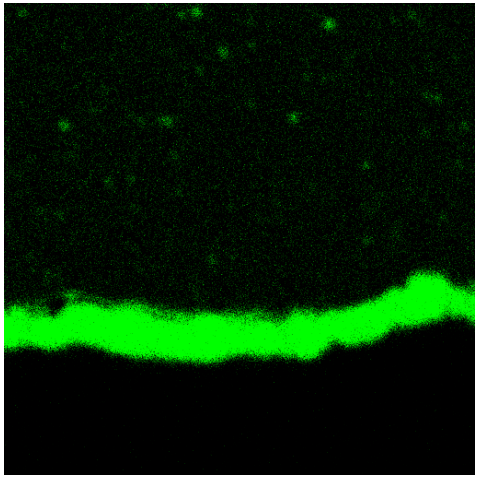

Al_kα 2000X

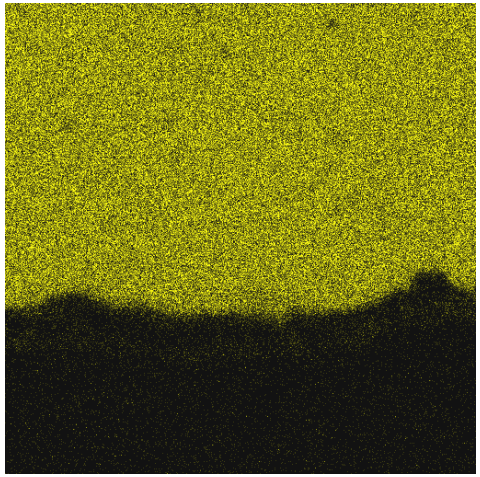

Cr_kα 2000X

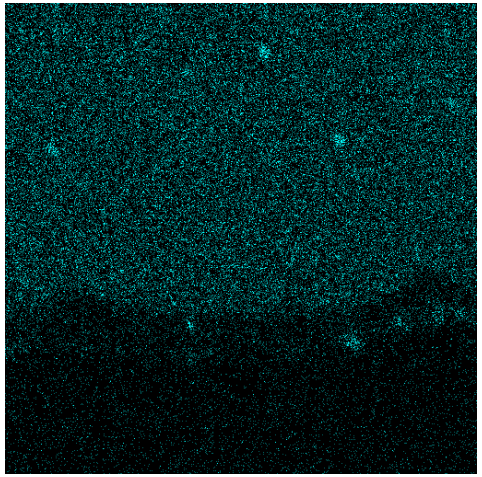

Ti_kα α 2000X

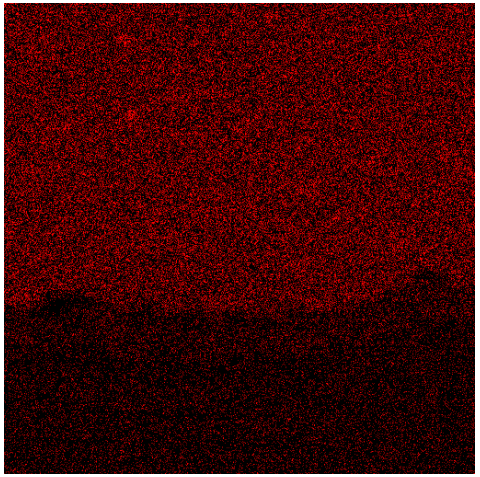

Y_lα 2000X

Exhibit 8-15
Elemental X-Ray Mapping, ODM 751, 1920 °F (1050 °C)

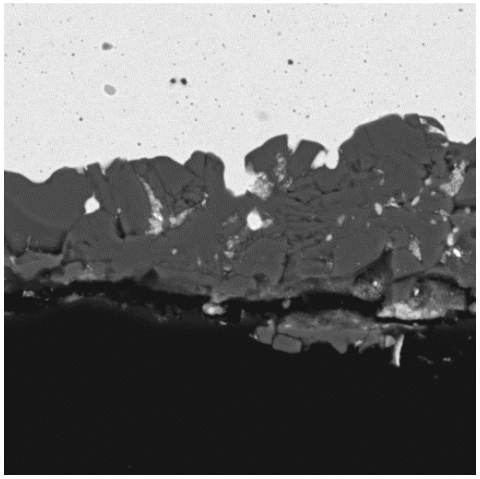

Backscatter Image 2000X

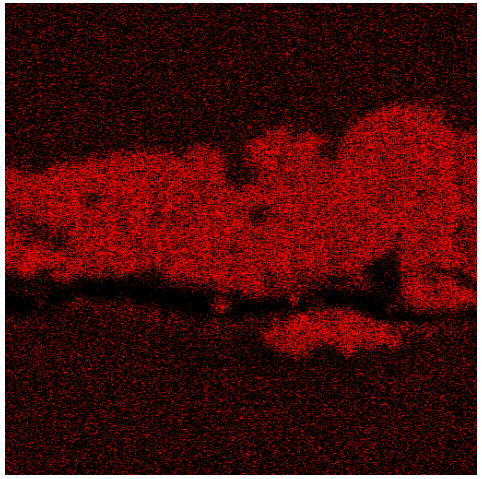

O_kα 2000X

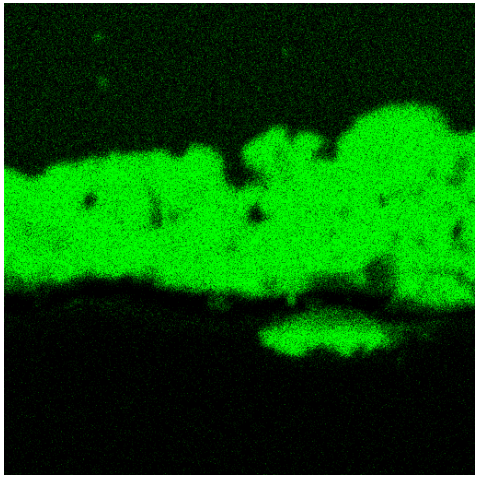

Al_kα 2000X

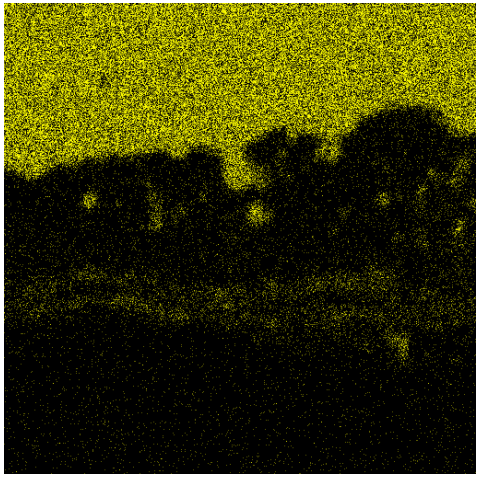

Cr_kα 2000X

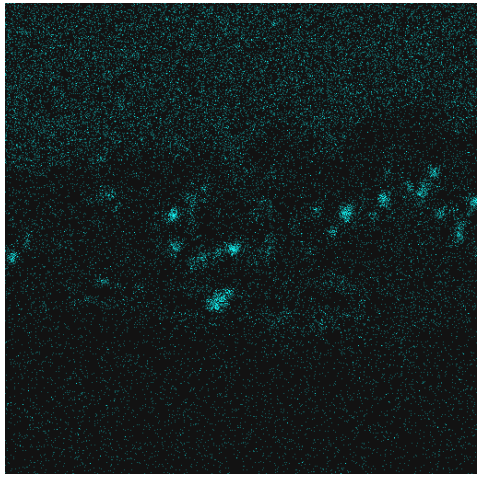

Ti_kα α 2000X

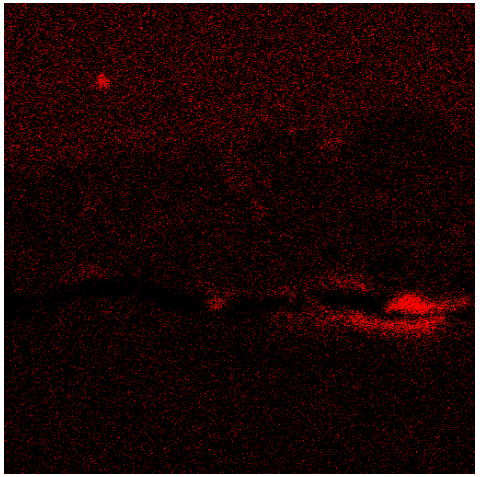

Y_lα 2000X

Exhibit 8-16
Elemental X-Ray Mapping, PM 2000, 1920 °F (1050 °C)

In the TLP process, a lower melting interlayer is placed between the two materials being joined. The sandwich is then heated to the bonding temperature and held for an appropriated time. The interlayer melts and interdiffusion occurs between the molten layer and the substrate, producing isothermal solidification of the molten material. MA 6000 material has been joined to itself employing each of the following alloys, (a) Ni-15Cr-4B, (b) Ni-12W-10Co-6Cr-4Ta-3B-2M0-0.25Y and (c) Ni-19Cr-8Si-1.3B (Tsuji and Mino, 1990). In each case, joining was accomplished by heating the materials at 2190 °F (1200 °C) for 16 to 20 hours under an applied stress of 29 psi (0.2 MPa) to 725 psi (5.0 MPa). In all cases, when tested, the joints exhibited strengths on the order of one third that of the base metal. Diffusion bonding involves simultaneously applying heat and pressure to a joint to produce solid state bonding with a minimum of macroscopic deformation. Diffusion bonding requires careful control over both surface cleanliness and material recrystallization. Surface preparation is generally cool, wet grinding to a nearly mirror finish. The polished parts are then stored in an inert liquid until joining. To achieve optimum high-temperature properties, growth of large, recrystallized grains across the prior joint interface is desired. Bucklow (1990) demonstrated that MA 956 can be joined by bonding recrystallized and unrecrystallized alloy at 2190 °F (1200 °C) and 29,008-43,511 psi (200-300 Mpa) pressure and then subjecting the bonded joint to an appropriate grain coarsening anneal. Verpoort (US patent 4,817,858) teaches that coarse grain ODS alloys can be joined successfully by hot isostatically pressing materials with finely machined surfaces, if pressure is not applied until after the material has been heated above cold-working temperatures. Pressing pressures are to be 14,504-43,511 psi (100-300 MPa), with bonding times ranging from 1-24 hours.

The alloy currently employed in the construction of the Radiant Heater is MA 754. It possesses the necessary high temperature mechanical and chemical properties demanded by the system. It and other members of the mechanically alloyed materials uniquely fit the bill. However as noted, joining is a serious undertaking and the processes previously described do not lend themselves easily to the construction of a full scale Radiant Heater. In the TLP process (Diffusion Brazing) the components to be joined are held under an applied load for prolonged duration at very high temperatures. In the diffusion bonding process, the mirror fine surfaces must also be held at reasonably high temperatures under very large applied loads. An objective for the future is the development of a process that combines the necessary features of both diffusion brazing and diffusion welding; processes that allow a metallurgical bond to occur at temperatures easily obtainable for field repairs, in environments obtainable in field repairs, and heat treating temperature and duration consistent with field repairs.

Initial experiments on joining were performed during this program. The experiments were designed to verify, amend and finally construct a set of jigs that allowed the experimenter to apply uniform pressures to specially prepared specimens of low carbon steel in order to demonstrate that the parts could be successfully bonded. Once the basic parameters were identified, MA 956 alloy was substituted for the low carbon steel and using the parameters from the study, the mechanically alloyed specimens were successfully joined. Metallographic examination confirmed that grains from the joined specimens obliterated the original interface. Equally important, the chemistry and quantity of the interlayer is reasonably well understood. All of the necessary forms and

discussions have been submitted to the legal staff. What need to be addressed are the details of the process and mechanical testing to accurately determine the true mechanical properties of the joints.

References for "Metals for the Radiant AIR Heater"

Bennet M.J., Romary H., and Price J.B., "The Oxidation Behavior of Alumina Forming Oxide Dispersion Strengthened Ferritic Alloys at 1200-1400°C", Heat-Resistant Materials, Proceedings of the First International Conference, September 1991.

Bucklow, I. A. "Diffusion Bonding a Creep Resistant Fe-ODS Alloy" Advances in Joining Newer Structural Materials, Elmsford NY: Pergamon, 1990 p 299.

Garcia-Alonso M. C., González-Carrasco J. L., Escudero M. L., and Chao J., "Oxidation Behavior of Fine-Grain MA 956 Superalloy", Oxidation of Metals, Vol. 53 Nos. 1 / 2, 2000.

Kazimierzak B., et al, "An ODS material with outstanding creep and oxidation resistance above 1100°C", Materials & Design, Vol. 13 No. 2, April 1992.

Lowell C. E., and Barrett C. A., "The Oxidation and Corrosion of ODS Alloys", NASA Technical Memorandum 102555, June 1990.

Malik A. U. and Natesan K., "Oxidation and Sulfidation Behavior of Fe-20CR-16Ni-4Al-1Y_2O_3 Oxide-Dispersion-Strengthened Alloy", Oxidation of Metals, Vol. 34 Nos. 5 / 6, 1990.

Quadakkers W. J., Holzbrecher H., Briefs K. G., and Beske H., "Differences in Growth Mechanisms of Oxide Scales Formed on ODS and Conventional Wrought Alloys", Oxidation of Metals, Vol. 32 Nos. 1 / 2, 1989.

Quadakkers W. J., "Growth mechanisms of oxide scales on ODS alloys in the temperature range 1000-1100°C", Werkstoffe und Korrosion 41, 659-668, 1990.

Quadakkers W. J., Schmidt K., Grümeier H., and Wallura E., "Composition, structure and protective properties of alumina scales on iron-based oxide dispersion strengthened alloys", Materials at High Temperatures, Vol. 10 No. 1, February 1992.

Tsuji and K Mino "Isothermal Forging and Subsequent Treatment of a Newly Developed ODS Alloy for Turbine Blade Applications", Structural Applications of Mechanical Alloying, ed. F.H. Froes and J.J. deBarbadillo, Metals Park OH:ASM Intern'l 1990.

Verpoort, I. C. US patent 4,817,858.

Versaci R. A., Clemens, D., and Quadakkers W. J., "Distribution and transport of yttrium in alumina scales on iron-based ODS alloys", Solid State Ionics 59 (1993) 235-242.

Weinbruch S., Anastassiadis A., Ortner H. M., Martinz H. P., and Wilhartitz P., "On the Mechanism of High-Temperature Oxidation of ODS Superalloys: Significance of Yttrium Depletion Within the Oxide Scales", Oxidation of Metals, Vol. 51 Nos. 1 / 2, 1999.

Refractory Ceramic Linings for the Radiant Air Heater

Initial Refractory Ceramic Candidate Selection

An initial selection of refractory candidates was made which was based primarily on the results of a 100 hour coal combustor/heat exchanger rig test conducted during the Phase I portion of the HIPPS program. This test identified several material families which showed promise for the RAH application, while also indicating which families of materials were not worth further consideration.

The materials which performed poorly in the 100 hour test included bonded fused grain alumina, bonded fused grain alumina-zirconia-silica (AZS), and the two castables: mullite bonded silicon carbide, and alumina bonded silicon carbide. Excessive infiltration, corrosion and erosion by the molten coal slags were evident. The interested reader is referred to the topical report written on this test. These families of materials just described were not considered for Phase II.

From the corrosion test results, all three of the fusion cast refractories performed well, including fusion cast α/β alumina, AZS, and 30% chromia-alumina. Bonded fused grain 30% chromia-alumina also held up to corrosion well. Both chrome oxide containing materials formed complex iron oxide/chrome oxide/aluminum oxide reaction layers which appeared to inhibit further corrosion. Based on these results, a broad list of potential refractory lining materials was compiled, which included the entire family of bonded fused grain chromia-alumina materials (from Harbison Walker), as well as fusion cast aluminas (Carborundum A2, Corhart SR504C), α/β aluminas (Carborundum Monofrax M, Corhart Jargal M), fusion cast chrome oxide containing refractories (Carborundum Monofrax E and K3, and Corhart ER2161), and several fusion cast AZS materials (Carborundum Monofrax S-3, S-4, S-5, and Corhart Unicore I and Unicore 501). This initial list of 14 candidate materials was made as broad as possible in order to select those few materials which would best meet the following requirements:

The chief requirements for the tile performance include:

- High as possible thermal conductivity (5 W/m- C @ 2400 °F (1316 °C)
- Corrosion resistance (<0.0005 in (0.13 mm)/1000 h at 2600 °F(1427 °C) – Illinois #6 coal Slag)
- Emissisvity (> 0.8 without coating @ 2000 °F (1093 °C))
- Elastic Modulus (< 137 GPa @ RT;< 40 GPa @ 2600 °F (1427 °C))

- Strength (> 3,046 psi (21 MPa) @ 2600 °F (1427 °C)
- Creep (< 1% at 1,015 psi (7 MPa) for 10,000 h)
- Tolerate high thermal gradient (50 °F (10 °C)/mm)
- Tile dimensions thin for large surface area (0.98-1.97 in thick x 17.99 in x 19.02 in (2.5-5.0 cm x 45.7 cm x 48.3 cm)

In addition, the material must be manufacturable and affordable (capable to machine in features, i.e., tongue/groove)

The chemical and microstructural composition (phases, grain size, porosity, grain boundary and other impurities) of the refractories have a major impact on their properties. In addition, the methods used to process and manufacture the refractories have a strong effect on their chemical and microstructural features. The refractories which are most likely to meet the requirements contain various combinations of the following constituents: Al_2O_3, MgO, mullite, ZrO_2, zircon, Cr_2O_3, $MgCr_2O_4$ (spinel), Al_2O_3-Cr_2O_3 (solid solution), SiO_2, plus various additives such as SiC and cements.

The choice of corrosion resistant refractories depends on many factors, including the specific slag and conditions of exposure. The results of study at ANL by Greenberg and Poeppel, where 8 different refractory materials were exposed to different liquid slags at 2910 °F (1600 °C) for 24 hours are as follows. The results indicate that the rate of recession of the refractories is strongly dependent upon the refractory type (composition, type of bonding, and hence processing), on the type of slag, on slag flow rate, and on impurities. The most erosion resistant refractory was processed by fusion casting, followed by the high fired, direct-bonded brick. The study concluded that refractory composition by itself is not a satisfactory guide in determining corrosion resistance, and that microstructural, manufacturing process, and other factors must be considered. In the present program, the testing of various types of refractories exposed to specific slags is a crucial part in arriving at the best refractories for application in the radiant heat exchanger panels.

The performance of the refractories is directly related to the choice of raw materials (minerals, oxides, purity, grain size, impurities); processing (forming the right combination of phases by heat treatment-calcining, fusing, etc.) and on the forming of the final refractory microstructures (final balance of phases, grain size distribution, porosity, etc.) and shape.

The fusion cast refractories appear to offer the best resistance to coal slags. Indeed, these refractories are widely used to line glass tank furnaces, and operate for many thousands of hours exposed to flowing glasses. Molten coal slag shares somewhat similar composition and behavior with glasses used for various applications (container, fiberglass, etc.). Some drawbacks of these types of refractories are (1) high cost, and (2) relatively poor thermal shock resistance.

Over 25 refractory materials were considered for the radiant air heater tiles. Not all could be manufactured to the desired size and shape. Those based on silicon ceramics (SiC, Si/SiC, and SiC composites) would be highly desirable because of their high thermal conductivity, and are typically used in heat exchangers. However, at the high

combustion temperatures required for the RAH tile hot face (> 2500°F (1370 °C)), the corrosive activity of the coal slags on these materials would be too great. The results of a previous screening study indicated that fusion-cast refractories would be promising candidate materials for the tiles. Based on these results and further screening tests (strength, thermal conductivity, emissivity, thermal gradients, slag corrosion, etc.), and microstructural examinations led to a family of high alumina and alumina/chrome fusion-cast materials. The measured properties of some of these materials are shown in Exhibit 8-17.

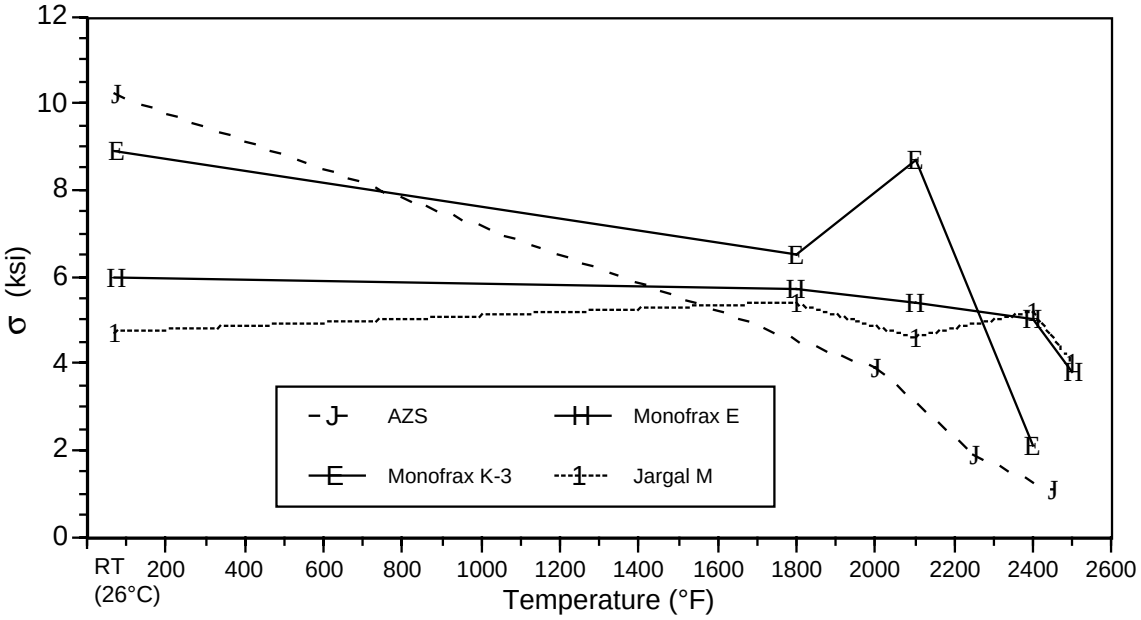

Exhibit 8-17
Four-Point Flexural Strength and Thermal Conductivity of Fusion-Cast Refractory Materials [ASTM C-202] (B).

Four-Point Flexural Testing

Specimens 3 in x 0.65 in x 0.30 in (7.62 cm x 1.65 cm x 0.76 cm) were machined from samples supplied by the vendors. The materials included Jargal M, Monofrax E, Monofrax K-3, and a composition similar to Monofrax S-4. The tests were conducted over a range of temperatures from ambient to 2500 °F (1370 °C). Exhibit 8.17 compares the flexure strength of the 4 materials from room temperature to 2500 °F (1370 °C). While the AZS samples were the strongest at room temperature, they were also the weakest at temperatures above 2400 °F (1316 °C). This was due to a large amount of glassy phase in the composition, which softens at the service temperature in order to accommodate the erratic thermal expansion behavior of the zirconia phase, and which enhances the deformation of the material under load. The Jargal M, which contains 95% Al2O3 is essentially free of glass, and while it was the lowest in strength at room temperature, it retained its strength up to 2500 °F (1370 °C) and was one of the strongest of the 4 materials tested at temperatures above 2400 °F (1316 °C), as shown in Exhibit 8-17 and 8.18. The strength of the chrome/alumina samples, which contain complex

magnesia-chrome-alumina spinel and other phases (Monofrax E and K-3), were intermediate at room temperature. With increasing temperature, the strength of the Monofrax E samples decreased slightly in strength up to 2400 F, while the strength of the high (78%) chrome sample (Monofrax K-3) was greatly reduced at this temperature (Exhibit 8-17). Both of these materials contain a glassy phase; the Monofrax K-3 contains the largest amount of glass (about 5% glass). The load/deflection (calculated stress-strain) curves of the four materials are compared in Exhibit 8-18.

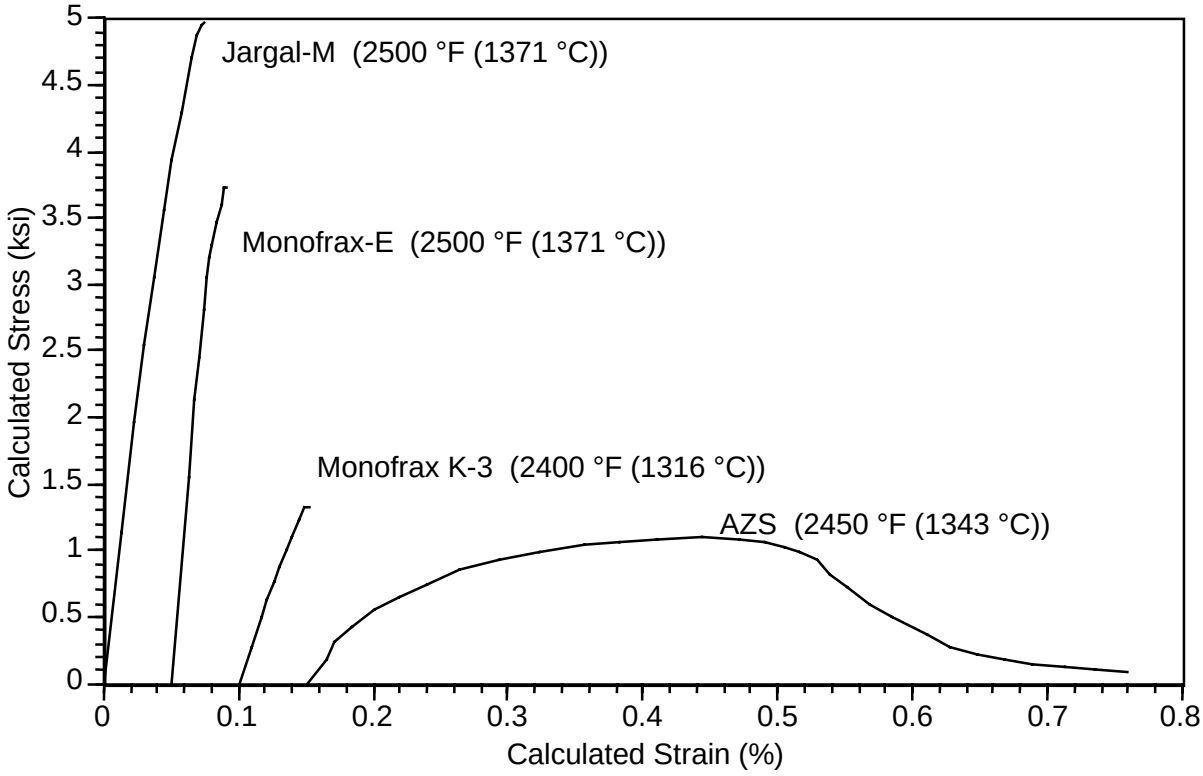

Exhibit 8-18
Comparison Of Calculated Stress-Strain Curves From 4-Point Flexure Tests For Several Refractory Material

Thermal Conductivity Measurements

Since the effectiveness of the design of the refractory lining for the RAH is dependent on accurate values of thermal conductivity, a brief review was conducted on the available thermal conductivity data for the candidate materials and on the measurement techniques used to generate the data. Of the five common methods to measure thermal conductivity, which include: 1) dynamic radial heat flow, 2) laser flash, 3) hot wire, 4) guarded hot plate, and 5) calorimeter; method 5 was considered to be the most reliable. Each of the measurement techniques has certain advantages over the others, but the method for obtaining the most reliable data for thick [>2 in (5.1 cm)] refractory samples with heterogeneous phases and relatively large pores and grain sizes is based on the calorimetric method commonly used for refractory brick (ASTM C201). The available

thermal conductivity data for Jargal M, and Monofrax E, K-3, and S-4 were measured by the laser flash method. it was decided to obtain additional samples of these materials and have the thermal conductivity measured by the calorimeter

Emissivity

There are no available data on the emissivity of the refractory candidates or on the metallic heat exchanger tubes. The emittance measurements of various surfaces at high temperatures will be made using a Thermogage emissometer available at Pratt and Whitney adjacent to UTRC. The test specimen is mounted on a graphite rod connected to a hydraulic actuator. This allows the specimen to be translated rapidly from the center of the black body furnace where it is surrounded by hot walls, to the end of the furnace where the sample surroundings are cool. A radiometer is positioned so that it can view the test specimen at both locations. A broad spectrum radiometer is used to obtain "total normal" emittance, while a narrow spectral band radiometer is used to obtain data in a particular spectral band.

The test procedure is as follows. The sample is brought up to the test temperature and allowed to equilibrate within the black body. The radiometer is positioned to obtain data and a trace on the oscilloscope is triggered. The radiometer is then shuttered (to obtain a zero energy base line). It is then unshuttered, the black body energy measured, and then the specimen is propelled out to the end fast enough that the change in specimen temperature is negligible. The emissivity of the specimen is calculated from the ratio of the energy emitted by the specimen at the end of the tube to the energy emitted by the specimen inside the black body. The refractory ceramics were tested in both "as cast" and machined surface conditions.

Slag Corrosion

Both static and dynamic slag tests were conducted on several of the refractories. The α/β-Al_2O_3 and MgO/Al_2O_3 samples were also tested in a dynamic slag testing facility at the EERC. The results showed that the α/β-Al_2O_3 material was more resistant than the MgO/Al_2O_3 material to corrosion/erosion by a liquid Illinois #6 coal slag after 100 hours at 2732 °F (1500 °C) (0.35 in/100h vs. 0.730 in/100h (0.89 cm/100h vs. 1.854 cm/100h) recession, respectively). However, in a Coal Creek Lignite slag test, the recession of the α/β-Al2O3 material was essentially unchanged, 0.310 in/100h (0.787 cm/100h), while that of the MgO/Al_2O_3 was even less, 0.216 in/100h (0.548 cm/100h). This shows the importance of slag composition as well as temperature on the corrosion resistance of a material to coal slags. The Illinois #6 coal is a bituminous coal with a high Fe content and relatively low Ca content. In contrast, the lignite sample has a relatively low Fe content but a high Ca content.

Static slag tests on Al_2O_3/Cr_2O_3 compositions showed significantly improved corrosion resistance to various coal slags over the alumina materials just described. However, the low thermal conductivity of these materials and possible problems in disposing of the spent material due to chromate leaching were a concern.

For the furnace runs to be conducted in the pilot test facility, it was decided to use the fusion-cast α/β-Al_2O_3 material because of its relatively high thermal conductivity and purity (see Table 8-4). It was commercially available in the sizes required and could be

machined to the desired features and shapes. The design for the tile shapes, dimensions and arrangement in the RAH was aided by detailed thermal and structural analyses performed by the team members.

Table 8-4
Refractory Materials Used in the Radiant Air Heater

Material	Process	RaH Used	Composition
Monofrax M	Fusion-cast*	Tile	α/βAl2O3 (95Al2O3 Na2O)
Aurex 30	Sintered**	Side Rail	Al2O3/30Cr2O3

* Monofrax, Inc. **Harbison Walker Refractories

Corrosion Testing of Refractories

Introduction

In order to determine the relative lifetime of refractories in most industrial applications, various slag tests have been developed. The most common are the cup slag test, drip slag test (American Society for Testing and Materials [ASTM] C 768), gradient slag test, rotary slag test (ASTM C 874), and dip-and-spin test. Among these tests, the cup slag test is the only static test method and the most commonly used, even though it cannot reproduce material erosion conditions or renew the slag charge. Early in the program, the EERC employed the static slag test for initial refractory screening tests. For flowing slag conditions, the rotary test is most often used. Although this test reproduces erosive conditions, the slag charge is still not renewed, so the slag can become saturated with corrosion products. Therefore, under the Combustion 2000 program, the EERC also developed a variation of the drip test that uses a continuous flow of slag to better simulate the mechanisms of slag corrosion and erosion of refractories in a slagging combustion system.

The initial focus of the work was to test the slag corrosion resistance of commercially available refractories and determine the mechanisms of their corrosion. Particular emphasis was placed on castable refractories since they are very inexpensive, although brick refractory blocks used to protect the RAH were also investigated. Once the corrosion mechanisms were determined, the focus shifted to improving the corrosion resistance of the materials, particularly by improving the bond phase between aggregate grains, since bonding phases normally have a lower melting point and lower corrosion resistance than does the bulk of the material. Other tests focused on the use of slag additives to decrease the corrosivity of the slag itself.

Experimental Methods

The easiest slag corrosion test to perform is the static test. In the static test, cubes 2 in. on a side with a 1-in^3 (16 cm^3) hole, or slag cup, in one surface were cast in a mold. After curing, the refractory cube was removed from the mold and fired at up to 2912 °F (1600 °C). Eleven grams of slag was placed into the slag cup and fired at 2732 °F (1500 °C) for 100 hours in air. The blocks were then cross-sectioned vertically through the slag cup, and the depth of slag penetration and surface recession was measured. The depth of slag penetration into the blocks is defined as the maximum depth at which measurable

concentrations of the primary slag constituents of Si, Ca, and Fe are found in the blocks, as determined by elemental mapping using an SEM.

For the dynamic slag corrosion tests, a dynamic slag application furnace (DSAF) was designed and built as part of the EERC work. The DSAF was designed to simulate conditions of dynamic corrosion on the vertical wall of the SFS. It is illustrated in Exhibits 8-19 and 8-20. The DSAF is a 23 in by 23 in (58.42 cm by 58.42 cm) double-chamber furnace, with each chamber gliding on rollers away from the other in the open mode. It has the capability of testing refractory samples up to a maximum of 3092 °F (1700 °C) and is designed to handle up to four test samples simultaneously. It uses eight molybdenum disilicide ($MoSi_2$) heating elements, with a 4 in (10.16 cm) thick insulation wall on the vertical walls and 5 in (12.7 cm) thick insulation wall on the horizontal walls.

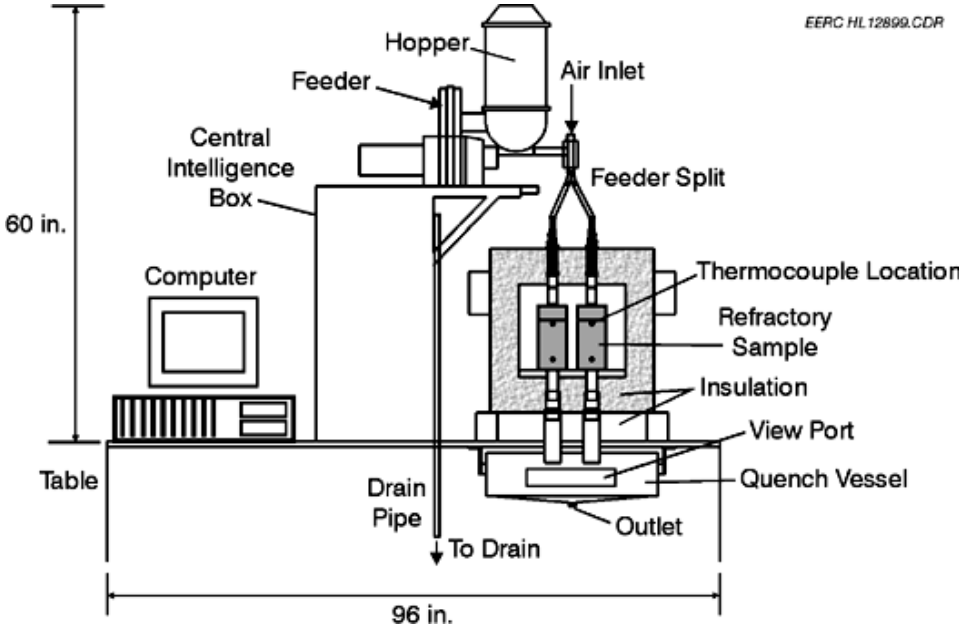

Exhibit 8-19
Schematic of the DSAF

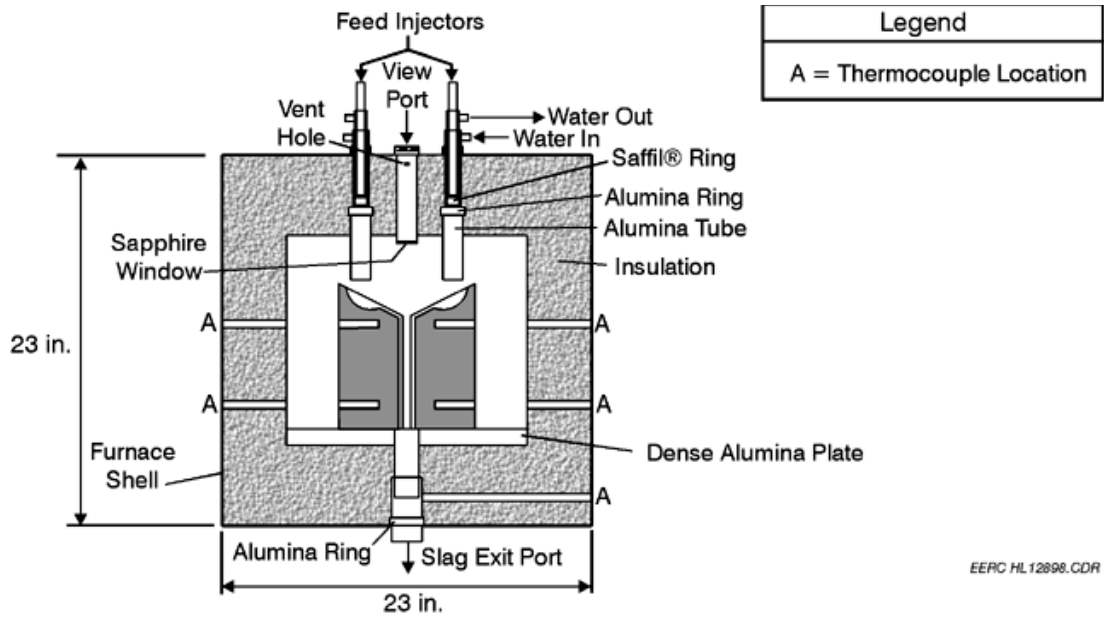

Exhibit 8-20
Schematic of the Inside of the DSAF with Refractory Block in Place

Four slag injector feed ports and two view ports are located on the top of the furnace. Each view port is a 6 in (15.24 cm) long, 99.8% dense, recrystallized alumina ceramic tube with a Vycor™ window at the cold junction and a sapphire window at the high-temperature junction. The injector feed tubes are designed in two stages: a water-cooled stainless steel tubing that goes 22 in (55.88 cm) into the furnace insulation and a 4 in (10.16 cm) alumina tube that hangs 2 in (5.08 cm) into the furnace chamber. Two exit ports for the spent slag are located at the bottom of the furnace. These are made of the same material as the view port. The spent slag exits through ceramic tubes into a water quench vessel.

The Ktron™ feeder is a precise low-rate volumetric feeder with a full hopper agitation made of 316 stainless steel material. The Ktron™ feeder can be controlled by either manual or remote methods. The transfer of the slag granules from the feeder is controlled by a double intermeshing set of augers. At the end of the transfer tube is a custom-designed feeder splitter to perform a 1- to 2- to 4-way split of the slag granules into the four feed injector entry ports, which are connected by high-temperature Tygon™ tubing to the water-cooled stainless steel feed injectors. The feeder is calibrated to deliver a slag area flow rate per unit refractory approximately equal to the maximum flow rate projected for the walls of the SFS. The calculated value was 0.11 lb (51 g) of slag through each feed injector entry port during a 1-hour time period, hence a total of 0.45 lb (204 g) of slag for all four entry ports. The feeder hopper can hold about 50 pounds of slag material (22,680 g), or enough for 100 hours of operation.

An air entry port is located on the top of the splitter, which is connected to the slag feeder. An air flow rate of 0.265 ft^3/hr (125 cm^3/min) is used for each entry port for DSAF experiments. The primary function of the air is to keep the hot air from rising up

through these feed entry ports and, secondly, to cause a positive air pressure for both the slag granules and melt to flow down through the exit ports.

The refractory test blocks are 4 in by 4 in by 9 in (10.16 cm by 10.16 cm by 22.86 cm) tall, with a 30-degree incline on the top surface. On this inclined surface is a well, 13 in by 0.125 in (33.02 cm by 0.318 cm) deep, which is drained by a 2 in (5.08 cm) wide by 3 in (7.62 cm) deep open vertical channel. The blocks are cast in rubber molds, cured, then prefired in the DSAF before the slag is introduced. With this design, for a slag with a viscosity of 100 poise using the feed rate stated above, the slag film thickness during a test is approximately 0.013 in (0.033 cm).

Results and Discussion

A total of five commercial and eight experimental castable refractories have been tested in the program, along with three types of brick materials and several types of additives and coatings. The refractories are listed in Table 8-5 along with the types of tests performed with them. The compositions of the refractories are listed in Table 8-6. The castable refractories have included alumina-bonded silicon carbide (SiC), chrome–alumina, and alumina-based materials. The SiC-based materials are useful to only 2550 °F (1400 °C) because above that temperature they are prone to active oxidation. Although useful to protect a heat exchanger, because in such a case they would be actively cooled, they are not useful as an uncooled material and, therefore, are not discussed in this report. Also, the chrome–alumina castable did show good corrosion resistance at higher temperatures, but because of environmental concerns about leaching of chrome from the spent material, work with these materials was limited, and therefore is also not discussed in this report.

Table 8-5
Refractories and Conditions of Slag Corrosion Tests Performed in This Program

Refractory Name	Firing Temp., °C	Test Temp., °C	Slag	Test Length, hr	Average Depth Recession, in.	Recession/Hour, in./hr
Descon 98	1600	1600	Illinois No. 6	5	0.06	0.01
Castolast G	1600	1600	Illinois No. 6	5	0.3 max *	0.06
Greencast 94	1600	1600	Illinois No. 6	5	0.3 max *	0.06
Hydrecon Tabcast	1600	1500	Illinois No. 6	45	0.2	0.004
(Cr/Al castable)						
Plicast 99	1500	1500	Illinois No. 6	91	0.5	0.005
	1600	1500	Illinois No. 6	63	0.08	0.001
	1625	1500	Coal Creek	4	Block cracked	No measurement
	Unknown	1400	Illinois No. 6	100	0.2	0.002
	1500	1500	Illinois No. 6 + 3%	100	0.2	0.002
+ 1% Y_2O_5	1500	1500	alumina	47	0.2	0.005
			Illinois No. 6			
Plicast 98	1625	1500	Illinois No. 6	103	0.3	0.003
	1500	1500	Illinois No. 6	54	0.6	0.01
	1625	1500	Cordero Rojo	10	0.2	0.02
	Uknown	1400	Illinois No. 6	100	0.1	0.001
w/Mullite Coating	1625	1500	Illinois No. 6	100	0.3	0.003
w/Alumina Coating	1625	1500	Illinois No. 6	90	0.3	0.003
Plicast 96	1600	1600	Illinois No. 6	5	0.1	0.02
	1600	1500	Illinois No. 6	140	0.3	0.002
	1625	1500	Cordero Rojo	10	0.2	0.02
Plicast 90MAV	1625	1500	Illinois No. 6	25	0.2	0.009
	1625	1500	Center (MRY)	25	0.2	0.009
Narcocast 60	1600	1500	Illinois No. 6	50	0.6	0.01
Monofrax L	1500	1500	Illinois No. 6	70	0.8	0.01
(fused cast)	1500	1500	Coal Creek	100	0.2	0.002
Monofrax M	1500	1500	Illinois No. 6	100	0.3	0.003
(fused cast)	1500	1500	Coal Creek	100	0.3	0.003
Kyocera Cr/Al (fused cast)	1500	1500	Illinois No. 6	103	0.09	0.0009
ALCOA	1625	1500	Illinois No. 6	8	0.05	0.006
SFL204AB3	1625	1500	Center (MRY)	10	0.2	0.02
ALCOA	1625	1500	Illinois No. 6	25	0.2	0.008
SFL214AB3	1625	1500	Center (MRY)	25	0.5	0.02
ALCOA	1625	1500	Illinois No. 6	8	0.08	0.01
SFL224AB3	1625	1500	Center (MRY)	10	0.4	0.04
SiC/Al 90/10	unknown	1400	Illinois No. 6	50	0.4 **	0.008

*Max recession value used – slag dissolved a hole through the slag well.
**Vertical channel was full of slag so measurement was done on width of the channel.

Table 8-6
Compositions of the Refractories Tested During the Program

Oxide, wt%:	SiC	Al_2O_3	SiO_2	Fe_2O_3	TiO_2	CaO	MgO	Cr_2O_3	Alkalies	Others
Material Name										
Descon A98	0	97.6	0.2	0.1	Trace	1.9	0.1	0	0.1	0
Castolast G	0	94	0.1	0.1	0	5.6	0.1	0	0.1	0
Greencast 94	0	94.5	0.1	0.2	0	4.5	0.2		0.3	0
Hydrecon	0	88.8	0.1	<0.1	<0.1	1.4	0	9.5	0.2	0
Tabcast										
Plicast 99	0	99.64	<0.1	<0.1	0	<0.1	0	0	0.2	0
Plicast 98	0	98.6	1	0.1	0	0.1	0	0	0.2	0
Plicast 96	0	95.3	3.8	0.1	0	0.1	0	0	0.2	0
Plicast 90 MAV	0	90	0	0	0	0	10*	0	0	0
Narcocast 60	0	62.2	28	1	1.7	2.8	0.1	0	0.2	0
Monofrax L	0	90	0	0	0	0	10	0	0	0
Monofrax M	0	94	1	0	0	0	0	0	4	1
Kyocera Cr/Al	0	88–90	0	0	0	0	0	10–12	0	0
ALCOA	0	100	0	0	0	0	0	0	0	0
SFL204AB										
ALCOA	0	88	0	0	0	0	12*	0	0	0
SFL214AB										
ALCOA	0	71	0	0	0	0	29*	0	0	0
SFL224AB										
SiC/Al 90/10	0	90	10	0	0	0	0	0	0	0

Comparison of Static to Dynamic Results

Exhibit 8-21 shows a comparison of static and dynamic corrosion blocks for three commercially available and one experimental refractory after testing with Illinois No. 6 slag. The static blocks were tested for 100 hr at 3090 °F (1700 °C), the larger dynamic blocks for only 5 hr at 2910 °F (1600 °C). The results for static blocks are typical of all alumina castable refractories tested by this method in that the slag completely soaks into the blocks making it difficult to discern the extent of the corrosion. A close analysis of penetration depth and surface recession indicates that the Plicast 96 was the least resistant to damage during the static tests. However, observation of the dynamic corrosion test blocks made of these same materials and tested in the DSAF with the same slag shows that the Plicast 96 material performed the best of all the commercially available materials. In fact, the other three materials performed so poorly during the dynamic tests that slag did not even build up in the slag well, but instead dissolved rapidly through the block itself.

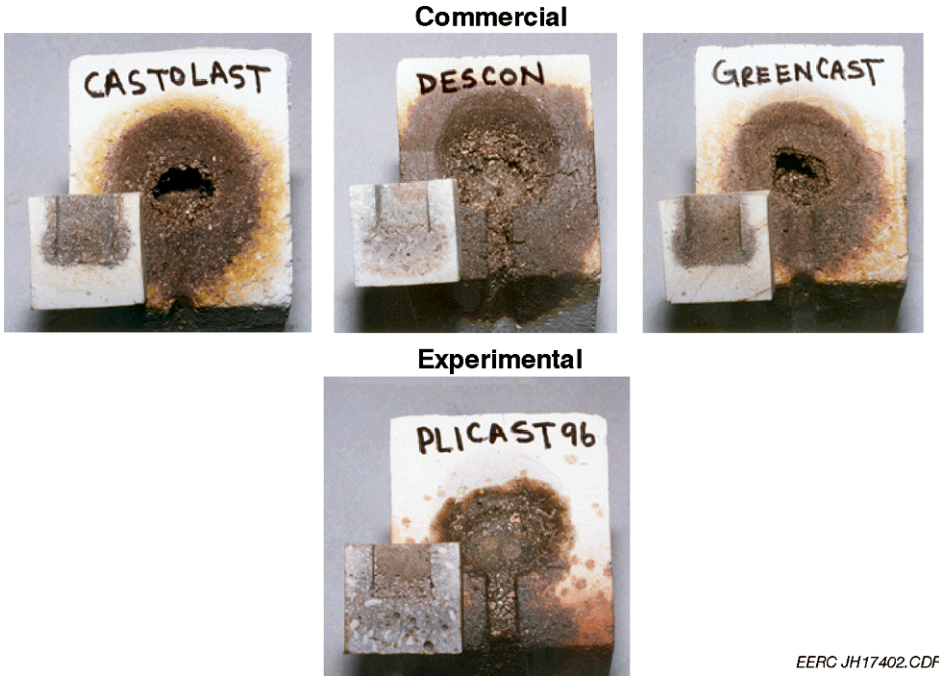

Exhibit 8-21
Comparison of Static and Dynamic Test Results for High-Alumina Castable Refractories

These results indicate that when the slag soaks into the block, the static test is not useful for differentiating between performance of the materials used under conditions involving flowing slag. They also show that higher-alumina-content refractories such as the Plicast 96 survive flowing acid slag corrosion at these temperatures much better than those with lower alumina levels. In addition, SEM analyses showed that the primary attack was against the cement material, not the aggregate. The cement for the three poorly performing materials was calcium aluminate-based, whereas for the Plicast, it is based on hydrated alumina. Other tests have shown that mullite-based cements perform somewhat better than the calcium aluminate cements, but not as well as the alumina-based cements. After these results, static tests were abandoned, as were lower-alumina-content refractories. For most of the ensuing tests, the EERC worked with the manufacturer of the Plicast refractory, Plibrico Company of Chicago, to test several experimental 98% and 99% alumina formulations using Alphabond, a hydrated-alumina cement manufactured by ALCOA.

The Effects of Refractory Temperature

One obvious way to reduce refractory corrosion rates is to reduce the surface temperature of the refractory either by subsurface cooling or by lowering the gas temperature. However, there are capital costs and efficiency penalties incurred in doing this. To determine the relative influence of a small variation in temperature on corrosion rates within the range of temperatures high enough for slag flow, blocks of Plicast 99 were tested with Illinois No. 6 slag at 2550 and 2730 °F (1400 and 1500 °C). It was not possible to test at lower temperatures with this slag because its viscosity was so high at 2550 °F (1400 °C) that it was prone to plugging the slag exit tube. Exhibit 8-22 shows the average surface recession within the flow channel as compared to the length of the test. The graph indicates two things. First, that corrosion rates by flowing slag

are nearly linear, except for a slightly higher initial rate while the excess cement at the surface of the material is dissolved away. In addition, the graph shows that for a 210 °F (100 °C) reduction in temperature, but still within the range of flowing slag, corrosion rates are cut nearly in half for this slag and refractory combination. However, corrosion rates were still too high, extrapolating to approximately 1.3 in (3.302 cm) after 1000 hr.

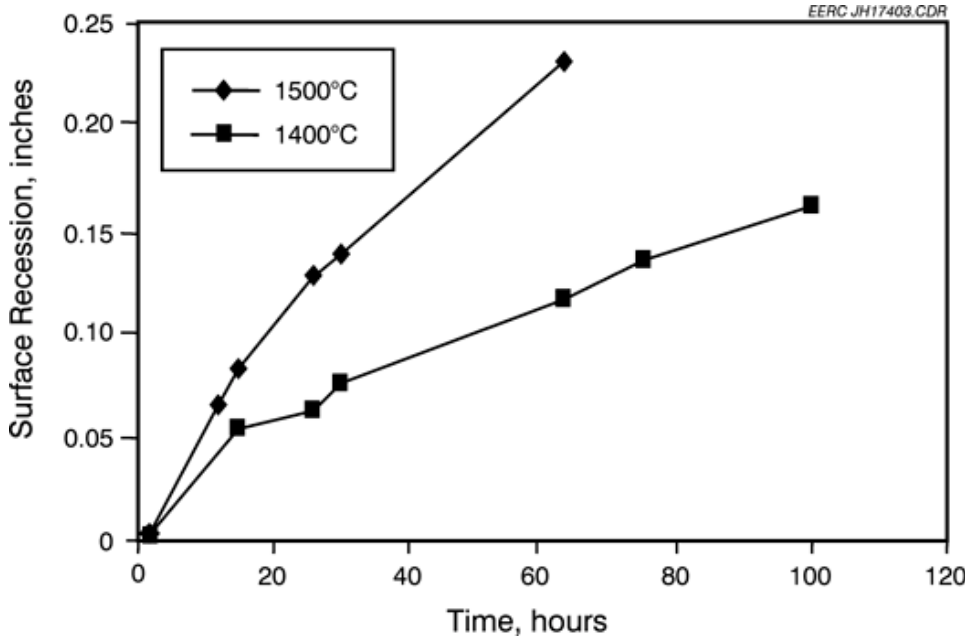

Exhibit 8-22
Corrosion Rate versus Time and Temperature for Plicast 99 Refractory and Illinois No. 6 Slag

The Effects of Coal Type

Tests in the pilot-scale flowing slag combustor system at the EERC have shown that more basic coal slags are much more corrosive to the Plicast refractory than the more acidic bituminous coal slags like the Illinois No. 6 slag. The basic slags are especially corrosive to new patches of refractory. However, older regions of refractory that have been previously exposed to less corrosive slags and fired to higher temperatures for longer times are much less corroded. To determine the effect of firing temperature on corrosion by a basic slag, blocks of the Plicast 99 were fired at 1730 and 2910 °F (1500 and 1600°C) and exposed to flowing slag formed from lignite provided by the Coal Creek Station power plant in North Dakota. Exhibit 8-23 shows the blocks after only short exposures to the slag. Although firing to the higher temperature did reduce corrosion somewhat, in both cases, the lignite slag penetrated the refractory and formed secondary crystallization products that expanded and caused the refractory to burst.

Exhibit 8-23 demonstrates that hydrated alumina is not a suitable binder for refractories exposed to lignitic slags. Therefore, four other refractories provided by Plibrico and ALCOA were tested with slag formed from lignite provided by the Milton R. Young Station (MRYS), North Dakota. Plibrico Plicast 90 MAV contains 10% magnesium–aluminate spinel and 90% alumina. The remaining three are from ALCOA. SFL214AB3 contains 12% magnesium aluminate spinel. SFL224AB3 contains 29% magnesium aluminate spinel. AFL204AB3, an all-

alumina self-flowing castable, is made with Alphabond 300, an experimental cement produced by ALCOA.

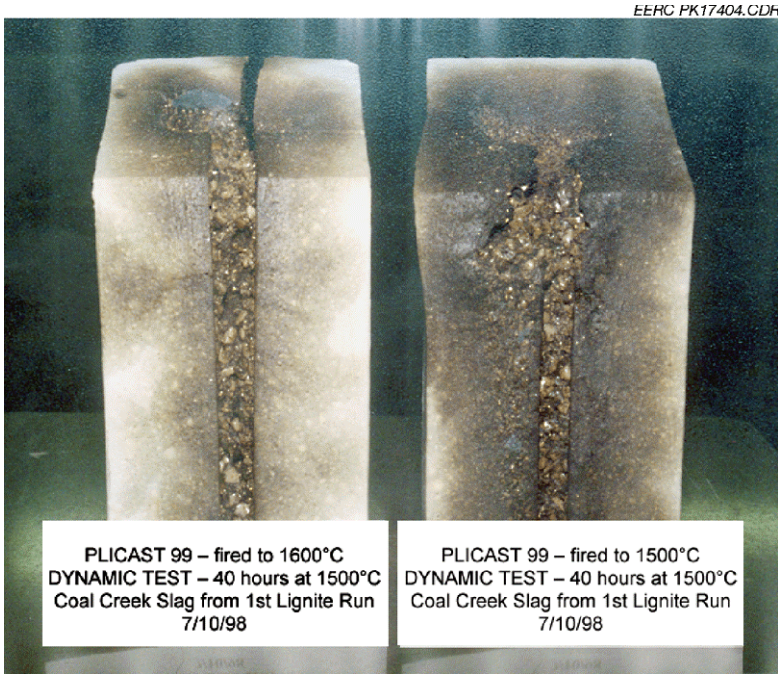

Exhibit 8-23
Blocks of Plicast 99 after Corrosion Testing with Lignitic Slag

The blocks were prefired to 2960 °F (1625°C) then tested at 2730 °F (1500 °C) using MRYS slag. The feed rate was approximately 50 grams per hour per injector. Exhibit 8-24 is a plot of the average measured recession versus time for the four samples. Since the rate of recession was so rapid for all four samples, the tests were stopped early. In contrast to the all-alumina Plibrico castables tested previously, the magnesium–aluminate spinel materials did not swell and crack. However, corrosion rates with the lignite slag are far too rapid even for the experimental samples, so none are recommended for use in a slagging combustion system firing a lignite without using an additive or a coating to reduce slag penetration. Tests were performed on the laboratory scale with a variety of coatings, but none were found to be as effective at preventing slag penetration as just coating the refractory with a less corrosive slag such as occurred in the SFS when firing a bituminous coal.

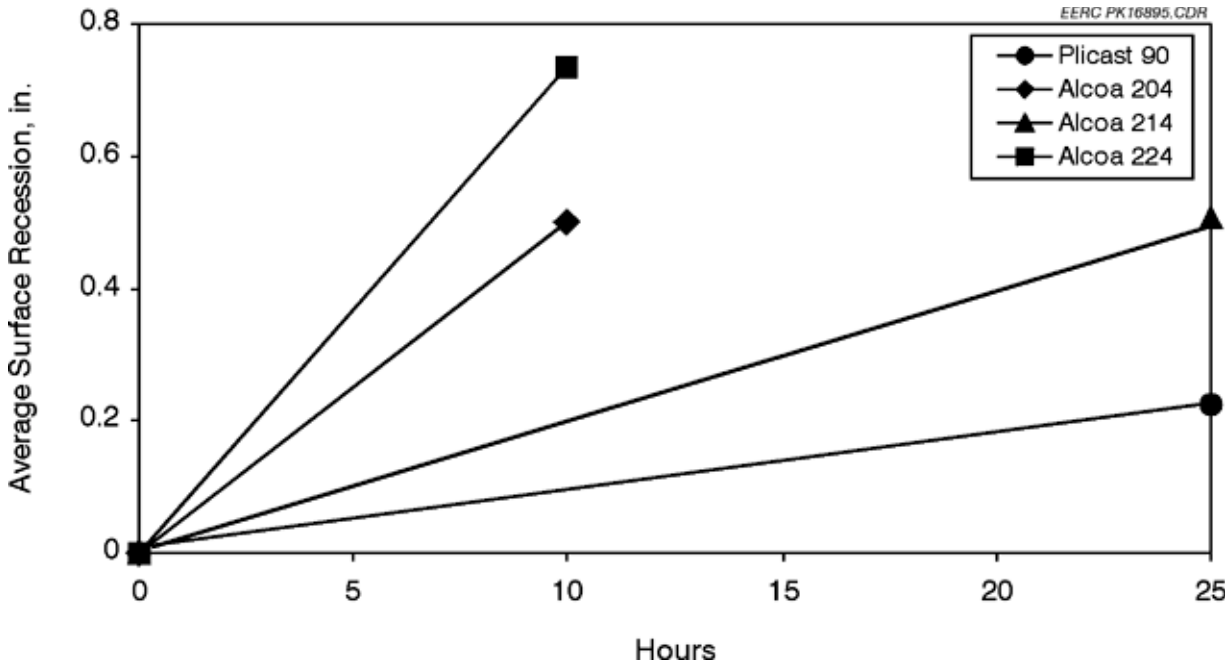

Exhibit 8-24
Plot of Average Recession versus Time for Alumina and Magnesium Aluminate Castable Materials after Dynamic Corrosion Test using MRYS Lignite Slag

The Effects of Refractory Additives

Alumina forms a complete series of crystalline solutions with the lanthanide or rare-earth oxides (REOs). Perovskites, $ReAl_2O_3$, where Re is a rare earth such as Y, La, Nd, Ce, Pr, Pm, Sm, or Eu, and the garnets, $Re_3Al_5O_{12}$, where Re can be Y, Tb, Dy, Er, Tm, Yb, or Lu, are all stable, high-melting-temperature materials. Therefore, yttria, neodymia, and lanthana were mixed in all combinations at proportions of 0.5% and 2.0% with the Plibrico 98 in order to determine if they could increase the corrosion resistance of the refractory to bituminous coal slag. Phase diagrams were used to identify stable high-melting-temperature materials within the lanthanide–alumina series that could modify the bonding phase of the alumina-based refractory. Two mechanisms for reducing corrosion were investigated. One was the formation of corrosion-resistant surface layers. The other was increased sintering to raise strength and seal continuous pores that would reduce slag penetration.

Three different processing methods were employed for fabricating the test samples: bulk mixing, impregnation, and surface coatings. Static cup tests were used initially to determine if the REOs formed corrosion-resistant surface layers that would prevent slag penetration. However, the Illinois No. 6 slag readily penetrated each of the blocks at 2730 °F (1500 °C), although the yttria-doped material showed the least penetration. Exhibit 8-25 shows a yttrium–aluminum–garnet (YAG) phase formed inside the yttrium-doped block. Although it survived the corrosion test, it was discontinuous and did not provide a barrier to penetration of the slag. Tests of pure YAG crystals showed that they were even less resistant to slag corrosion than the base alumina refractory. Therefore, the REO additions were not useful in developing corrosion-resistant layers in the alumina refractory. In addition to the corrosion tests, three-point modulus-of-rupture (MOR) tests were performed using the standard ASTM C 133 procedure to determine

if the addition of an REO improved the strength of the refractory. A strength increase would show that the refractory was more resistant to erosion. However, none of the REO additions increased the strength of the materials, so work with REO additions was dropped.

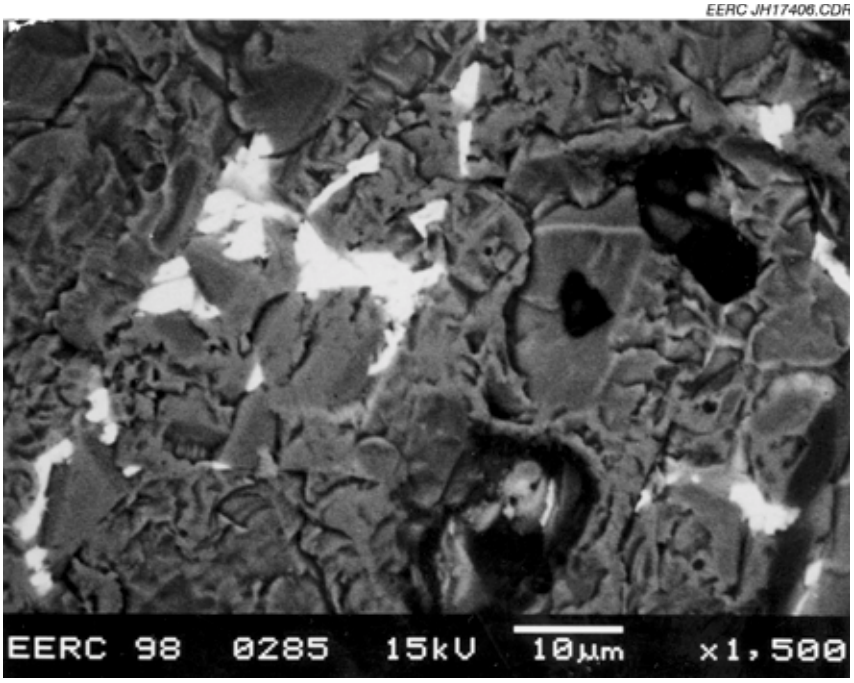

Exhibit 8-25
The Formation of YAG within the Plicast 99 Refractory

Flowing Slag Corrosion of Brick Refractories

In contrast to castable refractories which are fired in place, brick refractories can be prepared under more controlled conditions and fired at higher temperatures than those experienced within the furnace in which they are used. Therefore, brick refractories can be made with the highest possible corrosion resistance, although they are more difficult to deploy and are much more expensive than castable refractories. Three types of brick refractories were tested for resistance to corrosion by flowing slag in this project. They were the Monofrax L, a fusion-cast magnesia–alumina material, Monofrax M which is fusion cast 95% alumina, and Kyocera sintered chromia–alumina. Each of these materials were used to make panels for the front of the RAH to prevent the products of coal combustion from reaching the heat exchanger tubes.

Exhibit 8-26a is a photograph of the Kyocera chromia–alumina block after 103 hr of slag feed. The photograph shows that the surface of the block has very little corrosion and the discoloration caused by slag penetration into the block on either side of the vertical channel is minimal. The erosion of the chromia–alumina block was mainly concentrated at the center, creating a V-shaped channel instead of the usual broad U-shape observed in the Monofrax M block, as shown in Exhibit 8-26b. Exhibit 8-27 compares the measured recession rates for the three types of brick materials due to corrosion by flowing Illinois No. 6 slag. The overall surface recession rate for the Kyocera brick was much lower than that for the Monofrax bricks. Other tests with the castable refractories showed that the 99% alumina castable performed about as well as the Monofrax M material. After 103 hr of slag feed, the chrome-containing block had an

average measured recession of 0.09 in., which is a rate of 0.0009 in./hr. This is a 70% reduction compared with 0.35 in. (0.003 in./hr) for Monofrax M and a 91% reduction compared to the 0.73 in. (0.01 in./hr) after 70 hr for Monofrax L. In addition, because of the difference in corrosion channel shapes, the relative volume loss by the Kyocera material was much less than the ratios of recession depths would indicate. The much more narrow erosion channel for the chromia–alumina bricks should also substantially reduce the formation of slag flow rivulets that focus the slag corrosion of the Monofrax M panels in the SFS. The recession would most likely have been slightly higher for the Kyocera brick at a slag feed rate of 0.11 lb/hr (51 g/hr), but it is still apparent this refractory holds up very well in the presence of flowing slag.

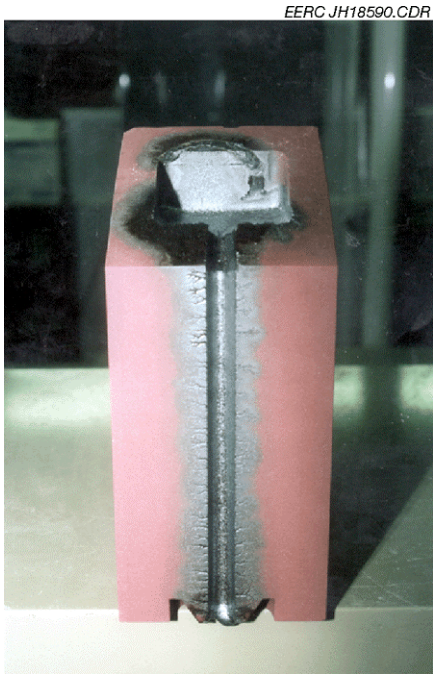

(a)

(b)

Exhibit 8-26
Photographs of Two Brick Materials after Corrosion by Illinois No. 6 Slag at 2730 °F (1500 °C): a) Kyocera Chromia–Alumina Brick after 103 hr; b) Monofrax M Brick after 100 hr

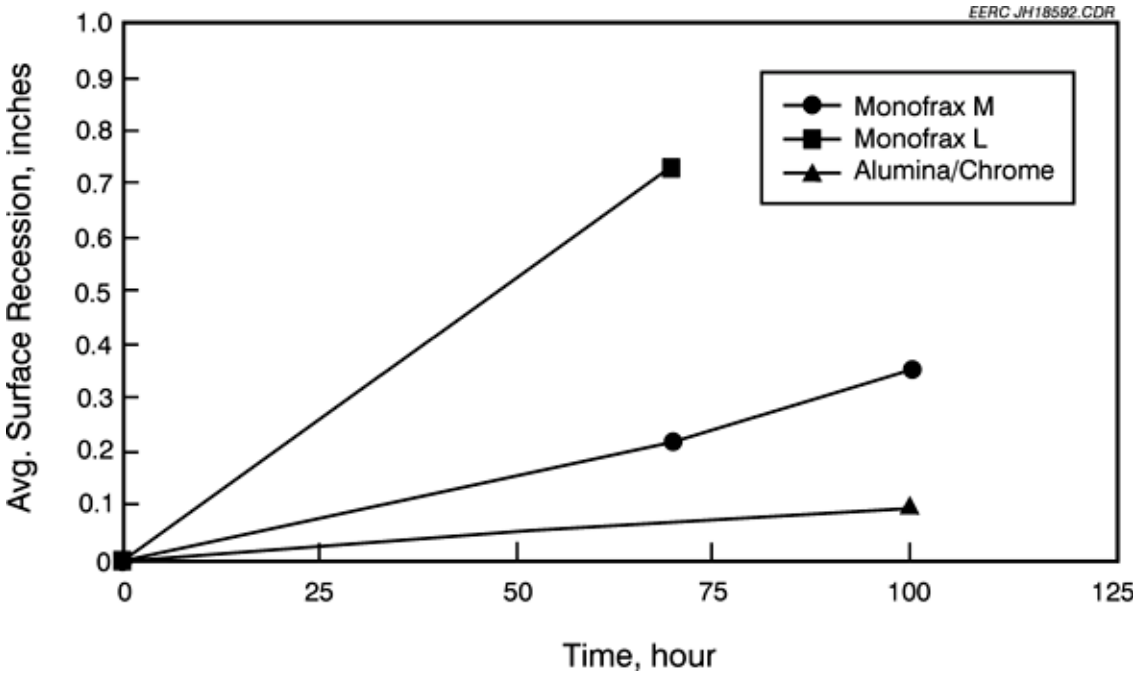

Exhibit 8-27
Surface Recession versus Time for the Brick Refractories Tested with Illinois No. 6 Slag at 2730 °F (1500 °C)

One problem with the use of chromia–alumina refractories is that slag that flows over them may pick up small amounts of chromia which may then leach into groundwater upon disposal of the slag. Therefore, the leachability of the spent slag from the DSAF test was analyzed by the toxicity characteristic leaching procedure (TCLP) EPA Test Method 1311. The leachate contained approximately 5 µg of chrome per liter. The measured value is 3 orders of magnitude below the EPA disposal limit of 5 mg/L and 1 order of magnitude below the drinking water limit of 50 µg/L. Wavelength-dispersive x-ray fluorescence (WDXRF) analyses of the spent slag showed at most 0.07% chromia in the slag that flowed over the Kyocera brick, whereas 0.02% chromia is found in slag that flowed over a 98% alumina-castable brick.

The Effects of Slag Additives

In all DSAF corrosion tests, it was found that surface recession at the bottom of the refractory block was always much less than at the top. Analyses of the spent slags also indicate that the slag is enriched by several percent in the material making up the refractory block. This indicates that as the slag dissolves some of the refractory, it becomes significantly less corrosive. To determine the relative effect of small amounts of additives on slag corrosivity, Plicast 99 blocks were tested at 1500EC with Illinois No. 6 slag with and without 3% alumina added. Exhibit 8-28 illustrates that even with such a small amount of additive, the corrosion rates dropped by a factor of 3. However, preliminary results from tests of the corrosion rates of Plicast 96 and 98 blocks with Illinois No. 6 slag and as much as 10% alumina addition show a much smaller decrease in corrosion rates, most likely because of the higher silica content in the cement used in those refractories. This indicates that the additive must be matched carefully to the composition of the refractory.

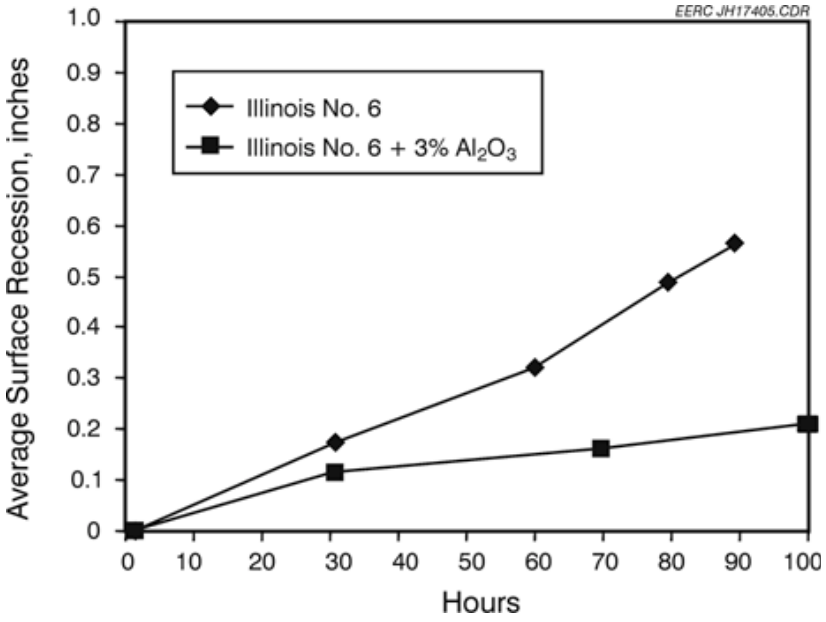

Exhibit 8-28
The Effect of Added Alumina on the Corrosivity of Illinois No. 6 Slag Toward Plicast 99 Refractory

The drop in corrosion rates when using slag additives occurs for two main reasons. The first is that alumina addition to this slag can increase its viscosity substantially. Exhibit 8-29 shows the variation in viscosity as a function of slag temperature for the Illinois No. 6 slag and the Illinois No. 6 slag with 10% alumina addition. The data show that the viscosity increases only slightly at the highest temperature measured 2535 °F (1390 °C). Since slag flow velocity in a thin film varies inversely with the cube root of the viscosity, such an increase would lead to a very minimal slag velocity increase. In addition, only 3% alumina was added to the slag for the corrosion test with the Plibrico 99, so the slight increase in slag viscosity at 2730 °F (1500°C) would not significantly increase either slag erosion due to higher flow rate or corrosion due to decreased transport rate in the boundary layer.

Another mechanism by which the alumina addition may decrease the corrosivity of the slag is simply by increasing its concentration to near that of saturation. As the saturation level is approached, dissolution rates of the 99% alumina refractory would be expected to decrease markedly and should drop to near zero as crystals rich in alumina begin to precipitate. In order to determine at what temperature this crystallization begins and determine the changes in crystallization behavior caused by the alumina addition, heated-stage x-ray diffraction (XRD) was used. With this technique, samples of the slag and slag plus alumina addition were heated on a platinum strip held in the XRD. Measurements of the types of crystals present in the slag were made periodically while the slag was heated to the melting point, then cooled back to room temperature. Unfortunately, because the slag is rich in network-forming elements (silicon, aluminum, and ferric iron), and relatively poor in network-modifying elements (calcium, magnesium, ferrous iron), the slag formed a glass that showed very little crystallization except for hematite upon cooling. However, the measurements did show that alumina-rich phases such as mullite ($Al_4Si_2O_{13}$) and anorthite ($CaAl_2Si_2O_8$) were present in the quenched DSAF slag upon heating, but not upon cooling. This may indicate that cooling the slag on a platinum strip, as is

done in XRD, suppresses crystallization. The suppression may occur because of supercooling made possible by the high network-former content of the slag which causes it to have a high viscosity and the lack of nucleation sites to be found on the platinum strip. This lack of crystallization on cooling rendered the XRD investigation inconclusive as to how the alumina addition reduces the corrosivity of the slag, but we believe that the hypothesis of slag saturation is still correct.

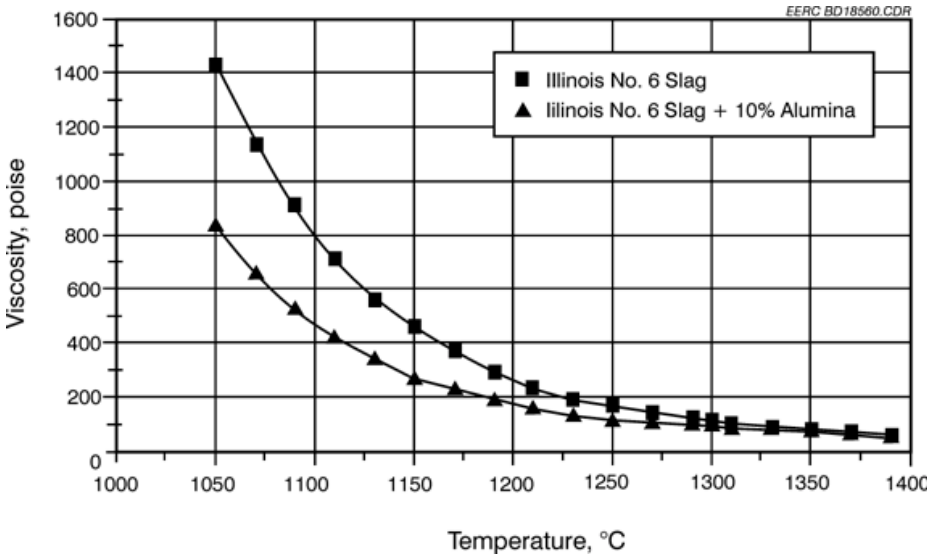

Exhibit 8-29
The Effect of Added Alumina on the Viscosity of Illinois No. 6 Slag as a Function of Temperature

Unlike the bituminous coals, however, lower-rank coals tend to have higher network-former concentrations, in particular calcium, in their slags. This makes the viscosity of the slags lower and allows crystallization to occur more readily. As reported above, these slags tend to be very corrosive towards high-alumina refractories, even causing bursting of the 98% and 99% alumina castables due to the formation of crystals in the pores of the refractory. In order to determine possible slag additives that may reduce the corrosivity of these slags, the crystallization and viscosity-versus-temperature behaviors of one Powder River Basin slag were analyzed. The slag chosen was created during the SFS test performed in March of 2000 with coal from the Cordero Rojo mine, Wyoming. This slag and slag plus additives were analyzed by heated-stage XRD, and measurements were made of the viscosity-versus-temperature curves for the same materials. Exhibit 8-30 shows the viscosity-versus-temperature curves for the Cordero Rojo slag and slag plus 10% of either calcia, alumina, or silica. The data show that this slag has a much lower viscosity and freezing temperature than the Illinois No. 6 data shown in Exhibit 8-29. The Exhibit 8-30 data show that the addition of silica to the Cordero Rojo slag increased its viscosity significantly at temperatures below approximately 2190 °F (1200 °C), but only slightly at higher temperatures. It also caused the slag to begin rapidly freezing at about 120 °F (50 °C) higher than without the silica, although this is not enough to cause the slag to freeze either on the surface or within the inner refractory layer of the SFS which may have reduced corrosion of that layer. In contrast, the alumina had little effect, and the calcia addition had the opposite effect, dropping the temperature at which it rapidly begins freezing by approximately 165 °F (75 °C).

In an attempt to determine if crystallization behavior of the Cordero Rojo slags could explain the viscosity-versus-temperature data shown in Exhibit 8-30, samples were analyzed by heated-stage XRD. Exhibit 8-31 shows the crystallization behavior of the slag and slag plus additives during cooling from a liquid state at 2640 °F (1450 °C). Before these measurements were taken, it was believed that the rapid solidification that occurs in low-rank coal slag during cooling was due to the formation of crystals in the slag. In contrast, the XRD data show that crystals are present in the original slag and slag plus calcia at much higher temperatures than those at which the slag begins to rapidly harden, about 1920 °F (1050 °C), according to the viscosity data. In fact, the slag plus silica sample, which began to harden at the highest temperature, formed no crystalline material until the temperature reached below 1830 °F (1000 °C). This suggests that adding silica, or possibly alumina, to the slag may reduce the formation of crystalline phases during cooling. By reducing the crystal formation, it may be possible to reduce the bursting of high-alumina castable refractories caused by crystallization in the slag that soaks into the refractories.

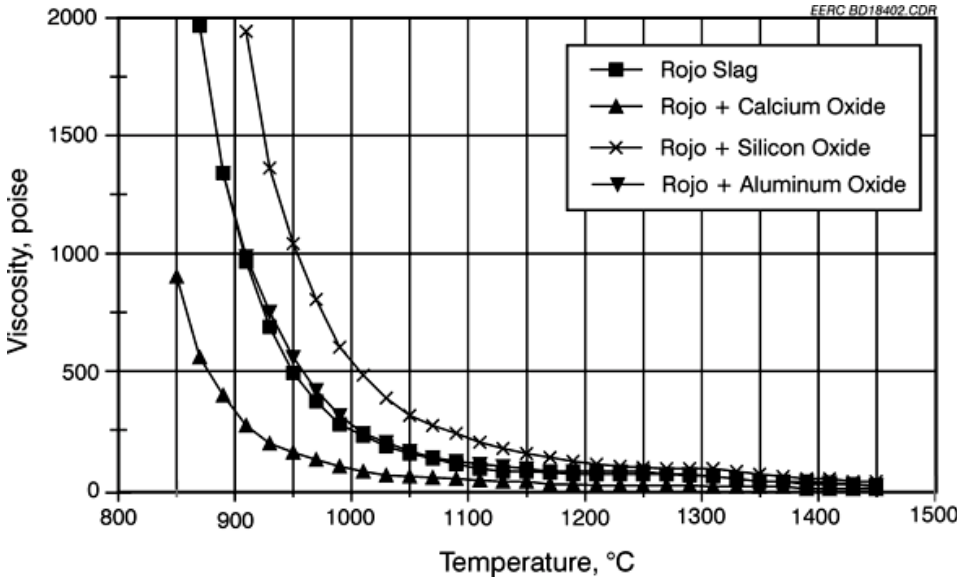

Exhibit 8-30
The Effects of Calcia, Alumina, and Silica Additives on the Viscosity of the Cordero Rojo Slag as a Function of Temperature

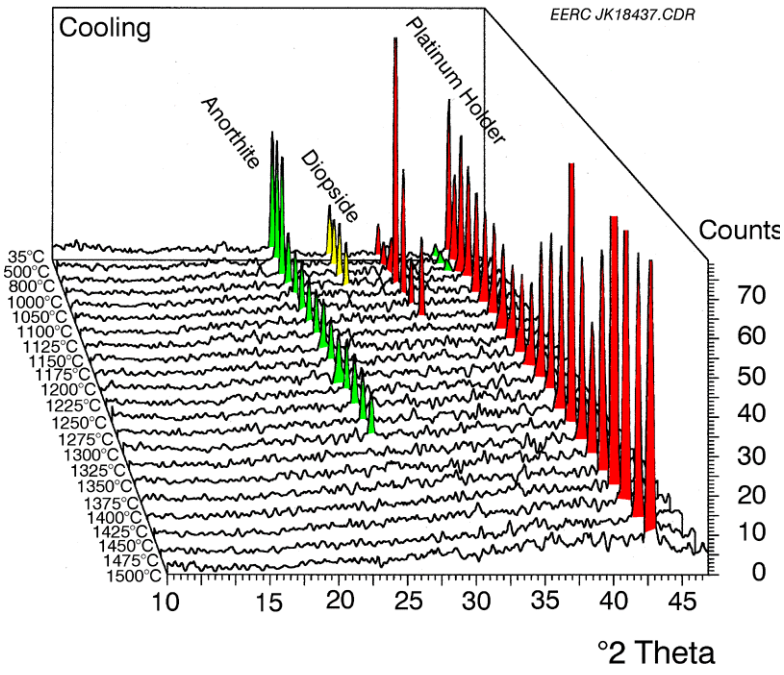

(a)

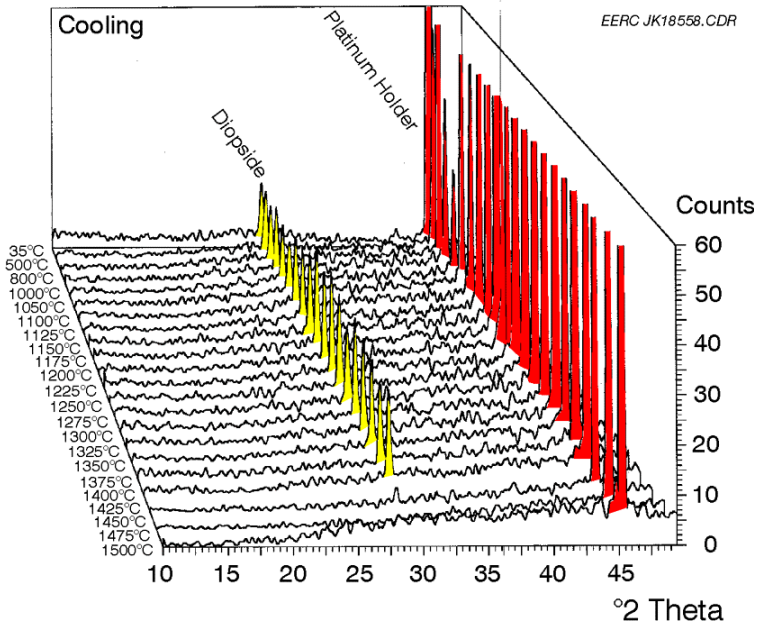

(b)

Exhibit 8-31 (a) and (b)
XRD Analysis of the Crystallization Behavior during Cooling of Cordero Rojo SFS Slag and Slag plus Additives: a) Slag b) Slag plus 10% Calcia

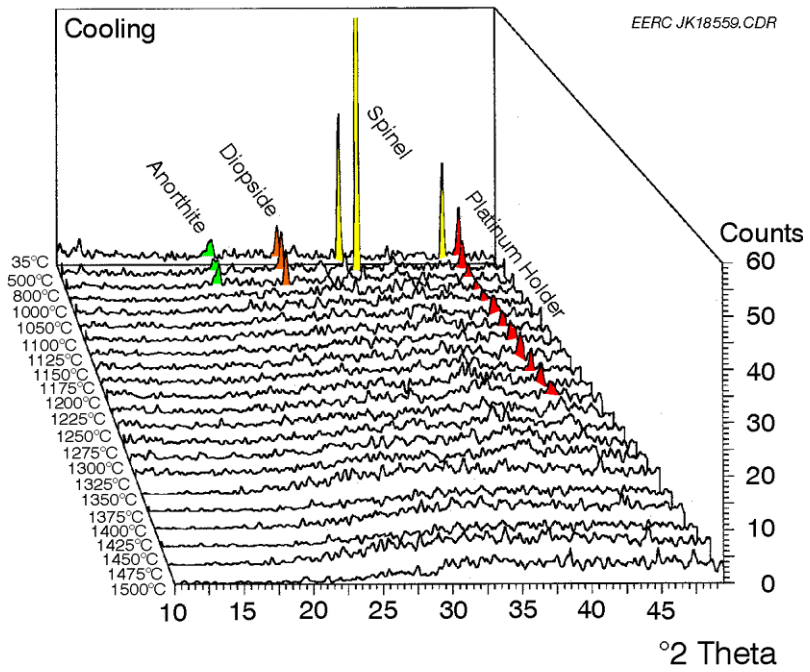

(c)

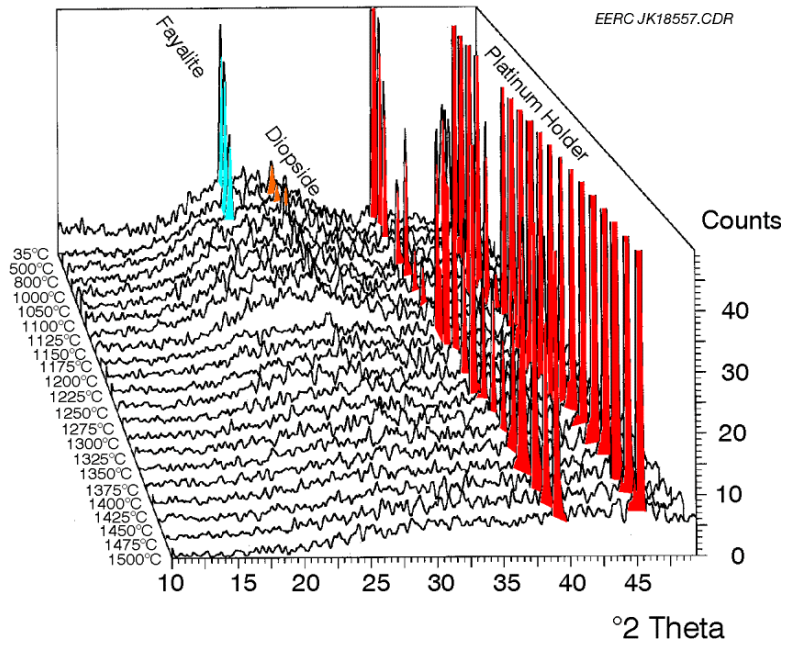

(d)

Exhibit 8-31 (Continued) (c) and (d)
XRD Analysis of the Crystallization Behavior during Cooling of Cordero Rojo SFS Slag and Slag plus Additives: c) Slag plus 10 % Alumina d) Slag plus 10% Silica

Conclusions

Static corrosion tests are poor indicators of refractory performance when the slag fully penetrates into the refractory as it does for castable alumina-based materials. Instead, dynamic tests where the slag flows over the refractory are much more indicative of performance in a large-scale application. At temperatures near 2730 °F (1500 °C), refractories made with alumina-based cements provide acceptable service for pilot-scale testing purposes, whereas calcium aluminate or mullite-based cements do not. However, none of the refractories were acceptable for long-term commercial service. No refractory is universal in performance toward all slags. Alumina–cement refractories perform much better with acidic slags, but are easily penetrated by basic slags and burst through secondary crystallization. Brick refractories had much lower porosity so slag penetration was much reduced, and they performed much better than castable refractories with the basic slags. With an acidic slag, the Plicast 99% alumina castable performed better than the Monofrax L and about as well as the Monofrax M material, but the Kyocera chromia–alumina brick refractory had by far the lowest corrosion rate of all of the materials tested with Illinois No. 6 slag.

Castable alumina refractories with magnesium aluminate spinel additions perform better than pure alumina materials with more basic slags, but still do not provide adequate corrosion resistance even for short-term testing. However, pilot-scale experience indicates that firing the refractory to higher temperatures and, especially, coating it with more benign aluminosilicates substantially increases the lifetime of castable refractories exposed to basic slags at 2730 °F (1500 °C). Rare-earth element additions to 99% alumina castables did not increase corrosion resistance or sintered strength. The most effective means of reducing alumina castable corrosion resistance may be addition of small amounts of alumina to the slag. An Illinois No. 6 slag to which only 3% alumina was added corroded an alumina castable by only one-third as much as the original slag at 2730 °F (1500 °C), although alumina additions did not reduce slag corrosivity nearly as much toward refractories that contained silica in their bonding cement. In addition, alumina or silica additions to low-rank, more basic, slags may help prevent the secondary crystallization that occurs when the slag soaks into castable refractories and which leads to their rapid failure.

Slag Corrosion of MA-754 Alloy

One way to dramatically decrease the size and cost of the RAH and drastically speed the commercialization of the technology would be to operate it without the ceramic panels which are significant impediments to heat transfer and have not yet been perfected in design or composition. Unfortunately, at the high temperatures at which the RAH operates, it has been assumed that the products of coal combustion would be too corrosive to the exposed alloy. However, in previous, separately funded work performed at the EERC, a temperature window was identified in the thermochemical behavior of the products of coal combustion in which it is believed the products may be much less corrosive toward structural materials than normally expected. The window ranges from a low temperature of approximately 2000 °F (1093 °C) to an upper, fuel-dependent temperature of approximately 2300 °F (1260 °C) (Hurley and Benson, 1995). Exhibit 8-32 shows the concentrations of silicon, sulfur, and calcium in ash deposits collected from a utility boiler burning a high-calcium coal as functions of approximate deposit temperature. The data show that above 2000 °F (1090 °C), condensed sulfates are not stable in the ash. Therefore, corrosion of alloy tubes by sulfates should not be significant above this

temperature. Also, below the upper limit of the temperature window, many coal ashes are solid, which makes mass transfer of corrodents to the structural materials relatively slow and allows a corrosion-reducing passive layer of corrosion products to exist. However, at higher temperatures, the slag is molten and readily dissolves the passive layer, leading to more rapid active corrosion. If such a low-corrosion temperature window does exist, then it may be possible to operate the RAH without the protective ceramic tiles between the heat exchanger tubes and the flame.

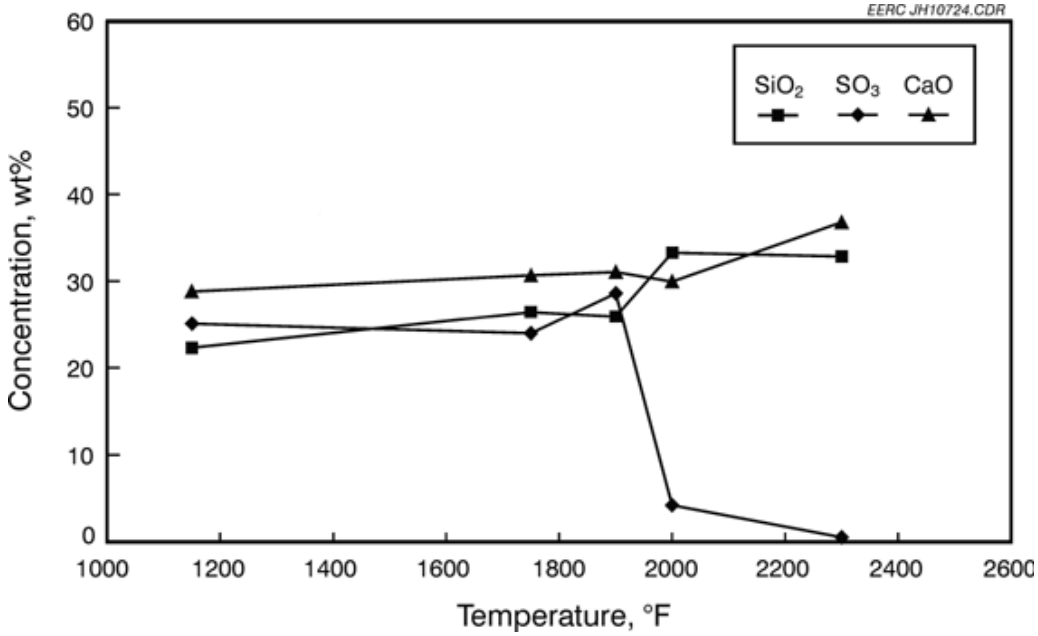

Exhibit 8-32
Temperature-Dependent Composition of Ash Deposits Collected from a Utility Boiler Burning a High-Calcium Wyoming Coal

To determine the overall corrosion rates of the RAH alloy exposed directly to the products of coal combustion and to determine whether corrosion of the alloy is reduced within the temperature window, alloy coupons were corroded under controlled laboratory conditions. The temperatures tested were 2100 °F (1150 °C) and 1830 °F (1000 °C). The higher temperature is approximately that experienced by the alloy tubes in the RAH when producing 2000 °F (1090 °C) pressurized air and is within the proposed low-corrosion temperature window. The lower temperature is approximately that of the tubes when producing 1730 °F (940 °C) air, but is in the range where condensed sulfates would be present on the surface of the tube.

For each test temperature, five coupons of Alloy MA-754 were cut into 1- × 5/8-in. (2.5- × 1.6-cm) coupons and exposed in an enclosed horizontal tube furnace equipped with gas inlet and outlet ports. The coupons were first subjected to 100 hr of oxidation at their respective test temperatures. The coupons for the lower-temperature tests were then covered with 0.6 g of Na_2SO_4 to simulate sulfate condensation and topped with a layer of powdered Illinois No. 6 slag to simulate high-temperature coal ash. The coupons for the higher-temperature test were covered with only the powdered slag. In both cases, the coupons were then heated in the presence of a simulated combustion gas for 500 hr at the test temperatures. The gas was composed of 13% CO_2, 4% O_2, 900 ppm SO_2, 9% water, and a balance of N_2 at a flow rate of 0.5 ft^3/hr (0.2 L/min). Coupons were removed after 100, 200, 350, and 500 hr of exposure for mass loss

calculations. A second coupon exposed for 500 hr was mounted in epoxy with the corrosion and ash layers intact and cross-sectioned for SEM analysis.

Corrosion rates were calculated by mass loss according to American Society for Testing and Materials (ASTM) Procedure G1-88. To perform the procedure, the coupons were sonically cleaned in successive chemical baths to remove corrosion products. The cleaned coupons were then weighed after drying, and mass loss from the original oxidized coupon was determined. From the mass loss, a corrosion rate can then be calculated. The weighing error for these samples should be no more than approximately 2% relative.

A plot of the cumulative corrosion for each temperature is shown in Exhibit 8-33. As the exhibit indicates, the corrosion rates were, in fact, lower at the lower temperature, indicating that sulfate corrosion was not significant for this alloy, although it may be for other, especially iron-based, alloys. However, in both cases, the corrosion rates were very low given the extreme conditions to which the samples were subjected. The cumulative corrosion after 500 hr at the higher temperature was found to be approximately 0.35 mil (9 μm), which suggests a maximum corrosion rate of 6.2 mil/year (157 μm/year). The cumulative corrosion after 500 hr at the lower temperature was found to be approximately 0.17 mil (4.4 μm), which suggests a maximum corrosion rate of 3 mil/year (76.4 μm/year). Although these corrosion rates are low, UTRC found during optical microscope analyses of the alloy coupon tested at 2100 °F (1150 °C) that numerous pores had formed within the alloy during the test by a mechanism that is not yet defined. The depth of the visible pore zone was found to be approximately one-third of the total cross-sectional area. The presence of these pores will adversely affect physical properties such as ductility and creep resistance. Therefore, although the surface recession was low, it was concluded that Alloy MA-754 is not suitable for commercial use at the higher temperature, but may be suitable for use in direct exposure to the products of coal combustion at the lower temperature.

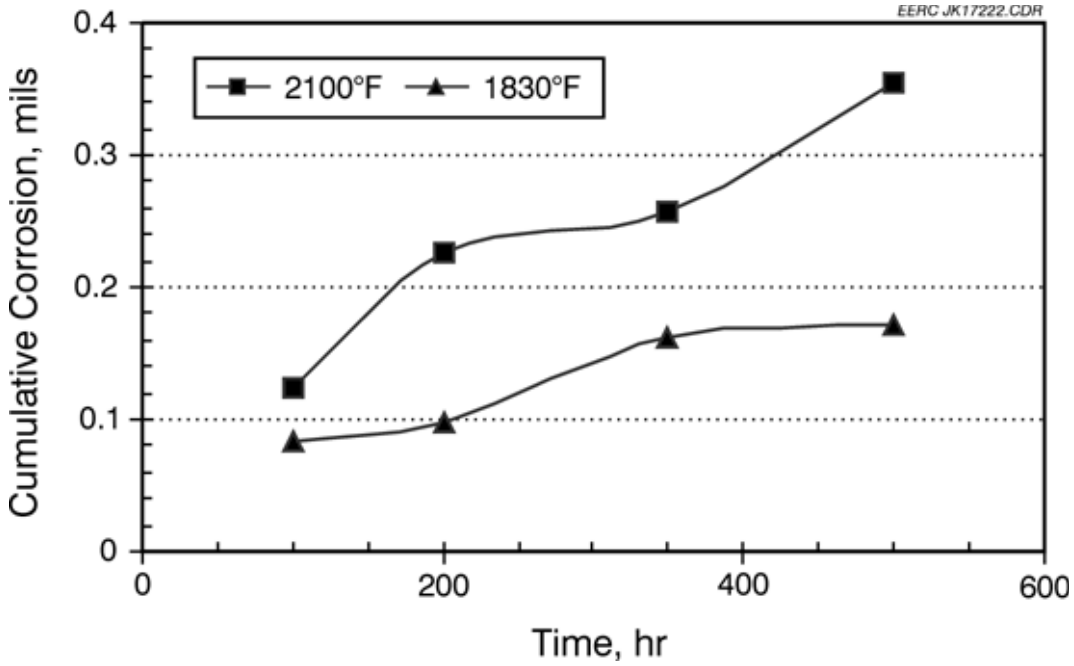

Exhibit 8-33
Cumulative Corrosion of Alloy MA-754 when Exposed to Simulated Coal Combustion Conditions at 1830 °F (1000 °C) and 2100 °F (1150 °C)

In order to better understand corrosion mechanisms, the coupon tested for 500 hr at 1830°F (1000°C) was examined by SEM had a discontinuous, irregular chromium oxide layer at the alloy–ash interface that ranged from approximately 0.02 to 0.15 mil (0.5–4 μm). The formation of small pits could be detected, which extended to a depth of 0.3 to 0.4 mil (8–10 μm). An SEM micrograph is shown in Exhibit 8-34. Evidence of chromium oxidation could be detected throughout the entire thickness of the alloy but was more concentrated in a surface zone 1.3 mil (30 μm) deep. The Illinois No. 6 slag had reacted with the sodium sulfate and formed a sintered, porous layer, which was lightly attached to the alloy surface. Sulfur was barely detectable in the oxidized zones.

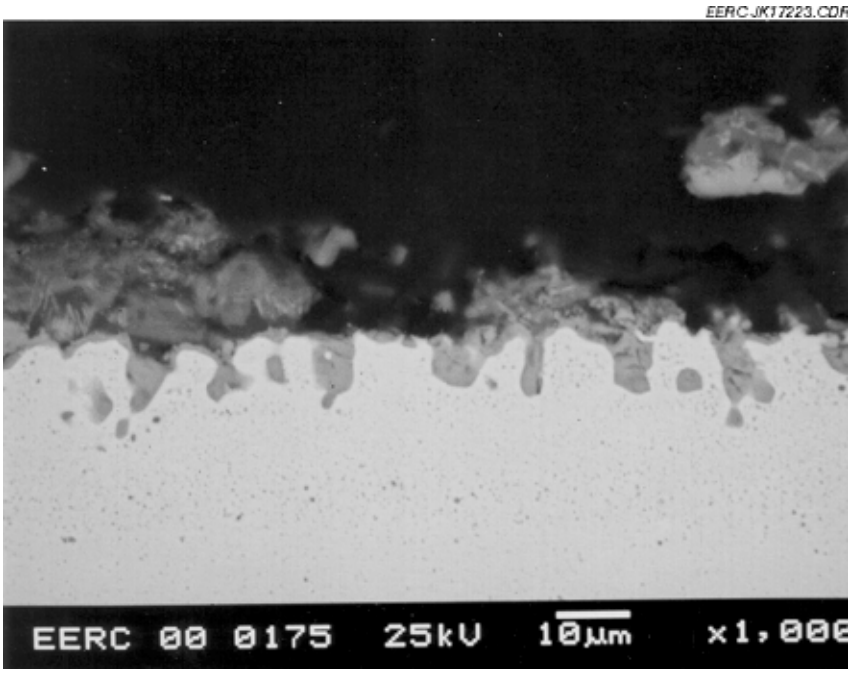

Exhibit 8-34
SEM Photograph of a Cross Section of the MA-754 Alloy when Exposed to Simulated Coal Combustion Conditions at 1830 °F (1000 °C)

Exhibit 8-35, whose field of view is 1.6 mil (41 µm), and Exhibit 8-36, with a field of view of 2.2 mil (55 µm), show x-ray maps generated during the SEM examination of the MA-754 alloy when exposed to simulated coal combustion conditions at 1830 °F (1000 °C). The chromium oxide layer can be clearly seen. Under these conditions, the chromium reacted with iron in the coal ash to form large iron/chromium oxide crystallites in the ash layer. These crystallites can be seen in the SEM micrograph shown in Exhibit 8-37. Above the oxide layer, contained in the slag, crystallites can be clearly seen. The formation of these crystallites was not detected in the alloy sample tested at 2100 °F (1150 °C). Table 8-7 shows the spot analysis of the crystallites, surface oxide layer, and zone of oxidation within the alloy.

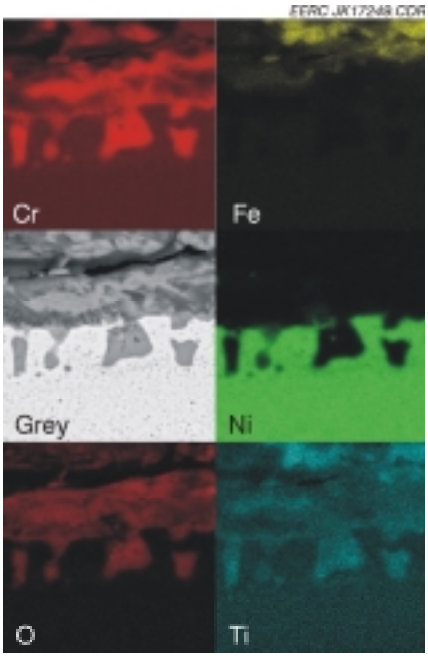

Exhibit 8-35
X-Ray Maps of a Cross Section of the Oxide Layer Formed on the MA-754 Alloy when Exposed to Simulated Coal Combustion Conditions at 1830 °F (1000 °C)

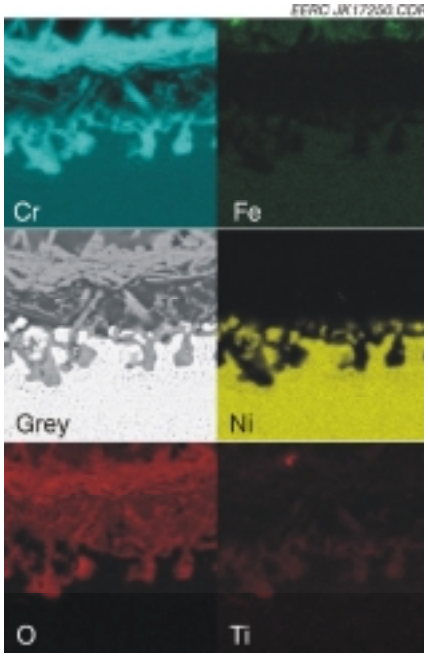

Exhibit 8-36
X-Ray Maps of a Cross Section of Crystallites Formed in the Slag Layer Next to the MA-754 Alloy when Exposed to Simulated Coal Combustion Conditions at 1830 °F (1000 °C)

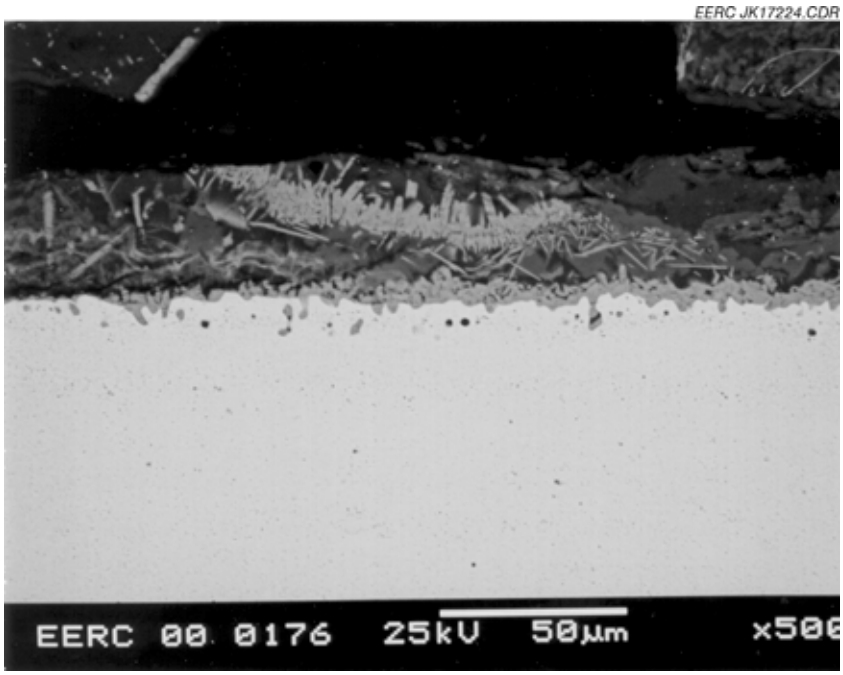

Exhibit 8-37
SEM Photograph of a Cross Section of Crystallites Formed in the Slag Layer next to the MA-754 Alloy when Exposed to Simulated Coal Combustion Conditions at 1830 °F (1000 °C)

Table 8-7
Elemental Concentrations of Oxidation Products, wt%

Element	Crystallites			**Surface Oxide Layer**			Oxidation Zone Within the Alloy		
Cr	5.5	34.5	8.4	73.4	63.2	69.5	64.5	66.0	63.8
O	22.8	22.1	23.3	22.0	18.7	24.8	21.0	23.4	20.0
Fe	52.5	39.3	48.0	0.6	1.0	2.0	<0.1	0.1	<0.1
Ni	0.2	0.2	0.3	0.9	8.7	1.0	11.2	7.3	10.2
Ti	1.3	0.7	2.0	1.5	1.4	1.0	1.7	1.7	2.8
Al	4.4	0.7	4.0	0.2	1.2	0.3	0.7	0.4	2.3
Ca	0.9	0.2	0.7	0.2	0.5	0.3	0.2	0.2	0.1
Nb	ND[1]	0.2	ND	ND	<0.1	<0.1	ND	0.2	ND
Si	8.6	0.9	6.9	0.8	4.5	0.7	<0.1	ND	<0.1
Na	2.6	0.4	4.3	ND	<0.1	<0.1	ND	ND	ND
S	0.2	0.1	<0.1	ND	0.1	<0.1	ND	ND	ND

[1] Not detected.

Although the laboratory tests are useful in determining corrosion mechanisms and relative rates as a function of temperature, they cannot show whether protective layers of slag would form under actual operating conditions. Therefore, a short probe was made by sliding a sleeve of MA 754 alloy tube over an air-cooled stainless steel probe and tested by direct exposure to the coal flame in the SFS while burning Kentucky coal. This exposure simulated conditions that the alloy tubes would experience if the RAH were operated without the ceramic panels in place.

The air-cooled probe was first inserted into the SFS furnace for a short time while firing on gas in order to cure a new layer of high-density refractory. However, the available process air required to control alloy temperature was insufficient, forcing the removal of the probe to avoid overheating the alloy. Changes were made to increase the quantity of process air available to support the probe prior to coal firing. As a result of the changes, it was possible to insert the MA 754 alloy probe into the slagging furnace once coal firing had been stabilized during the test in June 2000. The probe was left in place for nominally 130 hr of coal firing prior to switching to natural gas firing and a controlled furnace cooldown period. Alloy surface temperature (based on a thermocouple measurement) was controlled at nominally 1780 to 2000 °F (970 to 1090 °C) as a function of probe insertion depth and a process air flow rate of 95 to 100 scfm (2.7 to 2.8 m^3/min).

Measurements were made of the corrosion of the cooled MA 754 alloy probe to determine the relative amount of direct slag attack on the alloy surface. Measurements show an average surface recession of approximately 0.0024 in (60 μm)/130 hours, or 0.2 in (4 mm)/year. The end of the probe that was not efficiently cooled had melted, but corrosion was minimal right up to the point where the tube did melt. The slag layer that had formed on the surface of the tube during the test was only approximately 0.06 in (1.5 mm) thick and composed of three layers. A schematic of the layers is shown in Exhibit 8-38. During cooling, the slag layer spalled off of the tube, indicating that it was not intimately bonded to the tube. The innermost layer was sintered and approximately 0.002-0.0098 in (50–250 μm) thick. The fact that it was sintered implies that the ash would be relatively solid; therefore, corrosion of the alloy by this inner layer of ash would be low.

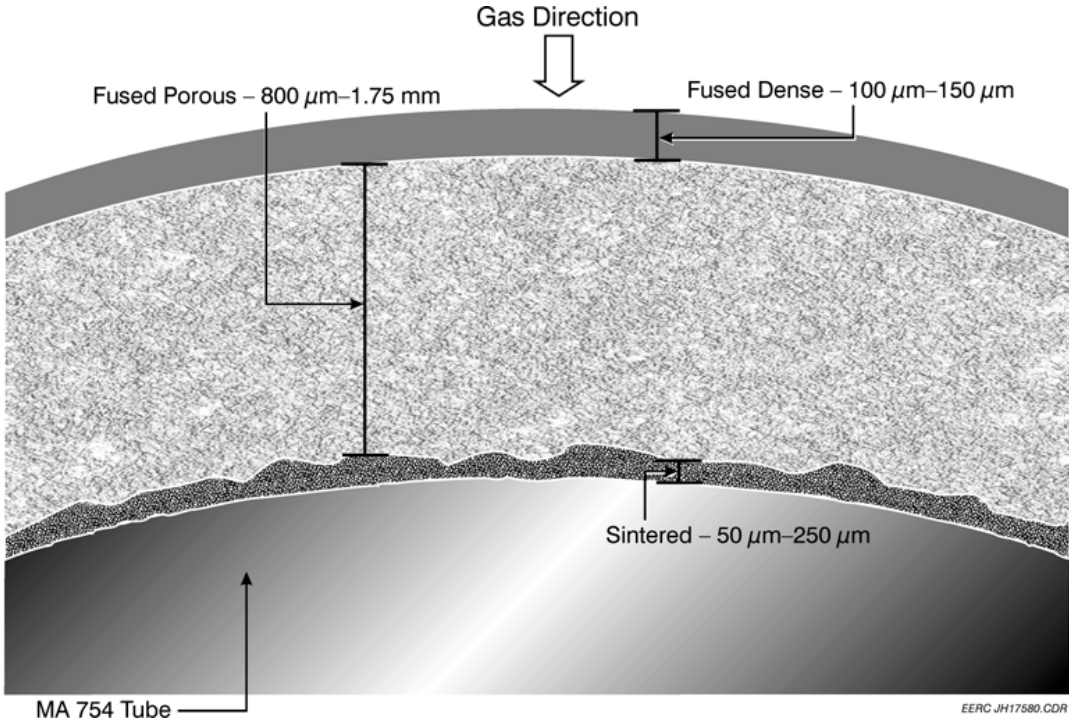

Exhibit 8-38
Schematic of the Slag Layers that Formed on the Cooled MA 754 Probe Exposed Directly to the Coal Flame in the SFS

On top of the sintered layer was a fused but porous layer approximately 0.0315 to 0.0689 in (800 to 1750 μm) thick. The fact that the layer was fused indicates that it would have a high thermal conductivity, but the porous nature indicates that it would not be flowing and so would provide a relatively permanent corrosion protection layer. The outer layer was fused and dense. It was approximately 0.0039 to 0.0059 in (100 to 150μm) thick. Its density indicates that it was likely molten at temperature and would, therefore, be constantly flowing off and replenished during exposure to slagging furnace conditions.

These results are very promising and indicate a protective slag layer would form on cooled alloy tubes exposed directly to the coal flame and that it would not be so thick as to seriously impede heat flow.

References for Slag Corrosion of MA-754 Ally Secion

Hurley, J.P.; Benson, S.A. Ash Deposition at Low Temperatures in Boilers Burning High-Calcium Coals: 1. Problem Definition. *Energy Fuels* **1995**, *9*, 775–781

Section 9 - Ash Management in HITAF

Abstract

The work reported in this section was performed under program task 2.3.1. The ash management aspects of our HIPPS design are complicated by the desire to be compatible with a wide range of US coals typical of current power plant usage. To be generally useful in the US market it was felt that the design should accommodate the full range of bituminous coals not just the Illinois #6 design coal. Our final design is in fact applicable to any solid fuel.

The wide range of coals also means a wide variation in the ash produced in the HITAF. For the high temperature regime the ash will be molten and free flowing. For the design coal, the slag layer will be only about 1mm thick on the furnace walls and the RAH tiles. In the HITAF, about half of the ash will be collected by the slag tap as runoff from the walls and the slag screen. Any ash particles that get past the slag screen will either deposit on the CAH tubes or be collected in the baghouse. All of this collected flyash will then be recycled into the fuel inlet so that all of the ash removed from the HITAF will have passed through the slag tap. This vitrified ash is a commercially viable product and therefore the ash disposal problem is resolved.

Initial sootblowing studies of the dry ash deposits on the CAH tubes indicate that these deposits can be readily removed and collected. A full discussion of the ash management part of the program is given below.

HITAF Overview

Over half the electricity generated in the U.S. is from coal combustion. Coal is burned primarily in pulverized coal (pc)-fired boilers and power is generated by steam turbines. The overall efficiency of state-of-the-art coal-fired power generation is approximately 35 percent. Improvements in thermal efficiency of existing plants will have a negligible impact on overall efficiency. Only minimal reductions in excess air levels and unburned carbon are possible.

The coal constituents that create environmental problems also affect pulverized coal-fired boiler performance and design. The size of the radiant furnace of a pulverized coal-fired boiler is dictated by the need to reduce gas temperatures below some critical level to prevent slagging or fouling and not by the time needed to complete the combustion of coal particles. Fireside deposition of ash, corrosion and erosion have a major impact on the availability of coal-fired power plants and therefore on the cost of power.

At the end of the twentieth century, approximately 50% of the coal-fired power plants that are in use will be 50 years old or older. If coal is to play a major role in the growth in power generation in the current century, four barriers must be overcome:

- The new coal-fired power plant must demonstrate a significant improvement in overall conversion efficiency (coal to bus bar) over existing plants.
- The new coal-fired power plant must satisfy environmental standards that approach those achieved by a gas-fired system.

- The cost of power generated by a new coal-fired power plant must be equivalent to or less than the power generated by a current state-of-the-art coal-fired power plant meeting today's environmental regulations.
- The new coal-fired power plant must have delivery and start-up schedules comparable to a natural gas-fired combined cycle system.

According to DOE, an indirect fired combined cycle using air as the working fluid is a promising concept that is not being vigorously pursued. The primary advantage of this approach is that, provided the working fluid is clean, current state-of-the-art gas turbines are available for turbine inlet temperatures of 2300 °F (1260 °C). If air can be heated to a minimum of 2500 °F (1371 °C) in a coal-fired air heater steam generator, then overall conversion efficiencies of approximately 47 percent are achievable. Since the turbine is available, the component that is needed is an environmentally acceptable coal combustor that can deliver high temperature air and that is at least as reliable as the turbine.

The High Temperature Advanced Furnace (HITAF) concept studied in this program has three operational functions:

1. It must provide for the safe, complete combustion of a wide range of coals with pollutant emissions less than 10% of current New Source Performance Standards.
2. It must raise the temperature of the two working fluids, air and water, to the level required to give an overall efficiency of at least 47%.
3. It must be constructed in such a way that new plants can be brought on line quickly which maintaining the cost of power at its current level.

The HITAF combustor has many features in common with conventional pulverized coal combustors. Yet there are certain key differences that necessitate a careful investigation of the management of ash in the combustor. The combustor would be "J" shaped with low-NO_x burners mounted on the top of the combustion chamber. The combustor would be octagonal through the reburn zone and then changes to a rectangular shape through the dilution and convective heat exchanger sections. The top of the furnace would be lined with refractory. Below this adiabatic section there would be a radiant air heater, composed of panels of alloy material in each of the eight sides. The panels would be covered with refractory. Temperatures would be high enough in the radiant heat transfer section to allow slag to flow down the walls to a wet bottom collector.

Injectors for burnout air and reburning fuel (if needed) would be located in the radiant zone. Vitiated air or turbine exhaust would be used to convey the reburn fuel (finely pulverized coal) into the combustion chamber. A wet ash hopper would be located directly underneath the combustion zone. The wet hopper should be designed as short and fat as possible with a 30-degree slope into the seal box. The hopper would also be equipped with clinker grinders, pumps, water control, and transport conveyor.

At the bottom of the combustion zone, below the radiant panels, the combustion gases would turn 90 degrees to enter the dilution/quench zone. At this point, the cross section of the furnace would changes from octagonal to rectangular. There would be a convergent section before the slag screen to increase the inlet gas velocity to approximately 200 ft/s (61.0m/sec). The

combustion gases would enter the slag screen at approximately 2780 °F (1527 °C). The slag screen would be made of a staggered array of refractory-covered water-cooled metal tubes.

Following the slag screen, dilution would be accomplished through injectors designed to deliver FGR and/or turbine exhaust into the duct at a velocity of 150 ft/s (45.7m/s). Since the gas temperature at the inlet to the dilution zone would still be high (2600 to 2690 °F or 1427 to 1477 °C), the injectors must be protected from build-up of wet slag. The injectors would be designed for removal to clean slag as required. The temperature of the gas exiting the dilution zone would be 2000 °F (1093 °C).

Following the dilution zone, the gas turns and would flow upward through a waterwall section with a cross section of 12.5 ft by 30 ft (3.8m by 9.1m). The waterwall section would be designed to reduce the gas temperature to 1800 °F (982 °C). Wall blowers would be installed to remove the dry ash that accumulates on the walls. A dry ash hopper would be located directly below the waterwall section. The hopper would remove ash that would be blown from the water walls or the convective air heater. The sloped sides of the ash hopper would be lined with waterwall surface. Above the waterwall section would be the SNCR area in which urea would be injected into the gas stream at a location allowing enough residence time for reduction of NO_x prior to the entrance to the convective air heater.

Flue gas would flow upward through the convective air heater at an inlet temperature of 1800 °F (983 °C) and leave at 1235 °F (668 °C). Air would be heated from 730 °F (388 °C) to 1300 °F (705 °C) in a two-pass, cross-counter flow heat exchanger consisting of parallel finned-tube sheets in the direction of hot gas flow. Dry ash accumulation on the convective air heater surface would be controlled by the use of retractable sootblowers. Ash would be directed into the dry ash hopper below.

If the advanced power generation cycle is to be commercially viable then availability of the HITAF is key. It must operate at full capacity, whenever required, for a period between outages that is as least as long as the gas turbine. Availability is a major factor in the cost of power therefore the HITAF must be reliable. The design must prevent problems from occurring because of the nature of the ash. Problems due to slagging, fouling, erosion and corrosion must be prevented either by controlling combustor conditions or the choice of appropriate materials. Also the HITAF must be perceived as a low risk device by the utility industry.

Deposition, corrosion, and erosion problems can only be avoided if careful consideration is paid to ash management issues throughout all stages of the system design and development. This is in contrast to traditional pulverized coal combustors, where the essential fundamentals of ash formation and deposition are not considered in design or frequently in operation. As part of the team led by UTRC, Physical Sciences, Inc. (PSI) had the charter of designing strategies for operation of the HITAF that minimize ash-related problems and provide superior control of the HITAF in order to maintain high availability and lower costs.

Impact of Coal on Operation

The choice of coal has a profound impact on the ash behavior during operation of the HITAF. The important coal characteristics, ash content and ash composition, control the operation of many of the in-situ particle removal devices and directly affect the heat transfer efficiency in the unit. For example, coals with a high viscosity ash may affect heat transfer in the

radiant zone by forming thick deposits on the walls. In some extreme cases the slag may freeze, causing a severe decrease in the heat transfer efficiency. Coals with lower viscosity, stickier ash (e.g., many Powder River Basin (PRB) coals) form much thinner flowing layers on the radiant zone walls, resulting in better heat transfer.

The ash viscosity is important in defining such operational parameters as the slag layer thickness on the radiant heater walls, and the maximum allowable temperature for the convective air heater. For example, the low viscosity Wyodak ash was calculated to form a very thin flowing slag layer on the radiant heater walls. For the higher viscosity Illinois No. 6 ash this thickness was approximately 0.22 in (0.56 cm) - resulting in a lower heat transfer efficiency (see the Section on the Slag Properties in the Radiant Zone). The ash viscosity also plays an important role in keeping the slag screen clear, since ash must flow freely from the slag screen into a slag tap.

The composition of the ash, particularly for the more fluid types of ash, determines the degree of corrosion of refractory surfaces. While ease of flow is beneficial for keeping heat transfer and slag screen surfaces clear, the increased corrosion that comes at the high temperatures needed to keep slag fluid can be very detrimental to operation.

Low viscosity ash may be desirable for operation of the radiant zone, but lower viscosity ash particles can form hard to remove, sintered, deposits in the dilution/quench and convective zones. The maximum allowable temperature for the surface of the convective air heater is defined as the temperature where significant sintering of the deposit occurs, resulting in difficult to remove deposits and decreased heat transfer (Table 9-1). Calculation of the maximum flue gas temperature is based on heat transfer considerations and the result was a temperature near 1800 °F (982 °C) (see the Section on Convective Air Heaters for details of this calculation).

Table 9-1
Maximum Deposit Surface Temperature in the Convective Air Heater Based on Sintering Criterion

Coal	Temperature °F (°C)
Illinois No. 6	1665 (902)
Wyodak	1385 (752)

The coal choice also plays a major role in the production of fine ash particles in the HITAF system. Due to the high temperatures required in the radiant zone for efficient radiative heat transfer, vaporization of many ash species may occur at higher rates than in conventional units. Vaporization of ash species from coal has been demonstrated at high particle temperatures. These vaporized ash species can then nucleate and condense, creating an increased loading of fine particles as compared to conventional units. Bituminous coals burned at particle temperatures typical of pulverized coal-fired power plants produce a submicron ash consisting of 0.9 to 1.7% of the total ash. This fume consists of primarily silicate with very little aluminum. Other constituents were FeO, MgO, K_2O, and Na_2O. Sub-bituminous coals burned generally have 1 to 3% of the ash in the submicron fume. In this case the fume consists of primarily MgO and Na_2O with minor amounts of SiO_2, FeO, CaO.

The results of previous laboratory experiments conducted using particle temperatures higher than those expected in pc-fired boilers show that amount of ash vaporized increases significantly as the particle temperature is increased. For example, increasing the particle temperature of Montana lignite from 3100 to 3500 °F (1704 to 1927 °C) resulted in an increase in the amount of ash vaporized, from 3% of total ash at the lower temperature to 10% at the higher temperature. As the submicron fume represents the particulate most likely to escape the control devices, it is important to address the issue of increased fume formation in the proposed design.

Ash Removal

Overview

A major component of any coal combustor design is the management of ash generated during combustion. The innovative HITAF design requires new solutions to the problems of removing ash while maintaining high availability. The HITAF is a down-fired, slagging combustor with radiant air heater surface integrated into the furnace walls and convective air heater surface located in the flow downstream of the radiant zone. Ash must be removed from the HITAF to maintain high heat transfer rates and low pressure drop.

In the current HITAF design several of the HITAF components act as in-situ particle collection devices. For example, approximately 1 to 2% of the ash is collected by turbulent diffusion on the walls of the radiant zone. This ash is molten and flows down the walls to a slag tap at the bottom of the furnace. The ash laden flue gas then passes through a slag screen where inertial impaction on the slag screen tubes removes approximately 50 to 60% of the molten ash. This ash also flows into the slag tap for removal. Additional ash deposits in the convective air heater by a combination of inertial impaction on the leading edge and particle diffusion to the heater surface. After the deposits are removed by sootblowing, the remaining ash is removed from the furnace by either a dry ash hopper or the baghouse.

As previously stated, the coal-fired high-temperature slagging furnace is expected to produce a fly ash having a smaller overall particle-size distribution than that typically found in today's commercial utility boiler systems (pulverized coal- and cyclone-fired). A smaller particle-size distribution is anticipated because of the higher furnace temperatures resulting in greater volatilization of ash species. Because the HITAF is a slagging furnace with a slag screen and a quench zone upstream of the convective air heater, a reduction in the overall fly ash loading in the flue gas stream after the convective air heater is also anticipated. Therefore, the particulate control device is expected to see a lower ash loading than currently experienced in utility systems, and the particle-size distribution is expected to be smaller, requiring a higher level of performance than that typically demanded of today's commercially available technology.

Fly ash particle sizes have been observed to range from 0.01 to 100 microns in conventional industrial and utility systems. Depending on system and fuel characteristics, mass mean diameters of 10 to 15 microns are typically observed. In order to meet the 0.003 lb/MM Btu ($1.36 g/10^6$ kJ) particulate emission limit stated as a goal in the program, effective control fine particulate emissions (particles <10 microns) will be very important.

The preliminary design work performed during Phase I suggested two major technical risks in the HITAF design. These risks are primarily caused by the criterion that the radiant section operate 'wet' - that is ash depositing on the radiant heater walls be molten and flow into the slag

tap. Experience has shown that molten slag can be extremely corrosive to conventional furnace refractory linings. Therefore, a better understanding of slag corrosiveness is necessary for optimum selection of the protective refractory. In addition the slag state, solid or liquid, and thickness have a profound effect on the heat transfer characteristics of the radiant section and the slag removal in the slag screen. Therefore it is important to ensure that either the slag continues to flow easily, forming layers of minimal thickness on the walls, under all operating conditions or preventative steps have been taken to minimize the effects of ash freezing.

As can be seen in the previous sections, the preliminary design work performed during Phase I illustrated several critical technical issues that were addressed in Phase II as follows

Slag properties in the radiant zone

Refractory corrosion in the radiant zone

Slag screen operation

Convective air heater cleaning

Convective air heater corrosion

Many of these issues are related the effect of molten slag and dry ash deposition on the operation and lifetime of the HITAF components. For example, molten slag can cause corrosion and reduced heat transfer in the radiant zone.

Slag Properties in the Radiant Zone

As mentioned above, experience in conventional power plants has shown that the physical state of the ash/slag dramatically effects heat transfer in the boiler. In the current HITAF design both the radiant zone and the slag screen are designed to operate under molten slag conditions. However, in the event that the gas temperatures in these sections cool below the critical point for slag to flow, provisions must be made to ensure that catastrophic loss in heat transfer efficiency does not occur. For example, during load following or furnace shut down the heat input into the furnace may drop below that required to maintain the molten slag layer. When this occurs, the slag layer on the radiant heater walls will freeze. Additional deposition on the walls will increase the ash layer thickness, and decrease the heat transfer to the working fluid with potentially catastrophic results.

Therefore, the design must include features to prevent freezing of the slag layer or operating procedures to manage the impact of a frozen slag layer. One possibility is the inclusion of small natural gas jets along the radiant heater walls and at the bottom of the furnace, in the slag tap. Under conditions where slag freezing may occur these jets may be enabled to ensure that the slag layer remains molten. As an added preventative measure, sootblowers may be required in the slag screen for deposit removal under dry ash conditions. This area will require additional work to minimize the risk associated with operating the HITAF under dry ash conditions by identifying combinations of operating conditions and coals which cause unacceptable freezing in the radiant zone.

In the case of a coal which does cause unacceptable freezing in the radiant zone, it may be desirable to control this thickness and the temperature at which the slag freezes to assure minimum slag corrosion rates, tapping problems, and deposition in the convective pass. Increasing slag viscosity may provide a means to protect the ceramic surface. In an oxidizing

atmosphere, a thin layer of SiO_2 forms on the surface of SiC and Al_2O_3 on aluminide alloys. The oxide layers can act as protective coatings to reduce corrosion rates by slowing the transport of oxygen to the underlying material unless it dissolves into the slag, leaving the material exposed directly to the slag. Since both SiC and aluminide alloys are non-oxides, they are not expected to be wetted well by the slag, and corrosion rates will depend on the rate of transport of directly corroding species. The preferred surface, oxide or non-oxide, is the one that dissolves most slowly.

The formation of the oxide layer depends on the partial pressure of oxygen at the ceramic surface; this can be influenced by the thickness of the slag layer (Ferber, 1984). A viscous slag layer would not allow rapid oxygen penetration to the ceramic surface because:

- it would form a deeper layer through which the oxygen must diffuse and,
- the diffusion rate is lower as a result of the relatively high concentration of bridging oxygen in a more viscous melt.

Also, the diffusion rates of corrosive ions such as iron to the SiC or calcium or magnesium to the aluminide (ASM Handbook, 1992) surfaces are much slower in a slag with higher viscosity and levels of bridging oxygen. Therefore, increasing slag viscosity next to the HITAF surface seems to be a plausible method to reduce slag corrosiveness as long as the amount of increase is tempered with other concerns such as slag tap operation.

The viscosity of a coal slag depends on the degree of oxygen bridging, molecular clustering, and crystal formation in the melt. These factors are in turn determined by the temperature and composition of the melt, as well as the gas stream composition. During HITAF operation with basalt, the gas temperature and composition are expected to be relatively fixed by burnout and efficiency requirements, although excursions for slag control will be possible. In addition, a great deal of flexibility is possible in slag composition by using blends of coals and possibly through the addition of small levels of naturally occurring nonfuel materials. Most important will be the ability to predict slag viscosity and corrosion rates as functions of gas composition, temperature, and slag composition.

Previous research at the EERC by Kalmanovitch and Frank (Kalmanovitch, 1990), and at Penn State by Jung and Schobert (Jung, 1992) has led to the development of methods to predict slag viscosity with good accuracy based on slag composition and temperature as long as the slag is fully liquid. However, equations for predicting the actual temperature of freezing are in the development stage, so freezing temperatures are still best determined by a combination of calculation of slag composition on better developed ash formation and deposition models, then measurement of the freezing temperatures by laboratory methods. Using these techniques, the EERC has shown that the freezing temperature of slags formed from PRB coals can be increased by over 390 °F (217 °C) by adding naturally occurring materials at rates of 2% on a coal weight basis (McCollor, 1994). Doing this during HITAF operation would cause a slag layer to be frozen next to the radiant heat exchanger surfaces, dramatically reducing slag corrosion.

As previously mentioned, the slag characteristics in the radiant zone greatly affect the heat transfer and ash removal. Slag/ash viscosity, for example, controls both the sticking probability and the flow characteristics of the slag. The thermal conductivity controls heat transfer to the working fluid. In the HITAF system these parameters are coupled to control the overall effectiveness of the slag screen. The viscosity of the slag controls the thickness of the flowing

slag layer, and the ease at which slag flows to the slag tap and is removed. The thermal conductivity controls, in part, the thickness of the frozen slag layer next to the refractory tubes and the heat transfer through the entire slag layer. Therefore, the combination of the two characteristics defines the ease of operation of the HITAF for given coal characteristics and operating conditions.

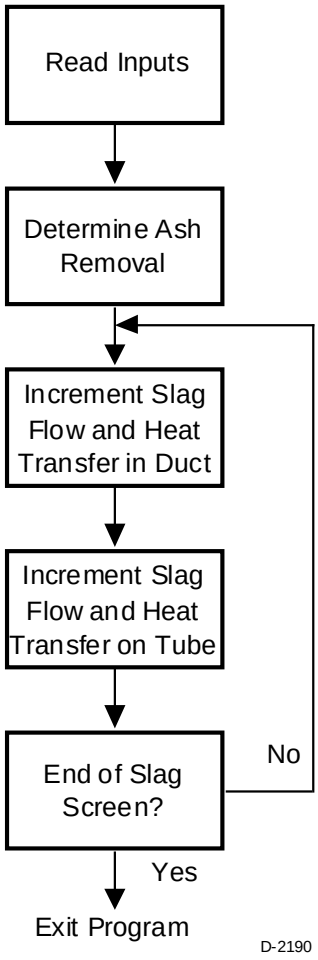

Exhibit 9-1
Components of Slag Screen Simulation Model

Slag Screen

Slag Screen Simulation Model

An overview of the slag screen model is shown in Exhibit 9-1. As can be seen from this figure, the model consists of three major components; mass collection on the tubes, slag flow and heat transfer in the duct, and slag flow and heat transfer on the tubes. By using these three components in an iterative routine, the model 'steps through' the slag screen beginning at furnace exit. First the mass collection routine is used to estimate the ash removal, and hence slag flow rate, at each tube bank. Then the model begins move into the duct for the heat and mass transfer calculations. At each step along the duct the flowing slag model developed by UTRC/PSI (presented in Phase I Quarterly and Final Reports) is used to calculate the thickness

of the flowing and frozen slag layers, and the gas temperature drop. When a tube bank is reached, the flowing slag model is used to calculate the slag thickness (flowing and frozen) on the tube and the heat removed by the bank of tubes. The model then 'steps around' the tube and continues along the duct until the next tube bank is reached. Each major submodel is discussed in more detail in the subsequent sections.

Model Inputs

As can be seen from Exhibit 9-1, the first operation in the model is to read the input parameters and calculate the duct dimensions. The required input parameters are shown in Table 9-2. These parameters include gas mass flow rates, desired gas velocity, and gas temperature at the slag screen inlet. Other parameters, such as the non-dimensional tube and row spacing, the tube radii, and the number of rows, are used to define the dimensions of the slag screen. Slag-related parameters include the ash composition (used to calculate the slag viscosity), the ash mass particle size distribution (psd) at the furnace exit, and the critical temperature required for the slag to flow.

Table 9-2
SSSiM Input Parameters

Gas Inlet Temperature
Gas Inlet Velocity
Gas Mass Flow Rate
Tube Coolant Temperature
Number of Tube Rows
Tube Diameter
Ash Mass Flow Rate
Ash Particle Size Distribution
Ash Composition (ASTM Analysis)
Ash Critical Viscosity Temperature
Gas Inlet Temperature

Calculation of Duct Dimensions and Number of Tubes Per Row

Based on the desired gas inlet velocity and the inlet mass flow rate the model then calculates the duct dimensions required for that velocity at the given mass flow rate and inlet gas temperature. This calculation assumes a rectangular duct twice as wide as it is tall. The calculated width is then used to determine the number of tubes per row according to:

$$N_{tubes} = \text{INTEGER}\left(\frac{W_{duct}}{2\, r_{tube}\, S_n} \right) \quad (1)$$

where:

W_{duct} = width of the duct

r_{tube} = outer radius of tube, including the refractory

S_n = non-dimensional tube spacing (tube spacing/tube diameter) normal to the flow

N_{tube} = number of tubes per row.

This relation assumes that some tubes will be placed next to the wall of the duct. The number of tubes per row is then used to determine the final duct width, which is subsequently used to calculate the final duct height. The velocity between the tubes is the critical factor, not open duct velocity.

Mass Collection in Slag Screen

Calculation of Tube and Row Capture Efficiencies

The method used to calculate the capture efficiencies of the individual tubes was discussed in detail in the Phase I Final Report. The capture efficiency of a collector in a high velocity flow field is mainly determined by an inertial parameter characterizing the particle motion, termed the Stokes number. The Stokes number can be viewed as the ratio of the characteristic stopping time of the particle to the characteristic flow time around the collector. For low Reynolds number flow, the particle stopping time may be computed by applying the Stokes drag law. The drag experienced by the particle in high Reynolds number flow is non-Stokesian. Israel and Rosner (Israel, 1983) developed engineering correlations for the inertial parameter for particle capture by a cylinder or a sphere as shown in Eq. (2).

$$Stk_{eff} = \psi(Re_p) \bullet Stk \tag{2}$$

where $Stk = \rho_p d_p^2 U/(18\mu)$, $Re_p = d_p \rho_g U_4/\mu g$, and $\varphi(Re_p)$ is the correction factor for non-Stokes behavior given by Eq. (3).

$$\psi(Re_p) = \frac{3}{0.0628\,Re_p}\left[(0.0628\,Re_p)^{1/3} - \tan^{-1}(0.0628\,Re_p)^{1/3}\right] . \tag{3}$$

For a circular cylinder collection geometry and $Stk_{eff} > 0.14$, the following correlation for the impaction efficiency was presented:

$$\eta_{cap} = \left[1 + 1.25\left(Stk_{eff} - \frac{1}{8}\right)^{-1} - 1.4 \times 10^{-2} \bullet \left(Stk_{eff} - \frac{1}{8}\right)^{-2} + 0.058 \times 10^{-4}\left(Stk_{eff} - \frac{1}{8}\right)^{-3}\right]^{-1} . \tag{4}$$

For the near-critical range the impaction efficiency is given by Eq. (5).

$$0.125 < Stk_{eff} < 0.14$$
$$\eta_{cap} = 0.043\left(Stk_{eff} - \frac{1}{8}\right)^{0.11} . \tag{5}$$

Once the impaction efficiency of a given tube is calculated, the model determines the particle removal efficiency for a row of tubes. If the particles are assumed not to disperse across the duct (via turbulent diffusion) the removal efficiency is simply given as:

$$\eta^*_{row}(d_p) = m(d_p)\,\eta_{row}(d_p)\,\frac{CA_{tubes}}{CA_{duct}} \tag{6}$$

where:

$\eta_{row}^{*}(d_p)$ = the mass removal efficiency of particles of size d_p in that row

$m(d_p)$ = the mass flow rate of particles of size d_p in the duct

Ca_{duct} = cross-sectional area of the duct

Ca_{tubes} = projected area of the tubes

In this case $m(d_p)$ is assumed to remain constant until after the total projected area of tubes equals the cross-sectional area of the duct (three rows in PSI design). At this point the inlet ash mass flow rate is corrected to account for the ash collected to that point. The mass flow rate of ash then remains constant until the total projected area of the tubes again equals the cross sectional area of the duct.

If the particles are assumed to fully disperse across the duct between rows, then the number of particles approaching a tube will depend on the removal efficiencies of the previous rows. Therefore $m(d_p)$ is corrected after each row to reflect the amount of ash removed by that row.

Slag Flow and Heat Transfer in the Duct

Once the amount of ash captured, and hence, the total slag flow, in the slag screen has been calculated as discussed in the previous section, the model begins to 'step through' the slag screen. At each point in the slag screen a modified version of the flowing slag model developed by UTRC/PSI in Phase I was used to determine the thickness of the flowing and frozen slag layers on the floor of the duct, and the heat transfer through the duct walls. The original model was modified slightly to account for flow in an angled duct. The model was also modified to include the shear force imparted on the slag by the gas flow through the slag screen. These modifications are discussed in detail below.

Modification for Flow on an Angled Surface

The original model was designed to calculate slag flow on the vertical walls of the radiant air heater. Although this model is also applicable to slag flow along the floor of the duct, a modification was required to make the model more generally applicable to non-vertical surfaces. For example, the floor of the duct is tilted away from vertical by some angle β (see Exhibit 9-2).

For the general case of flow of a falling film the equation of motion can be written as:

$$\frac{\partial \tau}{\partial y} = \rho\, g \cos\beta \tag{7}$$

Assuming a Newtonian fluid the equation can be written as:

$$\tau_s = \rho_s\, u_b^2\, (f/2) \quad . \tag{8}$$

Note that these equations are identical to those in the original model, except that for the vertical walls $\beta = 0$, and therefore, $\cos\beta = 1$. Therefore in the modified version of the model the equation of motion was changed to include the $\cos\beta$ term.

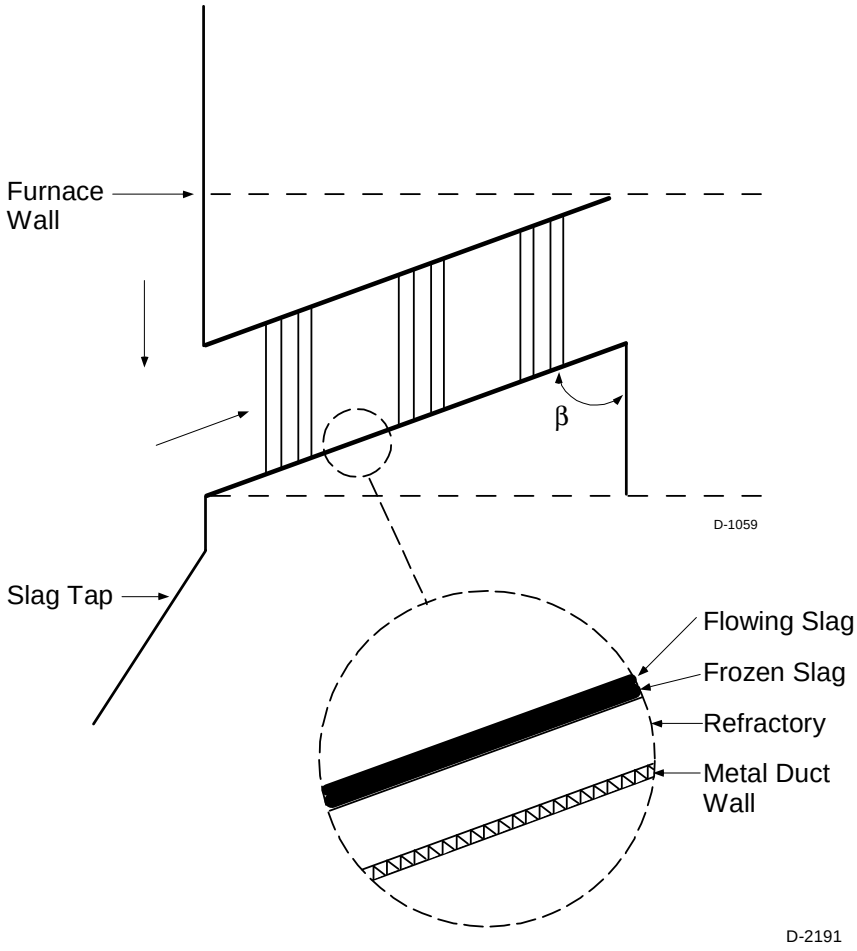

Exhibit 9-2
Schematic of Slag Screen

Shear Forces at the Slag Surface

Another departure from the original version of the flowing slag model is the fact that the high velocity gas in the slag screen is moving *counter* to the slag. This high gas velocity may cause a shear force at the slag-gas interface. In the original version the shear forces at the slag surface could be neglected because the gas velocities were relatively low and the gases were flowing in the same direction as the slag. This assumption may not be valid in the slag screen. Therefore the boundary conditions were modified to include the surface shear (τ_s), which is calculated according to (Kays, 1966):

$$\tau_s = \rho_g \, u_b^2 \, (f/2) \tag{9}$$

where ρ_g and u_b are the bulk gas density and velocity, respectively. The friction factor (f/2) is calculated from (Kzukauskas, 1972):

$$(f/2) = 0.0295(Re_x)^2 \quad . \tag{10}$$

The Reynolds number is defined according to Eq. (11).

$$Re_x = \frac{\rho_g \, u_b \, x}{\mu_g} \quad . \tag{11}$$

x is the distance from the entrance of the slag screen.

Heat Loss in the Duct Portion of the Slag Screen

Once the various modifications were made to the model, the system of equations are integrated to determine the surface temperature and the slag layer thickness. Note that the slag flowing at any location in the slag screen is assumed to be that collected from all the tubes *downstream* of that location, and *no* additional deposition occurs in the duct. The model repeats the calculations at each location until the temperature at the interface between the flowing slag and the frozen slag (see Exhibit 9-2) equals the critical viscosity temperature for the given coal.

The heat loss from the duct portion of the slag screen is calculated based on the elemental heat flux at each location. This elemental heat flux is defined as:

$$q_{duct} = (f_{wet} U_{wet} + (1 - f_{wet}) \, U_{clean}) \, (T_g \, T_a) \tag{12}$$

where f_{wet} is the fraction of the duct perimeter that is covered by slag. T_a is the temperature of the metal on the outside of the slag screen wall. The overall heat transfer coefficient through the slag (U_{wet}) is calculated from:

$$U_{wet} = \frac{1}{\frac{1}{h} + \frac{\delta_s}{k_s} + \frac{\delta_d}{k_d} + \frac{\delta_{ref}}{k_{ref}} + \frac{\delta_{wall}}{k_{wall}}} \tag{13}$$

where δ_s, δ_d, δ_{ref}, and δ_{wall} represent the thickness of the flowing slag layer, the frozen slag layer, the refractory, and the wall, respectively. Likewise, k_s, k_d, k_{ref}, and k_{wall} represent the thermal conductivity of the flowing slag layer, the frozen slag layer, the refractory, and the wall, respectively. The heat transfer coefficient from the gas to the slag, h, is calculated from Eqs. (14) through (18).

$$h = \frac{Nu \, k_g}{4 \, r_h} \tag{14}$$

$$Nu = 0.021 \, Pr^{0.5} \, Re^{0.8} \qquad \text{(Kays,1966)} \tag{15}$$

$$Pr = \frac{c_p \, \mu_g}{k_g} \tag{16}$$

$$Re = \frac{4 \, r_h \, u_b \, \rho_g}{\mu_g} \tag{17}$$

$$r_h = \frac{CA_{duct}}{Perim_{duct}} \quad . \tag{18}$$

$Perim_{duct}$ represents the perimeter of the duct. Finally, the overall heat transfer coefficient for the clean areas of the duct (i.e. the roof and the walls), U_{clean}, is calculated using equation 13 with the slag thickness set to 0. The decrease in the gas temperature from one step to the next is then given by:

$$\Delta T_g = \frac{Perim_{duct}\, \delta_{step}\, q_{duct}}{\dot{M}_g\, c_p} \tag{19}$$

where δ_{step} is step size from one point to the next in slag screen and M_g is the mass flow of gas in duct.

Results from these calculations are discussed in Subsection entitled Simulation Results.

Slag Flow and Heat Transfer on Tubes

The next major part of the model is the submodel to calculate the slag flow along the tubes in the slag screen. When the model reaches a tube bank this submodel is called to calculate the slag layer thickness along the length of the tubes. As with the submodel to calculate slag flow and heat transfer in the duct, this submodel is based on the UTRC/PSI flowing slag model. The model starts at the top of the tube (Exhibit 9-3) and solves the slag flow equations along the tube. Ash mass transfer to the individual tubes is given by the total ash deposition rate for the row of tubes (see Section on New Instrumentation for NOx Control in HITAF) divided by the number of tubes in the row and the length of the tube. Heat transfer to the tubes is given by radiation from the gas (as in the original model). In addition, a radiation term is also included for the tubes that "see" the back wall of the radiant air heater. This radiation term also takes into account that only the leading half of the tubes will see radiation from the wall.

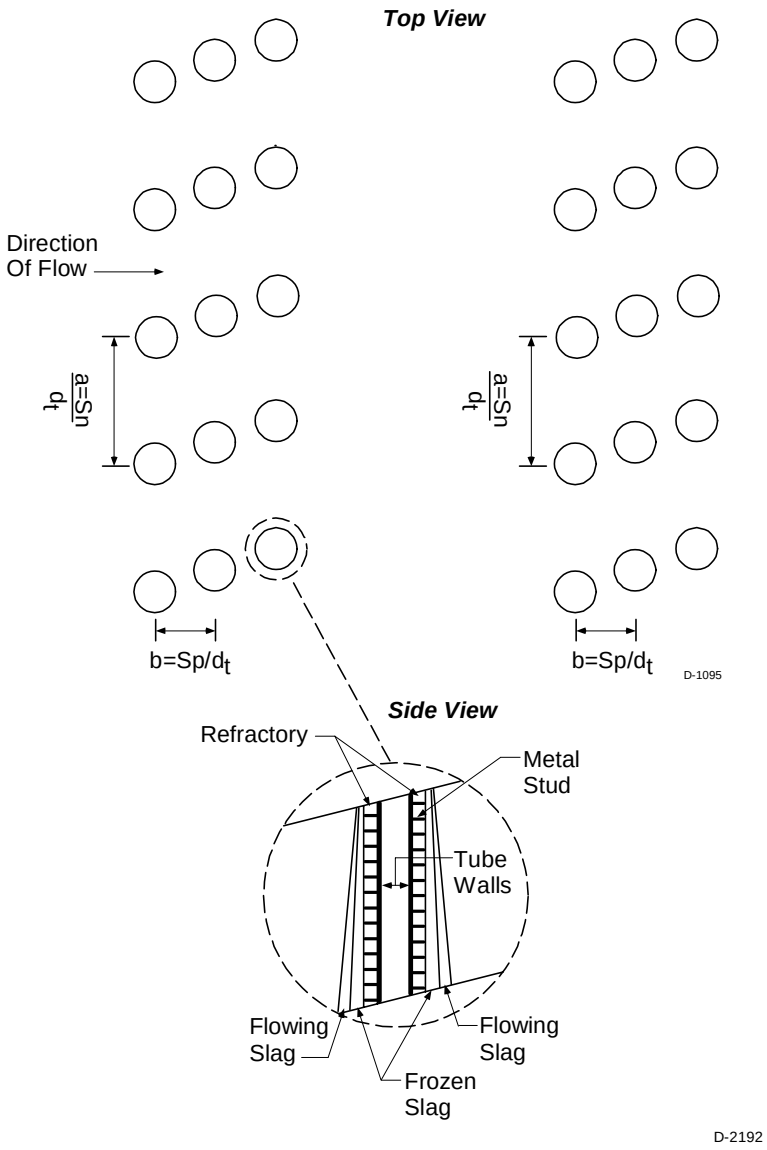

Exhibit 9-3
Tube Placement and Schematic of Individual Tube

The only major modification to the original model is the inclusion of a convective heat transfer term. This convective heat transfer coefficient is given by Eq. (20). The Nusselt number was calculated based on the Eq. (21) (Rodgers, 1979) as presented in the Phase I Final Report.

$$h = \frac{Nu\, k_g}{d_t} \tag{20}$$

$$Nu = c\, Re^{0.6}\, Pr^{0.36} \left(\frac{Pr_f}{Pr_w} \right)^{0.25} \tag{21}$$

where c is a constant that depends on the ratio of tube and row spacing, and Pr, Pr_f, and Pr_w are the Prandtl numbers for the bulk gas, the film, and the surface, respectively.

In the real slag screen tubes, it would be expected that deposits would form on only the leading and trailing edges of the tubes. The area between tubes would be clear of deposits. Therefore, in order to better simulate the temperature and slag flow on the slag screen tubes, only a fraction of the external area of the tube is covered by slag. The remainder of the tube is 'clean'. Therefore the calculation of the frozen and flowing slag layer thickness is based only on the 'wet' area of the tube (defined to be 75% of the tube area). The net heat transfer for a given tube is defined as the area weighted average of the heat transfer through the clean and slag covered areas of the tube. The net heat loss through a row of tubes is given by Eq. (22).

$$\Delta T_g = \frac{SA_{tubes}\, q_{avg}}{\dot{M}_g\, c_p} \quad . \tag{22}$$

Simulation Results

To further evaluate the current design for the full scale slag screen the model described in the previous sections was used to determine the effect of various variables on the collection efficiency of the slag screen, the slag layer thickness, and the temperature and pressure drops through the slag screen. Initially two coals were evaluated, and the 'worst case' coal used for the subsequent calculations. The important variables explored were the tube diameters and the gas velocity. Also explored was the assumption that the ash disperses across the duct between rows. Based on the simulations, a refined design was proposed and evaluated with the model.

Model Inputs

To explore the effect of coal ash properties on the slag screen, three different coals were used. These coals were a bituminous coal from the Illinois No. 6 seam, a PRB coal (denoted "Black Thunder") from the Wyodak-Anderson seam, and a PRB coal from the Wyodak-Rochelle seam. The ash particle size distributions (psd) from the Illinois No. 6 and the Black Thunder coals were fairly similar (Exhibit 9-4), while the ash composition showed some of the differences common between bituminous and PRB coals. The two PRB coals had slightly different ash compositions, but the ash particle size distribution was finer in the Wyodak-Rochelle coal. These ash psd's were used to generate the ash mass flow rates shown in Table 9-3. Ash compositions can be seen in Table 9-4.

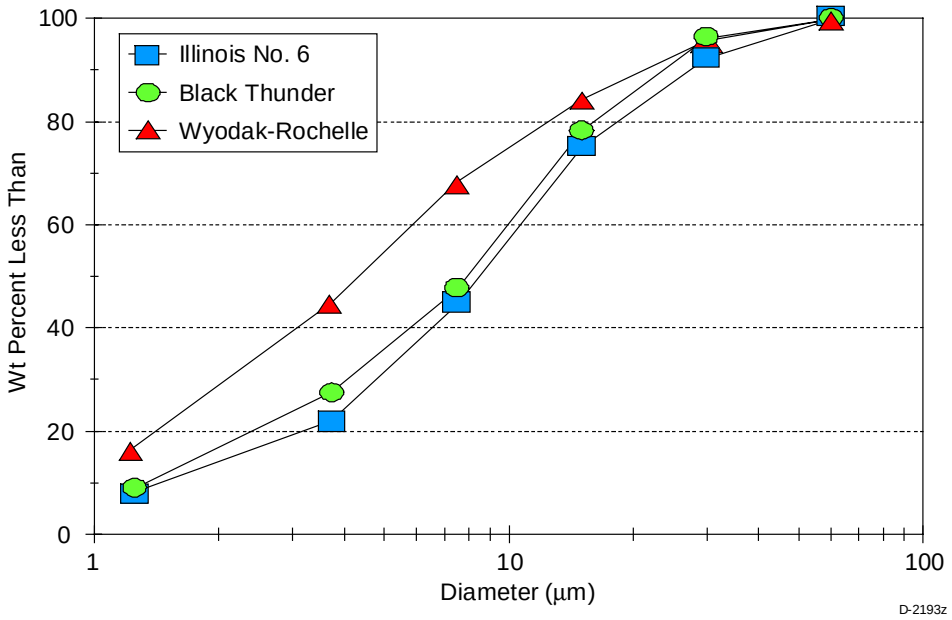

Exhibit 9-4
Ash Particle Size Distributions for Three Coals

Table 9-3
Ash Mass Flow Rate as a Function of Particle Size

d_p	Illinois No. 6		Wyodak-Anderson		Wyodak-Rochelle	
[micron]	[lb/hr]	[kg/sec]	[lb/hr]	[kg/sec]	[lb/hr]	[kg/sec]
1.25	533	0.067	333	0.042	632	0.080
3.75	908	0.114	706	0.089	1057	0.133
7.5	1483	0.187	746	0.094	884	0.111
15.0	1986	0.250	1159	0.146	602	0.076
30.0	1129	0.142	667	0.084	425	0.054
60.0	508	0.064	151	0.019	158	0.020

Table 9-4
Ash Composition

Component (wt %)	Illinois No. 6	Black Thunder (Wyodak-Anderson)	Wyodak-Rochelle
Na_2O	1.3	0.9	1.0
MgO	0.6	5.8	9.9
Al_2O_3	18.0	16.8	17.7
SiO_2	46.1	32.6	31.9
K_2O	2.1	0.2	0.3
CaO	5.3	22.0	24.6
Fe_2O_3	20.5	5.7	5.2
TiO_2	0.9	1.1	1.0
SO_3	5.2	14.9	8.4

Although several of the parameters were changed as part of this short parametric evaluation of the slag screen, many of the basic model inputs were kept constant in the calculations. These model inputs, and the assumed values, are listed in Table 9-5.

Table 9-5
Values of SSSiM Input Parameters

Input temperatures and flow rates:		
Gas mass flow rate:	160 lb/s	72.6 kg/s
Gas inlet temperature:	2780 °F	1527 °C
Water temperature:	572 °F	300 °C
Critical slag temperature:	2552 °F	1400 °C
RAH wall temperature:	3140 °F	1727 °C
Outside duct wall temperature:	390 °F	199 °C
Dimensions:		
Refractory in duct:	4 in	10.2 cm
Duct wall:	0.25 in	0.635 cm
Refractory on tubes[1]:	3 in	7.6 cm
Duct angle (β):	75 deg	75 deg

[1]Refractory (SiC) held on tubes with 2.5 in (6.35 cm) diameter studs, 280 studs/ft^2 (3000 studs/m^2)

Effect of Coal Ash Size and Composition

Based on the coal information shown in Tables 9-3 and 9-4, a series of simulations were performed. These simulations assumed 3 in (7.6 cm) Schedule 40 steel pipes (actual OD

approximately 3.5 in (8.9 cm)). Exhibit 9-5 shows the cumulative capture efficiency from the three coals as a function of tube row, assuming the ash does **not** disperse between tube rows. The data shown in this figure suggest that the capture efficiency is strongly dependent on the ash psd, as would be expected based on the impaction efficiency calculations shown in the Section on New Instrumentation for NOx Control in HITAF. The Illinois No. 6 has the largest ash, and also the largest cumulative capture efficiency. The Black Thunder has a slightly finer ash psd, and shows a slightly lower capture efficiency. Finally, the very fine Wyodak-Rochelle has a very low capture efficiency. The higher capture efficiency and ash loading of the Illinois No. 6 results in slightly thicker slag layers (Exhibit 9-6). The higher viscosity of the Illinois No. 6 slag as compared with the PRB coals also tends to increase this thickness.

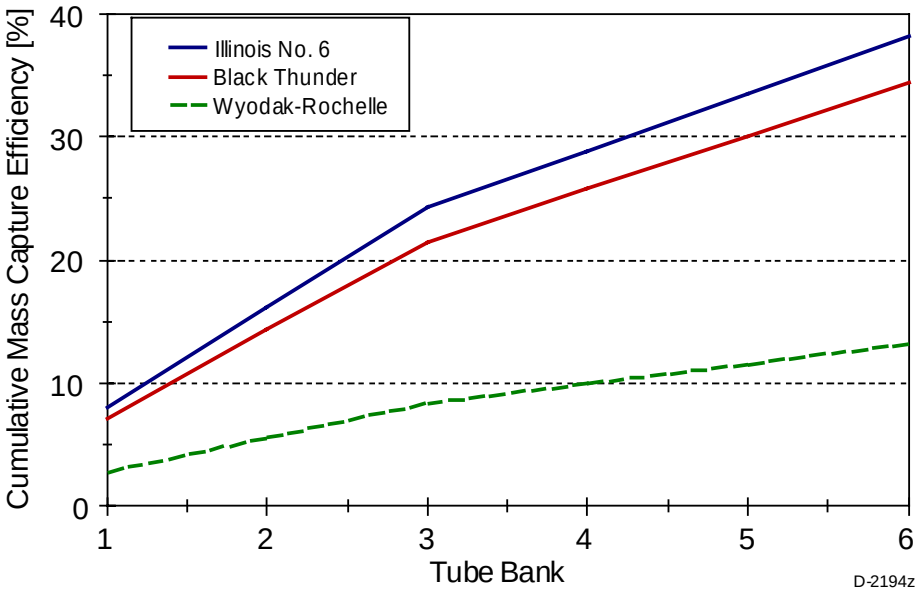

Exhibit 9-5
Slag Screen Capture Efficiencies for Three Coals
(no dispersion between rows)

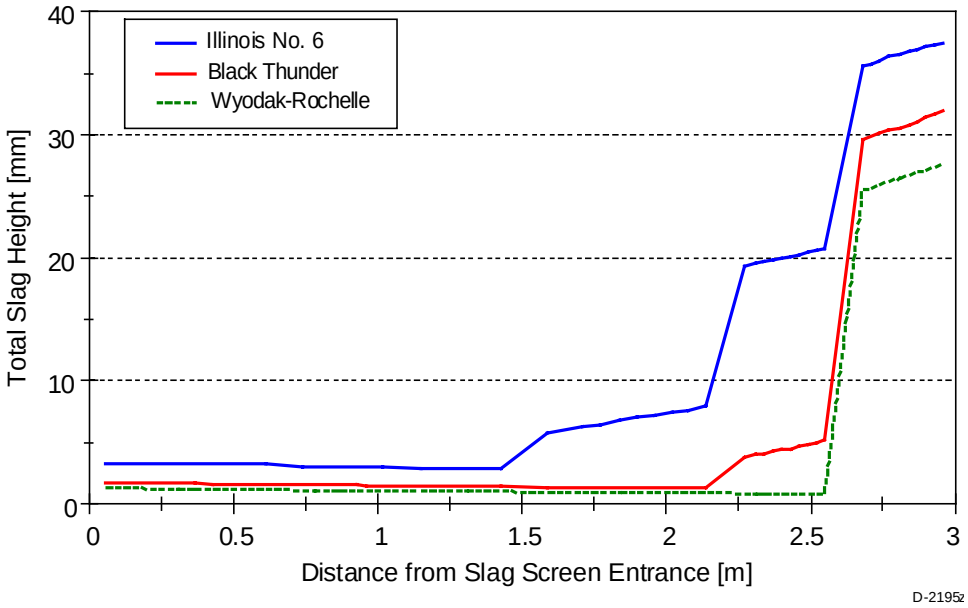

Exhibit 9-6
Thickness of Slag in Duct - Effect of Coal Ash Properties
(no dispersion between rows)

Another important effect of the ash composition is the critical viscosity temperature. Below this temperature, there is a sharp increase in viscosity and effectively the slag stops flowing. In general those coals with high calcium, sodium, or potassium content have much lower critical viscosity temperatures than those with high silica and alumina contents. For example, it has been estimated (Phase I Final Report) that the critical viscosity temperature for the Illinois No. 6 is approximately 2552 °F (1400 °C). However, for the PRB coals a critical viscosity temperature of approximately 2060 °F (1127 °C) is common. Exhibit 9-7 shows the effect of the critical viscosity temperature on the slag thickness on the duct using the Black Thunder coal. A much lower critical viscosity temperature yields a much lower slag thickness. Therefore, the slag thickness for PRB coals are likely to be much thinner than those predicted for the Illinois No. 6, or for PRB coals using 2552 °F (1400 °C) as the critical viscosity temperature. Therefore the Illinois No. 6 represents a 'worst case' and will be used for the subsequent calculations.

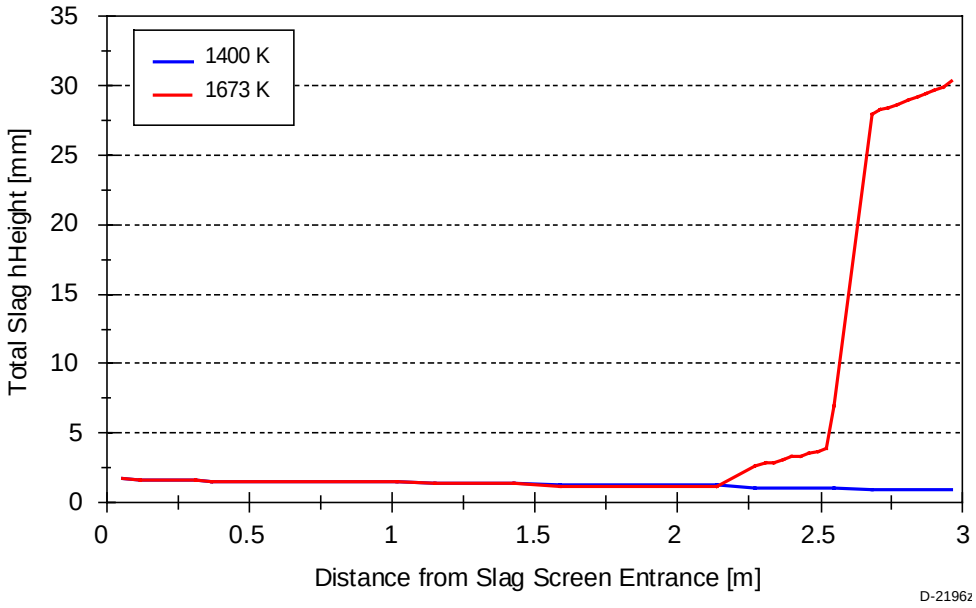

Exhibit 9-7
Effect of Critical Viscosity Temperature on Slag Thickness
(full dispersion between rows)

Effect of Tube Diameter

The effect of the tube diameter on the temperature drop across the slag screen and the cumulative collection efficiency can be seen in Exhibit 9-8. These results indicate that the temperature drop and the collection efficiency increase with decreasing tube diameter. However, the negative effect of tube diameter on the temperature drop is relatively small compared to the gain the in ash collection for the smaller tubes. The maximum slag thickness on the tubes (located at the bottom of the tubes in the last row) and the floor of the duct (at the exit of the duct) increase with decreasing tube diameter (Exhibit 9-9 and 9-10). This is due to the fact that more heat is removed by the smaller tubes (due to the larger number required) than the larger tubes. Therefore, the frozen layer is larger on the small tubes. The higher heat removed by the smaller tubes also decreases the gas temperature in the duct requiring thicker frozen layers on the floor of the duct to maintain a running slag flow. However, the thickness of slag layer on the floor only reduces the cross-section of the duct by 2 to 3%.

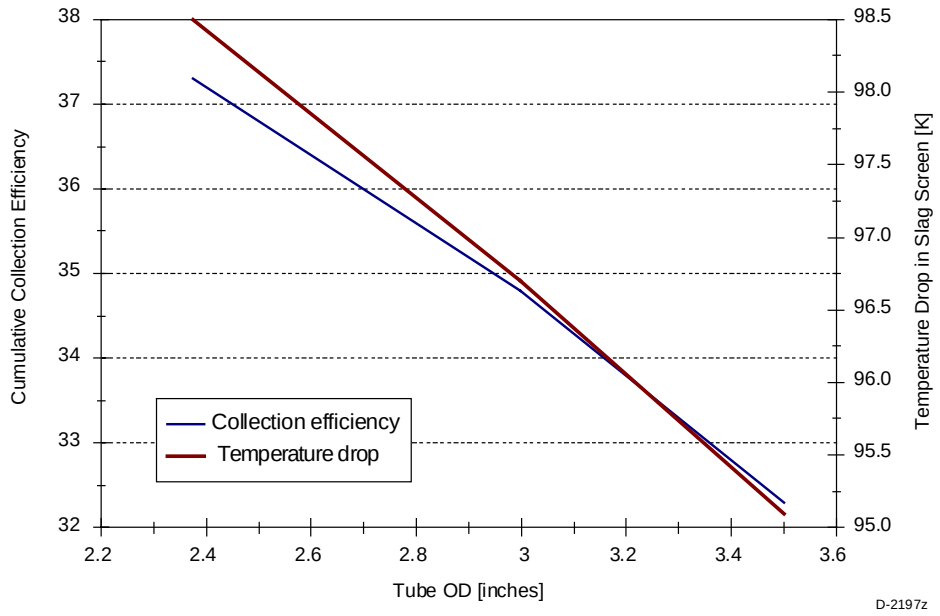

Exhibit 9-8
Effect of Tube Size on Temperature Drop and Collection Efficiency

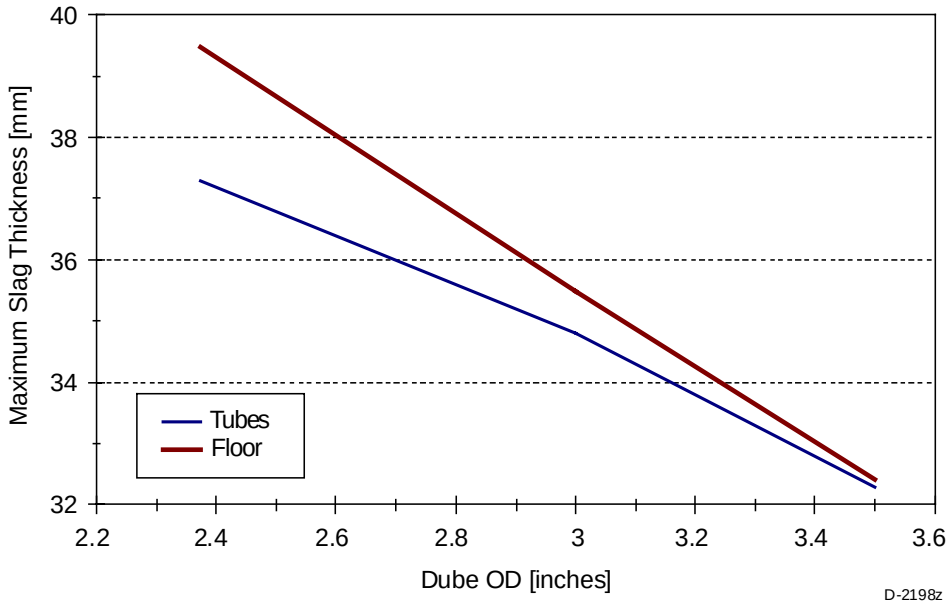

Exhibit 9-9
Effect of Tube Size on Maximum Slag Layer Thickness

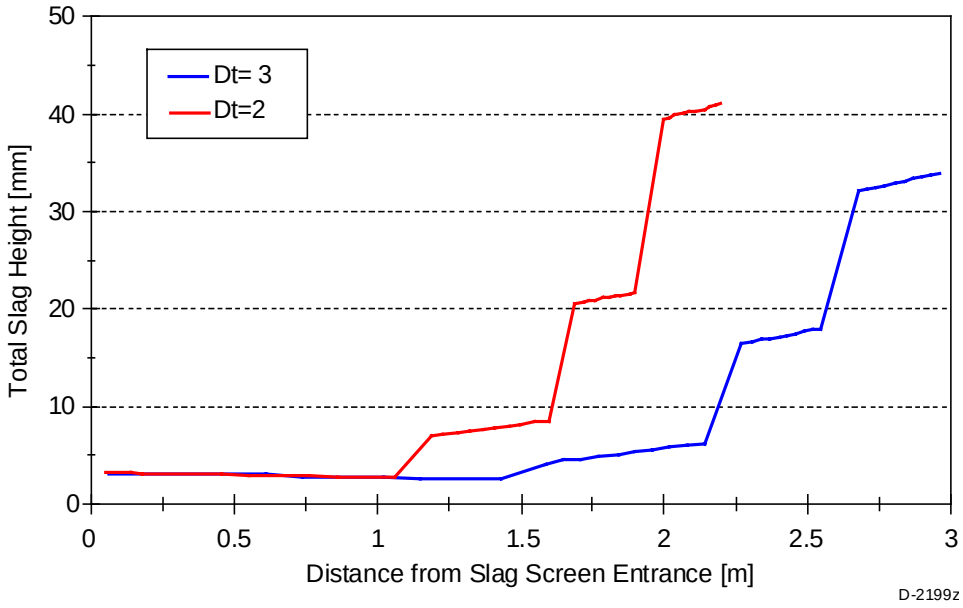

Exhibit 9-10
Effect of Tube Size on Slag Layer Thickness in Duct

In many slag screen designs the relatively thick slag layers on the tubes (approximately equal to the tube radius) would represent a serious cause for concern as the slag screen might plug. However, it is important to note that the PSI design precludes plugging of the slag screen due to slag build up. As discussed earlier in Subsection on Slag Flow and Heat Transfer on Tubes, only part of the tubes are actually covered by the slag layer. Industry experience has suggested that deposits typically grow primarily on the leading and trailing edges of the tubes, while the spaces between tubes remain fairly clean. This phenomenon makes sense as the deposition on the leading edge of the tube is primarily inertially driven. Deposition on the trailing edge, often much smaller or non-existent, is primarily due to turbulent deposition from the recirculation zones behind the tube. However, neither inertial deposition nor turbulent deposition is likely to occur in the spaces between the tubes. In those slag screen designs where the tube rows are staggered such that each subsequent row simply fills in the spaces in the previous rows (see Exhibit 9-11), growth of the deposits on the leading and trailing edges can quickly plug the slag screen. However, in the PSI design when the deposits on the leading and trailing edges are fully developed (typically on the order of a few hours in the large scale design) those tubes with large deposits simple re-direct the flow to the next row of tubes. In the case that all the tubes in a bank have large deposits (e.g. for the second bank of with the Illinois No. 6 coal), the collection efficiency of the bank may be dramatically decreased, ***but the bank will not plug***.

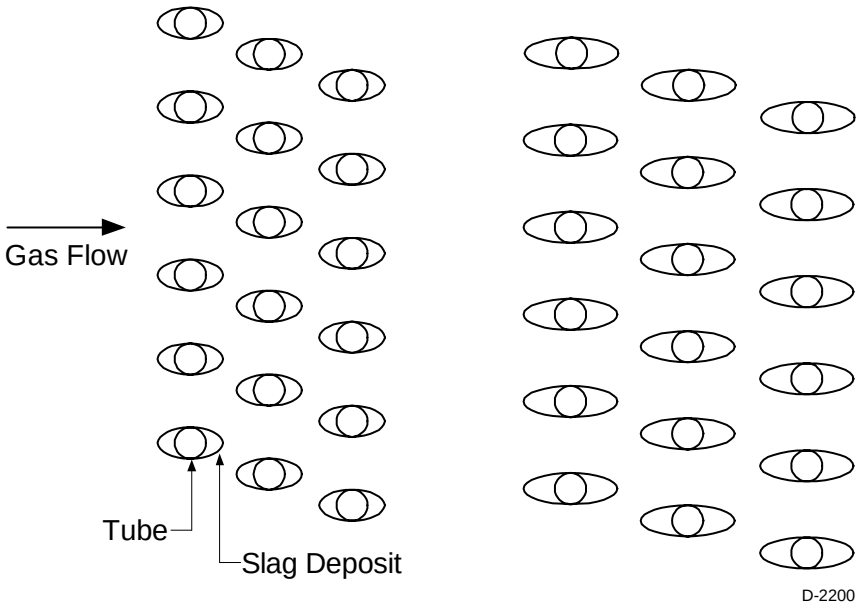

Exhibit 9-11
Schematic of Steady-state Slag Screen

Effect of Gas Velocity

One of the conclusions from the Phase I CFD calculations at UTRC was that the inlet velocity of the gas could be decreased slightly to decrease the pressure drop through the slag screen without dramatically affecting the collection efficiency of the slag screen. This is due the fact that the pressure drop changes as the square of the velocity while the impaction efficiency (see the Section on New Instrumentation for NOx Control in HITAF) has a much weaker dependence on velocity. Therefore calculations were done at 200 ft/s (61 m/s) and 164 ft/s (50 m/s). Based on the results from the previous subsection, these calculations were performed with 2 in (5.1 cm), Schedule 40 steel tubes (actual OD 2.375 in (6.0 cm)). The results of these calculations, summarized in Table 9-6, are in agreement with the CFD conclusions. The collection rate only decreased by 5% (based on the 200 ft/s (61 m/s) case) while the pressure drop decreased by 32%. However, the maximum slag thickness on the tubes also increased. In fact, calculations were attempted at 130 ft/s (40 m/s) but the frozen layer thickness became unacceptably high in the second tube bank. Therefore, based on these results 2.5 in (6.4 cm) Schedule 40 tubes will be used in the Phase II commercial slag screen design.

Table 9-6
Summary of Slag Screen Calculations -- Effect of Velocity

	200 ft/s (61 m/s)	164 ft/s (50 m/s)
Maximum Slag on tubes [mm]	49.5	62.7
Maximum Slag on floor [mm]	41.1	69.5
Cumulative collection efficiency	37	35
Pressure drop [inches H_2O]	5.7	3.9
Temperature drop °F (°C)	178 (99)	202 (112)

Effect of Ash Dispersion

One assumption that has often been made in the slag screen calculations is that the ash particles disperse across the duct between rows. This assumption is reasonable for widely spaced rows. However, it may not be completely valid for the current design. Therefore a set of calculations were performed using exactly the same conditions (Illinois No. 6, 3 in (7.6 cm) Schedule 40 tubes, and 197 ft/s (60 m/s)) to determine the effect of assuming full dispersion as compared to no dispersion between rows (see the Subsection on Mass Collection in Slag Screen). The results of these calculations, seen in Exhibit 9-12, suggest that the assumption of full dispersion only slightly reduces the predicted collection efficiency. It is important to note that the *effective* collection efficiency of any given row (Eq. (6) in the Subsection on Mass Collection in Slag Screen) is strongly dependent on the number of rows required to cover the entire cross section of the duct. The more rows required, the lower the effective collection efficiency. In addition, since the collection efficiencies are not added linearly to determine the cumulative collection efficiency, the cumulative collection efficiency is also reduced when more rows are required. Although this result suggests that the design proposed by UTRC, where only two rows are required to cover the cross section, would be the optimum, the results presented in the Subsection entitled Effect of Tube Diameter indicate that this design would be prone to plugging. However, by using three rows to cover the entire cross section we can prevent plugging with only a slight loss in the collection efficiency.

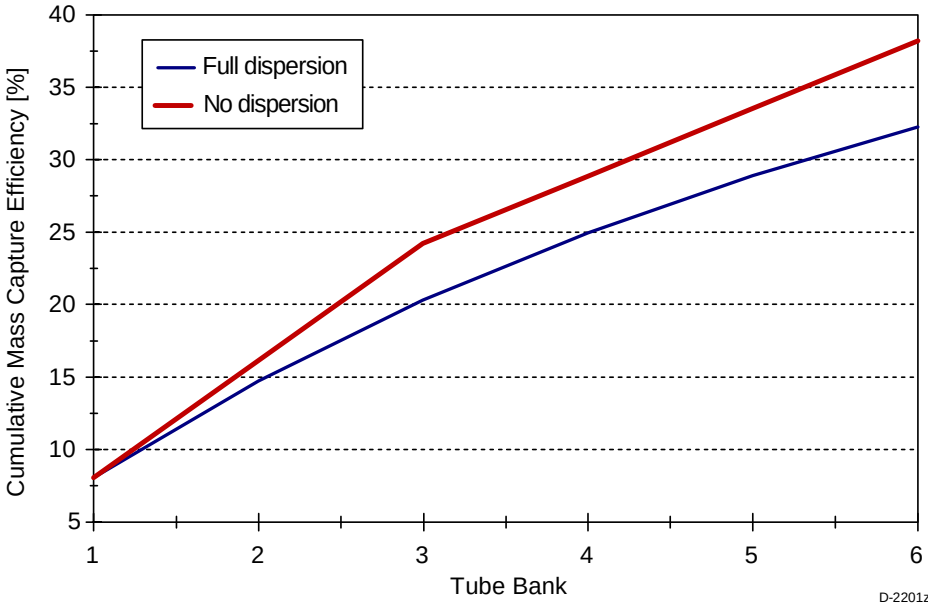

Exhibit 9-12
Effect of Ash Dispersion on Cumulative Capture Efficiency

Comparison with CFD Results

To provide a 'sanity' check for both the engineering model and the CFD calculations, SSSiM was used to simulate one of the conditions modeled with Fluent by UTRC personnel. This design was the PSI design discussed in previous sections using a gas velocity of 197 ft/s (60m/s) and 3 in (7.6 cm) (actual) tubes. The 3 in (7.6 cm) actual diameter consisted of 2 in (5.1 cm) Schedule 40 pipes wrapped with 0.47 in (1.19 cm) of refractory. The predicted capture

efficiencies of the entire slag screen can be seen in Exhibit 9-13. These results show that the predicted efficiencies are in good agreement for the largest sizes, but the discrepancy between the two models increases as the particle size decreases. This effect is due to the fact that PSI's engineering model assumes the deposition is dominated by inertial terms (and no non-inertial mechanisms are considered). The CFD calculations, on the other hand, include the effects of the non-inertial terms. As the CFD calculations are performed for clean, perfectly smooth, tubes it is likely that the actual capture efficiencies will be lower than predicted by this model. In addition, since non-inertial terms can play a role in the deposition of the finer particles, it is likely that the engineering model under-predicts the capture efficiencies. Therefore, the true capture efficiency curve lies somewhere between the two model predictions, and the models provide good upper and lower bounds.

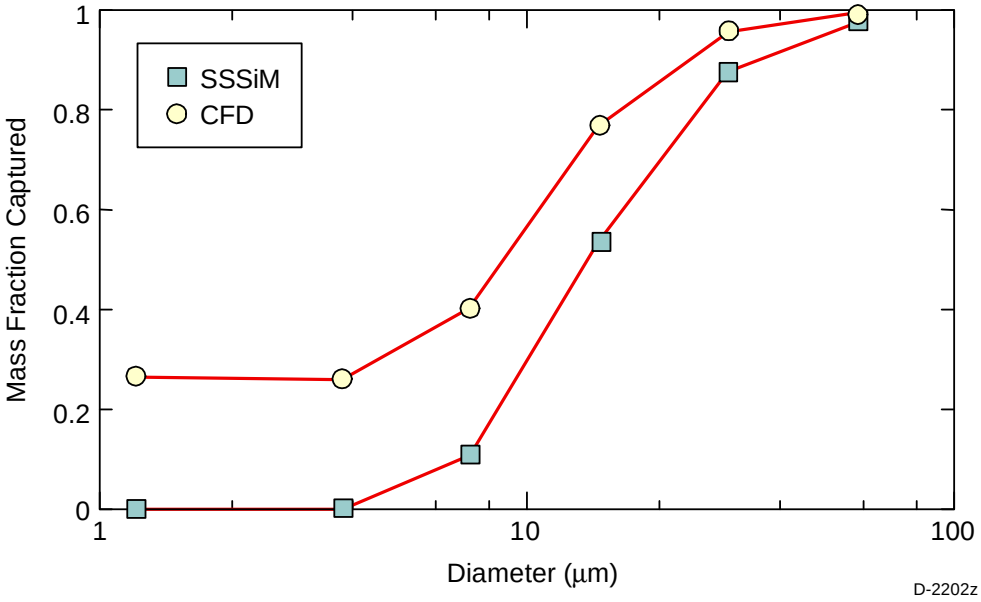

Exhibit 9-13
Comparison of CFD and SSSiM Collection Efficiency Predictions

Another important comparison between the two models is the predicted pressure drop across the slag screen. The CFD calculations predicted a pressure drop of 0.1835 psi (1.27 kPa) while SSSiM predicted 0.21 psi (1.45 kPa). The predicted pressure drops are in good agreement and both models indicate that this configuration yields an unacceptably high pressure drop. Therefore, this comparison between the two models indicate that SSSiM and the CFD calculations work well in combination to explore the slag screen designs. The SSSiM yields predictions for the slag thickness, the temperature drop, the pressure drop, and a lower bound for the collection efficiency. The CFD calculations provide an upper bound for the collection efficiency, and, more importantly, enable us to test the simplifying assumptions and identify problem areas that may be missed by the simple methods used by the PSI engineering model to handle fluid flow.

Commercial Slag Screen Design

Based on the calculations discussed above, a revised commercial slag screen design is proposed. This design uses 2.5 in (6.4 cm) Schedule 40 tubes (actual OD 2.875 in (7.3 cm)) and an inlet velocity of 164 ft/s (50 m/s). The design consists of two banks of three rows of tubes with the same normalized spacing as previous designs. The predicted cumulative capture efficiency, using the Illinois No. 6 with no ash dispersion, is shown in Exhibit 9-14. Although the cumulative collection efficiency is lower than desired, it is still acceptable, especially if it is taken at a lower bound. The slag thickness on the second tube bank are fairly high, which could potentially reduce the efficiency of these tube rows. (Exhibit 9-15). For example, the slag thickness as a function of location on the tube for the first row of tubes and the last row of tubes can be seen in Exhibit 9-16 and -17, respectively. As can be seen from these figures the thickness of the frozen layers dominates the overall slag layer thickness. The frozen layer on the tubes in the second tube bank, and on the duct floor in this region, are much higher due to the lower gas temperatures (Exhibit 9-18). However, due to the spacing of the tubes, as discussed in previous sections, the slag screen **cannot** plug, so this design will be acceptable. Further, the reduction in the flow area of the duct related to the frozen slag layer on the floor is minimal (less than 3%). Finally, the pressure drop, 0.14 psi (3.9 in (9.9 cm) of water, 0.097 kP) is probably acceptable, although just barely.

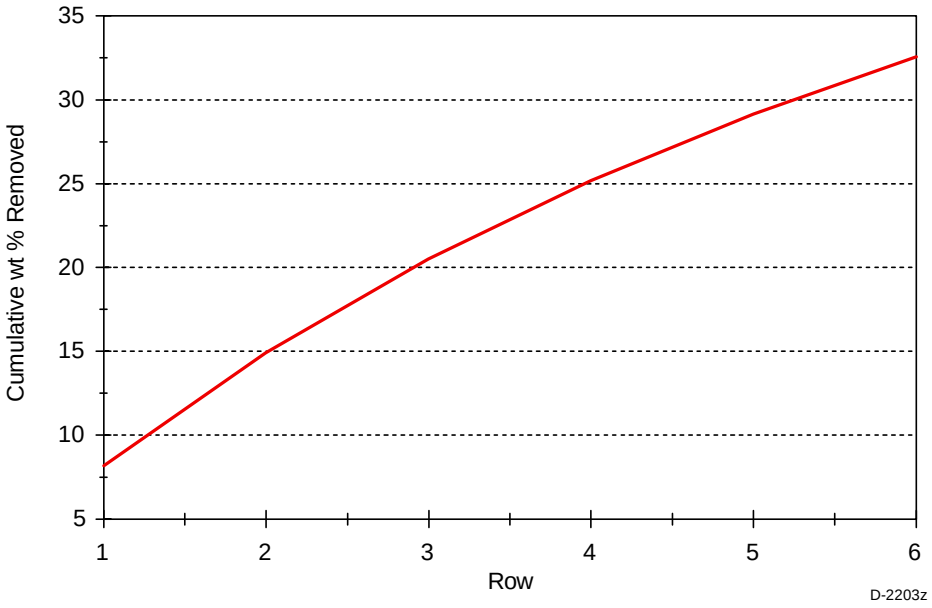

Exhibit 9-14
Cumulative Ash Capture Efficiency for Commercial Slag Screen Design (Illinois No. 6 ash)

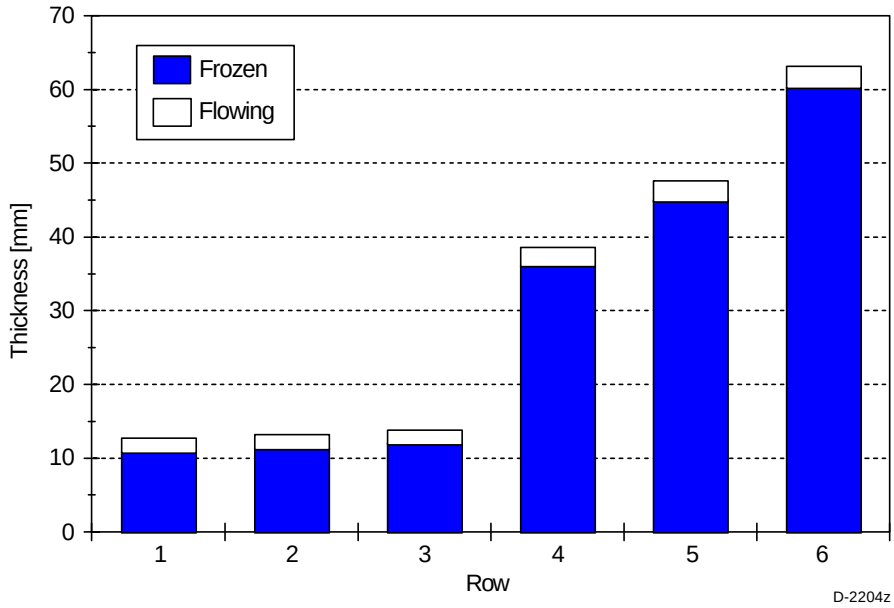

Exhibit 9-15
Slag Thickness on Tubes for Commercial Slag Screen
(Illinois No. 6 ash)

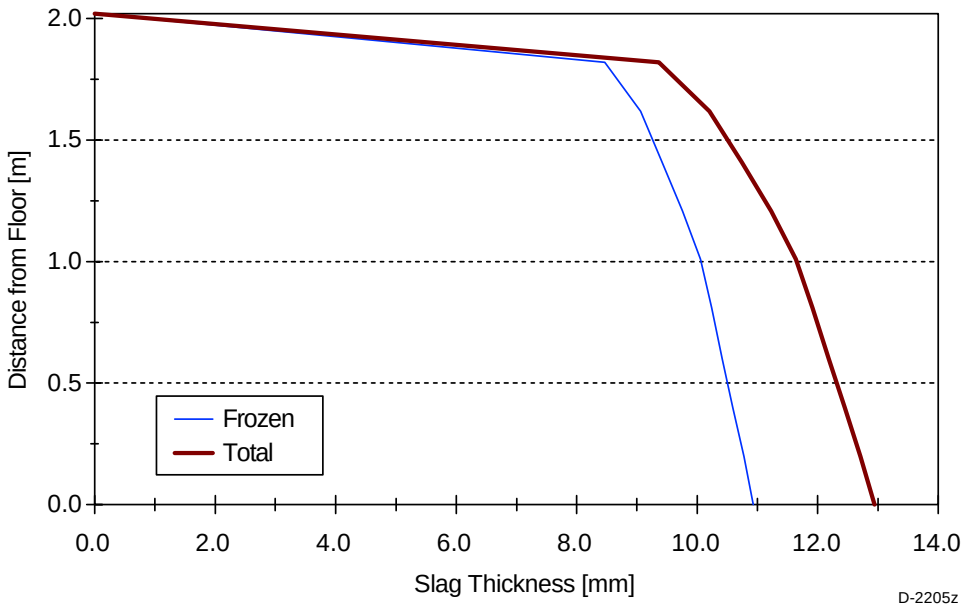

Exhibit 9-16
Slag Thickness on Tubes in First Row for Commercial Slag Screen
(Illinois No. 6 ash)

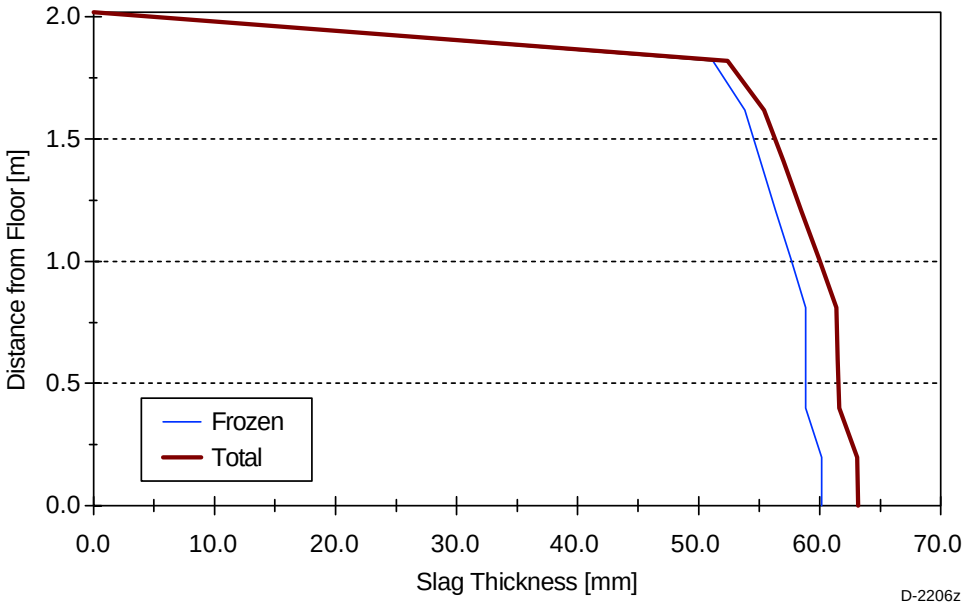

Exhibit 9-17
Slag Thickness on Tubes in Last Row for Commercial Slag Screen (Illinois No. 6 ash)

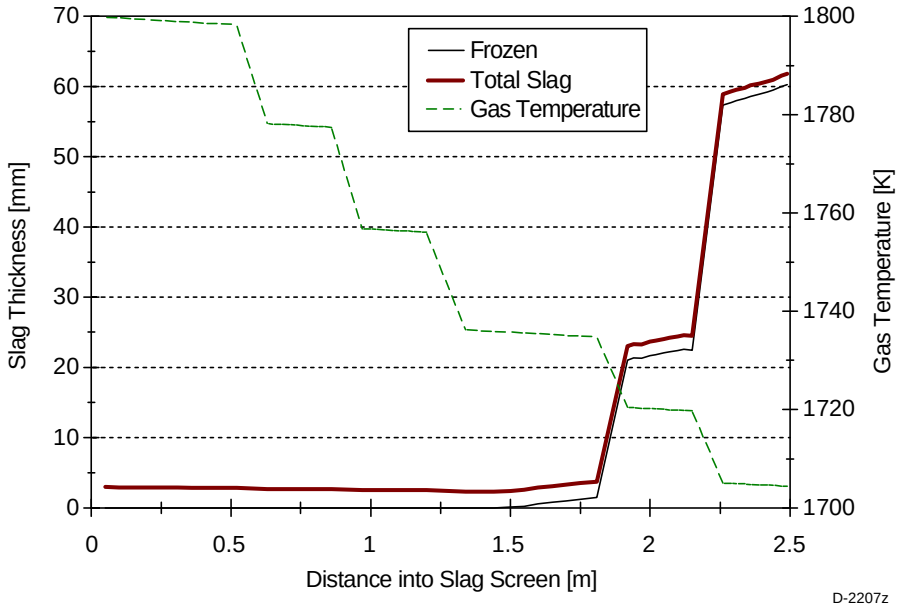

Exhibit 9-18
Slag Thickness and Gas Temperature in Duct for Commercial Slag Screen (Illinois No. 6 ash).

Convective Air Heater

Sintering of Convective Air Heater Deposits

In the Phase I program, criterion for deposit removability in the convective air heater was developed (described in the Phase I Final Report). These calculations were reviewed to determine how to improve them as required in Phase II. The results are briefly summarized below. The question that was addressed is as follows: what is the maximum flue gas temperature such that ash deposits on heat transfer surfaces can be removed easily?

Answering this question involves a three step process. First, it is necessary to establish a criterion for deposit removability by sootblowers. Based on earlier measurements of deposit strength, a minimum deposit porosity of 25% is established. The second step is to calculate sintering rates in the deposit to make sure that the deposit does not reach the "critical" porosity too quickly for easy removal. The result will be a maximum allowable deposit surface temperature. Finally, using the maximum allowable deposit surface temperature, a heat transfer calculation is performed to arrive at the maximum allowable flue gas temperature as a function of deposit thickness. The results depend on the composition of the coal ash.

Models for the sintering of coal ash deposits are based on viscous flow of the ash. The earliest work by Frenkel (Frenkel, 1945) concerned the rate of coalescence of two spheres such that the energy dissipated in viscous flow equals the energy gained by a decrease in surface area. Frenkel's model is applicable to the early stages of deposit sintering and can provide a qualitative indication of the degree of sintering (Hiram, 1983). Mackenzie and Shuttleworth (Mackenzie, 1949) developed a model for the shrinkage of closed pores which occurs in the later stages of densification. Scherer (Scherer, 1977) developed a more general model for sintering of open pores using an array of intersecting cylinders. He showed that his model reproduced the behavior of the Mackenzie and Shuttleworth model for values of porosity less than about 0.7.

For the purposes of modeling sintering of coal ash deposits from approximately 50% to 0% porosity, the model of Mackenzie and Shuttleworth will be used. This model describes the change in porosity as a function of time as follows:

$$\frac{\varepsilon}{\varepsilon_0} = e^{\frac{3t\sigma}{2r_0\mu}} \tag{23}$$

where ε_0 and ε are the deposit porosities initially and at some time t, respectively. The initial pore radius is r_0. The ash surface tension and viscosity are denoted by σ and μ.

In this analysis, viscosity is calculated based on the bulk composition of the ash. As discussed below, using bulk viscosity provides only an approximate answer since the composition of individual ash particles in the deposit can differ greatly from the bulk composition. A constant surface tension is assumed. For the sintering calculation, the ratio of surface tension to viscosity is the quantity of interest. Both surface tension and viscosity are functions of temperature. Surface tension depends approximately on the square root of temperature, while viscosity shows an exponential dependence on temperature (Rasak, 1985). Given that the viscosity changes by several orders of magnitude over the temperature range of interest, it is reasonable to neglect the variation of surface tension with temperature.

According to Raask (Rasak, 1985), viscosities in the range of 10^7 to 10^{11} poise (10^7 to 10^{11} Poise) are relevant to the formation of sintered deposits in coal-fired boilers. Senior and

Srinivasachar (Senior, 1995) developed a model for viscosity of silicates in the range of 10^5 to 10^9 poise (10^5 to 10^9 Poise). Other models of slag viscosity work well for flowing slag (i.e., viscosity less than about 10^3 poise (10^3 Poise), but cannot be applied to the much higher viscosities found in deposits. Using the ASTM ash composition for Illinois 6 and Wyodak coals (as reported in the Phase I Final Report), the viscosity was calculated as a function of temperature from 1340 to 2060 °F (727 to 1127 °C). Exhibit 9-19 displays the viscosity-temperature curves for oxidizing (all iron as $Fe+^3$) conditions calculated as described in Senior and Srinivasachar (Senior, 1995).

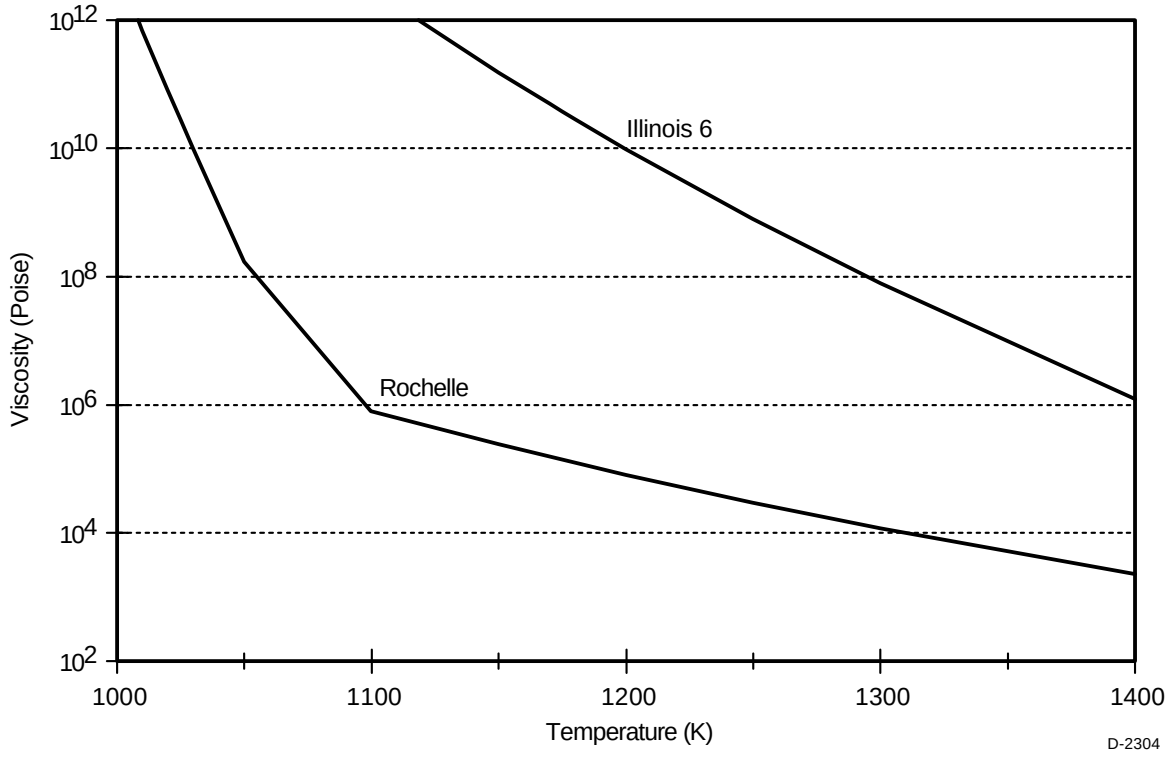

Exhibit 9-19
Viscosity-temperature Curves for Oxidizing Conditions

Densification calculations were performed using the method of Mackenzie and Shuttleworth (Mackenzie, 1949). The bulk ash composition was used to calculate the viscosity and a surface tension of 400 dyne/cm was assumed based on measurements of surface tension in a number of coal ash samples (Nowok, 1991). The initial deposit porosity was assumed to be 50% since deposits are observed to have low strength (implying little sintering) at this value of porosity. Based on Scherer's structural model for densification of a cubic lattice (Scherer, 1977), the pore radius was set equal to half the average particle diameter (Table 9-7).

Table 9-7
Ash Particle Size Distributions (in wt%)

Diameter, microns	Illinois 6	Wyodak-Rochelle
1-2.5	1.5	16.8
2.5-5	9.0	34.8
5-10	19.9	25.6
10-20	34.8	19.2
20-40	29.5	3.2
40-60	5.3	0.6
Weighted average diameter, microns	10.2	4.2

Exhibits 9-20 and -21 show densification as a function of time for Illinois 6 and Wyodak-Rochelle ash, respectively. The temperature at which porosity reaches the critical value of 25% in approximately 8 hours is 1646 °F (897 °C) for Illinois 6 and 1367 °F (742 °C) for Wyodak-Rochelle. These points correspond to a viscosity of approximately 3×10^{10} poise (3×10^{10} Poise) which is consistent with Raask's assessment of the range of viscosity for deposit sintering.

Having defined a maximum deposit surface temperature, T_s, such that the deposit can be easily removed, we can now compute the maximum flue gas temperature in the convective heat exchanger. In order to verify the approach, however, an example from a conventional coal-fired power plant will be presented first and then the results for the convective air heater conditions will be shown. Because we wish to find a maximum gas temperature, we will perform a steady state heat balance on the heat exchanger inlet using the maximum temperature for the working fluid.

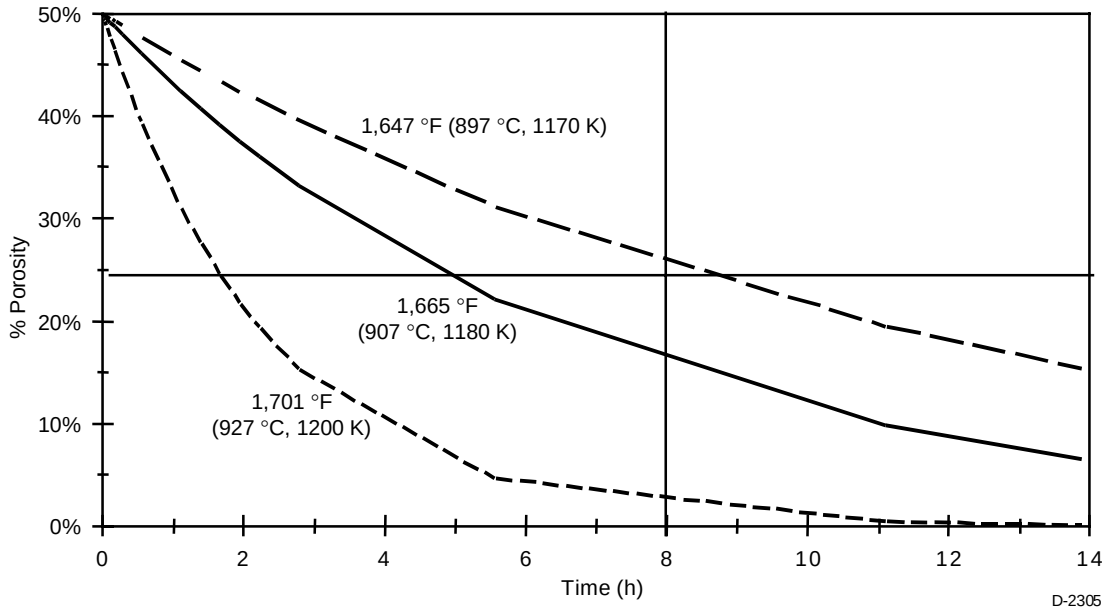

Exhibit 9-20
Densification of Illinois No. 6 Deposit

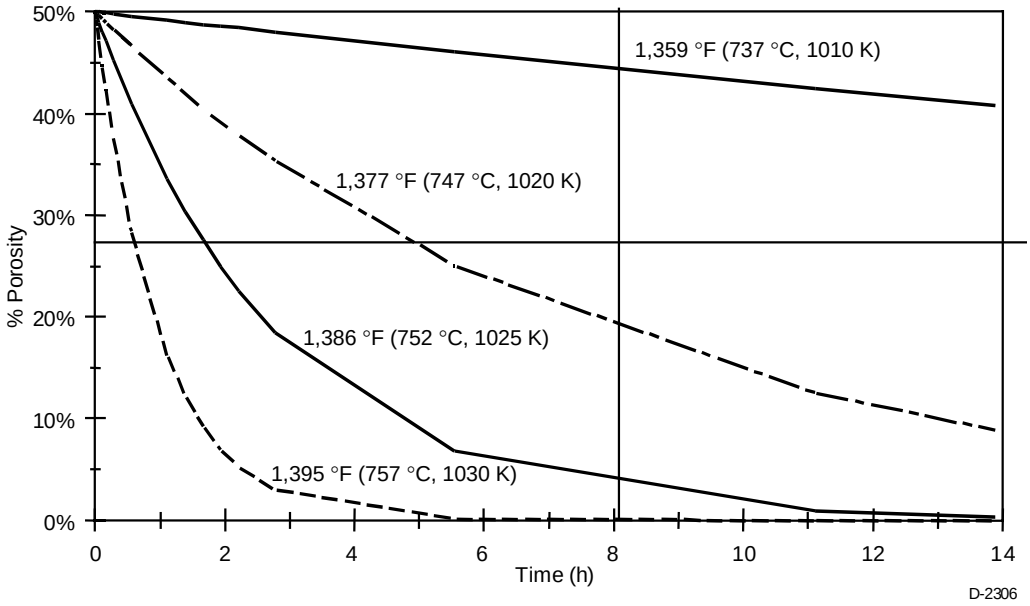

Exhibit 9-21
Densification of Wyodak-Rochelle Deposit

The gas temperature can be calculated by solving the steady state heat transfer problem given the air and deposit surface temperatures. This involves solving three equations for three unknowns:

$$h_{fluid}(T_{w_1} - T_{fluid}) = (k_{tube} / x_1)(T_{w_2} - T_{w_1}) = (k_{ash} / x_2)(T_s - T_{w_2}) = h_g(T_g - T_s) \qquad (24)$$

Variables are defined in Table 9-8. The equations are solved for gas temperature, T_g, as a function of ash thickness, x_2.

Table 9-8
Values Used to Calculate Steady State Heat Transfer

Parameter	Symbol [units]	Steam Reheater	HIPPS Air Heater
Working Fluid		Steam	Air
Working Fluid Temperature	T_{fluid} [°C]	344	705
Tube Material		Carbon Steel	Inconel
Tube Thermal Conductivity	k_{tube} [W/m- °C]	43.3	16
Tube thickness	x_1 [m]	0.0042	0.0032
Ash Thermal Conductivity	k_{ash} [W/m- °C]	0.65	0.65
Gas heat transfer coefficient	h_g [W/m^2- °C]	58.5	170
Working Fluid Heat transfer coefficient	h_{fluid} [W/m^2- °C]	1226	545

As a check on the calculated approach, the maximum allowable flue gas inlet temperature was estimated for a conventional steam convective air heater. Since the first bank of tubes in a power plant, the secondary superheater, sees a lot of radiation, the second bank, the reheater was modeled. The gas temperature entering the reheater is typically 2020 °F (1105 °C) burning an Illinois 6 coal (Stultz, 1992). Ash deposits of 0.5 in (1.3 cm) in 8 hrs are typical and can be removed easily.

Table 9-8 gives the parameters used for the steady state heat transfer calculation applied to a conventional steam reheater. The coal was assumed to be Illinois 6 coal having a maximum deposit surface temperature of 1647 °F (897 °C). The region marked “acceptable operation” in Exhibit 9-22 shows that at a maximum gas temperature of 2024 °F (1107 °C, 1380 K), deposits less than 1.25 in (3 cm) should be removable. This agrees with the experience in coal-fired power plants.

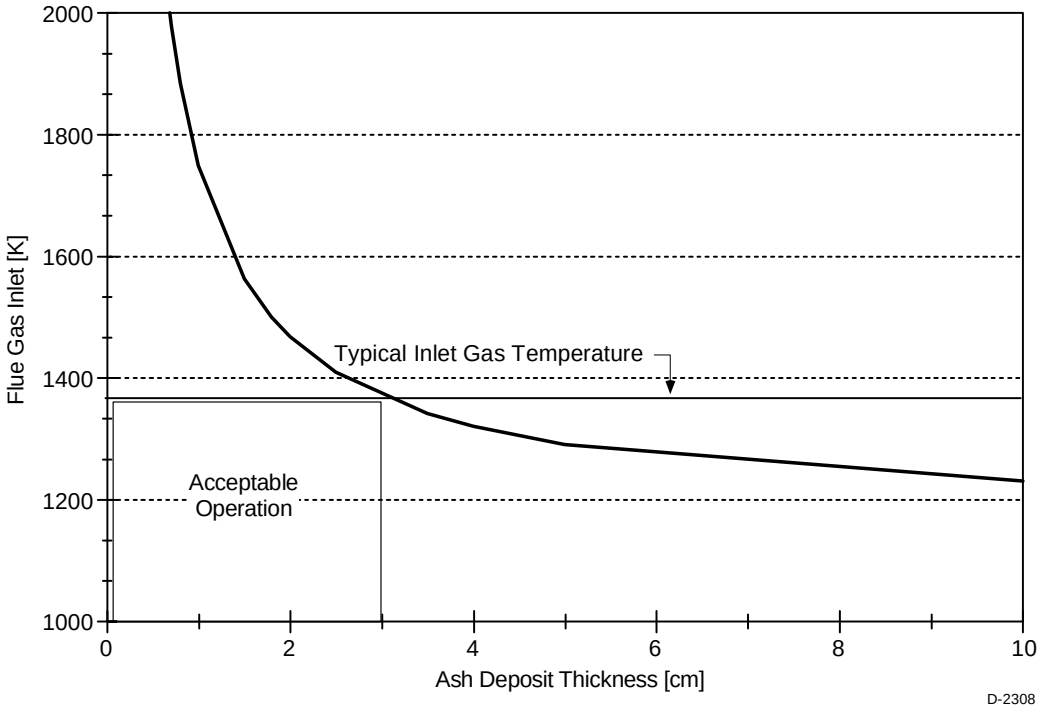

Exhibit 9-22
Maximum Allowable Flue gas Inlet Temperature for a Steam Reheater (Illinois No. 6 coal)

Exhibit 9-23 illustrates the effect of switching to a PRB coal on the maximum gas inlet temperature. For the same deposit thickness, the flue gas temperature must be decreased by about 360 °F (200 °C). Coal-fired boilers designed to burn high-fouling coals such as Wyodak-Rochelle employ furnace exit gas temperatures which can be 360 °F (200 °C) to 630 °F (350 °C) lower than those from units designed to burn bituminous coal (Borio, 1991). Thus, the method provides a means to estimate conditions for deposit removability. Next, it will be applied to the design of the convective air heater in the HIPPS furnace.

Results for the HIPPS convective air heater calculation are shown in Exhibit 9-24 for Illinois 6 and Wyodak-Rochelle. For Illinois 6 the maximum allowable flue gas inlet temperature is very sensitive to deposit thickness if the deposit thickness is less than 0.39 in (1 cm). If the convective air heater surface is 'clean,' the inlet gas temperature can be high, 2200 to 2700 °F (1227 to 1477 °C), for the bituminous coal. However, a clean surface cannot be expected during normal operation, especially at the inlet to the convective air heater where ash deposition is expected to be the highest. Modeling of deposition of the convective air heater (Sangiovanni, 1994) predicted a deposition rate about 0.025 in/hr (0.06 cm/hr). Deposits of less than 0.39 in (1 cm) are expected over an 8-hour period. Therefore, an inlet temperature of 1800 °F (982 °C) was chosen for the preliminary design for bituminous coals. Because the PRB coal, Wyodak-Rochelle, has a sintering temperature that is close to the working fluid temperature, the maximum allowable flue gas temperature is less than 1520 °F (827 °C).

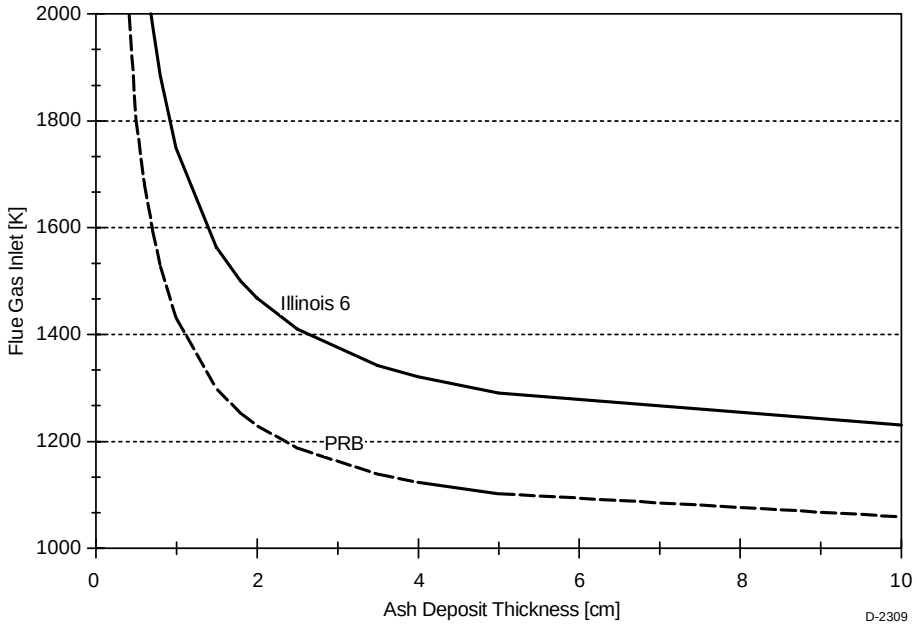

Exhibit 9-23
Maximum Allowable Flue gas Inlet Temperature for a Steam Reheater, Comparison of Illinois No. 6 Coal and PRB (Wyodak-Rochelle)

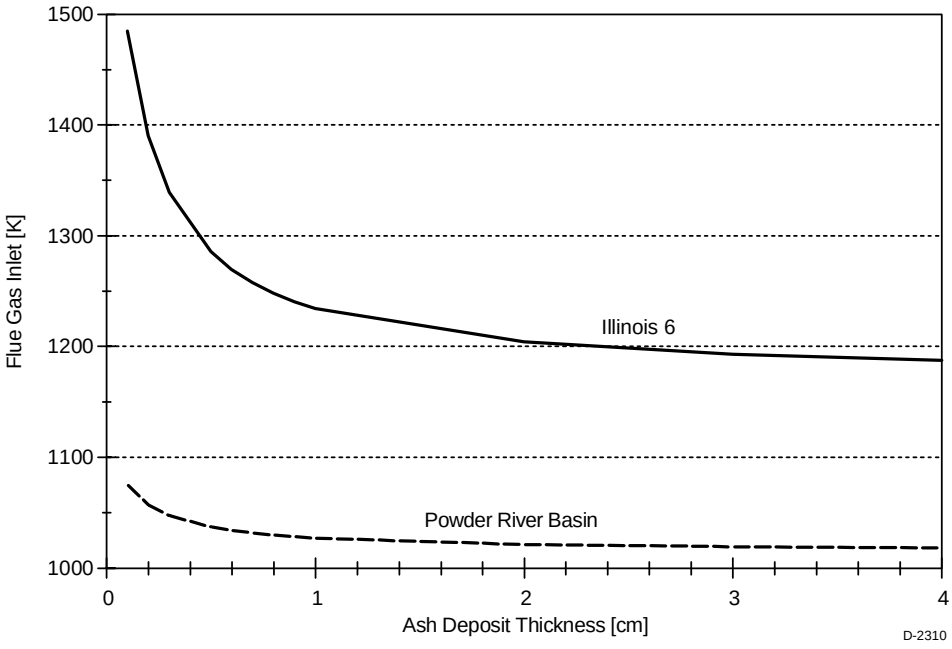

Exhibit 9-24
Maximum Allowable Flue Gas Inlet Temperature for HIPPS Convective Air Heater

Using the critical porosity and the bulk ash properties for bituminous and sub-bituminous coals, the maximum allowable deposit surface temperature and the maximum allowable flue gas

temperature in a convective heat exchanger were calculated. The calculation was carried out for conditions that represent the steam reheater section of a conventional pulverized coal-fired power plant and the result is consistent with observations from existing plants. As a result of this analysis, an inlet temperature of 1800 °F (982 °C) was chosen for the preliminary convective air heater design.

The accuracy of this method could be improved by adding more detail to the model for calculation of sintering rate in ash deposits. A single pore size and ash composition are not realistic assumptions. Pore size is probably not as big an issue as the composition, given the strong dependence of viscosity on composition (Senior, 1995). The composition of individual ash particles produced by a coal can vary widely as shown in Exhibit 9-25. For an eastern bituminous coal, the figure shows the frequency distribution of base/acid ratio based on the compositions of ash particles as compared with base/acid ratio determined from the bulk ash composition. A distribution of compositions implies that some ash particles will be relatively fluid at low temperatures while more refractory ones will not flow. Extending the sintering model to include a range of compositions will make the results more accurate.

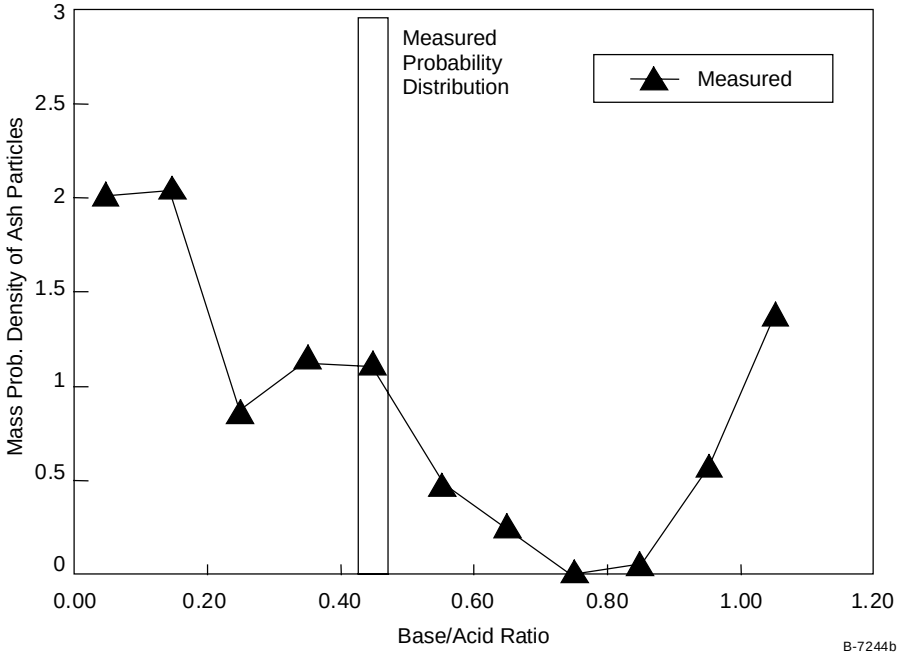

Exhibit 9-25
Distribution of Base/acid Ratio of Illinois No. 6 ash

The range of viscosity valves that is important for sintering of convective section deposits is high, 10^8 to 10^{10} poise (10^8 to 10^{10} Poise). No data on coal ash are available in this range, although there exist many measurements on simpler oxide systems at low temperatures (many of these references are cited in Senior and Srinivsaschar (Senior, 1995)). Well-controlled measurements of sintering rate in the laboratory can provide an indication of the viscosity (Scherer, 1977) and this may be a way to generate a better approximation. Furthermore, the formation of crystals in the deposit has not been accounted for. It is well known that heat treatment of ash causes crystallization and that this occurs in the boiler. Amorphous deposits

have higher strength than crystalline ones. Nowok et al. (Nowak, 1990) showed that heat treatment of a low rank coal ash reduced the strength. A more accurate method for calculating viscosity at low temperatures will also improve the accuracy and usefulness of the estimate.

Ash Mass Balance in HITAF

In the Phase I Final Report, an overall mass balance for ash in the commercial-scale HITAF was created for Illinois No. 6 coal. Prior to starting the designs for the commercial slag screen, quench zone, and convective air heater, it was important to revisit the ash mass balance, both to review the operational characteristics of the commercial unit and to ensure that the correct numbers for ash loading, etc were being used. In Phase II, PSI calculated the ash flow rates in HITAF as a function of particle size. Sticking probability of coal ash as a function of size and temperature was also provided.

Furthermore, a mass balance was calculated for an additional coal, Wyodak-Rochelle sub-bituminous coal because a sub-bituminous coal would be evaluated in the pilot-scale tests. Coals from the Powder River Basin (PRB) such as Wyodak are an important fuel for electric utilities. PRB coals are substantially different from eastern bituminous coals, both in their ash composition and combustion properties. Burning a PRB coal would require changes in the HITAF design and it was necessary to recognize this early in the design process.

Ash loading in the gas was calculated from the mass flow rates given in Table 9-9 for one HITAF combustor taken from the commercial plant design as outlined in the Phase II proposal. The flow rates for Wyodak coal were calculated using the ultimate, proximate, and heating value analyses for Wyodak-Rochelle coal, keeping the heat input to HITAF the same. Note that approximately the same amount of combustion air is required for both coals, even though the flow rate of Wyodak coal is higher than that of Illinois No. 6. This is because, while Wyodak has a lower heating value than Illinois No. 6, it also has a lower carbon content as well. Exhibit 9-26 shows the points in the HITAF that correspond to the flows in Table 9-9.

PSI's mineral transformation model (MMT) was used to generate an ash particle size distribution (psd) for Illinois No. 6 that is used as a starting point for the deposition calculations. The ash particle size and composition for Wyodak-Rochelle coal was calculated from a computer-controlled scanning electron microscopy (CCSEM) analysis of the ash as measured in Phase I.

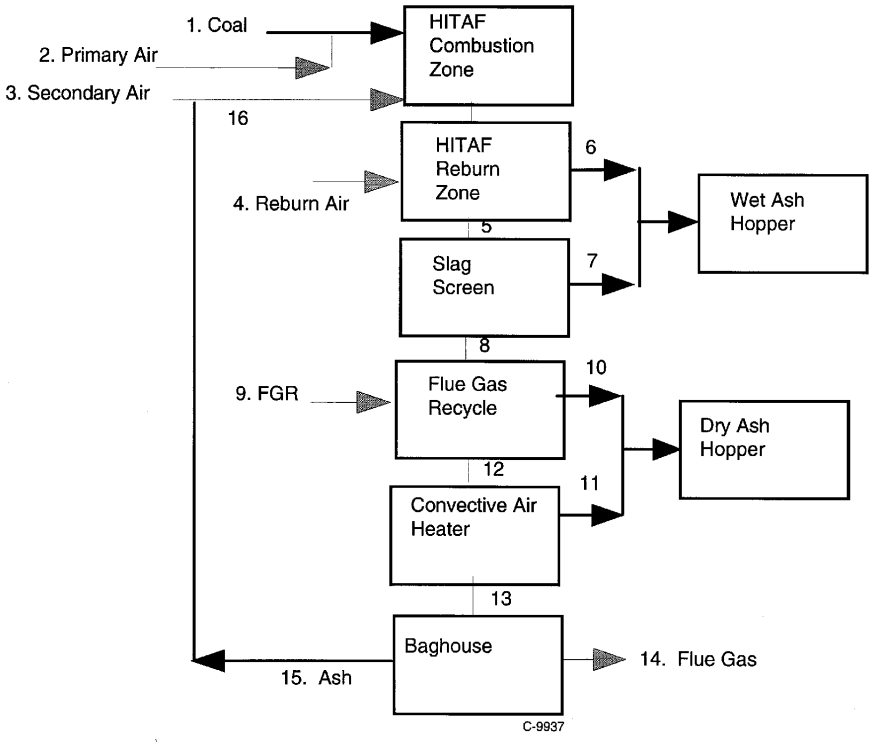

Exhibit 9-26
Ash Mass Balance in HITAF

Table 9-9
Baseline HITAF Flows for Ash Mass Balance
(Illinois No. 6 and Wyodak-Rochelle)

No.	Stream	T, °F (°C)	Illinois 6 Flow (lb/s)	Wyodak Flow (lb/s)
1	Coal	138 (59)	17.3	20.4
	Gas Flows:			
2	Primary Air	138 (59)	26.2	26.2
3	Secondary (vitiated) Air	1005 (540)	143.4	143.4
4	Reburn (vitiated) Air	1005 (540)	32.9	32.9
5	Slag Screen Inlet	2800 (1538)	217.9	217.9
8	Slag Screen Outlet	2650 (1455)	217.9	217.9
9	Flue Gas Recycle	256 (125)	117.0	117.0
12	Convective Air Heater Inlet	1800 (983)	334.9	334.9
13	Convective Air Heater Outlet	1190 (643)	334.9	334.9
14	Baghouse Outlet	350 (177)	334.9	334.9

Deposition in the Radiant Air Heater and Convective Air Heater was calculated as described in the Phase I Final Report. No deposition was assumed in the slag tap region or in the dilution/quench zone. The collection efficiency in the slag screen was taken to be the result from UTRC CFD calculation S96-2. This was considered to be an upper bound on slag screen collection, as discussed under the subsection of Comparison with CFD results. In the slag screen, all ash particles that strike the tubes were assumed to stick. In the convective air heater, the ash particles were assumed to have some probability of sticking (Tables 9-10 and -11). For the first three tubes of the convective air heater, a sticking probability corresponding to 2000 °F (1093 °C) was used. For the balance of the convective air heater the corresponding temperature was 1800 °F (982 °C). The collection efficiency for ash particles in the Radiant Air Heater, Slag Screen, and Convective Air Heater is summarized in Table 9-12.

Table 9-10
Adhesion Efficiency as a Function of Ash Particle Size and Temperature
Illinois No. 6-Burning Star

T, °F (°C)	TOTAL	<5 µm	5-10 µm	10-20 µm	20-40 µm	>40 µm
1800 (982)	0.01	0.04	0.01	0.00	0.00	0.00
2000 (1093)	0.05	0.10	0.09	0.02	0.05	0.06
2200 (1204)	0.11	0.22	0.19	0.09	0.05	0.06
2400 (1315)	0.55	0.71	0.60	0.55	0.45	0.58
2600 (1427)	0.72	0.84	0.77	0.72	0.68	0.64
2800 (1538)	0.84	0.89	0.83	0.82	0.87	0.70
3000 (1649)	0.84	0.89	0.85	0.83	0.87	0.70

Table 9-11
Adhesion Efficiency as a Function of Ash Particle Size and Temperature
Wyodak-Rochelle

T, °F (°C)	TOTAL	<2.5 µm	2.5-5 µm	5-10 µm	10-20 µm	20-40 µm	40-100 µm
1700 (927)	0.34	0.40	0.35	0.33	0.27	0.32	0.27
1800 (982)	0.38	0.44	0.39	0.37	0.36	0.36	0.31
2000 (1093)	0.48	0.57	0.50	0.47	0.46	0.46	0.40
2200 (1204)	0.64	0.75	0.67	0.63	0.62	0.62	0.53
2400 (1315)	0.70	0.80	0.72	0.69	0.66	0.66	0.56
2600 (1427)	0.72	0.82	0.75	0.71	0.63	0.68	0.58
2800 (1538)	0.79	0.90	0.82	0.78	0.69	0.74	0.63
3000 (1649)	0.79	0.90	0.82	0.78	0.69	0.74	0.63

Table 9-12
Total Ash Collection Efficiency for HITAF Components

Unit	Illinois No. 6	Wyodak-Rochelle
Radiant Air Heater	1.8%	1.2%
Slag Screen	63.7%	36.9%
Convective Air Heater	2.2%	35.6%

Since Illinois No. 6 has many large ash particles, it shows a high collection efficiency in the slag screen. On the other hand, very little Illinois No. 6 ash is predicted to deposit in the convective air heater because the ash particles are not very sticky below 2200 °F (1203 °C). Wyodak coal produces much finer ash that has a correspondingly lower collection efficiency in the slag screen. The ash is quite sticky at low temperatures which means that more deposition will take place in the convective air heater.

The effect of recycling ash from the baghouse to the furnace was also examined. In order to produce a high value ash product, the fine ash collected in the baghouse can be re-injected into the furnace. All ash then leaves the HITAF through the ash hoppers, primarily through the wet ash hopper. The glassy slag produced from the wet ash hopper can then be sold for aggregate material. The ash mass balance was calculated with and without recycle of the baghouse ash. The results of these calculations are given in Table 9-13.

Table 9-13
Ash Deposition Rates with and without Recycle

Unit	Illinois No. 6 Flow, lb/s		Wyodak Flow, lb/s	
	Baseline	With Recycle	Baseline	With Recycle
Radiant Air Heater	0.03	0.06	0.01	0.02
Slag Screen	1.20	1.80	0.35	0.56
Convective Air Heater	0.02	0.05	0.21	0.38

Recycling ash produces a 50% increase in the amount of ash deposition in the slag screen for both coals. The deposition in the convective air heater doubles for both coals. This is not very significant for Illinois No. 6 since the deposition rate in the convective air heater is so low. However, deposition in the convective air heater for Wyodak (and other low rank coals) could pose a problem.

The commercial-scale mass balance results provide some insight into design of the pilot-scale equipment. Illinois No. 6 should have relatively high deposition rates in the slag screen section which should run wet, unless the temperature falls below 2200 °F (1203 °C) - a potential problem during start-up. Not much deposition of ash is expected in the convective air heater test section as long as the temperatures stay below 2200 °F (1203 °C). A PRB coal, on the other hand, is expected to produce significant deposits in the convective air heater. Since these deposits should sinter rapidly, deposit removal should be investigated.

Pilot Scale Operation

Pilot Scale Slag Screen Design

Once the design on the commercial slag screen was completed, the design for the slag screen for the EERC pilot scale facility was initiated. Originally the slag screen for the pilot scale facility was going to be a scaled-down version of the commercial slag screen. The plan at that point was to utilize measurements from the pilot scale experiments to validate the models that will be used to finalize the commercial design. However, when the data required to fully validate the models was evaluated it was quickly realized that it wouldn't be cost-effective (or technically feasible in some cases) to collect the required data on the pilot scale slag screen. The small size of the slag screen, causing significant wall effects, would also prevent using the data developed to finalize the commercial slag screen design. Therefore, it was decided that the primary goal of the pilot scale slag screen will be to provide an ash psd entering the CAH that is comparable to that expected in the commercial plant thus providing a more realistic test for the convective air heater.

Based on discussions with EERC, the pilot scale slag screen was designed to meet the following criteria:

1. The slag screen must not plug in the event of large deposit buildup on the tube surface
2. Flow in the slag screen must not be restricted by slag buildup on the floor
3. The pressure drop in the slag screen must not exceed 2 in (5.1 cm) of water
4. The materials in the slag screen must be inexpensive and robust - this criterion will allow us to modify the design quickly if required,
5. The Reynolds number (based on the tube diameter) must not go below 2100 to ensure turbulent flow models apply.

Based on these criteria the PSI slag screen simulation model (SSSiM) was used to design a suitable pilot-scale slag screen. A simplified spreadsheet, based on the scaling equations, was used to estimate the acceptable tube size, tube spacing, and operating velocity. The resulting design was similar to the commercial scale design, but had a few minor variations. First, much smaller tubes and a slightly closer tube spacing were used in order to maximize the number of tubes in a row while still maintaining turbulent flow. Another change from the commercial scale design was the absence of a large space between the third and fourth rows of tubes. As it was anticipated that on-line cleaning of the tubes on the pilot scale would not be performed, and simulation of commercial scale was no longer being attempted, the path between rows 3 and 4 was removed to conserve space.

Once the spreadsheet was used to define the optimum tube parameters and operating conditions, the full SSSiM was used to determine the temperature drop across the slag screen. It was assumed that the gas within each mullite tube would be kept at some fraction of the gas temperature. This assumption was based on the fact that the tubes are sealed on both ends (no convective cooling) and that the heat loss due to conduction from the tube material to the wall is fairly low.

One effect of the smaller size that was immediately obvious was the higher heat loss in the smaller unit, due to a higher surface to volume ratio. In order to estimate the safe range of operation, the gas temperature inside the tube was varied from 90 to 99% of the gas temperature

outside the tube. At temperatures below 93% of the gas temperature (2500 °F (1371 °C)) the slag on the floor of the duct built up enough to severely constrict the flow. At temperatures above 95% of the gas temperature 2570 °F (1410 °C)) the flow was not constricted at all. As the tube is effectively isolated in the gas stream, and the flue gases could enter the tubes as discussed below, it was likely that the gas temperature inside the tubes (and the tube temperature) would equilibrate to a temperature very close to the bulk gas temperature. However, it was important to monitor this temperature inside the tubes to ensure that the tube walls are above the critical temperature at all times. To accomplish this it was recommended that thermocouples be placed into a tube in the first and last row.

The pilot-scale slag screen is shown to scale in Exhibits 9-27 and -28. The slag screen design information is outlined below.

- The tubes would consist of 1.5 in (3.8 cm) (OD) uncooled mullite tubes.
- There would be 6 rows of tubes, 3 tubes per row.
- The centerline spacing of tubes in each row would be 3¾ in (9.5 cm).
- The centerline spacing between rows would be 42 in (106.7 cm).
- There would be a 4 in (10.2 cm) layer of insulating refractory on all walls.
- There would be a 2 in (5.1 cm) layer of hard refractory on the side walls.
- There would be a 6 in (15.2 cm) layer of hard refractory on the roof and floor.
- The height of the duct would be 8¾ in (22.2 cm) (without refractory).
- The width of the duct would be 13 in (33.0 cm) (without refractory).
- The gas velocity entering the slag screen would be approximately 60 ft/s (18.3 m/s).

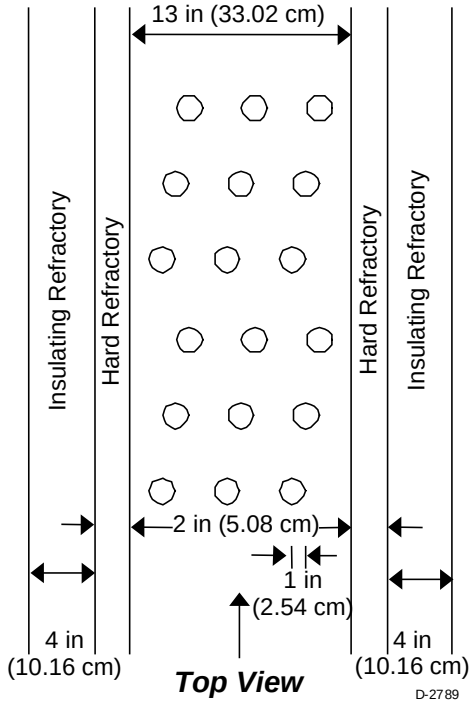

Exhibit 9-27
Top View of Pilot Scale Slag Screen

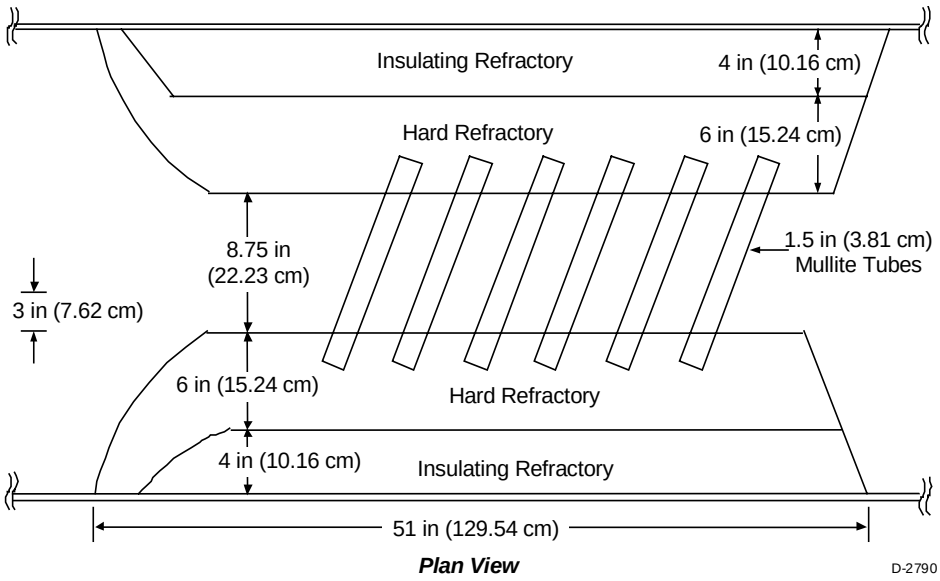

Exhibit 9-28
Plan View of Pilot Scale Slag Screen

Each of the mullite tubes was intended to have several breather holes drilled or cut into the sides. These holes would allow the pressure inside the tubes to balance with that in the slag screen during heat up to prevent the air trapped in the tubes during casting from cracking the tubes due to the increased pressure as the tubes are heated up. These holes would also allow the temperature inside the tubes to equilibrate with the gas temperature outside the tubes. By placing the holes on the side of the tubes (in between the tubes in a row) plugging of the holes by flowing slag could be avoided. The use of uncooled tubes would also prevent a large buildup of frozen ash on the tube surfaces.

Although the initial design called for mullite tubes, another material could be substituted based on the EERC slag corrosion data to prevent the slag from 'eating through' the tubes during the experiment. The final dimensions of the slag screen was intended to be approximately 25 in (63.5 cm) wide, 28¾ in (73.0 cm) tall, and 50 to 60 in (127.0 cm to 152.4 cm) long. The length included room for approximately 6 tube diameters at the entrance to allow the flow to settle down before entering the slag screen. EERC finalized the length based on the length of the duct between the furnace and the dilution zone. The slope of 20 deg included in the current EERC design should be sufficient to ensure that the slag flows from the slag screen into the slag tap.

The lower gas velocity (as compared to the commercial design) was expected to yield a pressure drop of less than 1 in (2.5 cm) of water, which was well within the design criteria. Another important feature of the slag screen design was the placement of the rows. As with the commercial slag screen, the rows in the smaller scale slag screen were offset so that even if the deposits on the leading edge and trailing edge of the tubes connect there would still be an open path through the slag screen. Therefore, although the efficiency of the slag screen would decrease if the tube deposits grew much larger than predicted, the design should prevent catastrophic plugging.

As mentioned above, the primary goal of the pilot scale slag screen was to generate an ash psd entering the CAH that is comparable to that expected in the full scale. A comparison of the collection efficiencies for both designs (assuming particle dispersion between rows) can be seen in Exhibit 9-29. As can be seen from this figure, the collection efficiencies are very similar, therefore we should get similar ash particle size distributions and loadings into the dilution zone.

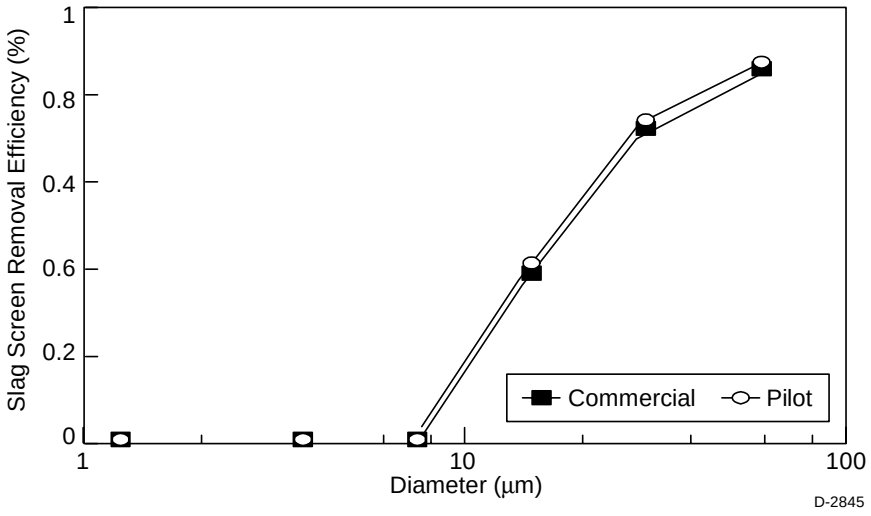

Exhibit 9-29
Removal Efficiencies of Pilot and Commercial Scale Slag Screens

Review of Pilot Scale Ash Behavior

Although the pilot scale combustor at EERC was not designed to remove ash in exactly the same way as a full-scale unit might, it is still useful to look at the performance of ash removal in the pilot scale system. Many different coals were burned in the pilot-scale unit as summarized in Table 9-14.

The slag screen and slag tap have been the places that have felt major ash impacts in the pilot scale high temperature slagging furnace. Excessive slag build up has not generally been reported on the radiant air panels, although the castable refractory at the bottom of the furnace did at one point become saturated with slag and slump into the slag tap. This indicates that slow buildup of ash on the furnace refractory surfaces will cause long term operating problems, even if there is not visible flowing slag layer in the furnace. The exception to this was with one of the lignite coals for which there was a great deal of flowing slag in the radiant section.

Table 9-14
Coals Burned in EERC Pilot-Scale Combustor in Phase II

Date	Coal	Rank
6/97	Illinois #6	Bituminous
9/97	Illinois #6	Bituminous
10/97	Wyodak (Rochelle)	Sub-bituminous
12/97	Illinois #6	Bituminous
2/98	Illinois #6	Bituminous
3/98	Wyodak (Rochelle)	Sub-bituminous
4/98	Coal Creek Station	Lignite
6/98	M R Young Station	Lignite
8/98	Illinois #6	Bituminous
1/99	Illinois #6	Bituminous
2/99	Eastern Kentucky	Bituminous
4/99	Illinois #6	Bituminous
5/99	Illinois #6	Bituminous
9/99	Prater Creek	Bituminous
12/99	Illinois #6	Bituminous
3/00	Cordero Rojo	Sub-bituminous
6/00	Eastern Kentucky	Bituminous
6/00	Prater Creek	Bituminous

The slag screen, in its final Phase II incarnation consisted of three to six rows of tubes (three tubes to a row). The tubes were made of castable refractory with water-cooled inner tubes. The initial outer diameter of the refractory was 1.5 in (3.8 cm), although this sometimes changed dramatically after operation with ash. Inside the refractory tube were water-cooled stainless steel tubes. There was an air gap between the refractory and the steel to prevent excessive removal of heat by the slag screen. The OD of the stainless steel tubes has been varied from 0.125 inches (0.3 cm) up to 0.375 inches (1.0 cm), depending on how high the inlet gas temperature to the slag screen needs to be. The tubes were embedded in castable refractory that formed the roof, walls, and floor of the slag screen section. The floor of the slag screen was sloped to allow slag to flow into the slag tap.

EERC concluded that the slag screen inlet temperature should be selected on the basis of the ash fusion data. They tried to operate the slag screen at a flue gas inlet temperature of 100 to 200 °F (56 to 112 °C) above the fluid temperature of the ash. If this is followed, then the inlet temperature should be 2400 to 2600 °F (1315 to 1427 °C) for the Wyodak coal and lignites and 2700-2900 °F (1482 to 1593 °C) for the bituminous coals.

For the operation of the slag screen, only three rows of tubes were used when firing the bituminous coals. (Every other row was removed, doubling the spacing between rows.) Presumably this was because of both the high ash content of these coals and the high ash fusion temperature. For very high ash fusion temperatures (e.g., the Eastern Kentucky bituminous coal), limestone was added to the coal to decrease the viscosity of the ash in the slag screen. For the low rank coals, six rows of tubes were used. The slag screen tubes do not last long. In some

cases, less than 100 hours of operation was enough for the slag to eat away the refractory entirely.

Nominally, 10% to 15% of the ash is removed in the baghouse. The rest is removed upstream. Approximately 70% of the ash is removed from the furnace, slag pot and dilution/quench zone; most of this is removed by the slag screen.

The dilution/quench zone experienced some ash build-up problems, particularly around the FGR nozzles. This problem was most evident when rows were removed from the slag screen, causing more ash to make it through. This could be dealt with by EERC without too much trouble. However, design of a larger scale system should involve consideration for how to design the dilution/quench zone for minimal ash build up. The convective air heater design appeared to work well in the pilot scale furnace with a gas inlet temperature of 1800 °F (982 °C).

References

ASM Handbook Volume 3: Alloy Phase Diagrams; ASM International, 1992; 2-42 and 2-48.

Borio, R.W.; Levasseur, A.A.; Chow, O.K.; Miemiec, L.S. "Ash Deposition: A Boiler Manufacturer's Perspective," *Inorganic Transformations and Ash Deposition During Combustion*; ASME: New York, NY; 1991.

Ferber, M.K.; Tennery, V.J. "Behavior of Tubular Ceramic Heat Exchanger Materials in Basic Coal Ash from Coal-Oil-Mixture Combustion," *Ceram. Bull*. **1984**, *63* (7), 898-904.

Frenkel, J. "Viscous Flow of Crystalline Bodies Under the Action of Surface Tension" *J.Phys.(Moscow)*, 1945, *9*, 385-391.

Hiram, Y.; Nir, A. "A Simulation of Surface Tension Driven Coalescence" *J. Colloid Inter. Sci.* 1983, *95*, 462-470.

Israel, R.; Rosner, D.E. *Aeros. Sci. Tech.*, **1983**, 2, 45-51.

Jung, B.; Schobert, H.H. "Improved Prediction of Coal Ash Slag Viscosity by Thermodynamic Modeling of Liquid-Phase Composition," *Energy and Fuels*, **1992**, *6*(4), 1992, 387–398.

Kalmanovitch, D.P.; Frank, M., "An Effective Model of Viscosity for Ash Deposition Phenomena," In *Mineral Matter and Ash Deposition From Coal*; The Engineering Foundation, 1990.

Kays, W.M. *Convective Heat and Mass Transfer*, McGraw-Hill, New York, NY, 1966.

Kzukauskas, A. *Advances in Heat Transfer*, J.P. Hartnet and T.F. Irvine Jr., Eds, **8**, Academic Press, New York, NY, 1972.

McCollor, D.P.; Zygarlicke, C.J.; Mann, M.D.; Hurley, J.P.; Timpe, R.C.; Bieber, J.C.; Ramanathan, M.C.; Strobel, T.M.; Nowok, J.W.; Swanson, M.L.; Jones, M.L., Weber, G.F. *Advanced Power Systems; topical report for task No. 3.0*, U.S. Department of Energy Cooperative Agreement DE-FC21-93MC30097; 1994, in press.

Mackenzie, J.K.; Shuttleworth, R., "Phenominological Theory of Sintering," *Proc. Phys.Soc.(London*), 1949 *B62*, 833-852.

Nowok, J.W.; Benson, S.A. *Inorganic Transformations and Ash Deposition During Combustion*; ASME: New York, NY; 1991, pp. 405-424.

Nowok, J.W.; Benson, S.A. Jones; Kalmanovitch, D.P., "Sintering behaviour and strength development in various coal ashes," *Fuel*, 1990, *69*, 1020-1027.

Raask, E. *Mineral Impurities in Coal Combustion*; Washington, D.C.: Hemisphere Publishing, 1985.

Rodgers, M.W. *Slag Layers in Coal-Fired MHD Generators*, PhD Dissertation, Stanford University, 1979

Sangiovanni, J.J.; Seery, D.J.; Chiappetta, L.; Senior, C.L. "Coal-Fired High Performance Power Generating System," ASME Paper 94-JPGC-PWR-3, 1994.

Scherer, G.W., "Sintering of Low-Density Glasses: I, Theory," *J.Am.Cer.Soc.*, 1977, *60*, 236-239.

Scherer, G.W.; Bachman, D.L., "Sintering of Low-Density Glasses: II, Experimental Study," *J.Am.Cer.Soc.*, 1977, *60*, 239-243.

Senior, C.L.; Srinivasachar, S. "Viscosity of Ash Particles in Combustion Systems for Prediction of Particle Sticking," *Energy & Fuels* 1995 *9*(2), 277-283.

Stultz, S.; Kitto, J. *Steam: Its Generation and Use*, 40th Edition; The Babcock & Wilcox Company: Barberton, OH; 1992.

Section 10 - Duct Heater

Abstract

Funded as Task 2.4, the Duct Heater development program goal was to develop a low NO_X emissions in-duct boost heater capable of raising the discharge temperature of the RAH to that required for the gas turbine. The design of the HIPPS cycle has assumed that materials limitations would require a boost heater to raise the RAH exhaust temperature to an appropriate inlet temperature. The state-of the-art gas turbines in the baseline cycle have turbine inlet temperatures around 2500 °F (1371 °C), well above the working temperature of available RAH containment materials. In the DOE requirements for the program 65% of the fuel input must be coal and 35% can be a premium fuel such as natural gas. The baseline UTRC HIPPS design, natural gas is used to boost the air temperature from 1700 °F to 2500 °F (930 °C to 1371 °C). The technical challenge is to mix the fuel (natural gas) with the high temperature air rapidly enough to avoid forming NOx.

The hot air stream must be mixed with the fuel gas to form a very lean (stoichiometry <0.2) mixture in a time that is shorter than the NOx formation time. In our designs, the centrifugal mixing approach was chosen to achieve this goal. Based on some experiments and detailed chemical kinetic calculations the UTRC duct heater design can mix rapidly enough to avoid significant chemical reaction at near stoichiometric conditions. The experimental studies on the duct heater mixing were ultimately truncated because of the program restructuring.

Nomenclature

a_r	Radial acceleration
C_{avg}	Fully-mixed jet mixture fraction
D	Jet orifice diameter (inches)
g	Gravity force (= 1 with body at rest)
J	Jet-to-Mainstream momentum flux ratio
LBM	Pounds mass
P	Pressure (psia)
R*	Richardson Number (defined in text)
r	Radius (inches)
ρ_b	Density of burned gas (lbm/ft^3)
ρ_u	Density of unburned gas (lbm/ft^3)
ρ_j	Density of gas jet (lbm/ft^3)
ρ_0	Density of free stream gas (lbm/ft^3)
σ	Mass-weighted standard deviation
T	Temperature
ΔT	Temperature standard deviation
U	Unmixedness Parameter (defined in text)
u	Axial velocity (ft/sec)
V_j	Jet velocity (ft/sec)
V_0	Velocity of free-stream gas (ft/sec)
W	Tangential velocity (ft/sec)
X	Axial distance (ft)

Z Distance along gas jet centerline (ft)

Preliminary Engineering Analysis

The combined cycle power plant described in this document will utilize a 161 MWe gas turbine powered generator. From thermodynamic analysis of the combined cycle it has been determined that the optimum input temperature for the power turbine should be 2495 °F (1370 °C) at 225 psia (1550 kPa) for an air mass flow rate of 726.5 lbm/s (330 kg/s). Since the high-temperature coal-fired air heater will operate with a discharge temperature of 1700 °F (930 °C), a boost heater is needed to provide the additional energy to operate the turbine at the required power output. The key requirements in the design of the boost heater are:

- Pressure drop less than 1.5% of airflow total pressure
- Uniform exit temperature profile
- Ultra-low emissions of NO_x and CO

These requirements can be met with mixer/combustor designs, which have been developed at UTRC as a result of research into gas turbine combustors for ground-based and aircraft turbines, and in micronized coal combustion research.

Heater Thermodynamics

The pressure drop through any combustor or mixer design is a direct function of the mass flow through the system. If the total mass flow of air to be heated is fixed, there is an optimum configuration which will provide the required heating rate, temperature profile, and pressure drop with piping that will match the physical dimensions of the gas turbine to be used. Based upon experience at UTRC on gas turbine combustor design, it is desirable to maintain duct velocities around 50 ft/s (15.2 m/s) to reduce piping losses and to obtain a boundary layer of moderate size. Gas velocities in practical combustors are maintained below 200 ft/s (61 m/s) for flame stability, and momentum ratios between air streams are typically 4 to 1 to aid in mixing. Using these criteria as general guidelines, the gas turbine air path was analyzed to determine the optimum method of providing the additional energy downstream of the air heat exchangers needed for the combined cycle.

Analysis shows that by splitting the flow into two streams, the size of ductwork, swirler dimensions, and mixing patterns can be optimized. However, each flow stream must experience a 795 °F (425 °C) temperature rise, with a total heat input of 3.567×10^8 Btu/h. To obtain this temperature rise, the flow could be further split so that 33% of the air would pass through a combustor, and 67% of the air would bypass the burner. This would reduce the overall pressure loss of the flow, since the burner is the high-pressure-loss side of the flow and only 1/3 of the airflow would experience this pressure drop. This flow split, however, is not practical because of the high temperatures required in the burner flow in order to provide the overall temperature rise of 795 °F (440 °C). Based upon the enthalpy of the total and split flow streams, the burner discharge temperature would approach 4000 °F (2205 °C). Not only would this present a materials problem, but also more importantly, it would present a serious thermal NO_x problem.

Studies of the production of NO_x in flames (Semerjian, 1977, Tacina, 1990, Merryman, 1975) have indicated that the production of "thermal" NO_x increases dramatically when

combustion temperatures exceed 2420 °F (1330 °C). Therefore, to reduce NO_x emissions from the boost heater, it is imperative that temperatures above this level be avoided. For this reason, the burner concept incorporating a 33% flow split cannot be used due to the high NO_x levels which would result. The optimum configuration will involve staged mixing which maintains a fuel-lean mixture at all times and prevents temperatures from exceeding 2420 °F (1330 °C). Premixing is not possible due to the high inlet temperature of the gas stream; the natural gas will oxidize very rapidly under the inlet conditions (reaction times < 30 msec). Residence times should be kept to a minimum at elevated temperatures in order to curtail reactions in the high temperature, very fuel lean flow that is proposed by the cycle analysis.

Mixer Aerodynamics

To provide rapid mixing with low-pressure-loss, the concept of centrifugal mixing, which utilizes density gradients within swirling flow to promote instability and mixing, will be utilized. This concept has been investigated for over 15 years at UTRC and Pratt & Whitney Aircraft (Vranos, 1982, Freihaut, 1989, Markowski, 1976, Johnson, 1986). Experiments detailed in Freihaut (1989) have demonstrated complete mixing of gaseous fueled diffusion flames in as little as 1.5 duct diameters under high intensity flame conditions. **It is emphasized here that the centrifugally enhanced mixer concept has been demonstrated successfully in reacting (combusting) flow in a previous DOE-sponsored contract.**

The concept of centrifugal mixing involves utilizing the instability created by density gradients within a swirling flow to enhance mixing between the flows. For an axisymmetric, swirling fluid with a small radial velocity, the condition for dynamic equilibrium is given by the equation:

$$\frac{\partial p}{\partial r} = -\rho_u \frac{w^2}{r} \tag{1}$$

Here ρ_u is the density of unburned flammable mixture, w is the tangential velocity, p is the static pressure, and r the distance from the center of rotation. If an annular element of flammable mixture is suddenly ignited along its periphery (as in the case of an annular pilot flame), a local density change is introduced, and the dynamic equilibrium is upset. This leads to a radial acceleration, so that

$$\frac{\partial p}{\partial r} = -\rho_b \frac{w^2}{r} + \rho_b a_r \tag{2}$$

Finally, the radial acceleration of a fluid element is then given as:

$$a_r = \frac{w^2}{r}\left(1 - \frac{\rho_u}{\rho_b}\right) \tag{3}$$

The subscripts u and b refer to unburned and burned fluid, respectively. If the combustion kinetics are sufficiently fast, the acceleration is tantamount to inward flame propagation, and the propagation rate is controlled by the density ratio of burned and unburned gases, and the acceleration term w^2 / r. An excellent correlation has been found between turbulent flame speed

and w^2 / r. It is believed that inertial effects induced by fluid rotation can substantially increase the rate of heat and mass transfer between the two streams. Experimental data and theory indicate that the centrifugal acceleration effects become pronounced when the centripetal acceleration exceeds 1000 g's.

In nearly every practical combustor design, gas temperature and local stoichiometry is controlled through the use of transverse jets which bring combustion or dilution air into the reaction zone. The design of a combustor incorporates airflow splits between dilution jets and the main flow to obtain the desired pressure loss, total mass flow, and staged stoichiometry to control emissions. Research conducted in the area of turbulent jet mixing in cross-flows has been conducted at UTRC for many years (Vranos, 1988). The results of these and other studies have indicated that the penetration of a jet of diameter D into a cross flow can be given by:

$$\frac{Y}{D} = 0.76 \left(\frac{\rho_j V_j^2}{\rho_o V_o^2} \right)^{0.52} \left(\frac{\rho_j}{\rho_o} \right)^{0.11} \left(\frac{X}{D} \right)^{0.29} \tag{4}$$

where subscript j refers to the jet, X is the distance downstream from the jet discharge, and Y is height above the orifice discharge. The design of a natural gas fired boost heater requires complete oxidation of the natural gas and complete penetration of the air jets within the combustor length. The above correlation was used to evaluate the boost heater to en-sure complete mixing in the length available.

Initially Proposed Heater Design

Based upon UTRC's experience in swirling flows, dilution jet mixing, NO_X formation chemistry, and rapid mixing, a design concept, shown in Exhibit 10-1, was analytically evaluated. This design was projected to provide a uniform hot gas stream to the turbine at minimum NO_X levels. The cycle analysis and heat exchanger design dictated that the airflow to the turbine would be divided into two gas streams. Therefore, two in-duct heaters would be required; the air mass flow through each heater would be 363.25 lbm/s (164.8 kg/s), and fuel flow would be 3.63 lbm/s (1.65 kg/s). The heater would operate with an inlet temperature of 1700 °F (930 °C) at 225 psia (1550 kPa), with a discharge temperature of 2495 °F (1370 °C).

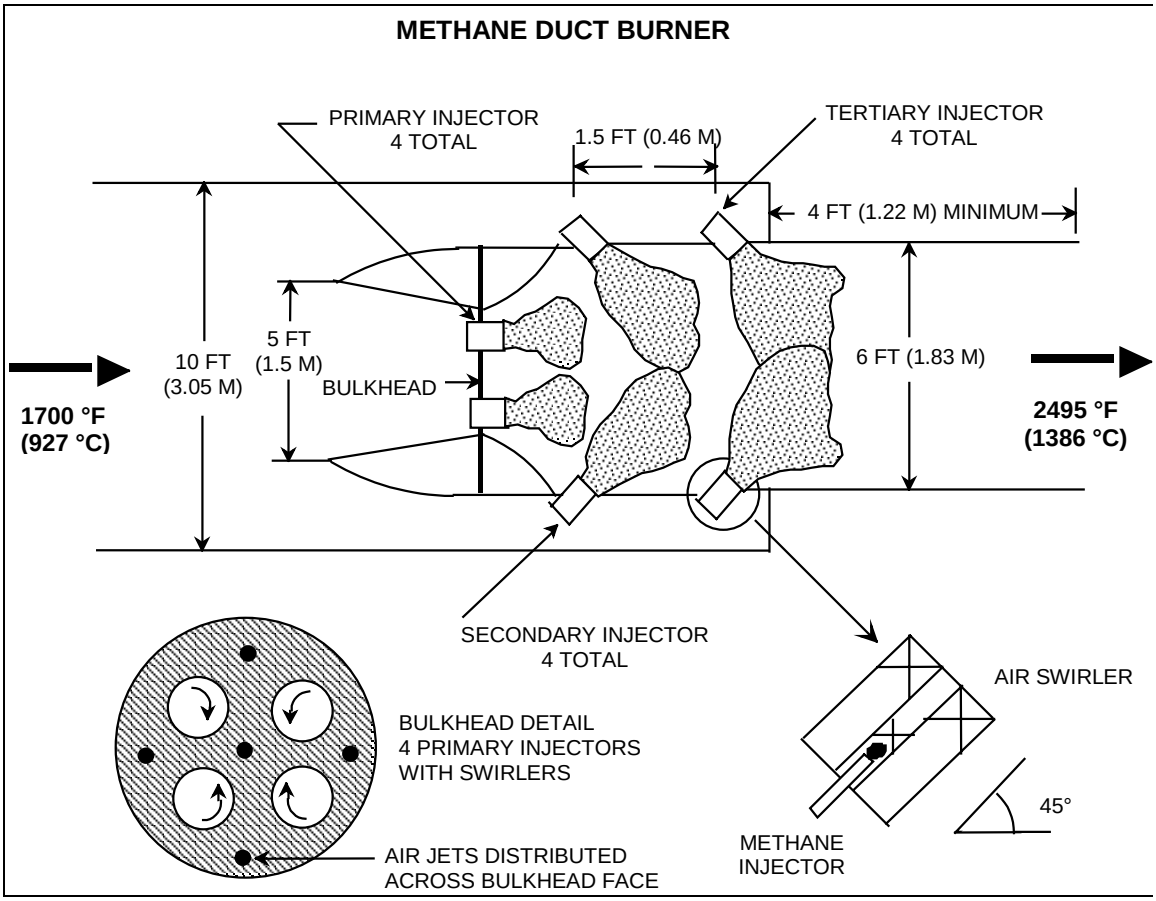

Exhibit 10-1
Initially Proposed Duct Heater Concept

To minimize NO_x emissions, the fuel input must be tailored to maintain constant fuel-lean conditions; in particular operation at stoichiometric conditions must be avoided. The kinetics of natural gas oxidation at the elevated temperature and pressure of the air stream were studied using a chemical-kinetics code (CHEMKIN©). The calculations determined that at an equivalence ratio (Φ) = 0.18, the fuel is completely oxidized in 29 msec. The important fact to note is that the inlet conditions to the heater promote rapid oxidation of the fuel. The heater is not a combustor in the conventional sense. No flame stabilization is required, no piloting zones, no recirculation for flame retention, and no dilution for temperature profiling is needed for this type of heater. What is most important is rapid mixing at minimum pressure loss, with stoichiometry carefully controlled to ensure complete oxidation with minimum NO_x production. This is the key concept of the design outlined below.

In the schematic representation of the duct heater as shown in Exhibit 10-1, the fuel is injected in three stages through a total of 12 centrifugally enhanced mixers. Each swirl module will pass 30.27 lbm/s (13.7 kg/s) of air, with fuel input through central injectors and swirlers to maintain Φ = 0.18. Each swirl module incorporates centrifugal mixing, due to the density ratio of 2.56 between the cold central fuel and the hot outer air. The swirl module is proposed to be of 9-in. (22.9 cm) outer diameter with a 1-in. (2.5 cm) inner swirl annulus for fuel flow. The mass-average velocity through the air swirler will be 195 ft/s (59.4 m/s), which will provide a

centripetal acceleration (V^2/r) of 7000 g's if a 45° swirl angle is used. Based on the results of past studies, this acceleration would promote very rapid mixing and ensure that the local stoichiometry would remain very lean to avoid temperature peaks. This rapid mixing is essential for low NO_x emissions. The spacing of injection stages was tailored to allow complete oxidation of each stage of fuel; the overall length of 7 ft (2.1 m) would ensure a uniform profile at the discharge plane. The swirl module dimensions, duct size, and duct length were chosen to theoretically provide complete penetration of the "jets" by the discharge plane, and the velocity levels in the swirlers were comparable to those tested in Freihaut (1989), Markowski (1976), Johnson (1986).

The largest impact of this type of heater design is in pressure drop imposed upon the system. Based upon the results of Markowski (1976) and Johnson (1986), and theoretical calculations, the expected pressure loss through the swirl modules would be less than 1.5% of the air flow total pressure. This pressure loss will not have a significant impact upon the overall system efficiency.

The output from the two in-duct heaters, each 6-ft. (1.8 m) diameter, would feed into a common duct to the power turbine. Overall swirl would be minimized due to the interaction of the individual swirl modules in each heater. The first stage swirlers would reinforce the swirl in the annulus between swirl modules, but there would not be an overall net swirl to the flow. The individual swirl modules would interact in regions of high shear that would further enhance small scale mixing. The discharge of the two heaters into a common duct to the turbine could be tailored to provide minimum duct pressure losses and to provide a uniform total pressure profile to the turbine.

Evaluation and Results of Preliminary Studies

The initial objective was to develop the concept for an in-duct gas fired heater which will raise the air temperature from 1700 °F (930 °C) (the discharge of the air heat exchanger) to 2495 °F (1370 °C), the temperature required at the turbine inlet for the proposed cycle efficiency. This heater was to have very low pressure-loss and produce very low levels of NO_X. The key items to be examined were the effectiveness of mixing with the injector, and the overall penetration of the fuel-air mixture into the main airflow path.

To develop a low-pressure-loss, rapid mixer for the in-duct boost heater, it was most cost effective to screen preliminary concepts in a reduced scale cold flow apparatus. Efficiency of the mixer can be determined using planar digital imaging and probe sampling with the goal of minimizing pressure losses within the duct heater while maintaining a uniform mixture profile. The cycle analysis performed as part of Phase 1 has indicated that the density ratio of the fuel to the main airflow in the in-duct heater will be 2.35, with a duct diameter of 6 ft. (1.83 m). In Phase 1 of the program, it seemed most efficient to examine the centrifugally enhanced mixing concept in a 1/12-scale model of the duct heater, use air to simulate the fuel, and a mixture of air and helium to simulate the hot gas stream. These gases provide the appropriate density ratio between the injected "fuel" and the heated "air". For ease of construction and to maintain manageable gas flows in a laboratory, the duct diameter was chosen to be 6 in. (15.2 cm), with centrifugally enhanced mixing injectors of 1-in. (2.5 cm) diameter. A mixture of helium and air (58% by volume of helium) was used in the outer swirl passage, with air in the central core. By seeding the central airflow with a methane trace gas, the high-density fuel in the actual duct heater was represented. A total unburned hydrocarbon analyzer utilizing a flame ionization

detector (FID) was used to probe the discharge of the swirler-injector at specific axial and radial locations in the duct to determine the concentration profile. Flow visualization was performed by seeding the central airflow with a mineral oil seed, and using Mie-scattered light intensity from an argon-ion laser to determine relative concentration of the seeded gas in the duct. Results from each of these investigations are discussed below.

Flow Visualization

The duct heater concept originally proposed utilizes an array of centrifugally enhanced mixers arranged in stages around the circumference of the duct as shown in Exhibit 10-1. The concept was based upon using the penetration of the individual jets into the main stream to provide a uniform exit temperature profile, while obtaining rapid mixing in each injector using the centrifugal mixing concept. To evaluate the mixing profile for an individual injector, tests were performed in a rectangular duct using planar digital imaging to determine concentration profiles of injected gas into the main flow. The jet flow was marked with mineral oil seed that was illuminated by sheets of light formed by an argon-ion laser and a rotating mirror system. The resultant image was captured and digitized by a CCD camera and associated data acquisition equipment. By normalizing the intensity of the image at any point in the duct with the intensity at the discharge of the jet into the duct, the relative concentration of jet fluid in the main flow can be determined. A conceptual representation of this apparatus is shown in Exhibit 10-2.

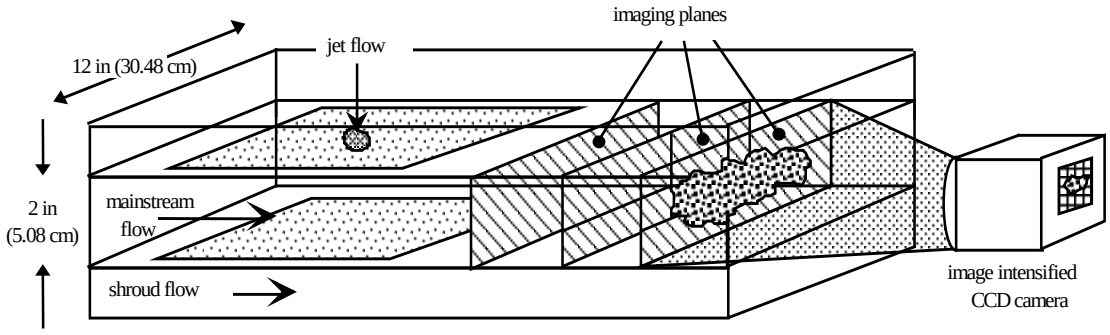

Exhibit 10-2
Flow Visualization Apparatus

The main duct velocity as proposed was approximately 50 ft/s (15.2 m/s), with each of the 12 injectors introducing 30.27 lbm/s (13.7 kg/s) of air at a velocity of 195 ft/s (59.4 m/s) and 0.302 lbm/s (0.14 kg/s) of fuel at a velocity of 87 ft/s (26.5 m/s). Using the target velocity ratios, the sub scale experiment in injector mixing was operated at a main flow velocity of 4 ft/s (1.2 m/s) in order to provide a flow field that could be imaged properly and ensuring that the marker particles would faithfully follow the flow. Although this experiment was approximately 1/12 scale, the momentum ratios were maintained as close as possible to that which would be expected in the full scale apparatus. As has been previously demonstrated, the momentum ratio is a critical parameter in cross-stream jet mixing if the jet diameter is normalized by duct height in analyses. The mainstream flow was constant, and imaging was performed at several locations down-stream of the injector location for several velocity ratios in order to explore the effect of velocity on the jet penetration. The injector consisted of a double swirl module of 0.87-in. (2.2 cm) diameter with 45° swirl vanes in the center and annular flows, similar to the proposed full-

scale device. The swirlers were designed and manufactured using stereo lithography and CAD techniques that could be used to optimize the swirler design for pressure drop and flow characteristics.

The results of the flow visualization experiments demonstrated that the centrifugal mixer works too well to provide adequate penetration of the jet into the main flow. From the concentration contours measured, it was evident that the swirler flow spreads radially along the wall, indicating very rapid transverse mixing, but the majority of the gas does not penetrate into the main flow. This would result in very poor temperature profiles in the duct heater and probably areas of high NO production. The heater exit pattern factor, defined as the deviation of local temperature from the average temperature, normalized by the average, would be large and would therefore present problems for the turbine inlet guide vanes and first stage rotor due to large thermal variations and accompanying stresses.

Mixer Concentration Measurements

Based upon the flow visualization results, a new duct heater concept was developed. This concept, shown in Exhibit 10-3, consists of 12 centrifugally enhanced mixers distributed in equal area sectors across the duct. Each injector will handle the same flows as listed above, and will be responsible for the fuel and airflow for each sector of 2.356 ft^2 (0.23 m^2) area. It was apparent that the centrifugal mixer provides very rapid transverse mixing at the velocity and density ratios to be found in the duct heater, so this characteristic was used to an advantage in designing the duct heater concept shown in Exhibit 10-3. To study the mixing in more detail, an experimental apparatus was built to perform probe sampling of the flow in both the near and far field of the mixer-injector. To accomplish this, the swirl module was designed with air flowing in the center passage (shown in Exhibit 10-4), and a mixture of air and helium flowing in the outer passage as described above. Based upon chemical kinetics studies using the CHEMKIN© computer code, the temperature rise needed in the duct heater is predicted to require an overall stoichiometry of 0.187, which calculates to a fuel mole fraction of 0.018. The more rapidly the mixer-injector can achieve this fuel mole fraction, the shorter the residence time at higher stoichiometries. Therefore the thermal NO_X can be minimized. The sub-scale test apparatus was designed with critical flow orifices or laminar flow elements used to meter the flows in each passage so that each gas flow could be measured accurately. The inner flow was seeded with methane tracer so that there was sufficient concentration at the discharge to measure with confidence while constantly monitoring the seed concentration to ensure it was stable. Typically, the inner air was seeded with 800 ppm of methane, with concentrations of 14 ppm measured when the flow was completely mixed. Once again, several flow velocity ratios were tested, with one being the anticipated ratio to be used in the full-scale device. The density ratio was determined by the fuel-air density ratio in the actual duct heater.

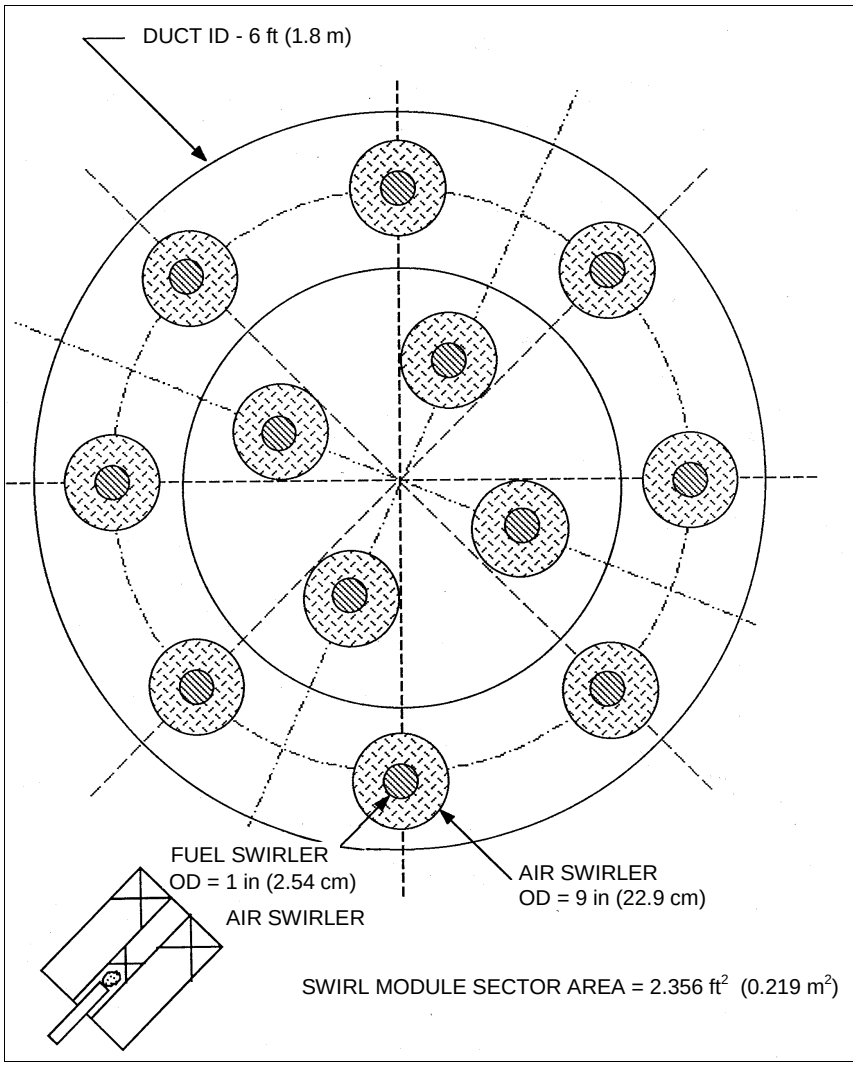

Exhibit 10-3
Second Design of Induct Boost Heater Injector Plane

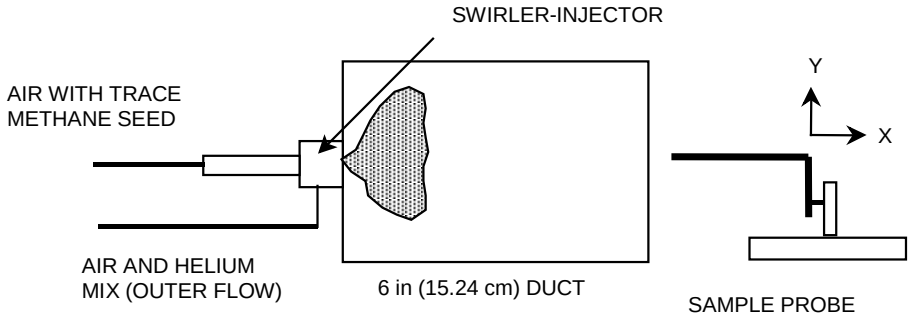

Exhibit 10-4
Schematic of Gas Composition Apparatus

The results of these gas composition experiments are shown for the expected density and velocity ratios in Exhibit 10-5. This figure shows radial composition profiles at five axial positions using a 0.0625 in (0.1588 cm) diameter sampling probe. The OD of the outer flow passage was 0.87 in (2.21 cm). From the figure, the data indicates that the inner and outer flows are completely mixed in 1.1 swirler diameters downstream of the swirler exit plane. Tests were also performed at various mass flows through the swirl module to determine the affective C_DA for the swirl module design. A larger diameter swirler (1.875-in. OD) was also tested to examine scaling effects. From the air flow data, the pressure drop that can be expected in the full scale device under the operating conditions listed in the proposal will be 1.3%, which is within the target of 1.5% total pressure drop.

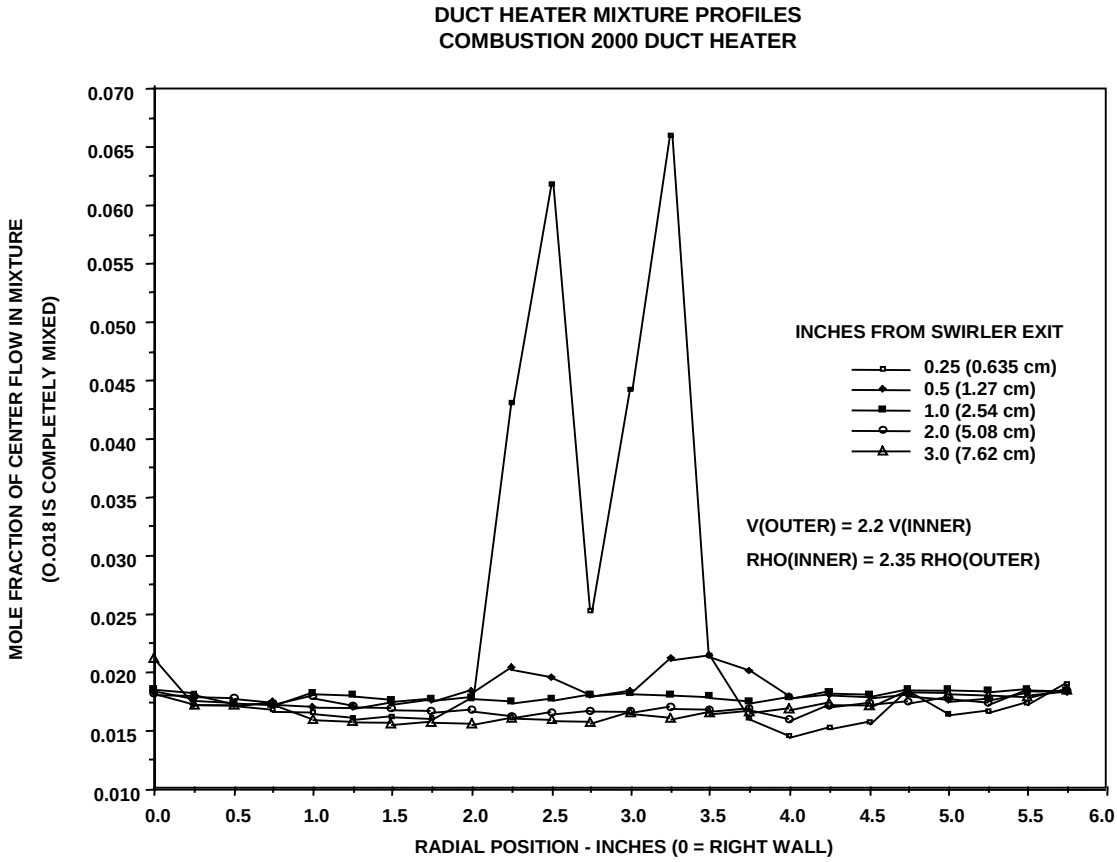

Exhibit 10-5
Cold Flow Mixing Profiles of Centrifugally Enhanced Mixer

Conclusions of Phase 1

The centrifugally enhanced mixer concept provides very rapid mixing of the fuel and air in the duct heater based upon projected mass flows and density ratios. The sub-scale model has demonstrated the viability of the concept. From these experiments, it has been determined that transverse injection of the fuel and air into the duct will not provide adequate penetration of the fuel-air mixture into the main stream and will therefore not provide a uniform exit temperature and composition profile. With a distributed array of coaxial mixers, the centrifugally enhanced

mixer-injector concept will provide complete mixing within 1.5 mixer diameters. This rapid mixing should keep the production of thermal NO_x at a minimum. Preliminary sub scale pressure drop measurements indicate that the total pressure drop through the mixer will be 1.3%, which meets the program goal.

Overview of Duct Heater Development

The Phase II boost heater program consisted of five phases: (1) review of existing mixing and injection test results, (2) turbulent flamelet and PSR modeling effort, (3) cold flow visualization and mixing studies, (4) sub scale hot flow facility development, and (5) testing at temperature and pressure. Different configurations for the boost heater were considered. The modes of operation ranged from a boost heater with a 1700 °F (930 °C) inlet and 2495 °F (1370 °C) outlet temperature, to a 100% natural gas fired combustor with a 730 °F (390 °C) inlet and 2495 °F (1370 °C) outlet temperature. Additionally, operation in a HAT cycle was considered. The results of Phase 1 demonstrated that centrifugally-enhanced mixing will provide rapid and complete mixing in a minimum physical length which will minimize NO_x production and provide a combustor pressure drop of ≈1.3%. The tasks outlined provided a logical path for development of a boost heater configuration that will adapt to the different modes of operation. The cold flow visualization coupled with a modeling effort provided the most efficient means for development of a mixer that will operate at 225 psia (1550 kPa) at an inlet temperature up to 1700 °F (930 °C). Sub scale testing of this mixer would have provided confidence in the performance to be expected in a full-scale demonstration facility.

The fifth phase of the duct heater development program involved the further experimental evaluation of low NO_x emission boost heaters operating with natural gas. Since the cycle analyses performed in Phase 1 enlarged the scope of the requirements of the boost heater, a much more extensive evaluation and test program was performed. Operation at high relative humidity (HAT Cycle) and gas turbine operation during startup firing with 100% natural gas, with the desire to utilize the existing combustor casing of the FT4000 gas turbine, have significantly altered the requirements of the boost heater. However, the basic mixing configuration for the FT4000 combustor and injector will still be centrifugally enhanced mixing. Under the present proposed design scheme, the compressor discharge air would be routed outboard to the air heater; this air will then be ducted back into the combustor casing where the centrifugally enhanced mixers will be located (at the standard 24 locations in the combustor dome). The natural gas injection at this location will result in a residence time of ≈ 30 msec, which will be sufficient for complete oxidation of the fuel by the discharge of the combustor. Provision will have to be made for sufficient bypass air from the compressor discharge in order to provide liner cooling. This scheme will provide the necessary design for operation under 100% natural gas firing, where the discharge air from the compressor will be heated to the 2495 °F (1370 °C) directly in the combustor. However, this type of operation may require piloting due to the very rapid mixing demonstrated in the Phase I testing of the boost heater and the tests reported in Freihaut (1989). Lean stability in the combustor may present a problem in the 100% natural gas fired case, especially in the HAT cycle based on the aero-derivative FT4000.

Sub scale Facility for Heater Evaluation

The intricate interaction between the aerodynamics of mixing and chemical kinetics had to be examined at the conditions that were anticipated for the FT4000 gas turbine to be used in the

HITAF combined cycle system, especially if the HAT Cycle is to be explored. To accomplish this, a sub scale facility was constructed at UTRC that included the capability of testing candidate centrifugally enhanced mixers/fuel injectors at up to 1700 °F (930 °C) inlet temperatures with a target discharge of 2495 °F (1370 °C). This facility was designed to operate with an air mass flow rate of 5 lbm/s (2.3 kg/s) and chamber pressures up to 40 atmospheres at the desired operating temperature. This provided the capability to test a 1/6-scale model of the boost heater mixer. A schematic of the heated flow mixer evaluation apparatus is shown in Exhibit 10-6. This facility utilized a gas-fired air heater on the first stage that can provide a maximum temperature of 900 °F (480 °C) at 20 lbm/s (9.1 kg/s); the heated air is not used in the combustion process. The air temperature was then increased via an electrically operated air heater manufactured by Phoenix Solutions, Inc. of Minneapolis, MN. The air supply for this system is capable of supplying up to 20 lbm/s at 400 psia (2760 kPa) at steady state conditions. However, for this experiment, the system was designed for an air mass flow rate of 5 lbm/s (2.3 kg/s) due to the high electrical energy requirements to heat this mass of air to 1700 °F (930 °C). This facility represents a major capital investment for UTRC, and is of great benefit to DOE because of the capabilities that are unique to UTRC are available for this and other programs.

The diagnostics designed to be used for evaluation of the performance of the boost heater mixer included: (1) axial and radial temperature profiles in the duct to determine the time-temperature history of flow mixing, and (2) axial and radial profiles of gas composition. The on-line gas analysis equipment to be used included NDIR CO and CO_2 analyzers, FID total unburned hydrocarbon analyzer, paramagnetic O_2 analyzer, and a TECO chemiluminescence NO_x analyzer. For detailed chemistry, a time-of-flight (TOF) mass spectrometer was available that is capable of measurement in the parts-per-billion (ppb) level for certain species. The analytical capability available for this program could be used to provide extremely detailed profiles of nearly any species of interest in the combustion process. Results of the detailed profiling can be used to refine combustion modeling efforts for enhancing the design process for the mixer and combustion system.

Initial experiments would have investigated the emissions from a fully premixed jet issuing into the air stream. Since this is the simplest case to study, it would have provided a baseline relationship to compare the jet mixing predictions (Vranos, 1988) and the combustion model calculations. Water injection to simulate HAT cycle operation would have been an additional step in the first group of experiments. The optimum configuration of the centrifugally enhanced mixer developed in the cold flow experiments would then be tested. To obtain a prediction of performance over a range of conditions, tests would be performed with air inlet temperatures ranging from 730 °F (390 °C) to 1700 °F (1370 °C), and at various pressures to determine the sensitivity of emissions to these variables. Water injection would have been an additional variable in order to investigate the viability of a centrifugally enhanced mixing injector in a HAT cycle combustor.

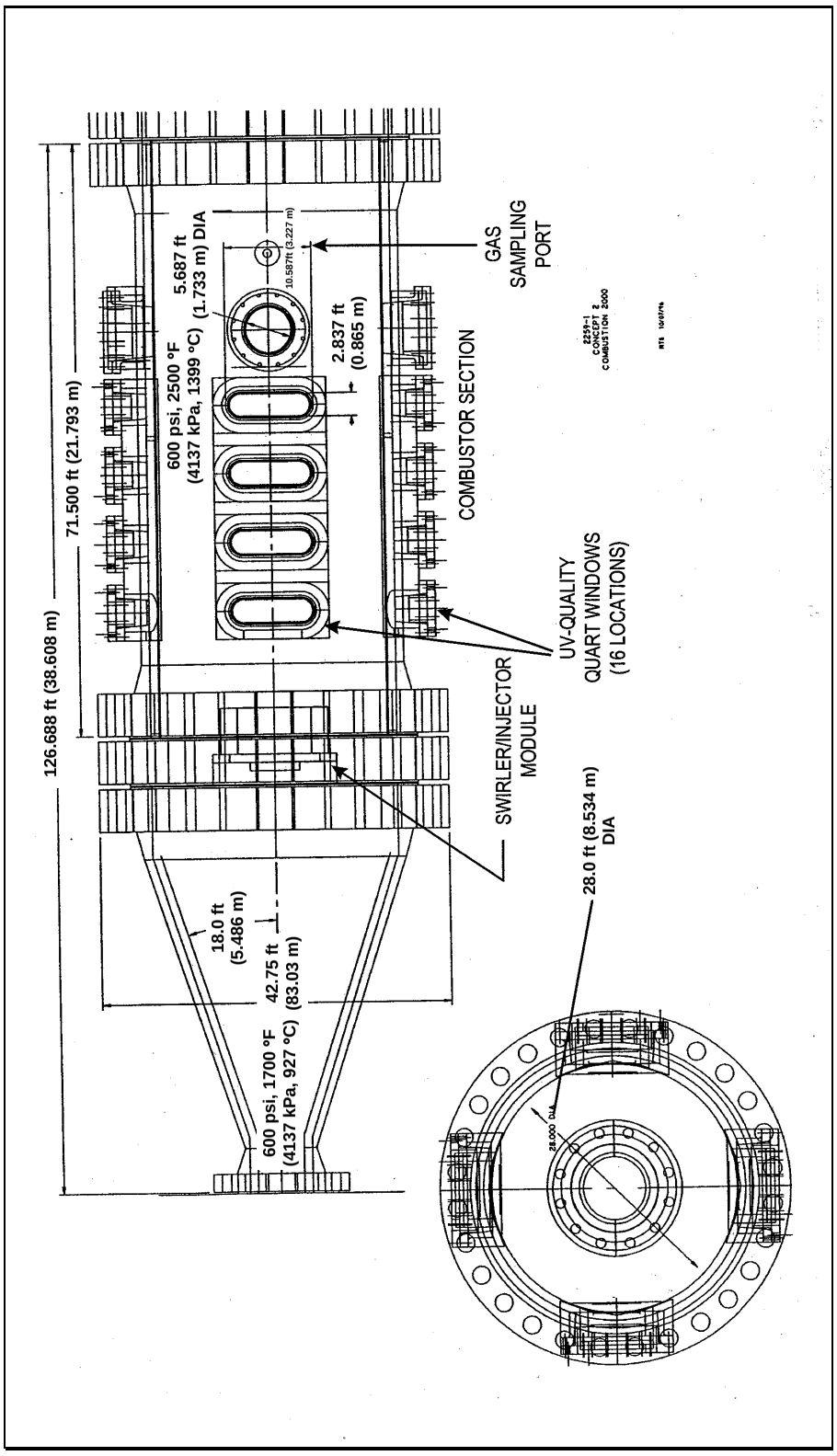

Exhibit 10-6
Original In-duct Boost Heater Sub-scale Test Combustor

One of the cycle analyses presented an option of startup operation with the gas turbine being operated with 100% natural gas firing. In consideration of this type of operation, it would appear that an optimum combustor configuration, one that would operate either with preheated air at to 1700 °F (1370 °C), or compressor discharge air at 730 °F (390 °C), would entail replacement of the fuel injectors and combustor dome with the centrifugal mixer/injector. The FT4000 combustor has 24 injectors distributed in an annulus; the combustion air and dilution air holes in the combustor liner are used to obtain the appropriate temperature distribution along the combustor length and to achieve an acceptable temperature distribution at the exit. By replacing each standard fuel injector with a centrifugally enhanced mixing injector, and modifying the combustor to eliminate the combustion air holes, it may have been possible to use the existing combustor envelope for the boost heater. With a design of this type, using the existing combustor modified to accept the centrifugal mixer, operation with 100% methane (no air preheating after the compressor discharge) may be possible. The residence time in the FT4000 combustor is estimated to be 5 msec based upon simple one-dimensional flow analysis. This scenario is based upon using the existing combustor envelope for the FT4000. In reality, since the compressor discharge will be taken off-board to the air heater and then brought back to the combustor, the final physical configuration will allow for a longer combustor and therefore a longer residence time if required.

Computer models were run to determine the adiabatic flame temperature with natural gas with an inlet temperature of 730 °F (390 °C) at 225 psia (1550 kPa). For these inlet conditions, a temperature of 2545 °F (1395 °C) can be achieved at an equivalence ratio of 0.45 ($\Phi = 0.45$). With the fuel input and air flow from the cycle analysis, the amount of air to be used in the combustion process can be calculated; the remaining air is used for cooling of the liner and dilution of the combustion products. This analysis determined that 45% of the air will be used in the combustion process and 55% will be cooling and dilution air. Based upon these flow splits, the maximum temperature that will be achieved in the combustor will be approximately 2900 °F (1595 °C); this will be diluted to the required discharge of 2495 °F (1370 °C). Iteration on equilibrium calculations then produced the results that the burner equivalence ratio (Φ) will be 0.55 to achieve that temperature. This requires 38% of the compressor discharge to enter the combustor and mix with the fuel for the combustion process; the remaining 62% will be liner cooling and dilution air. Calculated residence times were used as input to CHEMKIN® PSR (perfectly stirred reactor) calculations to determine the extent of reaction and predict NO emissions.

These results predict that in the case of 100% natural gas combustion in an FT4000 combustor (assuming a perfectly stirred reactor that is the closest approximation to the centrifugally enhanced mixer), NO production will be between 3-5 ppm. The fuel flow rate for 100% natural gas firing will be ≈ 19 lbm/s (8.6 kg/s). The calculated NO production from the natural gas flame will be ≈ 0.008 lbm per million Btu (3.4 g/10^6 kJ) of fuel input.

In the mode of operation where the compressor discharge air is directed off board to the air heater, the combustor can be used as the boost heater as generally described above. The air through the combustor will enter at 1700 °F (1370 °C) and the fuel will be oxidized to provide a discharge temperature of 2495 °F (1370 °C). The 24 centrifugally enhanced mixer/injectors will, based on Phase 1 mixing studies, provide a uniform mixing profile and low NO_X emissions using 3 in. (7.6 cm) diameter swirlers located in the 5 in. (12.7 cm) high dome region of the

FT4000 gas turbine combustor (modified for the new injector configuration). The exact combustor configuration will be determined by the design required for ducting the compressor discharge to the air heater, and by the desire to operate a humid air turbine (HAT) cycle. The residence time needed to provide complete combustion under the three scenarios would dictate the length of combustor needed. Flame stability and piloting will be an important consideration when operating with 100% natural gas firing.

Duct Heater Test Facility Preparation

Several variations to the combustor design were considered based upon the data that would be necessary to properly evaluate the performance of the low NO_X emission in-duct boost heater. Initially, a combustor with four planes of optical access was designed, but the combustor cost was prohibitive. This combustor design was scaled down to that shown in Exhibit 10-7. This combustor is designed for operation at 600 psia (4140 kPa) with a discharge temperature of 2550 °F (1400 °C) with an inlet temperature of 1700 °F (930 °C). The scaled-down combustor has four rectangular quartz windows located at the discharge plane of the mixer, followed by four round quartz windows for a second viewing plane downstream of the injector. Each of these quartz windows can be replaced with a steel insert into which a traversing thermocouple or gas sampling probe can be inserted. An instrumentation spool assembly with radial gas sampling ports and thermocouples was located at the exit of the combustor, prior to the converging section, to obtain an exit species and temperature profile. The combustor is lined with a high temperature alloy, backed by a ceramic insulation, so that carbon steel can be used in its construction.

The Facilities Instrumentation Group in the Jet Burner Test Stand (JBTS) obtained the necessary flow and temperature monitoring hardware for the combustor installation and operation. Of critical importance was the ability to monitor and interlock the operation of the JBTS facility with the Phoenix Solutions designed electric air heater to ensure that all operating parameters of the heater are within specification. In addition, there was a significant amount of combustor instrumentation necessary to ensure safe operation at the high exit temperatures of 2550 °F (1400 °C) and pressures (27 atmospheres). Data acquisition hardware was obtained so that the combustor exit temperature profiles, and combustor emissions could be measured. As outlined above, the optical system for planar imaging of mixing profiles within the combustor was designed and preliminary testing in laboratory flames was performed. Because of the very high centripetal acceleration to be experienced in the mixer/injector, Rayleigh scattering was used as the primary flow visualization technique in the combustor in lieu of Mie-scattering since the seed particles would not reliably follow the gas flow path.

The combustor (Exhibit 10-7) is capable of operation with natural gas or methane fuel with an exit temperature of 2550 °F (1400 °C) and pressure up to 40 atmospheres. The optical ports located at the discharge plane of the mixer/injector are of uv-grade quartz and are 3 x 10 in. (7.6 x 25.4 cm) in dimension. There are 4 ports at each axial station. There are also 4 round optical ports downstream of the rectangular windows. As stated above, each window location had an optional metal insert into which a traversing gas sample or thermocouple probe can be mounted. Because of the arrangement of the optical and sampling ports, a three-dimensional distribution of temperature and species can be produced which will aid in the evaluation of the mixer performance. The combustor outer shell is composed of carbon steel, with an Inconel liner and ceramic insulation layer on the ID to reduce heat loss to the walls and reduce the combustor wall

thickness. The windows are purged with nitrogen to maintain an acceptable quartz or metal temperature. The centrifugal mixer is housed in a modular insert located at the inlet to the combustor, just downstream of the inlet diffuser. Airflow, fuel flow, and purge flow are metered with venturis.

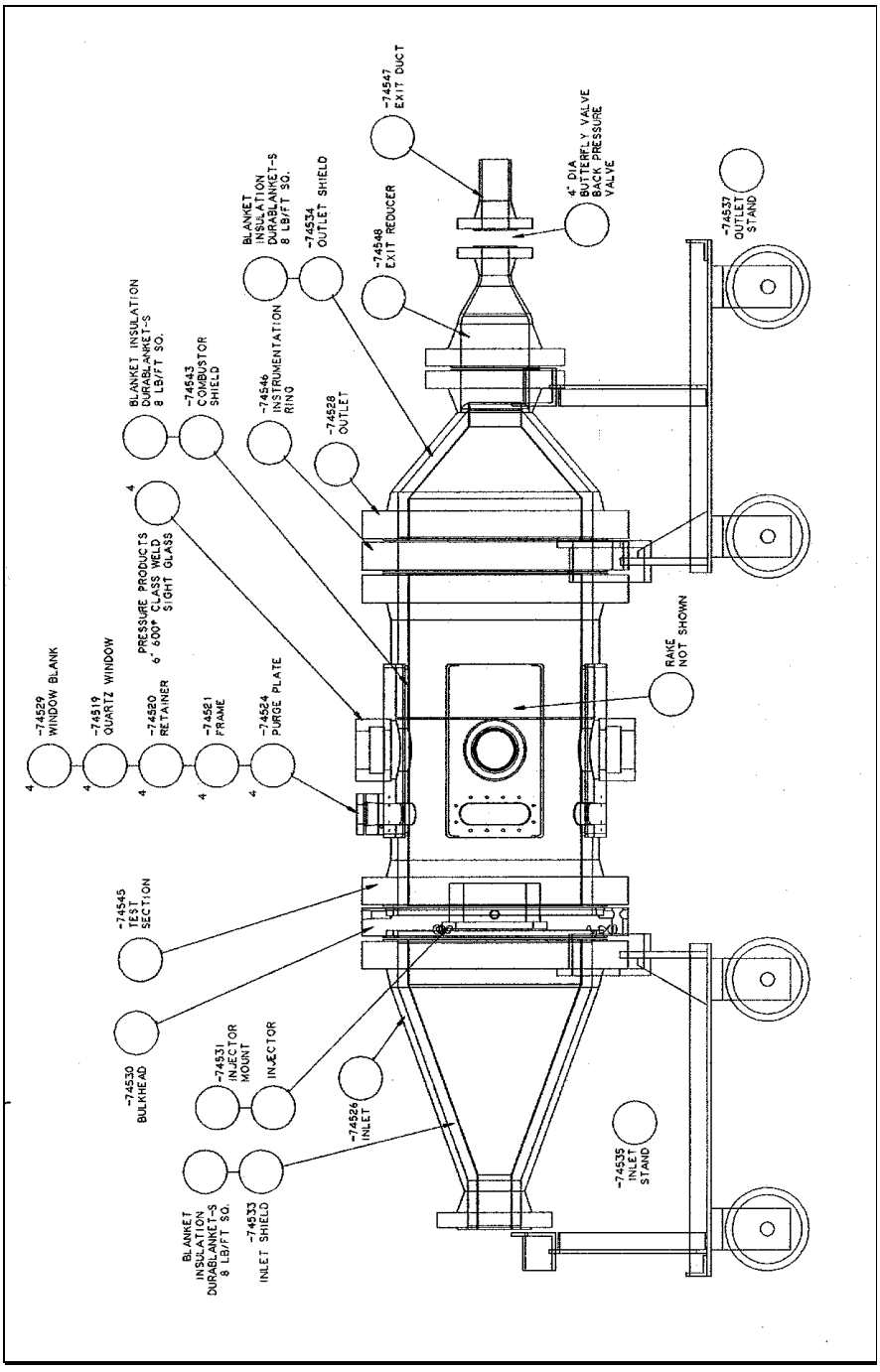

Exhibit 10-7
Reduced Optical Access Duct Heater Test Combustor and Support Stand

Exhibits 10-7 through 10-9 show the layout of the combustor, air heater, and inlet piping in the JBTS test facility. The inlet piping is unlined stainless steel, whereas the outlet piping from the electric air heater is lined stainless steel pipe. Stainless piping is required for the inlet to the electric heater to prevent any corrosion particles from the inlet pipe being transferred to the resistance screens. A double valve safety system is required by facility safety standards to allow two levels of shutoff from the air supply system to the combustor. The layout of the cell shows the relative positions of the electric power supply, air heater, and combustor.

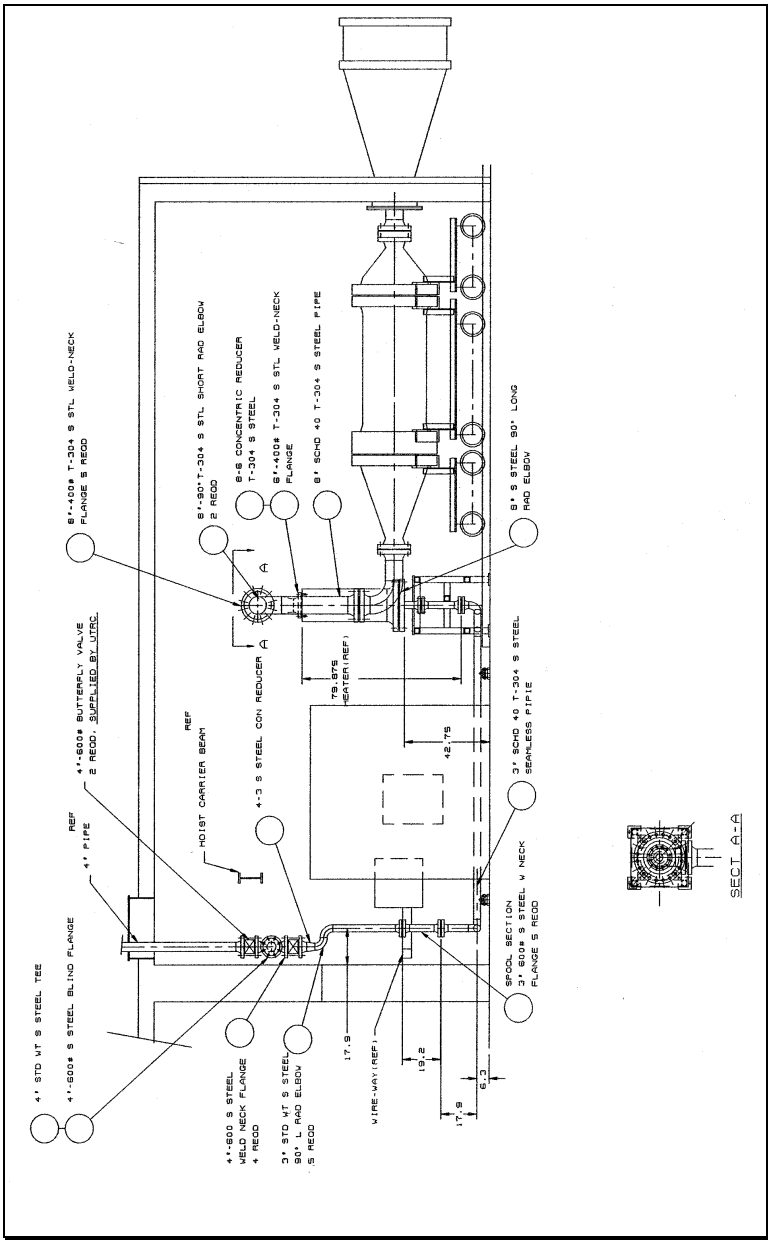

Exhibit 10-8
Duct Heater Test Facility Air Heater and Combustor Layout

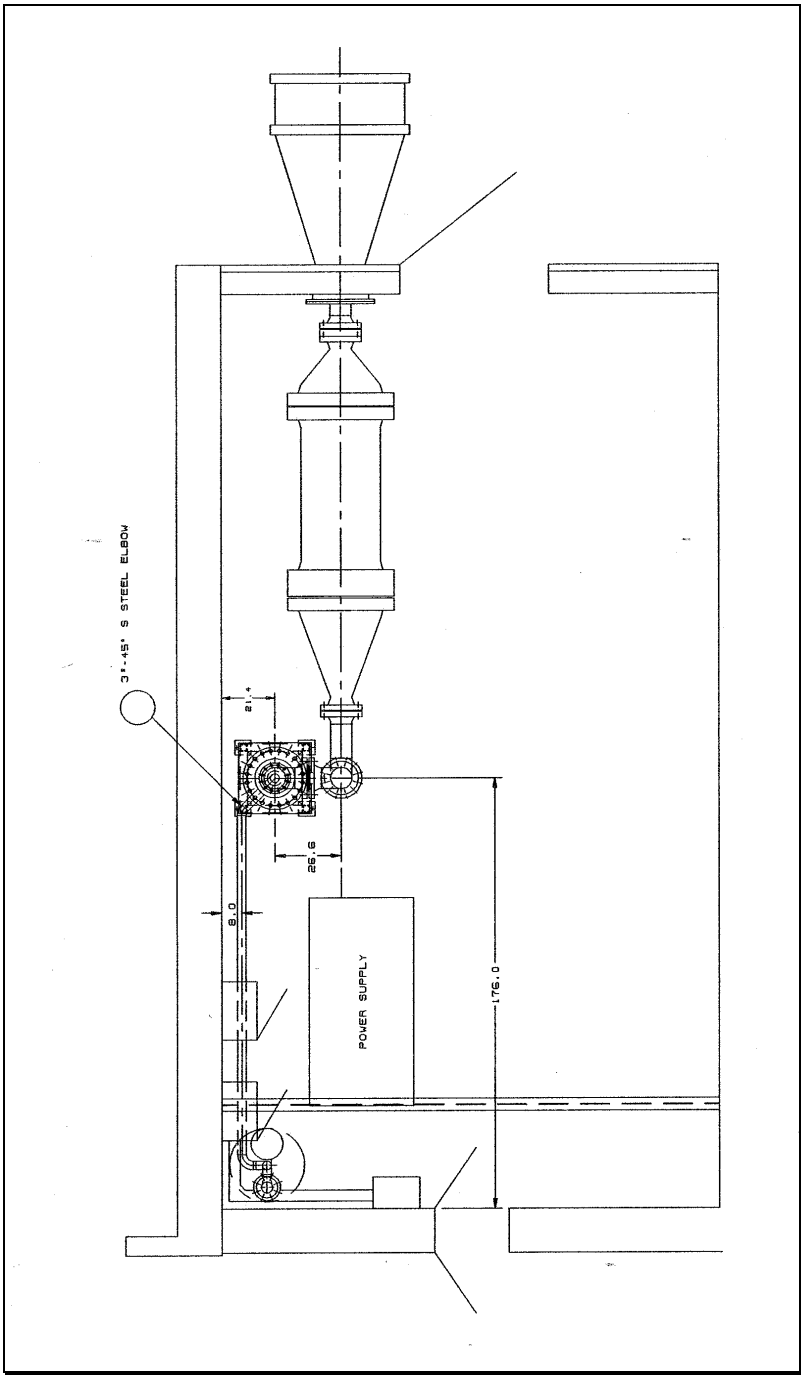

Exhibit 10-9
Plan View of Duct Heater Test Facility at UTRC JBTS

Cold Flow Mixer Evaluation

The sub scale testing and evaluation performed in Phase 1 demonstrated that the centrifugally enhanced mixing concept is a viable approach for an ultra-low NO_x emissions boost heater. To facilitate the cold flow mixer evaluation, candidate models were constructed using stereo lithography coupled with a CAD system and UV sensitive polymer resins. This rapid

prototyping enabled numerous candidate mixers to be developed and tested; the advantage was that the optimum mixer design existed on a CAD file and can be used to construct the mixer to be used in the hot test evaluation. Diagnostics included planar digital imaging, laser-induced fluorescence (LIF), Mie scattering flow visualization, and tracer gas concentration measurements. Testing on the reduced scale model were performed at UTRC in our 5 in. x 5 in. (12.7 cm x 12.7 cm) tunnel that was used for the testing reported in Phase 1. These two facilities provided scaling relationships that were used to design the mixer for the 1/6 scale hot test.

Mixer evaluations in cold flow were conducted prior to design and construction of the hot test mixer hardware. In order to obtain meaningful data on the performance of the centrifugal mixer for the duct heater, propane was used as the high-density marker gas in the cold flow facility. Propane has a large Rayleigh cross-section and a helium/air mixture was used in the outer flow to simulate the density ratio to be expected in the actual duct heater. Once again, Rayleigh scattering from the propane molecules was used to generate a planar image of the distribution of the center (fuel) flow in the overall fuel and air mixture. Based upon prior data, reported previously, nearly complete mixing is expected within 2 swirler diameters downstream of the injector.

The concept of centrifugal mixing, as previously described, was tested in a cold-flow facility designed for studying the mixing of variable density flows. The facility provides conditioned flow to a 3 in. (7.6 cm) diameter outer swirler (fabricated from an aluminum plate) and a 1 in. (2.5 cm) diameter inner swirler which are mounted flush within an 8 in. x 8 in. x 18 in. (20.3 cm x 20.3 cm x 45.7 cm). Plexiglas exhaust duct. The outer flow is primarily air from a 500-CFM blower while the inner flow is provided from compressed gas bottles. By mixing helium into the outer flow and using argon or carbon dioxide in the inner flow, density ratios up to 2:1 can be studied. Velocity ratios are introduced by independently controlling the mass flows and both the inner and outer swirler vane angles can be varied independently. The swirler and flow arrangement is shown schematically in Exhibit 10-10. The swirlers are circular, whereas the duct confinement is square.

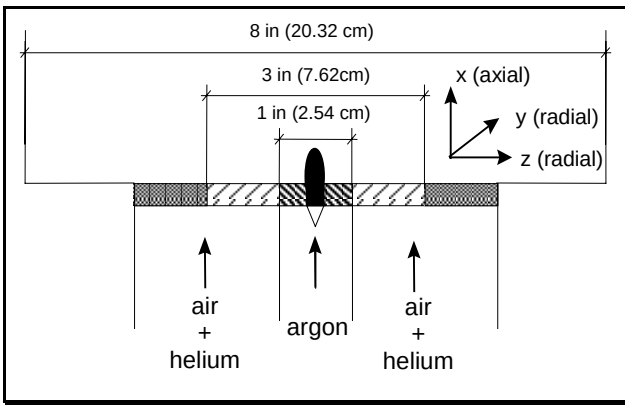

Exhibit 10-10
Schematic of the Cold-flow Test Facility Swirler and Flow Setup

The centrifugal mixing concept studied in the cold-flow facility is illustrated schematically in Exhibit 10-11. The concept exploits the Rayleigh instability, which occurs when a dense fluid of high angular momentum is introduced into the center of a flow that is less dense. In addition to the shear from the relative velocity mismatch at the interface between the flows, the centrifugal effect promotes instability and mixing. Previous work has indicated that the centrifugal effects become pronounced when the centripetal acceleration exceeds 1000. In a combusting system, the flame speed is significantly increased by this effect. In addition, the pressure drop of the system is less than that required to achieve an equivalent increase in flame speed driven by an increase in turbulence level alone.

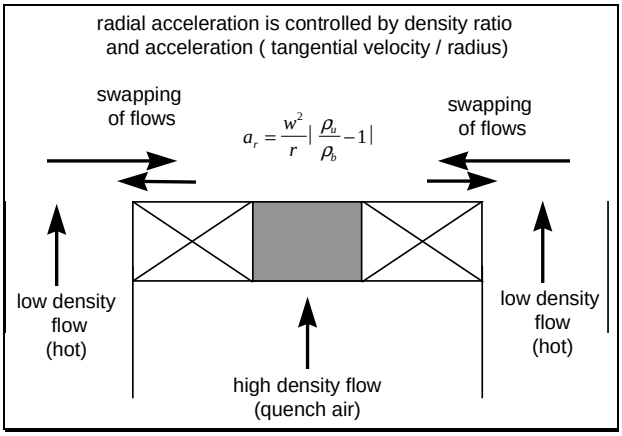

Exhibit 10-11
Centrifugal Mixing Concept

Test conditions were chosen to be able to determine the effect on mixing rate as the modified Richardson number (R*) is varied. The modified Richardson number is the ratio of centrifugal forces in a flow with density gradients to the shear forces. Rotation stabilizes the flow if R* >0 and destabilizes at R* <0 and is defined as:

$$R^* = \frac{1}{\rho}\left(\frac{\partial \rho}{\partial r}\right)\frac{w^2}{r} \Big/ \left(\frac{\partial u}{\partial r}\right)^2 \qquad (5)$$

By independently varying the density ratio and radial acceleration terms a correlation for mixing rate can be determined which will serve as a design guideline, i.e. the trade-off between radial acceleration which requires pressure drop and mixing rate.

Measurements of jet mass fraction distribution as a function of downstream and radial position have been made by introducing trace amounts of methane into the inner flow and using a gas sampling probe in conjunction with an online hydrocarbon analyzer to measure inner flow dilution as shown in Exhibit 10-12. For all of the data collected the outer vanes have been set parallel to the flow; i.e. the flow is non-swirling.

In Exhibit 10-13 the effect of swirl vane design is illustrated. A set of 6 swirlers fabricated with stereolithography were available that varied only in vane angle (0, 5, 10, 15, 30, and 45 deg). These swirlers had a 0.25 in. (0.6 cm) diameter hub and 12 flat vanes. The 0 and 45° results shown in Exhibit 10-13 are from this set. The 65° swirler has 6 curved vanes and a 0.5 in.

(1.3 cm) diameter hub. All three swirlers were tested without swirl in the outer flow at a velocity ratio of 1.4 and a density ratio of 1. A centerbody that extended 1 in. (2.5 cm) fore and aft of the hub was attached in all testing. As can be seen the measured spreading rate of the inner flow increased as a function of vane angle.

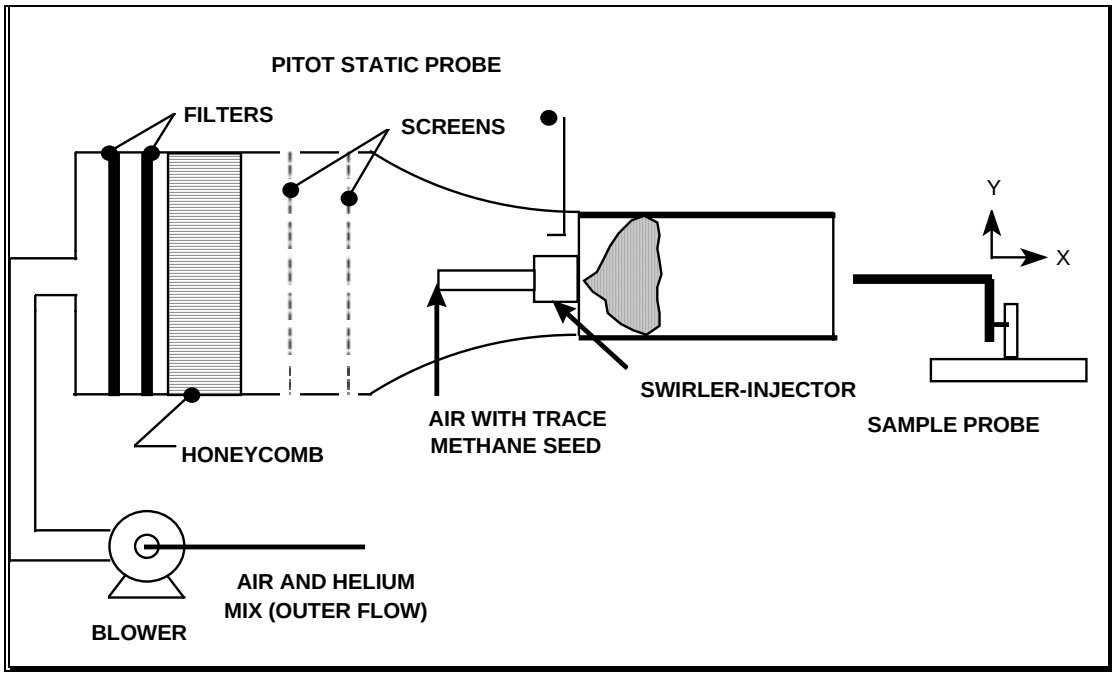

Exhibit 10-12
Cold Flow Mixing Test Apparatus with Trace Gas Seeding

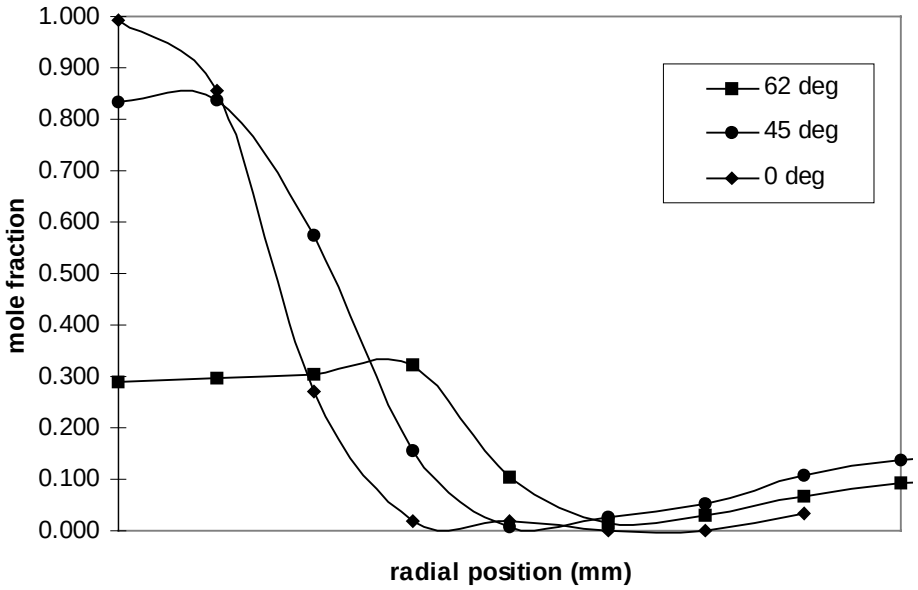

Exhibit 10-13
Effect of Vane Design on Inner Flow Distribution
(Downstream position = 1 inch, density ratio = 1.0, velocity ratio = 1.4)

At first it was puzzling that the 45° swirler had a relatively small effect on mixing rate. However upon closer inspection it was determined that a small "see-through" at the outer rim existed for the set of 6 flat vane swirlers. It is well known that in order to impart maximum swirl to a flow the vanes must overlap. Subsequent measurements with a pitot probe were not in agreement with calculated radial velocities based on swirl number, confirming the inefficiency of the vane design. It is clear from Exhibit 10-13 that the vane design will effect the mixing rate.

Flue Gas Recirculation Quench Zone

It was suggested that a rapid quench zone be developed at the discharge of the HITAF heater in order to reduce the gas temperature below the level at which the suspended ash particles would stick to the duct walls. This would prevent slag buildup and facilitate removal of the particulate at regular intervals from the walls through mechanical cleaning without excessive effort. This quench zone has been examined based upon experience in dilution jet mixing as applied to gas turbine combustors, where rapid quenching in very short distances are required. The previous research suggests a quench-zone design based on crossflow jets. Recent gas/gas mixing experiments in a cylindrical duct and a limited literature review suggests that quenching can be attained within two duct diameters with a crossflow configuration.

UTRC proposed that the quench-zone be located immediately downstream of the slag screen after transition to a 1 ft (0.3 m) diameter (round) duct. The quench-section would consist of a row of plenum fed jets injected from the wall of the duct as shown in Exhibit 10-14 (end-on view). Based on the flow parameters, it was calculated that eight round holes of 1.25 in. (3.2 cm) diameter located at 45 degree intervals around the circumference will quench the flue gas within two duct diameters.

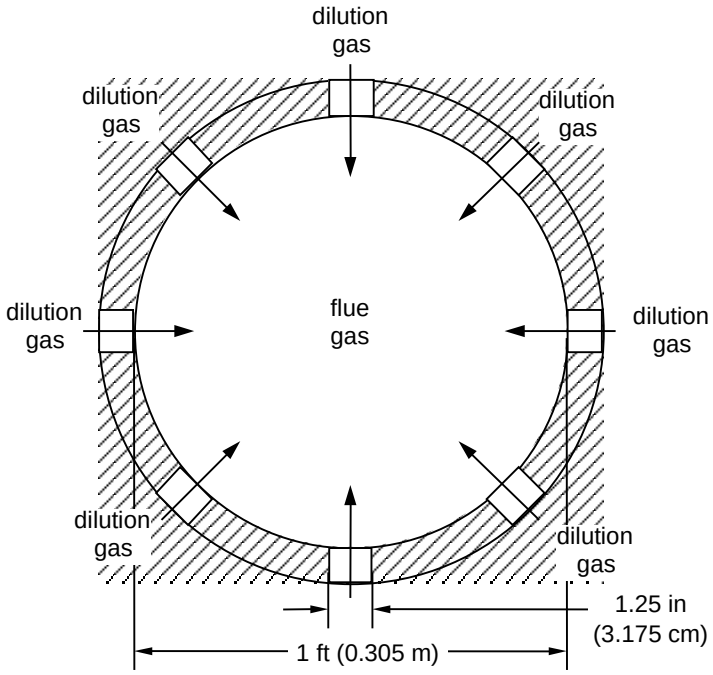

Exhibit 10-14
Proposed Quench Zone (end-on view)

Analysis of Flue Gas Recirculation

The correlation of Holdeman (1993) and Sowa (1994) for optimum mixing of wall injected jets into a cylindrical duct, shown below for reference, has been used as a design guideline. This is an empirical correlation developed for gas phase mixing based on many experimental and numerical investigations. The key to rapid mixing in a crossflow configuration is proper jet penetration, optimum at D/4, where D is the duct diameter. The correlation relates the primary variables and provides a guideline for optimum jet penetration.

$$n = \frac{\pi\sqrt{2J}}{C}$$

Where n is the number of orifices, J is jet-to-mainstream momentum-flux ratio, and C is a constant that has been found to be 2.5.

In order to minimize fabrication cost and pressure drop, eight injection locations have been selected. Although the above equation would predict a value for J of 20, as an iteration to the final design, a slightly higher value of J is recommended based on the author's experimental results in a similar mixing configuration Furthermore, with the particle laden stream, over-penetration vs. under-penetration would be desired. Using the given flow parameters in Table 10-1 and a J of 30 results in a quench-jet velocity of 171 ft/s (52.1 m/s) and a quench-jet diameter of 1.25 in. (the discharge coefficient is assumed to be 0.7).

Table 10-1
Assumed Flow Parameters for the Quench Zone Design

	Mass flow (lbm/s)	Temperature - °F (°C)	Density (lbm/ft^3)	Velocity (ft/s)
Flue Gas	0.8	2700 (1480)	0.013	64
Dilution Gas	0.4	300 (150)	0.052	171

The quench zone flow field was examined analytically to determine the particle temperatures and trajectories to determine if sufficient reduction of particle temperature can be achieved prior to the flow encountering any significant turns or obstructions. Preliminary results suggested that a staggering of dilution jets will provide better quenching of the core flow temperature. It has not been resolved why the computed flow field temperatures do not agree with measured degree of mixing (and hence, temperature) as determined experimentally.

Concentration distributions for a configuration with eight dilution jets injected perpendicular to a 3.875 in. (9.8 cm) diameter duct are shown in Exhibit 10-15 as a function of J and downstream position. C_{avg} is the fully mixed jet mixture fraction. Mixture uniformity is seen in general to increase with downstream position and vary as a function of J. The jets tend to under-penetrate with lower values of J and over-penetrate at higher values. Also note that the mixing rate is very rapid as indicated by the small number of contours at the downstream locations.

In Exhibit 10-16 the optimum value of J is indicated to be between 20 and 40 based on a plot of spatial unmixedness (a quantitative measurement similar to "percent mixed") at x/R of 1.2, i.e., ~1/2 duct diameter.

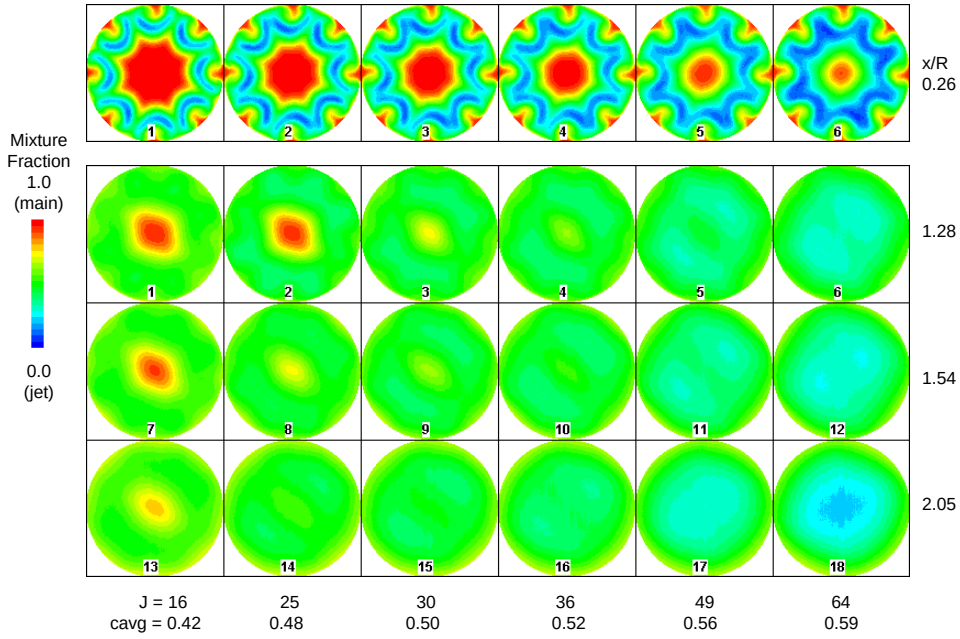

Exhibit 10-15
Concentration Distributions of 8 Round Jets Injected Perpendicular to a Cylindrical Mainstream

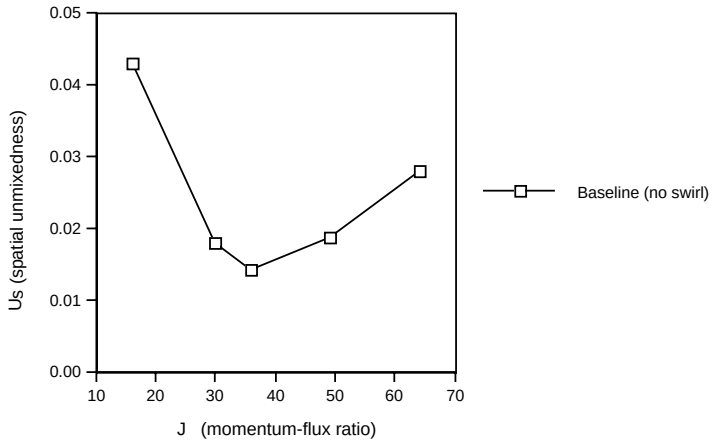

Exhibit 10-16
Comparison of Spatial Unmixedness at x/R = 1.2

Table 10-2 shows the results of the preliminary modeling effort using the FLUENT® CFD code, which is used extensively at UTRC for analyzing flows which include thermal gradients. In the table, the parameter ΔT is a temperature deviation parameter, defined as a temperature standard deviation; σ is the mass-weighted standard deviation from the CFD results. Included in the table is an "unmixedness" parameter (U) from previous experimental research, which is defined as:

$$U = \frac{C_{\text{var}}}{C_{avg}(1 - C_{avg})} \tag{6}$$

where,

$$c_{var} = \frac{1}{m}\sum_{i=1}^{m}(\bar{c}_i - c_{avg})^2 \tag{7}$$

= Spatial concentration variance

$\overline{C}_i$ = Time average concentration at measurement location (an image pixel)

C_{avg} = Fully mixed concentration

Table 10-2
Comparison of CFD Predictions and Measurements

Z/D	U	ΔT	σ
1	0.041	16 1	13
2	0.027	88	10
4	0.026	38	6
6	0.029	25	5

By definition, U=0 corresponds to a perfectly mixed system, while U=1 corresponds to a perfectly segregated system.

The results tabulated indicate that the measured mixing based upon planar digital imaging of jets in a crossflow is better than that indicated by the temperature deviation ΔT. The low sigma values suggest that there are large regions of essentially uniform flow. In the table, Z is the distance downstream from the dilution jet centerline, and D is the dilution jet hole diameter. In this comparison, ΔT and σ are based on a mass-weighted value; the unmixedness parameter (U) does not provide weighting for the boundary layer mass fluxes as is done with the CFD prediction. However, U is based upon c_{avg}, which is determined from all the pixels available in the imaging plane and therefore will account for boundary layer flow.

Duct heater facility

The combustor design that has been built is shown in Exhibit 10-17 below. This combustor is designed for operation at 600 psia (4140 kPa) with a discharge temperature of 2550 °F (1400 °C) with an inlet temperature of 1700 °F (930 °C). The combustor has 4 rectangular quartz windows located at the discharge plane of the mixer, followed by four round quartz windows for a second viewing plane downstream of the injector. A series of five gas sample and thermocouple rakes are located at the exit of the combustor, prior to the converging section, to obtain an exit species and temperature profile. The combustor is lined with a high temperature alloy, backed by a ceramic insulation, so that carbon steel was used in its construction.

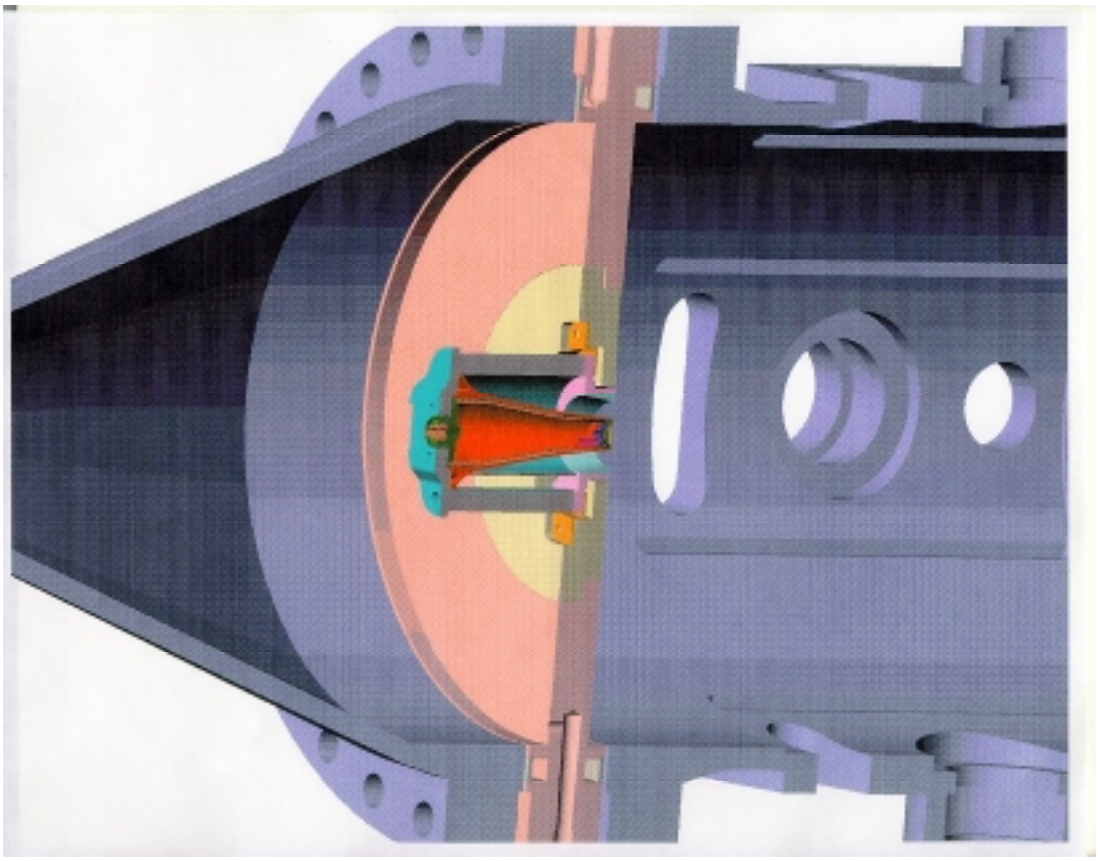

Exhibit 10-17
Injector Bulkhead and Sight Windows

The electric resistance air heater from Phoenix Solutions was repaired, tested at low power at Phoenix Solutions, and returned to UTRC. The (finally) carefully crated and marked heater was inspected for any transport damage; none was found. The unit has been placed in position in the test cell. All costs for repair of the heater have been borne by Phoenix Solutions and UTRC. In analyzing the structure of the heater and developing procedures for its installation and checkout, it was discovered that the existing Cell 4 crane does not have sufficient lifting height for the heater final assembly. A new auxiliary boom was designed and installed utilizing UTRC capital. Phoenix Solutions inspected the final installation of the air heater and approved the installation.

The installation, pressure checking, and certification of the high temperature, high pressure air piping and valving from the JBTS T-Thermal heater to Cell 4 where the Phoenix Heater will be installed has been completed. All of this piping has been designed and installed using UTRC capital funds. This piping has been used by another test program that utilized the Cell 4 test-centerline before the duct heater test combustor was installed. The wiring of power to the test cell was completed to accommodate the Phoenix Heater, including the vacuum contactor and emergency disconnects. A support stand for the heater including provisions for the water-cooled power cables from the power supply to the heater was designed and fabricated. In addition, all facility water lines and probe sample lines were fabricated and installed. The probe rakes have multiple ports; each can be sampled individually, or ganged together for an average gas sample. The thermocouples in the end plane will be sampled and recorded individually.

Isometric views of the combustor with the initially planned injector and with an advanced premixer are shown in Exhibits 10-18 through 10-21. Air is brought into the front end of the combustor through tangential entry slots on the bulkhead into which gaseous fuel is injected. The high swirl of the entry flow, combined with the centrifugal effects of the cold fuel swirling into the hot air will enhance mixing between the two fluids. Provision has been made for a centerbody flow to prevent flame attachment to the injector; fuel can be injected into this flow also.

During the initial phase of the air heater checkout, the power supply to the air heater, manufactured by NWL, Inc, failed catastrophically. This power supply, rated at 1.6 MWe, shorted instantaneously and burned out 3 of the 9 transformer coils. This was due, in part, to the internal erosion of the water-cooled coils as the unit sat in storage for nearly two years while funding issues and test cell occupancy issues were resolved. The power supply was shipped to the manufacturer after field representatives reviewed the damage. The repair of the power supply took nine months to complete. It was successfully tested with a dummy electrical load and certified operational. However, this long delay pushed the testing schedule for the combustor well into 2001. With the time available in the contract and the work needed to be done to prepare the facility, it was determined that in the best financial interest of DOE that no testing of the duct heater would be conducted.

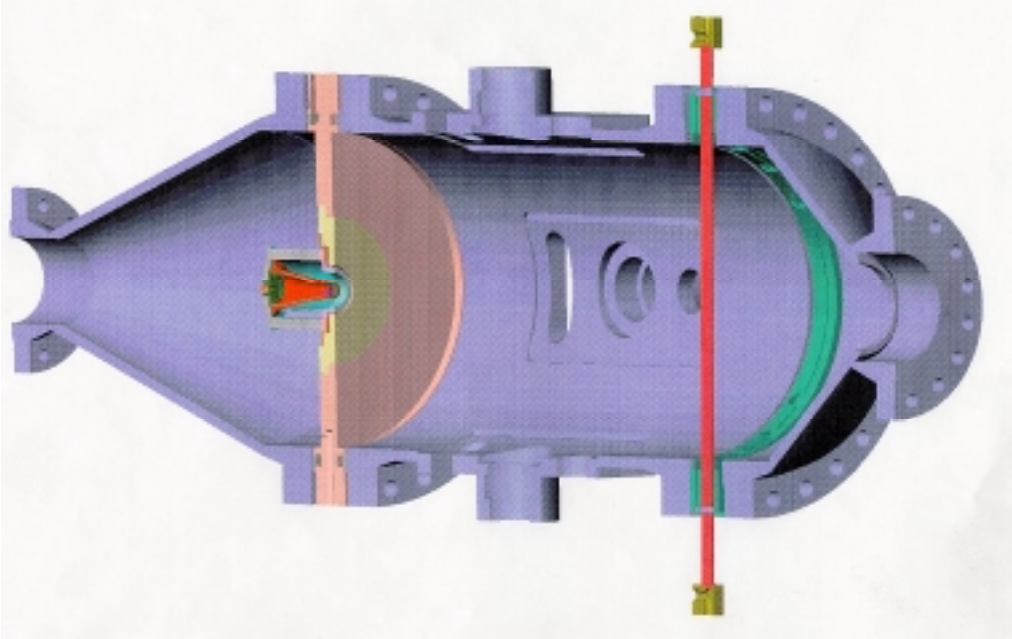

Exhibit 10-18
Combustor with One Sample Rake Shown

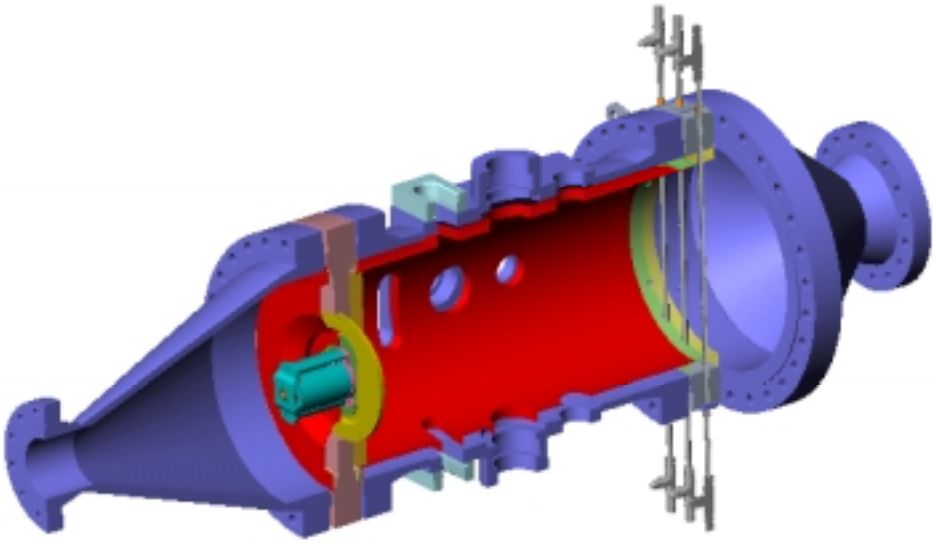

Exhibit 10-19
Combustor with Advanced Mixer and Multiple Rakes Shown

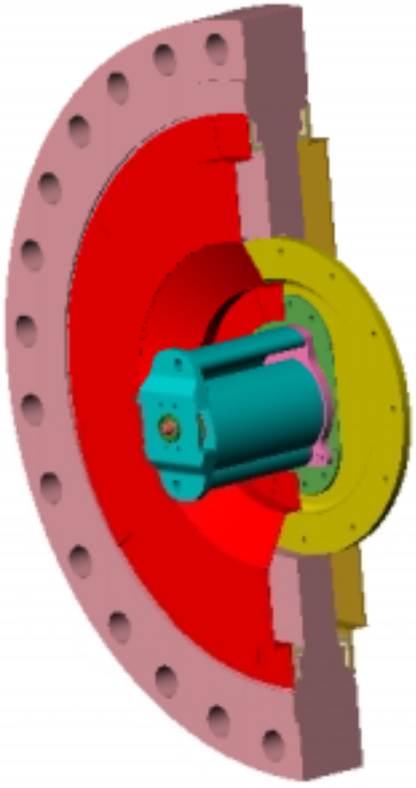

Exhibit 10-20
High Efficiency Premixer and Injector Mounted in Injector Flange

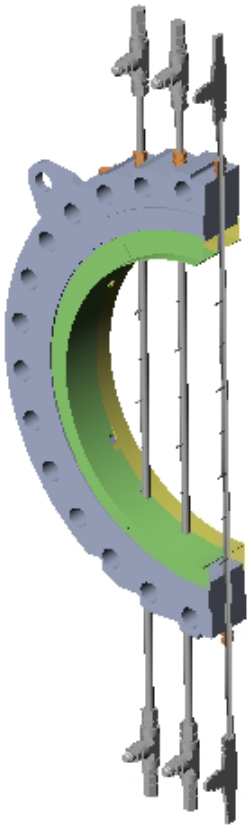

Exhibit 10-21
Gas Sampling and Thermocouple Rake in Instrumentation Flange

Conclusions

The duct heater development phase of the program has successfully demonstrated the applicability of the centrifugally enhanced mixing concept to provide very rapid mixing of fuel into the duct air stream. Experimental results in cold flow studies have verified the advantages of this rapid mixing concept. Flue gas recirculation and hot gas quench utilizing crossflow jets have been demonstrated successfully at UND. An air preheating system, capable of operation at 40 atmosphere pressure and inlet temperatures up to 1700 °F (1200K) has been obtained and installed in UTRC's test facility. A combustor that could evaluate the emissions and temperature profiles of the advanced centrifugal mixing concept in reacting flow was built. However, the restructuring of the program and the truncation of the schedule rendered testing of the mixing concepts in hot flow impractical. All of the cold flow testing and modeling, along with previous experimental results, indicates that the centrifugally enhanced mixing concept will result in a duct heater that has minimal pressure drop and NO_X emissions, and therefore meet the program goals.

References

Freihaut J.D., Proscia W., Knight B.A., "Combustion Properties of Micronized Coal for High Intensity Combustion Applications", Final Report DOE Contract DE-AC22-80263, April 1989.

Holdeman, J.D. (1993). Mixing of Multiple Jets With a Subsonic Crossflow. Prog. Energy Combust. Sci., Vol.19, pp. 31-70 (see also AIAA-91-2458 & NASA TM 104412).

Johnson B.V., Markowski S.J., Craig H.M., "Cold Flow and Combustion Experiments with a New Burner Air Distribution Concept", ASME Jrnl of Engineering for Power, pp. 370-375, April 1986.

Markowski S.J., Lohmann R.P., Reilly R.S., "The Vorbix Burner-A New Approach to Gas Turbine Combustors", ASME Jrnl of Engineering for Power, pp. 123-129, Jan. 1976

Merryman E.L., and Levy A.: Fifteenth Symposium (International) on Combustion, p. 1073, The Combustion Institute, 1975.

Semerjian H., Vranos A., "NO_X Formation in Premixed Turbulent Flames. Sixteenth Symposium (International) on Combustion, p. 169, The Combustion Institute, 1977.

Sowa, W.A., Kroll, J.T., Samuelsen, G.S., and Holdeman, J.D. (1994). Optimization of Orifice Geometry for Crossflow Mixing in a Cylindrical Duct. AIAA Paper 94-0219 (also NASA TM 106436).

Tacina Robert R., "Low NO_X Potential of Gas Turbine Engines, AIAA-90-0550.

Vranos A., Knight B.A., Zabielski M.F., "Centrifugal Mixing: A Comparison of Temperature Profiles in Non-Recirculating Swirling and Non-Swirling Flames", Combustion and Flame 48, pp. 109-119, 1982

Vranos A., Liscinsky D.S., "Planar Imaging of Jet Mixing in Crossflow", AIAA Journal, Vol. 26, No. 11, p. 1297, November 1988.

Section 11 - EERC Pilot-Scale Activities

Abstract

The work reported in this section was performed under program task 2.2.4. The testing of the individual air heater components were carried out with scale model test modules in a specially constructed furnace at UND/EERC. The pilot-scale slagging furnace system (SFS) consists of eight main components: 1) slagging furnace, 2) slag screen/slag tap, 3) dilution-quench zone, 4) process air preheaters, 5) convective air heater (CAH) section, 6) radiant air heater (RAH) panel, 7) tube-and-shell heat exchangers, and 8) pulse-jet baghouse.

High Temperature Advanced Furnace (HITAF), the major component development need for the HIPPS plant, was successfully completed. A nominally 3MMBtu/hr (3.18 x 10^6 kJ/hr) HITAF was designed, constructed, and tested with various coal and lignites to demonstrate the IFC concept. Consistently, 1700 °F, 150-psig process air was obtained demonstrating that the HIPPS baseline efficiency of 47% is achievable. In one instance, the furnace firing-rate was increased and the HITAF, the key HIPPS component, set a new record by heating pressurized air to 2000 °F. This accomplishment indicates that overall energy efficiency improvement by 35-60% and lowering of CO2 emissions by 28-40% compared to conventional pulverized coal boilers is achievable when HIPPS is ready for deployment. New heat exchange materials with temperature capabilities exceeding 2100 °F evolved out of this R&D. New metallurgy and new welding technologies evolved out of this study would potentially allow operation of high temperature heat exchangers using commercially available materials.

The design and fabrication of the pilot-scale slagging furnace and the performance of the CAH test module, and RAH panels are presented below.

The pilot-scale slagging furnace design is intended to be as fuel-flexible as possible, with maximum furnace exit temperatures of 2700 to 2900°F (1482 to 1593 °C) to maintain the desired heat transfer to the RAH panel and slag flow. The furnace has a nominal firing rate of 2.5 MMBtu/hr (2.65 x 10^6 kJ/hr) and a range of 2.0 to 3.0 MMBtu/hr (2.12 x 10^6 to 3.18 x 10^6 kJ/hr) using a single burner. The furnace design was based on Illinois No. 6 bituminous coal (11,100 Btu/lb [26,018 kJ/kg]) and a nominal furnace residence time of 3.5 sec. Flue gas flow rates range from roughly 425 to 645 scfm (12.0 to 18.3 m^3/min), with a nominal value of 535 scfm (15.1 m^3/min), based on 20% excess air. Firing a subbituminous coal or lignite increases the flue gas volume, decreasing residence time to roughly 2.6 sec. However, the high volatility of low-rank fuels results in high combustion efficiency (>99%).

RAH and CAH testing results

The RAH and CAH have been tested in the SFS for more than 2000 hrs while firing natural gas and for more than 1500 hrs firing coal and lignite. The heat transfer from both test modules was very close to the design estimates for the CAH and RAH. The implication of this is that our cycle analysis is realistic and that thermal efficiencies equal to or greater than 50% are achievable with our HIPPS design.

The test modules held up structurally with no apparent deterioration except slag corrosion of the protective tiles. The thermal expansion was accommodated by the design and the horizontal and vertical seams did not bind up with hardened slag. The corrosion rate of the tiles (especially

the high chrome tiles) was acceptable for most coals. The damage to the tiles came mostly from thermal cycling which induced cracks. The ceramic manufacturers believe this is a correctable flaw, and that with a blending of different particle size distributions in the initial material there would be a significant improvement in thermal shock resistance.

Introduction

The University of North Dakota Energy & Environmental Research Center (EERC) participated with United Technologies Research Center (UTRC) and UTRC subcontractors in Phase II of the Combustion 2000 High-Performance Power System project. EERC efforts included:

- laboratory - and bench-scale testing of materials used for the construction of key subsystems for the high-temperature advanced furnace (HITAF);
- testing methods to reduce problems related to coal slag flow and corrosion; and
- the design, construction, and operation of a pilot-scale slagging furnace system (SFS) to demonstrate essential HITAF subsystems.

EERC pilot-scale activities began in September 1995. In October 1995, the EERC submitted an application for a permit-to-construct to the North Dakota State Department of Health for the pilot-scale SFS to be constructed at the EERC. Because of the small size (2–4 MMBtu/h, or 2.1-4.2 x 10^6 kJ/hr) of the proposed system, the regulatory agency determined that a permit-to-construct was not necessary, but added the SFS as a listed source to the EERC permit-to-operate (Permit No. 078004).

Design and procurement activities related to the SFS began in September 1995. Design activities proceeded based on the primary purpose of the SFS, which was to evaluate heat transfer and material and slag/ash issues related to the performance of the radiant air heater (RAH) and convective air heater (CAH). Initial procurement activities focused on the acquisition of an overhead crane to be used in support of SFS fabrication and assembly activities. A final preliminary design package for the pilot-scale SFS was completed by the EERC and approved by UTRC in July 1996. The package contained a process description, process flow diagram, plan and elevation views of the major components, piping and instrumentation diagrams (P&IDs), and an instrumentation list. Primary SFS components included the

1) combustion air system (Area 100),
2) fuel feed system (Area 200),
3) slagging furnace (Area 300),
4) slag screen/quench zone/convective pass (Area 400),
5) flue gas system (Area 500),
6) process air system (Areas 600 and 700),
7) system instrumentation, and
8) data acquisition system.

The final SFS design included detailed design packages for major system components as well as support systems. These design packages contain specifications for purchased components, instruments, piping and electrical specifications, basic engineering design data, utility and raw material requirements, lists of fabrication materials and equipment, and fabrication drawings. Individual design packages were reviewed and approved in writing by UTRC before procurement and fabrication efforts were initiated by the EERC. Detailed design packages were prepared for the structural steel, slagging furnace, slag pot, primary and auxiliary burners, slag screen, dilution/quench zone, process air preheaters, tube-and-shell heat exchangers, pulse-jet baghouse, refractory selection and installation, coal feeder, system fans, SFS utility requirements (compressed air, water, compressed nitrogen, and electricity), CAH test section, and RAH test section. Although, the majority of design and procurement efforts were completed in September 1997, this activity continued through December 1997 with the installation and shakedown of the CAH tube bank and large radiant air heater (LRAH) panel. Subsequent design and procurement activities were limited to the installation of the small radiant air heater (SRAH) panel in April 1998 as well as support of CAH and RAH tests that continued through September 2000. The detailed design files for the SFS will be maintained at the EERC as long as the SFS remains on-site.

EERC construction activities began in December 1995 with structural steel installation. In May 1996, structural steel installation was essentially completed, and fabrication of system components began. Fabrication, assembly, and installation of major system components, excluding the process air preheaters, CAH tube bank, and RAH panels, were complete in April 1997. Process air preheater, CAH tube bank, LRAH panel, and SRAH panel installation were completed in July 1997, October 1997, November 1997, and April 1998, respectively. Shakedown of the SFS began in May 1997, with refractory curing completed in June. Subsequent shakedown tests continued periodically through December 1997 with the initial shakedown of the LRAH panel. Shakedown and initial testing of the SRAH panel occurred in April 1998 in conjunction with a SFS test firing a lignite fuel in support of a separate yet related project. A detailed description of the SFS is presented later in this section.

The original scope of work had plans for as many as 18 weeks (1500 hours of coal firing) of SFS operation in order to evaluate the performance of the CAH and RAH concepts once shakedown activities had been completed. However, funding cuts in FY98, FY99, and FY2000 only permitted the completion of 12 weeks of coal-fired SFS operation in support of this project, resulting in 1064 hours of coal firing. Fortunately, two related projects, one funded by the North Dakota Industrial Commission (NDIC) and the U.S. Department of Energy (DOE) National Energy Technology Laboratory (NETL) and a second funded by DOE NETL, supplied funding for the completion of 401 hours of additional coal/lignite-fired SFS operation in support of the overall effort (Collings, et al., April 1999; Collings, et al., December 1999). A test summary for the SFS for the period May 1997 through September 2000 is presented in Table 11-1. Information in the Table documents dates for SFS shakedown and other test periods completed; the type of fuel fired; whether or not individual test periods included the operation of the CAH tube bank, SRAH panel, and/or LRAH panel; hours of operation firing natural gas (including heatup, cooldown, and refractory curing); hours of operation firing coal or

Table 11-1
Slagging Furnace System Run Summary[1]

Dates	Run Number	Fuel Type	CAH Use	LRAH Use	SRAH Use	Natural Gas Firing, hr	Coal/ Lignite Firing, hr	Total Hours
5/20 to 5/21/97	Refractory cure/ shakedown	Natural gas	No	No	No	29	0	29
6/9 to 6/13/97	Refractory cure/ shakedown	Natural gas	No	No	No	99	0	99
6/17 to 6/20/97	High-temp. refractory cure/ shakedown	Natural gas	No	No	No	71	0	71
6/25 to 6/26/97	Shakedown	Illinois No. 6 bituminous coal	No	No	No	33	4	37
9/21 to 9/25/97	Shakedown SFS-IL6-0197	Illinois No. 6 bituminous coal	No	No	No	83	29	112
10/25 to 10/31/97	Shakedown SFS-RS1-0297	Rochelle subbituminous coal	Yes	No	No	98	47	145
11/30 to 12/4/97	SFS-RH1-0397	Natural gas	Yes	Yes	No	104	0	104
12/14 to 12/19/97	SFS-RH2-0497	Illinois No. 6 bituminous coal	Yes	Yes	No	80	35	115
2/9 to 2/13/98	SFS-RH3-0198	Illinois No. 6 bituminous coal	Yes	Yes	No	60	51	111
3/16 to 3/20/98	SFS-RH4-0298	Rochelle subbituminous coal	Yes	Yes	No	32	81	113
4/20 to 4/24/98	SFS-ND1-0398[2]	CCS lignite	Yes	Yes	Yes	120	50	170
6/8 to 6/12/98	SFS-ND2-0498[2]	MRYS/CCS lignite	Yes	Yes	Yes	61	52	113
8/7 to 8/19/98	SFS-RH5-0598	Illinois No. 6 bituminous coal	Yes	Yes	Yes	163	116	279
12/6 to 12/11/99	Refractory cure SFS-RC1-0698	Natural gas	Yes	No	No	86	0	86
1/24 to 1/29/99	SFS-RH6-0199[3]	Illinois No. 6 bituminous coal	Yes	Yes	No	55	60	115
2/14 to 2/19/99	SFS-RH7-0299[3]	Kentucky bituminous coal	Yes	Yes	No	63	38	101
4/4 to 4/15/99	SFS-RH8-0399[3]	Kentucky/Illinois No. 6 bituminous coal	Yes	Yes	No	63	201	264

Continued . . .

Table 11-1
Slagging Furnace System Run Summary[1] (continued)

Dates	Run Number	Fuel Type	CAH Use	LRAH Use	SRAH Use	Natural Gas Firing, hr	Coal/ Lignite Firing, hr	Total Hours
5/2 to 5/10/99	SFS-RH9-0499	Illinois No. 6 bituminous coal	Yes	Yes	No	79	109	188
8/20 to 8/26/99	Refractory cure SFS-RC2-0599	Natural gas	Yes	Yes	No	142	0	142
9/12 to 9/20/99	SFS-RH10-0699	Prater Creek bituminous coal	Yes	Yes	No	71	107	178
12/10 to 12/22/99	SFS-RH11-0799	Illinois No. 6 bituminous coal	Yes	Yes	No	95	202	297
2/14 to 2/16/00	SFS-RC3-0100	Natural gas	Yes	Yes	No	50	0	50
3/19 to 3/30/00	SFS-RH12-0200	Cordero Rojo subbituminous coal	Yes	Yes	No	63	200	263
5/29 to 6/2/00	SFS-RC4-0300	Natural gas	Yes	No	No	104	0	104
6/12 to 6/15/00	SFS-RH13-0400	Kentucky bituminous coal	Yes	Yes	No	59	13	72
6/19 to 6/27/00	SFS-RH13-0400	Prater Creek bituminous coal	Yes	Yes	No	53	150	203
9/19 to 9/21/00	SFS-RH14-0500	Natural gas	Yes	Yes	No	59	0	59
					Total Hours	2075	1545	3620

[1] Gas times include heatup and cooldown and refractory curing when necessary.
[2] These SFS tests were funded by NDIC and DOE NETL.
[3] These SFS tests were funded by DOE NETL.

lignite; and total hours of operation. Based on the data in the table, the SFS operated for a total of 3620 hours during the period May 1997 through September 2000.

Operating parameters were initially chosen for individual SFS tests based on SFS, RAH panel, and CAH tube bank design criteria. Once adequate operating experience was obtained and acceptable performance at baseline design conditions was documented, test parameters for subsequent SFS test periods were based on the results of previous tests and expanded performance objectives. Other test parameters included operating the RAH panel 1) at process air outlet temperatures that were higher than the original design criteria (>1700 °F [>927 °C]), 2) with ceramic tiles having different compositions, and 3) without ceramic tile protection.

Slagging furnace operation was evaluated based on furnace temperature (flue gas and refractory) and pressure measurements and on-line flue gas instrumentation readings (O_2, CO, CO_2, NO_x, and SO_2). A nominal coal firing rate of 2.5 MMBtu/h (2.6×10^6 kJ/hr) at an air-to-fuel ratio of about 1.2 was anticipated to achieve furnace gas temperatures of 2800 °F (1538 °C) near the furnace wall. Fuel selection was based on availability and properties such as ash fusion temperature and composition relative to potential impact on slag flow, RAH ceramic tile corrosion, and CAH tube bank deposition.

Special emphasis was placed on the collection of data to document the performance of the RAH panel located in the furnace wall. Performance of the RAH panel was evaluated relative to radiant heat transfer from the furnace to the hot process air stream and the impact of slag on the ceramic tiles protecting the high-temperature alloy heat-transfer surfaces. Temperature measurements were made at the surfaces of the ceramic tiles and alloy heat-transfer tubes as well as of the bulk inlet and outlet process air. The effects of the fuel type on the corrosion and erosion of the castable and brick refractory were evaluated based on observations before and after each week of operation. Photographs were taken to document observations.

Furnace exit, slag tap, and slag screen operating temperatures were selected based on ash fusion data for the specific fuels fired. These system temperatures are generally controlled at 100 to 200 °F (56 to 111 °C) above the fluid temperature of the slag under oxidizing conditions. Although the design and operation of these components are specific to the scale and design of the pilot-scale SFS, evaluating their performance was important to determining the impact of fuel properties on the relative performance of the RAH panel. The required flue gas recirculation (FGR) rate in the dilution/quench zone depends on the slag screen exit temperature. The FGR rate was controlled to achieve a flue gas temperature of 1800 to 1850 °F (983 to 1010 °C) entering the CAH tube bank.

Performance of the CAH tube bank was evaluated relative to heat transfer from the flue gas to the hot process air stream and the impact of ash deposition on the alloy tube surfaces. Temperature measurements were made to document the surface temperatures of the alloy heat-transfer surfaces as well as bulk inlet and outlet process air temperatures. Heat recovery from the CAH tube bank is integral to the preheating of process air for the RAH panel in the furnace. However, it was not necessary to remove ash deposits from the CAH tube surfaces in order to achieve the process air conditions required to effectively support the operation of the RAH panel. As a result, data concerning

deposition rate on the CAH heat-transfer surfaces were estimated based on the weight of deposits collected and the duration of coal firing for some test periods. During other test periods, the EERC attempted to sootblow the CAH tube bank on a regular basis in order to minimize heat-transfer degradation as a function of ash deposition.

CAH ash deposits collected during some of the tests that did not involve sootblowing were characterized to determine chemical composition and relative strength. Specific analyses included x-ray fluorescence (XRF), scanning electron microscopy (SEM) point count, and SEM morphology. Acquiring this information was important because the firing characteristics of the SFS concept represent a firing condition different from either pulverized coal (pc) or cyclone firing. Specifically, the flame is less turbulent to increase its length and reduce NO_x formation, yet flame and furnace temperatures are greater than in pc firing because of reduced radiant losses to the furnace walls. In addition, air-to-fuel ratios are higher than with cyclone firing.

Flue gas composition (O_2, CO, CO_2, NO_x, and SO_2) was monitored continuously using on-line instrumentation at the exit of the furnace and pulse-jet baghouse. Sulfur dioxide and nitrogen species data are reported on a lb/MMBtu and concentration basis. Particulate sampling was completed at the inlet and outlet of the baghouse during most of the SFS test periods. Sampling at the inlet of the baghouse documented particulate mass loading and size distribution. Sampling at the outlet of the baghouse documented mass and fine particulate emissions. Particulate emissions are reported on a lb/MMBtu and mass per unit volume basis.

Composite samples of coal, slag, and baghouse ash were collected for routine analysis. One composite coal sample was analyzed for each week of operation. Analyses included ultimate, proximate, Btu, dry sieve, ash fusion (oxidizing), XRF, computer-controlled scanning electron microscopy (CCSEM), and ash viscosity. Analysis of slag involved at least one composite sample for each week of operation and included ash fusion and composition. One baghouse ash composite sample was characterized for each week of operation. Analyses included Malvern particle size, carbon/hydrogen/nitrogen, and composition. Composite samples of ash from other locations in the system were collected on an as-needed basis. Analyses of these samples depended on system performance observations and data analysis.

Description of Pilot-Scale Slagging Furnace System

The EERC pilot-scale SFS was designed to simulate the conditions in a commercial-scale UTRC HITAF. The overall SFS is pictured in Exhibit 11-1, with a schematic of the system shown in Exhibit 11-2. The schematic in Exhibit 11-2 depicts the current SFS configuration as a result of system modifications made since construction of the original SFS was completed in 1997. Modifications in the last three years were limited to process piping changes, with no changes to major system components. A detailed description of the SFS is presented in Appendix A.

EERC GW16581.CDR

Exhibit 11-1
Photograph of the Pilot-Scale Slagging Furnace System

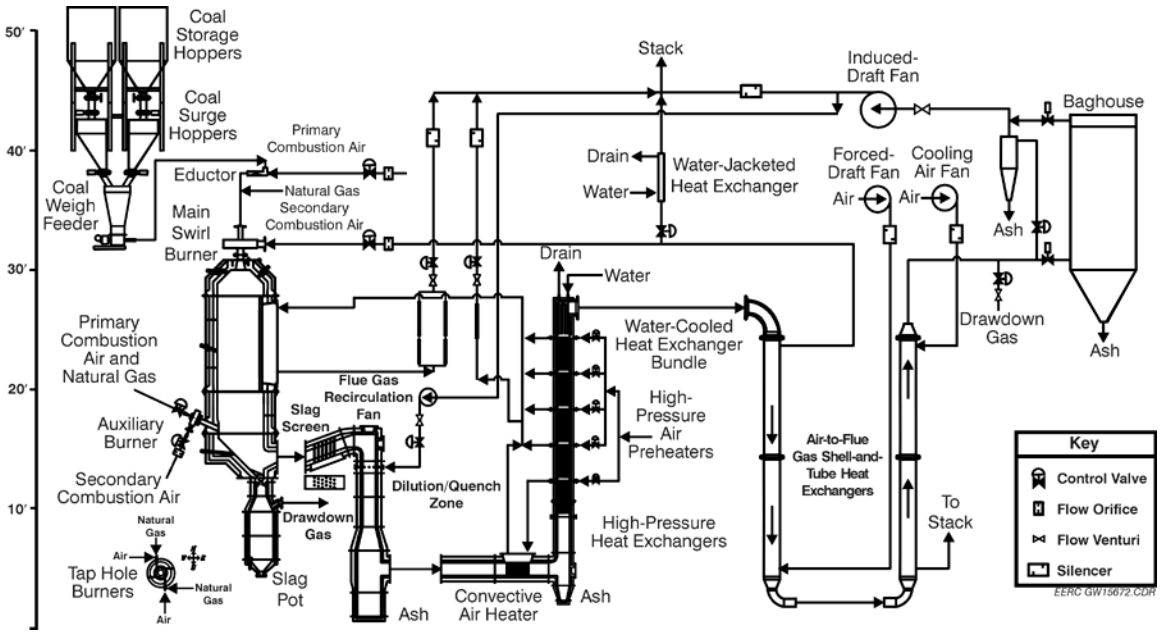

Exhibit 11-2
Combustion 2000 Slagging Furnace and Support Systems

Slagging Furnace

The pilot-scale slagging furnace is intended to be as fuel-flexible as possible, with maximum furnace exit temperatures of 2700 to 2900 °F (1483 to 1593 °C) to maintain the desired heat transfer to the RAH panel and slag flow. The furnace has a nominal firing rate of 2.5 MMBtu/h (2.6×10^6 kJ/hr) and a range of 2.0 to 3.0 MMBtu/h (2.1 to 3.2×10^6 kJ/hr) using a single burner. The design is based on Illinois No. 6 bituminous coal (11,100 Btu/lb [25,800 kJ/kg]) and a nominal furnace residence time of 3.5 s. Flue gas flow rates range from roughly 425 to 645 scfm (12.0 to 18.6 m^3/min), with a nominal value of 530 scfm (15 m^3/min), based on 20% excess air. Firing a subbituminous coal or lignite increases the flue gas volume, decreasing residence time to roughly 2.6 s, and decreases flame temperature due to the higher moisture content of these fuels. However, the high volatility of the low-rank fuels results in high combustion efficiency (>99%). The EERC oriented the furnace vertically (downfired) and based the burner design on that of a swirl burner used on two smaller EERC pilot-scale pc-fired units (600,000 Btu/h [633,000 kJ/hr]). Slagging furnace internal dimensions are 47 in. (119 cm) in diameter by roughly 16 ft (4.9 m) in total length.

The vertically oriented furnace shell was designed to include four distinct furnace sections. The top section of the furnace supports the main burner connection, while the upper-middle furnace section provides a location for installation of the RAH panels. The lower-middle furnace section supports the auxiliary gas burner; the bottom section of the furnace includes the furnace exit to the slag screen as well as the slag tap opening. Flue gas temperature measurements are made using two Type S thermocouples protruding 1 in. (2.5 cm) into the furnace through the refractory wall and three optical pyrometers (flame, flue gas along the furnace wall near the RAH panel, and flue gas at the furnace exit). Furnace temperature is also measured using thermocouples located at the interface

between the high-density and intermediate refractory layers and between the intermediate and insulating refractory layers. A pressure transmitter and gauges are used to monitor static pressures in order to monitor furnace performance. These data (temperatures and pressures) are automatically logged into the data acquisition system and recorded manually on data sheets on a periodic basis as backup.

The slag tap is intended to be as functional yet low-maintenance as possible. The tap is lined with highly corrosion-resistant refractory. Its diameter is nominally 4 in. (10 cm), which is small enough to reduce radiant heat losses out of the furnace while minimizing plugging, and it has a well-defined drip edge. A two-port natural gas-fired burner is used to maintain slag tap temperature for good slag flow. To further minimize heat losses slag is collected in an uncooled, dry container with refractory walls, rather than in a more typical water bath.

The refractory walls in the slagging furnace are composed of three layers of castable refractory. They consist of an inner 4-in. (10.2-cm) layer of high-density (14-Btu-in./ft^2 °F-hr, or 2.0-W/m-K) slag-resistant material, 4 in. (10.2 cm) of an intermediate refractory (4.0 Btu-in./ft^2 °F-hr, or 0.6 W/m-K), and a 3.25-in. (8.3-cm) outer layer of a low-density insulating refractory (1.3 Btu-in./ft^2 °F-hr, or 0.2 W/m-K). Three refractory layers were selected as a cost-effective approach to keeping the overall size and weight of the furnace to a minimum while reducing slag corrosion and heat loss. The inner layer is composed of an alumina castable, developed by the EERC in cooperation with the Plibrico Company, that was shown in laboratory tests to be extremely resistant to slag corrosion relative to other commercially available castable refractories. Table 11-2 summarizes properties for refractory material used in the SFS.

Table 11-2
Refractory Properties

Refractory:	**Plicast Cement-Free 99V KK/99V[1]**	**Plicast Cement-Free 98V KK/98V[1]**	**Plicast Cement-Free 96V KK/96V[1]**	**Narco Cast 60**	**Plicast LWI-28**	**Plicast LWI-20**	**Harbison-Walker 26**
Function	High density	High density	High density	High density	Insulating	Insulating	Insulating
Service Limit, °F	3400	3400	3300	3100	2800	2000	2600
Density, lb/ft^3	185	185	185	145	80	55	66
K, Btu-in./ft^2°F-hr @ 2000°F	14.5	14.5	14.0	6.5	4.0	NA[2]	2.2
K, Btu-in./ft^2°F-hr @ 1500°F	14.7	14.7	14.2	6.0	3.0	1.7	1.9
K, Btu-in./ft^2°F-hr @ 1000°F	15.5	15.5	15.0	5.6	2.7	1.3	1.7
Hot MOR[3] @ 2500°F, psi	650	750	1400	NA	NA	NA	NA
Hot MOR @ 1500°F, psi	–	–	2000	1000	250	100	110
Cold Crush Strength @ 1500°F, psi	–	–	10000	NA	750	400	350
Typical Chemical Analysis, wt% (calcined)							
Al_2O_3	99.6	98.6	95.5	62.2	54.2	39.6	53.8
SiO_2	0.1	1.0	3.8	28.0	36.3	31.5	36.3
Fe_2O_3	0.1	0.1	0.1	1.0	0.8	5.4	0.5
TiO_2	0.0	0.0	0.0	1.7	0.5	1.5	0.6
CaO	0.1	0.1	0.1	2.8	5.7	19.5	7.2
MgO	0.0	0.0	0.0	0.1	0.2	0.8	0.2
Alkalies	0.2	0.2	0.2	0.2	1.5	1.4	1.4

[1] The "KK" designation indicates the presence of fibers that promote dewatering during curing.
[2] Not applicable.
[3] Modulus of rupture.

Fuel Feed System

The SFS fuel feed system serves two primary functions, a natural gas-firing capability and a solid fuel-firing capability. The natural gas-firing capability supports preheating the SFS with the main burner as well as the operation of the auxiliary burner and the two-port slag tap burner. Each of the three burners has its own set of controls and flame safety system. The natural gas feed system is integrated into the overall process control and data acquisition system.

Solid fuel firing only supports the operation of the main burner. To date, solid fuel firing has included pulverized (70% <0.0030 in., or 75 µm, with a 300-µm top size) bituminous and subbituminous coal and lignite. Two sets of feeder screws were acquired so that the feeder gear ratio can be adjusted to achieve a fivefold change in feed rate capacity. Fuel feed rates have ranged from 150 to 400 lb/hr (68.1 to 181.6 kg/hr) with the potential for the feeder to deliver fuel at rates of >500 lb/hr (>227 kg/hr). The three primary components of the solid fuel feed system consist of two storage hoppers (2400 lb, 1090 kg each), two surge hoppers (500 lb, 227 kg each), and a weigh feeder. Each surge hopper has the capacity to refill the weigh feeder hopper twice, allowing for adequate time to change out the storage hoppers. Each surge hopper has a level indicator integrated with the process control and data acquisition system, which then opens and closes a valve supplying pulverized fuel from the storage hopper in auto mode. Refilling of the surge hoppers can also be operated in a manual mode. The weigh feeder in use at this time is a K-Tron solids feeder capable of operating in gravimetric (loss-in-weight) or volumetric feed modes using a twin screw design to provide a uniform nonpulsing feed.

Operation of the weigh feeder is integrated into the overall process control and data acquisition system using a user-programmable microprocessor and a 20-bit resolution load cell (high-resolution digital). Solids from the weigh feeder are discharged from the screws into an air eductor. The fuel is then pneumatically conveyed to the main burner through the primary air line. Refilling of the feed hopper can be operated in a manual or automatic mode.

The main burner is natural gas- and pulverized fuel-capable. The basic design is an International Flame Research Foundation (IFRF)-type adjustable secondary air swirl generator which uses primary and secondary air at approximately 15% and 85% of the total air, respectively, to adjust swirl. Increasing swirl to provide flame stability and increased carbon conversion can also affect the formation of NO_x. Carbon conversion has been >99% when bituminous and subbituminous coal and lignite are fired. High carbon efficiencies can be obtained at low swirl settings because of the high operating temperature and adequate residence time. Combustion air flow rates through the main burner range from about 400 to 600 scfm (11 to 17 m^3/min), depending on furnace firing rate and the fuel type (bituminous, subbituminous, or lignite).

An auxiliary gas burner (maximum firing rate of 850,000 Btu/h, or 896,750 kJ/hr) is located near the furnace exit in order to control furnace exit temperature, ensuring desired slag flow from the furnace and the slag screen. This auxiliary burner is used to compensate for heat losses through the furnace walls, sight ports, and RAH test panel. Use of the auxiliary gas burner is beneficial during start-up to reduce heating time and to

prevent slag from freezing on the slag screen tubes when the switch is initially made to coal firing.

Radiant Air Heater Panels

A key design feature of the furnace is accessibility for installation and testing of one LRAH panel and one SRAH panel. The LRAH panel was designed for testing material lifetimes and heat exchange coefficients and is 1.5 × 6.4 ft (0.46 × 1.96 m). This size was based on manufacturing constraints identified by UTRC, which designed and assembled the panels, as well as a desire to minimize furnace heat losses. The LRAH contains three vertically oriented tubes made of MA 754, a nickel-based oxide dispersion-strengthened alloy. The tubes were protected from slag corrosion by fusion-cast alumina refractory tiles. Process air for the LRAH panel is provided by an existing EERC air compressor system. Maximum air capacity available to support the LRAH is 270 scfm (7.6 m^3/min) at a delivery pressure of 150 psig (10.3 bar). As it passes through the LRAH panel, the process air is heated from nominally 1300 °F (705 °C) to as high as 1800 °F (982 °C). However, during one test, adjustments were made to the furnace firing rate and the process air flow rate and pressure to demonstrate that a LRAH process air exit temperature of 2000 °F (1094 °C) can be reached with the current design.

Backup process air is available from a smaller compressor at a delivery rate of nominally 150 scfm (4.2 m^3/min) and pressure of <100 psig (<7 bar). A tie-in to an existing nitrogen system was also installed as a backup to the existing air compressor system to prevent the panel from overheating in the event of a power outage. In the event of a failure of inlet process air piping, a backflow emergency piping system was installed so that overheating of the LRAH panel could be avoided. Photographs of the LRAH panel installed in the slagging furnace with and without tiles installed are presented in Exhibit 11-3.

EERC GW16622.CDR

EERC AH18414.CDR

Exhibit 11-3
Photographs of the LRAH Inside the Slagging Furnace with (top) and without (bottom) Tile Protection

Furnace design also permits the installation of a smaller 1.5- × 5.4-ft (0.46- × 1.65-m) SRAH panel. The purpose of the SRAH panel was to expose ceramic materials to slagging furnace conditions to evaluate their slag corrosion properties and material lifetimes rather than generating heat-transfer data. The SRAH was constructed with a variety of refractory tiles. A primary difference between the LRAH and SRAH panels

was that the SRAH panel was cooled with water rather than heated air using two sets of five vertically oriented 0.375-in. (0.952-cm)-outside-diameter (o.d.) stainless steel tubes. While the SRAH panel was 1 ft (0.3 m) shorter than the LRAH panel, both assemblies were the same width and use the same air-cooled frame support design. A central vertical ceramic rail was present in the SRAH panel, allowing the installation of either full-width (18-in. [46-cm]) or half-width tiles inside the furnace. In August 1998, severe tile deterioration and failure resulted in a technical and economic decision to remove the SRAH from service and make exclusive use of the LRAH panel for heat-transfer studies as well as evaluation of component performance relative to material lifetimes. As a result of this decision, the SRAH panel was not used for a majority of the SFS tests completed, and essentially no data were acquired. Therefore, subsequent discussion of the RAH panel in this report will refer exclusively to the LRAH.

Slag Screen

As the hot gases leave the combustion zone, they pass through a slag screen which is designed to remove the entrained ash as a nonleachable slag. The slag screen design for the pilot-scale SFS is the result of a cooperative effort between the EERC, UTRC, and Physical Sciences, Inc. (PSI). The primary objective for the slag screen is to reduce the concentration of ash particles entering the CAH.

Design criteria specific to the pilot-scale slag screen include

1) a simple design permitting modifications using readily available, inexpensive materials;
2) matching duct dimensions and flue gas flow rates to maintain turbulent flow conditions;
3) minimizing the potential for plugging as the result of slag deposit growth on tube surfaces or the sloped floor;
4) limiting differential pressure across the slag screen to 2-in. W.C. (4 mm Hg); and
5) limiting heat losses to ensure desired slag flow from the slag screen to the furnace slag tap.

The slag screen flue gas approach velocity is nominally 70 to 75 ft/s (21.4 to 22.9 m/s), depending on furnace firing rate and fuel type. The flue gas outlet temperature from the slag screen must be >2500 °F (>1371 °C) to minimize the potential for slag freezing in the slag screen.

The slag screen typically makes use of six rows of three 1.5-in. (3.8-cm)-diameter vertical tubes mounted in an upwardly sloped duct (20 degrees) to facilitate slag flow from the slag screen into the furnace slag tap. The center line-to-center line tube spacing in each row is 3.75 in. (9.5 cm). Center line-to-center line spacing between individual rows is 4 in. (10.2 cm). Internal duct dimensions for the slag screen are 10 in. × 13 in. × 3.5 ft (25 cm × 33 cm × 1.1 m). The resulting flue gas velocity through the slag screen is roughly 91 ft/s (28 m/s).

Slag screen tubes are fabricated using castable high-density refractory poured inside aluminum pipe. The aluminum pipe makes a structurally sound form during curing and eventually melts and runs into the slag pot as furnace temperatures rise. Water-cooled tubing inside of the refractory tubes and the floor of the furnace exit/slag screen inlet are intended to cool the refractory surfaces in order to minimize erosion and corrosion.

Based on slag screen-operating experience with bituminous coal, subbituminous coal, and lignite, EERC personnel have determined that the high-density refractory is an acceptable tube material and that the size of the water-cooled tubes inside of the high-density refractory must be changed depending on the type of fuel. During lignite- and subbituminous coal-fired tests, more cooling is necessary to build up a sufficiently thick frozen slag layer to protect the slag screen tubes from the severe erosion/corrosion attack that can occur within the slag screen.

The diameter of the stainless steel water tubes inside the slag screen tubes is typically 0.5 in. (1.3 cm) o.d. in the first row and, possibly, the second row (depending on ash fusion temperature data), and 0.375 in. (0.952 cm) o.d. in the remaining four rows. However, it was necessary to reduce the size of the water tubes to 0.25 in. (0.63 cm) o.d. in all but the first row for Illinois No. 6 bituminous coal firing, with the o.d. of the water tubes in the first row reduced to 0.375 in. (0.952 cm). For fuels with more refractory ash, such as an eastern Kentucky bituminous coal, only three rows of tubes were used in order to maintain slag flow out of the screen section. The first row used 0.375-in. (0.952-cm) o.d. water tubes, and the second and third rows used 0.25-in. (0.63-cm)-o.d. water tubes. The pilot-scale slag screen tubes will likely always require periodic replacement based on some level of erosion/corrosion and the fuels selected for testing. However, in a larger demonstration or commercial-scale unit, steam-cooled steel tubes could be used without a refractory coating, as long as a frozen slag layer can be maintained on the surface of the tubes.

Type S thermocouples (one each) in the vicinity of the first and last row of tubes are used to monitor slag screen temperature. However, these measured temperatures are believed to be less than the actual flue gas temperatures because the thermocouples are located behind individual water-cooled slag screen tubes and because of observed thermocouple deterioration by slag attack. Therefore, slag screen temperature control is based on an optical pyrometer measurement at the furnace exit/slag screen inlet. The EERC tries to operate the slag screen at flue gas temperatures of 100 to 200 °F (56 to 112 °C) above the fluid temperature of the fuel ash to ensure slag flow from the slag screen to the slag tap. Thermocouple data are automatically logged on the data acquisition system. To monitor and record slag screen differential pressure, taps were installed in the roof upstream and downstream of the tubes. As a backup to the data acquisition system, slag screen data are recorded manually on data sheets on a periodic basis. Mass balances were completed for all SFS operating periods in order to document the distribution of slag/ash in the system.

Dilution/Quench Zone

As the hot combustion gas leaves the slag screen, it is quenched with recirculated flue gas to 1850 °F (1010 °C) in order to reduce the stickiness of the remaining entrained ash

to minimize deposition on the CAH tubes. Because of the stickiness of the ash and the high turbulence caused by the injection of the recirculated flue gas, the quench zone is the only region in the furnace where hard slag/ash deposits form. These deposits are easily removed on-line by knocking them into a hopper at the bottom of the zone.

The design of the dilution/quench zone was a cooperative effort between the EERC and UTRC. The zone has a circular cross section and is oriented vertically so that ash deposits can be easily removed. It has a 1.17-ft (0.36-m) diameter in the area of the FGR nozzles and then expands to 2 ft (0.6 m) to provide adequate residence time within duct length constraints. The duct section containing the FGR nozzles is a water-cooled spool piece in order to permit easy changes to the size, number, and orientation of the FGR nozzles. The water-cooling wall appears to embrittle the slag deposits that form in this area, making them more prone to spontaneous shedding and generally easier to remove on-line. The vertically oriented dilution/quench zone is refractory-lined and located immediately downstream of the slag screen and upstream of the CAH duct. Routine cleaning of the dilution/quench zone is required during each weeklong coal- or lignite-fired test. A pressure transmitter is used to monitor and record differential pressure across the zone as an indication of slag deposition.

Convective Air Heater

The CAH design was a cooperative effort between the EERC and UTRC. It was constructed by UTRC and installed in September 1997. Flue gas flow rate to the CAH tube bank has been calculated by the EERC to range from 3553 to 4619 acfm at 1800 °F (101 to 131 m^3/min at 982 °C), depending on the fuel and firing rate in the SFS. A rectangular inside duct dimension of 1.17 ft^2 (0.11 m^2) results in a flue gas approach velocity of 50 to 73 ft/s (15 to 22 m/s) to the CAH tube bank. Heat is recovered from the flue gas to meet process air temperature requirements for the CAH as well as the RAH panel. The design process air exit temperature from the CAH is 1200 °F (649 °C) and is not permitted to exceed 1300 °F (705 °C). Process air flow rate is used to control process air exit temperature using a flow control valve.

The CAH tube bank originally consisted of twelve 2-in. (5-cm)-diameter tubes installed in a staggered three-row array. The first five tubes in the flue gas path were uncooled ceramic material, with the remaining seven tubes cooled using heated air. The uncooled ceramic tubes were replaced in May 1998 with uncooled stainless steel tubes because the ceramic tubes were repeatedly damaged when the tube bank was removed from the duct.

In September 1998, the uncooled tubes were again replaced. The replacement tubes were made of three high-temperature alloys, each with a different pipe size. They were 1.5-in. (3.8-cm) Schedule 80 INCOLOY MA956, 1-in. (2.5-cm) Schedule 40 INCOLOY MA956HT, and 0.75-in. (1.9-cm) Schedule 40 PM2000. Exhibit 11-4 illustrates the position, size, and alloy type for the five uncooled tubes. At the request of UTRC, two of these uncooled alloy tubes were removed from the CAH tube bank following a September 1999 test and returned to UTRC for characterization. The tubes removed from the CAH were composed of INCOLOY MA956HT and INCOLOY MA956. Replacement tubes were fabricated using 1.5-in. (3.8-cm) Schedule 40 stainless steel pipe. Exhibit 11-5

illustrates the position, size, and alloy type for the CAH tubes in place during the December 1999 test and all of the SFS tests performed in calendar year 2000.

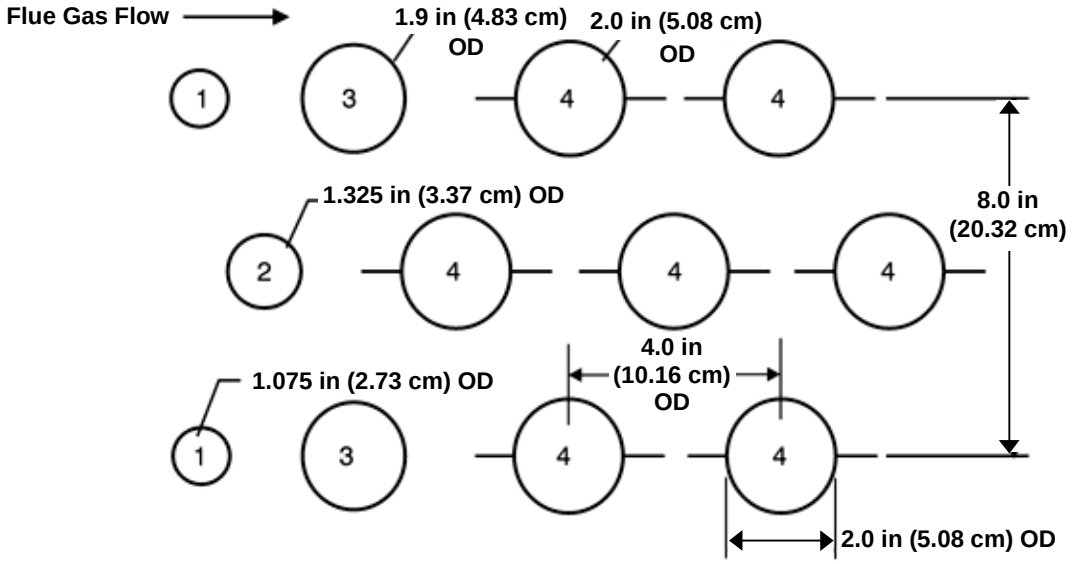

[1]Uncooled, PM 2000 (nominally 0.75 in (1.91 cm) Schedule 40 pipe).
[2]Uncooled, Incoloy Alloy MA956HT (nominally 1 in (2.54 cm) Schedule 40 pipe).
[3]Uncooled, Incoloy Alloy MA956 (nominally 1.5 in (3.81 cm) Schedule 80 pipe).
[4]Air-Cooled, Inconel 625 (2 in (5.08 cm) tubing, 0.188 in (0.478 cm) Wall.

Exhibit 11-4
Illustration of the Tubes in the CAH Tube Bank for the Period September 1998 through November 1999

Prior to an August 1998 test, fins were added to the air-cooled tubes in the CAH to improve heat transfer. The fins are 1-in. (2.5-cm) by 0.125-in. (0.318-cm) flat material and run the length of each tube on both the leading and trailing edges of the tube surface. Based on the subsequent data, it appears that the addition of the fins improved heat recovery during coal-fired test periods. The fins appear to have reduced the rate of heat-transfer degradation as ash deposits developed and helped to maintain a higher heat-transfer rate once the deposits had formed. However, no improvement in heat recovery was observed during natural gas-fired periods with clean tube surfaces. Exhibit 11-6 is a photograph of the CAH tube bank removed from the flue gas duct. The photograph shows the CAH tubes illustrated in Exhibit 11-5 after a SFS test completed in June 2000.

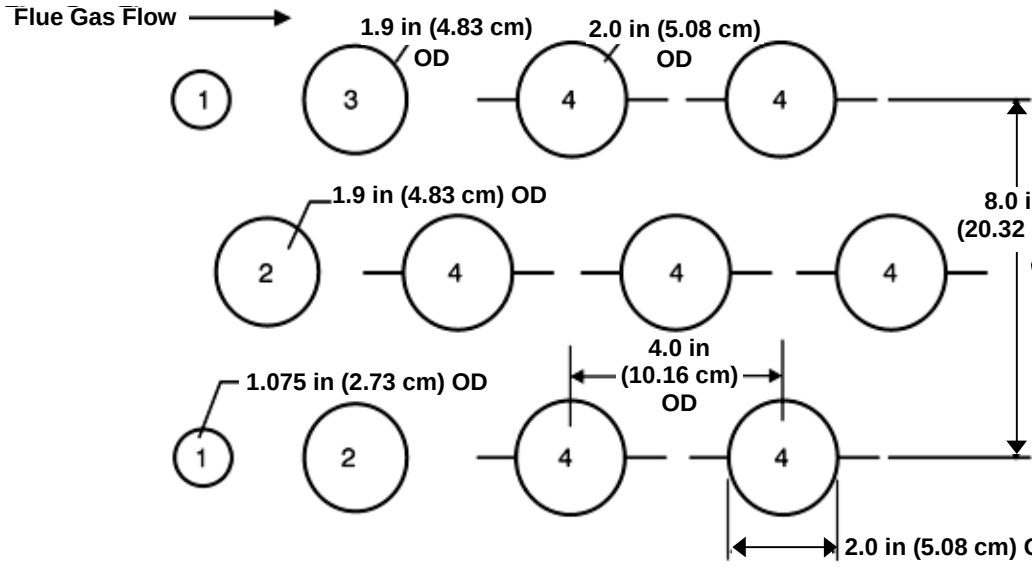

[1]Uncooled, PM 2000 (nominally 0.75 in (1.91 cm) Schedule 40 pipe).
[2]Replaced prior to December 1999 test, using 1.5 in (3.81 cm) Schedule 40 S.S. pipe.
[3]Uncooled, Incoloy Alloy MA956 (1.5 in (3.81 cm) Schedule 80 pipe).
[4]Air-Cooled, Inconel 625 (2 in (5.08 cm) tubing, 0.188 in (0.478 cm) Wall.

EERC GW17855.CDR

Exhibit 11-5
Illustration of the Tubes in the CAH Tube Ban for the Period December 1999 through December 2000

EERC AH18185.CDR

Exhibit 11-6
Photograph of CAH Tubes after a June 2000 SFS Test

Process Air Preheaters

Process air required for operation of the CAH tube bank and the RAH panel is preheated in five high-temperature alloy tube bundles located in the flue gas stream downstream of the CAH tube bank. The first tube bundle supports operation of the CAH tube bank, and the remaining four support the operation of the RAH panel. Because of high flue gas temperatures (1700 °F [927 °C]) in the vicinity of the first three process air preheaters and a nominal operating air pressure of 150 psig (10.3 bar), stainless steel could not be used for construction. Instead, an alloy capable of handling higher-temperature operation was required to maximize system flexibility and minimize the potential for material failure. Material options considered included a Haynes HR-120, HR-160, HA-230, and HA-556 and an RA253MA. Maximum temperatures for these five alloys at 150 psig (10.3 bar) are 1600, 1750, 1650, 1750, and 1650 °F (871, 955, 899, 955, and 899 °C), respectively. Based on material characteristics, availability, and cost, EERC personnel elected to use the RA253MA material for all five tube bundles exposed to flue gas, and HR-160 to transfer the heated process air to the RAH and CAH test sections. Use of the HR-160 alloy permitted the installation of electrical heaters to improve process air temperature control to the RAH and CAH test sections. The use of the two alloys in combination for the process air preheaters maximized system flexibility and minimized cost.

The tube bundles are mounted in a refractory-lined, vertically oriented, square duct. Duct dimensions are 12 in. by 12 in. (30.5 cm by 30.5 cm), with an overall duct length of 20.5 ft (6.2m). The refractory used in this section was a combination of Narco Cast 60 high-density refractory and Harbison-Walker 26 insulating refractory. All inlet and outlet process air lines supporting the CAH tube bank are insulated. Process air lines supporting the RAH panel are insulated and electrically heated.

During coal firing, it is possible to obtain process air temperatures of 1300 °F (705 °C) at flow rates of 200 scfm (5.7 m^3/min), even though the heat-transfer rate degrades with ash deposition on the tube surfaces. Further heating of the process air entering the RAH panel is achieved electrically and by recovering heat from the CAH tube bank. In addition, air compressor system and power failures have been encountered, resulting in the use of the nitrogen backup system. The nitrogen backup system has functioned as intended during these support system failures, supplying an emergency cooling media to the process air preheaters and, ultimately, supporting the CAH tube bank and RAH panel.

Flue Gas Heat Exchangers

The pilot-scale SFS has four tube-and-shell heat exchangers for heat recovery and flue gas temperature control and two water-cooled heat exchangers to reduce the heat load on system fans. Their location in the overall process layout is illustrated in Exhibit 11-2. The first two tube-and-shell heat exchangers reduce flue gas temperature and preheat the secondary air for the main burner. The third and fourth tube-and-shell heat exchangers are used to control flue gas temperature at the inlet of the pulse-jet baghouse.

The tube-and-shell heat exchangers have performed up to expectations during all test periods. The main burner secondary combustion air temperature is nominally 600 to 800

°F (316 to 427 °C), depending on ambient air temperatures. During winter months, the secondary air temperature can be controlled at the lower end of the range, and during summer months, temperature control is limited to the higher end of the range. Tube-and-Shell Heat Exchangers 3 and 4 perform very well, controlling the flue gas temperature at the baghouse inlet to <400 °F (<205 °C). Inspection during maintenance after each week of coal-fired operation indicates the presence of a scale-type ash layer on the surface of the tubes that must be removed in order to avoid deterioration of heat-transfer performance and corrosion of metal surfaces.

Two water-cooled heat exchangers were fabricated and installed in May 1998 to reduce the load on the FD (forced-draft), ID (induced-draft), and process air fans and ambient temperature on the upper levels of the SFS support structure. A water-cooled heat exchange tube bundle was installed in the flue gas stream between the five high-pressure process air preheater tube bundles and the first tube-and-shell heat exchanger. This water-cooled tube bundle reduces the cooling load on the FD and process air fans. A water-jacketed heat exchanger was installed on the secondary air bypass line to the stack to reduce the amount of heat being emitted to the immediate area and ambient temperature in the high bay in general.

Emissions Control

A pulse-jet baghouse is used for final particulate control for the SFS. The baghouse design permits operation at both cold-side (250 to 400 °F [121 to 205 °C]) and hot-side (600 to 700°F [316 to 371°C]) temperatures. The primary baghouse chamber and ash hopper walls are electrically heated and insulated to provide adequate temperature control to minimize heat loss and avoid condensation problems on start-up and shutdown. The main baghouse chamber was designed with internal angle iron supports to handle a negative static pressure of 20 in. W.C. (37 mm Hg).

Flue gas flow rates to the baghouse can range from a low of 630 scfm (17.8 m^3/min) at 350 °F (177 °C), to a maximum of 1063 scfm (30.1 m^3/min) at 700 °F (371 °C). Therefore, the baghouse design was based on an average flue gas flow rate of 850 scfm (24.1 m^3/min) at 350 °F (177 °C) or 1900 acfm (53.8 m^3/min) at 700 °F (371°C), based on a nominal furnace firing rate of 2.5 MMBtu/h (2.6×10^6 kJ/hr). The baghouse is sized to accommodate a maximum of 36 bags mounted on wire cages with 2-in. (5-cm) bag spacing. Bag dimensions are nominally 6 in. (15.2 cm) in diameter by 10 ft (3.0 m) in length, providing a total filtration area of 565 ft^2 (52.5 m^2).

Each filter bag is secured to the tube sheet using a snap band sewn into the top cuff. Stainless steel (304 SS) wire cages with 20 vertical wires and 6-in. (15-cm) ring spacing provide bag support. The pulse-jet baghouse is a single compartment capable of either on- or off-line cleaning. Pulse-jet cleaning can be triggered as a function of baghouse differential pressure or as a function of time. High-pressure/low-volume and low-pressure/high-volume cleaning options were included in the design of the pulse-air system. During heatup and off-line cleaning, flue gas flow is diverted through a cyclone. Two different sets of bags have been used during this project: a 16-oz/yd^2 (543-g/m^2)

Huyck felt material and a 22-oz/yd^2 (744-g/m^2) woven glass bag with a polytetrafluoroethylene (PTFE) membrane.

The SFS does not have a flue gas desulfurization system (FGD) for sulfur dioxide control. Dispersion modeling data developed by the North Dakota State Health Department indicate that the stack height, flue gas velocity at the stack exit, and dilution effect of the system process air that is exhausted through the stack permit a maximum sulfur dioxide emission rate of 20.8 lb/hr (9.4 kg/hr). However, based on operating experience with bituminous and subbituminous coal and lignite, the EERC never exceeded a sulfur dioxide emission rate of 17 lb/hr (7.7 kg/hr) during this project.

Instrumentation and Data Acquisition

The instrumentation and data acquisition components for the pilot-scale SFS address combustion air, flue gas, process air, process water, temperatures, static and differential pressures, and flow rates. The data acquisition system is based on a Genesis software package and three personal computers. Two sets of flue gas instrumentation (oxygen, carbon dioxide, carbon monoxide, sulfur dioxide, and nitrogen species) are dedicated to support the operation of the SFS. Flue gas is transferred from the sample point through a heated filter and sample line to the sample conditioner before it reaches the analyzers. Continuous flue gas sampling occurs between the slag screen and the dilution/quench zone to monitor and control slagging furnace operation. Flue gas is routinely sampled on a continuous basis at the exit of the baghouse to monitor the SFS for air leaks. Total flue gas flow rate through the SFS is measured using a venturi.

EERC Pilot-Scale Activities

The results of the pilot-scale SFS tests completed in support of this project are documented in this section of the report. These tests were performed between November 1997 and September 2000. SFS operating periods prior to November 1997 were focused on SFS shakedown efforts and are not discussed in this report. Also, natural gas-fired operating periods completed for the specific purpose of curing SFS refractory are not discussed. The discussion is based on the data and observations resulting from 12 SFS test periods completed in support of this project as well as referenced information resulting from two related projects (Collings et al., April 1999; Collings et al., December 1999). The 12 SFS operational periods involved natural gas firing during system heatup, cooldown, and to achieve test objectives; unplanned natural gas firing as a result of slag tap and slag screen plugging and cleaning of the dilution/quench zone; and 1064 hours of coal firing. Specific areas of discussion include SFS performance, CAH performance, RAH panel performance, and observations specific to the fuels fired and their potential impacts on HITAF performance. Conclusions based on the data are summarized as well as recommendations for further work where warranted.

Pilot-Scale Slagging Furnace System Performance

The pilot-scale SFS tests completed in support of this project involved the firing of natural gas and five different coal types. This section of the report will discuss fuel characteristics and SFS performance issues related to the slagging furnace, slag screen,

dilution/quench zone, process air preheaters, and pulse-jet baghouse. Specific examples of process data for these subsystems will be presented and discussed.

Fuel Characteristics

Table 11-3 summarizes analytical results for all of the fuels that have been fired in the pilot-scale SFS in support of this project as well as the two related projects previously identified (projects (Collings et al., April 1999; Collings et al., December 1999). These fuels were selected because of their commercial interest and because they represented a wide range of ash/slag properties. Actual fuel feed rates ranged from 150 to 200 lb/hr (68 to 91 kg/hr) for the bituminous coals, 230 to 280 lb/hr (104 to 127 kg/hr) for the subbituminous coals, and 345 to 400 lb/hr (157 to 182 kg/hr) for the lignite fuels. In most cases, fuel feed rate was adjusted and controlled to maintain a flue gas temperature near the RAH tile surfaces of 2800 °F (1538 °C). However, in the case of the lignite-fired tests, furnace temperature was limited to 2700 °F (1483 °C) because of the high fuel moisture content. In other tests, furnace firing rate was adjusted to achieve furnace temperatures of 2900 °F (1594 °C) and higher. Other than the Illinois No. 6 coal, the bituminous coals fired in the SFS were eastern Kentucky coals. Observations concerning furnace firing rate and temperature will be addressed in more detail later when discussing slagging furnace performance.

Table 11-3
Results of Fuel and Fuel Ash Analysis for Slagging Furnace Tests[1]

	Illinois No. 6 Bituminous Coal	Kentucky Bituminous Coal	Prater Creek Bituminous Coal	High-Ash-Fusion Bituminous Coal[2]
Proximate Analysis, wt%				
Moisture	2.8–10.3	2.3–2.5	1.7–2.0	2.2
Volatile Matter	35.9–39.9	38.2–38.7	37.9–38.7	36.9
Fixed Carbon	43.3–46.3	54.7–54.9	54.5–55.3	53.8
Ash	10.6–11.7	3.9–4.7	4.7–5.1	7.1
Ultimate Analysis, wt%				
Hydrogen	4.7–5.8	5.2–5.5	5.3–5.4	5.1
Carbon	61.6–67.6	77.5–78.2	77.5–78.3	74.8
Nitrogen	0.8–1.9	1.8	2.3–2.4	2.3
Sulfur	3.2–4.1	0.8–1.0	0.8–0.9	0.9
Oxygen	10.6–17.6	9.6–9.7	8.4–8.7	9.8
Ash	10.6–11.7	3.9–4.7	4.7–5.1	7.1
Heating Value, Btu/lb	11,015–11,658	13,861–14,120	13,538–14,167	13,103
Percent as Oxides, wt%				
SiO_2	49.3–53.9	42.5–44.8	38.2–38.4	56.4
Al_2O_3	19.8–21.5	28.9–29.8	24.4–25.0	32.5
Fe_2O_3	13.6–17.5	13.7–14.5	22.5–23.0	4.4
TiO_2	0.9–1.0	1.1	0.9–1.0	1.9
P_2O_5	0.1–0.2	0.1	0.1–0.2	0.1
CaO	2.6–3.6	1.9–2.8	3.6–3.8	0.8
MgO	1.5–2.0	2.2–2.4	1.9–2.1	1.3
Na_2O	1.1–1.5	1.1–1.3	0.3–0.6	0.3
K_2O	1.9–2.3	2.7–3.0	2.2–2.3	2.0
SO_3	2.5–4.0	2.4–3.8	4.6–4.9	0.2
Ash Fusion Temp., °F				
Initial	2315–2392	2398–2577	2474–2483	>2800
Softening	2342–2418	2440–2603	2490–2501	>2800
Hemisphere	2392–2448	2474–2621	2532–2544	>2800
Fluid	2491–2593	2588–2684	2571–2593	>2800
Sieve Analysis				
Screen Mesh Size		**Weight Percent Retained**		
100	1.8–25.2	8.1–11.4	13.6–14.9	9.8
140	0–14.9	12.9–13.9	10.4–15.1	8.1
170	0–14.9	NA[3]	NA	NA
200	9.6–13.5	11.4–13.5	12.4–12.9	11.6
230	0–16.2	8.7–9.4	8.0–8.3	8.7
270	0.5–14.6	0.7–1.6	0.8–1.2	1.9
325	7.4–14.7	11.9–12.7	10.9–11.9	12.0
400	0–4.7	NA	NA	NA
Pan	29.7–57.8	41.2–42.6	38.8–40.7	47.9
Total %	**99–100.2**	**99.9–100.1**	**99.9–100.0**	**100.0**

[1] Analysis is presented on an as-fired basis. Other than the Illinois No. 6 coal, the bituminous coals were eastern Kentucky fuels.
[2] This fuel was not successfully fired in the SFS. [3] Not available.

Continued

Table 3-1 (continued)
Results of Fuel and Fuel Ash Analysis for Slagging Furnace Tests[1]

	Cordero Rojo Subbituminous Coal	Rochelle Subbituminous Coal	Coal Creek Station Lignite	Milton R. Young Station Lignite
Proximate Analysis, wt%				
Moisture	25.3–26.1	21.6–24.3	31.6–37.9	33.8–37.1
Volatile Matter	35.8–36.5	35.6–37.4	29.4–31.5	30.4–32.1
Fixed Carbon	32.7–32.9	35.8–36.7	26.4–26.8	26.9–27.9
Ash	5.3–5.4	4.3–4.7	6.3–10.2	5.6–6.2
Ultimate Analysis, wt%				
Hydrogen	6.3	6.1–6.4	6.4–6.8	7.0–7.2
Carbon	49.4–49.7	53.0–55.2	38.5–40.9	41.1–43.4
Nitrogen	1.2	0.6–0.7	0.6	0.6
Sulfur	0.45	0.3	0.5–0.7	0.7–0.9
Oxygen	37.1–37.2	32.9–33.4	41.1–47.3	42.1–44.9
Ash	5.3–5.4	4.3–4.7	6.3–10.2	5.6–6.2
Heating Value, Btu/lb	8818–8853	9021–9328	6300–6708	6933–7144
Percent as Oxides, wt%				
SiO_2	26.7–26.8	26.7–27.1	31.8–35.5	11.2
Al_2O_3	17.1–17.5	15.5–16.3	11.7–12.0	8.6
Fe_2O_3	6.8–7.2	6.3–6.6	6.4–8.0	13.2
TiO_2	1.6	1.2–1.4	0.5	0.2
P_2O_5	1.1	0.7–0.9	0.3	0.1
CaO	26.1–26.2	21.6–24.3	17.0–18.7	21.3
MgO	5.2	6.7–6.9	6.5–7.0	7.3
Na_2O	1.0	1.5	2.9–3.2	11.7
K_2O	0.3–0.4	0.1–0.4	1.3	0.2
SO_3	13.4–13.7	15.6–17.0	16.0–19.0	26.2
Ash Fusion Temp., °F				
Initial	2221	2202–2295	2170–2188	2370–2371
Softening	2250–2251	2205–2308	2181–2196	2381–2384
Hemisphere	2262–2266	2214–2311	2189–2203	2384–2387
Fluid	2286	2221–2325	2196–2219	2392–2428
Sieve Analysis				
Screen Mesh Size		**Weight Percent Retained**		
100	11.0–13.5	7.6–8.8	6.4–10.3	14.9
140	15.0–15.1	14.2–15.4	12.3–13.8	15.7
170	NA[3]	NA	NA	4.6
200	13.3–14.2	14.3–14.4	11.9–12.3	8.5
230	8.0–9.0	8.4–9.1	3.7–8.5	NA
270	2.2–2.9	2.0–5.6	6.2–10.2	3.1
325	9.4–11.0	4.8–11.6	6.4–6.5	14.9
400	NA	NA	NA	NA
Pan	37.6–38.0	39.7–43.4	41.5–48.2	38.2
Total %	**100.0–100.2**	**98.6–100.6**	**98.3–99.9**	**99.9**

[1] *Analysis is presented on an as-fired basis.* [2] *This fuel was not successfully fired in the SFS.* [3] Not available.

Exhibits 11-7 to 11-9 are examples of SFS coal feed rate data for three fuel types. Exhibit 11-7 illustrates the coal feed rate data for an April 1999 test initially firing an eastern Kentucky bituminous coal. The EERC had planned to fire the eastern Kentucky coal for 200 hr. However, the quantity of available fuel was only sufficient for 150 hr of coal firing. Therefore, Illinois No. 6 coal was fired for the final 51 hr. During this test, coal firing was continuous for 184 hr, the longest continuous coal-fired period completed with the SFS. At that point, it was necessary to switch to natural gas firing in the main burner in order to facilitate the replacement of the slag pot. If it had not been necessary to switch to the Illinois No. 6 coal, the 200-hr test could have been completed without having to change out the slag pot.

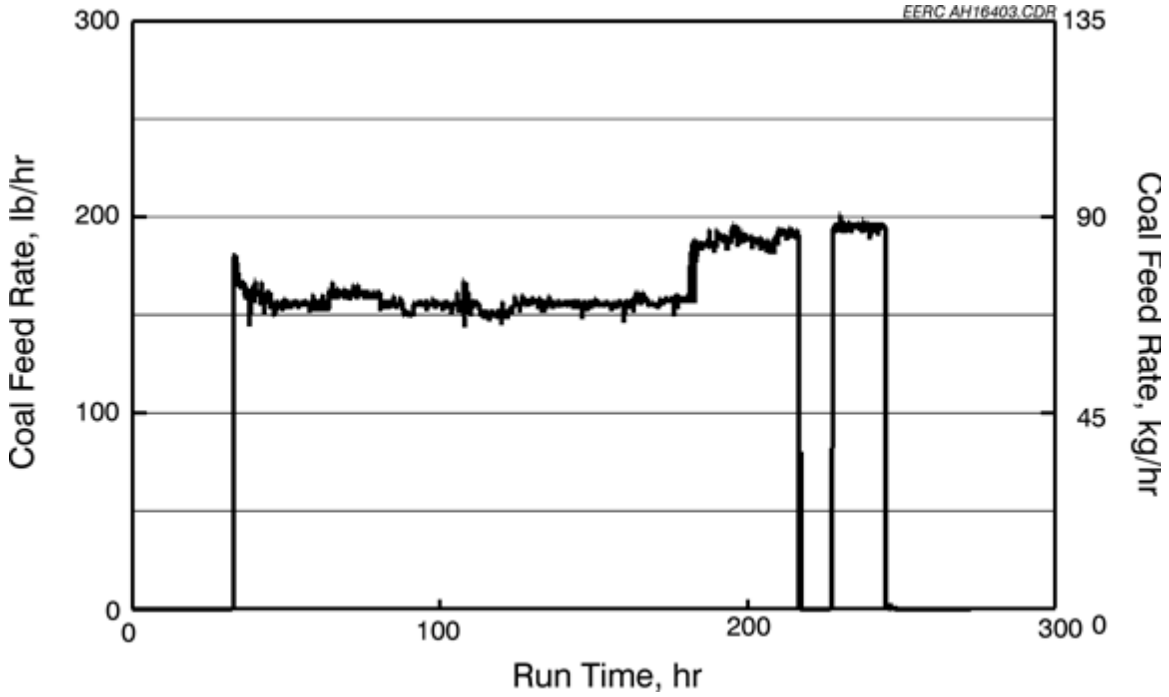

Exhibit 11-7
Coal Feed Rate versus Run Time for SFS Test SFS-RH8-0399

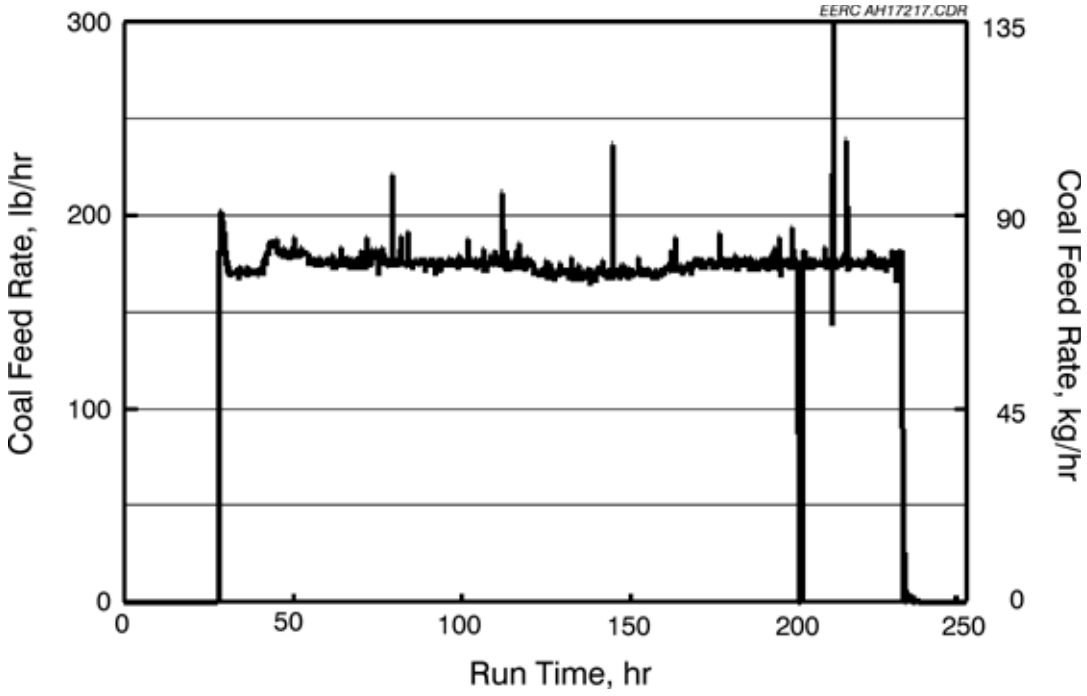

Exhibit 11-8
Coal Feed Rate versus Run Time for SFS Test SFS-RH11-0799

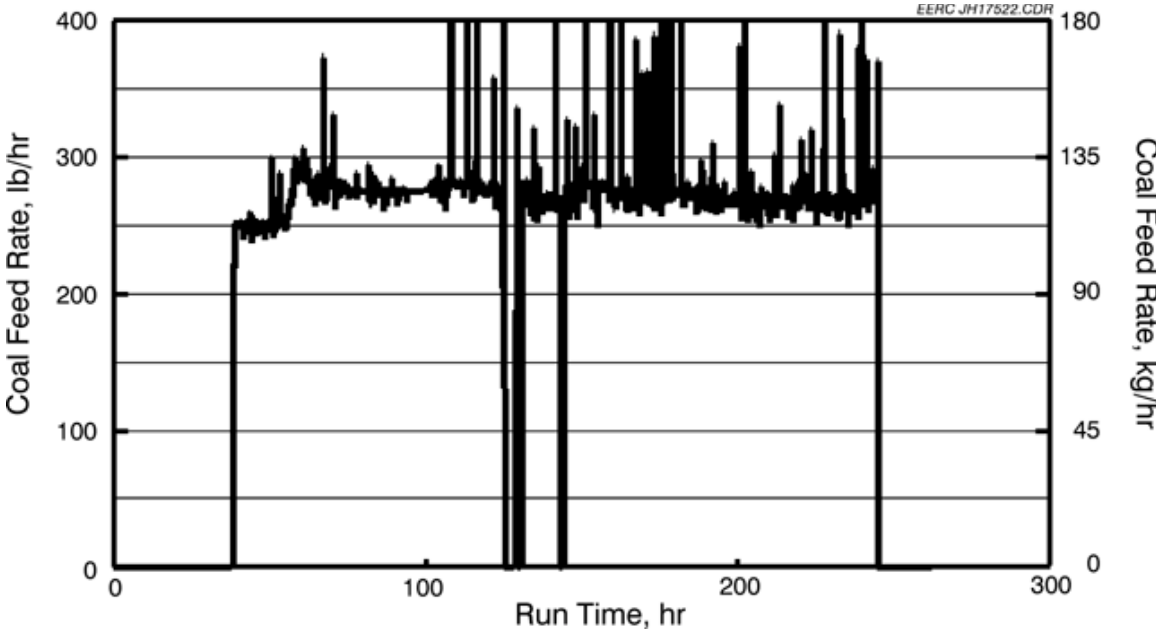

Exhibit 11-9
Coal Feed Rate versus Run Time for SFS Test SFS-RH12-0200

Exhibit 11-8 illustrates the coal feed rate data for a December 1999 test firing an Illinois No. 6 bituminous coal. Coal feed was continuous except for a 2-hr natural gas-fired period required to clean out the ash/slag pot below the dilution/quench zone after 160 hr of coal firing. Removal of ash/slag from this location was necessary to avoid a

potential plugging problem and a possible forced shutdown. In addition, the slag pot below the slag tap was changed once during this test, as planned, with no interruption of coal feed.

Exhibit 11-9 illustrates the coal feed rate data for a March 2000 test firing a Cordero Rojo subbituminous coal. Coal feed was continuous except for a 6-hr natural gas-fired period required to repair an electrical problem with the coal feeder and a 1.5-hr natural gas-fired period required for removing a plug from the slag tap. The slag pot below the slag tap was changed once during the March 2000 test, as planned, with no interruption of coal feed.

For all SFS tests, minor adjustments to coal feed rate were typically made in order to maintain a desired furnace temperature. Generally, coal feed rate was quite stable except for very short- duration (<30 seconds) spikes (high and low) associated with coal hopper refill cycles. In the case of the bituminous coals illustrated in Exhibits 11-7 and 11-8, spikes (high and low) caused by hopper refill cycles were minor. In the case of the subbituminous coal, these spikes were of greater amplitude, but they had no noticeable effect on SFS operation because of their short duration (<30 seconds).

As previously inferred, the fuels selected for this project represent a wide range of properties with respect to moisture, ash, and sulfur content; heating value; and ash/slag properties. For the bituminous coals, the analyses of the composite fuel samples indicated that the as-fired fuels contained 1.7–10.3 wt% moisture, 3.9–11.7 wt% ash, and 0.8–4.1 wt% sulfur. The heating values ranged from 11,015 to 14,167 Btu/lb (25,597 to 32,921 kJ/kg) on an as-fired basis. Fuel ash was analyzed for ash fusion properties under oxidizing conditions. Results indicate typical softening temperatures of 2342 to 2603 °F (1284 to 1429 °C) and typical fluid temperatures of 2491 to 2684 °F (1366 to 1474 °C). For one eastern Kentucky bituminous coal fired, the ash fusion temperatures were >2800 °F (>1538 °C). As a result, this fuel could not be fired successfully in the SFS because of plugging problems in the slag tap and slag screen.

For the subbituminous coals, the analyses of the composite fuel samples indicated that the as-fired fuel contained 21.6–26.1 wt% moisture, 4.3–5.4 wt% ash, and 0.3–0.5 wt% sulfur. The heating values ranged from 8818 to 9328 Btu/lb (20,491 to 21,676 kJ/kg) on an as-fired basis. Fuel ash analyses for the subbituminous coals indicated typical softening temperatures of 2205 to 2308 °F (1208 to 1265 °C) and typical fluid temperatures of 2221 to 2325 °F (1216 to 1274 °C).

For the lignite fuels, the analyses of the composite fuel samples indicated that the as-fired fuel contained 29.4–37.9 wt% moisture, 5.6–10.2 wt% ash, and 0.5–0.9 wt% sulfur. The heating values ranged from 6300 to 7144 Btu/lb (14,640 to 16,601 kJ/kg) on an as-fired basis. Fuel ash analyses for the lignite fuels indicated typical softening temperatures of 2181 to 2384 °F (1194 to 1307 °C) and typical fluid temperatures of 2196 to 2428 °F (1203 to 1331 °C).

Dry sieve analysis indicated that pulverizer performance during the course of the project was variable. For bituminous coals, data ranged from 50 wt% to 80 wt% <200 mesh (<74 µm). In cases where pulverizer efficiency was less than desired, either worn or improperly balanced hammers or deterioration of the hammer mill screen was found.

On a few occasions, reduced pulverization performance for bituminous coal is believed to have been caused by surface moisture. However, because of the high furnace-operating temperature, combustion efficiency was not adversely affected by variations in fuel particle size. For the bituminous coals, the carbon content of the fly ash collected in the baghouse was low, ranging from 0.1 to 0.7 wt%, with no observed correlation to fuel particle size.

For the subbituminous coals, pulverizer performance resulted in a nominal 60 wt% <200 mesh (<74 μm) fuel. This is a larger particle size than was desired and determined to be an indication of a need for pulverizer maintenance or adjustments. Also, the higher moisture content of these fuels has been observed to affect hammer mill efficiency. However, because of the high furnace- operating temperature and fuel volatility, combustion efficiency was not adversely affected by variations in fuel particle size. For both subbituminous fuels, the carbon content of the fly ash collected in the baghouse was low, 0.39 wt% for the Rochelle fuel (SFS-RH4-0298) and 0.40 wt% for the Cordero Rojo fuel (SFS-RH12-0200).

For the lignite fuels fired in the SFS, pulverizer performance resulted in 60–70 wt% <200-mesh (<74 μm) fuel. This is a somewhat larger particle size than was desired and determined to be the result of the higher moisture content of the fuels affecting hammer mill efficiency. However, because of the high furnace-operating temperature and fuel volatility, combustion efficiency was not adversely affected by variations in fuel particle size. For both lignite fuels, the carbon content of the fly ash collected in the baghouse was very low, 0.02 wt% for the CCS fuel (SFS-ND1-0398) and 0.01 wt% for the MRYS fuel (SFS-ND2-0498).

Compositions of the various fuel ashes, reported as oxides, are summarized in Table 3-3. A general comparison of the fuel ash data shows that the bituminous coal ashes contained significantly more silica and alumina than the subbituminous coal and lignite ash, while the subbituminous coal and lignite ashes contained significantly higher concentrations of alkali constituents such as calcium and magnesium. Interestingly, the potassium content of the bituminous coal ashes was higher than that observed in the subbituminous and lignite fuels. Iron content was higher in the bituminous fuels, with the exception of the high-ash-fusion-temperature bituminous coal that could not be successfully fired in the SFS because the slag fouled the slag screen tubes. With the exception of the one high-ash-fusion-temperature bituminous coal, which had lower iron than requested, the ash properties for the fuels fired in the SFS were about what was expected when the coals were ordered.

Although in some cases differences in ash chemistry appear small, they have noticeable effects on ash fusion temperature as well as deposition characteristics at lower temperatures. Therefore, ash chemistry, mineral size, and composition data as they relate to slag and ash properties are addressed in some detail relative to slag screen performance and CAH deposition later in this report.

Slagging Furnace Operation

The slagging furnace heatup rate during SFS tests completed in support of this and related projects was limited to 100 °F/hr (56 °C/hr) while natural gas was fired. This is

the heatup rate recommended for the RAH panel by UTRC. In a few cases, the furnace heatup rate was limited to 50 °F/hr (28 °C/hr) in order to cure new refractory in accordance with manufacturers' recommendations. When the furnace reached the desired operating temperature, 2800 °F (1538 °C) for most test periods, the main burner was switched from natural gas to coal firing, and coal feed rate adjustments were made to maintain furnace temperature. For a few higher- temperature SFS tests, the switch from natural gas to coal firing was also made at 2800 °F (1538 °C). However, this was done to simplify reaching an operating temperature of >2800 °F (>1538 °C). For lignite-fired tests, the switch from natural gas to lignite firing occurred at 2700 °F (1483 °C) because the high moisture content of the fuel made it impossible to reach a furnace temperature of 2800 °F (1538 °C).

As examples of furnace temperature and firing rate data, Exhibits 11-10 and 11-11 show the respective data for a bituminous coal-fired test (SFS-RH8-0399) completed in April 1999. The furnace was fired with eastern Kentucky coal for 150 hours and Illinois No. 6 coal for 51 hours. The total furnace firing rate (main plus auxiliary burners) ranged from 2.7 to 2.8 MMBtu/h (2.8 to 2.9 × 10^6 kJ/hr). The main burner firing rate ranged from 2.1 to 2.2 MMBtu/h (2.2 to 2.3 × 10^6 kJ/hr), accounting for 76% to 81% of the total energy input. The resulting flue gas temperature near the furnace wall/RAH panel was 2740 to 2830 °F (1505 to 1555 °C). This temperature was established initially using two Type S thermocouple measurements and two optical pyrometer measurements. As thermocouple performance degraded with slag corrosion, furnace temperatures were measured using the two optical pyrometers and maintained with adjustments to the coal feed rate. Furnace refractory temperatures ranged from 1055 to 1300 °F (569 to 705 °C) for the hot side of the insulating refractory to as high as 2430 °F (1333 °C) for the cold side of the high-density refractory.

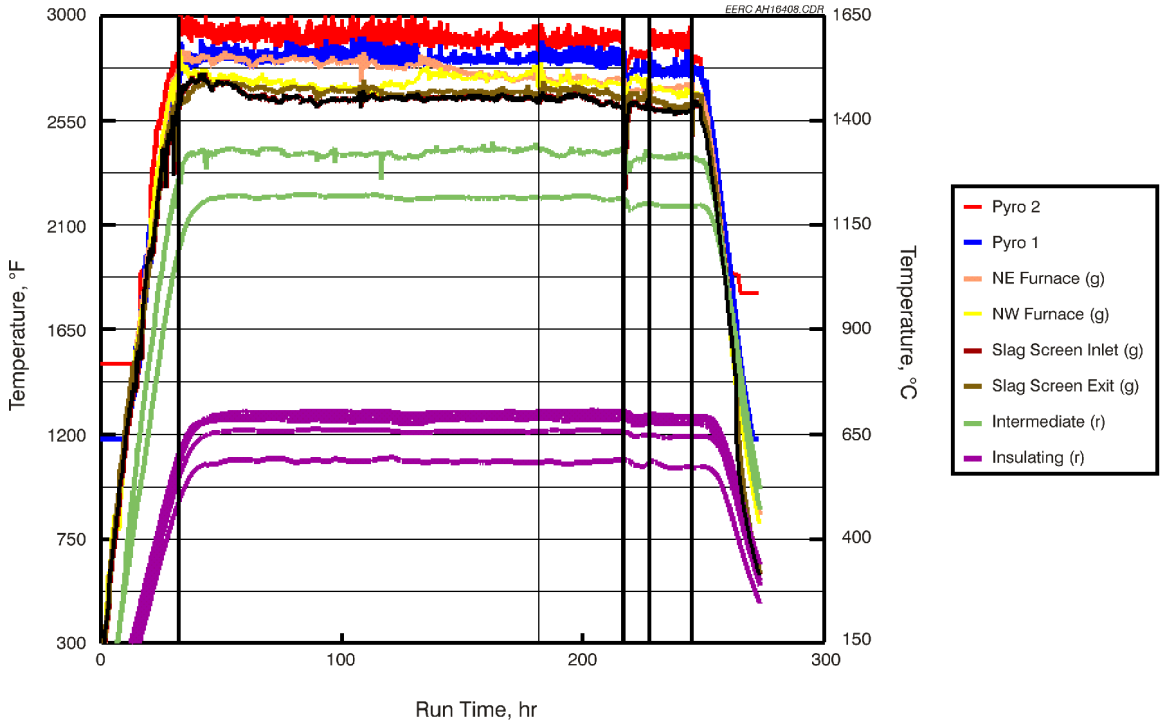

Exhibit 11-10
Furnace and Slag Screen Temperatures versus Run Time for SFS Test SFS-RH8-0399

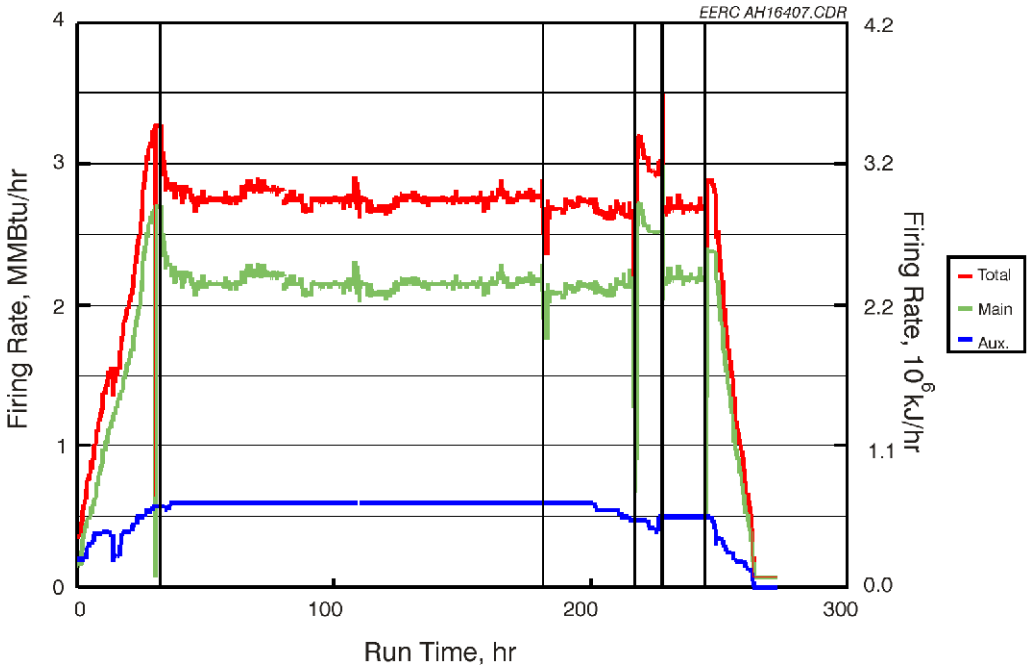

Exhibit 11-11
Slagging Furnace Firing Rate versus Run Time for SFS Test SFS-RH8-0399

No operating problems were encountered during the April 1999 test. The use of limestone to modify slag chemistry was a successful mitigation step taken to avoid slag screen and slag tap performance problems anticipated based on previous tests with the higher-ash-fusion-temperature eastern Kentucky fuel. Details concerning slag screen performance will be addressed later in this report. Excess slag deposits were found in the slag tap at the conclusion of the April test as a result of very viscous slag flowing from the slag screen during cooldown. However, these deposits did not plug the slag tap and were removed from the slag tap during routine maintenance. Inspection of the furnace refractory after the April 1999 test indicated that the new high-density refractory, cured in December 1998, was in excellent condition.

Examples of furnace temperature and firing rate data, respectively, for an Illinois No. 6 bituminous coal-fired test (SFS-RH11-0799) are shown in Exhibits 11-12 and 11-13. The data are for a 202-hr test completed in December 1999. The total furnace firing rate (main plus auxiliary burners) ranged from 2.5 to 2.6 MMBtu/h (2.6 to 2.7 × 10^6 kJ/hr). The main burner firing rate ranged from 2.0 to 2.1 MMBtu/h (2.2 to 2.3 × 10^6 kJ/hr), accounting for 80% of the total energy input. Resulting flue gas temperature near the furnace wall/RAH panel and furnace exit was 2795 to 2865 °F (1535 to 1574 °C). This temperature measurement was made using an optical pyrometer with secondary measurements using two Type S thermocouples. Furnace refractory temperatures ranged from 1130 to 1395 °F (610 to 758 °C) for the hot side of the insulating refractory to as high as 2620 °F (1438 °C) for the cold side of the high-density refractory.

No operating problems were encountered during the December 1999 test, and modification of slag chemistry was not necessary to maintain satisfactory slag screen and slag tap performance. Slag screen and slag tap plugging were avoided using temperature control and one on-line preemptive cleaning of the slag tap. Inspection of the furnace refractory after the December 1999 test indicated that the high-density refractory, cured in December 1998, was in good condition.

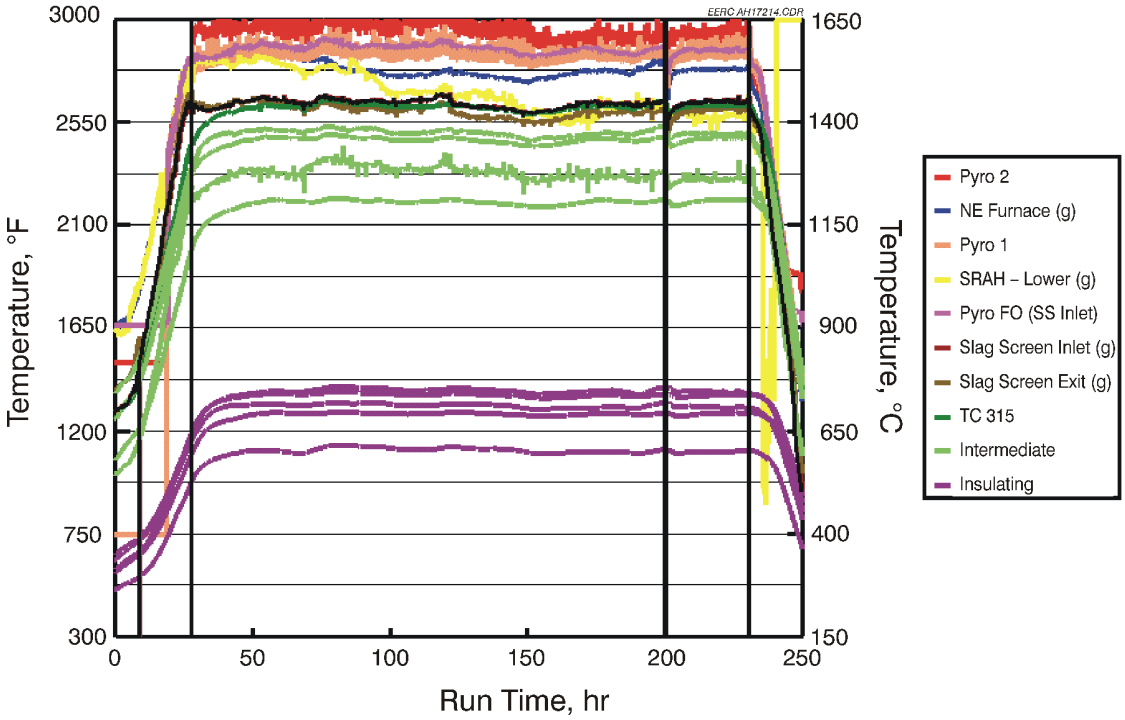

Exhibit 11-12
Furnace and Slag Screen Temperatures versus Run Time for SFS Test SFS-RH11-0799

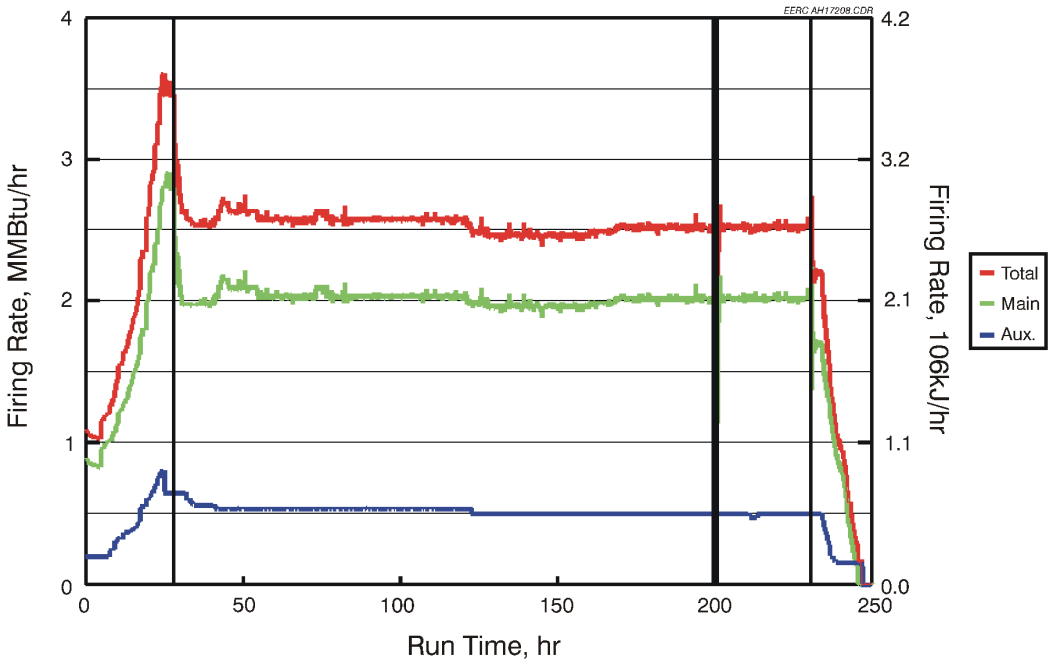

Exhibit 11-13
Slagging Furnace Firing Rate versus Run Time for SFS Test SFS-RH11-0799

Exhibits 11-14 and 11-15 represent furnace temperature and firing rate data, respectively, for a subbituminous coal-fired test (SFS-RH12-0200) completed in March 2000. The furnace was fired with a Cordero Rojo coal for 200 hr. The total furnace firing rate (main plus auxiliary burners) ranged from 3.2 to 3.3 MMBtu/h (3.4 to 3.5 × 10^6 kJ/hr). The main burner firing rate ranged from 2.4 to 2.5 MMBtu/h (2.5 to 2.6 × 10^6 kJ/hr), accounting for 74% to 76% of the total energy input. Resulting flue gas temperature near the furnace wall/RAH panel was 2800 to 2850 °F (1538 to 1566 °C). Measured furnace exit temperature typically matches the furnace wall temperature. However, during this test, the furnace exit temperature was nominally 85 °F (47 °C) lower. The reason for this temperature difference was determined to be the development of a crack in the high-density refractory near the target for the optical pyrometer measuring furnace exit temperature. Development of the crack created a small area of heat loss affecting the optical pyrometer measurement. Subsequent replacement of the high-density refractory in the furnace exit eliminated the crack as well as the differential in furnace temperature measurements.

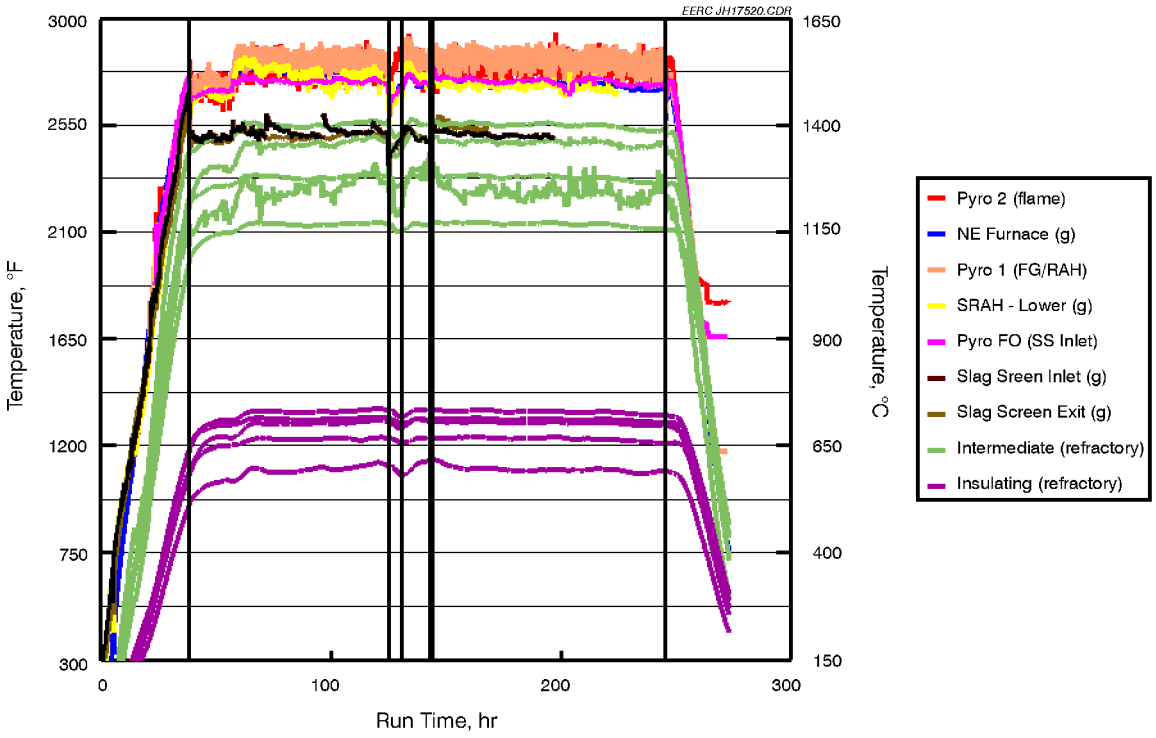

Exhibit 11-14
Furnace and Slag Screen Temperatures versus Run Time for SFS Test SFS-RH12-0200

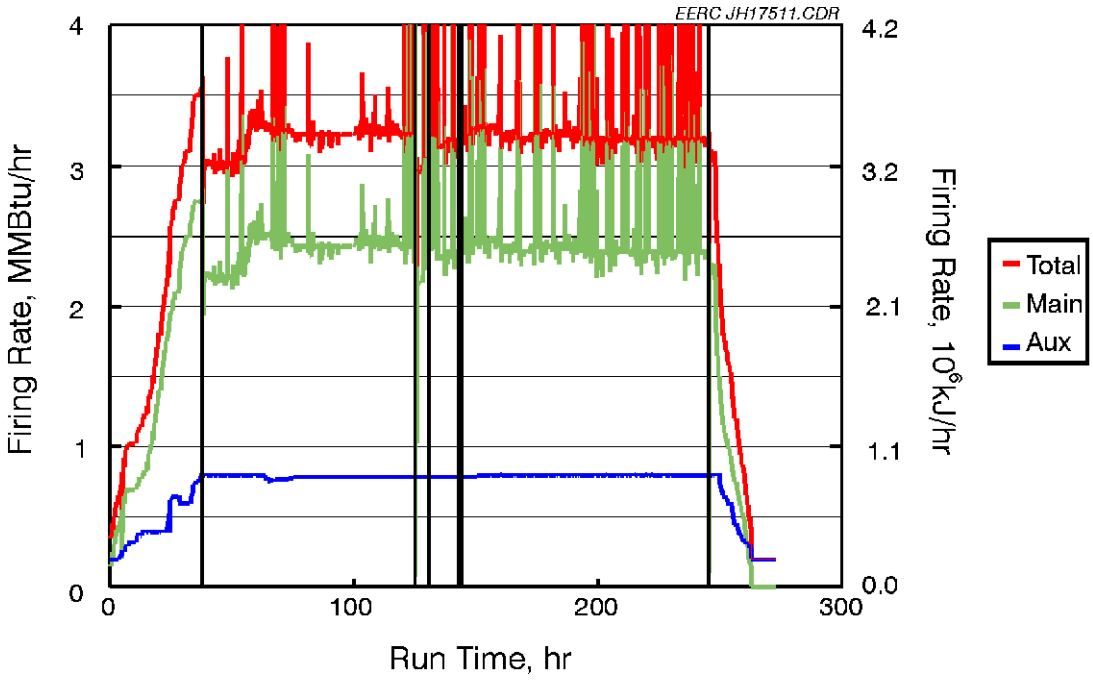

Exhibit 11-15
Slagging Furnace Firing Rate versus Run Time for
SFS Test SFS-RH12-0200

Furnace refractory temperatures ranged from 1090 to 1355 °F (588 to 735 °C) for the hot side of the insulating refractory to as high as 2550 °F (1399 °C) for the cold side of the high-density refractory. Compared to the December 1999 test period firing Illinois No. 6 coal, the insulating refractory temperatures were 40 °F (22 °C) lower, and high-density-refractory temperatures were 65 to 80 °F (36 to 44 °C) lower. These lower refractory temperatures were observed even though the total furnace firing rate in March 2000 was 27% to 28% higher than the firing rate in December 1999. In addition, the main burner firing rate in March 2000 was 20% higher than that required in December 1999, 2.4 to 2.5 MMBtu/h (2.5 to 2.6 × 10^6 kJ/hr) versus 2.0 to 2.1 MMBtu/h (2.1 to 2.2 × 10^6 kJ/hr). However, the result was a 100 °F (56 °C) lower relative furnace flame temperature in March 2000, nominally 2850 °F (1566 °C) versus 2950 °F (1621 °C). The lower furnace temperatures observed in March 2000 with a higher firing rate were the result of a higher fuel moisture content, nominally 26 wt% (Cordero Rojo subbituminous coal) in March 2000 versus 3 wt% (Illinois No. 6 bituminous coal) in December 1999.

Slag tap performance was a problem during the March 2000 test because of the corrosive nature of the Cordero Rojo slag and the resulting refractory damage observed in the bottom of the slagging furnace, the slag tap, and below the slag tap. In addition, furnace inspection following the test revealed refractory deterioration in the top furnace section as well. Therefore, the EERC elected to replace the high-density refractory in all four furnace sections prior to any future SFS tests.

The high-density refractory liner in the furnace was initially installed and cured in the second quarter of 1997. Complete replacement of the high-density refractory was required twice during the course of the project. However, high-density refractory

replacement was not necessarily completed in all four furnace sections at the same time. Repairs to the intermediate and insulating refractory layers were required in some areas of the furnace as a result of damage that occurred when the high-density layer was removed, but general replacement of intermediate and insulating refractory was not necessary.

The primary reason for replacing the high-density furnace liner the first time was the extensive cracking that had developed in the liner as a result of its initial curing and subsequent heating and cooling cycles. However, refractory deterioration in the bottom section of the furnace because of slag corrosion was the reason for high-density refractory replacement in this section of the furnace. In order to avoid cracking problems observed with the first liner, the new high-density liner was poured in such a way that it would not bond to the middle or intermediate refractory layer and would be divided into approximately 2-ft-square wall sections to allow the liner to move independently during heatup and cooldown. This design was very successful in preventing the extensive cracking that was seen in the original furnace liner. Replacement of the high-density furnace liner in the second quarter of 2000 was required because of slag corrosion and plans for high-temperature (>2900 °F [>1594 °C]) furnace operation in the future.

Another observation made during the course of this project concerning the high-density furnace liner was obvious color changes. When new high-density refractory was poured, it was a gray color. Upon curing, the color changed to a bright white. Subsequently, with each coal-fired test, the color of the high-density liner darkened. The EERC believes that the darkening of the refractory was the result of slag penetration into the surface of the high-density liner. This change in appearance may indicate the potential for a failure of the high-density furnace liner if the refractory chemistry is sufficiently modified. However, the degree of slag impaction on the vertical walls is believed to be small, and there were no plans to expose the refractory liner to low-melting-temperature slag for any duration. Exhibit 11-16 contains photographs illustrating the observation. The top photograph shows a newly cured refractory surface, with the bottom photograph showing the same refractory surface after 100 hr of coal firing. The observation concerning color change was consistent for each coal-fired test completed.

Exhibit 11-16
Photographs of the Slagging Furnace Interior after Refractory Curing (Top) and Again After 100 Hours of Coal Firing (Bottom)

The area of the high-density furnace liner that showed the greatest deterioration from test to test was below the RAH panel where slag from the panel was dripping onto the horizontal surface below. However, because of the small area impacted, no refractory repairs or replacement were required to solely address the resulting refractory damage.

On one occasion, coatings were applied to specific areas of the high-density refractory surface to improve its slag corrosion resistance. These coatings are evident in the top photograph in Exhibit 11-16 (lower left and lower right sides of the photograph). However, after only 60 hr of coal firing, there was no evidence of the coatings on the refractory surface. Apparently, the coatings were eroded from or absorbed into the surface of the high-density refractory. The two coatings tested in the slagging furnace were selected based on bench-scale observations. Pilot-scale observations indicate that further bench-scale development work is necessary before additional coating tests would be warranted in the pilot-scale slagging furnace.

Variations in furnace refractory temperatures observed during the course of this project are believed to be the result of several factors. First, fuel moisture differences can affect flame intensity and furnace temperatures for a given firing rate. The planned gap/air space between the high-density and intermediate refractory layers utilized when the high-density refractory layer was replaced the first time would have a definite effect on insulating refractory temperatures. Another possibility is poor temperature data because of aging thermocouples. However, all of the thermocouples measuring furnace refractory temperatures were inspected periodically and replaced when sheath deterioration was apparent. Thermocouple replacement requirements in this application were minimal. Any changes in the thermal properties of the high-density refractory liner with time would affect all refractory temperature measurements. The emissivity, reflectivity, or conductivity properties of the high-density furnace liner would affect refractory temperature measurements. This issue and its potential implications concerning the performance of the RAH panel are discussed later in this report.

Minor pressure surges (a few tenths to a couple of inches of W.C.) are not uncommon in the slagging furnace. They happen on a periodic basis as a result of baghouse cleaning, opening of access ports to clean the dilution/quench zone and CAH tube bank, opening of access ports to insert or remove sampling probes, and when flue gas flow distribution through the baghouse or cyclone is altered. However, pressure surges in the furnace as a result of the activities identified did not cause any operating problems during the SFS test periods completed in support of this project.

The duration of coal-fired test periods completed in support of this and related projects ranged from 4 hr for one shakedown test to nominally 200 hr for three SFS tests. Coal-fired test periods of <60 hr were all impacted in some way by fuel ash properties which affected the performance of the slag screen, slag tap, or both. In other cases, tests planned for a duration of 200 hr were terminated early because of a power failure, a compressor failure, the development of a process air leak to the RAH, the failure of RAH ceramic tiles, and a refractory failure in the bottom section of the furnace. However, overall, the slagging furnace has proven to be a reliable, relatively simple system to operate in support of the HITAF concept. Table 11-4 summarizes operating time for the SFS representing 27 heating and cooling cycles.

Table 11-4
Summary of SFS Operating Hours Through December 2000[1]

	Natural Gas Firing, hr	Coal/Lignite Firing, hr	Total Operation, hr
Slagging Furnace System	2075	1545	3620

[1]Natural gas firing includes heatup, cooldown, and refractory curing.

Main and Auxiliary Burners

The main and auxiliary burners performed well in support of this project. For all SFS test periods, the main burner swirl was maintained at a minimum (about 20%), while the auxiliary burner swirl setting was nominally 80%. Carbon efficiency for all of the fuels fired was >99.5% because of the high furnace-operating temperature and adequate residence time. Higher carbon levels were observed on three occasions because of problems encountered with system fans for the fuel feed system. Based on slagging furnace-operating experience, the EERC intends to continue minimum main burner swirl as necessary to establish a stable flame, to establish uniform temperatures over the length of the furnace, and to minimize NO_x emissions for any future SFS tests. However, in the event of furnace operation at lower firing rates and lower temperatures, it may be necessary to increase main burner swirl in order to maintain flame stability.

Slag Screen Performance and Slag Analysis

Commercial slag screen design and the materials used by vendors are specific to the given application. Therefore, the observations made in this report concerning slag screen performance are probably less relevant to the performance of a commercial HITAF system design than the observations made with respect to other SFS components (RAH, CAH, and pulse-jet baghouse). This is true regardless of the fuel type (bituminous coal, subbituminous coal, or lignite) being fired. Therefore, evaluating slag screen performance was not a high priority for the project. However, the slag screen did impact the operation of the SFS in general and the dilution/quench zone and CAH tube bank specifically. As expected, fuel ash properties had a significant effect on slag screen performance. Slag screen operating temperature was selected on the basis of ash fusion data for the fuel to be fired. The EERC attempted to operate the slag screen at flue gas temperatures of 100 to 200 °F (56 to 112 °C) above the fluid temperature of the fuel ash to ensure slag flow from the slag screen through the slag tap. However, this was not possible for all fuel types fired in the slagging furnace. Therefore, it was necessary for the EERC to modify the slag screen configuration to match fuel ash properties as previously discussed. For high-ash- fusion fuels, such as the eastern Kentucky bituminous coal, it was necessary to reduce the number of tubes in the slag screen from 18 to nine as well as reduce the water-cooled surface in each 1.5-in. (3.8-cm) refractory tube to limit cooling capacity. These steps were necessary to prevent slag accumulation

and plugging of the slag screen, resulting in a high slag screen differential pressure and a potential forced SFS shutdown. Other successful mitigation steps taken when firing an eastern Kentucky coal included the use of limestone to modify slag chemistry and higher-temperature operation of the furnace (2900 °F/1594 °C) and slag screen (2700 °F/1483 °C) to reduce slag viscosity.

Exhibit 11-17 presents photographs of the slag screen inlet following SFS tests completed in February 1999 (SFS-RH7-0299) and April 1999 (SFS-RH8-0399). In both cases, an eastern Kentucky bituminous coal was fired, resulting in comparable furnace temperatures and nearly comparable slag screen temperatures. The upper photograph shows that the first row of tubes experienced some erosion/corrosion and significant slag buildup on the floor of the slag screen in the vicinity of the second, third, and fourth rows of tubes. As the degree of slag screen plugging developed, differential pressure eventually exceeded 8 in. W.C. (14.9 mmHg), forcing a termination of the coal feed and a SFS shutdown. The lower photograph shows the effectiveness of the mitigation steps taken for the April 1999 test. In this case, the combination of fewer slag screen tubes and some limited limestone injection permitted the completion of a 200-hour coal-fired test without any slag screen-operating problems encountered. The effectiveness of the limestone addition with the fuel was evaluated for limestone feed rates ranging from 0.25 to 2 lb/hr (113 to 908 g/hr). Ultimately, slag screen differential pressure was stabilized and effectively controlled at 0.5 in. WC (0.9 mmHg) using a limestone feed rate of 0.5 lb/hr (227g/hr). The 0.5-lb/hr (227-g/hr) limestone feed rate increased the total solids rate into the slagging furnace by nominally 0.3 wt%. The corresponding relative increase in the ash rate into the slagging furnace was 3.7 wt% based on the calcium oxide addition to the ash.

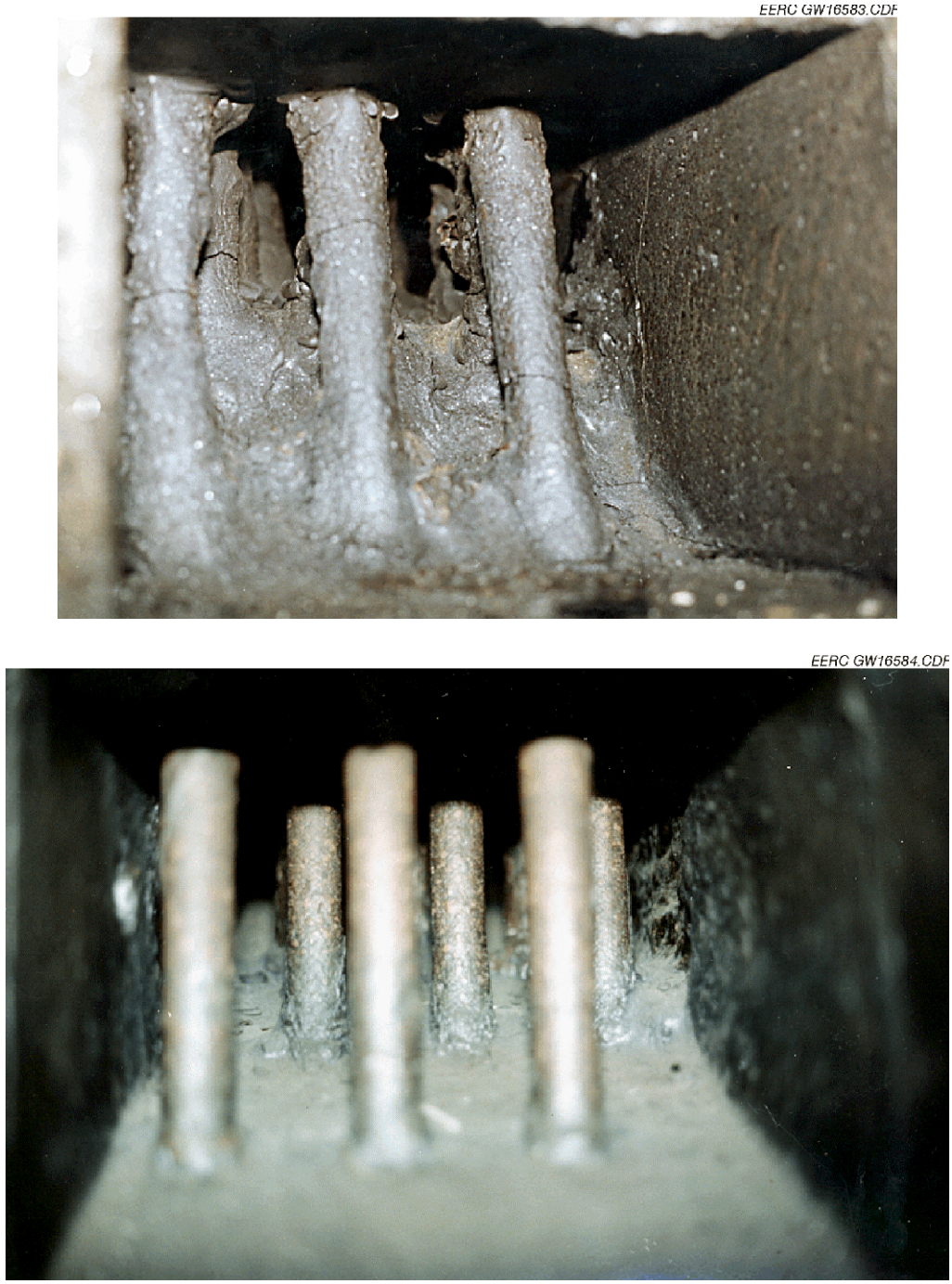

Exhibit 11-17
Photographs of Slag Screen Tubes Showing Slag Accumulation and Plugging for a February 1999 Test (Top) and the Effectiveness of Mitigation Measures Applied During an April 1999 Test (Bottom)

The composition of the Kentucky coal ash as compared to the composition of slag samples collected from the slag pot and slag screen following the February 1999 test are shown in Tables 11-5 and 11-6. The values are reported on an oxide basis normalized to an SO_3-free basis, while the SO_3 numbers are reported on a basis normalized with the

other oxides. The slag pot samples were collected from the bottom and top of the slag collected in the slag pot and from the slag tap itself to determine if the composition of the slag dripping into the slag pot changed during the course of the test. This was done in order to explain why the slag initially flowed quickly into the pot from the slag screen, but later in the test it appeared to become more viscous, ultimately leading to the formation of a slag dam.

The data show that all of the slag samples contained much less calcia, slightly less alumina, slightly more silica, and much more iron oxide than the original coal ash. CCSEM analyses of the minerals in the coal indicate that the alumina and silica in the coal were concentrated in clay particles, with the larger clay particles being more enriched in silica compared to the smaller clay particles. The calcia in the coal was concentrated in larger limestone particles and the iron in larger pyrite particles. The reduced alumina content in the slag pot samples most likely occurred because the smaller, alumina-rich clay particles stayed entrained in the gas stream as it passed around the slag screen tubes rather than impacting the tubes. The alumina content in the slag did increase, however, as the run proceeded, possibly because the slag screen efficiency increased slightly, causing more of the smaller clay-derived particles to be captured. The lower calcia content in the slag samples as compared to the coal ash is most likely due to the limestone fragmenting on heating, forming small particles that also passed around the tubes. Note that the calcia content did not increase in the samples collected higher in the pot, indicating that any increase in capture efficiency later in the test was not enough to begin significant capture of limestone-derived particles. The enrichment in iron oxide in the slag is due to the high capture efficiency for the relatively large pyrite-derived ash particles.

Table 11-5
February 1999 Kentucky Coal Ash, Slag Pot, and Slag Tap Samples

Oxides,[1] wt%	Kentucky Coal	Slag Pot Bottom	Slag Pot Top	Slag Tap
SiO_2	40.4	45.6	43.6	46.8
Al_2O_3	30.8	23.6	27.7	26.9
Fe_2O_3	10.6	16.4	17.4	17.9
TiO_2	1.1	1.0	0.9	0.9
P_2O_5	0.1	0.1	0.1	0.1
CaO	10.9	6.6	4.9	2.0
MgO	2.3	4.0	2.5	1.9
Na_2O	1.5	1.0	1.1	1.0
K_2O	2.3	1.7	1.9	2.6
SO_3[2]	6.7	0.1	0.1	0.1

[1] Oxide concentrations normalized to an SO_3-free basis.

[2] SO_3 concentrations normalized with other oxides.

Table 11-6
February 1999 Kentucky Coal Ash and Slag Screen Samples

Oxides,[1] wt%	Kentucky Coal	Screen Front	Screen Back	Quench Entrance
SiO_2	40.4	49.5	48.2	49.4
Al_2O_3	30.8	26.4	28.3	25.1
Fe_2O_3	10.6	15.6	13.9	11.1
TiO_2	1.1	1.0	1.1	0.9
P_2O_5	0.1	0.1	0.0	0.1
CaO	10.9	1.9	2.7	8.0
MgO	2.3	1.9	2.2	1.9
Na_2O	1.5	1.1	1.2	1.7
K_2O	2.3	2.6	2.3	1.9
SO_3 [2]	6.7	0.1	0.1	0.1

[1] Oxide concentrations normalized to a SO_3-free basis.

[2] SO_3 concentrations normalized with other oxide.

The composition of the residual slag held in the dam in the slag screen itself are compared to that of the coal ash in Table 11-6. As is true for the slag pot samples, the slag dam was depleted in alumina and calcia and enriched in silica and iron. However, the enrichment in silica was greater than, and the iron less than, the enrichment found in the slag pot samples. These changes would give the slag dam samples even higher viscosities than the slag pot samples. However, slag flow patterns in the main furnace indicate that essentially all of the slag in the slag pot flowed from the slag screen. The fact that the higher-viscosity slag remained in the screen and the lower-viscosity slag flowed out through the slag tap into the slag pot may indicate that the slag is a mixture of high- and low-viscosity materials.

The composition of the eastern Kentucky coal ash as compared to the composition of slag samples collected from the slag pot during the individual limestone injection tests completed in April 1999 is shown in Table 11-7. Analyses were completed for limestone feed rates of 0.25, 0.5, 1, and 2 lb/hr (114, 227, 454, and 908 g/hr). The oxide values for the slag samples are reported on a normalized oxide basis, while the coal ash sample is normalized to an SO_3-free basis.

As expected, the data show that the calcia content of the slag samples increased with increased limestone feed rate relative to the coal ash chemistry. However, the calcia content did not increase as much as it would have if the limestone were depositing in the slag at the same rate as the coal ash, indicating some limestone fragmentation. Also, the composition of the slag was sufficiently variable that a direct dilution effect for other slag components was not consistently evident in the samples. Ash fusion temperature data generated under oxidizing conditions did show the desired effect of limestone addition to the fuel. The highest ash fusion temperatures were observed for the coal ash, with ash fusion temperatures decreasing as the limestone feed rate was increased.

When firing an Illinois No. 6 bituminous coal the slag screen performed as intended with 18 tubes installed. Desired slag flow could be maintained with appropriate temperature control using a combination of the main and auxiliary burners. It was not necessary to use limestone addition to modify slag chemistry. The ash fusion fluid temperature for the Illinois No. 6 bituminous coal fired in support of this project ranged from 2491 to 2593 °F (1366 to 1423 °C). Therefore, a slag screen temperature of 2600 to 2700 °F (1399 to 1427 °C) was adequate to avoid plugging problems in the slag screen when firing the Illinois No. 6 fuel. Table 3-6 presents coal ash and slag composition and ash fusion data for SFS tests completed firing an Illinois No. 6 bituminous coal (SFS-RH11-0799) and a Cordero Rojo subbituminous coal (SFS-RH12-0200). As in the case of the eastern Kentucky fuel, some enrichment of the iron concentration along with depletion of alkali components was observed when comparing Illinois No. 6 coal ash and slag composition data, resulting in the general increase of ash fusion temperatures.

Table 11-7
April 1999 Kentucky Coal Ash and Slag Tap Samples

Oxides,[1] wt%	Kentucky Coal Ash[2]	Limestone 2 lb/hr	Feed 1 lb/hr	Rate 0.5 lb/hr	0.25 lb/hr
SiO_2	45.9	43.4	42.2	44.6	44.8
Al_2O_3	29.6	28.4	30.1	27.9	26.2
Fe_2O_3	14.8	14.5	15.2	16.4	19.9
TiO_2	1.1	1.0	0.9	0.9	1.0
P_2O_5	0.1	0.1	0.1	0.1	0.1
CaO	2.0	7.1	6.1	5.0	2.6
MgO	2.3	2.2	2.2	2.2	2.0
Na_2O	1.1	0.8	0.7	0.7	0.6
K_2O	3.1	2.4	2.3	2.2	2.9
SO_3	–	0.1	0.1	0.1	0.1
Ash Fusion Temp., °F					
Initial	2577	2436	2441	NM[3]	NM
Softening	2603	2441	2446	NM	NM
Hemisphere	2621	2467	2474	NM	NM
Fluid	2684	2537	2537	NM	NM

[1] Oxide concentrations normalized to 100% closure.
[2] SO_3-free basis.
[3] Not measured.

When firing a Cordero Rojo subbituminous coal, the slag screen performed as intended, with 18 tubes installed. Desired slag flow could be maintained as a function of temperature control using a combination of the main and auxiliary burners. It was not necessary to use an additive to modify slag chemistry. The ash fusion fluid temperature for the Cordero Rojo subbituminous coal fired in support of this project was 2286 °F (1253 °C). Because the test called for a furnace temperature of 2800 °F (1538 °C), slag screen temperatures were nominally 2700 °F (1483 °C). As a result, plugging problems in the slag screen were nonexistent. However, slag erosion/corrosion of the high-density refractory in the furnace exit, slag tap, and slag screen was more severe than it would have been if furnace exit and slag screen temperatures had been limited to 2600 °F (1427

°C). The coal ash and slag composition data in Table 11-8 show silica and alumina enrichment and significant alkali depletion for the slag, consistent with the increase in ash fusion temperature observed. Alkaline earth element depletion in the slag for the Cordero Rojo fuel was significant relative to the bituminous coal slag because those constituents represented nearly 40 wt% of the Cordero Rojo ash. The calcia and magnesia depletions in the slag occur because those elements are primarily bound in the coal as salts of organic acids. As such, they readily volatilize upon coal combustion and recondense as micron-sized particles that easily stay entrained in the combustion gas and pass around the slag screen tubes.

Table 11-8
Illinois No. 6 and Cordero Rojo Coal Ash and Slag Tap Samples[1,2]

Oxides, wt%	Illinois No. 6 Coal Ash	Illinois No. 6 Slag	Cordero Rojo Coal Ash	Cordero Rojo Slag
SiO_2	51.1–53.2	49.4–51.1	30.9–31.0	37.9–38.3
Al_2O_3	21.0–22.2	20.9–21.0	19.8–20.2	21.1–24.6
Fe_2O_3	14.8–18.1	18.9–20.7	7.7–8.4	7.3–7.7
TiO_2	0.9–1.0	0.9	1.9	1.6–1.7
P_2O_5	0.2	0.2	1.3	0.6–0.7
CaO	2.7–3.3	2.7–3.0	30.2–30.3	23.0–24.7
MgO	1.8–1.9	1.6	6.0	3.5–4.4
Na_2O	1.5	1.1–1.3	1.1	1.0–1.2
K_2O	2.1–2.4	2.1–2.3	0.4	0.3
SO_3	–	–	–	–
Ash Fusion Temp., °F				
Initial	2390–2392	2479–2482	2221	2248–2274
Softening	2417–2418	2496–2517	2250–2251	2262–2285
Hemisphere	2448	2573–2574	2262–2266	2275–2290
Fluid	2586–2593	2579–2581	2286	2477–2513

[1] Oxide concentrations normalized to 100% closure.
[2] SO_3-free basis.

Following each SFS test, slag and ash from system components and piping were collected and weighed in order to prepare a mass balance. A total theoretical ash quantity was calculated on the basis of the total coal feed and the measured ash content of the composite coal sample. Total slag and ash recovery for individual SFS tests was nominally 80–85 wt%. Some slag loss to high-density refractory in the furnace, slag screen, and slag tap are evident after each test based on the observed darkening of the refractory. On two occasions, slag and ash recovery was >90 wt%. However, in these cases, evidence of erosion/corrosion of high-density refractory in the furnace, slag screen, or slag tap indicated that some of the mass recovered as slag was actually refractory. In two cases, mass balance closure was only 70 wt%. These two cases occurred as a result of firing a low-ash eastern Kentucky coal. In one case, plugging problems in the slag

screen resulted in a significant quantity of slag that was unrecoverable. The other case represented the first SFS test completed after replacing the high-density refractory in the bottom section of the furnace. Therefore, the EERC believes that a larger quantity of slag was absorbed into the new high-density refractory. On one occasion, firing a lignite fuel, slag and ash recovery was only 61 wt%. Inspection of the furnace following this test revealed a significant color change, indicating that a significant amount of coal ash/slag may have been absorbed into the high-density refractory liner.

Slag recovery from the furnace, slag pot, and dilution/quench zone depended on the fuel fired and the slag screen configuration employed. When the slag screen configuration employed 18 tubes, 56–72 wt% of the fuel ash was recovered as slag. When the nine-tube configuration was employed for higher ash fusion fuels, 45–53 wt% of the fuel ash was recovered as slag. The EERC estimates that unrecoverable slag in the furnace, slag screen, and dilution/quench zone for any given test period may represent as much as 10% of the theoretical ash.

Fly ash recovered from other system components (drawdown gas line, CAH duct, process air preheater tubes, tube-and-shell heat exchangers, cyclone, baghouse, and flue gas piping) represented 10–32 wt% of the theoretical ash, depending on slag screen performance. Nominally, 10–20 wt% of the ash in the fuels fired in the SFS was recovered in the pulse-jet baghouse.

Dilution/Quench Zone

The dilution/quench zone was effectively used to control the temperature of the flue gas entering the CAH tube bank at 1800 °F (983 °C). The FGR required to achieve this objective ranged from 250 to 380 scfm (7.1 to 10.8 m^3/min), depending on the furnace firing rate, furnace exit temperature, and flue gas flow rate. On a weekly basis, it was necessary to replace the Type K thermocouple used as the temperature control point. Thermocouple replacement was necessary because of the sheath deterioration that occurred as a function of flue gas temperature and sulfate corrosion.

Slag deposits formed in the vicinity of the FGR nozzles during all of the coal-fired SFS tests completed in support of this and related projects. As a result, it was necessary to clean slag deposits from the area of the FGR nozzles on a periodic basis after the initial 24 to 48 hours of coal firing. Subsequent cleaning frequency depended on slag screen efficiency as well as the quantity of ash in the fuel and fuel ash characteristics. Occasionally, it was necessary to remove slag deposits every 2 hours. However, for most SFS tests, removal of slag deposits was required every 4–8 hours. The addition of a water-cooled wall in the FGR nozzle spool piece resulted in slag deposits being removed more efficiently because of slag embrittlement. Installation of the water-cooled metal surface significantly reduced the damage done to the high-density refractory in the area as a function of slag removal. Also, the use of a water-cooled lance simplified the removal of slag deposits. Downstream of the FGR nozzles, a small quantity of weakly sintered ash was typically observed on the refractory walls. This material was easily removed during SFS maintenance between test periods.

Material recovered from the dilution/quench zone as a result of SFS tests was <15% of the total ash when the slag screen configuration was properly matched to the fuel fired.

Larger percentages of total ash showed up in the dilution/quench zone as a result of damaged or too few tubes installed in the slag screen for a given fuel type. During one SFS test, a larger percentage of the fuel ash was recovered as slag in the dilution/quench zone because of plugging problems in the slag screen. Plugging in the slag screen increased flue gas velocities, increasing the slag screen collection efficiency. However, because of a slag dam between the second and third rows of tubes, the collected slag pooled in the slag screen until the level reached a point where it began to run into the dilution/quench zone. In this case, 34% of the fuel ash was collected as slag in the dilution/quench zone and 38% was collected as slag in the slag pot.

Process Air Preheaters

Process air for the CAH tube bank and the RAH panel was heated using air preheater tube bundles located downstream of the CAH. Exhibits 11-18 through 11-20 summarize process air preheater temperature data as a function of run time for SFS tests completed in April 1999, December 1999, and March 2000, respectively. The data are shown because they represent typical data when firing a Kentucky bituminous, Illinois No. 6 bituminous, and Cordero Rojo subbituminous coal, respectively. Further heating of the process air entering the RAH panel was achieved electrically and by recovering heat from the CAH tube bank. Process air for the CAH tube bank is supplied by the first air preheater tube bundle. During the April 1999 test (SFS-RH8-0399), process air entering the CAH tube bank was controlled at set points ranging from 1075 to 1140 °F (580 to 616 °C) for nominal process air flow rates of 77 to 108 scfm (2.2 to 3.1 m^3/min). Process air temperatures at the exits of the other four preheater tube bundles were nominally 1205 to 1320 °F (652 to 716 °C) for combined flow rates totaling 100 to 150 scfm (2.8 to 4.2 m^3/min).

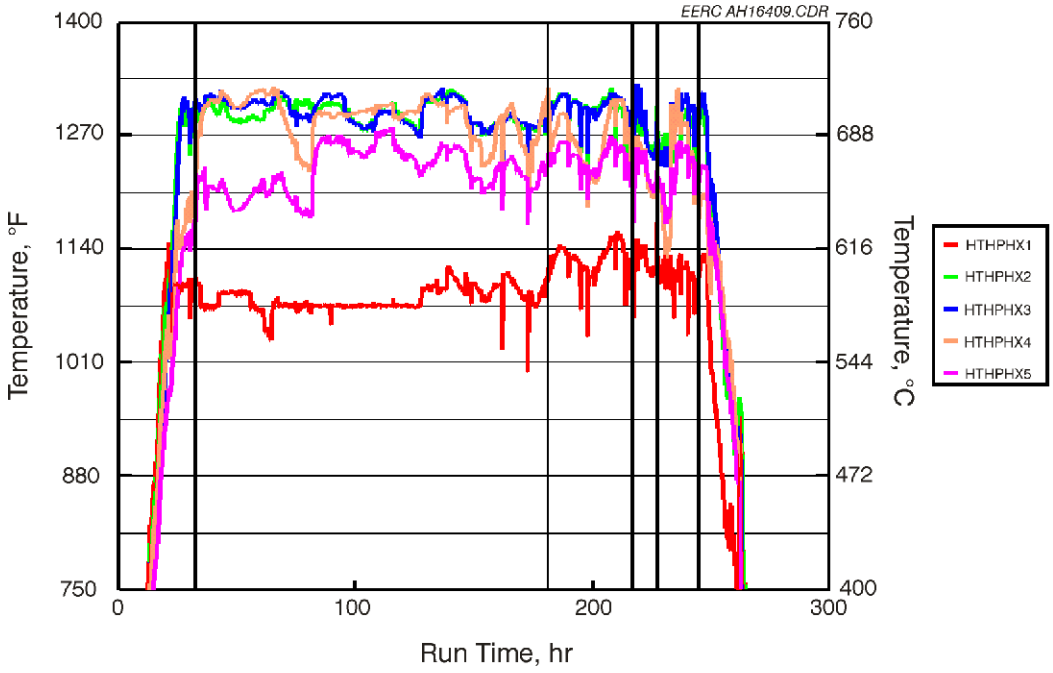

Exhibit 11-18
Process Air Preheater Temperatures versus Run Time for SFS Test SFS-RH8-0399

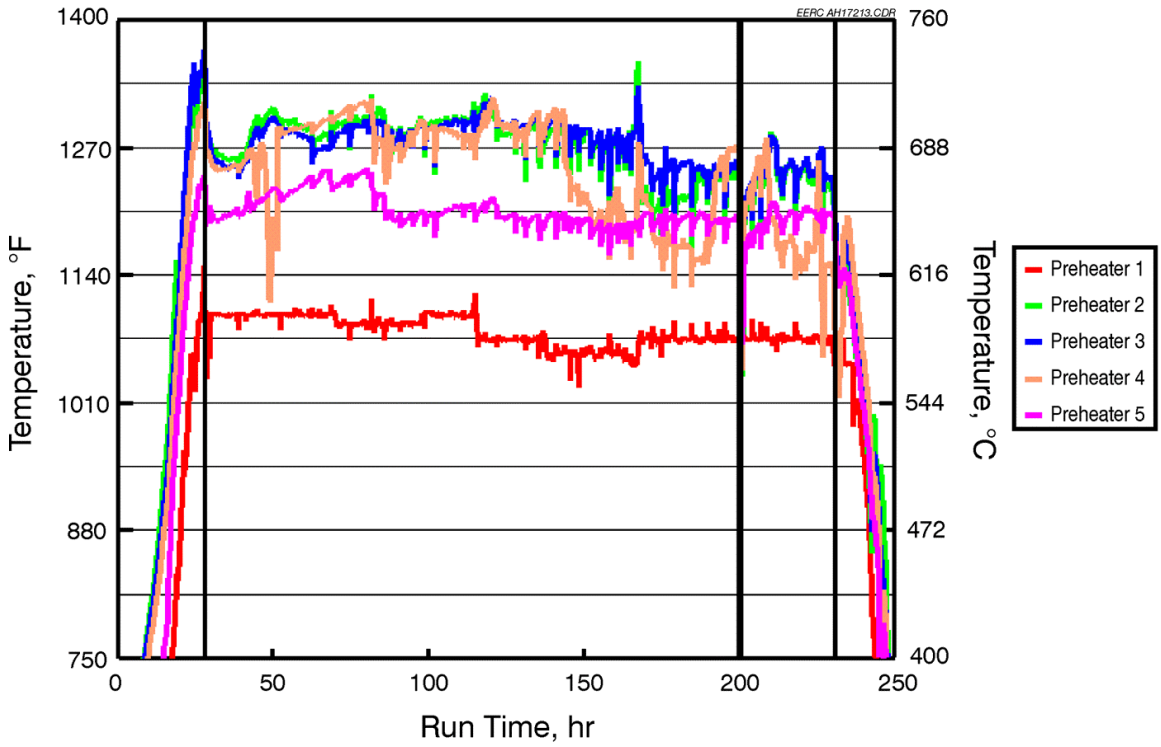

Exhibit 11-19
Process Air Preheater Temperatures versus Run Time for SFS Test SFS-RH11-0799

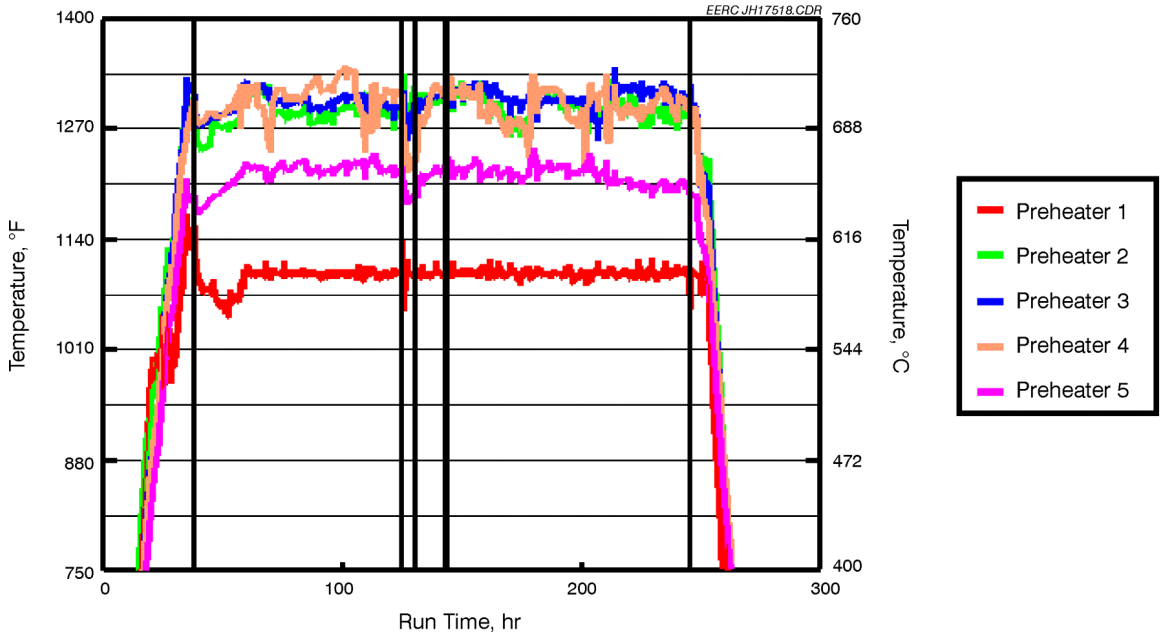

Exhibit 11-20
Process Air Preheater Temperatures versus Run Time for SFS Test SFS-RH12-0200

During the December 1999 test, process air entering the CAH tube bank was controlled at set points ranging from 1060 to 1100 °F (571 to 594 °C) for nominal process air flow rates of 90 to 105 scfm (2.5 to 3.0 m^3/min). Process air temperatures at the exits of the other four preheater tube bundles were nominally 1180 to 1300 °F (638 to 705 °C) for combined flow rates totaling 150 to 200 scfm (4.2 to 5.7 m^3/min).

During the March 2000 test, process air entering the CAH tube bank was controlled at a set point of 1090 (588 °C) for nominal process air flow rates of 100 to 110 scfm (2.8 to 3.1 m^3/min). Process air temperatures at the exits of the other four preheater tube bundles were nominally 1205 to 1310 °F (652 to 710 °C) for combined flow rates totaling 150 to 200 scfm (4.2 to 5.7m^3/min).

Process air preheater heat-transfer rate degraded with time as ash deposits developed on the tube surfaces for all of the fuel types fired in support of this and related projects. However, process air temperature and flow rate control were adequate to support operation of the CAH tube bank and RAH panel for all of the test periods completed regardless of the fuel type (eastern Kentucky bituminous coal, Illinois No. 6 bituminous coal, two Powder River Basin subbituminous coals, and two northern plains lignite fuels) fired. Ash deposits collected on these tube surfaces were easily removed during SFS maintenance between test periods.

Particulate Emissions

The characteristics of fly ash generated in the high-temperature SFS are different than those observed for a given fuel fired in a conventional pc-fired system. Specific differences observed include a reduction in mass loading and particle size and changes in ash chemistry related to particle size. The lower mass loading and smaller particle size

were anticipated based on the use of a slag screen at the furnace exit to promote ash collection as slag. Changes in fly ash chemistry were also anticipated as a function of volatilization and condensation mechanisms as well as slag screen performance.

The initial set of filter bags installed in the pulse-jet baghouse were 16-oz/yd^2 (454-g/m^2) Huyck felt material. This filter media generally demonstrated good particulate control. However, on-line cleanability and differential pressure control were inconsistent for most fuel types. Therefore, in late 1998 a new filter media was installed. The new filter media was a 22-oz/yd^2 (624-g/m^2) woven glass with a PTFE membrane. As a result, on-line cleaning effectively controlled baghouse differential pressure for the bituminous and subbituminous coals fired in 1999 and 2000. Improvements in on-line filter cleanability are believed to be due to the PTFE membrane facilitating dust cake release at lower pulse pressures, minimizing ash reentrainment.

During gas- and coal-fired furnace operation, baghouse temperatures and temperature profiles were nominal, and the electrical heaters worked well, limiting the potential for condensation on start-up and shutdown. Baghouse temperature ranged from 315 to 390 °F (158 to 199 °C), with typical values of 330 to 350 °F (166 to 177 °C). Exhibit 11-21 presents baghouse temperature data versus run time for a March 2000 SFS test firing Cordero Rojo subbituminous coal. Temperature data are stable except for spikes (high and low) associated with dilution/quench zone cleaning cycles and CAH sootblowing cycles. Dilution/quench zone cleaning has the greatest effect on downstream flue gas temperatures. Changes in baghouse inlet set point temperatures are evident in the data at run hours of approximately 95 and 190. In each case, the set point was increased by 5 °F (3 °C) in order to reduce the load on the cooling-air fan, which is used to control flue gas temperature entering the baghouse. Flue gas temperature is very uniform over the length of the baghouse (5 °F [3 °C] differential), indicating the electrical wall heaters were working well. The overall temperature differential from the baghouse inlet to outlet flanges was 25 °F (14 °C).

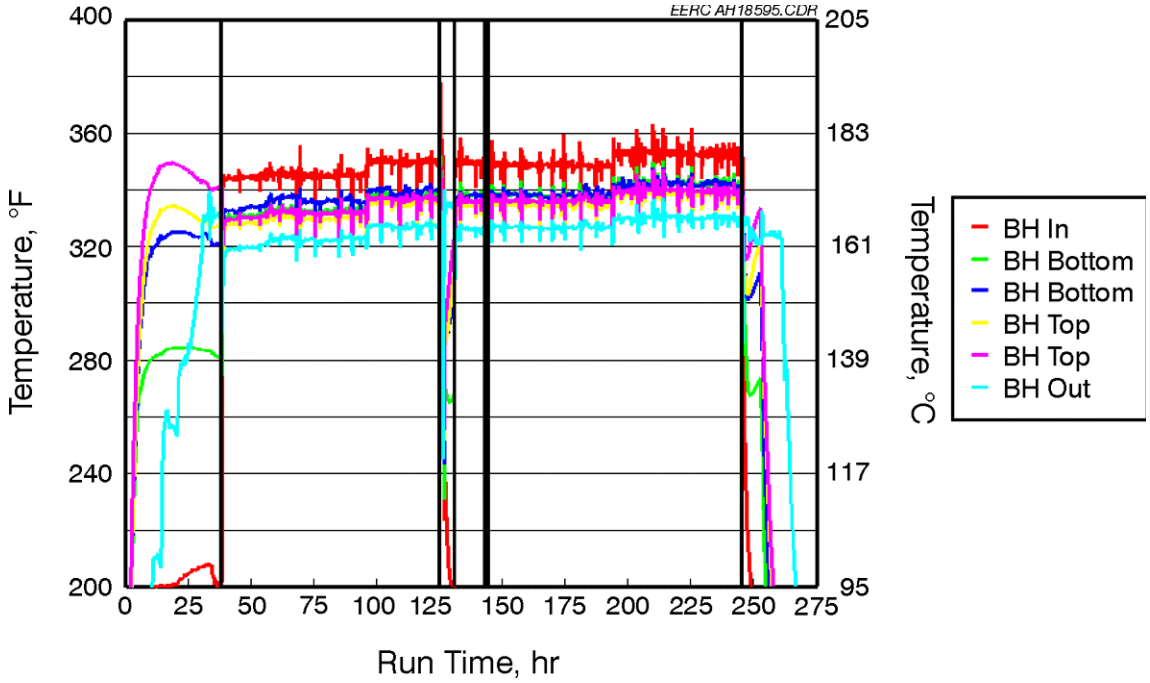

Exhibit 11-21
Baghouse Temperatures versus Run Time for SFS Test SFS-RH12-0200

Flue gas flow rates ranged from 880 to 1165 scfm (24.9 to 33.0 m^3/min), with typical values of 900 to 1050 scfm (25.5 to 29.7 m^3/min). Actual flue gas flow rates through the baghouse were typically 1380 to 1700 acfm (39.0 to 48.1 m^3/min) and ranged from 1365 to 1950 acfm (38.7 to 55.2 m^3/min). The 36 bags (total filtration area of 565 ft^2 [52.5 m^2]) used in the baghouse resulted in filter face velocities of 2.4 to 3.5 ft/min (0.73 to 1.1 m/min). These filter face velocities are low compared to conventional pulse-jet filtration systems typically operating at or near 4 ft/min (1.2 m/min).

Mass loading measured at the inlet of the pulse-jet baghouse ranged from 0.0428 gr/scf (98.02 mg/Nm^3) to 0.29 gr/scf (664 mg/ Nm^3). The low end of the range represented a low- moisture (2.5 wt%), low-ash (3.9 wt %), high-heating-value (14,120 Btu/lb/32,812 kJ/kg) bituminous coal and a moderate level of ash collection (53%) as slag. The high end of the range represented a lignite containing 35 wt % moisture and 6 wt% ash, with a heating value of nominally 7000 Btu/lb (16,267 kJ/kg). For the lignite, only 43 wt% of the ash was collected as slag. In general, the fly ash mass loading measured at the inlet of the pulse-jet baghouse was an order of magnitude lower than would be expected for a conventional pc- or lignite-fired system. Ultimately, in commercial systems, the mass loading, particle-size distribution, and chemistry of the fly ash reaching a control device will depend on the fuel ash content, ash chemistry, and design and operating conditions of the system in which the fuel is being used.

Mass loading measured at the outlet of the pulse-jet baghouse ranged from 0.0002 gr/scf (0.46 mg/Nm^3) to 0.0061 gr/scf (13.97 mg/ Nm^3). Values >0.001 gr/scf (>2.29 mg/ Nm^3) represented tests where sulfur trioxide condensation was observed and found to have contributed in some manner to filter weight gains. Measurements were made to document sulfur trioxide concentrations downstream of the pulse-jet baghouse. For

Illinois No. 6 bituminous coal, 45 ppm sulfur trioxide was observed. For low-sulfur bituminous coal, the sulfur trioxide concentration was <5 ppm. Sulfur trioxide measurements were not made for subbituminous and lignite fuels because sulfur trioxide present in the flue gas would quickly react with fly ash alkali constituents. In order to limit the impact of sulfur trioxide condensation on particulate measurements and cleanup/maintenance requirements downstream of the pulse-jet baghouse when firing Illinois No. 6 coal, the EERC injected calcium oxide into the flue gas upstream of the baghouse at a rate of 0.5 lb/hr (227 g/hr). This quantity of calcium oxide reduced sulfur trioxide concentrations downstream of the pulse-jet baghouse to <5 ppm. As a result, outlet mass loading was reduced and downstream flue gas piping showed no evidence of acid condensation.

Calculated particulate emissions from the pulse-jet baghouse ranged from 0.0007 to 0.0233 lb/MMBtu. Values >0.003 lb/MMBtu represented tests where the use of a high-sulfur fuel resulted in sulfur trioxide condensation which contributed to filter weight gains. During all tests, regardless of the fuel fired, the pulse-jet baghouse limited particulate emissions to <0.03 lb/MMBtu. When sulfur trioxide condensation and filter media damage were not evident, particulate emissions were controlled at <0.003 lb/MMBtu.

In addition to the standard U.S. Environmental Protection Agency (EPA) Method 5 sampling completed during the coal-fired test periods, respirable mass emissions (defined below) were measured at the outlet of the pulse-jet baghouse using a TSI Inc. aerodynamic particle sizer (APS-33). This real-time measurement method measures particle mass in the range of 0.5 to 15 µm. The primary advantages of this system are the high spatial resolution and the short sampling time. In the APS-33, particle-laden air is passed through a thin-walled orifice, with the particles lagging behind the gas because of their higher inertia. The velocity lag is related to the aerodynamic diameter of the particles, allowing the determination of the aerodynamic dynamic diameter of a particle by measuring the velocity of a particle as it exits the orifice. To measure the particle velocity, the APS-33 employs a laser beam split into two beams and refocused onto two rectangular planes a set distance apart in front of the orifice. The light scattered by a particle passing through these beams is collected and focused onto a photomultiplier tube, which emits two pulses separated by the time taken for the particle to cross the distance between the two planes. This time interval is measured electronically and used to calculate the particle's aerodynamic diameter.

Respirable mass is a calculated value defined by the American Council of Governmental and Industrial Hygienists for particles in the size range of 2 to <10 µm, based on aerodynamic diameter. Exhibits 11-22 and 11-23 present respirable mass emissions data for an Illinois No. 6 bituminous coal and an eastern Kentucky bituminous coal, respectively. The data are presented on a mg/m^3 basis versus sampling time and are representative of tests using the woven glass/ PTFE membrane bags. For the Illinois No. 6 coal, the average respirable mass emission rate integrated over 4 hours was 0.0025 mg/m^3 with individual measurements ranging from 0.0006 to 0.004 mg/m^3. During the Kentucky coal-fired test, the integrated average was 0.0004 mg/m^3 for a 2-hour sampling period, and individual measurements ranged from 0.0001 to 0.0015 mg/m^3.

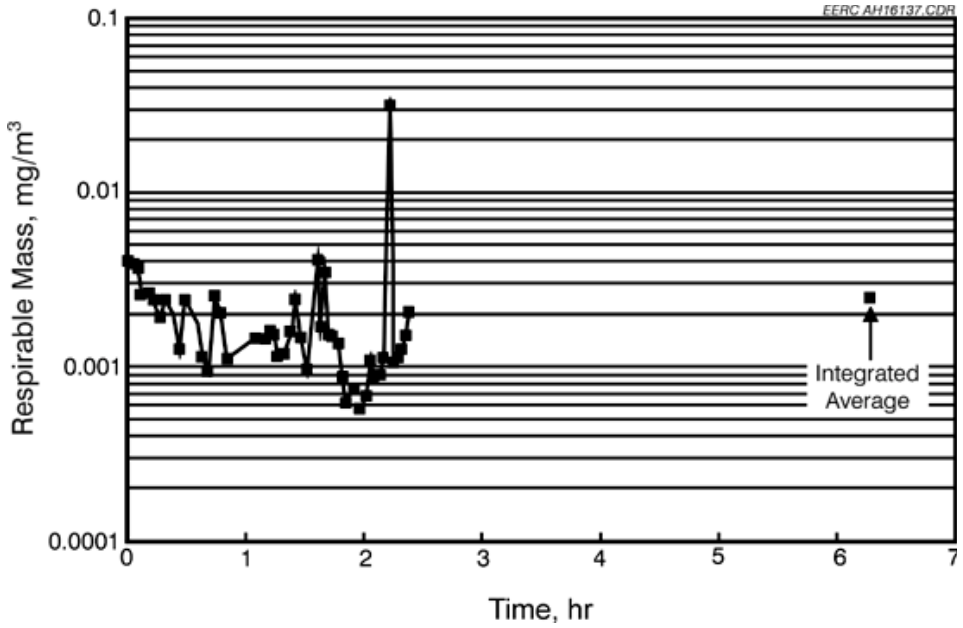

Exhibit 11-22
Respirable Mass Emission Data for an Illinois No. 6 Bituminous Coal, SFS-RH6-0199

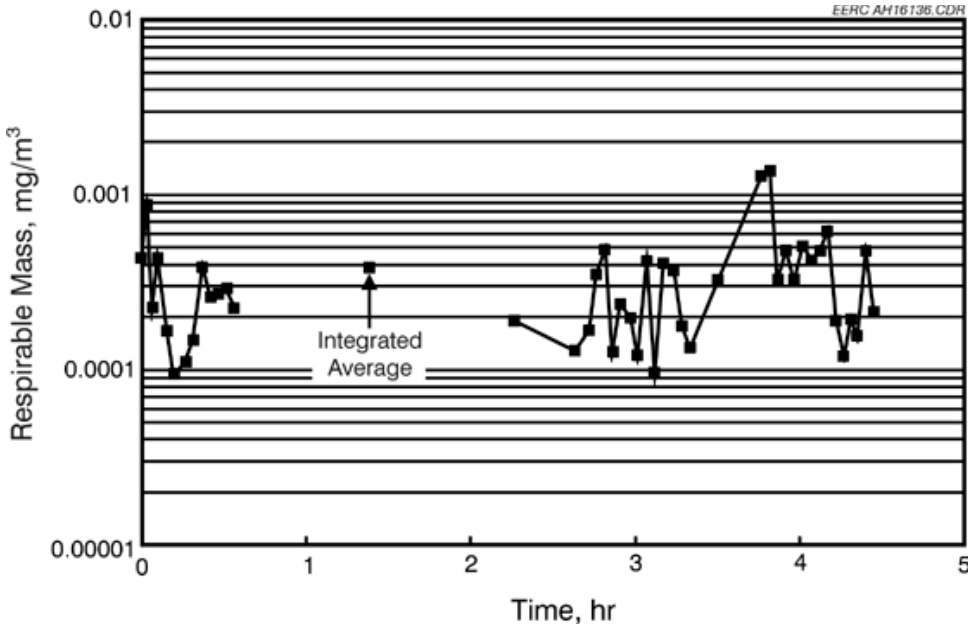

Exhibit 11-23
Respirable Mass Emission Data for an Eastern Kentucky bituminous Coal, SFS-RH7-0299

No valid respirable mass data were available for two subbituminous coal-fired tests completed. Data collected during the Cordero Rojo subbituminous coal-fired test were determined to be invalid as a result of a high-vacuum static pressure condition (>15 in. W.C. [>28 mmHg]) at the sampling point. The reason for the high-vacuum static

pressure condition was the high flue gas flow rate through the SFS, the resulting system differential pressure, and the required operating speed of the ID fan to maintain desired furnace static pressure.

Exhibits 11-24 and 11-25 present respirable mass emissions data for a lignite-fired test and an Illinois No. 6 coal-fired test, respectively, while using the Huyck felt bags. For the lignite, the average respirable mass emission rate integrated over a cleaning cycle was 0.003 mg/m^3 versus 0.02 mg/m^3 for the Illinois No. 6 coal, nearly an order-of-magnitude difference. This relative difference is also evident in the emission spikes observed as a result of each cleaning cycle. Cleaning cycle emission spikes for the lignite and Illinois No. 6 coal were 0.02 mg/m^3 and 0.2 mg/m^3, respectively. Since the difference in emission rates between cleaning cycles was less significant, the higher particulate emission rates observed for the Illinois No. 6 coal appear to be the result of emission spikes during fabric filter cleaning cycles.

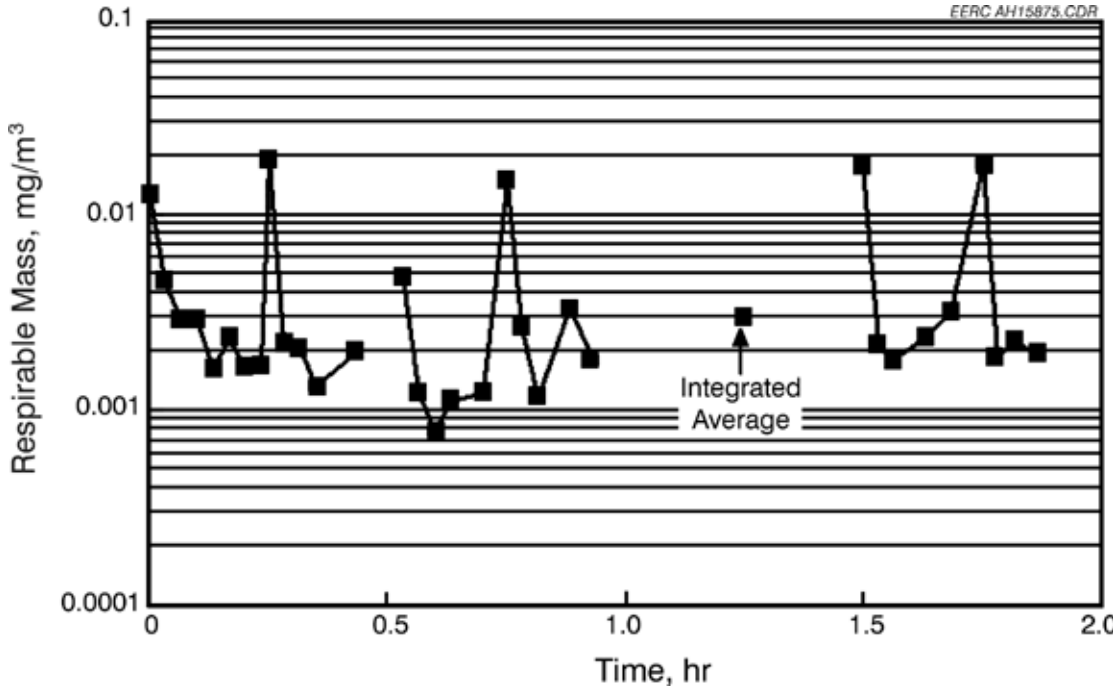

Exhibit 11-24
Respirable Mass Emission Data for a Lignite, SFS-ND1-0398

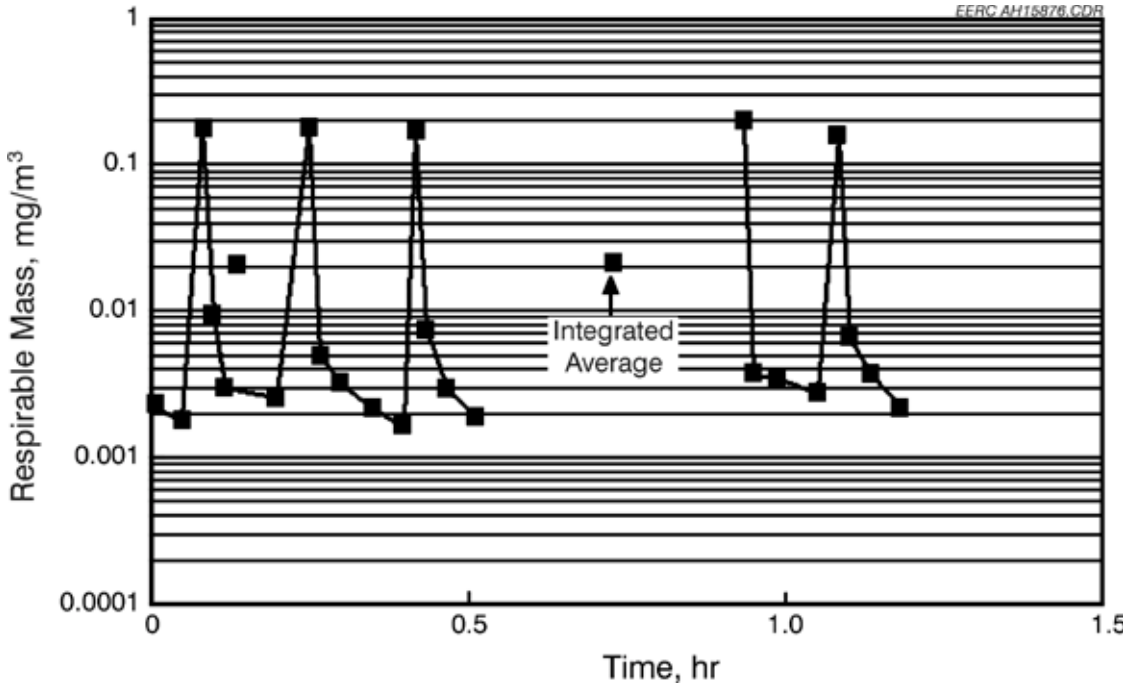

Exhibit 11-25
Respirable Mass Emission Data for an Illinois No. 6 Bituminous Coal, SFS-RH5-0598

Comparing Exhibits 11-22 and 11-25, the data indicate a near order-of-magnitude difference in respirable mass emissions. The lower emissions observed in Exhibit 3-16 are believed to be due to the fabric type used, the 22-oz/yd^2 (624-g/m^2) woven glass with a PTFE membrane, resulting in a significantly less frequent cleaning cycle. Cleaning frequency for the woven glass/PTFE membrane filter media was 3 to 6 hr versus 10 minutes for the Huyck felt filter media.

The baghouse clean air plenum was inspected following each test period to determine whether acid condensation or ash tracking on the tube sheet were evident. Periodically, filter bags were removed from the baghouse for inspection and occasional cleaning. In all cases, the tube sheet appeared to be very clean, with occasional evidence of acid condensation, consistent with sulfur trioxide measurements downstream of the baghouse. At this time, the 22-oz/yd^2 (624-g/m^2) woven glass/PTFE membrane filters installed in the baghouse are in good condition.

Geometric particle-size analysis was completed for a composite ash sample collected from the baghouse hopper for all SFS tests. Exhibit 11-26 summarizes the data for the fuel types fired (bituminous coal, subbituminous coal, and lignite, respectively) in the SFS. Overall, the data show that, with the exception of one ash sample, 80 wt% of ash was <10 µm and 50 wt% was <6 µm. For the Illinois No. 6 bituminous coal, the data show the ash to be 100 wt% <20 µm, 80 wt% <6–9 µm, and 50 wt% <3–6 µm. With the exception of one ash sample, the eastern Kentucky bituminous coal resulted in a similar baghouse ash particle-size range. The subbituminous fuels fired generally resulted in ash particle sizes in the range reported for the Illinois No. 6 coal. However, for one sample 5

wt% of the fly ash mass indicated particle sizes ranging from 20–50 µm. For the other subbituminous ash sample, 100 wt% of the ash was <11 µm. The two lignite fuels fired in the slagging furnace demonstrated very similar ash particle sizes, 100 wt% <30 µm, 80 wt% <10 µm, and 50 wt% <5 µm. Factors believed to influence ash particle size at the baghouse inlet included ash chemistry, furnace operating conditions, slag screen performance, dilution/quench zone performance, and the application of sootblowing at the CAH tube bank.

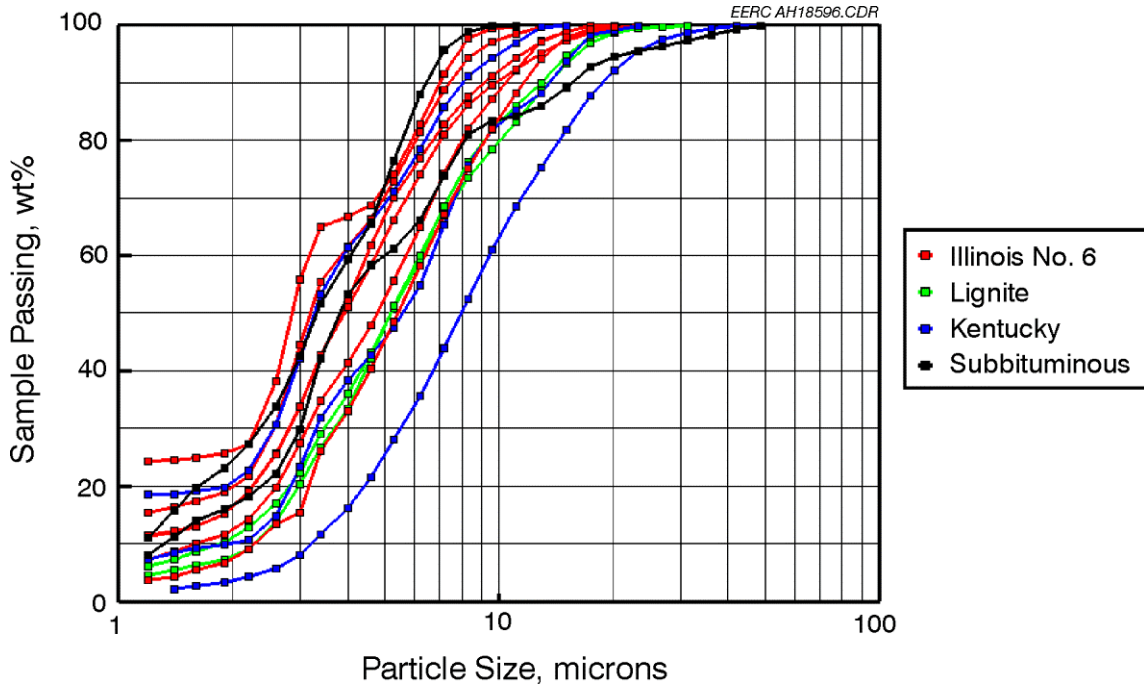

Exhibit 11-26
Baghouse Ash Particle-Size Data for All Fuel Types Fired in the SFS

One data set representing an eastern Kentucky coal-fired test resulted in a larger-than-average fly ash particle-size distribution. This SFS test (SFS-RH13-0400) was the only test completed during which CAH sootblowing effectively controlled tube surface temperature and heat recovery for the duration of the test. Therefore, that data set in Exhibit 11-26 would indicate that effective CAH sootblowing would have the greatest effect on ash particle size at the inlet to the baghouse.

One data set representing a subbituminous coal-fired test resulted in a larger-than-average fly ash particle-size distribution for the upper 20 wt%. This SFS test (SFS-RH4-0298) was a test during which the slag screen tubes were reduced from a diameter of 1.5 in. (3.8 cm) to <0.5 in. (<1.3 cm) as a result of slag erosion/corrosion. Therefore, this data set would indicate the effect of poor slag screen performance on ash particle size at the inlet to the baghouse, where particle size increased from 20 wt% 5.5–11 µm to 20 wt% 8–50 µm.

Multicyclone sampling data for the same fuel types are summarized in Exhibit 11-27. In general, the multicyclone sampling data indicate an aerodynamic particle size of 40–70 wt% <8 µm and 10–50 wt% <2 µm.

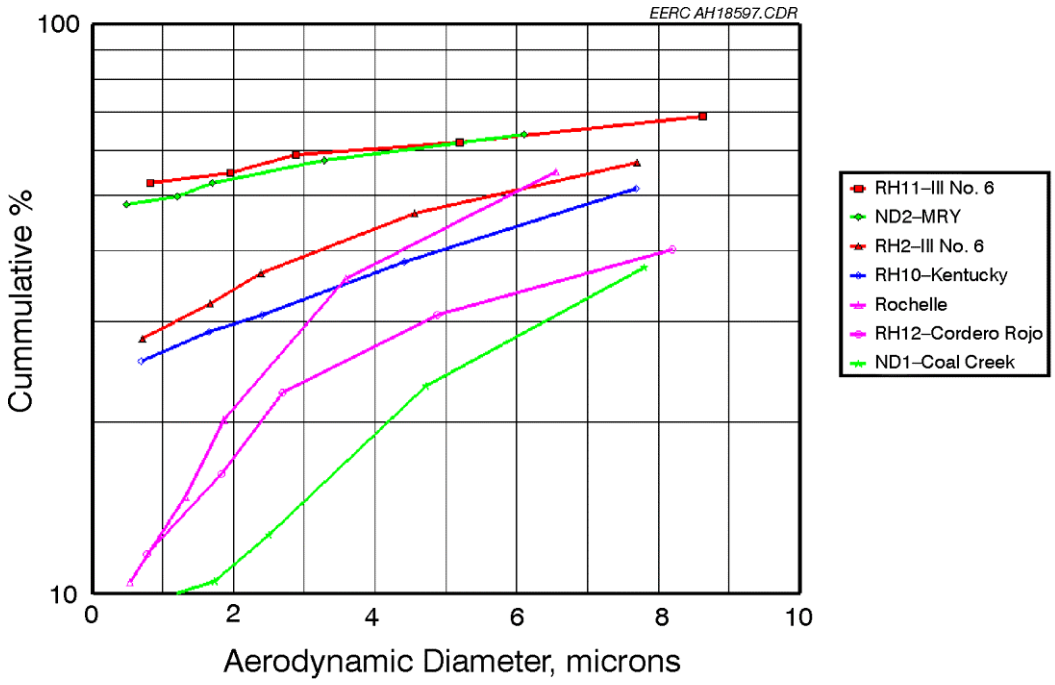

Exhibit 11-27
Multicyclone Data resulting from Baghouse Inlet Sampling

Carbon content in the baghouse ash was measured to determine combustion efficiency for each SFS test. The carbon content of the baghouse ash ranged from 0.01 to 0.70 wt% for all fuels fired and was generally <0.5 wt%. However, there was no correlation with fuel type, fuel particle-size distribution, or furnace operating conditions. Therefore, the EERC believes that low baghouse ash carbon content consistently observed was primarily a function of the residence time and high operating temperature of the slagging furnace.

As previously stated, on-line cleaning alone did not consistently control baghouse differential pressure for all fuels when using the Huyck felt filter media. Also, cleaning cycle frequency for the Huyck felt filter media was routinely measured in minutes rather than hours. After installation of the 22-oz/yd^2 (624-g/m^2) woven glass/PTFE membrane filters, pulse cleaning of the bags was accomplished on-line using a reservoir pulse-air pressure of nominally 40 to 60 psig (2.8 to 4.2 bar) for all fuels fired. The baghouse differential pressure cleaning set point was typically 6 in. W.C. (11 mmHg). Once the initial dust cake was formed, the cleaning frequency was 4 to 8 hours when the eastern Kentucky coal was fired and 3 to 6 hours when the Illinois No. 6 coal was fired. For the Cordero Rojo subbituminous coal, the cleaning frequency was nominally 2 hours. The bags consistently cleaned to a differential pressure of nominally 2 in. W.C. (4 mmHg) for the bituminous coals and 4 in. W.C. (7 mmHg) for the subbituminous coal. Variations in cleaning cycle frequency for a given fuel type were the result of variations in furnace operating conditions and resulting particulate mass loading and flue gas flow rate.

Exhibits 11-28 through 11-30 present baghouse differential pressure as a function of run time for three fuel types, respectively.

Exhibit 11-28 (SFS-RH8-0399) shows a uniform baghouse cleaning cycle through roughly Run Hour 180. At that point, the EERC switched from the eastern Kentucky fuel to an Illinois No. 6 fuel, resulting in more frequent bag cleaning as a result of increased mass loading. However, on-line cleaning did effectively control baghouse differential pressure.

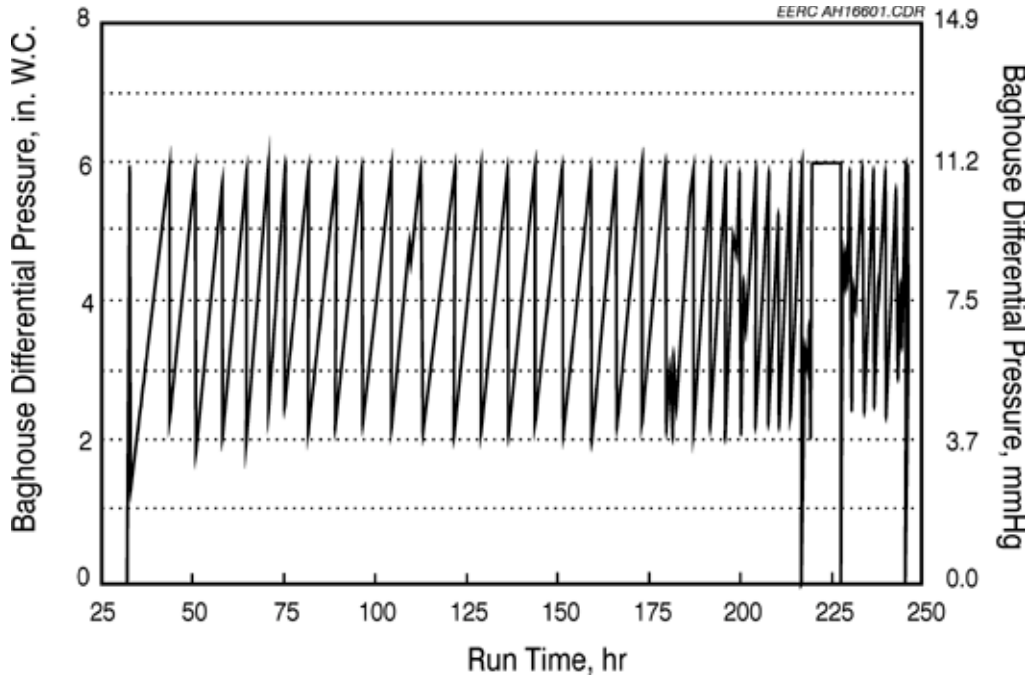

Exhibit 11-28
Baghouse Differential Pressure versus Run Time for an Eastern Kentucky Coal-fired Test

Exhibit 11-29 illustrates baghouse differential pressure for a test firing Illinois No. 6 coal (SFS-RH11-0799). Again, on-line cleaning effectively controlled differential pressure. However, at roughly Run Hour 160 the cleaning cycle set point was reduced from 6 to 5 in. W.C. (11 to 9 mmHg). The change was made in an attempt to mitigate system upset conditions caused by the change in overall system pressures following baghouse cleaning. This set point change resulted in a smaller swing in system differential pressure and was a beneficial change in operating protocol.

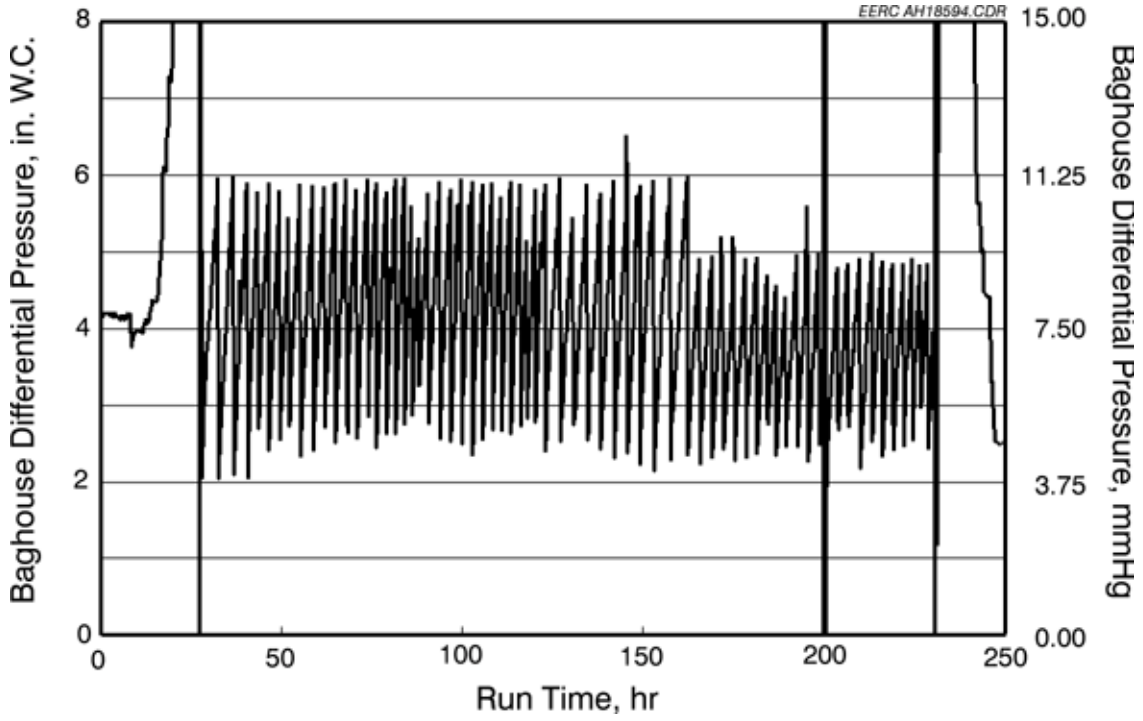

Exhibit 11-29
Baghouse Differential Pressure versus Run Time for an Illinois No. 6 Coal-fired Test

Exhibit 11-30 illustrates baghouse differential pressure for a test firing Cordero Rojo subbituminous coal (SFS-RH12-0200). In this case, the baghouse differential pressure cleaning-cycle set point was initially 5 in. W.C. (9 mmHg). However, after 100 hr of coal firing, on-line cleaning was occurring at a 50-minute interval, and the differential pressure after cleaning was >3 in. W.C. (>6 mmHg). The cleaning cycle set point was increased to 6 in. W.C. (11 mmHg), and the on-line cleaning frequency was reduced to nearly a 2-hr cycle. The differential pressure after cleaning was <4 in. W.C. (<7.5 mmHg).

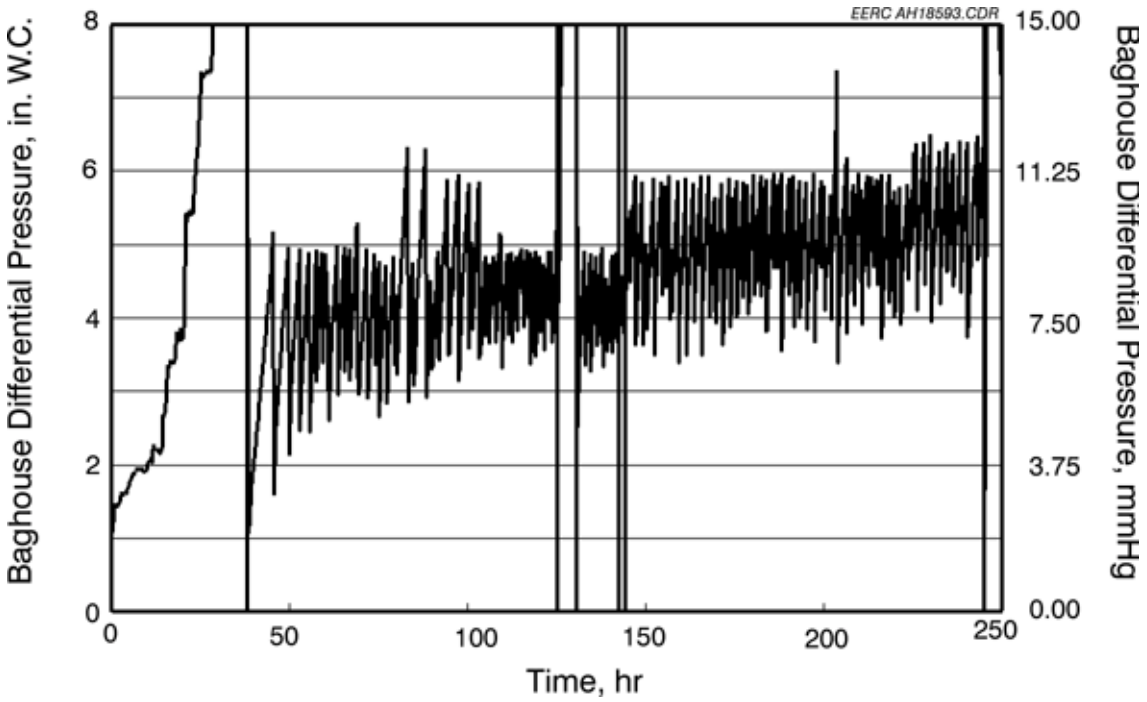

Exhibit 11-30
Baghouse Differential Pressure versus Run Time for a Subbituminous Coal-fired Test

If development of the HITAF concept continues, it will be necessary to continue fly ash characterization efforts in order to properly select the type of particulate control technology (ESP, fabric filter, or hybrid approach) to be used. Also, this information will be necessary for the preparation of detailed system designs and the implementation of an appropriate approach to operation. Based on SFS pulse-jet baghouse experience to date, there are questions yet to be answered concerning the appropriate filter face velocity, fabric type, and approach to cleaning that will effectively achieve performance and cost objectives relative to the control of particulate emissions and differential pressure for a range of fuel types.

Flue Gas Composition

Table 11-9 shows the average gaseous emissions measured during SFS tests completed with the various fuel types fired. The oxygen (O_2), carbon dioxide (CO_2), and carbon monoxide (CO) data are based on furnace exit measurements made in the slag screen outlet. Sulfur dioxide (SO_2) and nitrogen species (NO_x) data are based on flue gas sampling downstream of the pulse-jet baghouse. Ranges for oxygen concentration are similar for all of the fuel types fired in the slagging furnace. For a given fuel type, the oxygen concentration range was a function of changes in air-to-fuel ratio and furnace firing rate to achieve a range of desired furnace temperatures. Carbon dioxide concentration data followed the oxygen data.

The CO concentrations exceeding 10 ppm were indicative of some combustion occurring in the slag screen. This was observed for all fuel types fired in the slagging

furnace as well as for natural gas fired in the auxiliary burner. However, no CO was observed at the baghouse outlet sampling location unless the slag tap burners were operated in a fuel-rich condition. Therefore, the CO observed in the slag screen was oxidized in the dilution/quench zone and CAH section. The CO observed in the slag screen is a function of the main burner operating at a low swirl condition. Increasing main burner swirl would reduce CO concentrations in the slag screen but would also increase temperature variations over the length of the furnace.

Table 11-9
Flue Gas Composition for All Fuel Types Fired in the Slagging Furnace

Illinois No. 6 Bituminous Coal	Concentration	lb/MMBtu
O_2	2.8%–5.0%	
CO_2	12.6%–15.0%	
CO	5–50 ppm	
NO_x	360–610 ppm	0.4–1.4
SO_2	1680–3140 ppm	5.2–6.9
Eastern Kentucky Bituminous Coal		
O_2	2.6%–5.9%	
CO_2	12.0%–15.3%	
CO	5–60 ppm	
NO_x	450–780 ppm	0.8–1.5
SO_2	280–850 ppm	0.9–1.6
Powder River Basin Subbituminous Coal		
O_2	3.0%–5.8%	
CO_2	12.6%–14.7%	
CO	5–80 ppm	
NO_x	440–605 ppm	0.6–1.4
SO_2	150–320 ppm	0.5–0.9
Northern Plains Lignite		
O_2	3.0%–4.0%	
CO_2	14.0%–15.3%	
CO	10–40 ppm	
NO_x	400–620 ppm	0.64–0.84
SO_2	630–720 ppm	1.2–1.6

NO_x Emissions

NO_x concentrations in the flue gas ranged from 360 to 780 ppm. Total NO_x emissions (reported as nitrogen dioxide) were determined to range from 0.4 to 1.5 lb/MMBtu. NO_x emissions were higher during individual test periods, represented by higher average coal feed rates and furnace temperatures. NO_x emissions were marginally higher when the eastern Kentucky fuel was fired compared to the Illinois No. 6 fuel because of higher furnace temperatures. Excess air levels and fuel moisture content also influenced NO_x emissions. The auxiliary burner firing condition is also believed to have affected the NO_x emissions; however, no specific tests were conducted to document the effect of the auxiliary burner on NO_x emissions.

SO_2 Emissions

No attempt at controlling sulfur dioxide emissions was made. Therefore, sulfur dioxide emissions were dependent on fuel sulfur content, fuel feed rate, and the presence of alkali species in the flue gas available for sulfation reactions. Calculated rates were based on the coal feed rate through the main burner and the sulfur content and heating value of the fuel determined for the composite fuel samples analyzed. For the Illinois No. 6 bituminous coal, calculated theoretical sulfur dioxide emissions were 8.7 to 16.8 lb/hr (3.9 to 7.6 kg/hr). Measured flue gas composition at the stack indicated SO_2 concentrations of 1680 to 3140 ppm and emission rates of 8.8 to 15.4 lb/hr (4.0 to 7.0 kg/hr) or 5.2 to 6.9 lb/MMBtu. For the eastern Kentucky bituminous coals, calculated theoretical sulfur dioxide emissions were 2.4 to 3.2 lb/hr (1.1 to 1.4 kg/hr). Measured flue gas composition at the stack indicated SO_2 concentrations of 280 to 850 ppm and emission rates of 2.0 to 3.5 lb/hr (0.9 to 1.6 kg/hr) or 0.9 to 1.6 lb/MMBtu. For the bituminous coals, the most likely explanation for the difference between calculated and measured SO_2 emission rates is that the composite fuel samples analyzed for any given test period did not adequately represent fuel sulfur content documented by the flue gas sulfur dioxide analyzers.

For the subbituminous coals, calculated theoretical sulfur dioxide emissions were 0.9 to 2.6 lb/hr (0.4 to 1.2 kg/hr). Measured flue gas composition at the stack indicated SO_2 concentrations of 150 to 320 ppm and emission rates of 0.8 to 2.3 lb/hr (0.4 to 1.0 kg/hr) or 0.5 to 0.9 lb/MMBtu. For the lignite fuels, calculated theoretical sulfur dioxide emissions were 5.5 to 6.3 lb/hr (2.5 to 2.9 kg/hr). Measured flue gas composition at the stack indicated SO_2 concentrations of 630 to 720 ppm and emission rates of 3.0 to 4.3 lb/hr (1.4 to 2.0 kg/hr), or 1.2 to 1.6 lb/MMBtu. For the subbituminous and lignite fuels, the most likely explanation for the difference between calculated and measured SO_2 emission rates is sulfation of alkali ash constituents contained in the fuel. In all of the SFS tests with these fuels, measured SO_2 emissions were lower than those calculated based on fuel analyses and feed rate.

Convective Air Heater Tube Bank Performance

The CAH tube bank was installed and initially evaluated during a shakedown test completed in October 1997. CAH tube bank performance met all test objectives relative to heat transfer and its support of the RAH panel. Performance differences relative to fuel ash properties were as expected. Table 11-10 summarizes operating hours for the CAH tube bank, representing 22 thermal cycles.

Exhibit 11-31 illustrates the location of thermocouples in the CAH tube bank, and Table 3-9 presents a list of thermocouple descriptions that pertain to the results discussed in this report. Prior to an August 1998 test, all of the CAH thermocouples were replaced or repaired in conjunction with the installation of fins on the air-cooled tubes. However, one tube surface thermocouple (CAHIT3) was damaged when the tube bank was installed in the flue gas duct. One additional CAH thermocouple failed during both an August and December 1998 test, and a fourth thermocouple failed at the beginning of a January 1999 test. Therefore, during several of the tests discussed in this report, only one of the five surface thermocouples was functioning properly.

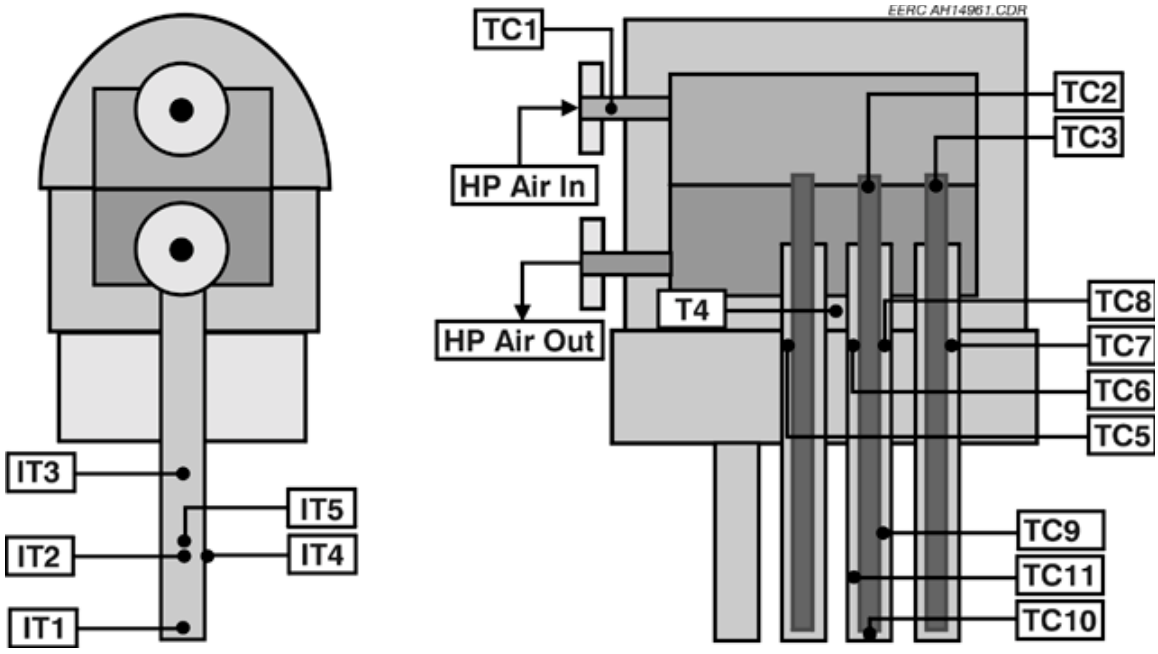

Exhibit 11-31
Thermocouple Locations in the CAH Tube Bank

Sootblowing

In November 1999, the EERC developed a probe or lance for sootblowing the CAH tube bank. The components of the sootblowing system included stainless steel tubing and a nozzle, high-pressure hose, ball valve, regulator, and pipe fittings. The sootblowing media was compressed nitrogen gas delivered to the lance at a pressure of 200 psig (13.8 bar) and a flow rate of 188 scfm (5.3 m^3/min). The lance was manually inserted and removed through an access port to the tube bank. In addition, the probe was rotated up and down approximately 45° while moving in and out of the CAH tube bank. This approach permits sootblowing between two rows of tubes. The duration of an actual sootblowing event did not exceed 15 seconds. However, the potential effectiveness of sootblowing was not adequately addressed during this project. Sootblowing was attempted during only a few tests near the end of the project with fins attached to the leading and trailing edges of the tubes.

Based on this limited work, an 8-hr sootblowing frequency is adequate for the eastern Kentucky coal fired in the SFS. However, all of the other fuel types (bituminous, subbituminous, and lignite fuels) fired in the SFS will likely require more frequent (4-hr cycle) sootblowing to achieve a comparable result. Also, improved sootblowing effectiveness may require a modification to the methodology employed to increase the tube surface area affected by each sootblowing event.

Table 11-10
Summary of CAH Tube Bank Operating Hours Through December 2000[1]

	Natural Gas Firing, hr	Coal/Lignite Firing, hr	Total Operation, hr
CAH Tube Bank	1760	1512	3272

[1] Natural gas firing represents heatup, cooldown, and refractory curing.

Table 11-11
Description of CAH Thermocouple Locations[1]

Category	No.	Label	Description
Air Inlet	1	CAHTC1	Bulk flow entering the inlet header
	2	CAHTC2	Air entering center tube
	3	CAHTC3	Air entering most downstream tube
Air Outlet	4	CAHTC6	Air leaving center tube
	5	CAHTC7	Air leaving most downstream tube
	6	CAHTC5	Air leaving most upstream tube
	7	CAHTC8	Air leaving side tube
Air in Active Region	8	CAHTC10	Bottom of center tube
	9	CAHTC11	4 in. up outside annulus, center tube
	10	CAHTC9	8 in. up outside annulus, center tube
Tube Surface	11	CAHIT1	1 in. up center tube, facing upstream (failed)
	12	CAHIT2	5 in. up center tube, facing upstream
	13	CAHIT3	8 in. up center tube, facing upstream (failed)
	14	CAHIT4	5 in. up center tube, facing to side (failed)
	15	CAHIT5	5 in. up center tube, facing downstream (failed)
Header Shell	16	CAHTC4	Next to shell on outside, between return air pipes (failed)

[1] Thermocouple locations are illustrated in Exhibit 3-31.

No attempt had been made to sootblow the CAH tubes prior to the installation of fins. Therefore, conclusions cannot be drawn concerning the potential advantages of the fins when routine sootblowing is effectively used to maintain desired CAH heat recovery. Also, the presence of the fins may actually inhibit the effectiveness of sootblowing. For the balance of this discussion, the performance of the CAH tube bank is discussed with respect to the fuel types (bituminous and subbituminous coals) fired in the SFS during this project.

Operation with Illinois No. 6 Bituminous Coal

As an example of operating data when firing Illinois No. 6 coal, Exhibits 11-32 through 11-34 summarize CAH tube bank surface and flue gas temperatures, process air temperatures, and process air flow rate data, respectively, for a SFS test completed in December 1999 (SFS-RH11-0799). Based on the single thermocouple measurement, the clean tube surface temperatures were nominally 1540 °F (838 °C), with the surface temperature decreasing to 1190 °F (644 °C) as ash deposits developed and adjustments were made to the process air flow rate. Attempts to sootblow the CAH tube bank are evident in the data as step increases in surface temperature. The general decline in measured surface temperature over the initial 120 hr of coal firing demonstrates that the sootblowing approach used during this test was not effective. However, the surface temperature data during the last 50+ hr of coal firing indicate that an equilibrium may have been reached and that continued sootblowing would have maintained surface temperatures in the range of 1190 to 1280 °F (644 to 694 °C).

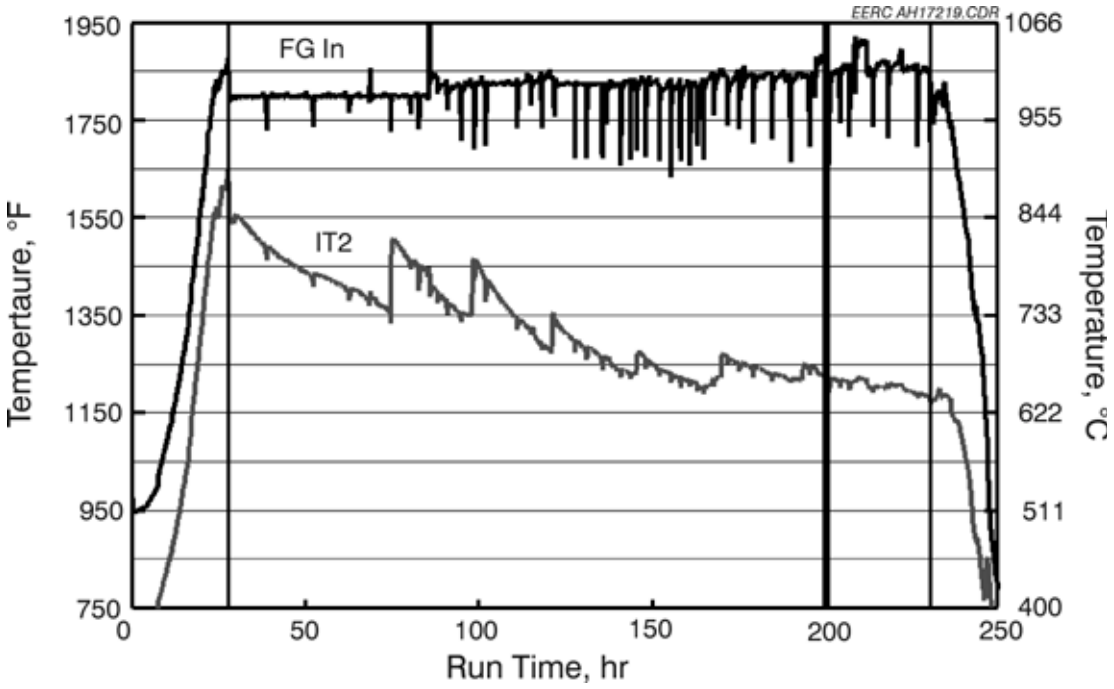

Exhibit 11-32
CAH Tube Surface and Flue Gas Temperatures versus Run Time for SFS Test SFS-RH11-0799

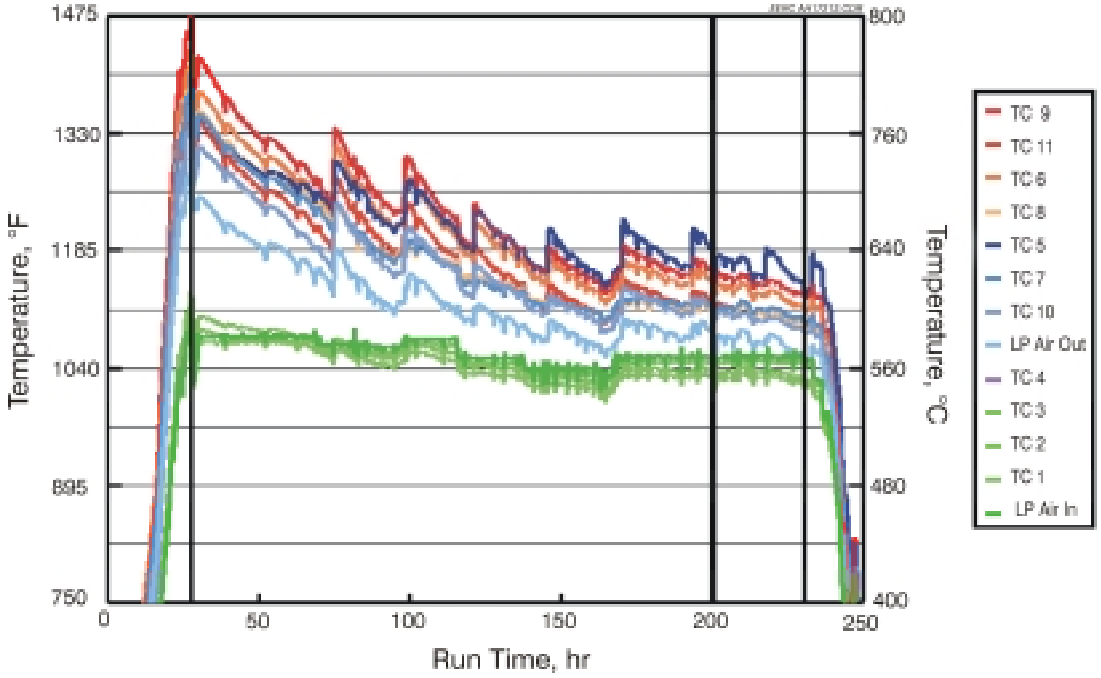

Exhibit 11-33
CAH Process Air Temperatures versus Run Time for SFS Test SFS-RH11-0799

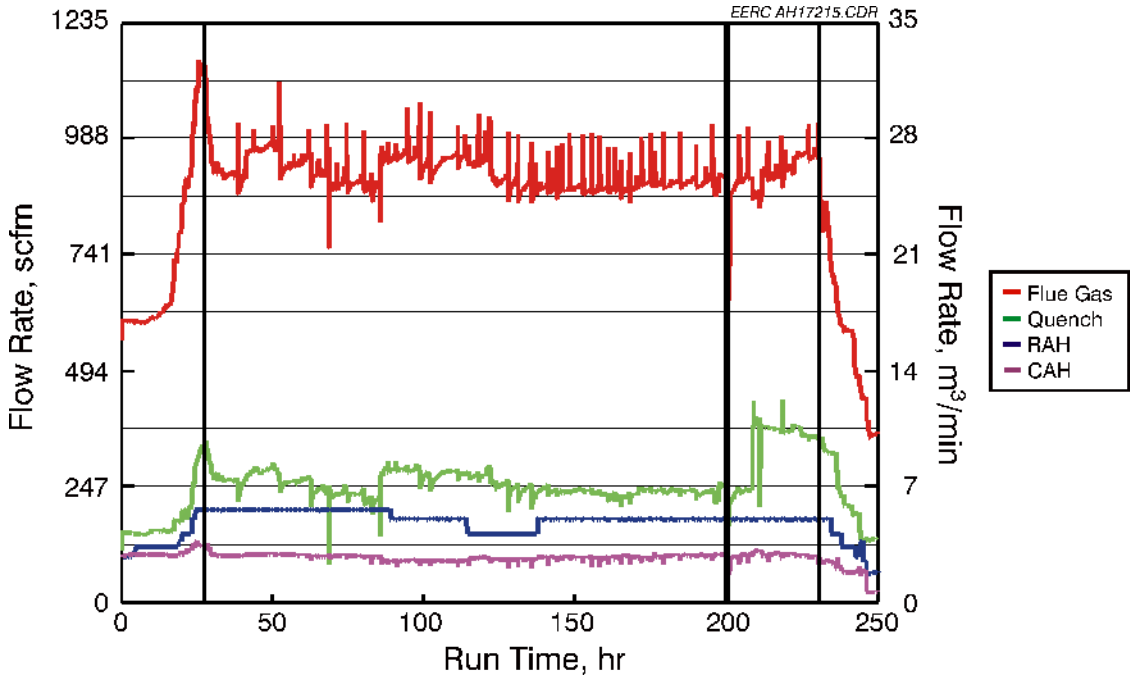

Exhibit 11-34
CAH Process Air, RAH Process Air, Quench Gas, and Flue Gas Flow Rates versus Run Time for SFS Test SFS-RH11-0799

While natural gas was fired and the tubes were clean (prior to coal firing), heat recovery from the CAH tube bank was roughly 40,000 Btu/h (42,200 kJ/hr). This result was observed for the following conditions:

- Process air flow rate of 120 scfm (3.4 m^3/min) at 150 psig (10.3 bar)
- Inlet process air temperature of 1090 °F (588 °C)
- Outlet process air temperature of 1245 °F (674 °C)
- Flue gas temperature of 1800 °F (982 °C) entering the CAH tube bank

Exhibit 11-35 presents heat recovery in the CAH as a function of run time for SFS Test SFS-RH11-0799.

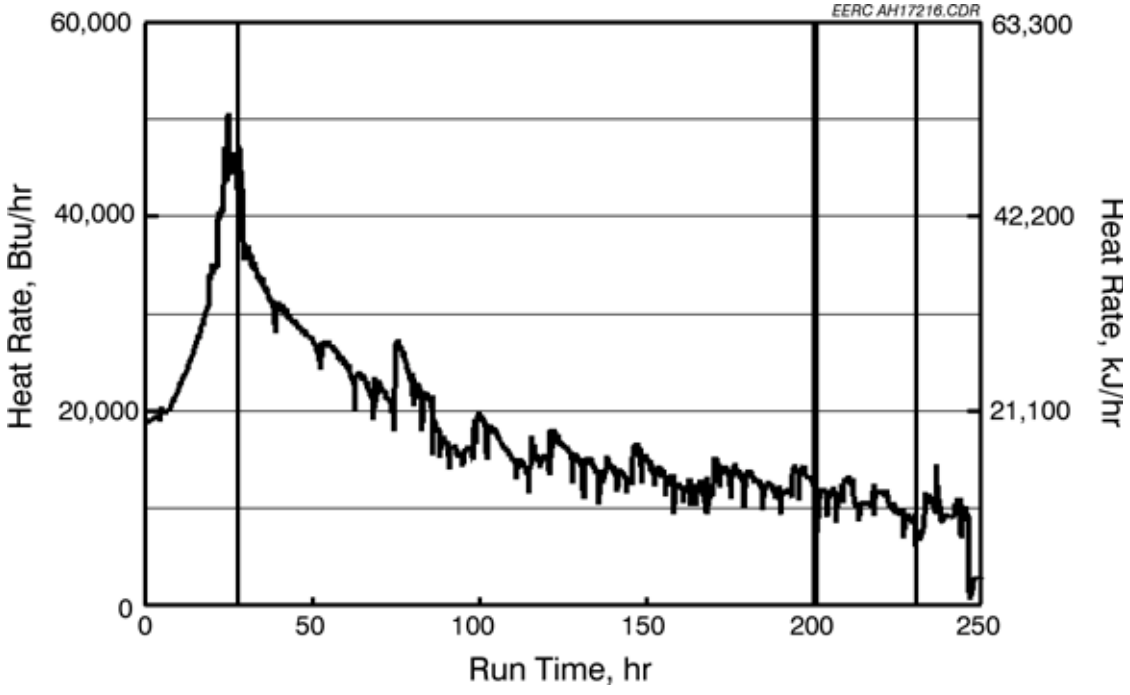

Exhibit 11-35
CAH Heat Recovery versus Run Time for SFS Test SFS-RH11-0799

When coal firing began, surface temperatures initially decreased at a rate of nominally 4.5 °F/hr (2.5 °C/hr) over nearly 25 hr as ash deposits developed on the surface of the tubes. After 45 hr of coal firing, an attempt was made to sootblow the CAH tube bank. As a result, the tube surface temperature increased from 1355 °F (735 °C) to 1505 °F (819 °C), and the heat recovery rate increased from 20,000 Btu/h (21,100 kJ/hr) to 27,300 Btu/h (28,802 kJ/hr). After an additional 24 hr of coal firing, CAH sootblowing was repeated. A tube surface temperature increase was again observed, 1345 °F (730 °C) to 1460 °F (794 °C). However, the heat recovery rate increase, 16,200 Btu/h (17,091 kJ/hr) to 19,400 Btu/h (20,467 kJ/hr), was lower because it was necessary to reduce the process air flow rate (103 to 90 scfm [2.9 to 2.5 m^3/min]) in order to maintain process air temperature in support of RAH operation. Based on the data in Exhibit 11-35, it appears that sootblowing should have begun after 4–8 hr of coal firing and repeated every 4–8 hr

in order to maintain a heat recovery rate in the CAH tube bank of >30,000 Btu/h (>31,650 kJ/hr).

Because of the attempts to sootblow the CAH tube bank during this test and previous characterization of CAH ash deposits resulting from Illinois No. 6 coal-fired tests, CAH ash deposits were not collected for characterization following the test. The deposits that formed were limited to the leading and trailing edges of the tubes. Exhibit 11-36 presents a photograph of the ash deposits on the surface of the tubes following the test. The photograph shows substantial leading- and trailing-edge deposits. However, CAH tube bank plugging was not a problem. No deposits were observed bridging the flue gas paths between the tubes. However, these deposits did bridge areas between the tubes in the direction of the flue gas flow.

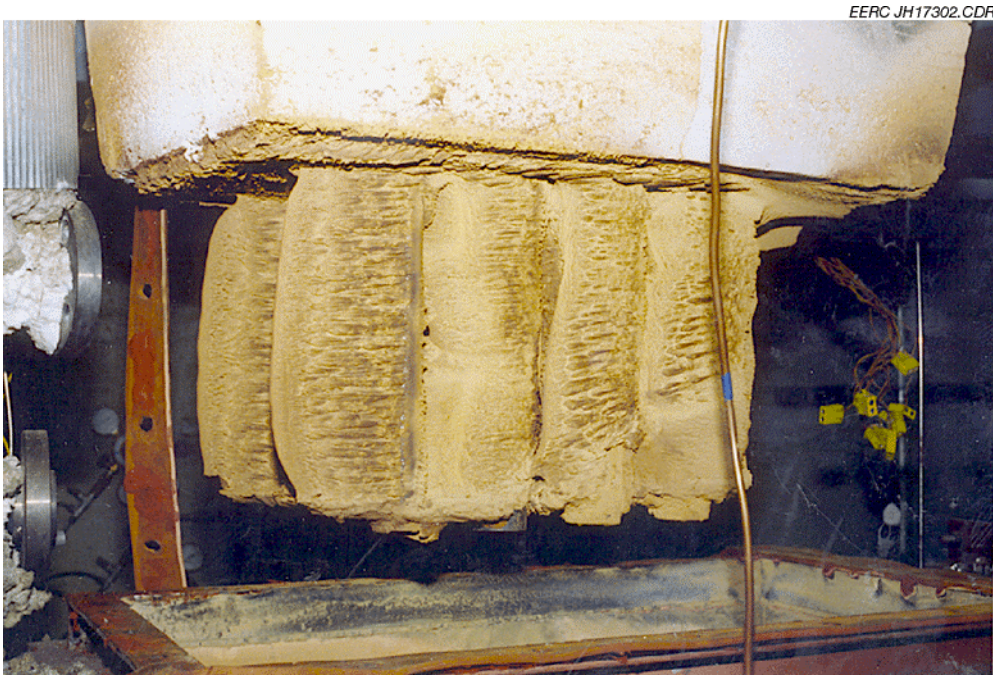

Exhibit 11-36
Photograph of Ash Deposits on the CAH Tubes Following SFS Test SFS-RH11-0799 Firing Illinois No. 6 Bituminous Coal

Deposit strength is a function of ash chemistry, particle size, and temperature history. The relative strength of the deposits is indicated by the fact that the deposits remained intact when the CAH tube bank was removed from the duct. This observation is consistent with results from other tests firing Illinois No. 6 bituminous coal. The total weight of the deposits collected from the CAH tubes and duct was 165 lb (74.9 kg). The total weight of the deposits collected from the CAH tubes was 24 lb (11 kg). On a mass-per-unit-time basis, the ash deposition rate for this Illinois No. 6 coal-fired test would be 0.12 lb/hr (54.5 g/hr) of coal firing. Incorporating the surface area of the tube bank (6.28 ft^2 or 0.58 m^2) results in a value of 0.019 lb/hr-ft^2 (93.97 g/hr-m^2). On a coal-firing-rate basis, the CAH ash deposition rate would be 0.06 lb/MMBtu (25.9 g/10^6 kJ). These values are higher than those observed for Illinois No. 6 coal-fired tests in September 1998

and May 1999. The higher ash deposition rate observed in December 1999 is believed to result from lower slag screen efficiency. Slag screen efficiency was lower because there were only nine tubes present versus 18 tubes typically used during tests firing Illinois No. 6 coal.

Exhibit 11-37 illustrates CAH heat recovery for a SFS test firing Illinois No. 6 coal completed prior to the installation of fins on the tubes. In this case, as ash deposits developed on the tube surfaces, surface temperatures initially decreased at a rate of nominally 15 °F/hr (8 °C/hr). After roughly 20 hr of coal firing, that rate dropped to about 8 °F/hr (4 °C/hr). Overall heat recovery from the CAH tube bank decreased from roughly 40,000 Btu/h (42,200 kJ/hr) to 10,000 Btu/h (10,550 kJ/hr). These and similar data are the basis for the observation stated early concerning improved CAH heat recovery while firing coal with the addition of fins to the leading and trailing edges of the tubes. The fins appear to reduce the rate of heat-transfer degradation as ash deposits develop and help to maintain a higher heat-transfer rate once the deposits have formed. However, no improvement in heat recovery was observed while firing natural gas with clean tube surfaces.

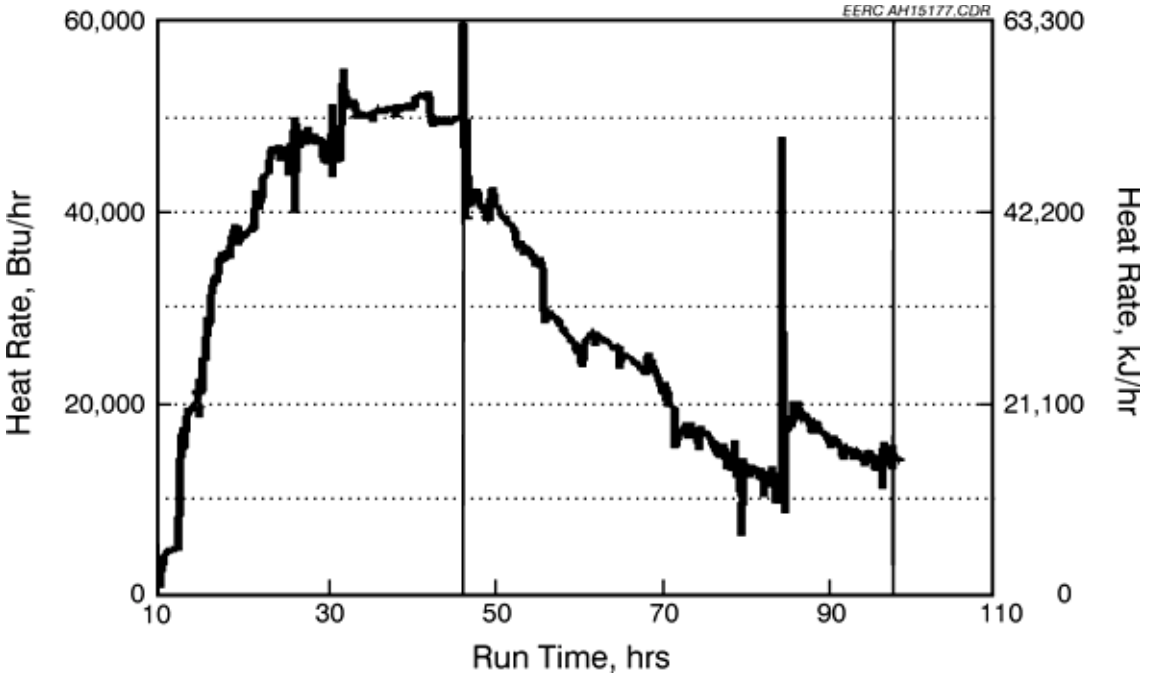

Exhibit 11-37
CAH Heat Recovery versus Run Time for SFS Test SFS-RH3-0198

Table 11-12 summarizes ash composition data for a leading-edge CAH ash deposit as well as fuel, slag, and baghouse ash for an Illinois No. 6 coal-fired SFS test (SFS-RH3-0198). The compositions of the deposits that formed on the air-cooled tubes are dominated by larger particles showing some depletion in alumina and iron and, possibly, some limited enrichment in silica.

The deposits on the tube surfaces grew directly into the gas flow, forming a very thin fin with an apex several inches from the tube. Although this deposit shape is common in utility boilers when high-calcium subbituminous coals are burned, it is not common for bituminous coal deposits. Exhibit 11-38 is a backscattered SEM photograph of a polished cross section of one of the CAH deposits. Exhibit 11-39 is a higher-magnification micrograph of some of the brighter inclusions in the deposits. The elemental compositions of the marked points on the two micrographs are given in Table 11-13.

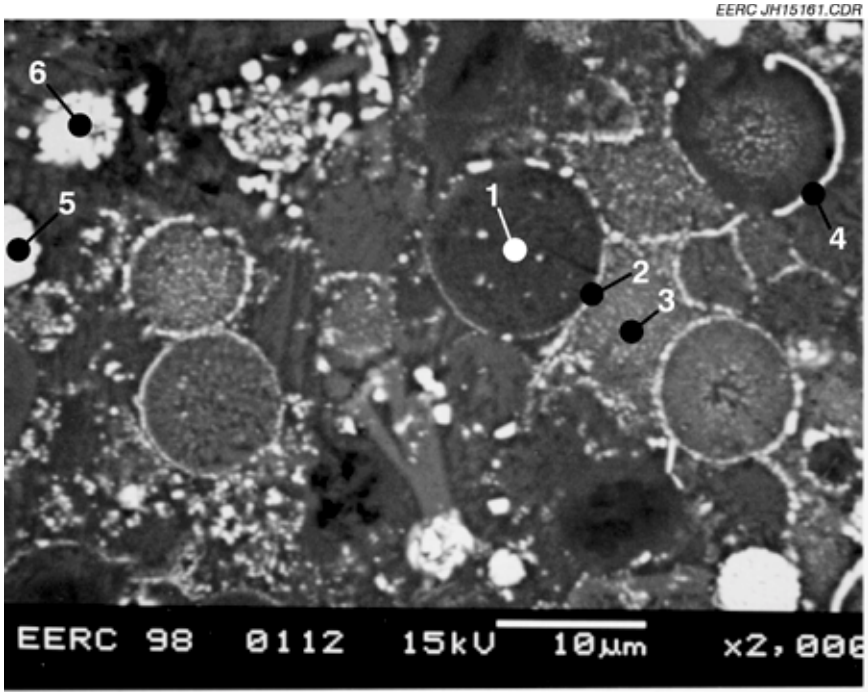

Exhibit 11-38
Backscattered Electron Micrograph of a Polished Cross Section of One of the CAH Deposits from an Illinois No. 6 Coal-fired Test

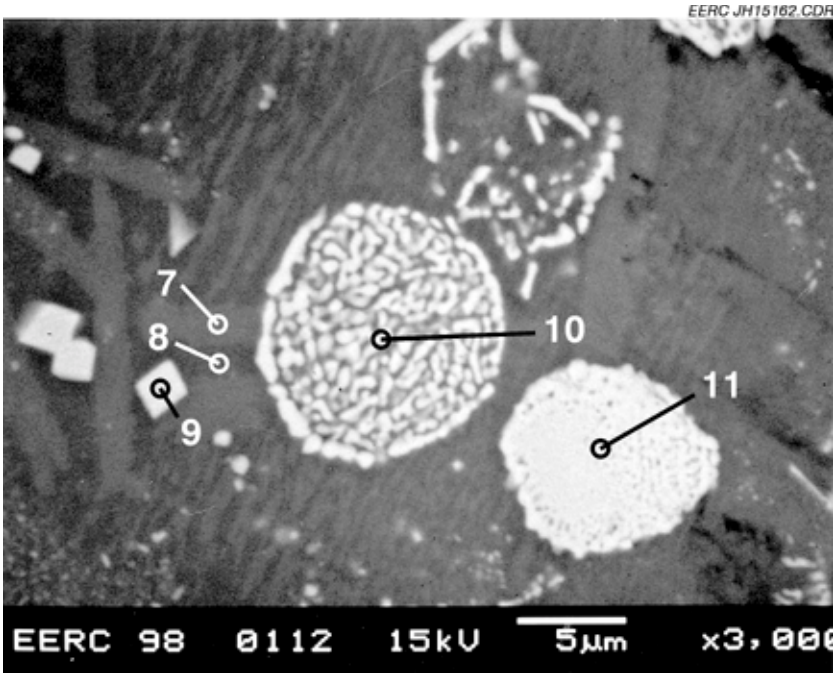

Exhibit 11-39
A Higher Magnification of Some of the Brighter Inclusions in the Deposits

Table 11-12
XRF Analysis Results for Fuel, Slag, and Ash Samples Collected During a SFS Test Firing Illinois No. 6 Coal

Oxides,[1] wt%	Illinois No. 6 Coal Composite	Slag Pot Composite	CAH Leading Edge	Baghouse Ash Composite
SiO_2	54.4	54.8	54.5	51.7
Al_2O_3	21.3	19.8	19.4	20.4
Fe_2O_3	14.7	16.5	14.4	16.4
TiO_2	0.9	0.9	1.1	1.2
P_2O_5	0.1	0.1	0.2	0.6
CaO	3.6	3.6	5.5	3.7
MgO	1.6	1.2	1.3	1.5
Na_2O	1.2	1.1	1.3	1.6
K_2O	2.1	2.1	2.3	2.9
SO_3[2]	–	0.5	0.2	3.8

[1] Oxide concentrations normalized to an SO_3-free basis.

[2] SO_3 concentrations normalized with other oxides.

Table 11-13
Composition of Points Marked in Exhibits 11-38 and 11-39, atom %

Point No.	O	Na	Mg	Al	Si	S	K	Ca	Ti	Fe
1	59	0	0	17	20	0	2	0	0	1
2	57	1	1	13	16	0	1	3	1	8
3	56	2	1	13	20	0	0	4	1	4
4	59	1	0	10	22	0	2	0	0	6
5	48	1	1	3	1	0	0	0	1	46
6	57	1	1	5	12	0	1	0	10	12
7	58	0	0	14	19	0	0	7	0	1
8	61	1	1	7	25	0	2	2	0	1
9	47	3	3	4	3	0	0	1	3	37
10	49	2	1	6	8	0	0	1	1	32
11	48	2	0	3	4	0	0	0	0	42

The data in the table are presented on a mole or atom percent basis rather than an oxide weight percent basis to make it easier to determine the oxidation state of the material.

The exhibits and table show that the deposits are composed primarily of ash particles with diameters less than 10 μm along with a secondary aluminosilicate-rich melt phase. Unlike deposits formed during tests with a high-calcium subbituminous coal, the Illinois No. 6 deposits do not contain any sulfur-rich material. The small size of the particles is similar to that of the particles that typically make up deposits formed when a high-calcium coal is fired and indicates why they have the shape that they do. Particles in this size range usually do not separate significantly from the gas stream and so tend to form only very thin, finlike deposits. In a utility boiler firing a bituminous coal, the deposits are usually bombarded with larger ash particles that tend to spread out the deposit. However, because of the slag screen and dilution/quench zone in the SFS, the larger particles are mostly removed, leaving only the small particles to make up the deposit, hence causing the shape of the deposit to become finlike.

The dominant composition of the particles in the deposit is similar to that of Points 1 and 3, i.e., aluminosilicates derived from kaolin and montmorillonite clays that have sintered and formed secondary iron and sometimes calcium-rich phases at the particle interfaces. The general composition of this interface material falls near a eutectic composition in the $FeO–SiO_2$–anorthite ($CaO–Al_2O_3–2SiO_2$) phase diagram with a melting point of 1960 °F (1071 °C).

Exhibit 11-39 shows more clearly some of the iron-rich species, derived from iron oxide-rich particles left from the oxidation of pyrite, such as Points 10 and 11. It also shows secondary crystals formed from the melt that are rich in iron and titanium (Point 9)

as well as anorthite (Point 7). Exhibit 11-40 shows an x-ray map of the same field as that of Exhibit 11-39, which shows the general distribution of the elements within the area. The figure indicates that silicon and aluminum are distributed widely throughout the matrix, with iron primarily concentrating in small areas and calcium somewhat concentrated in what appear to be anorthite crystals. X-ray diffraction analysis shows that the only major crystalline materials in the deposits are hematite (Fe_2O_3), although the SEM analyses indicate that FeO is more likely, and plagioclase feldspar, for which anorthite is one end member. Minor species include quartz (SiO_2) and mullite ($3Al_2O_3$–$2SiO_2$). This implies that the great mass of the deposits is aluminosilicate glass that does not strongly diffract x-rays. With time, deposits of this composition and size distribution of particles could sinter more completely and become quite hard and difficult to remove. However, over the length of this test, the deposit was very porous and, although stronger than the deposits formed during subbituminous coal tests, was weak enough that it should be easily removed with a sootblower.

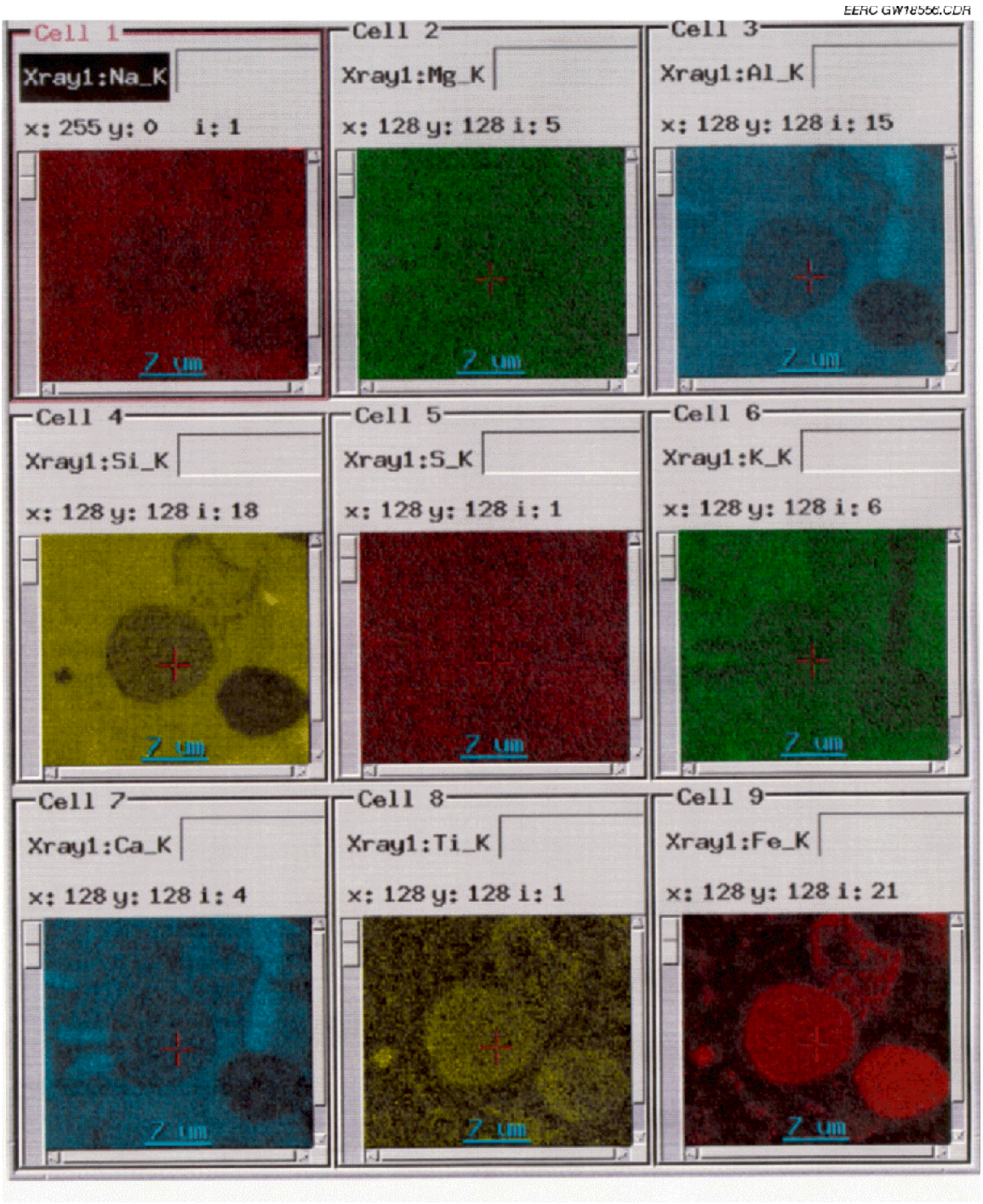

Exhibit 11-40
An X-ray Map of the Same Field as That of Exhibit 11-39 That Shows the General Distribution of the Elements Within That Area

Operation with Subbituminous Coal

As an example of operating data when firing a subbituminous coal, Exhibits 11-41 through 11-43 summarize CAH tube bank surface and flue gas temperatures, process air temperatures, and process air flow rate data for a SFS test (SFS-RH12-0200) completed in March 2000. During this test a Powder River Basin subbituminous coal from the Cordero Rojo mine was fired. On the basis of a single thermocouple measurement, the clean tube surface temperatures were nominally 1580 °F (860 °C). During the March 2000 SFS test, the EERC began sootblowing after 8 hr of coal firing and then repeated sootblowing every 8 hr for the duration of the test. The components of the sootblowing system and methodology used have been previously described.

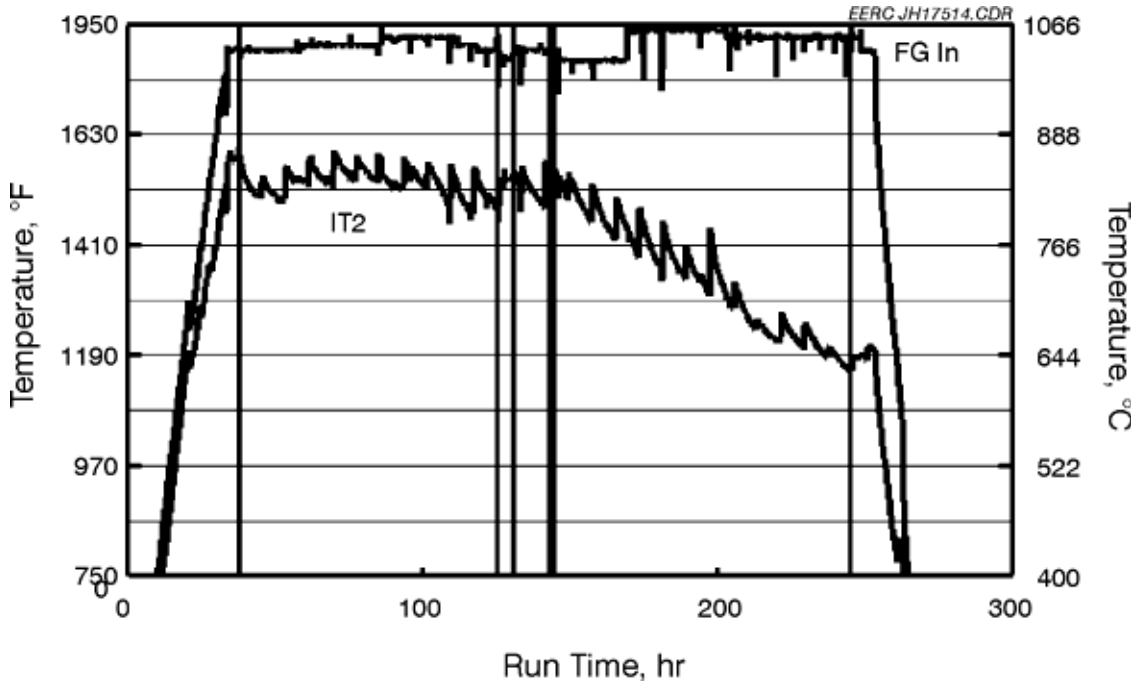

Exhibit 11-41
CAH Tube Surface and Flue Gas Temperatures versus Run Time for SFS Test SFS-RH112-0200

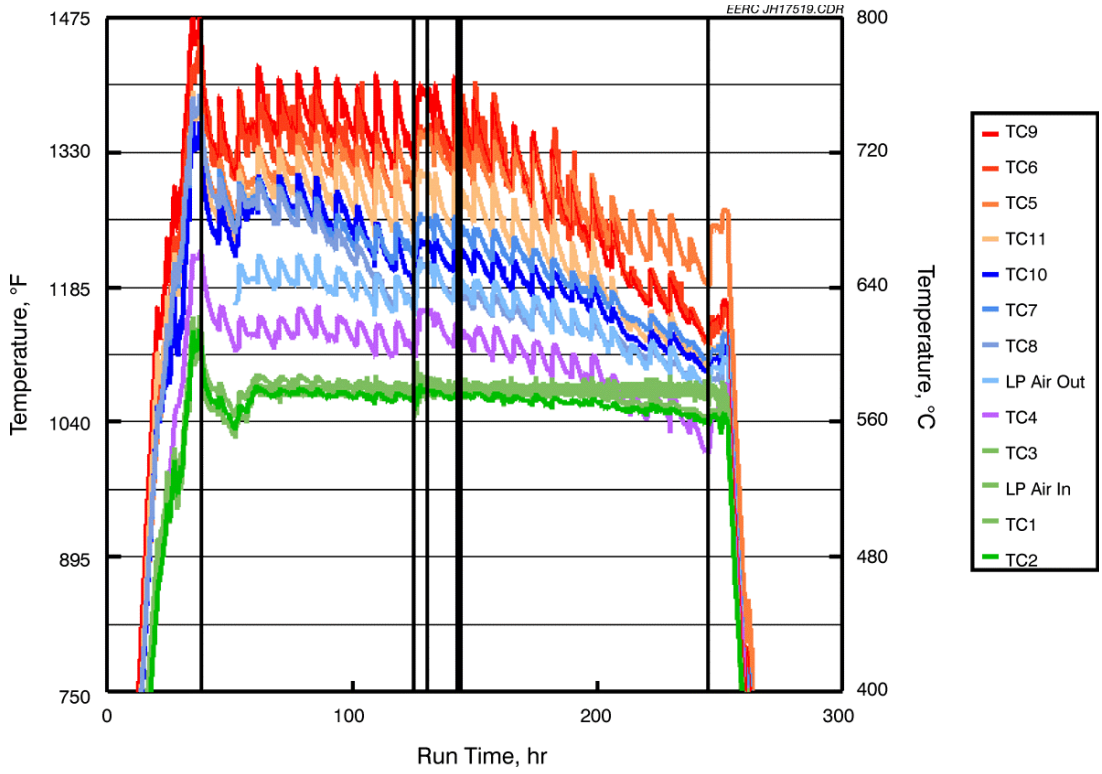

Exhibit 11-42
CAH Process Air Temperatures versus Run Time for the SFS Test SFS-RH12-0200

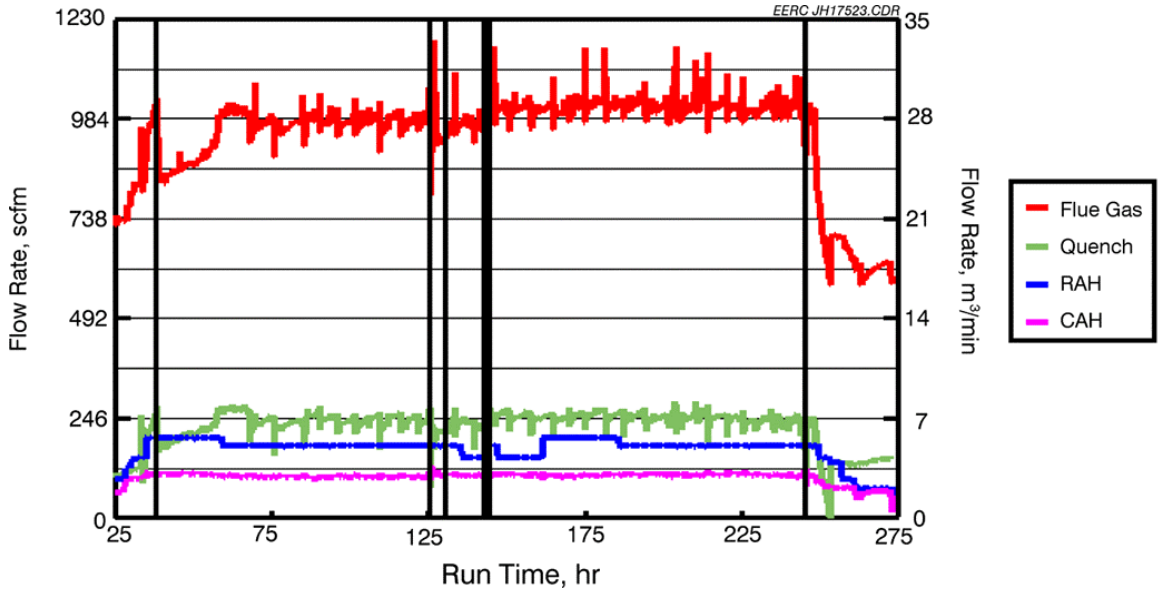

Exhibit 11-43
CAH Process Air, RAH Process Air, Quench Gas, and Flue Gas Flow Rates versus Run Time for SFS Test SFS-RH12-0200

As a result of the sootblowing approach employed, the surface temperature remained relatively stable in the range of 1470 to 1580 °F (799 to 860 °C) during the first 100 hr of coal firing. However, after a short natural gas-fired period to repair the coal feeder, the tube surface temperature gradually decreased to 1160 °F (627 °C) over the final 100 hr of coal firing. This decrease occurred even though sootblowing was repeated every 8 hr. Process air flow rate adjustments were limited during the test, resulting in flow rates of 100–110 scfm (2.8–3.1 m^3/min). Attempts to sootblow the CAH tube bank are evident as step increases in the tube surface and process air temperature data as well the heat recovery data. A hypothesis is not available at this time to explain why the sootblowing approach was initially effective in controlling tube surface temperature but became less effective after 100 hr of coal firing and the short natural gas-fired period.

While natural gas was fired and the tubes were clean, heat recovery from the CAH tube bank was roughly 38,000 Btu/hr (40,090 kJ/hr), comparable to other SFS tests. This result was observed for the following conditions:

- Process air flow rate of 110 scfm (3.1 m^3/min) at 150 psig (10.3 bar)
- Inlet process air temperature of 1110 °F (599 °C)
- Outlet process air temperature of 1310 °F (710 °C)
- Flue gas temperature of 1800 °F (983 °C) entering the CAH tube bank

Exhibit 11-44 presents heat recovery in the CAH as a function of run time for the test.

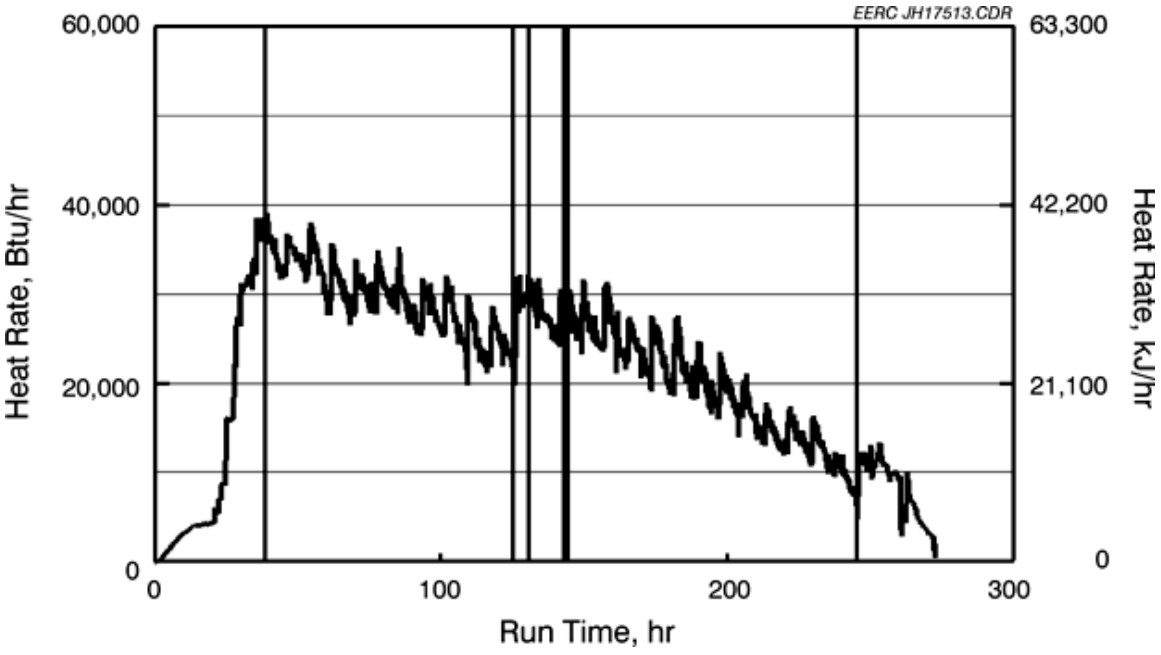

Exhibit 11-44
CAH Heat Recovery versus Run Time for SFS Test SFS-RH12-0200

Once coal firing was stabilized, CAH heat recovery was initially 36,150 Btu/hr (38,138 kJ/hr) and decreased as ash deposits developed on the surface of the tubes. After 8 hr of coal firing, CAH heat recovery had decreased to 32,115 Btu/hr (33,881 kJ/hr) and sootblowing was attempted. This first attempt to sootblow the CAH tubes effectively restored heat recovery. CAH heat recovery was effectively controlled in this range for roughly 50 hr, or six sootblowing cycles, before heat recovery began to degrade over a 24-hr period. An increase in the flue gas recirculation rate in the dilution/quench zone and total flue gas flow rate through the CAH tube bank stabilized heat recovery for about 24 hr. However, during the last 100 hr of coal firing, CAH heat recovery continued to degrade, consistent with the tube surface temperature observed. Although each sootblowing event resulted in an increase in tube surface temperature and heat recovery, after 200 hr of coal firing, heat recovery in the CAH degraded to nominally 10,000 Btu/hr (10,550 kJ/hr). The overall degradation of CAH heat recovery during the March 2000 test indicates that the sootblowing approach employed was not adequate. The data in Exhibit 11-44 indicate that more frequent sootblowing should improve CAH heat recovery, but there is no guarantee that the degradation in heat recovery observed during this test would not recur. Sootblowing every 4 hr when a subbituminous coal is fired should be attempted in the future if the opportunity occurs. Improved sootblowing effectiveness may require a modification to the methodology employed to increase the tube surface area affected by each sootblowing event.

As with the other fuels fired in the SFS, data support the conclusion that the addition of the fins to the air-cooled tubes improves heat recovery during the coal-fired test periods. The fins appear to reduce the rate of heat-transfer degradation as ash deposits develop and help to maintain a higher heat-transfer rate once the deposits have formed. However, no improvement in heat recovery was observed during the natural gas-fired periods with clean tube surfaces.

Because of the attempts to sootblow the CAH tube bank during the March 2000 test and previous characterization of CAH ash deposits resulting from a subbituminous coal-fired test, CAH ash deposits were not collected for characterization following the March 2000 test. The deposits that formed were generally limited to the leading and trailing edges of the tubes. Exhibit 11-45 presents photographs of ash deposits on the surface of the tubes following the March 2000 test. The top photograph shows three uncooled tubes that were free of ash deposits as a result of sootblowing efforts. The sidewall of one air-cooled tube is partially visible, indicating a degree of sootblowing effectiveness. The bottom photograph shows an uncooled tube with a clean trailing edge as well as two air-cooled finned tubes with roughly one-third of their surfaces cleaned to a degree. These photographs support the observed need for greater sootblower coverage. Substantial leading- and trailing-edge deposits are visible in both photographs. However, CAH tube bank plugging was not a problem. No deposits were observed bridging the flue gas path between the tubes.

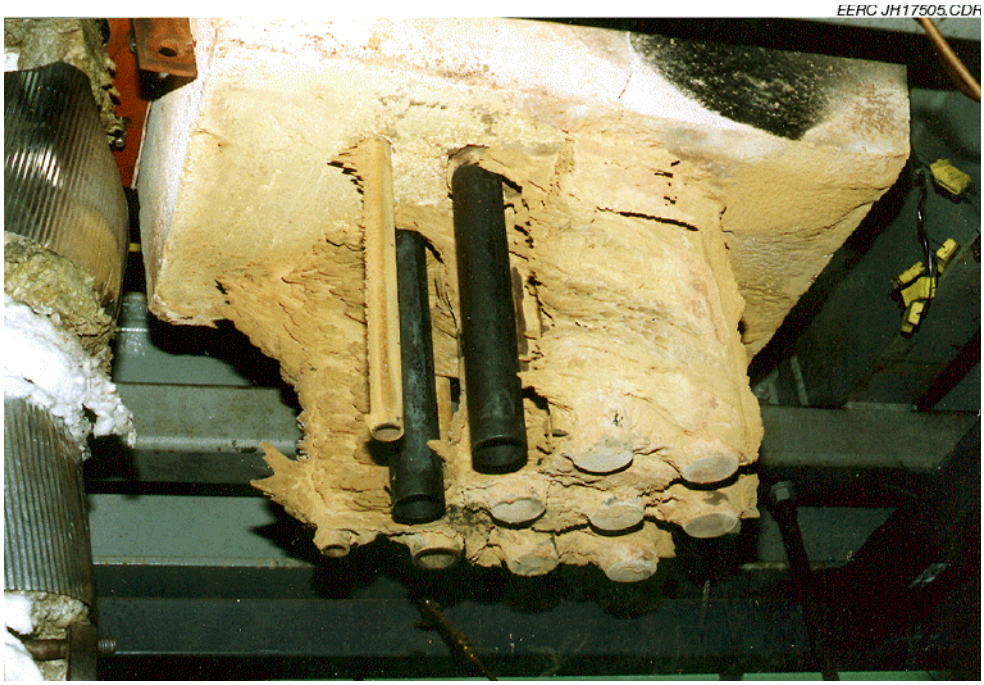

Exhibit 11-45
Photographs of Ash Deposits on the CAH Tubes Following the March 2000 Test Firing Cordero Rojo Subbituminous Coal

Deposit strength is a function of ash chemistry, particle size, and temperature history. The relative strength of the deposits is indicated by the fact that the deposits remained intact when the tube bank was removed from the duct. This observation is consistent with results from previous tests with other fuel types. However, a direct comparison with a previous subbituminous coal-fired test is not possible because of differences in test duration and the presence of fins on the CAH tubes during the March 2000 test. The total weight of the deposits collected from the CAH tubes and duct was 55 lb (25 kg). The total weight of the deposits collected from the CAH tubes was 21 lb (9.5 kg). On a mass-per-unit-time basis, the ash deposition rate on the CAH tubes would be 0.10 lb/hr (45.4 g/hr) of coal firing. Incorporating the surface area of the tube bank (6.28 ft^2, or 0.58 m^2) results in a value of 0.017 lb/hr-ft^2 (78.3 g/hr-m^2). On a coal-firing-rate basis, the CAH ash deposition rate would be 0.04 lb/MMBtu (18.2 g/10^6 kJ). Although a comparison with a previous subbituminous coal-fired test is not possible, a comparison with Illinois No. 6 coal-fired tests indicates similar ash deposition rates based on the ash content and heating value of the fuel. On a lb/MMBtu (g/10^6 kJ) basis, the ash content of the Cordero Rojo coal was 62% of that observed for the Illinois No. 6 coal. Calculated ash deposition rates for the March 2000 test firing the Cordero Rojo coal were nominally 66% of those calculated for the Illinois No. 6 coal-fired test completed in December 1999. However, the relative value of this comparison is limited because the slag screen configuration was different (18 tubes in March 2000 versus nine tubes in December 1999) as was the approach to CAH sootblowing (8-hr frequency in March versus 24 hr in December). Comparisons with other SFS tests are not appropriate because sootblowing of the CAH tube bank was only routinely used during tests completed in December 1999, March 2000, and June 2000.

Exhibit 11-46 illustrates CAH heat recovery for a SFS test (firing a subbituminous coal) completed prior to the installation of fins on the tubes. In this case, as ash deposits developed on the tube surfaces, surface temperatures initially decreased at a rate of nominally 25 °F/hr (14 °C/hr). After roughly 20 hr of coal firing, that rate dropped to about 5 °F/hr (3 °C/hr). Overall heat recovery from the CAH tube bank decreased from roughly 31,200 Btu/hr (32,916 kJ/hr) to 11,500 Btu/hr (12,132 kJ/hr). These and similar data are the basis for the observation stated early concerning improved CAH heat recovery while firing coal with the addition of fins to the leading and trailing edges of the tubes. The fins appear to reduce the rate of heat-transfer degradation as ash deposits develop and help to maintain a higher heat-transfer rate once the deposits have formed. However, no improvement in heat recovery was observed while firing natural gas with clean tube surfaces.

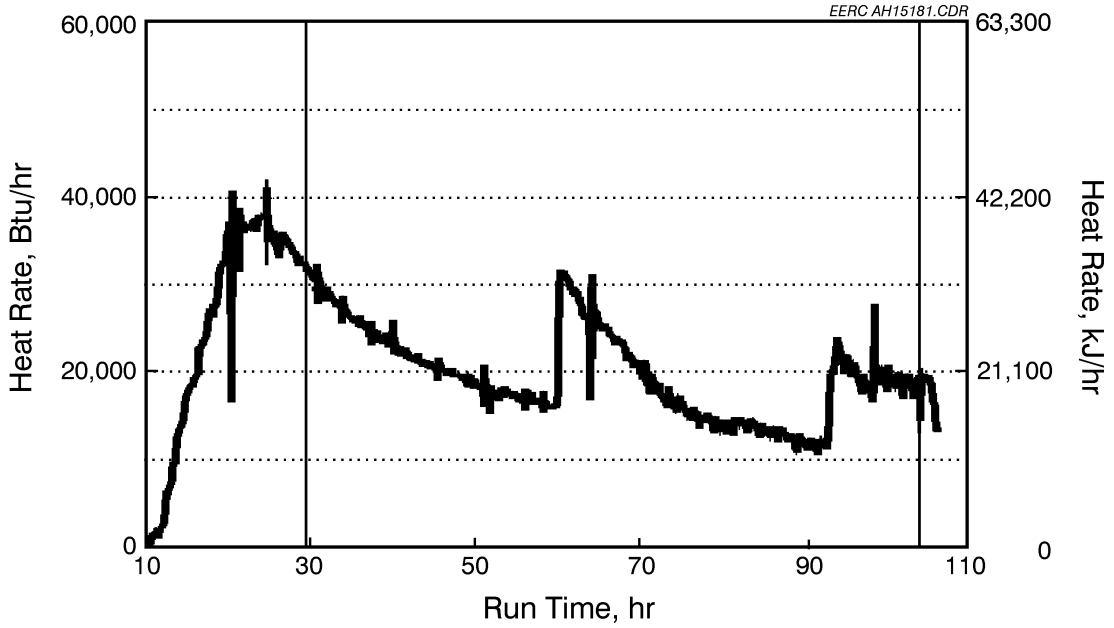

Exhibit 11-46
CAH Heat Recovery versus Run Time for SFS Test SFS-RH4-0298

Table 11-14 shows the composition of the original coal ash as compared to deposits formed on the air-cooled alloy surfaces in the CAH tube bank as a result of firing a subbituminous coal in the SFS in October 1997 (SFS-RS1-0297). The data are presented on a normalized SO_3-free basis, with SO_3 content added for comparison. The as-measured closure of the analytical data is also included to indicate the relative accuracy of the analyses. The relatively low silica and high calcia concentrations in the CAH deposits as compared to the bulk coal ash indicate that they are composed of smaller ash particles than the bulk fuel ash. The relatively uniform compositions of the CAH deposits indicate that they are composed of similar-size particles, because larger particles are usually more enriched in silica than smaller particles.

In a typical pc-fired utility boiler, different types of deposits usually are composed of different ash particle sizes because they form from differing depositional processes such as inertial impaction (leading-edge deposits), eddy deposition (trailing-edge deposits), or thermophoresis (inner layer of air-cooled alloy tube deposit). Therefore, the uniformity in the SFS deposits is in contrast to deposits formed on steam tubes in the front or higher-temperature region of the convective pass of utility boilers firing Powder River Basin coals. In this region of a utility boiler, larger particles (lower calcium) typically form the outer front deposits, smaller particles (higher calcium) form downstream deposits, and the smallest particles (highest calcium) form the inner layers on cooled tubes. The difference between the deposits formed on these CAH tubes and those found in utility boilers is most likely caused by the removal of the larger particles in the SFS by the slag screen and in the quench zone.

Table 11-14
XRF Analysis Results for Fuel Ash and CAH Ash Samples Collected During a SFS Test Firing a Subbituminous Coal

Oxides,[1] wt%	Rochelle Coal Composite	Leading-Edge Outer Deposit	Leading-Edge Inner Deposit	Trailing-Edge Outer Deposit
SiO_2	31.7	24.4	26.1	27.9
Al_2O_3	18.4	18.6	17.1	18.0
Fe_2O_3	7.5	8.0	8.0	7.3
TiO_2	1.4	1.6	1.6	1.4
P_2O_5	1.1	1.4	1.1	1.5
CaO	28.8	35.8	35.7	33.0
MgO	8.2	7.9	7.5	6.9
Na_2O	1.8	1.1	1.4	2.3
K_2O	0.1	0.1	0.1	0.6
BaO	0.7	0.7	0.8	0.9
SrO	0.3	0.3	0.3	0.3
ZrO_2	0.0	0.1	0.1	0.0
SO_3[2]	15.6	11.9	15.3	25.9
Total Closure	99.4	96.1	95.9	98.8

1 Oxide concentrations normalized to an SO3-free basis.

2 SO3 concentrations normalized with other oxides.

In contrast to the CAH deposits, samples of slag collected from the slag pot, slag tap, and quench zone were all found to have relatively high levels of silica and alumina and reduced levels of calcia as compared to the coal ash. These levels reflect the concentrations typically found in larger ash particles formed during the combustion of Powder River Basin coals. Conversely, the baghouse ash has a slightly lower level of silica and a slightly higher level of calcium, indicating that it is composed of somewhat smaller particles than the bulk ash. Table 11-15 summarizes the composition data for these samples. For this data set, all closures are good except for the slag pot and quench zone samples, which are relatively low for an unknown reason.

Table 11-15
XRF Analysis Results for Fuel Ash, Slag, and Ash Samples Collected During a SFS Test Firing a Subbituminous Coal

Oxides,[1] wt%	Rochelle Coal Composite	Slag Pot Slag	Slag Tap Slag	Quench Zone	Baghouse Ash
SiO_2	31.7	38.5	43.4	38.3	26.6
Al_2O_3	18.4	29.0	19.5	29.6	20.0
Fe_2O_3	7.5	6.9	6.5	7.0	7.3
TiO_2	1.4	1.2	1.3	1.1	1.2
P_2O_5	1.1	0.3	0.4	0.3	1.8
CaO	28.8	18.5	21.0	18.0	32.3
MgO	8.2	3.1	4.5	3.0	7.6
Na_2O	1.8	1.6	2.3	1.8	1.3
K_2O	0.1	0.1	0.2	0.1	0.5
BaO	0.7	0.5	0.5	0.4	0.9
SrO	0.3	0.2	0.2	0.2	0.3
ZrO_2	0.0	0.1	0.1	0.1	0.1
SO_3[2]	15.6	0.1	0.5	0.1	6.5
Total Closure	99.4	87.3	93.4	91.7	99.8

1 Oxide concentrations normalized to an SO3-free basis.

2 SO3 concentrations normalized with other oxides.

Operation with Eastern Kentucky Bituminous Coal

As an example of operating data when firing an eastern Kentucky bituminous coal, Exhibits 11-47 through 11-49 summarize CAH tube bank surface and flue gas temperatures, process air temperatures, and process air flow rate data for SFS Test SFS-RH8-0399. While natural gas was fired and the tubes were clean, heat recovery from the CAH tube bank was roughly 40,000 Btu/hr (42,200 kJ/hr). This result was observed for the following conditions:

- Process air flow rate of 111 scfm (3.1 m^3/min) at 150 psig (10.3 bar)
- Inlet process air temperature of 1080 °F (582 °C)
- Outlet process air temperature of 1270 °F (688 °C)
- Flue gas temperature of 1790 °F (977 °C) entering the CAH tube bank

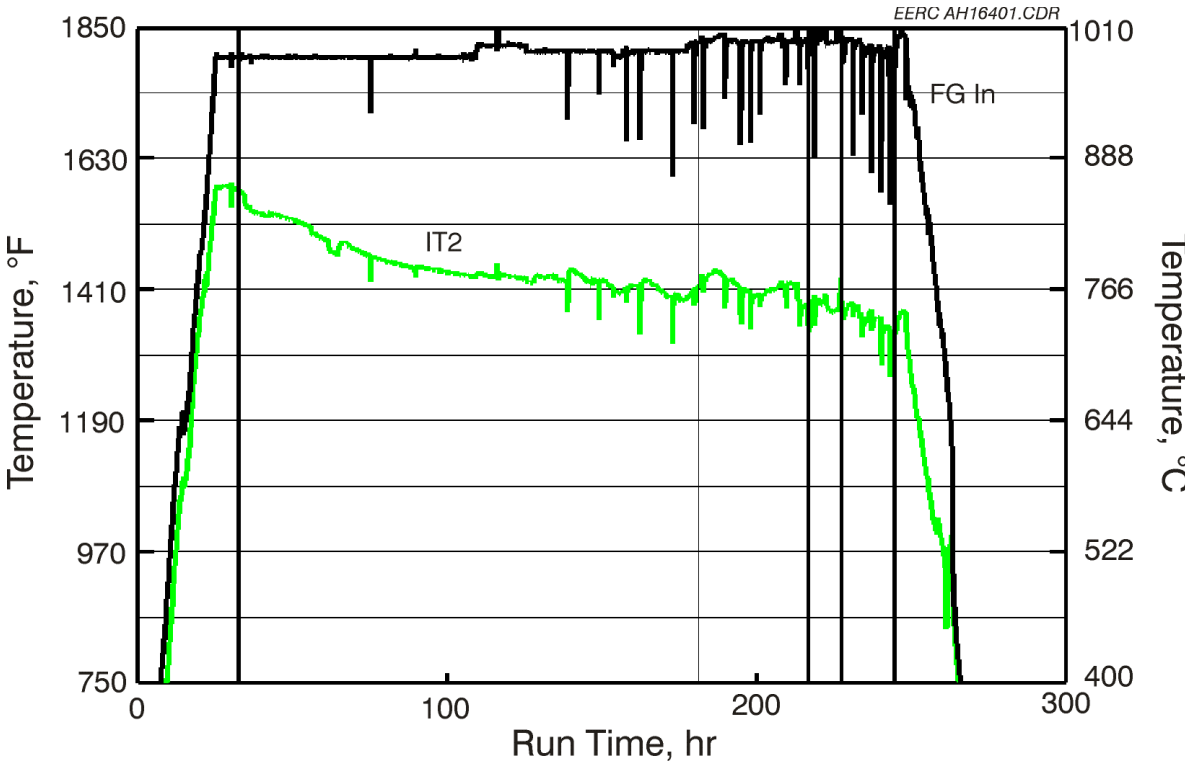

Exhibit 11-47
CAH Tube Surface and Flue Gas Temperatures versus Run Time for SFS Test SFS-RH8-0399

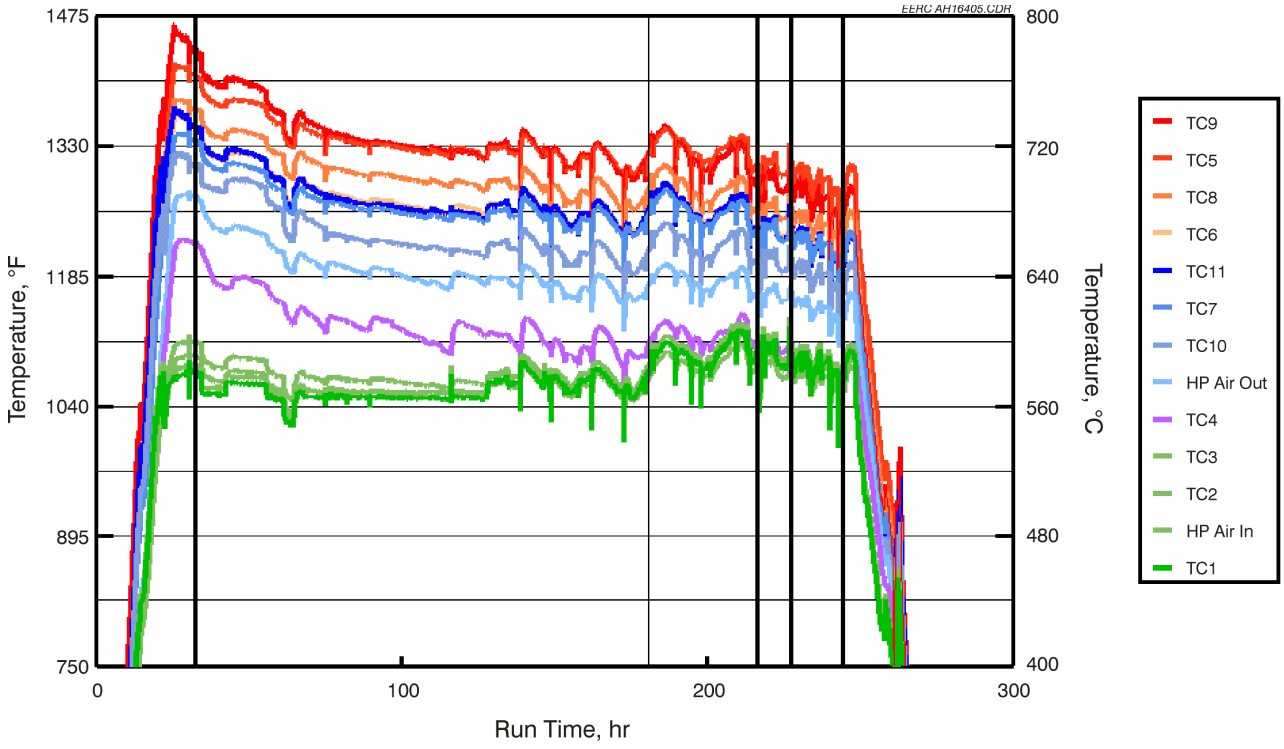

Exhibit 11-48
CAH Process Air Temperatures versus Run Time for SFS Test SFS-RH8-0399

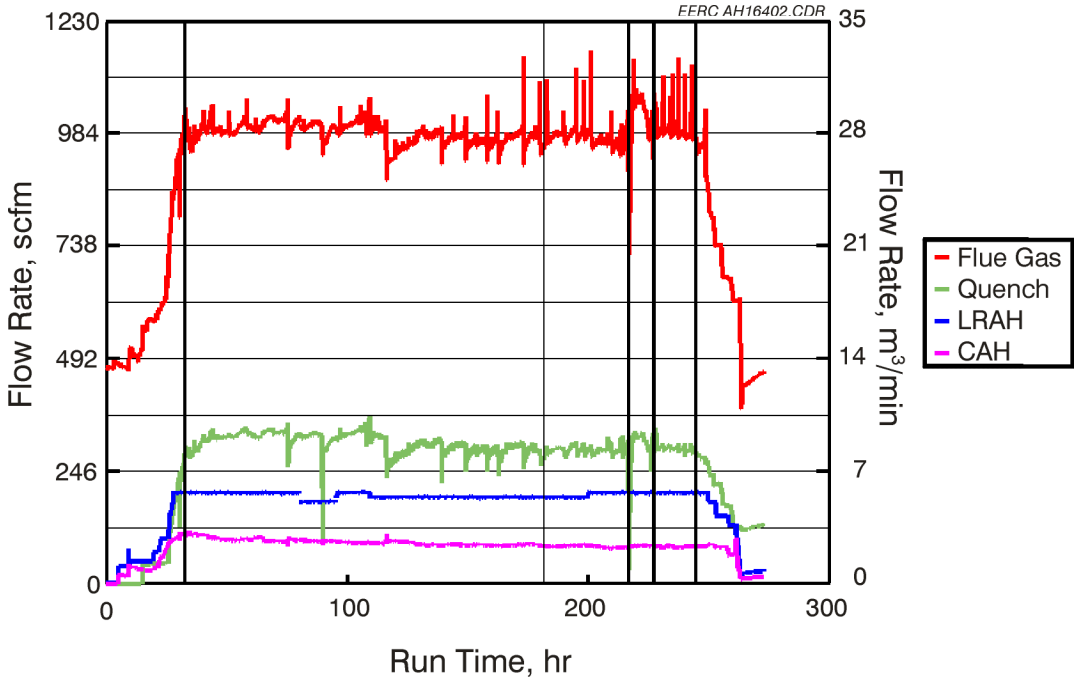

Exhibit 11-49
CAH Process Air, RAH Process Air, Quench Gas, and Flue Gas Flow Rates versus Run Time for SFS Test SFS-RH8-0399

Exhibit 11-50 presents heat recovery in the CAH as a function of run time for SFS Test SFS-RH8-0399.

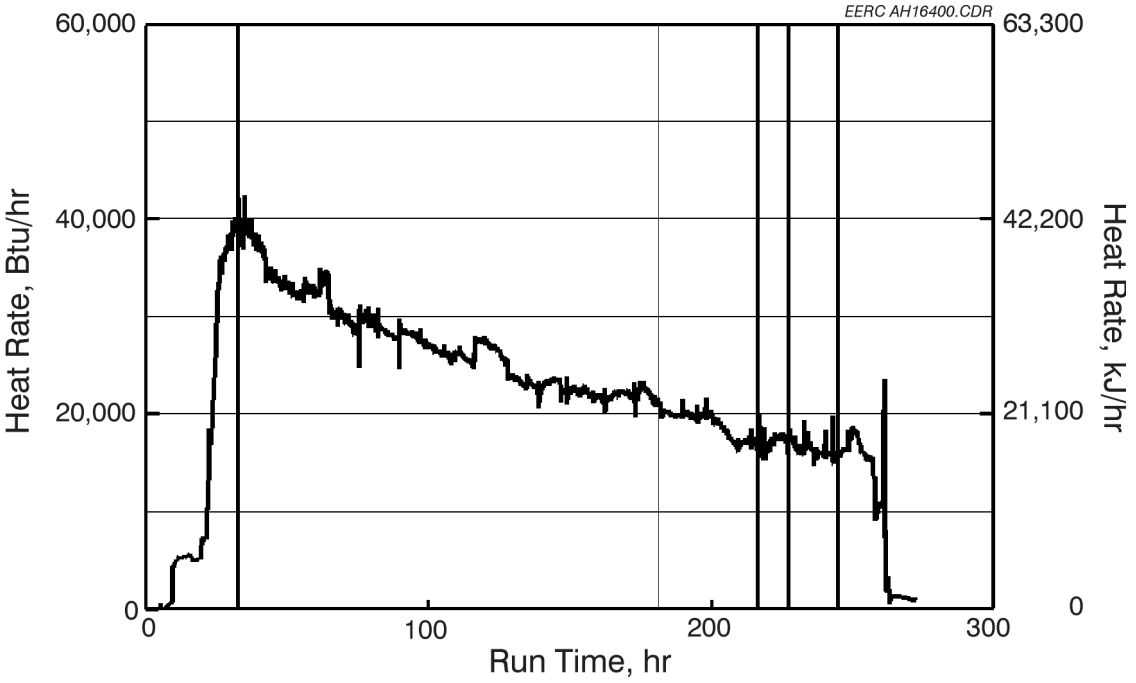

Exhibit 11-50
CAH Heat Recovery versus Run Time for SFS Test SFS-Rh8-0399

When coal firing began, surface temperatures initially decreased at a rate of nominally 5 °F/hr (3 °C/hr) over nearly 10 hr as ash deposits developed on the surface of the tubes. After 40 hr of coal firing, the rate decrease was 0.7 °F/hr (0.4 °C/hr). No further decrease in tube surface temperature was noted, other than changes related to flue gas flow rates, flue gas temperatures, process air flow rates, and process air temperatures, until the eastern Kentucky coal was replaced by the Illinois No. 6 coal. It must be noted that process air flow rates were also decreasing (0.1 scfm/ 0.003 m^3/min) over these time frames in an attempt to maintain a relatively constant process air exit temperature. The minimum process air flow rate through the CAH tube bank was 77 scfm (2.2 m^3/min). As ash deposits developed on the tube surfaces, heat recovery from the CAH tube bank decreased from roughly 40,000 Btu/hr (42,200 kJ/hr) to 21,200 Btu/hr (22,366 kJ/hr) when the eastern Kentucky coal was fired. Heat recovery from the CAH tube bank remained at this level for nearly 42 hours prior to the switch to the Illinois No. 6 coal. One reason for the steady heat recovery rate may have been spontaneous shedding of the ash-fouling deposits from the CAH tubes, as indicated by piles of ash at the bottom of the tubes. CAH ash deposit composition, resulting from eastern Kentucky coal, is discussed later in this report.

Over the final 51 hours of coal firing (Illinois No. 6), the heat recovery from the CAH tube bank decreased and eventually stabilized at 16,000 Btu/hr (16,880 kJ/hr) prior to termination of the coal feed. These data are generally consistent with the other SFS tests firing eastern Kentucky coal as well as Illinois No. 6 coal. A comparison of the results shows a nominal 30% higher heat recovery rate in the CAH tube bank when the eastern Kentucky coal is fired, probably because of its relatively low ash content and spontaneous ash deposit shedding. However, these

data do not address the potential for improved heat recovery for either fuel type as a function of an effective sootblowing system. These data support the conclusion, previously stated, that the addition of the fins to the air-cooled tubes improves heat recovery during the coal-fired test periods.

EERC personnel did not clean the CAH tube bank during SFS Test SFS-RH8-0399, and ash deposits were not characterized, because of the need to switch fuels during the 200-hour test. CAH tube bank plugging was not a problem. No deposits were observed bridging the flue gas path between the tubes. The deposits that formed were limited to the leading and trailing edges of the tubes. However, these deposits did bridge the area between the tubes in the direction of the flue gas flow. Deposit bridging between tubes in the direction of the flue gas flow may have been the result of a longer eastern Kentucky coal-fired period or occurred as a result of firing the Illinois No. 6 coal during the last 51 hours. EERC personnel believe the latter scenario more likely.

Exhibit 11-51 presents a photograph of ash deposits on the surface of the tubes following the April 1999 test. The photograph shows three of the five uncooled tubes as well as two of the seven air-cooled finned tubes. The leading- and trailing-edge deposits are readily visible, with bare metal surfaces visible on the back half of the uncooled tubes. The pieces of tube deposit missing from the photograph of the air-cooled tubes fell off as the tube bank was removed from the duct. Because two different fuels were fired during this test, a discussion of deposit strength, weight, and deposition rate is not warranted.

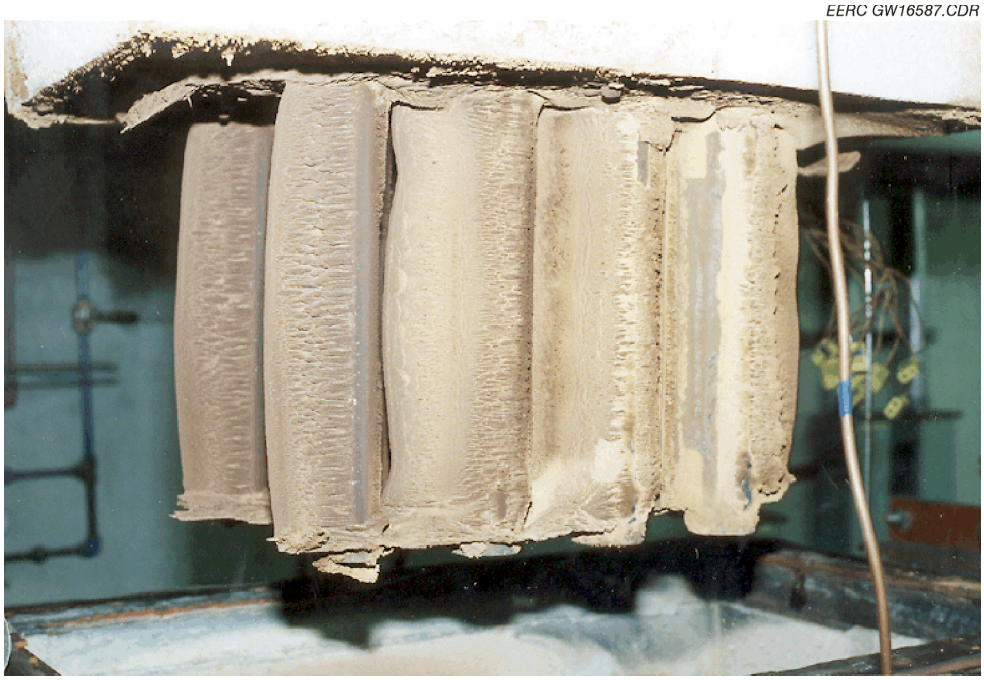

Exhibit 11-51
Photograph of Ash Deposits on the CAH Tubes Following SFS Test SFS-RH8-0399 Firing Eastern Kentucky and Illinois No. 6 Bituminous Coal

In June 2000, a similar SFS test (SFS-RH13-0400) was completed while firing an eastern Kentucky coal. In this case, sootblowing was effectively used to control tube surface temperature and the resulting CAH heat recovery. Exhibit 11-52 presents CAH tube surface temperature for SFS Test SFS-RH13-0400. On the basis of a single thermocouple measurement, the clean tube surface temperatures were nominally 1570 °F (855 °C). During the June 2000 SFS test, the EERC began sootblowing after 8 hr of coal firing and then repeated sootblowing every 8 hr for the duration of the test. The components of the sootblowing system were previously described along with the media, media pressure and flow rate, and general approach.

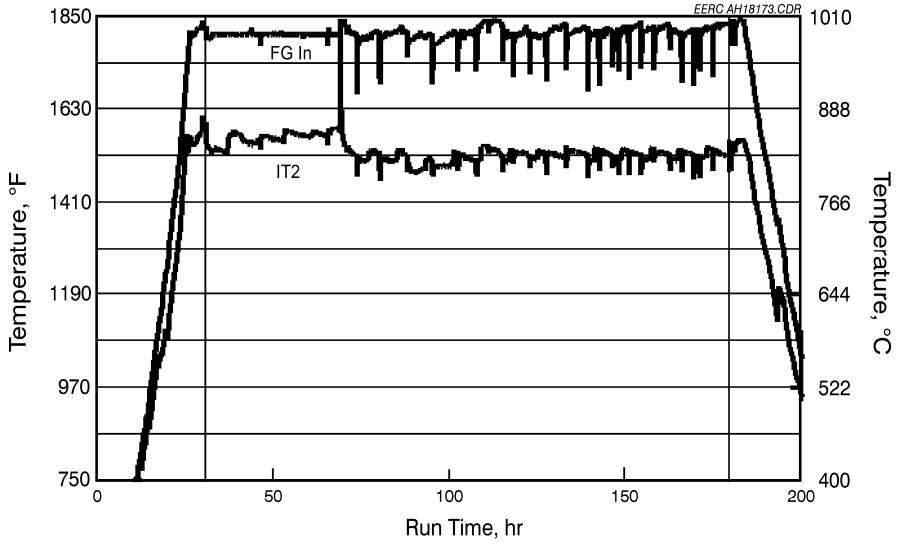

Exhibit 11-52
CAH Tube Surface and Flue Gas Temperatures versus Run Time for SFS Test SFS-RH13-0400

As a result of the sootblowing approach employed, the surface temperature remained relatively stable in the range of 1530 to 1580 °F (833 to 860 °C) during the first 40 hr of coal firing. However, after replacement of a failing thermocouple and required adjustments to the flue gas recirculation rate in the dilution/quench zone, the tube surface temperature decreased to a nominal range of 1510 to 1545 °F (821 to 841 °C) which was maintained over the final 110 hr of coal firing. Based on the tube surface temperature measurement, the sootblowing approach used in June 2000 prevented any measurable deterioration in the performance of the CAH tube bank due to ash deposition. Process air flow rate adjustments were limited during the test, resulting in flow rates of 95–124 scfm (2.7–3.5 m^3/min) during the first 40 hr of coal firing and nominally 95 scfm (2.7 m^3/min) during the final 110 hr. Sootblowing events in the CAH tube bank are somewhat evident in Exhibit 11-52 as step increases in the tube surface temperature data. However, the effect is masked to a significant degree in the surface temperature and heat recovery data by temperature and flue gas flow rate fluctuations during on-line cleaning of the dilution/quench zone. Based on the observed effectiveness of CAH sootblowing in June 2000 (firing an eastern Kentucky bituminous coal), sootblowing frequency for other fuels fired in the SFS will have to be 8 hr or less to achieve a comparable result.

Exhibit 11-53 presents heat recovery in the CAH as a function of run time for SFS Test SFS-RH13-0400. Once coal firing was stabilized, CAH heat recovery was initially 37,600 Btu/hr (39,668 kJ/hr) and initially decreased as ash deposits developed and adjustments were made to process air flow rates even though sootblowing was occurring every 8 hr. After 40 hr of coal firing, CAH heat recovery had decreased to 31,100 Btu/hr (32,810 kJ/hr). After replacing a failed flue gas thermocouple and adjusting the flue gas recirculation rate in the dilution/quench zone, CAH heat recovery was effectively controlled at 24,090 to 28,220 Btu/hr (25,415 to 29,772 kJ/hr) for 110 hr while maintaining an 8-hr sootblowing frequency. The data in Exhibit 11-53 indicate that an 8-hr sootblowing frequency was adequate for this eastern Kentucky bituminous coal once adjustments to flue gas and process air flow rates were completed.

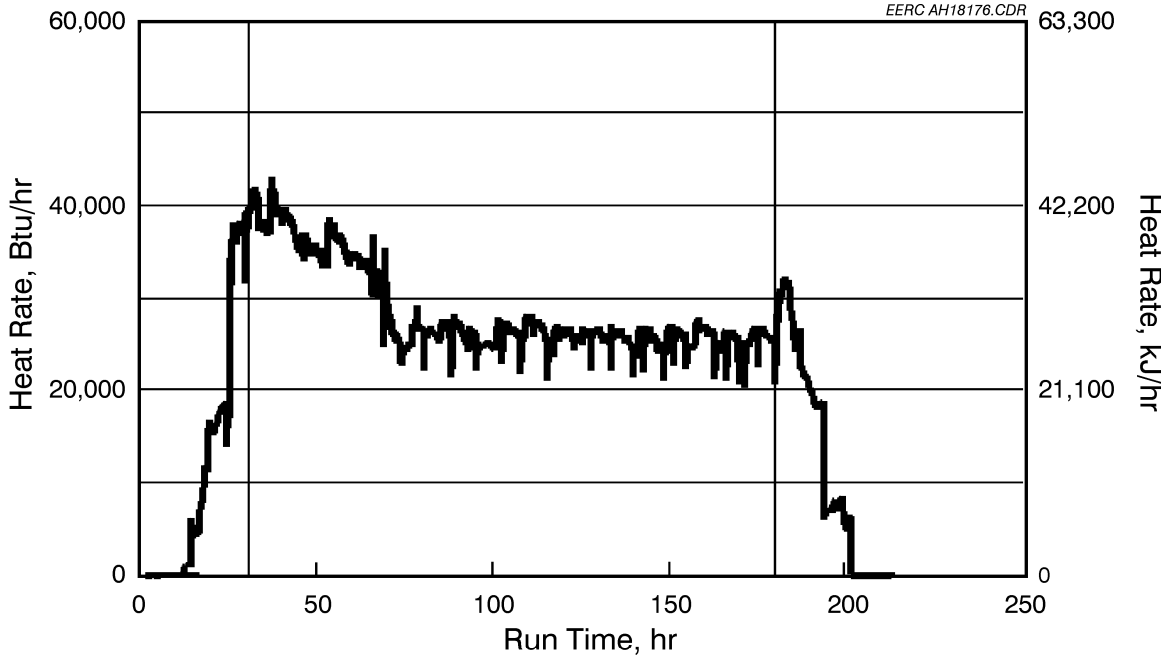

Exhibit 11-53
CAH Heat Recovery versus Run Time for SFS Test SFS-RH13-0400

The deposits that formed on the CAH tubes during the June 2000 test were limited to the leading and trailing edges of the tubes. Exhibit 11-54 presents photographs of ash deposits on the surface of the tubes following the June 2000 test. The top photograph shows three uncooled tubes that were free of ash deposits as a result of sootblowing efforts. The sidewall of the air-cooled tubes in this photo has a visible ash layer but no real evidence of deposit development. However, ash deposits are observed bridging the gaps between finned tubes in the center row. The bottom photograph shows additional uncooled surfaces with no visible ash deposits. In this photo, the cooled surfaces are relatively clean as a result of their more direct exposure to each sootblowing event. Both photographs support the conclusion that CAH ash deposits were effectively controlled during the June 2000 SFS test and CAH tube bank plugging was not a problem. No deposits were observed bridging the flue gas path between the tubes.

Exhibit 11-54
Photographs of Ash Deposits on the CAH Tubes Following
SFS Test SFS-RH13-0400 Firing Eastern Kentucky Bituminous Coals

Based on CAH operating experience, all of the other fuel types fired in the SFS may require more frequent sootblowing in order to control CAH heat recovery at a comparable level. When firing an Illinois No. 6 bituminous coal or a subbituminous coal, a 4–8-hr sootblowing frequency should be utilized. Also, improved sootblowing effectiveness may require a modification to the methodology employed to increase the tube surface area affected by each sootblowing event.

No attempt had been made to sootblow the CAH tubes prior to the installation of fins. Therefore, conclusions cannot be drawn concerning the potential advantages of the fins when routine sootblowing is effectively used to maintain desired CAH heat recovery. Also, the presence of the fins may actually inhibit the effectiveness of sootblowing.

During a February 1999 SFS test (SFS-RH7-0299) firing an eastern Kentucky bituminous coal, EERC personnel did not clean the CAH tube bank in order to facilitate the development of ash deposits for characterization. Deposit strength is a function of ash chemistry, particle size, and temperature history. The deposits remained intact when the CAH tube bank was removed from the duct. However, the small quantity of deposit and, therefore, minimal weight may have been the primary reason the deposit remained intact. Also, the deposits from the air-cooled tubes were not generally removed intact from the tube surfaces. The total weight of the deposits collected from the CAH tubes and duct was 2.2 lb (1.0 kg). The total weight of the deposits collected from the CAH tubes was 1 lb (0.5 kg). On a mass-per-unit-time basis, the ash deposition rate for this Kentucky coal-fired test would be 0.03 lb/hr (13.6 g/hr) of coal firing. Incorporating the surface area of the tube bank (6.28 ft^2, or 0.58 m^2) results in a value of 0.005 lb/hr-ft^2 (23.4 g/hr-m^2). On a coal-firing-rate basis, the CAH ash deposition rate would be 0.01 lb/MMBtu (5.9 g/10^6 kJ). These calculated values are nominally a factor of 3 smaller than those observed for the Illinois No. 6 coal, consistent with the eastern Kentucky coal's lower ash content and higher heating value.

Table 11-16 summarizes ash composition data for leading- and trailing-edge CAH ash deposits as well as fuel, slag, and baghouse ash for an eastern Kentucky coal-fired SFS test (SFS-RH7-0299). The CAH deposits formed contained nominally 50% silica, and all alkali and alkaline-earth species were present in very low concentrations, so limited sintering at the temperatures of the CAH would be expected. These compositions indicate that the deposits are dominated by larger particles enriched in silica and depleted in alumina. It is unusual that the compositions of the upstream and downstream deposits are so similar, since the upstream deposits are usually more enriched with larger particles and the downstream deposits usually more enriched with smaller particles. SEM analyses showed that essentially all of the different deposits were composed of complex silicates, except for a thin powder layer adjacent to the tube, which contained approximately 15% sulfate material.

Table 11-16
XRF Analysis Results for Fuel Ash, Slag, and Ash Samples Collected During a SFS Test Firing an Eastern Kentucky Bituminous Coal

Oxides,[1] wt%	Kentucky Coal Composite	Slag Pot Composite	CAH Leading Edge	CAH Trailing Edge	Baghouse Ash Composite
SiO_2	44.2	43.0	53.2	53.2	41.6
Al_2O_3	31.0	25.4	20.7	20.6	24.5
Fe_2O_3	14.2	17.4	14.5	14.1	15.1
TiO_2	1.1	1.0	1.3	1.3	1.3
P_2O_5	0.1	0.1	0.3	0.3	0.6
CaO	2.9	6.4	3.3	2.4	6.1
MgO	2.5	3.8	1.8	1.9	3.0
Na_2O	1.3	1.0	1.8	2.5	2.9
K_2O	2.8	1.9	3.1	3.8	4.9
SO_3[2]	–	0.1	1.0	0.4	9.2

1 Oxide concentrations normalized to an SO3-free basis.

2 SO3 concentrations normalized with other oxides.

Radiant Air Heater Panel Performance

Initial shakedown of the RAH panel took place in December 1997 and testing continued through September 2000. RAH panel performance met all design objectives relative to process temperatures, heat transfer, and its ability to produce a pressurized hot-air stream within design limits for all of the fuel types (bituminous coal, subbituminous coal, and lignite) fired.

A critical aspect of RAH panel performance was the ability of the ceramic tiles to withstand the slag attack and thermal cycling conditions in the slagging furnace. Two types of Monofrax and one type of Kyocera brick material were evaluated for slag corrosion resistance, and one type of Monofrax and the Kyocera materials were employed as tiles on the RAH. Unfortunately, both types of tiles cracked during testing in the SFS. The cracks are believed to result from residual stresses created during tile fabrication, which include both the actual casting/cooling process and the machining of the tiles. The cracks grew, sometimes to the point of failure, because of thermal cycling in the furnace. The stresses and the resulting cracks could be reduced if the tiles could be formed in near net shapes, eliminating the need for machining. Also, the recession rates observed for Monofrax tiles as a function of slag attack were greater than desired for potential commercial applications.

All of the coal-fired tests utilized ceramic tiles to protect the MA 754 alloy tubes from furnace conditions. A comparison of the coal-fired test data with tiles and natural gas-fired data without tiles demonstrated that the RAH panel heat recovery without tiles were 22% to 82% higher for a process air flow rate of 200 scfm (5.7 m^3/min). This increase occurred even though the coal-fired data with tiles represent furnace temperatures ranging from 2800 to 2950 °F (1538 to 1621 °C), while the natural gas-fired data without tiles were for a furnace temperature of only 2300 °F (1260 °C). The implication is the potential for significantly higher heat-transfer rates for a given surface area as well as the considerable simplification and cost reduction of the RAH concept if the tiles can be eliminated.

The commercial potential of the RAH panel will depend on demonstrating options (repowering and new plant concepts) for using the high-temperature heat exchanger without tile protection or the development of ceramic tile material that is less susceptible to cracking as a function of fabrication methodology and thermal cycling. Table 11-17 summarizes operating hours for the RAH Panel MA 754 alloy tubes, representing 19 thermal cycles.

RAH Panel Ceramic Tile Performance

Prior to fabrication of ceramic tiles for testing in the SFS, bench-scale flowing slag erosion/corrosion tests were completed. Initial work compared fusion-cast Monofrax tiles designated L and M. Results from the bench-scale flowing-slag tests demonstrated that surface recession was greater for the Monofrax L material. Therefore, the Monofrax M material was selected for fabrication of the first set of tiles installed in the RAH panel in November 1997. Subsequent bench-scale work identified a sintered chromia–alumina material that demonstrated a greater resistance to slag erosion/corrosion than the Monofrax M material. As a result, RAH tiles were also fabricated using the sintered chromia–alumina material developed by Kyocera.

Table 11-17
Summary of RAH Panel Operating Hours Through December 2000[1]

	Natural Gas Firing, hr	Coal/Lignite Firing, hr	Total Operation, hr
RAH Panel	1472	1465	2937

[1]Natural gas firing represents heatup, cooldown, refractory curing, and SFS-RH14-0500.

During the course of this project, the performance of four different sets of tiles was evaluated. Each set of tiles was thoroughly inspected upon initial installation and following each SFS test. The first and second sets of tiles, installed in November 1997 and January 1999, respectively, were new fusion-cast 95% alumina Monofrax M tiles. Exhibit 11-55 is a photograph of the first set of Monofrax M tiles installed in the RAH panel. Newly installed Monofrax M tiles were generally a bright white color. Exposure to natural gas firing had no impact on tile color. Exhibit 11-56 is a photograph of two of the Monofrax M tiles following 35 hr of coal firing. The photograph demonstrates the dramatic color change that occurred as a result of exposure to slag.

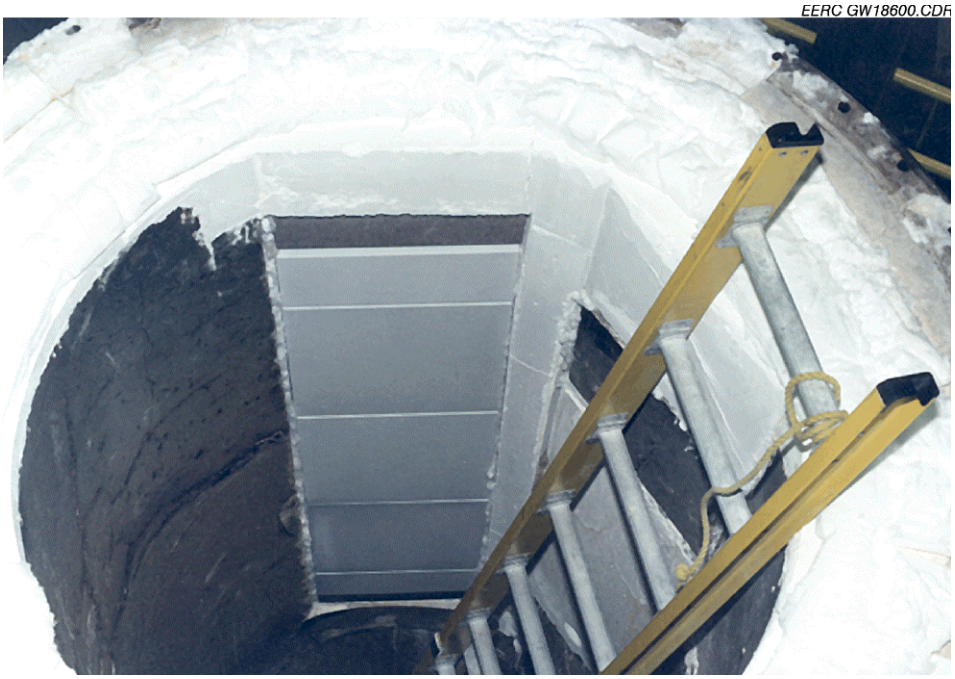

Exhibit 11-55
Photograph of New Monofrax M Tiles Inside of the Slagging Furnace

Exhibit 11-56
Photograph of Two Monofrax M Tiles after 35 hr of Coal Firing

The third set of tiles installed in the RAH panel was a combination of new and used fusion-cast alumina Monofrax M tiles and one new sintered chromia–alumina Kyocera tile. Only one new Kyocera tile was installed because a second tile had four broken corners as well as a large number of small cracks extending from each edge. The damage to the second Kyocera tile occurred as a function of curing and machining prior to shipment to the EERC. The new Kyocera tile was installed in the center tile position and did not have any visible cracks. However, the upper right corner of the Kyocera tiles was broken as a result of some machining that was performed at the EERC prior to its installation. Because only one large new Monofrax M tile was available, it was necessary to reuse one of the Monofrax M tiles originally installed in January 1999 as a replacement for the second Kyocera tile.

The fourth and final set of tiles included three new corrosion-resistant, sintered chromia–alumina tiles made by Kyocera and two new Monofrax M half-tiles. No half-tiles were fabricated using the Kyocera material. The balance of this discussion will summarize data and observations concerning the performance of the second (new Monofrax M tiles) and fourth (new Monofrax M and Kyocera tiles) sets of tiles evaluated in the SFS.

The second set of Monofrax M tiles was installed in the RAH panel in January 1999. Following installation of the tiles, SFS tests were completed in January (SFS-RH6-0199), February (SFS-RH7-0299), and April 1999 (SFS-RH8-0399), respectively, in support of a related but separately funded DOE project (Task 3.3 Cooperative Agreement Contract No. DE-FC26-98FT40320). Inspection of the new Monofrax M tiles upon installation revealed the minor cracks in two of the five tiles. Exhibit 11-57 is a photograph of the new Monofrax M tiles installed on the RAH panel inside of the slagging furnace prior to the January 1999 test. The cracks visible at the time were hairline cracks in the large upper and lower tiles. The vertical crack in the large upper tile is visible in the photograph as a result of the application of a blue dye. In addition, rough surface pitting of the tile is evident at the end of the vertical crack in the upper center of

the tile. The large lower tile had one crack originating on the left edge and a few rough surface pits along the right edge near the middle of the tile. Neither the crack nor the surface pits in the large lower tile is visible in the photograph.

Exhibit 11-58 shows the furnace interior after the January 1999 SFS test (SFS-RH6-0199). The photograph, when compared to Exhibit 11-59, illustrates the color change of the Monofrax M tiles as a result of coal firing. Exposure to slag darkened the tiles because a residual slag layer was left on the surface. No additional tile color change occurred because of subsequent SFS tests. Although not obvious in the photo, the slag layer on the tiles is thin and appears to be uniform, with no evidence of any extensive buildup. While there was some slag present in the seams between the tiles, there was no evidence of any fusion between adjacent tiles. Therefore, a 4-hour period of natural gas firing prior to SFS cooldown was adequate to prevent buildup of excess slag on the surface of the tiles or in the seams between tiles for the Illinois No. 6 and Kentucky bituminous coals. Also, any quantity of slag present in the seams between tiles cracked as a result of cooldown and tile movement.

Exhibit 11-57
Photograph of New Monofrax M tiles Installed on the RAH Panel in January 1999

Exhibit 11-58
Photograph of the Monofrax M Tiles Following SFS Test SFS-RH6-0199

Exhibit 11-59 illustrates the visible cracks found in the Monofrax M tiles following the January (left) and February (right) 1999 tests. Overall, the tiles appeared to be in good condition. Following the January test, visible cracks were only evident in two tiles, the small and large upper tiles. The small crack evident in the large lower tile prior to coal firing was covered with slag and was not visible following the January test. The vertical crack in the large upper tile did not appear to have changed as a result of the January and February tests. However, the combination of cracks in the large upper tile was considered potentially problematic as a function of future thermal cycles. The only other change in tile cracking that was observed following the February test was the appearance of a new crack originating on the lower right edge of the small upper tile.

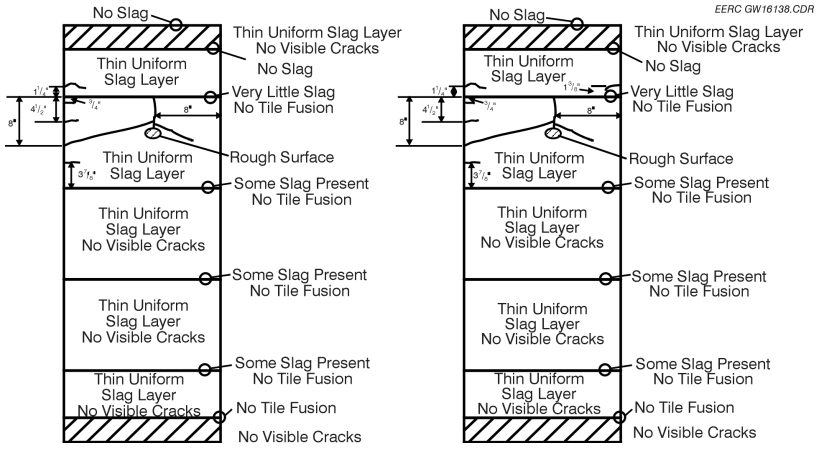

Exhibit 11-59
Illustration of Cracks Found in the Monofrax M tiles Following SFS Tests SFS-RH6-0199 (left) and SFS-RH7-0299 (Right)

Exhibit 11-60 illustrates the visible cracks found in the Monofrax M tiles following the April 1999 test. Overall, the condition of the tiles deteriorated somewhat with each test, with the small lower tile showing the greatest degree of erosion/corrosion. This is believed to result from the combination of its higher surface temperature and the greater quantity of slag flowing over its surface relative to the other tiles. The surface temperature of the small lower tile, although not measured, is believed to be higher than the three larger tiles because the backside of this tile is insulated within the radiation cavity and is not directly cooled by the heat-transfer surfaces. The greatest quantity of slag flows over this tile because of its location below the other tiles.

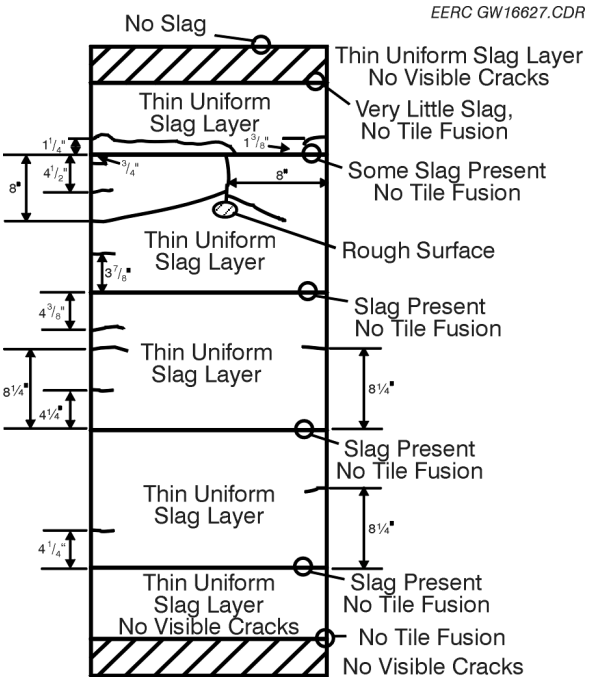

Exhibit 11-60
Illustration of Cracks Found in the Monofrax M Tiles Following SFS Test SFS-RH8-0399

The cracks in the large lower and middle tiles were hairline cracks posing no concern following the April 1999 test. The large upper tile had the most extensive cracking and, therefore, posed a concern with respect to potential failure. Thermal cycles are believed to be the primary cause of Monofrax M tile cracking and the propagation of cracks formed during tile fabrication, with slag contributing to erosion/corrosion of surfaces and imparting stresses on the tiles as it finds its way into seams between tiles. Exhibit 11-61 is a photograph of the small lower tile and the lower edge of the large lower tile following the February 1999 test. Exhibit 11-62 presents a photograph of the Monofrax M tiles from inside of the furnace following the April 1999 test. Both photographs show where the flow of slag has caused erosion/corrosion of the tile surfaces. This observation is consistent with those made concerning the original RAH tiles installed in December 1997 and removed subsequent to failure in August 1998. In addition, the photographs illustrate the small quantity of slag found in the seams between the tiles.

Exhibit 11-61
Photograph of the Small Lower Tile and the Lower Edge of the Large Lower Tile Following SFS Test SFS-RH7-0299

Exhibit 11-62
Photograph of the Monofrax M Tiles from Inside the Furnace Following SFS Test SFS-RH8-0399

The surface temperatures of the tiles on the cavity side during the SFS tests completed in January, February, and April 1999 ranged from nominally 2000 to 2205 °F (1094 to 1208 °C). These temperatures were based on measurements made at the center of each of the three large tiles once the SFS had stabilized thermally. Higher tile surface temperatures (furnace side), 2620 to 2693 °F (1438 to 1479 °C), were measured near the center of the large middle tile. Surface temperatures during these SFS test periods were somewhat higher yet comparable to the temperatures observed during the first RAH coal-fired test completed in December 1997. However, the furnace-side tile temperature was a new thermocouple location for these tests. Therefore, a direct comparison with previous data is not appropriate.

SFS tests with the second set of Monofrax M tiles were concluded with two coal-fired SFS tests completed in May (SFS-RH9-0499) and September (SFS-RH10-0699) 1999. Exhibit 11-63 is a photograph of the tiles inside the slagging furnace following SFS Test SFS-RH10-0699. The condition of the individual tiles is not clear in this photograph. However, the broken corners on the lower edge of the small upper tile are evident. Exhibit 11-64 illustrates the visible cracks found in the Monofrax tiles following the September 1999 test. Overall, the condition of the tiles deteriorated with each test subsequent to their installation in January 1999. The small and large upper tiles exhibited the most severe cracking. Only the small lower tile was observed to be free of cracks. However, the small lower tile showed the greatest degree of erosion/corrosion because of its higher surface temperature and the greater quantity of slag flowing over its surface relative to other tiles.

Exhibit 11-63
Photograph of the Monofrax M Tiles Inside the Furnace Following SFS Test SFS-RH10-0699

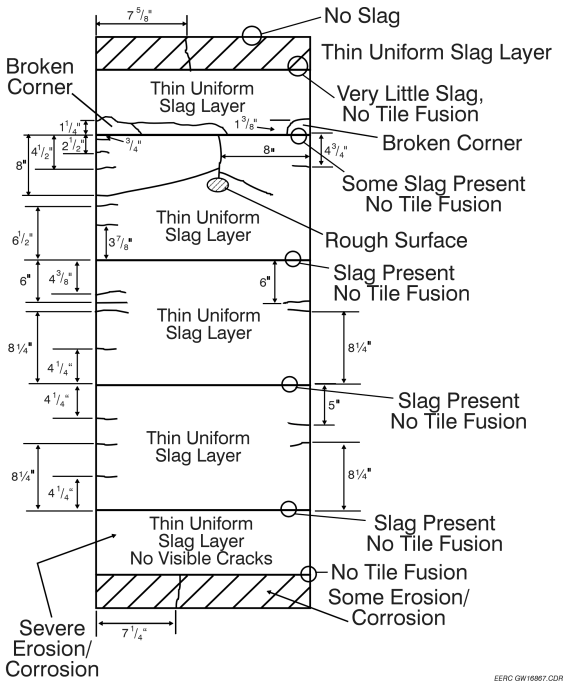

Exhibit 11-64
Illustration of Cracks Found in the Monofrax M tiles Following SFS Test SFS-H10-0699

The second set of Monofrax M tiles was removed from the RAH panel in November 1999 in preparation for the installation of new tiles. Subsequent to their installation in January 1999, this set of tiles had experienced 988 hr of slagging furnace operation, representing 473 hr of natural gas firing (including heatup, cooldown, and refractory curing), 515 hr of coal firing and six thermal cycles. Based on the tile cracking and surface recession observed for these Monofrax M tiles, they do not appear to be a viable option for use in a commercial RAH application.

Five large corrosion-resistant sintered chromia–alumina tiles made by Kyocera were delivered to the EERC in May 2000. Three of these tiles had been machined and drilled for use. They were installed in the RAH in early June 2000 and represent the fourth and final set of tiles installed on the RAH panel. These tiles appeared to be free of cracks, but one tile did have a minor chip in one edge. The two large Kyocera tiles that had not been machined did have visible cracks. No half-tiles were fabricated using the Kyocera material. Therefore, half-tiles made of the Monofrax M material were used.

The top photograph in Exhibit 11-65 shows the new Kyocera (reddish hue) and Monofrax M (white) tiles prior to a June 2000 SFS test (SFS-RH13-0400). As previously stated, no visible cracks were observed in the three large Kyocera tiles. One hairline vertical crack was visible in the small upper Monofrax M tile. However, the hairline crack is not visible in the photograph.

Exhibit 11-65
Photographs of RAH Tiles Before and After SFS Test SFS-RH13-0400

The RAH panel ceramic tiles were thoroughly inspected following the June test. The lower photograph in Exhibit 11-65 shows the RAH tiles following the June test. As expected, based on previous observations, the color of the upper and lower Monofrax M half-tiles changed from white to a brown/black as a result of slag coating the surface. The broken lower left corner of the small upper Monofrax M tile is evident in the photograph. Although the condition of the Kyocera tiles is not clearly depicted in this photograph, cracks are evident in the large upper and center

tiles, and a bottom portion of the lower tile is broken. A surface color change is also evident for the Kyocera tiles, having lost the reddish hue observed in the upper photograph, taking on a more gray coloration. Although not obvious in the photograph, the degree of erosion/corrosion is more pronounced on the Monofrax M tiles. However, the degree of crack propagation was much more severe for the Kyocera tiles.

The slag layer on the tiles is generally thin and appears to be uniform, with the exception of the lower edges of the Kyocera tiles and areas of the center and lower Kyocera tiles where a wavy layer of frozen slag appears to be evident. However, no evidence of any extensive slag buildup was noted. While slag is present in the seams between the tiles, there is no evidence of any fusion between adjacent tiles. Also, any quantity of slag present in the seams between tiles appears to crack as a result of cooldown and tile movement.

Exhibit 11-66 shows the large upper Kyocera tile. The top photograph shows it in the furnace following the June 2000 test, and the bottom photograph shows the cavity side of the tile after it was removed from the RAH panel. Numerous cracks are evident in the furnace-side photograph, with most of the cracks appearing to be fused shut with slag. In the cavity-side photograph, the degree of cracking is more evident. The accumulation of slag near the bottom edge of this tile appears as dark spots in the upper photograph. Rivulets where slag flowed over the surface of the tile are also evident in the photograph.

Exhibit 11-67 presents photographs of the large center Kyocera tile. The top photograph shows the tile in the furnace following the June 2000 test and the bottom photograph shows the cavity side of the tile after it was removed from the RAH panel. The only obvious cracks from the furnace side are the two horizontal cracks, one across the middle of the tile and the second through the upper half of the tile. A broken corner on the lower left edge of the tile is also visible. With the exception of the horizontal crack across the middle of the tile, the cracks appear to be fused shut with slag. In the cavity-side photograph, the degree of cracking is again more evident and the broken lower corner is actually missing in this photograph. As previously observed for the upper tile, the accumulation of slag near the bottom edge of this tile appears as dark spots in the furnace-side photograph, and slag rivulets are also evident. Fewer points of slag accumulation and rivulets are evident in the center tile when compared to the upper tile. However, the right half of the center tile has a wavy appearance, apparently due to the collection of crystalline material in the slag, leading to some limited slag accumulation.

Exhibit 11-68 presents photographs of the large lower Kyocera tile. The top photograph shows the tile in the furnace following the June 2000 test, and the bottom photograph shows the cavity side of the tile after it was removed from the furnace. Obvious cracks from the furnace side are apparent across the center of the tile and in the upper left corner. In addition, a large piece of the tile's lower edge is broken. The cracks in the upper left quadrant of the tile appear to be fused shut with slag. In the cavity side photograph, the severity of cracking experienced by this tile is clearly evident. Rivulets as well as the wavy surface of the tile indicate slag flow over the surface similar to the center tile. Accumulation of slag on the right half, near the top edge of this tile, appears as a wavy surface in the furnace-side photograph. Slag rivulets are evident on the left half of the tile.

Exhibit 11-66
Photographs of Large Upper Kyocera Tile Before and After SFS Test SFS-RH13-0400

Exhibit 11-67
Photographs of Large Center Kyocera Tile Before and After SFS Test SFS-RH13-0400

Exhibit 11-68
Photographs of Large Lower Kyocera Tile Before and After SFS Test SFS-RH13-0400

The most significant area of erosion/corrosion is observed at the top edge of each tile where slag dripped from the tile above. This occurs even though the least corrosion occurred near the bottom of the tile immediately above. One would think that if the slag was saturated with the corrosion products from the tile above, the corrosion of the lower tile would also be limited. However, it appears that a portion of the corrosion products from the upper tile would often form

a crystalline mass that remained along the bottom of the tile and within the solid drip structure, possibly because the tile was thinner and therefore cooler at the joint. SEM analyses showed that the crystalline material was composed primarily of alumina or iron aluminate spinel which has a melting point above the surface temperature of the tiles. This left the slag that continued to flow off of the drip body less saturated and able to dissolve additional tile material. The separation of the crystalline material implies that the act of dripping from one tile to another in a sense makes the slag more corrosive again. Therefore, if dripping from one tile to the next can be eliminated, the corrosion rate of the tiles may be reduced. Slag channels that developed on the surface of the Kyocera tiles were not nearly as deep or as wide as those observed for Monofrax M tiles. In addition, the slag did not appear to penetrate into the Kyocera tile nearly as much as into the Monofrax M tiles.

Exhibit 11-69 illustrates the visible cracks found in the RAH tiles following the June 2000 test. Overall, the condition of the Monofrax M half-tiles was good following the test. However, the degree of cracking observed for the Kyocera tiles was extensive. Following completion of the test, only the small lower Monofrax M half-tile was free of visible cracks. The crack in the small upper Monofrax M half-tile before the test was covered with slag during the test and was no longer visible. However, this tile was found to have a broken lower left corner following the test.

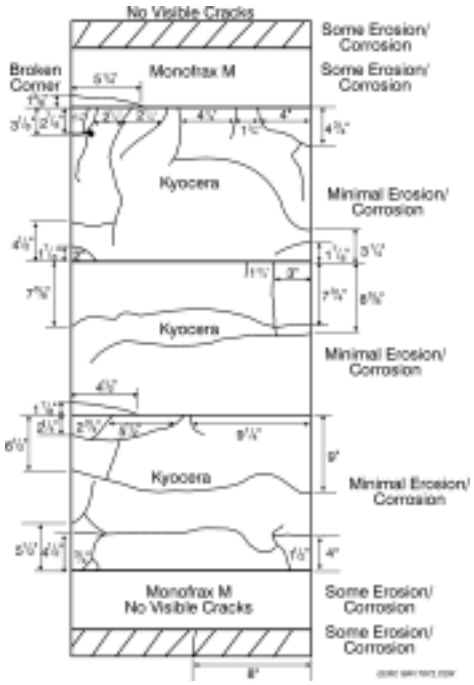

Exhibit 11-69
Illustration of Cracks Found in the RAH Tiles Following SFS Test SFS-RH13-0400

There were no visible cracks in the Kyocera tiles prior to the June 2000 test. As previously discussed in reference to the photographs, the three large Kyocera tiles were extensively cracked following the test. Twelve cracks were evident in the upper and lower tiles and four in the center tile. Based on the degree of cracking, the use of these Kyocera tiles would not be an option in future SFS tests.

The fourth and final set of tiles (a combination of new Monofrax M half-tiles and three new Kyocera tiles) was removed from the RAH panel in September 2000 in preparation for a natural gas-fired SFS test to be performed without tiles installed in the RAH panel. Subsequent to their installation in June 2000, the fourth set of tiles had experienced 275 hr of slagging furnace operation, representing 112 hr of natural gas firing (including heatup and cooldown), 163 hr of coal firing, and two thermal cycles.

Heatup/cooldown cycles are believed to be the primary cause of tile crack propagation for both the Monofrax M and Kyocera tiles. However, the cracks are believed to actually form during tile casting, curing, and machining. The fourth set of RAH tiles had only experienced two thermal cycles. Slag contributes to erosion/corrosion of surfaces and may impart stresses on the ceramic tiles as it finds its way into seams between tiles. However, the quantity of slag found in the seams between the tiles is small and always cracks during cooldown.

RAH Panel Heat-Transfer Performance with Tiles

Fifteen coal- and lignite-fired SFS tests were completed in support of this and related projects to evaluate the performance of the RAH panel with Monofrax M and/or Kyocera tiles. The primary function of the tiles was to protect the MA 754 alloy surfaces from ash and slag and flame impingement. For the purpose of this report, examples of RAH process data will be presented from two of these test periods, SFS-RH8-0399 (April 1999, eastern Kentucky bituminous coal, Monofrax M tiles) and SFS-RH13-0400 (June 2000, eastern Kentucky bituminous coal, Kyocera tiles). Discussions concerning heat recovery data will address the potential influence of the condition and type of RAH tiles, the condition of high-density refractory in the furnace, and fuel properties.

Exhibits 11-70 through 11-72 summarize the RAH ceramic tile temperatures, tube surface temperatures, and process air temperatures for the April 1999 test (SFS-RH8-0399, eastern Kentucky bituminous coal and Monofrax M tiles). The process air flow rate data for the RAH panel were summarized in Exhibit 11-49. Exhibit 11-73 illustrates the location of thermocouples in the RAH panel for the test, and Table 11-18 describes the RAH thermocouple locations. The cavity-side tile surface temperatures ranged from nominally 2000 to 2140 °F (1094 to 1171 °C), based on measurements made at the center of each of the three large tiles once the SFS had stabilized thermally (Run Hours 50 through 248). Furnace-side tile surface temperatures of 2400 to 2630 °F (1316 to 1444 °C) were measured near the center of the large middle tile. There is no obvious explanation for the drop in the furnace-side tile surface temperature that occurred just prior to Run Hour 100.

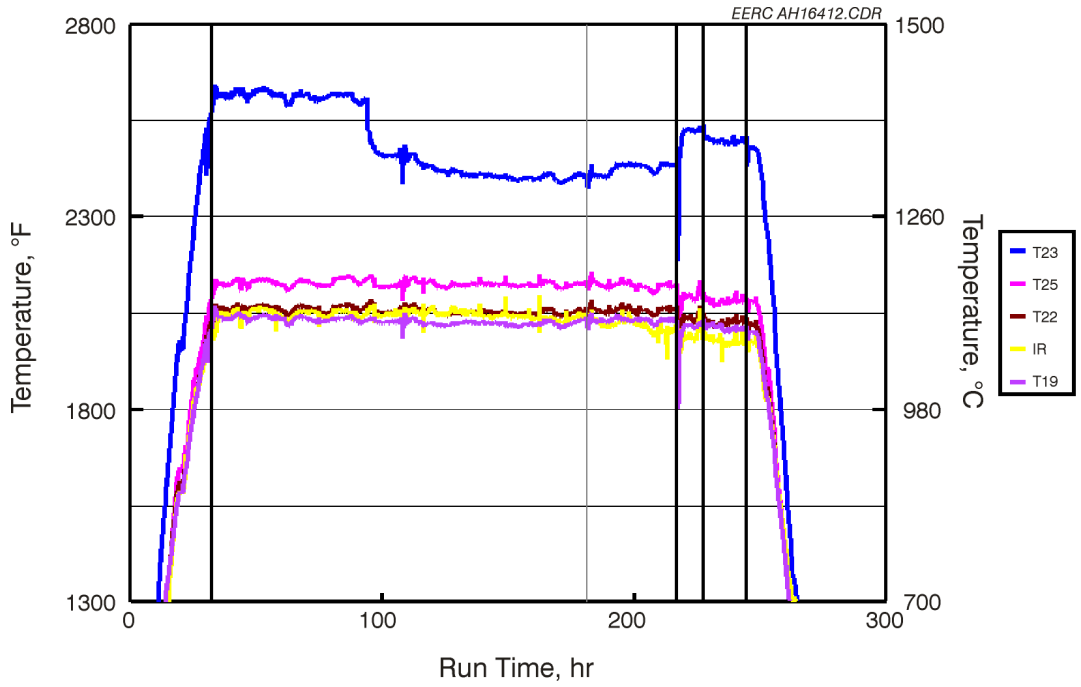

Exhibit 11-70
RAH Ceramic Tile Temperatures versus Run Time for SFS Test SFS-RH13-0400

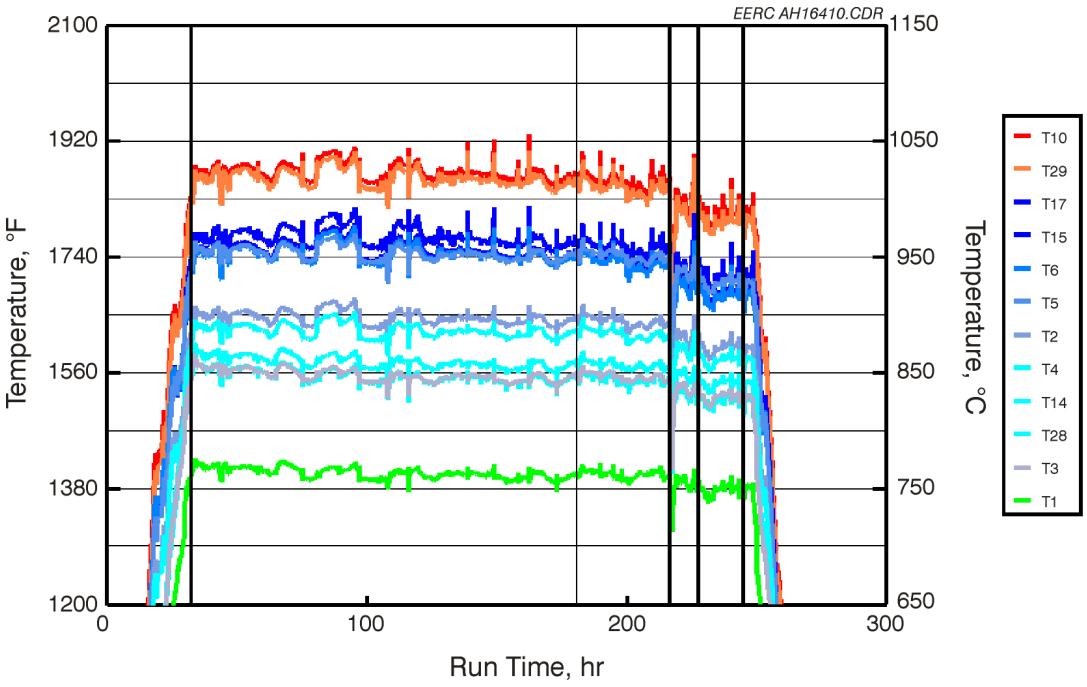

Exhibit 11-71
RAH Tube Surface Temperatures versus Run Time for SFS Test SFS-RH8-0399

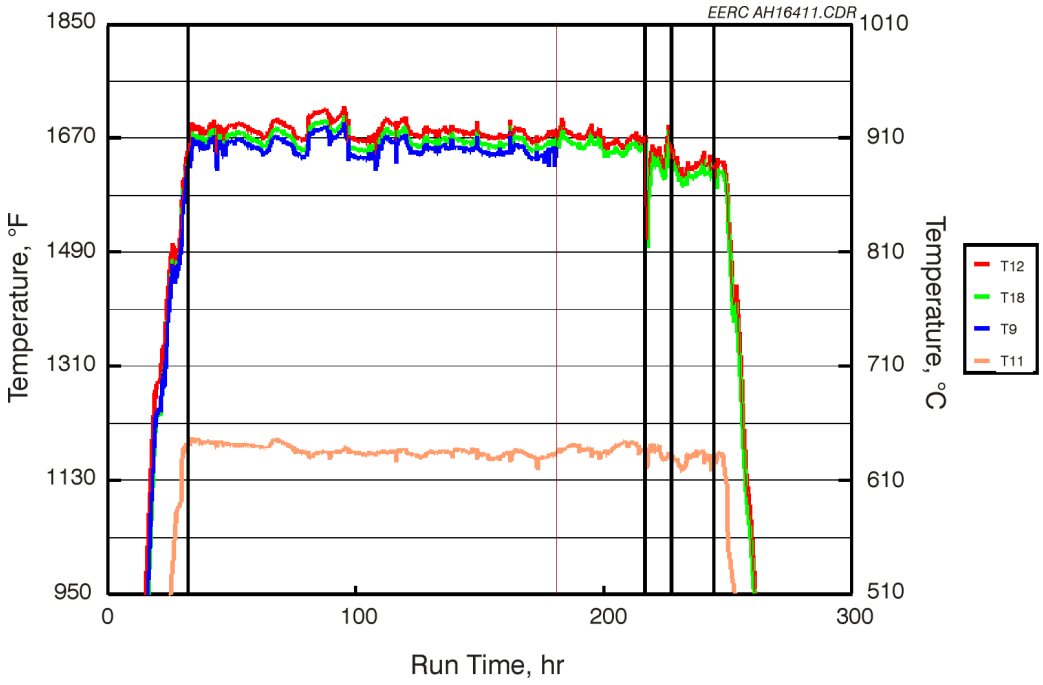

Exhibit 11-72
RAH Process Air Temperatures versus Run Time for SFS Test SFS-RH8-0399

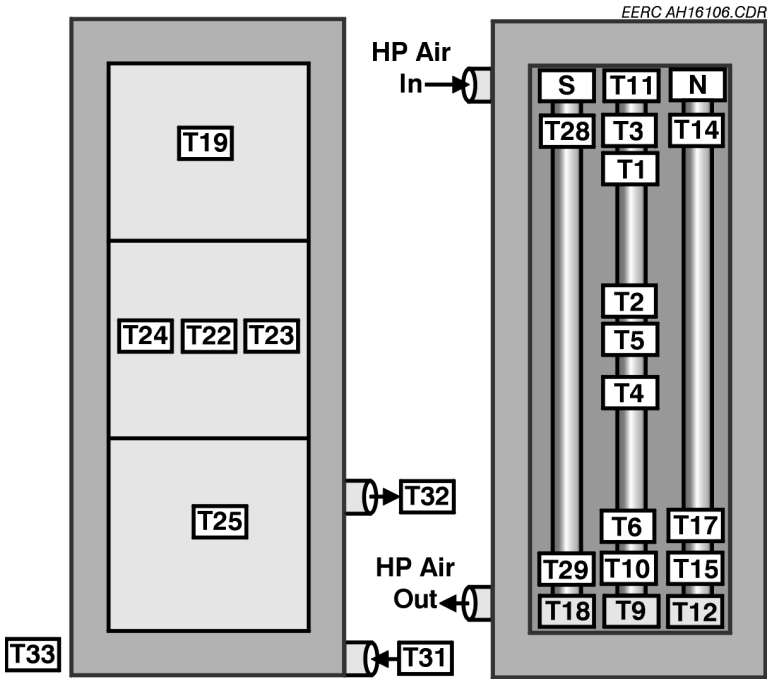

Exhibit 11-73
Thermocouple Locations in the RAH Panel for SFS Test SFS-RH8-0399

One possibility is the degradation of the thermocouple junction as a result of slag erosion/corrosion of the tile surface. The thermocouple must have been effectively attached, and measuring a relative furnace-side temperature or the reading would have resulted in a decrease to a value at or below the values indicated by TC19, TC22, and TC25 (cavity-side tile surface temperatures). Tile surface temperatures of 40 to 65 °F (22 to 36 °C) higher were observed during RAH coal-fired tests in January and February 1999. The implication of these temperature differences will be discussed later.

RAH process air flow rates during the April 1999 test were controlled at 180, 190, and 200 scfm (5.1, 5.4, and 5.7 m^3/min), with 200 scfm (5.7 m^3/min) used primarily. Changes in process air flow rates had a definite effect on tile surface temperatures as observed for all SFS tests. As process air flow rates were reduced, tile surface temperature increased. Subsequently, when process air flow rates were increased, tile surface temperatures decreased. This effect was most evident for process air flow rate changes at Run Hours 80, 95, 109, and 200.

RAH tube surface temperatures ranged from nominally 1390 to 1900 °F (755 to 1038 °C). The low end of the temperature range represents the back side of the tube surfaces near the process air inlet, with the high end of the temperature range representing the front side of the tube surfaces near the process air outlet. Changes in process air flow rates had noticeable effects on all tube surface temperatures. Tube surface temperature step changes were most noticeable for surface temperature measurements near the process air exit and on the front side of the tubes. Consistent with the tile temperature data previously discussed, tube surface temperatures in April 1999 were comparable to all previous bituminous coal-fired tests. However, the high end of the range was somewhat lower, 70 to 80 °F (39 to 44 °C), when compared to data from tests in January and February 1999. Again, the implication of these temperature differences will be discussed later.

Process air inlet temperatures ranged from 1145 to 1195 °F (619 to 646 °C) but were nominally 1160 to 1190 °F (644 to 666 C) for most of the coal-fired operational period. Outlet process air temperatures ranged from nominally 1610 to 1710 F (877 to 932 °C). The effect of process air flow rate can be seen in the process air outlet temperature data. As process air flow rate decreases, process air exit temperature increases, as expected. These process air flow rate changes are noted at Run Hours 80, 95, 109, and 200.

Heat recovery data from the RAH panel are presented in Exhibit 11-74 for the April 1999 test. At process air flow rates of 180, 190, and 200 scfm (5.1, 5.4, and 5.7 m^3/min), the heat recovered from the RAH panel was 115,385 to 118,750 Btu/hr (121,731 to 125,281 kJ/hr), 115,385 to 119,710 Btu/hr (121,731 to 126,294 kJ/hr), and 120,670 to 125,000 Btu/hr (127,307 to 131,875 kJ/hr), respectively. The heat recovery ranges are a function of minor adjustments to the coal feed rate, combustion air flow rates, and changes in furnace pressure. The main burner firing rate was nominally 2.1 to 2.3 MMBtu/hr (2.2 to 2.4 × 10^6 kJ/hr). Comparisons of heat recovery data for various SFS tests will be discussed later in the report.

Table 11-18
Description of RAH Panel Thermocouple Locations for SFS Test SFS-RH8-0399[1]

Category	No.	Label	Description
Air Inlet	1	HP Air In	Provided by the EERC, in pipe before inlet header
	2	RAHT11	Air entering RAH through center tube
Air Outlet	3	RAHT18	Air leaving left (south) tube
	4	RAHT9	Air leaving middle tube
	5	RAHT12	Air leaving right (north) tube
MA Tube Surface	6	RAHT1	Top of middle tube facing cold side
	7	RAHT2	Middle of middle tube facing other tube
	8	RAHT3	Top of middle tube facing toward furnace
	9	RAHT4	Middle of middle tube facing cold side
	10	RAHT5	Middle of middle tube facing toward furnace
	11	RAHT6	Bottom of middle tube facing cold side
	12	RAHT7	Removed
	13	RAHT8	Removed
	14	RAHT10	Bottom of the middle tube facing toward furnace
	15	RAHT13	Removed
	16	RAHT14	Top of north tube facing toward furnace
	17	RAHT15	Bottom of north tube facing toward furnace
	18	RAHT16	Removed
	19	RAHT17	Bottom of north tube facing toward side wall
	20	RAHT28	Top of south tube facing toward furnace
	21	RAHT29	Bottom of south tube facing toward furnace
Inner Surface of Monofrax Bricks	22	RAHT19	Top tile, center
	23	RAHT20	Removed
	24	RAHT21	Removed
	25	RAHT22	Middle tile, center
	26	RAHT23	Middle tile, right center hot-side surface
	27	RAHT24	Middle tile, left side rail
	28	RAHT27	Removed
	29	RAHT25	Lower tile, center
	30	RAHT26	Removed

[1] Thermocouple locations are illustrated in Exhibit 11-73.

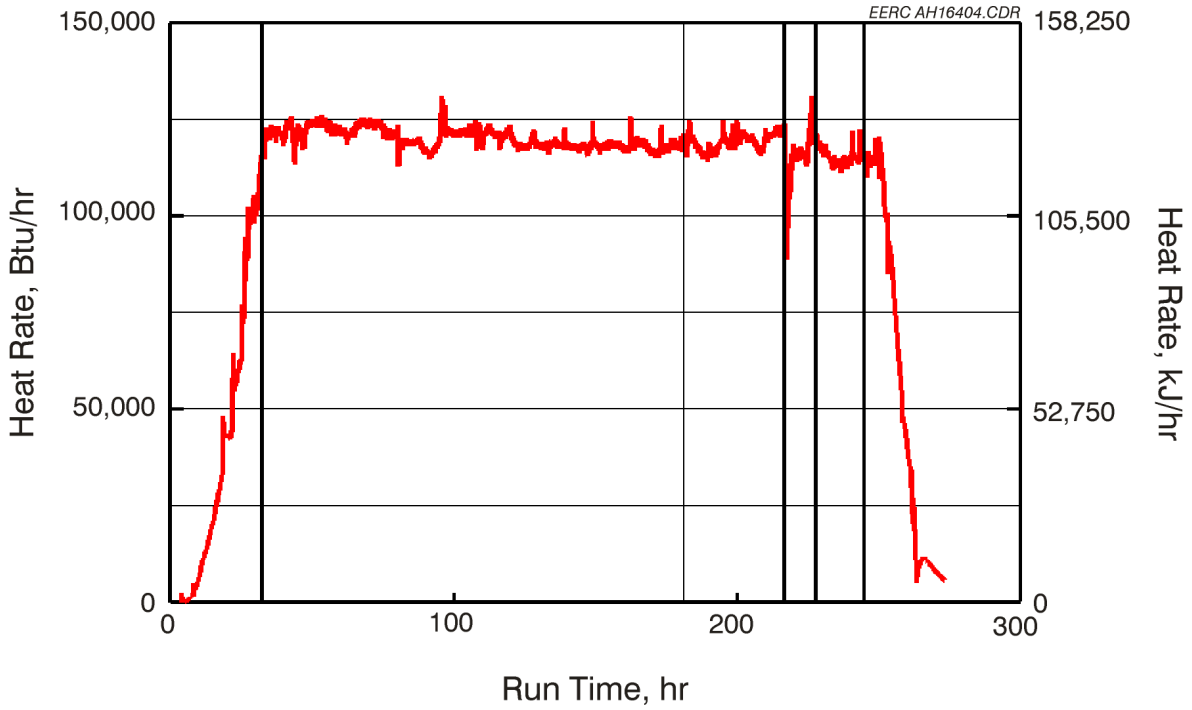

Exhibit 11-74
RAH Heat Recovery versus Run Time for SFS Test SFS-RH8-0399

Exhibits 11-75 through 11-77 summarize the RAH ceramic tile temperatures, tube surface temperatures, and process air temperatures for a June 2000 test (SFS-RH13-0400, eastern Kentucky bituminous coal, Kyocera tiles). The process air flow rate data for the RAH panel are summarized in Exhibit 11-78. Exhibit 11-79 illustrates the location of thermocouples in the RAH panel for the test, and Table 11-19 describes the RAH thermocouple locations. The indicated ceramic tile surface temperatures (cavity side) ranged from nominally 1720 to 2060 °F (938 to 1127 °C), based on measurements made at the center of the middle and lower large tiles once the SFS had stabilized thermally (Run Hours 40 through 180). The cavity-side thermocouple on the upper tile failed during tile installation. These measured cavity-side temperatures are significantly lower (80–280 °F [44–156 °C]) than those observed during the April 1999 SFS test firing the same fuel at similar conditions. These thermocouple measurements were determined to be valid as a result of an RAH panel inspection following the June 2000 test. Therefore, the lower cavity-side tile temperatures indicate that the Kyocera tiles have a lower thermal conductivity than the Monofrax M tiles, which would necessitate a larger RAH if the Kyocera tiles are used.

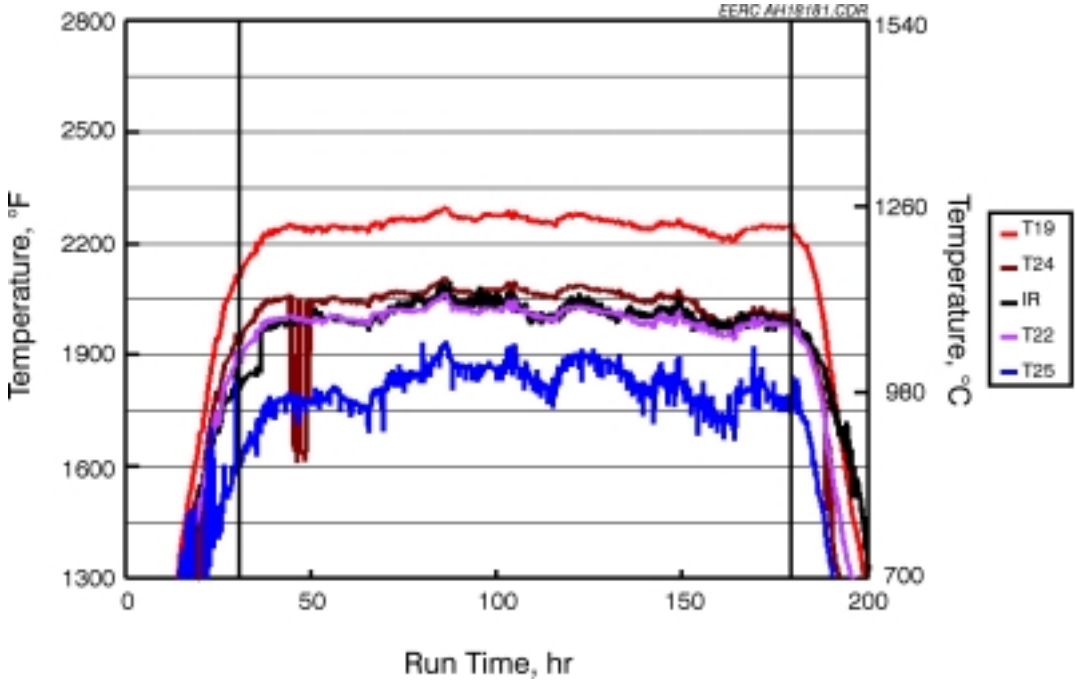

Exhibit 11-75
RAH Ceramic Tile Temperatures versus Run Time for SFS Test SFS-RH13-0400

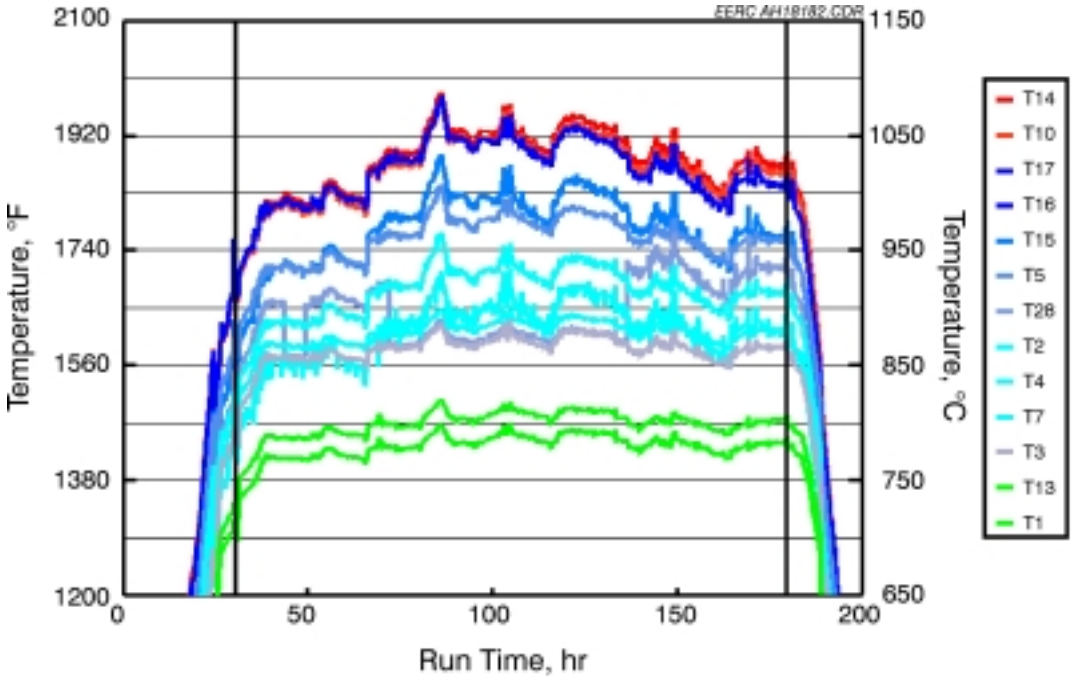

Exhibit 11-76
RAH Tube Surface Temperatures versus Run Time for SFS Test SFS-RH13-0400

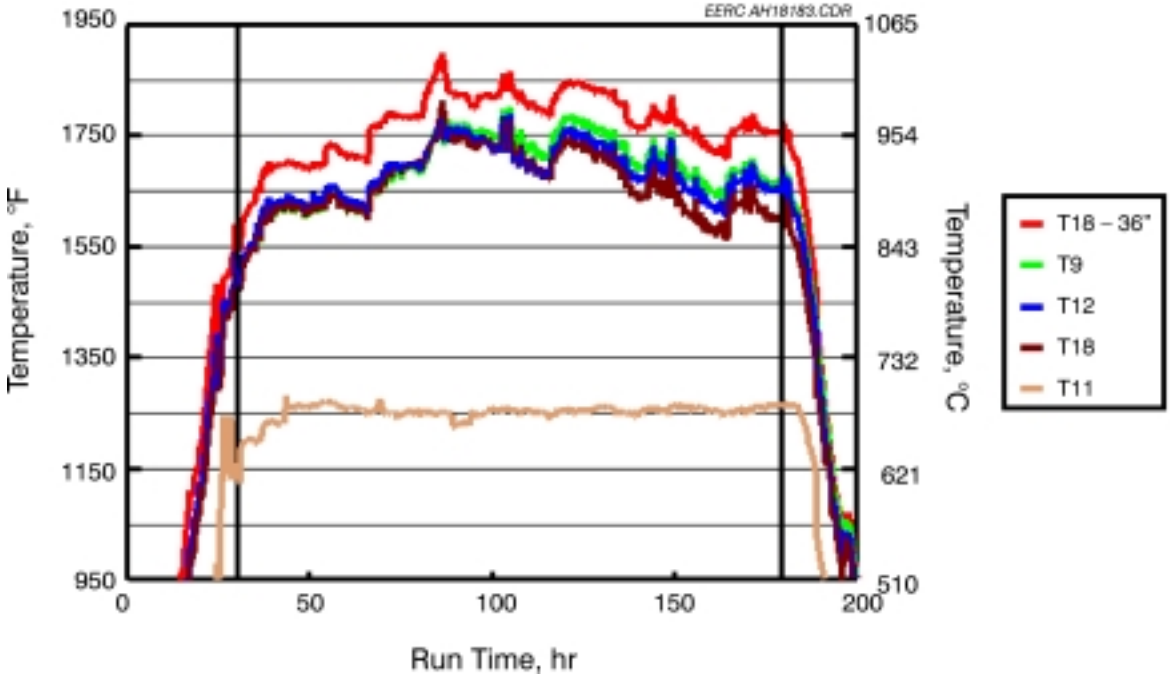

Exhibit 11-77
RAH Process Air Temperatures versus Run Time for SFS Test SFS-RH13-0400

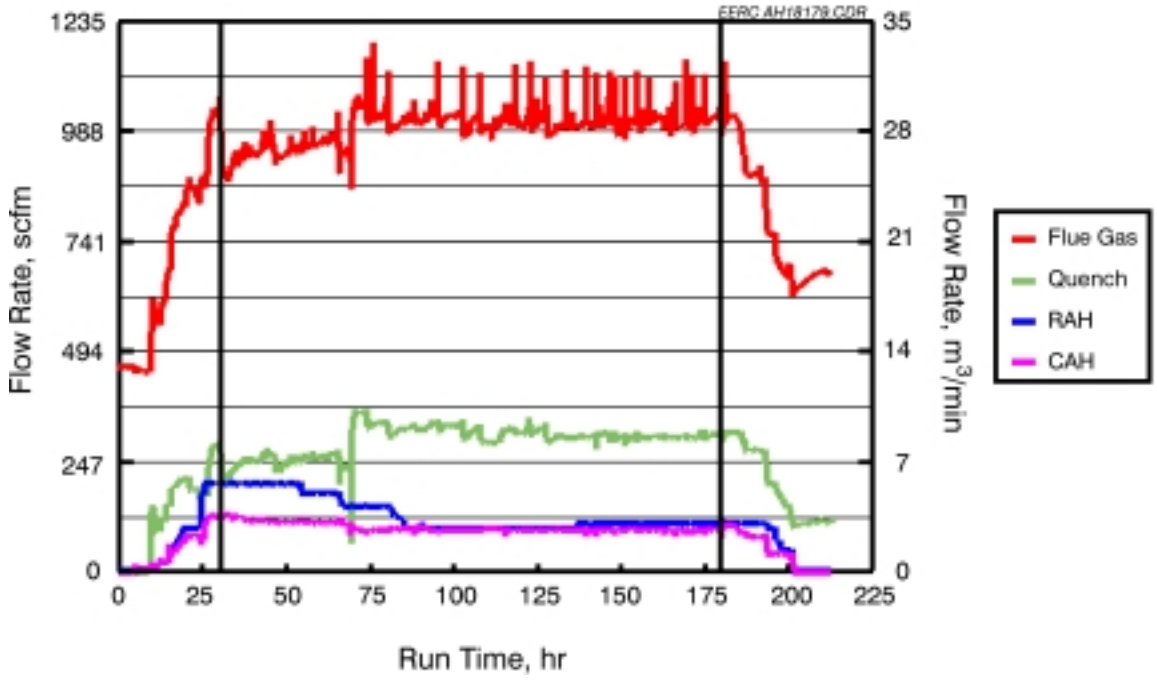

Exhibit 11-78
CAH Process Air, RAH Process Air, Quench Gas, and Flue Gas Flow Rates versus Run Time for SFS Test SFS-RH13-0400

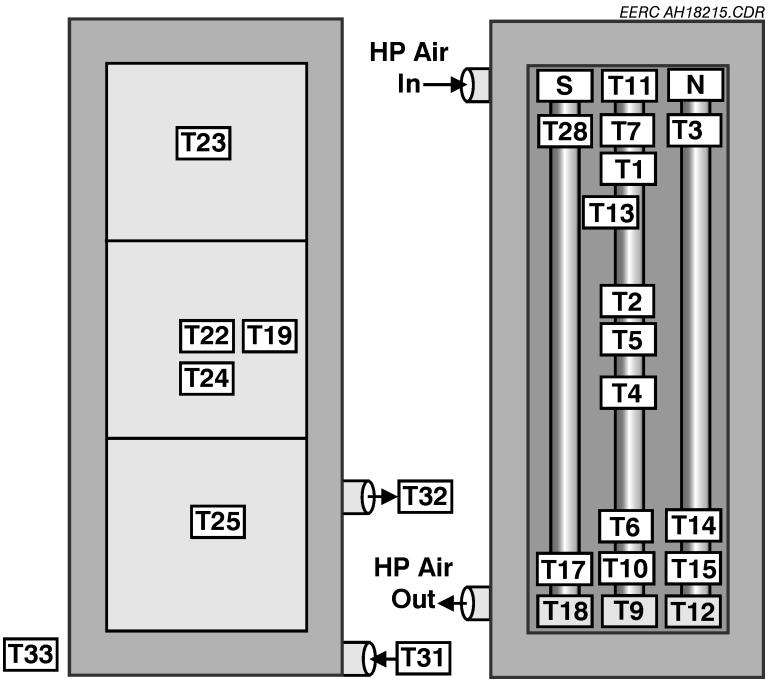

Exhibit 11-79
Thermocouple Locations in the RAH Panel for SFS Test SFS-RH13-0400

Thermocouple T24 was installed in the center tile prior to the June test to measure a furnace-side tile surface temperature. However, the available diamond tooling was inadequate to drill through the tile to the hot-side surface. Therefore, a furnace-side tile surface temperature measurement was not available, and the actual thermocouple location represented a position halfway between the cavity- and hot-side locations. The ceramic tile temperature measured by this thermocouple ranged from nominally 1980 to 2100 °F (1082 to 1149 °C). This temperature range is consistent with cavity-side temperatures measured for the Monofrax M tiles, again indicating that the thermal resistance of the Kyocera tiles appears to be significantly greater than for the Monofrax M tiles.

RAH process air flow rates during the June 2000 test were controlled at 150, 180, and 200 scfm (4.2, 5.1, and 5.7 m^3/min). Test periods attempted at lower process air flow rates (after Run Hour 87) were invalid because of a process air leak that developed in a flange connection in the RAH process air outlet header. For the test periods completed before the air leak developed, changes in process air flow rates had a definite effect on tile surface temperatures measured. As flow rates were reduced, tile surface temperature increased. This effect is evident for flow rate changes at

Run Hours 54 and 66. Temperature step changes observed after Run Hour 78 are related to adjustments in process air pressure and efforts to document the process air leak that developed at roughly Run Hour 87.

Table 11-19
Description of RAH Panel Thermocouple Locations for SFS Test SFS-RH13-04001

Category	No	Label	Description
Air Inlet	1	HP Air In	Provided by the EERC, in pipe before inlet header
	2	RAHT11	Air entering RAH through center tube
Air Outlet	3	RAHT18	Air leaving left (south) tube
	4	RAHT9	Air leaving middle tube
	5	RAHT12	Air leaving right (north) tube
MA Tube Surface	6	RAHT1	Top of center tube facing cold side
	7	RAHT2	Middle of center tube facing other tube
	8	RAHT3	Top of north tube facing toward furnace
	9	RAHT4	Middle of center tube facing cold side
	10	RAHT5	Middle of center tube facing toward furnace
	11	RAHT6	Bottom of center tube facing cold side
	12	RAHT7	Removed
	13	RAHT8	Removed
	14	RAHT10	Bottom of the center tube facing toward furnace
	15	RAHT13	Top of center tube, facing south tube
	16	RAHT14	Bottom of north tube facing toward furnace
	17	RAHT15	Bottom of north tube facing toward furnace
	18	RAHT16	Removed
	19	RAHT17	Bottom of south tube facing toward furnace
	20	RAHT28	Top of south tube facing toward furnace (failed)
	21	RAHT29	Removed
Inner Surface of Monofrax Bricks	22	RAHT19	Center tile, left side rail
	23	RAHT20	Removed
	24	RAHT21	Removed
	25	RAHT22	Center tile, cavity side center
	26	RAHT23	Top tile (failed June 2000)
	27	RAHT24	Center tile, quasi-furnace side center
	28	RAHT27	Removed
	29	RAHT25	Lower tile, cavity side center
	30	RAHT26	Removed

[1] Thermocouple locations are illustrated in Exhibit 11-79.

RAH tube surface temperatures ranged from nominally 1410 to 1895 °F (766 to 1035 °C). The low end of the temperature range represents the back side of the tube surfaces near the process air inlet, with the high end of the temperature range representing the front side of the tube surfaces near the process air outlet. Changes in process air flow rates had noticeable effects on all tube surface temperatures. Tube surface temperature step changes were most noticeable for

surface temperature measurements near the process air exit and on the front side of the tubes. Tube surface temperatures during the test were comparable to those for all previous bituminous coal-fired tests. However, when comparing temperature data for the June 2000 and previous tests firing the same fuels at the same conditions, maximum tube surface temperatures at the process air exit were nominally 5 to 30 °F (3 to 17 °C) lower in June. Again these temperature data support the observation that the Kyocera tiles have a lower thermal conductivity than the Monofrax M tiles.

Process air inlet temperatures ranged from 1250 to 1270 °F (677 to 688 °C) during the coal-fired operational period prior to the air leak. Outlet process air temperatures ranged from nominally 1595 to 1725 °F (869 to 941 °C) during the tests successfully completed prior to the air leak. The effect of process air flow rate can be seen in the process air outlet temperature data. As process air flow rate decreases, exit temperature increases, as expected. These flow rate changes are noted at Run Hours 54 and 66.

Heat recovery data from the RAH panel are presented in Exhibit 11-80 for the June 2000 test. At process air flow rates of 150, 180, and 200 scfm (4.2, 5.1, and 5.7 m^3/min), the heat recovered from the RAH panel was 75,280 to 77,530 Btu/hr (79,420 to 81,790 kJ/hr), 81,120 to 87,640 Btu/hr (85,580 to 92,460 kJ/hr), and 89,890 to 94,380 Btu/hr (94,830 to 99,570 kJ/hr), respectively. The heat recovery ranges are a function of minor adjustments to the coal feed rate, combustion air flow rates, and changes in furnace pressure. The main burner firing rate was nominally 2.2 to 2.3 MMBtu/hr (2.3 to 2.4 $\times$ 10^6 kJ/hr).

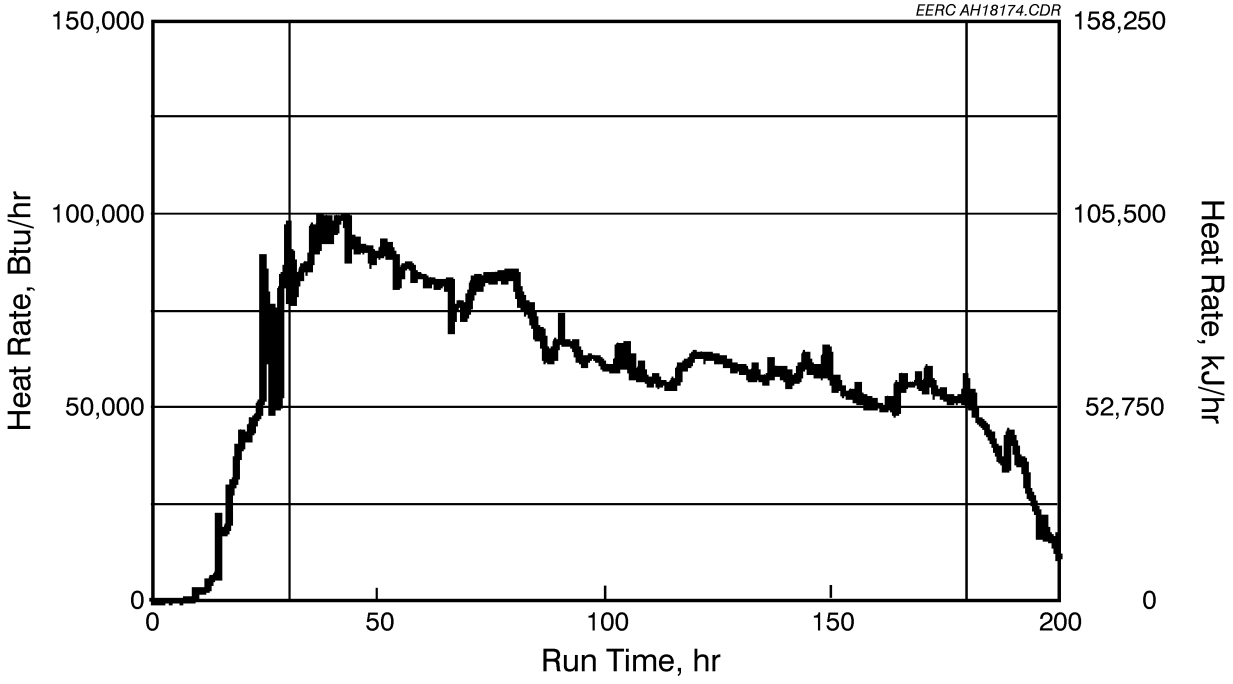

Exhibit 11-80
RAH Heat Recovery versus Run Time for
SFS Test SFS-RH13-0400

Exhibit 11-81 summarizes RAH heat recovery data at process air flow rates of 180 and 200 scfm (5.1 and 5.7 m^3/min) for bituminous coal-fired tests completed in 1999 through June 2000 and the subbituminous coal-fired test completed in March 2000. SFS tests in 1997 and 1998 are not included in the comparison because additional heat exchange surface (the SRAH) was present in those tests, the short duration of many test periods, and some differences in SFS operating conditions. Therefore, direct comparisons of RAH heat recovery are only valid for tests completed during the period January 1999 through June 2000 (RH6, RH7, RH8, RH9, RH10, RH11, RH12, and RH13).

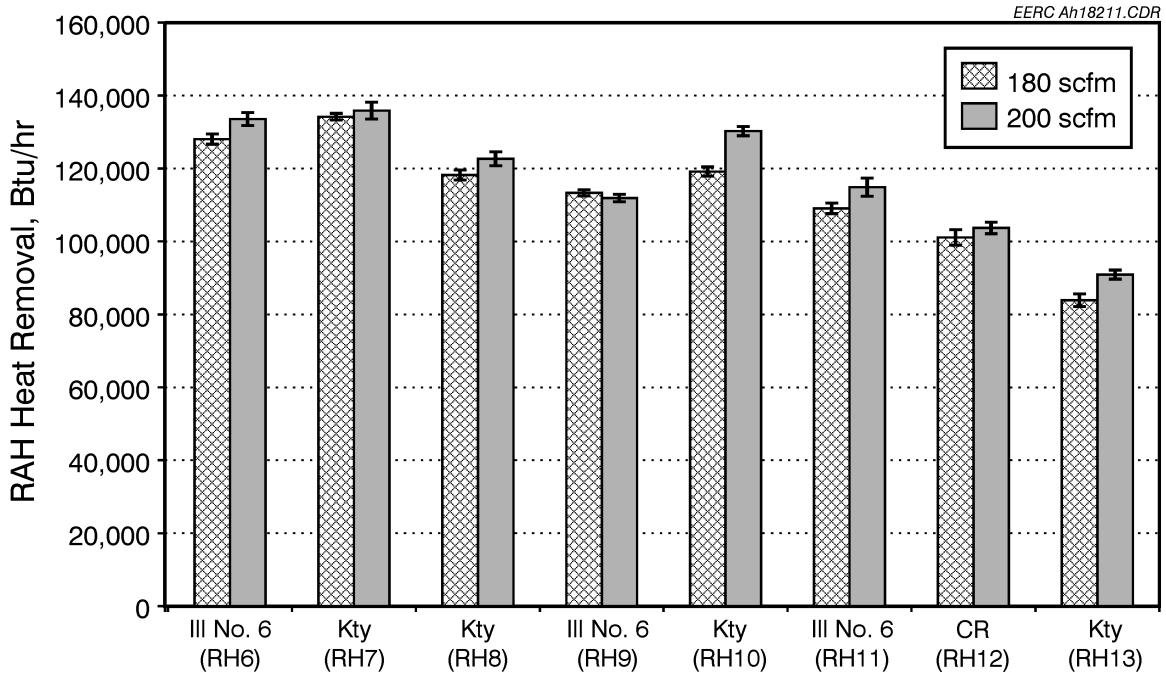

Exhibit 11-81
RAH Heat Recovery for Bituminous Coal-fired Tests Completed in 1999 and 2000 and a Subbituminous Coal-Fired test Completed in 2000

A comparison of eastern Kentucky coal-fired test data from February (RH7), April (RH8), and September 1999 (RH10) with June 2000 (RH13) shows that the RAH panel heat recovery in June 2000 was 30%–37% less than that observed in the previous tests. Comparisons with bituminous and subbituminous coal-fired tests completed in 1999 and 2000 show that the RAH panel heat recovery rate in June 2000 was lower than for all of the other test periods by 15%–37%. These data, along with the temperature data previously discussed, indicate that the Kyocera tiles significantly reduced the heat recovery rate of the RAH panel as a result of their lower thermal conductivity when compared to the Monofrax M tiles. Therefore, based on the extensive cracking observed and their impact on the RAH heat recovery rate, the Kyocera tiles are not a viable option at this time for further pilot-scale testing.

Besides the use of two different types of tiles, there were other factors influencing the RAH panel heat recovery rate data observed during the course of this project. First, the SRAH previously mentioned, which removed heat from the furnace and reduced the heat recovery rate by the RAH panel. However, after the August 1998 test, the SRAH was removed from the

system. A second reason for heat recovery variability in the RAH can be seen in comparisons of RH6 and RH9 (firing Illinois No. 6 coal) and RH7 and RH8 (firing eastern Kentucky coal). In both cases, heat recovery by the RAH was lower for the second test for each coal type. These data indicate that the heat recovery rate for the RAH panel was decreasing with each week of operation.

The reason for this reduction in heat recovery with time is not well understood, but EERC personnel believe that several factors influenced the reduction. One possibility is a potential change in heat flux to the RAH tiles, resulting in a decrease in the heat transfer to the radiation cavity. The flame-side surface of the RAH tiles did darken as a result of slag coating and absorption during the January 1999 test (RH6). However, it is not clear what the effect would be on radiant heat absorption or emission, or thermal conductivity. Also, no additional color changes were noted following subsequent test periods. One possibility is that the changing heat flow was related to tile deterioration with each week of coal-fired furnace operation as a result of slag erosion/corrosion. Erosion/corrosion of the tiles may have affected their heat-transfer properties. Another possibility would be a significant difference in thermal properties of the slag layer on the surface of the tiles. Although the residual slag layer present on the surface of the tiles is thin (a millimeter or less), it may have reduced the overall tile thermal conductivity.

Another potential contributing factor to the decreasing RAH heat flow may be the high-density furnace refractory color change observed with each week of operation. Newly cured high-density refractory in the furnace was a bright white color. As the high-density refractory darkened with each week of operation, it is possible that the reflectivity or emissivity characteristics of the furnace liner changed, resulting in a decrease in radiation to the RAH panel. A comparison of the RAH panel data for the April 1999 (RH8) and the February 1999 (RH7) tests, firing the same fuel and evaluating the same set of tiles, indicates that there was a decrease in the heat recovery rate of 12%. A similar effect was observed when comparing RH6 and RH9. This effect may be an indication of a potential reduction in refractory reflectivity/emissivity as previously stated or a change in its thermal conductivity, resulting in an increase in heat loss through the furnace wall. Heat loss through the furnace wall was probably not the key factor, since the EERC fired the furnace to achieve a specific furnace temperature. Therefore, increased heat loss through the furnace wall would have been accounted for by increased furnace firing rate. However, in the case of the June 2000 test, the thermal conductivity of the Kyocera tiles apparently influenced the performance of the RAH panel to a much greater degree than the properties of the new high-density refractory in the slagging furnace.

A combination of effects due to changes in tile and high-density refractory characteristics may be a reasonable explanation for the changes in heat recovery. That combination of factors would explain a lower RAH heat recovery rate in December 1999 (RH11, new tiles and aged high-density refractory) when compared to January 1999 (RH6, new tiles and high-density refractory) yet a comparable RAH heat recovery rate when compared to May 1999 (RH9, aged tiles and high-density refractory).

The magnitudes of these “naturally” occurring variations in heat recovery made it difficult to determine the effects of some of the more subtle variations in operations or RAH modifications. In particular, one small modification was a UTRC attempt to affect RAH heat transfer by applying coatings to the cavity-side surface of the Monofrax M tiles. Data obtained during subsequent SFS test periods indicated that the natural variations in heat recovery were greater

than the effects of the coatings so that no conclusion could be reached about the ability of the coatings to improve RAH tile cavity-side heat transfer.

Fuel properties, as they relate to furnace performance, also have the potential to influence the performance of the RAH panel. For example, when firing subbituminous coal (22–26 wt% moisture) in the slagging furnace it was necessary to fire the furnace at a higher rate (10%–20%) when compared to the bituminous coals to maintain a 2800 °F (1538 °C) furnace temperature. A 2900 °F (1594 °C) furnace temperature was not possible when firing a subbituminous coal in the slagging furnace because of capacity limitations associated with controlling flue gas flow rate and furnace static pressure. In the case of firing lignite fuels (32–38 wt% moisture), slagging furnace temperature was limited to 2700 °F (1482 °C). Compared to the Illinois No. 6 bituminous coal, lignite firing resulted in a 100 °F (56 °C)-lower furnace temperature at a firing rate that was 10% to 12% higher.

A calculation of adiabatic flame temperatures, based on 24% excess air, indicated a difference of 480 to 490 °F (267 to 272 °C) for Illinois No. 6 coal versus the lignite fuels. Therefore, it is unlikely that a 2800 °F (1538 °C) furnace temperature could be achieved with either lignite fired in the slagging furnace without the fuel moisture content being reduced. Without increasing the furnace temperature for a given RAH surface area, it is not likely that high-moisture fuels can achieve the same level of heat recovery observed when a bituminous coal is fired. However, calculations completed by UTRC show that lignite firing in the HITAF incurs a 2% efficiency penalty when compared to the Illinois No. 6 coal but should still reach approximately 45% overall system efficiency.

Overall, the RAH panel design developed by UTRC met or exceeded all process temperature and heat-transfer objectives based on the pilot-scale tests completed. However, the Monofrax M and Kyocera tiles did not meet performance objectives. Therefore, further development of the RAH concept must focus on development of an improved tile and/or the application of the RAH panel without tiles. Based on the potential advantages, substantially reduced cost, and shorter development time line, a focused effort to determine the potential application of the RAH panel without tiles for repowering and new plant concepts is warranted.

RAH Panel Heat-Transfer Performance Without Tiles

As discussed in the previous section, the use of the ceramic panels to protect the heat exchanger tubes leads to most of the operational problems with the current RAH design. Ideally, if the RAH could be operated without the ceramic tiles, the design would be greatly simplified and the heat exchange coefficients would rise dramatically. Additionally, cost would be significantly reduced because the RAH could be much smaller so less of the expensive alloy would be needed for construction, and the cost of the ceramic panels themselves would be eliminated. Laboratory data developed late in the program (and discussed in a separate section of this report) indicated that it may be possible to expose the oxide dispersion-strengthened alloy tubes carrying the process air in the RAH directly to the products of coal combustion and still expect reasonably long lifetimes. The laboratory data showed that as long as the surface temperature of the alloy was below that of the melting point of the ash impacting the surface, metal recession rates were very low. Therefore, for the June 2000 test, the EERC installed an air-cooled MA 754 alloy probe in the slagging furnace to evaluate the corrosion resistance of the alloy when it is exposed directly to the coal flame and slag as if the RAH were operated without

the tiles in place. The installed probe can be seen in the lower right corner of the top photograph of Exhibit 11-65.

The MA 754 alloy probe was inserted into the slagging furnace for a short period of time in May while new high-density refractory was cured in the furnace, slag tap, and slag screen. However, the available process air required to control alloy temperature was insufficient, forcing the removal of the probe to avoid overheating the alloy. Changes were made to increase the quantity of process air available to support the probe prior to the June 2000 SFS test. As a result of the changes, it was possible to insert the MA 754 alloy probe into the slagging furnace once coal firing had been stabilized. The probe was left in place for nominally 130 hr of coal firing prior to switching to natural gas firing and a controlled furnace cooldown period. Alloy surface temperature (based on a thermocouple measurement) was controlled at nominally 1780 to 2000 °F (971 to 1094 °C) as a function of probe insertion depth and a process air flow rate of 95 to 100 scfm (2.7 to 2.8 m^3/min). During the test, the uncooled ends of the MA 754 sleeve melted, but the cooled portion showed very little damage. The slag layer on the surface of the probe was only a few millimeters thick and detached from the probe on cooldown. Details concerning the slag layer on the surface of the probe are discussed in a separate section of this report.

Based on the results with the MA 754 alloy probe, a short (3-day) natural gas-fired SFS test was completed in September 2000. The purpose of the test (SFS-RH14-0500) was to evaluate the performance of the RAH panel without tiles to protect the heat-transfer surfaces from furnace conditions. This short test would allow the identification of system limitations, such as process air capacity, that must be addressed so that the RAH can be operated without the tiles while firing coal. If the RAH can be operated without tiles, then the cost and impedance to heat transfer caused by the tiles can be eliminated. In addition, the size of the RAH and time to commercialization can be substantially reduced.

During the gas-fired test, the furnace and RAH heatup rates were limited to 100 °F/hr (56 °C/hr). Thermocouples and an optical pyrometer were used to monitor the surface temperature of the MA 754 alloy tubes. Alloy surface temperatures were not permitted to exceed 2000 °F (1094 °C). Furnace firing rate and exit temperature and process air flow rate were controlled to prevent the MA 754 alloy surfaces from being overheated. Burner swirl was adjusted to minimize the potential for flame impingement on the alloy surfaces. Exhibits 11-82 and 11-83 summarize furnace firing rate and furnace temperatures as a function of run time for the September 2000 test.

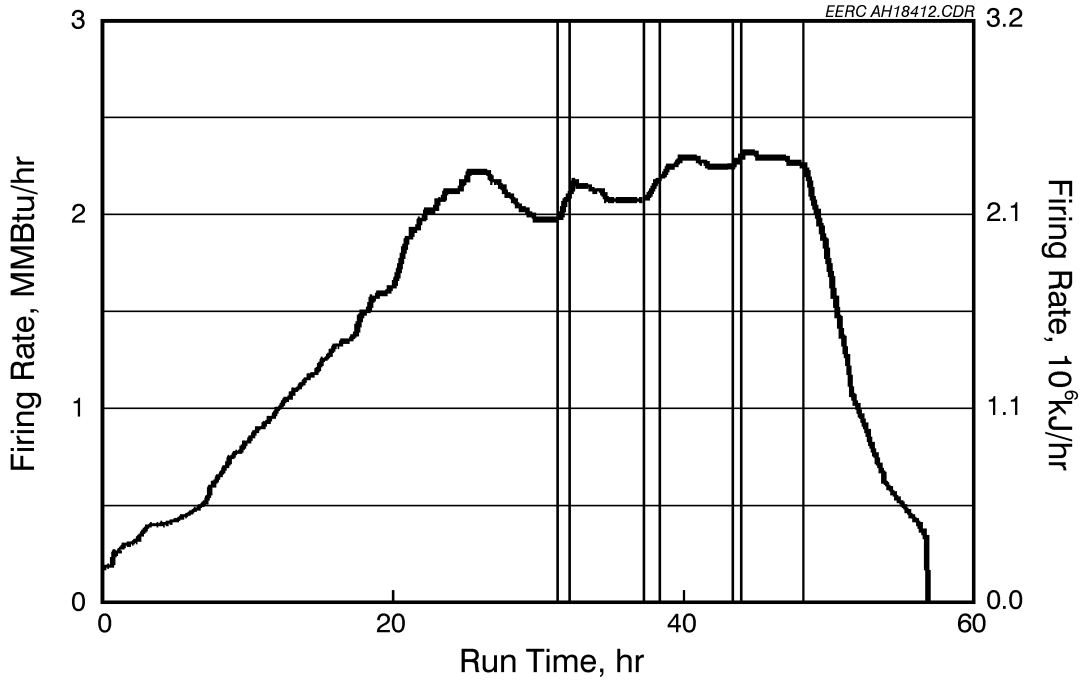

Exhibit 11-82
Furnace Firing Rate versus Run Time for
SFS Test SFS-RH14-0500

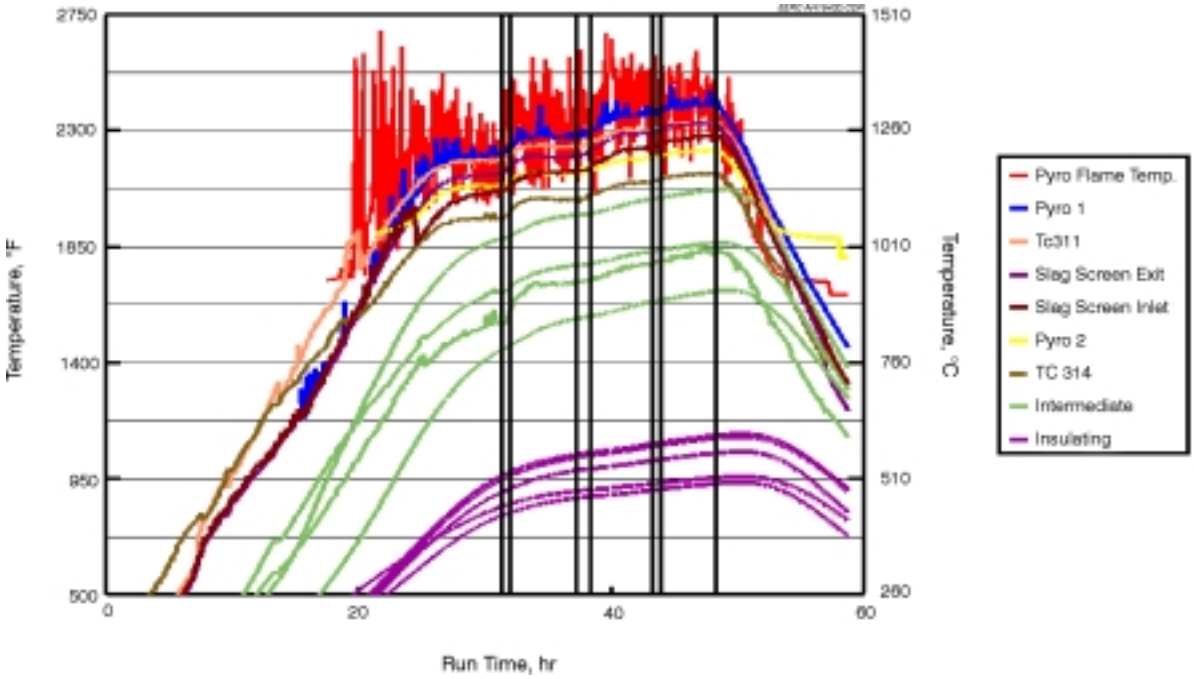

Exhibit 11-83
Furnace and Slag Screen Temperatures versus Run Time for
SFS Test SFS-RH14-0500

Exhibit 11-84 is a photograph of the RAH with the tiles removed before the September SFS test. The photograph shows the position of the MA 754 tubes in the RAH cavity. Low-density insulating board was installed behind the tubes and at the top and bottom of the cavity to protect high-temperature fibrous mat insulation from furnace conditions. The low-density insulating board also provided further protection to the machined elbows at the top and bottom of each MA 754 tube and minimized heat transfer to those surfaces. Other observations concerning the photograph include the presence of the upper and lower Monofrax M half-tiles and some high-density refractory repairs above the RAH panel. The Monofrax M half-tiles were left in place because they were in good condition and to protect insulating material from furnace conditions. High-density refractory repairs above the RAH panel were necessary because of cracks that had developed during the June 2000 test.

Exhibit 11-84
Photograph of RAH Panel Prior to SFS Test SFS-RH14-0500

Exhibit 11-85 is a photograph of the RAH after completing the September SFS test. The only differences when compared to Exhibit 11-84 are the white color of the new high-density refractory as a result of curing and some sintering (blackening) of the edges of some fibrous insulation below the RAH cavity. There were no observed changes to the surface of the MA 754 alloy tubes or the Type K thermocouples used to measure surface temperatures. However, the EERC does not expect the Type K thermocouples to survive even low-temperature furnace conditions for any duration. Therefore, if further testing of the RAH panel occurs without tile protection, it will be necessary to replace the Type K thermocouples with a combination of Type R or S thermocouples and one or more optical pyrometers.

Exhibit 11-85
Photograph of RAH panel following SFS Test SFS-RH14-0500

Exhibits 11-86 and 11-87 summarize the RAH tube surface temperatures and process air temperatures for the September 2000 test (SFS-RH14-0500). The process air flow rate data for the RAH panel are summarized in Exhibit 11-88. Exhibit 11-89 illustrates the location of thermocouples in the RAH panel, and Table 11-20 describes the RAH thermocouples that were used during the September 2000 test. Because the tiles were removed from the RAH panel prior to the test, there are no tile surface temperature data to discuss.

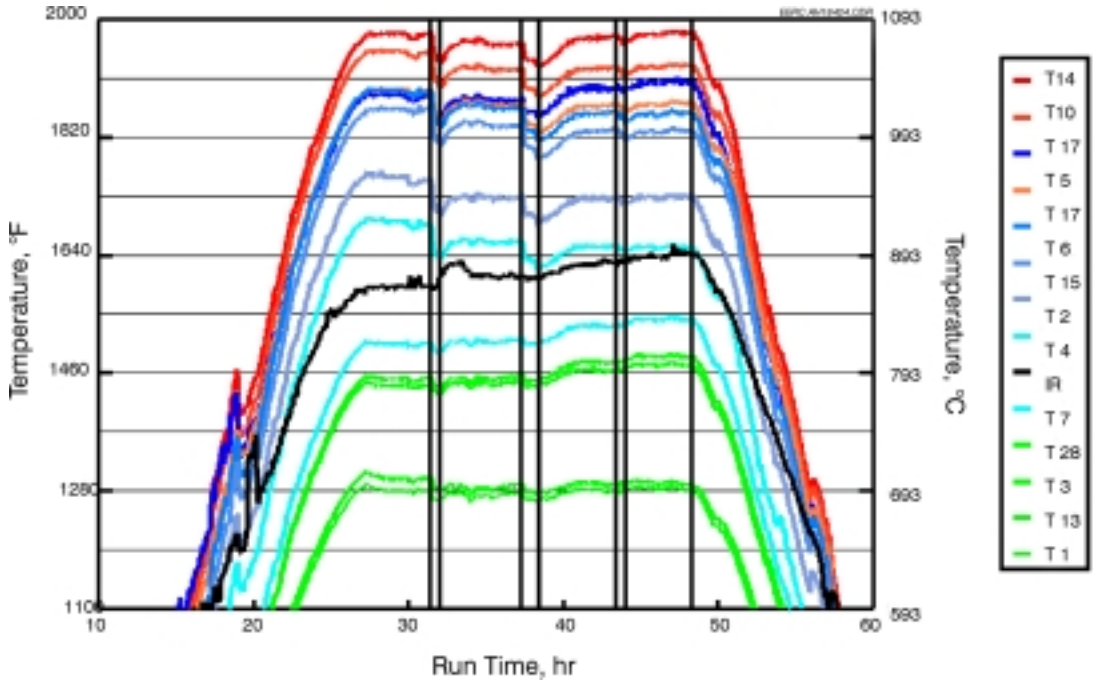

Exhibit 11-86
RAH Tube Surface Temperatures versus Run Time for SFS Test SFS-RH14-0500

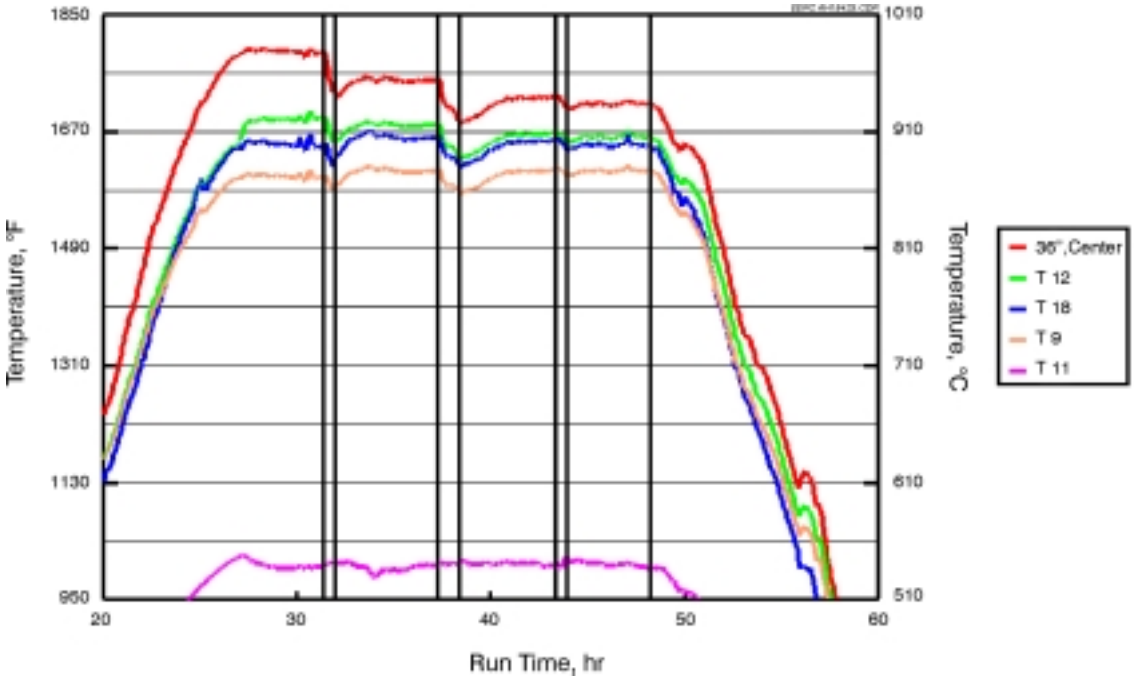

Exhibit 11-87
RAH Process Air Temperatures versus Run Time for SFS Test SFS-RH14-0500

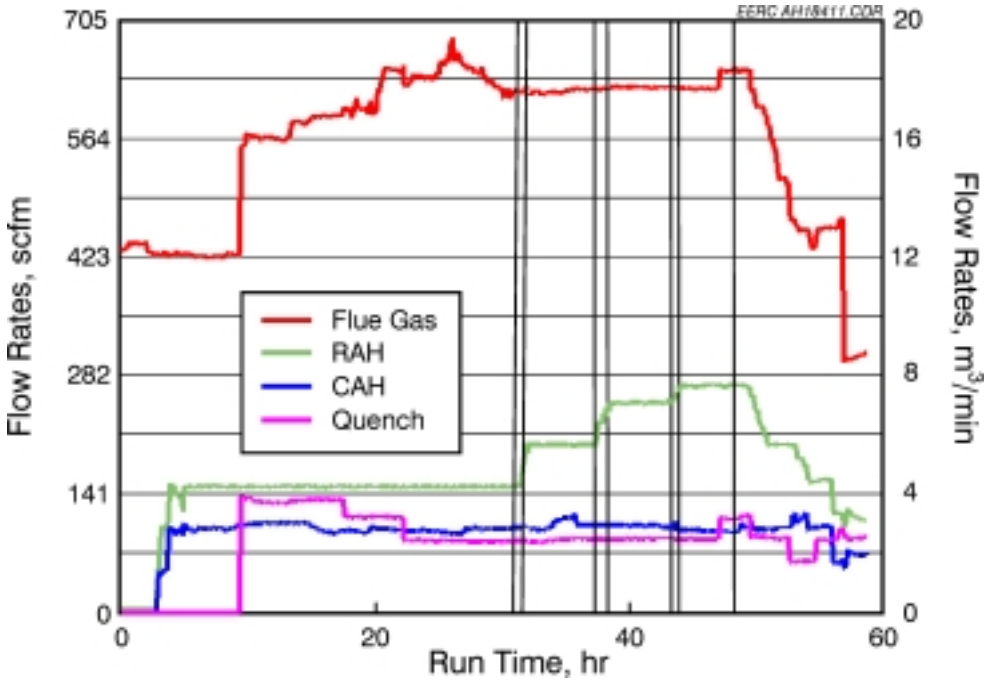

Exhibit 11-88
CAH Process Air, RAH Process Air, Quench Gas, and Flue Gas Flow Rates versus Run Time for SFS Test SFS-RH14-0500

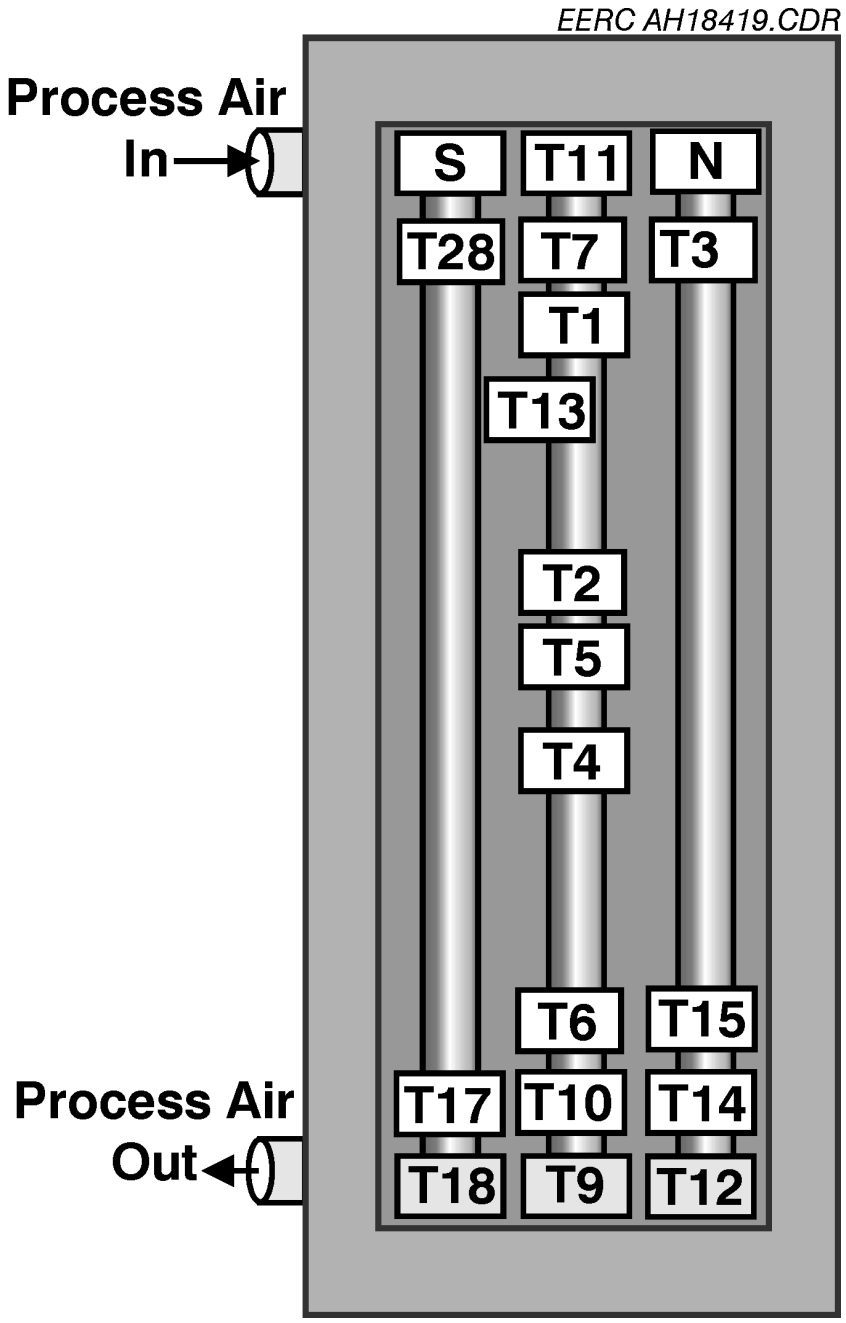

Exhibit 11-89
Thermocouple Locations in the RAH Panel for SFS Test SFS-RH14-0500

Table 11-20
Description of RAH Panel Thermocouple Locations for SFS Test SFS-RH14-0500[1]

Category	No.	Label	Description
Air Inlet	1	HP Air In	Provided by the EERC, in pipe before inlet header
	2	RAHT11	Air entering RAH through center tube
Air Outlet	3	RAHT18	Air leaving left (south) tube
	4	RAHT9	Air leaving middle tube
	5	RAHT12	Air leaving right (north) tube
MA Tube Surface	6	RAHT1	Top of center tube facing cold side
	7	RAHT2	Middle of center tube facing adjacent tube
	8	RAHT3	Top of north tube facing toward furnace
	9	RAHT4	Middle of center tube facing cold side
	10	RAHT5	Middle of center tube facing toward furnace
	11	RAHT6	Bottom of center tube facing cold side
	12	RAHT7	Top of center tube facing toward furnace
	13	RAHT8	Removed
	14	RAHT10	Bottom of the center tube facing toward furnace
	15	RAHT13	Top of center tube, facing south tube
	16	RAHT14	Bottom of north tube facing toward furnace
	17	RAHT15	Bottom of north tube facing cold side
	18	RAHT16	Removed
	19	RAHT17	Bottom of south tube facing toward furnace
	20	RAHT28	Top of south tube facing toward furnace
	21	RAHT29	Removed

[1] Thermocouple locations are illustrated in Exhibit 11-89.

RAH process air flow rates during the September test were controlled at 150, 200, 250, and 270 scfm (4.2, 5.7, 7.0, and 7.6 m^3/min). These individual RAH process air flow rates were set, then furnace firing rate was increased until tube surface temperatures approached 2000 °F (1094 °C). The furnace firing rate was then maintained for 4 hr before the process air flow rate was increased to the next set point and furnace firing rate increased accordingly. In order to avoid exceeding the 2000 °F (1094 °C) temperature limit established for the MA 754 tubes, it was necessary in some cases to marginally reduce firing rate during a 4-hr test period as furnace refractory continued to heat. A process air flow rate of 270 scfm (7.6 m^3/min) was the maximum flow rate available to support the RAH panel.

RAH tube surface temperatures ranged from nominally 1270 to 1990 °F (688 to 1088 °C). The low end of the temperature range represents the back side of the tube surfaces near the process air inlet, with the high end of the temperature range representing the front side of the tube surfaces near the process air outlet. Changes in process air flow rates had noticeable effects on all tube surface temperatures. Tube surface temperature step changes were most noticeable for surface temperature measurements near the process air outlet and on the front side of the tubes. Tube surface temperatures in September 2000 were comparable to those for all previous coal-

fired tests near the process air outlets because, for a given process air flow rate, the EERC adjusted furnace firing rate to maintain tube surface temperatures at these locations near limits established for the MA 754 alloy. However, the tube temperatures near the process air inlet were generally 100 to 200 °F (56 to 111 °C) cooler than typically observed when firing coal. The reason for this difference was the temperature of the process air entering the RAH. RAH inlet process air temperatures during the September test were nominally 1000 °F (538 °C), roughly 200 °F (111 °C) lower than inlet process air temperatures observed during coal-fired tests. These lower process air temperatures were the result of reduced heat transfer at the CAH and air preheater tube bundles because of lower flue gas flow rates and temperature, all related to the lower furnace firing rates.

As previously stated, process air inlet temperatures were nominally 1000 °F (538 °C) during the September 2000 test. Outlet process air temperatures ranged from nominally 1600 to 1690 °F (871 to 921 °C) during the test. The effect of process air flow rate can be seen in the process air outlet temperature data. When process air flow rate was increased, exit temperature decreased. As furnace firing rate was increased to maintain desired tube surface temperatures, the process air exit temperatures returned to nominal values. These flow rate changes are noted at Run Hours 32, 37, and 43.

Heat recovery data from the RAH panel versus run time are presented in Exhibit 11-90 for the September 2000 test. At process air flow rates of 150, 200, 250, and 270 scfm (4.2, 5.7, 7.0, and 7.6 m^3/min), the heat recovered from the RAH panel was 122,470 Btu/hr (129,210 kJ/hr), 165,310 Btu/hr (174,400 kJ/hr), 201,590 Btu/hr (212,680 kJ/hr), and 218,590 Btu/hr (230,610 kJ/hr), respectively. These are mean values for individual test periods of 3 to 4 hours. The main burner firing rate ranged from nominally 2.0 to 2.3 MMBtu/hr (2.1 to 2.4×10^6kJ/hr).

Exhibit 11-91 summarizes RAH heat recovery data at process air flow rates of 180 and 200 scfm (5.1 and 5.7 m^3/min) for bituminous coal-fired tests completed in 1999 through June 2000, the subbituminous coal-fired test completed in March 2000, and the natural gas-fired test completed in September 2000. All of the coal-fired tests utilized ceramic tiles to protect the MA 754 alloy tubes from furnace conditions. A comparison of the coal-fired test data with tiles and the September 2000 (RH14) natural gas-fired data without tiles shows that the RAH panel heat recovery in September was 22% to 82% higher for a process air flow rate of 200 scfm (5.7 m^3/min). The coal-fired data with tiles represents furnace temperatures ranging from 2800 to 2950 °F (1538 to 1621 °C) while the natural gas-fired data without tiles represents a furnace temperature of nominally 2300 °F (1260 °C).

Exhibit 11-90
RAH Heat Recovery versus Run Time for
SFS Test SFS-RH14-0500

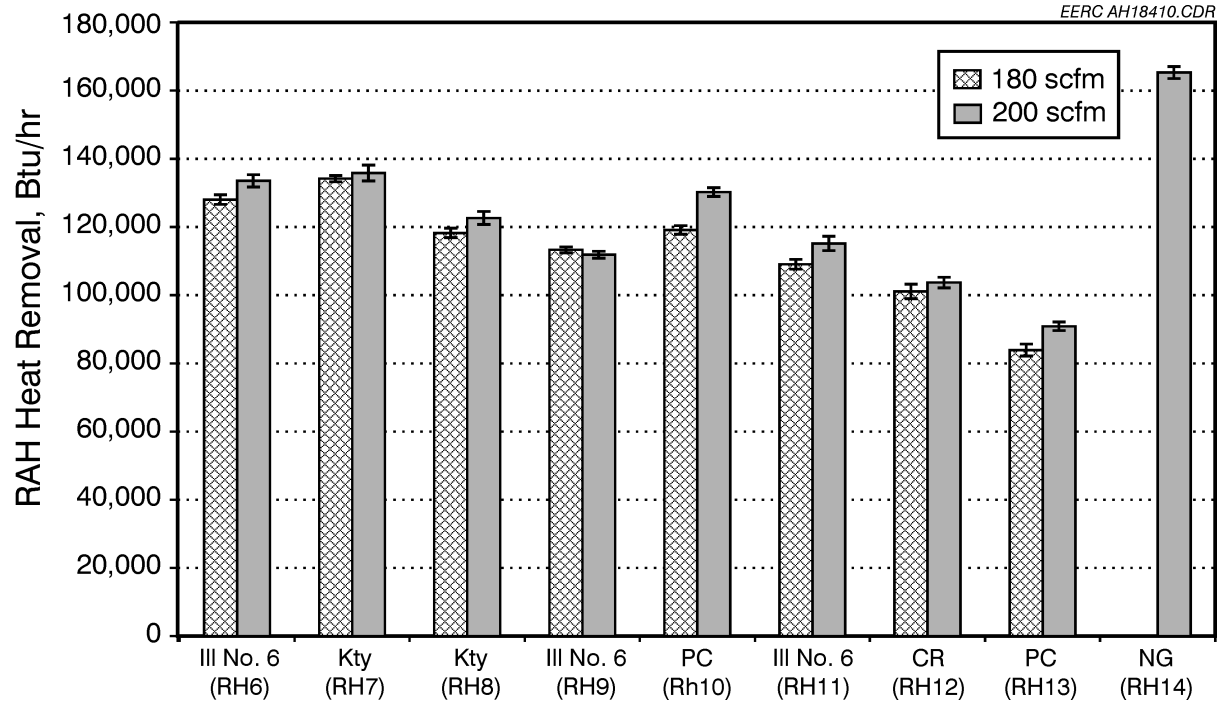

Exhibit 11-91
RAH Heat Recovery for Coal-Fired Tests Completed in 1999 and 2000
and the Natural Gas-fired Test Completed in September 2000

In August 1999, SFS Test SFS-RC2-0599 was performed for the primary purpose of curing new high-density refractory in the slagging furnace. Natural gas firing through the main burner at 3.0 MMBtu/hr (3.1×10^6 kJ/hr) resulted in a furnace temperature of nominally 2800 °F (1538 °C). The RAH panel was installed and Monofrax M tiles were in place, shielding the MA 754 alloy tubes from furnace conditions. At a process air flow rate of 200 scfm (5.7 m^3/min), the RAH panel heat recovery rate was 112,000 Btu/hr (118,160 kJ/hr). Although these conditions were only maintained for a short duration and the furnace had not reached thermal equilibrium, comparing the SFS-RC2-0599 and SFS-RH14-0500 data suggests that removal of the Monofrax M tiles resulted in a 47% increase in RAH heat recovery even though furnace temperature during SFS-RH14-0500 was 500 °F (278 °C) lower.

RAH heat recovery and process air flow rate are plotted versus furnace temperature for the September 2000 test in Exhibit 11-92. The data generally appear linear for the limited furnace temperature range represented. Whether this indicated trend is real or simply a function of the small data set is uncertain. If additional process air capacity were available to support the RAH panel, this data set could be expanded to document RAH heat recovery without tile protection at higher furnace temperatures. The implication is the potential for significantly higher heat-transfer rates for a given surface area. Assuming success firing natural gas, future coal-fired tests would be warranted to address issues concerning ash and slag deposition on the MA 754 alloy surfaces as well as heat transfer.

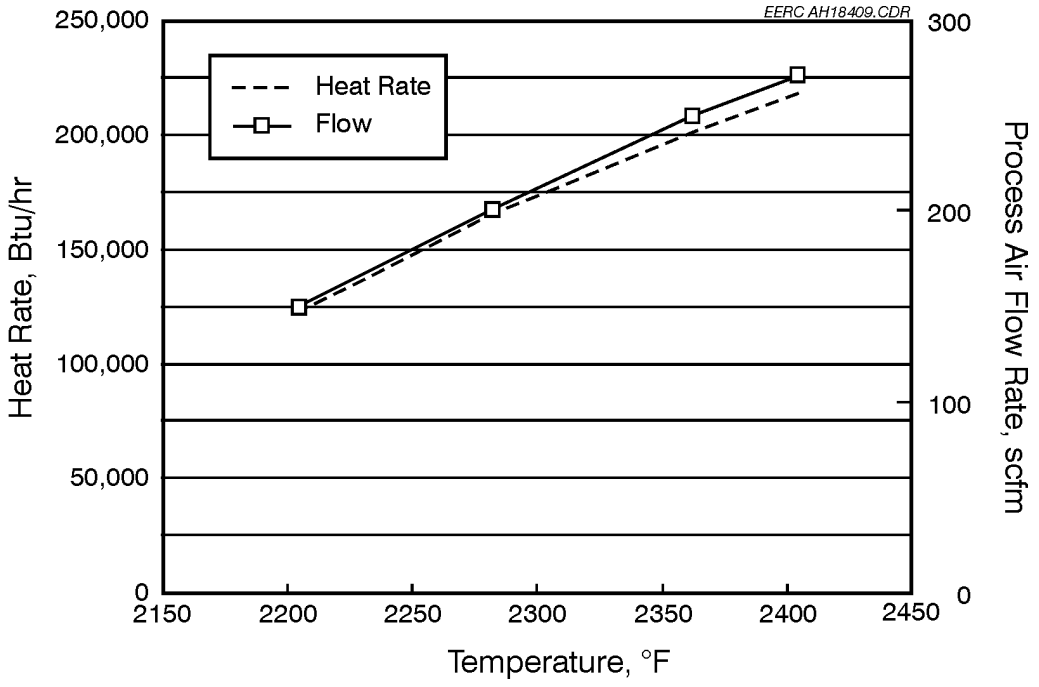

Exhibit 11-92
RAH Heat Recovery and Process Air Flow Rate versus Furnace Temperature for SFS Test SFS-RH14-0500

Additional compressor capacity is available to support further testing of the RAH panel. However, a new process air line will need to be installed to access the available compressor capacity. Installation of a second process air line would permit the use of two existing compressors to support SFS operation. In this scenario, a smaller compressor would be used to meet all air requirements other than the process air required to support the CAH tube bank and RAH panel. The air capacity available for the CAH and RAH would be a minimum of 400 scfm (11.3 m^3/min), and may be as high as 450 scfm (12.7 m^3/min), depending on compressor performance and line losses. Other modifications to the SFS process air system may be necessary to address other potential limiting factors such as control valve capacity, capacity of flow measurement devices, and process air heating and cooling capacity.

References

Collings, M.E.; Dockter, B.A.; Eylands, K.E.; Hajicek, D.R.; Henderson, A.K.; Hurley, J.P.; Kleven, P.L.; Lillemoen, C.M.; Weber, G.F. *Lignite Testing in a Pilot-Scale High-Temperature Advanced Furnace*; Final Report for U.S. Department of Energy Contract No. DE-FC26-98FT40321 and North Dakota Industrial Commission Contract No. FY98-XXX84; EERC Publication 99-EERC-03-06; Energy & Environmental Research Center: Grand Forks, ND, April 1999.

Collings, M.E.; Dockter, B.A.; Hajicek, D.R.; Henderson, A.K.; Hurley, J.P.; Kleven, P.L.; Weber, G.F. *High-Temperature Heat Exchanger Testing in a Pilot-Scale Slagging Furnace System*; Final Topical Report for U.S. Department of Energy Contract No. DE-FC26-98FT40320; EERC Publication 99-EERC-08-12; Energy & Environmental Research Center: Grand Forks, ND, Dec 1999.

Appendix A - Pilot-Scale Slagging Furnace System: A Facility Description

Introduction

The University of North Dakota Energy & Environmental Research Center (EERC) participated with United Technologies Research Center (UTRC) and UTRC subcontractors in Phase II of the Combustion 2000 project. EERC efforts were focused on laboratory- and bench-scale testing of materials used for the construction of key subsystems for a high-temperature advanced furnace (HITAF); testing of methods to reduce problems related to coal slag flow and corrosion; and the design, construction, and operation of a pilot-scale slagging combustion system to test the design and operation of key HITAF subsystems.

Work on the pilot-scale slagging furnace system (SFS) began in September 1995. A preliminary overall system design was completed in December 1995, and work began that same month on the fabrication and installation of the structural steel for the system. The area occupied by the SFS is roughly 24 × 48 ft (7.3 × 14.6 m) and six floors in elevation. Design and construction activities continued into April 1997, with refractory curing completed in May and initial system shakedown activities beginning in June. Installation of key components, system shakedown, and system modifications continued into December 1997. Testing of critical HITAF components began in December 1997 and continued through September 2000. This section presents a detailed description of the pilot-scale SFS designed, constructed, and operated by the EERC in support of the UTRC Combustion 2000 project.

Pilot-Scale Slagging Furnace System

A design package for the pilot-scale SFS was completed by the EERC and approved by UTRC in July 1996. The package contained a process description, process flow diagram, plan and elevation views of major components, piping and instrumentation diagrams (P&IDs), and an instrumentation list. P&IDs can be found in Addendum-A, with plan and elevation views presented in Addendum-B. Addendum-C contains start-up, shutdown, and emergency procedures. Exhibits 11A-1 and 11A-2 are a photograph and simplified illustration, respectively, of the SFS.

Exhibit 11A-1
Photograph of the Pilot-Scale Slagging Furnace System

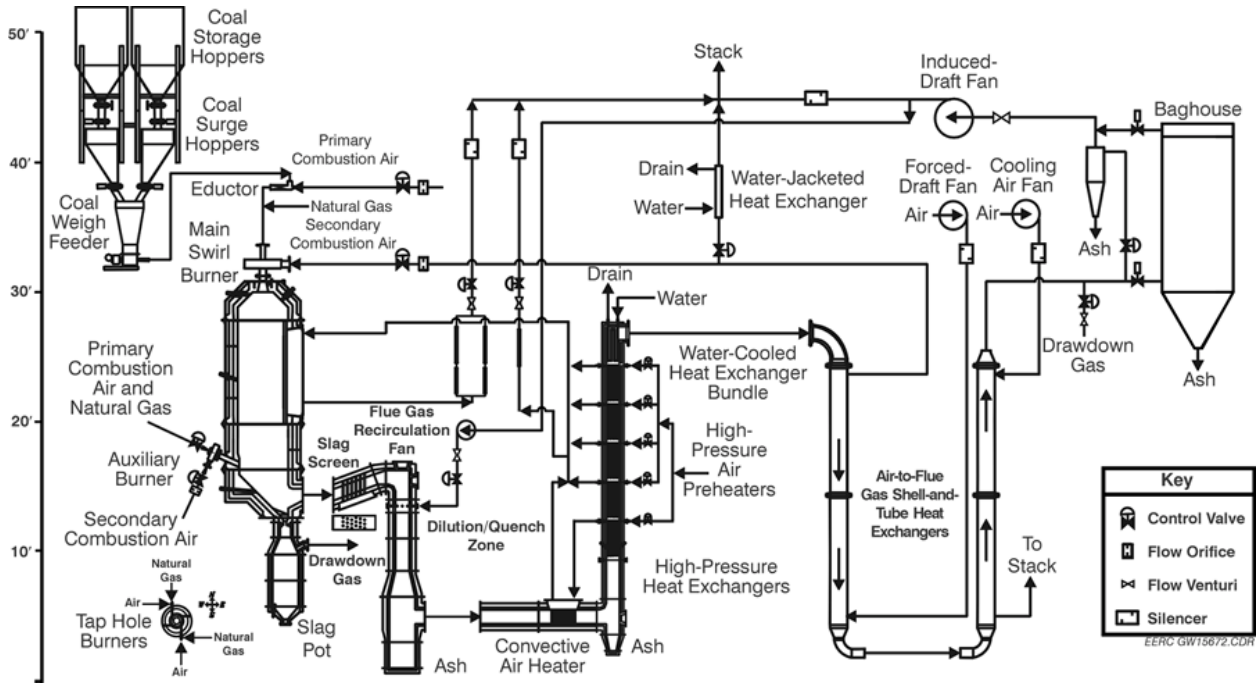

Exhibit 11A-2
Illustration of the Pilot-Scale Slagging Furnace and Support Systems

The SFS is divided into seven primary process areas: 1) combustion air (Area 100), 2) fuel feed system (Area 200), 3) slagging furnace (Area 300), 4) slag screen–quench zone–convective pass (Area 400), 5) flue gas system–baghouse (Area 500), and 6) process air system (Areas 600 and 700). These area identification numbers are the basis for component identification and numbering. The individual areas are identified in the overall process P&IDs in Addendum-A.

Installation of electrical lighting and 110-, 208-, and 440-volt circuits was initiated in July and continued through September 1996. Light fixtures were installed on all six floors, and emergency lights were installed in the high-bay stairwell at three elevations. Weatherproof instrument and electrical wire trays were run on all six floors and into the control room. Electrical circuits (110-volt) to support installation of the various system components were installed on all six floors early in the construction process once the majority of the structural steel installation was complete. Installation of circuit breaker panels (110-, 208-, and 440-volt) was completed in December 1996, with wiring activities completed in March 1997. The focus of electrical work through December 1997 was final electrical connections as system components were installed.

Structural Steel

Structural steel design, drafting, and procurement activities began in late 1995 and were essentially completed in April 1996; fabrication and erection were completed in May 1996; and priming and painting continued through June. Some limited structural steel work continued through late 1996 in conjunction with the installation of key HITAF components. Detailed structural steel design files and drawings were completed for the SFS. This information is on file at the EERC and available upon request. Copies of detailed structural steel drawings for the SFS

were submitted to UTRC for informational purposes in early 1998. The photograph in Exhibit 11A-1 shows the general layout of SFS structural steel and component installation.

Fuel Feed System

Coal feeder specifications were submitted to UTRC for review and approval in July 1996. Coal feeder specifications included pulverized coal density (40 lb/ft^3 [641 kg/m^3]) and particle size (70% <0.0030 in. [75 μm; 300-μm top size]). Other specifications included feed rate range (200–500 lb/hr [91–227 kg/hr]), minimum hopper capacity (10 ft^3 [0.3 m^3]), nonpulsing feed (twin-screw), gravimetric (loss-in-weight) feed mode, minimum 20-bit resolution load cell (high-resolution digital), and user-programmable microprocessor control. Following UTRC approval, a bid package was distributed to several vendors requesting formal bids on the coal feeder.

Coal feeder bids were received from four prospective vendors in August 1996, and a purchase order was subsequently issued to Winger Associates for a K-Tron coal feeder. The coal feeder arrived in late October and was installed on the fourth floor of the high-bay structure in November. Fabrication drawings for two intermediate coal hoppers were completed in early December, followed by material procurement. Fabrication of the coal hoppers began in December 1996. Fabrication and installation of two intermediate coal hoppers was completed in February 1997, along with installation of the valves for the coal feed system. The use of two coal hoppers minimizes the possibility of coal feed interruptions caused by plugging, bridging, or valve failure in a single intermediate hopper. Level indicators for the intermediate coal hoppers were added in June, along with hopper vents and dust collectors and final wiring of valves and weigh cells. The programming of the controller for the coal feeder and its integration with the data acquisition system began in December 1996 and was completed in January 1997. Installation of the main and auxiliary burners was completed in March 1997, along with natural gas connections to both burners and primary air lines (including coal feed to the main burner). Secondary air connections were completed to the auxiliary and main burners in March and April 1997, respectively.

Shakedown of the coal feed system began in June and was completed in December 1997 as a function of SFS operation. A new set of screws was installed in the coal feeder in November in an attempt to eliminate short-term feed rate instability observed during hopper fill cycles. It appeared that the original screws were flooding to some degree during fill cycles. The new set of screws eliminated the flooding problem. Initial feed rate limitations with the new set of screws was overcome by changing the coal feeder gear ratio, resulting in a fivefold increase in feed rate capacity. Installation of the original set of screws would be necessary to achieve a feed rate of >300 lb/hr (136 kg/hr). The maximum potential coal feed rate is believed to be about 1500 lb/hr (681 kg/hr). However, feed rates >400 lb/hr (182 kg/hr) have not been demonstrated. The photographs in Exhibit 11A-3 show two coal storage hoppers, the stands for the coal storage hoppers, the two intermediate coal hoppers, and the gravimetric coal feeder.

EERC GW18537.CDR

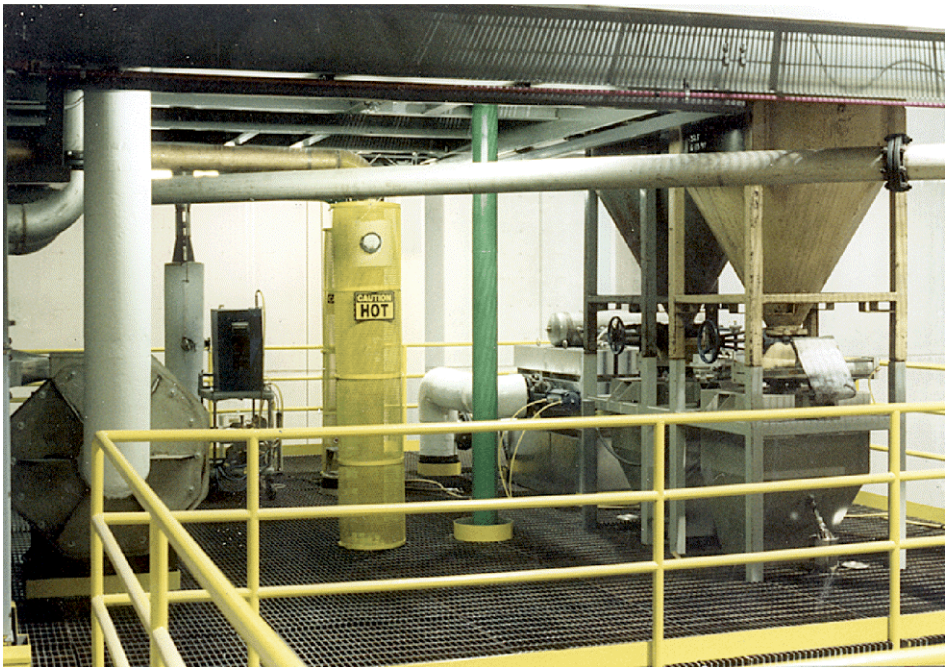

EERC GW18549.CDR

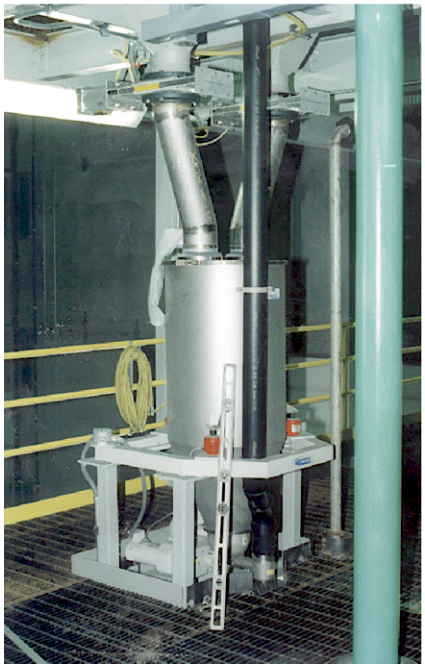

Exhibit 11A-3
Photographs of Coal Storage Hoppers, Intermediate Coal Hoppers, and Coal Feeder

Natural gas line size, header size, and delivery pressure requirements were finalized with the local supplier in August 1996. The local supplier installed a 2-in. (5-cm) meter and regulator to deliver natural gas at about 12 psig (0.9 bar). Based on the components installed by the gas supplier, the EERC elected to design and fabricate a 2-in. (5-cm) natural gas header to be operated at 8 psig (0.6 bar). This header supplies natural gas to the main and auxiliary burners as

well as a two-port burner in the slag tap. Header design, fabrication, and installation were completed in late 1996. Installation of the natural gas piping, valve/control system, and flame safety system for the main and auxiliary burners was completed in March 1997, and pressure testing was completed in April. Shakedown and verification of the natural gas system was completed in June 1997 as a function of refractory-curing activities and initial firing tests with the auxiliary and primary burners.

Pilot-Scale Slagging Furnace

The pilot-scale slagging furnace design is intended to be as fuel-flexible as possible, with maximum furnace exit temperatures of 2700 to 2900 °F (1483 to 1593 °C) in order to maintain the desired heat transfer to the radiant air heater (RAH) panel and slag flow. It has a nominal firing rate of 2.5 million Btu/hr (2.6×10^6 kJ/hr) and a range of 2.0 to 3.0 million Btu/hr (2.1 to 3.2×10^6 kJ/hr) using a single burner. The design is based on a bituminous coal (Illinois No. 6 – 11,100 Btu/lb, or 25,800 kJ/kg) and a nominal furnace residence time of 3.2 s. Resulting flue gas flow rates range from roughly 425 to 645 scfm (12.0 to 18.6 m^3/min), with a nominal value of 530 scfm (15 m^3/min) based on 20% excess air. Firing a subbituminous coal or lignite increases the flue gas volume, decreasing residence time to roughly 2.6 s. However, the high furnace temperature and volatility of the low-rank fuels result in high combustion efficiency (>99%). The EERC oriented the furnace vertically (downfired) and based the burner design on that of a swirl burner currently used on two EERC pilot-scale pulverized coal (pc)-fired units that are fired at 600,000 Btu/hr (633,000 kJ/hr). Slagging furnace dimensions are 47 in. (119 cm) inside diameter (i.d.) by roughly 16 ft (4.9 m) in length. Table 11A-1 summarizes the volumetric flow rate and temperature data upon which the furnace design was based. Furnace refractory pouring activities were completed in March 1997, and the furnace was installed in the high bay.

The vertically oriented furnace shell was designed to include four distinct furnace sections that, when bolted together, make up the pilot-scale slagging furnace. The top section of the furnace supports the main burner connection and is shown in the photograph in Exhibit 11A-4. The upper-middle furnace section, shown in the Exhibit 11A-5 photograph, provides a location for installation of two RAH panels (on the opposite wall). The lower middle furnace section supports the auxiliary gas burner; the bottom section of the furnace includes the furnace exit to the slag screen as well as the slag tap opening. Exhibit 11A-6 is a photograph of the two lower sections of the furnace showing the auxiliary burner, furnace exit, several sight ports, slag tap, top of the slag pot, drawdown gas flange, slag screen, and upper sections of the dilution/quench zone.

EERC GW18543.CDR

Exhibit 11A-4
Photograph of Top Furnace Section with Primary Burner Installed

EERC GW18546.CDR

Exhibit 11A-5
Photograph of Upper-Middle Furnace Section

EERC GW18544.CDR

Exhibit 11A-6
Photograph of the Two Lower Furnace Sections

Construction materials for the furnace shell were mostly carbon steel. The only exceptions were the flanged pipe connections for the main and auxiliary burners and the sight ports, since their refractory protection is limited. The main burner piping connection to the furnace is 8-in. (20-cm) Schedule 40 stainless steel material. The auxiliary burner piping connection to the furnace is 3.5-in. (8.9-cm) Schedule 40 stainless steel material. Copper pipe and flow control panels can also be seen in the furnace photographs. These components supply cooling water to the slag screen tubes, refractory support surfaces in the furnace, several sight ports, and high-density refractory in the vicinity of the main and auxiliary burners. The control panel on the right in the lower furnace photograph supplies combustion air and natural gas to the slag tap burner.

Table 11A-1
Theoretical Flow and Heat-Transfer Data for the Slagging Furnace and Refractory Ducts Based on Illinois No. 6 Bituminous Coal

Furnace Firing Rate, MMBtu/hr:	2.0	2.5	3.0		2.0	2.5	3.0
Furnace				Furnace Exit/Slag Screen			
Furnace i.d., in.	47	47	47	Total Flue Gas Flow, scfm	592	646	663
Furnace Length, ft	16	16	16	Total Flue Gas Flow, acfm	3598	3926	4029
Refract. 1 Thickness, in.	4	4	4	Furnace Exit Vel., ft/s	33.2	36.2	37.2
Refract. 2 Thickness, in.	4	4	4	Slag Screen Exit Gas Vel., ft/s	66.4	72.5	74.4
Refract. 3 Thickness, in.	3.25	3.25	3.25				
Furnace Weight, tons	14.4	14.4	14.4	Dilution Gas Requirements			
				Inlet Gas Temp., °F	2520	2535	2540
Inlet Gas Temp., °F	2900	3000	3100	Gas Velocity In, ft/s	61.3	67.3	69.2
Avg. Gas Temp., °F	2800	2850	2900	Exit Gas Temp., °F	1855	1851	1850
Exit Gas Temp., °F	2700	2700	2700	Dilution Gas Temp., °F	300	300	300
Refract. 1 Surf. Temp., °F	2677	2728	2777	Dilution Gas Flow, scfm	248	280	289
Refract. 2 Surf. Temp., °F	2431	2477	2521	Total Flue Gas Flow, scfm	840	926	952
Refract. 3 Surf. Temp., °F	1751	1783	1815	Flue Gas Flow Rate Out, acfm	3740	4115	4229
Furnace Skin Temp., °F	275	279	283	Gas Velocity Out, ft/s	67.6	74.4	76.5
Coal Feed Rate, lb/hr	176	220	264	Dilution Gas Nozzles			
Airflow Rate, scfm	398	497	597	Nozzle Diameter, in.	1.25	1.25	1.25
Flue Gas Flow Rate, scfm	428	536	643	No. of Nozzles	8	8	8
Flue Gas Flow Rate, acfm	2683	3412	4155	Dilution Gas Flow, acfm	362	409	422
Furnace Gas Velocity, ft/s	3.7	4.7	5.7	Dilution Gas Velocity, ft/s	89	100	103
Flue Gas Residence Time, s	4.1	3.2	2.6				
				Convective Air Heater			
Auxiliary Burner, scfm	164	110	20	Gas Temp., °F	1800	1800	1800
Auxiliary Burner, kBtu/hr	890	560	110	Flue Gas Flow Rate, acfm	3651	4025	4138
Total Firing Rate, kBtu/hr	2890	3060	3110	Gas Velocity, ft/s	52.2	57.5	59.1
Wall Losses, kBtu/hr	194	202	209				
RAH Losses, kBtu/hr	190	190	190				

Assumption: Excess air is 20%.

Temperature measurement in the furnace is extremely important. Methods to characterize furnace temperature during shakedown included Type S thermocouples and a high-velocity thermocouple (HVT). An optical method was considered; however, instrument vendors in 1997 determined that the cross-sectional area of the slagging furnace was too small for an industrial-grade instrument to be effective. Four Type S thermocouple locations were designated for the furnace interior in the final design. Two Type S thermocouple locations were included in the design of each of the temporary RAH panel doors. Once the large radiant air heater panel (LRAH) was installed, two of the Type S thermocouples were relocated in sight ports in the furnace wall. Thermocouples are also located at the interface between the high-density and intermediate refractory layers as well as between the intermediate and insulating refractory layers.

In the third quarter of 1998, two optical pyrometers were purchased to replace two Type S thermocouples that required weekly replacement because of slag corrosion. These optical pyrometers were mounted in relatively permanent locations to measure furnace flame temperature and flue gas temperature near the ceramic tile surfaces of the LRAH panel. A third optical pyrometer with fiber optics was also installed and is used to measure flue gas and surface temperatures at multiple locations in the furnace and slag screen. Final installation of the optical pyrometers was completed in early December 1998, following delivery of the third optical pyrometer and completion of furnace refractory work. Operating experience has shown optical pyrometer performance to be acceptable when compared with Type S thermocouples while firing natural gas and pulverized coal. Verification of optical pyrometer performance is accomplished during each SFS operating period using Type S thermocouple data while firing natural gas and pulverized coal.

Thermocouple data are automatically logged into the data acquisition system. A pressure transmitter and gauges are used to monitor static pressures in order to monitor furnace performance. These data are automatically logged into the data acquisition system and are recorded manually on data sheets on a periodic basis as backup. An example of furnace temperature data plotted as a function of run time can be found in Addendum-D. Furnace temperature measurements are presented on a schematic of the furnace in Addendum-E.

Observation ports were located in the furnace to permit visual observation of the main burner flame, auxiliary burner flame, RAH panels, slag screen, and slag tap. One sight port is located in the wall of each of the four sections of the slag pot to permit observation of slag buildup and determine when to break up stalagmitelike deposits to make better use of the available volume in the slag pot. With the exception of the furnace exit (inlet to the slag screen) and a few furnace sight ports, there is one sampling port in the furnace wall. This port was installed in May 2000 to permit installation of an air-cooled probe fabrication using the MA 754 alloy, the same alloy used to fabricate the RAH heat-transfer surfaces. This port is located near the bottom of the blank door installed when the SRAH panel was permanently removed. When the LRAH panel is not installed, additional access ports are available in the temporary blank door.

The slag tap was intended to be as simple and functional as possible. To that end, the original design was a simple refractory-lined hole in the bottom of the furnace. The diameter of the slag tap was 6 in. (15 cm), with the potential to change the diameter by simply removing or repouring refractory. To minimize heat losses, slag is collected in an uncooled, dry container with refractory walls. Because of plugging problems experienced during system shakedown, the slag tap refractory was replaced, reducing the diameter of the hole to nominally 4 in. (10 cm) and creating a well-defined drip edge. In addition, a two-port natural gas slag tap burner was added in early 1998. Another design feature of the slag tap involves drawing a small amount of flue gas through the slag tap to help maintain temperature and promote slag flow. The flow rate of the drawdown gas is 25 to 40 scfm (0.71 to 1.13 m^3/min), depending on the desired slag tap temperature and burner firing rate. As a result, although some slag tap deposits do form and slag tap erosion is observed, the slag tap only plugged twice during nearly seven weeks of SFS operation in 1998. Since the slag tap burner was added, plugging problems encountered in the slag tap were either related to refractory failures or fuel ash fusion temperatures that were higher than anticipated.

The combination of a slag tap burner and the drawdown gas feature has resulted in a slag tap with limited plugging problems. The drawdown gas temperature is reduced using indirect cooling before combining upstream of the baghouse with the bulk of the flue gas. Cleaning of the entrance of the drawdown gas line is required occasionally to maintain gas flow in the desired range.

The slag pot consists of several refractory-lined modular sections. Three of these modular sections are shown hanging from the bottom of the furnace in the left foreground of the photograph in Exhibit 11A-7. The refractory in the slag pot consists of two layers: 1.5 in. (3.8 cm) of high-density material and 2.5 in. (6.4 cm) of insulating refractory. The high-density refractory was intended to be sacrificial. However, the removal of slag from the slag pot has not resulted in refractory damage. The slag pot has a 2-ft (0.6-m) i.d. and allows for a variable length (3 to 7 ft [0.9 to 2.1 m]) with the installation of as many as three spool piece sections. Depending on the frequency and duration of system operation, it is necessary to have two complete slag pots. The use of a single slag pot for a week of operation is desirable. However, continuous operation of the SFS for more than a week requires that the slag pot be changed to accommodate the volume of slag collected. Changing the slag pot containers can be accomplished on-line while firing coal.

Exhibit 11A-7
Photograph Showing the Cooling Water Recirculation Tank and pumps, Furnace Slag Pot, Lower Sections of the Dilution/Quench Zone, and CAH Duct

Construction materials for the slag pot shell were carbon steel. The only exception was the flanged pipe connection for the drawdown gas, because its refractory protection is limited. The drawdown gas piping connection to the slag pot is 6-in. (15-cm) Schedule 10 stainless steel material. Two observation ports were installed at the top of the slag pot to permit visual evaluation of slag tap performance. The key to their value is the ability to keep them clean and

limit their impact as heat sinks for slag flowing through the slag tap. A limited nitrogen purge is effectively used to keep system sight ports clean.

Temperature is useful as an indicator of slag tap burner and slag tap performance. Therefore, a thermocouple is located in the immediate vicinity of the slag tap. In addition, if the slag tap burners are fired fuel-rich, this condition results in a carbon monoxide spike at the baghouse exit as a result of the drawdown gas flow to the inlet side of the baghouse. Thermocouple data and flue gas data are automatically logged into the data acquisition system. A pressure indicator is used to monitor static pressure in the same location in order to monitor slag tap performance. These data are recorded manually on data sheets on a periodic basis.

Secondary combustion air preheat control capabilities for the main burner are limited at this time. The present range of control is 600 to 800 °F (316 to 427 °C), depending on ambient air temperatures and forced draft (FD) fan capacity. Two tube-and-shell heat exchangers are operated in series to recover heat from the flue gas to preheat secondary combustion air for the main burner. Primary combustion air for the main burner is not heated at this time. Heated primary air may be necessary to successfully fire low-heating-value fuels, although two lignites have been successfully fired using unheated primary air. It may also be necessary to add an electric air preheater in the future to achieve the desired flexibility with respect to secondary combustion air temperature control. The need for an electric air preheater will be based on performance data developed during system operation and future test plans. Since the auxiliary burner is only natural gas-fired, neither the primary nor secondary air sources for this burner are heated.

Detailed fabrication drawings for the furnace and slag pot shells were prepared and approved prior to material procurement and fabrication. Fabrication of the furnace and slag pot shell sections were initiated in September 1996 and completed in October. Installation of the furnace shell and furnace penetrations was completed in December 1996. Furnace fabrication drawings were updated, with penetrations added for thermocouples, pressure taps, and sight ports. These updated drawings were submitted to UTRC for informational purposes and are on file at the EERC.

The refractory walls in the slagging furnace consist of three castable refractory layers: 4 in. (10.2 cm) of high-density (14 Btu-in./ft^2-°F-hr [2.0 W/m-K]) slag-resistant material; 4 in. (10.2 cm) of an intermediate refractory (4.0 Btu-in./ft^2-°F-hr [0.6 W/m-K]); and 3.25 in. (8.3 cm) of a low-density insulating refractory (1.3 Btu-in./ft^2-°F-hr [0.2 W/m-K]). Three refractory layers were selected as a cost-effective approach to keep the overall size and weight of the system to a minimum while reducing slag corrosion and heat loss.

Because of its structural strength and high corrosion resistance, Plibrico Plicast Cement-Free 98V KK alumina castable was originally used as the inner layer in the top three furnace sections, in the exit of the furnace, and in the top section of the dilution/quench zone. Plicast Cement-Free 99V KK was used in the bottom furnace section (except for the exit), slag tap, slag screen, and transition to the dilution/quench zone because of its even greater resistance to slag attack. Refractory procurement began in December 1996, and refractory-pouring activities for most of the system (four furnace sections, slag pot sections, dilution/quench zone, convective air heater [CAH] duct, and cooling air preheater duct) were completed in March 1997. Refractory pouring for the slag screen and several drawdown gas piping sections was completed in April 1997.

Complete replacement of the high-density refractory has been required twice since the original refractory was installed in 1997. However, high-density refractory replacement was not necessarily completed in all four furnace sections at the same time. Repairs to the intermediate and insulating refractory layers were required in some areas of the furnace as a result of damage that occurred when the high-density layer was removed; general replacement of intermediate and insulating refractory was not necessary.

After several weeks of furnace operation, refractory repairs were made to the high-density refractory in the top section of the furnace and the upper middle furnace section. In the top section of the furnace, the Plibrico Plicast Cement-Free 98V KK refractory was replaced with a Narco Cast 60 castable refractory. Replacement was necessary because of the shrinkage found in the Plibrico Plicast Cement-Free 98V KK. The Narco Cast 60 refractory was selected as a replacement because of past success with its use in other furnace systems. Although the Narco Cast 60 is much more prone to slag corrosion, operating experience with bituminous and subbituminous coal had shown that slag deposition was not significant in the top section of the furnace. After nearly 7 weeks of operation, the Narco Cast 60 refractory appeared to be in good shape, although refractory deterioration was evident in the top section of the furnace after 2 weeks of lignite firing. Therefore, the high-density refractory in the top section of the furnace was replaced with a Plibrico Plicast Cement-Free 96V refractory in the fall of 1998. This material is less prone to corrosion than the Narco Cast 60 refractory, yet stronger and less prone to shrinkage than the Plibrico Plicast Cement-Free 98V KK refractory previously used in this section of the furnace.

The upper middle section of the furnace showed more severe refractory damage as a result of lignite firing. Some patching of the high-density refractory in the upper middle furnace section was necessary after the lignite test periods, especially where the refractory was itself a fresh patch. EERC personnel believe that the newly repaired/patched portions of the refractory corroded excessively because the system was not fired to as high a temperature before coal/lignite feed was begun as the older refractory had been during the original system shakedown. As part of an August 1998 test period, the EERC attempted to cure new refractory patches at 2900 to 3000 °F (1594 to 1649 °C) in order to improve corrosion resistance. However, using natural gas with both RAH panels installed limited maximum furnace temperatures to 2850 °F (1566 °C). Based on an inspection of the furnace interior following the August 1998 test, the EERC elected to replace the entire high-density refractory liner.

The primary reason for replacing the high-density furnace liner in the two middle furnace sections in 1998 was the extensive cracking that had developed in the liner as a result of its initial curing and subsequent heating and cooling cycles. Refractory deterioration in the bottom section of the furnace because of slag corrosion was the reason for high-density refractory replacement in this section of the furnace. In order to avoid cracking problems observed with the first liner, the new high-density liner was poured in such a way that it would not bond to the middle or intermediate refractory layer and would be divided into approximately 2-ft-square wall sections to allow the liner to move independently during heatup and cooldown. This design was very successful in preventing the extensive cracking that was seen in the original furnace liner.

Following a March 2000 SFS test, the EERC determined that the top and bottom sections of the furnace were in poor condition as a result of 10 heating and cooling cycles and slag corrosion over an 18-month period involving nearly 1700 hr of SFS operation. However, the EERC elected

to replace the entire high-density furnace liner in the second quarter of 2000 because of plans for high-temperature (>2900 °F [>1594 °C]) furnace operation in the future.

Another observation made during the course of SFS operation concerning the high-density furnace liner was obvious color changes. When new high-density refractory was poured, it was gray in color. Upon curing, the color changed to a bright white. Subsequently, with each coal-fired test, the color of the high-density liner darkened. The EERC believes that the darkening of the refractory was the result of slag penetration into the surface of the high-density liner. This change in appearance may indicate the potential for a failure of the high-density furnace liner if the refractory chemistry is sufficiently modified. However, the degree of slag impaction on the vertical walls is believed to be small; therefore, frequent (annual) refractory replacement is not anticipated.

The area of the high-density furnace liner that shows the greatest deterioration from test to test is below the RAH panel where slag from the panel drips onto the horizontal surface below. However, because of the small area impacted, no refractory repairs or replacement have been required to solely address the resulting refractory damage.

Complete replacement of the high-density furnace refractory was anticipated on a periodic basis. However, the frequency of high-density refractory replacement is uncertain because of the variable slag deposition and chemistry that occur as a result of the various fuels fired and changing furnace conditions necessary to meet individual test objectives. Table 11A-2 summarizes properties for refractory used in the pilot-scale SFS, and Exhibit 11A-8 illustrates refractory layout for the slagging furnace.

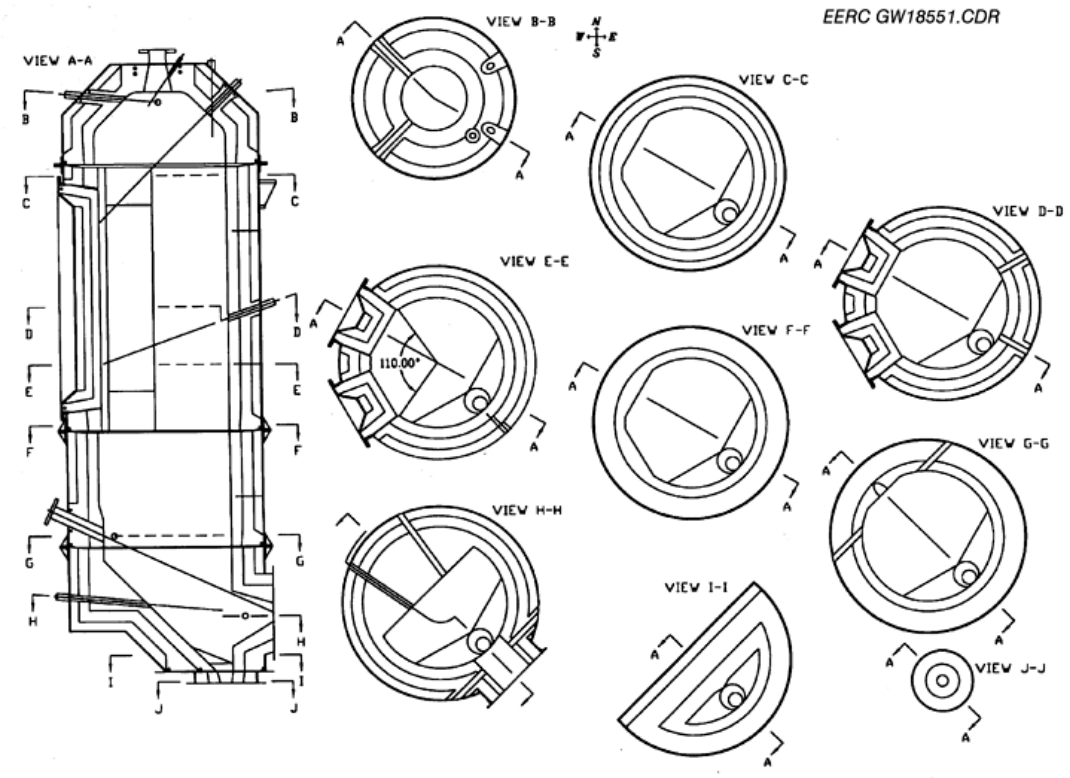

Exhibit 11A-8
Cross-Sectional Views of the Furnace Refractory Layout

Main and Auxiliary Burners

The main burner is natural gas- and pulverized coal (pc)-capable, 70% – 200 mesh (70% – 75 µm). Burner development and testing were not objectives within the scope of work. However, some burner turndown was desirable and was factored into the burner design. Flame stability is assessed by observing the flame and its relation to the burner quarl as a function of secondary air swirl and operating conditions at full load and under turndown conditions. The basic burner design, an International Flame Research Foundation (IFRF)-type adjustable secondary air swirl generator, is illustrated in Exhibits 11A-9 and 11A-10. An IFRF-type adjustable secondary air swirl generator uses primary and secondary air at approximately 15% and 85% of the total air, respectively, to adjust swirl between 0 and a maximum of 1.9.

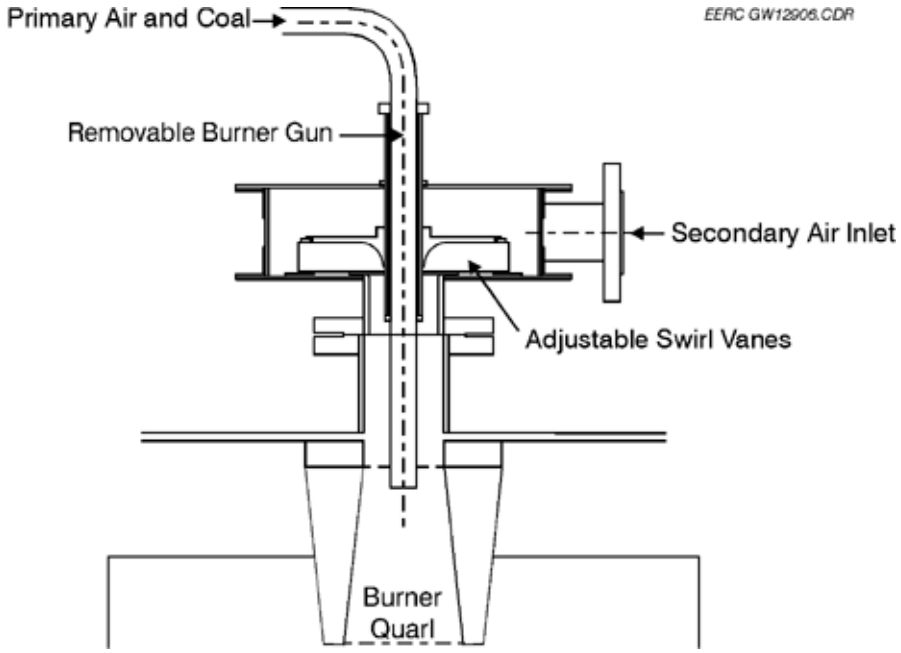

Exhibit 11A-9
IFRF Adjustable Swirl Burner

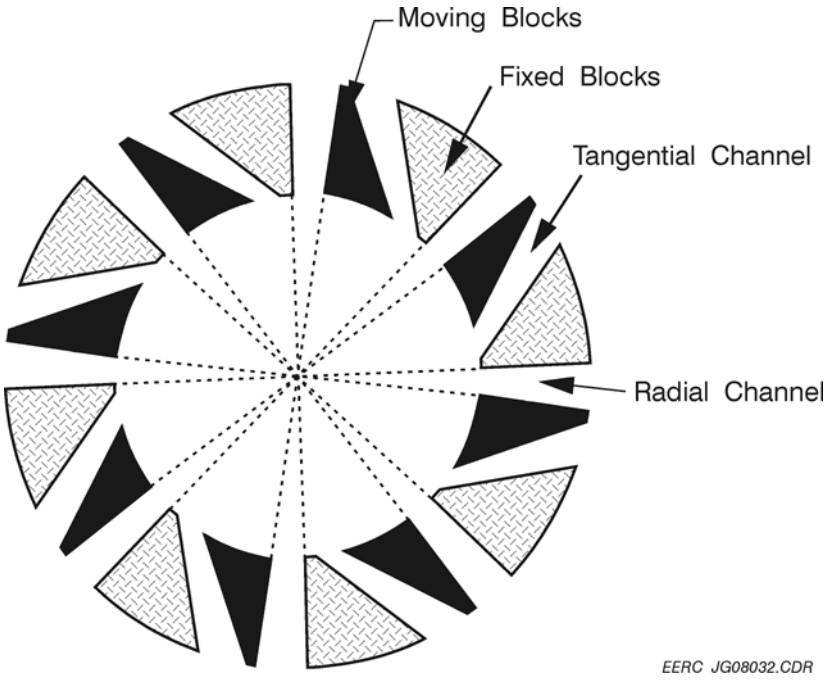

Exhibit 11A-10
Cross Section of a Burner Movable Block Assembly

"Swirl" is defined as the ratio of the radial (tangential) momentum to axial momentum imparted to the secondary air by movable blocks internal to the burner and is used to set up an internal recirculation zone (IRZ) within the flame that allows greater mixing of combustion air and coal. Swirl is imparted by moving blocks to set up alternate paths of radial flow and

tangential flow, creating a spin on the secondary air stream that increases the turbulence in the near-burner zone. At the fully open position of the swirl block, the secondary air passes through the swirl burner unaffected, and the momentum of the stream has only an axial component (the air enters the combustion chamber as a jet). As the angle of the blocks changes, the air begins to spin or swirl, and the radial component to the momentum is established, creating the IRZ in the near-burner region. It is the ratio of this radial component of the momentum to the axial component that establishes the quantity defined as swirl.

The adjustable swirl burners currently used by the EERC consist of two annular plates and two series of interlocking wedge-shaped blocks, each attached to one of the plates. The two sets of blocks can form alternate radial and tangential flow channels, such that the airflow splits into an equal number of radial and tangential streams, which combine farther downstream into one swirling flow, as shown in Exhibit 11A-10. By a simple rotation of the movable plate, radial channels are progressively closed and tangential channels opened, so that the resulting flux of angular momentum increases continuously between zero and a maximum value. This maximum swirl depends on the total airflow rate and the geometry of the swirl generator. Swirl can be calculated from the dimensions of the movable blocks (the ratio of the tangential and radial openings of the blocks) or from the measurement of the velocity of the airstream (obtaining both radial and axial components). The following description of that calculation is provided by Beer and Chigier (1972):

Table 11A-2
Refractory Properties

Refractory:	Plicast Cement-Free 99V KK/99V[1]	Plicast Cement-Free 98V KK/98V[1]	Plicast Cement-Free 96V KK/96V[1]	Narco Cast 60	Plicast LWI-28	Plicast LWI-20	Harbison-Walker 26
Function	High density	High density	High density	High density	Insulating	Insulating	Insulating
Service Limit, °F	3400	3400	3300	3100	2800	2000	2600
Density, lb/ft^3	185	185	185	145	80	55	66
K, Btu-in./ft^2 °F-hr @ 2000°F	14.5	14.5	14.0		4.0	NA2	2.2
K, Btu-in./ft^2 °F-hr @ 1500°F	14.7	14.7	14.2	6.0	3.0	1.7	1.9
K, Btu-in./ft^2 °F-hr @ 1000°F	15.5	15.5	15.0	5.6	2.7	1.3	1.7
Hot MOR[3] @ 2500°F, psi	650	750	1400	NA	NA	NA	NA
Hot MOR @ 1500 °F, psi	–	–	2000	1000	250	100	110
Cold Crush Strength @ 1500 °F, psi	–	–	10000	NA	750	400	350
Typical Chemical Analysis, wt% (calcined)							
Al_2O_3	99.6	98.6	95.5	62.2	54.2	39.6	53.8
SiO_2	0.1	1.0	3.8	28.0	36.3	31.5	36.3
Fe_2O_3	0.1	0.1	0.1	1.0	0.8	5.4	0.5
TiO_2	0.0	0.0	0.0	1.7	0.5	1.5	0.6
CaO	0.1	0.1	0.1	2.8	5.7	19.5	7.2
MgO	0.0	0.0	0.0	0.1	0.2	0.8	0.2
Alkalies	0.2	0.2	0.2	0.2	1.5	1.4	1.4

[1] The “KK” designation indicates the presence of fibers that promote dewatering during curing.

[2] Not applicable.

[3] Modulus of rupture.

When rotating motion is imparted to a fluid upstream of an orifice, the fluid emerging from the orifice has a tangential velocity component in addition to the axial and radial components encountered in the nonswirling jets. The presence of the swirl results in radial and axial pressure gradients, which in turn, influence the flow field. In the case of strong swirl, the adverse axial pressure gradient causes reverse flow along the axis, setting up the internal recirculation zone.

In swirling free jets or flames, both axial flux of the angular momentum (G_x) and the axial thrust (G_ψ) are conserved. These can be written as

$$G_\psi = \int_0^R \left[(\mathrm{Wr})\Delta U^2 \mathrm{Br}\right] \mathrm{dr} = \mathrm{const} \tag{1}$$

$$G_x = \int_0^R \left[U\Delta U^2 \mathrm{Br}\right] \mathrm{dr} + \left[\mathrm{p2Br}\right] \mathrm{dr} = \mathrm{const} \tag{2}$$

where *U*, W, and p are the axial and tangential components of the velocity and static pressure, respectively, in the cross section of the jet. Since both of these momentum fluxes can be considered to be characteristic of the aerodynamic behavior of the flame, a nondimensional criterion based on these quantities can describe the swirl intensity as:

$$S = G_\psi / G_x R \quad (R = \text{exit radius of the burner nozzle}) \tag{3}$$

Experiments have shown that the swirl number S indicates the flow similarity between swirling jets produced by geometrically similar swirl generators. Other similarity criteria, which take into account nonisothermal conditions and confinement of jet flow by walls, can also be applied in conjunction with the swirl number. The calculation of swirl in other types of swirl generators, such as the air registers on a utility boiler, are also described by Beer and Chigier (1972), although not mentioned here.

Secondary air swirl is used to stabilize the flame. In the absence of swirl, loss of flame may result, increasing the risk of a dust explosion. As swirl is applied to the combustion air, coal particles are entrained in the IRZ, increasing the heating rate of the particles, leading to increased release of volatiles and char combustion. The flame becomes more compact and intense as swirl is increased to an optimum level, which is characterized in EERC pilot-scale test facilities as the point at which the flame makes contact with the burner quarl. Increasing swirl beyond this level can pull the flame into the burner region, unnecessarily exposing metal burner components to the intense heat of the flame and possible combustion in the coal pipe.

Increasing swirl to provide flame stability and increased carbon conversion can also affect the formation of NOx. The high flame temperatures and increased coal–air mixing associated with increased swirl create an ideal situation under which NOx may form. In full-scale burners with adjustable vanes, swirl is often increased to reach the optimum condition and then decreased slightly to reduce the production of NOx. Although NOx emissions are of interest, their control is not a key objective for the SFS. Therefore, burner operational settings are based on achieving desired furnace exit temperatures and slag conditions in the furnace. Flame stability under turndown conditions is characterized by firing the primary burner at reduced load (typically 66% to 85% of the full load rate), maintaining the same primary airflow, and adjusting the secondary airflow to meet excess air requirements.

The SFS main burner design is simply a scaled-up version of two existing burners used at the EERC based on increased combustion air volumetric flow rates. Materials of construction for the main burner are entirely stainless steel because of the combustion air (up to 800 °F [427 °C]) temperature ranges to which it is exposed. Combustion air flow rates through the main burner range from about 400 to 600 scfm (11 to 17 m^3/min), depending on furnace firing rate and fuel type (bituminous, subbituminous, or lignite) fired. Exhibit 11A-4 is a photograph showing the main burner installed on top of the slagging furnace, including the primary air gun/coal pipe and the secondary air piping. Natural gas piping is also visible in the photograph, along with ultraviolet (UV) flame sensors.

An auxiliary gas burner (850,000 Btu/hr [896,750 kJ/hr]) is located near the furnace exit in order to control furnace exit temperature, ensuring desired slag flow from the furnace and slag screen. This auxiliary burner is used to compensate for heat losses through the furnace walls, sight ports, and RAH test panels. The use of the auxiliary gas burner is beneficial during start-up to reduce heatup time and to prevent the freezing of slag on the slag screen when initially switching to coal firing. The auxiliary gas burner firing rate is dependent on main burner fuel properties, desired furnace exit temperature, and heat losses from the furnace. The auxiliary burner is a smaller version of the main burner design. Materials of construction for the auxiliary burner are entirely stainless steel. The auxiliary burner is shown attached to the furnace in the photograph in Exhibit 11A-11 along with the primary air gun, secondary air line, natural gas piping, spark plug ignitor, and UV flame sensor.

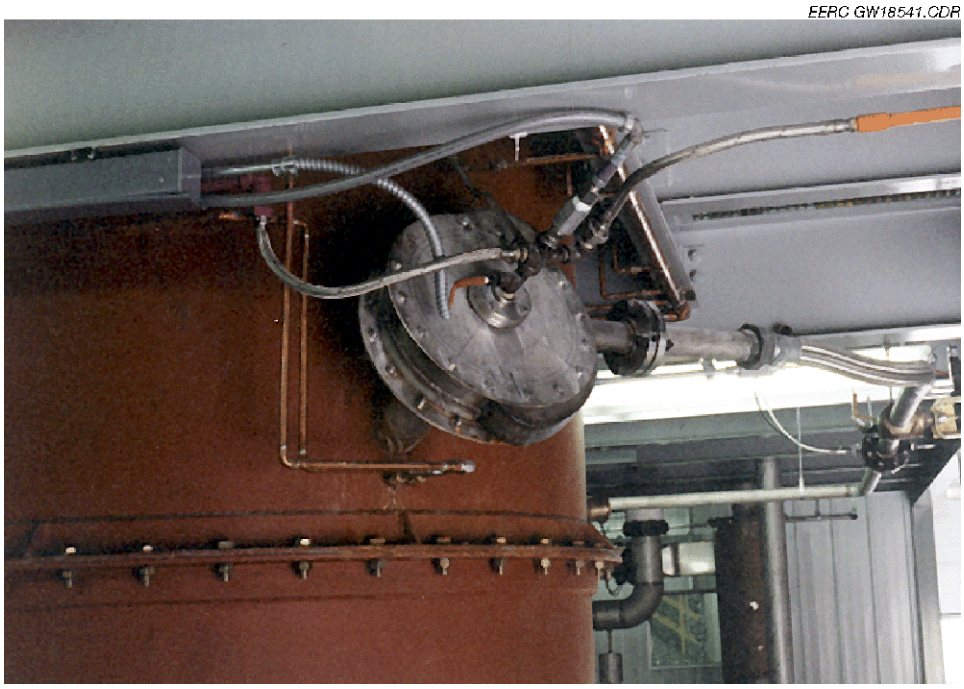

Exhibit 11A-11
Photograph of Auxiliary Burner Installed on the Slagging Furnace

Inlet combustion air piping to the main burner is mostly insulated 6-in. (15-cm) Schedule 5 stainless steel for the secondary air and 1-, 2-, and 4-in. (2.5-, 5-, and 10-cm) Schedule 10 and 40 stainless steel for the primary air/coal feed line. The main burner piping connection to the furnace

is 8-in. (20-cm) Schedule 40 material. For the auxiliary burner, inlet combustion air piping sizes are 1-in. (2.5-cm) Schedule 40 and 2-in. (5-cm) Schedule 5 and 10 material. The auxiliary burner piping connection to the furnace is 3.5-in. (9-cm) Schedule 40 material.

Thermocouples were installed to measure inlet combustion air temperatures for each burner. Thermocouple data are automatically logged into the data acquisition system. Pressure transmitters and gauges are used to monitor static and differential pressures in order to monitor burner performance and measure combustion air flow rate. These data are automatically logged into the data acquisition system, and flow control valves are used to adjust and maintain desired combustion air flow rates. As a backup, burner data are recorded manually on data sheets on a periodic basis.

Cleaning and maintenance of the burners are minimal. When the top of the slagging furnace is removed to inspect the interior, it is necessary to first disconnect the combustion air and fuel feed lines and remove the main burner. Burner fabrication was completed in September 1996, except for the primary air guns/coal pipes, which were completed in March 1997. These short, flanged sections of straight pipe were cut to the appropriate length, fabricated, and installed once the refractory-lined furnace had been assembled and final measurements were made. Initial burner testing began in May 1997 and was completed in conjunction with overall furnace shakedown later in the year.

Replacement of the primary air/fuel nozzle on the main burner was necessary in May 2000 after nearly 3000 hr of SFS operation. Measurements indicated that roughly 4 in. (10.2 cm) of the nozzle had been lost (oxidized and eroded) since the burner was fabricated and originally installed. Inspection indicated that a similar repair was also necessary for the auxiliary burner.

Radiant Air Heater Panels

A key design feature of the furnace is accessibility for installation and testing of one LRAH panel and one small radiant air heater (SRAH) panel. The furnace design will accept one LRAH panel with a maximum active size of 1.5 × 6.4 ft (0.46 × 1.96 m). This size was selected to minimize furnace heat losses and based on panel-manufacturing constraints identified by UTRC. Flame impingement on the RAH panels is not necessarily a problem. Process air for the LRAH panel is provided by an existing EERC air compressor system. Maximum air capacity available to support the LRAH is 270 scfm (7.6 m^3/min) at a delivery pressure of 150 psig (10.3 bar). As it passes through the LRAH panel, the process air is heated from nominally 1300 °F (705 °C) to as high as 1800 °F (982 °C). However, during a single test, adjustments were made to the furnace firing rate and the process air flow rate and pressure to demonstrate that a LRAH process air temperature of 2000 °F (1094 °C) can be reached with the current design.

Backup process air is available from a smaller compressor at a delivery rate of nominally 150 scfm (4.2 m^3/min) and a pressure of <100 psig (<7 bar). A tie-in to an existing nitrogen system was also installed as a backup to the existing air compressor system. In the event of a failure of inlet process air piping to the LRAH panel, a backflow emergency piping system was installed so that overheating of the LRAH panel could be avoided.

It was necessary to heat the process air to achieve the desired LRAH inlet temperature of 1300 °F (705 °C). Outlet process air temperature from the LRAH panel is generally controlled at 1800 °F (982 °C) or less by adjusting process air flow rate using flow control valves. Based on

EERC and UTRC heat-transfer calculations, the process air flow rate necessary to cool the LRAH panel was expected to be 200 scfm (5.7 m^3/min). Based on operating experience, 150 to 200 scfm (4.3 to 5.7 m^3/min) is adequate to control the LRAH panel temperature with ceramic tiles in place to protect the alloy heat-transfer surfaces from furnace conditions. The SFS uses flue gas heat exchange (CAH and process air preheaters) and electrical heating to meet heated process air temperature requirements for the LRAH panel. The advantage of combining heat sources for the process air stream at this scale is greater flexibility and range of control. Proper insulation and thermocouple location were required to minimize and document LRAH edge effects, respectively, as well as adequately define surface temperature distributions, total heat absorption, and local heat flux.

The LRAH test panel arrived at the EERC on September 15, 1997. Final assembly and installation of the LRAH panel into the furnace took place in November 1997, with initial shakedown and testing of the LRAH panel occurring in December 1997. Testing of the LRAH panel to date has focused on evaluating LRAH panel performance relative to heat transfer, tile and tube temperatures, and process air temperatures and flow rates while firing bituminous coal, subbituminous coal, and lignite. Generally, the performance of the LRAH panel was as anticipated, with no significant process problems. However, a forced shutdown occurred in August 1998 because two ceramic tiles failed, falling into the bottom of the furnace.

In September 2000, the performance of the alloy heat-transfer surfaces was evaluated without tile protection during a short natural gas-fired test period. Alloy surface temperatures were limited to 2000 °F (1094 °C), limiting furnace temperature to 2400 °F (1316 °C) because of a maximum available process air flow rate of 270 scfm (7.6 m^3/min) at 150 psig (10.3 bar). In December 2000, a second process air line was installed in order to increase the volume of process air available to support the LRAH panel. However, further modifications will be necessary before a new process air capacity limit is determined. These modifications are expected to include installation of a new process air dryer, installing additional process air preheat surface, upgrading materials of construction for some existing process air components, adding cooling capacity to protect process air measurement and flow control devices and should be completed in the second quarter of 2001.

LRAH panel tiles and support bricks were replaced on several occasions. In some cases, replacement was necessary because of tile failures. In other cases, tiles were replaced because of a desire to evaluate new materials. Replacement of siderail support bricks occurred twice because of damage to retaining ledges. Periodic inspection of the LRAH tubes has indicated that they are in good condition even after the temperature excursion they experienced in August 1998 as a result of the tile failure. The tubes did not appear to have warped. Also, no ash/slag appeared to be imbedded in the surface of the tubes. A light ash dusting was observed on the surface of the tubes that were not directly exposed to the furnace flame. The metal surfaces exposed directly to the furnace flame appeared to be somewhat sintered, but no damage was evident. Inspection of the alloy surfaces after exposure to furnace conditions in September 2000 in a controlled manner also indicated that the tubes were in good condition.

The inlet and outlet cooling air headers of the LRAH panel were unbolted periodically to permit the inspection and replacement of gaskets that had begun leaking as a function of repeated heating and cooling cycles. As a result of the August 1998 test, the gaskets in the outlet header were found to be in very poor condition. Also, threaded thermocouple fittings on the process air

outlet header were replaced occasionally because they developed leaks. Disassembly and reassembly of the LRAH panel was completed on a few occasions, and difficulties were encountered as a result of frozen nuts on stud bolts and frozen stud bolts in threaded flanges.

As of December 2000, the LRAH panel had been exposed to a range of furnace-firing conditions for a total of 2937 hr. Natural gas firing represented 1472 hr, and coal–lignite firing represented 1465 hr. In addition, the LRAH panel was exposed to 19 heating and cooling cycles. The longest continuous coal-fired period was 184 hr, completed in April 1999.

Furnace design also permits the installation of a nominally sized 1.5- × 5.4-ft (0.46- × 1.65-m) RAH panel. The purpose of the SRAH panel was to expose refractory materials to furnace slagging conditions rather than generate heat-transfer data. A primary difference between the LRAH and SRAH panels was that the SRAH panel was cooled with water rather than heated air. The SRAH panel was water-cooled using two sets of five vertically oriented 0.375-in. (0.952-cm)-outside diameter (o.d.) stainless steel tubes. While the SRAH panel was 1 ft (0.3 m) shorter than the LRAH panel, both assemblies were the same width and used the same air-cooled frame support design. A central vertical ceramic rail was present in the SRAH panel, allowing the installation of either full-width (18-in. [46-cm]) or half-width panels inside the furnace. The SRAH panel was delivered the first week of April 1998 and installed prior to a weeklong lignite test period completed April 19–24. Shakedown and initial testing of the SRAH panel were completed in April 1998.

As a result of damage sustained by the SRAH panel during a August 1998 test period, the panel was removed from the slagging furnace. UTRC personnel determined that rebuilding the SRAH panel was not warranted and that further materials testing could be accomplished using the LRAH panel. Therefore, the area of the slagging furnace in which the SRAH panel was located was filled in with insulating, intermediate, and high-density refractory as part of the high-density refractory replacement activity in late 1998.

UTRC designed and fabricated the LRAH test panel. Exhibit 11A-12 illustrates the UTRC RAH concept, and Exhibit 11A-13 illustrates the LRAH panel installed in the slagging furnace with thermocouple locations indicated. Table 11A-3 describes the thermocouple locations illustrated in Exhibit 11A-13. Exhibit 11A-14 presents photographs of the completed LRAH panel assembly from both the exterior and interior of the furnace. Examples of LRAH data plotted as a function of run time can be found in Addendum-D. LRAH screen prints are presented in Addendum-E.

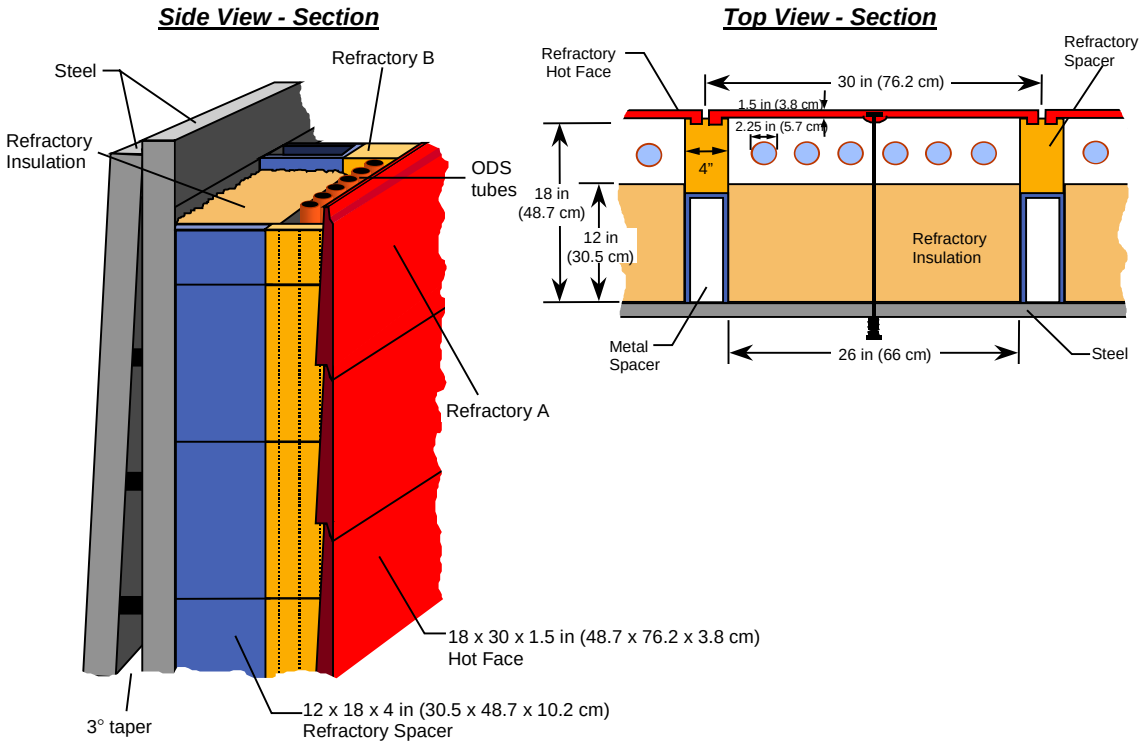

Exhibit 11A-12
Illustration of UTRC RAH Concept

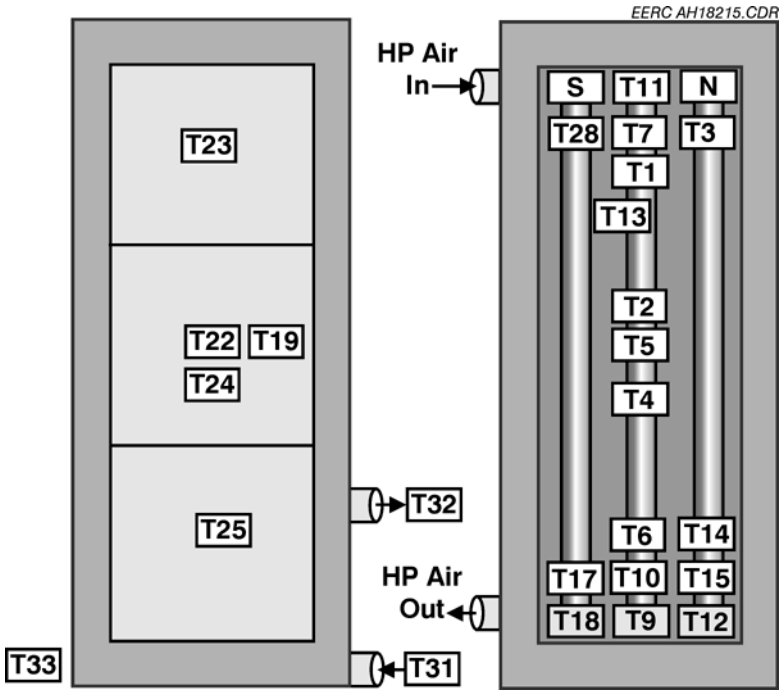

Exhibit 11A-13
Illustration of LRAH Panel and Thermocouple Locations

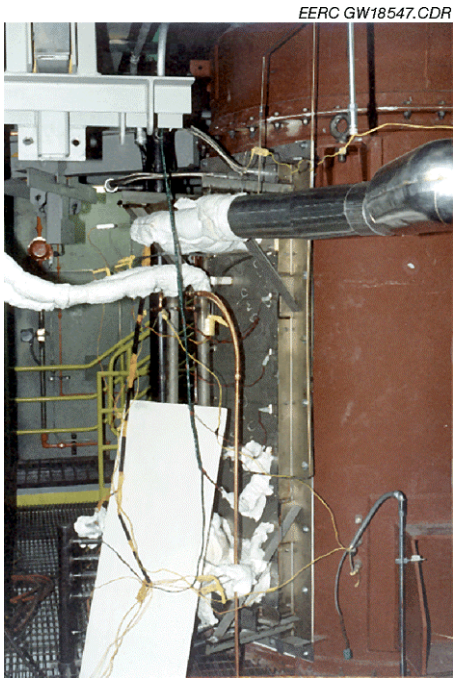

Exhibit 11A-14
Photographs of the Installed LRAH Panel from the Interior (Left) and Exterior (Right) of the Furnace

Table 11A-3
Description of RAH Panel Thermocouple Locations[1]

Category	No.	Label	Description
Air Inlet	1	HP Air In	Provided by the EERC, in pipe before inlet header
	2	RAHT11	Air entering RAH through center tube
Air Outlet	3	RAHT18	Air leaving left (south) tube
	4	RAHT9	Air leaving center tube
	5	RAHT12	Air leaving right (north) tube
MA Tube Surface	6	RAHT1	Top of center tube facing cold side
	7	RAHT2	Middle of center tube facing adjacent tube
	8	RAHT3	Top of north tube facing toward furnace
	9	RAHT4	Middle of center tube facing cold side
	10	RAHT5	Middle of center tube facing toward furnace
	11	RAHT6	Bottom of center tube facing cold side
	12	RAHT7	Removed
	13	RAHT8	Removed
	14	RAHT10	Bottom of the center tube facing toward furnace
	15	RAHT13	Top of center tube, facing south tube
	16	RAHT14	Bottom of north tube facing toward furnace
	17	RAHT15	Bottom of north tube facing toward furnace
	18	RAHT16	Removed
	19	RAHT17	Bottom of south tube facing toward furnace
	20	RAHT28	Top of south tube facing toward furnace (failed)
	21	RAHT29	Removed
Inner Surface of Ceramic Tiles	22	RAHT19	Center tile, left side rail
	23	RAHT20	Removed
	24	RAHT21	Removed
	25	RAHT22	Center tile, cavity side center
	26	RAHT23	Top tile (failed June 2000)
	27	RAHT24	Center tile, quasi-furnace side center
	28	RAHT27	Removed
	29	RAHT25	Lower tile, cavity side center
	30	RAHT26	Removed

[1] Thermocouple locations are illustrated in Exhibit 11A-13.

Slag Screen

The slag screen design for the SFS was the result of a cooperative effort between EERC, UTRC, and Physical Sciences, Inc. (PSI), personnel. The primary purpose for the pilot-scale slag screen is to reduce the concentration and affect the size distribution of ash particles entering the CAH tube bank. The design is intended to result in an ash particle-size distribution comparable to that expected in the commercial plant. Other design criteria specific to the pilot-scale slag screen include:

1) a simple design permitting modifications if necessary using readily available, inexpensive materials;

2) matching duct dimensions and flue gas flow rates to maintain turbulent flow conditions;

3) minimizing the potential for plugging as the result of slag deposit growth on tube surfaces or the sloped floor;

4) limiting differential pressure across the slag screen to 2 in. W.C. (4 mm Hg); and

5) limiting heat losses to assure desired slag flow from the slag screen to the furnace slag tap. Exhibits 11A-2 and 11A-6 illustrate and show, respectively, the slag screen and its relationship to the slagging furnace and dilution/quench zone.

The slag screen flue gas approach velocity is nominally 70 to 75 ft/s (21.4 to 22.9 m/s), depending on furnace firing rate and fuel type. The flue gas outlet temperature from the slag screen must be >2500 °F (>1371 °C) to minimize the potential for slag freezing in the slag screen. For some high-ash-fusion-temperature fuels, the slag screen flue gas temperature must approach 2800 °F (1538 °C) to avoid slag accumulation and plugging. The use of limestone injection has been effectively used in some cases to modify slag chemistry and improve slag flow from the slag screen through the slag tap.

The slag screen typically makes use of six rows of three 1.5-in. (3.8-cm)-diameter vertical tubes mounted in an upwardly sloped duct (20 degrees) to facilitate slag flow from the slag screen into the furnace slag tap. The center line-to-center line tube spacing in each row is 3.75 in. (9.5 cm). Center line-to-center line spacing between individual rows is 4 in. (10.2 cm). Internal duct dimensions for the slag screen are 10 in. × 13 in. × 3.5 ft (25 cm × 33 cm × 1.1 m). The resulting flue gas velocity through the slag screen is roughly 91 ft/s (28 m/s).

Originally, EERC personnel had recommended the use of uncooled high-alumina-content tube material for the slag screen to minimize heat loss and avoid slag freezing in the last few rows of tubes. EERC and PSI personnel agreed that a high-alumina-content material had the best chance of surviving the slagging conditions in the slag screen. Solid rods had been considered for the first three rows, but were subsequently eliminated as an option because of thermal shock concerns. PSI ordered tubes having a wall thickness of 0.125 in. (0.32 cm) because they were readily available and much less expensive than thicker wall tubes. Each tube was vented on the downstream side to prevent internal pressure increases upon the heating of trapped air in the tubes and to allow thermal equilibrium between the interior and exterior of the tubes. Promoting thermal equilibrium between the flue gas and interior of the tubes was expected to facilitate the use of Type S thermocouples (one each) in the first and last row of tubes to monitor slag screen temperature without exposing the thermocouples to the slag. Thermocouple data are automatically logged on the data acquisition system. Pressure taps were installed in the roof upstream and downstream of the tubes to monitor and record slag screen differential pressure. As a backup to the data acquisition system, slag screen data are recorded manually on screen prints (see Addendum-E) on a periodic basis.

EERC personnel were somewhat concerned about the survivability of the thin-walled tubes with respect to slag attack. However, if the first two or three rows of slag screen tubes were lost to erosion/corrosion, the EERC did not expect a dramatic effect on system operability. Routine on-line cleaning of the slag screen was not anticipated to be a requirement. However, two sight ports were installed in the vertical sidewalls of the slag screen to permit visual observation and the use of an air lance for periodic cleaning, if necessary. Placement of sight ports in the walls of

the slag screen was a heat loss and materials concern. Therefore, the actual size of the sight ports in the wall of the slag screen was limited to 2 in. (5 cm). If heat loss or material problems were identified during shakedown tests, the 2-in. (5-cm) holes could be easily plugged with refractory. Sight ports located in the furnace exit and at the inlet of the dilution/quench zone permit visual observation of the inlet and outlet of the slag screen. Two additional ports in the furnace exit along with the sight ports in the dilution/quench zone inlet provide access for flue gas sampling around the slag screen. Each of these sight/sample ports is 2.3 in. (5.8 cm) i.d. Continuous flue gas sampling occurs between the slag screen and the dilution/quench zone to monitor and control slagging furnace operation.

The refractory component of the slag screen consists of two refractory layers. The inner high-density layer is a Plicast Cement Free 98V KK, with an outer insulating layer of Harbison-Walker Castable 26. The high-density refractory is 2.25 in. (5.7 cm) thick in the sidewalls and 4 in. (10.2 cm) thick in the roof and floor of the slag screen. The insulating refractory is 3.75 in. (9.5 cm) thick in the sidewalls, roof, and floor. A Plicast LWI-28 refractory was used around the sight ports in the wall of the slag screen. Properties for the high-density and insulating refractory selected for use in the slag screen are summarized in Table 11A-2. Exhibit 11A-15 presents plan and elevation views of the slag screen showing critical tube and refractory dimensions. Exhibit 11A-16 presents photographs of the slag screen inlet showing slag accumulation in one case and a relatively clean slag screen in another case. The construction material for the slag screen shell is carbon steel. The final design package for the slag screen was completed in September 1996, and fabrication and installation of the slag screen was completed in April 1997.

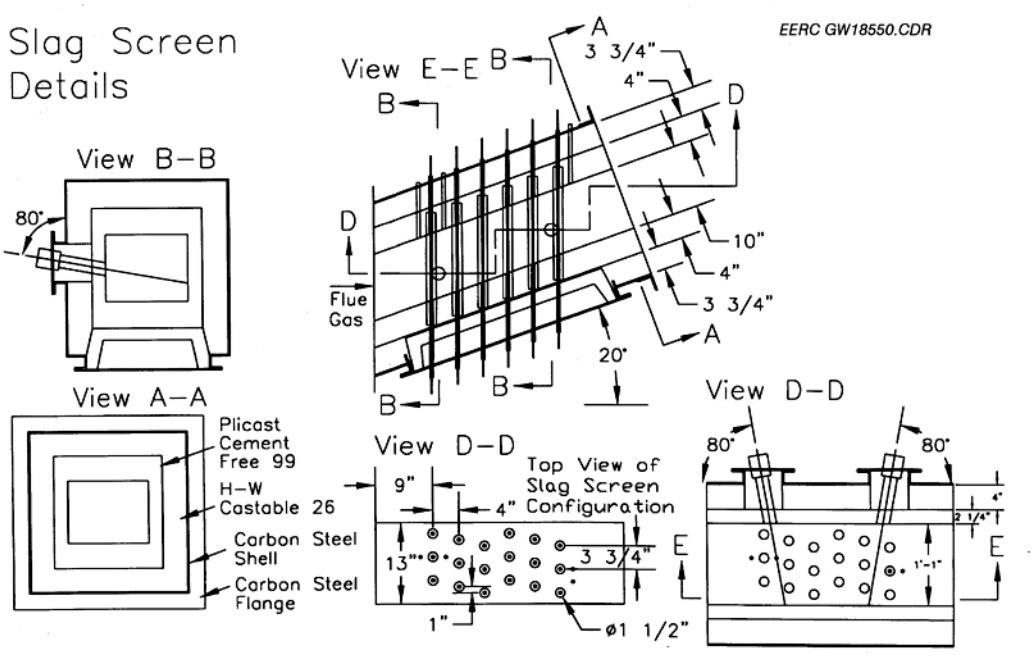

Exhibit 11A-15
Plan and Elevation Views of Slag Screen

EERC GW18536.CDR

EERC GW18535.CDR

Exhibit 11A-16
Photographs of Slag Screen Tubes Showing Slag Accumulation and Plugging For a February 1999 Test (Top) and the Effectiveness of mitigation measures applied During a April 1999 Test (Bottom)

The original high-alumina content slag screen tubes were damaged as a result of severe erosion/corrosion during two initial weeks of SFS shakedown tests. In addition, refractory (Plicast Cement Free 99V KK and 98V KK)-filled tubes sustained similar damage. The front half

of each tube was severely eroded/corroded, often completely missing. Even though the first few rows of slag screen tubes were lost to erosion/corrosion, there was no apparent effect on system operability. The operating conditions experienced by the slag screen were reviewed with PSI personnel to determine what steps would be taken to prevent similar damage in the future. Alternative material options for the slag screen tubes were considered, as well as cooling the tubes and reducing gas temperatures when the slag tap is operating efficiently.

As a result of discussions with PSI personnel and subsequent heat-transfer calculations, the EERC elected to install water-cooled surfaces inside of the 1.5-in (3.8-cm) ceramic and/or high-density refractory tubes using 0.125-in. (0.32-cm) 316 stainless steel tubing. The water-cooled surfaces ran the length of each tube and were centered in a 0.31-in. (0.79-cm) hole. Leaving an air gap between the refractory surface and the water-cooled surface was believed to be necessary to achieve the desired heat transfer. Most of the slag screen tubes were fabricated using castable high-density refractory poured inside aluminum pipe. The aluminum pipe makes a structurally sound form during curing and eventually melts and runs into the slag pot as furnace temperatures rise. However, six tubes were fabricated by pouring high-density castable refractory into high-alumina-content ceramic tubes. The purpose for trying both material combinations was to determine which would result in acceptable tube life. Using the high-density castable refractory would be less costly if its durability were equivalent to the high-alumina-content ceramic tubes.

Observations during a subsequent test period indicated that the water cooling resulted in a tube surface temperature about 150 °F (83 °C) cooler than the flue gas temperature. Inspection of the slag screen after two weeks of operation with Illinois No. 6 coal indicated that all of the tubes were intact and would not require immediate repair or replacement. However, the front half of each tube in the first and second rows had been severely eroded/corroded. The remaining tubes all had a slag layer over the surface of the refractory or ceramic. EERC personnel elected to increase the diameter of the water-cooled 316 stainless steel tubing in the first and second rows from 0.125-in. (0.32-cm) to 0.188-in. (0.476-cm) and eliminate the air gap. By increasing the diameter of the tubing in the first and second rows of tubes and eliminating the air gap, the EERC hoped to further reduce the surface temperature of these tubes and the resulting erosion/corrosion observed.

Based on slag screen operating experience to date, slag screen tubes are currently fabricated using castable high-density refractory poured inside aluminum pipe. Water-cooled surfaces inside of the refractory tubes and the floor of the furnace exit/slag screen inlet are intended to cool the high-density refractory surface and minimize the erosion/corrosion observed. Based on slag screen operating experience with bituminous coal, subbituminous coal, and lignite, EERC personnel have determined that the high-density refractory is an acceptable tube material and that the size of the water-cooled tubes inside of the high-density refractory must be changed depending on the type of fuel. During lignite- and subbituminous coal-fired tests, more cooling is necessary to build up a sufficiently thick frozen slag layer to protect the slag screen tubes from the severe erosion/corrosion attack that can occur within the slag screen. The diameter of the stainless steel tubes installed in the slag screen tubes would be 0.5 in. (1.3 cm) o.d. in the first row and, possibly, the second row (depending on ash fusion temperature data), and 0.375 in. (0.952 cm) o.d. in the remaining four rows. However, it was necessary to reduce the size of the stainless steel tubes to 0.25 in. (0.63 cm) o.d. in all but the first row for Illinois No. 6 bituminous coal firing, with the o.d. of the stainless steel tubes in the first row reduced to 0.375 in. (0.952

cm). For fuels with more refractory ash, such as an eastern Kentucky bituminous coal, only three rows of tubes were required. The first row used 0.375-in. (0.952-cm)-o.d. tubes, and the second and third rows were 0.25 in. (0.63 cm) o.d. The slag screen tubes will likely always require periodic replacement based on some level of erosion/corrosion and the fuels selected for testing.

Type S thermocouples (one each) in the vicinity of the first and last row of tubes are used to monitor slag screen temperature. However, these measured temperatures are believed to be less than the actual flue gas temperatures because the thermocouples are located behind individual water-cooled slag screen tubes and because of observed thermocouple deterioration by slag attack. Therefore, slag screen temperature control is based on an optical pyrometer measurement at the furnace exit/slag screen inlet. The EERC tries to operate the slag screen at flue gas temperatures of 100 to 200 °F (56 to 112 °C) above the fluid temperature of the fuel ash to ensure slag flow from the slag screen to the slag tap.

Inspection of the slag screen and furnace interior following each week of operation indicates that the slag observed flowing through the slag tap comes from the slag screen and sloped floor of the furnace. While there is evidence of slag flowing down the surface of the LRAH panel, there is no evidence of slag flowing into the slag tap from the panel or furnace walls when firing bituminous or subbituminous coals.

Mass balances are completed for all SFS operating periods in order to document the distribution of slag/ash in the system. Based on operating experience with bituminous coal, subbituminous coal, and lignite, 56% to 72% of the fuel ash is captured in the SFS as slag when 18 tubes are used in the slag screen. When the nine tube configuration was employed for the higher-ash-fusion fuels, 45–53 wt% of the fuel ash was recovered as slag. The EERC estimates that unrecoverable slag in the furnace, slag screen, and dilution/quench zone for any given test period may represent as much as 10% of the theoretical ash. Fly ash recovered from other system components (drawdown gas line, CAH duct, process air preheater tubes, tube-and-shell heat exchangers, cyclone, baghouse, and flue gas piping) represents 10–32 wt% of the theoretical ash, depending on slag screen performance. Nominally, 10 to 20 wt% of the ash in the fuels fired in the SFS is reaching the baghouse.

Dilution/Quench Zone

The dilution/quench zone design for the SFS was the result of a cooperative effort between EERC and UTRC personnel. The circular dilution/quench zone is oriented vertically, maintains a 1.17-ft (0.36-m) diameter in the area of the flue gas recirculation (FGR) nozzles, and then expands the duct diameter to 2 ft (0.6 m) to provide adequate residence time within duct length constraints. The duct section containing the FGR nozzles is a spool piece in order to accommodate potential changes to the size, number, and orientation of the FGR nozzles.

The dilution/quench zone is refractory-lined and located immediately downstream of the slag screen. The top three sections contain Plicast Cement Free 98V KK high-density refractory and Harbison-Walker 26 insulating refractory. The bottom three sections contain Narco Cast 60 high-density refractory and Harbison-Walker 26 insulating refractory. Flue gas recirculation is used to cool the flue gas in the dilution/quench zone and freeze entrained slag particles. A centrifugal-type FGR fan draws flue gas from the system immediately downstream of the induced-draft (ID) fan. The 4-in. (10.2-cm) Schedule 10 stainless steel piping transporting the dilution gas is insulated to avoid condensation problems. Dilution gas is injected into the dilution/quench zone

through eight 1.25-in. (3.18-cm) nozzles at a total flow rate of 250 to 380 scfm (7.1 to 10.8 m^3/min), depending on furnace firing rate and fuel fired. The design assumed a dilution gas temperature of 300 °F (149 °C) and a flue gas exit temperature from the dilution/quench zone of 1850 °F (1010 °C). A flow control valve is used to control the FGR rate to achieve the desired flue gas temperature entering the CAH tube bank. Care must be taken to maintain a minimum FGR rate to avoid overheating metal surfaces.

Fabrication drawings for the dilution/quench zone were completed in October 1996, material procurement was completed in November, and fabrication and initial assembly were completed in early January 1997. The pouring of refractory and final assembly of the dilution/quench zone were completed in March 1997. In the Exhibit 11A-6 and A-7 photographs, the top and bottom sections of the dilution/quench zone can be seen on the second and first floors of the high-bay area bolted to the slag screen and CAH duct, respectively.

Inspection of the dilution/quench zone after each week of coal firing in 1997 and early 1998 revealed that significant slag deposits had formed in the vicinity of the FGR nozzles. In some cases, it appeared that as the deposit grew in size, the combination of high flue gas velocity and deposit weight resulted in a form of self-cleaning. This was evident by the quantity of slag found in the slag/ash hopper at the bottom of the dilution/quench zone. However, during all of these initial coal-fired test periods, it was necessary to dislodge slag deposits from the dilution/quench zone on a periodic basis to avoid severe plugging and system shutdown. The sight port at the top of the dilution/quench zone was successfully used for on-line cleaning. Downstream of the FGR nozzles, the small quantity of ash observed on the refractory walls was weakly sintered. Based on this early operating experience, EERC personnel expected that on-line cleaning of the dilution/quench zone would be necessary on a routine basis.

Because routine cleaning of the dilution/quench zone was required during initial coal-fired SFS test periods, a differential pressure transmitter was purchased and installed in April 1998 in order to better monitor and document the slag deposition in the dilution/quench zone. Based on observations during an August 1998 test period and the frequent cleaning required, the EERC modified the spool piece section of the dilution/quench in late 1998. The specific modification involved the addition of a water-cooled wall around the FGR nozzles. This water-cooled wall serves to embrittle the slag deposits that form in this area, making them more prone to spontaneous shedding and generally easier to remove on-line using a water-cooled lance. The additional heat loss to the waterwall also reduced the volume of FGR required to control the temperature of flue gas entering the CAH tube bank.

The overall performance of the dilution/quench zone with FGR has been very good with respect to controlling the temperature of the flue gas entering the CAH duct during 3620 hours of combined natural gas- and coal-firing. The temperature of the flue gas entering the CAH tube bank section can be effectively controlled at various temperature set points during heatup and cooldown periods. During stable coal-fired operation, an 1800 °F (982 °C) or 1850 °F (1010 °C) set point is maintained.

Convective Air Heater

The CAH design was a cooperative effort between the EERC and UTRC. The flue gas flow rate to the CAH tube bank is 3550 to 4620 acfm at 1800 °F (100 to 131 m^3/min at 982 °C), depending on the fuel type and furnace firing rate. A rectangular inside duct dimension of 14 in.

× 12 in. (36 cm × 30 cm) results in a cross sectional area of 1.17 ft^2 (0.11 m^2) and a flue gas approach velocity of 50 to 73 ft/s (15 to 22 m/s) to the CAH tube bank. The CAH tube bank originally consisted of twelve 2-in. (5-cm)-diameter tubes installed in a staggered three-row array. The first five tubes in the flue gas path were uncooled ceramic material, with the remaining seven tubes cooled using heated air. Tube spacing is 4 in. (10.2 cm) on center. The length of the duct occupied by the tube bank is nominally 20 in. (51 cm). Primary and backup process air for the CAH tubes is provided by the same EERC air compressor system described for the LRAH panel. Heat is recovered from the flue gas to meet process air temperature requirements for the CAH tube bank.

Process air heating and flow rate control are necessary to achieve the 700 °F (371 °C) minimum–1000 °F (538 °C) maximum inlet process air temperature desired, effectively controlling surface temperatures, and provide for an inside heat-transfer coefficient similar to the commercial design. The CAH process air flow rate and operating pressure are nominally 100 scfm (2.8 m^3/min) and 150 psig (10.3 bar), respectively. The design process air exit temperature from the CAH is 1200 °F (649 °C) and is not permitted to exceed 1300 °F (705 °C). Process air flow rate is used to control process air exit temperature using a flow control valve.

Four sight ports and one tube fitting port were installed in the walls of the CAH duct to permit observation and sootblowing. Fabrication drawings for the CAH shell sections were completed and approved in November 1996. Material procurement for and fabrication of the CAH shell were completed in December. Once final fit was verified, locations for pressure tap, thermocouple, and sight port penetrations were identified. The shell sections were disassembled, and shell penetrations were installed. Refractory pouring and final assembly and installation of the CAH duct were completed in March 1997. All three sections contain Narco Cast 60 high-density refractory and Harbison-Walker 26 insulating refractory. The photographs in Exhibit 11A-17 show the three shell sections comprising the CAH, the two horizontal sections, the transition section between the CAH and the process air preheaters, the CAH tube bank installed in the duct, and the insulated inlet and outlet process air lines.

EERC GW18542.CDR

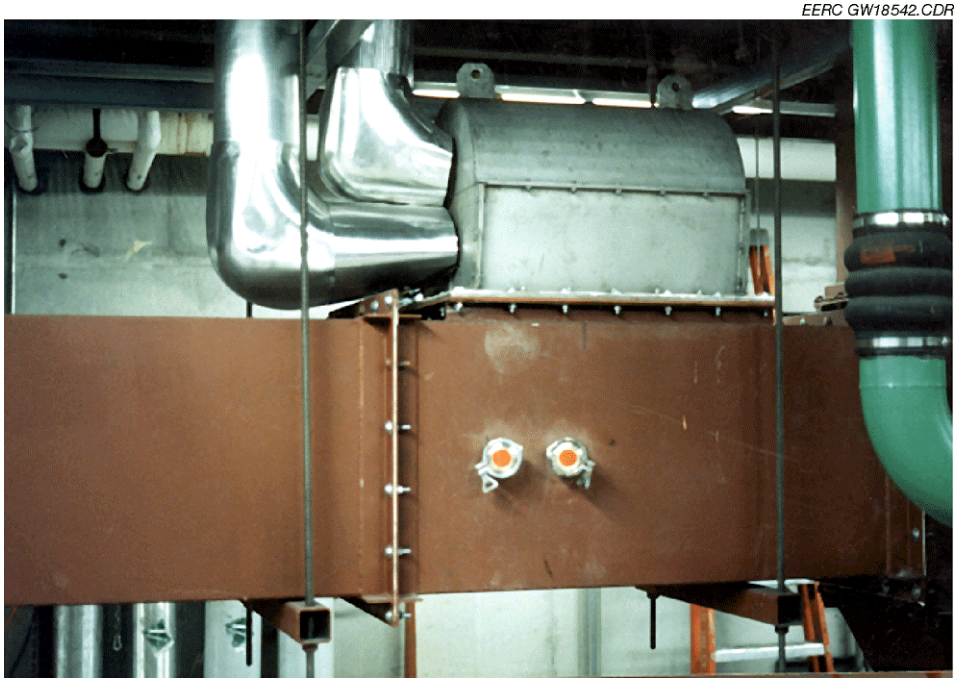

EERC GW18540.CDR

Exhibit 11A-17
Photographs of the CAH Duct and the Installed CAH Tube Bank

UTRC assumed responsibility for the design and fabrication of the CAH tube bank. Components for the CAH tube bank arrived at the EERC in August 1997, and assembly of the CAH tube bank was completed in September. Initial testing of the CAH tube bank occurred in October and December 1997. Process air flow rate to the CAH is adequate, and temperature control is good. Addendum-D contains illustrations of CAH tube bank surface temperatures, process air temperatures, and process air flow rate and CAH heat rate data as a function of run

time. Exhibit 11A-18 illustrates UTRC's conceptual design for the CAH tube bank installed in the SFS (Addendum-E contains a screen print of the CAH temperatures and process air flow rate and pressure). Exhibit 11A-19 identifies the location of thermocouples in the CAH tube bank, and Table 11A-4 describes the thermocouple locations. SFS operating experience has shown that when the tubes are clean, it is necessary to either increase the process air flow rate to a level >100 scfm (>2.83 m3/min) or reduce the temperature of the flue gas entering the CAH tube bank from 1800 to 1700 °F (982 to 927 °C) to prevent the overheating of the alloy tube surfaces.

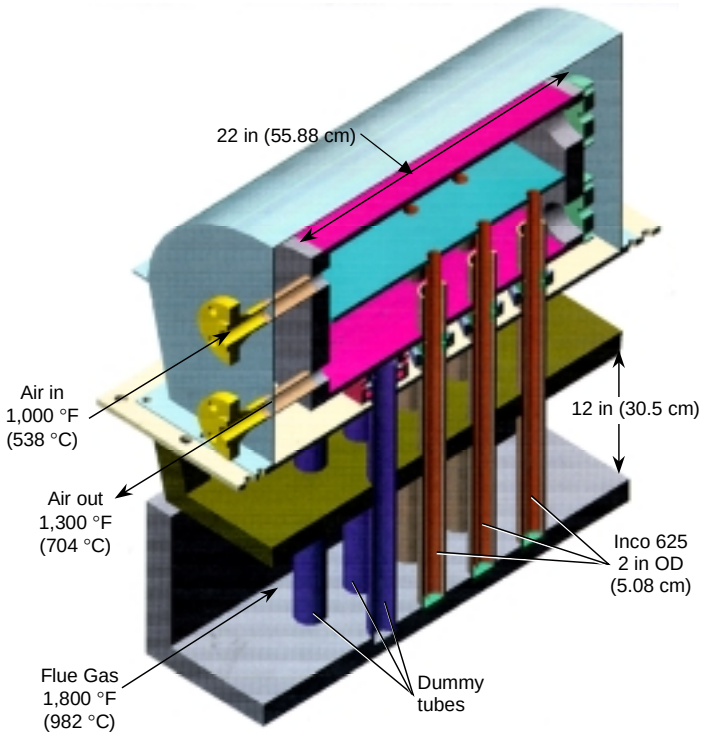

Exhibit 11A-18
Illustration of the CAH Tube Bank

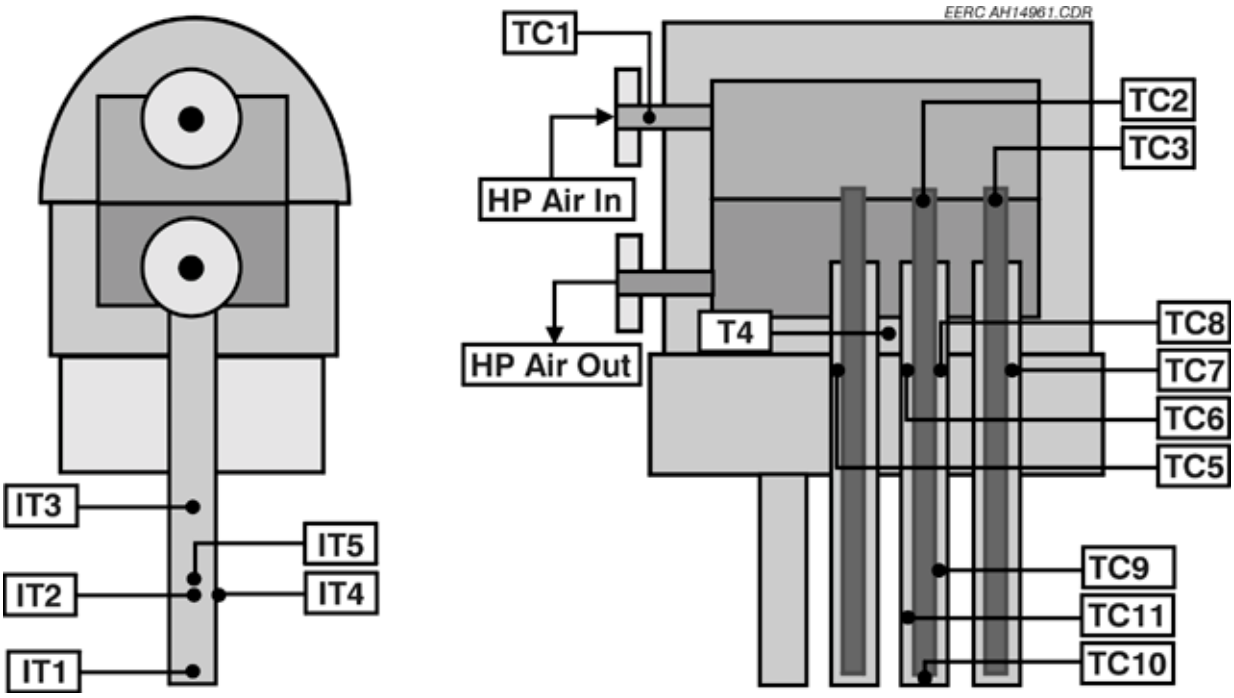

Exhibit 11A-19
Thermocouple Locations in the CAH Tube Bank

Table 11A-4
Description of CAH Thermocouple Locations[1]

Category	No.	Label	Description
Air Inlet	1	CAHTC1	Bulk flow entering the inlet header
	2	CAHTC2	Air entering center tube
	3	CAHTC3	Air entering most downstream tube
Air Outlet	4	CAHTC6	Air leaving center tube
	5	CAHTC7	Air leaving most downstream tube
	6	CAHTC5	Air leaving most upstream tube
	7	CAHTC8	Air leaving side tube
Air in Active Region	8	CAHTC10	Bottom of center tube
	9	CAHTC11	4 in. up outside annulus, center tube
	10	CAHTC9	8 in. up outside annulus, center tube
Tube Surface	11	CAHIT1	1 in. up center tube, facing upstream (failed)
	12	CAHIT2	5 in. up center tube, facing upstream
	13	CAHIT3	8 in. up center tube, facing upstream (failed)
	14	CAHIT4	5 in. up center tube, facing to side (failed)
	15	CAHIT5	5 in. up center tube, facing downstream (failed)
Header Shell	16	CAHTC4	Next to shell on outside, between return air pipes (failed)

[1] Thermocouple locations are illustrated in Exhibit 11A-19.

The five uncooled ceramic tubes were replaced in May 1998 with uncooled stainless steel tubes. Replacement of the ceramic tubes was necessary because they were repeatedly damaged when the tube bank was removed from the duct after the test periods in February, March, and April. After a lignite-fired test in June 1998, the air-cooled tubes were removed from the tube bank, cleaned, and fins were added to the leading and trailing edges. The purpose of adding fins to the air-cooled tubes was to increase heat transfer. Based on operating experience to date, it appears that the addition of the fins to the air-cooled tubes improved heat recovery during coal-fired test periods. The fins appear to have reduced the rate of heat-transfer degradation as ash deposits developed and helped to maintain a higher heat-transfer rate once the deposits had formed. However, no improvement in heat recovery was observed during natural gas-fired periods with clean tube surfaces.

Prior to an August 1998 test, all of the CAH thermocouples were replaced or repaired in conjunction with the installation of fins on the air-cooled tubes. However, one tube surface thermocouple (CAHIT3) was damaged when the tube bank was installed in the flue gas duct. One additional CAH thermocouple failed during both the August and December 1998 tests, and a fourth thermocouple failed at the beginning of a January 1999 test. Therefore, at this time, only one of the five surface thermocouples is functioning properly. There are no plans to replace these thermocouples at this time because of the time and expense that would be required.

In September 1998, the uncooled tubes were again replaced. The replacement tubes represented three high-temperature alloy types (INCOLOY MA956, INCOLOY MA956HT, and PM2000) and three pipe sizes (1.5-in. [3.81 cm] Schedule 80, 1-in. [2.54 cm] Schedule 40, and 0.75-in. [1.905 cm] Schedule 40, respectively). Exhibit 11A-20 illustrates the position, size, and alloy type for the five uncooled tubes. The five uncooled tubes were arranged such that the first two tubes in the flue gas path were the 0.75-in. (1.9-cm) Schedule 40 PM2000 material. The third tube was the 1-in. (2.5-cm) Schedule 40 INCOLOY

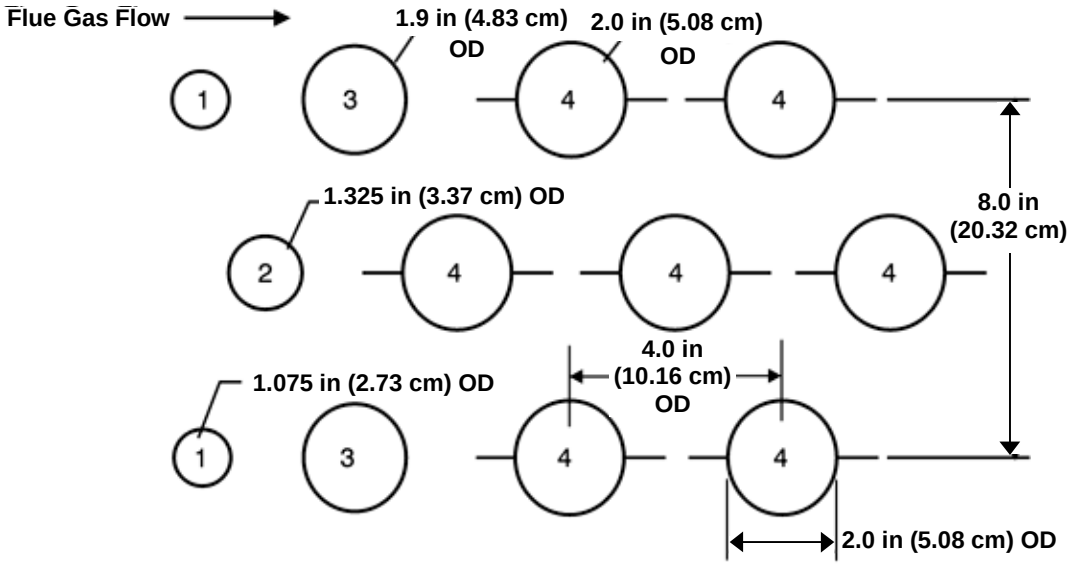

[1]Uncooled, PM 2000 (nominally 0.75 in (1.91 cm) Schedule 40 pipe).
[2]Uncooled, Incoloy Alloy MA956HT (nominally 1 in (2.54 cm) Schedule 40 pipe).
[3]Uncooled, Incoloy Alloy MA956 (nominally 1.5 in (3.81 cm) Schedule 80 pipe).
[4]Air-Cooled, Inconel 625 (2 in (5.08 cm) tubing, 0.188 in (0.478 cm) Wall.

EERC GW15683.CDR

Exhibit 11A-20
Illustration of the Tubes in the CAH Tube Bank from September 1998 through November 1999

MA956HT material, and the last two tubes were the 1.5-in. (3.8-cm) Schedule 80 INCOLOY MA956 material. Exhibit 11A-21 is a photograph of the CAH tube bank with the uncooled alloy tubes as well as the air-cooled finned tubes.

EERC GW18538.CDR

Exhibit 11A-21
Photograph of the Uncooled and Finned Tubes Installed in the CAH Tube Bank

At the request of UTRC, two uncooled alloy tubes installed in the CAH tube bank in September 1998 were removed following a September 1999 test and returned to UTRC for characterization. The tubes removed from the CAH represent the alloys designated INCOLOY MA956HT and INCOLOY MA956. Replacement tubes were fabricated using stainless steel pipe. Exhibit 11A-22 illustrates the tubes in the CAH tube bank as of January 2001.

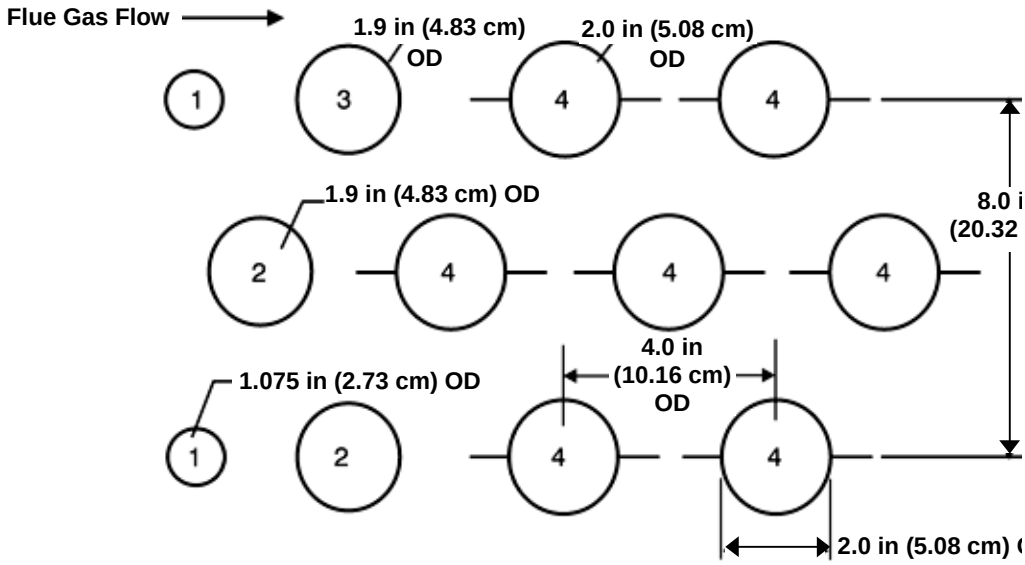

[1]Uncooled, PM 2000 (nominally 0.75 in (1.91 cm) Schedule 40 pipe).
[2]Replaced prior to December 1999 test, using 1.5 in (3.81 cm) Schedule 40 S.S. pipe.
[3]Uncooled, Incoloy Alloy MA956 (1.5 in (3.81 cm) Schedule 80 pipe).
[4]Air-Cooled, Inconel 625 (2 in (5.08 cm) tubing, 0.188 in (0.478 cm) Wall.

EERC GW17855.CDR

Exhibit 11A-22
Illustration of the Tubes in the CAH Tube Bank from December 1999 through January 2001

When coal firing is initiated, CAH tube surface temperatures decrease. Process air flow rates are also decreasing as a function of time in an attempt to maintain a relatively constant process air exit temperature. Stable temperatures and flow rates are only observed during natural gas-fired periods and when a sootblowing methodology is effectively applied during coal firing. However, when firing coal, it is not necessary to clean the surface of the metal tubes to maintain acceptable process air flow rate and temperature control. Therefore, ash deposits can be generated to permit a relative determination of ash deposition rate and characterization of CAH tube deposits. Based on SFS operating experience to date with bituminous, subbituminous, and lignite fuels, CAH plugging for fuel-fired periods of up to 200 hr is not a problem. The deposits that form are limited to the leading and trailing edges of the tubes. The issue of CAH plugging could become a concern during longer-term tests. However, periodic cleaning of the CAH tube bank should adequately mitigate any plugging problems encountered.

An ash deposition rate can be expressed in many ways for the CAH tube bank. The simplest is mass per unit time, lb/hr (g/hr), based on the mass of ash recovered from the CAH tubes and the fuel firing duration. Incorporating the surface area of the tube bank (6.28 ft^2, or 0.58 m2) results in units of lb/hr-ft^2 (g/hr-m2). On a fuel-firing-rate basis, the CAH ash deposition rate would be expressed as lb/MMBtu (g/kJ). In order to compare fuel ash deposition rates in the CAH tube bank and determine deposit composition, it is necessary to fire the slagging furnace at a constant rate and for a specific time frame for each fuel without attempting to sootblow the tube surfaces. Exhibit 11A-23 is a photograph of the CAH tube bank following a December 1999 test firing an Illinois No. 6 coal. In this case, sootblowing was not effectively applied, resulting in significant leading- and trailing-edge deposits. However, CAH tube bank plugging was not a problem. No deposits were observed bridging the flue gas path between the tubes.

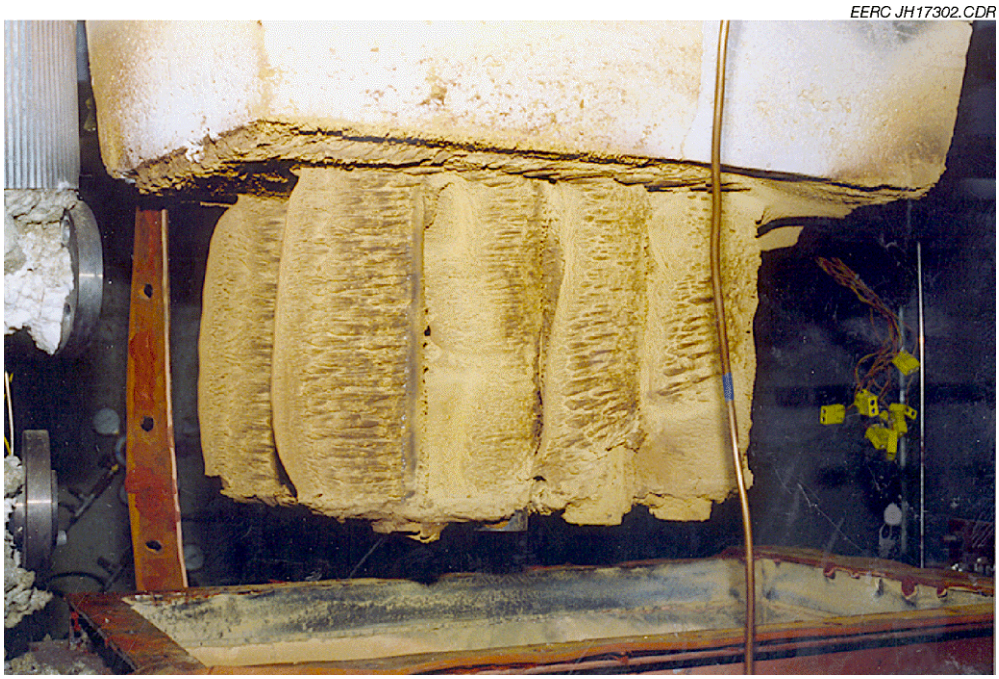

Exhibit 11A-23
Photograph of Ash Deposits on the CAH Tubes Following a December 1999 Test Firing Illinois No. 6 Bituminous Coal

In November 1999, the EERC developed a probe for sootblowing the CAH tube bank. The components of the sootblowing system included stainless steel tubing and a nozzle, high-pressure hose, a ball valve, a regulator, and pipe fittings. The sootblowing medium is compressed nitrogen gas delivered to the lance at a pressure of 200 psig (13.8 bar) and a flow rate of 188 scfm (5.3 m^3/min). The approach simply involves the manual insertion and removal of the lance through an access port to the tube bank. This approach permits sootblowing between two rows of tubes. The duration of an actual sootblowing event does not exceed 15 s.

Based on CAH operating experience to date, an 8-hr sootblowing frequency is adequate for the eastern Kentucky coal fired in the SFS. Exhibit 11A-24 is a photograph of the CAH tubes following that June 2000 test. Although some ash deposits are visible on the air-cooled finned tubes, they are minimal when compared to ash deposits observed without sootblowing. However, all of the other fuel type (bituminous, subbituminous, and lignite fuels) fired in the SFS will likely require a 4-hr sootblowing frequency to achieve a comparable result. Also, improved sootblowing effectiveness may require a modification to the methodology employed to increase the tube surface area affected by each sootblowing event.

Exhibit 11A-24
Photograph of Ash Deposits on the CAH Tubes Following a June 2000 Test Firing an Eastern Kentucky Bituminous Coal

No attempt had been made to sootblow the CAH tubes prior to the installation of fins. Therefore, conclusions cannot be drawn concerning the potential advantages of the fins when routine sootblowing is effectively used to maintain desired CAH heat recovery. Also, the presence of the fins may actually inhibit the effectiveness of sootblowing.

Process Air Preheaters

Design activities for the process air preheaters, which support operation of the LRAH panel and CAH tube bank, were essentially completed in September 1996. Because of flue gas temperatures (1700 °F or 927 °C) in the vicinity of the first three process air preheaters, EERC personnel reviewed material options for fabricating the tube bundles and the inlet process air piping to the LRAH test panel. These components were to be operated at a nominal air pressure of 150 psig (10.3 bar). Stainless steel was ruled out for the first three process air preheaters. An alloy capable of handling higher-temperature operation was required to maximize system flexibility and minimize the potential for material failure.

Material options considered included a Haynes HR-120, HR-160, HA-230, and HA-556 and an RA253MA. Maximum temperatures for these five alloys at 150 psig (10.3 bar) are 1600°, 1750°, 1650°, 1750°, and 1650 °F (871°, 955°, 899°, 955°, and 899 °C), respectively. Based on material characteristics, availability, and cost, EERC personnel elected to use the RA253MA (1650 °F at 150 psig [899 °C at 10.3 bar]) material for all five tube bundles exposed to flue gas and the HR-160 (1750 °F at 150 psig [955 °C at 10.3 bar]) material to transfer the heated process air to the LRAH and CAH test sections. Use of the HR-160 alloy permitted the installation of electrical heaters to improve process air temperature control to the LRAH test section. The use of RA253MA and HR-160 in combination for the process air preheaters maximized system

flexibility and minimized cost. Reduced flue gas temperature would have allowed the fourth and fifth process air preheaters supporting operation of the LRAH panel to be fabricated using stainless steel. However, because of an RA253MA minimum purchase requirement, all five tube bundles were fabricated using this material. The tube bundles are mounted in a refractory-lined, vertically oriented, square duct. Duct dimensions are 12 in. by 12 in. (30.5 cm by 30.5 cm) with an overall duct length of 20.5 ft (6.2 m).

Fabrication drawings for the process air preheaters were completed in October 1996, with material procurement and shell fabrication completed in November. Initial assembly and installation of the process air preheater shell sections were completed in January 1997, along with the final fit fabrication of the elbow connection between the exit of the process air preheaters and the inlet to the tube-and-shell heat exchangers. Once final fit was verified, locations for pressure tap, thermocouple, and sight port penetrations were identified. The shell sections were disassembled, and shell penetrations were installed in February. Refractory pouring for these sections was completed in March 1997 using Narco Cast 60 high-density refractory and Harbison-Walker 26 insulating refractory, and the sections were reassembled in the high bay. The location of the process air preheaters in the SFS is illustrated in Exhibit 11A-2. Fabrication of piping runs to and from the CAH tube bank and LRAH panel was completed in October and November 1997, respectively. All inlet and outlet process air lines supporting the CAH tube bank are insulated. Process air lines supporting the RAH panel are insulated and electrically heated.

Shakedown tests completed in September and October 1997 documented the performance of the process air preheater tube bundles, piping subsystem, and process control scheme. Observations and data demonstrated that the process air preheater system worked quite well. In addition, air compressor system failures were encountered, resulting in an unscheduled test of a nitrogen backup system. The nitrogen backup system functioned as intended when the air compressor shut down, supplying an emergency cooling media to the process air preheaters.

Examples of process air preheater temperature data are shown in Addendum-D. Addendum-E shows a screen print of the process air temperatures, pressures, and flow rates. Data representing natural gas- and coal-firing periods are indicated. Because of higher flue gas flow rates during natural gas firing, the air temperature exiting the process air preheater tube banks is higher when compared to coal-fired periods at comparable process air flow rates. However, during coal-firing, it is still possible to obtain exit temperatures of 1300 °F (705 °C) at process air flow rates of 200 scfm (5.7 m^3/min), even though the heat-transfer rate degrades with ash deposition on the tube surfaces. Further heating of the process air entering the LRAH panel is achieved electrically and by recovering heat from the CAH tube bank.

Slagging Furnace System Heat Exchangers

The pilot-scale SFS includes four tube-and-shell heat exchangers for heat recovery and flue gas temperature control and two water-cooled heat exchangers to reduce the heat load on system fans. Their location in the overall process layout is illustrated in Exhibit 11A-2. The first two tube-and-shell heat exchangers reduce flue gas temperature and preheat the secondary air for the main burner. The third and fourth tube-and-shell heat exchangers are used to control flue gas temperature at the inlet of the baghouse. Construction materials for the tube-and-shell heat exchangers are a combination of 304 stainless steel and carbon steel. Fabrication of the tube-and-shell heat exchangers was completed in August 1996. Installation and insulation activities were

completed in October and November 1996, respectively. Installation of flue gas piping/valves began in December 1996 and was completed in January 1997.

The tube-and-shell heat exchangers have performed up to expectations during all test periods. The main burner secondary combustion air temperature is nominally 600 to 800 °F (316 to 427 °C), depending on ambient air temperatures. During winter months, the secondary air temperature can be controlled at the lower end of the range, and during summer months temperature control is limited to the higher end of the range. Tube-and-shell heat exchangers 3 and 4 perform very well, controlling the flue gas temperature at the baghouse inlet to <400 °F (<205 °C). Inspection during maintenance after each week of coal-fired operation indicates the presence of a scale-type ash layer on the surface of the tubes that must be removed in order to avoid deterioration of heat-transfer performance, corrosion of metal surfaces, and potential plugging.

Two water-cooled heat exchangers were fabricated and installed in May 1998 to reduce the load on three SFS fans and ambient temperature on the upper levels of the SFS support structure. A water-cooled heat exchange tube bundle was installed in the flue gas stream between the five process air preheater tube bundles and the first tube-and-shell heat exchanger. This water-cooled tube bundle reduces the cooling load on the fans supporting the tube-and-shell heat exchangers. A water-jacketed heat exchanger was installed on the secondary air bypass line to the stack to reduce the air volume entering the stack and the amount of heat being emitted to the immediate area.

System Fans

The pilot-scale SFS has five fans: a combustion air FD fan, two cooling-air FD fans, an ID fan, and a FGR fan. Table 11A-5 summarizes the fan specifications. All five fans are centrifugal-type fans, with variable-speed drives (speed controllers) installed on the four large fans. The combustion air FD blower supplies ambient air to tube-and-shell heat exchanger Nos. 1 and 2, plus combustion air to the auxiliary burner. A portion of the heated air exiting the heat exchangers is used as secondary combustion air to the main burner, with the rest exiting the system through the stack. Valves and orifice plates and venturis are used to control and measure, respectively, the air and flue gas flow in the SFS.

Table 11A-5
Pressure, Temperature, and Flow Specifications for Slagging Furnace System Blowers

	Inlet Pressure, psig	Exit Pressure, psig	Avg. Inlet Temp., °F	Min. Inlet Temp., °F	Max. Inlet Temp., °F	Max. Inlet Flow, scfm	Max. Inlet Flow, acfm	Avg. Inlet Flow, acfm	Motor Horse-power
FD Blower	0	3.0	60	20	100	1200	1292	1200	40
Cooling-Air Blower	0	1.5	60	20	100	1200	1292	1200	20
ID Blower	1	0.5	350	250	450	1200	2255	1755	25
FGR Blower	0	1.5	350	250	450	450	788	701	10
Cooling-Air Blower	0	2.0	80	60	100	200	200	200	5

The cooling-air blower supplies ambient air to tube-and-shell heat exchanger Nos. 3 and 4, providing final cooling of the flue gas before it enters the baghouse. The heated air leaving the heat exchangers exits the system through the stack. An electronic speed controller on the fan is used to adjust the airflow from 0 to 1200 scfm (0 to 34 m^3/min) to maintain a desired flue gas temperature entering the pulse-jet baghouse. This approach permits the baghouse to be operated at either cold-side (350 °F [177 °C]) or hot-side (650 °F [344 °C]) conditions.

Flue gas exiting the baghouse is drawn through the ID blower and discharged through the stack. The blower speed is regulated with an electronic speed controller to maintain a zero-pressure balance point in the slagging furnace. A portion of the hot flue gas (nominally 350 °F [177 °C]) from the ID fan exit is drawn through the FGR blower for use as dilution gas in the dilution/quench zone. A combination of an electronic speed controller on the blower motor, a venturi flowmeter, and a flow control valve are used to regulate the FGR flow to maintain the desired flue gas temperature at the inlet of the CAH tube bank.

The small FD fan provides cooling air to the RAH panel door frames. Each RAH door frame requires 100 scfm (2.8 m^3/min) of cooling air. The fan was installed in November 1997, along with an inlet muffler and air filter. Two valves and flow measurement devices permit measurement and control of cooling air flow rate to each of the RAH door frames.

Fan specifications were submitted to UTRC for review in mid-July 1996. Based on UTRC approval, vendor recommendations, and the bids received from four prospective vendors, a purchase order was issued to Winger Associates, representing American Fan Company, for the four large system fans in late August 1996. Installation of the four large fans was completed in early 1997. Two FD water-cooled radiators were installed in May 1998 on the combustion air FD and ID fan motors to protect them from overloading due to the high ambient temperatures on the sixth level of the support structure. The radiators generate cool air that circulates over the electric motors.

The performance of the system fans during shakedown and subsequent test periods has been excellent. However, to reduce noise in the high bay, the EERC added mufflers to the outlet piping of the four large SFS fans, the process air lines downstream of the high-pressure control

valves, and the discharge lines from the RAH frame-cooling process air lines. The mufflers on the ID and two large FD fans also reduced noise levels at the stack and exterior intakes, respectively.

Emission Control

A pulse-jet baghouse is used for final particulate control on the pilot-scale SFS. The baghouse design permits operation at both cold-side (250 to 400 °F [121 to 205 °C]) and hot-side (600 to 700 °F [316 to 371 °C]) temperatures. The primary baghouse chamber and ash hopper walls are electrically heated and insulated to provide adequate temperature control to minimize heat loss and avoid condensation problems on start-up and shutdown. Inlet and outlet piping and the clean air plenum are insulated. Because of the planned and anticipated operating conditions, materials of construction are primarily 304L stainless steel. The main baghouse chamber was designed with internal angle iron supports to handle a negative static pressure of 20 in. W.C. (37 mmHg).

Flue gas flow rates to the baghouse can range from a low of 630 scfm (17.8 m^3/min) (981 acfm [27.8 m^3/min]) at 350 °F (177 °C), based on a furnace firing rate of 2 MMBtu/hr [2.1×10^6 kJ/hr]) to a maximum of 1060 scfm (30.0 m^3/min) (2365 acfm [67.0 m^3/min] at 700 °F [371 °C]), based on a furnace firing rate of 3 MMBtu/hr [3.16×10^6 kJ/hr]). Therefore, the baghouse design was based on an average flue gas flow rate of 850 scfm (24.1 m^3/min) (1324 acfm [37.5 m^3/min] at 350 °F [177 °C] or 1896 acfm [53.7 m^3/min] at 700 °F [371 °C], based on a nominal furnace firing rate of 2.5 MMBtu/hr [2.64×10^6 kJ/hr]). The baghouse is sized to accommodate a maximum of 36 bags mounted on wire cages with 2-in. (5.1-cm) bag spacing.

Bag dimensions are nominally 6 in. (15.2 cm) in diameter by 10 ft (3.0 m) in length, providing a total filtration area of 565-ft^2 (52.5 m^2). Arranging the bags in six rows of six bags each allows the number of bags on-line to be changed by installing different tube sheets. For example, when the baghouse is operated at 350 °F [177 °C] and 850 scfm (24.1 m^3/min) (1324 acfm [37.5 m^3/min]), only 24 bags are required to achieve a filter face velocity of 3.5 ft/min (1.1 m/min). If all 36 bags were installed, the filter face velocity would be roughly 2.3 ft/min (0.7 m/min). In the event that the baghouse is operated at a hot-side condition (1896 acfm [53.7 m^3/min] at 700 °F [371 °C]), 30 bags would result in a filter face velocity of 4.0 ft/min (1.2 m/min), and 36 bags would decrease the face velocity to 3.4 ft/min (1.0 m/min). At a maximum potential flow rate of 2365 acfm (67.0 m^3/min) (1060 scfm [30.0 m^3/min]) at 700 °F (371 °C), 36 bags would result in a filter face velocity of 4.2 ft/min (1.3 m/min).

To date, only one tube sheet has been constructed, permitting the installation of 36 bags (565-ft^2 [52.5 m^2] of filtration area) arranged in a six-by-six array. Installing the maximum number of bags permits the SFS to be operated over the broadest potential range of conditions while minimizing the potential impact of the baghouse on overall system performance. Each filter bag is secured to the tube sheet using a snap band sewn into the top cuff. Stainless steel wire cages with 20 vertical wires and 6-in. (15.2-cm) ring spacing provide bag support. The pulse-jet baghouse is a single compartment capable of either on- or off-line cleaning. Flue gas enters the baghouse in an area just below the bottom of the cage-supported bags and above the ash hopper. Access to the filter bags and stainless steel wire cages is gained by removing the clean air plenum at the top of the baghouse. The baghouse ash hopper is supported at the fourth level (roughly

40-ft [12.2-m] elevation), providing access to the clean air plenum on the fifth level to facilitate installation, inspection, and removal of filter bags and cages.

Low-watt-density heat cable made for conductive surfaces was installed to preheat the surface of the baghouse chamber to prevent moisture condensation during start-up and to minimize baghouse heat losses over the operating range of interest (350-700 °F [177-371 °C]); heat cable was run vertically on each of the four baghouse walls spaced on 6-in. (15.2-cm) centers. The individual elements were wired in parallel to minimize the impact of single-element failures. The baghouse ash hopper is heated in a similar manner. Five temperature controllers are used to control electrical resistance heating on the pulse-jet baghouse.

Pulse-jet cleaning can be triggered as a function of baghouse differential pressure or as a function of time. The baghouse pulse-jet cleaning system is operated/controlled by a program written for the Genesis data acquisition software that permits adjustment of cleaning frequency and pulse duration. Timers are used to set pulse duration and off time, while total baghouse operating time and test time in hours and total and test cleaning cycles are documented by the data acquisition system and data sheets. Filter bag cleaning occurs when the program opens the solenoid-operated valves between the pulse-air reservoir and the six pulse-air manifold lines. Each manifold line provides pulse air to six filter bags. Six filter bags are cleaned simultaneously, with a short delay between each set of filter bags to allow air pressure to recover in the pulse-air reservoir. The cleaning sequence is set to avoid cleaning adjacent rows. Row cleaning order is 1, 3, 5, 2, 4, 6.

Air for bag cleaning is provided by the same EERC air compressor system that supports the LRAH panel and CAH tube bank. High-pressure/low-volume and low-pressure/high-volume cleaning options were included in the design of the pulse-air system. In order to operate at a low-pressure/high-volume condition, a pulse volume of 0.03 ft^3/ft^2 (0.009 m^3/m^2) of fabric surface, or roughly 0.5 ft^3 (0.01 m^3)/bag, is necessary at a pulse-air reservoir pressure of <40 psig (<3 bar). The pulse volume for each set of six bags would be 3 ft^3 (0.08 m^3). For a high-pressure/low-volume case, 0.01 to 0.02 ft^3/ft^2 (0.003 to 0.006 m^3/m^2) of fabric surface is common, and the pulse-air reservoir pressure will be 40 to 100 psig (3 to 7 bar). Therefore, a maximum pulse volume of 1.9 ft^3 (0.05 m^3) will be required to clean one set of six bags. The required pulse duration to achieve a desired pulse-air volume as a function of pulse pressure was determined during system shakedown. Assembly of the pulse-air manifold and installation of compressed air piping to the pulse-air reservoir were completed in November 1996. Filter bags were installed in the baghouse in May 1997 to support refractory curing and the initial firing of coal in the slagging furnace.

Flue gas sample ports were installed in the inlet and outlet piping of the baghouse to permit flue gas sampling for gaseous/vapor-phase constituents as well as fly ash. Flue gas filters and heat trace lines were installed to support three sample locations. The first location is in the exit of the slag screen, the second is upstream of the baghouse and/or cyclone, and the third is downstream of the baghouse and/or cyclone. If necessary, these sample lines can be relocated or additional sample ports added to the SFS. Specific routine flue gas measurements are made to determine carbon monoxide, carbon dioxide, oxygen, sulfur dioxide, and nitrogen oxide concentrations using on-line instruments. Fly ash particle-size distribution and mass loading are determined periodically using standard U.S. Environmental Protection Agency (EPA) methods. Hazardous air pollutants (HAPs) can be measured using EPA Method 29 as well as other

methods. Sight ports (4 in. [10.2 cm] o.d.) are located at two elevations in the baghouse to permit inspection of bag surfaces on the dirty side and two locations in the clean air plenum to permit visual inspection of the tube sheet surface and the exit of several bags.

Thermocouples were installed in the inlet and outlet piping, as well as at four locations along the length of the baghouse chamber. Differential pressure across the chamber and static pressure at the outlet of the chamber are monitored continuously with pressure transducers. Gauges are also used as a backup to monitor baghouse differential and static pressure at the main control panel. Baghouse thermocouple and pressure transducer data are automatically logged on the data acquisition system. As a backup, baghouse data are recorded manually on data sheets on a periodic basis. Examples of baghouse data can be found in Addendum-D, and a screen print can be found in Addendum-E.

Baghouse ash removal is accomplished by opening a 6-in. (15.2-cm) knife valve at the bottom of the hopper, allowing ash material to drain through a 6-in. (15.2-cm) stainless steel pipe into a 55-gal (208-L) drum on the main floor level. Ash containers of this size facilitate handling and are adequate for ash accumulation during 100-hr and longer test periods, with only periodic replacement required. The photograph in Exhibit 11A-1 shows the baghouse and ash removal line and valves.

The bag/fabric type initially chosen for use in the SFS was a 16-oz (454-g) Huyck felt material. For multiple fuel types (Illinois No. 6 bituminous coal, Rochelle subbituminous coal, and two lignites) particulate emissions were effectively controlled to levels at or below 0.003 lb/MMBtu during test periods completed with undamaged bags. Baghouse differential pressure and the ability to control it were quite different for each of the four fuel types fired in the SFS. Depending on the fuel, combinations of on-line and off-line cleaning were necessary and on-line cleaning frequency was always <20 minutes. In all cases, baghouse differential pressure was controlled at <10-in. W.C. (19 mmHg).

In December 1999, a new set of bags was installed in the pulse-jet baghouse. The bag/fabric type was a 22-oz (624-g) woven glass with a polytetrafluoroethylene (PTFE) membrane. This bag/fabric type was selected in an attempt to improve the cleanability/differential pressure control, with expectations of as good if not better particulate control. Coal-fired test periods completed in 1999 and 2000 demonstrated comparable control of particulate emissions (0.0004-0.0028 lb/MMBtu vs. 0.0002-0.0030 lb/MMBtu) and improved control of baghouse differential pressure. The new bags were effectively cleaned on-line as a function of differential pressure using a set point of 6 in. W.C. (11 mmHg) and a pulse duration of 0.1 s. Reservoir pulse-air pressure can be adjusted for each fuel type to ensure that differential pressure after on-line cleaning is <3 in. W.C. (6 mmHg). Typically, a 60 psig (4.2 bar) pressure has been successfully used to control baghouse differential pressure. Cleaning frequency was typically >60 minutes for a filter face velocity ranging from 2.4 to 3.2 ft/min (0.7 to 1.0 m/min).

Particle-size distribution at the baghouse inlet has been determined using a five-stage multicyclone for several fuel types (three bituminous coals, two subbituminous coals, and two lignites). Although there is some variation between fuel types, typical data show 100% of the mass to be <10 microns, with 50% of the mass <2–8 microns, depending on fuel/ash properties. Factors affecting particle-size distribution in addition to fuel/ash properties include the performance of the slag screen and CAH tube bank.

The SFS does not have a sulfur dioxide control system, and there are no plans to install one at this time. Dispersion modeling data developed by the North Dakota Department of Health indicate that the stack dimensions (height and diameter) and volumetric flow rate permit a 20.8-lb/hr (9.4-kg/hr) sulfur dioxide emission rate. Sulfur dioxide emissions are limited to 20.8 lb/hr (9.4 kg/hr) to avoid potentially exceeding the ambient air standard. However, based on operating experience with bituminous, subbituminous, and lignite fuels, the EERC has never exceeded a sulfur dioxide emission rate of 17 lb/hr (7.7 kg/hr). Emission of nitrogen oxides has been 1.4 lb/MMBtu or less (<650 ppm at 3% oxygen in the flue gas).

Instrumentation and Data Acquisition

The instrumentation and data acquisition components for the pilot-scale SFS address combustion air, flue gas, process air, cooling water, and other appropriate measurements (temperatures, static and differential pressures, and flow rates). Flue gas is monitored for oxygen, sulfur dioxide, carbon monoxide, carbon dioxide, and total nitrogen species (nitric oxide and nitrogen dioxide) on a continuous basis at the furnace exit using on-line analyzers. A second set of gas analyzers (oxygen, carbon monoxide, carbon dioxide, sulfur dioxide, and nitrogen species) is used to monitor a second system location (baghouse inlet or outlet) simultaneously. Surface temperature measurements are made for the LRAH panel and CAH tube bank as well as furnace refractory in several locations. Orifice plates and venturis (monitored with pressure transducers and gauges on the main control panel) were installed to measure combustion air flow rate, flue gas flow rate, FGR rate, drawdown gas flow rate, and process air flow rates.

The data acquisition system is based on a Genesis software package and three personal computers with battery backup power supplies. This type of data acquisition system is currently used at the EERC on a number of pilot-scale combustion and gasification process systems. All process data points are logged on the data acquisition system and stored in a series of historian files. Integrated process control has been implemented extensively throughout the SFS, although all system processes can be controlled manually. System areas making use of integrated process control include the

1) fuel feed system,
2) furnace static pressure,
3) drawdown gas flow control,
4) combustion air flow control,
5) cooling-air flow control to the tube-and-shell heat exchangers,
6) process air flow rate and temperature control to the CAH tube bank,
7) process air flow rate and temperature control to the LRAH panel,
8) FGR rate to the dilution/quench zone, and
9) baghouse cleaning and temperature control.

Detailed P&IDs and an instrumentation list were submitted to UTRC for review and approval in July 1996. Following UTRC approval, the EERC initiated procurement of system instrumentation and components for the data acquisition system in August.

References

Beer, J.M.; Chigier, N.A. *Combustion Aerodynamics;* John Wiley & Sons: New York, 1972; pp 100–146.

Addendum A -Piping & Instrumentation Diagrams
(Appendix A)

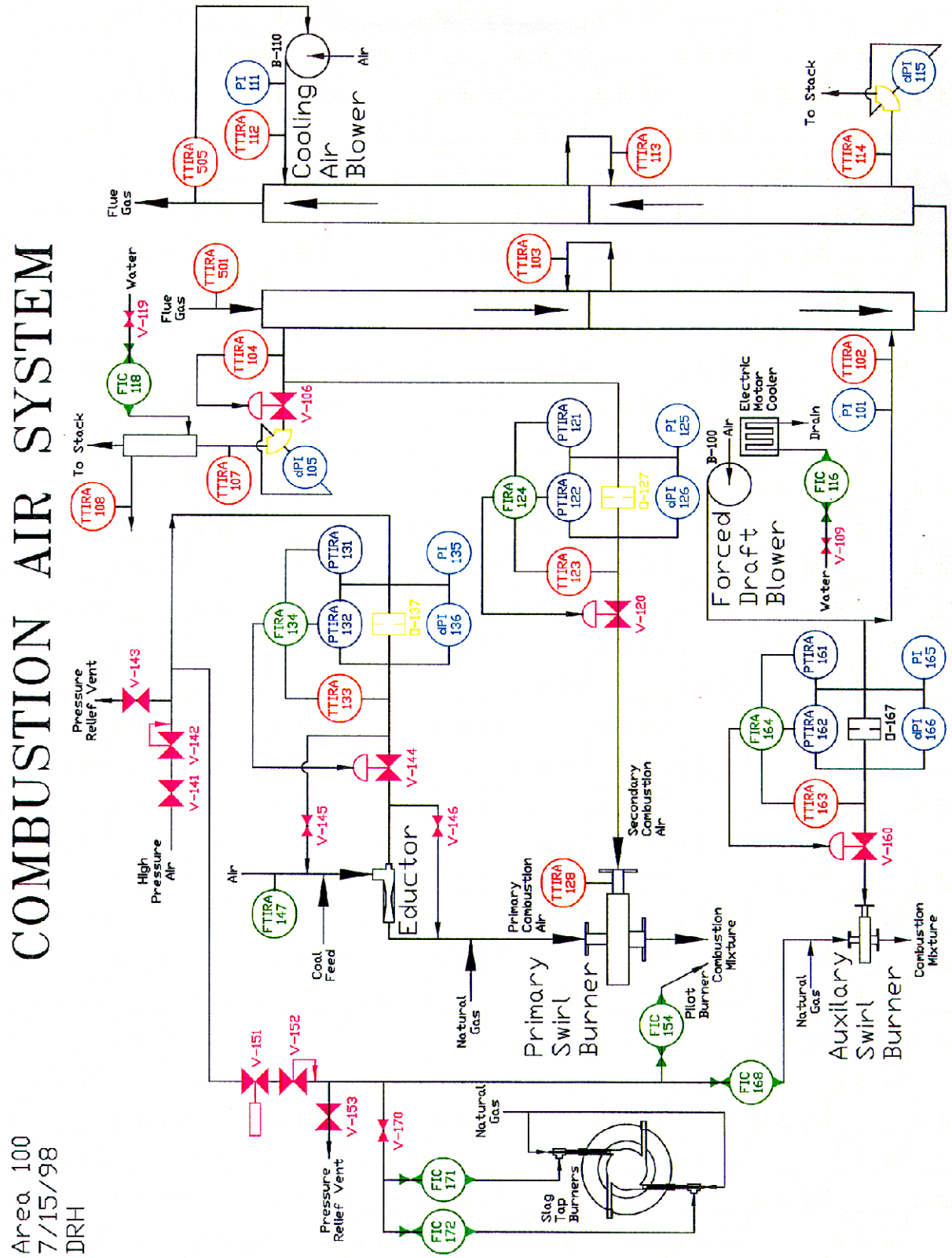
COMBUSTION AIR SYSTEM
Area 100
7/15/98
DRH
Cooling Air Blower
B-110
Air
Flue Gas
To Stack
Water
V-119
FIC 118
TTIRA 505
TTIRA 112
PI 111
TTIRA 501
TTIRA 104
TTIRA 107
dPI 105
V-106
TTIRA 108
TTIRA 103
TTIRA 113
TTIRA 114
dPI 115
TTIRA 102
PI 101
Electric Motor Cooler
Drain
B-100
Forced Draft Blower
FIC 116
V-109
Water
PTIRA 121
PTIRA 122
FIRA 124
TTIRA 123
D-127
dPI 126
PI 125
V-120
PTIRA 131
PTIRA 132
FIRA 134
TTIRA 133
D-137
dPI 136
PI 135
Pressure Relief Vent
V-143
V-142
V-141
High Pressure Air
V-144
V-145
V-146
Air
FTIRA 147
Cool Feed
Eductor
Primary Combustion Air
TTIRA 128
Secondary Combustion Air
Natural Gas
Primary Swirl Burner
Pilot Burner
Combustion Mixture
FIC 154
PTIRA 161
PTIRA 162
FIRA 164
TTIRA 163
D-167
dPI 166
PI 165
V-160
Natural Gas
Auxilary Swirl Burner
Combustion Mixture
FIC 168
V-151
V-152
V-153
V-170
Pressure Relief Vent
Natural Gas
FIC 171
FIC 172
Slag Tap Burners

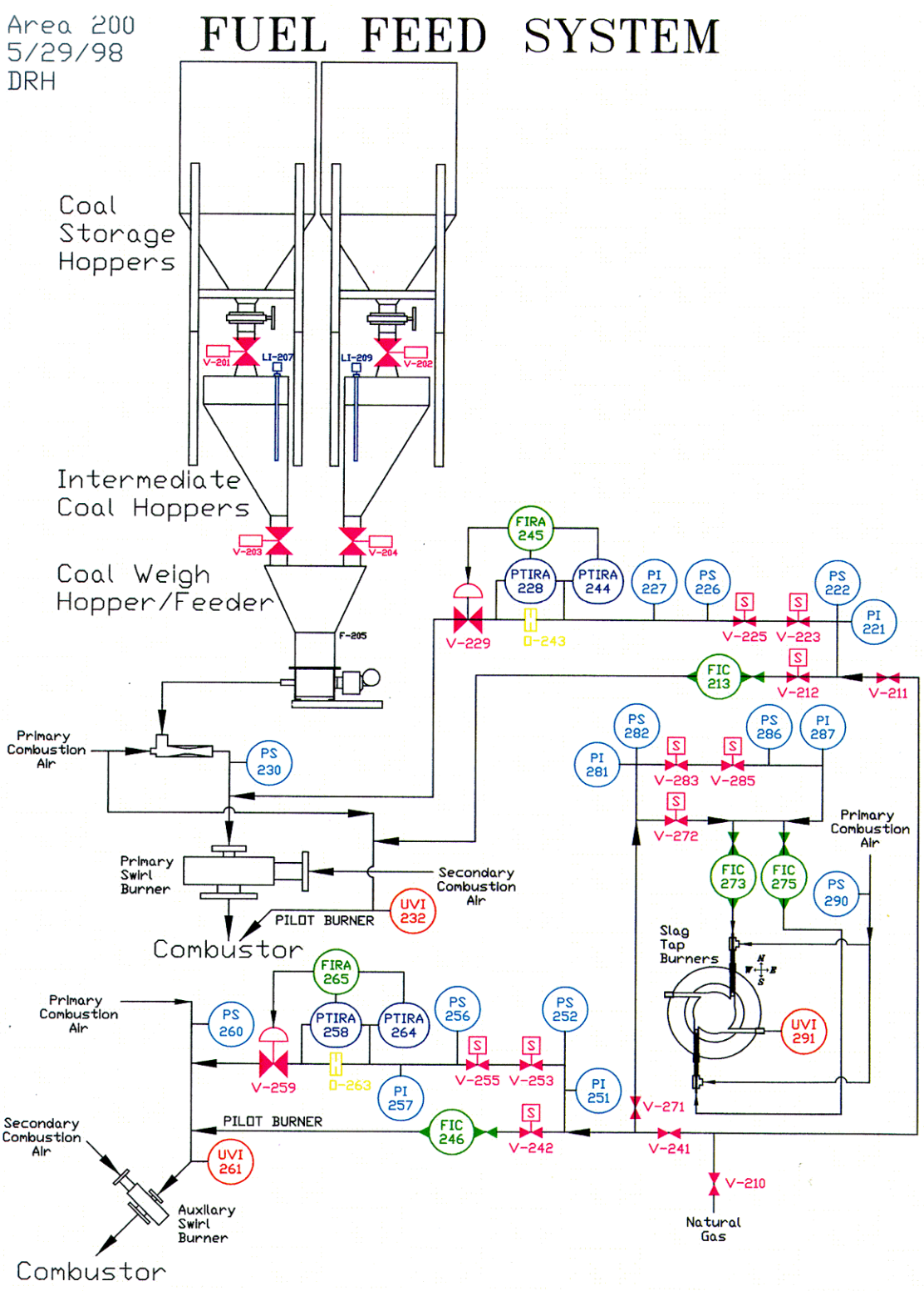
Area 200
5/29/98
DRH
FUEL FEED SYSTEM
Coal Storage Hoppers
V-201
LI-207
LI-209
V-202
Intermediate Coal Hoppers
V-203
V-204
Coal Weigh Hopper/Feeder
F-205
FIRA 245
PTIRA 228
PTIRA 244
PI 227
PS 226
PS 222
PI 221
V-229
D-243
V-225
V-223
FIC 213
V-212
V-211
Primary Combustion Air
PS 230
PS 282
PS 286
PI 287
PI 281
V-283
V-285
V-272
Primary Combustion Air
Primary Swirl Burner
Secondary Combustion Air
UVI 232
PILOT BURNER
Combustor
FIC 273
FIC 275
PS 290
Slag Tap Burners
UVI 291
FIRA 265
Primary Combustion Air
PS 260
PTIRA 258
PTIRA 264
PS 256
PS 252
V-259
D-263
V-255
V-253
PI 257
PI 251
V-271
PILOT BURNER
FIC 246
V-242
V-241
Secondary Combustion Air
UVI 261
V-210
Auxiliary Swirl Burner
Natural Gas
Combustor

Area 300
7/22/98
DRH

COMBUSTOR & WATER COOLING

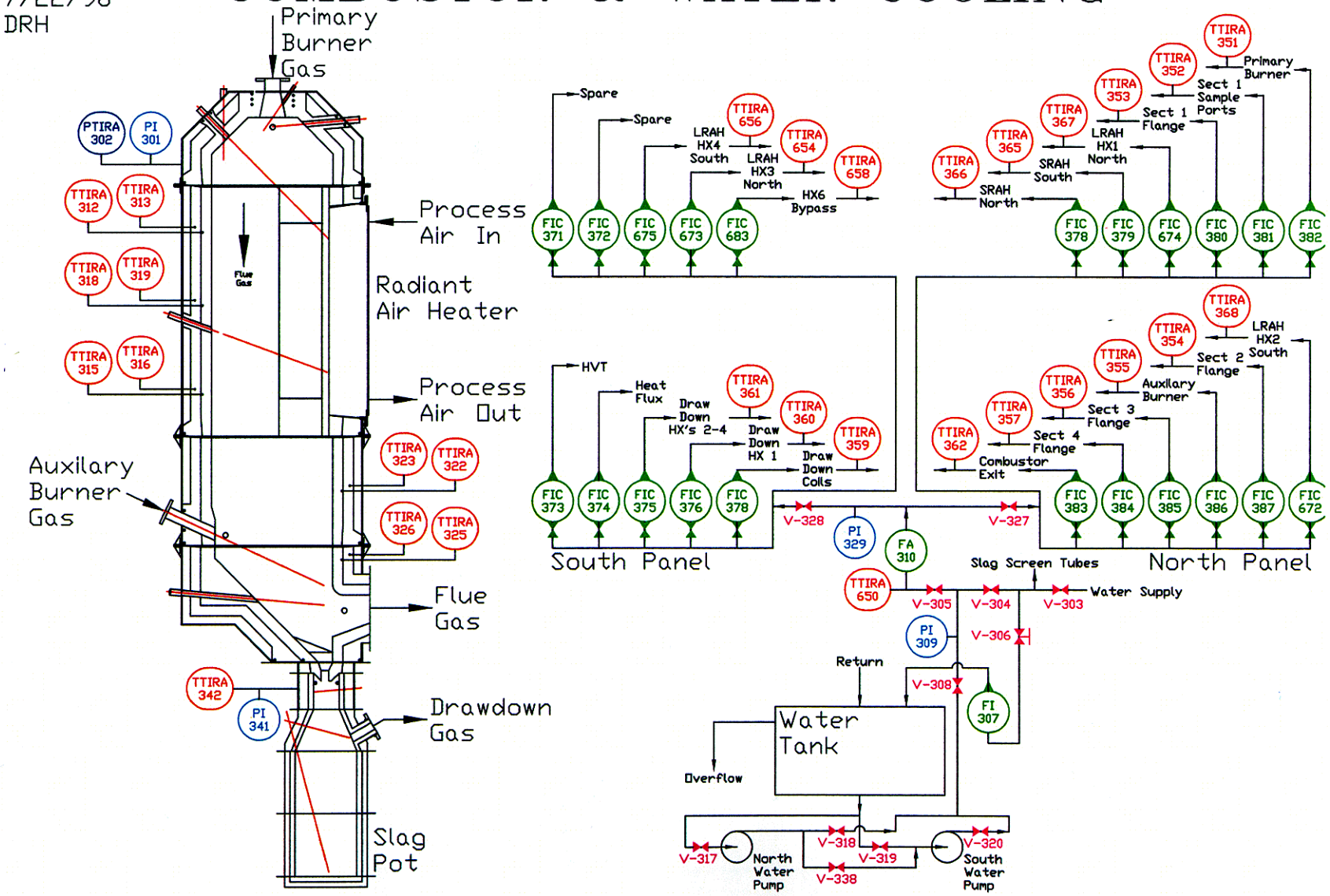

Area 400
7/16/98
DRH

SLAG SCREEN, QUENCH ZONE & CONVECTIVE PASS

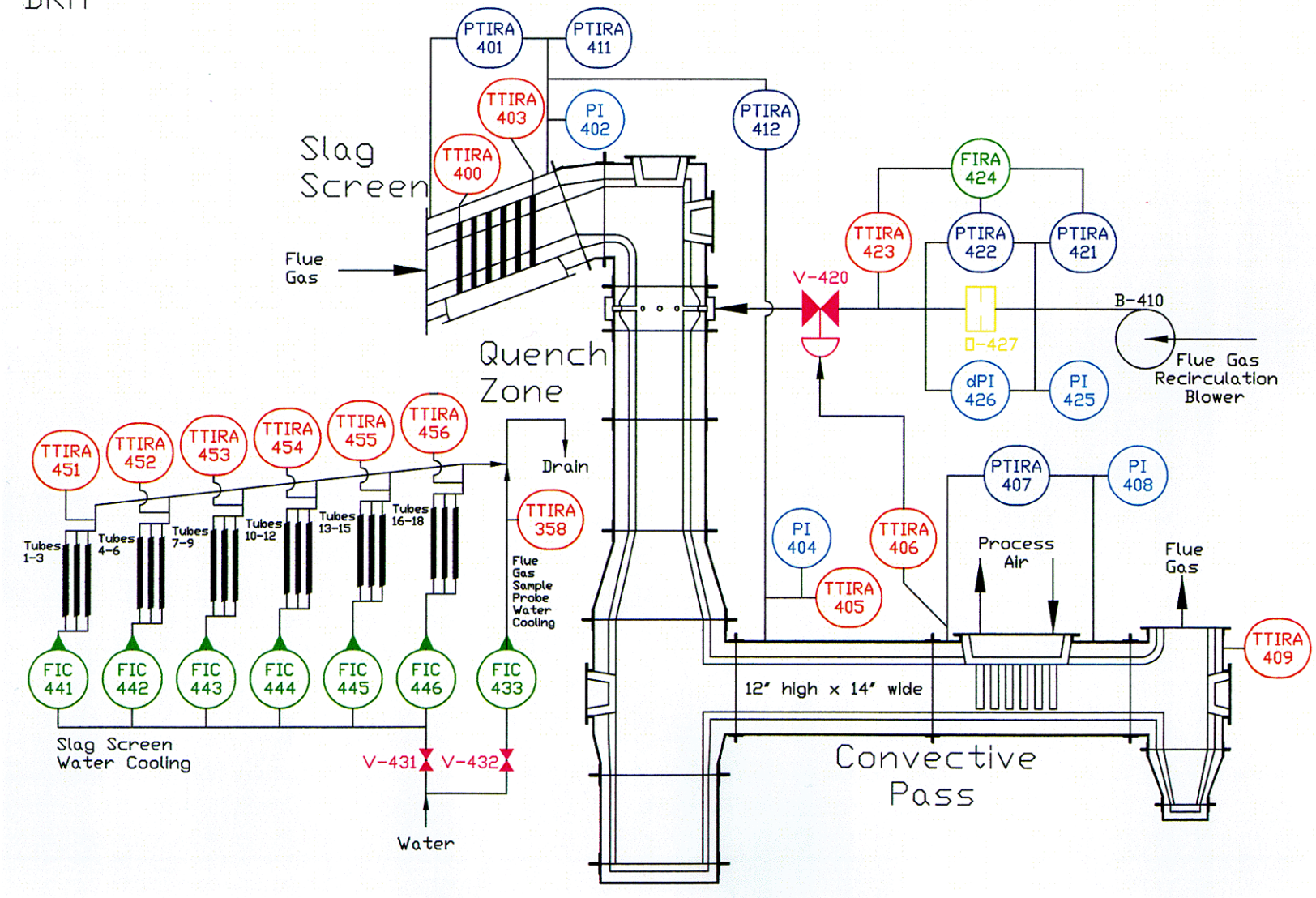

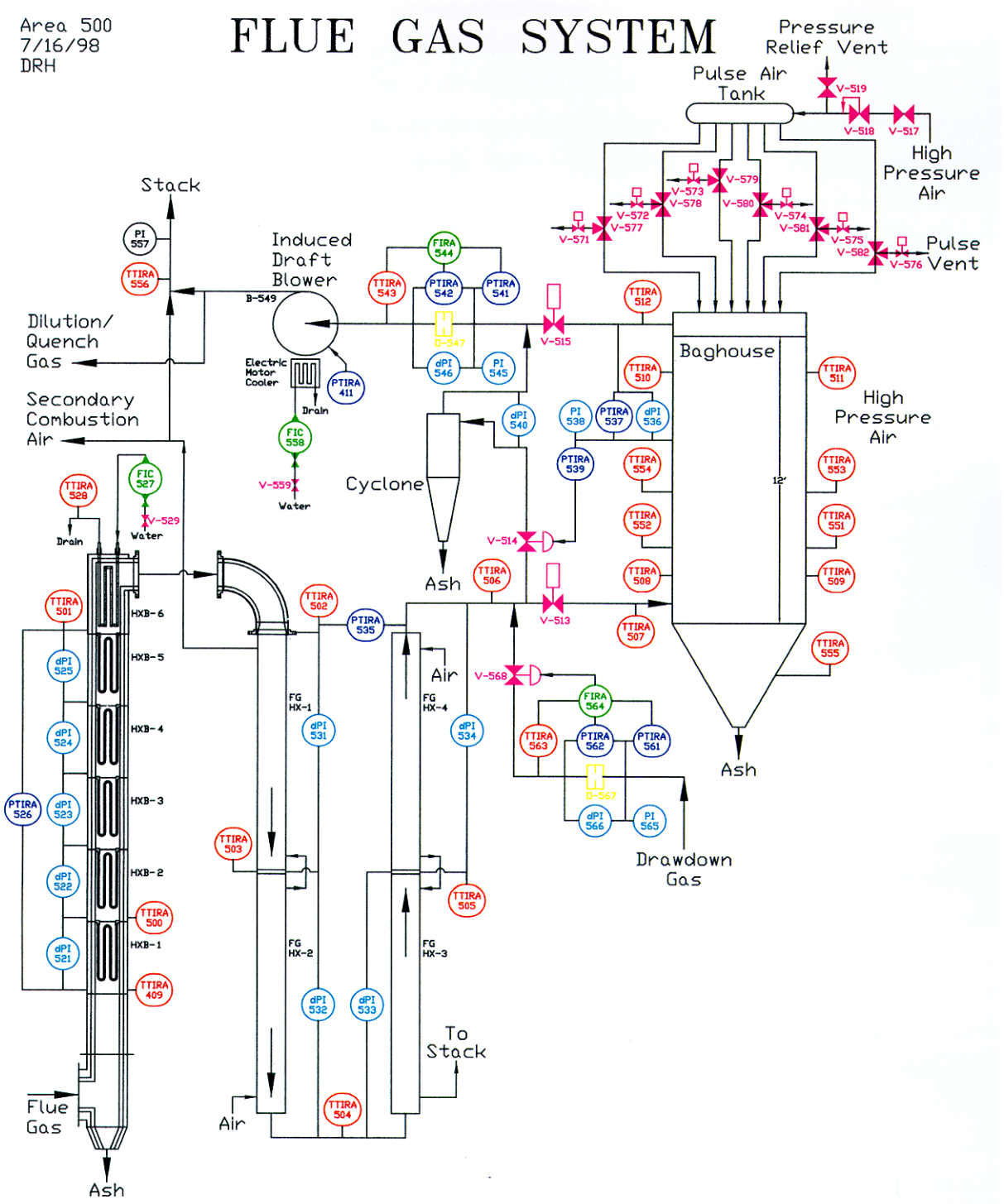
Area 500
7/16/98
DRH
FLUE GAS SYSTEM
Pressure Relief Vent
Pulse Air Tank
V-519
V-518
V-517
High Pressure Air
V-579
V-573
V-578
V-580
V-572
V-577
V-574
V-581
V-571
V-575
V-582
V-576
Pulse Vent
Stack
PI 557
TTIRA 556
Induced Draft Blower
B-549
Dilution/ Quench Gas
Secondary Combustion Air
Electric Motor Cooler
PTIRA 411
Drain
FIC 558
V-559
Water
FIRA 544
TTIRA 543
PTIRA 542
PTIRA 541
D-547
dPI 546
PI 545
V-515
TTIRA 512
Baghouse
TTIRA 510
TTIRA 511
High Pressure Air
dPI 540
PI 538
PTIRA 537
dPI 536
PTIRA 539
TTIRA 554
TTIRA 553
12'
Cyclone
TTIRA 552
TTIRA 551
V-514
Ash
TTIRA 506
TTIRA 508
TTIRA 509
V-513
TTIRA 507
TTIRA 555
TTIRA 528
FIC 527
V-529
Water
Drain
TTIRA 501
HXB-6
TTIRA 502
PTIRA 535
Air
V-568
FIRA 564
TTIRA 563
PTIRA 562
PTIRA 561
FG HX-1
FG HX-4
dPI 525
HXB-5
dPI 531
dPI 534
dPI 524
HXB-4
Ash
PTIRA 526
dPI 523
HXB-3
D-567
dPI 566
PI 565
Drawdown Gas
TTIRA 503
dPI 522
HXB-2
TTIRA 505
TTIRA 500
dPI 521
HXB-1
FG HX-2
FG HX-3
TTIRA 409
dPI 532
dPI 533
To Stack
Flue Gas
Air
TTIRA 504
Ash

Area 600/700
7/16/98
DRH

HIGH TEMPERATURE/PRESSURE HEAT EXCHANGERS

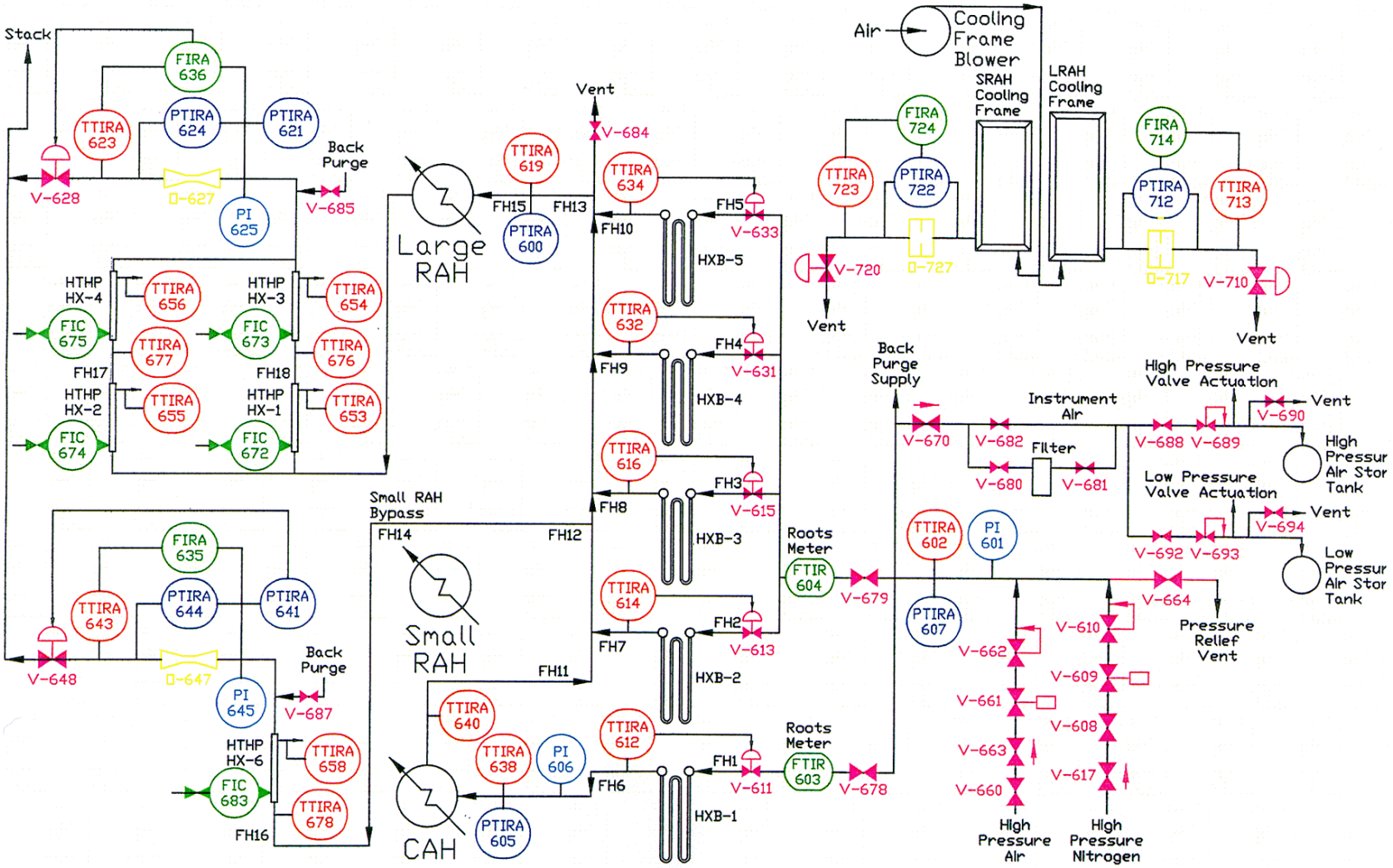

Addendum B -Plan and Elevation Views
(Appendix A)

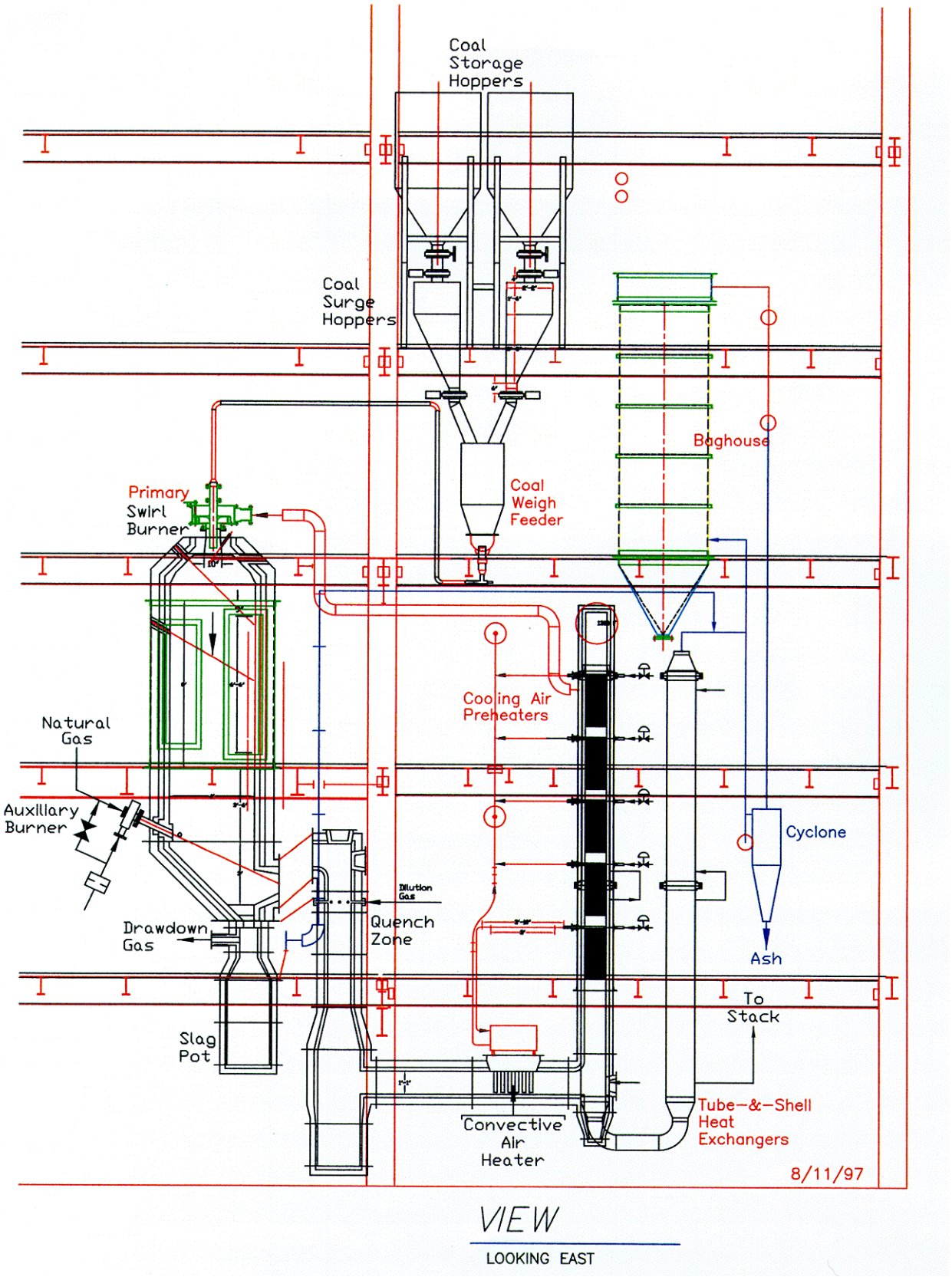
Coal
Storage
Hoppers
Coal
Surge
Hoppers
Baghouse
Primary
Swirl
Burner
Coal
Weigh
Feeder
Cooling Air
Preheaters
Natural
Gas
Auxiliary
Burner
Cyclone
Dilution
Gas
Quench
Zone
Drawdown
Gas
Ash
To
Stack
Slag
Pot
Tube-&-Shell
Heat
Exchangers
Convective
Air
Heater
8/11/97
VIEW
LOOKING EAST

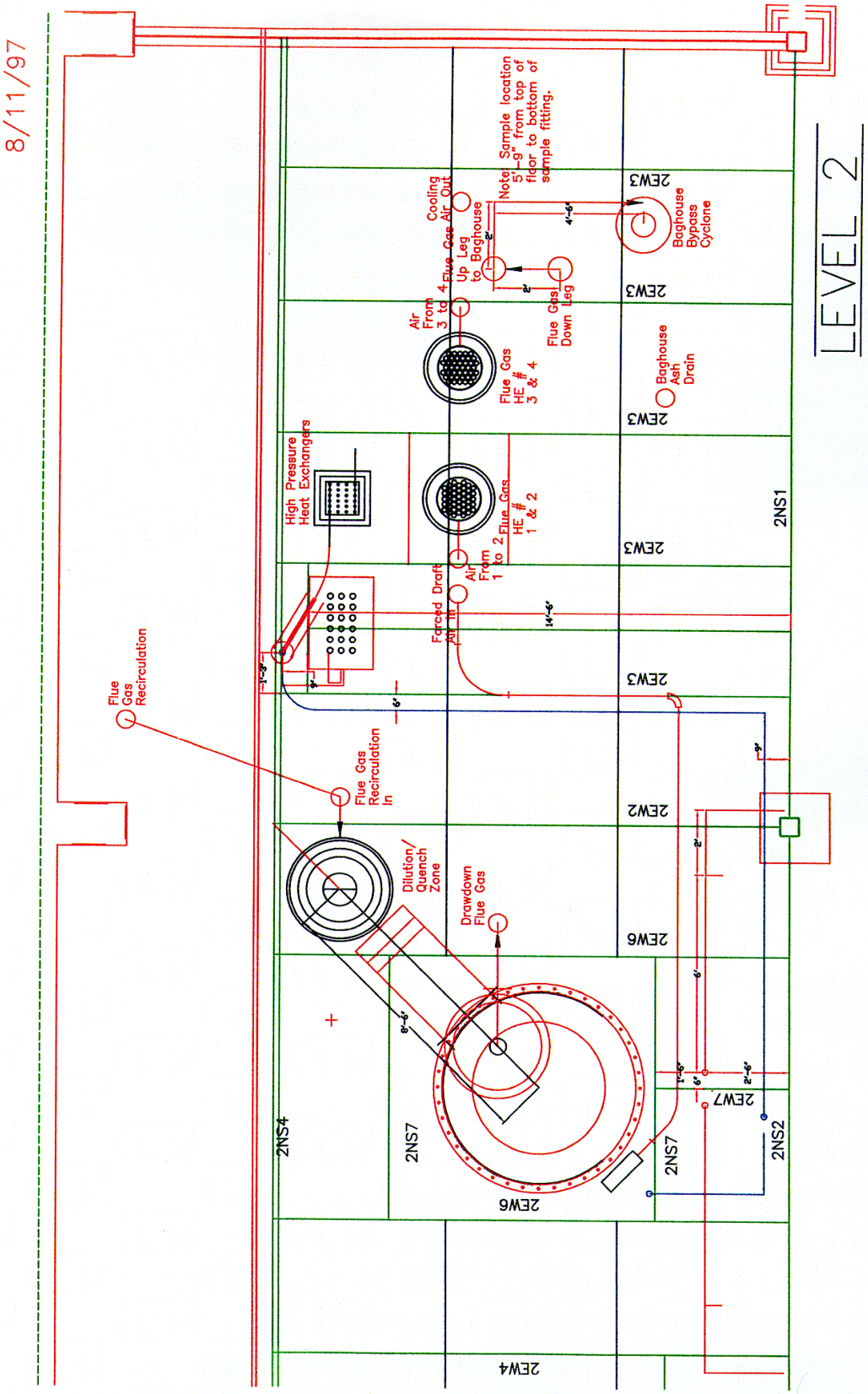
8/11/97
LEVEL 2
Note: Sample location 51-0" from top of floor to bottom of sample fitting.
Cooling Air Out
Flue Gas Up Leg to Baghouse
Flue Gas Down Leg
Baghouse Bypass Cyclone
Air From 3 to 4
Flue Gas HE # 3 & 4
Baghouse Ash Drain
High Pressure Heat Exchangers
Flue Gas HE # 1 & 2
Air From 1 to 2
Forced Draft Air In
Flue Gas Recirculation
Flue Gas Recirculation In
Dilution/ Quench Zone
Drawdown Flue Gas
2EW3
2EW2
2EW6
2EW7
2EW4
2NS1
2NS2
2NS4
2NS7

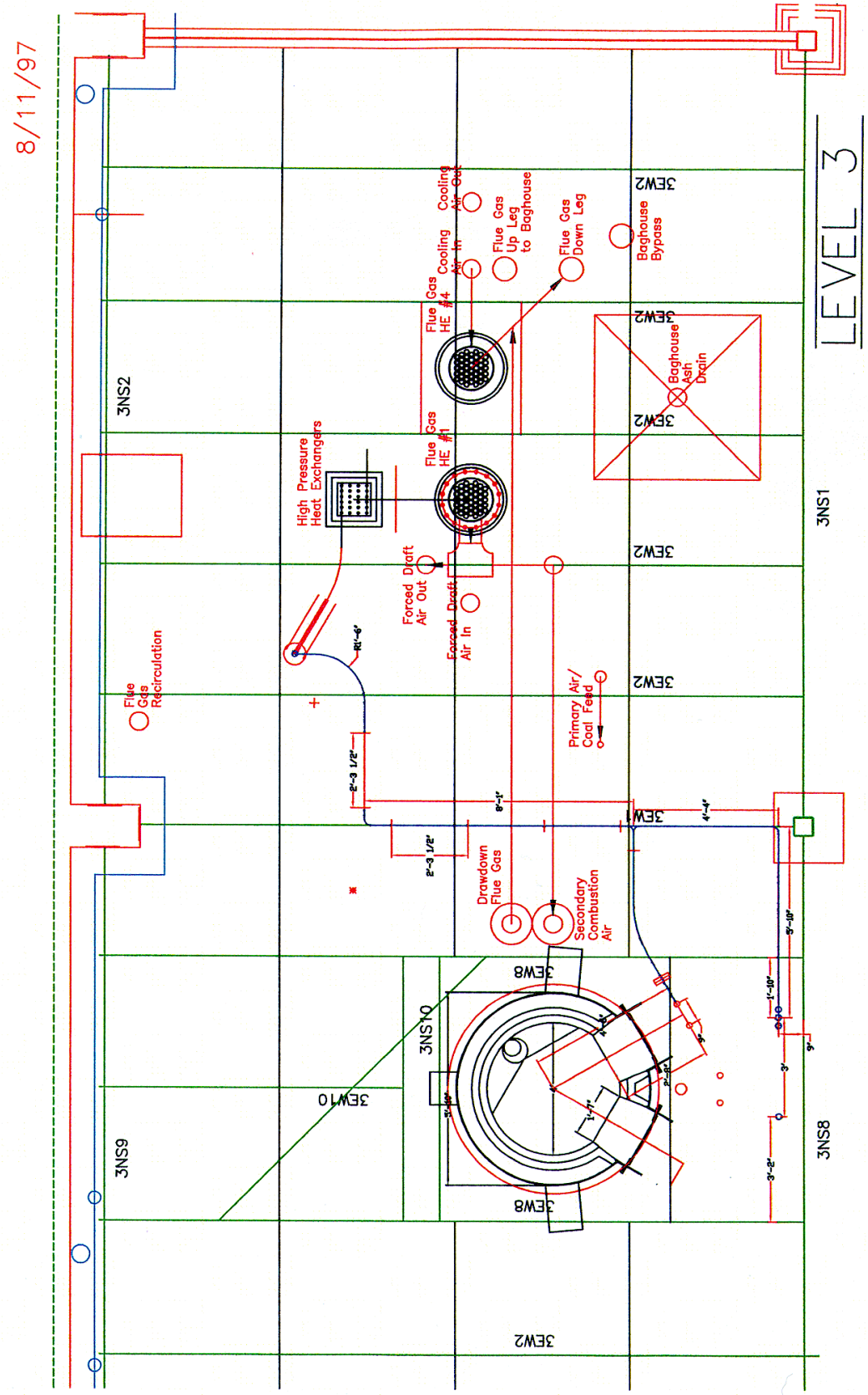
8/11/97
LEVEL 3
3NS1
3NS2
3NS8
3NS9
3NS10
3EW2
3EW8
3EW10
Cooling Air Out
Cooling Air In
Flue Gas Up Leg to Baghouse
Flue Gas Down Leg
Baghouse Bypass
Flue Gas HE #4
Baghouse Ash Drain
Flue Gas HE #1
High Pressure Heat Exchangers
Forced Draft Air Out
Forced Draft Air In
Flue Gas Recirculation
Primary Air/ Coal Feed
Drawdown Flue Gas
Secondary Combustion Air

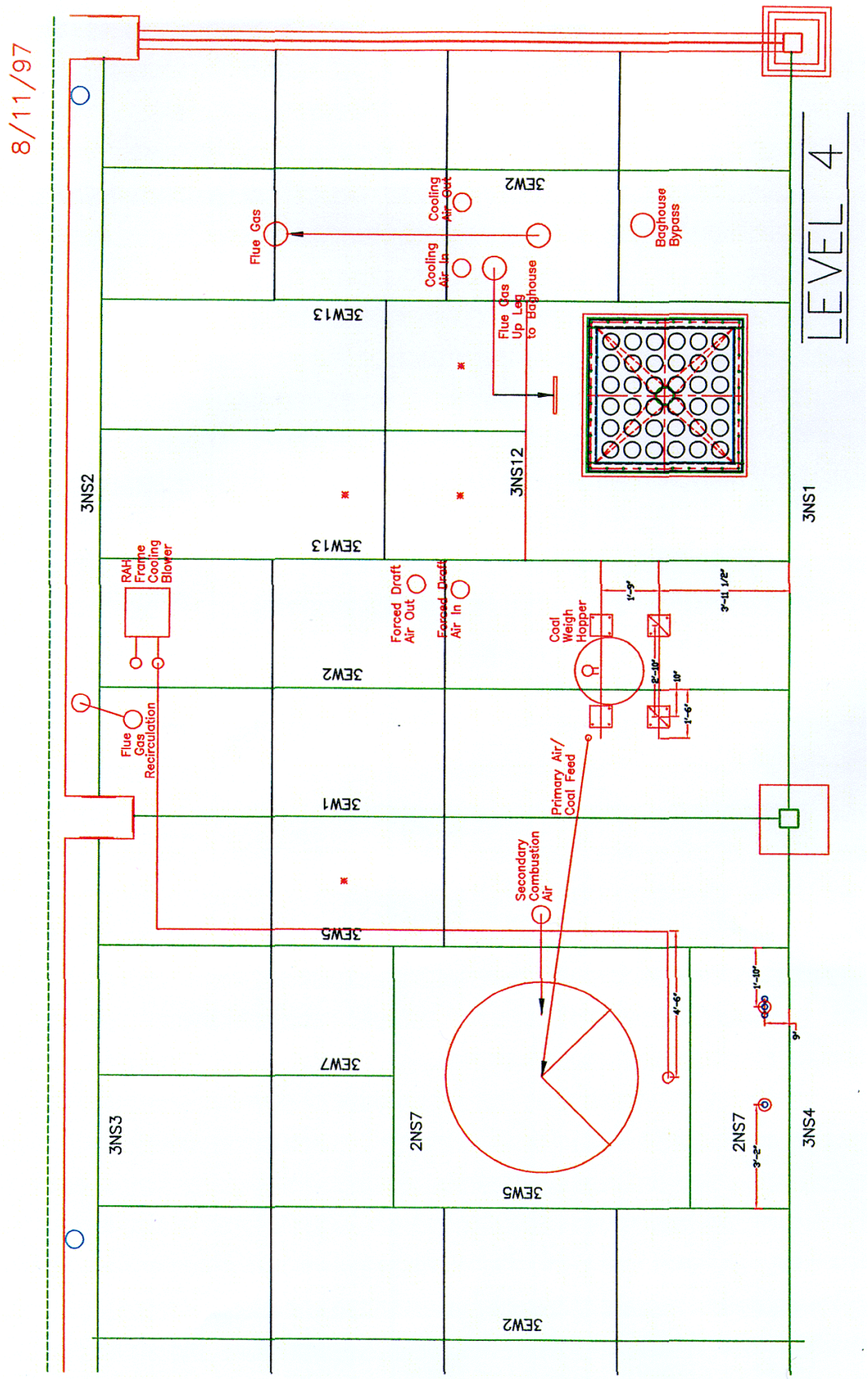
8/11/97
LEVEL 4
3EW2
Flue Gas
Cooling Air Out
Cooling Air In
Baghouse Bypass
Flue Gas Up Leg to Baghouse
3EW13
3NS12
3NS2
3NS1
RAH Frame Cooling Blower
Forced Draft Air Out
Forced Draft Air In
Coal Weigh Hopper
Flue Gas Recirculation
3EW1
Primary Air/ Coal Feed
Secondary Combustion Air
3EW5
3EW7
3NS3
2NS7
3NS4

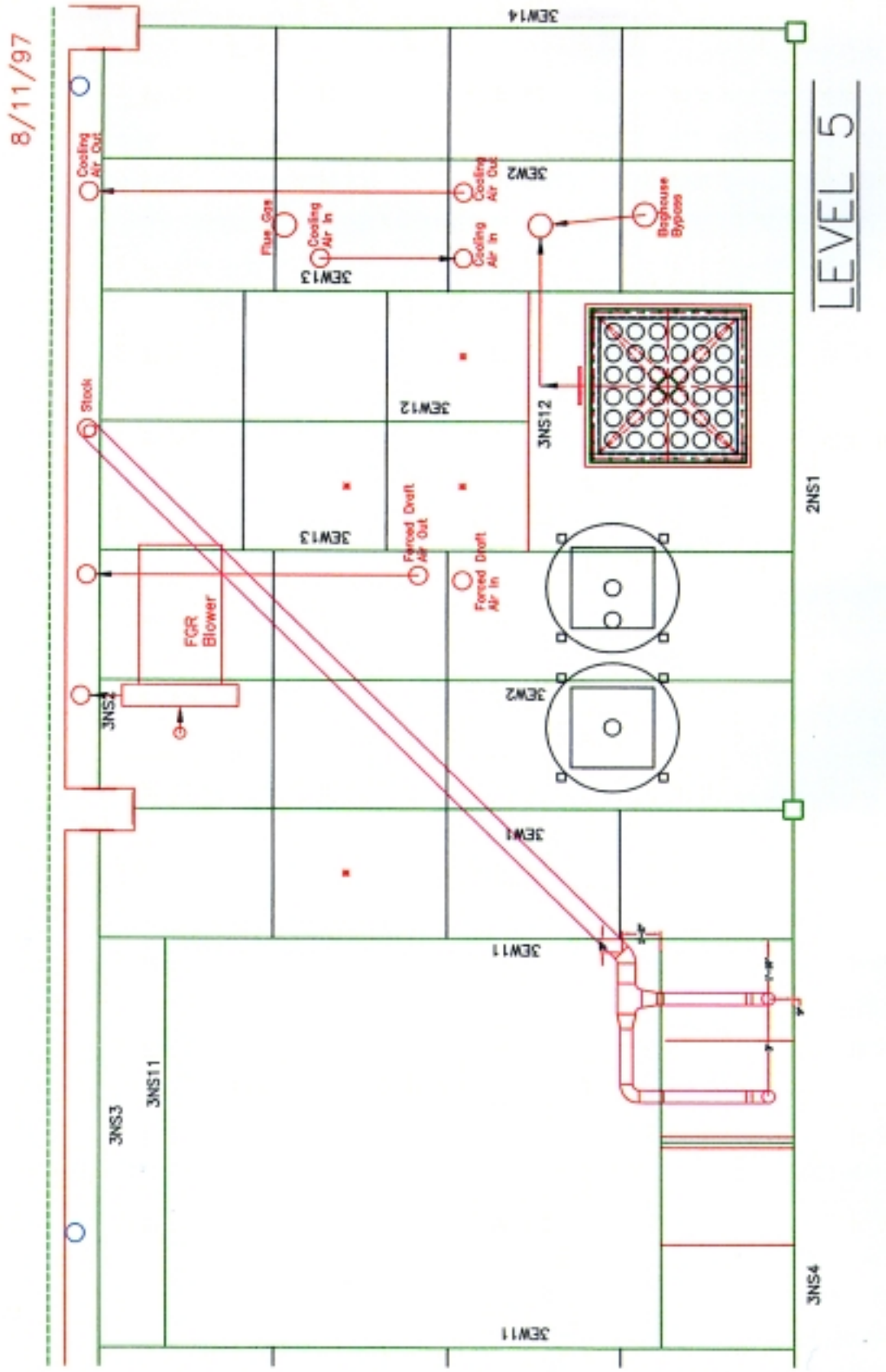
8/11/97
LEVEL 5
3EW14
3EW2
3EW13
3EW12
3EW1
3EW11
Cooling Air Out
Cooling Air In
Flue Gas
Baghouse Bypass
Stack
3NS12
2NS1
Forced Draft Air Out
Forced Draft Air In
FGR Blower
3NS2
3NS3
3NS11
3NS4

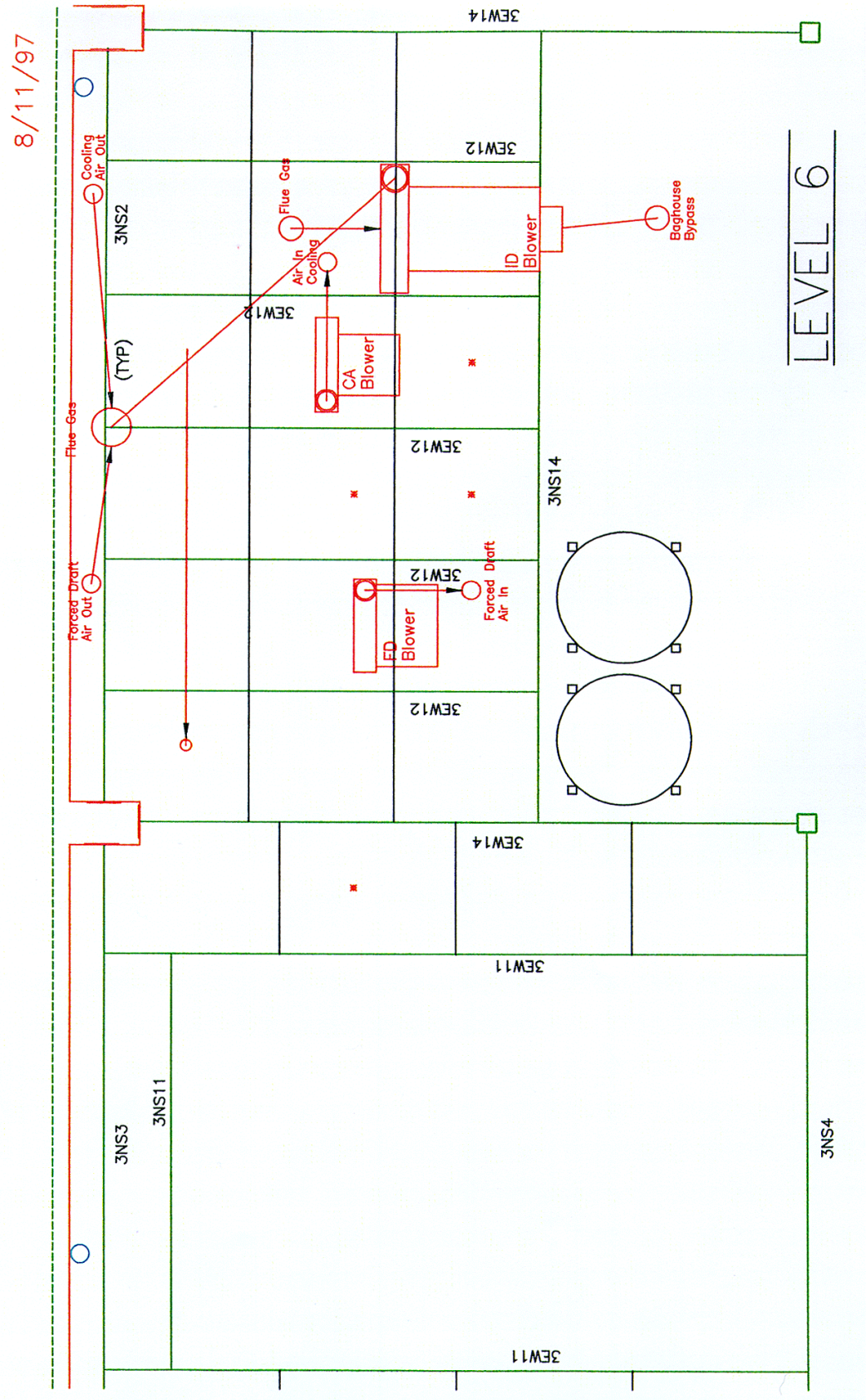
8/11/97
LEVEL 6
3EW14
3EW12
3EW12
3EW12
3EW12
3EW14
3EW11
3EW11
3NS2
3NS14
3NS3
3NS11
3NS4
Cooling Air Out
Flue Gas
Air In Cooling
ID Blower
Baghouse Bypass
(TYP)
CA Blower
Flue Gas
Forced Draft Air Out
Forced Draft Air In
FD Blower

Addendum C - SFS Operating Procedures
(Appendix A)

Slagging Furnace System (SFS) Start-Up Procedure

Pressurization of instrument air lines

1) Hand valves (V678, V679) to HP-HT manifold below roots meters and the main HP-air trunk line (V660) should be closed.

2) If not already running, start the Atlas-Copco compressor (SW comer of compressor building) by following the specific instructions attached to the compressor panel.

3) SLOWLY crack HV V608 to house N2 in front of air pressure regulator on 2nd floor. If the pressure gage does not show any pressure, valve V609 may be stuck in closed position. If this is the case, the valve has to be opened manually by applying compressed air to the bottom of the actuator. Close valve V608, manually open V609, then crack V608 to fill instrument air lines and tanks. The pressure gage above the Roots meters should read about 150 psig (10.34 bar) when the lines are full.

   NOTE: If the pressure gage already reads 100 psig (6.89 bar) then the hand valve (V660) to the air line is open and the high-pressure air flow has not been diverted and/ or the wrong compressor is running. If the pressure gage reads 165 psig (11.38 bar), then the air hand valve (V660) is probably open in addition to the nitrogen valves.

   If the hand valve to the high-pressure air is open, temporarily close this valve to verify that the nitrogen regulator is adjusted to 150 psig (10.34 bar)! Be sure to open it again after performing nitrogen pressure check, to ensure the availability of instrument air for valve operation.

Valve Cycling

The data acquisition system is downloaded with the proper start-up default values, however the actual positions of the double-acting solenoid valves are not reliable until they are cycled once. If the valve is actuated without a noticeable sound of air release, then the valve was not in the proper position. In any case, the start-up positions of the DeZurik valves should be visually verified prior to any further action.

This is best accomplished using the ‘MANUAL" screen selection from the main CONTROL screen.

Switch all of the valves listed below from "A" to "M" and fully cycle each valve.

NOTE: BE SURE TO LEAVE VALVES IN “AUTO” WHEN COMPLETE. The PID controls will not function in MANUAL mode.

Upper Baghouse (V515)

Lower Baghouse (V513)

FGR Control Valve (V420)

Primary Burner SCA (V120)

Primary Bumer SCA Bypass (V106)

Cyclone Inlet Control Valve (V514)

All control valves on HT-HP HX systems: V611, V613, V615, V631, V633, V648, V628

At this time prepare flue gas loop of the combustor for operation by verifying the following on the "Control" screen:

- Baghouse Bypass PID is in Manual Mode, and valve position is 100% (visually inspect to verify valve is open).
- Upper and Lower Baghouse Valves are closed (V515, V513).
- High-pressure pilot-air (V151), HP nitrogen (V609), and HP air (V651) are in Manual mode and in open position.
- FD and FGR fans are in Manual mode.
- System dP PID is in Auto mode and set to -0.50 in (-1.27 cm) H_20 as the set point.
- BH inlet temp, Main SCA, and Quench temperature are all in Manual mode.

Main and Auxiliary Natural Gas Burners

1) Open high-pressure air valve V661 from control screen.
2) *If not already open, slowly open compressed air HV (V660) feeding SFS bay. This valve is for the HP-HT-HX circuit and instrument air (under 2nd floor grating, East wall, South control room door). This valve can be accessed through 2nd floor grating access panel. The pressure should rise to about 165 psig (11.38 bar).*

   NOTE: In addition to the natural gas piping, there are 3 other safety interlocks that need to be satisfied before the burners can light: 1) FD fan is running, 2) the ID fan is running, and 3) the primary air is flowing to each burner.

3) Set FD fan to 40% of capacity on Control screen. After the fan has reached this speed, enter a set-point of 200 scfm for the Main Burner SCA and WAIT for the flow to reach the set-point, and for the ID fan to catch-up to the flow, i.e., return system dP (dPT411) back to -0.5 cm (-1.27 cm) H20.
4) Adjust the Main Burner PCA to 70 scfm on the control screen and wait for system to equilibrate. Likewise, adjust the Aux. Burner SCA to 40 scfm (1.133 m^3/m) on the control screen.
5) On 3rd Floor, adjust the Auxiliary Burner PCA rotameter to 400 scfh (11.33 m^3/h), and the Main Burner Pilot-Air to 400 scfh (11.33 m^3/h). Enter the Aux. PCA value in the area provided on the Control screen.
6) Set both burners to minimum swirl position, i.e. fully clockwise.
7) The natural gas pilot rotometers need to be adjusted to the following positions:

   Aux. Burner: open 2 full turns (note: this will be off scale when running. This is OK, after a flame is established the meter can be adjusted back to 50 scfh (1.416 m^3/h) if desired).

Main Burner: open approximately 1-1/4 turn to get 75 scfh (2.124 m^3/h).

8) At this point both burners should be ready to ignite. If all interlocks have been satisfied, a white light will illuminate when the flame safety control is placed in the start position. Quickly turn each flame safety on/off switch to the "on" and "off"' position to verify that the interlocks are satisfied.

9) Aux. Burner: Turn flame safety switch ON Main Burner: Turn flame safety switch ON (note: while burner tries to ignite, there is a 3 second interval in which adjustments can be made to the main burner natural gas rotameter).

Slag Tap Natural-Gas Burners

1) The slag-tap burners use thermal ignition for starting. The temperature for natural-gas auto-ignition is over 1400 °F (760 °C). To attain this temperature, the main furnace has to be heated to the operating temperature. The drawdown gas valve (V568) should be operated at 100% open during the furnace heatup period.

3) Adjust the south burner air rotameter to 400 scfh (11.33 m^3/h) (right-hand side of the 2nd floor panel). Safety interlocks for the air and natural gas system are built into the South slag-tap burner. Try to ignite this burner first before proceeding to the North slag-tap burner.

4) If the interlocks have been satisfied, a white light will illuminate when the flame safety control is placed in the start position. Quickly turn each flame safety on/off switch to the "ON" and "OFF" position to verify that the interlocks are satisfied.

5) When the flame safety system starts the "flame check" slowly open the natural gas rotameter to approximately 40 scfh (1.133 m^3/m). This is a trial and error procedure to establish the correct fuel air mixture. When a stable flame is established the North slag-tap burner can be ignited.

6) After the refractory and slag-tap area temperature has reached 2000 °F (1093 °C), check the flue gas analyzers for carbon monoxide and adjust the fuel/air ratio accordingly.

Heating the Furnace

During the heating process, the temperature entering the slag screen should be maintained at the same temperature as the upper furnace to minimize the temperature gradient across the LRAH and furnace walls. The furnace is heated to operating temperature using natural gas only. The maximum heating rate allowable by the refractory, slag screen tubes, and the LRAH panel must follow this schedule:

Ambient to 300 °F (149 °C): Immediate

300–Maximum: 150 °F/hr (66 °C/hr)

Primary Burner

The primary burner is difficult to operate at such low firing conditions. Initially the pilot burner can be used to achieve the 300 °F (149 °C) starting temperature. In order to achieve the specified temperature ramp with the Primary burner, the natural gas needs to be bled into the primary air line. This gas does not burn efficiently, and is too lean to support a primary burner flame. The primary burner can be operated in automatic mode down to 100 scfh (2.83 m^3/h).

Auxiliary Burner

These rates can be easily achieved using the pilot-gas rotameter for the auxiliary burner in conjunction with the control valve operated from the "Control" computer screen. This burner can be operated in automatic mode after the full range of the pilot rotameter is exhausted. When switching to automatic mode the rotameter may need to be turned off temporarily to achieve the lower temperatures.

Both burners are more easily ignited when the swirl is minimized; however, after the combustor is above the auto-ignition temperature of natural gas (1500 °F [816 °C]), increased swirl will improve combustion, especially with the auxiliary burner. In the case of the primary burner, do not increase the SCA flow rate until the stoichiometric air/fuel ratio is reached. The SCA tends to extinguish the pilot flame.

Coal Feed/Steady-State Operation

The coal feeder is very responsive and therefore reaches the feed rate set-point within 15 seconds. If the coal feed screws and feed factor have not changed since the last run, the easiest way to transition from gas to coal is just turn off the gas to the primary burner by entering zero for the primary burner natural gas flow rate. Prior to doing this, a coal feed rate should be calculated based on the Btu content of the fuel to supply about 80% of the natural gas heating rate. Set the primary burner swirl at 25% (minimum) for all bituminous and subbituminous coals and lignite. Additional swirl adjustments should be made based on EOS directions. At the time of transition, turn on coal feed and wait for the first sign of temperature increase in the furnace temperature. Quickly turn off gas supply and watch temperature closely. Fine adjustments can be made to the coal feed to return the temperature to specification. Turn off the primary burner flame-safety system to prevent accidental natural gas ignition, and turn off the pilot rotometer.

If the screws or feed factor have been changed since the previous run, it is best to transition to coal feed gradually. Do this by decreasing the natural gas feed rate and increasing the coal feed rate by equivalent percentages; for example, start by reducing the natural gas feed rate to 80% and start coal feed at 20% of the full load rate. This prevents serious temperature fluctuations while the coal feeder adjusts to the new parameters. As the coal feed rate stabilizes at the setpoint, make the next adjustment to both natural gas and coal feed rates. When the coal feed rate stabilizes right away following an adjustment, it is safe to go to 100 % coal feed.

Additional Procedures

Additional procedures pertaining to specific test equipment (LRAH, SRAH, CAH, slag probe) can be found in the Experimental Operating Specification (EOS). The limits concerning flows, pressures, and temperatures contained in the EOS takes precedence over any procedures outlined in this text.

Slagging Furnace System (SFS) Shut-Down Procedures

The most important aspect of the furnace shut-down is the rate of cooling. This is best accomplished using natural gas, although coal feed could be used. The maximum cooling rate allowable by the refractory, slag screen tubes, and the LRAH panel must follow this schedule:

Maximum–300 °F: 150 °F/hr (149 °C: 66 °C/hr)

The shut-down procedure assumes that the furnace is first transitioned back to natural gas using the following procedure:

1) Check function of primary burner pilot 1 to 2 hours before discontinuing coal feed.
2) Open rotameter supplying gas to the Primary pilot burner 1-1/4 turns.
3) Adjust primary burner pilot-air rotameter to 400 scfh (11.33 m^3/h).
4) Toggle Primary burner flame safety system switch to ON position to determine if all interlocks are satisfied THEN immediately turn OFF.
5) Check the control screen to be sure that the primary natural gas flow rate setting is set to zero.
6) Go to "energy" screen and check the total heat input from the coal source. The equivalent gas feed rate is approximately this value divided by 1000, i.e., 2,000,000 Btu/hr = 2000 scfh (2,110,112 kJ/hr = 56.63 m^3/h) gas flow.
7) Turn on primary burner flame safety system and wait for pilot burner to light. If the burner ignites (indicated by lights on flame safety panel), turn off coal feed and type in equivalent gas feed rate. Additional adjustments can be made by observing the relative change in furnace temperature. NOTE: Because the coal flame can obscure to UV detector, the coal feed may have to be terminated before the pilot flame will ignite. In this case, simply turn on the flame safety system and allow the unit to cycle (one attempted start/ 30 seconds); if the flame does not start, turn off coal feed and let the system continue to cycle. If the flame still does not ignite, go back to coal feed and start trouble shooting the flame safety system (closed valves, improper flows, electrical failures, etc.). After a gas flame is established, immediately reduce swirl to the main burner to minimum (full clockwise position).
8) After 30 minutes of gas firing to remove acid gases and residual particulate, bypass baghouse SLOWLY by first opening bypass valve to cyclone in 10% increments. After each increment, wait for ID fan to reestablish pressure set-point (dP411). When valve is fully open, close both baghouse knife valves (V513, V515) from control screen starting with the upper (exit) valve (V515) first. Turn baghouse heaters off.
9) When slag flow stops, turn off slag tap burner flame safety system and natural gas and air rotometers.
10) Slowly ramp down temperature according to the above cooling schedule. As furnace temperature drops, ramp down convective air heater set point in 50 °F (10 °C) increments to maintain a 100 scfm (2.83 m^3/m)quench flow. (Note: Failure to change the quench set point can cause the PID to shut off the flow to the quench zone. To prevent this, the PID control can be put in manual mode). At a temperature below 1500 ° F (816 °C), the natural gas can be turned off completely and the primary and auxiliary burner air rates can be reduced to minimal values to keep burners cool. Suggested values are given below:

    Primary Burner: PCA = 20 scfm (0.57 m^3/m) SCA = 50 scfm (1.42 m^3/m)

    Auxiliary Burner: PCA = 400 scfh (11.33 m^3/h) SCA = 10 scfm (0.28 m^3/m)

11) Reduce FD and FGR fan speeds to 30% or as required to maintain flows.

12) Put quench temperature PID (V420) into manual mode and set valve position percentage to allow 50 scfm (1.42 m^3/m) flow into the quench zone.

13) Reduce total flow through the high-pressure loop to a minimum (30-50 scfm [0.49-1.42 m^3/m]). This can be accomplished by placing the 5 inlet valves into manual (V611, V613, V615, V631, V633) and reducing the valve percentages. Maintain small flow rates (5-10 scfm [0.14-0.28 m^3/m]) through each of these valves. Flows through each valve can be verified by changes in the total flow through the Roots meters. Close back-pressure valve V628 and open LRAH flow valve V648 to minimize pressure and direct the flow solely through the LRAH panel.

14) When the LRAH pressure is reduced, switch from the Atlas-Copco compressor to house air.

Additional Procedures

Additional procedures pertaining to specific test equipment (LRAH, SRAH, CAH) can be found in the Experimental Operating Specification (EOS). The limits concerning flows, pressures, and temperatures contained in the EOS takes precedence over any procedures outlined in this text.

Emergency Procedures: Short Term Loss of Power

This scenario is for normal power return with generator.

The data acquisition system and main computer are equipped with uninterruptable power supplies (UPS) in the event of Center-wide power failure. Even though the back-up generator should be functional in less than a minute, several systems will still be affected. These include water pumps, air compressors, fans, and coal and natural gas feeds.

First Action: **Turn off coal feed and natural gas using red-colored switches on the control panel.** This will prevent an attempted restart by these systems. Even though these systems still could restart after 45 seconds, it is a waste of time since they are not sustainable until the main compressor is restarted and the fans are reset.

Second Action: Send operator to restart Atlas-Copco compressor.

Third Action: Check pressure gage above roots meter. If reading is steady at approximately 150 psig (10.34 bar), the nitrogen back-up system to the CAH/RAH loop is functioning properly. If the pressure is falling then open all valves prior to the nitrogen regulator (V608, V609) above south control room door.

Fourth Action: Switch cooling water system from pumps to City water if the pumps do not restart. Like the fans, the water pumps may need to be reset by toggling the control panel switch off then back on again.

Fifth Action: **Enter "zero" for all combustion air and natural gas flow rates to close these valves.** Reduce manual setting for FD and FGR fans to about 40%. If the fans do not restart on their own, reset fans by toggling each of the control panel switches on-off-on. If the fans still do not respond, the breakers for these fans may need to be reset or switched off-on. **NOTE: failure to zero-out flow rates could result in 100% open valves when trying to restart system!**

Sixth Action: Enter values for secondary combustion air flow rates and allow ID fan to catch up by returning system pressure back to set point. This should prevent the burners from overheating until the compressor is operating.

By this time the system should be safe and stable. The compressor should also be back on line. Check pressure gage above roots meter to see if pressure has returned to 165 psig (11.38 bar). In addition the FGR fan may need adjustment, and/or the quench zone set-point may need to be reduced.

Seventh Action: Set primary combustion air flow rates for restarting burners. **Turn ALL THREE flame safety systems off outside of control room on second floor.** Switch burner control switch on control panel to on position, and restart burners according to normal procedures.

Emergency Procedures: Permanent Loss of Power

This scenario is for a loss of power that outlasts the protection supplied by the UPS

If the generator does not retain power immediately, then the engineer must proceed on the assumption that total loss of control by the computer is inevitable. In this case, all valves will return to their fail-safe positions. Because of this circumstance, the high-pressure loop (CAH/RAH) should be stabilized while there is feedback from the data acquisition system. The fail safe positions for all of the pressure valves are wide open.

NOTE: The constant influx of alarms may make it difficult to operate the computer. Either use another computer (SIX), or terminate Alarm Worx program altogether on main computer by clicking on the "X" in the upper right-hand corner of the alarm screen.

First Action: **Turn off coal feed and gas red switches on the control panel.** This will prevent an attempted restart by these systems. Even though these systems still could restart after 45 seconds, it is a waste of time since they are not sustainable until the main compressor is restarted and the fans are reset.

Second Action: Check pressure gage above roots meter. If reading is steady at approximately 150 psig (10.34 bar), the nitrogen back-up system to the CAH/RAH loop is functioning properly. If the pressure is falling then open all valves prior to the nitrogen regulator (V608, V609) above south control room door.

Third Action: Switch cooling water system from pumps to City water.

Fourth Action: Close hand valves (V678, V679) to high-pressure manifold. Quickly open all five HP manifold inlet control valves (V611, V613, V615, V631, V633) in manual mode. The manifold hand valves should then be cracked to maintain a positive flow through the heat exchangers and RAH panel to maintain the MA tubes of the panel below maximum allowable temp (2000 °F (1093 °C) surface, 1700 °F (927 °C) bulk). When the pressure in the RAH inlet is reduced to its lowest level (gauge on control room south panel or "pressure" screen), open the back-pressure and RAH flow valves to 100% (V628, V648). Readjust flow through RAH by cracking hand valves to achieve allowable temperatures in the MA tubes. The system should now be ready for loss of data acquisition and control.

Fifth Action: With remaining time, bypass baghouse, set all natural gas, PCA, and SCA flows to zero. Close all natural gas trunk line hand valves (V210, V241, V211).

At this point there is very little that can be done to protect the remaining components. When power is restored, the first priority is to start FD, FGR, and ID fans to cool overheated stainless steel parts.

Sixth Action: Enter values for secondary combustion air flow rates and allow ID fan to catch up by returning system pressure back to set-point (dPT411, -0.50 in (-1.27 cm) H_2O). This should prevent the burners from overheating until the compressor is operating.

Seventh Action: If the problem resulting in loss of power is corrected, set primary combustion air flow rates for restarting burners. **Turn ALL THREE flame safety systems off outside of control room on second floor.** Switch burner control switch on control panel to on position, and restart burners according to normal procedures. Reset HT-HP cooling system based on normal operating procedures.

Emergency Procedures: Flex-Hose Failure

This scenario is for a high-pressure hose failure that requires a shutdown of the flow through the HT-HP heat exchangers. This can occur if the flex hose failure results in inadequate cooling of the MA tubes of the RAH panel.

First Action: Assess the failure as minor or catastrophic. From this point the procedure varies depending if the failure is a minor failure / small crack or a catastrophic failure / inadequate MA tube cooling.

Minor Failure/Small Crack

Second Action: If minor, reduce the pressure of the HP system as much as possible while maintaining adequate cooling to RAH MA tubes.

Third Action: Proceed with normal shutdown to reduce temperature in furnace. When temperature in furnace is below 2000 °F (1093 °C) and the RAH MA tube surface temperatures (RAHTC10, RAHTC16, RAHTC29) are below 2000 °F (1093 °C), depressurize high-pressure manifold by closing manifold hand valves (V678, V679) below roots meters.

Fourth Action: Replace failed flex-hose if parts are available and continue operation by ramping temperature to experimental operating specification (EOS), or proceed with shutdown.

Catastrophic Failure/ Inadequate MA Tube Cooling

Second Action: Reduce fuel feed, either gas or coal, by 30-50% on the Main burner only. This is intended to be a quick action without regard to a target drop in temperature of the furnace. This action can be delayed if the MA tube temperature rise is critical-- GO to next two steps and return to this later.

Third Action: Close hand valves (V678, V679) to high-pressure manifold below roots meters. Proceed to 4th floor and crack emergency bypass valve (V684) using handle hanging on valve body. When pressure is drained from system, open valve fully. Immediately open emergency back-flush valve (V685) located on 4th floor next to West hand rail (North, round wheel). Adjust this valve (V685) until adequate cooling of MA tubes is attained.

Fourth Action: Quickly open to 100% all five HP manifold inlet control valves (V611, V613, V615, V631, V633). The manifold hand valves (V678, V679) should then be cracked to maintain a small positive flow through the heat exchangers to prevent back -flow and overheating of the cold-side Teflon flex hoses. Close the back-pressure and RAH flow valves completely to avoid loss of cooling air (V628, V648). Readjust flow through RAH if necessary using emergency back-flush valve (V685) to achieve allowable temperatures in the MA tubes (2000 °F (1093 °C) surface, 1700 °F (927 °C) bulk air).

Fifth Action: Isolate area where flex hose failure occurred since a significant flow will still escape through the rupture point. **CAUTION**: the gas will be extremely hot and will be a burn/fire hazard.

Sixth Action: Proceed with normal shutdown to reduce temperature in furnace. When temperature in furnace is below 2000 °F (1093 °C) and the RAH MA tube temperatures (RAHTC10, RAHTC16, RAHTC29) are below 2000 °F (1093 °C), stop flow to through RAH panel and allow flex hose to cool.

Seventh Action: Replace failed flex-hose if parts are available and continue operation by ramping temperature to experimental operating specification (EOS), or proceed with shutdown procedure.

Addendum D - Example of Process Data
(Appendix A)

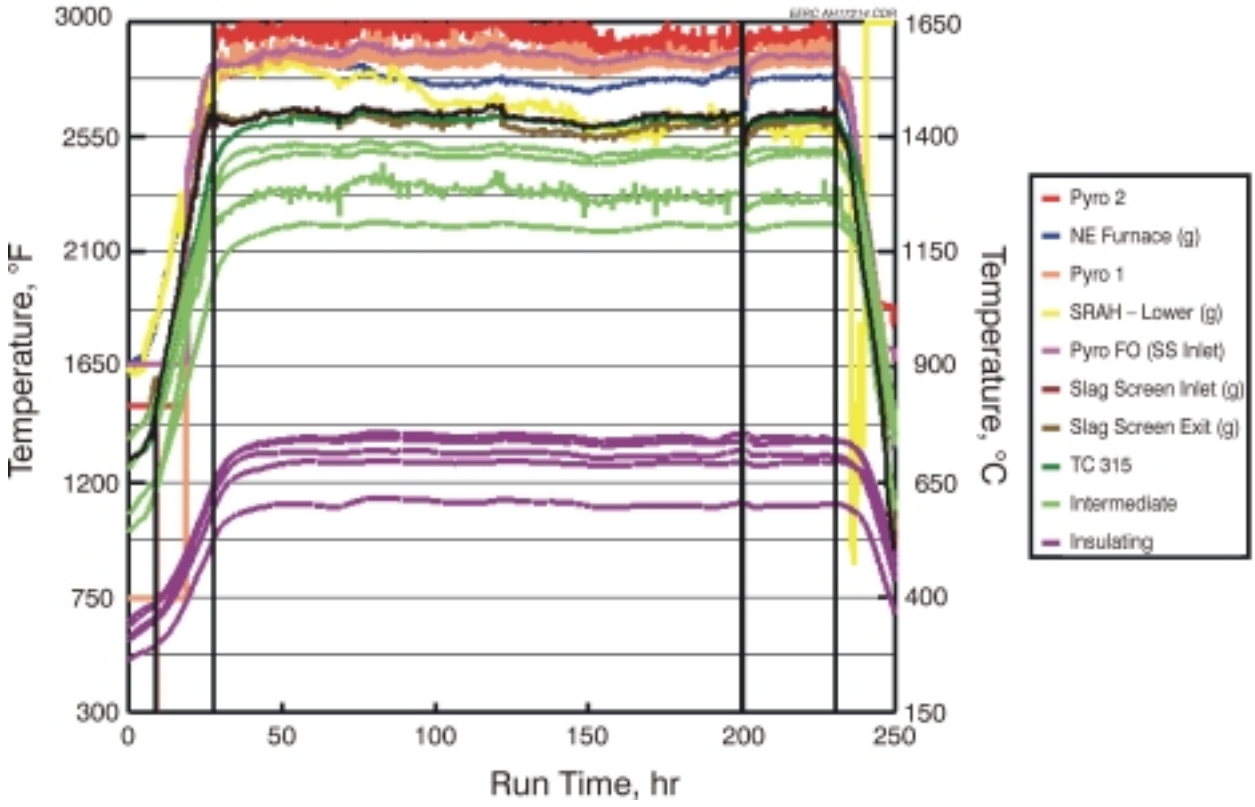

Furnace and Slag Screen Temperatures versus Run Time

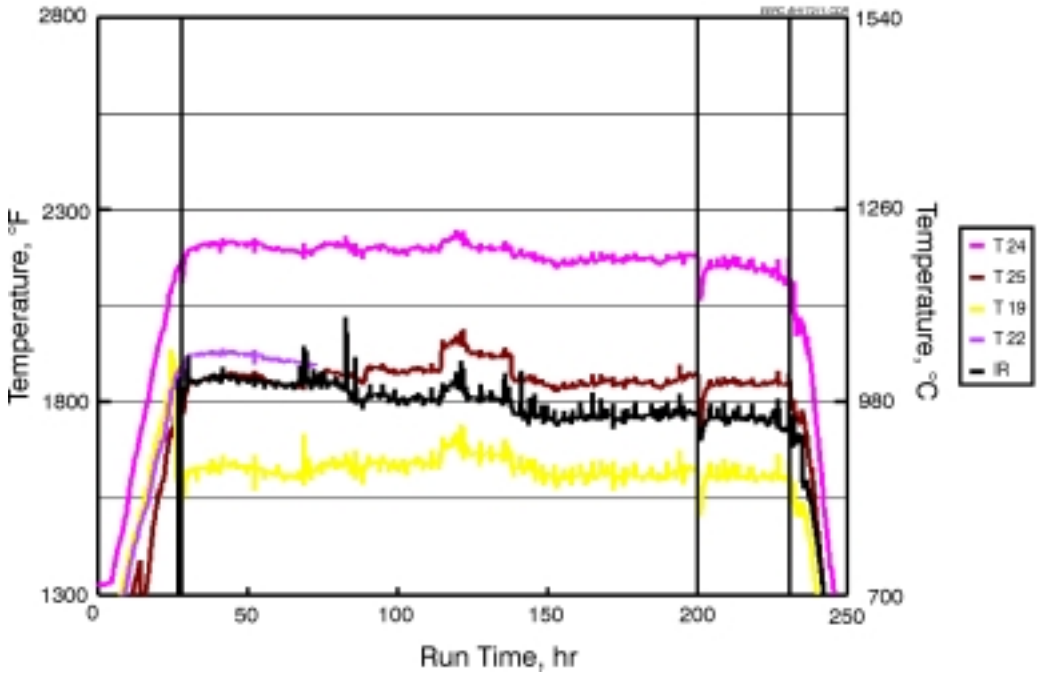

RAH Ceramic Tile Temperatures versus Run Time

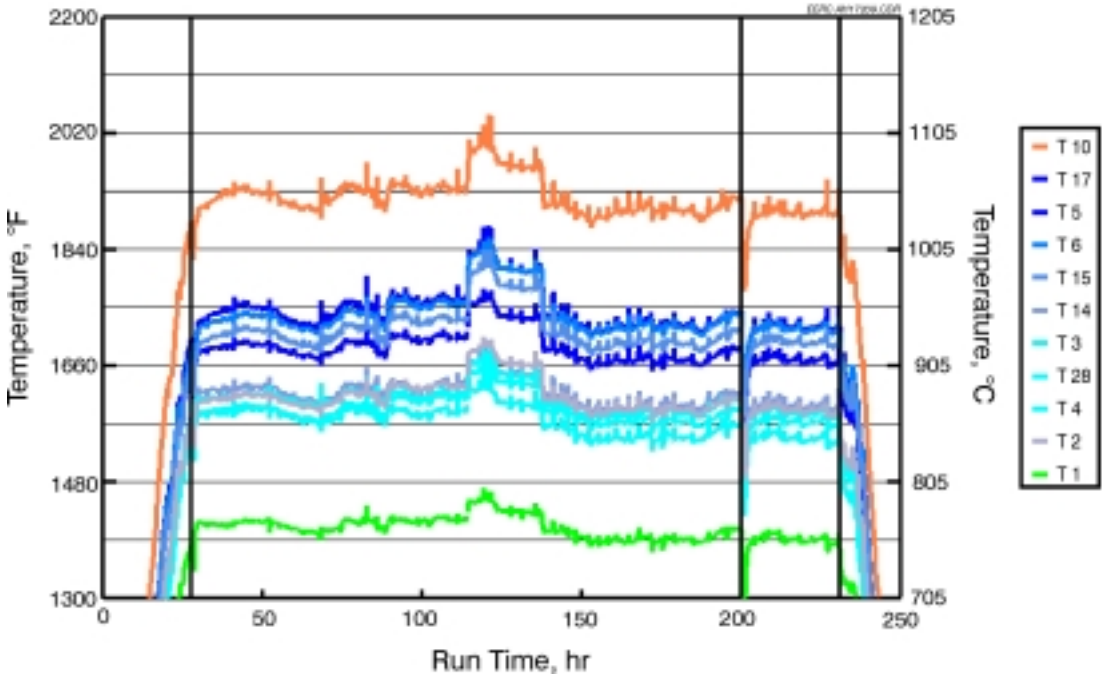

RAH Tube Surface Temperatures versus Run Time

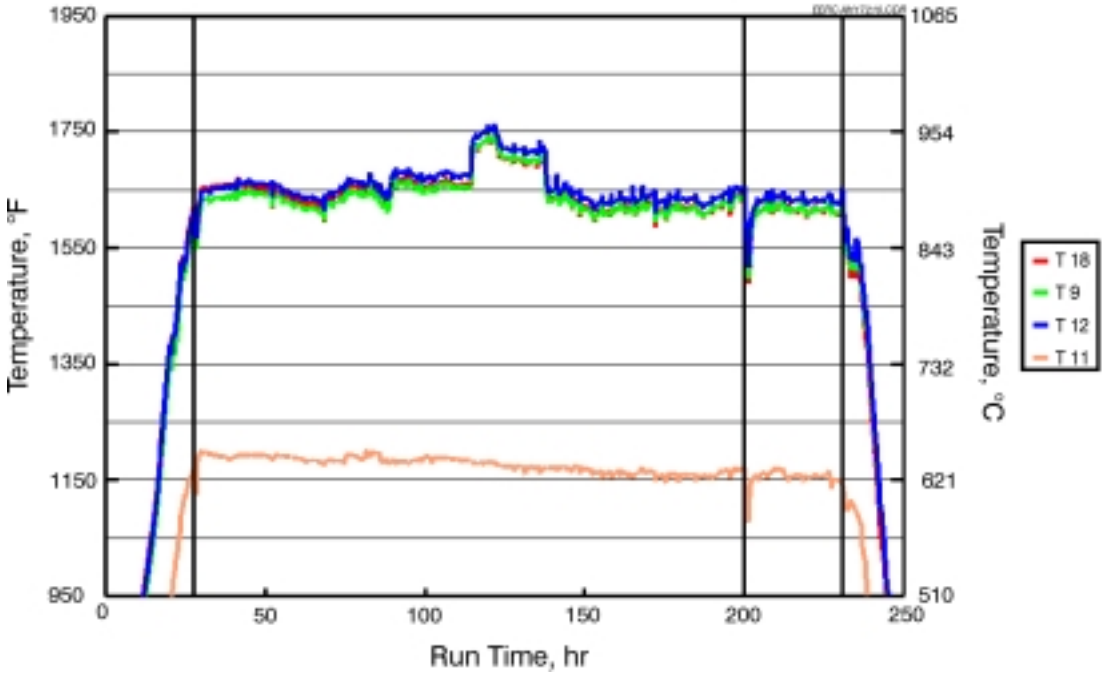

RAH Process Air Temperatures versus Run Time

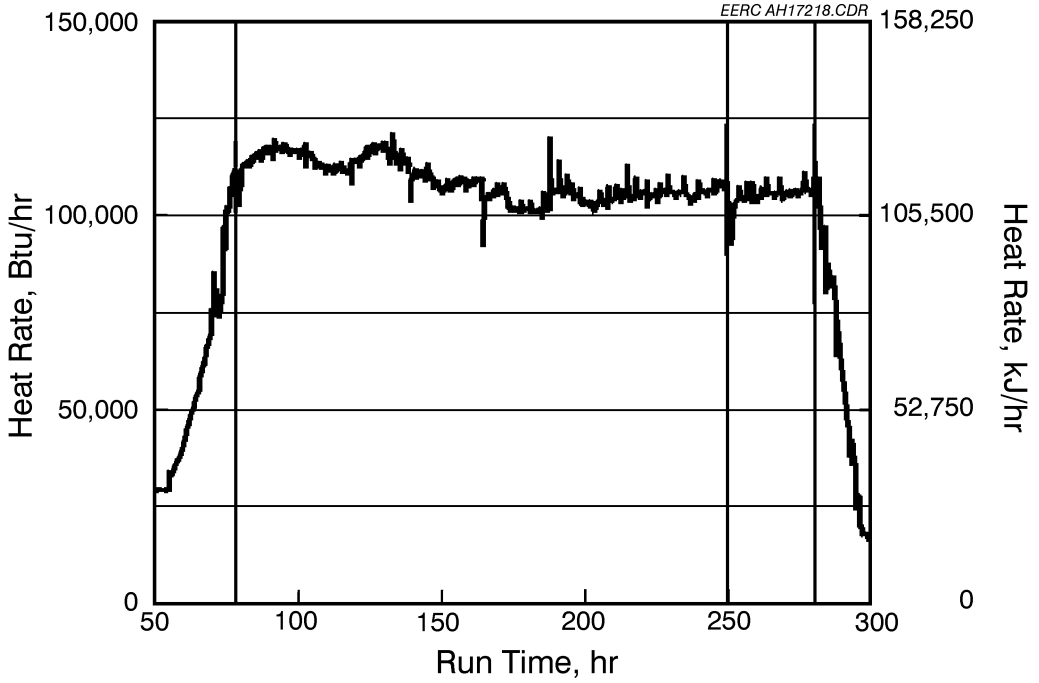

RAH Heat Recovery versus Run Time

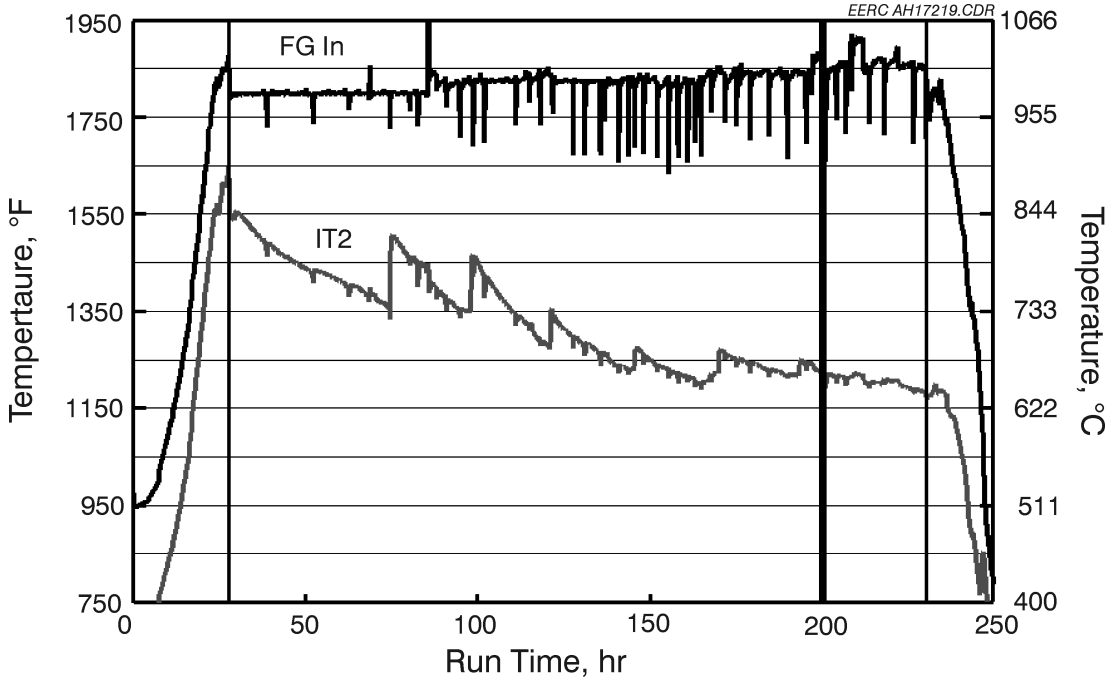

CAH Tube Surface and Flue Gas Temperatures versus Run Time

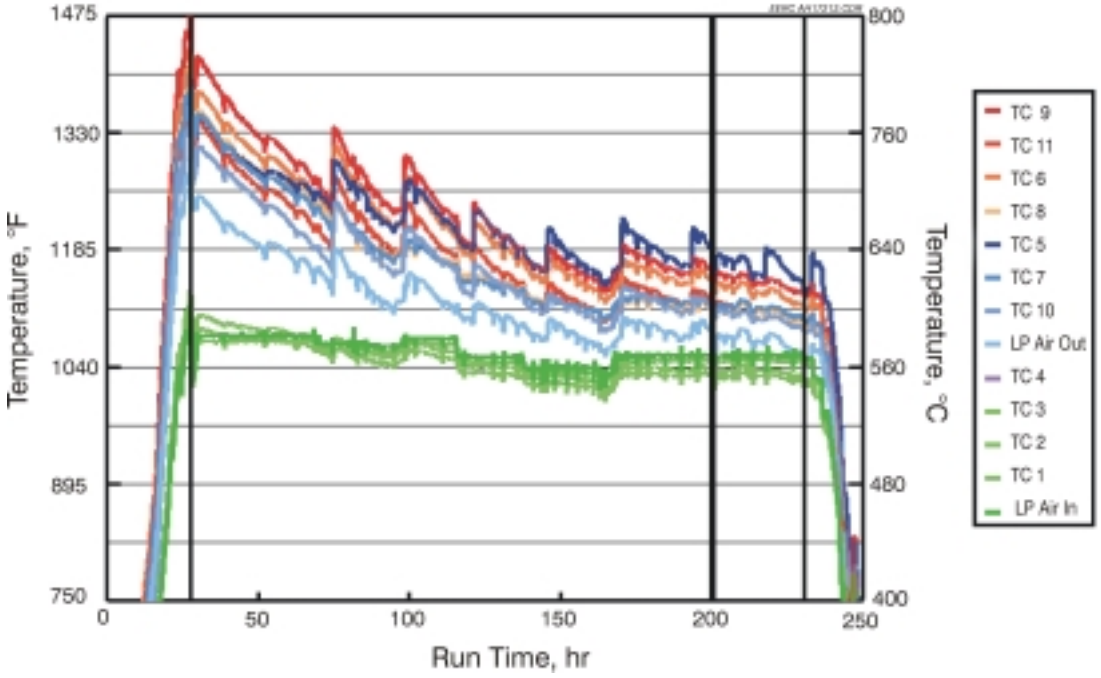

CAH Process Air Temperatures versus Run Time

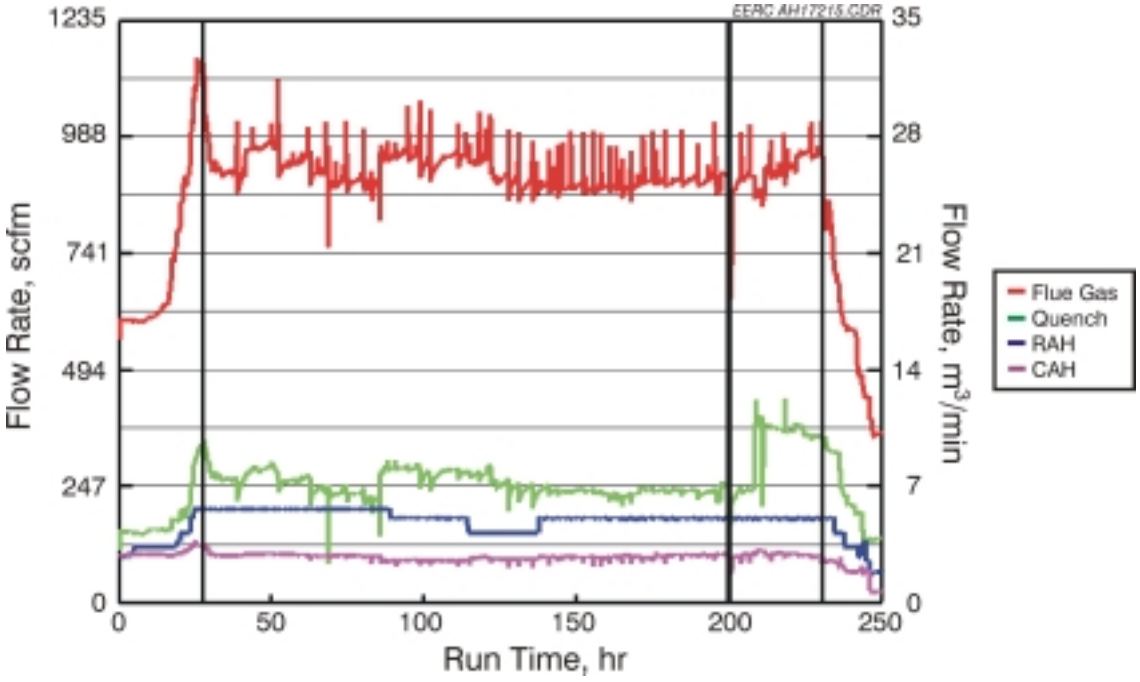

CAH Process Air, RAH Process Air, Quench Gas, and Flue Gas Flow Rates versus Run Time

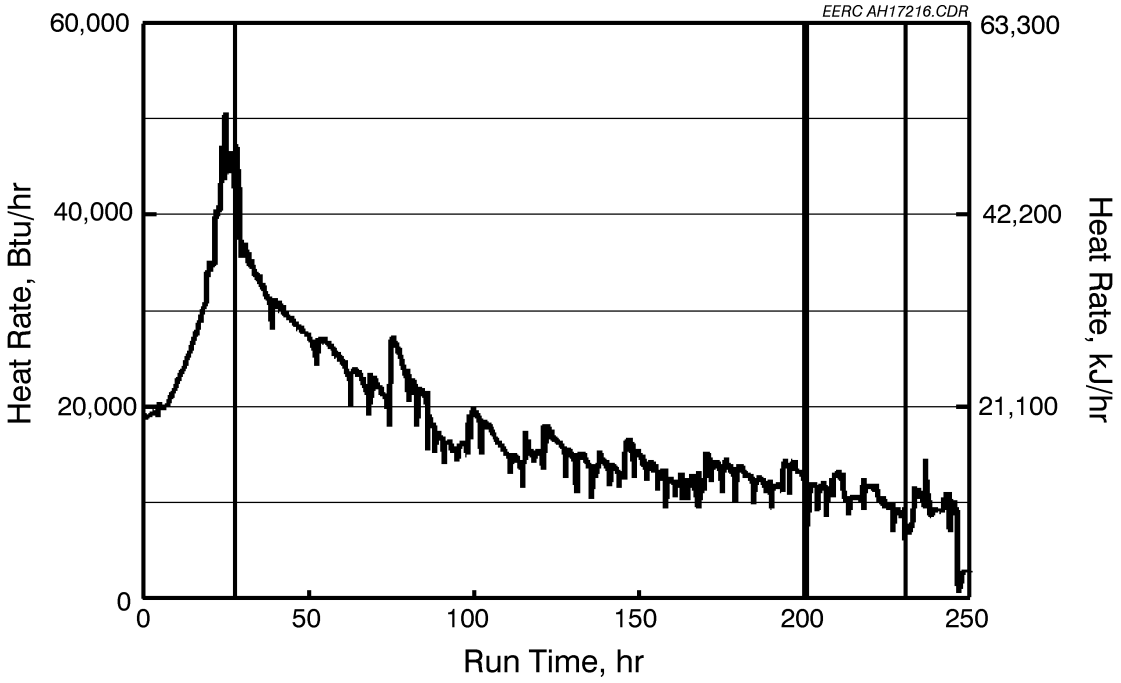

CAH Heat Recovery versus Run Time

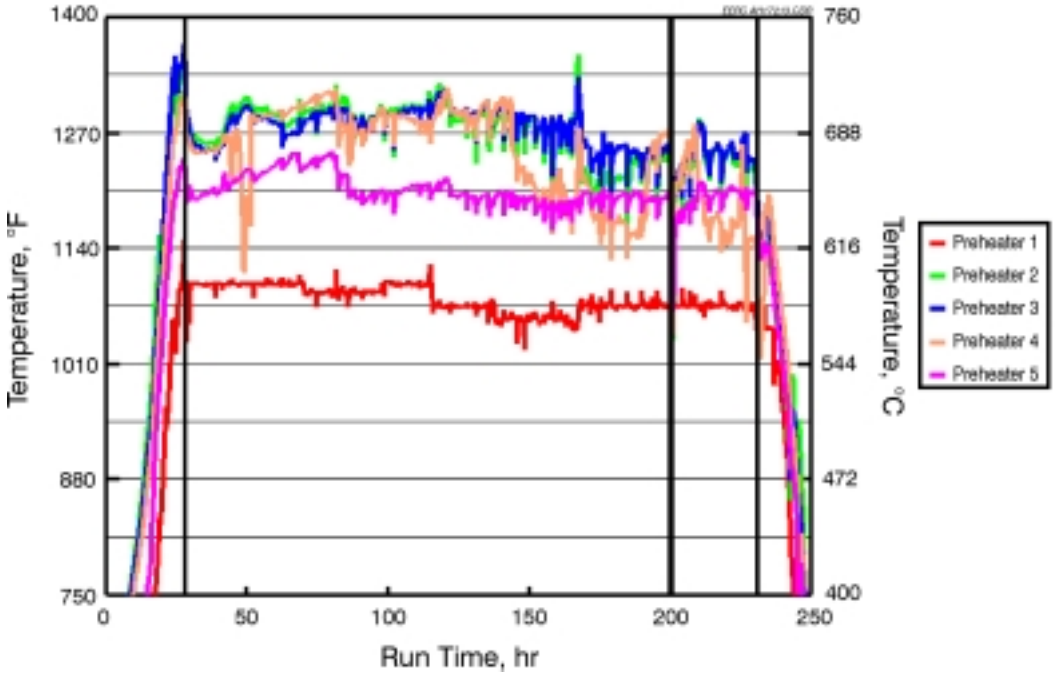

Process Air Preheater Temperatures versus Run Time

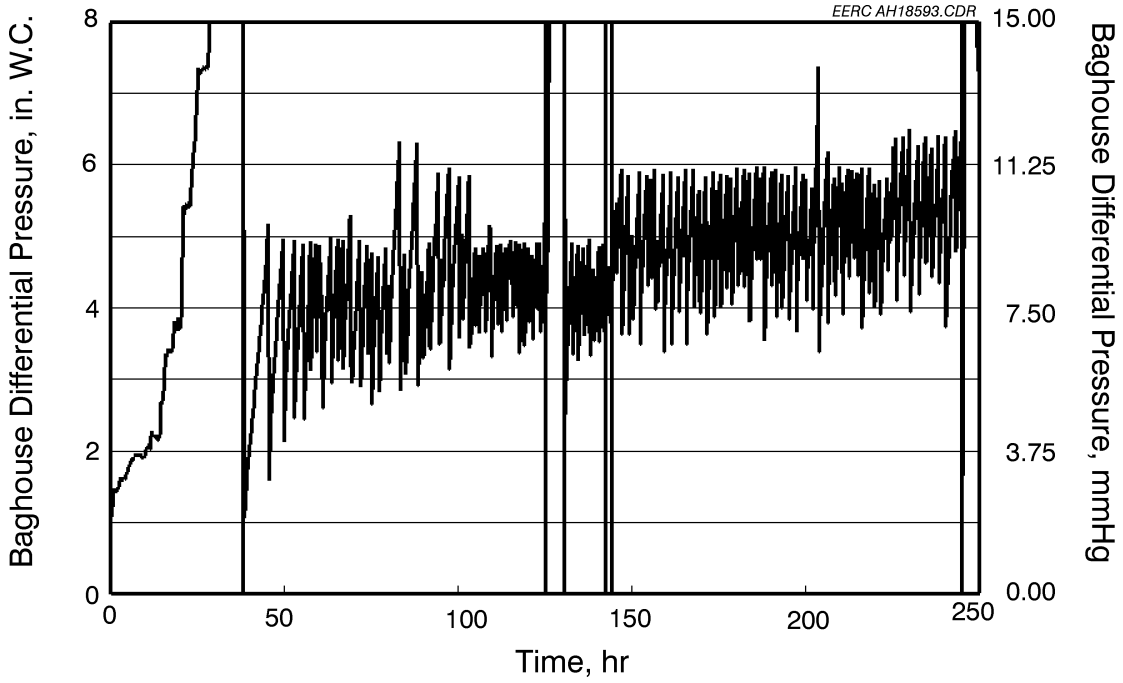

Baghouse Differential Pressure versus Run Time

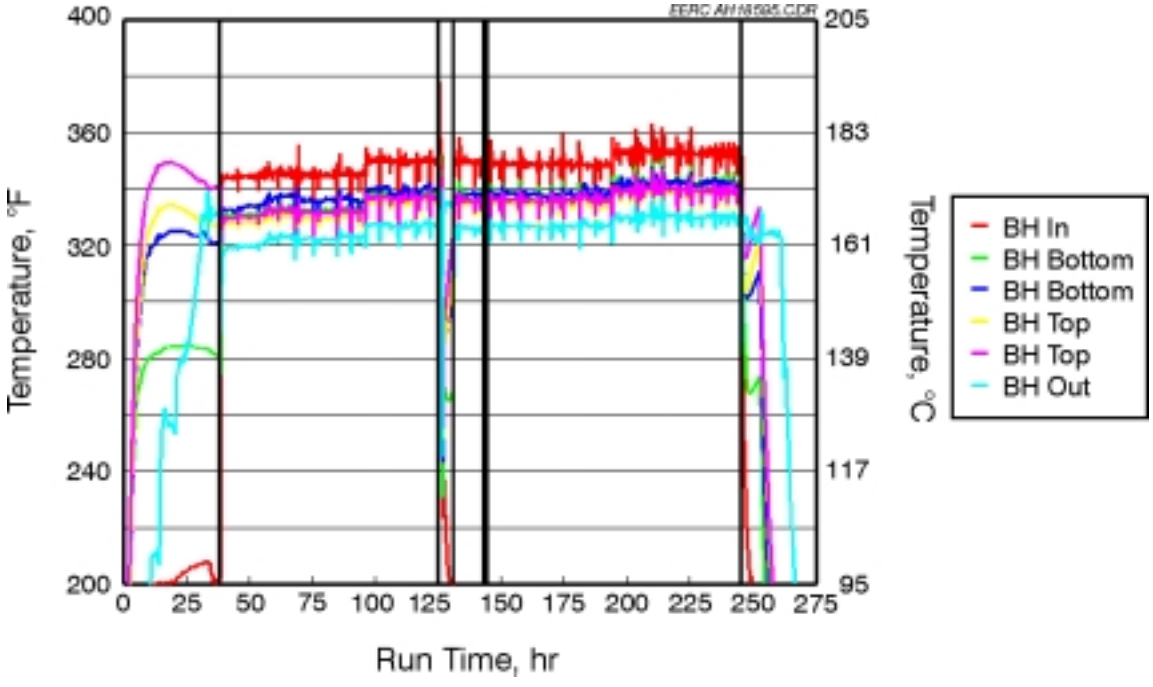

Baghouse Temperatures versus Run Time

Addendum E - Examples of System Data Sheets
(Appendix A)

C2000 DATA SHEET 1 - SYSTEM PRESSURES (Page 1 of 4)

Run No._____

Date								
Time								
Operator's Initials								

Magnehelics, left panel (All units in inches H_2O, unless otherwise noted)

Cooling Air Blower Static PI - 111								
HX 2 Air Inlet Static PI - 101								
Aux SCA Static PI - 165								
Main SCA Static PI - 125								
Main PCA Static (psig) PI - 135								
Main PCA dP dPI - 136								
Aux SCA dP dPI - 166								
Main SCA dP dPI - 126								
Combustor Static PI - 301								
Slag Pot Static PI - 341								
Slag Screen Static PI - 402								
CAH Inlet Static PI - 404								
CAH Exit Static PI - 406								

Page_____of_____

C2000 DATA SHEET 1 - SYSTEM PRESSURES (Page 2 of 4)

Run No._____

Date								
Clock Time								
Operator's Initials								

Flue Gas Pressures, left panel (inches H_2O)

Baghouse Static PI - 538								
Flue Gas Orifice Static PI - 545								
ID Fan Inlet Static PI - 557								
HTHPHX Sect 1 dP dPI - 521								
HTHPHX Sect 2 dP dPI - 522								
HTHPHX Sect 3 dP dPI - 523								
HTHPHX Sect 4 dP dPI - 524								
HTHPHX Sect 5 dP dPI - 525								

C2000 DATA SHEET 1 - SYSTEM PRESSURES (Page 3 of 4)

Run No._____

Date								
Clock Time								
Operator's Initials								

Baghouse Pulse Times, center panel (seconds)

BH Pulse Delay								
BH Pulse Duration								

Heat Trace Line Output Temperatures, center panel

Slag Screen								
Baghouse In								
Baghouse Out								

HTHP Air Heaters (Watlow), center panel

1								
2								
3								
4								

Baghouse Heaters, center panel

Baghouse S								
Baghouse W								
Baghouse N								
Baghouse E								
Baghouse B								

Page_____of_____

C2000 DATA SHEET 1 - SYSTEM PRESSURES (Page 4 of 4)

Run No._____

Date								
Clock Time								
Operator's Initials								

Flue Gas Pressures, right panel (inches H_2O)

S&T HX 1 dP dPI - 531								
S&T HX 2 dP dPI - 532								
S&T HX 3 dP dPI - 533								
S&T HX 4 dP dPI - 534								
Baghouse dP dPI - 536								
Cyclone dP dPI - 540								
FG Orifice dP dPI - 546								
Drawdown Orifice dP dPI - 566								
Drawdown Orifice Static dPI - 565								

Air Heater Pressures, right panel (psig)

Large RAH inlet static PI - 601								
CAH inlet static ** OUTSIDE **								
LRAH venturi static PI - 625								
Bypass venturi static PI - 645								

Page_____of_____

C2000 DATA SHEET 2 - WATER, AIR AND NATURAL GAS FLOW RATES (Page 5 of 3)

Run No._____

Date								
Time								
Operator's Initials								

Air Flow to Optical Pyrometers (scfh)

SR (FO)								
SA								
SR								

High Pressure and Drawdown Heat Exchangers - 3rd Floor, South panel (All values are in gpm.)

LRAH HX4								
LRAH HX3								
HP Bypass HX6								
Drawdown HX 2, 4								
Drawdown HX 1								
Drawdown Coils								

Combustor Heat Exchangers - 3rd Floor, North Panel (all values are gph unless otherwise indicated)

Section 1 Inside, gpm								
LRAH Coil, gpm								
LRAH HX N, gpm								
Sect. 1 Flange								
Sect. 1 Sight Ports								
Main Burner, gpm								
Slag Screen Floor								
Sect. 4 Flange								
Sect. 3 Flange								
Aux. Burner								
Sect. 2 Flange								
LRAH HX S, gpm								

Page_____of_____

C2000 DATA SHEET 2 - WATER, AIR AND NATURAL GAS FLOW RATES (Page 6 of 3)

Run No._____

Date								
Time								
Operator's Initials								

Aux Burner Flow Rate - 3rd Floor, North Panel (scfh)

Pilot Air								
Aux PCA								

Main Pilot Gas Flow - 3rd Floor Stairwell (scfh)

Main Pilot Gas								

Aux Pilot Gas Flow - 2nd Floor Stairwell (scfh)

Aux Pilot Gas								

Tap Burners - 2nd Floor (scfh)

Gas Flow, left								
Gas Flow, right								
Air Flow, left								
Air Flow, right								

Slag Screen Water Flow Rates - 2nd floor (from left to right)(gpm)

Slag Tubes 16 - 18								
Slag Tubes 13 - 15								
Slag Tubes 10 - 12								
Slag Tubes 7 - 9								
Slag Tubes 4 - 6								
Slag Tubes 1 - 3								
Quench Zone								
Sample Port, gph								

Page_____of_____

C2000 DATA SHEET 2 - WATER, AIR AND NATURAL GAS FLOW RATES (Page 7 of 3)

Run No._____

Date								
Time								
Operator's Initials								

NOTE: THESE VALUES ONLY NEED TO BE RECORDED ONCE PER SHIFT!

HX Water Flow Rates, 4th floor (gpm)

HTHPHX 6 (east)								
FD Bypass HX (west)								

Frame Cooling Blower Outlet Static, 4th Floor (inches H_2O)

Blower Static								

Elbow dP's, 5th floor (inches H_2O)

FD bypass (north)								
Cooling air (south)								

Condenser Water Flow Rates, 6th floor (gpm)

ID Fan (south)								
FD Fan (north)								

Page_____of_____

C2000 DATA SHEET 6 - COAL RECORD

Run No._____

COAL HOPPERS

Date	Clock Time Start	Clock Time Stop	Hopper Letter	Hopper Location	Gross Wt (lbs)	Tare Wt (lbs)	Net Wt (lbs)	Operator Initials

Page_____of_____

C2000 DATA SHEET 7 - ASH INVENTORY RECORD (Page 9 of 2)

Run No._____

BAGHOUSE ASH

Barrel No.	Test No.	Start			Stop			Gross (lbs)	Tare (lbs)	Net (lbs)
		Date	Time	Name	Date	Time	Name			

Page_____of_____

C2000 DATA SHEET 7 - ASH INVENTORY RECORD (Page 10 of 2)

Run No._____

CYCLONE ASH

Barrel No.	Test No.	Start			Stop			Gross (lbs)	Tare (lbs)	Net (lbs)
		Date	Time	Name	Date	Time	Name			

Page_____of_____

C2000 DATA SHEET 10 - FLUE GAS ANALYSIS

Run No._____

Date								
Clock Time								
Operator's Initials								

Analyzer Panel A (left-hand side)

O_2 (% of scale) Scale =								
CO_2 (% of scale) Scale =								
CO (% of scale) Scale =								
SO_2 (ppm) Scale =								
NO_x (ppm) Scale =								
Sample Location								

Analyzer Panel B (right side)

O_2, %								
CO_2, %								
CO, ppm								
SO_2, ppm								
NO_x, ppm								
Sample Location								

Page_____of_____

C2000 DATA SHEET 11 - SOLIDS INVENTORY RECORD

Run No._____

Location	Weight	Units	Operator's Initials
Slag Pot			
Slag tap			
Drawdown piping			
Quench zone bottom			
Quench zone sides			
N shell & tube heat exchanger			
S shell & tube heat exchanger			
shell & tube heat exchanger - top elbow			
shell & tube heat exchanger - bottom elbow			
High pressure heat exchanger			
Baghouse			
Cyclone			
CAH Duct			
CAH probe ash:			
Ceramic - front			
Ceramic - back			
Metal - front			
Metal - back			
Coal Leakage			

Page_____of_____

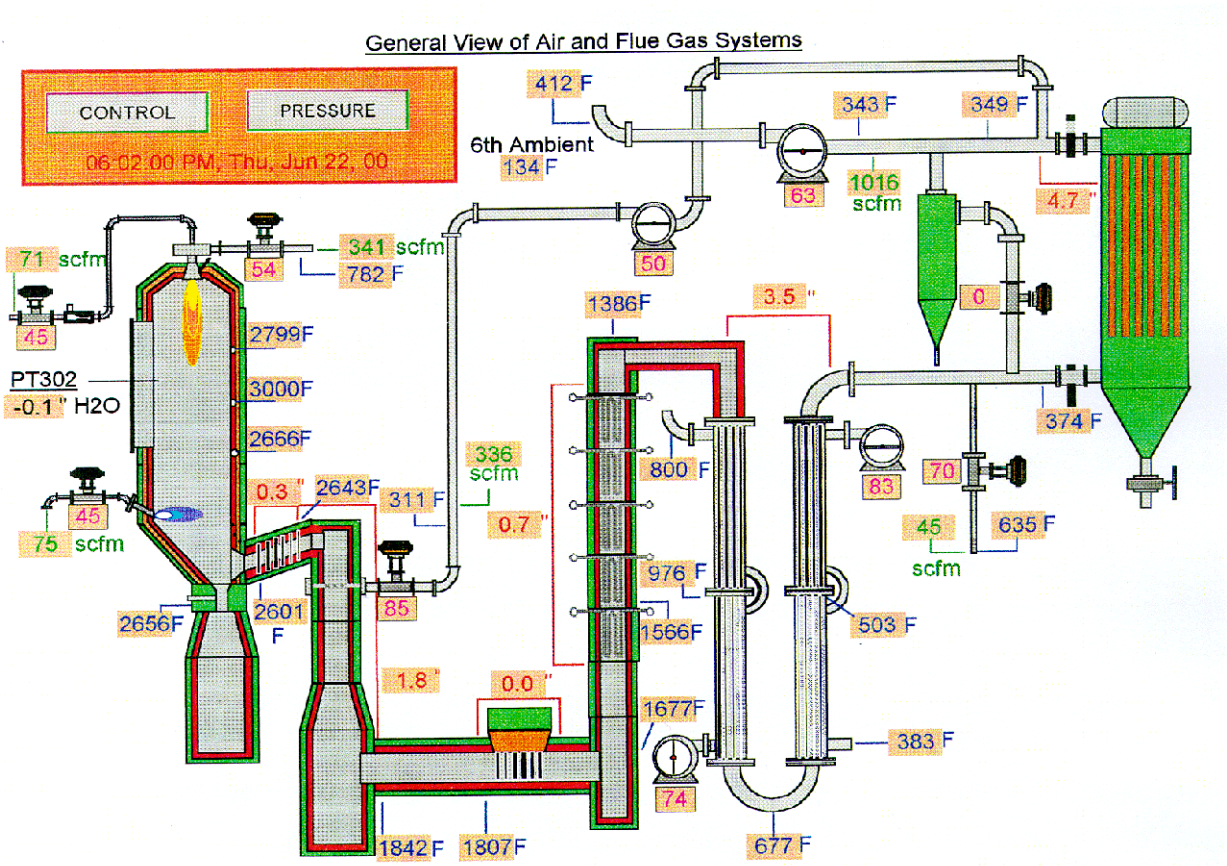
General View of Air and Flue Gas Systems
CONTROL
PRESSURE
06:02:00 PM, Thu, Jun 22, 00
412 F
6th Ambient
134 F
343 F
349 F
63
1016
scfm
4.7 "
50
71 scfm
45
54
341 scfm
782 F
PT302
-0.1 " H2O
2799F
3000F
2666F
0.3 "
2643F
311 F
336
scfm
0.7 "
45
75 scfm
2656F
2601
F
85
1386F
3.5 "
800 F
976 F
1566F
1.8 "
0.0 "
1677F
74
1842 F
1807F
677 F
503 F
383 F
0
374 F
70
83
45
scfm
635 F

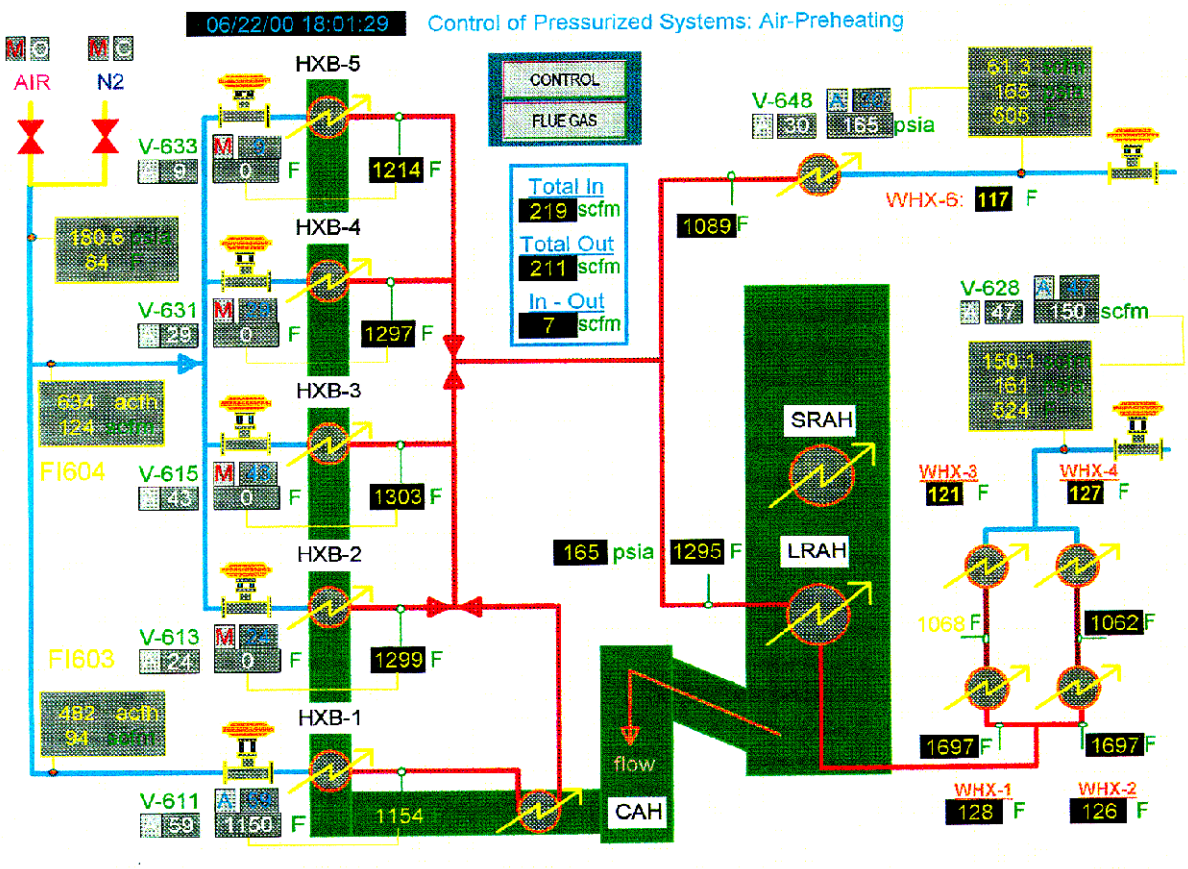
06/22/00 18:01:29
Control of Pressurized Systems: Air-Preheating
AIR
N2
HXB-5
HXB-4
HXB-3
HXB-2
HXB-1
V-633
V-631
V-615
V-613
V-611
FI604
FI603
CONTROL
FLUE GAS
Total In
219 scfm
Total Out
211 scfm
In - Out
7 scfm
1214 F
1297 F
1303 F
1299 F
1154 F
1089 F
V-648
30
165 psia
WHX-6: 117 F
V-628
47
150 scfm
SRAH
LRAH
165 psia
1295 F
WHX-3
121 F
WHX-4
127 F
1068 F
1062 F
1697 F
1697 F
WHX-1
128 F
WHX-2
126 F
flow
CAH

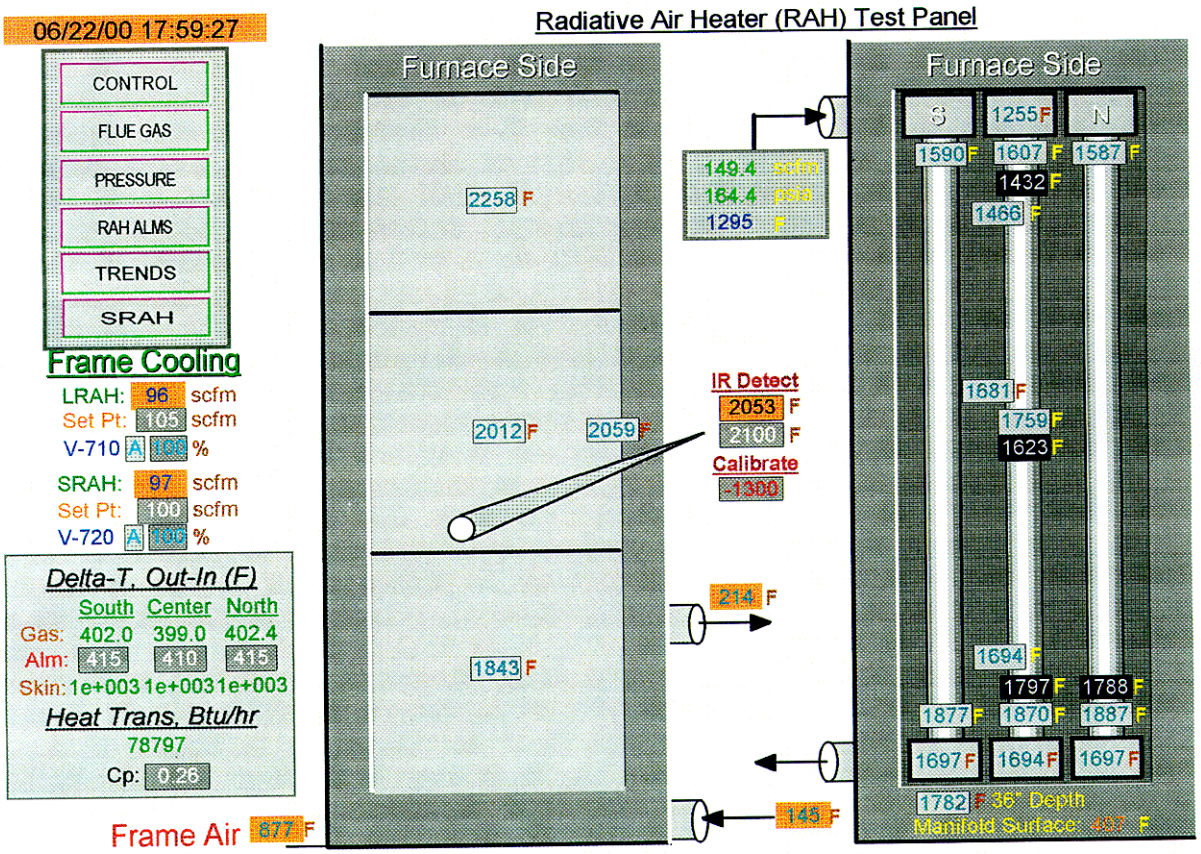
Radiative Air Heater (RAH) Test Panel
06/22/00 17:59:27
CONTROL
FLUE GAS
PRESSURE
RAH ALMS
TRENDS
SRAH
Frame Cooling
LRAH: 96 scfm
Set Pt: 105 scfm
V-710 A 100 %
SRAH: 97 scfm
Set Pt: 100 scfm
V-720 A 100 %
Delta-T, Out-In (F)
South Center North
Gas: 402.0 399.0 402.4
Alm: 415 410 415
Skin: 1e+003 1e+003 1e+003
Heat Trans, Btu/hr
78797
Cp: 0.26
Frame Air 877 F
Furnace Side
2258 F
2012 F
2059 F
1843 F
149.4 scfm
164.4 psig
1295 F
IR Detect
2053 F
2100 F
Calibrate
1300
214 F
145 F
Furnace Side
S
1255 F
N
1590 F
1607 F
1587 F
1432 F
1466 F
1681 F
1759 F
1623 F
1694 F
1797 F
1788 F
1877 F
1870 F
1887 F
1697 F
1694 F
1697 F
1782 F 36" Depth
Manifold Surface: 402 F

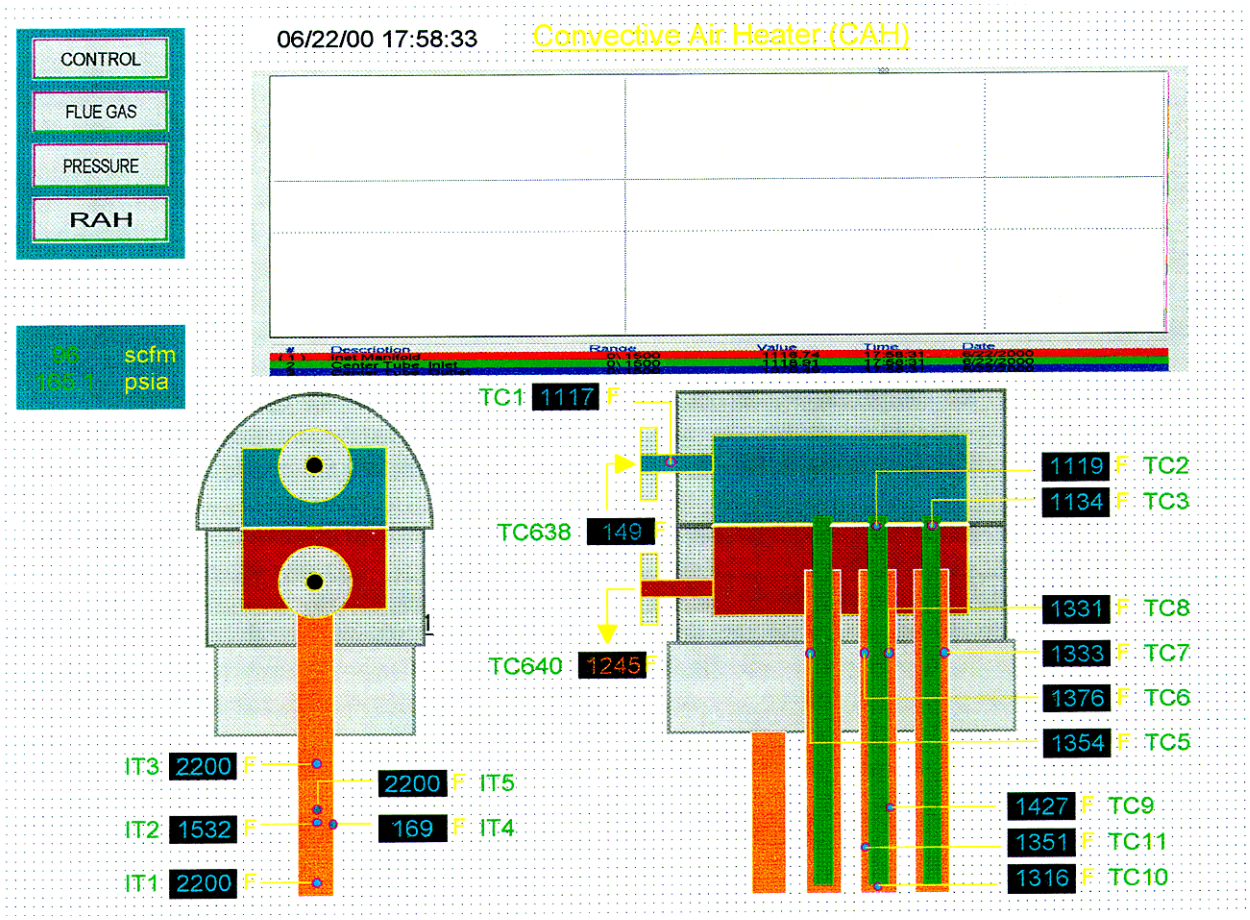
CONTROL
FLUE GAS
PRESSURE
RAH
06/22/00 17:58:33
Convective Air Heater (CAH)
scfm
psia
TC1 1117 F
1119 F TC2
1134 F TC3
TC638 149 F
1331 F TC8
1333 F TC7
TC640 1245 F
1376 F TC6
1354 F TC5
IT3 2200 F
2200 F IT5
IT2 1532 F
169 F IT4
IT1 2200 F
1427 F TC9
1351 F TC11
1316 F TC10

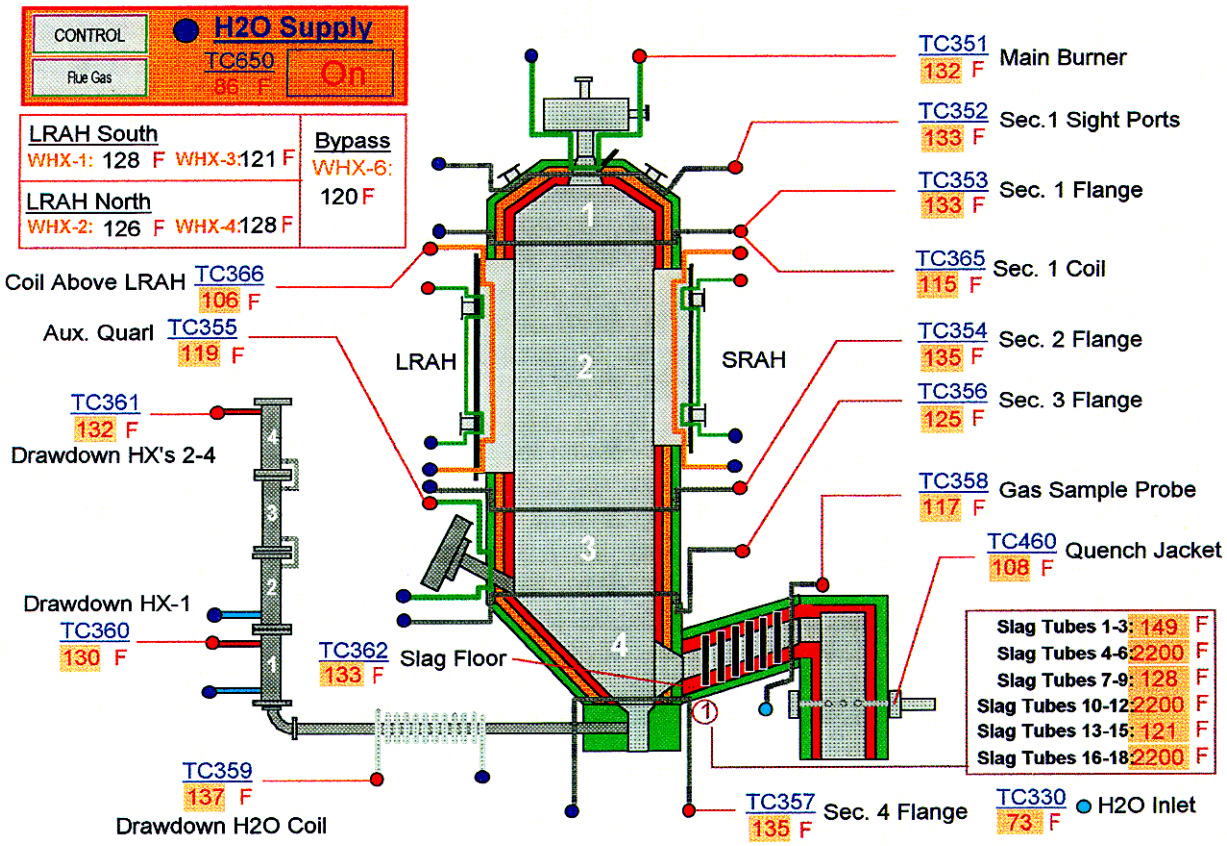
CONTROL
Flue Gas
H2O Supply
TC650
86 F
On
LRAH South
WHX-1: 128 F WHX-3:121 F
LRAH North
WHX-2: 126 F WHX-4:128 F
Bypass
WHX-6:
120 F
TC351
132 F
Main Burner
TC352
133 F
Sec.1 Sight Ports
TC353
133 F
Sec. 1 Flange
TC365
115 F
Sec. 1 Coil
TC354
135 F
Sec. 2 Flange
TC356
125 F
Sec. 3 Flange
TC358
117 F
Gas Sample Probe
TC460
108 F
Quench Jacket
Slag Tubes 1-3: 149 F
Slag Tubes 4-6:2200 F
Slag Tubes 7-9: 128 F
Slag Tubes 10-12:2200 F
Slag Tubes 13-15: 121 F
Slag Tubes 16-18:2200 F
TC366
106 F
Coil Above LRAH
TC355
119 F
Aux. Quarl
LRAH
SRAH
TC361
132 F
Drawdown HX's 2-4
Drawdown HX-1
TC360
130 F
TC362
133 F
Slag Floor
TC359
137 F
Drawdown H2O Coil
TC357
135 F
Sec. 4 Flange
TC330
73 F
H2O Inlet